
18 - 22 MARCH, SHARJAH - UAE
META'13
4th International Conference on Metamaterials,
Photonic Crystals, and Plasmonics

ISBN: 978-2-9545460-0-1
ISSN: 2429-1390

META'13 Sharjah - United Arab Emirates

The 4th International Conference on Metamaterials, Photonic Crystals and Plasmonics

Proceedings

March 18 – 22, 2013
Sharjah, United Arab Emirates

www.metaconferences.org

META'13 Sharjah - United Arab Emirates

The 4th International Conference on Metamaterials, Photonic Crystals and Plasmonics

Edited by

Said Zouhdi | Paris-Sud University, France
Hamid Al-Naimiy | University of Sharjah, UAE

Contents

META'13 ORGANIZATION 1
SPONSORS AND SUPPORTERS 2
META'13 VENUE 2
GUIDELINES FOR PRESENTERS 2
META'13 TECHNICAL PROGRAM 4

META'13 ORGANIZATION

META'13 General Chair

Said Zouhdi, Paris Sud University, France

META'13 General Co-Chair

Hamid Al-Naimiy, University of Sharjah, UAE

Organizing Committee

Hussein M. Elmehdi (Chair), UAE
Laurent Santandrea (Co-Chair), France

Nadjib Brahimi, UAE
Ihsan Shehadah, UAE
AbdulKadir Hamid, UAE
Muhammad Bawa'aneh, UAE
Omar Adwan, UAE
Rafea Haffa, UAE
Kifah Taqez, UAE
Khadijah Al Housani, UAE
Ghada Amer, UAE
Romain Corcolle, France
Tahsin Akalin, France
Mohamed Ahachad, Morocco
Mounia Ajdour, Morocco

International Advisory Committee

Hamid M. K. Al-Naimiy, UAE
Nader Engheta, USA
Mathias Fink, France
Sailing He, Sweden
Tatsuo Itoh, USA
Yuri Kivshar, Australia
Ricardo Marques, Spain
Graeme W. Milton, USA
Raj Mittra, USA
Susumu Noda, Japan
Masaya Notomi, Japan
Yahya Rahmat-Samii, USA
Vladimir Shalaev, USA
Ari Sihvola, Finland
Sergei Tretyakov, Finland
J. C. Vardaxoglou, UK
Alexey Vinogradov, Russia
Martin Wegener, Germany
Nikolay Zheludev, UK

Technical Program Committee

S. Maier (Chair), UK
J.Aizpurua, Spain
T. Akalin, France
A. Alu, USA
W. L. Barnes, UK
X. Begaud, France
S. Bozhevolnyi, Denmark
K. Busch, Germany
C. T. Chan, Hong Kong
A. Chipouline, Germany
J. Christensen, Spain
C. Craeye, Belgium
A. Dmitriev, Sweden
I. El-Kady, USA
D. Felbacq, France
W. Fritzsche, Germany
F. J. Garcia, Spain
H. Giessen, Germany
O. Hess, UK
R. Hillenbrand, Spain
D. Kim, Rep. Of Korea
J. Krenn, Austria
K. Leosson, Iceland
J. Li, Hong Kong
M. McCall, UK
L. M. Moreno, Spain
P. Nordlander, USA
T. Odom, USA
D. Pawlak, Poland
C.-W. Qiu, Singapore
M. Qiu, Sweden
D. R. Smith, USA
T. Tanaka, Japan
A. Urbas, USA
J. K. W. Yang, Singapore
A. V Zayats, UK
X. Zhang, USA
L. Zhou, China

Special Session Organizers

Christophe Craeye, Belgium
Ozlem Ozgun, Turkey
Tahsin Akalin, France
Samel Arslanagic, Denmark
Radu Malureanu, Denmark
Dorota A. Pawlak, Poland
Wounjhang Park, USA
Mady Elbahri, Germany
Carsten Rockstuhl, Germany
Mohamed Farhat, Saudi Arabia
Pai-Yen Chen, USA
Fernando Moreno, Spain
Manuel Nieto-Vesperinas, Spain
Mohamed Swillam, Egypt
Henri Benisty, France
Anatole Lupu, France
Zhengtong Liu, Singapore
Jiaming Hao, France
Beatrice Dagens, France
Johan Christensen, Denmark
Vicent Romero Garcia, Spain
Nayla El-Kork, UAE

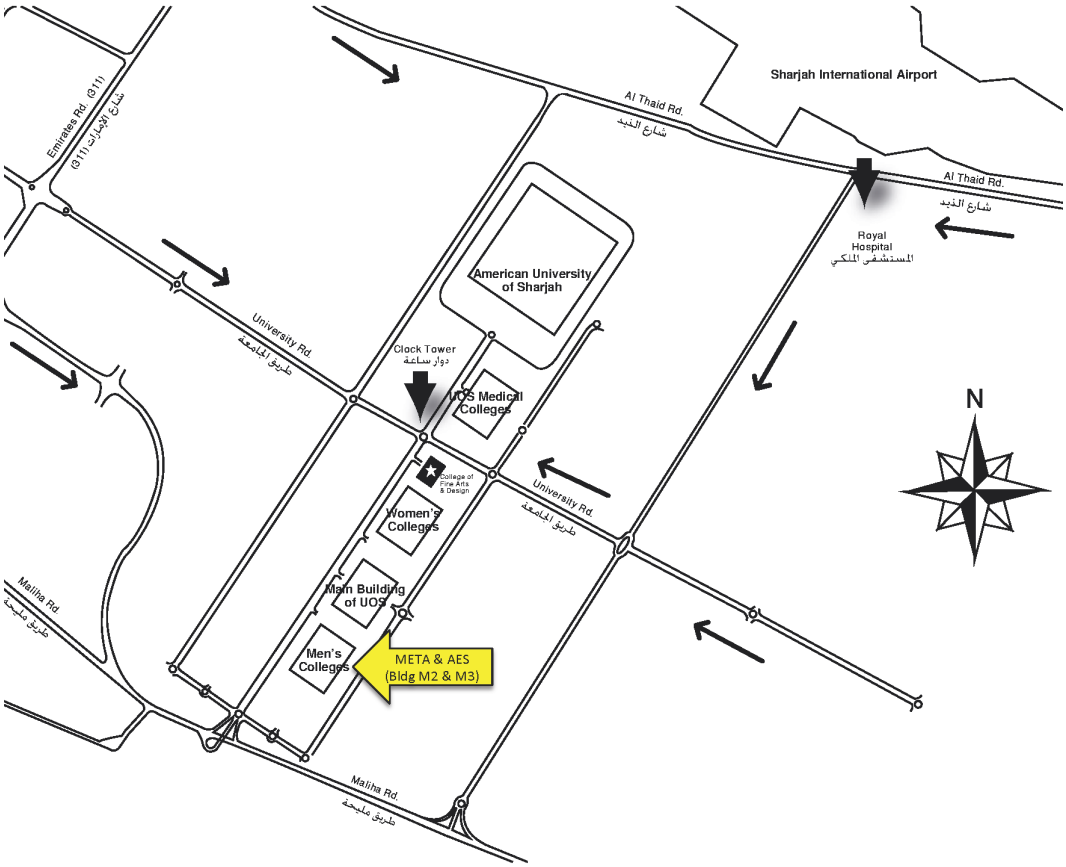
SPONSORS AND SUPPORTERS

We wish to thank the following organizations for their contribution to the success of this conference :

University of Sharjah, UAE
LGEP-SUPELEC, France
Paris-Sud University, France
Institut Français, UAE
Office of Naval Research Global, UK
IOP Publishing, UK
EPL, UK
CST-ME , Egypt
IEEE-APS, USA
URSI, Belgium

META'13 VENUE

META'13 will be held on March 18-22, 2013, at the University of Sharjah, Sharjah, United Arab Emirates.



GUIDELINES FOR PRESENTERS

Oral Presentations

Each session room is equipped with a stationary computer connected to a LCD projector. Presenters must load their presentation files in advance onto the session computer. Technician personnel will be available to assist you.

Scheduled time slots for presentation are 20 mn for regular and invited prensentations, 45 mn for plenary talks, and 30 mn for keynote talks, including questions and discussions. Presenters are required to report to their session

room and to their session Chair at least 15 minutes prior to the start of their session.

The session chair must be present in the session room at least 15 minutes before the start of the session and must strictly observe the starting time and time limit of each paper.

Poster Presentations

Presenters are requested to stand by their posters during their session. One panel will be available for each poster. Pins or thumbtacks are provided to mount your posters on the board. All presenters are required to mount their papers one hour before the session and remove them at the end of their sessions.

General Papers

Giant magnetoimpedance in thin amorphous and nanocrystalline microwires (pp. 14)
Arcady Zhukov, Ahmed Talaat, Mihail Ipatov, Margarita Churyukanova, Sergei Kaloshkin, Valentina Zhukova,

Multi-Band, highly absorbing, microwave metamaterial Structures (pp. 20)
Theofano Kollatou, Alexandros Dimitriadis, Stylianos Assimonis, Nikolaos Kantartzis, Christos Antonopoulos,

Effect of concentration of Cd on structural and optical properties of ZnO:Cd thin films prepared by sol-gel method (pp. 26)
Ausama I. Khudiara, M. Zulfequar, Zahid H. Khan,

Metamaterials and negative index materials

Tuniable microwave filter using split ring resonator (pp. 30)
Mondher Labidi, Oussama Tabbebi, Fethi Choubani,

Unidirectional amplification and shaping of optical pulses by three-wave mixing with negative phonons (pp. 34)
Alexander K. Popov, Mikhail I. Shalaev, Sergey A. Myslivets, Vitaly V. Slabko,

This work investigates the quality and quantity of a cylindrical cloak made of PMMA material filled with gold, silver, and mixed nano-particles. The effective material parameters together with their transformed permittivity and permeability are calculated by a home-made computational code. The form of the three different cloaks will be compared pictorially. (pp. 40)
Hamid Nadgaran, Mohammad Mehdi Sadeghi, N. Niakan,

Coupled equation of electromagnetic wave in a nonlinear metamaterial waveguide (pp. 45)
Mina Azari, Mohsen Hatami,

Microwave propagation at the interface between nonlinear MTMs and anisotropic materials (pp. 50)
Hala Jarallah El-Khozondar, Rifa Jarallah El-Khozondar, Said Zouhdi,

Finite difference time-domain modelling of metamaterials: GPU implementation of cylindrical cloak (pp. 54)
Attique Dawood,

Graphene metamaterials

The spontaneous down-conversion of laser light focused on metal-dielectric interface is considered. In this case the working second-order susceptibility is enhanced due to excitation of plasmon-polaritons. It is found that strong enhancement of the process takes place for the laser intensity close to the critical intensity. The further increasing of intensity will cause weakening of the process. The crossover of the efficiency takes place if the amplitude of oscillations of the eikonal coincides with the wavelength of excitation. (pp. 63)
Vladimir Hizhnyakov, Helle Kaasik, Imbi Tehver,

Acoustic metamaterials

On the feasibility of a 2D acoustic cloak using layers of elastic materials (pp. 70)
Cecile Dutrion, Frank Simon,

Plasmonics and nanophotonics

Enhanced emission of waveguide thermal emitter by incorporating metal nanoparticles in periodic hole arrays (pp. 79)
Pei-Wen Wu, Hung-Hsin Cheng, Hung-Hsin Chen, Si-Chen Lee,

Optical property of double-layered metal films with periodic structure (pp. 83)
Mohamed Boutria, Rachid Oussaid,

Four Vertical Prolate Spheroids with a Center Gap as Nanoantenna (pp. 87)
Mahdieh Khosravi, Ramezan Ali Sadeghzadeh, Mohammad Sadegh Abrishamian,

Coupled nano-plasmons (pp. 90)
Marian Apostol, Stelian Ilie, Aurel Petrut, Marcel Savu, Stefan Toba,

Study on PL enhancement of GaAs/InGaAs quantum well emission by gold nanoparticle arrays (pp. 96)
Hongwei Gao, Jinghua Teng, Soo Jin Chua, Ning Xiang,

Deep subwavelength double metal disk cavity and applications (pp. 100)
Soon-Hong Kwon,

Strong emission from nano-iron using laser induced breakdown spectroscopy technique (pp. 106)
Fareed Faris Rashid, Ashraf El-sherbini El-sherbini, Abdulsalam Al-Muhammady,

Parameter dependency of dipole nanoantenna in infrared range (pp. 112)
D. Bala Sekhar, Avanish Bhadauria, William R. Taube,

Metamaterial-inspired bandpass filter for the terahertz goubau line (pp. 117)
Ali Karami Horestani, Withawat Withayachumnankul, Christophe Fumeaux, Derek Abbott, Tahsin Akalin,

Silicon nanowire photodetector enhanced by a bow-tie antenna (pp. 119)
Gordana Klaric Felic, Feras Al-Dirini, Faruque M. Hossain, Thanh Chong Nguyen, E. Skafidas,

Wide band silicon mirror based grating coupler for silicon integrated photonics (pp. 122)
Md Asaduzzaman, Masuduzzaman Bakaul, Stan Skafidas, Md Rezwanul Haque Khandokar,

Atomistic approach for simulating plasmons in nanostructures (pp. 127)
Arto Sakko, Tuomas Rossi, Jussi Enkovaara, Risto Nieminen,

Optical forces induced by metal nanoparticle clusters (pp. 132)
Jordi Sancho-Parramon, Salvador Bosch,

Dielectric sensing based on energy tunneling in wire-loaded microstrip cavities (pp. 137)
Abdullah Nauroze, Omar Siddiqui, Rashad Ramzan, Omar Ramahi,

Hybrid and quantum materials

The influence of debonding on the mechanical properties of hybrid nanocomposites (pp. 142)
Waleed K. Ahmed,

Exact numeric resolution of the system globally non linear Schrodinger-Poisson in order to study the influence of different technological parameters on the performance of AlGaAs/GaAs heterojunction (pp. 148)

Boubeb Ilhem, M. Marir Benabbas, A. Houam, F. Kerrour,

Photonic crystals

Soft and Hard regimes of Gap Solitons generation in planar Bragg grating (pp. 157)
Alexander Sadovnikov, Andrew Rozhnev, Nikita Riskin,

Photonic crystal fiber propagation characteristics (pp. 163)
R. H. Thaher,

Construction of dirac points using triangular supercrystals (pp. 170)
Mohammad Hasan Aram, Roya Mohajeri, Sina Khorasani,

Propagation effects in a polymer-based photonic liquid crystal fiber (pp. 176)
Tomasz R. Wolinski, Marzena Tefelska, Karolina Milenko, Katarzyna Rutkowska, Andrzej W. Domanski, Slawomir Ertman, Kamil Orzechowski, Kasia Rutkowska, Marek Sierakowski, Edward Nowinowski-Kruszelnicki,

Influence of Ag doping on structural and optical properties of ZnO thin films synthesized by sol-gel technique (pp. 182)
Azeddine Chelouche, Djamel Djouadi, Hamid Merzouk, Ali Aksas,

Inverse design and topology optimization of novel photonic crystal broadband passive devices for photonic integrated circuits (pp. 187)
Imanol Andonegui, Isidro Calvo, Angel Javier Garcia-Adeva,

Eigenmodes Analysis in 2-D Lorentz-Type Frequency-Dependent Photonic Crystals (pp. 193)
Amin Gul Hanif, Toru Uno, Takuji Arima,

Plasmon-enhanced photovoltaics, photocatalysis, and solar fuels

Enhanced light absorption in thin-film tandem solar cells using a Bottom Metallic Nanograting (pp. 200)
Xuanru Zhang, Wei Wang, Zhiang Li, Honglei Cai, Jijun He, Randy Knize, Bin Xiang, Yalin Lu,

VO2-based multilayers with enhanced luminous transmittance and switching properties (pp. 205)
Yuan Zhao, Xuanru Zhang, Randy Knize, Yalin Lu,

Broadband spectroscopy of nanoporous-gold promoter (pp. 210)
Satoko Kuwano Nakatani, Youn-Hee Han, Toshiharu Takahashi, Teruyoshi Awano,

Design consideration for plasmonic solar cells based on Ag nanoparticles (pp. 216)
Razan R. Najm, Mousa I. Hussein, Ahmed Ayesh,

Transformational electromagnetics

Fundamentals of designing cylindrical high order transformation optics invisibility cloaks using silver-silica metamaterials (pp. 220)
Kareem Salah Elassy,

Frequency selective structures and high impedance surfaces

Analytical model of a self-complementary connected antenna array on high impedance surface (pp. 228)
Xavier Begaud, Fabrice Linot, Michel Soiron, Christian Renard,

Design and measurement of a thin and light absorbing material for space applications (pp. 234)
Yenny Pinto, Julien Sarrazin, Anne Claire Lepage , Xavier Begaud, Nicolas Capet,

Conception of compact patch antenna loaded with CRLH metamaterial (pp. 239)
Oussama Tabbabi, Mondher Labidi, Fethi Choubani, Jacques David,

Analytical and numerical modelling of complex materials and structures

Microwave scattering diagrams of three-layered SiC-metamaterial/ gyrotropic ferrite-SiC cylinders (pp. 243)
J. Bucinskas, L. Nickelson, R. Martavicius,

The wave functions of the crystal lattice energy bands (pp. 249)
Klara Amanovna Iskakova, Rif Akhmaltdinov, Aysara Amanova,

Theory and simulation of cavity quantum electro-dynamics in multi-partite quantum complex systems (pp. 252)
Moslem Alidoosty Shahraki, Sina Khorasani, Mohammad Hasan Aram,

The investigation of the photonic waveguide structure made of silicon carbide by means of the method of the singular integral equations (pp. 258)
T. Gric, L. Nickelson, R. Martavicius,

Electrodynamical analysis of metamaterial waveguides coated with silicon carbides (pp. 263)
L. Nickelson, A. Bubnelis, S. Asmontas,

Technologies and applications

Simulation and design of a bandpass filter on metasubstrates (pp. 269)
Valdemir Praxedes Silva Neto, Cristhianne Linhares Vasconcelos, Maria Rosa Medeiros Lins Albuquerque, Adaildo Gomes d'Assuncao,

Metamaterial-Inspired Displacement Sensor with High Dynamic Range (pp. 274)
Zahra Shaterian, Ali Karami Horestani, Christophe Fumeaux,

Planar metamaterial-based MIMO Antennas (pp. 277)
Dimitra Ketzaki, Dimitrios Ntaikos, Ioannis Rekanos, Traianos Yioultsis,

Nano-aperture design to enhance optical transmission using the shape optimization procedure (pp. 280)
Heeseung Lim, Namjoon Heo, Jae Seok Choi, Jeonghoon Yoo,

Recent progress on numerical methods for metamaterial analysis

On the use of a hierarchical multi-level building block basis function scheme in periodic plasmonic structures (pp. 286)
Xuezhi Zheng, Ventsislav K. Valev, Vladimir Volskiy, Guy A. E. Vandenbosch, Victor V. Moshchalkov,

Selective mode suppression in microstrip differential lines by means of electric-LC (ELC) and magnetic-LC (MLC) resonators (pp. 291)

Jordi Naqui, Miguel Duran-Sindreu, Ferran Martin,

Multifrequency and low profile metamaterial-inspired antennas (pp. 297)
Saber Dakhli, Hatem Rmili, Jeans-Marie Floc'h, Fethi Choubani, Kouroch Mahdjoubi,

A Robustness analysis of the numerical computation of green's dyadics in bianisotropic media (pp. 302)
Ignace Bogaert,

Multifrequency and low profile metamaterial-inspired antennas (pp. 306)
Saber Dakhli, Hatem Rmili, Jean-Marie Floc'h, Fethi Choubani, Kouroch Mahdjoubi,

Antennas on quasi synthetic media (pp. 311)
Chinwe C. Njoku, William G. Whittow, J. C. Vardaxoglou,

Plasmonic antennas, lenses and metasurfaces

Long-range interaction of localized surface plasmons in periodic and random patterns of Au nano-particles (pp. 318)
Yoshiaki Nishijima, Lorenzo Rosa, Saulius Juodkazis ,

Metamateria patch antenna radiation pattern Agility (pp. 324)
S. M. Chaker, M. Bouzouad,

Active Terahertz Metamaterials

Terahertz band gaps based on TEM mode by photonic crystals inside parallel-plate waveguide (pp. 330)
Eui Su Lee, Tae-In Jeon,

A bottom-up approach towards metamaterials and plasmonics

Plasmonic collective coherent radiance and collective resonance state at the loss compensation condition near metal nanoparticle (pp. 335)
Vitaliy Pustovit, Arkadi Chipouline, Augustine Urbas,

Plasmonic nanocomposites

Enhancement of GaAs/InGaAs quantum Well emission by disordered gold nanoparticle arrays (pp. 340)
Hongwei Gao, Jinghua Teng, Soo Jin Chua, Ning Xiang,

Tunable metamaterials and plasmonics devices

Plasmonic waveplate: Incident polarization modulation (pp. 345)
Shan Huang, Jie Li, Feng Lin, Zheyu Fang, Xing Zhu,

New advances in optically magnetic materials for nanophotonics

Scattering forces on magneto-dielectric particles and the electromagnetic momentum density (pp. 353)
Manuel I. Marques, Juan J. Saenz,

Emerging technology in plasmonics

Optimizing silicon-plasmonic waveguides for x(3) nonlinear applications (pp. 359)
Alexandros Pitilakis, Odysseas Tsilipakos, Emmanouil E. Kriezis,

Rigorous characterization of surface plasmonic waveguides and guided-wave devices for THz systems (pp. 364)
B. M. A. Rahman, C. Themistos, H. Tanvir, A. Quadir, C. Markides,

Singularities & broken symmetries of systems with gain and loss structures

Soliton scattering in the chain of optical waveguides including PT - symmetric defect (pp. 370)
Sergey Suchkov, Sergey Dmitriev, Andrey Sukhorukov, Igor V. Barashenkov, Elina R. Andriyanova, Karina M. Badgetdinova, Yuri Kivshar,

PT-Symmetric nonlinear metamaterials and zero-dimensional systems (pp. 376)
Giorgos P. Tsironis, Nikos Lazarides,

Plasmonic Biosensors

Metal island film based structures for sensing using spectrophotometry and ellipsometry (pp. 387)
Vesna Janicki, Ordi Sancho-Parramon, Salvador Bosch, Hrvoje Zorc,

Nanoparticles and nanosystems

Assemblies from metallic and semiconducting nanocrystals (pp. 392)
Ingolf Kahle, Stefan Krause, Cornelius Krasselt, Alexander Jakob, Alexander Oehlke, Colin Georgi, Steffen Schulze, Heinrich Lang, Michael Hietschold, Stefan Spange,

The study of magnetic properties of Ge nanoparticles (pp. 407)
Yung Liou,

General Papers

Giant magnetoimpedance in thin amorphous and nanocrystalline microwires

Arcady Zhukov[1,2,*], Mihail Ipatov[1], Ahmed Talaat[1], Margarita Churyukanova[3], Sergei Kaloshkin[3] and Valentina Zhukova[1]

[1]Dpto. de Fís. Mater., UPV/EHU San Sebastián 20018, Spain
[2] IKERBASQUE, Basque Foundation for Science, 48011 Bilbao, Spain
[3]National University of Science and Technology «MISIS», Moscow, 119049, Russia
*corresponding author, E-mail: arkadi.joukov@ehu.es

Abstract

We present the results on Giant magneto-impedance effect (GMI) effect in amorphous and nanocrystalline microwires at frequencies till 4 GHz paying special attention to tailoring the frequency and magnetic field dependence of GMI effect. Correlation between magnetoelastic anisotropy and magnetic field dependences of diagonal and off-diagonal impedance components are observed

1. Introduction

Ferromagnetic thin wires (with typical diameters from 5 till 120 μm) gained considerable interest owing to their good soft magnetic properties and giant magneto-impedance, GMI, effect [1, 2]. Industrial applications required miniaturization of the magnetic sensors. Therefore soft magnetic wires with reduced dimensionality recently gained much attention [1, 2]. GMI effect, consisting of large sensitivity of the impedance of magnetically soft conductor on applied magnetic field, attracted great attention [2, 3] due to excellent magnetic field sensitivity. The shape of magnetic field dependence of the GMI effect (usually presented as magnetic field dependence of magnetoimpedance ratio, $\Delta Z/Z$) is determined by the magnetic anisotropy [1-3] Magnetic anisotropy of amorphous and nanocrystalline microwires is determined mostly by the magnetoelastic term and can be tailored by the metallic nucleus composition and by the thermal treatment [1,4, 5].

Latest development of industrial applications required miniaturization of the magnetic sensors. Therefore reduction of diameters of magnetically soft wires is one of the prioritary tasks in the field of applied magnetism. Consequently families of soft magnetic wires with reduced dimensionality and outstanding magnetic characteristics, such as melt extracted wires (typically with diameters of 40-50 μm) [6, 7] and glass-coated microwires with even thinner diameters (between 1-40 μm) [4, 5] recently gained much attention. The advantage of the Taylor-Ulitovski method allowing the fabrication of glass-coated metallic microwires consists of controllable fabrication of long (up to few km long continuous microwire) and homogeneous thin composite wires [1,4].

Recently, certain progress on achievement of excellent soft magnetic properties and high GMI effect of glass coated microwires has been reported at the laboratory level [1,4]. This gives rise to development of industrial applications for low magnetic field detection in various industrial sectors [8]. Cylindrical shape and high circumferential permeability observed in amorphous wires is quite suitable for achievement of high GMI effect [4, 9]. It is worth mentioning, that the cylindrical shape is quite suitable for achieving of high GMI effect [1-9].

As mentioned above, the magnetic field dependence of the GMI ratio is intrinsically related with the magnetic anisotropy and peculiar surface domain structure of amorphous wires [1-4]. Magnetic anisotropy of amorphous microwires in the absence of magnetocrystalline anisotropy is determined mostly by the magnetoelastic term [5, 10, 11]. Therefore the magnetic anisotropy can be tailored by thermal treatment [4, 13, 14]. On the other hand at certain conditions of thermal treatment and for certain composition amorphous microwires can exhibit nanocrystalline structure after partial crystallization [15, 16]. In some cases, nanocrystallization allows achieving good magnetic softness and enhanced GMI effect in ferromagnetic microwires [15-17]. Such soft magnetic character is though to be originated because the magnetocrystalline anisotropy vanishes and the very small magnetostriction value when the grain size approaches 10 nm [15-18]. Like for conventional nanocrystalline Finmet-type materials, average anisotropy for randomly oriented α-Fe(Si) grains is negligibly small when the average grain is about 10-20 nm. Low values of the magnetostriction are essential to avoid magnetoelastic anisotropies arising from internal or external mechanical stresses.

As mentioned above in the case of amorphous glass-coated microwires the magnetic anisotropy in the absence of magnetocrystalline anisotropy has mostly the magnetoelastic origin, i.e. determined by the metallic nucleus composition and by the internal stresses [5, 10, 11]. The strength of internal stresses is mostly determined by the ratio, ρ, between the metallic nucleus diameter, d, and total

composite wire diameter, D, (ρ=d/D). Such stresses arising during simultaneous solidification of the composite wires originate from the difference in thermal expansion coefficients of metallic alloy and glass coating [10-11].

The magnetoelastic energy, K_{me}, is given by

$$K_{me} = 3/2\ \lambda_s \sigma, \qquad (1)$$

where $\sigma = \sigma_i + \sigma_a$ – total stresses, σ_i –are the internal stresses, σ_a – applied stresses and λ_s - magnetostriction constant [19]. As regarding the magnetostriction constant, λ_s, in system $(Co_xFe_{1-x})_{75}Si_{15}B_{10}$ λ_s changes from $-5x10^{-6}$ at x= 1, to $\lambda_s \approx 35\ x10^{-6}$ at x≈0.2, exhibiting nearly-zero values at Co/Fe ration of about 70/5 [19, 20].

Consequently, the magnetoelastic anisotropy of amorphous microwires can be tailored either through the metallic nucleus composition and by changing the samples geometry (ρ-ratio) or by thermal treatment [1,4].

Consequently in this paper we studied the GMI effect (GMI ratio, ΔZ/Z,) and hysteretic magnetic properties in ultra-thin amorphous and nanocrystalline glass-coated microwires with vanishing magnetostriction constant and report results on correlation of GMI effect with magnetic anisotropy and possibilities to tailor magnetic field dependence of GMI effect.

2. Experimental details and discussion

We have measured dependences of the diagonal Z_{zz} and GMI ratio on external axial magnetic field H in amorphous as-prepared and annealed microwires, as described elsewhere [4, 19].

The magneto impedance ratio, *ΔZ/Z,* is defined as usually accepted [1-4]:

$$\Delta Z/Z = [Z\,(H) - Z\,(\mathrm{Hmax})] / Z\,(\mathrm{Hmax}), \qquad (2)$$

where H_{max} is the axial *DC*-field with maximum value up to few kA/m.

The microwires were placed in a specially designed microstrip cell. One wire end was connected to the inner conductor of a coaxial line through a matched microstrip line while the other was connected to the ground plane [21]. The wire impedance was measured using vector network analyzer. The frequency range for the diagonal impedance component has been measured till 4 GHz.

Hysteresis loops have been measured by the induction method, as described elsewhere [4].

We studied Finemet-type $Fe_{70.8}Cu_1Nb_{3.1}Si_{14.5}B_{10.6}$, $Fe_{70.8}Cu_1Nb_{3.1}Si_{16}B_{9.1}$, $Fe_{71.8}Cu_1Nb_{3.1}Si_{15}B_{9.1}$ and $Fe_{73.8}Cu_1Nb_{3.1}Si_{13}B_{9.1}$; amorphous $Co_{69.12}Fe_{4.01}Ni_{1.46}B_{11.63}Si_{10.83}Mo_{1.46}C_{1.49}$, $Co_{66.87}Fe_{3.66}C_{0.98}Si_{11.47}B_{13.36}Mo_{1.52}$ and $Co_{69.4}Fe_{4.3}Ni_{1.5}B_{11.7}Si_{11.9}Mo_{1.2}$ microwires with different diameters of metallic nucleus, d, total diameters, D, and consequently different ρ - ratios (ρ=d/D) fabricated by the Taylor-Ulitovsky method [4]. Finemet-type samples have been annealed at conventional furnace. X-ray diffraction (XRD) measurements were carried out by means of a D8-Advance (BRUKER) diffractometer CuKα (λ = 1.54 Å) radiation was used in all the patterns.

3. Results and discussion

3.1. Magnetic properties and GMI effect of amorphous microwires

As mentioned above, value of GMI ration and magnetic field dependences of GMI effect are intrinsically related with magnetic softness of magnetic materials, which is determined by the magnetic anisotropy. In the case of amorphous materials there are a few sources of magnetic anisotropy, such as surface defects, clusters, magnetoelastic anisotropy related with internal and applied stresses [4, 10,11].

Effect of ρ–ratio (which affects the internal stresses) on hysteretic properties of $Co_{69.12}Fe_{4.01}Ni_{1.46}B_{11.63}Si_{10.83}Mo_{1.46}C_{1.49}$ amorphous as-prepared microwires with similar metallic nucleus diameter, d, ranging between 9.8 and d=12.4 μm and with ρ–ratios ranging between 0.53 and 0.86 is illustrated in Fig.1. All studied samples present similar values of coercivities (about 3 A/m), but magnetic anisotropy field and consequently magnetic permeability of these samples are rather different: microwires with thicker glass coating and consequently with stronger internal stresses present higher magnetic anisotropy field and lower magnetic permeability (Fig.1). It is worth mentioning, that samples with rather different diameters of metallic nucleus (11 and 12.4 μm) and glass coating thickness, but with similar ρ - ratio present quite similar hysteresis loops with

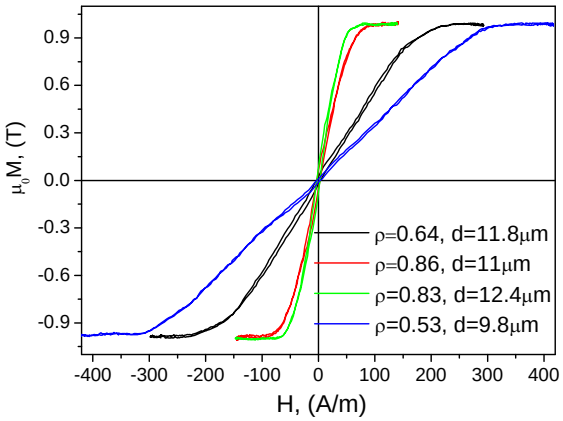


Figure 1: Effect of microwires geometry on hysteresis loops of $Co_{69.12}Fe_{4.01}Ni_{1.46}B_{11.63}Si_{10.83}Mo_{1.46}C_{1.49}$ microwires

similar magnetic anisotropy field and consequently similar magnetic permeability (Fig.1). Similar dependences have been observed in other Co-rich microwires [4, 22]

Accordingly magnetic field dependences of GMI effect measured in $Co_{69.4}Fe_{4.3}Ni_{1.5}B_{11.7}Si_{11.9}Mo_{1.2}$ microwires of the same composition and different geometry are also different (see Figs.2). Here we present dependences of GMI ratio, ΔZ/Z on magnetic field, H, measured for microwires with metallic nucleus diameters 6.0 and 21.0 μm and with rather different ρ-ratios (0.53 and 0.92 respectively). General features of measured ΔZ/Z dependences on magnetic field,

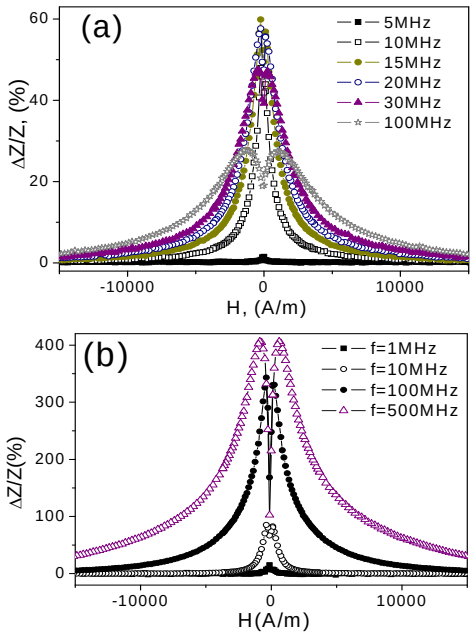


Figure 2: ΔZ/Z(H) dependences of $Co_{69.4}Fe_{4.3}Ni_{1.5}B_{11.7}Si_{11.9}Mo_{1.2}$ microwires with different ρ–ratios: ρ=0.59; d=6; D=10.2μm (a) and ρ=0.92; d=21 μm; D=22.8 μm (b).

H, is that the magnetic field of maximum shifts to the higher field region increasing the frequency, *f*.

From Fig. 2 we can also conclude, that ΔZ/Z and its frequency dependence are strongly affected by the magnetoelastic anisotropy determined by the ratio ρ. Much higher ΔZ/Z ratio has been obtained for the simple with thicker metallic nucleus diameter. On the other hand significant GMI effect has been obtained even for thin microwires (with metallic nucleus diameter about 6 μm). Frequency dependence of maximum ΔZ/Z ratio, $\Delta Z/Z_{max}$ present maximum for both samples (see Fig.3), but both $\Delta Z/Z_{max}$ and frequency of maximum are rather different. For both samples there is an optimal frequency where the $\Delta Z/Z_{max}$ exhibit maximum value.

We measured GMI ratio, ΔZ/Z, at different

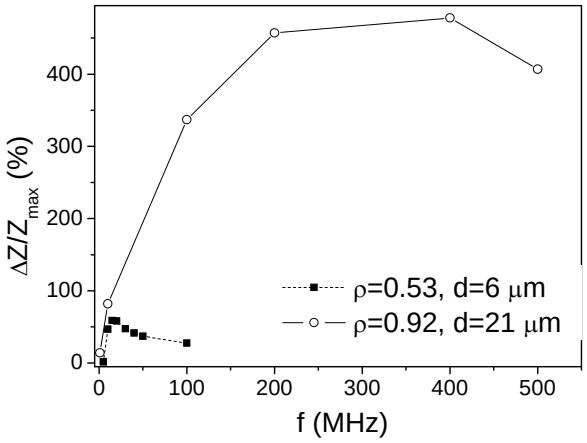


Figure 3: Frequency dependence of $Co_{69.4}Fe_{4.3}Ni_{1.5}B_{11.7}Si_{11.9}Mo_{1.2}$ microwires with different metallic nucleus diameters

frequencies in considerable amount of $Co_{66.87}Fe_{3.66}C_{0.98}Si_{11.47}B_{13.36}Mo_{1.52}$ microwires with metallic nucleus diameters between 8.5 and 9 μm and presented obtained results in the similar way as in Fig.3, i.e. $\Delta Z/Z_{max}$ (f). For these samples the optimum frequency for achievement of highest GMI ratio is between 100 and 200 MHz (see Fig.4). Additionally all the samples exhibited similar $\Delta Z/Z_{max}$ (f) dependences. The origin of the maximum on $\Delta Z/Z_{max}$(f) dependences might be determined by the magnetic anisotropy field. Therefore one can expect similar $\Delta Z/Z_{max}$(f) dependences for microwires with similar ρ-ratios.

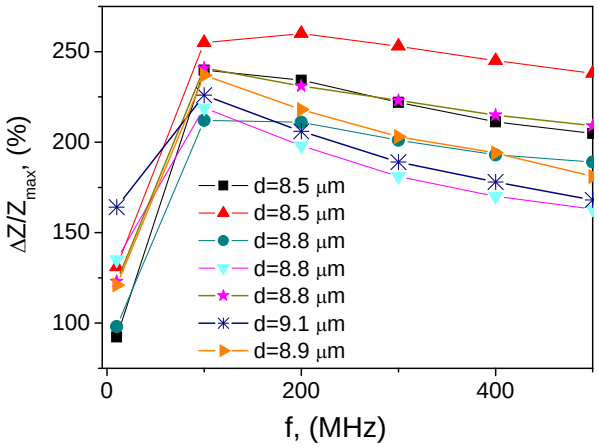


Figure 4: Frequency dependence of $Co_{66.87}Fe_{3.66}C_{0.98}Si_{11.47}B_{13.36}Mo_{1.52}$ microwires with similar metallic nucleus diameters and similar ρ-ratios.

3.2. Magnetic properties and GMI effect in nanocrystalline microwires

All as-prepared and even annealed below first crystallization process Finemet-type microwires present squired hysteresis loops similar to Fe-rich amorphous microwires (Fig.5). Like in other amorphous Fe-rich microwires, coercivity, H_c, exhibit remarkable dependence on ρ-ratio (Figs. 5, 6).

Generally we observed that annealing results in decrease of coercivity, H_c, and hysteresis loops present rectangular shape at least until relatively high annealing temperature, T_{ann}.

Annealing temperature dependence of coercivity of $Fe_{71.8}Cu_1Nb_{3.1}Si_{15}B_{9.1}$ microwires shown in Fig.7 present considerable magnetic softening at T_{ann} between 800 and 900 K as previously observed in other Finemet-type materials and Finemet-type microwires [15, 23]. Generally GMI effect in as-prepared Finemet-type microwires (like for all amorphous Fe-rich microwires) is rather small. Some exceptions are partially crystalline microwires, where some amount of nano-sized crystals has been observed in as-prepared state.

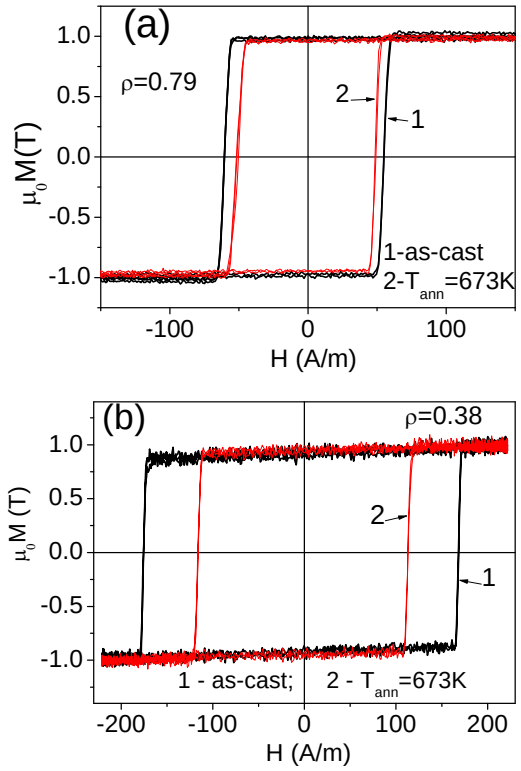


Figure5: Hysteresis loops of as-prepared and annealed at 673 K $Fe_{70.8}Cu_1Nb_{3.1}Si_{14.5}B_{10.6}$ microwires with different ρ=d/D ratios: a) ρ=0.79, b) ρ=0.38.

Particularly in as-prepared $Fe_{73.8}Cu_1Nb_{3.1}Si_{13}B_{9.1}$ microwire we observed existence of α-Fe nanocrystallites with average grain size about 12 nm (Fig.8a). The grain size has been estimated the average grain size can be estimated from the width of the crystalline peak using the Debye–Scherrer equation. For comparison X-ray diffraction pattern of completely amorphous as-prepared $Fe_{70.8}Cu_1Nb_{3.1}Si_{14.5}B_{10.6}$ microwire is shown in Fgi.8b. In as-prepared $Fe_{73.8}Cu_1Nb_{3.1}Si_{13}B_{9.1}$ microwire we observed GMI effect ($\Delta Z/Z \approx 10\%$ at 600 MHz, see Fig. 9). After annealing we observed increasing of the GMI effect (Figs.9a and 9b).

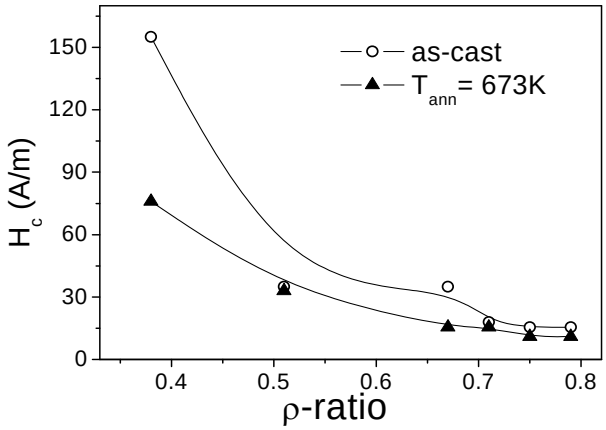


Figure 6: Coercivity dependence on ρ-ratio for as-prepared and annealed at 673 K $Fe_{70.8}Cu_1Nb_{3.1}Si_{14.5}B_{10.6}$microwires.

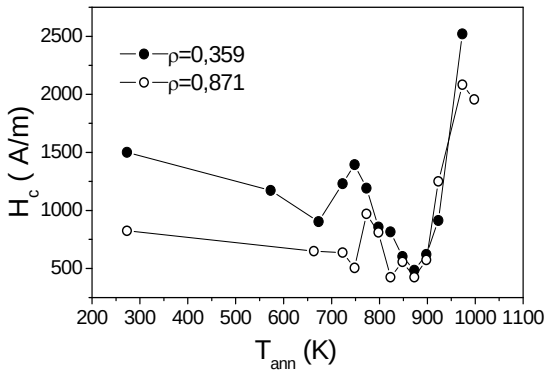


Figure 7: Annealing temperature dependence of coectivity of $Fe_{71.8}Cu_1Nb_{3.1}Si_{15}B_{9.1}$ microwires with different ρ-ratios.

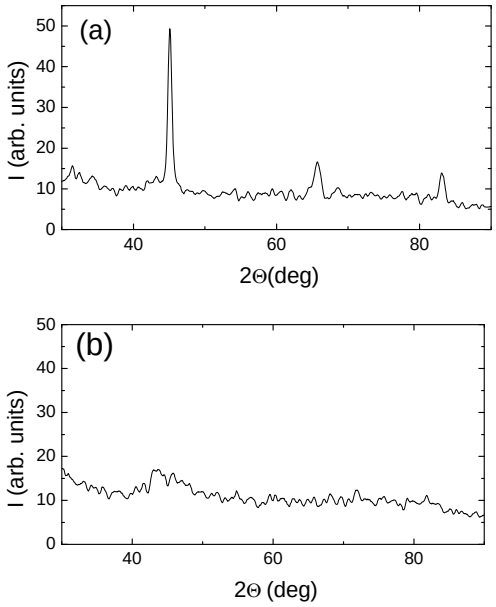


Figure 8: X-ray diffraction patterns of as-prepared $Fe_{73.8}Cu_1Nb_{3.1}Si_{13}B_{9.1}$ (a) and $Fe_{70.8}Cu_1Nb_{3.1}Si_{14.5}B_{10.6}$ (b) microwires.

For comparison we present GMI results for as-prepared and annealed at 673 K $Fe_{70.8}Cu_1Nb_{3.1}Si_{14.5}B_{10.6}$ microwires (d=8.2 μm, D=16.6 μm, ρ = 0.49) with amorphous structure (Fig.10).

As-prepared $Fe_{70.8}Cu_1Nb_{3.1}Si_{14.5}B_{10.6}$ amorphous sample exhibit much lower maximum $\Delta Z/Z$ values, $\Delta Z/Z_{max}$(3% at 600 MHz, see Fig. 10a). Like in the case of $Fe_{70.8}Cu_1Nb_{3.1}Si_{14.5}B_{10.6}$ nanocrystalline microwires we observed improvement of $\Delta Z/Z_{max}$ after annealing at 673K (Fig.10b)

Higher GMI effect in as-prepared $Fe_{73.8}Cu_1Nb_{3.1}Si_{13}B_{9.1}$ microwire must be related to it nanocrystalline structure. In fact previously partially crystalline structure consisting of nano-sized grains embedded in amorphous matrix have been already reported [15, 24].

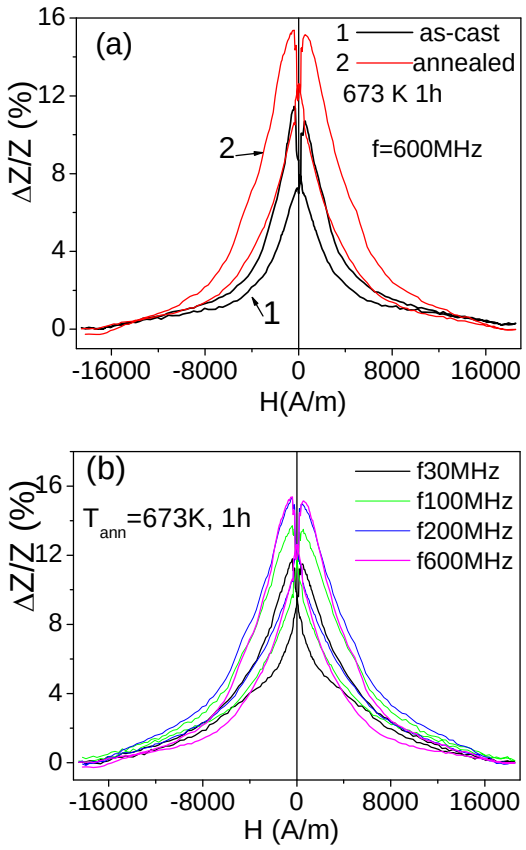


Figure 9: ΔZ/Z(H) dependences of $Fe_{73.8}Cu_1Nb_{3.1}Si_{13}B_{9.1}$ microwires (d=20.3μm, ρ=0.71) measured in as-prepared and annealed at 673 K samples at 600 MHz (a) and in annealed at 673 K $Fe_{73.8}Cu_1Nb_{3.1}Si_{13}B_{9.1}$ microwires at different frequencies (b).

Enhancement of the ΔZ/Z ratio must be related enhancing of magnetic softening observed in studied microwires after annealing (Figs. 5, 6).

Observation of GMI effect in as-prepared $Fe_{73.8}Cu_1Nb_{3.1}Si_{13}B_{9.1}$ microwires must be attributed to lower magnetostriction constant in partially crystalline samples containing nanocrystallites.

Finally we measured GMI effect in Finemet-type microwires with different ρ–ratio. ΔZ/Z (H) dependences for $Fe_{73.8}Cu_1Nb_{3.1}B_{9.1}Si_{13}$ are presented in Fig.11. As can be appreciated although generally GMI is rather small, the samples with higher ρ–ratio (lower internal stresses) generally present higher $\Delta Z/Z_{max}$ values.

Generally, measurements of the GMI effect in nanocrystalline microwires involve preparation of the electrical contacts of rather brittle nanocrystalline samples obtained by recrystallization of amorphous samples after annealing. Therefore preparation of less brittle nanocystalline microwires directly by rapid quenching of composite microwire from the melt might be useful from the point of view of applications. The work on optimization of the GMI ratio during nanocrystallization is in progress.

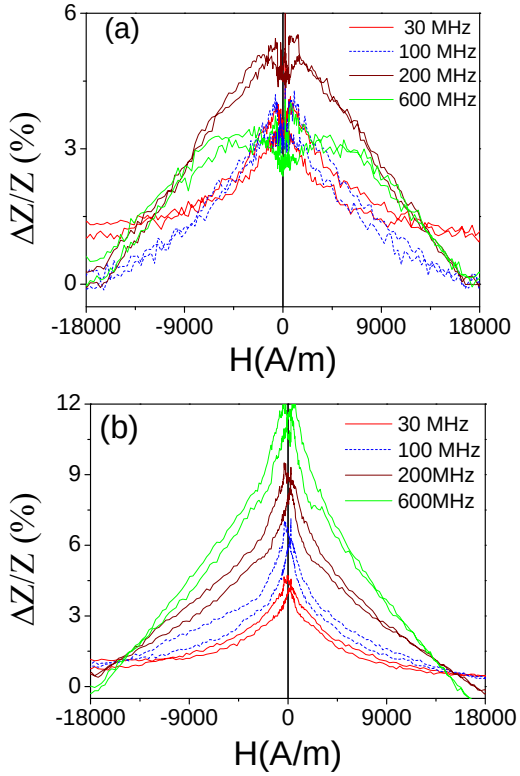


Figure 10: ΔZ/Z(H) dependences of in as-prepared (a) and annealed (b) $Fe_{70.8}Cu_1Nb_{3.1}Si_{14.5}B_{10.6}$ microwires (d=8.2μm, ρ=0.49) measured at different frequencies.

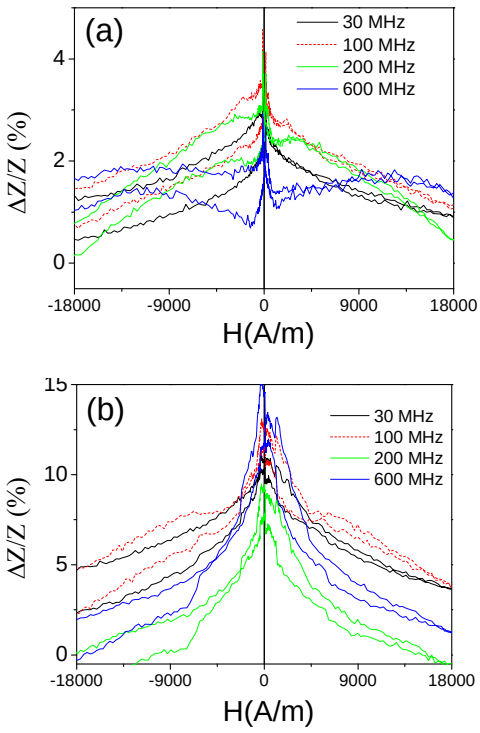


Figure 11: ΔZ/Z(H) dependences of as-prepared $Fe_{73.8}Cu_1Nb_{3.1}B_{9.1}Si_{13}$ with ρ =0.56, d=12.3 μm (a) and ρ=0.87, d=25.1 μm (b) measured at different frequencies.

4. Conclusions

GMI magnetic field and frequency dependences and magnetic softness of composite microwires produced by the Taylor-Ulitovski technique can be tailored either controlling magnetoelastic anisotropy of as-prepared microwires or by heat treatment. The magnetic softness, magnetic field and frequency dependences of GMI effect are determined by the magnetoelastic anisotropy. GMI effect has been observed in as-prepared Fe-rich microwires with nanocrystalline structure.

Acknowledgements

This work was supported by EU ERA-NET programme under project "SoMaMicSens" (MANUNET-2010-Basque-3), by EU under FP7 "EM-safety" project, by Spanish Ministry of Science and Innovation, MICINN under Project MAT2010-18914, by the Basque Government under Saiotek 12 MEMFOMAG (S-PE12UN139) project and by federal target program "Scientific and scientific-pedagogical personnel of innovative Russia", state contract no 14.A18.21.0783.

References

[1] M. Vazquez, H. Chiriac, A. Zhukov, L. Panina, and T. Uchiyama, On the state-of-the-art in magnetic microwires and expected trends for scientific and technological studies, *Phys Status Solidi A*, 208: 493–501, 2011.

[2] L.V. Panina and K. Mohri, Magneto-impedance effect in amorphous wires, *Appl Phys Lett* 65: 1189-1191, 1994.

[3] N. A. Usov, A. S. Antonov and A. N. Lagar`kov, Theory of giant magneto-impedance effect in amorphous wires with different types of magnetic anisotropy, *J. Magn Magn Mater* 185: 159-173, 1998.

[4] A.F. Cobeno, A. Zhukov, A.R. de Arellano - Lopez, F. Elías. J.M. Blanco, V. Larin and J. Gonzalez, Physical properties of nearly zero magnetostriction Co-rich glass-coated amorphous microwires, *J Mater Res* 14: 3775-3783, 1999.

[5] H. Chiriac, T.-A- Ovari and A. Zhukov, Magnetoelastic anisotropy of amorphous microwires, *J Magn Magn Mater* 254-255: 469-471, 2003.

[6] V. Zhukova, A. Zhukov, V. Kraposhin, A. Prokoshin and J. Gonzalez, *Sensors and Actuators (A)* 106: 225-229, 2003.

[7] P. Ciureanu, G. Rudkowska, L. Clime, A. Sklyuyev, A. Yelon, Anisotropy optimization of giant magnetoimpedance sensors, *J Optoelectronics and Advanced Materials* 6: 905-910, 2004.

[8] Y. Honkura, Development of amorphous wire type MI sensors for automobile use, *J Magn Magn Mater* 249: 375-381, 2002.

[9] V. Zhukova, N.A. Usov, A. Zhukov and J. Gonzalez, Length effect in Co-rich amorphous wire, *Phys Rev B* 65: 134407-1-7, 2002.

[10] H. Chiriac, T. A. Ovari, and Gh. Pop, Internal stress distribution in glass-covered amorphous magnetic wires, *Phys Rev B* 42**:** 10105-10113, 1995.

[11] A. S. Antonov, V. T. Borisov, O. V. Borisov, A. F. Prokoshin and N. A. Usov, Residual quenching stresses in glass-coated amorphous ferromagnetic microwires, *J Phys D: Appl Phys* 33; 1161-1168, 2000.

[12] A. Zhukov, Design of magnetic properties of Fe-rich glass – coated magnetic microwires for technical applications, *Adv Func Mat* 16: 675-680, 2006.

[13] J.M. Blanco, A. Zhukov and J. Gonzalez, Asymmetric torsion stress giant magnetoimpedance in nearly-zero magnetostrictive amorphous wires, *J Appl Phys* 87: 4813-4815, 2000.

[14] V. Zhukova, A.F. Cobeño, A. Zhukov, J.M. Blanco, S. Puerta, J.González and M. Vázquez, Tailoring of magnetic properties of glass coated microwires by current annealing, *J Non-Cryst Solids* 287: 31-36, 2001

[15] J. Arcas, C. Gomez-Polo, A. Zhukov, M. Vázquez, V. Larin, A. Hernando, Magnetic properties of amorphous and devitrified FeSiBCuNb glass-coated microwires, *Nanostructured Materials* 7: 823-834, 1996.

[16] M. Churyukanova, V. Zhukova, S. Kaloshkin, A. Zhukov, Effect of magnetoelastic anisotropy on properties of Finemet-type microwires, *J. Alloy Compd* 536S: S291– S295, 2012.

[17] C. Dudek, A.L. Adenot-Engelvin, F. Bertin and O. Acher, Engineering of the magnetic properties of Finemet based nanocrystalline glass-coated microwires, *J Non-Cryst Solids* 353: 925-927, 2007.

[18] G. Herzer, Amorphous and Nanocrystalline Materials in Encyclopedia of Materials: Science and Technology, ISBN: 0-08-0431526, Elsevier Science Ltd, pp. 149-157, 2001.

[19] Y. Konno and K. Mohri, Magnetostriction measurements for amorphous wires, *IEEE Trans Magn* 25, No.5: 3623-3625, 1989.

[20] A. Zhukov, V. Zhukova, J. M. Blanco, A. F.Cobeño, M.Vazquez and J Gonzalez, Magnetostriction in glass-coated magnetic microwires, *J Magn Magn Mater* 258-259: 151-157, 2003.

[21] M. Ipatov, V. Zhukova, A. Zhukov, J. Gonzalez, and A. Zvezdin, Low-field hysteresis in the magnetoimpedance of amorphous microwires, *Phys Rev B* 81: 134421, 2010.

[22] A. Zhukov, M. Ipatov, M. Churyukanova, S. Kaloshkin, V. Zhukova, Giant magnetoimpedance in thin amorphous wires: From manipulation of magnetic field dependence to industrial applications, *J Alloy Compd* http://dx.doi.org/10.1016/j.jallcom.2012.10.082, 2012.

[23] V. Zhukova, A.F. Cobeño, A. Zhukov, J.M. Blanco, V. Larin and J. Gonzalez, Coercivity of glass-coated $Fe_{73.4-x}Cu_1Nb_{3.1}Si_{13.4+x}B_{9.1}$ ($0 \le x \le 1.6$) microwires, *Nanostructured Materials* 11: 1319-1327, 1999.

[24] C. Garcia, A. Zhukov, J. Gonzalez, V. Zhukova, R. Varga, J.J. del Val, V. Larin and J.M. Blanco, Studies of a structural and magnetic properties of glass-coated nanocrystalline $Fe_{79}Hf_7B_{12}Si_2$ microwires, *J Alloy Compd* 423: 116-119, 2006.

Multi-Band, Highly Absorbing, Microwave Metamaterial Structures

T. M. Kollatou*, A. I. Dimitriadis, S. D. Assimonis, N. V. Kantartzis, and C. S. Antonopoulos

Department of Electrical and Computer Engineering, Aristotle University of Thessaloniki,
GR-54124 Thessaloniki, Greece
*corresponding author: fanikollatou@gmail.com

Abstract

The idea presented in this paper concerns the design of new, ultra-thin, polarization-insensitive, wide-angled metamaterial absorbers that operate in mutli-frequency bands within the microwave regime. The basic structure geometry is presented firstly and used to create multi-band highly absorbing structures, exploiting the scalability property of the metamaterials. Simulation results verify the high absorption of the structure. The multi-band absorbers are promising candidates as absorbing elements in scientific and technical applications because of its multiband absorption, polarization insensitivity, and wide-angle response. Finally, the current distribution for those structures is presented to gain an insight into the physics behind the multiple absorption mechanism.

1. Introduction

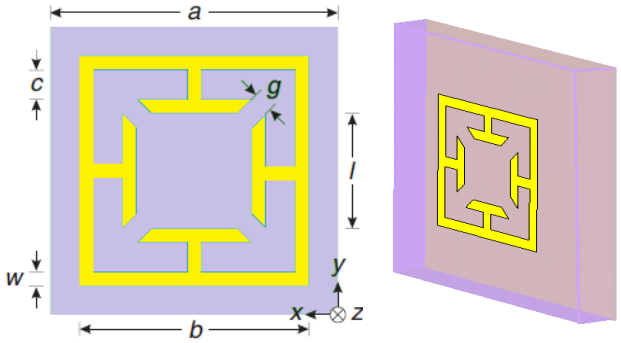
Metamaterials have been effectively used to produce highly absorbing structures which led the microwave engineers to research a new scientific field, with a direct impact on modern microwave systems. Since metamaterial absorbers are thinner than the traditional microwave absorbers, due to diffraction limit restrictions, they are perfect candidates to replace them as absorbing elements in scientific and technical applications. Essentially, metamaterials are inherently inhomogeneous structures, usually fabricated from metallic particles embedded in a host dielectric medium, and their properties mainly arise from the geometric details rather than their constituting material properties. Since the size of the comprising particles is often much smaller than the free-space wavelength, they are frequently described via effective-medium theories, i.e. by extracting effective electromagnetic parameters [1]. In the meanwhile, a considerable variety of metamaterial structures have been proposed in order to produce almost perfect absorption in the microwave, terahertz, and infrared frequency regions [2-5]. The initial proposed designs were fabricated in low-cost FR-4 substrate by means of standard photolithographic techniques and have been very sub-wavelength (around $\lambda_0/35$ at the resonant frequency). However, their performance has often been angle- and polarization-dependent, while the absorption bandwidth is usually narrow, due to the resonant behavior of metamaterial elements. Since there is still need for improvement of their performance, a lot of research is carried out in order to produce a wide range of incident angles and bandwidth-enhanced frequency spectrum [6-10]. This is a subject of huge importance for many different electromagnetic interference/electromagnetic compatibility (EMI/EMC) problems.

The purpose of this paper is to present a family of ultrathin, polarization-insensitive, metamaterial structures with wide angles of incidence that can achieve high absorption in multiple frequencies within the microwave regime. Having determined the optimized unit-cell dimensions [11] for an absorber operating in the middle of the microwave X-band (8.2-12.4 GHz) we proceed to the design of multi-band absorbers. They consist of a periodic array of different scales of square electric ring resonators (S-ERRs) [12] and a full metal back plate separated by a 1mm thick FR-4 dielectric substrate, resulting in an electrically thin structure. The proposed concept is successfully used in various cases of oblique incidence. The absorbing capability of the proposed absorber is directly resulted from the resonant structures of the unit cell. Through simply scaling up and down the dimensions of the original S-ERR it is possible to tune the absorbing frequency over a significant electromagnetic frequency spectrum.

2. Theoretical background and S-ERR absorber design

Absorbers are incorporated in various applications to eliminate unwanted scattering electromagnetic energy. In free space this is accomplished by presenting an impedance to an incoming wave equal to the impedance of free space. At a material interface, the incident, reflected and refracted waves must obey the boundary condition which states that the sum of both electric and magnetic fields of the waves must be continuous. This requirement of continuity of the amplitudes leads to the well known Fresnel's equations. For the design of an efficient and reliable metamaterial absorber, it is necessary to minimize both the reflection and transmission of the incident waves, exploiting the complex interactions of the metamaterial with the impinging radiation. Such a requirement stems from the definition of the absorption, obtained in terms of the *S*-parameters, as $A(\omega) = 1 - R(\omega) - T(\omega)$, with $R(\omega) = |S11|^2$ and $T(\omega) = |S21|^2$ being the reflectance and transmittance, respectively.

Following the theoretical analysis, our proposed structure of an efficient metamaterial absorber, is realized by imptinting a S-ERR at the front face of a 1 mm thick FR-4 dielectric substrate with a relative permittivity $\varepsilon_r = 4.1$ and loss $\tan\delta = 0.025$ (at 10 GHz) as in Fig.1(a). Note that the substrate is ultra thin and lightweight and determines the overall design's characterization as ultrathin. The bottom layer is a full copper plane to ensure zero transmission through the slab and is designed such that the incident magnetic field drives circulating currents between the two layers. The metallic parts are made of copper, which behaves as a perfect electric conductor (PEC) at the microwave regime. The specific S-ERR has been chosen due to its four-fold rotational symmetry around z-axis that renders the structure's response insensitive to the polarization of the impinging waves. An array of infinite unit cells is formed by applying periodic boundary conditions along the *x*- and *y*-axis. All simulations in this paper are carried out through the frequency domain solver of CST MWS™ computational package [13].



(a) (front view) **(b) (side view)**

Figure 1: Optimized unit cell with a = 8 mm, b = 4.2 mm, c = 0.5 mm, l = 1.9 mm, g = 0.56 mm, and w = 0.32 mm. Thickness of the copper layer (yellow color) is 35 μm, while the thickness of the substrate (purple color) is 1 mm.

The absorption peak (Fig. 2) of 95.8 % occurs at the frequency of 10.3 GHz, while the reflectance is minimized at the same frequency.

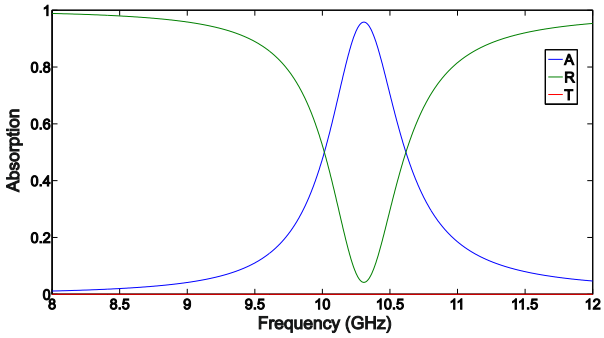


Figure 2: Absorption A, reflectance R and transmittance T of the proposed metamaterial absorber described in Figure 1. The peak value for the absorption is found to be 95.8% at 10.3 GHz.

The wide-angle performance of the proposed structure is verified in Fig.3 where high absorption curves, centered almost at the same frequency as the one referring to normal incidence, are acquired even for large angles of incidence. In the first case, the electric field component is parallel to the *x*-axis and we vary the angle theta between the wavevector and the *z*-axis on the *yz*-plane. In the second case we keep the magnetic field component parallel to the *y*-axis and modify the angle phi between the wavevector and the *z*-axis on the *xz*-plane. Note that, due to the absorber's four-fold rotational symmetry around the *z*-axis, these two cases are equivalent to the propagation of TE- and TM-polarized plane waves, respectively.

Finally, an interesting observation points out how sensitive the structure is to changes of the substrate's dielectric properties. When the electric permittivity of the dielectric fluctuates from $\varepsilon_r = 4$ to $\varepsilon_r = 4.3$, the geometric features of absorption curve remain unchanged whereas the center frequency is slowly up- and down-shifted. Depending on the application's operating frequency a small change in the dielectric properties of the substrate can significantly influence the accuracy of the results.

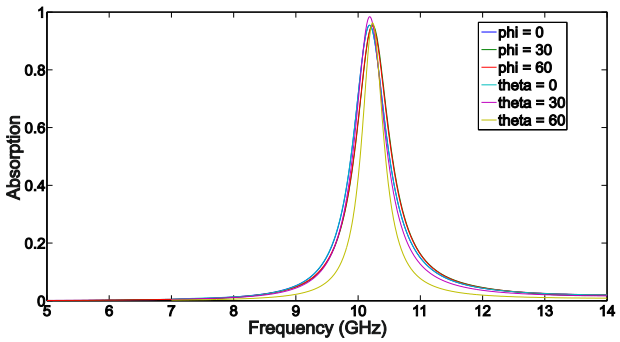


Figure 3: Absorption efficiency of the proposed device for obliquely-incident waves for two different cases.

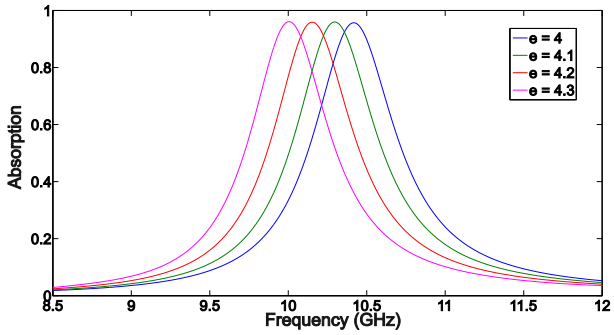


Figure 4: Absorption curves for various values of ε_r.

Table 1: Different values of ε_r.

Electric permittivity	Absorption	Frequency
4	95.8%	10.42GHz
4.1	95.8%	10.3GHz
4.2	95.8%	10.15GHz
4.3	95.8%	10GHz

3. Towards multi-band absorption

Designing an absorber that operates efficiently in the desired frequency band, for oblique incident waves is of major importance when at the same time it can work as a multi- or broad band absorber. Multi-band metamaterial absorbers can be implemented by properly scaling the original structure. Specifically, by multiplying the dimensions of the original S-ERR along the *x*- and *y*-axis by a scaling factor *s*, the center absorption frequency can be downshifted ($s > 1$) or up-shifted ($s < 1$), without changing the absorption curve's original shape and fractional bandwidth. This property, frequently called metamaterial scalability property, will be, herein, used for the synthesis of multiband absorbers. This feature can also be used to offer broad-band absorbers [14, 15] by very slightly changing the scaling. Generally, the realization of broadband metamaterial absorbers can be seen as the borderline case of multi-band designs, with scaling factors of the respective ERRs approaching unity. It is important to highlight that no scaling is applied along the *z*-direction, since the metal thickness has no efect on the overall behavior of the absorbers. An example confirming the scalability feature for different scales of the original structure is presented in Fig.5.

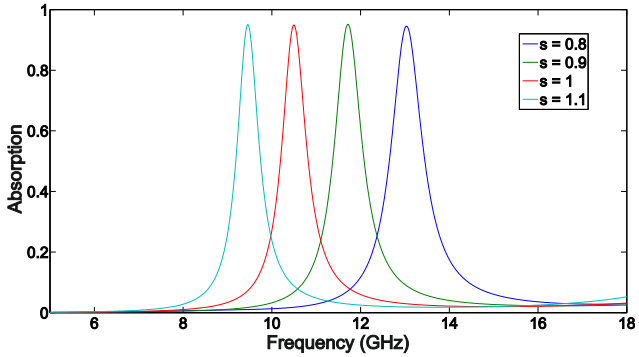


Figure 5: Absorption curves of the scaled versions of the proposed device.

Table 2: Different scales of the ERR.

Scales s	Absorption	Frequency
0.80	95.8%	13GHz
0.90	95.8%	11.7GHz
1.00	95.8%	10.3GHz
1.10	95.8%	9.46GHz

3.1. Dual-band absorption

Utilizing the conclusions drawn in the previous paragraph, we proceed in the design of a dual-band metamaterial absorber. Four electric resonators are imprinted at the front face of an FR-4 dielectric substrate, as in Fig. 6. The S-ERRs that are placed along the same diagonal have the same dimensions. Two of them are scaled versions of the original S-ERR structure illustrated in Fig. 1(a), with a scaling factor $s_2 = 0.90$, while the other two have the dimensions of the original ERR, and thus can be considered to be scaled by $s_1 = 1.00$. The opposite side of the dielectric is covered by a full copper plane to guarantee zero transmission through the slab in order to enhance the absorption.

From the results of the absorption curve in Fig. 7, two distinct absorption peaks can be observed, as expected. The first is located at the frequency of 10.4 GHz, producing an almost perfect absorption of 99.3%, while the second occurs at 11.7 GHz and is reaching the value of 96%. Furthermore, note that the absorption peak of the original S-ERR (in Fig.1) is increased from 95.8% to 99.3% in the dual-band structure showing that the addition of a second scaled S-ERR in the unit cell is slightly enhancing the structure's absorbing efficiency as well as offering another high absorption peak.

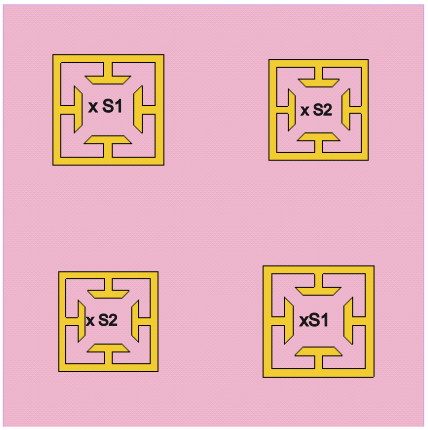


Figure 6. Unit cell of a dual-band metamaterial absorber, consisting of four properly scaled S-ERRs where $s_1 = 1.00$ and $s_2 = 0.90$.

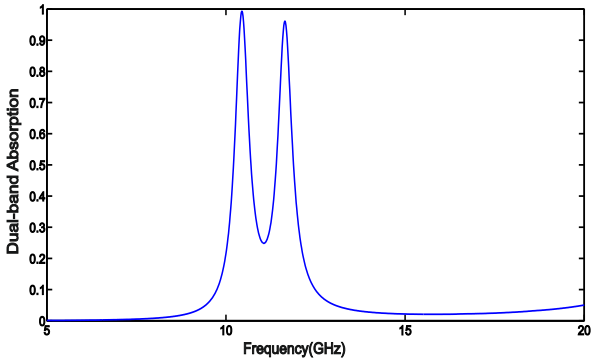


Figure 7. Absorption spectrum of the dual-band structure. The first peak reaches a maximum of 99.3% at the frequency of 10.4 GHz, while the second one corresponds to 96% absorption at 11.7 GHz.

Equally important to the multi-bandwidth performance of the absorber is proven to be its ability to absorb obliquely incident waves, even for large angles of incidence. To this end, an analysis of the absorbing efficiency is held for two cases of oblique incidence.

Varying the angle theta, while retaining the angle phi=0^0, results in a very promising peak absorbances over 70% up to a 60^o angle at almost the same center frequencies as in the case of normal incidence. The absorbing efficiency

deteriorates beyond that critical angle, yet remains at a 70% peak for an incidence of 80° (omitted for clarity reasons). This deterioration phenomenon is attributed to the fact that the incident magnetic field can no longer efficiently drive circulating currents between the two metallic layers due to polarization. On the other hand, for the variation of angle phi, the absorber's performance remains almost unchangeable and up to 99% and 96% respectively verifying the wide-angle dual-band characteristic of the proposed structure.

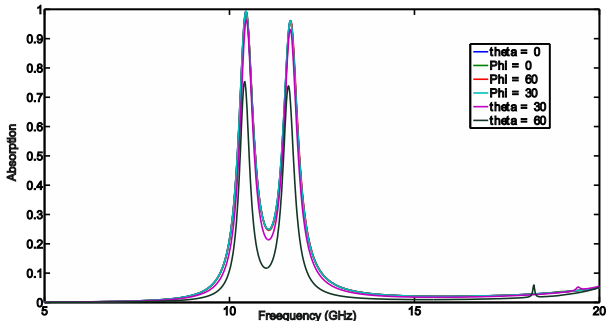


Figure 8: Absorption efficiency of the dual-band absorber for obliquely-incident waves in two different cases.

Table 3: Various angles of incidence for the dual-band.

Angle of incidence	Degrees	Abs. peak 1	Abs.peak 2
φ(phi)	0^0	99.3%	96%
φ	30^0	99.3%	96%
φ	60^0	99.3%	96%
θ(theta)	0^0	99.3%	96%
θ	30^0	96%	93%
θ	60^0	75%	74%

For various scaled versions of the S-ERR (Fig.9), the dual-band absorber exhibits high absorptive regions in different resonant frequencies. Observe the transition from dual-band absorption to broad-band, compared to the original S-ERR, in the cases where $s_1 = 1.00$ and $s_2 = 0.97$. Although two distinct peaks can be clearly identified in the resulting curve, the broadband structure absorbs over 85% for twice the frequency band than the original structure (Fig.1).

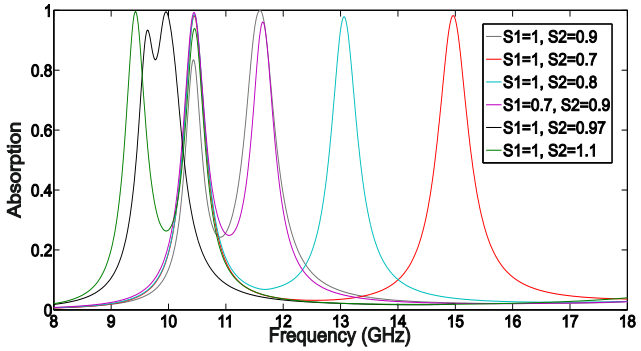


Figure 9. Absorption curves of the scaled versions of the dual-band structure.

Table 4: Dual-band absorber scaled variations.

Scale S1	Scale S2	Abs.peak 1	Abs.peak 2
1.00	0.70	98%	98%
1.00	0.80	98.4%	97%
1.00	0.90	99.3%	96%
1.00	1.10	99.5%	94%
0.70	0.90	84%	97%
1.00	0.97	93%	99%

3.2. Triple-band absorption

The design concept of the dual-band structure can be easily extended to the construction of multi-band devices. A more complicated setup is the triple-band absorber, presented in Fig. 9. The unit cell consists of a set of 3x3 S-ERR scaled elements. The selected scaling factors are *s*1 = 1.00, *s*2 = 0.80, and *s*3 = 0.70 for the larger, medium, and smaller ERRs, respectively. From the simulation results depicted in Fig. 10, we observe three discrete absorption peaks. The first peak corresponds to an almost perfect 99.7% at the frequency of 10.4 GHz, the second one to 95.8% absorption at 13 GHz, while the third one reaches a maximum of 95.5%, at the frequency of 15 GHz.

Electric ring resonators with the same scaling factors can be combined in different ways inside the complex unit cell. Multiple variations were simulated in order to test the effect of their arrangement on the performance of the structure. The outcomes of the comparison unveiled that the proposed structure is the optimal choice for the specific triple-band absorber. It is also possible to change the scaling of each S-ERR depending on the applications requirements, as was exemplified in the case of the dual-band absorber in the previous section.

The wide angle performance is investigated also for the case of the triple-band absorber, proving the structures efficient operation for the various scenarios of oblique incidence. Firstly, we vary the angle theta which leads to high absorption rate over 75% up to a 60° angle at almost the same center frequencies as in the case of normal incidence. Secondly varying the angle phi, we observe that the performance of the proposed triple-band structure remains almost unchangeable and up to 99% and 96% respectively verifying the wide-angle triple-band feature of the absorber.

Furthermore, the surface current distributions at the three resonant frequencies are illustrated in Fig.12. From this result, we can better interpret the absorption mechanism of the triple-band absorber. At 10.4 GHz, surface currents indicate the resonant behavior of the larger S-ERRs, while at 13 GHz the electric resonance of the medium S-ERRs is apparent.

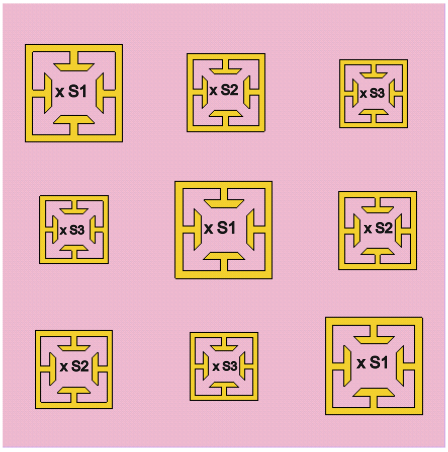


Figure 10. Unit cell of a triple-band absorber, consisting of nine properly scaled ERRs. The dimensions of the bigger, medium, and smaller ERRs are those of Fig. 1 scaled by $s1 = 1$, $s2 = 0.8$ and $s3 = 0.7$, respectively.

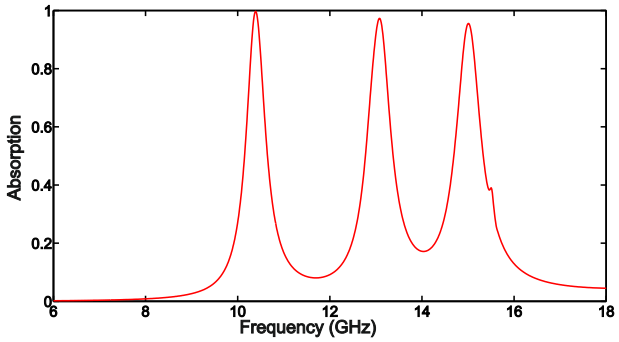


Figure 11: Absorption spectrum of the triple-band device. The first peak reaches 99.7% at 10.4 GHz, the second one to 95.8% at 13 GHz, while the third one reaches a 95.5%, at 15 GHz.

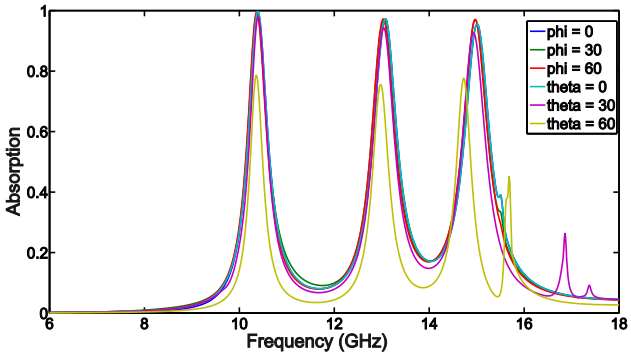


Figure 12. Absorption efficiency of the triple-band absorber for obliquely-incident waves in two different cases.

Table 5: Various angles of incidence.

Angle	Degrees	Absorption %	Absorption %	Absorption %
φ(phi)	0^0	99.7%	97%	96%
φ	30^0	98.8%	97%	96%
φ	60^0	98.8%	96.6%	97%
θ(theta)	0^0	99.7%	97%	96%
θ	30^0	98%	94%	92%
θ	60^0	76%	75%	77%

Finally at 15GHz the smaller S-ERRs are responsible for the resonance. These outcomes suggest that the combination of unit cells with different absorbing frequencies can yield the superposition of their absorptive spectra, verifying our idea for the realization of multiband components.

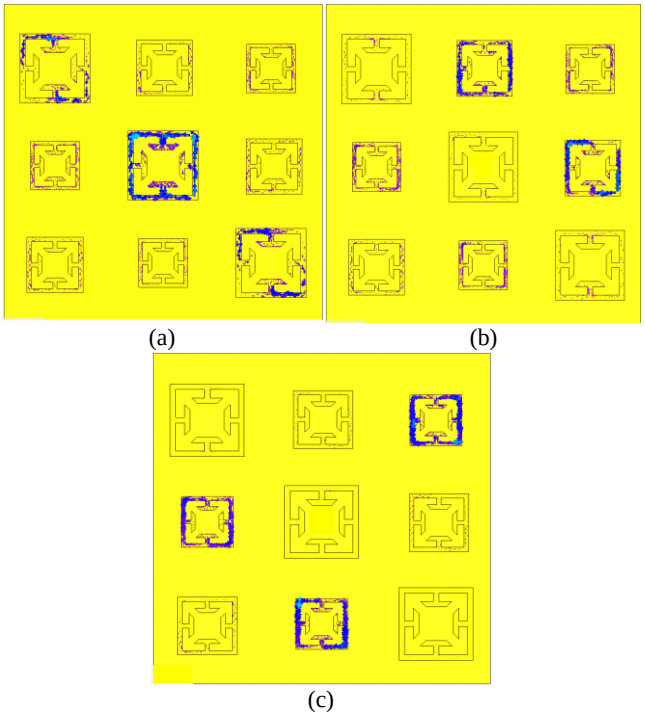


Figure 13. Surface current distributions on the front side of the triple-band absorber at (a) 10.4 GHz, (b) 13 GHz and (c) 15 GHz. The lower absorption frequency is due to the resonance of the bigger ERRs, the intermediate peak corresponds to the resonance of the medium-sized ERRs while the higher one can be attributed to the resonant behavior of the smaller ERRs.

4. Conclusions

The concept of designing new, polarization-independent, wide-angled, multi-band metamaterial absorbers in the microwave regime has been introduced. The proposed structures have been proven to exhibit several attractive characteristics by remaining electrically thin at the resonance frequency implementing a low-cost FR-4 dielectric substrate. By exploiting the geometrical scalability of the S-ERR elements, we have achieved multiple absorption peaks at the desired frequencies, thus extending our idea to dual-band and triple-band structures. Using this feature, these absorbers could be designed to work at other EM frequency range with nearly perfect absorption. Furthermore, the possibility to create broad-band absorbers was successfully exemplified using the dual-band arrangement with closely-located resonances. The presented results from various incident angles constitute a strong indication for the angle-insensitive performance of the proposed absorbers. Finally, current distributions for the triple band structure verified our idea towards the realization

of multi-band absorbers by combining unit cells with different absorbing frequencies. Such a composite microwave metamaterial may find numerous applications ranging from the active element in a bolometer to stealth technology. Future work will focus on the quantitative explanation of the power loss mechanism within the structure as well as the experimental verification of the acquired numerical results by measuring fabricated prototypes for the triple- and dual-band absorbers.

References

[1] Smith, D., Schultz S., Markoš P., and Soukoulis C., Determination of effective permittivity and permeability of metamaterials from reflection and transmission coefficients, *Phys. Rev. B*, vol. 65, no. 19,pp. 195104(1–5), 2002.

[2] Caloz, C. and T. Itoh, *Electromagnetic Metamaterials: Transmission Line Theory and Microwave Applications: The Engineering Approach*. John Wiley & Sons, New York ,2006.

[3] Marqués, R., F. Martín, and M. Sorolla, *Metamaterials with NegativeParameters: Theory, Design, and Microwave Applications*. John Wiley & Sons, New York, 2008.

[4] Bilotti, F., A. Toscano, K. B. Alici, E. Ozbay, and L. Vegni, Design of miniaturized narrowband absorbers based on resonant-magnetic inclusions, *IEEE Trans. Electomagn. Compat*., Vol. 53, No. 63, 63-72, 2011.

[5] Zhu, W., X. Zhao, B. Gong, L. Liu, and B. Su, Optical metamaterial absorber based on leaf-shaped cells, Appl. *Phys.A - Mater*., Vol. 102, No. 1, 147-151, 2011.

[6] Kollatou, T., A. Dimitriadis, Kantartzis, N., Hinaje, M., Antonopoulos C., A class of multi-band, polarization-insensitive, microwave metamaterial absorbers in EMC analysis, in *International Symposium on Electromagnetic Compatibility (EMC EUROPE)*, 2012.

[7] Tao, H., C. Bingham, A. Strikwerda, D. Pilon, D. Shrekenhamer, N. Landy, K. Fan, X. Zhang, W. Padila, and R. Averitt, Highly flexible wide angle of incidence terahertz metamaterial absorber: Design, fabrication and characterization, *Phys. Rev. B*, vol. 78, no. 24, pp.241103(1–4), 2008.

[8] Xiaopeng, S., Tie J. C., J. Zhao, H. F. Ma, W. X. Jiang, and H. Li, Polarization-independent wide-angle triple-band metamaterial absorber, *Optics Express*, Vol. 19, Issue 10, pp. 9401-9407 (2011).

[9] Huang, L. and H. Chen, Multi-band and polarization insensitive metamaterial absorber, *Progress In Electromagnetics Research*, Vol. 113, 103-110, 2011.

[10] Cheng, Y. Z., Y. Wang, Y. Nie, R. Z. Gong, X. Xiong, and X. Wang, Design, fabrication and measurement of a broadband polarization-insensitive metamaterial absorber based on lumped elements, *J. Appl. Phys.*, Vol. 111, 044902, 1-4, 2012.

[11] Kollatou, T., A. Dimitriadis, S. Assimonis, N. Kantartzis, and C. Antonopoulos, A family of ultra-thin, polarization-insensitive, multi-band, highly absorbing metamaterial structures, *Progress In Electromagnetics Research*, Vol. 136, 579-594, 2013

[12] Chen, H. T., J. F. O'Hara, A. J. Taylor, R. D. Averitt,C. Highstrete, M. Lee, and W. J. Padilla, Complementary planar terahertz metamaterials, *Opt. Express*, Vol. 15, 1084-1095, 2007.

[13] CST MWSTM: Computer Simulation Technology: Microwave Studio, Computer Simulation Technology Std., 2011.

[14] Gu, S., J. P. Barrett, T. H. Hand, B. I. Popa, and S. A. Cummer, A broadband low-reflection metamaterial absorber, *J. Appl.Phys.*, Vol. 108, 064913, 1-6, 2010.

[15] Sun, J., L. Liu, G. Dong, and J. Zhou, An extremely broad band metamaterial absorber based on destructive interference, *Opt.Express*, Vol. 19, No. 22, 21155-21162, 2011.

Effect of concentration of Cd on structural and optical properties of ZnO:Cd thin films prepared by sol-gel method

Ausama I. Khudiar[a,*], M. Zulfequar[b] and Zahid H. Khan[b]

[a]Center of Applied Physics, Ministry of Science and Technology, Baghdad, Iraq.

[b]Department of Physics, Jamia Millia Islamia (A Central University), Jamia Nagar, New Delhi-110025, India.

*corresponding author, E-mail: ausamaikhudiar@yahoo.com

Abstract

Cadmium doped zinc oxide polycrystalline thin films were prepared by sol-gel process. The sol was prepared from zinc acetate dehydrate and cadmium acetate was used to it. Methoxyethanol and monoethanolamine were used as solvent and stabilizer, respectively. The quantity of cadmium in the sol was 0, 1, 5 and 10 at % Cd. Structural investigation including microstructure was carried out by X-ray diffraction (XRD) analysis. The films give a hexagonal wurtzite structure with diffraction peaks at (100), (002) and (101). It is found that the particle size of the films change with Cd doping. Optical properties of the thin films were determined by using UV-VIS-NIR spectrometer. It was found that the band gap of the thin films decreased from 3.16 eV to 2.6 eV as the concentration of Cd was increased. Such films can be applied on silicon solar cells as the changes in the band gap are acceptable as a requirement for good anti-reflecting coating element.

1. Introduction

Zinc oxide is an inexpensive n-type semiconductor having direct band gap of 3.3 eV which crystallizes in hexagonal Wurtzite structure (c = 5.025 and a = 3.249) [1]. Due to large exciton binding energy of 60 meV, they have potential applications in Optoelectronic devices such as in solar cells, Optical wave guide, Light emitting diodes (LED). Various gas, chemical and biological sensors were based on ZnO thin film. Thin films of Zinc oxide can be prepared by various techniques; among them are Sputtering, Chemical Vapor Deposition (CVD), Laser ablation, Sol- gel methods [2- 4]. Properties of ZnO thin films show dependence on the technique used. Apart from doping, to increase the functionality of ZnO thin film, the effect of preparation conditions on the properties have to be considered for its effective technological applications. In the present work we have used sol-gel methods to prepare ZnO liquid and spin coating process for film preparation. Zinc acetate dihydrate was used as the precursor material. The Sol-gel process has the advantages of controllability of compositions, simplicity in processing and is cost effective [5]. We have studied the effect of concentration of Cd on the structural and optical properties of ZnO thin films. X-ray diffraction (XRD) was used for structural characterization. UV-Vis spectrometry was used for optical characterization.

2. Experimental details

Zinc acetate dehydrate ($Zn(CH_3COO)_2$_2H2O) and cadmium hexahydrate were dissolved in a solution of isopropanol and monoethanolamine. The molar ratio of MEA to zinc acetate was 1.0 and the concentration of zinc acetate was 0.7 mol/l. The quantity of cadmium in the sol was 0, 1, 5 and 10 at % Cd. The resultant solution was stirred at 50 °C for 1 h to yield a clear and homogeneous solution. The solution was finally aged at room temperature for 24 h. Cd-doped ZnO (AZO) films were prepared on glass substrate by repeated coating. Spin coating was performed at room temperature, with a rate of 3000 rpm for 30 s. After depositing each times, the films were preheated in air at 275 8C for 10 min. After repeating the coating procedure five times for the final film thickness of approximately 200 nm, the films were finally postheated at 500 °C for 1 h in air using an electronic furnace. For measuring the optical absorption of thin films, a double beam UV/VIS/NIR Spectrophotometer (Camspec-M550) was used. The XRD measurements were carried out using an X-Ray Diffractometer PW 1830 PANalytical which has tube anode; copper using the wavelength 1.54056Å.

3. Results and Discussion

3. 1. Structural Properties

The structure of ZnO:Cd thin films were studied using high resolution X-ray diffraction (XRD). XRD spectra of the thin films were showed in Fig. 1. The XRD peaks of 31.48°, 35.26° and 37.17° were correspond to ZnO (100), (002) and (101) respectively in Fig. 1 A. Theses peaks confirmed that the film was polycrystalline in nature and the type of structural was a hexagonal wurzite[5]. The crystalline size (grain diameter (D)) of the crystallites can be determined using the Scherrer's formula from the full width at half maximum (FWHM) β [6, 7];

$$D = 0.94\lambda/\beta\cos\theta \qquad (1)$$

where λ is the wavelength of the X-ray used, β is the FWHM and θ is the angle between the incident and scattered X-ray. The grain size of ZnO was 32.01 nm.

Fig. 1 B, C and D show XRD of ZnO: Cd thin film when concentration of Cd are 1% , 5% and 10%. The structural of ZnO: Cd thin films were a hexagonal wurzite. The full width at half maximum (FWHM) of the thin films increased after Cd doping. The grain size of ZnO: Cd thin films were 13.65, 13.65 and 18.42 nm.

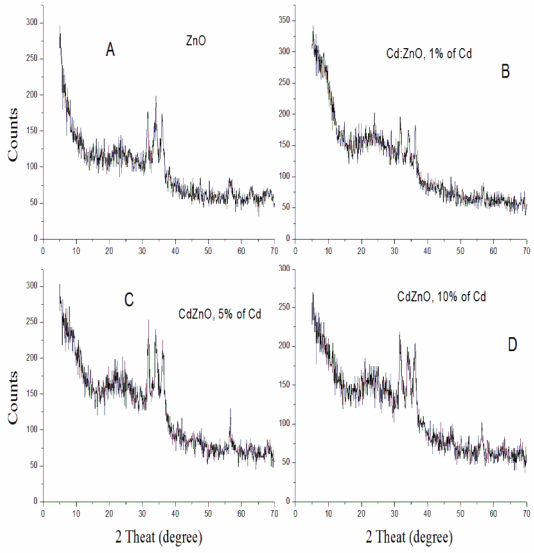


Figure 1: XRD of ZnO: Cd thin films before and after Cd doping.

3.2: Optical properties

The optical absorption spectra of ZnO and ZnO: Cd thin films, Cd concentration 1%, 5% and 10%. The thin films deposited onto a glass substrate were studied at room temperature in the range of wavelengths 300–750 nm. Figure 2 shows the variation of absorption spectra with wavelength (λ).

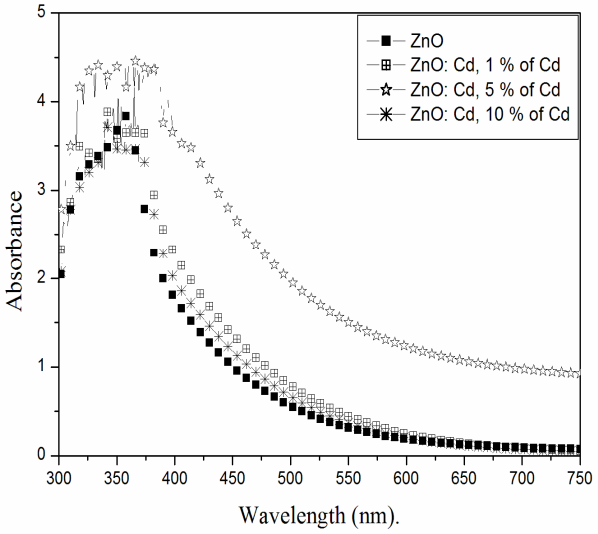


Figure 2: Absorbance spectra with wavelength (λ). For ZnO: Cd system films.

The value of optical band gap 'E_g' is calculated using the following relation [8,9];

$$\alpha = A\,(h\nu - E_g)^{n}/h\nu \qquad (2)$$

where A is a constant and n is equal to 1/2 for direct band gap semiconductors. The plots of $(\alpha h\nu)^2$ versus hν are shown in Fig. 3 for ZnO and ZnO: Cd system films. We find the optical band gap decreased with Cd content. The decrease in the optical band gap on the addition of Cd in the ZnO system films may be explained on the basis of the model of density of states in amorphous semiconductor proposed by Mott and Davis [10]. According to this model, the width of localized states near the mobility edges depends on the degree of disorder and defects presented in the amorphous structure. In particular, it is known that unsaturated bonds together with some saturated bonds [11] are produced as a result of insufficient number of atoms deposited in the amorphous films [12]. The unsaturated bonds are responsible for the formation of some defects in the films. Such defects produce localized states in the amorphous solids.

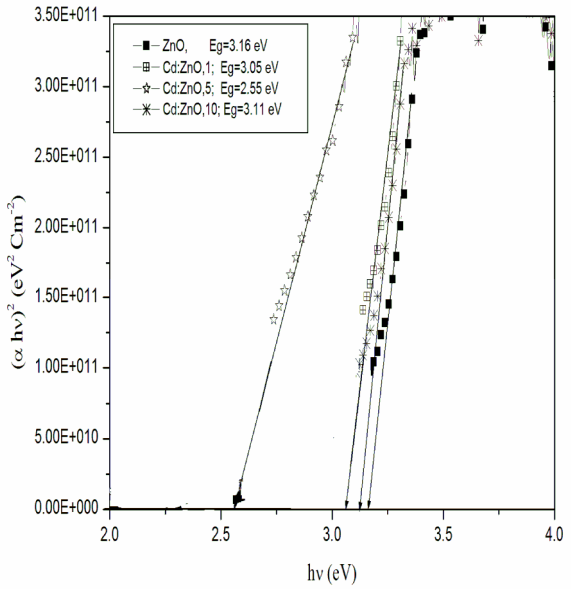


Figure 3. Optical band gap of Zno: Cd thin films.

4. Conclusion

We have instigated the optical and structure propties of the ZnO thin films. In spit of the insignificant change in the structure with the variation of (Cd) content the grain size decreased for thin films variation of Cd increase, it is found that the optical band gap decrease with increasing (Cd) content, a result has been attributed to the increase in the localized tail states.

References

[1] K.J. Chen, T.H. Fang, F.Y. Hung, L.W. Ji, S.J. Chang, S.J. Young, Y.J. Hsiao, *Applied Surface Science* 254: 5791–5795, 2008.

[2] J.H. Park, S.J. Jang, S.S. Kim, B.T. Lee, *Appl. Phys. Lett*. 89: 121108, 2006.

[3] J.J. Chen, M.H. Yu, W.L. Zhou, K. Sun, L.M. Wang, *Appl. Phys. Lett*. 87: 173119, 2005.

[4] S.Y. Kuo, W.C. Chen, Cheng F C.P., *Superlattices Microstruct.* 39: 162–170, 2006.

[5] Canyun Zhang, *Journal of Physics and Chemistry of Solids* 71: 364–369, 2010.

[6] Ausama I. Khudiar, M. Zulfequar, Zahid H. Khan, *Journal of Non-Crystalline Solids* 357: 1264–1269, 2011.

[7] Young-Sung Kim, Weon-Pil Tai, *Applied Surface Science* 253: 4911–4916, 2007.

[8] Chien-Yie Tsay, Min-ChiWang, *Ceramics International* 39: 469–474, 2013.

[9] Nanda Shakti, P.S.Gupta, *Applied Physics Research* 2: 91, 2010

[10] N. F. Mott, E. A. Davis, *Electronic Processes in Non-Cryst. Mater*. pp. 382 & 428 Clarendon, Oxford 1979.

[11] S. R. Ovshinsky, D. Adler *Contemp. Phys.* 19: 109,1978.

[12] M. L. Theye, *Proceeding of the Fifth International Conference on Amorphous and Liquid Semiconductors* 1: 479, 1973.

Metamaterials and negative index materials

Tuniable microwave filter Using Split Ring resonator

Mondher LABIDI, Oussama TABBEBI, Jamel BEL HADJ TAHAR and Fethi CHOUBANI
Innov'com Research Laboratory, Higher School of Communications of Tunis,
Sup'Com University of Carthage, Tunisia

Abstract— The idea aim of this paper is to describe the potentiality of sub-wavelength resonators, namely, Split-Ring Resonators, complementary split-ring resonators, and related structures to the suppression of undesired spurious bands in microwave filters, a key aspect to improve their rejection bandwidths. The utilization of such resonant structures as efficient microwave filter is also demonstrated. The coupling between 7- SRRs can be quite complex and strongly depends on their geometrical arrangement. These materials have in certain bands a frequency of negative permittivity and permeability with promising applications in the field of microwaves such as: antenna, waveguides, filter…First of all we will examine the electromagnetic behavior of those materials focusing mainly on their response on an external electric field and its crucial role in the achievement of left-handed behaviour. Later we will study the applications of these metamaterials in the filter design.

INTRODUCTION

Metamaterials show negative permittivity and permeability in certain frequency range or what is known as left-handed material (LHM), it provides another alternative to the existing right-hand rule. With this theory, it offers a new dimension to the antenna applications as well as optic. The negative refractive index [1,2] and the convergence of the electromagnetic waves when passing through the metamaterial is benefit for optical applications. Also, the relationship between different dimensions can affect the frequency response in order to understand the metamaterial structure and its properties.

The structure is optimized to get the left-handed properties in X-band frequency which is around 8GHz-12GHz. Although, the metamaterials structure gives a limited negative range within the X-band, it fits the theory with the co-existence of both negative permittivity and negative permeability [3]. the simulation via HFSS simulation tools is used to optimize and confirm the theoretical result. Then the simulation being performed on the filter with metamaterial structure is observed and analyzed so we notice a frequency shift occurs.Our study aims to represent recent investigations about implementation to the left handed metamaterials in the design of band pass filter and cutoff band filter.

The introduction includes the definition of the metamaterials, the early theory to the negative index of refraction, the structure that shows the left-handed properties and the applications to the Left Handed Materials (LHM) in the filter. The rest of the search is organized as follows. In section II, we tried to introduce the left handed material, the Split Ring Resonator « SRR ». The design procedure various prototype devices of the filter and their simulated frequency responses will be presented in section III. Section IV is reserved for the conclusion.

STUDY OF METAMATERIALS

This part consists of brief theory of metamaterial, which includes the properties of metamaterial in electromagnetic field, the behavior of negative index of refraction, and the other prominent properties of metamaterial that is refraction and the Snell's Law. Besides, there are also discussions based on few literatures in metamaterials areas performed by other researchers. The idea of metamaterial or negative index of refraction was first proposed theoretically in 1968 by V.G.Veselago [4]. This metamaterial exhibits a negative permittivity and permeability which is also known as left – handed material (LHM). The negative permittivity is easily obtained by an array of metallic wires and was theorized in 1996 [1,2]. JB Pendry [5]also theorized the structure of negative permeability which was established in 1999 with split ring resonator (SRR) structure. The transmission – reflection problem is translated by the inversion method,[1,2] which is calculating the effective permittivity and the effective permeability μeff from the coefficients of transmission and reflection. These two coefficients are obtained from simulations under the software HFSS:

$$t^{-1} = \left[\cos(nkd) - \frac{i}{2}\left(z + \frac{1}{z}\right)\sin(nkd)\right] e^{ikd} \quad (1)$$

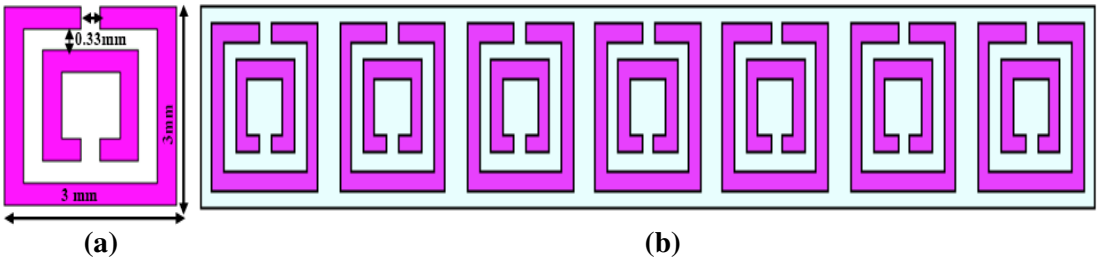


Figure 1. (a) SRR single structure. (b) Array of SRRs structure

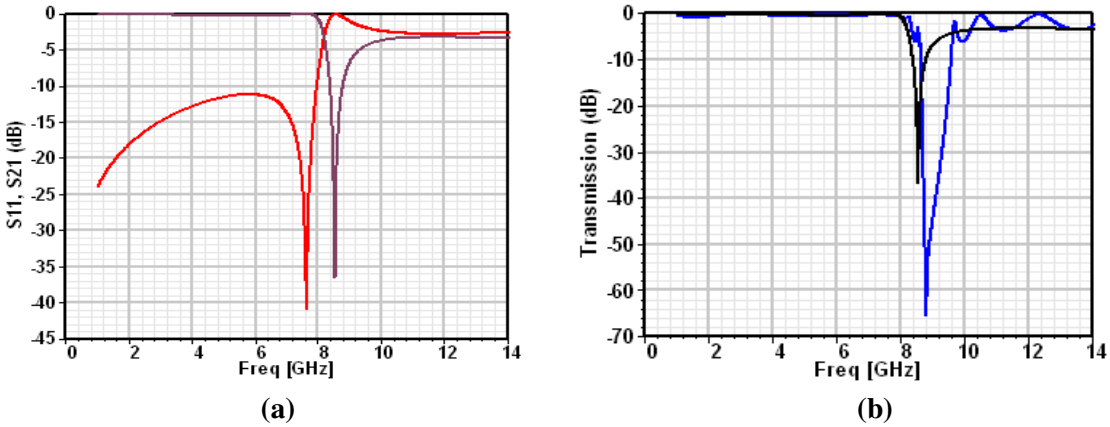


Figure 2. (a) Transmission and reflection coefficient of single SRR. (b) Transmission for single and array of SRRs in dB.

Where $k = \frac{\omega}{c}$ is the wavenumber of the incident wave, the length d and n is the refraction index. The reflection coefficient is also related to n and z by:

$$\frac{r}{t'} = -\frac{i}{2}\left(z - \frac{1}{z}\right)\sin(nkd) \qquad (2)$$

Equations (1) and (2) can be inverted to find n and z as functions of t and r. The permittivity ε and the permeability μ can be easily obtained from the following relations:

$$\varepsilon = \frac{n}{z} \qquad \mu = nz \qquad (3)$$

$$\text{when}: \cos(nkd) = \frac{1}{2t}(1 - r^2 + t^2) \text{ And:}$$

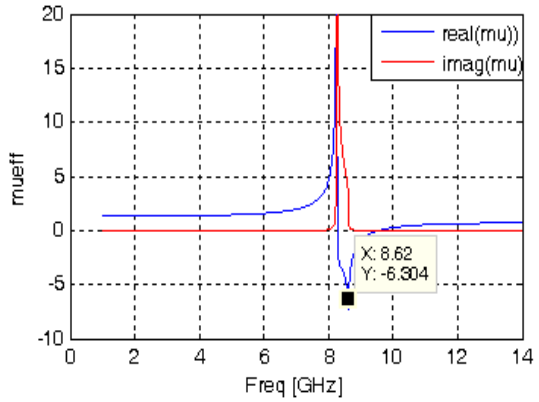
$$z = \pm\sqrt{\frac{(1+r^2) - t^2}{(1-r^2) - t^2}}$$

According to studies by Kafesaki, M. et.al. (2005), magnetic resonance with negative permeability μ, can be calculated using Split Ring Resonator SRR. The various dimensions of the squared SRR for a functioning in band X [8,2 GHz; 12,4 GHz] are given figure 1. Figure 1 shows the square for double-ring SRR, dielectric used is the Rogers R04003 with ε=3.38 and tanδ = 0.0027. figure 2(a) shows the reflection and transmission coefficients for the single SRR, SRRs give a dip in the transmission coefficient which is associated with a negative permeability regime. The frequency of this dip, that is the magnetic resonance frequency. In this resonance frequency at 8.55GHz, the transmission coefficient is -36.44 dB for the single SRR. However, in figure 2(b), we compare the characteristics between the single and the array of SRR as part of our study on the filter. The resonance frequency of array of SRRs presented is 8.75 GHz with a transmission of -65.16 dB. Real and imaginary permeability are given in figure 3, such as in figure 3(a), we note that at 8.62 GHz the real part of permeability goes negative with a bandwidth 0.9 GHz. Figure 3(b) shows the real and imaginary parts of the permeability for the array of 7 SRRs, as configured in figure 2(b). we notice a region of negative permeability over the range from 8.4 GHz to 9.3 GHz. This is consistent with the region of attenuated transmission.

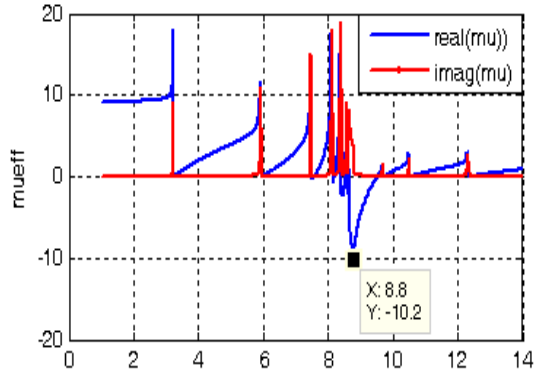
III. STUDY OF FILTER USING SRRs

A band-pass filter is a device that passes frequencies within a certain range and rejects (attenuates) frequencies outside that range. An example of an analogue electronic band-pass filter is an RLC circuit. These filters can also be created by combining a low-pass filter with a high-pass filter

This section is devoted to a bandpass filter under SRRs and microstrip resonators. here, we represent the characteristics of band-pass structure composed of microstrip resonators. Then, we associate the SRRs with the microstrip resonators and we comment on the results of simulation. In the first part we describe a filter-pass using microstrip resonator only [6]. Several values for width and length of microstrip resonators are taken to behave bandpass to22 GHz. The resonators are five in number and each have a length of 3.43 mm and a width of 1.2 mm. The input lines and output have



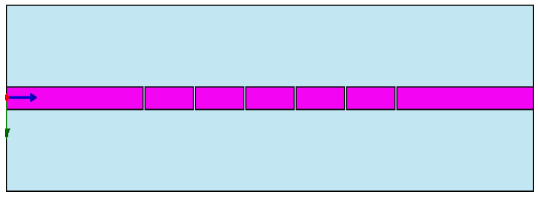
(a)



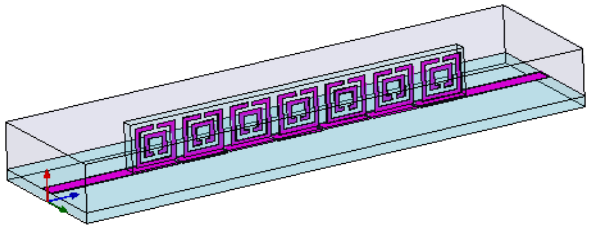
(b)

Figure 3. (a) Real and imaginary effective permeability for a single SRR. (b) Effective parameters for an array of SRRs.

the same width and a length of 9.825 mm. The width of gaps is 0.2 mm. The total length of the circuit is 38 mm as shown in Figure 4 (a) and the substrate used is ROGERS RO4003C with 3.38 of permittivity and 0.0027 of tangδ. The results obtained from numerical simulations using Ansoft's HFSS show a band-pass character for the filter on use around 22 GHz frequency. Noticing transmission curve, structure shows high insertion loss. This does not in any way considered a problem. In fact, the frequency band of interest here is below the bandpass, where the signal is not transmitted. The second part is devoted to describe the second type of the filter in use. Here, structure represented is made from a blend of microstrip resonators, Split Ring Resonators and an electrical shielding (Figure 4.(b)). The microstrip resonators are used to realize the bandpass filter modeled in the previous section, whose center frequency is 22 GHz with a bandwidth of 0.8 GHz (Figure 5(a)). The input and output lines of bandpass filter can also feed SRRs. Indeed, SRRs produce a resonance effect mainly when magnetic field penetrates through the rings. Thus, an electromotive force is generated around the ring giving rise to the creation of a current flowing on them. This current disappears in the cut rings and many charges of opposite sign accumulate at the ends of each ring. In our case, the magnetic field of the fundamental mode, from microstrip resonators forms a loop around the ribbons. As a result, SRRs must be placed along the axis of propagation perpendicular to the tape drivers to

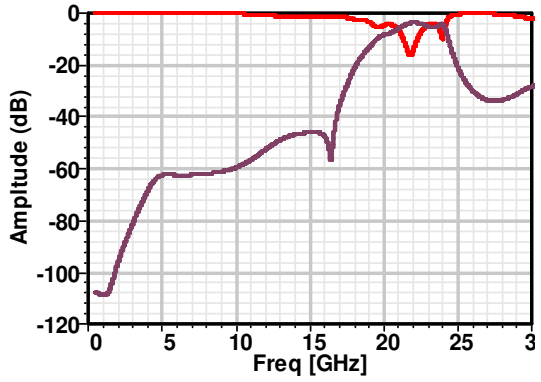


(a)

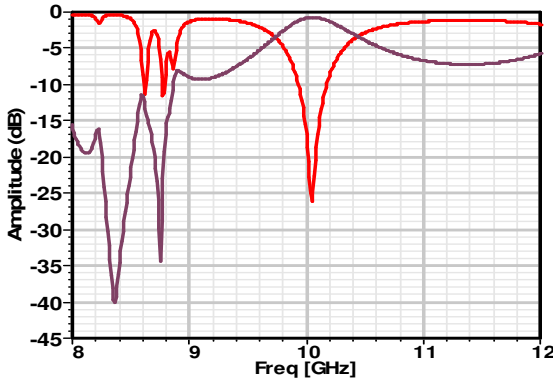


(b)

Figure 4. (a) Pass-band filter using microstrip resonator. (b) Associated SRRs to microstrip resonator



(a)



(b)

Figure 5. (a) Transmission and Reflection Coefficients for pass band filter without SRRs, (b) Transmission and reflection Coefficients for band pass filter using SRRs.

ensure good magnetic coupling. The type of substrate used for SRRs is the same as for the bandpass filter in Figure 4.(a), in other words the RO4003C having a relative permittivity of 3.38, tangential loss of 0.0027, a thickness of 0.81 mm, a height of 3.63 mm, a length of 25.41 mm, a copper layer on each side of 35µm thickness and periodicity of elements is 3.63 mm.

The guide shaped shield has a cross section of 4, 475 × 10 mm2. This shielding reduces the insertion loss of the structure by creating a capacitive effect. As the dimensions of SRRs were calculated for a resonance X-band [8.2 GHz, 12.4 GHz], simulation results (figure 5.(b) show behavior bandpass centered around 10 GHz instead of 22 GHz (figure 5.(a)) with a bandwidth of 0.3 GHz.

CONCLUSION

This part is devoted; on the one hand to the study of Split Ring Resonator and their application in bandpass filter on the other hand. The structure of microstrip resonators used is coupled with capacitive gaps to obtain a bandpass filter. The most interesting area to us is the band offset being below the bandwidth, where we have the resonance of SRRs. By combining the SRRs microstrip resonators and the use of an electrically shielded, we would have transmission in the evanescent field of microstrip resonators. This study shows that it is possible to lower the center frequency of a bandpass filter in combination with SRRs.

REFERENCES

[1] J. B. Pendry, “Negative refraction makes a perfect lens”, Physical Review Letters, vol. 85, no.18, pp. 3966–3969, October 2000.

[2] D. R. Smith and N. Kroll, “Negative refractive index in left-handed materials”, Physical Review Letters, vol. 85, no. 14, pp. 2933–2936, October 2000.

[3] D. R. Smith, D. C. Vier, N. Kroll, and S. Schultz, “Determination of effective permittivity and permeability of metamaterials from reflection and transmission coefficients”, Physical Review B,vol. 65, no. 19, April 2002.

[4] V. G. Veselago, “The electrodynamics of substances with simultaneously negative values of ε and µ”, Soviet Physics USPEKHI, vol. 10, no. 14, pp. 509–514, January-February 1968.

[5] J. B. Pendry, A. J. Holden, D. J. Robbins, and W. J. Stewart, “Magnetism from conductors and enhanced nonlinear phenomena”, IEEE Transactions on Microwave Theory and Techniques, vol.47, no. 11, pp. 2075–2084, November 1999.

[6] S. N. Burokur, M. Latrach, and S. Toutain, “Split Ring Resonators and Slot Split Ring Resonators: Influence on microstrip line transmission and possible applications”, in 11th International Symposium on Antenna Technology and Applied Electromagnetics, St-Malo, June 2005.

Unidirectional Amplification and Shaping of Optical Pulses by Three-Wave Mixing with Negative Phonons

Alexander K. Popov[1*], Mikhail I. Shalaev[2], Sergey A. Myslivets[3], and Vitaly V. Slabko[2]

[1]University of Wisconsin-Stevens Point, Stevens Point, WI 54481, USA
[2]Siberian Federal University, 660041 Krasnoyarsk, Russian Federation
[3]Institute of Physics of Russian Academy of Sciences, 660036 Krasnoyarsk, Russian Federation
*corresponding author, E-mail: apopov@uwsp.edu

Abstract

A possibility to greatly enhance frequency-conversion efficiency of stimulated Raman scattering is shown by making use of extraordinary properties of three-wave mixing of ordinary and backward waves. Such processes are commonly attributed to negative-index plasmonic metamaterials. This work demonstrates the possibility to replace such metamaterials that are very challenging to engineer by readily available crystals which support elastic waves with contra-directed phase and group velocities. The main goal of this work is to investigate specific properties of indicated nonlinear optical process in short pulse regime and to show that it enables elimination of fundamental detrimental effect of fast damping of optical phonons on the process concerned. Among the applications is the possibility of creation of a family of unique photonic devices such as unidirectional Raman amplifiers and femtosecond pulse shapers with greatly improved operational properties.

1. Introduction

Extraordinary features of coherent nonlinear optical NLO energy conversion processes in negative-index metamaterials (NIMs) that stem from wave-mixing of ordinary and backward electromagnetic waves (BEMW) and the possibilities to apply them for compensating optical losses have been investigated in [1–10]. Essentially different properties of three-wave mixing (TWM) and four-wave mixing processes on one hand and second harmonic and third harmonic generation have been revealed in [1, 11–18]. Ultimately, it was shown that NLO propagation processes that involve BW enable a great enhancement of energy-conversion rate at otherwise equal nonlinearities and intensities of input waves. A review can be found in [11, 12].

In [19], three-wave mixing (TWM) of continuous waves (CW) was investigated in the scheme of stimulated Raman scattering (SRS) as an analog of parametric interaction of waves in a medium with negative dispersion. Two of the coupled waves were ordinary electromagnetic waves and the third one was backward elastic wave corresponding to optical phonons which exhibit negative dispersion $d\omega_v(k)/dk$. The latter gives rise to contra-directed group and phase velocities of propagation of lattice vibrations, i.e. backward elastic waves. Such waves exist in crystals containing more than one atom per unit cell. Indeed, backwardness is a main property of EM waves propagating in NIMs. Such BWs were predicted by L. I. Mandelstam in 1945 [20], who also had pointed out that negative refraction is a general property of the BWs. Optical phonons with wave vector much smaller than the reciprocal lattice vector have been considered in [19]. The focus was placed on a coupling scheme where the fundamental radiation was converted to co-propagating Stokes and contra-propagating vibrational waves under the phase-matched conditions. The possibility of the extraordinary SRS was shown, which is typical for TWM whereas one of the coupled waves possesses negative dispersion [1, 2]. The latter results in gain of the Stokes component along the medium much greater than the exponential growth [21].

The basic idea underlying the proposed concept is as follows. The dispersion curve $\omega(k)$ for optical phonons is

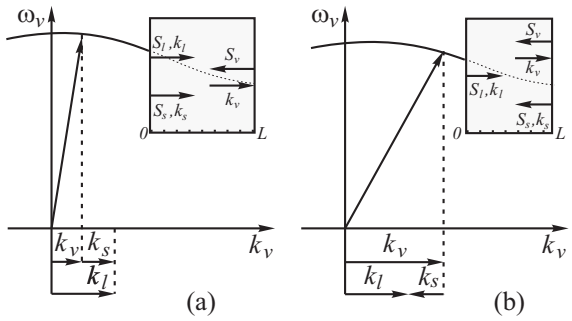


Figure 1: Negative dispersion of optical phonons and two phase matching options for short- and long-wave vibrations: (a) – co-propagating, (b) – contra-propagating fundamental, control, and Stokes, signal, waves. Insets: relative directions of the energy flows and the wave-vectors.

depicted in Fig. 1. It is negative in the range from zero to the boundary of the first Brillouin's zone. Hence, the group velocity of such phonons, $\mathbf{v}_v^{gr}$, is antiparallel with respect to its wave-vector, $\mathbf{k}_v^{ph}$, and phase velocity, $\mathbf{v}_v^{ph}$, because

$$\mathbf{S} = \mathbf{v}_g U, \quad \mathbf{v}_g = (\mathbf{k}/k)[\partial\omega/\partial k], \quad \partial\omega(k)/\partial k < 0. \quad (1)$$

Optical vibrations can be excited by the light waves due to the two-photon (Raman) scattering. The latter gives

the ground to consider such a crystal as the analog of the medium with negative refractive index at the phonon frequency and to employ the processes of parametric interaction of three waves, two of which are ordinary EM waves and the third is the wave of elastic vibrations with the directions of the energy flow and of the wave-vector opposite to each other. For continuous wave SRS in the coupling geometry depicted in Fig. 1(a) and diamond crystal, estimates made in [19] have shown that the minimum intensity of the fundamental field $I_{\min}$, required to reach the aforementioned extraordinary Raman amplification is on the order of $I_{\min} \sim 10^{18}$ W/cm^2, which exceeds optical breakdown threshold. The main process that determines such a high intensity is fast phonon damping, which is characterized by the optical phonon relaxation rate on the order of $\tau_v = 6 \cdot 10^{-12}$ s, and relatively small group velocity of the elastic oscillation $v_v \sim 10^2 \div 10^3$ cm/s for optical phonons with small optical wave vectors [22, 23]. Diamond is a representative of a wide class of transparent crystals which support optical phonons [22–26].

The *goal of this work* is to show that this seemingly formidable obstacle can be removed and the threshold intensity of the fundamental field $I_{\min}$ required to realize such extraordinary coupling can be significantly reduced. It is possible by making use of short laser pulses with duration τ_p less then the lifetime of the vibrational oscillation of τ_v. Some of the properties of the output fundamental and Stokes pulses, such as duration and pulse shape are investigated.

2. Equations and model

Consider lowest-order SRS process [27, 28]. The waves are given by equations

$$E_{l,s} = (1/2)\varepsilon_{l,s}(z,t)e^{ik_{l,s}z - i\omega_{l,s}t} + c.c., \quad (2)$$

$$Q_v = (1/2)Q(z,t)e^{ik_v z - i\omega_v t} + c.c. \quad (3)$$

Here, $\varepsilon_{l,s}$, Q, $\omega_{l,s,v}$ and $k_{l,s,v}$ are the amplitudes, frequencies and wave-vectors of the fundamental, Stokes and vibrational waves; $Q_v(z,t) = \sqrt{\rho}x(z,t)$; x is displacement of the vibrating particles, ρ is the medium density. With account for the frequency and phase matching exppressions,

$$\omega_l = \omega_s + \omega_v\,(k_v)\,, \quad \vec{k}_l = \vec{k}_s\,(\omega_s) + \vec{k}_v,$$

one obtains following partial differential equations for the slowly varying amplitudes in the approximation of the of first order of Q in the polarization expansion:

$$\begin{aligned} \frac{\partial \mathcal{E}_l}{\partial z} + \frac{1}{v_l}\frac{\partial \mathcal{E}_l}{\partial t} &= i\frac{\pi\omega_l^2}{k_l c^2} N \frac{\partial \alpha}{\partial Q}\mathcal{E}_s Q \\ \frac{\partial \mathcal{E}_s}{\partial z} + \frac{1}{v_s}\frac{\partial \mathcal{E}_s}{\partial t} &= i\frac{\pi\omega_s^2}{k_s c^2} N \frac{\partial \alpha}{\partial Q}\mathcal{E}_l Q * \\ \frac{\partial Q}{\partial z} + \frac{1}{v_v}\frac{\partial Q}{\partial t} + \frac{Q}{l_v} &= i\frac{1}{4\omega_v v_v} N \frac{\partial \alpha}{\partial Q}\mathcal{E}_l \mathcal{E}_s^*. \end{aligned} \quad (4)$$

Here, $v_{l,s,v}$ are the projections of the group velocities of the fundamental, Stokes and vibration waves on the z-axis, N is the number density of the vibrating molecules, α is the molecule polarizability, $l_v = \tau_v v_v$ is the mean free path of phonons.

For the sake of simplicity, we consider model of a rectangular pulse of input fundamental radiation with duration much shorter that the phonon lifetime τ_v. In the coordinate frame associated with this pulse and within the fundamental pulse range, complex amplitudes of two other interacting fields become time independent, and Eqs. (4) transform into set of ordinary differential equations whose solution is known in the approximation of constant pump amplitude or can be relatively easily found numerically when depletion of the pump is accounted for. Here, the boundary conditions must be fulfilled not at the boundaries of the medium but at the boundaries of the fundamental pulse. The latter is correct for the period of time after the instant when generated waves reach the boundaries of the fundamental pulse due to the difference in their group velocities or direction of propagation. Such approximation becomes true after travailing a distance $l > L_g^{\max}$, where $L_g^{\max} = \max\{L_g^s, L_g^v\}$. Here, $L_g^{s,v}$, which is further referred to as group length, is defined as

$$L_g = \tau_p v_l^2/|v_{s,v} - v_l|, \quad (5)$$

where $v_{s,v}$ are negative if their energy fluxes are opposite to that of the fundamental wave. Hereinafter, the waves are referred to as co-propagating waves if Poynting vector of the Stokes wave is co-directed with that of fundamental wave (Fig. 1a), and as counter-propagating in the opposite case (Fig. 1b). In the approximation of constant pump amplitude, in the coordinate frame locked to the pump pulse and within the pulse, equations for generated Stokes and backward vibration waves take the form:

$$\begin{aligned} d\,Q/d\xi &= -ig_v\mathcal{E}_s^* - QK_v/l_v \\ d\,\mathcal{E}_s/d\xi &= ig_s Q^*, \end{aligned} \quad (6)$$

where $g_v = -K_v N(d\alpha/dQ)\mathcal{E}_l/(4\omega_v v_v)$, $K_{v,s} = v_{v,s}/(v_{v,s} - v_l)$, $g_s = K_s N(d\alpha/dQ)\mathcal{E}_l \pi\omega_s^2/(k_s c^2)$. Here, intensity of the laser beam is taken constant. Depletion of the fundamental beam is neglected. Equations (6) may describe significant amplification of the Stokes signal, however they remain valid until only relatively small part of the strong input laser beam is converted. Equations (6) do not depend on time and are similar to those describing CW TWM [19]. Here, group velocities $v_v < 0$, $v_s > 0$ and wave vector $k_s > 0$ for co-propagating and $v_s < 0$, $k_s < 0$ for counter-propagating phase matching configurations. Since the Stokes frequency is less than that of the fundamental one, $v_s > v_l$ and is much greater than the magnitude of phonon group velocity v_v.In the case of co-directed laser and Stokes waves, the boundary conditions take the form:

$$\mathcal{E}_s(\xi = 0) = \mathcal{E}_s^0, \quad Q(\xi = l_p) = 0. \quad (7)$$

In the opposite case of counter-propagating Stokes and laser waves, the boundary conditions are given by equations

$$\mathcal{E}_s(\xi = l_p) = \mathcal{E}_s^{l_p}, \quad Q(\xi = l_p) = 0. \quad (8)$$

Here, $l_p = \tau_p v_l$ is length of the fundamental pulse.

Solution to Eqs. (6) can be presented in the form:

$$T_s^{\uparrow\uparrow} = \left| \frac{e^{\gamma' \xi'} \{R_1 \cos Z + \gamma' \sin Z\}}{R_1 \cos(R_1) + \gamma' \sin(R_1)} \right|^2,$$
$$T_s^{\uparrow\downarrow} = \left| \frac{\beta_1 e^{\beta_2 (1-\xi')} - \beta_2 e^{\beta_1 (1-\xi')}}{2R_2} \right|^2. \quad (9)$$

Here, $T_s^{\uparrow\uparrow} = \left|\mathcal{E}_s(\xi)/\mathcal{E}_s^0\right|^2$ and $T_s^{\uparrow\downarrow} = \left|\mathcal{E}_s(\xi)/\mathcal{E}_s^{l_p}\right|^2$ are transparency (amplification) factors, $\gamma' = \gamma l_p$, $\gamma = -K_v/(2l_v)$, $R_{1,2} = \sqrt{g'^2 \mp \gamma'^2}$, $Z = R_1(1-\xi')$, $\xi' = \xi/l_p$, $\beta_{1,2} = \gamma \pm R_2$, $g' = g l_p$, $g = \sqrt{g_v^* g_s}$.

For $\gamma \ll g$, phonon damping can be neglected and Eqs. (9) take the form

$$T_s^{\uparrow\uparrow} = \left| \frac{\cos[g l_p (1-\xi')]}{\cos(g l_p)} \right|^2,$$
$$T_s^{\uparrow\downarrow} = \left| \left[e^{g l_p (1-\xi')} + e^{-g l_p (1-\xi')} \right] /2 \right|^2. \quad (10)$$

3. Enhancing coherent energy transfer between electromagnetic waves through backward optical phonons

In the given approximation of neglected depletion of the fundamental wave, solution to Eq. (10) tends to infinity for certain pulse length and intensity. This indicates the possibility to greatly enhance the conversion efficiency provided that the following requirements are met:

$$\cos(g l_p) = 0; \quad l_p = (\pi/2)/\sqrt{g_v^* g_s} \quad (11)$$

Corresponding threshold intensity of the fundamental field $I_{\min}^p$, which is required for realization of great enhancement of energy conversion due to NLO coupling with BW phonon, is given by equations:

$$g > \gamma, \quad I_{\min}^p = \frac{K_v}{K_s} \frac{c n_s \lambda_{s0} \omega_v}{16\pi^3 v_v \tau_v^2} \left| N \frac{\partial \alpha}{\partial Q} \right|^{-2} \quad (12)$$

Here, n_s is refractive index at Stokes frequency, λ_{s0} is Stokes wavelength in the vacuum.

3.1. Factors discriminating BW SRS in continuous wave and pulsed regimes

Threshold intensity of fundamental radiation required for realization of BW SRS in CW regime is given by [19]

$$I_{\min} = \left(c n_s \lambda_{s0} \omega_v / 8\pi^3 l_p \tau \right) |N \partial\alpha/\partial Q|^{-2}. \quad (13)$$

It differs from the threshold value in pulse regime by factor

$$\frac{I_{\min}^p}{I_{\min}} = -\frac{K_v}{K_s} \approx -\frac{v_v}{v_l} \frac{v_s - v_l}{v_s}. \quad (14)$$

For the same typical crystal parameters as employed in [19], Eq. (14) yields $I_{\min}^p / I_{\min} \approx 10^{-11}$. Hence, $I_{\min}^p$ decreases down to $I_{\min}^p \sim 10^7$ W/cm^2, which is achievable with commercial femtosecond lasers and falls below optical breakdown threshold for most transparent crystals.

Equation (14) displays two factors that determine substantial decrease of $I_{\min}^p$ in pulsed regime compared to that in CW one. First factor is ratio of phonon group velocity to fundamental pulse velocity $-v_v/v_l$ which is of the order of $\sim 10^{-8}$. This factor is attributed to the fact that phonons generated in the front edge of the laser pulse propagate in opposite direction and hence exit from the fundamental pulse area very fast, practically with the optical group velocity. Hence, effective phonon mean free pass becomes commensurable with the fundamental pulse length, which mitigates detrimental effect of phonon damping. Second factor in Eq. (14) that determines substantial decrease in $I_{\min}^p$ is due to small optical dispersion in the transparency region of the crystal. Hence, Stokes pulse surpasses slowly the fundamental one, which also increases NLO coupling length.

3.2. Numerical simulations, $\tau_p \ll \tau_v$.

Numerical analysis is done for the model with parameters typical for diamond crystal [22, 23]: carrying wavelength of the fundamental pulse $\lambda = 800$ nm, pulse duration $\tau_p = 60$ fs, $\omega_v = 1332$ cm^{-1}, vibrational transition width $(c\tau_v)^{-1} = 1.56$ cm^{-1}, $v_l = 1.228 \cdot 10^{10}$ cm/s, $v_s = 1.234 \cdot 10^{10}$ cm/s, $v_v = 100$ cm/s for co-propagating and $v_v = 2000$ cm/s for counter-propagating waves, $N d\alpha/dQ = 3.78 \cdot 10^7$ (g/cm)$^{1/2}$. Partial differential equations (4) were solved numerically in three steps: TWM in the vicinity of the entrance to the Raman medium, TWM and propagation through the medium and TWM in the vicinity of the exit from the Raman slab. Numerical simulation for the first and third medium intervals were made in the laboratory reference frame with the boundary conditions applied to the corresponding edges of the slab. NLO propagation process inside the slab was simulated in the moving frame of reference with the boundary conditions applied to the pulse edges. Such a computing approach allows for significant reduction of the computation time since, for each given instant, integration is required only through a space interval covered by the fundamental pulse and not through the entire medium. Shape of the fundamental pulse was chosen nearly rectangular and symmetric with respect to its center

$$\mathcal{E}_l = \frac{1}{2} \mathcal{E}_l^0 \{\tanh[(t_0 + t_p - t)/t_f] - \tanh[(t_0 - t)/t_f]\},$$

the slope $t_f = 0.1$, the pulse duration at half-maximum $t_p = 1$ and pulse delay $t_0 = 0.6$ were scaled to the fundamental pulse width τ_p. The amplitude of input CW Stokes signal was chosen $\mathcal{E}_s^0 = 10^{-5} \mathcal{E}_l^0$.

Figure 2 displays output quantum conversion efficiency $\eta_{sq} = (\omega_l/\omega_s) \cdot \int_t I_s(z,t) dt / \int_t I_l(z=0,t) dt$ vs. input pulse intensity (the same as vs. input pulse energy) both for co-propagating ($z = L$) and counter-propagating ($z = 0$) geometries. A great increase of the conversion efficiency due to BW effect in the case of co-propagating waves is

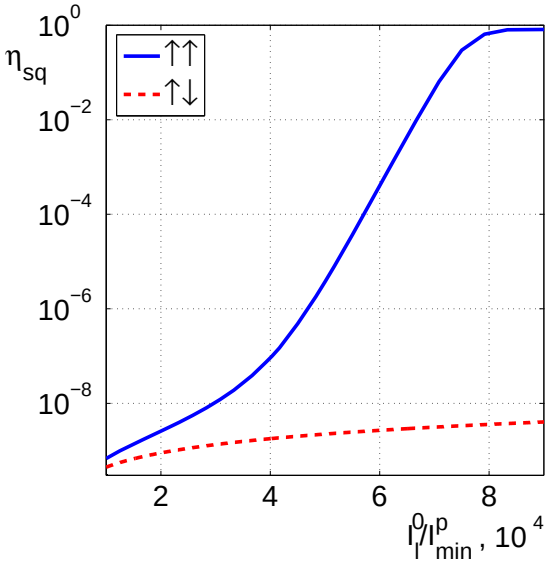


Figure 2: Quantum conversion efficiency vs. intensity (energy) of the input pulses for co-propagating and contra-propagating phase matching geometries.

explicitly seen. Saturation at $I_l^0/I_{min}^p \approx 7 \cdot 10^4$ is due to depletion of fundamental radiation caused by conversion to Stokes radiation.

Simulations also show that shape of the output Stokes and fundamental pulses differ and vary significantly depending on the intensity of the input fundamental wave. Input seeding signal at Stokes frequency is assumed a weak CW broadband radiation. Figure 3 depicts amplified output pulse $T_s = \left|\mathcal{E}_s(L,t)/\mathcal{E}_s^0\right|^2$ of Stokes radiation for relatively small amplification of the signal and small depletion of the fundamental beam. Here, shape of the fundamental pulse remains unchanged. Pulse shape of amplified Stokes signal is different and determined by the fact that $v_s > v_l$ and Stokes pulse surpasses fundamental one. In contrast, at $I_l^0/I_{min}^p = 8.3 \times 10^4$ and $I_l^0/I_{min}^p = 1.67 \times 10^5$ (Figs. 4a,b), conversion efficiency becomes significant ($\eta_q = 0.8$ and $\eta_q = 0.93$, respectively). Corresponding depletion of the output fundamental pulse and changes in its shape is explicitly seen. Note that in the case shown in Fig. 4(b), the output Stokes pulse significantly overtakes the pump pulse. In the latter case, major conversion occurs in the middle of the medium, after which both pulses propagate almost without interacting and inde-

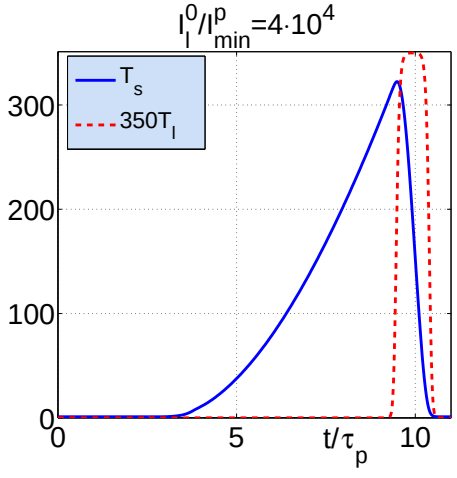


Figure 3: Pulse shape of amplified Stokes radiation at the exit of crystal of length L = 1 cm, $T_s = \left|\mathcal{E}_s(L,t)/\mathcal{E}_s^0\right|^2$ (solid line). Pulse shape of the output fundamental pulse $T_l = \left|\mathcal{E}_l(L,t)/\mathcal{E}_l^0\right|^2$ is depicted by dashed line. Here, $I_l^0/I_{min}^p = 4 \times 10^4$.

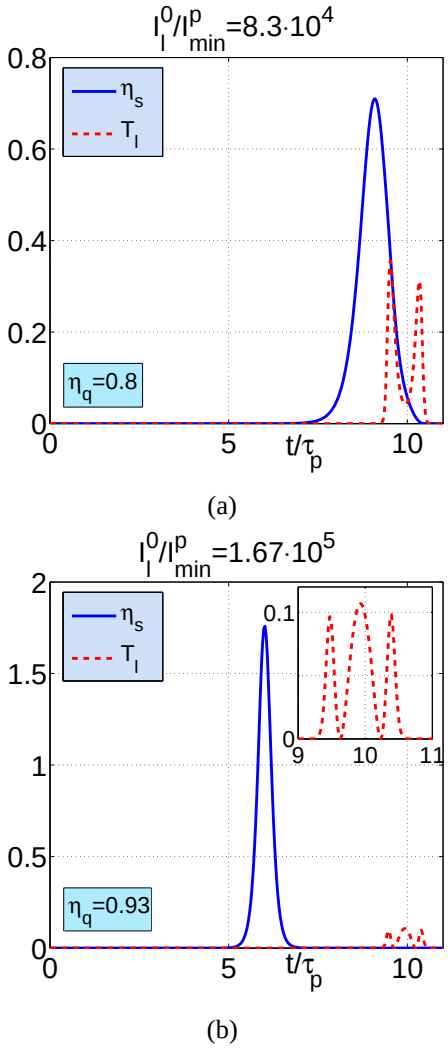


Figure 4: Pulse shape of amplified Stokes radiation (solid line) and of transmitted fundamental radiation (dashed line) at the exit of crystal of L = 1 cm. $\eta_s = (\omega_l/\omega_s) \cdot \left|\mathcal{E}_s(L,t)/\mathcal{E}_l^0\right|^2$ is conversion efficiency, $T_l = \left|\mathcal{E}_l(L,t)/\mathcal{E}_l^0\right|^2$ is transmittance. a. $I_l^0/I_{min}^p = 8.3 \times 10^4$. b. $I_l^0/I_{min}^p = 1.67 \times 10^5$

pendently from each other. It is seen that output Stokes pulse narrows with increase of the input fundamental intensity. Here, crystal length of 1cm corresponds to more than 1000 input pulse lengths ($T/t_p = L/L_p$ = 1357). Threshold intensity $I^p_{min} = 6 \cdot 10^6$ W/cm^2, which corresponds to 60 fs pulse of 5 μJ focused to the spot of diameter D = 100 μm. Intensity of seeding Stokes signal was chosen $I^0_s/I^0_l = 10^{-10}$.

Described NLO propagation processes are in striking contrast with their counterparts in crystals where only phonons with positive group velocity exist [27, 28]. Such NLO properties are also different from those inherent to phase-matched mixing of EM and acoustic waves for the cases where the latter have energy flux and wave vector directed against EM waves [21]. Elaboration of the proposed concept allows to utilize revealed extraordinary features for creation of a family of unique photonic devices made of ordinary Raman crystals such as optical switches, filters, amplifiers and cavity-free optical parametric oscillators. Proposed here concept is different from earlier proposed in [29] and does not require periodic poling of quadratic nonlinear susceptibility of crystals at the nanoscale as described in [30] (and references therein).

4. Conclusions

While the physics and applications of NIMs are being explored world-wide at a rapid pace, current mainstream focuses on fabrication of specially shaped nanostructures which enable negative optical magnetism. It is challenging task that relies on sophisticated methods of nanotechnology. Engineering a strong fast quadratic NLO response by such mesoatoms also presents a challenging goal not yet achieved. This paper proposes to mimic similar extraordinary backward-wave extraordinary nonlinear-optical propagation processes, however, making use readily available Raman active crystals. Among the prospective application is a family of photonic devices with advanced functional properties. Basic underpinning idea is to replace one of the coupled backward electromagnetic wave by optical phonons - elastic waves with negative group velocity.Operation in short pulse regime is proposed to remove such a severe detrimental factor as fast phonon damping. Significant decrease of the required minimum intensity of fundamental radiation compared with that in continuous-wave regime is shown down to that provided by commercial lasers. Unusual properties of the investigated processes are numerically simulated and the possibilities of pulse shape tailoring are predicted. There are many Raman active transparent crystals that support optical phonons with negative group velocity can be utilized, some of them, such as calcite, may offer further optimization of operational characteristics of the proposed photonic devices.

Acknowledgement

This work was supported in parts by the by the US AFOSR under Grant No FA950-12-1-298, by the US National Science Foundation under Grant No ECCS-1028353 and by the Russian Federal Program on Science, Education and Innovation under Grant No 14.A18.21.1942.

References

[1] A. K. Popov and V. M. Shalaev, Negative-index metamaterials: second-harmonic generation, Manley Rowe relations and parametric amplification, *Applied Physics B: Lasers and Optics* 84: 131-137, 2006.

[2] A. K. Popov and V. M. Shalaev, Compensating losses in negative-index metamaterials by optical parametric amplification, *Opt. Lett.* 31: 2169–2171, 2006.

[3] A. K. Popov, S. A. Myslivets, T. F. George, and V. M. Shalaev, Four–wave mixing, quantum control, and compensating losses in doped negative-index photonic metamaterials," *Opt. Lett.* 32: 3044–3046, 2007.

[4] A. K. Popov and S. A. Myslivets, Transformable broad-band transparency and amplification in negative-index films, *Applied Physics Letters* 93: 191117(3), 2008.

[5] A. K. Popov, S. A. Myslivets, and V. M. Shalaev, Resonant nonlinear optics of backward waves in negative-index metamaterials, *Applied Physics B: Lasers and Optics* 96: 315–323, 2009.

[6] A. K. Popov, S. A. Myslivets, and V. M. Shalaev, Microscopic mirrorless negative-index optical parametric oscillator, *Opt. Lett.* 34: 1165–1167, 2009.

[7] A. K. Popov, S. A. Myslivets and V.M. Shalaev, Plasmonics: nonlinear optics, negative phase and transformable transparency (Invited Paper), in *Plasmonics: Nanoimaging, Nanofabrication, and their Applications V*, edited by Satoshi Kawata, Vladimir M. Shalaev, Din Ping Tsai, *Proc. of SPIE* 7395: 73950Z-1(12), 2009.

[8] A. K. Popov, S. A. Myslivets, and V. M. Shalaev, Coherent nonlinear optics and quantum control in negative-index metamaterials, *J. Opt. A: Pure Appl. Opt.* 11: 114028(13), 2009.

[9] A. K. Popov and S. A. Myslivets, Numerical Simulations of Negative-Index Nanocomposites and Backward-Wave Photonic Microdevices, *"ICMS 2010 : International Conference on Modeling and Simulation," Proc. of WASET* 37: 107–121 2010; `http://www.waset.org/journals/waset/v37/v37-16.pdf`.

[10] A. K. Popov and T. F. George, Computational studies of tailored negative-index metamaterials and microdevices, a chapter in *Computational Studies of New Materials II: From Ultrafast Processes and Nanostructures to Optoelectronics, Energy Storage and Nanomedicine*, Edited by T. F. George, D. Jelski, R. R. Letfullin, and G. Zhang, World Scientific, Singapore, 2011.

[11] A. K. Popov, Nonlinear optics of backward waves and extraordinary features of plasmonic nonlinear-optical microdevices, *Eur. Phys. J. D* 58: 263–274, 2010 (topical issue on Laser Dynamics and Nonlinear Photonics).

[12] A. K. Popov and V. M. Shalaev, "Merging nonlinear optics and negative-index metamaterials," *Proc. SPIE* 8093-06: 1–27, 2011; arXiv:1108.0867.

[13] I. V. Shadrivov, A. A. Zharov, and Yu. S. Kivshar, Second-Harmonic Generation in Nonlinear Left-Handed Metamaterials, *J. Opt. Soc. Am.* B23: 529–534, 2006.

[14] M. Scalora, G. D'Aguanno, M. Bloemer, M. Centini, N. Mattiucci, D. de Ceglia and Yu. S. Kivshar, Dynamics of Short Pulses and Phase Matched Second Harmonic Generation in Negative Index Materials, *Opt. Express*, 14: 4746–4756, 2006.

[15] A. K. Popov, V. V. Slabko, and V. M. Shalaev, Second harmonic generation in left-handed metamaterials, *Laser Phys. Lett.* 3: 293–296, 2006.

[16] A. I. Maimistov and I. R. Gabitov, E. V. Kazantseva, Quadratic solitons in media with negative refractive index, *Opt. Spectrosc.* 102, 90–97 2007.

[17] A. I. Maimistov and I. R. Gabitov, Nonlinear optical effects in artificial materials, *Eur. Phys. J. Special Topics* 147: 265286, 2007

[18] S. O. Elyutin, A. I. Maimistov, and I. R. Gabitov, On the third harmonic generation in a medium with negative pump wave refraction, *JETP* 111: 157–169, 2010.

[19] M. I. Shalaev, S. A. Myslivets, V. V. Slabko and A. K. Popov, "Negative group velocity and three-wave mixing in dielectric crystals, *Optics Lett.* 36: 3861–3863, 2011.

[20] L. I. Mandelstam, Group velocity in a crystall lattice, *ZhETF* 15: 475–478, 1945.

[21] D. L. Bobroff, Coupled-modes analysis of the phonon-photon parametric backward-wave oscillator, *J. Appl. Phys.* 36: 1760–1769, 1965.

[22] E. Anastassakis, S. Iwasa and E. Burstein, Electric-Field-Induced Infrared Absorption In Diamond, *Phys. Rev. Lett.* 17: 1051–1054, 1966.

[23] Y. Chen and J. D. Lee, Determining material constants in micromorphic theory through phonon dispersion relations, *International J. of Engineering Science* 41: 871–886, 2003.

[24] *Light Scattering in Solids*, Ed.M. Cardona, Ch.2 in *Topics in Applied Physics*, vol. 8, Springer-Verlag, Berlin, Heidelderg, NY, 1975.

[25] R. R. Alfano and S. I. Shapiro, Optical Phonon Lifetime Measured Directly with Picosecond Pulses, *Phys. Rev. Lett.* 26: 1247–1251, 1971.

[26] V. S. Gorelik, *Contemporary problems of Raman spectroscopy*, Moscow, Nauka Publishing Co., 1978 in Russian), pp. 28–47.

[27] Y. R. Shen and N. Bloembergen, Theory of stimulated brillouin and raman scattering, *Phys. Rev.* 137: A1787-A1805, 1965.

[28] R. W. Boyd, *Nonlinear Optics*, Third Edition (Amsterdam: Academic Press, 2008.

[27] Sukhorukov A.P., Schadnova A.K. Parametric light amplifiction in modulated field of laser wave, *Zh. Eksp. Teor. Fiz.* 60: 1251–1258, 1971 (in Russian).

[28] Sushchik M.M., Fortus V.M. Freidman G.I. Parametrically-coupled wave imprisonment by pulses and beams of pumping radiation, *Izv. Vyssh. Uchebn. Zaved. Radiofiz.* 12: 293-299, 1969 (in Russian).

[29] S. E. Harris, Proposed backward wave oscillations in the infrared, *Appl. Phys. Lett.* 9: 114–117, 1966.

[30] J. B. Khurgin, Mirrorless magic, *Nat. Photonics* 1: 446–448, 2007 (and ref. therein).

Determination of the effective material parameters of PMMA filled with gold, silver nano-particles for a cylindrical cloak

H. Nadgaran*, M.M. Sadeghi, N. Niakan

Physics Department, Shiraz University, Shiraz 71454, Iran.
*corresponding author, E-mail: nadgaran@susc.ac.ir

Abstract

Permitivity and permeability distribution of a PMMA metamaterial host containing silver and gold nano-particles are calculated at optical frequencies. The effect of the two nanoparticles on the material parameters of the host metamaterial through tunability of the plasmonic interactions between the metallic nano-particles is compared.

1. Introduction

Metamaterials with unusual properties and vast applications are usually inaccessible in nature. They can be fabricated artificially in various structures. Their applications for imaging beyond the diffraction limit [1-6] and realization of negative refractive index materials [7-15] have made them very much attractive in recent years. The key element of these applications returns back to the field of transformation optics [16,17]. Implementation of many interesting features such as invisibility cloaks [16,18,19] and superlenses [20, 21] can be feasible through transformation optics, thanks to invariance of the Maxwell's equations under coordinate transformations. There have been many proposals for the realization of the cylindrical cloak for TM-polarized radiation [22]. In this reference radially elongated metal wires of sub wavelengths dimensions were embedded in a dielectric host material. In such works the most theoretical model which was used is Maxwell-Garnet effective medium theory (MGT) where the interactions between metal particles and plasmon excitations is not taken into account [23,24].

This paper however is devoted to gold spherical nano-particles embedded in a host medium of PMMA in array forms and compares the results with the case of silver nano-particles [25]. Utilizing spherical nano-particles has many advantages compared to nano-wires: for example symmetry of the spherical nano-particles does not necessitate specific orientation of the nano-particles within the host medium.

2. Ideal versus reduced parameter sets

For cylindrical cloaks, using cylindrical coordinate, transformation is given by [25]:

$$r = \left(1 - \frac{a}{b}\right) r' + a \quad \varphi = \varphi' \quad z = z' \tag{1}$$

where a and b are the inner and outer radii of the cloak, r, φ, z and r', φ', z' are the transformed and untransformed coordinates. The results of this transformation are the following material parameters of the cloaking shell [16], called ideal parameters:

$$\varepsilon_r = \mu_r = \frac{r-a}{r} \tag{2}$$

$$\varepsilon_\varphi = \mu_\varphi = \frac{r}{r-a} \tag{3}$$

$$\varepsilon_z = \mu_z = \left(\frac{b}{b-a}\right)^2 \frac{r-a}{r} \tag{4}$$

The dependency of permeability on the distance should be removed somehow to avoid their divergence in the case of r approaches a. This task can be performed through various ways and one of those simple ways to do that is to use polarized incident beam where the magnetic field vector is taken along the z-axis (TM polarization). By utilizing specific polarization similar to one mentioned, the so-called reduced parameter set for cylindrical cloak can be obtained:

$$\varepsilon_r = \left(\frac{b}{b-a}\right)^2 \left(\frac{r-a}{r}\right)^2 \tag{5}$$

$$\varepsilon_\varphi = \left(\frac{b}{b-a}\right)^2 \tag{6}$$

$$\mu_z = 1 \tag{7}$$

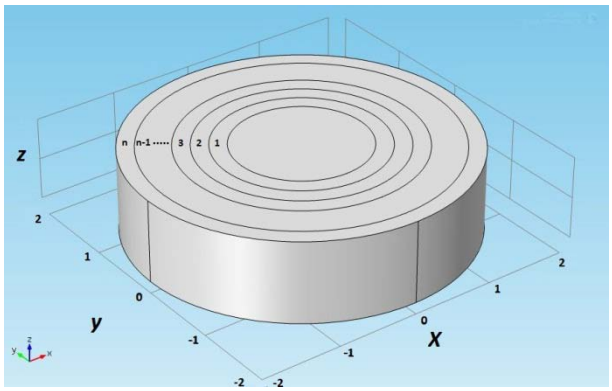


Figure 1: Coaxial cylinder for cylindrical cloak that composed of n shell segment with equal thickness$(b-a)/n$.

Ideal and reduced parameter sets are also called continuous-ideal and continuous-reduced parameters and the reason behind this nomenclature is that the cylindrical cloak is considered as a continuum based material as a whole. On the other hand a set of discrete-reduced parameters is usually defined in the literature and that refers to a set of parameters when the cloak material is assumed to be composed of n cylindrical layers of equal thickness$(b-a)/n$. The permittivity values of each layer were calculated in the middle of each layer and it is kept constant within the layer (Fig.1).

3. Simulation method

The procedure and all parameter values in this work has been taken from reference [25] except that they have calculated the effective material parameters of PMMA containing nano-silver particles while our work is devoted to the case when nano-gold particles are embedded in PMMA. The main purpose of our work is to compare the values of the PMMA material parameters for both cases and to see the effect of the plasmonic excitations in each case. CST commercial software were employed to obtain reflection and transmission coefficients S_{11} and S_{21} . PMMA permittivity was taken to 2.25. The nano-particle diameter was assumed to be 12nm. The gold nano-particles were assumed to being in the middle of rectangle unit cells and the unit cells are exposed to two different TM-polarized light propagating in the k direction as shown in the Figure (2).

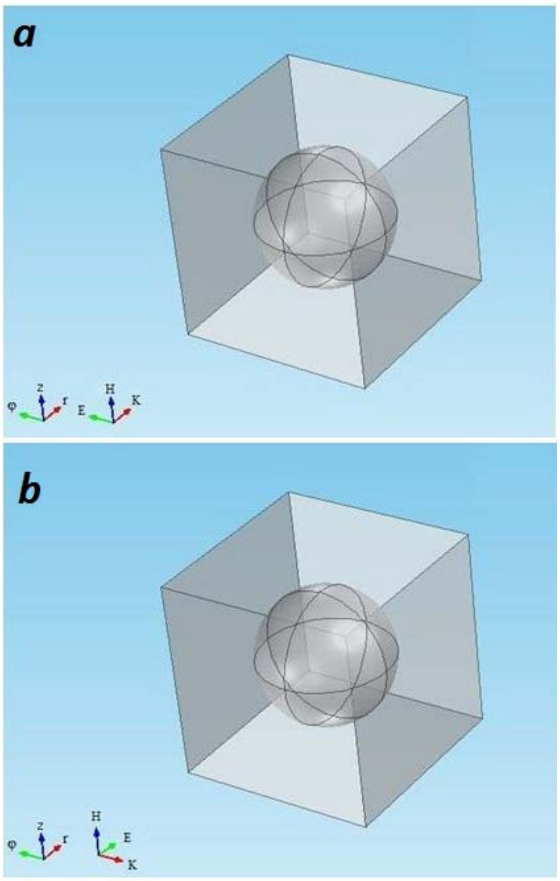


Figure 2: Unit cell with its dimension(l_r, l_φ, l_z) with a gold nano sphere in the center of unit cell (a) unit cell irradiated by a TM-polarized electromagnetic wave in k direction, incident along the r-direction and (b) incident along φ-direction.

4. S_{21} and ε_r

Figures (3) and (4) show the work of Diedrich *et al* [25] for the case of nano-silver and our work for the case of nano-gold, respectively. Close inspection of the two figures for the absolute value of $|S_{21}|$ (transmission) shows that the range of frequency working for nano-silver case is higher and broader whereas this range for nano-gold case tends toward lower frequencies that is one may conclude that nano-gold particles embedded in PMMA makes the cloak suitable for infrared regimes that is longer wavelengths and pushes the frequency range out of visible regime. Figure (3) and (4) also show that the direction of the shift of the value of S_{21} and ε_r toward higher frequencies by increasing l_r is the same. Moreover, the second branch occurring for the smallest value of l_r which was seen in the nano-silver case is also appeared in the nano-gold case except that its intensity is lower than that of the silver case. As the two branches are related to plasmonic resonances of the nano-particle metals, one can conclude that at least in the frequency vicinity of the second branch, the plasmonic resonance of nano-gold case is weak and cannot be well exploited if good cloaking is desired.

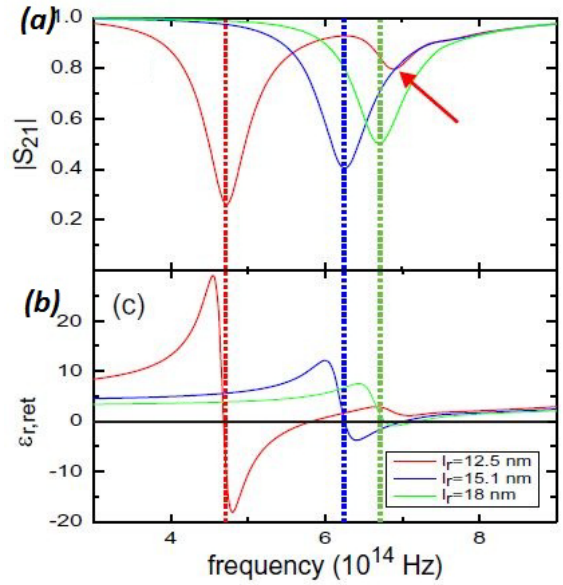


Figure 3: (a) Magnitude of transmission coefficient for silver nano-particle versus frequency for different size of unit cell in r-direction. Red curve shows $|S_{12}|$ with $l_r = 12.5nm$. Diameter of sphere is 12nm. Blue curve shows $|S_{12}|$ with $l_r = 15.1nm$ and green curve shows $|S_{12}|$ with $l_r = 18nm$ (b) Retrieved radial permittivity corresponding to values of S_{21} above.

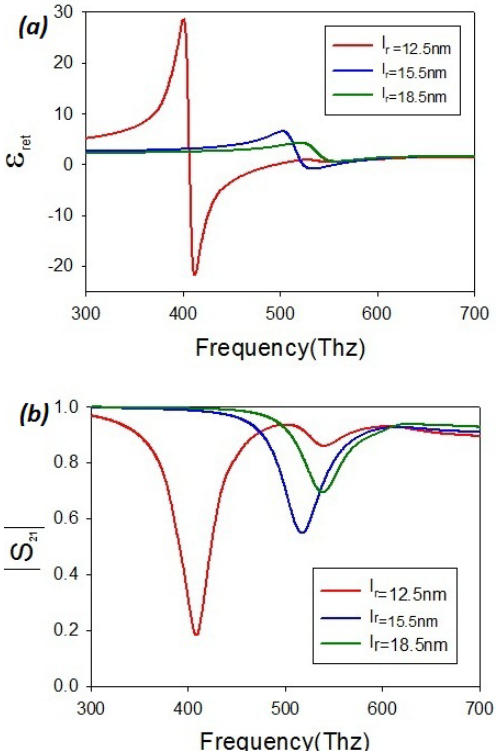


Figure 4: (a) Retrieved radial permittivity corresponding to values of S_{21}. (b) Magnitude of transmission coefficient for gold nano-particle versus frequency for different size of unit cell in r-direction. Red curve shows $|S_{12}|$ with $l_r = 12.5nm$. Diameter of sphere is 12nm. Blue curve shows $|S_{12}|$ with $l_r = 15.1nm$ and green curve shows $|S_{12}|$ with $l_r = 18nm$

5. Cloak

Figures (5) and (6) show the quality of cloak and the component of E_y for the two cases of nano-silver and nano-gold. The figures show that the cloak as a result of the ideal parameter set is almost the same for both cases. The cloak coming out of continuous-reduced parameter set is better for the nano-silver case than that of the nano-gold case. The comparison of the cloak for the discrete-reduced parameter set for the two cases shows that it is getting worse for the nano-gold case, so that one cannot safely recommend nano-gold particles embedded in PMMA for the optical frequency cloak.

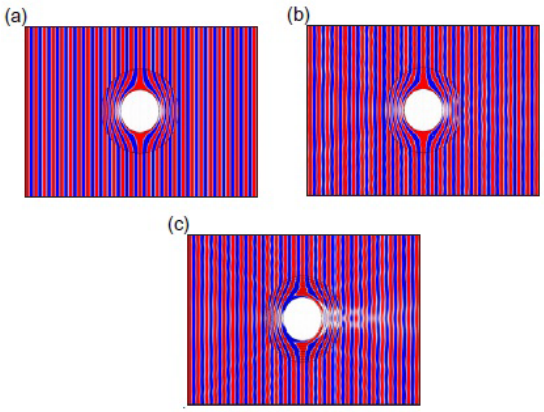


Figure 5: TM-polarized plane wave of frequency $f = 6.65 \times 10^{14} Hz$ irradiating the cloak device with (a) continuous-ideal materials (b) Reduced-continuous materials (c) Discrete-reduced materials

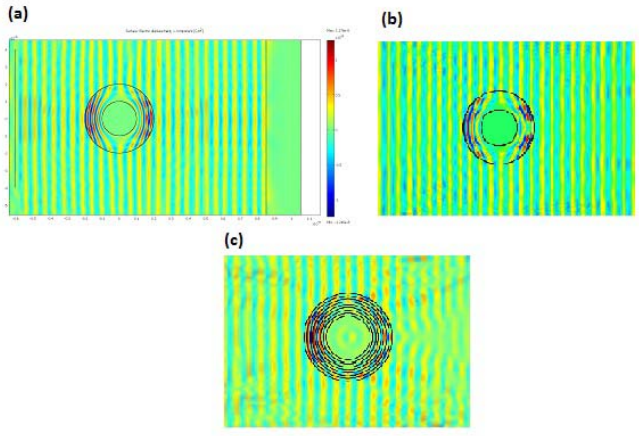


Figure 6: TM-polarized plane wave of frequency $f = 5.23 \times 10^{14} Hz$ irradiating the cloak device with (a) continuous-ideal materials (b) Reduced-continuous materials (c) Discrete-reduced materials

6. Radial and tangential permittivity

Based on the discrete-reduced cloak composed of $n = 8\ layers$, Table (1) shows the calculated radial and tangential permittivity values. This table can be compared with Table (2) of reference [25] which is for the case of nano-silver. The comparison shows that 1) the range of l_r for the case of nano-gold is shorter than that of nano-silver and this makes the nano-gold experimental work harder. Also, the change of filling factor (t, the last column of tables) is almost the same for both cases which points out that good cloaking for both cases from filling factor point of view has the same difficulties.

Table 1: Radial and tangential permittivity value for discrete , reduced cloak in PMMA medium filled with golden nanoparticle. $l_\varphi = 21nm\ and\ l_z = 20nm\ are\ constant$

Layer	ε_r	ε_r^{ret}	ε_φ	$\varepsilon_\varphi^{ret}$	l_r	t
1	0.0138	0.933	4.09	4.085	12.504	0.172
2	0.099	0.802	4.09	4.087	12.545	0.172
3	0.226	0.669	4.09	4.088	12.590	0.171
4	0.370	0.517	4.09	4.087	12.645	0.171
5	0.518	0.347	4.09	4.087	12.700	0.170
6	0.663	0.230	4.09	4.089	12.760	0.169
7	0.803	0.095	4.09	4.088	12.830	0.168
8	0.937	0.020	4.09	4.086	12.878	0.167

Table 2:Radial and tangential permittivity value for discrete , reduced cloak in PMMA medium filled with silver nanoparticle. $l_\varphi = 28nm\ and\ l_z = 20nm\ are\ constant$

Layer	ε_r	ε_r^{ret}	ε_φ	$\varepsilon_\varphi^{ret}$	l_r	t
1	0.01	0.04	4.09	4.04	13.37	0.12
2	0.01	0.14	4.09	4.07	13.30	0.12
3	0.22	0.23	4.09	4.07	13.13	0.12
4	0.37	0.38	4.09	4.10	12.97	0.12
5	0.52	0.51	4.09	4.10	12.82	0.13
6	0.66	0.67	4.09	4.10	12.74	0.13
7	0.80	0.76	4.09	4.11	12.66	0.13
8	0.94	0.94	4.09	4.15	12.56	0.13

7. Conclusion

We calculated the effective material parameters of PMMA containing nano-silver and nano-gold particles. Although much of the behavior of the material for both cases are similar, one can note that nano-gold cloak tends to have good cloak for frequencies less than optical frequencies and it is mostly suited for infrared regimes and higher wavelengths. Also, we can note the lesser plasmonic resonances of the gold nano-particle case compared with nano-silver one. Calculated radial and tangential permittivity components show that both cases suffer from short range of l_r (distance between nano-particles) and smallness of nano-particle filling factors.

Acknowledgements

H.N thanks the Shiraz University Research council for the support of this work.

References

[1] Pendry J B , Negative refraction makes a perfect lens *Phys. Rev. Lett.* **85** 3966–9,2000
[2] Houck A A, Brock J B and Chuang I L, Experimental observation of a left-handed material that obeysSnell's law *Phys. Rev. Lett.* **90** 13,2003
[3] Grbic A and Eleftheriades G V, Overcoming the diffraction limit with a planar left-handed transmissionlinelens *Phys. Rev. Lett.* **92** 117403,2004
[4] Taubner T, Korobkin D, Urzhumov Y, Shvets G and Hillenbrand R, Near-field microscopy through a SiCsuperlens *Science* **313** 1595 ,2006
[5] Liu Z, Lee H, Xiong Y, Sun C and Zhang X, Far-field optical hyperlens magnifying subdiffractionlimited Objects *Science* **315** 1686,2007
[6] Schwaiger S, Broell M, Krohn A, Stemmann A, Heyn C, Stark Y, Stickler D, Heitmann D and Mendach S, Rolled-up three-dimensional metamaterials with a tunable plasma frequency in the visible regime, *Phys. Rev. Lett.* **102** 163903, 2009
[7] Smith D R, Padilla W J, Vier D C, Nemat-Nasser S C and Schultz S ,Composite medium withsimultaneously negative permeability and permittivity *Phys. Rev. Lett.* **84** 4184–7, 2000
[8] Shelby R A, Smith D R and Schultz S, Experimental verification of a negative index of refraction *Science* **292** 77–9, 2001
[9] Linden S, Enkrich C, Wegener M, Zhou J, Koschny T and Soukoulis C M, Magnetic response ofmetamaterials at 100 terahertz *Science* **306** 1351–3, 2004
[10] Shalaev V M, CaiW, Chettiar U K, Yuan H-K, Sarychev A K, Drachev V P and Kildishev A V, Negative index of refraction in optical materials *Opt. Lett.* **30** 3356–8, 2005
[11] Zhang S, FangW, Panoiu N C, Malloy K J, Osgood R M and Brueck S R J, Experimental demonstrationof near-infrared negative-index metamaterials *Phys. Rev. Lett.* **95** 137404, 2005
[12] Dolling G, Wegener M, Soukoulis C M and Linden S, Negative-index metamaterial at 780 nmwavelength *Opt. Lett.* **32** 53–5, 2007
[13] Valentine J, Zhang S, Zentgraf T, Ulin-Avila E, Genov D A, Bartal G and Zhang X, Three-dimensionaloptical metamaterial with a negative refractive index *Nature* **455** 376, 2008
[14] Xiao S, Chettiar U K, Klidishev A V, Drachev V P and Shalaev W M, Yellow-light negative-indexmetamaterials*Opt. Lett.* **34** 3478–80, 2009
[15] Rottler A, Harland M, Br¨oll M, Schwaiger S, Stickler D, Stemmann A, Heyn C, Heitmann D and Mendach S, Rolled-up nanotechnology for the fabrication of three-dimensional fishnet-type GaAs–metalmetamaterials with negative refractive index at near-infrared frequencies *Appl. Phys. Lett.***100** 151104, 2012
[16] Pendry J B, Schurig D and Smith D R, Controlling electromagnetic fields *Science* **312** 1780–2, 2006
[17] Leonhardt U, Optical conformal mapping *Science* **312** 1777–80, 2006
[18] Cummer S A, Popa B-I, Schurig D, Smith D R and Pendry J B, Full-wave simulations of electromagneticcloaking structures *Phys. Rev*. E **74** 036621, 2006
[19] Schurig D, Pendry J B and Smith D R, Calculation of material properties and ray tracing in transformation media *Opt. Express* **14** 9794–804, 2006
[20] Han S, Xiong Y, Genov D, Liu Z, Bartal G and Zhang X, Ray optics at a deep-subwavelength scale: a transformation optics approach *Nano Lett.* **8** 4243–7
[21] Kildishev A V and Narimanov E E 2007 Impedance-matched hyperlens*Opt. Lett.* **32** 3432–4, 2008
[22] Cai W, Chettiar U K, Kildishev A V and Shalaev V M, Optical cloaking with metamaterials *NaturePhotonics* **1** 224–7, 2007
[23] Riikonen S, Romero I and Garcia de Abajo F J, Plasmon tunability in metallodielectricmetamaterials*Phys. Rev*. B **71** 235104, 2005
[24] Alu A, Yaghjian A D, Shore R A and Silveirinha M G , Causality relations in the homogenization of metamaterials*Phys. Rev.* B **84** 054305, 2011
[25] Diedrich D, Rottler A, Heitmann D and Mendach S,Metal Dielectric metamaterials for transformation optic and gradient index devices in the visible regime, *New Journal of Physics**14** 053042(17pp),2012*

.

Coupled Equation of electromagnetic wave in a nonlinear metamaterial waveguide

Azari. Mina [1], Hatami. Mohsen [1,2]

[1] Atomic and Molecular Group, Faculty of Physics, Yazd University, Yazd, Iran
[2] Physics Group, Faculty of Science, Shiraz University Of Technology, Shiraz, Iran

[1] mina_azari_101@yahoo.com
[2] mhatami@yazduni.ac.ir

Abstract

We have derived nonlinear couple wave equations in a metmaterial waveguide for both electric and magnetic component of electromagnetic wave. The coupled equations are not symmetric respect to electric and magnetic field. We also simulated the propagation of fundamental soliton in a nonlinear metamaterial waveguide and studied its behavior.

1. Introduction

It is evident that the two electromagnetic parameters of material i.e ε and μ, determine the behavior of the external fields widely. However the manifestation of artificial structure to manipulation electromagnetic properties is too marvelous so that novel phenomenon expose which have never seen before in nature intrinsically. This class of man-made materials is called metamaterials [1].

The "metamaterial" was terminated initially by Rodger M. Walser in 1999 at university of texas [2]. The idea of synthetic materials with both negative ε and μ is referred to Victor Veselago in 1968 [3] who theoretically survived several unusual properties in left-handed materials like negative index refraction, the reversal of Cherenkov radiation, the reversal of the Doppler shift and strikingly the reversal of Snell's law. Shelby et.al observed negative refraction experimentally primarily [4]. Pendry was the first one to propose a new design as split-ring-resonators to attain LHM [5]. However the revolution of metamaterials commenced by D. R. Smith and his team at the university of California [6] when they experimentally proved the possibility of contemporary negative ε and μ by Pendry's idea.

The backward of verification in this field is so extensive that we can hardly mention all of them. But we can specify some of numerous and appealing applications such as perfect lenses [7], cloaking devices [8-9-10], sub-wavelength waveguides [11] and the enhancement of magnetic resonance imaging (MRI) [12].Stopping light [13], compact cavities, adaptive lenses, tunable mirrors, security imaging, bio molecular fingerprinting, remote sensing [14] are some other attractive applications in this new field.

So far, linear features of metamaterials were studied predominantly when both ε and μ are intended to be independent of the intensity of the electromagnetic field. A nonlinear metamaterial is a tunable metamaterial to achieve nonlinearity more than nature materials. If we have authority to adjust varactors in unit cells of metamaterials, it is feasible to overcome and control and tune permittivity and permeability beyond their linear response. However variable capacitance diodes can be inserted into the split-ring-resonators to upgrade linear medium to nonlinear metamaterials [15-17]. Nonlinear phenomena are developed by new structures such as harmonic generation [18-19], down-conversion [20] or tenability [21].

In this work we want to derive nonlinear couple wave equations in a metmaterial waveguide for both electric and magnetic component of electromagnetic wave. Besides that it is available to obtain refractive index for a special kind of metamaterial waveguide.

2. Equations

The planer waveguide system which we have considered here has boundaries in the x-y plane while the direction of propagation is taken to be in the z-axis. Here we presume that the core of the metamaterial waveguide consists of nonlinear split ring resonator units combined with straight thin copper wires. For simplicity we consider single gap SRR. Although the nonlinear aspect can be introduced in any circuit elements, the field amplification within the capacitive gaps estimates the best nonlinear response in the high-field regions of the circuit. Such system is influenced by an electromagnetic filed.

So we assume that only the capacitance C(q) has a nonlinear response. The nonlinearity reaction can be yield by mounting a varactor onto the slit of SRRs. By this aforementioned illustration, it is feasible for our purpose to choose a Skyworks SMV 1231-079 hyper-abrupt tuning varactor. This approach suggests the nonlinear voltage-dependent capacitance C (V_D), as the following model [22]:

$$C(V_D) = C_0(1 - V_D / V_P)^{-K} \qquad (1)$$

Where C_0 is the zero basic capacitance, K is the gradient coefficient and V_P is the intrinsic potential and V_D is the voltage across the diode. For small field amplitudes, the time-dependent charge as a function of voltage can be computed as follows according to this chosen model:

$$Q = \int_0^{V_D} C(V_D')dV_D' = \frac{C_0 V_P}{1-K}(1-(1-\frac{V_D}{V_P})^{1-K}) \quad (2)$$

Where V_p is the intrinsic potential and K is the gradient coefficient. If we assume that $V_D \prec V_P$, then the voltage across the diode can be offered as a function of charge:

$$V_D(q) = V_P[1-(1-q\frac{1-K}{V_P})^{1/1-K}] \quad (3)$$

Overtly, according to equation (3) the inserted varactor exhibits the nonlinear relationship between charge and voltage [22].
The electromotive force $\varepsilon(t)$, turns out a current I so that:

$$L\frac{dI}{dt} + RI + V_D = \varepsilon(t) = -\frac{\partial \varphi_m}{\partial t} \quad (4)$$

In this equation L, R and $V_D = \frac{1}{C}\int_0^t I(\tau)d\tau$ are subsequently the distributed inductance, distributed resistance and the induced voltage.

As we mentioned before, only the capacitance C (q) has a nonlinear response. So after expanding V_D in a Taylor series the equation (4) can be abbreviated to:

$$\ddot{q} + \varsigma\dot{q} + \omega_0^2 q + \alpha q^2 + \beta q^3 = \omega_0^2 \varepsilon(t) \quad (5)$$

Where $\alpha = a\omega_0^2$, $\beta = b\omega_0^2$, a and b are the nonlinear structural parameters and ς is the linear damping constant. It is necessary to introduce ω_0 as the resonance frequency.

As regards the SRR submits a dominantly magnetic response, ultimately after solving equation (5) by standard methods [23], the intensity-dependent permeability is given by [24]:

$$\mu_{eff} = 1+\frac{F\omega^2}{D(\omega)} + 3\frac{F\omega_0^6\omega^4 A^2\mu_0^2|H|^2}{D(\omega)^3 D(\omega)^*}(\frac{4a^2\omega_0^2}{3D(0)} + \frac{2a^2\omega_0^2}{3D(2\omega)} - b) \quad (6)$$

In this equation, F is the structural constant, and $D(\omega) = \omega_0^2 - \omega^2 - i\gamma\omega$ and γ is a loss parameter.
As we illustrated previously, SRRs are synthesize with straight thin wires. The major portion of nonlinear dielectric permittivity function is related to this part.

For simplicity the metallic structure is embedded into a nonlinear dielectric with a permittivity that depends on the severity of the electric field and the nonlinear dependence is relevant to Kerr nonlinearity.

Finally the expression for the effective nonlinear dielectric permittivity is obtained [25]:

$$\varepsilon_{eff} = \varepsilon_{D0} + \alpha\frac{|E|^2}{|E_c|^2} - \frac{\omega_p^2}{\omega(\omega - i\gamma_\varepsilon)} \quad (7)$$

Where: $\gamma_\varepsilon = c^2 \big/ 2\sigma S\ln(d/r)$ and $\omega_p \approx (c/d)[2\pi/\ln(d/r)]$.

The planer waveguide system which we have considered here has boundaries in the x-y plane while the direction of propagation is taken to be in the z-axis.

According to Maxwell's equations:

$$\vec{\nabla}\times\vec{H} = \vec{J} + \frac{\partial\vec{D}}{\partial t} = \sigma\vec{E} + \frac{\partial\vec{D}}{\partial t} \quad (8)$$

$$\vec{\nabla}\times\vec{E} = -\frac{\partial\vec{H}}{\partial t} \quad (9)$$

We could obtain Helmholtz equation as follows:

$$\nabla^2\vec{H} + \omega^2\mu_{eff}\varepsilon_{eff}\vec{H} + i\omega\sigma\mu_{eff}\vec{H} = 0 \quad (10)$$

If we insert magnetic field in equation so that it propagates through z direction:

$$\vec{H} = g(x,y)B(\omega,z)e^{ik_0 z} \quad (11)$$

We would acquire two below equations by utilizing the separation of values method [26]:

$$\frac{\partial^2 g}{\partial x^2} + \frac{\partial^2 g}{\partial y^2} + [\omega^2(\mu_{eff}\varepsilon_{eff}) + i\omega\sigma\mu_{eff} - \breve{\beta}^2]g = 0 \quad (12)$$

$$2ik_0\frac{\partial B}{\partial Z} + [\breve{\beta}^2 - k_0^2]B = 0 \quad (13)$$

Nevertheless we have:

$$\frac{\omega^2}{k_0^2}[(\mu_{eff}\varepsilon_{eff}) + \frac{i\sigma\mu_{eff}}{\omega}] = (n+\Delta n)^2 \cong n^2 + 2n\Delta n \quad (14)$$

Eventually the refractive index is attained:

$$n = [\varepsilon_{D_0}c^2(1+\frac{F\omega^2}{D(\omega)})(1-\frac{\omega_P^2}{\varepsilon_{D_0}\omega(\omega-i\gamma_\varepsilon)} + \frac{i\sigma}{\varepsilon_{D_0}\omega})]^{1/2} \quad (15)$$

And

$$\Delta n = R(\omega)|H|^2 + Q(\omega)|E|^2 + P(\omega)|H|^2|E|^2 \quad (16)$$

Where its coefficients are:

$$R(\omega)=\varepsilon_{D_0}c^2(1-\frac{\omega_P^2}{\varepsilon_{D_0}\omega(\omega-i\gamma_\varepsilon)}+\frac{i\sigma}{\varepsilon_{D_0}\omega})\times(3\frac{F\omega_0^6\omega^4A^2\mu_0^2}{D(\omega)^3D(\omega)^*})$$
$$\times(\frac{4a^2\omega_0^2}{3D(2\omega)}+\frac{2a^2\omega_0^2}{3D(2\omega)}-b)(\frac{1}{2n(\omega)}) \quad (17)$$

$$Q(\omega)=(\frac{\alpha c^2}{|E_c|^2})(\frac{1}{2n(\omega)})(1+\frac{F\omega^2}{D(\omega)}) \quad (18)$$

$$P(\omega)=(\frac{\alpha c^2}{|E_c|^2})(3\frac{F\omega_0^6\omega^4A^2\mu_0^2}{D(\omega)^3D(\omega)^*})\times(\frac{4a^2\omega_0^2}{3D(2\omega)}+\frac{2a^2\omega_0^2}{3D(2\omega)}-b)(\frac{1}{2n(\omega)}) \quad (19)$$

We presented eigenvalue according to this equation:

$$\bar{\beta}(\omega)=\beta(\omega)+\Delta\beta \quad (20)$$

Where:

$$\Delta\beta=k_0\frac{\iint\Delta n|T(x,y)|^2dxdy}{\iint|T(x,y)|^2dxdy} \quad (21)$$

On the other hand, we selected magnetic and electric fields as following relations:

$$H(x,y)=g(x,y)B(\omega,z)e^{ik_0z} \quad (22)$$
$$E(x,y)=F(x,y)A(\omega,z)e^{ik_0z} \quad (23)$$

Now we can insert equation (16) in (21) and gain this equation:

$$\Delta\beta=k_0\{R(\omega)|B|^2+Q(\omega)|A|^2+P(\omega)|B|^2|A|^2\} \quad (24)$$

In equation (13) we can use this approximation:

$$\bar{\beta}^2(\omega)-k_0^2\cong 2k_0(\beta(\omega)+\Delta\beta-k_0) \quad (25)$$

It is helpful to approximate $\beta(\omega)$ in a Taylor series toward ω_0 :

$$\beta(\omega)=k_0+(\omega-\omega_0)\beta_1+\frac{1}{2}(\omega-\omega_0)^2\beta_2+\frac{1}{6}(\omega-\omega_0)^3\beta_3+... \quad (26)$$

In such a manner we approximated other coefficients and substituted them in equation (16). Lastly converting $(\omega-\omega_0)$ to $(i\partial/\partial t)$ leads us to have equation (13) in time-domain:

$$\frac{\partial B}{\partial Z}=ik_0\{|B|^2R(\omega_0)+|A|^2Q(\omega_0)+|B|^2|A|^2P(\omega_0)\}B$$
$$-\frac{\partial}{\partial t}\{\beta_1+R_1(\omega)k_0|B|^2+k_0|A|^2Q_1(\omega)+k_0|A|^2|B|^2P_1(\omega)\}B$$
$$-\frac{i}{2}\frac{\partial^2}{\partial t^2}\{\beta_2+R_2(\omega)k_0|B|^2+k_0|A|^2Q_2(\omega)+k_0|A|^2|B|^2P_2(\omega)\}B$$
$$+\frac{1}{6}\frac{\partial^3}{\partial t^3}\{\beta_3+R_3(\omega)k_0|B|^2+k_0|A|^2Q_3(\omega)+k_0|A|^2|B|^2P_3(\omega)\}B \quad (27)$$

In equation (27) subscripts 1, 2 and 3 are respectively the first, the second and the third derivative of coefficients toward ω_0.

For simplicity we disregard the term $\frac{\partial^3}{\partial t^3}$.Let us to introduce a time scale normalized and similarly a length scale one to the input pulse width as:

$$\tau=t/t_0 \quad (28)$$
$$\xi=Z/L \quad (29)$$

At the same time we introduce normalized amplitudes for both magnetic and electric fields as follows:

$$u=B/\sqrt{p_0} \quad (30)$$
$$v=A/\sqrt{q_0} \quad (31)$$

Where q_0 and p_0 are the peak power of the incident pulse. In the end, this procedure derives us to these two uncoupled equations:

$$\frac{\partial u}{\partial\xi}=ia'u|u|^2+ib'u|v|^2+ic'(u|u|^2|v|^2)+id'\frac{\partial u}{\partial\tau}$$
$$-\frac{i}{2}e'\frac{\partial^2u}{\partial\tau^2}+if'\frac{\partial}{\partial\tau}(u|u|^2)+ig'\frac{\partial}{\partial\tau}(u|v|^2)$$
$$+ih'\frac{\partial}{\partial\tau}(u|u|^2|v|^2)+ik'\frac{\partial^2}{\partial\tau^2}(u|u|^2)$$
$$+im'\frac{\partial^2}{\partial\tau^2}(u|v|^2)+in'\frac{\partial^2}{\partial\tau^2}(u|u|^2|v|^2) \quad (32)$$

$$\frac{\partial v}{\partial \xi} = ia'v|u|^2 + ib'v|v|^2 + ic'(v|u|^2|v|^2) + id'\frac{\partial v}{\partial \tau}$$
$$-\frac{i}{2}e'\frac{\partial^2 v}{\partial \tau^2} + if'\frac{\partial}{\partial \tau}(v|u|^2) + ig'\frac{\partial}{\partial \tau}(v|v|^2)$$
$$+ ih'\frac{\partial}{\partial \tau}(v|u|^2|v|^2) + ik'\frac{\partial^2}{\partial \tau^2}(v|u|^2)$$
$$+ im'\frac{\partial^2}{\partial \tau^2}(v|v|^2) + in'\frac{\partial^2}{\partial \tau^2}(v|u|^2|v|^2) \quad (33)$$

Where the coefficients are formed as:

$$a' = (1 - \frac{\omega_P^2}{\varepsilon_{D_0}\omega(\omega - i\gamma_\varepsilon)} + \frac{i\sigma}{\varepsilon_{D_0}\omega}) \times (3\frac{F\omega_0^6\omega^4 A^2\mu_0^2}{D(\omega)^3 D(\omega)^*})$$
$$\times (\frac{4a^2\omega_0^2}{3D(0)} + \frac{2a^2\omega_0^2}{3D(2\omega)} - b)(\frac{\varepsilon_{D_0} c\omega p_0 L}{2n(\omega)})_{\omega_0} \quad (34)$$

$$b' = (\frac{Lq_0 c\omega\alpha}{2n(\omega)})(1 + \frac{F\omega^2}{D(\omega)})_{\omega_0} \quad (35)$$

$$c' = (\frac{p_0 q_0 \alpha\omega c}{2n(\omega)E_c^2})(3\frac{F\omega_0^6\omega^4 A^2\mu_0^2}{D(\omega)^3 D(\omega)^*}) \times (\frac{4a^2\omega_0^2}{3D(0)} + \frac{2a^2\omega_0^2}{3D(2\omega)} - b)_{\omega_0} \quad (36)$$

$$d' = -\frac{L\beta_1}{t_0} \quad (37)$$

$$e' = \frac{L\beta_2}{t_0^2} \quad (38)$$

$$f' = (\frac{Lp_0\varepsilon_{D_0}}{t_0})\frac{d}{d\omega}[(1 - \frac{\omega_P^2}{\varepsilon_{D_0}\omega(\omega - i\gamma_\varepsilon)} + \frac{i\sigma}{\varepsilon_{D_0}\omega}) \times (3\frac{F\omega_0^6\omega^4 A^2\mu_0^2}{D(\omega)^3 D(\omega)^*})$$
$$\times (\frac{4a^2\omega_0^2}{3D(0)} + \frac{2a^2\omega_0^2}{3D(2\omega)} - b)(\frac{1}{2n(\omega)})]_{\omega_0} \quad (39)$$

$$g' = (\frac{Lq_0\alpha}{t_0 E_c^2})\frac{d}{d\omega}[(\frac{\omega c}{2n(\omega)})(1 + \frac{F\omega^2}{D(\omega)})]_{\omega_0} \quad (40)$$

$$n' = (\frac{Lq_0 p_0\alpha}{t_0 E_c^2})\frac{d}{d\omega}[(3\frac{F\omega_0^6\omega^4 A^2\mu_0^2}{D(\omega)^3 D(\omega)^*})$$
$$\times (\frac{4a^2\omega_0^2}{3D(0)} + \frac{2a^2\omega_0^2}{3D(2\omega)} - b)(\frac{c\omega}{2n(\omega)})]_{\omega_0} \quad (41)$$

$$k' = (\frac{Lp_0}{2t_0^2})\frac{d^2}{d\omega^2}[(1 - \frac{\omega_P^2}{\varepsilon_{D_0}\omega(\omega - i\gamma_\varepsilon)} + \frac{i\sigma}{\varepsilon_{D_0}\omega}) \times (3\frac{F\omega_0^6\omega^4 A^2\mu_0^2}{D(\omega)^3 D(\omega)^*})$$
$$\times (\frac{4a^2\omega_0^2}{3D(0)} + \frac{2a^2\omega_0^2}{3D(2\omega)} - b)(\frac{c\omega Lp_0\varepsilon_{D_0}}{2n(\omega)})]_{\omega_0} \quad (42)$$

$$m' = (\frac{Lq_0}{2t_0^2})\frac{d^2}{d\omega^2}[(\frac{\alpha\omega c}{2n(\omega)})(1 + \frac{F\omega^2}{D(\omega)})]_{\omega_0} \quad (43)$$

$$n' = (\frac{Lp_0 q_0}{2t_0^2})\frac{d^2}{d\omega^2}[(3\frac{F\omega_0^6\omega^4 A^2\mu_0^2}{D(\omega)^3 D(\omega)^*})$$
$$\times (\frac{4a^2\omega_0^2}{3D(0)} + \frac{2a^2\omega_0^2}{3D(2\omega)} - b)(\frac{\omega}{2n(\omega)})]_{\omega_0} \quad (44)$$

As we are eager to achieve the standard Schrödinger equation, it is advantageous to omit some coefficients of equations (32) and (33). Afterwards, we altered the variable ξ to $n(\omega)\eta$ and also τ to $T\sqrt{n(\omega)e'}$ .So two coupled equations reduced to:

$$\frac{\partial v}{\partial \eta} = imv|u|^2 + inv|v|^2 + ip(v|u|^2|v|^2) - \frac{i}{2}\mathrm{sgn}(\beta_2)\frac{\partial^2 v}{\partial T^2} \quad (45)$$

$$\frac{\partial u}{\partial \eta} = imu|u|^2 + inu|v|^2 + ip(u|u|^2|v|^2) - \frac{i}{2}\mathrm{sgn}(\beta_2)\frac{\partial^2 u}{\partial T^2} \quad (46)$$

Here m, n and p are coefficients associated with metamaterial core construction.

After inserting experimental results [22], [24] and [25] in the coefficients of the equations (45) and (46), we can simulate and survey the behavior of fundamental soliton as follows:

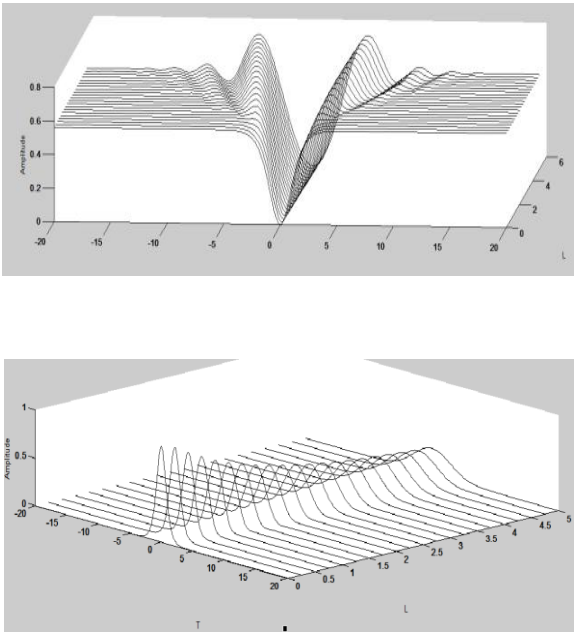


Figure 1: The simulation of propagation of electromagnetic wave in a metamaterial waveguide according to equation (45) and (46).

3. Discussion

In spite of a regular nonlinear waveguide, fundamental soliton does not preserve its shape in a metamaterial waveguide. So it would better find another coupled soliton solution.

4. Conclusions

In this article we presented a waveguide with a metamaterial core. We have presented the effective permeability coefficient and the effective permittivity for this nonlinear structure. We perceived that the dependence of magnetic and electric fields is obvious in these two parameters. While the straight thin copper wires are responsible to provide electric nonlinearity, the SRR obtained the magnetic nonlinearity. In addition we tried to solve the Helmholtz equation for propagating electromagnetic waves. For this special structure we could compute the refraction index. On the other hand, by using standard methods, we acceded propagating electromagnetic wave equations in this nonlinear meamaterial medium. Finally we normalized these two equations and omitted some coefficients to achieve standard nonlinear Schrödinger equations. We realized that these two equations are not symmetric but they are coupled. After that the behavior of fundamental soliton was survived and it was seen that the fundamental soliton is not a soliton solution of nonlinear metamaterial coupled electromagnetic wave equations.

References

[1] J. B. Pendry, Focus issue: negative refraction and metamaterials – introduction, *Opt Express*, 11, 7, pp 639, 2003.

[2] A. Lakhtakia, T. G Mackay, *Meet the metamaterials*, Opt Photon News, 18, pp 32–39, 2007.

[3] V. G. Veselago, The electrodynamics of substances with simultaneosly negative values of ε and μ, *Sov. Phys. Usp*, 47, 509, 1968.

[4] R. A. Shelby, D. R. Smith, S. Schultz, Experimental verification of a negative index of refraction, *Science* 292, 5514, pp 77–79, 2001.

[5] J. B. Pendry, A. J. Holden, D. J. Robbins and W. J. Stewart, Magnetism from conductors and enhanced nonlinear phenomena, *IEEE Trans. Microwave Theory Tech*, 47, pp 2075, 1999.

[6] D. R .Smith, W. J. Padilla, D. C. Vier, S. C. Nemat-Nasser, S. Schultz, Composite medium with simultaneously negative permeability and permittivity, *Phys. Rev. Lett*. 84, 4184, 2000.

[7] J. B. Pendry, Negative refraction makes a perfect lens, *Phys. Rev. Lett*. 85, 3966 , 2000.

[8] A. Alu, N. Engheta, Achieving transparency with plasmonic and metamaterial coatings, *Phys. Rev. E* 72, 016623, 2005.

[9] U. Leonhardt, Optical conformal mapping, *Science*, 312, 1777, 2006.

[10] J. B. Pendry, D. Schurig, D. R. Smith, Controlling electromagnetic fields, *Science* 312, 1780, 2006.

[11] A. Alu, N. Engheta, Guided modes in a waveguide filled with a pair of single-nagative (SNG), double-negative (DNG), and/or double-positive (DPS) layers, *IEEE Trans. Microwave theory Technol*, 52, 199, 2004.

[12] M. C. K. Wiltshire, J. B. Pendry, I. R. Young, D. J. Larkman, D. J. Gilderdale, J. V. Hajnal, Microstructured magnetic materials for RF flux Guides in magnetic resonance imaging, *Science*, 291, 849, 2001.

[13] W. T. Lu, S. Sridhar, Slow light, open-cavity formation, and large longitudinal electric field on a slab waveguide made of indefinite permittivity metamaterials, *Phys Rev A*, 82, 013811, 2010.

[14] T. J. Yen, W. J. Padilla, N. Fang, D. C. Vier, D. R. Smith, J. B. Pendry, D. N. Basov, and X. Zhang, Terahertz magnetic response from artificial materials, *Science*, 303, 5663, pp. 1494–1496, 2004.

[15] D. A. Powell, I. V. Shadrivov, Y. S. Kivshar, M. V. Gorkunov, Self-tuning mechanisms of nonlinear split-ring resonators, *Appl. Phys. Lett*, 91, pp. 144107, 2007.

[16] C. M. Krowne, Y. Zhang, *Physics of Negative Refraction and Negative Index Materials: Optical and Electronic Aspects and Diversified Approaches*, Springer-Verlag. pp 331, 332, ISBN 9783540721314, 2007.

[17] A. A. Zharov, I. Shadrivov, Y. Kivshar, Nonlinear properties of left-handed metamaterials. *Physical Review Letters*, 91, 3, 037401, 2003.

[18] I. V. Shadrivov, A. B. Kozyrev, D. W. Van der Weide and Y. S. Kivshar, Tunable transmission and harmonic generation in nonlinear metamaterials, *Appl. Phys. Lett*, 93 161903, 2008.

[19] M. W. Klein, M. Wegener, N. Feth, S. Linden, Experiments on second- and third-harmonic generation from magnetic metamaterials, *Opt. Express*, 15, 5238, 2007.

[20] A. B. Kozyrev, D. W. Van der Weide, Nonlinear left-handed transmission line metamaterials, *Appl. Phys*, 41, 173001, 2008.

[21] I. V. Shadrivov, S. K. Morrison, Y. S. Kivshar, Tunable split-ring resonators for nonlinear negative-index metamaterials, *Opt. Express*, 14, 9344, 2006.

[22] B. Wang, J. Zhou, T. Koschny, C. M. Soukoulis, Nonlinear properties of split-ring resonators, *Opt. Express*, 16, 20, pp 16058-16063, 2008.

[23] R. Boyd, *Nonlinear Optics*, Academic press, New York, 2007.

[24] E. Poutrina, D. Huang, D. R. Smith, Analysis of nonlinear electromagnetic metamaterials, *New Journal Of Physics*, 12, 093010,pp 1-27, 2010.

[25] A. A. Zharov, I. V. Shadrivov, Y. S. Kivshar, Nonlinear properties of left-handed metamaterials, *Phys. Rev. Lett*, 91, 3,pp 37401–37404, 2003.

[26] P. G. Agrawal, *Nonlinear Fiber Optics*, Academic press, New York, 2007.

Microwave Propagation at the interface between Nonlinear MTMs and Anisotropic Materials

Hala J. El-Khozondar[1], Rifa J. El-Khozondar[2], Said Zouhdi,

[1]Department of Electrical Engineering, IUG, P. O. Box 108, Gaza, Palestine
[2]Physics Department, Al-Aqsa University, P.O. box 4051, Gaza, Palestine
[3]Laboratorie do Génie Electrique de Paris, Université Paris Sud 11, France
*corresponding author, E-mail: hkhozondar@iugaza.edu

Abstract

Metamaterials which have both negative permeability and negative permittivity have potential applications in optoelectronics and communications. These materials are fabricated in laboratories which is an added advantage. The focus of this work is on the propagation of surface wave at the interface between nonlinear MTMs and anisotropic materials in the optical range. The dispersion equation is derived from Maxwell's equations. The dispersion equation is solved numerically to study the characteristics of the propagated wave. Only TE modes are considered. Results display the dependence of the propagating waves on the characteristics of the structure composite materials.

1. Introduction

The importance of anisotropic materials is due to the fact that they can be used as directional means for different optical equipment like fibers and convertors [1-4]. A dramatic research on wave propagations in anisotropic medium has been done [5-7]. It is shown that the propagation is coupled and depends on polarization.

Metamaterials labeled a Left-Handed material as they satisfy the characteristic laws for left-handed substances. These materials were first theoretically investigated by Veselago [8]. Pendry *et al*. [9] presented a periodic group of nonmagnetic directing units having an effective permeability to broaden the electromagnetic properties range of effective media. The effective permeability is enhanced by making the basic units resonant. This leads to large positive effective permeability close to the low frequency side of the resonance and negative effective permeability near the high frequency side of the resonance. The materials of negative effective permeability attracted attention because they can be united with negative permittivity materials to produce metamaterials. The split ring resonator (SSR) can be used to create a material with negative permeability which can be used to build metamaterials.

Smith *et. al.* [10] treated metamaterial as a square matrix of periodic arrays. An array encompasses splitting-ring resonators and conducting wires. This combined structure shows a frequency in the microwave region with negative permeability and negative permittivity. These MTMs have several engineering applications because their permeabilities and permittivities can be adapted according to particular necessities. MTMs have various applications in sensors [11-13] and isolators [14-20].

The term negative index of refraction is an essential development of metamaterials. To get negative refraction, both permeability and permittivity should be negative. This can be done by using metamaterials where the frequency of negative permittivity can be reduced using wires whereas the negative permeability can be attained with resonant particles [21-24]. Furthermore, theoretical [25] and experimental [26-28] researches demonstrate that the properties of negative refraction occur in some anisotropic media labeled anisotropic-MTMs media.

Nonlinear electromagnetic responses in MMs is established by the addition of nonlinear elements inside the MMs, for example by inserting the split-ring resonators (SRRs) in a Kerr-type dielectric [29], or by introducing certain nonlinear elements like diodes in the split-ring resonators [30]. When ultrashort pulses propagate in nonlinear electric polarization MTMs, the permeability combined with the nonlinear polarization leading to a self-steepening effect and a higher order nonlinear term [31-34].

The purpose of this work is to study surface wave propagation at the interface between nonlinear MTMs (NMTMs) and anisotropic materials. Next section is dedicated to introduce the proposed structure and the theory of the problem. In section 3, results are presented followed by discussion in section 4. Conclusion is given in section 5.

2. Structure of the problem and dispersion equation

In this work, we propose to study the effect of nonlinear metamaterials (NMTMs) on the propagation of the surface waves at the interface of the anisotropic media. Fig. 1 shows the proposed structure. The structure consists of two semi-infinite planes. The lower half of the space $x<0$ is filled by NMTMs and the upper half $x>0$ is filled by anisotropic media. We considered two cases of anisotropy: anisotropic dielectric with positive permittivity and permeability and the second case is by replacing dielectric anisotropic media with anisotropic-media with negative permittivity and negative permeability (anisotropic-MTMs).

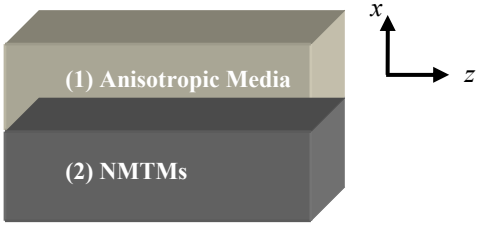


Figure 1: The proposed configuration.

The nonlinear MTMs have characteristic parameters defined as follows:

$$\varepsilon_2^{NL}(\omega) = \varepsilon_2(\omega) + \alpha I, \quad (1)$$

$$\mu_2^{NL}(\omega) = \mu_2(\omega) + \alpha I, \quad (2)$$

where I is the field intensity, α is the strength of the nonlinear term taken to be equal $2\text{x}10^{-9}$.
In general, anisotropic media has the following dielectric tensor:

$$\varepsilon = \begin{pmatrix} \varepsilon_{xx} & \varepsilon_{xy} & \varepsilon_{xz} \\ \varepsilon_{yx} & \varepsilon_{yy} & \varepsilon_{yz} \\ \varepsilon_{zx} & \varepsilon_{zy} & \varepsilon_{zz} \end{pmatrix} \quad (3)$$

The material is chosen such that only diagonal elements are not zero. We assumed the fields are oscillatory and have the following TE polarization as follows,

$$\vec{E} = \left(0,\ E_y,\ 0\right)\exp\left[i\left(\omega t - \beta z\right)\right], \quad (4)$$

$$\vec{H} = \left(H_x,\ 0,\ H_z\right)\exp\left[i\left(\omega t - \beta z\right)\right], \quad (5)$$

where $\beta = n_{eff}\, k$ denotes the propagation constant, n_{eff} the effective refractive index, $\omega = ck$ the frequency, k is the propagation constant in free space, and c is the speed of light.
Applying equation (4) and equation (5) into Maxwell's equations, we get the field equations and their solutions in the two media.

For $x<0$, the field equation and its solution are written as follows

$$\frac{d^2E_y^{(2)}}{dx^2} + \left(-\beta^2 + k^2\left(\varepsilon_2\mu_2 + \alpha\mu_2\left|E_y^{(2)}\right|^2\right)\right)E_y^{(2)}, \quad (6)$$

$$\mathrm{E}_{\mathrm{y}}^{(2)} = \frac{q_2}{k}\sqrt{\frac{2}{\alpha\mu_2}}\,\mathrm{sec}\,h\left(q_2\left(x - x_0\right)\right), \quad (7)$$

where $q_2 = \sqrt{\beta^2 - k\,\mu_2\varepsilon_2}$, and x_0 is the integration constant and indicates the location of the maximum power.
For $x>0$, the field equation and its solution are expressed as

$$\frac{d^2E_y^{(1)}}{dx^2} - \left(-\beta^2 + k^2\left(\varepsilon_1\mu_1\right)\right)E_y^{(1)} = 0, \quad (8)$$

$$\mathrm{E}_{\mathrm{y}}^{(1)} = A\,\mathrm{e}^{-q_1 x}, \quad (10)$$

where A is the constant of integration can be found from boundary conditions and $q_1 = \sqrt{\beta^2 - k\,\mu_1\varepsilon_1}$.

The dispersion equation can be easily derived by imposing the boundary condition at x=0 into the field equations.

$$\tanh\left(q_2 x_0\right) = \frac{q_1}{q_2}\frac{\mu_2}{\mu_1} \quad (11)$$

Equation (11) shows the relation between the characteristic constants of the two media and gives the needed information about the propagated surface waves between the two media. The time averaged power flowing in the z direction per unit beam width is calculated:

$$P = -\frac{1}{2}\,\mathrm{Re}\int_{-\infty}^{\infty}\left(HxE^*\right)_z dx \quad (12)$$

The dispersion equation (11) is solved numerically for the range of $\tanh(q_2x_0)$ between -1 to +1. The value of n_{eff} is used to obtain the power of the propagated waves.
The fields (equations (7) and equation (9)) in the two media are also solved numerically. In all the calculations, the linear parts of equation (1) and equation (2) values are taken in the optical range at λ = 812 nm [35] where the permittivity ε and permeability μ are simultaneously negative.

3. Discussion

Fig.2 illustrates the propagated power flow at the interface between the NMTMs and the dielectric anisotropic media where we notice that as the wave goes from the nonlinear media to the anisotropic media the power increases until it saturates around the cutoff at n_{eff} = 2. Moreover, the power has a definite power threshold where the surface waves starts to propagate. The field distribution at different values of n_{eff} at different positions for the proposed structure is plotted in Fig. 3. It is noticeable that increasing the wave index increases the field maximum which explains the increase in the power as the index increases.

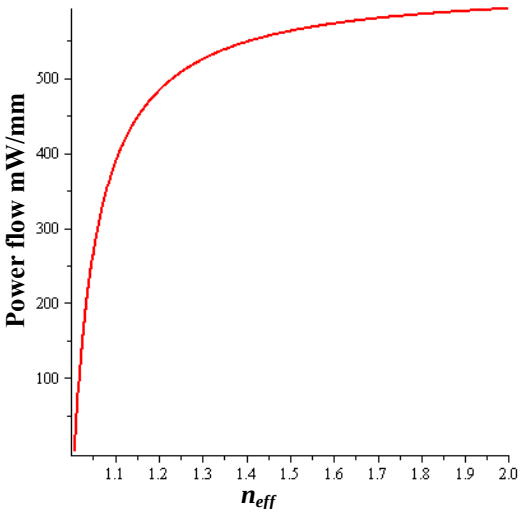


Figure 2 The variation of the total power flow at the NMTMs/anisotropic dielectric interface with n_{eff}.

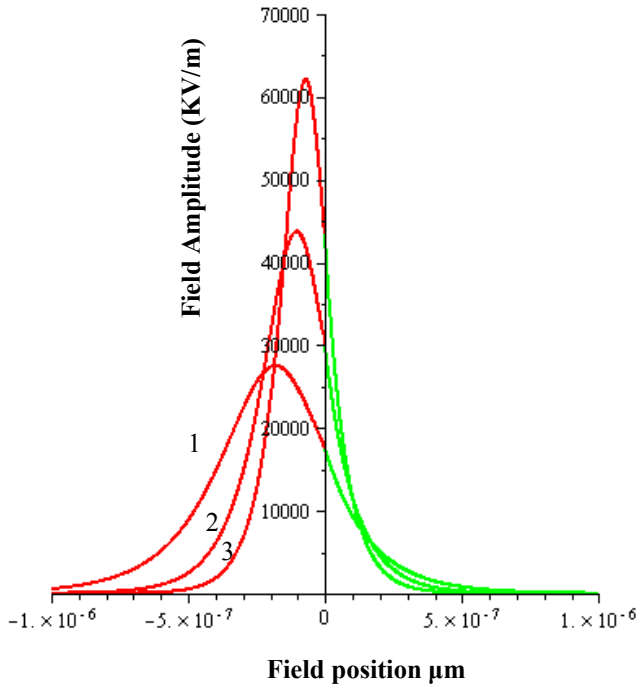


Figure 3 The field amplitude as a function of position for different values of n_{eff}: 1.2 for curve 1, 1.5 for curve 2 and 1.9 for curve 3.

Replacing the dielectric-anisotropic material with anisotropic-MTMs media we get the power distribution for the proposed structure as shown in fig. 4. We noticed that the power has no saturation value.

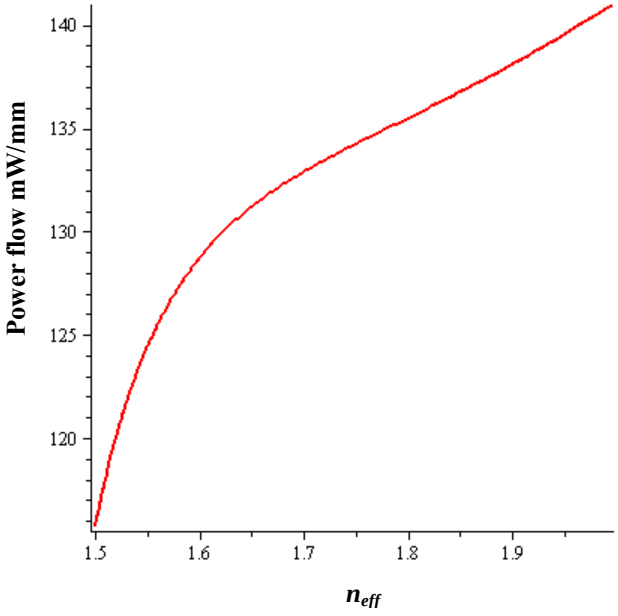


Figure 4 The dependence of the total power flow at the NMTMs/anisotropic-MTMs interface on n_{eff}.

4. Conclusions

In this work we studied the surface wave propagation at the interface between nonlinear-MTMs and anisotropic media. We studied two cases of anisotropic media: one case in which the anisotropic media has positive permittivity and permeability and the second case both permittivity and permeability is negative. We found that the dispersion equations which explain the behavior of the surface waves. In the first case we noticed that the power increases as wave index increases and has a saturation limit. While in the second case we found that the power increase as the wave index increases without saturation limit. The field amplitude distribution at different wave index for different positions is plotted. The plot shows that as the wave index increases the maximum of the amplitude increases.

Acknowledgements

The first and third authors would like to acknowledge the French government for funding the work through Al-Maqdisi program grant.

References

[1] C. L. XU, w. P. Huang, J. Chrostowski, and S. K. Chaudhuri, A Full-VectoriaI Beam Propagation Method for Anisotropic Waveguides, *J Lightwave Technol* 12:1926-1931, 1994.

[2] R. C. Alferness, Effective waveguide electro-optic TE+TM mode converter/waveguide filter, *Appl. Phys. Lett.* 36: 513-5 15, 1980.

[3] R. H. Stolen, V. Ramaswamy, P. Kaiser, and W. Pleibel, Linear polarization in birefringent single-mode fibers, *Appl. Phys. Lett.* 33: 699-701, 1978.

[4] D. N. Payne, A. J. Barlow, and J. J. Hansen, Development of low- and high-birefringence fibers, *IEEE J. Quantum Electron.* 18: 477487, 1982.

[5] L. Thylen and D. Yevick, Beam propagation method in anisotropic media, *Appl. Opt.* 21: 2751-2754, 1982.

[6] J. A. Fleck, Jr. and M. D. Feit, Beam Propagation in uniaxial anisotropic media, *J. Opt. Soc. Am.* 73: 920-926, 1983.

[7] J. M. Liu and L. Gomelsky, Vectorial beam propagation method, *J. Opt. Soc. Am.* 9: 1574-1585, 1992.

[8] V.S. Veselago, The electrodynamics of substances with simultaneously negative values of ε and µ, *Sov. Phys. Usp.* 10: 509-514, 1968.

[9] J. B. Pendry, A. J. Holden, D. J. Robbins, and W. J. Stewart, Magnetism from Conductors and Enhanced Nonlinear Phenomena, *IEEE Trans. Microwave Theory Tech.* 47: 2075-2083, 1999.

[10] D. R.Smith, W. J. Padilla, D. C. Vier, S. C. Nemat-Nasser, and S. Schultz, Composite medium with

simultaneously negative permeability and permittivity, *Phys. Rev. Lett.* 84: 4184-4187, 2000.
[11] H. El-Khozondar, R. El-Khozondar, M. Shabat, A. Koch, Metallic nonlinear magnetooptical nonreciprocal isolator, *OPTIK* 122: 256–258, 2011.
[12] H. El-Khozondar, R. El-Khozondar, M. Shabat, Characteristics of Magetooptical Integrated Metamaterials Isolator *Int. J. Mod. Phys. B* 23, 4675-4683, 2009.
[13] R. El-Khozondar, H. El-Khozondar, M. Shabat, Applications of Metamaterials in Optical Waveguide Isolator, *J. Al-Aqsa Univ.* 12: 35-50, 2008.
[14] H.J. El-Khozondar, R.J. El-Khozondar, M.M. Shabat, Double-Negative Metamaterial Optical waveguide Behavior Subjected to Stress. *Islamic university journal for natural science and Engineering* 16 (1), 9-20, 2008.
[15] R. El-Khozondar, H. El-Khozondar, M. Shabat, A. Koch, TM waves propagation at magnetoplasma-MTMs, *World J. Condens. Matter Phys*. 2: 171-174, 2012.
[16] H. J. El-Khozondar, R. J. El-Khozondar, S. Zouhdi, Surface waves at the interface between tunable LC–MTMs and nonlinear media, *Appl. Phys. A: Mater. Sci. Process.*109:865–867, 2012
[17] H. El-Khozondar, M. Müller, R. El-Khozondar, M. Shabat, A. Koch, 2012. Sensitivity of double-negative metamaterial optical sensor, *Int. J. Pure Appl. Sci. Technol.* 11: 29-35, 2012.
[18] H. El-Khozondar, M. Müller, R. El-Khozondar, A. Koch, Influence of magnetic field inhomogeneity on a magneto-optical current sensor, *Journal of sensor technology* 2: 19-22, 2012.
[19] H. El-Khozondar, R. El-Khozondar, M. Müller, A. Koch, Sensitivity of TM Nonlinear Magnetooptical Integrated Optical Sensor, Multidiscipline Modeling in Materials and Structures (MMMS), 8: 32-42, 2011.
[20] R. El-Khozondar, H. El-Khozondar, M. Shabat, Surface wave propagation in Ferroelectric/MTMS interface, *Integr Ferroelectr* 130: 50-57, 2011.
[21] J.B. Pendry, Negative refraction makes a perfect lens, *Phys. Rev. Lett.* 85, 3966-3969, 2000.
[22] R.A. Shelby, D.R. Smith, and S. Schultz, Experimental verification of a negative index of refraction, *Science* 292, 77-79, 2001.
[23] D.R. Smith and N. Kroll, Negative refraction index in left-handed materials, *Phys. Rev. Lett.* 85, 2933-2936, 2000.
[24] I. V. Lindell, S. A. Tretyakov,K. I. Nikoskinen, and S. Ilvonen, Bw media-media with negative parameters capable of supporting backward waves, *Microw Opt Techn Let* 31: 129-133, 2001.
[25] A. J. Hoffman, L. Alekseyev, S. S. Howard, K. J. Franz, D. Wasserman, V. A. Podolskiy, E. E. Narimanov, D. L. Sivco, and C. Gmachl, Negative refraction in semiconductor metamaterials, *Nat Mater* 6: 946–950, 2007.
[26] X. H. Hu and C. T. Chan, X. H. Hu and C. T. Chan, Photonic crystals with silver nanowires as a near-infrared superlens, *Appl Phys Lett* 85: 1520-1522, 2004.
[27] D. R. Smith and D. Schurig, Electromagnetic Wave Propagation in Media with Indefinite Permittivity and Permeability Tensors, *Phys. Rev. Lett.* 90: 077405-077408, 2003.
[28] D. R. Smith, D. Schurig, J. J. Mock, P. Kolinko, and P. Rye, Partial focusing of radiation by a slab of
indefinite media, *Appl. Phys. Lett.* 84: 2244, 2004.
[29] A.A. Zharov, I. V. Shadrivov, and Y. S. Kivshar, Nonlinear properties of left-handed meta-materials, *Phys. Rev. Lett.* 91: 037401-037404, 2003.
[30] M. Lapine, M. Gorkunov, and K. H. Ringhofer, Nonlinearity of metamaterial arising fromdiode insertions into resonant conductive elements, *Phys. Rev. E* 67: 065601-065604, 2003.
[31] Wen, S., Y. Wang, W. Su, Y. Xiang, X. Fu, and D. Fan, Modulation instability in nonlinear negative-index material, *Phys. Rev. E* 73: 0366171-0366176, Copyright @ 2006, Optical Society of America, March 24, 2006.
[32] Wen, S., Y. Xiang, W. Su, Y. Hu, X. Fu, and D. Fan, Role of the anomalous self-steepening effect in modulation instability in negative-index material, *Opt. Express* 14: 1568-1575, Copyright @ 2006, Optical Society of America, February 22, 2006.
[33] Wen, S., Y. Xiang, X. Dai, Z. Tang, W. Su, and D. Fan, Theoretical models for ultrashort electromagnetic pulse propagation in nonlinear metamaterials, *Phys. Rev. A* 75, 033815-033818, 2007.
[34] N. Lazarides and G. P. Tsironis, Coupled nonlinear Schrödinger field equations for electro-magnetic wave propagation in nonlinear left-handed materials, *Phys. Rev. E* 71, 036614-036617, 2005.
[35] U. K. Chettiar, A. V. Kildishev, H.-K. Yuan, W. Cai, S. Xiao, V. P. Drachev, and V. M. Shalaev, Double Negative Index Metamaterial: Simultaneous Negative Permeability and Permittivity at 812 nm, Proc. Photonic Metamaterials: from Random to Periodic, Jackson Hole, WY, June 4-7, 2007.

Finite Difference Time–Domain Modelling of Metamaterials: GPU Implementation of Cylindrical Cloak

Attique Dawood

Department of Electrical Engineering,
National University of Computer and Emerging Sciences (FAST), Islamabad, Pakistan
E-mail: attique.dawood@nu.edu.pk

Abstract

Finite difference time–domain (FDTD) technique can be used to model metamaterials by treating them as dispersive material. Drude or Lorentz model can be incorporated into the standard FDTD algorithm for modelling negative permittivity and permeability. FDTD algorithm is readily parallelisable and can take advantage of GPU acceleration to achieve speed–ups of 5x–50x depending on hardware setup. Metamaterial scattering problems are implemented using dispersive FDTD technique on GPU resulting in performance gain of 10x–15x compared to conventional CPU implementation.

1. Introduction

Standard FDTD algorithm cannot cater for negative values of permittivity or permeability. This is because of the Courant stability criterion. As soon as the permeability or permittivity becomes less than unity the algorithm will not be stable. A metamaterial object can be modelled as a dispersive substance using either the Lorentz or Drude dispersive models. These models can yield negative values of permittivity (or permeability) for certain frequency ranges [1]. Using these dispersive models, FDTD update equations are modified and permittivity and permeabilities are replaced with terms dependent on frequency of operation.

Two problems are chosen for GPU implementation. First is the electromagnetic wave scattering by a slab with negative permittivity and permeability; also known as DNG (double negative) medium. Second problem is the simulation of cylindrical cloak. An incident Gaussian pulse on DNG slab will undergo dispersion resulting in different frequency components being separated. Refractive index and transmission coefficient are calculated numerically to ascertain the validity of implementation. The cylindrical cloak was first proposed and tested by Pendry et. al. [2]. The first FDTD implementation was by Zhao et. al [3] and implemented on Comsol, a commercial electromagnetic simulation software. Simulations are implemented on Matlab, C++ and GPU. Performance comparison reveals a 10–15 times increase in performance with GPU implementations. Performance gain is greater for larger problem sizes and greater simulation times.

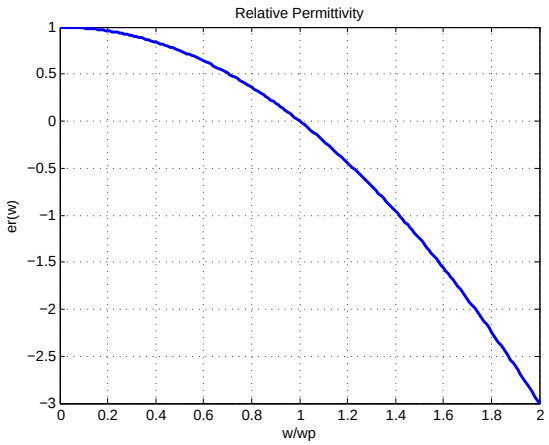


Figure 1: ϵ_r plotted against ω/ω_p for $\epsilon_\infty = 1$ and $\gamma = 0$

2. Drude Dispersion Model

In ideal conditions the permittivity (and permeability) of a material remain constant for any frequency and throughout the structure of that material. Speed of electromagnetic waves in such a medium remain constant if frequency changes. Additionally, there is no loss in energy as the waves pass through the medium.

In reality, such a material does not exist. Speed of EM waves varies with frequency of operation. Also, there is a loss associated with the material. A material is dispersive if its permittivity or permeability is dependent on frequency [4, Ch. 10].

The relative permittivity in Drude model is given by

$$\hat{\epsilon_r}(\omega) = \epsilon_\infty - \frac{\omega_p^2}{\omega^2 - j\gamma\omega}. \qquad (1)$$

Where, ω_p is plasma frequency and γ is collision frequency. Setting $\gamma = 0$ and $\epsilon_\infty = 1$, relative permittivity comes out to be negative for $\omega/\omega_p > 1$ (figure 1). Thus, Drude model can be effectively used to model metamaterials with permittivity or permeability less than one by incorporating it into FDTD update equations.

3. FDTD Update Equations

Faraday's Law and Ampere's Law in differential form are given by

$$\nabla \times \mathbf{E} = -\frac{\partial \mathbf{B}}{\partial t}, \tag{2}$$

$$\nabla \times \mathbf{H} = \frac{\partial \mathbf{D}}{\partial t}. \tag{3}$$

From [5], the update equations for a wave propagating in z direction are given by

$$H_y^{n+\frac{1}{2}}\left[k+\frac{1}{2}\right] = H_y^{n-\frac{1}{2}}\left[k+\frac{1}{2}\right] + \frac{\Delta t}{\mu \Delta x}\left(E_x^n[k] - E_x^n[k+1]\right), \tag{4}$$

$$E_x^{n+1}[k] = E_x^n[k] + \frac{\Delta t}{\epsilon \Delta x}\left(H_y^{n+\frac{1}{2}}\left[k-\frac{1}{2}\right] - H_y^{n+\frac{1}{2}}\left[k+\frac{1}{2}\right]\right). \tag{5}$$

In the conventional FDTD algorithm future magnetic field components are first computed from past electric field components (eq. 4). Using the updated magnetic field components, future electric field components are then calculated (eq. 5) and the simulation proceeds in a leap–frog manner [5].

4. FDTD Update Equations Based on Drude Model

Electric flux density and electric field are related by

$$\mathbf{D} = \epsilon \mathbf{E}. \tag{6}$$

Where $\epsilon = \epsilon_r \epsilon_0$ and ϵ_r for Drude model is given by equation 1. Substituting Drude model ϵ_r, equation 6 can be written as

$$\omega^2 \mathbf{D} - \gamma(j\omega)\mathbf{D} = \epsilon_\infty \omega^2 \mathbf{E} - \omega_p^2 \mathbf{E} - \epsilon_\infty \gamma(j\omega)\mathbf{E}. \tag{7}$$

Following the treatment of [3] and [4], frequency domain quantities can be converted to time–domain using the relationships $j\omega \rightarrow \partial/\partial t$ and $\omega^2 \rightarrow -\partial^2/\partial t^2$. Moreover, fields multiplying with ω_p^2 are averaged in time. Second–order difference scheme is used, both for single and double derivatives to keep all the terms in accordance with the second–order nature of whole expression. This will result in easier implementation. The final form is given by

$$E_x^{n+1} = a_e\left(D_x^{n+1} - 2D_x^n + D_x^{n-1}\right) + b_e\left(D_x^{n+1} - D_x^{n-1}\right) + c_e\left(2E_x^n - E_x^{n-1}\right) + d_e\left(2E_x^n + E_x^{n-1}\right) + e_e E_x^{n-1}. \tag{8}$$

This is also known as the auxiliary update equation for electric field where a_e–e_e are scalars given by

$$a_e = 4/g,\ b_e = \gamma(2\Delta t)/g,\ c_e = 4\epsilon_0\epsilon_\infty/g,$$
$$d_e = -\epsilon_0\omega_p^2(\Delta t)^2/g,\ e_e = \epsilon_0\epsilon_\infty\gamma_e(2\Delta t)/g,$$
$$g = 4\epsilon_0\epsilon_\infty + \epsilon_0\omega_p^2(\Delta t)^2 + \epsilon_0\epsilon_\infty\gamma(2\Delta t)$$

A similar procedure can be carried out to obtain auxiliary update equation for magnetic field.

$$H_y^{n+1} = a_m\left(B_y^{n+1} - 2B_y^n + B_y^{n-1}\right) + b_m\left(B_y^{n+1} - B_y^{n-1}\right) + c_m\left(2H_y^n - H_y^{n-1}\right) + d_m\left(2H_y^n + H_y^{n-1}\right) + e_m H_y^{n-1}. \tag{9}$$

For a wave propagating in z direction, FDTD update equations are

$$B_y^{n+1}(k) = B_y^n(k) + \frac{\Delta t}{\Delta z}\left(E_x^n(k) - E_x^n(k+1)\right) \tag{10}$$

and

$$D_x^{n+1}(k) = D_x^n(k) + \frac{\Delta t}{\Delta z}\left(H_y^{n+1}(k-1) - H_y^{n+1}(k)\right). \tag{11}$$

Equations 10 and 11 drive the FDTD algorithm which give future values of By and Dx from past fields. Equations 8 and 9 are auxiliary equations which give future fields H_y and E_x at $n+1$. A dry run without any scatterer is carried out before actual simulation to record incident fields. After simulation any post–processing is done to calculate required parameters like refractive index. The whole algorithm is depicted in figure 2.

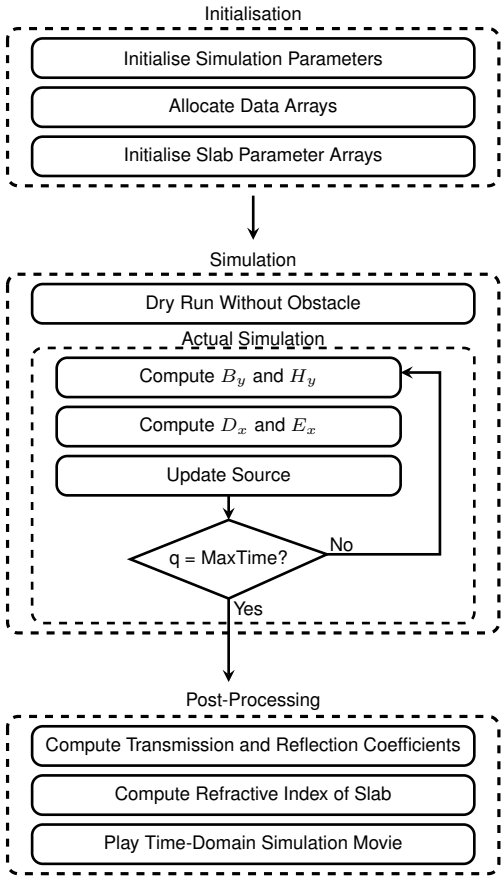


Figure 2: FDTD algorithm

5. GPU Considerations

With the evolution of 3D graphics arose a need for faster computing means to handle real–time graphics processing. The graphics processing unit or GPU was originally meant to act as a separate processor to handle graphics computations. A modern GPU has several hundred small processors that can work in parallel. Generally, these processors are referred to as shaders. The idea is to divide a problem into smaller sub–problems meant to execute in parallel. To take advantage of GPU acceleration a problem must have either task–parallel or data–parallel nature.

5.1. Task–Parallelism

In task–parallelism computation consist of several independent tasks that run concurrently. These tasks may be completely unrelated but the end result is dependent on their outputs. Consider summation of a series, where we want to compute the value of e^x from Taylor series. The mathematical expression is given by

$$e^x = 1 + \frac{x^1}{1!} + \frac{x^2}{2!} + \frac{x^3}{3!} + \frac{x^4}{4!} + \frac{x^5}{5!} + \frac{x^6}{6!} + ... + \frac{x^n}{n!} \quad (12)$$

A single–threaded conventional implementation would have to calculate all the terms one–by–one and then sum up the result in the end. However, in a multi–threaded implementation, each thread would calculate only one term. All the treads will perform their computation in parallel and the end result is then summed up. The computation–intensive task of calculating factorials and higher powers of x is parallelised and results in significant reduction of computation time.

5.2. Data–Parallelism

In data–parallelism same operation is performed on individual elements of data. A simple example is that of scalar matrix multiplication. Consider an array of size n being multiplied with a scalar constant c. The result of each multiplication can be calculated independently by assigning a separate thread for the task. This is illustrated in figure 3 where input array is `A[]` and resultant array is `B[]`. Data–parallelism applies to any scenario where values in resultant data array only depends on values from input array. FDTD is a good example of data–parallelism and a GPU implementation can take advantage of accelerated computing.

6. Simulation of 1D DNG Slab

6.1. Problem Specification

An electromagnetic wave travelling in z direction is incident on a slab with negative values of permittivity and permeability (DNG) at the frequency of operation [6]. Sinusoidal wave, Gaussian pulse and Ricker wavelet are used as sources. Transmission and reflection coefficients are calculated at the air–slab interface. Refractive index of slab for a range of frequencies is also computed. By varying parameters, the simulation can be scaled to any desired frequency or wavelength.

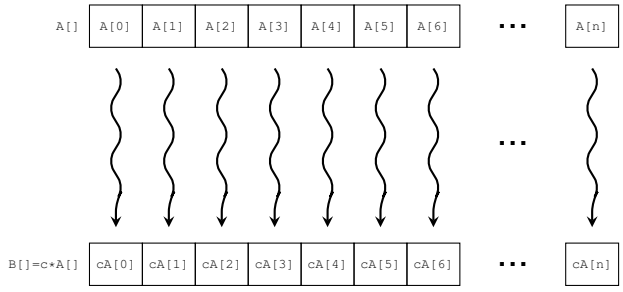


Figure 3: Data–parallelism

6.2. Simulation Results

The simulation is run for both lossless and lossy cases with sinusoidal, Gaussian and Ricker wavelet sources. The slab parameters are set such that at frequency of operation, f_0, the permittivity and permeability of slab are both negative and result in a refractive index $n = -1$.

6.3. Simulation Parameters

The number of spatial steps is set as 4096 and simulation is run for 4×4096 time steps. The slab is located between steps 1365 and 2731. Δz or spatial step is set as 3 mm and time step, Δt, is set as 50 ps. Frequency of operation is $f_0 = 0.1953125$ GHz and Courant number for this configuration comes out to be $S_c = 0.5$. In order to obtain relative permittivity and permeability of -1 at required f_0, plasma frequencies are set as $\omega_{pm}^2 = \omega_{pe}^2 = 2 \times (2\pi f_0)^2$ with $\epsilon_\infty = \mu_\infty = 1$. First order absorbing boundary condition (ABC) are applied on fields at end points.

6.4. Incident and Transmitted Fields

Simulation with Gaussian pulse reveals that low frequency components are reflected at the interface which is confirmed from the transmission and reflection coefficients obtained for the air–slab interface. At f_0, the transmission coefficient is 1 and there are no reflections when a sinusoidal source with f_0 is incident on the slab. Under steady–state conditions, transmitted wave inside the slab has negative phase velocity while energy is propagating in $+\hat{z}$ direction as expected.

6.5. Refractive Index

Following [6], the refractive index was calculated from

$$n_{FDTD} = \frac{1}{jk_0(z_1 - z_2)} log \left| \frac{E_x(\omega, z_2)}{E_x(\omega, z_1)} \right|. \quad (13)$$

Where, k_0 was the wave number set as ω_0/c and the fields were recorded at locations $z_1 = 1415\Delta z$ and $z_2 = 1424\Delta z$. For both, Gaussian pulse and Ricker wavelet, $Re(n)$ was -1 at f_0 while $Im(n)$ was sufficiently close to 0.

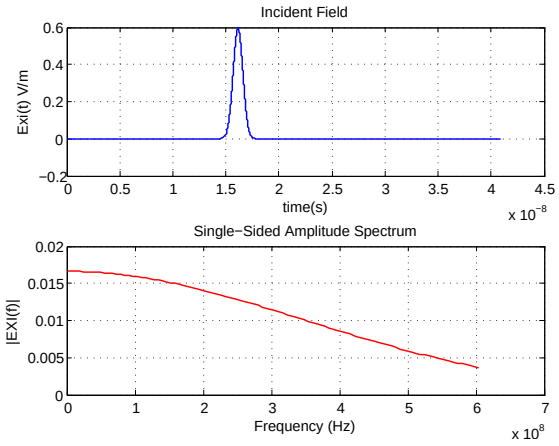


Figure 4: Incident Gaussian pulse

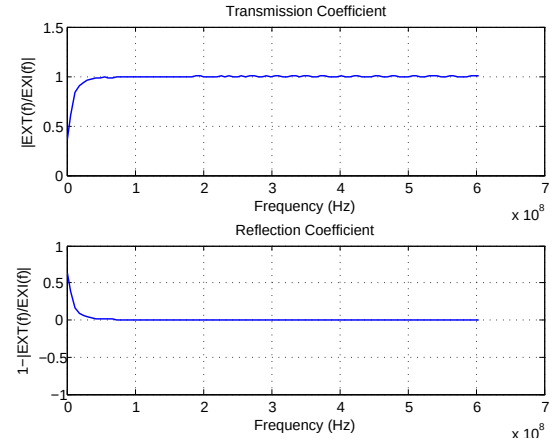


Figure 5: Transmission and reflection coefficients

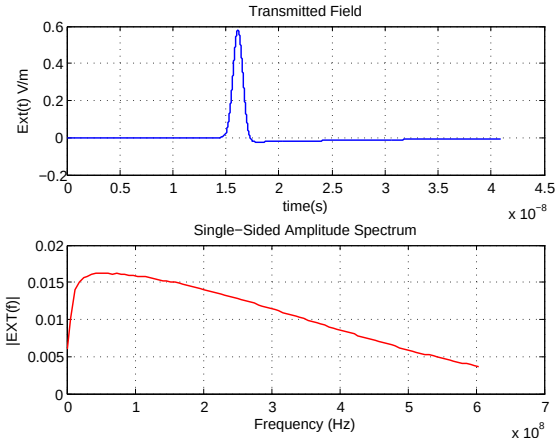


Figure 6: Transmitted Gaussian pulse

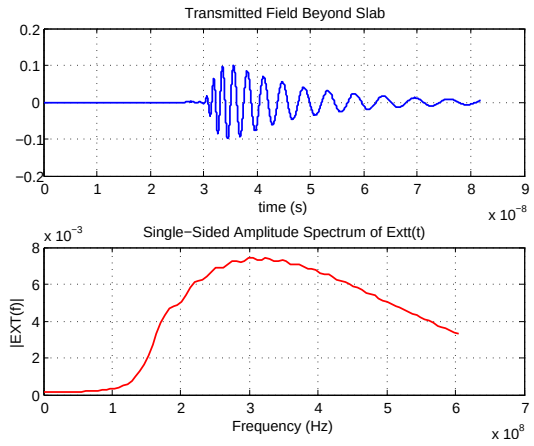


Figure 7: Transmitted Gaussian pulse beyond slab

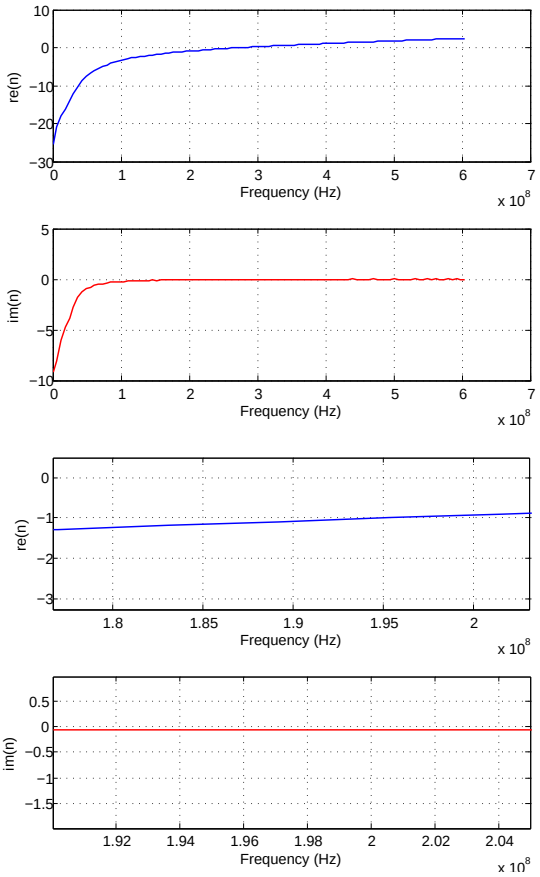


Figure 8: Refractive index

7. Simulation of 2D DNG Slab

7.1. Update Equations

The most common 2D configurations are TE^z or TM^z polarisation where the problem space is confined to xy–plane. In TE^z, electric field components are transverse to z–axis and vice versa. For 2D simulation of DNG slab, TM^z polarisation is assumed. The field components of interest would be E_z, H_x and H_y. Following the approach for 1D

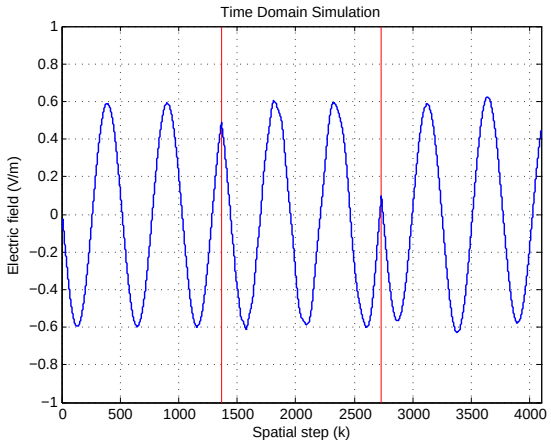


Figure 9: Steady-state under lossless conditions

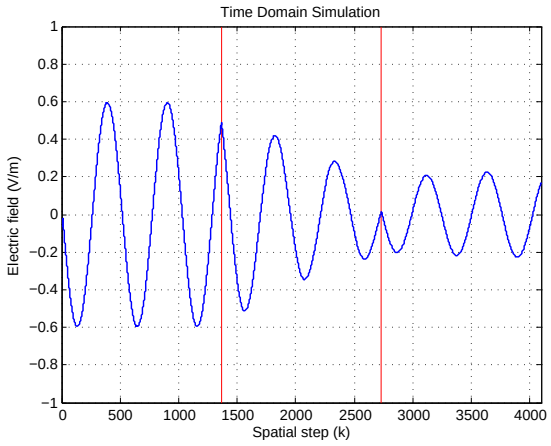


Figure 10: Steady-state under lossy conditions

case FDTD update equations are

$$D_z^{n+1}[i,j] = D_z^n[i,j] + \frac{\Delta t}{\Delta}\left(H_y^{n+\frac{1}{2}}\left[i+\frac{1}{2},j\right] - H_y^{n+\frac{1}{2}}\left[i-\frac{1}{2},j\right] - H_x^{n+\frac{1}{2}}\left[i,j+\frac{1}{2}\right] + H_x^{n+\frac{1}{2}}\left[i,j-\frac{1}{2}\right]\right), \tag{14}$$

$$B_x^{n+\frac{1}{2}}\left[i,j+\frac{1}{2}\right] = B_x^{n-\frac{1}{2}}\left[i,j+\frac{1}{2}\right] + \frac{\Delta t}{\Delta}\left(-E_z^n[i,j+1] + E_z^n[i,j]\right) \tag{15}$$

and

$$B_y^{n+\frac{1}{2}}\left[i+\frac{1}{2},j\right] = B_y^{n-\frac{1}{2}}\left[i+\frac{1}{2},j\right] + \frac{\Delta t}{\Delta}\left(E_z^n[i+1,j] - E_z^n[i,j]\right). \tag{16}$$

It is important to note here that DNG slab medium is assumed anisotropic. The auxiliary update equations (9 and 8) to obtain electric and magnetic fields, E_v and H_v ($v \in x, y, z$), from corresponding flux densities, D_v and B_v, remain unchanged.

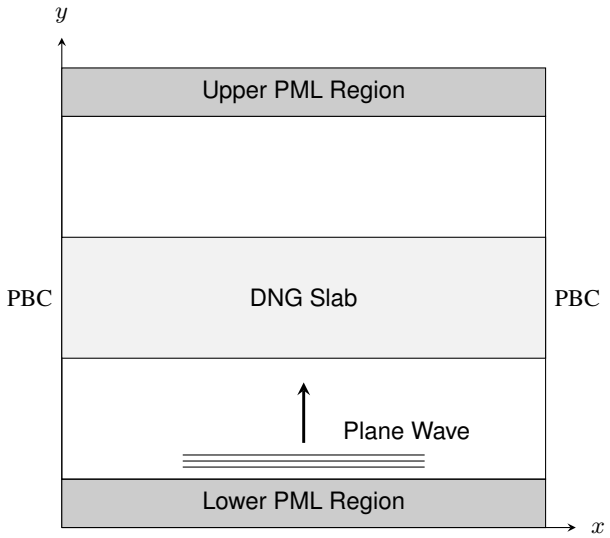


Figure 11: Simulation geometry

7.2. Simulation Geometry

The DNG slab interface is perpendicular to incident plane wave propagating in $+y$ direction. Periodic boundary conditions (PBC) are applied at $x = 0$ and $x = x_{max}$. In y direction the grid is terminated at both ends by perfectly matched layer (PML) to absorb any incoming waves. The solution geometry is depicted in figure 11. The arrangement of field nodes is shown in figure 12. Magnetic field components are updated first and then used to update electric field.

The solution space is bounded in y direction at both ends by H_x which acts as the boundary for PML. H_x at these end points is set to 0 so that any out–going fields are reflected back into PML. Essentially, the j size of H_x arrays is one greater than H_y and E_z arrays.

7.3. Simulation Parameters and Results

The solution space is 512 cells in both x and y directions without taking into account the width of PML, which is 50 cells wide. The plane wave source is located 10 cells from the lower PML layer. The spatial and temporal steps are set as $\Delta x = \Delta y = \Delta = 3$ mm and $\Delta t = 50$ ps, respectively; with a Courant number of 0.5. Frequency of operation is $f_0 = 1.5625$ GHz. The DNG slab parameters are same as in the case of 1D DNG simulation.

Figure 13 shows the refractive index obtained for a range of frequencies with a Gaussian pulse excitation. Again, real part of refractive index at f_0 is close to -1, whereas, imaginary part is close to 0.

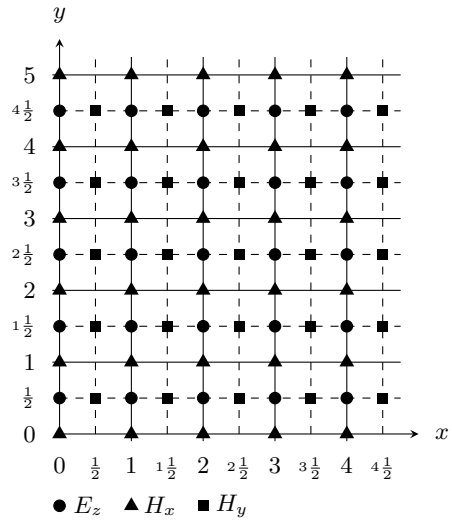


Figure 12: Arrangement of field nodes

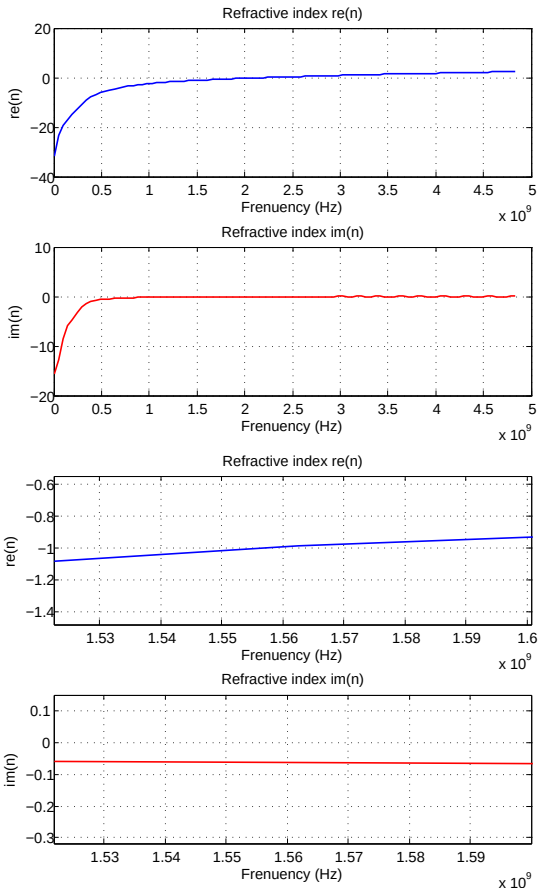


Figure 13: Refractive index of 2D DNG slab

8. FDTD Modelling of Lossless Cylindrical Cloak

8.1. The Electromagnetic Invisibility Cloak

It is well known that we can only see things when light bounces off them and reaches our eyes. This is the reason why transparent objects can sometimes be difficult to spot,

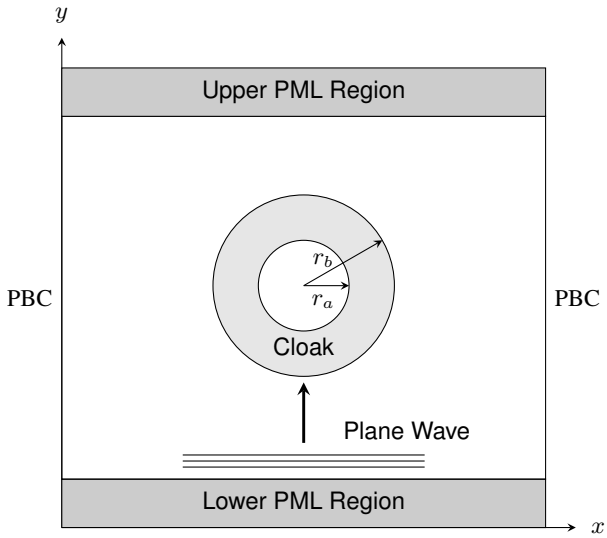


Figure 14: Simulation geometry

like window panes. If we can somehow make light bend around the corners of an object so that it continues on its trajectory then that object will appear invisible. Invisibility has, for ages, remained confined to only fiction books but in modern day world of optical transformations and artificially engineered materials, this no longer is a mystery.

An electromagnetic cloak at microwave frequencies was proposed and tested for the first time by Pendry et. al. [2]. The cloak is cylindrical in shape meant to hide a circular object. This is probably the simplest implementation sufficient for proof of concept. To bend light around the circular object the cloaking material must exhibit negative values of permittivity and permeability. The cloaking medium itself is anisotropic. The first attempt at modelling this electromagnetic cloak using the FDTD algorithm was by Zhao et. al. [3]. Their FDTD implementation was tested using simulation software Comsol.

8.2. Problem Specification

The implementation in [3] is for TE^z while in this paper TM^z approach is followed as in the case of DNG slab problems. The cloaking parameters are same and given by

$$\mu_r(r) = \frac{r - r_a}{r}, \tag{17}$$

$$\mu_\phi(r) = \frac{r}{r - r_a}, \tag{18}$$

$$\epsilon_z(r) = \left(\frac{r_b}{r_b - r_a}\right)^2 \frac{r - r_a}{r}. \tag{19}$$

Here, r_a and r_b are the inner and outer radii of cloaking shell. r_a and r_b are chosen as 0.1 m and 0.2 m respectively. The FDTD implementation is first tested on Matlab, then implemented using C++ and finally on GPU. The problem geometry is depicted in figure 14. The FDTD update equations for TM^z are completely analogous to those for

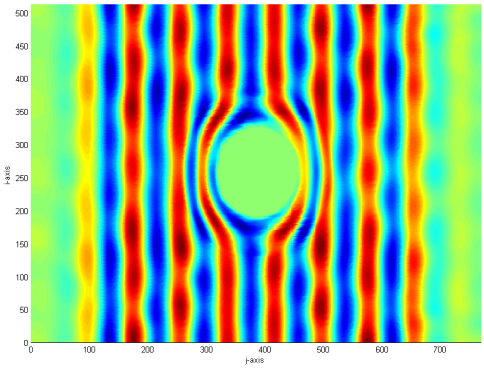


Figure 15: Ez under steady state for lossless cloak

	Platform/ Configuration	Compiler/ Toolchain
Matlab	x64	NA
C++	x64/O3	VC++, gcc/g++
OpenCL	x64/O3	VC++, gcc/g++
CUDA	x64/O3	nvcc for win/linux

Table 1: Operating system, platform/configuration and compiler/toolchain used for performance testing

TE^z presented in [3]. The update equations for D_z, H_x and H_y remain the same as in the case of 2D DNG problem. Figure 15 shows E_z under steady–state. All simulation c1odes are available at `http://code.google.com/p/computational-electromagnetics/`

9. Performance Analysis

9.1. Hardware and Software Set–up

Matlab, C++, CUDA and OpenCL implementations are tested with respect to space and time. Operating system, platform/configuration and compiler/toolchain for these implementations are listed in table 1. Simulations use `double` data type for arrays on 64 bit optimised platform. The CPU is an Intel Core 2 Duo E8400 @3.00 GHz with 4 GB RAM. For CUDA simulations, GPU is GTX 500 Ti with 192 shaders and 1 GB of memory. Visual C++ 2010 Express is the IDE used on 64 bit Windows 7. The flavour of linux is Fedora 14 64 bit. Hardware and software configuration is listed in table 2.

10. Conclusions

The goal of this paper was to analyse GPU performance gain of dispersive FDTD and GPU implementation of lossless cylindrical cloak. It was shown that materials with negative permeability and permittivity can be effectively modelled using Drude dispersive model. The numerical results showed good agreement with theoretical values in the case of DNG slab problem

CPU	Intel Core 2 Duo E8400 @3.00 GHz
RAM	4.00 GB DDR2
GPU	nVidia Geforce GTX 550 Ti 1 GB
Matlab	2010a 64 bit
Linux	Fedora 14 64 bit
Windows	Win7 64 bit
Cygwin	64 bit on Win7

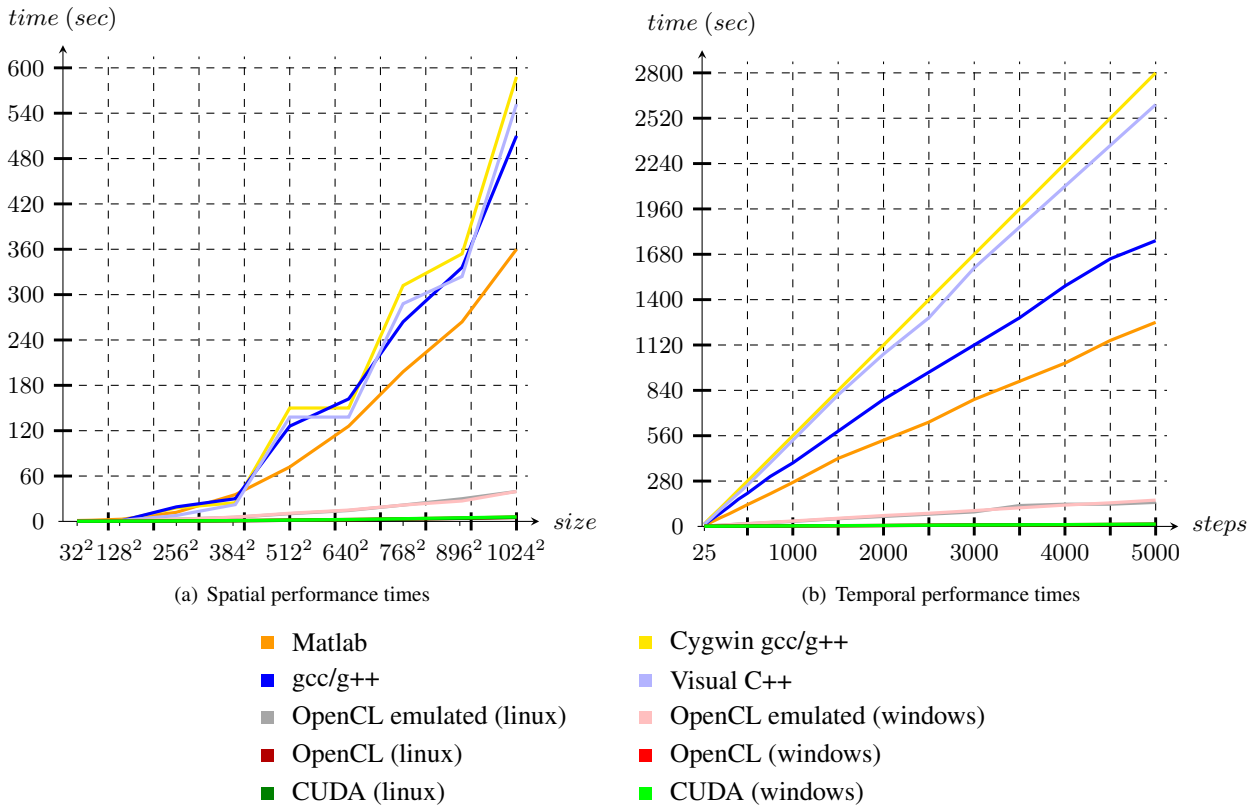
Table 2: Hardware and software used for performance testing

The 1D and 2D cases of slab problem was then implemented using C++ and GPU. A comprehensive performance analysis showed that GPU was able to perform much better both, as the problem domain and maximum time stepping are increased. For smaller problems, however, it is better to use Matlab or C++ due to data copying overhead associated with GPU implementation.

The lossless case of cylindrical cloak, as presented by Zhao et. al. in [3], was implemented using Matlab, C++ and finally on GPU with minor modifications. The simulations showed adequate similarity to accepted results.

Acknowledgement

I would like to thank Dr. Rashad Ramzan for his guidance.



(a) Spatial performance times

(b) Temporal performance times

Figure 16: Performance comparison

References

[1] S. G. et al, "Metamaterials and fdtd based numerical modeling studies," *ELECO*, Sep 2007.

[2] D. Schurig, J. J. Mock, B. J. Justice, S. A. Cummer, J. B. Pendry, A. F. Starr, and D. R. Smith, "Metamaterial Electromagnetic Cloak at Microwave Frequencies," *Science*, vol. 314, no. 5801, pp. 977–980, 2006.

[3] Y. H. Argyropoulos C., Yan Zhao, "A radially-dependent dispersive finite-difference time-domain method for the evaluation of electromagnetic cloaks," *IEEE Transactions on Antennas and Propagation*, vol. 57, pp. 1432–1441, May 2009.

[4] J. B. Schneider, *Understanding the Finite Difference Time-Domain Method*. www.eecs.wsu.edu/~schneidj/ufdtd, 2010.

[5] K. Yee, "Numerical solution of inital boundary value problems involving maxwell's equations in isotropic media," *IEEE Transactions on Antennas and Propagation*, vol. 14, pp. 302–307, May 1966.

[6] R. W. Ziolkowski and E. Heyman, "Wave propagation in media having negative permittivity and permeability," *Physical Review*, vol. 64, October 2001.

Graphene metamaterials

Spontaneous nonparametric down-conversion of light

Vladimir Hizhnyakov[1], Helle Kaasik[1] and Imbi Tehver[1*]

[1]Institute of Physics, University of Tartu, Riia 142, 51014 Tartu, Estonia
*corresponding author, E-mail: tehver@fi.tartu.ee

Abstract

The spontaneous down-conversion of laser light in a dielectric plate and/or metal-dielectric interface is considered. It is found that strong enhancement of the process takes place near the critical intensity of excitation. The further increasing of intensity will cause weakening of the emission. The crossover of the efficiency takes place if the amplitude of oscillations of the eikonal coincides with the wavelength of excitation.

1. Introduction

Spontaneous nonparametric down-conversion of photons – the creation of photon pairs on the expense of the single photons of laser in case of absence of the feedback is the nonlinear quantum phenomenon which takes place due to existence of the zero-point fluctuations. In this process the laser field, due to second-order nonlinear interaction perturbs the refractive index which causes the periodical in time perturbation of the zero-point state and the emission of the photon pairs [1-11]. The process belongs to the phenomena of general importance while it is a consequence of the fundamental fact established by the quantum theory that the vacuum of space is not empty: it is full of quantum fluctuations. The latter show up e.g. as emitted photons if the zero-point state undergoes the time-dependent perturbations. It is of remarkable interest also from practical point of view while generated photon pairs are in the entangled state. At the usual conditions the process has extremely low probability and is observed only in case of positive feedback, e.g. in parametric oscillators. However, at present there exist possibilities not only to use strong laser light but also to enhance the interaction of light with matter using e.g. surface plasmon-polaritons, and in this way to increase the intensity of the down-conversion.

The time-dependence of the zero-point state of the field can also be achieved if the boundary conditions in time are changed, e.g. by taking a resonator and modulating in time its length. The two-photon emission, which arises in this case, is called the dynamic Casimir effect [10-15], referring to the fact that the usual (static) Casimir effect [12] - the attraction of the mutually parallel light reflecting plates, displays the existence of the zero-point energy of the electromagnetic field. The emission, which is generated in a resonator with periodically changing boundary conditions has been studied by several authors (see, e.g. [12-21]). In this case, the frequency of the one or several modes of the resonator is periodically changed. If the half of the period of modulation of frequency coincides with the period of the mode then the parametric resonance takes place resulting in the excitation of the mode. In this case the energy of the mode is exponentially growing in time.

However, this mechanism of the enhancement of radiation takes place only in case of a resonator (cavity) having discrete modes with rather different frequencies: only in this case the periodical change of the frequency of a mode will not mix it with other modes of the cavity which would destroy the parametric resonance. This mechanism can be used for the microwaves, when the characteristic size of the resonator is of the order of cm. In case of visible light this mechanism cannot be used due to very small size of the resonator which in this case should be comparable to the wave length of light. The dynamical Casimir effect for microwaves was recently observed in [22, 23].

In this communication we consider the two-photon emission in visible frequency excited by the standing laser wave in a dielectric plate or a metal/dielectric interface. In the latter case the plasmon-polaritons can be generated. Here the field enhancement takes place allowing one to increase the intensity of the down conversion. Two possible geometries of the set-up are considered: the wave front of the standing wave of the laser is 1) parallel or 2) perpendicular to the interface. In the first case the dielectric is supposed to have the non-zero second-order susceptibility $c^{(2)}$. In the second case this non-zero value of $c^{(2)}$ of the dielectric is not needed while for the waves propagating along the interface the required components of $c^{(2)}$ differ from zero due to the inherent asymmetrical structure of the interface.

The arising emission results from the field-induced fast modulation of the optical length (eikonal) in time which, in its turn, leads to a fast modulation of the zero-point state of the quantum field. In the case under consideration the emitting system is open, i.e. the feedback coupling is absent. The process under consideration is (quasi)stationary. The emission has a noticeable intensity only if the velocity V of the oscillations of the optical length is approaching the velocity of light c_0. Although usually the latter condition is very difficult to fulfill, modern light sources may have sufficient power to modulate the dielectric so strongly that the case with $V = c_0$ or even with $V > c_0$ can be achieved. Obviously it is of interest to know how the light conversion

depends on the laser power in this case. Below we propose an answer to this question.

2. Emission of dielectric with oscillating in time optical length

Let us first consider the quantum emission of a dielectric with a periodically time-dependent refractive index $n(t)$. The time-dependence of n may be achieved, e.g. if the dielectric is exposed in a strong standing laser wave. We restrict ourselves to the consideration of the emission in a fixed direction. Then the equation for the field operator has the form [9-11]

$$\left[\partial^2/\partial t^2 - (c_0/n(t))^2\,\partial^2/\partial x^2\right]\hat{A} = 0, \qquad (1)$$

where $n(t) \approx n + n_0' \cos w_0 t$, $n_0' = c^{(2)} E_0$, E_0 is the amplitude of the standing laser wave, c_0 is the velocity of light in vacuum. For the convenience of consideration, we suppose that the dielectric is placed into a resonator, the length of which L_0 tends to infinity. We also suppose that only a part of the dielectric is excited; at that the refractive index slowly changes with x. This allows one to use Eq. (1) with $n(t)$ replaced by $n(t,x)$. The field operator satisfies the boundary conditions, which means that it turns to zero at the borders at any time moment. Taking for the coordinates of the mirrors $x_0 = 0$ and $x_1 = L_0$, both, Eq. (1) and the boundary conditions are satisfied if $\hat{A}(x,t)$ is chosen in the form

$$\hat{A}(x,t) = \sum_k \sin(p\,kl(t,x)/l(t))\hat{A}_k(t), \qquad (2)$$

where $k = 0, \pm 1, \pm 2 \ldots$, $l(t,x) = \int_0^x dx' n(t,x')$ is the optical length (eikonal) at the coordinate x and the time moment t, $l(t)$ is the full optical length.

Full paper should be submitted electronically via `http://metaconferences.org/ocs/index.php/META/index/pages/view/submission/` as a processed PDF. Acknowledgement of receipt of the submission will be sent to the contact-author e-mail address.

To find the rate of emission caused by the time-dependence of $n(t)$ we will calculate the correlation function $D_k(t,t') = \langle 0|\hat{A}_k(t)\hat{A}_k(t')|0\rangle$, where $|0\rangle$ is the zero-point state of the field. Here we refer to [24,25], where it was shown that in the large t, t' this limit

$$D_k(t,t') = \frac{1}{2w_k}\left(\left(1+|n_k|^2\right)e^{-iw_k(t-t')} + |n_k|^2 e^{iw_k(t-t')}\right),$$

where the coefficient $|n_k|^2$ describes the number of the generated photons N_k with the frequency w_k. The intensity of emission is then given by $d|n_k|^2/dt$.

To find N_k we insert Eq. (2) into Eq. (1) and neglect the terms $\propto dn(t,x)/dx$. We get

$$\sum_k \left[\partial^2/\partial t^2 + (p\,ck/l(t))^2\right]\hat{A}_k(t)\sin(p\,kl(t,x)/l(t)) = 0. \qquad (3)$$

Let us consider x outside the excited area. For such x Eq. (1) reduces to the usual wave equation of a non-dispersive dielectric with a constant refractive index n_0. Inserting Eq. (3) into this equation, we find for large L_0

$$\sum_k \left[\frac{\partial^2 \hat{A}_k}{\partial t^2} + w_k^2 \hat{A}_k - \frac{kpx}{L_0^2}\left(2\dot{L}\dot{\hat{A}}_{k,\tilde{q}} + \ddot{L}\hat{A}_k\right)\cos\left(\frac{pkx}{L_0}\right)\right] = 0, \qquad (4)$$

where $w_k = p\,ck/L_0$, $c = c_0/n$ is the velocity of light (polariton) in the dielectric. Taking into account the identity

$$x_0 = -\left(2L_0/p\right)\sum_1^\infty (-1)^m m^{-1}\sin(p\,mx/L_0)$$

we get

$$\left(\partial^2/\partial t^2 + w_k^2\right)\hat{A}_k + w_k \hat{B}_k \simeq 0, \qquad (5)$$

where

$$\hat{B}_k = \tfrac{1}{pc}\sum_{j\neq k}(-1)^{j-k}\, j(2\dot{L}(t)\dot{\hat{A}}_j + \ddot{L}(t)\hat{A}_j)/(j^2-k^2),$$
$$j = 0, \pm 1, \pm 2 \ldots.$$

Eq. (5) can be presented in the following integral form:

$$\hat{A}_k(t) = \hat{A}_k^{(0)}(t) - \int_0^t dt_1 \sin(w_k(t-t_1))\hat{B}_k(t_1), \qquad (6)$$

where $\hat{A}_k^{(0)}(t)$ is the field operator in vacuum. From Eq. (6) it follows that in the $t \to \infty$ limit the operator $\hat{A}_k(t)$ consists of the terms $\propto e^{-iw_k t}$ and $\propto e^{iw_k t}$. The terms with $w_k + w_j \simeq w_0$ make a largest contribution to the integral; other terms are small and may be neglected (this corresponds to the RWA, which holds in case when the laser field is weaker than the atomic field). Therefore, the only essential contribution to this integral comes from the terms with $L(t_1)\hat{A}_j(t_1) \propto \mathrm{e}^{\pm i(w_0 - w_j)t_1}$, for which $2\dot{L}(t)\,\partial\hat{A}_j(t)/\partial t + \ddot{L}(t)\hat{A}_j(t) \propto j^2 - k^2$. As a result, the factor $j^2 - k^2$ in the equation for $\hat{B}_k$ is cancelled and we get

$$\hat{B}_k(t) \approx V\cos(w_0 t)\,\hat{Q}(t), \qquad (7)$$

$$\hat{Q}(t) = k_0^{-1}L_0^{-1}\sum_{j=-k_0}^{k_0}(-1)^k\, j\hat{A}_j(t), \qquad (8)$$

k_0 is the integer part of $w_0 L_0/pc$. From Eqs. (6) and (7) it follows that the number of the emitted photons in the large t limit equals

$$N_k \simeq \left(V^2 c_0 k/2\right)\int\int_0^t dt_1 dt_1' e^{i(w_0 - w_k)(t_1 - t_1')} D(t_1, t_1'), \qquad (9)$$

where $D(t,t') = \langle 0|\hat{Q}(t)\hat{Q}(t')|0\rangle$. One can see that the number of the emitted photons is determined by the Fourier transform of the pair correlation function $D(t,t')$ for the large t and t'.

3. Low velocity limit

If $V \ll c$ then one can replace in Eq. (8) for $\hat{Q}$ the field operator $\hat{A}_j$ by $\hat{A}_j^{(0)}$. In this approximation

$$D_k(t) = d_{0,k}(t) = \frac{\hbar}{2k_0^2 L_0^2}\sum_{j=1}^{k_0} j^2 w_j^{-1} e^{iw_j t} \qquad (11)$$

Replacing the sum over j by the integral over $w_j = jw_0/k_0$ one gets the following equation for the Fourier transform of $d_{0,k}(t)$:

$$d_0(w_k) = \frac{\hbar n'(w-w_k)}{w_0^3 c_0 L_0} \qquad (12)$$

where $n' = n(w-w_k)$ is the refractive index for the frequency $w-w_k$. This gives the following rate of generation of photons of the mode k:

$$\dot{N}_{0k} = \frac{V^2 nn' w_k (w_0 - w_k)}{2L_0 w_0^3 c_0}. \qquad (13)$$

We take now into account that the full number of modes passing through the irradiated area in the spectral interval between w and $w+dw$ equals

$$r(w)dw = \mathrm{N}L_0 dw/p\,c_0, \qquad (14)$$

where

$$\mathrm{N} \sim p^2 (S/2\bar{l}^2)(n_0^2 - 1) \qquad (15)$$

is the number of the modes with frequency w in the irradiated area of the dielectric with the cross section $S, n_0 = n(w_0)$, $\bar{l}$ is the characteristic wave length. Taking into account that photons are emitted by pairs with the frequencies w and $w_0 - w$ we get

$$\bar{l}^{-2} = \left(w^2 n^2 + (w_0 - w)^2 n'^2\right)/8w_0^2 l_0^2$$

where $l_0 = w_0/c$. Therefore in the case $v = V/c_0 \ll 1$ the spectral rate of emitting photons equals

$$\dot{N}_0(w) \approx \frac{p\,v^2 nn' S}{2w_0^2 \bar{l}^2}(n_0^2 - 1) w (w_0 - w) \qquad (16)$$

(here $n \equiv n(w)$ and $n' \equiv n(w_0 - w)$ are the refractive indexes for the frequencies w and $w_0 - w$). We see that the emission under consideration is different from the emission in small resonator considered in Refs. [1,4-8,12-21]: it is stationary, its spectrum is broad, while in the case of small resonator it is non-stationary (exponentially increasing in time) and quasi-monochromatic.

The full rate of the generating of photons in the small velocity v limit is

$$\dot{N}_0 \approx \int_0^{w_0} \dot{N}(w)dw \approx \frac{pV^2 w_0 S}{160c^2 l_0^2}(n_0^2 - 1). \qquad (17)$$

4. Arbitrary velocity

To find the emission for an arbitrary velocity, we follow the calculations given in [9-11] (see part 2.2.1, the k=2 case). We use the equation of motion for the operator $\hat{Q}$:

$$\hat{Q}(t) = \hat{Q}^{(0)}(t) + 2vw_0\int_0^t dt_1 G(t-t_1)\cos(w_0 t_1)\hat{Q}(t_1) \qquad (18)$$

($t \le t_0$), which directly follows from Eqs. (6) – (7). Here $\hat{Q}^{(0)}$ is given by Eq. (8) for $\hat{Q}$ with $\hat{A}_j^{(0)}$ instead of $\hat{A}_j$,

$$G(t) = (\Theta(t)/pk_0^2)\sum_{k=1}^{k_0} k \sin w_k t$$

is the Green function. Using Eq. (18) once again (this time for $\hat{Q}(t_1)$) and inserting it into $D(t,t')$ we find

$$D(t,t') \simeq d(t,t') + 2vw_0\int_0^t dt_1 G(t-t_1)\cos(w_0 t_1) D_1^*(t_1,t')$$
$$+ v^2 w_0^2 \int_0^t dt_1 \int_0^{t_1} dt_2 G(t-t_1)G(t_1-t_2)e^{-iw_0(t_1-t_2)}D(t_2,t'),$$

where $d(t,t') = \langle 0|\hat{Q}^{(0)}(t)\hat{Q}(t')|0\rangle$, and an analogous equation for $d^*(t',t)$. We take into account only $e^{iw_0(t_1-t_2)}$ term of the factor $4\cos(w_0 t_1)\cos(w_0 t_2)$; other terms oscillate fast and drop out. Above the term $\propto v$ may be omitted while it also oscillates fast. Taking into account that in the large time limit the correlation functions $D(t,t')$ and $d(t,t')$ depend on the time difference and using the relation

$$\int_0^\infty dt \int_0^t dt_1 \int_0^{t_1} dt_2 e^{iwt} = \int_0^\infty dt_2 e^{iwt_2}\int_0^\infty dt_1 e^{iwt_1}\int_0^\infty dt\, e^{iwt}$$

($t' \to \infty, t = t - t_1, t_1 = t_1 - t_2$), one gets the following equation for $D(w)$ [3-5] (the factor $e^{iwt'}$ cancels):

$$D(w) \simeq d(w) + v^2 G(w)G(w-1)D(w),$$

where

$$G(w) = \frac{1}{p}\left[1 + \frac{w}{2}\ln\frac{|1-w|}{|1+w|}\right] + \frac{iw}{2}\Theta(1-|w|),$$

and an analogous equation for $d^*(w)$ (we take $w_0 = 1$ for the frequency units). As a result, the number of the emitted photons with the frequency w per unit time and frequency equals:

$$\dot{N}(w) = \frac{\dot{N}_0(w)}{|1 - v^2 nn' G^*(w) G(1-w)|^2}. \qquad (19)$$

This expression describes the spectrum of emission under consideration for any value of v (see Fig. 1). It is important to note that this spectrum is continuous although the excitation was monochromatic. This property of the emission under consideration was primarily predicted in [9-11] and it was recently experimentally verified in [22,23].

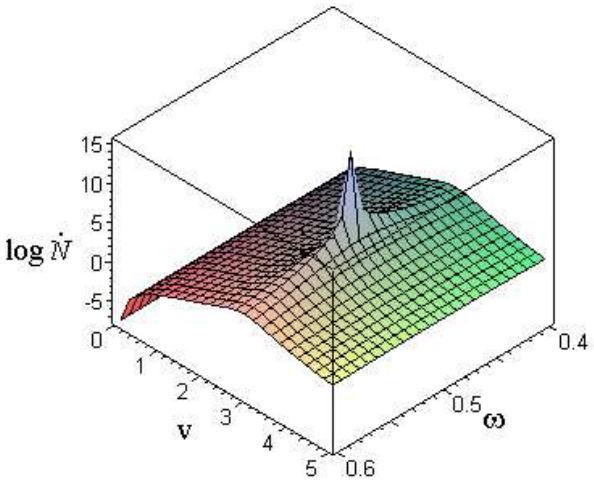


Figure 1: The logarithm of the rate of the emission of photons $\dot{N}$ by a medium with periodically time-dependent refractive index $n = n_0 + n' \cos w_0 t$ as a function of the frequency of emission w and maximal velocity v of the optical length (the units $w_0 = 1$ and $c_0 = 1$ are used).

If $v \ll 1$, then the intensity of the emission increases quadratically with v. However, if $v \gg 1$, then the dependence on v is the opposite: $\dot{N} \propto v^{-2}$. If v approaches the value $v_r = 4p / \sqrt{p^2 + (4 - \ln 3)^2} \approx 2.94$, then the resolvent diverges at $w = 1/2$ and the emission is resonantly enhanced (Fig. 2). This corresponds to a very intense conversion of laser photons to other photons. The given value of v_r is close to p, i.e. the value of v, which corresponds to the resonance between the oscillation of the optical length and the generated wave, when the amplitude of oscillations coincides with the wavelength of the emitted photons with the main frequency close to $w_0 / 2$.

5. Estimation of the number of generated photons

Let us present an estimation of the number of generated photons at the spontaneous down-conversion in a dielectric plate. First we estimate the velocity (v) of the periodical change of the optical length in the plate under the laser excitation with frequency w_0 in visible. To this end we consider the field generated by the laser pulse with the energy $\mathcal{E} = 10^{-5}$ J and duration $t = 10^{-11}$ sec focused on the

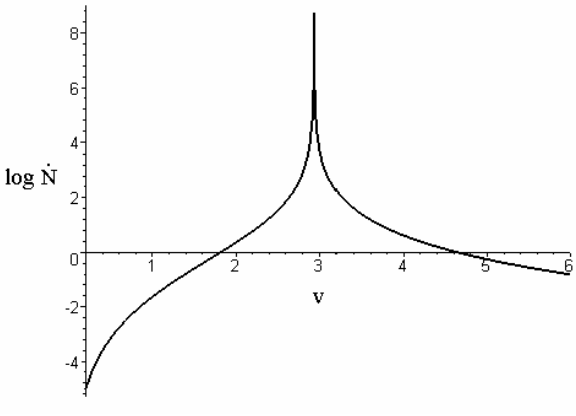


Figure 2: The intensity of the emission $I = \int w \dot{N}(w) dw$ as a function of $v = V/c \propto I_0$ in the case of a monochromatic excitation (I_0 is the laser intensity).

area $S = L \times a$, where $L = 0.01$ m is the length and $a = 10^{-4}$ m (0.1 mm) is the width of the irradiated area. This corresponds to $S = 10^{-6} \mathrm{m}^2$. The intensity of light is $I = \mathcal{E}/tS = 10^{12}\ \mathrm{W/m}^2$. This light intensity corresponds to the following strength of the electric field

$$E = 1.9 \cdot 10^7\ V/m.$$

The velocity v can be estimated as follows:

$$V = c^{(2)} EL/l$$

We take $c^{(2)} = 10$ pm/V and $l = 10^{-6}$ m (1 μm). We get

$$V \approx 1.9c$$

The number of generated photon per excitation pulse for the pulse $w_0 t = 10^5$ equals

$$N = t \int_0^{w_0} \dot{N}(w) dw \sim \frac{p t w_0 S}{160 l_0^2} \left(n_0^2 - 1\right) \frac{v^2}{c^2} \sim 10^7$$

i.e around million photons per light pulse. For repetition rate this means that *ca* one of every million of photons of the frequency w_0 will be converted to two photons with the frequencies $\approx w_0/2$.

The efficiency of the conversion may be remarkably enhanced using plasmon-polaritons for which the nonlinear susceptibility $c^{(2)}$ may have much larger values than used here typical for usual dielectrics value of $c^{(2)} = 10$ pm/V. Another possibility is given by the resonance $v = V/c = 2.9$: a careful choice of the of excitation condition together with the dielectric or metal-dielectric interface would also allow one to essentially increase the efficiency of the spontaneous down conversion.

6. Down conversion in a SNOM tip

Presented theory may be applied also for generation of entangled photon pairs in the metal-coated SNOM tip. If the pump laser beam is accessing the tip through the fiber (along its symmetry axis z), the inversion symmetry along this axis, should be broken. In these conditions, only three nonzero components of $c^{(2)}$ exist: $c^{(2)}_{zzz}$ and $c^{(2)}_{zxx} = c^{(2)}_{zyy}$ (here the first index corresponds to the electric field component of the pump photon, while the second and the third indices – respectively to the electric field components of the signal and of the idler photons). One should interpret the action of these nonzero components in the following way. At the tip the incident pump wave has in addition to the transversal electric field also a longitudinal (z-polarized) electric field component. Therefore the $c^{(2)}_{zzz}$ component describes the generation (at the tip output) of photon pairs of vanishing evanescent waves, while $c^{(2)}_{zxx}$ and $c^{(2)}_{zyy}$ components describe the generation, in addition to the photons of vanishing near-field waves, the pairs of collinearly polarized (i.e. polarization-entangled) two photons propagating in the far field. Therefore the two photons of an entangled pair can be found propagating outside of the tip. In directions close to z the polarization of photons is arbitrary; however both photons have the same polarization (i.e. their polarization states are entangled). The metal (gold) coating of the tip allows one to excite surface plasmons and to enhance the efficiency of the down conversion.

7. Conclusions

A theory of the nonparametric spontaneous down conversion of monochromatic light in dielectric with non-zero value of the second-order nonlinear susceptibility is proposed. The photons in the process are generated by pairs and they are in the entangled states. The intensity of emission is determined by the maximum of change of the velocity of the optical length (eikonal) in time caused by the laser light. The spectrum of emission is continuous. The later, in its turn linearly depends on the intensity of the light. In case of weak excitation the intensity of emission depends quadratically on the laser intensity. At strong excitation the dependence of the process on the laser intensity changes drastically. It is found that a strong enhancement of the emission takes place near the critical intensity of excitation. The emission then is quasimonochromatic; its frequency equals half of the frequency of the laser light. The further increasing of intensity will cause weakening and de-monochromatization of the emission. The crossover of the process occurs if the amplitude of oscillations of the optical length (eikonal) coincides with the wavelength of excitation. Numerical consideration shows that the efficiency of the down conversion under consideration for usual experimental conditions may be a pair of photons per million of exciting photons or more.

Acknowledgements

The research was supported by Estonian research projects SF0180013s07, IUT2-27 and by the European Union through the European Regional Development Fund (project 3.2.0101.11-0029).

References

[1] Moore, G. Quantum theory of the electromagnetic field in a variable-length one-dimensional cavity. *J. Math. Phys.* 11: 2679–2691, 1970.

[2] E. Yablonovitch, Accelerating reference frame for electromagnetic waves in a rapidly growing plasma: Unruh-Davies-Fulling-DeWitt radiation and the nonadiabatic Casimir effect, *Phys. Rev. Lett.* 62: 1742–1745, 1989.

[3] V. Hizhnyakov, Quantum emission of a medium with a time-dependent refractive index, *Quantum Optics* 4: 277–280, 1992.

[4] A.A. Lobashov, V.V. Mostepanenko, Quantum effects associated with parametric generation of light and the theory of squeezed states, *Theor. Mat. Phys.* 88: 913–925, 1991.

[5] V.V. Dodonov, A.B. Klimov, D.E. Nikonov, Quantum phenomena in nonstationary media, *Phys. Rev. A* 47: 4422–4429, 1993.

[6] H. Johnston, S. Sarkar, Moving mirrors and time-varying dielectrics, *Phys. Rev. A* 51: 4109–4115, 1995.

[7] H. Saito, H. Hyuga, The dynamical Casimir effect for an oscillating dielectric model. *J. Phys. Soc. Japan* 65, 3513–3523, 1996.

[8] M. Cirone, K. Rzazewski, J. Mostowski, Photon generation by time-dependent dielectric: A soluble model, *Phys. Rev. A* 55: 62 (1997).

[9] V. Hizhnyakov, Strong two-photon emission by a medium with periodically time-dependent refractive index, arXiv:quant-ph/0306095v1 (13 June 2003).

[10] V. Hizhnyakov, H. Kaasik, Dynamical Casimir effect: quantum emission of a medium with time-dependent refractive index, *IEEE Conference Proceedings: Northern Optics 2006*, IEEE Operations Center, Bergen, Norway, pp. 7–11, 2006.

[11] V. Hizhnyakov, H. Kaasik, Quantum emission of light by medium with time-dependent refractive index. *Proceedings of SPIE: ICONO 2007: Physics of Intense and Superintense Laser Fields; Attosecond Pulses; Quantum and Atomic Optics; and Engineering of Quantum Information, Minsk, 28.05-01.06.2007*. SPIE - International Society for Optical Engineering, 6726: 67262R-1–10, 2007.

[12] M. Bordag (editor), The Casimir Effect 50 Years Later: Proceedings of the Fourth Workshop on Quantum Field Theory under the Influence of External Conditions, World Scientific, Leipzig, 1999.

[13] V. Dodonov, Current status of the dynamical Casimir effect. *Phys. Scripta* 82: 038105, 2010.

[14] V.V. Dodonov, Nonstationary Casimir effect and analytical solutions for quantum fields in cavities with moving boundaries, *Modern Nonlinear Optics*, Part I, 119, (*Adv. Chem. Phys.* 119), second edition (ed M. W. Evans), Wiley, New York, pp. 309–394, 2002.

[15] D. A. R. Dalvit, P. A. Maia Neto, & F. D. Mazzitelli, Fluctuations, dissipation and the dynamical Casimir effect. Preprint http://arXiv.org/abs/1006.4790v2, 2010.

[16] C.K. Law, Effective Hamiltonian for the radiation in a cavity with a moving mirror and a time-varying dielectric medium. *Phys. Rev. A* 49: 433- 437, 1994.

[17] C.K. Law, Interaction between a moving mirror and radiation pressure: A Hamiltonian formulation, *Phys. Rev. A* 51: 2537–2541, 1995.

[18] M. Janowicz, Evolution of wave fields and atom-field interactions in a cavity with one oscillating mirror, *Phys. Rev. A* 57; 4784–4790, 1998.

[19] D.F. Mundarain, P.A. Maia Neto, Quantum radiation in a plane cavity with moving mirrors, *Phys. Rev. A* 57: 1379–1390, 1998.

[20] V.V. Dodonov, Generation of photons in a lossy and detuned cavity with an oscillating boundary, *Phys. Lett. A* 244: 517–522, 1998.

[21] G. Schaller, R. Schützhold, G. Plunien, G. Soff, Dynamical Casimir effect in a designed leaky cavity, *Phys. Lett. A* 297: 81–86, 2002.

[22] J. R. Johansson, G. Johansson, C. M. Wilson, F. Nori, Dynamical Casimir effect in superconducting microwave circuits. *Phys. Rev. A* 82: 052509, 2010.

[23] C. M. Wilson, G. Johansson, A. Pourkabirian, M. Simoen, J. R. Johansson, T. Duty, F. Nori, P. Delsing, Observation of the dynamical Casimir effect in superconducting circuit, *Nature*, 479: 376–379, 2011.

[24] V. Hizhnyakov, Multiphonon anharmonic decay of a quantum mode. *Europhysics Letters* 45: 508–513, 1999.

[25] V. Hizhnyakov, H. Kaasik, I. Tehver, High-order vibrational relaxation: a nonperturbative theory, *Eur. Phys. J. B*, 28: 271–276, 2002.

Acoustic metamaterials

On the feasibility of a 2D acoustic cloak using layers of elastic materials

Cécile Dutrion, Frank Simon

Department of Aerodynamics and Energetics Modeling,
Onera - The French Aerospace Lab
*corresponding author, E-mail: cecile.dutrion@onera.fr

Abstract

This paper examines the possibility of designing an acoustic cloak using a multilayered elastic cylindrical shell to eliminate the acoustic field scattered from a rigid cylinder impinged by plane waves. This scattered field is calculated by a semi-analytical code and depends on the dimensional and mechanical characteristics of the elastic layers. Optimization by genetic algorithm is led to determine the characteristics of the layers minimizing the scattering. Realizable elastic coatings leading to scattering reduction are eventually proposed.

1. Introduction

In the last years, different methods have been proposed to make an obstacle transparent to acoustic waves. There are two major approaches.

The first one is based on transformational acoustics and consists in designing a cloak able to guide waves around an object, without scattering. Indeed, thanks to a coordinate transformation method similar to that employed by Pendry [1] in the electromagnetic domain, Cummer and Schurig [2] demonstrated that perfect acoustic cloaking could be achieved in surrounding the obstacle with a specific anisotropic and inhomogeneous fluid. No such material can be found in nature, however the recent development of metamaterials offered new possibilities, and lately, some experimental realizations of materials having effective properties close to those prescribed by the transformational acoustics theory have been reported [3, 4].

The second type of solutions, called scattering cancellation techniques, has been introduced by Alù and Engheta [5]. The idea is to design a layer that permits a drastic reduction of the total scattering cross-section of the obstacle over a given frequency bandwidth. This approach has first been developed for electromagnetic cloaking, and has been extended afterwards to acoustic waves. Different proposals have been made. Bobrovnitskii [6, 7] studied the possibility of realizing coatings with tailored surface impedances. Chen and Farhat [8, 9] proposed a pattern structure with appropriate acoustic surface impedance leading to significant reduction of the scattering of a sphere. In a different way, but still relying on the minimization of the scattered field, García-Chocano *et al.* [10] designed an acoustic cloak for a cylindrical obstacle in surrounding it with an important number of cylinders of small diameter appropriately placed to minimize the scattering. Guild [11, 12] showed numerically that a drastic scattering reduction could be achieved with a single isotropic layer wrapped around an elastic or fluid sphere.

In this study, a scattering cancellation approach is adopted. We examine the possibility of acoustic scattering reduction with devices based on elastic vibration. The aim is to determine if layers of elastic materials could be employed to significantly reduce the scattering in the case of a rigid cylinder submitted to normal plane waves. First, the method used to evaluate the scattered pressure field in this configuration is described. Then, the inverse problem consisting in searching the parameters of the layers allowing a reduction of the acoustic scattering is exposed. The results of numerical minimization using genetic algorithm in the case of a bi-layer coating fixed on a rigid cylinder are presented, and finally a realizable configuration is proposed.

2. Evaluation of the scattered pressure field

2.1. Statement of the problem

Let us consider an infinite rigid cylinder of radius a placed in a fluid of mass density ρ and speed of sound c. A coating made of N layers of orthotropic viscoelastic materials is fixed on it. A plane acoustic wave of angular frequency ω is impinging normally on the covered cylinder. $\mathrm{e}^{-i\omega t}$ harmonic time dependence is assumed. Coordinates systems are chosen such that the direction of the incident wave coincides with the x-axis in cartesian coordinates and corresponds to $\theta = \pi$ in cylindrical coordinates. The geometry of the problem is depicted in Fig. 1.

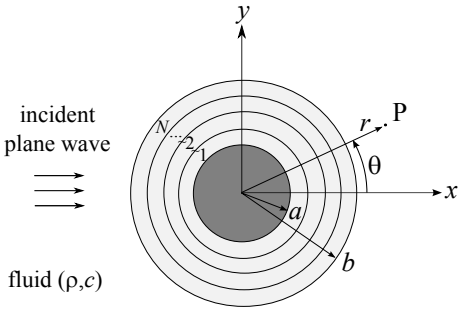


Figure 1: Multilayered coating made of N orthotropic viscoelastic materials and fixed on a rigid cylinder excited by a plane wave.

2.2. Pressure field in the exterior fluid

The acoustic pressure field in the exterior fluid p satisfies the Helmholtz equation

$$\triangle p + k^2 p = 0, \tag{1}$$

where $k = \omega/c$ is the wave number. This pressure field can be splitted up into two parts: the incident pressure p_{inc} and the scattered pressure p_{scat}. The scattered pressure is composed of a reflected part p_{refl}, corresponding to the reflection of the incident wave on a rigid cylinder of radius b, and a radiated part p_{el}, due to the vibration of the surface of the elastic coating. The sum of the incident pressure and the reflected pressure forms the blocked pressure.

$$p = \overbrace{p_{inc} + \underbrace{p_{refl}}_{p_{scat}}}^{p_{blocked}} + p_{el} \tag{2}$$

The aim is to cancel the scattered pressure, that is to say to tailor the elastic coating so that the radiated pressure p_{el} cancels the reflected one p_{refl}.

2.2.1. Incident pressure

The pressure due to a plane wave of amplitude p_0 travelling in the positive x-direction is usually written

$$p_{inc} = p_0 \, \mathrm{e}^{-i(\omega t - kx)}, \tag{3}$$

but it can also be represented as a series of cylindrical Bessel functions of integer order as follows:

$$p_{inc} = p_0 \, \mathrm{e}^{-i\omega t} \sum_{n=0}^{+\infty} i^n \epsilon_n J_n(kr) cos(n\theta) \tag{4}$$

where

$$\epsilon_n = \begin{cases} 1 & \text{if} \quad n = 0, \\ 2 & \text{if} \quad n \geqslant 1. \end{cases}$$

2.2.2. Scattered pressure

The scattered pressure must satisfy the Helmholtz equation and the Sommerfeld radiation condition (*i.e.* there can only be cylindrical waves travelling from the scatterer to infinity). Thus the scattered pressure can be written

$$p_{scat} = \mathrm{e}^{-i\omega t} \sum_{n=0}^{+\infty} A_n(\omega) H_n(kr) cos(n\theta) \tag{5}$$

where $A_n(\omega)$ is the unknown scattering coefficient and $H_n(x)$ is the cylindrical Hankel function of the first kind of order n.

The scattering coefficient $A_n(\omega)$ is determined using the boundary condition on the outer surface of the coating, stating that the acoustic radial velocity (resp. displacement) at $r = b$ is equal to the radial velocity (resp. displacement) of the external surface of the coating. Thanks to the projection of the linearized Euler equation in the radial direction

$$\omega^2 \rho u_r = \frac{\partial p}{\partial r}, \tag{6}$$

we obtain a relation between the displacement $u_r^N(b, \theta)$ of the external surface of the coating and the unknown scattering coefficient $A_n(\omega)$:

$$\begin{aligned} u_r^N(b,\theta) = \frac{\mathrm{e}^{-i\omega t}}{\omega \rho c} \sum_{n=0}^{+\infty} [p_0 i^n \epsilon_n J_n'(kb) \\ + A_n(\omega) H_n'(kb)] \, cos(n\theta). \end{aligned} \tag{7}$$

Thus, it is necessary to study the vibrations of the coating excited by a plane wave. A semi-analytical code has been developed to solve the equations of orthotropic elasticity in cylindrical configuration, evaluate $u_r^N(b, \theta)$, and finally p_{scat}.

2.3. Vibration analysis

In each layer k considered as lineraly elastic medium, the equations of motion are, in terms of stress components (σ_{ij}) and in the polar coordinates system (r, θ):

$$\begin{aligned} \frac{\partial \sigma_{rr}^k}{\partial r} + \frac{\partial \sigma_{r\theta}^k}{r \partial \theta} + \frac{1}{r}(\sigma_{rr}^k - \sigma_{r\theta}^k) = \rho_s^k \frac{\partial^2 u_r^k}{\partial t^2}, \\ \frac{\partial \sigma_{r\theta}^k}{\partial r} + \frac{\partial \sigma_{\theta\theta}^k}{r \partial \theta} + \frac{2}{r} \sigma_{r\theta}^k = \rho_s^k \frac{\partial^2 u_\theta^k}{\partial t^2}. \end{aligned} \tag{8}$$

where ρ_s^k is the mass density of the solid material composing the layer k, and (u_r, u_θ) represents the material displacement.

For a cylindrically orthotropic material, the generalized Hook's law can be written as:

$$\begin{pmatrix} \sigma_{rr}^k \\ \sigma_{\theta\theta}^k \\ \sigma_{r\theta}^k \end{pmatrix} = \begin{pmatrix} c_{11}^k & c_{12}^k & 0 \\ c_{12}^k & c_{22}^k & 0 \\ 0 & 0 & c_{33}^k \end{pmatrix} \begin{pmatrix} \epsilon_{rr}^k \\ \epsilon_{\theta\theta}^k \\ 2\epsilon_{r\theta}^k \end{pmatrix} \tag{9}$$

where c_{ij} are the elastic constants, and ϵ_{ij} are strain components.

Moreover the strain components are related to the displacements by the equations:

$$\begin{aligned} \epsilon_{rr}^k &= \frac{\partial u_r^k}{\partial r}, \\ \epsilon_{\theta\theta}^k &= \frac{\partial u_\theta^k}{r \partial \theta} + \frac{u_r^k}{r}, \\ \epsilon_{r\theta}^k &= \frac{1}{2} \left(\frac{\partial u_r^k}{r \partial \theta} + \frac{\partial u_\theta^k}{\partial r} - \frac{u_\theta^k}{r} \right). \end{aligned} \tag{10}$$

In the case of orthotropic material, the system obtained by substition of (9) and (10) into (8) is not readily solvable analytically. Therefore two approximate methods have been employed here.

2.3.1. Method 1

The first method was proposed by Skelton and James [13] and is based on a wave number domain approach and approximations classically used in the finite element method.

Circumferential variations of field quantities are represented by Fourier series, which gives, for instance for the

displacements:

$$\begin{pmatrix} u_\theta^k \\ u_r^k \end{pmatrix} = \sum_{n=-\infty}^{\infty} \mathrm{e}^{in\theta} \begin{pmatrix} u_{\theta,n}^k \\ u_{r,n}^k \end{pmatrix} \mathrm{e}^{-i\omega t}. \tag{11}$$

To take into account the propagation of waves in the radial direction due to a possible important thickness or softness of the elastic materials, spectral displacements are represented by quadratic functions in r, and radial variations of other field quantities are approximated by the finite element method. In each layer, the dynamic stiffness matrix $\mathbf{S}_n^k$ is calculated using a method of minimization of energy functional, as described in [13, 14]. It relates spectral displacements $\mathbf{u}_n^k$ and spectral excitations $\mathbf{F}_n^k$ at the inner and outer surfaces of the element ($r = a_{k-1}$ and $r = a_k$) and can be written

$$\mathbf{S}_n^k \mathbf{u}_n^k = \mathbf{f}_n^k \tag{12}$$

with $\mathbf{u}_n^k = \left(u_{\theta,n}^k(a_k), u_{r,n}^k(a_k), u_{\theta,n}^k(a_{k-1}), u_{r,n}^k(a_{k-1})\right)^T$ and $\mathbf{f}_n^k = \left(f_{\theta,n}^k(a_k), f_{r,n}^k(a_k), f_{\theta,n}^k(a_{k-1}), f_{r,n}^k(a_{k-1})\right)^T$.

A spectral dynamic stiffness "matrix" is also defined for the exterior fluid, where it can be derived from equations (5), (7) and (11) that

$$\rho\omega c \frac{H_{|n|}(kb)}{H'_{|n|}(kb)} u_{r,n}^N(b) = f_{r,n}(b). \tag{13}$$

The N element stiffness matrices are assembled together with the matrix of the exterior fluid in a ($2N$+2)x($2N$+2) block matrix, which gives the following matrix equation, expressing the continuity of displacements and stresses at layer interfaces:

$$\mathbf{Z}_n \mathbf{u}_n = \mathbf{e}_n, \tag{14}$$

where $\mathbf{Z}_n$ is the system spectral stiffness matrix, $\mathbf{u}_n$ is a vector containing the spectral displacements at the interfaces, and $\mathbf{e}_n$ a vector containing the spectral excitations at the interfaces.

Boundary conditions are applied (no displacement at the inner surface and radial excitation due to the blocked pressure on the outer surface). Finally the solution of the system of equations (14) gives the spectral displacements at the layer interfaces, and particularly at the outer surface, which allows the determination of the scattered field in all the exterior fluid.

2.3.2. Method 2

The second method, similar to that employed by Chen [15], Hasheminejad [16] and Jamali [17], is based on state space formulation, wave function expansion and transfer matrix approach.

Equations (8), (10) and (9) may be written as follows:

$$\frac{\partial \mathbf{Y}^k}{\partial r} = \mathbf{M}^k \mathbf{Y}^k, \tag{15}$$

where $\mathbf{Y}^k = \left(u_\theta^k, u_r^k, \sigma_{rr}^k, \sigma_{r\theta}^k\right)^T$ is called the state vector and $\mathbf{M}^k$ is a 4x4 complex matrix given in appendix.

The state vector $\mathbf{Y}^k$ is expanded in terms of unknown modal coefficients as

$$\mathbf{Y^k} = \begin{pmatrix} u_\theta^k \\ u_r^k \\ \sigma_{rr}^k \\ \sigma_{r\theta}^k \end{pmatrix} = \sum_{n=0}^{\infty} \begin{pmatrix} b u_{\theta,n}^k(\xi)\sin(n\theta) \\ b u_{r,n}^k(\xi)\cos(n\theta) \\ c_{44}^N \sigma_{rr,n}^k(\xi)\cos(n\theta) \\ c_{44}^N \sigma_{r\theta,n}^k(\xi)\sin(n\theta) \end{pmatrix} \mathrm{e}^{-i\omega t}, \tag{16}$$

where ξ is the dimensionless radial coordinate $\xi = r/b$.

The orthogonality of trigonometric functions gives

$$\frac{d\mathbf{V}_n^k}{d\xi} = \mathbf{P}_n^k(\xi)\mathbf{V}_n^k, \tag{17}$$

where $\mathbf{V}_n^k = \left(u_{\theta,n}^k, u_{r,n}^k, \sigma_{rr,n}^k, \sigma_{r\theta,n}^k\right)^T$ is the modal state vector. The modal matrix $\mathbf{P}_n^k$ is given appendix.

Layers are assumed to be thin enough to consider the matrix $\mathbf{P}_n^k(\xi)$ constant within each layer. This constant matrix can be evaluated at $\xi = \xi_{k-1}$, the inner interface of the k-th layer. Then, it comes:

$$\mathbf{V}_n^k(\xi) = \exp\left[(\xi - \xi_{k-1})\mathbf{P}_n^k(\xi_{k-1})\right]\mathbf{V}_n^k(\xi_{k-1}), \tag{18}$$

where $\xi_{k-1} \leqslant \xi \leqslant \xi_k$ and $k = 1, 2, ..., N$, which gives at the outer surface of the k-th layer:

$$\mathbf{V}_n^k(\xi_k) = \exp\left[h_k \mathbf{P}_n^k(\xi_{k-1})/b\right]\mathbf{V}_n^k(\xi_{k-1}), \tag{19}$$

where h_k is the thickness of the considered layer.

For each layer, the state vector at the outer surface is related to the state vector at the inner surface. Continuity conditions at all interfaces between layers enable to relate the state variables at the outer surface of the coating ($\xi_N = 1$) to the state variables at its inner surface ($\xi_0 = a/b$).

$$\mathbf{V}_n^N(\xi_N) = \mathbf{T}_n \mathbf{V}_n^1(\xi_0), \tag{20}$$

with

$$\mathbf{T}_n = \prod_{k=N}^{1} \exp\left[h_k \mathbf{P}_n^k(\xi_{k-1})/b\right] \tag{21}$$

the global modal transfer matrix.

The boundary conditions at the inner and outer surfaces of the coating are given by:

$$\begin{aligned} \sigma_{rr}^N(b,\theta) &= -p(b,\theta) \\ \sigma_{r\theta}^N(b,\theta) &= 0 \\ u_r^0(a,\theta) &= 0 \\ u_\theta^0(a,\theta) &= 0. \end{aligned} \tag{22}$$

Their transcription in conditions on the modal coefficients leads to the following system:

$$\begin{pmatrix} -1 & 0 & T_{n,13} & T_{n,14} \\ 0 & -1 & T_{n,23} & T_{n,24} \\ 0 & -\beta_n & T_{n,33} & T_{n,34} \\ 0 & 0 & T_{n,43} & T_{n,44} \end{pmatrix} \begin{pmatrix} u_{\theta,n}^N(\xi_N) \\ u_{r,n}^N(\xi_N) \\ \sigma_{rr,n}^0(\xi_0) \\ \sigma_{r\theta,n}^0(\xi_0) \end{pmatrix} = \begin{pmatrix} 0 \\ 0 \\ \alpha_n \\ 0 \end{pmatrix}, \tag{23}$$

with

$$\alpha_n = -\frac{2p_0 i^{n+1}\epsilon_n}{\pi b c_{33}^N H_n'(kb)}$$
$$\beta_n = -\omega\rho c b \frac{H_n(kb)}{H_n'(kb)}.$$

The solution of this system gives, in particular, $u_{r,n}^N(\xi_N)$, which allows the calculation of the pressure in the exterior fluid:

$$p(r,\theta,\omega) = \mathrm{e}^{-i\omega t}\sum_{n=0}^{\infty}\left[\underbrace{p_0 i^n \epsilon_n\left(J_n(kr) - \frac{J_n'(kb)}{H_n'(kb)}H_n(kr)\right)}_{p_{blocked}} + \underbrace{\omega\rho c b u_{r,n}^N(\xi_N)\frac{H_n(kr)}{H_n'(kb)}}_{p_{el}}\right]\cos(n\theta). \quad (24)$$

2.3.3. Discussion

Both methods rely on series expansion of the displacements with regard to the circumferential variable θ. In the first case, general Fourier series is used, whereas the second case is based on particular solutions in sine and cosine valid for cylindrical configurations.

Another difference lies in the fact that the continuity of displacements and stresses at the interfaces is not written in the same way in the two approaches. In the first one, a (2N+2)x(2N+2) matrix corresponding to the whole multi-layered shell is formed. In the second approach, the matrix corresponding to the total system is of constant size (4x4), independently of the number of layers. A comparison of the two methods in terms of computational time (cf Figure 2) showed that the CPU time increases linearly with the number of layers N with the first method, whereas it stays roughly constant with the second one, which is consistent with the above remark. Besides, it can be noted that method 2 is interesting for a significant number of layers ($N \geqslant 10$), and method 1 seems more appropriate for coatings with few layers. For the next step, *i.e.* the search of parameters of the different layers conducting to a scattering reduction, the study has been restricted to bi-layer coatings, and the simulations have thus been conducted with the first method.

Finally, the pressure fields obtained on a set of configurations with these two methods are very similar and fully comparable to those obtained for the same cases with the finite element simulation software COMSOL, which validates both approaches.

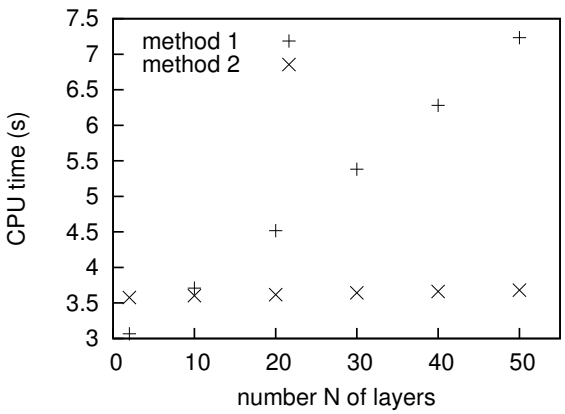


Figure 2: Comparison of CPU times with the two methods (same configurations)

3. Search for parameters minimizing the scattering

3.1. Method

Optimization techniques have been employed to find the dimensional and mechanical characteristics of the elastic layers leading to scattering reduction. Those parameters, that constitute the optimization variables, are, for each layer:

- thickness h,
- Young modulus in the radial direction E_r,
- Young modulus in the tangential direction E_θ,
- shear modulus $G_{r\theta}$,
- Poisson's ratio $\nu_{r\theta}$,
- mass density ρ,
- structural loss factor η.

The study has been restricted to bi-layer coatings to limit the number of optimization variables.

A genetic algorithm (SOGA from the DAKOTA software) has been coupled with the vibro-acoustic approach described above. Simulations have been conducted to find the parameters of the layers minimizing the objective function, defined as the ratio of the scattering cross-section σ_{sc} in the "cloaked" case to the scattering cross-section in the "uncloaked" case.

$$F_{obj} = \frac{\sigma_{sc}^{(cloaked)}}{\sigma_{sc}^{(uncloaked)}} \quad (25)$$

The scattering cross-section is defined as

$$\sigma_{sc} = \int_S \frac{< I_{sc} >}{< I_{inc} >} dS, \quad (26)$$

where I is the acoustic active intensity in the radial direction

$$I = -i\omega p u_r, \quad (27)$$

and $< . >$ denotes a time-averaged quantity. As a result of the non-absorption of the fluid medium, the acoustic energy

conservation law allows us to calculate the intensity on any surface enclosing the obstacle. Here, it has been chosen to evaluate it on a cylinder of radius 0.75 m (for tests with a rigid cylinder of radius comprised between 0.05 m and 0.2 m).

The scattering gain σ_{gain} provided by the coating is mesured in decibel as follows:

$$\sigma_{gain} = 10 \log_{10} \left[\frac{\sigma_{sc}^{(cloaked)}}{\sigma_{sc}^{(uncloaked)}} \right]. \qquad (28)$$

3.2. Numerical results

3.2.1. Bi-layer coating

In the first simulations, the elastic and dimensional parameters characterizing the two elastic layers have all been considered as independent optimization variables, and could therefore vary independently of each other. Each parameter has been allowed to vary between bounds corresponding to existing materials, but no condition ensured that these parameters could all be achieved simultaneously. However this first step permitted us to note that a very good scattering reduction could be obtained with bi-layer coatings composed of an external isotropic and stiff layer, and an internal orthotropic and soft layer. For instance, in the case of a rigid cylinder 30 cm in diameter placed in air, a scattering reduction of 13 dB in comparison with the uncloaked case theoretically occurs at 380 Hz. The corresponding pressure fields are represented in Fig. 3.

As said previously, it is very unlikely that such materials could be found in pratice, but these simulations highlighted the importance of the orthotropy of the internal layer. Indeed, optimization have also been conducted with coatings made of two isotropic layers, but no configuration leading to scattering reduction coul be found so. Considering an internal orthotropic layer and an external isotropic one, scattering reduction has been observed when the Young modulus of the internal layer in the radial direction was much smaller than the Young modulus in the tangential direction.

Table 1: Elastic and dimensional parameters obtained through optimization on a bi-layer coating made of an internal orthotropic layer and an external isotropic layer. Rigid cylinder 30 cm in diameter, optimization frequency: 380 Hz.

layer	1	2
h (mm)	2.4	0.6
E_r (MPa)	0.1	800
E_θ (MPa)	0.8	800
$G_{r\theta}$ (MPa)	0.25	308
$\nu_{r\theta}$	0.4	0.3
ρ (kg/m^3)	100	1200
η (%)	0.5	1

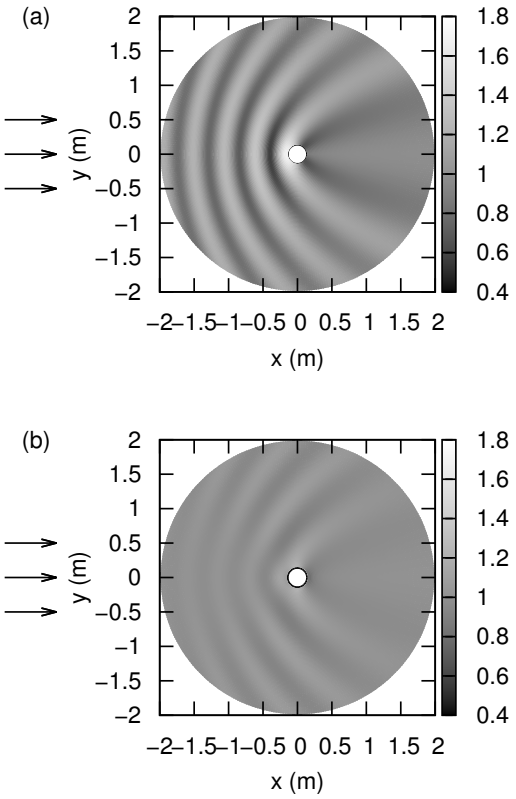


Figure 3: Absolute value of the complex pressure field around an uncloaked (a) or a cloaked (b) cylinder 30 cm in diameter, excited by a unit plane wave at 380 Hz. Coating entirely determined by optimization, cf Table 1.

3.2.2. Realizable cloak

Further investigations have then been conducted for different sizes of obstacle, using a 10 mm orthotropic polyethylene foam for the internal layer, the aim being to find an existing material for the external layer that could lead to a substantial reduction of the acoustic scattering. Thanks to the genetic algorithm, interesting values of the thickness h_2 and the structural loss factor η_2 of the external layer have been determined, as well as the interesting frequency range. With all these parameters fixed, direct computation of the scattering cross-section σ_{sc} as a function of the Young modulus E_2 and the mass density ρ_2 of the external layer has been carried out. It appeared that, for a given size of obstacle, scattering reduction is only possible with a few pairs (E_2, ρ_2), and that, although the attenuation is not as important with these coatings as it is with those founded in the first step, the phenomenon can still be observed. An example is given in Fig. 4 and Table 2, with a scattering gain of 5 dB. For smaller cylindrical obstacles, the curve representing the interesting zone moves towards lower (E_2, ρ_2), and the frequency at which the scattering reduction occurs becomes higher (and inversely if a bigger obstacle is considered), cf Fig. 5.

As a concrete example, according to these simula-

tions and for an appropriate choice of obstacle size and frequency, coatings composed of orthotropic polyethylene foam and polymers like polymethylpentene, polycarbonate or poly(methyl methacrylate) can enable scattering reduction.

Table 2: Elastic and dimensional parameters given by optimization on a bi-layer coating having as internal layer a 10 mm polyethylene foam. Rigid cylinder 26.6 cm in diameter, optimization frequency: 680 Hz.

layer	1	2
h (mm)	10	1
E_r (MPa)	1.2	1820
E_θ (MPa)	14	1820
$G_{r\theta}$ (MPa)	0.1	700
$\nu_{r\theta}$	0.3	0.3
ρ (kg/m^3)	89	661
η (%)	11	9

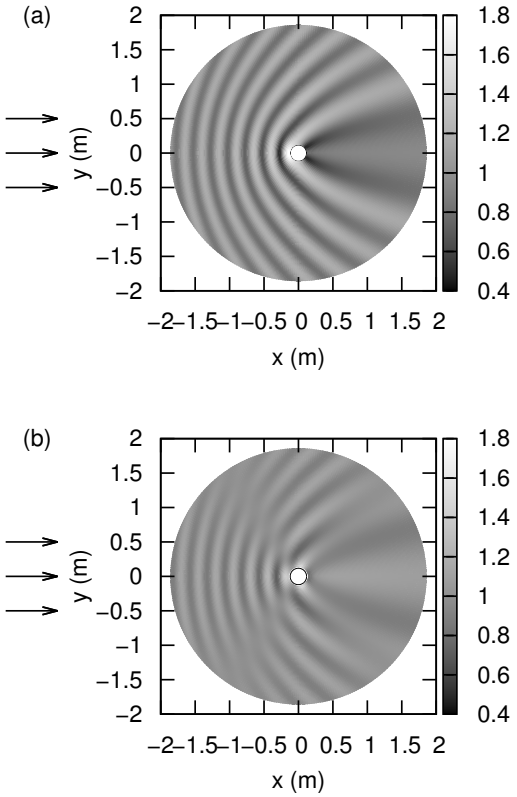


Figure 4: Absolute value of the complex pressure field around an uncloaked (a) or a cloaked (b) cylinder 26.6 cm in diameter, excited by a unit plane wave at 680 Hz. Coating with an internal layer of polyethylene foam and an external layer determined by optimization, cf Table 2.

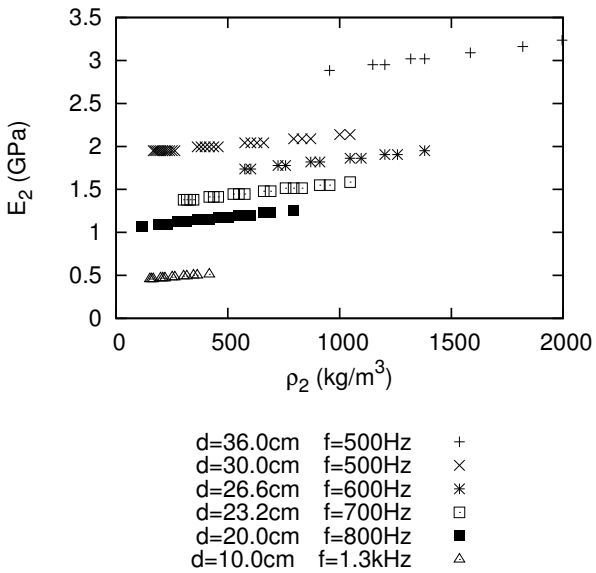


Figure 5: (E_2, ρ_2) leading to a scattering gain of at least 4 dB, in the case of an internal layer of polyethylene foam and an external isotropic layer with $h_2 = 1\ mm$ and $\eta_2 = 9\%$.

3.3. Frequency band

The observed scattering reduction is effective on a narrow frequency band. The scattering gain of the configurations described in Table 1 and Table 2 is represented with regard to the frequency in Fig. 6. The configuration corresponding to the example 1 has a 3 dB-bandwidth of 142 Hz, whereas the configuration of the example 2 has a 3 dB-bandwidth of 48 Hz.

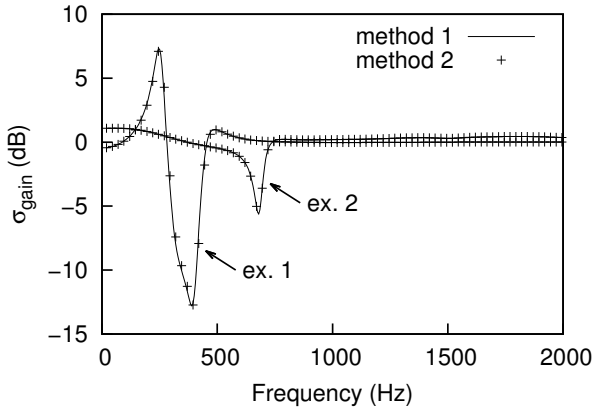


Figure 6: Variations of the scattering gain with frequency for the coatings described in Table 1 (example 1) and Table 2 (example 2).

4. Conclusions

Numerical simulations involving genetic algorithm showed that scattering reduction could be achieved by fixing an

elastic coating made of an internal orthotropic layer and an external isotropic layer on a rigid cylinder excited by a plane wave. Practical configurations have been proposed and are now to be tested experimentally in order to validate these numerical results. Further studies are considered to try to broaden the frequency range on which the coating effectively reduces the scattering. The effects of a greater number of layers are also going to be investigated.

5. Appendix

$$\mathbf{M}^k = \begin{pmatrix} m_{11}^k & m_{12}^k & m_{13}^k & m_{14}^k \\ m_{21}^k & m_{22}^k & m_{23}^k & m_{24}^k \\ m_{31}^k & m_{32}^k & m_{33}^k & m_{34}^k \\ m_{41}^k & m_{42}^k & m_{43}^k & m_{44}^k \end{pmatrix}$$

where

$$\begin{aligned}
m_{11}^k &= \frac{1}{r} \\
m_{12}^k &= -\frac{\partial}{r\partial\theta} \\
m_{13}^k &= 0 \\
m_{14}^k &= \frac{1}{c_{33}^k} \\
m_{21}^k &= -\frac{c_{12}^k}{c_{11}^k}\frac{\partial}{r\partial\theta} \\
m_{22}^k &= -\frac{1}{r}\frac{c_{12}^k}{c_{11}^k} \\
m_{23}^k &= \frac{1}{c_{11}^k} \\
m_{24}^k &= 0 \\
m_{31}^k &= \frac{e^k}{r^2}\frac{\partial}{\partial\theta} \\
m_{32}^k &= \rho_s^k \frac{\partial^2}{\partial t^2} + \frac{e^k}{r^2} \\
m_{33}^k &= \frac{1}{r}\left(\frac{c_{12}^k}{c_{11}^k} - 1\right) \\
m_{34}^k &= -\frac{\partial}{r\partial\theta} \\
m_{41}^k &= \rho_s^k \frac{\partial^2}{\partial t^2} - \frac{e^k}{r^2}\frac{\partial^2}{\partial\theta^2} \\
m_{42}^k &= -\frac{e^k}{r^2}\frac{\partial}{\partial\theta} \\
m_{43}^k &= -\frac{c_{12}^k}{c_{11}^k}\frac{\partial}{r\partial\theta} \\
m_{44}^k &= -\frac{2}{r}
\end{aligned}$$

with

$$e^k = c_{22}^k - \frac{{c_{12}^k}^2}{c_{11}^k}.$$

$$\mathbf{P}_n^k = \begin{pmatrix} p_{n,11}^k & p_{n,12}^k & p_{n,13}^k & p_{n,14}^k \\ p_{n,21}^k & p_{n,22}^k & p_{n,23}^k & p_{n,24}^k \\ p_{n,31}^k & p_{n,32}^k & p_{n,33}^k & p_{n,34}^k \\ p_{n,41}^k & p_{n,42}^k & p_{n,43}^k & p_{n,44}^k \end{pmatrix}$$

where

$$\begin{aligned}
p_{n,11}^k &= \frac{1}{\xi} \\
p_{n,12}^k &= \frac{n}{\xi} \\
p_{n,13}^k &= 0 \\
p_{n,14}^k &= \frac{c_{33}^N}{c_{33}^k} \\
p_{n,21}^k &= -\frac{c_{12}^k}{c_{11}^k}\frac{n}{\xi} \\
p_{n,22}^k &= -\frac{1}{\xi}\frac{c_{12}^k}{c_{11}^k} \\
p_{n,23}^k &= \frac{c_{33}^N}{c_{11}^k} \\
p_{n,24}^k &= 0 \\
p_{n,31}^k &= \frac{e^k}{c_{33}^N}\frac{n}{\xi^2} \\
p_{n,32}^k &= \frac{1}{c_{33}^N}\left(-\rho_s^k\omega^2 b^2 + \frac{e^k}{\xi^2}\right) \\
p_{n,33}^k &= \frac{1}{\xi}\left(\frac{c_{12}^k}{c_{11}^k} - 1\right) \\
p_{n,34}^k &= -\frac{n}{\xi} \\
p_{n,41}^k &= \frac{1}{c_{33}^N}\left(-\rho_s^k\omega^2 b^2 + \frac{e^k n^2}{\xi^2}\right) \\
p_{n,42}^k &= \frac{e^k}{c_{33}^N}\frac{n}{\xi^2} \\
p_{n,43}^k &= \frac{c_{12}^k}{c_{11}^k}\frac{n}{\xi} \\
p_{n,44}^k &= -\frac{2}{\xi}
\end{aligned}$$

Acknowledgement

Funding for this work was provided by the "Direction Générale de l'Armement" and the "région Midi-Pyrénées".

References

[1] J.B. Pendry, D. Schurig, D.R. Smith, Controlling electromagnetic fields, *Science* 312, 2006.

[2] S.A. Cummer, D. Schurig, One path to acoustic cloaking, *New J. Phys.* 9, 45, 2007.

[3] S. Zhang, C. Xia, N. Fang, Broadband acoustic cloak for ultrasound waves, *Phys. Rev. Lett.* 106, 024301, 2011.

[4] B.-I. Popa, L. Zigoneanu, S.A. Cummer, Experimental acoustic ground cloak in air, *Phys. Rev. Lett.* 106, 253901, 2011.

[5] A. Alù, N. Engheta, Achieving transparency with plasmonic and metamaterial coatings, *Phys. Rev. E* 72, 016623, 2005.

[6] Y.I. Bobrovnitskii, A new imedance-based approach to analysis and control of sound scattering, *J. Sound Vib.* 297: 743-760, 2006.

[7] Y.I. Bobrovnitskii, Impedance acoustic cloaking, *New J. Phys.* 12, 043049, 2010.

[8] P.-Y. Chen, M. Farhat, S. Guenneau, S. Enoch, A. Alù, Acoustic scattering cancellation via ultrathin pseudo-surface, *Appl. Phys. Lett.* 99, 191913, 2011.

[9] M. Farhat, P.-Y. Chen, S. Guenneau, S. Enoch, A. Alù, Frequency-selective surface acoustic invisibility for three-dimensional immersed objects, *Phys. Rev. B* 86, 174303, 2012.

[10] V.M. García-Chocano, L. Sanchis, A. Díaz-Rubio, J. Martínez-Pastor, F. Cervera, R. Llopis-Pontiveros, J. Sánchez-Dehesa, Acoustic cloak for airborne sound by inverse design, *Appl. Phys. Lett.* 99, 074102, 2011.

[11] M.D. Guild, A. Alù, M.R. Haberman, Cancellation of acoustic scattering from an elastic sphere, *J. Acoust. Soc. Am.* 129, 3, 2011.

[12] M.D. Guild, M.R. Haberman, A. Alù, Plasmonic cloaking and scattering cancelation for electromagnetic and acoustic waves, *Wave Motion* 48: 468-482, 2011.

[13] E.A. Skelton, J.H. James, Acoustics of an anisotropic layered cylinder, *J. Sound Vib.* 161, 2, 1993.

[14] O.C. Zienkiewicz, *La méthode des éléments finis*, McGraw-Hill, third edition, 1979.

[15] W.Q. Chen, Z.G. Bian, H.J. Ding, Three-dimensional vibration analysis of fluid-filled orthotropic FGM cylindrical shells, *Int. J. Mech. Sci.* 46: 159-171, 2004.

[16] S.M. Hasheminejad, M. Rajabi, Acoustic scattering characteristics of a thick-walled orthotropic cylindrical shell at oblique incidence, *Ultrasonics* 47: 32-48, 2007.

[17] J. Jamali, M.H. Naei, F. Honarvar, M. Rajabi, Acoustic scattering from functionally graded cylindrical shells, *J. Mech.* 27, 2: 227-243, 2011.

Plasmonics and nanophotonics

Enhanced Emission of Waveguide Thermal Emitter by Incorporating Metal Nanoparticles in Periodic Hole Arrays

Pei-Wen Wu, Che-Hsuan Cheng, Hung-Hsin Chen, and Si-Chen Lee*

Graduate Institute of Electronics Engineering, National Taiwan University, Taipei, Taiwan
*corresponding author, E-mail: sclee@ntu.edu.tw

Abstract

The enhanced emission of waveguide thermal emitter (WTE) by incorporating metallic nanoparticles in periodic hole arrays is investigated in the mid-infrared regime. Different metallic films were deposited inside the holes and then annealed to form randomly sized nanoparticles. It is found that the randomly distributed nanoparticles significantly enhanced the emission intensity of the WTE. It is believed that the plasmoinc-like resonance between different nano-sized particles is greatly enhanced by accumulative scattering events from all directions that leads to the enhancement. This unique design by integrating localized and propagating surface plasmons together provides an easy way to improve the emission intensity of waveguide thermal emitter and a better device for IR application.

1. Introduction

Recently, numerous studies have been conducted to investigate the emission and transmission properties through the periodic hole arrays by using various metallic nanoparticles (NPs) [1,2] and coupled structures since the discovery of the extraordinary optical transmission (EOT) in 1998 by Ebbesen *et al.* [3-5]. This phenomenon was attributed to the generation of surface plasmon polaritons (SPPs) at the interface between the metallic and dielectric films [3]. However, very few studies focused on the mid-infrared regime due to the weak intensities of infrared sources. Numerous applications of nanoparticles have been applied in plasmonic devices, biosensors, solar cells, and surface enhanced Raman scattering (SERS) etc. [6-9] to improve the performance. In this paper, we incorporate different kinds of nanoparticles into micro-scaled periodic hole arrays of the WTE [10] and investigate its emission properties in the mid-infrared regime. The coupling between the localized surface plasmons (LSPs) and propagating SPPs is expected to enhance infrared emission of the WTE. This provides a new way to increase the emission in the mid-infrared regime.

2. Experimental

Fig.1 displays the fabrication processes of WTE structure embedded with metallic nanoparticles. The WTE consists of tri-layer Au / SiO_2 / Au deposited on the front surface whereas a 450 nm Molybdenum (Mo) layer was sputtered on the back surface of the silicon substrate as electrode. The bottom 150nm Au layer was deposited by E-gun evaporation as a reflector. Then a 2 μm SiO_2 layer was deposited on top of Au by PECVD at 350°C. The top Au film with circular holes arranged in hexagonal lattice was produced by thermal evaporation of Au on patterned photoresist and lifted-off. The hole array has a period of 2.3μm and hole diameter of 1.15μm. Next, different kinds of 3 nm thick metallic film were deposited inside the holes followed by rapid thermal annealing (RTA) at 450°C for 2 minutes to form randomly sized nanoparticles. The SEM pictures of a single empty hole and 3 nm thick Au, Ag and Cr film after RTA are shown in Fig. 2 (a), (b), (c) and (d), respectively. The outer part (white) of the circular hole (black) is the metal array. The nanoparticles are scattered around at the bottom of the hole. The electric current was sent into Mo layer to heat up the WTE and the waveguide mode was excited by black body radiation from the oxide film and emitted through the holes on the top metal. Fourier Transform Infrared Spectrometer (FTIR) Bruker IFS 66 v/s and PERKIN ELMER 2000 were used to measure the reflection and emission spectra of WTE in the normal direction.

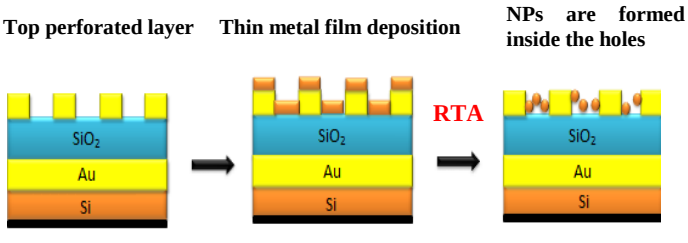


Fig. 1 Schematic diagrams showing the Fabrication processes of the WTE with metallic nanoparticles embedded inside the holes by rapid thermal annealing.

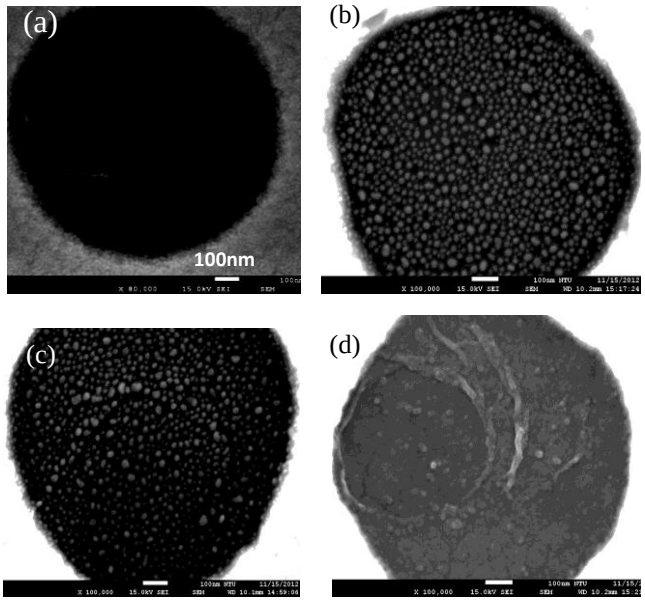


Fig. 2 SEM pictures of (a) an empty hole, hole with the random sized NPs made of (b) Au, (c) Ag, and (d) Cr. The magnification of SEM is 100,000X.

Three samples were fabricated and deposited with Au, Ag, and Cr, respectively. The corresponding sample definitions are listed in Table. 1.

Table 1: Sample definitions

Metal	Before Deposition	After Deposition Of 3 nm film	After RTA
Au	A1	A2	A3
Ag	B1	B2	B3
Cr	C1	C2	C3

3. Results and discussion

The AFM landscape graph of samples A3, B3, and C3 are shown in Fig. 3. It is clear that the NPs are uniform in A3 and B3, and NPs are sphere-like and smaller. However, for C3, the sample deposited with Cr, the NPs are island-like and bigger. In average, the widths of NPs in sample A3, B3, and C3 are about 20 nm, 30 nm, and 70 nm, respectively. The heights of NPs range from 20 to 25 nm for A3, 10 to 15 nm for B3, and 10 to 20 nm for C3. In addition, the gaps between neighboring NPs are larger than the NP size. So, the different gap sizes of random NPs may sustain sufficiently strong antenna-like plasmonic resonances in the mid-infrared. And these resonances may couple with the waveguide modes.

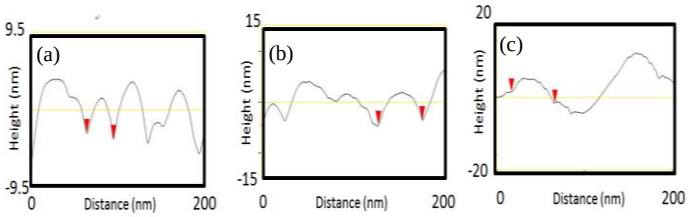


Fig. 3: AFM landscape measurements of three samples.(a) A3, (b) B3, and (c) C3

3.1. Reflection Spectra

During the reflection measurement, the samples were placed in xy plane and light incident in z direction. Fig. 4 (a), (b) and (c) display the normalized reflection spectra of sample groups A, B and C, respectively. Here the normalization is based on the noise signal of the background. The dip around 5.8 μm is the waveguide mode. The theoretical wave guide mode wavelength is given by [10]

$$\lambda_{\mathrm{WM}} = \frac{2n_{\mathrm{SiO_2}}}{\sqrt{\frac{16}{(3\times a^2)} \times (k^2 - k \times \ell + \ell^2) + \left(\frac{m}{t_{\mathrm{ox}}}\right)^2}} \qquad (1)$$

According to this equation, the theoretical peak wavelength is 5.6μm. The experimental result is very close to tis value.
WTE with Cr NPs (C3) shows lower reflection intensity as compared to samples C1 and C2 The decrease is larger than those using Au (A3) and Ag (B3) NPs. It is also found that the reflection of WTE become lower as holes were covered by thin metal film as samples A2, B2 and C2. After treated with RTA at 450^{o}C for 2 minutes, the reflectance is even lower for samples A3,B3 and C3. By calculating the change in reflectance, A3 is 32.7% lower than that of A1, B3 is 27.3% lower than that of B1, and C3 is 15.1%lower than that of C1. So, the excitation of plasmon inside the cavity of NPs may lead to the less reflection light.

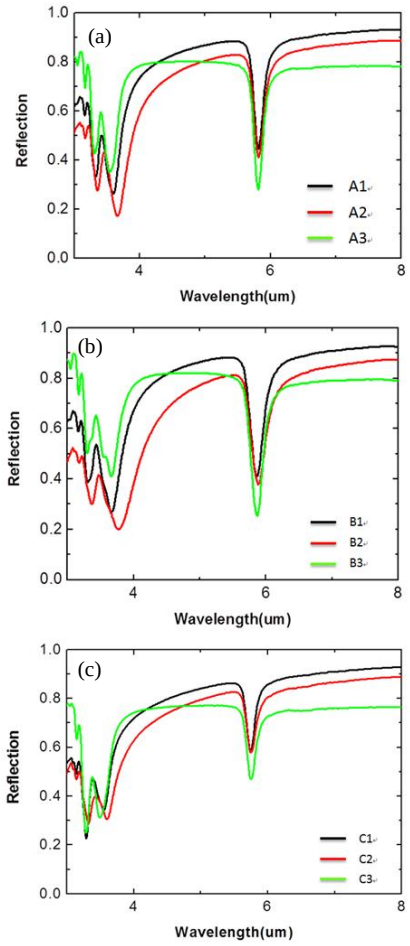


Figure . 4 The reflection spectra of sample groups of (a) A, (b) B, and (c) C, which includes all samples w/ and w/o metallic film and w/ NPs.

3.2. Emission Spectra

Fig. 5 shows the emission spectra of WTE operated at 150°C. It is clear that the emission peak positions stay the same whatever the metal is. The maximum increase in emission intensity was found for WTE A3 with Au NPs, and the second one is WTE B3 with Ag NPs. The increase of emission intensity for samples A3, B3, and C3 are 35%, 27%, and 13%, respectively. Theoretically, holes with random nanoparticles inside should screen out part of the emission light and result in lower emissivity. However, the results are opposite. Random metal NPs enhance the emission intensity due to the excitation of plasmon. It is believed that the plasmon resonance between different nano-sized particles are enhanced by accumulative scattering effect from all directions.

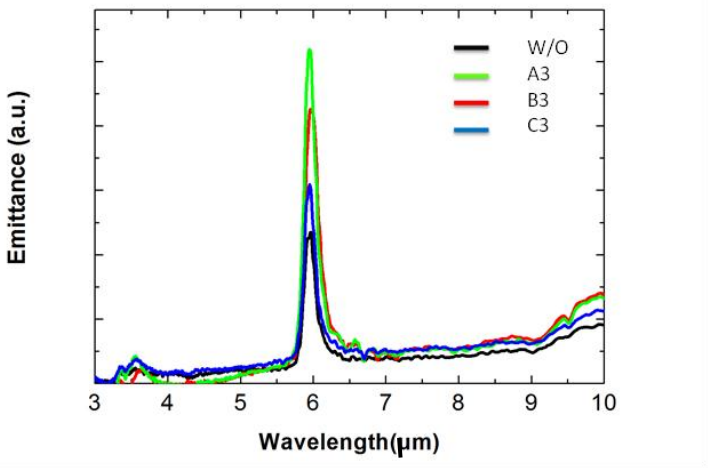


Figure. 5 The emission spectra of WTE incorporated w/o different kinds of metallic NPs

4. Conclusions

In conclusions, the enhanced emission with random metallic NPs embedded in periodic hole arrays were demonstrated. Different kinds of metallic films were deposited in hole arrays then annealed to form random NPs. There were no change in peak emission wavelength with different metal embedded. And the emissivity enhancement of samples with Au and Ag NPs are much larger than that with Cr NPs. It is due to the large accumulative scattering effect from all directions and plasmonic-like resonances between NPs. This unique design by integrating localized and propagating surface plasmons together provides a platform for electrical field confinement within individual hole and an easy way to improve the emissivity of WTE. It can be used as a better device for IR application, such as biosensors, solar cells, and surface enhanced SERS.

References

[1] Brian K Canfield, Sami Kujala, Konstantins Jefimovs, Tuomas Vallius, Jari Turunen, d Martti Kauranen, *J. Opt. A: Pure Appl. Opt*. **7,** 2005.

[2] Hong Wei, Daniel Ratchford, Xiaoqin (Elaine) Li, Hongxing Xu, and Chih-Kang Shih, *Nano Lett.* Vol.9 No. 12, 2009.

[3] T. W. Ebbesen, H. J. Lezec, H. F. Ghaemi, T. Thio, and P. A.Wolff, "Extraordinary optical transmission through sub-wavelength hole arrays," *Nature*, vol. 391, pp. 667–669, Feb. 1998.

[4] T. Søndergaard, S. I. Bozhevolnyi, J. Beermann, S. M. Novikov, E.Devaux, and T. W. Ebbesen, "Extraordinary

optical transmission with tapered slits: Effect of higher diffraction and slit resonance orders," *J.Opt. Soc. Amer. B*, vol. 29, no. 1, pp. 130–137, 2012.
[5] Y. T. Chang, T. H. Chuang, M. W. Tsai, L. C. Chen, and S. C. Lee,"Observation of Fabry–Pérot-type surface plasmon on Ag film with perforated short-range 3×3 hole array arranged in long-range periodic structure," *Appl. Phys. Lett.*, vol. 91, no. 25, pp. 251105-1–251105-3,2007.
[6] B. K. Canfield, S. Kujala, K. Jefimovs, T. Vallius, J. Turunen, and M. Kauranen, "Polarization effects in the linear and nonlinear optical responses of gold nanoparticle arrays," *J. Opt. A, Pure Appl. Opt.*, vol. 7, no. 2, p. S110, 2005.
[7] C. L. Nehl, H. Liao, and J. H. Hafner, "Optical properties of starshaped gold nanoparticles," *Nano Lett.*, vol. 6, no. 4, pp. 683–688, 2006.
[8] T. Zhai, *et al.*, "Random laser based on waveguided plasmonic gain channels," *Nano Lett.*, vol. 11, no. 10, pp. 4295–4298, 2011.
[9] L. H. Qian, X. Q. Yan, T. Fujita, A. Inoue, and M. W. Chen, "Surface enhanced Raman scattering of nanoporous gold: Smaller pore sizes stronger enhancements," *Appl. Phys. Lett.*, vol. 90, no. 15, pp. 153120-1–153120-3, 2007.
[10] Y. T. Wu, Y. T. Chang, H. H. Chen, H. F. Huang, D. C. Tzuang, Y. W. Jiang, P. E. Chang, and S. C. Lee, IEEE *Photon. Tech. Lett.*, **22**, 1159-1161, 2010
[11]Y. C. Chen, Y. T. Chang, H. H. Cheng, F.T. Chuang, C. H. Chen, and S. C. Lee, IEEE *Photon. Tech. Lett.*, **25,** 1041-1135, 2013

Optical property of double-layered metal films with periodic structure

M. Boutria and R. Oussaid*

Houari Boumediene University of Sciences and Technology, Instrumentation Laboratory
Box n°32 El Alia Bab Ezzouar 16111 Algiers, Algeria
*corresponding author, E-mail: roussaid@usthb.dz

Abstract

This paper reports optical property of double-layered metal films with periodic structure, which works as a half-wave plate by itself. The advantage of this structure is that it can tune the rotation angle of optical activity, with high transmittance, by changing the relative angle of two films. We analyze the optical property of the structure using numerical calculation with conventional transfer matrix method and FDTD method. We propose the design of an anisotropic and chiral structure (3-D). The chirality is controlled by simply changing the angle between the two plates. The optical rotation is accompanied by a transmission up to 80%. The proposed structure opens the way to the design of a new kind of chiral plates in the terahertz or microwave domains.

1. Introduction

Since the emergence of nano-optics (near-field optics, photonic crystals, plasmonics, metamaterials, etc.) in the 1990s, scientists in the electromagnetic domain have tried to generate artificial optical activity (chirality) using the original properties exhibited by metamaterials. Consequently, the main objective in the development of artificial chiral periodic structures is to produce simultaneously a large optical activity and a high transmittance. Another property that gives importance to artificial planar structures is their ability to exhibit nonlinear optical properties due to their unusual broken symmetry imposed by the chirality. Different phenomena observed in planar metamaterials have attracted researchers in this field[1-8]. Chirality in general and particularly chiral structures, have driven for a long time researches in physics and are still being very attractive. The optical activity characterizes the rotation of the polarization plane of linearly polarized waves. Many researches were done in this field [1, 2, 3, 4, 5]. In these studies, a large optical rotation is sometimes achieved, but often with relatively low transmission. In this paper, we present a design of a chiral structure based on a 3-D metamaterial composed of two identical nanostructured metallic films each one playing the role of a half-wave plate and working at normal incidence [6]. Our chirality is obtained through a provoked optical rotation induced by breaking the symmetry of one plate to get artificial intrinsic chiral material with an enhanced transmission up to 80%.

2. The proposed Structure

In the proposed Structure**,** the second plate is rotated by an angle (α) with regard to the first one (see fig. 1). We assume that the two plates are spaced by a distance *d*. For sake of simplicity, we assume that the two plates are free-suspended in vacuum and that the cavities are also devoid of dielectric. Each layer consists of a perfectly conducting metallic film similar to the one studied in ref [7]. With the geometrical parameters of that reference, the metallic layer behaves as a half-wave plate for a wavelength around $\lambda=1.223p$.

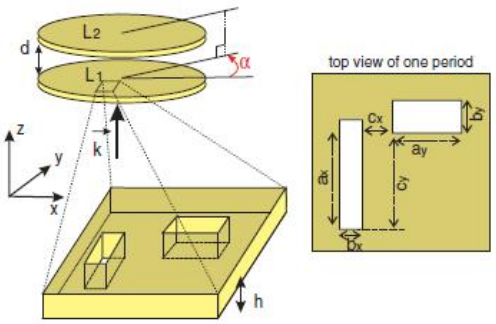


Figure 1: Schematic of the proposed structure composed of two half-wave plates (L_1, L_2) rotating by an α one with regard to the other. A zoom-in over one unit cell of L_1 is presented to show one array pattern composed of two rectangular apertures. The top view made over one period shows the geometrical parameters of the slits.

To demonstrate the optical rotation, we have to calculate the transmission spectra for two incident orthogonal polarization states. Unfortunately, for an arbitrary value of α, the whole structure ($L1$,$L2$) becomes no longer periodic. Consequently, two different approaches are developed below. The first one is based upon a semianalytical calculation of the total transmission that considers the two plates as a conventional Fabry-Perot inter- ferometer. Only

far-field transmission and reflection properties of each layer are needed and the near-field coupling is then neglected (only multireflections of homogeneous propagating waves between the two elements are taken into account). The second one is a homemade 3D-periodic FDTD code, used to simulate the transmission spectrum of the whole structure when the Bravais lattice of the two layers is the same (only patterns of the second layer are rotated).

2.1. Semi analytical Approach

We consider the two plates as a conventional Fabry-Perot interferometer. So, the near-field coupling between the two plates is neglected and only multi-reflections of homogeneous propagating waves between the two elements are considered. The second plate is rotated by an angle (α) with respect to the first one (figure 2). Each plate is completely described by its corresponding transmission and reflection Jones matrices T_i and R_i (i = 1, 2), respectively. For the first plate, T_1 and R_1 are calculated using a homemade FDTD code. Contrary to L_1, the matrices T_2 and R_2 of the second plate (L_2) are numerically derived from T_1 and R_1 by a rotation of (α) through the relations:

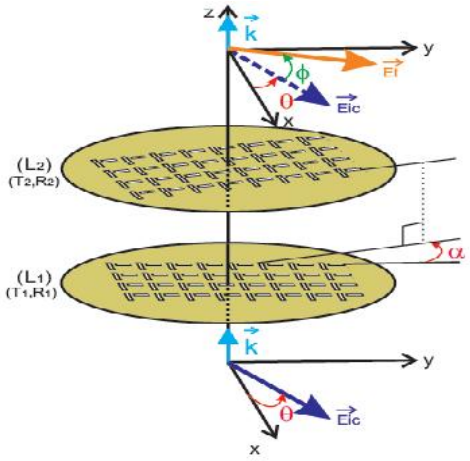


Figure 2: Cascaded structure consisting of two plates (L_1 and L_2), the second is rotated by (α) with respect to the first one. The polarization plane rotation is named ϕ.

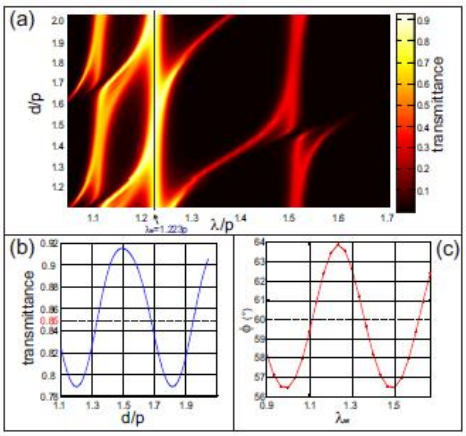


Figure 3: (a) Semi-analytical calculated transmission spectra versus the distance d separating the two plates. The incident beam is polarized at θ = 45° from Ox and the angle between the two plates is set to α=30°. (b) Transmission variations at the operating wavelength of $\lambda=1.223p$ as a function of d. (c) Rotation angle ϕ function of the operating wavelength.

$$T_2 = \Re^{-1}(T_1)\Re \quad and \quad R_2 = \Re^{-1}(R_1)\Re\,, \tag{1}$$

Where $\Re$ is the rotation matrix of angle α.

The transmitted field through the whole structure can then be calculated with an algorithm similar to the one used for a multilayered structure [8], and it can be expressed as:

$$\vec{E}_t = \hat{T}\cdot\vec{E}_t\,, \tag{2}$$

Where $\hat{T}$ is the transmission Jones matrix of the whole structure in the linear basis (xOy) given by:

$$\hat{T} = T_2\left(1 - R_1R_2e^{-2i\phi}\right)^{-1}T_1\,, \tag{3}$$

φ is the phase change due to the propagation between the two plates. The optical activity is then deduced by determining the rotation angle of the transmitted field with regard to the incident one. This angle can simply be calculated through the expression of the transmission Jones matrix when expressed in the circular basis. This Jones matrix in circular basis is obtained by:

$$T_c = \Lambda^{-1}\hat{T}\Lambda = \begin{pmatrix} T_{++} & T_{+-} \\ T_{-+} & T_{--} \end{pmatrix}, \tag{4}$$

Where $\Lambda = \frac{1}{\sqrt{2}}\begin{pmatrix} 1 & 1 \\ i & -i \end{pmatrix}$ is the matrix of the basis change.

With this transformation, the transmission matrix directly relates the incident and transmitted electric fields in terms of right-handed (RCP), and left-handed (LCP), circularly polarized components. The angle of rotation is then directly deduced from the diagonal elements of T_c .

$$\phi = \frac{1}{2}\arg\left(\frac{T_{--}}{T_{++}}\right), \tag{5}$$

This corresponds to the phase difference between the transmitted RCP and LCP waves.

The optical activity is then deduced by determining the rotation angle of the transmitted field with regard to the incident one. The case of two plates separated by a distance $d=1.8p$ and rotated by $\alpha=30°$ was studied. This leads to a rotation by ($\phi=56.47°$) instead of $2x30°=60°$. This discrepancy is due to the fact that the transmission through a single plate at this wavelength is not perfect (equal to $0.92<100\%$). Therefore, the transmission is affected by the multiple reflections between the two plates as shown in figure 3c where a maximum of relative error of 4° is obtained on the rotation angle.

The obtained results demonstrate that the double layered structure behaves as an anisotropic tunable chiral plate because the polarization plane of the transmitted wave rotates through an angle that depends almost exclusively on the position of the second plate relative to the axis of the first plate and independently of the incident polarization direction. We note that, in this first method, only the zero-diffracted orders, in transmission and reflection, are taken into account while the diffracted evanescent waves are neglected. Consequently, we use the FDTD which is a rigorous method, in order to involve these waves in the whole structure transmission coefficient. For this reason, we chose the distance between the two plates larger than one wavelength (here $d = 1.8p = 1.47\lambda w$).

2.2. 3D-FDTD simulations of the whole structure

The FDTD is a method which is usually used to study periodic structures. Because of the periodicity breaking due to the rotation of the second plate, instead of rotating the second plate, the patterns (rectangular apertures) of this latter are rotated (see figure 4a) by the same angle considered above (α) without modifying the periodicity directions, Although the effect of rotating the pattern instead of the whole plate is very weak on the transmission spectra, it greatly affects the transmission properties of the double-layered structure but the optical activity is still present. We are in front of a real limitation of periodic methods to treat such cascaded structures. Only semi analytical approaches can be accurate within their domain of validity.

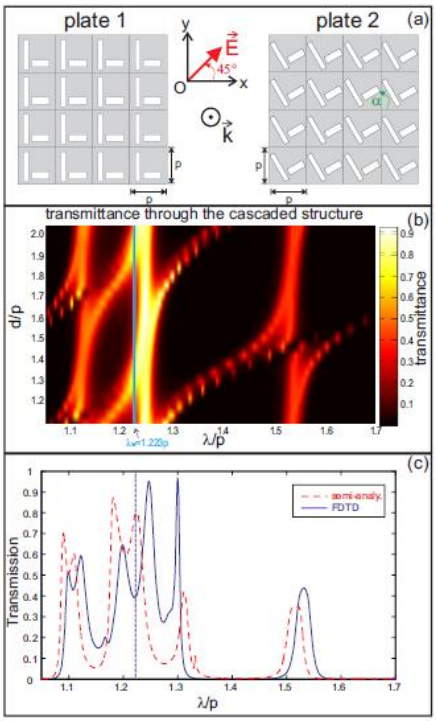


Figure 4: (a) Schema of *4*x*4* periods of the plate with non-rotated (left) and rotated (right) rectangular apertures. (b) Transmission spectra of the two plates calculated by FDTD with the same parameters as in fig.3b . (c) Comparison between the spectra obtained by the two methods for *d=1.8p*.

The transmission coefficient of the double-apertured-double-layered structure calculated by the 3D-FDTD is presented in Fig. 4(b) as a function of both the wavelength and the distance *d* between the two plates. This result should be compared with that of Fig. 3(a) obtained within the semi-analytical approach. In both cases, the incident plane wave is polarized at $\theta = 45°$ from the *Ox* axis. Quantitatively, there is a very good agreement even if the semi-analytical approach does not take into account evanescent components of the electromagnetic field generated by the light diffraction on the sub-wavelength apertures. Only diffracted zero order is considered. In fact, the coupling through the evanescent, i.e., nonpropagative, waves occurs only for small values of the distance *d.* By considering $d > \lambda$, we almost cancel the contribution of all these waves, i.e., the tunneling is negligible.

3. Conclusions

This paper reports optical property of double-layered metal films with periodic structure. In this paper, we have presented a design of a chiral structure based on a 3D metamaterial composed of two identical nanostructured metallic films, each one playing the role of a half-wave plate and working at normal incidence. The second plate is rotated by an angle (α) with regard to the first one. In the optical domain, it is well known that the combination of these two half-wave plates is equivalent to an optical rotator (rotation angle of 2α). Thus, chirality is obtained through a rotation of one plate that breaks the symmetry of the whole structure, creates a 3D intrinsic chirality, and induces optical activity. We have presented an artificial chiral structure based on the cascading of two identical half-wave plates. We have analyzed the optical property of the structure using numerical calculation. The optical activity is demonstrated through a semi-analytical approach and a homemade 3D-periodic FDTD code. The advantage of this structure is that it can tune the rotation angle of optical activity, with high transmittance by changing the relative angle of two films. An exalted transmission (up to *80%)* at the operating wavelength is obtained accompanied by a tunable rotation corresponding to twice the angle between the two plates. The designed structure deserves to be experimentally tested.

Acknowledgements

The authors thank the Department of Optical PM Duffieux FEMTO-ST (Besançon, France) for their collaboration.

References

[1] F. I. Fedorov, on the theory of optical activity in crystals, *Opt. Spectrosc* 6: 49, 1958.

[2] Thomas Paul Christoph Menzel, Carsten Rockstuhl and Falk Lederer, retrieving effective parameters for quasiplanar chiral metamaterials, *Applied Physics Letters,* 93:233106, 2008.
[3] Benfeng Bai, Janne Laukkanen, Anni Lehmuskero, and Jari Turunen, simultaneously enhanced transmission and artificial optical activity in gold film perforated with chiral hole array, *Physical Review B ,* 81:115424, 2010.
[4] Masanobu Iwanaga, subwavelength orthogonal polarization rotator, *Optics Letters ,* 35, No.2, 2010.
[5] Christian Helgert, Ekaterina Pshenay-Severin, Matthias Falkner, Christoph Menzel, Carsten Rockstuhl, Ernst-Bernhard Kley, Andreas Tunnermann, Falk Lederer, and Thomas Pertsch, chiral metamaterial composed of three-dimensional plasmonic nanostructures, *Nano Letters,* 11 (10): 4400–4, 2011.
[6] M. Boutria, R. Oussaid, D. Van Labeke and F. I. Baida, Tunable artificial chirality with extraordinary transmission metamaterials, *Phys. Rev. B 86*, 155428*,* 2012.
[7] F. I. Baida, M. Boutria, R. Oussaid, and D. Van Labeke, Enhanced-transmission metamaterial as anisotropic plates, *Phys. Rev. B,* 84:035107, 2011.
[8] J. M . Vigoureux, Polynomial formulation of reflection and transmission by stratified planar strutures. *J. Opt. Soc. Am. A*, 8(11):1697–1701, November 1991.

Four Vertical Prolate Spheroids with a Center Gap as Nanoantenna

Mahdieh Khosravi[1], Ramezan Ali Sadeghzadeh[1], Mohammad Sadegh Abrishamian[1]

[1]School Department of Electrical and Computer Engineering, K. N. Toosi University of Technology, Shariati Street, PO Box 16314, Tehran, Iran

*corresponding author, E-mail: *m_khosravi@ee.kntu.ac.ir*

Abstract

In this paper, we first investigate the properties of a single prolate nanospheroid of different materials to determine basic element. Next, we study the behavior of a structure of four vertical prolate spheroids of same dimension with a center gap (g). Finally, simulation results for different parameters variation (element size and gap distance) have been presented by order. As a result, this semi-turnstile nanoantenna produces intense optical field enhancement when illuminated at the resonant wavelength.

1. Introduction

Properly designed plasmonic nanoantennas could have various applications in many fields such as optical communications, biological and medical sensors. Basically, an optical antenna is a dramatically miniaturized version of its much larger RF counterpart [1-2]. In antenna theory, antenna parameters are directly related to the wavelength λ of incident radiation, but this scaling fails at optical frequencies where metals behave as strongly coupled plasmas [3]. Recent advances in nano technology have opened doors to several next generation devices and sensors. Characterizing nanoplasmonic particles and structures in a simple and effective way is imperative for monitoring and detecting processes at nano scale in a variety of environments.

As stated above, the development of plasmonic structures as nanoantennas has become an important topic, and different numerical simulations have been used for their design and optimization. CST is a convenient software for this purpose. An important requirement of this software for the study of dispersive media is the need of an analytical law of dispersion. Here, it seems good to use Drude model for describing the dispersion of metals at optical frequencies [4]. However, the parameters of modeled materials have to be applicable over broad frequency bands in order to perform broadband calculations. Since the constitutive parameters (ε, μ, σ, and τ) must be specified as constants in simulations, the modified Debye model (MDM) is used here to describe the frequency-dependent behavior of metals [5].

Because of the resonant behavior at certain frequencies (plasmon generation) an accurate setting is demanded. For exact simulations, it is required to refine mesh resolution by setting its properties, locally. As incident light, a plane wave is used to excite the structure. For direct extraction of the Extinction Cross Section (ECS) the broadband scattering response is extracted. Ii is worth to mention that ECS of antenna element peaks at its resonance frequency, since an increase in antenna current result in greater scattering and absorption, and also more amount of field enhancement.

2. Basic element: simulation and results

As first step, we investigate the properties of a single prolate nanospheroid of different materials to make best choice for basic element (Fig.1 (a)). Main advantage of using the spheroidal particle is providing a means of adjusting the scattering resonant frequency by changing the ratio of radii. Also, what metals to use for optical antenna design is an open question, since metals behave very differently in optical domain. As an answer, noble metals such as gold and silver are good candidates for optical antenna design, mainly due to their specific optical property. The final choice for metal is silver whose permittivity at the frequencies of interest is well described by modified Drude model.

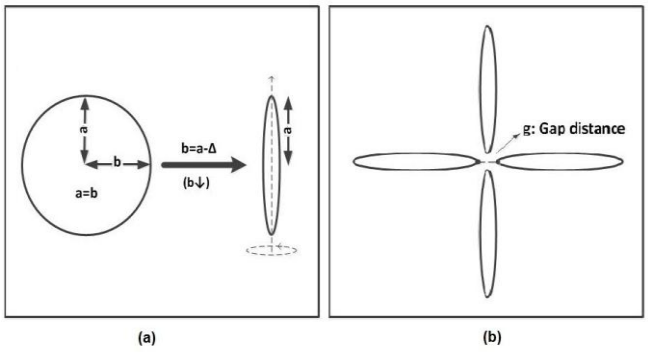


Figure 1: (a) Single prolate spheroid as basic element (b) Semi-turnstile arrangement.

In conclusion, a concentric (core-shell) spheroidal nanoparticle made of a given plasmonic material (silver) and an ordinary dielectric (silica) is employed to be the structural block of semi-turnstile nanoantenna in next step. This is because of the fact that one can tailor the resonant frequency in a wide range by properly controlling the

geometrical parameters (the cover thickness and the ratio of radii).

Extinction Cross Section (ECS) for the cases of a nano-sphere in both forms of pure metal (1 layer) and core-shell model (2 layer) versus frequency is plotted in (Fig. 2) for two different metal materials. The core which made of silica with permittivity 2.08 has a radius of 38 nm, while the shell has a thickness of 10 nm and it is made either of silver or gold. The peaks occur at wavelength around 920 THz for the case of silver sphere, while at frequency larger than 630 THz for gold one. So, it is clear from the figure that replacing silver with gold causes a considerable enhancement in resonant value of electric field intensity. Although, single layer silver shows higher enhancement, but for the reason of more adjustability silver coated silica will be our final choice as antenna element.

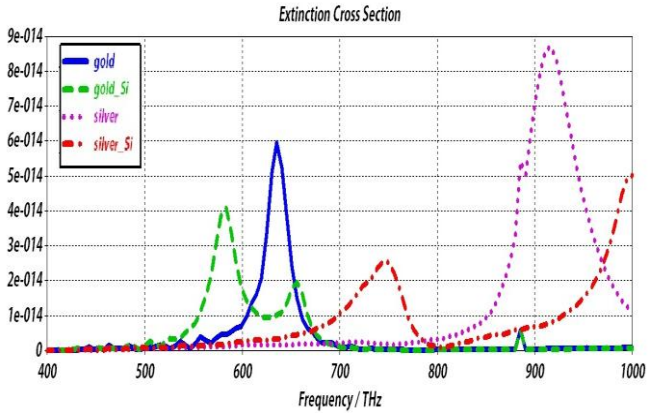


Figure 2: ECS vs. frequency for gold, silica covered with gold, silver, and silica coated by silver nanoparticle.

3. Final structure: simulation and results

During the rest of this paper, we model a structure of four vertical prolate spheroids of same dimension (a [major axis] × b [minor axis] × b) having common feed gap of width g at its center (Fig.1 (b)). This structure of vertical nanoparticles is normally illuminated by a plane wave source. Before performing calculations for our actual structures, we verify our model by the results published by the researchers in recent years [5-6]. The overall goal of this work is to investigate effects of cover thickness (h), the difference among major and minor axis (Δ) and gap size (g) using CST Microwave Studio. As final step, the near field pattern was calculated at resonance wavelengths for optimized antenna.

As first step of this section, effect of exerting gradual increase in metallic cover thickness (h) for a silica nano-ellipsoid with fixed dimension is considering. It is evident from (Fig. 3) that resonant field intensity will be greater for thicker metallic cover. The peaks occur at frequency around 350 THz for the case of h = 4, while at frequency larger than 500 THz for h = 4. So, it is clear from the figure that an increase in metallic cover thickness causes a red-shift in the resonance.

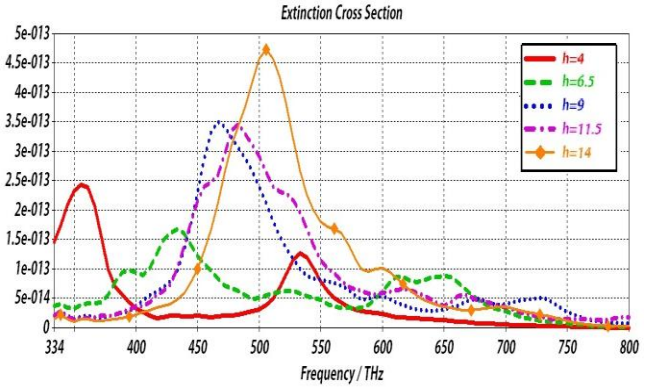


Figure 3: ECS vs. frequency for different thicknesses (h) of outer silver layer.

As blow diagram shows, a gradual increase in Δ and transforming from sphere to ellipsoid will cause a change in both resonant frequency and in maximum amount of ECS. All of these variations will happen as gradual as variation in Δ. Based on (Fig.4), field enhancement is more considerable for Δ lower than 25 and greater than 40. Blue-shift in resonant frequency is another result of increasing Δ. Also, multi-resonance can be observed for this structure, which has many potential applications.

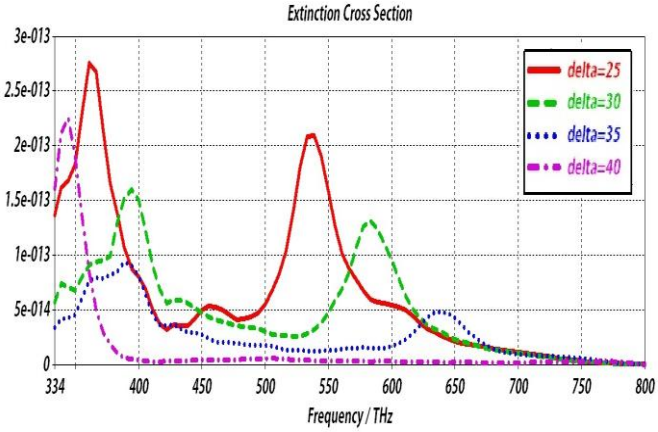


Figure 4: ECS vs. frequency to introduce an optimized value for difference among major and minor axis (Δ).

The feed-gap size of proposed model greatly influences the enhancement of near-field intensity. Smaller feed-gap gives rise to higher field enhancement. On reducing the feed-gap of this antenna from 17 to 11 nm, the intensity enhancement was found to be almost obvious. However, the geometry of the antenna puts a lower limit on its feed-gap dimension, which should be greater than the minor radii of nano-spheroid comprising it. There are two different resonances for each g in 300 to 800 THz frequency ranges. It can be seen in (Fig. 5) that all the curves have nearly overlapped in second resonant frequency. The peak occurs at frequency around 370 THz for the case of g = 11, while at frequency larger than 400 THz for other values of g.

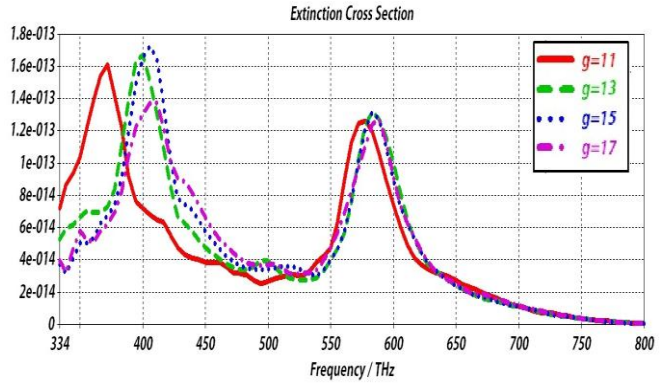


Figure 5: ECS vs. frequency in order to do an optimization for gap distance (g).

The strong field enhancement localized in the feed-gap of optical semi-turnstile antenna can be seen in (Fig. 6). Key dimensions of this final optimum structure are a = 48, Δ = 30, and h = 5. As it has been shown, the greatest value of field enhancement occurs at the center gap.

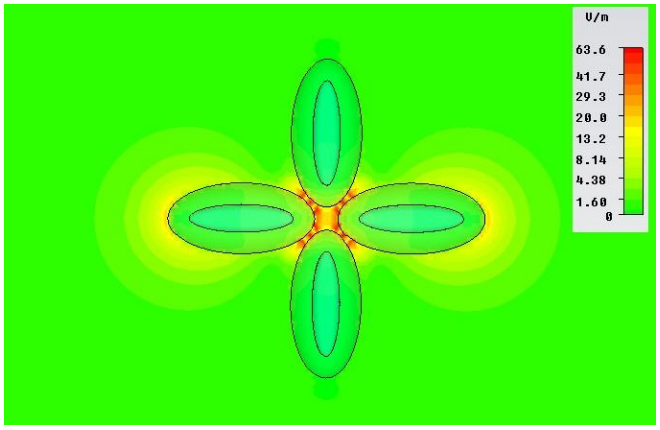


Figure 6: Near field behavior of optimized antenna including 4 vertical elements.

4. Conclusions

All over this paper, we study the resonances behavior of nano-sized models under study. Special attention is focused on Extinction Cross Section (ECS) as output of simulations, because it experiences a peak at resonance frequency and its enhancement is also considerable for dimensions of this scale. We also calculated the electric field distribution around the vertical assembly of nano spheroidal particles in the presence of an incident electromagnetic field (a linearly polarized plane wave). And as final result, simulation outputs verify that a wise adjustment of gap size and two other parameters (cover thickness (h) and the difference among major and minor axis (Δ)) will lead to a considerable field enhancement in center gap of this novel structure of offered element.

Acknowledgements

The authors have special thanks to Faculty of Micro-Electronic (FME), and also Islamic Azad University (Khomein Branch, Faculty of Engineering) for their financial supports.

References

[1] Bharadwaj, P.; B. Deutsch, and L. Novotny, "Optical antennas," *Adv. Opt. Photon*, No. 1, 438–483, 2009.

[2] Guzatov, D., and V. Klimov, "Optical properties of a plasmonic-nano-antenna: an analytical approach," *New JNL. of Phys.*, 2011.

[3] Novotny, L., "From near-field optics to optical antennas feature," *Physics Today*, 47-52, July 2011.

[4] Ordal, M. A., "Optical properties of the metals Al, Co, Cu, Au, Fe, Pb, Ni, Pd, Pt, Ag, Ti, and W in the infrared and far infrared", *J. App. Optics*, Vol. 22, No. 7, Apr. 1983.

[5] Gai, H., J. Wang, and Q. Tian, "Modified Debye model parameters of metals applicable for broadband calculations", *Applied Optics*, Vol. 46, No. 12, 2229-2233, 2007.

[6] Thomas, R., J. Kumar, R. S. Swathi, and K. G. Thomas, "Optical effects near metal nanostructures: towards surface-enhanced spectroscopy," *Current Science*, Vol. 102, No. 1, Jan. 2012.

Coupled nano-plasmons

M. Apostol[1,2*], S. Ilie[2,3], A. Petrut[3], M. Savu[2], and S. Toba[3]

[1]Department of Theoretical Physics, Institute of Atomic Physics, Magurele-Bucharest MG-6, POBox MG-35, Romania
[2]MiraTechnologies Ltd, Teiul Doamnei 2, Bucharest
[3]MiraTelecom, Grigorescu 13, 075100 Otopeni-Bucharest
*corresponding author, E-mail: apoma@theory.nipne.ro

Abstract

A simple model of coupled plasmons arising in two neighbouring nano-particles is presented. The coupled oscillations and the corresponding eigenfrequencies are computed. It is shown that the plasmons may be periodically trasferred between the two particles. For larger separation distances between the two particles the retardation is included. The oscillation eigenmodes are the polaritons in this case. There are distances for which the particles do not couple to each other, *i.e.* the polaritonic coupling gets damped. The van der Waals-London-Casimir force is estimated for the two particles; it is shown that for large distances the force is repulsive. We compute also the polarizabilities of the two coupled nano-particles and their cross-section under the action of an external monochromatic plane wave, which exhibit resonances indicative of light trapping and field enhancement. A resonant force is also identified, acting upon the particles both on behalf of the external field and of each other.

1. Introduction

Enhanced and locally confined optical fields associated with nanoparticles, nanostructures and nanoaggregates enjoy an increasing interest in nanoscale manipulation of active devices,[1, 2] nanoantennas,[**?**]-[6] surface enhanced Raman spectroscopy,[7] light trapping,[8] etc. The phenomenon is obviously related to dipolar fields, resonances and, as it was shown recently, hybridization,[9, 10] charge building in narrow nano-gaps and quantum tunneling within nanodimers.[11]-[21] All this dynamics is governed by coupled nano-plasmons.

Plasmons is an old and fundamental concept in condensed matter physics:[1] they are long-wavelength longitudinal oscillations of the charge density in matter. In a simple model, which is usually called the Drude-Lorentz model, matter can be represented as a plasma, consisting of identical mobile charges q of mass m and concentration (density) n (*e.g.*, electrons) moving uniformly and collectively against a quasi-rigid background of neutralizing charges $-q$ (*e.g.*, ions). The practical realization of long wavelength limit implies finite-size polarizable bodies, which entail, in turn, boundary conditions. Consequently, we may have many branches of plasmons: for instance, in a homogeneous conducting sphere the plasmon spectrum is given by $\Omega_l = \omega_p\sqrt{l/(2l+1)}$, where $\omega_p = \sqrt{4\pi nq^2/m}$ is called the plasma frequency and $l = 1, 2...$ is the azymuthal quantum number. A much more convenient representation simplifies the things to point particles, which may be a reasonably useful model for the nowadays nano-plasmonics.

[1]There is an enormous and ubiquituos plasmon literature, which makes a formal list of references both impossible and pointless.

2. Matter polarization

As it is well known, the Maxwell equations in matter imply four unknowns: $\mathbf{E}$ (electric field), $\mathbf{D}$ (electric displacement), $\mathbf{H}$ (magnetic field) and $\mathbf{B}$ (magnetic induction); and only two independent equations (Faraday and Maxwell-Ampere equations, which contain the $curl$ and the time derivatives). In order to solve them, we introduce constitutive relations between these unknowns through the semi-phenomenological and quasi-empirical dielectric function ε and magnetic permeability μ. A large class of matter is quasi-non-magnetic, such that we may equal $\mathbf{H}$ and $\mathbf{B}$ and put $\mu = 1$; still, we have three unknowns ($\mathbf{E}$, $\mathbf{D}$ and $\mathbf{H}$) and two equations.

On the other hand, the motion of the mobile charges in polarizable matter can be described by a displacement field $\mathbf{u}(t, \mathbf{r})$, which is a function of the time t and position $\mathbf{r}$. In the classical limit of small and slow variations (corresponding to classical electromagnetism), this displacement field generates a polarization charge density $\rho = -nqdiv\mathbf{u}$ and a corresponding current density $\mathbf{j} = nq\dot{\mathbf{u}}$. These charge and current densities generate in matter an electric field $\mathbf{E}$ and a magnetic field $\mathbf{H}$; but we still have two independent equations and three unknowns: $\mathbf{E}$, $\mathbf{H}$ and $\mathbf{u}$**.** However, the displacement field obeys an equation of motion, which, in this classical limit, is the Newton equation of motion

$$m\ddot{\mathbf{u}} = q(\mathbf{E} + \mathbf{E}_0) - m\omega_c^2\mathbf{u} - m\gamma\dot{\mathbf{u}} \ ; \qquad (1)$$

$\mathbf{E}$ is the internal (polarization) electric field, $\mathbf{E}_0$ is an external electric field, ω_c is a characteristic frequency and γ is a damping coefficient (much smaller than any relevant frequency). The magnetic part of the Lorentz force is absent in equation (1) because the velocities of the charges in matter are much smaller than the speed of light; the internal magnetic field is also absent, in accordance with our

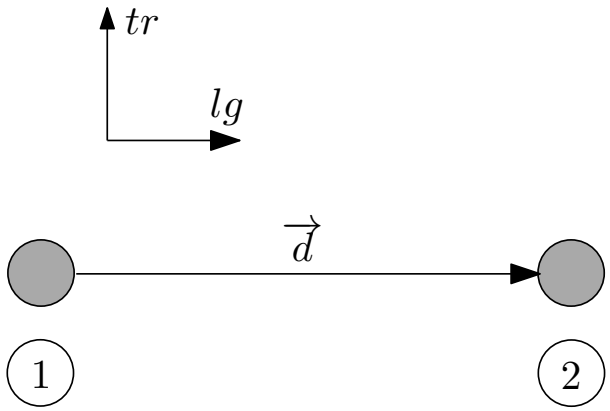


Figure 1: Two point dipoles

assumption of small $\mathbf{u}$ and non-magnetic matter. Equation (1) is the missing equation (the third equation), which helps solving the Maxwell equations.[22]-[24]

Obviously, $\mathbf{P} = nq\mathbf{u}$ is the polarization (density of dipole moments); equation (1) leads immediately to the well-known Drude-Lorentz (plasma) dielectric function $\varepsilon(\omega) = (\omega^2 - \omega_c^2 - \omega_p^2)/(\omega^2 - \omega_c^2 + i\omega\gamma)$, where only the optical dispersion is included (through the dependence on the frequency ω). As it is well known, $\omega_c = 0$ corresponds to conductors, while $\omega_c \neq 0$ describes dielectrics. The model and equation (1) can be generalized in multiple ways. We limit ourselves here to use equation (1) in conjunction with Maxwell equations, in order to describe a simple situation regarding coupled nano-plasmons.

The longitudinal internal (polarization) electric field in Gauss equation $div\mathbf{E} = -4\pi nq div\mathbf{u}$ is given by $\mathbf{E} = -4\pi nq\mathbf{u}$ (*i.e.*, $\mathbf{E} = -4\pi\mathbf{P}$). In the long-wavelength limit, the finite size of the body is usually taken into account by a (de-) polarizing factor f, such as the field is given by $\mathbf{E} = -4\pi nqf\mathbf{u}$; for instance, for a sphere $f = 1/3$. Introducing this polarization field in equation (1), taking the Fourier transform and leaving aside the coefficient γ, we get

$$(\omega^2 - \omega_c^2 - f\omega_p^2)\mathbf{u} = -\frac{q}{m}\mathbf{E}_0 \ ; \qquad (2)$$

we can see that we have a plasmon resonance at frequency $\sqrt{\omega_c^2 + f\omega_p^2}$; for a conducting sphere with $\omega_c = 0$ and $f = 1/3$, we get the plasmon frequency $\omega_p/\sqrt{3}$, in accordance with the frequencies Ω_l given above for $l = 1$.[24]

3. Coupled nano-plasmons

We consider two point particles, denoted by 1 and 2, each with its own plasmon frequency $\omega_{1,2}$, separated by the position vector $\mathbf{d}$. We describe the motion of the mobile charges in each particle by a displacement vector $\mathbf{u}_{1,2}$; equation (2) becomes

$$(\omega^2 - \omega_{1,2}^2)\mathbf{u}_{1,2} = -\frac{q}{m}\mathbf{E}_{02,1} \ , \qquad (3)$$

where $\mathbf{E}_{01,2}$ is the electric field generated by particle 1 (2) at the position of the particle 2 (1). In the long wavelength limit this is the field generated by a point dipole

$$\mathbf{E}_{01,2} = v_{1,2}n_{1,2}q\frac{3(\mathbf{u}_{1,2}\mathbf{d})\mathbf{d} - \mathbf{u}_{1,2}d^2}{d^5} \ , \qquad (4)$$

where $v_{1,2}$ are the volumes of the two particles and $n_{1,2}$ are the concentration of the mobile charges in the particles; equation (4) is valid in the near-field region $c/\omega \gg d$, where c is the speed of light.[25] Since the particles are considered point-like, we have also $v_{1,2}^{1/3} \ll d$. Introducing this field in equations (3) we get two coupled equations for the displacement vectors. It is convenient to use the projection of the displacement vectors on the vector $\mathbf{d}$ and on a direction perpendicular to the vector $\mathbf{d}$; we call the former the longitudinal displacements and denote them by $u_{l1,2}$, while the latter, denoted by $\mathbf{u}_{t1,2}$, are called transverse displacements. The equations for the longitudinal displacements are decoupled from those corresponding to the transverse displacements; both sets of equations have the same structure. We limit ourselves here to the longitudinal displacements

$$(\omega^2 - \omega_{1,2}^2)u_{l1,2} = -\frac{\omega_{p2,1}^2 v_{2,1}}{2\pi d^3}u_{l2,1} \ . \qquad (5)$$

The solution of these coupled-oscillators equations is straightforward. The factor $v_{1,2}/d^3$ plays the role of a weak-coupling constant. The eigenfrequencies of equations (5) are close to the plasmon frequencies $\omega_{1,2}$, which should satisfy the condition $c/\omega_{1,2} \gg d$; $c/\omega_{1,2}$ is usually called the plasma wavelength. For typical values $\omega_{1,2} \simeq 10^{15}s^{-1}$ we get a critical distance of the order $d \simeq 0.1\mu m$; the treament given here holds for smaller distances, while for larger distances we need to take into account the retardation in estimating the polarization field.

An interesting situation occurs for two identical conducting particles $\omega_{c1} = \omega_{c2} = 0$, $\omega_{p1} = \omega_{p2} = \omega_p$ and $v_1 = v_2 = v$; in order to simplify the things we take also $\omega_1 = \omega_2 = \omega_p$. In this case the eigenfrequencies are given by

$$\Omega_{l1,2} = \omega_p\left(1 \pm \frac{v}{2\pi d^3}\right)^{1/2} \simeq \omega_p\left(1 \pm \frac{v}{4\pi d^3}\right) \ . \qquad (6)$$

The displacement vectors for the initial condition $u_{l2}(t = 0) = 0$ read

$$\begin{aligned} u_{l1}(t) &= 2Ae^{i\omega_p t}\cos\tfrac{v}{4\pi d^3}t \ , \\ u_{l2}(t) &= -2iAe^{i\omega_p t}\sin\tfrac{v}{4\pi d^3}t \ ; \end{aligned} \qquad (7)$$

we can see that the two coupled oscillations exhibit "beats", and the plasmons can be transferred periodically between the two particles, as expected. A similar situation holds for the transverse oscillations, with the factor 2π replaced by 4π in the above formulae. The corresponding eigenfrequencies are given by

$$\Omega_{t1,2} = \omega_p\left(1 \pm \frac{v}{4\pi d^3}\right)^{1/2} \simeq \omega_p\left(1 \pm \frac{v}{8\pi d^3}\right) \ . \qquad (8)$$

4. van der Waals-London-Casimir force

A polarizable point-like particle can be approximated by a dipole, with the current density $\mathbf{j} = vnq\dot{\mathbf{u}}\delta(\mathbf{r})$ and charge density $\rho = -vnq(\mathbf{u}grad)\delta(\mathbf{r})$, where v is the volume of the particle placed at the origin. For these charge and current distributions we can compute easily the electromagnetic potentials (Fourier transforms):

$$\mathbf{A} = -i\lambda vnq\mathbf{u}\frac{e^{i\lambda r}}{r} \ , \ \Phi = -vnq\frac{\mathbf{ur}}{r}\frac{\partial}{\partial r}\frac{e^{i\lambda r}}{r} \ , \quad (9)$$

where $\lambda = \omega/c$. The polarization electric field is given by $\mathbf{E} = -(1/c)\partial\mathbf{A}/\partial t - grad\Phi$, so that we can include the retardation in the equation of motion (1). For the longitudinal oscillations of two identical conducting particles (ω_1=$\omega_2 = \omega_p$) we get

$$(\omega^2 - \omega_p^2)u_{l1,2} = -\frac{\omega_p^2 v}{2\pi d^3}(1 - i\lambda d)e^{i\lambda d}u_{l2,1} \quad (10)$$

(and a similar set of equations for the transverse oscillations). We can see that in the non-retarded limit $\lambda d \ll 1$ equations (10) go into equations (5) derived above. We are interested now in the wave-zone limit $\lambda d \gg 1$. The eigenfrequencies of equations (10) are given by

$$(\omega^2 - \omega_p^2)^2 = \frac{\omega_p^4 v^2}{(2\pi d^3)^2}(1 - i\lambda d)^2 e^{2i\lambda d} \ , \quad (11)$$

or

$$\tan\lambda d = \lambda d \ , \ (\omega^2 - \omega_p^2)^2 = \frac{\omega_p^4 v^2}{(2\pi d^3)^2}(1 + \lambda^2 d^2) \ . \quad (12)$$

It is convenient to introduce the notations $g = v/2\pi d^3 \ll 1$ and $\omega_p d/c = A$; the solution can be found as a series of powers of g:

$$\begin{aligned}\Omega = \omega_p[1 \pm \tfrac{1}{2}g(1 + A^2)^{1/2} + \\ + \tfrac{1}{8}g^2(A^2 - 1) + ...] \ ;\end{aligned} \quad (13)$$

it should satisfy the equation $\tan(\Omega d/c) = \Omega d/c$, which, in the limit $g \ll 1$ becomes $\tan A \simeq A$ ($\Omega \simeq \omega_p$); for large values of A we get $A = \omega_p d/c \simeq n\pi$. We can see that there are real solutions for the eigenfrequencies only for certain values of the distance $d_n \simeq n\pi c/\omega_p$, which are approximate multiples of the plasma wavelength (in this limit). The corresponding oscillations are usually called polaritons. For intermediate values of d the eigenfrequencies are complex, *i.e.* the coupling between the two particles is damped (the damping parameter γ in the equation of motion (1) should be retained in this case). We can equally well say that the two particles are not coupled in this case.

The zero-point (vacuum fluctuations) energy can be estimated as $\mathcal{E} = \sum \hbar\Omega/2$, where the summation extends over all the eigenfrequencies. The motion of the transverse degrees of freedom leads to the eigenfrequencies equation

$$\begin{aligned}\tan\lambda d = \tfrac{\lambda d}{1-\lambda^2 d^2} \ , \ (\omega^2 - \omega_p^2)^2 = \\ = \tfrac{\omega_p^4 v^2}{(4\pi d^3)^2}(1 + 3\lambda^2 d^2 + \lambda^4 d^4) \ .\end{aligned} \quad (14)$$

The solution is given by

$$\begin{aligned}\Omega = \omega_p[1 \pm \tfrac{1}{4}g(1 + 3A^2 + A^4)^{1/2} + \\ + \tfrac{1}{32}g^2(3A^4 + 3A^2 - 1) + ...] \ .\end{aligned} \quad (15)$$

Now we can compute the zero-point energy (the transverse degrees of fredom have a double multiplicity):

$$\mathcal{E} = \hbar\omega_p\left[3 + \frac{g^2}{16}(3A^4 + 5A^2 - 3)\right] \quad (16)$$

and the corresponding force

$$F = \frac{\hbar\omega_p v^2}{32\pi^2}\left(\frac{3\omega_p^4}{c^4 d^3} + \frac{10\omega_p^2}{c^2 d^5} - \frac{9}{d^7}\right) \ . \quad (17)$$

We can see that in the non-retarded limit ($\omega_p d/c \ll 1$) the force is attractive and goes like $-1/d^7$; this is the van der Waals-London force; it comes from the longitudinal degrees of freedom. In the opposite, retarded limit $\omega_p d/c \gg 1$ the force is repulsive and goes like $1/d^3$; this is the limit of the Casimir force, coming entirely from the transverse oscillations.[26] The force changes sign around $\omega_p d/c \preceq 1$ and has a maximum for $\omega_d d/c \succeq 1$. For intermediate distances the numerical coefficients in equation (17) are not reliable, since the transverse oscillations do not occur at the same distances d_n as the longitudinal ones; increasing the distance, the longitudinal and transverse oscillations contribute alternately to the repulsive force.

5. External field

We consider the two point dipoles acted by an external monochromatic plane wave with the electric field $\mathbf{E}_0(t, \mathbf{r}) = \mathbf{E}_0\cos(\omega t - \mathbf{kr})$, $\omega = ck$ and $\mathbf{E}_0\mathbf{k} = 0$. The two particles separated by the distance d lie along the z-axis and the external field (wavevector**k**) makes an incidence angle α with the z-axis. For a p- (parallel) wave we have both a longitudinal (E_{0z}) and a transverse (E_{0x}) component of the external field, while for an s- (senkrecht) wave we have only a transverse component E_{0y}. We assume further the most interesting situation of two identical point dipoles with $v^{1/3} \ll d \ll c/\omega$ (optical excitation), as well as $d \ll c/\omega_p$. The equation of motion (1) gives

$$\begin{aligned}\ddot{u}_{l1,2} + \omega_p^2 u_{l1,2} - \tfrac{v\omega_p^2}{2\pi d^3}u_{l2,1} = \tfrac{q}{m}E_{0l}\cos\omega t \ , \\ \ddot{u}_{t1,2} + \omega_p^2 u_{t1,2} + \tfrac{v\omega_p^2}{4\pi d^3}u_{t2,1} = \tfrac{q}{m}E_{0t}\cos\omega t \ ,\end{aligned} \quad (18)$$

where we have neglected the position dependence of the external field at the location of the two point dipoles. The solution of this equations is given by

$$\begin{aligned}u_{1l} = u_{2l} = -\tfrac{q}{m}E_{0l}\tfrac{1}{\omega^2 - \Omega_{2l}^2}\cos\omega t \ , \\ u_{1t} = u_{2t} = -\tfrac{q}{m}E_{0t}\tfrac{1}{\omega^2 - \Omega_{1t}^2}\cos\omega t \ ,\end{aligned} \quad (19)$$

where

$$\Omega_{2l}^2 = \omega_p^2\left(1 - \frac{v}{2\pi d^3}\right) \ , \ \Omega_{1t}^2 = \omega_p^2\left(1 + \frac{v}{4\pi d^3}\right) \ . \quad (20)$$

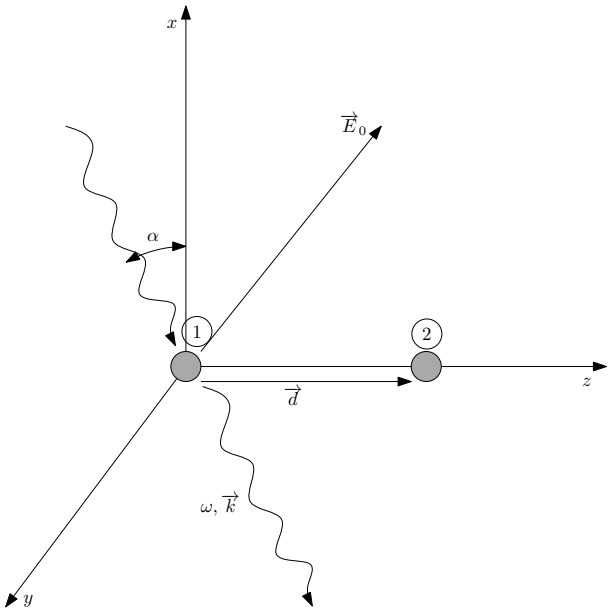


Figure 2: Two coupled point dipoles subjected to an external field

Equations (19) give the polarizabilities of the two coupled point dipoles ($\mathbf{P} = nq\mathbf{u}$ is the polarization). It is worth noting that there exist two resonant frequencies Ω_{2l} (shifted to the red with respect to the characteristic frequency ω_p of the isolated dipole) and Ω_{1t} (shifted to the ultraviolet). At these resonances the light is trapped by the two coupled dipoles, and the field is enhanced appreciably.

Having known the displacements $\mathbf{u}_{1,2}$ we can use the potentials given by equations (9) to compute the field in the wave zone ($r \gg d$). The calculations are straightforward. We can use the results for estimating the cross-section defined as $d\sigma = \mathbf{S}\mathbf{r}d\Omega/S_0 r^3$, where $\mathbf{S}$ is the Poynting vector of the scattered field and $\mathbf{S}_0$ is the Poynting vector of the incident field. We get the total cross-sections

$$\sigma_p = \frac{2\omega_p^4 v^2}{3\pi c^4}\omega^4 \left[\frac{\sin^2\alpha}{\left(\omega^2-\Omega_{2l}^2\right)^2} + \frac{\cos^2\alpha}{\left(\omega^2-\Omega_{1t}^2\right)^2}\right] \ , \qquad \sigma_s = \frac{2\omega_p^4 v^2}{3\pi c^4}\cdot\frac{\omega^4}{\left(\omega^2-\Omega_{1t}^2\right)^2} \tag{21}$$

for the p- and, respectively, the s-wave. We can see the resonant cross-section (especially the longitudinal resonance at lower frequencies), which indicates again the phenomenon of light trapping and field enhancement.

6. Resonant force

Under the action of an external field the particles get polarized; the displacement field given by equations (19) generates charge and current densities; for instance, the particle placed at $\mathbf{r} = 0$ acquires a charge density $\rho(\mathbf{r}) = -vnq(\mathbf{u}grad)\delta(\mathbf{r})$, where $\mathbf{u}$ denotes its displacement field. The external field acts upon this charge by a drift force given by

$$\mathbf{F}_d = \int d\mathbf{r}\rho(\mathbf{r})\mathbf{E}_0(t,\mathbf{r}) \ ; \tag{22}$$

the calculations are straightforward and we get

$$\mathbf{F}_d = vnq(\mathbf{k}\mathbf{u})\mathbf{E}_0 \sin\omega t \ . \tag{23}$$

A similar drift force acts upon the particle placed at $\mathbf{r} = \mathbf{d}$. We can see that an external s-wave, as well as an external plane wave acting upon an isolated particle brings no drift force. Making use of equations (19) for a p-wave (and identical particles), we get the drift force

$$\mathbf{F}_d = \frac{3v^2\omega_p^4\omega}{64\pi^2 cd^3}\cdot\frac{\sin 2\alpha \sin 2\omega t}{(\omega^2-\Omega_{2l}^2)(\omega^2-\Omega_{1t}^2)}E_0\mathbf{E}_0 \ . \tag{24}$$

We note the resonant character of this force for frequency ω approaching the frequencies Ω_{2l} or Ω_{1t}.

There is also an interaction force acting between the two particles. For instance, we get the force acting upon the particle placed at $\mathbf{r} = 0$ on behalf of the particle placed at $\mathbf{r} = \mathbf{d}$ by using the (dipole) field given by equation (4) in equation (22). We get an interaction force

$$F_{12l} = \frac{3v^2\omega_p^4}{16\pi^2 d^4}\left[\frac{2E_{0l}^2}{(\omega^2-\Omega_{2l}^2)^2} - \frac{E_{0t}^2}{(\omega^2-\Omega_{1t}^2)^2}\right]\cos^2\omega t \ , \qquad F_{12t} = -\frac{6v^2\omega_p^4}{16\pi^2 d^4}\cdot\frac{E_{0l}E_{0t}}{(\omega^2-\Omega_{2l}^2)(\omega^2-\Omega_{1t}^2)}\cos^2\omega t \ . \tag{25}$$

We note again the resonant character of this force, as well as its non-central character, in general (for a p-wave it gives rise to a torque).

In estimating these forces we limited ourselves only to the polarization (displacement field) generated by the external field. In general, we should also take into acount the field generated by the particles in estimating the displacement field. The contribution of this "internal" field (which acts as an external field for each particle) is proportional to the volume v of the particles, and for a finite number of particles it may be neglected. However, for a large number of particles, its contribution is important. It is worth noting also that under the action of such resonant interaction forces the nano-particles can get organized in super-structures.

7. Conclusion

We have analyzed here the electromagnetic coupling between two polarizable point-like particles, modelled as point dipoles. This may be a reasonably useful model of coupled nano-plasmons and nano-polaritons. For small separation distances between the two particles (smaller than the plasma wavelength), where the non-retarded coupling regime dominates, the two particles exhibit coupled plasmons, which can be transferred from one particle to other. The zero-point fluctuations give the attractive van der Waals-London force in this case, acting between particles and behaving like $-1/d^7$, where d is the separation distance. For distances larger than the plasma wavelength

the retardation comes into play and the coupling is realized through polaritons. This may happens only for certain discrete sets of separation distances (different for longitudinal and transverse oscillations of the charge density, with respect to the separation vector), in between the coupling being damped (non-coupling); it is realized either by longitudinal or transverse oscillations of the charge density, in turn. Immediateley after distances of the order of the plasma wavelength, the zero-point energy force acting between particles becomes repulsive, arising from transverse oscillations (polaritons) and going at infinity like $1/d^3$.

The polarizabilities of the two coupled nano-particles exhibit plasmonic resonances, which are also present in the cross-section of the scattered field as well as in the resonant force acting upon the particles both on behalf of the external field and of each other.

Acknowledgement

The authors are indebted to the members of the Seminar of the Institute of Atomic Physics and the Laboratory of Theoretical Physics, Magurele, Bucharest, for useful discussions and a careful reading of the manuscript. This work was supported by the Romanian Government Research Agency Grant #306/SMIS 26614.

References

[1] P. J. Schuck, D. P. Fromm, A. Sundaramurthy, G. S. Kino and W. E. Moerner, Improving the mismatch between light and nanoscale objects with gold bowtie nanoantennas, *Phys. Rev. Lett.* 94: 017402, 2005.

[2] R. W. Taylor, T.-C. Lee, O. A. Scherman, R. Esteban, J. Aizpurua, F. M. Huang, J. J. Baumberg, and S. Mahajan, Precise subnanometer plasmonic junctions for SERS within gold nanoparticle assemblies using cucurbit[n]uril "glue", *ACS Nano* 5: 3878-3887, 2011.

[3] P. Muhlschlegel, H. Eisler, O. Martin, B. Hecht and D. Pohl, Resonant optical antennas, *Science* 308: 1607-609, 2005.

[4] E. Cubukcu, E. A. Kort, K. B. Crozier and Federico Capasso, Plasmonic laser antenna, *Appl. Phys. Lett.* 89: 093120, 2006.

[5] A. G. Curto, G. Volpe, T. H. Taminiau, M. P. Kreuzer, R. Quidant and N. F. van Hulst, Unidirectional emission of a quantum dot coupled to a nanoantenna, *Science* 329: 930-933, 2010.

[6] L. Novotny and N. van Hulst, Antennas for light, *Nature Photon.* 5: 83-90, 2011.

[7] H. Xu, E. J. Bjerneld, M. Käll and L. Börjesson, Spectroscopy of single hemoglobin molecules by surface enhanced Raman scattering, *Phys. Rev. Lett.* 83: 4357-4360, 1999.

[8] H. A. Atwater and A. Polman, Plasmonics for improved photovoltaic devices , *Nature Mater.* 9: 205-213, 2010.

[9] E. Prodan, C. Radloff, N. J. Halas and P. Nordlander, A hybridization model for the plasmon response of complex nanostructures, *Science* 302: 419-422, 2003.

[10] P. Nordlander, C. Oubre, E. Prodan, K. Li and M. I. Stockman, Plasmon hybridization in nanoparticle dimers, *Nano Letters* 4: 899-903, 2004.

[11] T. Atay, J.-H. Song, and A. V. Nurmikko, Strongly interacting plasmon nanoparticle pairs: from dipole-dipole interaction to conductively coupled regime, *Nano Lett.* **4** 1627-1631 (2004).

[12] I. Romero, J. Aizpurua, G. W. Bryant and F. J. García de Abajo, Plasmons in nearly touching metallic nanoparticles: singular response in the limit of touching dimers, *Opt. Express* 14: 9988-9999, 2006.

[13] P. K. Jain, W. Huang and M. A. El-Sayed, On the universal scaling behavior of the distance decay of plasmon coupling in metal nanoparticle pairs: a plasmon ruler equation, *Nano Lett.* 7: 2080-2088, 2007.

[14] M. Danckwerts and L. Novotny, Optical frequency mixing at coupled gold nanoparticles, *Phys. Rev. Lett.* 98: 026104, 2007.

[15] J. B. Lassiter, J. Aizpurua, L. I. Hernandez, D. W. Brandl, I. Romero, S. Lal, J. H. Hafner, P. Nordlander and N. J. Halas, Close encounters between two nanoshells, *Nano Lett.* 8: 1212-1218, 2008.

[16] A. Aubry, D. Y. Lei, S. A. Maier and J. B. Pendry, Interaction between plasmonic nanoparticles revisited with transformation optics,*Phys. Rev.* 105: 233901, 2010.

[17] K. J. Savage, M. M. Hawkeye, R. Esteban, A. G. Borisov, J. Aizpurua and J. J. Baumberg, Revealing the quantum regime in tunnelling plasmonics, *Nature* 491: 574-577, 2012.

[18] R. Esteban, A. G. Borisov, P. Nordlander and Javier Aizpurua, Bridging quantum and classical plasmonics with a quantum-corrected model, *Nature Commun.* 3: 825, 2012 (1-9).

[19] F. van Beijnum, C. Retif, C. B. Smiet, H. Liu, P. Lalanne and M. P. van Exter, Quasi-cylindrical wave contribution in experiments on extraordinary optical transmission, *Nature* 492: 411-414, 2012.

[20] J. A. Scholl, A. L. Koh and J. A. Dionne, Quantum plasmon resonances of individual metallic nanoparticles, *Nature* 483: 421-427, 2012.

[21] D. R. Ward, F. Huser, F. Pauly, J. C. Cuevas and D. Natelson, Optical rectification and field enhancement in a plasmonic nanogap, *Nature Nanotech.* 5: 732-736, 2010.

[22] M. Apostol and G. Vaman, Electromagnetic field interacting with a semi-infinite plasma, *J. Opt. Soc. Am. A* 26: 1747-1753, 2009.

[23] M. Apostol and G. Vaman, Reflection and refraction of the electromagnetic field in a semi-infinite plasma, *Opt. Commun.* 282: 4329-4332, 2009.

[24] M. Apostol and G. Vaman, Plasmons and diffraction of an electromagnetic plane wave by a metallic sphere, *Progr. Electrom. Res. (PIER)* 98: 97-118, 2009.

[25] M. Apostol, S. Ilie, A. Petrut, M. Savu and S. Toba, A generalization of the dipolar force, *J. Appl. Phys.* 112: 024905, 2012.

[26] M. Apostol, On the molecular forces acting between macroscopic bodies, *Physica B* 409: 57-62, 2013

Study on PL enhancement of GaAs/InGaAs Quantum Well Emission by Gold Nanoparticle Arrays

Hongwei Gao[1], Jinghua Teng[2], SooJin Chua[1,2], Ning Xiang[1]

[1] Department of Electrical and Computer Engineering, National University of Singapore, Singapore 117576, Singapore

[2] Institute of Material Research and Engineering, Singapore 117602, Singapore

*corresponding author, E-mail: elexn@nus.edu.sg

Abstract

Enhancement of photoluminescence(PL) intensity for InGaAs/GaAs quantum well (QW) caused by coupling effect of surface plasmon(SP) resonance generated by Au nanodisk arrays with QW emission is demonstrated experimentally. To increase the coupling efficiency, a thin layer SiO_2 is introduced between Au nanodisk and GaAs surface. To match SP wavelength with QW emission wavelength (945 nm),Au nanodisk arrays with periodicity of 290 nm, radius of 70 nm, and thickness of 10 nm is fabricated. 2.17-fol d enhancement is observed.

1. Introduction

Surface plasmons (SPs), arising from resonant interactions between surface charge oscillations from metal and electromagnetic fields, have drawn much attention in optics and photonics.[1]Pioneering studies showed that metallic nanostructures, which generate surface plasmon resonance (SPR),are able to be used as near-field antennas because they can redistribute the local photonic mode density,[2] concentrate electromagnetic energy into small volumes,[3] and affect the excitation and emission rate of neighbouring chromophores. Due to the last promising property, they can produce enhancements in Raman scattering,[4-8] fluorescence,[9,10]photoinduced charge generation,[11] photochemistry,[12] and nonlinear optical response.[13,14] Recently, there has been much progress in enhancing the efficiency of spontaneous emission (fluorescence) using the SPR effect in the vicinity of a metal-dielectric boundary. The first important example of the improvement was achieved in GaN photoluminescence by depositing a thin layer of Ag film on top of the GaN.[15]Subsequently,90-fold enhancement of the spontaneous recombination rate from a similar structure was reported.[16]Since then, SPR was employed in many different light emitting media[17–21]to enhance the spontaneous emission, for example, Si emitters.[22]The coupling of surface plasmon polariton (SPP)modes with the radiation mode has been obtained by one dimensional (1D) dielectric gratings,[17,18,21]two-dimensional (2D) corrugated silver films,[20,23]and more complicated cavity like structures.[24]This interaction could be accomplished in two ways to enhance the PL intensity. The first approach occurs during the optical excitation stage, which is to couple the incident light directly into tightly confined SPs modes generated by metallic nanostructure to increase the excitation energy density in the vicinity of the quantum well (QW) region.[25-28]The second approach takes place during the emission stage, which is to enhance energy-emission efficiency of the QW through Purcell effect.[29]They have already been demonstrated through InGaN/GaN and AlGaAs/GaAs systems, of which emission wavelength falls in visible region; however, there has been very few reports regarding the SP effects on InGaAs QWs systems, of which emission wavelength located in near infrared (NIR) range. It is known InGaAs is a very important optoelectronic material. It is used in high-power and high-frequency electronics due to its superior electron velocity with respect to the more common semiconductors silicon and gallium arsenide. It is popular in infrared detectors mainly attributes to lower dark current. Moreover, it also can be used as a laser medium. The reason of few reports in NIR range is probably because it is easy to generate SPR in short-wavelength range by Ag or Au (which are often used for generating SPs). Although using periodically nanostructure with such metals can tune SPR to a little longer wavelength, how to extend it to near infrared (NIR) range on GaAs in an efficient way is still a big challenge. Here, we simply introduce a thin SiO_2 film under Au nanodisk arrays to modify the Au SPR properties which could provide efficient coupling with InGaAs/GaAs QWs. Meanwhile, this thin SiO_2 layer may also serves as passivation layer to reduce

surface states of GaAs top layer, which maybe important if the active layer is very close to the surface (20nm, in present study). In our studied set-up, more than 2 fold enhancement of light emitting from the InGaAs/GaAs QWs by Au SPR has been observed. To our knowledge, It is the first enhancement achieved based on InGaAs/GaAs system.

2. Experiment

Fig.1 (a) shows the fabrication process for Au nanodisk arrays. A 50nm SiO_2 is deposited on the InGaAs/GaAs quantum wells (QWs) which consists of 4 periods of 8nm InGaAs wells separated by 20nm GaAs barrier layers. Followed by a negative photoresist (NR-200P) spun on top of SiO_2 at 3000rpm for 40s with acceleration of 2000rpm. The photoresist is then proceed to exposure twice orthogonally, and developing to form photoresist nanohole arrays as a mask. The periodicity is determined by laser wavelength and angle between incident beam and reflected beam. Radius is adjusted by developing time for photoresist after exposure. The Au nanodisk array is constructed by evaporating 10 nm Au into the photoresist nanoholes. The thickness of deposited Au is monitored by quartz crystal during electron beam evaporation process. After Au deposition, a standard lift-off process is performed to form the Au nanodisk arrays (wafer A). According to simulation result, radius of Au nanodisk here is chosen to be 70 nm to match SPR wavelength toInGaAs/GaAs QWs emission wavelength (945 nm).Fig.1 (b) shows one of scanning electron microscope (SEM) image of formed Au nanodisk arrays. It is observed that circular shaped Au nanodisk arrays with excellent uniformity both in shape and periodicity is formed on top of QWs. Optical properties of wafer are measured to investigate the SP effects on QW emission intensity.

In our experiment, a 632 nm line of Ar+ laser is employed as excitation source to perform PL measurement. A 0.85 m double-grating monochromator and a PMT detector are used to collect the signal in lock-in mode. The reflectance spectrum is measured by a UV spectrophotometer (Shimadzu) from normal incidence.

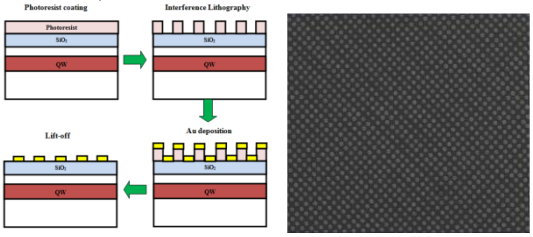


Fig.1.(a) Schematic illustration of sample fabrication process.

Figure 1b The SEM image of Au nanodisk arrays on top of QW.

3. Result and discussion

Fig 2 shows room temperature PL result of sample A (red), on top of which are a 50 nm SiO_2 layer and Au nanodisk arrays. For comparing, PL result of the original wafer, which is grown side by side, is also displayed (black). In the PL spectra, two main peaks have been observed. One is located around 880nm, which should be resulted from GaAs barrier layers (or GaAs substrate). The other one is at 945nm. It should be emitted from InGaAs QWs. It is clearly observed that the QWs peak is enhanced 2.17 times by SiO_2 film/Au nanostrctures, while the peak of GaAs barriers is reduced to about half of its original intensity. Moreover, there is a 5 nm blue-shift of QW PL from sample A compared with that from as-grown sample. However, for the signal emitted from substrate, the peak remains at the same wavelength.

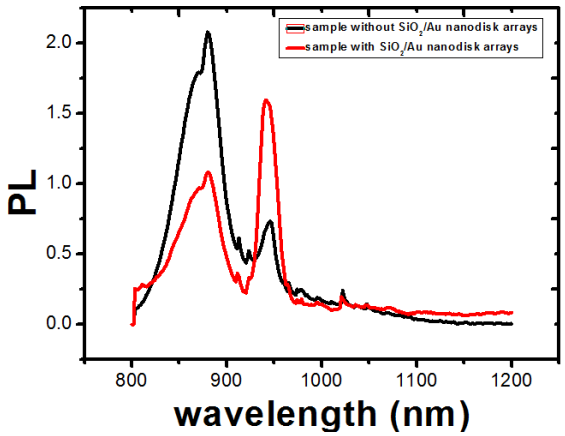


Fig.2.PL spectra of as-grown sample (black curve) and compact sample with SiO2/Au nanodisk arrays (red curve)

Normally, the pumping light from laser generates electron-hole pairs in both InGaAs QWs and GaAs barriers. Some of carriers generated in GaAs barriers diffuse into InGaAs QWs, because the ground energy of InGaAs QW is lower. Then, they are terminated by radiative recombination and nonradiative recombination. The radiative recombination leads to InGaAs QW's PL and GaAs barrier's PL, while, the nonradiative recombination results in loss. For sample A, PL peaks are located at 945 nm and 880 nm respectively.

In the case of the existence of Au nanodisk arrays, some issues which can affect the optical properties of InGaAs/GaAs quantum system should be considered, because the intensity of pumping light and of emitting light may be reduced due to the absorption by Au in our interesting regions. For wafer A, the area ratio of Au nanodisk is ~18%. However, the peak intensity from the InGaAs QWs is increased much due to Au nanodisk arrays fabricated on a 50 nm SiO_2 film on top of InGaAs/GaAs QWs. Two possible mechanisms may explain this phenomenon. One is the pumping light may be increased due to 2D photonic crystal and SP effects of Au nanodisk arrays, which means more photons are absorbed by the InGaAs/GaAs quantum system. The more absorption energy can increase the number of excited carriers in InGaAs QWs and GaAs barriers, resulting in more light emitted from QWs and GaAs barriers. However, our experimental results show that only the PL intensity from InGaAs QWs has been enhanced, while the PL emitted from GaAs barriers is reduced. It must be the other mechanism leads to the enhancement of the PL emission from InGaAs QWs. It is possible that electron-hole pairs generated by laser pumping release to ground energy of both InGaAs QWs and GaAs

barriers, and then recombine radiatively to emit light from QWs and GaAs barriers as displayed spectrum (black) in Fig 2. However, the emitted photons from InGaAs QWs excites the resonance oscillation of the SPs from Au nanodisk arrays which results in strong confined electric field. Due to the short distance between SPs and QWs, this strong confined electric field of SP can act on QWs, leading to the increased carrier recombination rate which enhances the PL intensity of InGaAs QWs. The electron oscillation energy of the SPs does not match with GaAs barrier bandgap, so no such enhancement occurs in the GaAs barrier. Therefore, more carriers generated in GaAs barriers will diffuse into InGaAs QWs because of its higher recombination rate, leading to the reduction of the PL of GaAs barriers as seen from red curve in Fig 2.

To verify the role of the thin SiO_2 film, Au nanodisk arrays, with the same periodicity and thickness with wafer A, but smaller radius (~60 nm), are created directly on a similar InGaAs/GaAs wafer (wafer B). Smaller radius is to ensure SPR generated by this Au nanodisk arrays to be located close to this InGaAs/GaAs QW emission wavelength (1004 nm).

Fig 3 shows room temperature PL results for sample B (red curve) and its as-grown sample (black curve). It is clearly observed that the intensity of PL emitted from the InGaAs QWs is reduced to about 87% compared to that from original wafer, also with a 5 nm blue-shift. While, there is almost no change for the peak wavelength emitted from GaAs barriers.

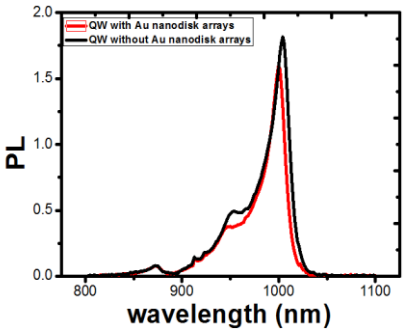


Fig. 3 PL spectra of as-grown sample and compact sample, black curve is PL spectrum for sample without Au nanodisk arrays, red curve is PL spectrum for sample with Au nanodisk arrays

For sample B, PL from InGaAs QWs is lowered to 87% compared with original QW PL intensity, and PL from GaAs barriers is also lowered. Although the .resonance oscillation wavelength of SPs is designed to match with InGaAs QWs emission wavelength, the observed PL is not enhanced much if we consider the Au absorption of pumping and emission light (26%). One possible reason is that the surface state of GaAs is increased by Au nanodisk, resulting in more nonradiative recombination, which offsets the increasing of radiative recombination rate caused by SP-QWs coupling. Another possible reason is the radiative enhancement rate is also determined by density of state of the SPPs. To further investigate the enhancement mechanism, measurement of reflectance spectra for these two wafers are conducted. Fig 4 shows the experimental results. A sharp dip is clearly observed around 940nm for sample A (black curve), of which Au nanodisk arrays are created on a 50 nm SiO_2 atop InGaAs/GaAs system, while a broader dip is observed around 1004 nm for sample B, of which Au nanodisks are fabricated directly on the GaAs surface. The arrows indicate the relative InGaAs QWs emission line as shown in Fig.2.It reveals the SP-QWs coupling is well. However, the thin SiO_2 film inserted between the Au nanodisk and the GaAs surface narrows the resonance oscillation band, e.g. concentrating the density of state of the SPP. Therefore, much enhancement of the radiative recombination rate can be obtained by the efficient SP-QWs coupling such as sample A.

In addition, it has been noticed that the wavelength of the QWs PL shifts to high energy side (Fig.2 and Fig.3) by the strong confined electric field caused by SPR for both samples. The blue-shifted should be due to the interaction of the SPR and QWs. The strong electric field of the excited SP by the photons emitted from QWs increases the energy level of the InGaAs QWs.

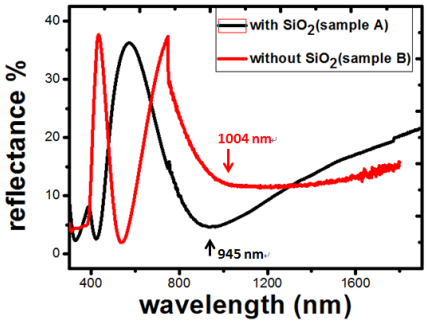


Fig. 4.Black curve :Reflectance spectrum of sample A: Au nanodisc arrays on SiO2 atop as-grown sample(PL ~945 nm), Red curve :Reflectance spectrum of sample B :Au nanodisc arrays atop as-grown sample(PL ~1004 nm)

4. Conclusion

In conclusion, surface plasmon effects on InGaAs/GaAs quantum wells (an important NIR optoelectronic medium) have been investigated. When Au nanodisk arrays are fabricated directly on the GaAs top layer, the enhancement of PL is very low although SP-QWs coupling occurs. We attribute this low enhancement to the wider resonance oscillation band of SPs, e.g. low density of state of SPP. When a thin SiO_2 film inserted between Au nanodisk and GaAs surface, much narrower resonance oscillation band of SPs has been observed experimentally. Due to the efficient coupling of SP-QWs, more than 2 fold PL enhancement has been first, as our best knowledge, achieved for the InGaAs/GaAs QWs.

Acknowledgements

This work is supported by Singapore Ministry of Education (grant number MOE2009-T2-1-086).

References

[1] W. L. Barnes, A. Dereux, and T. W. Ebbesen, Nature (London)**424**, 824(2003).

[2] Barnes, W. L. J. Mod. Opt. 45 (4), 661–699 (1998).

[3] Schuller, J. A.; Barnard, E. S.; Cai, W.; Jun, Y. C.; White, J. S.; Brongersma, M. L. Nat. Mater. 9 (3), 193–204 (2010)

[4] Nikoobakht, B.; El-Sayed, M. A. J. Phys. Chem. A, 107 (18), 3372–3378(2003).

[5] Alivisatos, P. Nat. Biotechnol. 22 (1), 47–52(2004).

[6] Willets, K. A.; Van Duyne, R. P. Annu. Rev. Phys. Chem, 58, 267–297(2007).

[7] Lal, S.; Link, S.; Halas, N. J. Nat. Photonics, 1 (11), 641–648(2007).

[8] Stoerzinger, K. A.; Hasan, W.; Lin, J. Y.; Robles, A.; Odom, T. W. J. Phys. Chem. Lett., 1 (7), 1046–1050(2010).

[9] Shimizu, K. T.; Woo, W. K.; Fisher, B. R.; Eisler, H. J.; Bawendi, M. G. Phys. Rev. Lett., 89 (11), 117401(2002).

[10] Kinkhabwala, A.; Yu, Z.; Fan, S.; Avlasevich, Y.; Mullen, K.; Moerner, W. E. Nat. Photonics, 3 (11), 654–657(2009).

[11] Kulkarni, A. P.; Noone, K. M.; Munechika, K.; Guyer, S. R.; Ginger, D. S. Nano Lett., 10 (4), 1501–1505(2010).

[12] Watanabe, K.; Menzel, D.; Nilius, N.; Freund, H. J. Chem. Rev. 106 (10), 4301–4320(2006).

[13] Wenseleers, W.; Stellacci, F.; Meyer-Friedrichsen, T.; Mangel, T.; Bauer, C. A.; Pond, S. J. K.; Marder, S. R.; Perry, J. W. J. Phys. Chem. B, 106 (27), 6853–6863(2002).

[14] Gryczynski, I.; Malicka, J.; Shen, Y. B.; Gryczynski, Z.; Lakowicz,J. R. J. Phys. Chem. B, 106 (9), 2191–2195(2002).

[15] I. Contijo, M. Boroditsky, E. Yablonovich, S. Keller, U. K. Mishra, and S. P. DenBaars, Phys. Rev. B **60**, 11564 (1999).

[16] A. Neogi, C. W. Lee, H. O. Everitt, T. Kuroda, A. Takemuchi, and E. Yablonovich, Phys. Rev. B **66**, 153305 (2002).

[17] K. Okamoto, I. Niki, A. Shvartser, Y. Narukawa, T. Mukai, and A. Scherer, Nat. Mater. **3**, 601 (2004).

[18] K. Okamoto, I. Niki, A. Scherer, Y. Narukawa, T. Mukai, and Y. Kawakami, Appl. Phys. Lett. **87**, 071102 (2005).

[19] T. D. Neal, K. Okamoto, and A. Scherer, Opt. Express **13**, 5522 (2005).

[20] J. Feng, T. Okamoto, and S. Kawata, Opt. Lett. **30**, 2302 (2005).

[21] S. Wedge, J. A. E. Wasey, W. L. Barnes, and I. Sage, Appl. Phys. Lett. **85**, 182 (2004).

[22] S. Pillai, K. R. Catchpole, T. Trupke, G. Zhang, J. Zhao, and M. A. Green, Appl. Phys. Lett. **88**, 161102 (2006).

[23] P. T. Worthing and W. L. Barnes, Appl. Phys. Lett. **79**, 3035 (2001).

[24] J. Vuckovic, M. Loncar, and A. Scherer, IEEE J. Quantum Electron. **36**, 1131 (2000).

[25] N. E. Hecker, R. A. Hopfel, N. Sawaki, T. Maier, and G. Strasser, Appl. Phys. Lett. **75**, 1577 (1999).

[26] H. R. Stuart and D. G. Hall, Appl. Phys. Lett. **69**, 2327 (1996).

[27] T. W. Ebbesen, H. J. Lezec, H. F. Ghaemi, T. Thio, and P. A. Wolff, Nature _London_ **391**, 667 (1998).

[28] J. A. Porto, F. J. Garcia-Vidal, and J. B. Pendry, Phys. Rev. Lett. **83**, 2845 (1999).

[29] G. Sun,J. B. Khurgin,and R. A. Soref,APPLIED PHYSICS LETTERS **94**, 101103 (2009)

[30] T. Klar, M. Perner, S. Grosse, G. von Plessen, W. Spirkl, and J. Feldmann, Phys. Rev. B 80, 4249 (1998).

[31] N. E. Hecker, R. A. Höpfel, N. Sawaki, T. Maier, and G. Strasser, Appl. Phys. Lett. 75, 1577 (1999).

[32] R. R. Chance, A. Prock, and R. Silbey, "Comments on the classical theory of energy transfer," ***J.*** *Chem. Phys.*, vol. 62, pp. 2245-2253, (1975).

[33] (33) K. Okamoto, I. Niki, A. Shvartser, Y. Narukawa, T. Mukai, and A. Scherer, Nat. Mater. **3**, 601 (2004).

[34] (34) A. Neogi and H. Morkoc, Nanotechnology **15**, 1252 (2004).

Deep Subwavelength Double Metal Disk Cavity and Applications

Soon-Hong Kwon

[1]Department of Physics, Chung-Ang University, Seoul 156-756, Korea
*corresponding author, E-mail: soonhong.kwon@gmail.com

Abstract

We propose a plasmonic whispering-gallery-mode cavity comprising of a dielectric disk with sub-hundred nanometer thickness sandwiched by two silver disks. By reducing radius and thickness carefully based on the investigated resonant wavelength dependencies, the surface-plasmon-polariton cavity mode with a resonant wavelength of 1550 nm can be confined in a disk with a radius of 88 nm and a thickness of 10 nm, where the physical size of the cavity is 0.000064 λ_0^3 (λ_0: free space wavelength). The cavity mode has a deep subwavelength mode volume of 0.010 $(\lambda/2n)^3$ and a high quality factor of 1900 at 40K, consequently, a large Purcell factor of 1.1 x 10^5. The proposed double metal disk cavity can be used to measure refractive index change of the environmental material or gap thickness change.

1. Introduction

Light confinements in wavelength-scale nanocavites have been a topic that has been attracting considerable attention, owing to their ability to strongly enhance light-matter interactions. Strong interactions, represented by a high quality (Q) factor and a small mode volume (V_{mode}), enables nanocavities as one of key components for novel photonic devices such as low-threshold lasers [1-3], efficient single photon sources [4,5], optical switch [6,7], and optical memories [8]. Recently, metal coated dielectric cavities demonstrated the smallest mode volumes in dielectric cavities [3,9-11], however, further size reduction is intrinsically limited by the diffraction-limit, order of wavelength in material. In contrast to dielectric cavities, plasmonic cavities allow light confinement in the subwavelength mode volume [12-18].

On the other hand, among dielectric cavities, whispering-gallery-mode (WGM) excited at disk or ring cavities have been studied over a wide range of applications such as optical switch [7], memory [8], channel-drop filters [19], and laser [20] by applying its unique modal characteristics of high Q factor, efficient waveguide coupling, and mode degeneracy [21,22]. However, as the radius of a cavity decreases, radiation loss of the WGM tends to increase due to weaker total internal reflection [21,22]. Therefore, conventional WGM based on dielectric cavities has the limitation of size reduction, which becomes the main obstacle to miniaturize photonic devices based on the WGM. Very recently, the plasmonic WGM based on surface-plasmon-polaritons (SPPs) has been reported [12,16,23]. Whereas there are few studies on theoretical analysis to reduce cavity size to the deep-subwavelength dimension while the high Q and same resonant wavelength are kept.

Due to its small size, the plasmonic WGM cavity, which supports WGM properties in subwavelength size, can be a new building block for the high-density integration of photonic devices. In this letter, we propose a deep-subwavelength-sized plasmonic WGM cavity by intricately reducing radius (R) and thickness (t) simultaneously. In this cavity with R = 88 nm and t = 10 nm, the physical volume of $(\lambda_0/30)^3$ (λ_0: free space wavelength), large Q of 1900 at 40K and ultrasmall mode volume (V_{mode}) of 0.010 $(\lambda/2n)^3$ are achieved, which results in a high Purcell Factor (F_p) of 1.1 x 10^5. In addition, by modifying the plasmonic cavity, we suggest the possibilities of the applications for refractive index sensing and gap thickness sensing.

2. Plasmonic whispering-gallery-mode cavity for different azimuthal number

Figure 1(a) shows a schematic diagram of the plasmonic disk cavity consisting of a dielectric disk with radius of R and thickness of t sandwiched by two silver disks with the same radii. The thicknesses of silver disks are 200 nm. This plasmonic WGM cavity can be efficiently excited by electrical injection through top and bottom metal disks [11]. In a cavity with R = 476 nm and t = 100 nm, plasmonic WGM with an azimuthal number (N) of 6 can be excited at a resonant wavelength of 1550 nm through a three-dimensional (3D) finite-difference time-domain simulation, as shown in the electric field (E_z) profiles of Fig. 1(b) and 1(c). The horizontal view shows a similar field profile with the transverse-magnetic (TM)-like WGM in the conventional dielectric disk [21,22], however, in the vertical direction, the electric fields in the cross-sectional view are only tightly confined inside the dielectric disk due to the top and bottom silver disks in contrast to the field extension of the conventional WGM over air [21,22].

The dielectric was assumed to have a high refractive index of 3.4 (e.g. InP, Si or GaAs) and silver was modeled by the Drude model: $\varepsilon(\omega) = \varepsilon_\infty - \omega_p^2 / (\omega^2 + i\gamma\omega)$. Experimentally determined dielectric functions of silver were fitted by the background dielectric constant ε_∞ of 3.1, the plasma frequency ω_p of 1.4 x 1016 s-1 and the collision

frequency γ at room temperature of 3.1 x 10^{13} s^{-1}, respectively [15-18,24]. A spatial resolution of 1 nm was used for these calculations. We used a home-made FDTD code for numerical simulation. To excite the plasmonic WGM, a dipole emitter was placed 1 nm away from the bottom of the silver surface. The mode volume was defined as the ratio of the total energy density of the mode to the peak energy density, where the effective refractive index of metal was used [14-17].

In order to investigate the effects of size reduction regarding the plasmonic WGM, Q factors at 40K were calculated as a function of the azimuthal number (Fig. 2). The Q factor is defined as $Q = \omega_0$(Stored Energy)/(Power Loss), and calculated from the time decay of the cavity energy. The cavity thickness is fixed at t = 100 nm and the resonant wavelength is kept at 1550 nm for fair comparison. Thus, the radius of the cavity decreases with decreasing the azimuthal number to provide the same resonant wavelength, which is shown from the corresponding radius for a given azimuthal number at the top axis in Fig. 2.

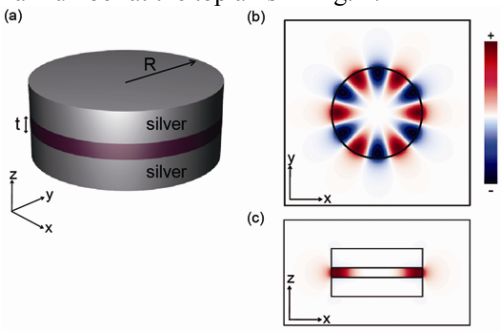


Figure 1: (a) Schematic diagram of the plasmonic disk cavity consisting of silver (gray)/dielectric (red)/silver. R and t indicate the radius of the disk and thickness of the dielectric, respectively. (b) Horizontal and (c) cross-sectional views of the electric field (E_z) profiles of the plasmonic WGM mode with the azimuthal number, N = 6 for the cavity with R = 476 nm and t = 100 nm.

The Q factor calculated at 40K can provide a lower limit of Q for the solid-state quantum electrodynamics (QED) experiments since the operation temperature for single photon source or strong coupling is usually lower than 40K [4,5,14,17]. The Q factor is calculated from the time decay of the mode energy. Silver at low temperature was described by scaling down the damping collision frequency, γ, by a ratio of the conductivity at low temperature and the room temperature conductivity [3,14-18].

For the fixed thickness, the total Q factor (Q_{total}) decreases with the decreasing azimuthal number or radius in Fig. 2. Total loss of the plasmonic cavity can be divided into an optical loss by radiation and absorption loss by metallic ohmic loss. In order to systematically investigate the dependence of Q factors on the azimuthal number (or radius), $Q_{optical}$ and $Q_{absorption}$ were calculated separately where $Q_{optical}$ was estimated by setting the damping constant as zero. Here, $Q_{optical}$ and $Q_{absorption}$ are inversely proportional to the radiation loss and absorption loss, respectively. Since the real part of the metal permittivity is barely affected by the damping constant in the telecommunication wavelength, where γ is orders of magnitude smaller than the resonant frequency, ω, zeroing γ allows calculating $Q_{optical}$ separately. Interestingly, when azimuthal number is larger than 4, Q_{total} is limited by $Q_{absorption}$ and, when N is smaller than 3, Q_{total} is limited by $Q_{optical}$. In contrast to that $Q_{absorption}$ almost remains constant as 5500 for the cavities with a fixed thickness of 100 nm regardless of the azimuthal number, $Q_{optical}$ exponentially decreases with a decreasing azimuthal number, which can be understood by larger radiation loss due to the smaller radius of the curvature [21,22]. On the other hand, the plasmonic WGM with N=1, corresponding to the dipole resonance, serious radiation loss degrades Q to only 10 as in the case of a metal nanoparticle [25]. Therefore, unfortunately, simply decreasing radius (or azimuthal number) to miniaturize cavity size seriously deteriorates the Q factor due to increasing radiation loss.

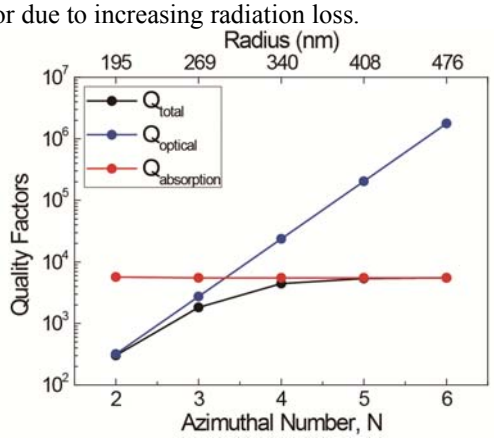


Figure 2: Q factors of plasmonic WGM for different azimuthal numbers. The top axis shows the corresponding radius of the cavities to the azimuthal number, having the same resonant wavelength of 1550 nm. Q_{total}, $Q_{optical}$, and $Q_{absorption}$ are indicated by black, blue, and red lines, respectively.

3. Size reduction of plasmonic WGM cavity

In order to further reduce cavity size with the same resonant wavelength while a high Q is maintained, the wavelength, Q factor, and mode volume (V_{mode}) were systematically investigated in Fig. 3 by varying the structure parameters of the plasmonic disk, radius (R) and thickness (t) for the cavity mode with N = 2, where Q_{total} is limited by $Q_{optical}$. At a fixed thickness of 100 nm, the resonant wavelength decreases linearly as the radius decreases [21,22]. On the other hand, at a fixed radius, the resonant wavelength increases considerably for a thinner thickness due to the stronger coupling of SPPs excited at the top and bottom silver/dielectric interfaces [15,17,26]. The calculated resonant wavelengths were plotted as a function of R and t in Fig. 3(a). In the color map, red (top left) and violet (bottom right) represent longer and shorter wavelengths, respectively. Although the resonant wavelength of conventional nanocavites usually decreases with a reduction in size [21,22], the proposed plasmonic WGM cavity can have the same resonant wavelength for even a smaller

cavity by cleverly decreasing R and t. Indeed, black squares in Fig. 3(a) indicate structure parameter sets (R, t) having the resonant wavelength of 1550 nm. It should be noted that the resonance remains at the same wavelength while the physical volume ($\pi R^2 t$) of the dielectric disk reduces considerably for the cavities with (R, t) ranging from (195 nm, 100 nm) to (88 nm, 10 nm) where the physical volume changes from 1.2 x 10^{-2} μm^3 to 2.4 x 10^{-4} μm^3. Here, V_{mode} was defined as the ratio of the total electric field energy density to the peak energy density of the mode, considering the effective refractive index of metal [14-18].

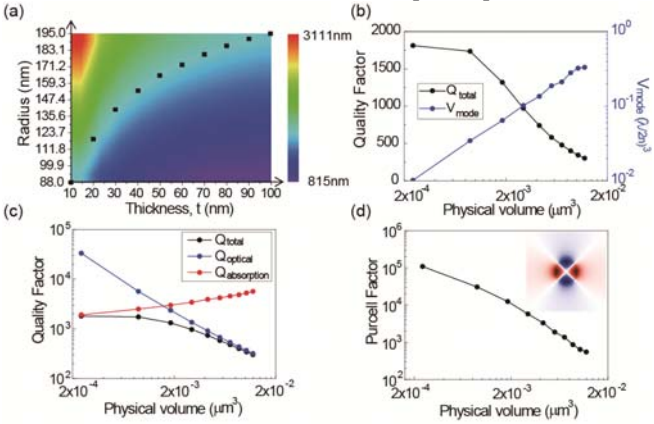


Figure 3: Resonant wavelengths, Q factors, and mode volume for the plasmonic WGM with the azimuthal number, N = 2. (a) Resonant wavelength color map as a function of R and t. Black squares indicate (R, t) sets having resonant wavelength of 1550 nm. (b) Q factors at 40 K (black) and Vmode (blue) calculated as a function of the physical volume ($\pi R^2 t$) of the dielectric disk. (R, t) varies from (195 nm, 100 nm) to (88 nm, 10 nm), corresponding to black squares in (a). (c) Q factors vs. the physical volume. (d) Purcell factor vs. the physical volume. The inset shows the electric field profile of the cavity mode with N = 2.

As shown in Fig. 2, the Q factor of the cavity with R = 195 nm and t = 100 nm was limited by $Q_{optical}$, related to radiation loss. However, as the physical volume decreases, $Q_{optical}$ increases exponentially by two orders of magnitude in Fig. 4(c). Because a thinner metal-insulator-metal waveguide has a larger effective refractive index [26], and radiation loss of WGM decreases. In contrast, $Q_{absorption}$ modestly decreases to three times the size from 5700 to 1900 due to increasing metallic absorption loss. As result, Q_{total} rather increases from 320, limited by radiation loss, to 1900, limited by absorption loss, even though cavity size reduces 50 times smaller from (R, t) = (195 nm, 100 nm) to (88 nm, 10 nm). However, if the thickness becomes smaller, Q factor decreases due to increasing absorption loss. V_{mode} reduces from 0.33 $(\lambda/2n)^3$ to 0.010 $(\lambda/2n)^3$ with decreasing the physical volume in Fig. 4(b). As a result of the increasing Q factor and exponentially decreasing V_{mode} with decreasing cavity size, F_p increases dramatically upto 1.1 x 10^5 in Fig. 4(d). Considering the average positioning of an emitter inside the cavity, still large average F_p of 2.9 x 10^4 was also calculated.

4. Applications

4.1. Refractive index sensing

Surface-plasmon-polaritons (SPPs) cavities locate most of the energy in the background material outside the metal, also resulting in high sensitivity devices. In addition to high sensitivity, the miniaturization of refractive index sensors is required to realize compact photonic integrated lab-on-a-chip devices. However, reduction of the sensing volume in plasmonic index sensors has not yet been studied extensively.

In order to measure the refractive index change of an environmental material, we modified the plasmonic WGM cavity by separating two metal disks with a nano-scaled gap [27]. The cavity could be miniaturized by simultaneously reducing the radius (R) and gap thickness (t) [11], showing deep subwavelength-scale sensing volumes with the same resonant wavelength. By investigating Q factors, sensitivity (S = wavelength shift per refractive index unit (RIU)), and figure of merit (FOM = S/linewidth = SQ/λ) numerically, we were able to optimize the FOM of the plasmonic cavity

We propose a plasmonic cavity consisting of two metal disks with radii of R, separated by a gap of thickness t, as shown in Fig. 4 (a). Silver is chosen as the metal because of its low ohmic loss; the background material is assumed to be water, the most common analyte in chemical analysis. The refractive index of the water is set to 1.319, the value at 1550 nm telecommunications wavelength. The thickness of each silver disk is 200 nm, chosen because it is sufficiently thick to avoid SPP excitation at the outer disk surfaces.

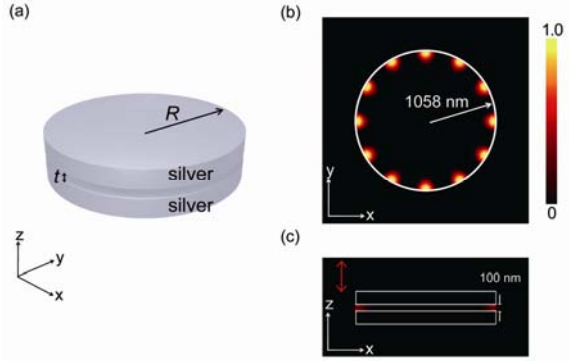


Figure 4: (a) Schematic diagram of plasmonic disk cavity for refractive index sensing. (b) Top view and (c) side view of electric field intensity profiles of TM WGM. The red arrow indicates the direction of the dominant electric field. The electric field intensity is normalized by its maximum value.

In the cavity with (R, t) = (1058 nm, 100 nm), transverse-magnetic (TM)-like WGM with a wavelength of 1550 nm can be excited, as shown in the electric field intensity mode profiles in Fig. 4(b) and 4(c) [11]. Because the 100 nm gap distance is much smaller than half of the wavelength in the water, λ/2n = 588 nm, the transverse-electric (TE)-like WGM cannot be allowed in this subwavelength disk cavity. However, because the z-directional electric field component of the TM-like WGM is dominant and the direction is normal to the surface of the

silver disk, the TM-like WGM can be observed as the plasmonic cavity mode. Even though there is no physical boundary in the gap sandwiched between two silver disks, it is interesting to know that the plasmonic WGM is well-confined in the gap region, defined by radius of R and thickness of t, as light confinements in the conventional dielectric disk cavities. Although there is no index difference between the inside and outside gap regions, the cavity mode is horizontally confined by the total internal reflection (TIR) due to the high effective index of metal-insulator-metal (MIM) plasmonic waveguide mode, where the strong coupling between SPPs excited at the two metal surfaces sandwiching the gap occurs [26]. As the electric field of this plasmonic cavity mode is largely overlapped with background materials, it is expected that optical properties such as resonant wavelengths would be very sensitive.

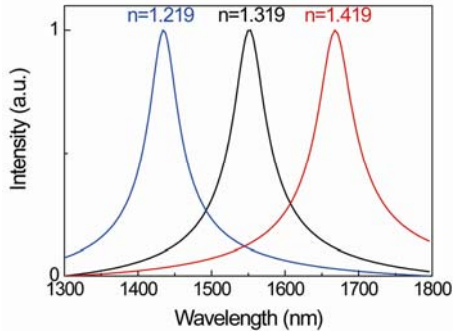


Figure 5: Resonant spectrum of the plasmonic WGM for the background liquids with different refractive index of 1.219 (red), 1.319 (black), and 1.419 (blue). The cavity size is defined by (R, t) = (1058 nm, 100 nm).

In order to investigate the effect of the background material on the cavity mode, the resonant spectrum is calculated for the cavity with (R, t) = (1058 nm, 100 nm) as the refractive index of the liquid changes from 1.219 to 1.419, in Fig. 5. When the refractive index is 1.319, the resonant peak is observed at 1550 nm with a full-width half-maximum (FWHM) linewidth of 40 nm. As the index decreases to 1.219, also reducing the effective cavity size, the resonance blue-shifts to 1435 nm; for an index of 1.419, it red-shifts to 1668 nm. For an index change of 0.1, a large wavelength shift of 116.5 nm was estimated. It should be noted that this sensitive cavity to environmental index changes has a subwavelength physical volume of 0.094 λ_0^3, which indicates an ability to measure the refractive index change of a tiny amount of analyte. Here, λ_0 is the free space wavelength of the cavity resonance, 1550 nm.

In order to further miniaturize the size of the plasmonic index sensor, the corresponding radius, R, which provides the cavity with the resonant wavelength of 1550 nm, is carefully calculated as the gap thickness decreased from 100 nm to 5 nm, as indicated in Table.1. It should be noted that although the wavelength and mode numbers are kept constant, both size parameters of the plasmonic cavity, thickness and radius, decreased, and as similarly observed in Fig. 3. It is therefore possible to further miniaturize the plasmonic WGM cavity by decreasing both R and t, as shown in Table. 1, while keeping the resonant wavelength constant.

Table 1: The gap thickness and the corresponding radius for the plasmonic WGM cavities, having the resonant wavelength of 1550 nm.

Thickness (nm)	Radius (nm)	Thickness (nm)	Radius (nm)
5	435	60	986
10	585	70	1011
20	744	80	1031
30	843	90	1046
40	909	100	1058
50	953		

As a result, the physical volume of the gap layer, considered the minimum volume of the analyte required for the analysis, reduces dramatically with decreasing thickness. Here, the physical volume is obtained by calculating $\pi R^2 t$ for the plasmonic WGM cavities in the Table. 1. For a cavity with (R, t) = (1058 nm, 100 nm), the physical volume is 0.094 λ_0^3, 0.35 μm^3. As the thickness decreases to 5 nm (the corresponding R is 435 nm), the physical volume decreases to 0.00080 λ_0^3, 0.0030 μm^3 = 3.0 attoliter, which is the lowest sensing volume ever reported [28].

On the other hand, in order to use a cavity as resonant index sensor, two parameters should be considered, the sensitivity to the index change and the spectral resolution. Because the spectral resolution is determined by the resonance linewidth, the Q factor, which is inversely proportional to the resonance linewidth ($\Delta\lambda_{FWHM}$), must be maximized as a function of the gap thickness of the plasmonic WGM cavities. For a plasmonic WGM cavity with (R, t) = (744 nm, 20 nm), the Q factor has a maximum value of 105, giving a minimum linewidth of 14.8 nm. The physical volume of the gap layer is 0.0093 λ_0^3 = 0.035 μm^3 = 35 attoliter, 10 times smaller than the cavity with (1058 nm, 100 nm) and 100 times smaller than the cube of the free space wavelength. Therefore, the plasmonic WGM cavity enables the measurement of deep subwavelength-scaled volumes of analyte (35 attoliter) with relatively sharp linewidth (14.8 nm) and high sensitivity of 1160 nm/RIU.

4.2. Plasmonic ruler

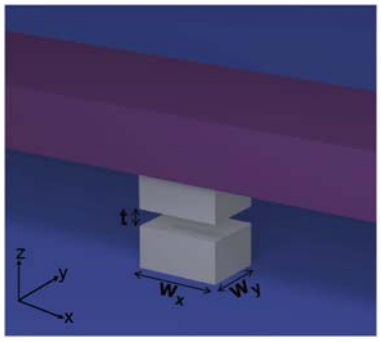


Figure 6: Schematic diagram of a plasmonic cavity for a plasmonic ruler.

The resonant wavelength of the plasmonic cavity, where strong SPP mode is sandwiched between metal blocks, depends on gap thickness very sensitively. Figure 6 shows the schematic diagram of a plasmonic ruler. The plasmonic cavity consists of two silver blocks separated by a gap of t. Each block has a rectangular cross-section sized by w_x and w_y. Between the gaps, a plasmonic cavity mode can be excited by injecting linearly polarized light. The resonant wavelength of the cavity mode can be measured by observing transmission curve of linearly polarized white light/tunable light source, which determines the gap thickness precisely.

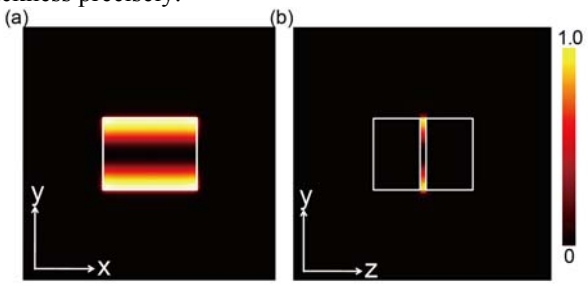


Figure 7: Electric field intensity profiles of (a) top view and (b) side view for the plasmonic cavity of Fig. 6.

For a cavity with w_x = 200 nm, w_y = 150 nm, and t = 10 nm, plasmonic cavity mode with a wavelength of 879 nm is strongly confined inside the air gap, as shown in Fig. 7. In this paper, w_x and w_y are fixed for the cavities to be discussed. Even though there is no physical boundary in xy plane, effective refractive index because of strong coupling of SPPs between two metal-air interfaces at the air gap enables strong horizontal confinement of SPPs. The Q factor of 53 and deep subwavelength mode volume of 0.001 λ_0^3 is estimated.

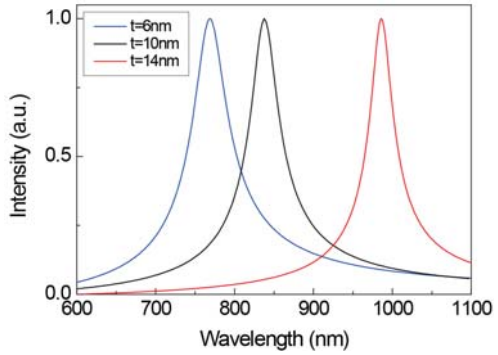


Figure 8: Resonant spectrum of the plasmonic WGM for the background liquids with different gap thickness (t) of 6 nm (blue), 10 nm (black), and 14 nm (red).

We investigated the response of the resonant peak of the plasmonic cavity mode to the change of the gap thickness for different gap of 6 nm, 10 nm, 14 nm in Fig. 8. First, resonant wavelength increases for thinner gap thickness. For 14 nm thickness, resonance blue-shifts to 750 nm, contrary, for 6 nm, the resonance red-shifts to 1000 nm while resonance exists at 879 nm for t = 10 nm. Second, larger resonance shift ($\Delta\lambda$) is observed in the case of decreasing t than increasing t. When t decreases to 6 nm, $\Delta\lambda$ is +220 nm, but when t increases to 14 nm, $\Delta\lambda$ is -130 nm.

5. Conclusions

In this paper, we proposed a plasmonic WGM cavity having an extremely small mode volume of 0.010 $(\lambda/2n)^3$ and high Q factor of 1900 at 40K. In the dielectric disk sized by a radius of 88 nm and a thickness of 10 nm with an ultra-small physical volume of 0.000032 λ_0^3 (λ_0: free space wavelength), SPPs with a wavelength of 1550 nm were strongly confined by two silver disks [29]. The deep subwavelength mode volume allowed obtaining a large Purcell factor of 1.1 x 10^5 at 40 K. Even though at room temperature, where metallic absorption loss seriously increases, the low Q factor of 60 is calculated, thanks to the small mode volume, still a high Purcell factor of 3600 could be achieved. The proposed plasmonic WGM cavity can be one of key components for a wide range of applications such as refractive index sensing and gap thickness sensing. As refractive index sensor, the cavity with the radius of 744 nm and gap thickness of 20 nm shows the highest FOM of 80, due to a narrow resonance linewidth (14.8 nm) and high sensitivity (S = 1160 nm/RIU) to the index change of the background material, while having remarkably the ability to measure ultra-small volume (0.035 μm^3 = 35 attoliter) of analyte. In addition, as gap thickness sensor, 220 nm resonant wavelength shift is estimated for the small gap thickness change of only 4 nm.

Acknowledgements

This research was supported by the Basic Science Research Program through the National Research Foundation of Korea (NRF) funded by the Ministry of Education, Science and Technology (Grant No. 2012-0003438).

References

[1] S H.-G. Park, S.-H. Kim, S.-H. Kwon, Y.-G. Ju, J.-K. Yang, J.-H. Baek, S.-B. Kim, and Y.-H. Lee, Electrically driven single-cell photonic crystal laser, *Science* 305: 1444–1447, 2004.

[2] B. Ellis, M. A. Mayer, G. Shambat, T. Sarmiento, J. Harris, E. E. Haller, and J. Vuckovic, Ultralow-threshold electrically pumped quantum dot photonic-crystal nanocavity laser, *Nat. Photon.* 5: 297–300, 2011.

[3] M. T. Hill, Y.-S. Oei, B. Smalbrugge, Y. Zhu, T. de Vries, P. J. van Veldhoven, F. W. M. van Otten, T. J. Eijkemans, J. P. Turkiewicz, H. de Waardt, E. J. Geluk, S.-H. Kwon, Y.-H. Lee, R. Nötzel, and M. K. Smit, Lasing in metallic-coated nanocavities, *Nat. Photon.* 1: 589–594, 2007.

[4] D. Englund, D. Fattal, E. Waks, B. Zhang, T. Nakaoka, Y. Arakawa, Y. Yamamoto, and J. Vuckovic, Controlling the spontaneous emission rate of single quantum dots in a two-dimensional photonic crystal, *Phys. Rev. Lett.* 95: 013904, 2005.

[5] J. P. Reithmaier, G. Sek, A. Loffler, C. Hofmann, S. Kuhn, S. Reitzenstein, L. V. Keldysh, V. D. Kulakovskii, T. L. Reinecke, and A. Forchel, Strong coupling in a single quantum dot-semiconductor microcavity system, *Nature* 432: 197–200, 2004.

[6] K. Nozaki, T. Tanabe, A. Shinya, S. Matsuo, T. Sato, H. Taniyama, and M. Notomi, Sub-femtojoule all-optical switching using a photonic-crystal nanocaviy, *Nat. Photon.* 4: 477–483, 2010.

[7] L. Liu, R. Kumar, K. Huybrechts, T. Spuesens, G. Roelkens, E.-J. Geluk, T. de Vries, P. Regreny, D. Van Thourhout, R. Baets, and G. Morthier, An ultra-small, low-power, all-optical flip-flop memory on a silicon chip, *Nat. Photon.* 4: 182–187, 2010.

[8] M. T. Hill, H. J. S. Dorren, T. De Vries, X. J. M. Leijtens, J. H. Den Besten, B. Smalbrugge, Y. S. Oei, H. Binsma, G. D. Khoe, and M. K. Smit, A fast low-power optical memory based on coupled micro-ring lasers, *Nature* 432(7014), 206–209 (2004).

[9] K. Yu, A. Lakhani, and M. C. Wu, Subwavelength metal-optic semiconductor nanopatch lasers, *Opt. Express* 18: 8790–8799, 2010.

[10] M. P. Nezhad, A. Simic, O. Bondarenko, B. Slutsky, A. Mizrahi, L. Feng, V. Lomakin, and Y. Fainman, Room-temperature subwavelength metallo-dielectric lasers, *Nat. Photon.* 4: 395–399, 2010.

[11] C. Manolatou, and F. Rana, Subwavelength nanopatch cavities for semiconductor plasmon lasers, *IEEE J. Quantum Electron.* 44: 435–447, 2008.

[12] M. Kuttge, F. J. García de Abajo, and A. Polman, Ultrasmall mode volume plasmonic nanodisk resonators, *Nano Lett.* 10: 1537–1541, 2010.

[13] R. F. Oulton, V. J. Sorger, T. Zentgraf, R.-M. Ma, C. Gladden, L. Dai, G. Bartal, and X. Zhang, Plasmon lasers at deep subwavelength scale, *Nature* 461: 629–632, 2009.

[14] Y. Gong, and J. Vuckovic, Design of plasmon cavities for solid-state cavity quantum electrodynamics applications, *Appl. Phys. Lett.* 90: 033113, 2007.

[15] M.-K. Seo, S.-H. Kwon, H.-S. Ee, and H.-G. Park, Full three-dimensional subwavelength high-Q surface-plasmon-polariton cavity, *Nano Lett.* 9: 4078–4082, 2009.

[16] S.-H. Kwon, J.-H. Kang, C. Seassal, S.-K. Kim, P. Regreny, Y.-H. Lee, C. M. Lieber, and H.-G. Park, Subwavelength plasmonic lasing from a semiconductor nanodisk with silver nanopan cavity, *Nano Lett.* 10: 3679–3683, 2010.

[17] J.-H. Kang, Y.-S. No, S.-H. Kwon, and H.-G. Park, Ultrasmall subwavelength nanorod plasmonic cavity, *Opt. Lett.* 36: 2011–2013, 2011.

[18] J.-H. Kang, H.-G. Park, and S.-H. Kwon, Room-temperature high-Q channel-waveguide surface plasmon nanocavity, *Opt. Express* 19: 13892–13898, 2011.

[19] B. E. Little, S. T. Chu, H. A. Haus, J. Foresi, and J. P. Laine, Microring resonator channel dropping filters, *J. Lightwave Technol.* 15: 998–1005, 1997.

[20] M. Fujita, A. Sakai, and T. Baba, Ultrasmall and ultralow threshold GaInAsP-InP microdisk injection lasers: design, fabrication, lasing characteristics, and spontaneous emission factor, *IEEE J. Sel. Top. Quantum Electron.* 5: 673–681, 1999.

[21] K. Vahala, *Optical microcavities*, World Scientific, Singapore, 2004.

[22] R. K. Chang, and A. J. Campillo, *Optical processes in microcavities*, 1st ed, World Scientific, Singapore, 1996.

[23] B. Min, E. Ostby, V. Sorger, E. Ulin-Avila, L. Yang, X. Zhang, and K. Vahala, High-Q surface-plasmon-polariton whispering-gallery microcavity, *Nature* 457: 455–458, 2009.

[24] P. B. Johnson, and R. W. Christy, Optical constants of the noble metals, *Phys. Rev. B* 6: 4370–4379, 1972.

[25] M. A. Noginov, G. Zhu, A. M. Belgrave, R. Bakker, V. M. Shalaev, E. E. Narimanov, S. Stout1, E. Herz, T. Suteewong, and U. Wiesne, Demonstration of a spaser-based nanolaser, *Nature* 460: 1110–1113, 2009.

[26] H. T. Miyazaki, and Y. Kurokawa, Squeezing visible light waves into a 3-nm-thick and 55-nm-long plasmon cavity, *Phys. Rev. Lett.* 96: 097401, 2006.

[27] S. H. Kwon, Deep Subwavelength-scale Metal-Insulator-Metal Plasmonic Disk Cavities for Refractive Index Sensors, *IEEE Photonics Journal*, DOI: 10.1109/JPHOT.2013.2244206

[28] B.Wang, M. A. Dündar, R. Nötzel, F. Karouta, S. He, and R. W. van der Heijden, Photonic crystal slot nanobeam slow light waveguides for refractive index sensing, *Appl. Phys. Lett*. 97:151105, 2010.

[29] S.-H. Kwon, Deep subwavelength plasmonic whispering gallery-mode cavity, *Opt. Express* 20: 24918–24924, 2012.

Strong Emission From Nano-Iron Using Laser Induced Breakdown Spectroscopy Technique

F.F. Rashid[1]*, A. M. ELSherbini [2],A. Al-Muhamady[2]

[1] :Department of Laser and Opto-Electronic Engineering, University of Technology, Baghdad, IRAQ
[2]:Lab. of Lasers and New Materials, Faculty of Science, Cairo University, Dep. of Phys., Giza, Egypt

Corresponding author : fareedfrasheed@yahoo.com

Abstract

In this paper we report a strong enhanced emission from laser produced plasma in air from iron oxide nanomaterial in comparison with the corresponding bulk samples. The enhancement strength differs with different Nd:YAG laser harmonics wavelengths. The analysis showed that such enhancement increased exponentially with the plasma evolution time, while, it declines as the laser fluence increased.

Experimental data analysis clearly showed that the observed enhancement is mainly associated with the change in the plasma electron density. We claim that this strong enhanced optical emission from laser produced plasma is due to surface plasmon resonant excitation preferably on nano oxide materials. Such experimental findings could improve the LIBS-sensitivity down to extremely low concentrations.

1. Introduction

Laser induced breakdown spectroscopy (LIBS) technique can be used for elemental analysis [1,2], cleaning [3], studying of old archeology [4], metals in soils [5]. This technique utilizes the light emitted from plasma produced by the interaction of pulsed lasers with matter. These emission lines, when analyzed, give the different matrix elements in target material, while the spectral shape and radiance can provide both of plasma electron density and temperature, respectively [6,7].One problem is the relatively small signal to background ratio and hence the poor the ability of the LIBS technique to detect the very small concentration of the different elements [8,9]. Different techniques were devised to overcome this difficulty, namely signal enhancement, such as the double pulse technique [10-11] in which the target material is irradiated by consequent double laser pulses separated by a certain delay time. The first excites plasma while the next interacts with this rarefied medium. Moreover, the introduction of the femtosecond laser source provides one basic advantage is the very small continuum component appeared under the lines, hence the large the signal to background ratio [12,13].

Nano-based materials are those having structured components with at least one dimension less than 100 nm. Materials that have one dimension in the nano-scale are layers, such as a thin films or surface coatings. While materials that are nano-scale in two dimensions include nano-wires and nano-tubes. Three dimensional materials are nano-scale particles, for example precipitates, colloids and quantum dots. Nano-crystalline materials, made up of nanometer-sized grains, also fall into this category, which may give an overview of the properties, and the significant applications of some nano-materials [14].

Nowadays, the accelerating progress in the field of nano-material science may provide a new facility to reach signal enhancement. In this work we will demonstrate the combination of the nano-material target with LIBS technique to get enhancement in Iron oxide (Fe_3O_4) emission.

2. Experimental

The experimental setup can be seen in figure.1.

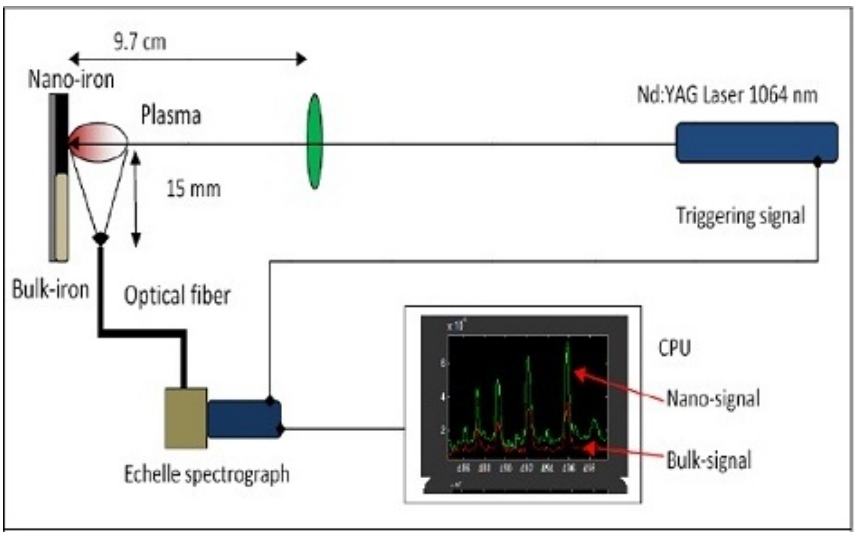


Figure 1 Experimental set-up

The laser system (Nd: YAG) delivers 650, 300 and 150 mJ per pulse at different harmonics of 1064, 532 and 355 nm, respectively at constant duration of 5 ns. Equal laser fluence was achieved by varying the laser focal spot size at the target (focal spot diameters of 1.5, 1.1, 0.75 mm, respectively at different laser harmonics) in order to compare the results at the different laser harmonics. The laser energy was varied using a set of previously calibrated absorbing sheets. Both of the nano and bulk targets were compressed (~ 5 ton/cm^2) to a disk shape and positioned side by side perpendicular to laser axis on an xy-translational stage. The processing of the experimental data was carried out using home-made routine under the MATLAB$^{7®}$package. Each data was taken three times on fresh target condition which enables us to account for any fluctuations in measurements. The Fe_3O_4 (MKN-Fe3O4-025) almost spherical nano material powder samples were purchased from "mk$_{NANO}$ -CANADA" and used without further purification with particle sizes of diameter 25 nm. The relative concentration (stoichiometry) of the nano with respect to the bulk was measured spectroscopically utilizing the Boltzmann plot method [15,16] which indicated almost similar stoichiometry, (Analysis to be published later [17]) .The relative spectral response of the camera MCP and spectrograph including optical fiber was measured using a deuterium lamp (type, DH-2000-CAL).

3. Results and discussion

A comprehensive preview to the observed enhanced spectral lines emission from laser produced iron plasma at 532nm laser wavelength, under constant fluence (34 J/cm^2), gate and delay time (5 μs), is shown in figure (2):

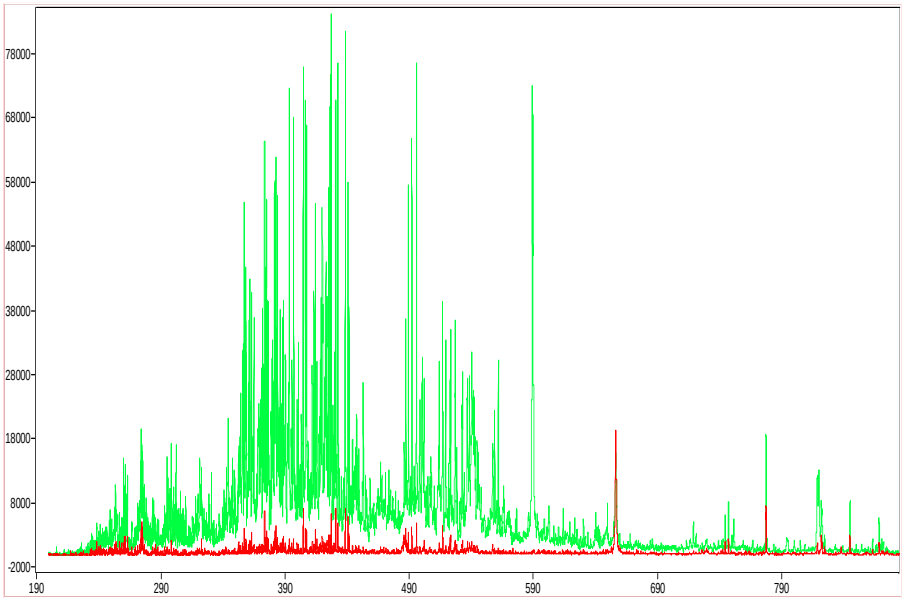


Figure 2 A comparison between bulk verses nano iron Spectra

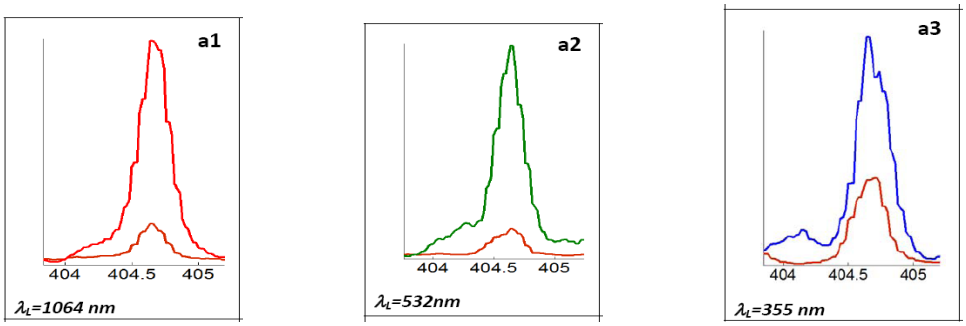


Figure 3 Some emission lines under different laser harmonics excitation.

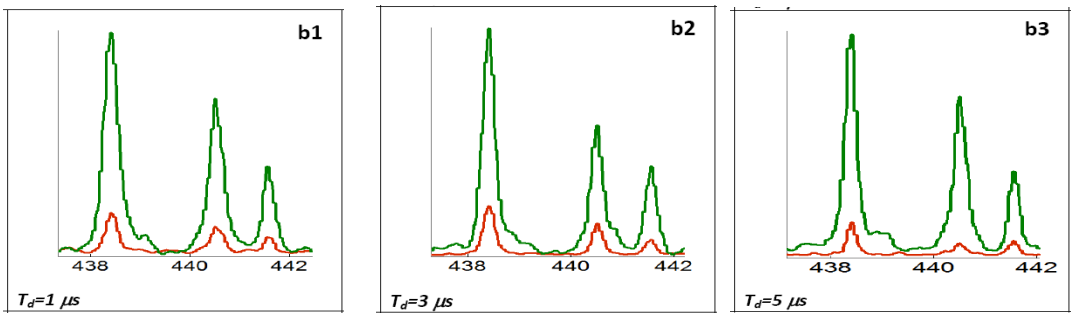


Figure 4 Effect of delay time on enhanced emission

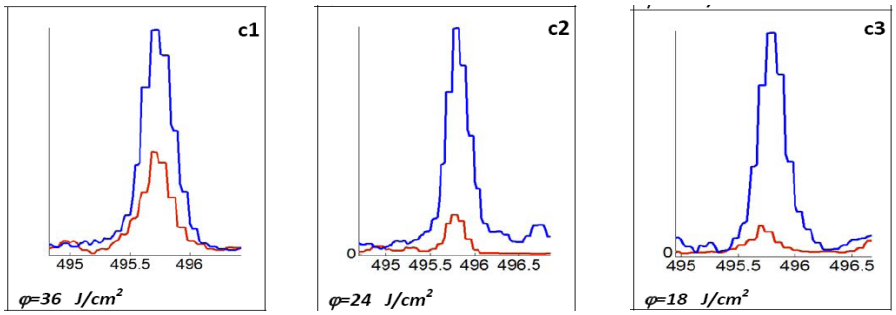


Figure 5 The effect of laser fluence on enhancement

A focused look on the spectrum details can be seen in figure 3(*a1, a2,a3*) Were a general comparison between emitted signal intensity (vertical axis (au)), from Fe I lines from both of nano and bulk targets. (a1, 2, 3) shows the effect of irradiation by different laser harmonics, all at fixed laser fluence of 34 J/cm^2, gate of 1 μs and delay time of 3 μs.

Figure 4(b1, 2, 3) shows the behavior of emitted optical lines from nano and bulk iron with delay time in the range from 1 to 5 μs utilizing the laser second harmonic (532nm) and constant fluence of 34 J/cm^2 is shown.

Moreover, the effect of laser fluence on enhancement from iron nanomaterials is also shown in figure5 (*c1,c2,c3*), while fixing the laser wavelength at the third harmonic at 355 mm and delay gate times at 1 μs.

A careful inspection of figure3, elicits an enhancement-laser wavelength dependence. This behavior points to a resonance like phenomenon plausibly linked with favorable resonant optical excitation of surface plasmons by nano structured materials [18], and was confirmed for the nano ZnO material utilizing absorption spectroscopy where a higher absorption at the shorter wavelength region was verified [19] and also confirmed through an experimental study for the nano ZnO study by the authors[20].

An elaborate assessment of enhancement phenomena (figures 4,5) showing a trend of enhancement as we go to later plasma evolution times and lower laser fluence, respectively.

This is confirmed by calculations of the average enhancement factors over some of the emission spectral lines arising from nano structured iron (Fe I lines at 340.74, 404.58, 438.35, 492.05, 561.56 and 613.66 nm) (see figures 6,7). This trend was found to be due to the faster decline in signal height (spectral radiance) emerging from bulk material plasma. However, a prominent fall in enhancement with plasma evolution was found in case of the third harmonic laser irradiation of iron as illustrated in figure, which may be due to mismatching in surface plasmon resonance frequency off the incident laser radiation. In contrast, an exponential decline of enhancement is observed with increasing laser fluence, (figure7, colored squares).

A systematic calculation of the relative plasma electron density, was carried out in order to gain some insight of the implication of enhancement in terms of the relevant plasma parameters. The ratio of plasma electron densities of nanostructured to bulk targets (n_{eN}/n_{eB}) was estimated from the relative Stark broadening component of the same spectral lines appeared in both of nano and bulk plasmas.

Temporal evolution of estimated relative plasma electron densities n_{eN}/n_{eB} utilizing the Stark broadening of the Fe I lines at 340.74 , 404.58, 438.35 nm is shown in figures 6,7 (triangles of different colors). Though both plasmas from nano and bulk targets are created under the same condition, one can notice that the electron density of the plasma emerging from the nano target is superior to that from bulk.

Moreover, the relative plasma electron density increases in accordance with that of the enhancement along with plasma evolution. However, incompatible decline in the emission intensity is accompanied with

third harmonic laser irradiation (figures 6,7), this indicates that nano iron inherent surface plasmons would resonate better with green 532 nm laser light.

In general, electron density measurement usually probes the intensity of electric fields in the plasma medium. Our results revealed the existence of extra electric fields in the nano-structured plasma. This is not strange, since localized surface plasmons in the vicinity of nano particles was certified in number of articles [21-23]. Moreover, the observed change in enhancement upon switching the laser between different wavelengths confirms the resonance of such surface plasmons with the incident laser frequency. We allege that origin of this extra electron density coming from the incident strong laser field liberating the electronic surface waves (plasmons) inherent to nano structured materials. This conclusion may be drawn from the peculiar dependence of both of enhancement and relative electron density on laser fluence which would suggest the liberation of surface plasmons as the main mechanism responsible for the pronounced measured electron density.

Further examination of enhancement–plasma electron density relation would suggest a series of medium term experiments in which the effect of nanomaterial grain size, laser polarization state under different ambient conditions should carefully be addressed.

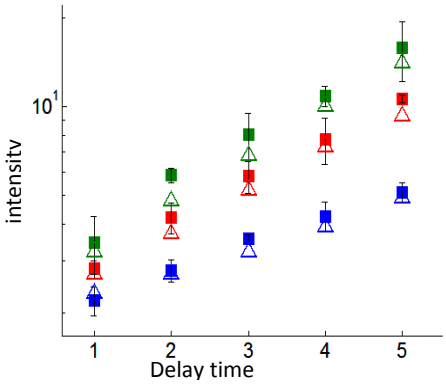


Figure.6 The intensity against Delay time

For Iron nano samples

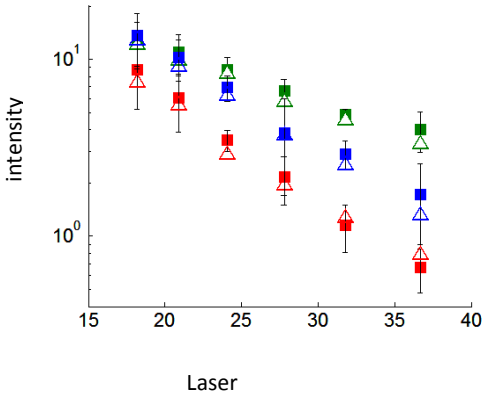


Figure.7 Signal enhancement versus laser fluence for iron.

Squares; represents the enhancement factors.
Open triangles; denotes the relative electron density (n_{eN} / n_{eB}).

4.Conclusions

A lowest possible fluence just sufficient to release surface plasmons from nano particles at the largest delay and suitable laser wavelength would be favorable choice for certain material to sustain optical signal enhancement.

Acknowledgment

This work is financially supported by The Iraq scholar rescue fund project, Institute of international education (IEE), Washington,D.C.

The authors would like to thank Prof. N.Omentto, Prof. H J Kunze and A El Dawyyan for their valuable discussions.

References

[1] D. A. Rusak, B. C. Castle, B. W. Smith and J. D. Winefordner, Fundamentals and applications of laser- induced breakdown spectroscopy, *Crit. Rev. Anal. Chem*., 27**:** 257–290, 1997.

[2] K. Song, Y. I. Lee and J. Sneddon, Applications of laser induced breakdown spectrometry, A*ppl. Spectrosc. Rev*., 32: 183–235, 1997.

[3] M. Jankowsk and G. S´liwin´ski, Acoustic monitoring for the laser cleaning of sandstone, *Journal of Cultural Heritage***,** 4: 65s–71s, 2003.
[4] M. Chappé, J. Hildenhagen, K. Dickmann and M. Bredol, Laser irradiation of medieval pigments at IR VIS. and UV wavelengths, *Journal of Cultural Heritage*, 4: 264s–270s, 2003.
[5] F. Hilbk-Kortenbruck, R. Noll, P. Wintjens, H. Falkb and C. Becker, Analysis of heavy metals in soils using laser-induced breakdown spectrometry combined with laser-induced fluorescence, *Spectrochim Acta, B* 56: 933-945, 2001.
[6] H. J. Kunze, *Introduction to plasma spectroscopy*, Springer Series on Atomic, Optical and Plasma Physics 56 Springer, 2009.
[7] H. R. Griem, *Plasma Spectroscopy*, McGraw-Hill, New York, 1964.
[8] V. Lazic, F. Colao, R. Fantoni, V. Spizzicchino, Laser-induced breakdown spectroscopy in water: Improvement of the detection threshold by signal processing, *Spectrochim. Acta, B* 60: 1002–1013, 2005.
[9] K. A. Tereszchuk, J. M. Vadillo and J. J. Laserna, Depth profile analysis of layered samples using glow discharge assisted Laser-induced Breakdown Spectrometry (GD-LIBS), *Spectrochim. Acta, B* 64: 378–383, 2009.
[10] V. I. Babushok, F. C. DeLucia Jr., J. L. Gottfried, C. A. Munson, and A. W. Miziolek, Double pulse laser ablation and plasma: Laser induced breakdown spectroscopy signal enhancement, *Spectrochim. Acta, B* 61: 999–1014, 2006.
[11] C. Sánchez-Aké, M. Bolaños and C. Z. Ramírez, Emission enhancement using two orthogonal targets in double pulse laser-induced breakdown spectroscopy, *Spectrochim. Acta, B* 64: 857–862, 2009.
[12] V. Piñon and D. Anglos, Optical emission studies of plasma induced by single and double femtosecond laser pulses, *Spectrochim. Acta, B* 64: 950–960, 2009.
[13] D. E. Roberts, A. du. Plessis, J. Steyn, L. R. Botha, C. A. Strydom and I. J. Van Rooyen, Femtosecond laser induced breakdown spectroscopy of silver within surrogate high temperature gas reactor fuel coated particles, *Spectrochim. Acta, B* 65: 918–926, 2010.
[14] C. P. Poole Jr and F. J. Owens, *Introduction to Nanotechnology*, John Wiley & Sons Inc., 2003.
[15] C. Aragón and J. A. Aguilera, Characterization of laser induced plasmas by optical emission spectroscopy: A review of experiments and methods, *Spectrochim. Acta, B* 63: 893-916, 2008.
[16] A. P. M. Michel, Applications of single-shot laser-induced breakdown spectroscopy, *Spectrochim. Acta, B* 65: 185-191, 2010.
[17] A. M. ELSherbini, F. F. Rashid, Temperature and stochiometry analysis of LIBS Spectra for nano-iron oxide, (To be published).
[18] J. R. Sambles, G. W. Bradbery and F. Yang, Optical excitation of surface plasmons: An introduction, *Contemporary Phys.*, 32: 173-183, 1991.
[19] B. Krishnan, L. Irimpan, V. P. N. Nampoora and V. Kumar, Synthesis and nonlinear optical studies of nano ZnO colloids, *Physica, E* 40: 2787–2790, 2008.
[20] A. M. ELSherbini, F. F. Rashid, A. M. Aboulfotouh, Th. M. ELSherbini, S. H. Allam, and A. Al-Muhamady, Laser produced plasma From Zinc oxide nanomaterials), *Proceeding of The First National conference for Engineering Sciences FNCES '12*, Baghdad-IRAQ, PP. 382-387, 2012.
[21] C. Yeonho, P. Younggeun, K. Taewook and P. L. Luke, Selective and sensitive detection of metal ions by plasmonic resonance energy transfer-based nanospectroscopy, *Nature Nanotech.*, 4: 742-746, 2009.
[22] Y. Choi, Y. Park, T. Kang and L. P. Lee, Selective and sensitive detection of metal ions by plasmonic resonance energy transfer-based nano spectroscopy, *Nature Nanotech.*, 4: 742 – 746, 2009.
[23] H. Joerg, Plasmonics: Surfing the wave, *Nature*, 461: 720-722, 2009.

Parameter Dependency of Dipole Nanoantenna in Infrared Range

D. Bala Sekhar, Avanish Bhadauria* and William R. Taube
CSIR-Central Electronics Engineering Research Institute, Pilani-333031, India
*corresponding author, E-mail: avanish@ceeri.ernet.in

Abstract

This paper presents the study of field intensity enhancement of dipole nanoantenna and parameters that effect on the field intensity enhancement in the infrared wavelength range. The dipole nanoantenna consists of gold (metal) dipole arms separated by a gap of nm range. Metal was considered as plasma and its plasmonic behavior has been considered according to drude theory. To investigate the parametric dependencies of dipole nanoantenna the finite element method (FEM) based software High Frequency Structure Simulator (HFSS) has been used. The influence of thickness of metal, feed gap and polarization angle of incident light of dipole nanoantenna was studied, where they strongly effects the dipole nanoantenna characteristics of resonance wavelength and electric field enhancement. This study helps to optimize the dipole nanoantenna structure for the better performance.

1. Introduction

Since the past one decade the Nanoantenna has attracted many researchers due to their outstanding optical properties, like strong enhancement [1] and sub-wavelength confinement of the electrical field and light capturing [2] due to localized surface plasmons. The size of nanoantennae is the order of the wavelength of light. In this wavelength range even novel metals like silver and gold do not behave as perfect conductors and show frequency dependent complex dielectric behavior.

The possibility of coupling between photons and electrons in the nanoantennae are the basis of their properties. When these 3D structures couples with incident light the electrons get to oscillate within structures which are similar than the wavelength of incident light and causes surface plasmon resonance. These resonance leads to the strongly localized field enhancement. Furthermore nanoantennae can also be used to couple propagating optical wave as evanescent wave. Hence they are promising as intermediate component between nanoscale optical and electronic device and optical fields. And hence the field enhancement phenomenon can find applications in the area of sensing like field enhanced fluorescence [3], surface enhanced Raman scattering [4], super lenses [5], nanoscale imaging [6], spectroscopy [7], lasers [8], thermal detectors [9], energy harvesting [10], higher harmonic generation [11], photodetectors [12].

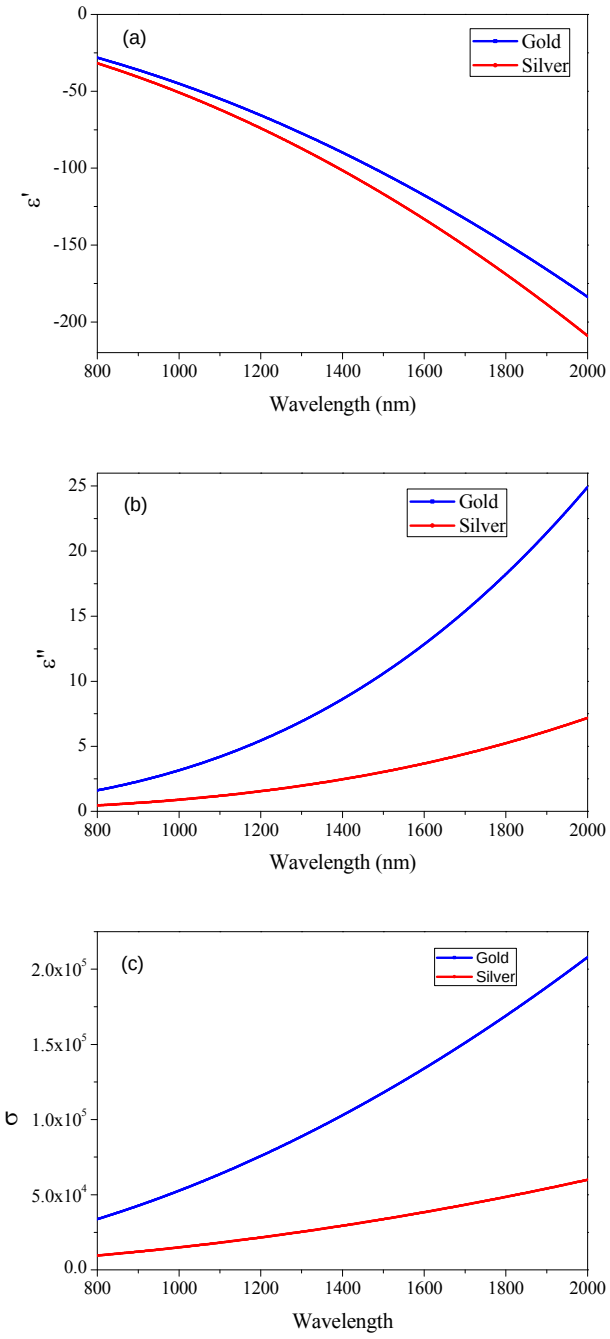


Figure 1. Wavelength dependency of (a) real, (b) imaginary parts of complex dielectric function and (c) conductivity of Gold and Silver metals.

2. Dielectric Properties of Metals at Optical Range

Noble metals are known for their high conductivity, which is because of ocean of free electrons. They can be considered as electron gas in bulk and modeled as plasma. Due to plasmon nature of metals at high frequency i.e., optical range the metals behave completely different than the static case. Hence the behavior of metal at optical range can be described as frequency dependent complex dielectric function, which can be explained by drude theory of free electron gas. According to the drude theory the complex dielectric function $\varepsilon^*(\omega)$ of metals can be described as

$$\varepsilon^*(\omega) = \varepsilon' - j\varepsilon'' = \varepsilon_{in} - \frac{\omega_p^2}{\omega^2 + i\gamma\omega} \quad (1)$$

where, ω_p is plasma frequency which depends on free electron density of metal and γ is collision frequency, which is responsible for losses. For the nanoantennae simulation gold has been used. ε_{in} includes effect of free electrons and bound electrons and is 1 for silver and 2 for gold. The frequency dependent complex dielectric functions of gold and silver were modeled using above model. Model parameters were fitted according to the calculations made by Johnson and Christy from the experimental data [13] and the plasma frequency ω_p and collision frequency γ of gold are 1.296×10^{16} rad/s and 1.265×10^{14} Hz respectively and silver are 1.37×10^{16} rad/s and 3.21×10^{13} Hz respectively. The conductivity of metal (gold) can be expressed as

$$\sigma(\omega) = \omega\varepsilon_0\varepsilon'' \quad (2)$$

where ω is angular frequency of light and ε_0 is free space permittivity.

3. Surface Plasmon Resonance

When the nanoantennae are excited by light, surface plasmons will couple with photons and collective oscillations of electrons will occur. These oscillations will propagate along metal and dielectric interface called as surface plasmon polariton (SPP). Surface plasmons are electromagnetic excitations at the interface of metal and dielectric and propagate along the interface.

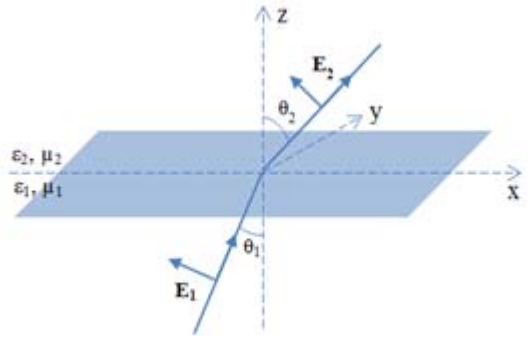


Figure.2. Interface between medium 1 and medium 2 with dielectric functions ε_1, ε_2 respectively.

When plane polarized wave is illuminated on two medium systems having plain interface as shown in the Figure 2, the electric field (E_i, i corresponds to medium) can be obtained from wave equation [14]

$$\nabla \times \nabla \times \vec{E}_i - \frac{\omega^2}{c^2}\varepsilon_i \vec{E}_i = 0, \qquad \text{i=1,2} \quad (3)$$

By solving the above equation using suitable boundary conditions we got the following conditions for generation of surface plasmons at the interface

$$\left.\begin{aligned} \varepsilon_1(\omega) \times \varepsilon_2(\omega) < 0, \\ \varepsilon_1(\omega) + \varepsilon_2(\omega) < 0 \end{aligned}\right\} \quad (4)$$

Because of localization of electromagnetic field due to surface plasmon resonance can contribute field intensity enhancement at interface.

4. Simulation of nanoantennae

To study the behavior of nanoantennae we have carried out our analysis using FEM based software ANSOFT's High Frequency Structure Simulator (HFSS) [15]. The gold dipole nanoantenna was designed on SiO_2 substrate as shown in the Figure 3. The gold relative permittivity and conductivity have been computed according to drude model and assigned as material property in HFSS. The relative permittivity of SiO_2 has been considered as 3.9. The dipole nanoantenna was illuminated by plane polarized EM wave from substrate side and intensity enhancement was calculated at middle of feedgap. The antenna was divided into tetrahedra of typical size 3nm and rest will divided into 70 nm tetrahedra. The perfectly matched layer (PML) boundary condition has been used.

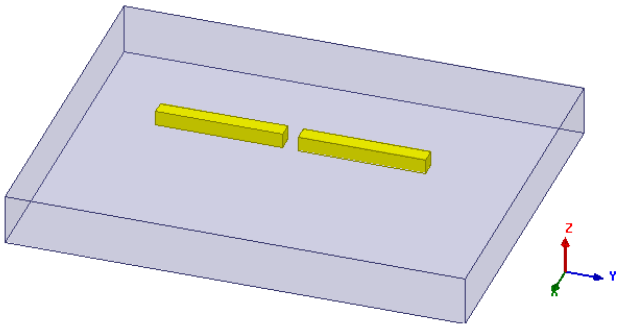


Figure 3. Dipole Nanoantenna

The dipole Nanoantenna of each dipole arm length 250nm, 100nm width, and 30nm thickness with a feedgap of 30nm was designed over SiO_2 substrate. The polarization angle of the plane wave was varied from 0^0 to 90^0 in the steps of 15^0. The intensity enhancement was calculated and that's varies with polarization angle. In our study the feedgap of nanoantenna was varied from 20 nm to 60 nm by keeping constant dipole length. The intensity enhancement is strongly dependent on the feedgap. Next we varied the dipole metal thickness from 20nm to 90nm keeping other parameters constant. It has been observed that the intensity enhancement decreases with increase of gold thickness with change in resonance wavelength. Further the variation of dipole nanoantenna length has been studied. The length was varied from 230 nm to 530 nm with 40 nm steps. The resonance wavelength of dipole nanoantenna varies with change in length, which is similar in case of classical RF antenna.

5. Results and Discussion

The dependency of intensity enhancement of dipole nanoantenna has been analyzed by varying different parameters like polarization angle of incident plane wave, gap between dipole arms, thickness of gold under constant dipole arm width and changing arm width according to gold thickness, dipole nanoantenna. These dependencies have been studied with variation of wavelength in infrared region.

The variation of intensity enhancement with change in polarization angle was plotted in Figure 4. It was observed that as the polarization angle varies from 0^0 to 90^0, the intensity enhancement decreases. The maximum intensity enhancement was obtained at 0^0 polarization angle as the incident plane wave was aligned in the direction of dipole nanoantenna axis. If the polarization angle varies the electric field component along the direction of dipole axis varies and attains minimum value at 90^0 polarization angle, which shows there is no enhancement if the incident plane wave is perpendicular to dipole axis.

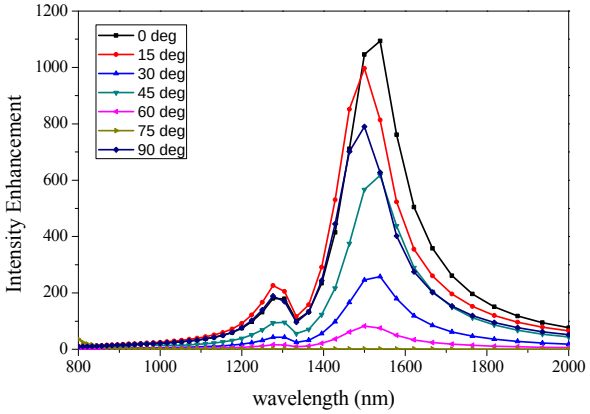


Figure 4. Intensity Enhancement variation with wavelength at different incident wave polarization angles.

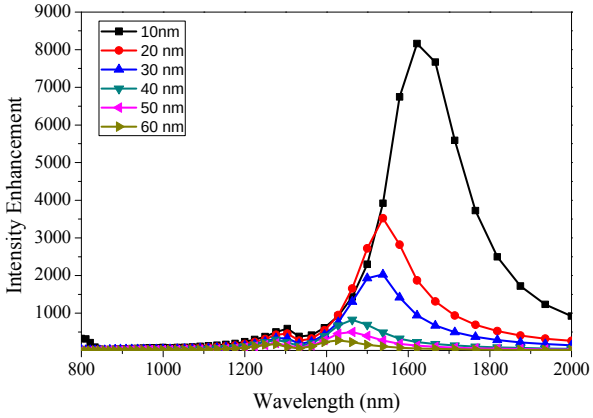


Figure 5. Intensity Enhancement variation with wavelength at different feedgaps.

The variation of intensity enhancement with feedgap was shown in the Figure 5. The dipole nanoantenna of length 530nm width 100 nm and thickness 30nm with varying feedgap was designed over SiO_2 substrate. The feedgap of dipole nanoantenna was varied from 10 nm to 60 nm keeping constant length of dipole antenna. It was observed that the field intensity enhancement decreases as the feedgap increasing. With the change in feedgap not only intensity enhancement effected but also the maxima of intensity shifts at different wavelengths. The shift of maxima is a result of change in the gap.

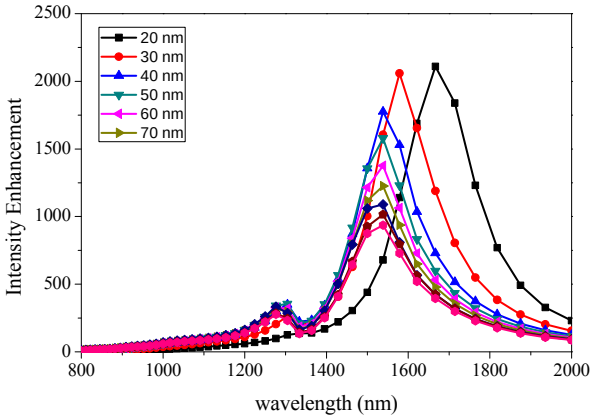


Figure 6. Intensity Enhancement variation with wavelength at different thicknesses of gold.

The variation of intensity enhancement with gold thickness was plotted in the Figure 6. The dipole nanoantenna of each dipole arm of length 250 nm, width 100nm with a feedgap of 30nm was designed. The dipole metal thickness (gold) was varied from 20nm to 70 nm in increment of 10nm. As the thickness of gold decreases; the field strongly confines between dipole arms, which results increased intensity enhancement. Therefore the higher intensity enhancement can be obtained choosing lower gold thicknesses. It can be seen from the figure that if the thickness decrease below 40nm; the wavelength corresponds to maxima of intensity shifts with decrease of thickness in the dipole nanoantenna towards higher wavelengths.

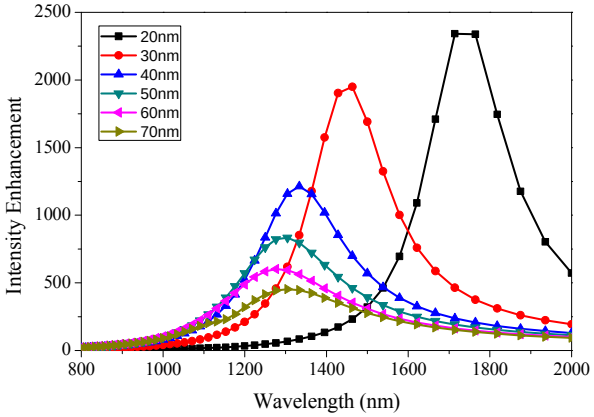


Figure 7. Intensity Enhancement variation with with wavelength at different thickness maintaining thickness to dipole width ratio as one.

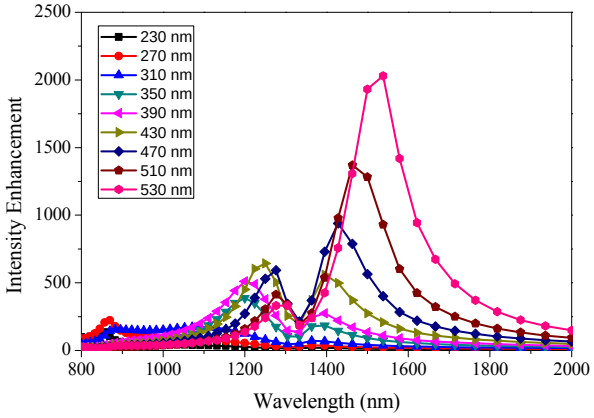


Figure 8. Intensity enhancement variation with wavelength at different antenna lengths.

In the Figure 7 the variation of intensity enhancement for different dipole arm thicknesses (maintaining thickness to dipole width ratio as one) was shown. If we increase the thickness the intensity enhancement changes with shift in maxima of intensity enhancement.

The intensity enhancement variation for different dipole lengths has been shown in the Figure 8. Keeping fixed dipole arm width of 100 nm the dipole length was varied with fixed feedgap of 30nm. The maxima of intensity enhancement shift with the length of dipole nanoantenna. The intensity enhancement increases rapidly with increase in the dipole length.

From Figure 5 the dipole nanoantenna which results maximum enhancement i.e., 10nm feedgap antenna was considered for plotting field intensity enhancement distribution. The intensity enhancement distribution of mentioned dipole nanoantenna was calculated at its resonance wavelength (1621.6 nm) and shown in the Figure9. The intensity distribution was plotted for difference planes shown in this figure. It was clearly observed that the field is concentrated at the center and edges of dipole Nanoantenna. In Figure 9 (a) and (b) the planes at center of dipole nanoantenna and above the nanoantenna that are parallel to dipole plane have been taken and intensity enhancement distribution of respective planes were shown. The intensity at center plane of dipole nanoantenna has 10^3 times of the incident field. But in outer plane the intensity falls to 500 times. This signifies that the intensity enhancement confines to metal surface and reducing drastically if we move above the surface. From the Figure 9.(c) it was observed that the maximum field is concentrated at edges of dipole arm. In the Figure 9 (d) the intensity enhancement distribution of plane along dipole edge has been shown. It indicates most of the field confines within the interface.

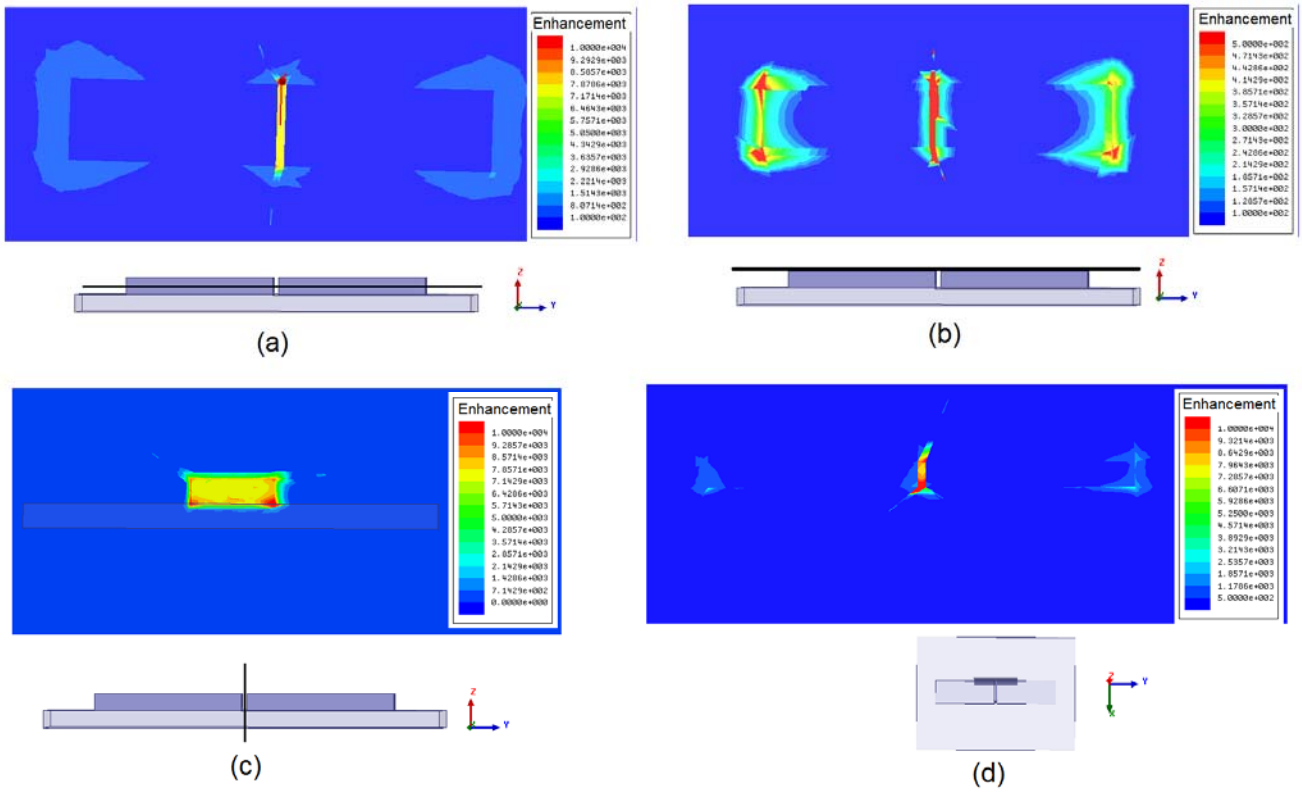


Figure 9. Intensity Enhancement distribution for Dipole Nanoantenna at different planes.

6. Conclusions

The geometric dependencies of dipole nanoantenna and its effects on intensity enhancement and resonance wavelength were studied with numerical computations. The study will be useful to optimize the nanoantenna of proper choice. It may find the applications in Surface Enhanced Raman Scattering (SERS) based sensor, spectroscopy and optical communication areas.

Acknowledgements

The authors gratefully acknowledge to the Dr. Chandra Shekhar, Director and Dr. Jamil Akhtar, Head, Sensors & Nanotechnology group, CSIR-CEERI Pilani for their continuous support and encouragement.

References

[1] Z. Li, H.T. Hattori, P. Parkinson, J. Tian et al, "A Plasmonic Staircase Nanoantenna device with strong electric field enhancement for Surface Enhanced Raman Scattering (SERS) Applications", Journal of Physics D: Applied Physics, vol. 45, No. 30, 2012.

[2] M. P. Busson, B. Rolly, B. Stout, N. Bonod, S. Bidault, "Accelerated Single Photon Emission from Dye Molecule-driven Nanoantennas Assembled on DNA", Nature Communications, vol. 3, No. 962, 2012.

[3] Kuhn S. et al., "Enhancement of Single Molecule Fluorescence using a Gold Nanoparticle as an Optical Nanoantenna," Physical Review Letters, vol. 97, No. 017402, 2006.

[4] D. Wang, W. Zhu, Y. Chu, K.B. Crozier, "High Directivity Optical Antenna Substrates for Surface Enhanced Raman Scattering", Advanced Materials, vol. 24, Iss. 32, 4376-4380, 2012.

[5] Z. Liu, E. Li, V.M. Shalaev, A.V. Kildishev, "Near field Enhancement in Silver Nanoantenna superlens system", Applied Physics Letters, vol. 101, No. 021109, 2012.

[6] J.Y. Kim, V.P. Drachev, H.K. Yuan et al., "Imaging Contrast Under Aperture Tip-Nanoantenna Array Interaction", Applied Physics B, vol. 93, 189-198, 2008.

[7] Y. Zou, P. Steinvurzel, T. Yang, K.B Crozier, "Surface Plasmon Resonances of Optical Antenna Atomic Force Microscope Tips", Applied Physics Letters, vol. 94, No. 171107, 2009.

[8] D. Das Gupta, G.V. Maltzahn, S. Ghosh et al., "Probing Nanoantenna-Directed Photothermal Destruction of Tumors using Noninvasive Laser Irradiation", Applied Physics Letters, vol. 95, No. 2333701, 2009.

[9] H. Zhu, F. Yi, E. Cubukcu, "Nanoantenna Absorbers for Thermal Detectors", IEEE Photonics Technology Letters, vol. 24, No. 14, 2012.

[10] Kotter D.K. et al., "Solar Nantenna Electromagnetic Collectors", Proceedings of 2nd International Conference on Energy Sustainability, Florida, USA, August 2008.

[11] M. Rajput, R.K. Sinha, S. Rawal, S.K. Varshney, "UV Emission from Left-Handed materials through Second Harmonic Generation: Optical Nanoantenna and Imaging Applications", Micro & Nano Letters, vol. 6, Iss. 8, 575-578, 2011.

[12] L. Cao, J.S. Park, P. Fan et al., "Resonant Germanium Nanoantenna Photodetectors", Nano Letters, vol. 10, 129-1233, 2010.

[13] P.B. Johnson, R.W. Christy, "Optical Constants of the Noble Metals", Physics Review B, vol. 6, No. 12, 4370-4379, 1972.

[14] L. Novotny, B. Hecht, "Principles of Nano-Optics", Cambridge University Press, 2006.

[15] High Frequency Structure Simulator, www.ansys.com/hfss.

Metamaterial-Inspired Bandpass Filter for the Terahertz Goubau Line

Ali K. Horestani[1*,2], Withawat Withayachumnankul[1], Christophe Fumeaux[1], Derek Abbott[1], and Tahsin Akalin[3†]

[1]School of Electrical & Electronic Engineering, The University of Adelaide, Adelaide, SA 5005, Australia
[2]Ministry of Science, Research and Technology, Tehran, Iran
[3]Institut d'Electronique de Microelectronique et de Nanotechnologie IEMN, France
*corresponding author, E-mail: akarami@eleceng.adelaide.edu.au
†corresponding author, E-mail: tahsin.akalin@iemn.univ-lille1.fr

Abstract

Recently, it has been shown that a single wire Goubau line that supports surface wave propagation can be used as an effective terahertz waveguide with low attenuation and low dispersion. In order to fully exploit Goubau lines in terahertz systems, for example for communication applications, structures such as different types of passive filters are required. This paper demonstrates that metamaterial elements can be used as building blocks for realization of compact bandpass Goubau line filters.

1. Introduction

Despite the emerging interest in terahertz systems and their applications in sensing, imaging and communications, there is still a need for efficient low-loss waveguides in the terahertz regime. Even though hollow waveguides and two-conductor transmission lines such as coaxial cables and microstrip lines are efficient for low to moderate radio-frequency operation, scaling these waveguides for terahertz applications is not an efficient solution because of the finite conductivity of metals at this higher frequency range. On the other hand, in spite of their high efficiency, conventional optical interconnections such as optical fibers are bulky and can not be integrated in planar technologies [1, 2]. Surface electromagnetic waves that propagate along the interface of a dielectric and a conductor, so-called surface-plasmon polaritons (SPPs), are one possible solution that has been proposed for realization of high speed on-chip interconnections, where thin metal circuitry can be used for carrying both the optical signals and electrical currents [1]. In particular, it was shown in [3] that a bare Goubau-like single metal wire that supports the propagation of surface waves [4, 5, 6] can be used as an efficient terahertz waveguide with low attenuation and low dispersion.

In order to exploit the propagation of surface waves on single wire in real applications, effective passive structures such as various types of filters are required. A bandstop filter based on the corrugated planar Goubau line (PGL) has been studied in [7]. It was shown that the structure provides a stopband characteristic for surface plasmon polariton propagation. More recently, an application of metamaterial resonators for filtering was investigated in [2]. A stopband in the transmission characteristics of the guided surface electromagnetic waves on a PGL was demonstrated computationally and experimentally. Also, split ring resonators (SRRs) and complementary split ring resonators (CSRRs) have been used for the design of bandpass or bandstop filters in microstrip and coplanar wave guide technologies [8, 9]. However, to the authors' knowledge, no study has been conducted on bandpass structures for PGL. In this paper we present a metamaterial-inspired bandpass filter for a modified PGL operating at sub-terahertz frequencies around 200 GHz.

2. Bandpass Filter for the Terahertz Goubau Line

In previously published work [10] Akalin et al. have presented a high-efficiency planar launching structure for a plasmonic wave on a PGL. The structure consists of a coplanar waveguide with a tapered section, which effectively converts the coplanar waveguide mode to the Goubau mode. It was also shown that adding a gap in the Goubau line results in almost no energy transmission, proving that the transmitted energy in the original structure is not due to the direct coupling of the launching sections. In the present paper, it is shown that if the gapped Goubau line is properly coupled to a pair of SRRs, as illustrated in Fig. 1, the surface wave can be transmitted across the gap via coupling through the SRRs at the resonant frequency of the ring resonators. Therefore, the resonance condition of the SRR creates a narrow passband, and there is virtually no transmission of energy in the rest of the spectrum.

The concept has been investigated with full-wave 3D electromagnetic simulation using a 400 μm thick quartz crystal with a relative permittivity $\epsilon_r = 3.78$ as the substrate. The dimensions of the coplanar waveguide to Goubau line launching structure are $w = 50$ μm, $w_{\mathrm{gnd}} = 190$ μm, $s = 5$ μm and $l_l = 650$ μm. The Goubau line has a width $w_G = 5$ μm and a total length $l_G = 2100$ μm including the 50 μm gap in the middle. The gap is loaded with a pair of SRRs with $a = 140$ μm, $g = 10$ μm and $c = 10$ μm. Since the electromagnetic wave along the PGL propagates in a quasi-TEM mode, which is strongly confined around the line and decays exponentially in the

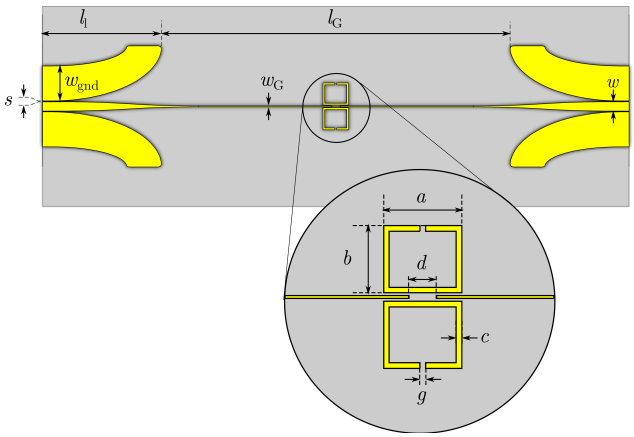


Figure 1: (a) Top view of the metamaterial inspired bandpass Goubau line structure excited by coplanar waveguide launching sections.

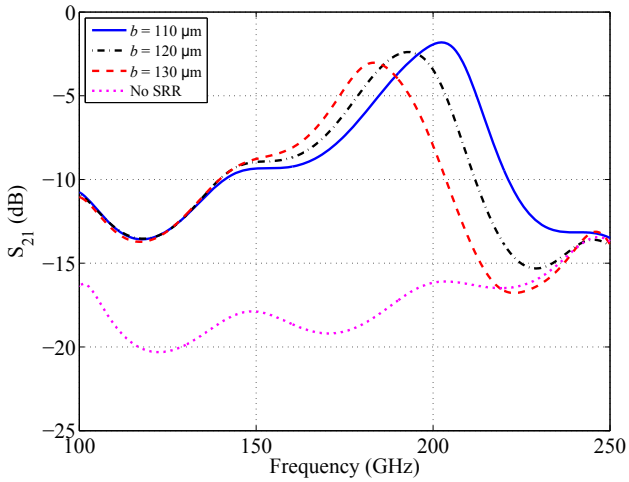


Figure 2: Simulated normalized transmission coefficients of the structure for three lateral dimensions of the SRRs, i.e. $b = 110\ \mu\text{m}, 120\ \mu\text{m}$, and $130\ \mu\text{m}$ as well as the structure without SRRs.

transverse plane, the pair of single-ring SRRs are placed close to the PGL in order to maximize the magnetic coupling between both structures.

Fig. 2(b), depicts the simulated transmission coefficient of the structure for three different values of the SRRs' lateral dimension b. Note that in order to exclude the launching sections loss, the transmission coefficients of the bandpass structure are normalized to that of a structure without the gap and SRRs. Simulation results clearly demonstrate the bandpass behavior of the proposed structure with a with a central frequency that can be controlled by tuning the SRRs dimensions. More details about higher order bandpass filters for PGL and controlling the filter's bandwidth will be presented elsewhere.

3. Conclusion

This paper presents an application of metamaterial elements in the realization of bandpass filters for the PGL at subterahertz frequencies. Due to the exponentially decaying transverse electromagnetic field in the Goubau mode, a pair of SRRs needs to be placed in close proximity to a gapped Goubau line for strong coupling. This strong coupling results in transmission of energy exclusively in a narrow band around the SRRs resonance. The frequency and bandwidth of the passband can be controlled by optimizing the dimensions of the SRRs. Ongoing work includes structure fabrication and measurement.

References

[1] E. Ozbay, "Plasmonics: Merging photonics and electronics at nanoscale dimensions," *Science*, vol. 311, no. 5758, pp. 189–193, 2006.

[2] W. Chen, J. Mock, D. Smith, T. Akalin, and W. Padilla, "Controlling gigahertz and terahertz surface electromagnetic waves with metamaterial resonators," *Physical Review X*, vol. 1, no. 2, 2011, art. no. 021016.

[3] K. Wang and D. Mittleman, "Metal wires for terahertz wave guiding," *Nature*, vol. 432, no. 7015, pp. 376–379, 2004.

[4] G. Goubau, "Open wire lines," *IRE Transactions on Microwave Theory and Techniques*, vol. 4, no. 4, pp. 197–200, 1956.

[5] M. King and J. Wiltse, "Surface-wave propagation on coated or uncoated metal wires at millimeter wavelengths," *Antennas and Propagation, IRE Transactions on*, vol. 10, no. 3, pp. 246–254, 1962.

[6] J. Brown, "The types of wave which may exist near a guiding surface," *Proceedings of the IEE-Part III: Radio and Communication Engineering*, vol. 100, no. 68, pp. 363–364, 1953.

[7] T. Akalin, E. Peytavit, and J. Lampin, "Bendings and filters with single strip THz plasmonic waveguides," in *Joint 32nd International Conference on Infrared and Millimeter Waves, 2007 and the 2007 15th International Conference on Terahertz Electronics. IRMMW-THz.*, 2007, pp. 75–76.

[8] F. Martin, F. Falcone, J. Bonache, R. Marques, and M. Sorolla, "Miniaturized coplanar waveguide stop band filters based on multiple tuned split ring resonators," *Microwave and Wireless Components Letters, IEEE*, vol. 13, no. 12, pp. 511–513, 2004.

[9] M. Gil, J. Bonache, and F. Martín, "Metamaterial filters: A review," *Metamaterials*, vol. 2, no. 4, pp. 186–197, 2008.

[10] T. Akalin, A. Treizebré, and B. Bocquet, "Single-wire transmission lines at terahertz frequencies," *IEEE Transactions on Microwave Theory and Techniques*, vol. 54, no. 6, pp. 2762–2767, 2006.

Silicon nanowire photodetector enhanced by a bow-tie antenna

Gordana Klaric Felic[1], Feras Al-Dirini[2,1], Faruque M. Hossain[1,2], Thanh Cong Nguyen[2,1], Efstratios Skafidas[2,1]

[1]National ICT Australia, The University of Melbourne, Parkville VIC 3010, Australia
[2]The University of Melbourne, Electrical and Electronic Engineering, Parkville VIC 3010, Australia

*corresponding author, E-mail: fhossain@unimelb.edu.au, gordana.felic@nicta.com.au

Abstract

Properties of surface plasmon polaritons (SPP) can be exploited for the minituarisation of photonic circuits below the optical wavelength scale. Smaller and more sensitive photodetectors can be made by using sub-wavelength semiconductor elements such as germanium or silicon nanowires in combination with nanometer-scale antennas. Proposed nanowire photodetector enables on-chip optical sensing applications.

1. Introduction

Excellent electronic transport properties of silicon nanowires can be exploited for biomolecule detection in the dc and frequency dependent detection system [1]. Germanium and silicon-based nanowire devices can absorb and transduce light to photocurrent [2-4]. The addition of optical antennas in the nanowire device enhances photodetection by concentrating radiation into a semiconductor nanowire. This is due to the fact that optical nano-antennas can increase the absorption cross-section and provides better signal-to-noise ratio. They also may enable manipulating optical fields at nanometer-scale thus help enhancing the efficiency of nano-scale photo-detectors. This property of optical antenna comes from the unique optical behavior of metals that that enable collective electron excitations, known as surface plasmons [5]. In this paper we present and discuss how a bow-tie dipole antenna can be exploited to confine the radiated power into a silicon nanowire. Using principle of field enhancement by metal antenna structures a subwavelength metal-semiconductor-metal detector can be built [2].

2. Device construction

The silicon nanowire device is patterned on a silicon-on-insulator (SOI) wafer in order to maintain the ease with planner CMOS fabrication process compatibility. The silicon dioxide insulator layer is 150 nm thick and the top silicon device has a thickness of 50 nm. Figure 1(a) shows a perspective view of the proposed device. Silicon nanowire is shown as traced through the gap of printed gold antenna (bow-tie and/or Hertz-dipole). Gold pads at two ends of the nanowire (to form electrical contacts) and bow-tie antenna may be patterned and deposited at one process step. The length and diameter of the Si nanowire are considered to be 500 nm and 50 nm respectively. The total length of our designed antenna is 380 nm and the gap between the metal arms is 100 nm.

3. Results and discussion

To quantify the enhancement of light absorption, simulation has been performed using the CST (Computer Simulation Technology) Microwave Studio, Time Domain (TD) Solver [6]. The simulation model is based on the previously constructed nanowire device without antenna [2]. The computation of power flow on the surface of the nanowire is obtained by integration of the power density over the nanowire surface.

3.1. Power Flow Computation

According to the conservation theorem [7], the power flowing into the circuit is equal to the rate of change of the energy stored and the rate of energy dissipation. In theoretical generalization, the energy is distributed through space with an energy density W (J/m3), and the power is dissipated at a local rate of dissipation per unit volume P_d (W/m3). As the power on the nanowire flows with a density **S** (W/m2), a vector, the power crossing the nanowire surface surface, S_a is given in [7] by

$$\oint_{S_a} \mathbf{S} d\mathbf{a} \tag{1}$$

With these field-theoretical generalizations, the power flowing into the nanowire volume V, enclosed by the surface S is given in [7] by

$$-\oint_{S_a} \mathbf{S} d\mathbf{a} = \frac{d}{dt}\int_V W dV + \int_V P_d dV \tag{2}$$

where the minus sign indicates that the term on the left is the power flowing into the volume. According to the right hand side of the equation, input power is equal to the rate of increase of the total energy stored plus the power dissipation. The total energy is expressed as an integral over the volume of an energy density, W and the total power dissipation is the integral over the volume of a power dissipation density P_d.

3.2. Optical Bow-Tie Antenna

When a bow-tie antenna is illuminated with electromagnetic radiation, currents are induced in the arms of the antenna and guided towards the open circuits terminal (gap) region. The accumulated charge at the open terminals results in displacement current across the gap (field enhancement region). Considering, a fundamental resonance, the effective wavelength of the bow-tie antenna depends on the length L and the effective index of the localized SPP along the bow-tie antenna gap, n_{eff} [8]

$$\lambda \approx 2 \int_{-L/2}^{L/2} n_{eff}(x)dx + \delta \qquad (3)$$

where δ is the offset due to the antenna gap and reflections. The above equation is a simple linear scaling law for λ_{eff} where n_{eff} has a dimension of antenna length depending on the geometry and dielectric properties of the metal at optical frequencies (plasma wavelength).

3.3. Results

When the photodetector with the antenna is illuminated with a plan wave in perpendicular direction to the nanowire (along the gap of the bow-tie antenna), the electric field intensity will increase. This will drive the increased light absorption in the nanowire. Power flow (absorption) distribution profile for the nanowire with bow-tie antenna and dipole antenna are given in Figure 2. The near-field and power flow distribution of the detector have been calculated for the plane wave excitations at wavelengths from 300 nm to 1.6 μm.

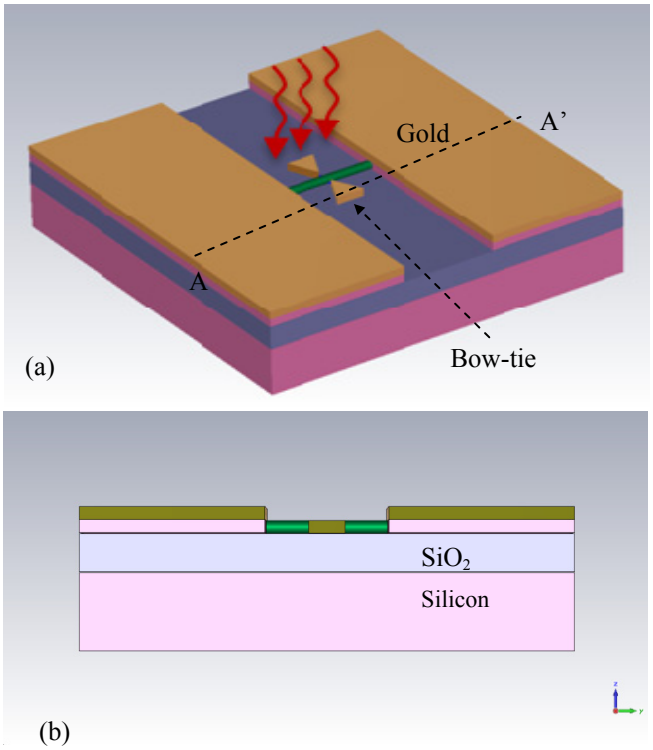


Figure 1: Schematic illustration of the semiconductor nanowire device used for photo detection. (a) Perspective view (b) Cross-sectional view of the device (AA').

The ability of a bow-tie antenna to concentrate radiation in the silicon element (absorption enhancement) is illustrated in Figure 3. The plane wave polarised in the bow-tie direction was incident from the top of the nanowire device. The structure with bow-tie antenna resonates at a wavelength of 850 nm with highest electric field in the gap region. In order to compare the effect of the antennas (bow-tie and Hertz dipole) on light absorption enhancement, power density is integrated on the face of the wire (absorbed power) for the given range of wavelengths. The power absorption of the system with antennas is then compared with the power absorption of the silicon wire. The comparison between the power absorption for a half-wave Herzian dipole antenna and bow-tie antenna is given in Figure 4. It shows that the bow-tie antenna enhances the power absorption for the entire range of wavelength (300-1600 nm) and that the absorption enhancement is greater than the absorption enhancement of the half-wave Hertz dipole antenna. These results indicate the ability of bow-tie antennas of reducing semiconductor detector's area many-fold and thus the enhancement of sensitivity at several orders of magnitude.

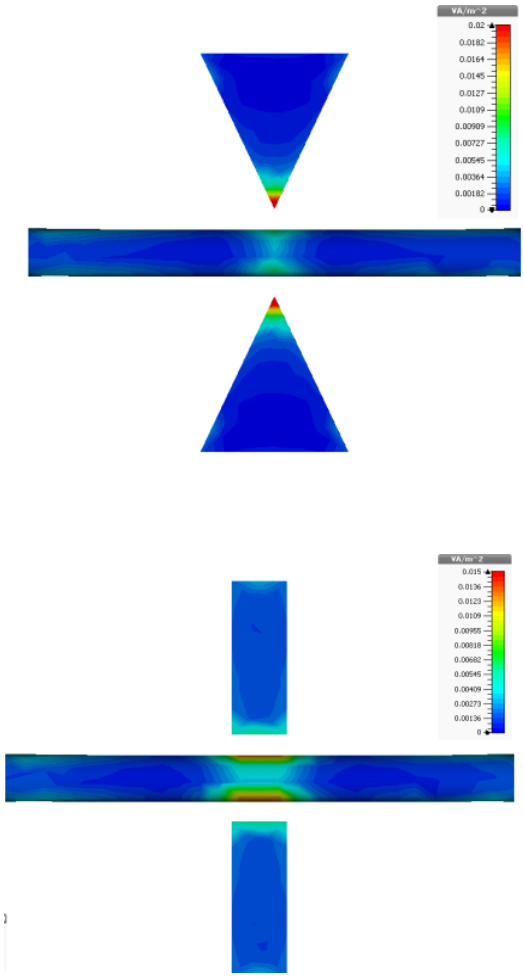


Figure 2: The distribution profile of power flow (VA/m^2) for the nanowire system with bow-tie and dipole antenna (antenna length, 380 nm, silicon wire diameter, 50 nm, at 850 nm).

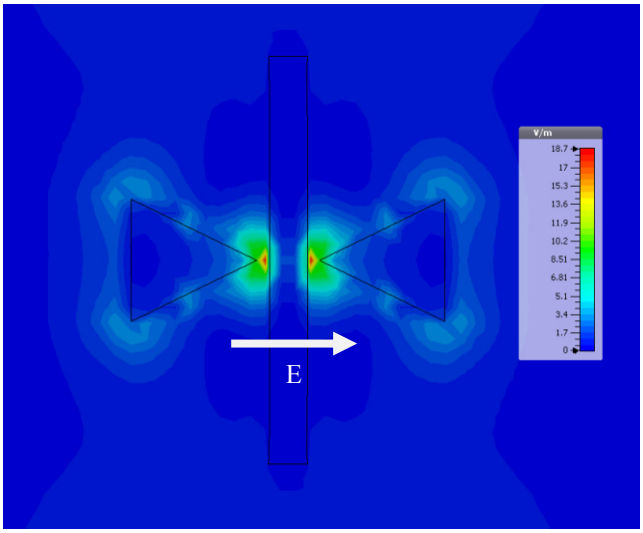


Figure 3: The distribution profile of electric field for the nanowire detection system with bow-tie antenna at wavelength, λ=850 nm.

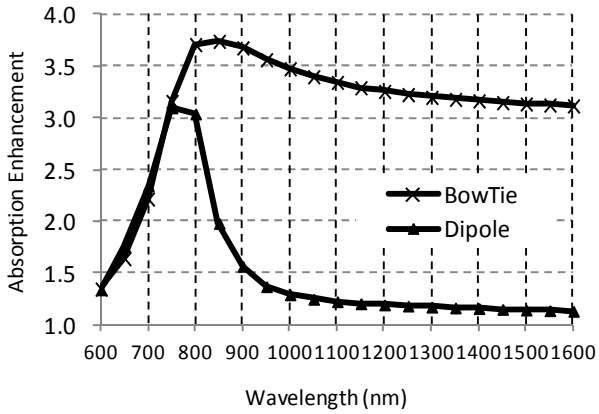


Figure 4: Spectra of light absorption enhancement for the nanowire system with bow-tie antenna and dipole antenna (wire length: 500 nm, diameter: 50 nm).

4. Conclusion

In this paper we have shown that the inclusion of bow-tie antenna can increase the ability to absorb light for a wide range of wavelength and can provide the enhancement of sensitivity of the semiconductor photodetector without involving far-field radiation. Thus the designed nano-wire based nano-antenna system holds promise for both highly sensitive photodetection and photovoltaics applications.

Acknowledgements

NICTA is funded by the Australian Government as represented by the Department of Broadband, Communications and the Digital Economy and the Australian Research Council through the ICT Centre of Excellence program.

References

[1] Nguyen T.C, Qiu W. Z. and Skafidas E. "Functionalised Nanowire-Based Antigen Detection Using Frequency-Based Signals, IEEE Transactions on Biomedical Engineering, VOL. 59, NO. 1, January 2012.

[2] Tang, L. et al. "Nanometre-scale germnium photodetector enhanced by a near-infrared dipole antenna," Nature Photonics, VOL. 2, 226–229, 2008.

[3] Fan P, Chettiar U. K., Cao L, Afsinmanesh F., Engheta N. and Brongersma M. L., "An invisible metal-semiconductor photodetector," Nature Photonics, VOL. 6, 380-385, 2012.

[4] Pengyu F., Huang C.Y., Linyou C. and Brongersma M. L., "Redesigning Photodetector Electrodes as an Optical Antenna," Nanolett.

[5] J.A. Schuller et al., "Plasmonics for extreme light concentration and manipulation", *Nature Materials*, VOL 9, 193-204, 2010.

[6] http://www.cst.com/

[7] Haus, Hermann A., and James R. Melcher. Electromagnetic Fields and Energy. Englewood Cliffs, NJ: Prentice-Hall, 1989

[8] L. Novotny, "Effective Wavelength Scaling for Optical Antennas," *Physical Review Letters*, PRL 98, 266802 (2007)

Wide Band Silicon Mirror Based Grating Coupler for Silicon Integrated Photonics

Md Asaduzzaman[1,2], Masuduzzaman Bakaul[1], Stan Skafidas[1,2], Md Rezwanul Haque Khandokar[1,2]
[(1)] *Department of Electrical & Electronic Engineering, The University of Melbourne, Parkville, Australia,*
[(2)] *NICTA (National ICT Australia Ltd.), Department of Electrical & Electronic Engineering, The University of Melbourne, Parkville, Australia*
Author e-mail address: m.asaduzzaman@student.unimelb.edu.au

Abstract

A CMOS compatible silicon (Si) grating waveguide coupler has been designed and simulated by finite difference time domain (FDTD) method. A highly efficient (90%) wide band (40 *nm* at 3dB) coupling has been achieved by exploiting the combined effects of surface grating and multilayer silicon mirrors.

1. Introduction

Silicon-On-Insulator (SOI) provides the compatibility with well matured CMOS technology which opens the potentiality to integrate photonic devices with nano-electronic circuits. The high index contrast between silicon and oxide allows designing photonic devices in submicron scale with high density integration [1]. One of the key issues of such nano-scale devices is their integration with micro-scale optical links [2], for example, the coupling of standard single-mode fiber with nano-scale photonic waveguides with typical cross-sections of 63.6 μm^2 and 0.1 μm^2 respectively [3].

A variety of techniques have been proposed to perform such coupling including prism coupling, butt coupling, and grating coupling. Among them butt coupling and grating coupling have attracted a lot of attention in the recent past due to their higher compatibility CMOS process technology. Butt coupling which requires accurate polishing and dicing in tapering the waveguide edge relies on highly precision fabrication technology which increases the cost [4-7]. Fortunately grating couplers can overcome these limitations significantly, in addition to enabling wafer level testing for mass production [8].

Despite the advantages of grating couplers in fabrication simplicity, one of the major limitations of grating couplers is their poor coupling efficiency and lower coupling bandwidth. Several approaches have been proposed to obtain high coupling efficiencies, including through grating couplers by optimizing various grating parameters and structures including photonic crystals and manipulating back reflection [9-13]. One of the main sources of coupling losses in grating couplers includes light propagation towards substrate (35%-45%) [2]. But very few concentrate on the light which is propagating through Buried Oxide (BOX) and coupled into the substrate. The use of metallic mirror [14] and distributed Bragg reflector [15] have been proposed for this purpose.

However none of them discussed about the silicon mirror which is one of the primary requirements in silicon photonic devices and to be compatible with standard CMOS processing technology.

In this work, we have designed a high efficient, high bandwidth silicon coupler for interconnection between fiber and nano-scale waveguides by simultaneously applying techniques of light redirection, mirror-reflection, and surface gratings. We took the advantages of using silicon-mirror in grating coupler that effectively overcome the efficiency limiting factors associated with coupling through the buried oxide (BOX) layer [16] and low bandwidth response of coupled light [11].

The ultimate coupling efficiency of the coupler is determined by the directionality of power propagation as shown in Fig. 1. The incident light (Pin) from optical fiber on the gratings diffracted in two different directions through silicon layer just below the gratings, one part (Pw) is diffracted towards waveguide where a photodetector is assumed to be placed while another part (Po) is diffracted in the opposite direction and contributed in the coupling loss.

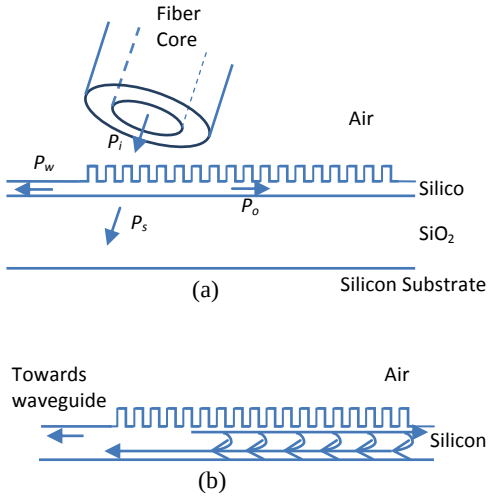


Fig. 1: (a) Power propagation directions of fiber-to-waveguide grating couplers (b) Enlarged view of diffracted light of P_o

However a big portion of this light again diffracted back to the direction of the waveguide continuously as it faces several numbers of gratings as shown in Fig. 1 (b) and

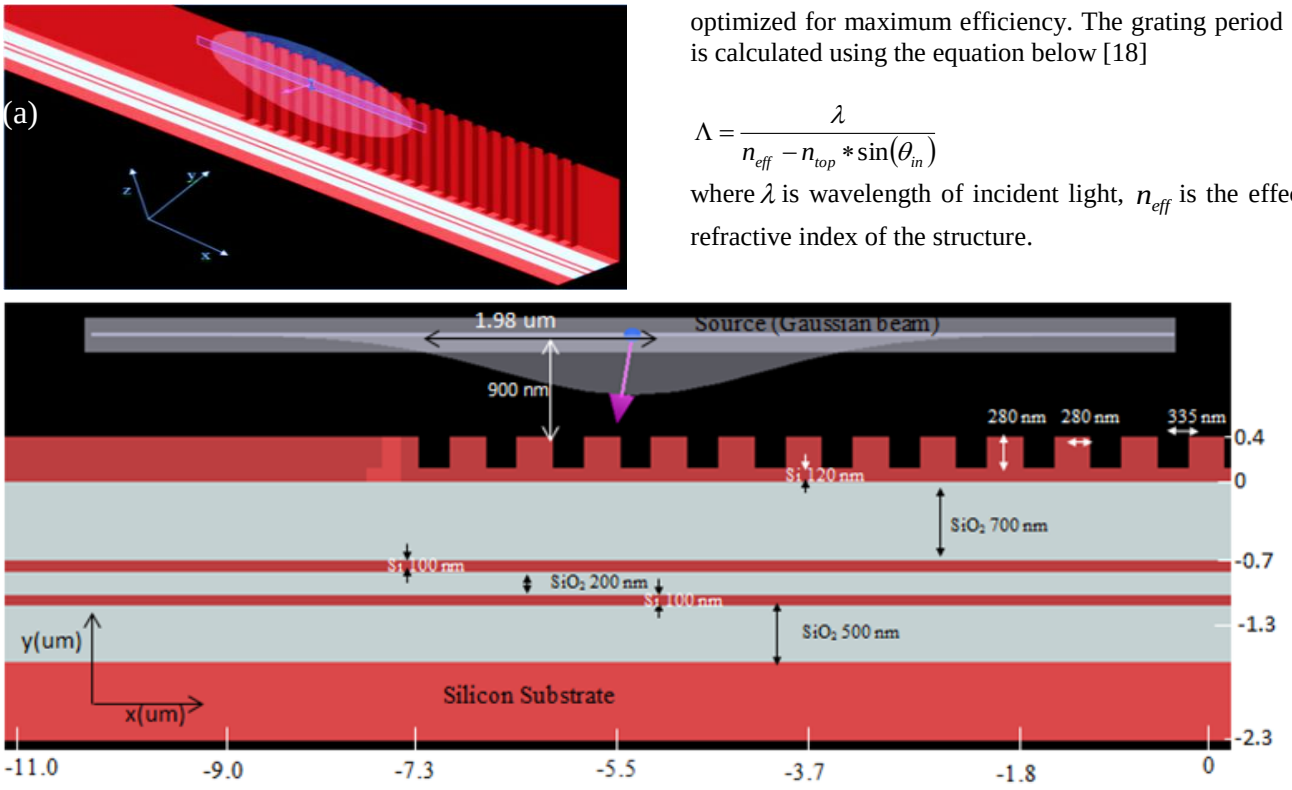


Fig. 2: (a) Perspective view and (b) cross-section of the device structure

consequently improves the coupling efficiency of the coupler.

Another part of light (P_s) transmitted through the Buried Oxide (BOX) layer and coupled into the silicon substrate. This transmitted light highly contributed to the coupling losses. The power received at the end of the waveguide where the photodetector is assumed to be placed is calculated using the equation (1).

$$P_w = P_{in} - (P_o + P_s) \quad (1)$$

where $(P_o + P_s)$ is simply propagation loss in the coupler. To improve the coupling efficiency these losses must be minimized. As descried above in Fig. 1(b), mostly of P_o is diffracted back towards waveguide due to gratings. Therefore, P_s which is transmitted through BOX is remain as the main source of losses and causes in poor coupling efficiency of the coupler.

In our design we have introduced a new technique to redirect this light towards the waveguide by using multilayer silicon mirrors.

2. Design and simulations

The structure of the proposed multilayer mirrored grating coupler is designed using a SOI wafer with dimensions of top-Si: 400 *nm* and BOX: 1600 *nm* with grating at the top layer and a simple modification in the BOX layer as shown in Fig. 2. The position of two 100 *nm* thin Si mirror layers is optimized for maximum efficiency. The grating period (Λ) is calculated using the equation below [18]

$$\Lambda = \frac{\lambda}{n_{eff} - n_{top} * \sin(\theta_{in})} \quad (2)$$

where λ is wavelength of incident light, n_{eff} is the effective refractive index of the structure. n_{top} is the refractive index of top cladding, θ_{in} is the incident angle with normal to the surface (y-axis) of the structure. The extracted value of n_{eff} is found 2.38 using a fully vectorial mode solver [17].

The calculated value of Λ is 615 *nm* for the input optical wavelength of $\lambda = 1550$ *nm*, $n_{top} = 1$ (air) and, for incident angle $\theta_{in} = -8^0$. For clarity, this slight tilt angle helps enhancing the coupling of predominant first order diffraction by minimizing the effect of second order diffraction [3].

Based on the optimized design, the calculated grating depth (*d*) and width (*w*) are found 280 *nm* and 335 *nm* respectively using $\Lambda = 615$ *nm* and filling factor (w/Λ) = 0.545. The novel features of this design can be explained by analysing intensity profiles along three propagation directions.

3. Results and discussion

The design is simulated using widely use commercial software package "Lumerical Solutions" based on Finite Difference Time Domain (FDTD) method [18]. Fig. 3 and 4 show the TE mode intensity distribution in the BOX and the Si waveguide region including the impinging Gaussian beam region. For a clear visualization and comparison of coupling intensity between the point of incidence (grating region) and

several microns away along the waveguide (where a photo detector is assumed to be located), a wide region is covered. A significant enhancement intensity coupling occurs in presence of surface grating and Si mirrors in BOX region.

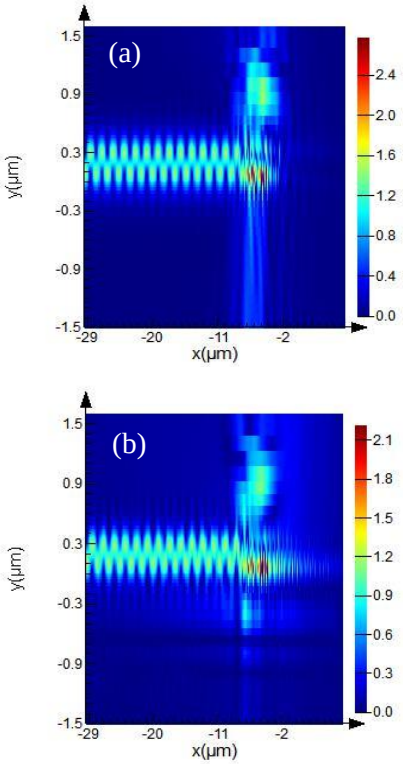


Fig. 3: TE mode intensity distribution in the waveguide (grating region inclusive) at 1550 *nm* (a) without mirror (b) with mirror.

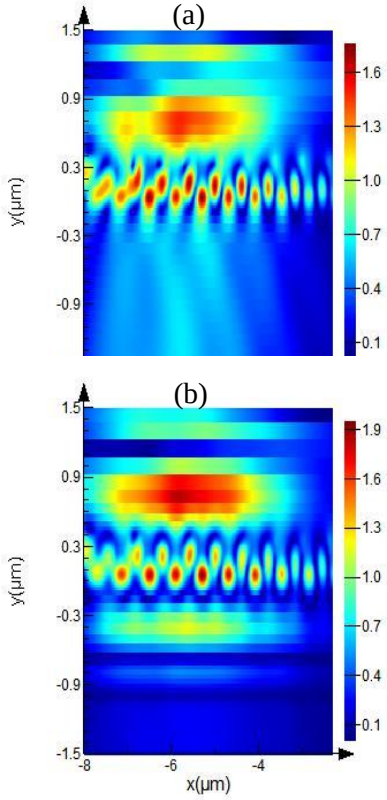


Fig. 4: Enlarged view of TE mode intensity distribution in the grating region along the direction of incident at 1550 *nm* (a) without mirror (b) with mirror.

Fig. 5 shows the intensity profiles in the same regions as in Fig. 3, which can further be explained by interference and scattering phenomena. The incident light is scattered by surface gratings and then fractionally coupled through +x, –x, and –y (direction of incidence) directions. The propagating waves along +x/-x directions are in the wave-guided modes reflect back from the periodic grating trench edges, resulting an interference with the incident light. Consequently, a standing wave forms with resonance around the point of incidence localized in the grating region. The period of modulated interference patterns is determined by the grating patterns (depth, width, and shape). Hence the highest intensity level occurs at the point of incident (at x = -5.5 *μm* in our design). The wave stabilized as it propagates along the silicon waveguide. The interference patterns of the waves are clearly distinguishable between the structure in the absence of silicon mirrors and in the presence of silicon mirrors as shown in Fig. 5 (a) and (b) respectively. This is because without mirrors in the BOX layer, no light is reflected toward the waveguide and only interference occurs with P_0 in the waveguide. Hence the wave

On the other hand in the presence of mirrors in the BOX region, the transmitted light in the direction of incident is reflected towards the waveguide. Therefore, a three-way (P_w, part of P_o and part of P_s) interference occurs in this case and takes longer propagation distance to be stabilized as depicted in Fig. 5(b). Comparison of Fig. 5(a), without silicon mirrors, and (b), with silicon mirrors, indicates an efficient enhancement of light intensity (from 50% to ~90%) in the waveguide region in presence of buried Si mirrors in the BOX layer. We have achieved 90% theoretical coupling efficiency in terms of intensity ratio in our novel design of Si grating coupler.

In our structure, we have achieved a very wide band width of coupling efficiency which is one of the major limitations in the grating couplers. Fig. 6 shows the wavelength dependent coupling efficiency of the coupler. The maximum efficiency (90%) is observed at 1565 *nm* and a wide frequency band is shown that coupled strongly around the standard telecommunication band. Moreover, for 80 *nm* bandwidth 63% coupling efficiency has been achieved.

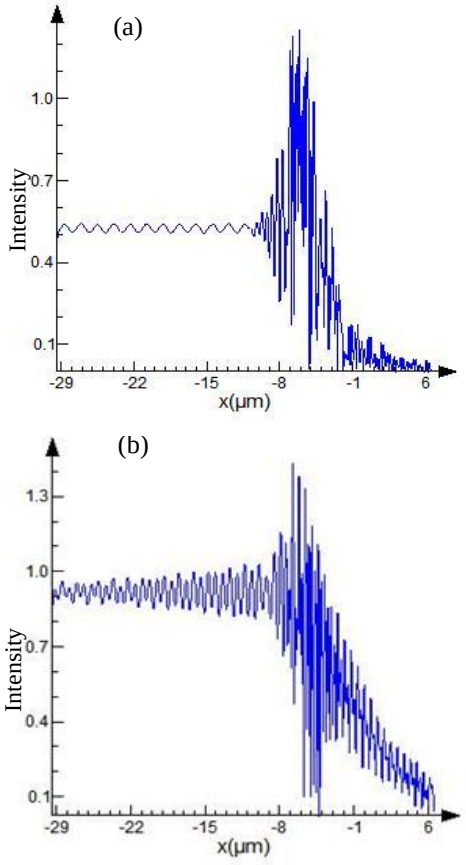


Fig. 5: TE mode intensity profile at 1550 *nm* (a) without mirror (b) with mirror.

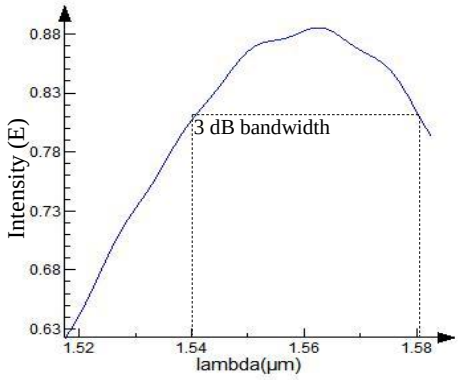


Fig. 6: Wavelength dependent coupling efficiency.

6. Conclusion

In this paper, we have designed a multilayer silicon mirror based grating coupler, which can couple the light efficiently between single-mode fiber and SOI waveguide. The obtained 90% coupling efficiency is very high comparing with other grating couplers of this type at telecom wavelength of 1550 *nm* and this structure provides 3-dB bandwidth of 40 *nm*. The other advantages of this design, it is compact and efficient, no polishing is required at the waveguide facets for interfacing which allows wafer lever testing and packaging, hence reduced the cost significantly. Moreover our structure can be fabricated using standard CMOS processing technology.

References

[1] Xiaochuan Xu, Harish Subbaraman, John Covey, David Kwong, and A. Hosseini, "Complementary metal-oxide-semiconductor compatible high efficiency subwavelength grating couplers for silicon integrated photonics," *Appl. Phys. Lett.*, vol. 101, pp. 0311091-4, 2012.

[2] D. Vermeulen, S. Selvaraja, P. verheyen, G. Lepage, W. Bogaerts, P. Absil, D. Van Thourhout, and G. Roelkens, "High-efficiency fiber-to-chip grating couplers realized using an advanced CMOS-compatible Silicon-On-Insulator platform," *Opt. Express*, vol. 18, pp. 18278-18283, 2010.

[3] G. Roelkens, D. Vermeulen, D. Van Thourhout, S. B. R. Baets, P. G. P. Lyan, and J.-M. Fédéli, "High efficiency diffractive grating couplers for interfacing a single mode optical fiber with a nanophotonic silicon-on-insulator waveguide circuit," *Appl. Phys. Lett.*, vol. 92, pp. 1311101-2, 2008.

[4] Graham T. Reed and Andrew P. Knights, *Silicon Photonics an Introduction*. West Sussex , England: John Wiley & Sons Ltd, 2004.

[5] T. Shoji, T. Tsuchizawa, T. Watanabe, K. Yamada, and H. Morita, "Low loss mode size converter from 0.3 μm square Si wire waveguides to singlemode fibres," *Electron. Lett*, vol. 38, pp. 1669-1670, 2002.

[6] V. R. Almeida, R. R. Panepucci, and M. Lipson, "Nanotaper for compact mode conversion," *Opt. Lett*, vol. 28, pp. 1302-1304, 2003.

[7] S. McNab, N. Moll, and Y. Vlasov, "Ultra-low loss photonic integrated circuit with membrane-type photonic crystal waveguides," *Opt. Express*, vol. 11, pp. 2927-2939, 2003.

[8] Christophe Kopp and Alexei Chelnokov, "Fiber grating couplers for silicon nanophotonic circuits: Design modelling methodology and fabrication tolerances," *Optics Communications*, vol. 282, pp. 4242-4248, 2009.

[9] Chao Qiu, Zhen Sheng, Le Li, Albert Pang, Zhiqi Wang, Aimin Wu, Xi Wang, Shichang Zou, and Fuwan Gan, "Poly-Silicon Grating Couplers for Efficient Coupling With Optical Fibers," *IEEE Photonics Technology Letters*, vol. 24, pp. 1614-1617, 2012.

[10] G. Roelkens, D. Van Thourhout, and R. Baets, "“High efficiency Silicon-on-Insulator grating

coupler based on a poly-Silicon overlay," *Opt. Express*, vol. 14, pp. 11622-30, 2006

[11] Liu Liu, Minhao Pu, Kresten Yvind, and Jørn M. Hvam, "High-efficiency, large bandwidth silicon-on-insulator grating coupler based on a fully-etched photonic crystal structure," *Appl. Phys. Lett.*, vol. 96, pp. 0511261-3, 2010.

[12] Zhe Xiao, Feng Luan, Tsung-Yang Liow, Jing Zhang, and Ping Shum, "Design for broadband high-efficiency grating couplers," *Opt. Express*, vol. 37, pp. 530-532, 2012.

[13] Neil Na, Harel Frish, I-Wei Hsieh, Oshrit Harel, Roshan George, Assia Barkai, and Haisheng Rong, "Efficient broadband silicon-on-insulator grating coupler with low backreflection," *Opt. Lett*, vol. 36, pp. 2101-2103, 2011.

[14] F. Van Laere, G. Roelkens, J. Schrauwen, D. Taillaert, P. Dumon, W. Bogaerts, D. Van Thourhout, and R. Baets, "Compact grating couplers between optical fibers and Silicon-on-Insulator photonic wire waveguides with 69% coupling efficiency," presented at the Conference on Optical Fiber Communication (IEEE), 2006.

[15] D. Taillaert, P. Bienstman, and R. Baets, "Compact efficient broadband grating coupler for silicon-on-insulator waveguide," *Opt. Lett.* , vol. 29, pp. 2749-51, 2004.

[16] Dirk Taillaert, Wim Bogaerts, Peter Bienstman, Thomas F. Krauss, Peter Van Daele, Ingrid Moerman, Steven Verstuyft, Kurt De Mesel, and Roel Baets, "An Out-of-Plane Grating Coupler for Efficient Butt-Coupling Between Compact Planar Waveguides and Single-Mode Fibers," *IEEE Journal of Quantum Electronics*, vol. 38, pp. 949-955, 2002

[17] "Lumerical Solutions inc. ," *http://www.lumerical.com/tcad-products/mode*.

[18] "Lumerical Solutions inc.," *http://www.lumerical.com/tcad-products/fdtd*.

Atomistic Approach for Simulating Plasmons in Nanostructures

Arto Sakko*, Tuomas Rossi, Jussi Enkovaara, Risto M. Nieminen

COMP Centre of Excellence, Department of Applied Physics,
Aalto University, Finland
*corresponding author, E-mail: arto.sakko@aalto.fi

Abstract

Recent experimental and theoretical works have demonstrated that quantum mechanical effects play an important role in materials design of some novel nano-plasmonic materials. In this work, electronic structure calculations are used to study these effects for the optical properties of metal nanostructures and small flakes of graphene. Their optical response is shown to depend on their exact atomic composition, and their similarities (size-dependent resonance frequency) and differences (metallic vs. semiconducting material) are discussed. The open-source computer code GPAW is used for the simulations, which can be done for systems of thousands of valence electrons. The calculations automatically include quantum effects such as tunneling, nonlocal response, and molecular orbital hybridization.

1. Introduction

Present-day materials design benefits from reliable computer simulations, which yield the materials' characteristics only from the knowledge of their structure and composition. Optical properties are typically calculated using Maxwell's equations, which describe the scattering, absorption, and propagation of light in materials whose dielectric permittivity and permeability are known.[1] With sophisticated nanofabrication techniques, such as litography, self-assembly, and surface chemistry, it is possible to create materials with sub-nm-scale features, leading to a new regime where quantum mechanical effects must be accounted for in order to understand the optical response.[2, 3, 4]

One attractive strategy for adding quantum effects into the simulations of the optical response is to extend Maxwell's equations by incorporating nonlocality in the dielectric permittivity.[5] Such an approach avoids quantum simulations and is thus very efficient, but the general form for the nonlocal terms may not be known. A more general approach is to use fully quantum mechanical electronic structure calculations.[6] Some pioneering works have recently used the time-dependent generalization of the density functional theory (TDDFT) for such situations, and explored the tunneling and nonlinear response between nanoparticles in close contact.[4, 7, 8] Our calculations in this work are similar, but whereas the cited works employ the "jellium" approach, where the nuclear charges are replaced by positive charge continuum, we also account for the atomistic structure of the material. Our approach thus describes molecular orbital hybridization and the bonding between atoms. The atomic description is also relevant for the optical response of molecules whose electronic transition frequencies depend on the discrete energy levels of the quantum mechanical system. The molecular excitations localized at specific parts of the plasmonic system, e.g. metallic nanoparticle with optically active adsorbate molecules, can couple with surface plasmons in a non-trivial way. The materials design of these systems requires sophisticated electronic structure calculations, possibly in conjunction with multi-scale approaches that combine quantum and classical electrodynamical simulations.[9, 10, 11]

In this work we describe a general method for predicting the optical response of nanoscale systems. We review the theoretical background, computational method, and the used computer code. We first calculate the optical response of metal atom chains, and demonstrate how their resonance frequencies depend on their structure at the atomic level.[12] Then we show that the same phenomenon is observed also in more realistic graphene-based nanomaterials, which can be chemically fabricated.[13] In both cases the main resonance wavelength can be selectively tuned in a wide range across the near-infrared and visible part of the electromagnetic spectrum. Despite this similarity, these resonances have quite different origins, as we demonstrate with comparative calculations for the infinite and finite systems. Furthermore, in order to get more insight into the characteristics of the resonances, we visualize the spatial distribution of the electron polarization from our quantum mechanical predictions. Thus, our work here integrates the classical and quantum mechanical treatments for the optical phenomena, exemplifies the need for quantum treatment in two optically interesting systems, and encourages and helps the scientists working with nano-optics to start using the electronic structure calculations when necessary.

2. Method

Optical properties of all materials depends on how their charge carriers respond to applied light. In the classical electromagnetism, this response is hidden in the material-specific macroscopic dielectric function $\epsilon_M(\omega)$. The dielectric function determines how light propagates inside the material, scatters, or is absorbed. From the microscopic point of view, the electrons are quantum mechanical particles with discrete energy levels and delocalized wavefunctions. In metallic systems, the (nearly) free-electron approximation is often valid, and Drude-type approxima-

tions for the electronic mobility simplify the situation considerably. Nevertheless, at small length scales ($\lesssim$5 nm) the approximation breaks down, and quantum mechanical effects must be included. Numerous electronic structure calculation schemes can be used to simulate optical excitations,[14] and in this work we use TDDFT.[15, 16]

2.1. Time-dependent density functional calculation scheme

In the time-dependent density functional method, one studies the electronic density under an influence of an external electric field. First, the ground state electronic structure is calculated by solving the Kohn-Sham orbitals $\phi_j(\mathbf{r})$ and energies ε_j from the eigenvalue equation

$$\left[-\frac{1}{2}\nabla^2 + V_{\mathrm{Hxc}}[\rho](\mathbf{r}) + V_{\mathrm{ext}}(\mathbf{r})\right]\phi_j(\mathbf{r}) = \varepsilon_j\phi_j(\mathbf{r}), \quad (1)$$

where the electronic density $\rho(\mathbf{r}) = \sum_j |\phi_j(\mathbf{r})|^2$ determines the Hartree-exchange-correlation potential $V_{\mathrm{Hxc}}[\rho](\mathbf{r})$ that includes all electron-electron interactions, and V_{ext} is the external potential. In the absence of external electric fields, the external potential contains only the Coulomb interaction between electrons and nuclei:

$$V_{\mathrm{ext}}(\mathbf{r}) = \sum_n \frac{-Z_n}{|\mathbf{r} - \mathbf{R}_n|}, \quad (2)$$

where $\mathbf{R}_n$ and Z_n are the position and charge of the n:th nucleus, respectively. Since $V_{\mathrm{Hxc}}(\mathbf{r})$ depends on the Kohn-Sham orbitals, Eq. 1 is solved iteratively. After obtaining the ground state, one can apply an external electric field to excite the system. The time evolution of the electron density then follows time-dependent Kohn-Sham equation

$$\left[-\frac{1}{2}\nabla^2 + V_{\mathrm{Hxc}}[\rho](\mathbf{r},t) + V_{\mathrm{ext}}(\mathbf{r},t)\right]\phi_j(\mathbf{r},t) = i\frac{\partial\phi_j(\mathbf{r},t)}{\partial t}. \quad (3)$$

The time-dependent density can be related to the material's optical constants through the (linear) response theory. For instance, the electric susceptibility χ is the linear response function between external potential and the induced density:

$$\delta\rho(\mathbf{r},t) = \int_{-\infty}^{t} dt' \int d^3\mathbf{r}'\chi(\mathbf{r},\mathbf{r}',t-t')\delta V_{\mathrm{ext}}(\mathbf{r}',t') + O(V_{\mathrm{ext}}^2). \quad (4)$$

The susceptibility is directly connected to the macroscopic dielectric function, photoabsorption spectrum, energy loss function, and other usual experimental observables.[17]

The practical implementation for calculating these quantities depends on the use of periodic boundary conditions and whether the response functions are solved in the time or in the frequency domain. For non-periodic systems, equations (3) and (4) can be directly solved in time domain for a specific external perturbation: To calculate the response to optical light, one excites the system by dipole electric field at all frequencies ω, using

$$\delta V_{\mathrm{ext}}(\mathbf{r},\omega) = -\mathbf{E}\cdot\mathbf{r}, \quad (5)$$

which is in the time domain $V_{\mathrm{ext}}(\mathbf{r},t) = -\mathbf{E}\cdot\mathbf{r}\delta(t)$. Then the photoabsorption spectrum is obtained from the Fourier tranformation of the time-dependent induced dipole moment $\delta\mu(t)$, i.e. the photoabsorption cross section is $\sigma_{\mathrm{abs}}(\omega) \propto \mathrm{Im}\,[\delta\mu(\omega)]$. The equivalent calculation for the photoabsorption spectrum can also be formulated in the frequency space by solving the induced dipole moment in terms of the electron-hole basis.[18]

For periodic systems, one can utilize the Bloch's theorem and the concept of the reciprocal space, so that all calculations consider only the unit cell of the system.[14] The density response function can then be written as

$$\chi(\mathbf{r},\mathbf{r}',\omega) = \frac{1}{N_q V}\sum_{\mathbf{qGG'}} e^{i(\mathbf{q}+\mathbf{G})\cdot\mathbf{r}}\chi_{\mathbf{GG'}}(\mathbf{q},\omega)e^{-i(\mathbf{q}+\mathbf{G'})\cdot\mathbf{r}'}, \quad (6)$$

where $\mathbf{G}$ and $\mathbf{G}'$ are reciprocal lattice vectors, $\mathbf{q}$ is a wave vector in the first Brillouin zone, N_q is the number of $\mathbf{q}$-vectors, and V is the unit cell volume. The density response function can be solved from the matrix equation

$$\chi_{\mathbf{GG'}}(\mathbf{q},\omega) = \chi^0_{\mathbf{GG'}}(\mathbf{q},\omega) + \sum_{\mathbf{G}_1\mathbf{G}_2}\chi^0_{\mathbf{GG}_1}(\mathbf{q},\omega)K^{\mathrm{Hxc}}_{\mathbf{G}_1\mathbf{G}_2}(\mathbf{q})\chi_{\mathbf{G}_2\mathbf{G'}}(\mathbf{q},\omega), \quad (7)$$

where χ^0 is the noninteracting density response function that can be evaluated from the ground-state Kohn-Sham orbitals and eigenvalues in a straightforward way, and K^{Hxc} contains all electron-electron interactions. After $\chi_{\mathbf{GG'}}(\mathbf{q},\omega)$ is solved, the inverse microscopic and the macroscopic dielectric functions can be calculated from

$$\epsilon^{-1}_{\mathbf{GG'}}(\mathbf{q},\omega) = \delta_{\mathbf{GG'}} + \frac{4\pi}{|\mathbf{q}+\mathbf{G}|}\chi_{\mathbf{GG'}}(\mathbf{q},\omega) \quad (8)$$

and

$$\epsilon_M(\mathbf{q},\omega) = \frac{1}{\epsilon^{-1}_{00}(\mathbf{q},\omega)}, \quad (9)$$

respectively.[17]

3. Calculations

The TDDFT calculations in this work are carried out using the open-source GPAW computer code.[19, 20] In GPAW the time-dependent wavefunctions, electron density, and potentials are expressed on uniform real space grid. The derivative operators are generated by the finite-difference method, and since they are almost local, the approach provides exceptionally good computational parallelizability. This formulation is similar to the finite-difference time-domain (FDTD) method that is widely used for solving

classical electrodynamics problems.[1] Another advantageous feature of GPAW is that only the valence electronic degrees of freedom need to be included in calculations. This is possible because the core electrons and the strong potential near the nuclei are treated with the projector-augmented wave method, which enables efficient calculations of the elements throughout the periodic table.[21] Using large supercomputers, GPAW can be applied to systems of thousands of valence electrons. Calculations can be done efficiently for molecules, surfaces, interfaces, as well as for crystalline materials, because the periodic boundary conditions can imposed in 0–3 directions.

In the beginning of the calculation, one must define system geometry (a set of atoms and their coordinates), spacing between grid points, and the calculation box size. If non-periodic boundary conditions are used, the time-dependent Kohn-Sham equations can be solved either in the time or in the frequency space.[18] With periodic boundary conditions, TDDFT calculation must be done in the frequency space.[17] In our present calculations we used the adiabatic local density approximation (ALDA) for including the exchange and correlation effects, i.e. for approximating V_{Hxc} and K^{Hxc} in Eqs. (1), (3), and (7). ALDA is based on the electron gas theory and in general it performs well for the plasmonic properties.[16]

3.1. Na chains

We carried out time-domain TDDFT calculations for isolated Na_N chains of up to $N = 22$. In these calculations, the non-periodic (zero) boundary conditions were imposed, the bond length was 2.89 Å, grid spacing was 0.30 Å, and 10.0 Å of vacuum was added around the atoms. The time propagation was followed up to 33 fs, which yields the energy resolution of ∼0.15 eV. The photoabsorption spectrum for infinitely long Na chain was calculated using periodic boundary conditions, 0.30 Å spacing, 24Å of vacuum, 30 k-points along the dimension of the chain axis, and with a large number of electronic bands.

3.2. Graphene nanoflakes

Frequency space TDDFT calculations were used to calculate the photoabsorption spectrum of isolated graphene nanoflakes of various sizes. Time-domain calculations yielded very similar spectra. Spacing between grid points was 0.32 Å, and the vacuum size around the system was 6.4 Å. The calculation of graphene nanoribbon was performed with the periodic boundary conditions using 30 k-points along the ribbon axis.

4. Results and discussion

Metal atom chains are the simplest atomistic systems that contain plasmon-type electronic excitations.[12] In Fig. 1 we show the optical response (photoabsorption spectrum) of these structures, and the electron density change that is associated with the L_0 resonance that dominates the low-energy region of the spectrum. The energy of this longitudinal excitation clearly redshifts with increasing chain length, as expected from the classical plasmon theory and previous works.[12] The density profile that is typical for nearly-free electron gas, is evident from the shown transition charge density. The red curve next to the transition density map shows the transition density integrated over the slice perpendicular to the chain. Its oscillations along the chain originate from the quantum mechanical treatment of the electrons, similar to the Friedel oscillations of the electron density near the surfaces or impurities of bulk metals.

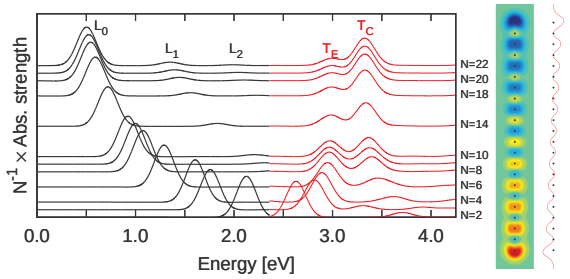


Figure 1: The photoabsorption spectrum of Na_N chains (left), separated into longitudinal (black) and transversal (red) parts, and the transition charge density of Na_{22} associated with the L_0 transition (right).

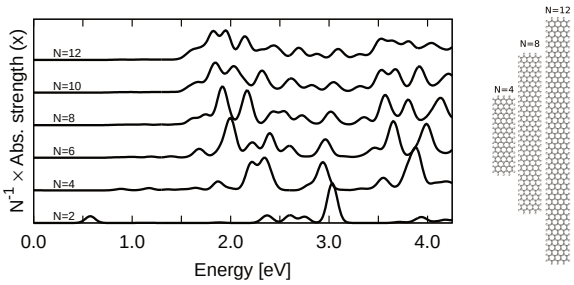


Figure 2: The length dependence of the photoabsorption spectrum of graphene nanoflakes, for the polarization along the long axis of the flake.

In addition to the metallic nanoclusters and wires, also many other types of nanostructures have tunable optical response. Graphene nanoflakes have attracted a wealth of interest lately, as their electrical and optical properties depend strongly e.g. on their size and termination type.[22, 23] Fig. 2 shows how the photoabsorption spectrum of graphene flakes changes as the length of the ribbon increases. The calculation demonstrates that the optical properties of graphene nanoflakes can be tailored systematically by changing the flake length. Flakes of various sized can actually be realized with chemical synthesization methods.[13]

We additionally analyze how the optical response of Na chains and graphene flakes behaves at the limit of infinite length, i.e. we used periodic boundary conditions in the elongated direction. The results are shown in Fig. 3.

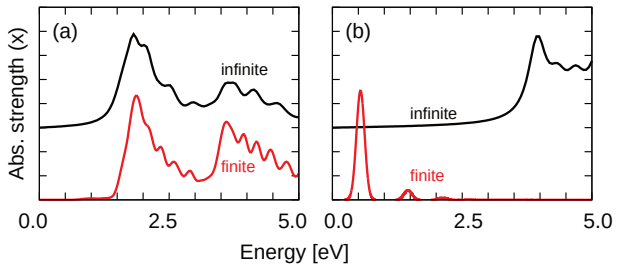


Figure 3: Photoabsorption spectrum along the long axis of the graphene nanoflake (a) and Na chain (b), with periodic boundary conditions (black curves) and finite system (red curves).

The optical spectrum of a large flake is very similar to the infinitely long ribbon: both systems show two main features at 1.9 eV and 3.6 eV. We thus conclude that tuning the optical properties of graphene flakes is only possible for relatively small flakes. In contrast to the graphene flakes, the photoabsorption spectrum of infinitely long Na chain is very different from the spectrum of Na_{20}. The difference between these two cases can be addressed to the different types of excitation: in contrast to a semiconducting graphene nanoribbon, Na chain is a metallic system that supports plasmonic resonances. Because light cannot couple with volume plasmons, it is not possible to directly observe plasmonic response by the photoabsorption spectroscopy.[24]

Thanks to the improving nanofabrication techniques, the need for including quantum effects in the optical materials design will keep increasing. In addition to the direct atomistic effects demonstrated here, electronic structure calculations can be useful in many related problems in nano-photonics and engineering. For example, the nonlocality of the dielectric response could be studied and parametrized using TDDFT, by exploring the $\mathbf{q}$-dependence of the density response function.[25] By combining quantum and classical electrodynamical simulations, one could describe on the same footing both the chemical and electrical effects that contribute in the surface enhanced Raman scattering technique.[9] Such a hybrid approach could be utilized also for studying the coupling of surface plasmons with light emitters.[26] Electronic structure calculations can also answer recently raised questions concerning the accuracy of the plasmonic simulations at the microscopic level. In particular, there is some evidence that reliable calculations of nearly touching silver contacts (where "charge transfer plasmon" appears) require more sophisticated approximations than ALDA for the electronic exchange and correlation.[27] This work paves way for studying these kinds of nano-optical phenomena with atomistic TDDFT simulations using the GPAW computer code. Free access, good performance, and user-friendly Python scripting interface make it an attractive tool for studying these effects.

Acknowledgement

We thank the Academy of Finland (Centres of Excellence Program) for the financial support, and Aalto Science-IT project and Finnish IT Center for Science (CSC) for computational resources.

References

[1] A. Taflove, S. C. Hagness *Computational Electrodynamics: The Finite-Difference Time-Domain Method, 3rd ed.*, Artech House, Norwood, MA, 2005.

[2] J. A. Scholl., A. L. Koh, J. A. Dionne, Quantum plasmon resonances of individual metallic nanoparticles, *Nature*, 483: 421, 2012.

[3] F. J. G. de Abajo, Nonlocal Effects in the Plasmons of Strongly Interacting Nanoparticles, Dimers, and Waveguides, *J. Phys. Chem. C* 112: 17983–17987, 2008.

[4] J. Zuloaga, E. Prodan, P. Nordlander, Quantum Description of the Plasmon Resonances of a Nanoparticle Dimer, *Nano Lett.* 9: 887–891, 2009.

[5] J. M. McMahon, S. K. Gray, G. C. Schatz, Nonlocal Optical Response of Metal Nanostructures with Arbitrary Shape, *Phys. Rev. Lett.* 103: 097403, 2009.

[6] S. M. Morton, D. W. Silverstein, L. Jensen, L., Theoretical Studies of Plasmonics using Electronic Structure Methods, *Chem. Rev.* 111: 3962, 2011.

[7] K. J. Savage, M. H. Hawkeye, R. Esteban, A. G. Borisov, J. Aizpurua, J. J. Baumberg, Revealing the quantum regime in tunnelling plasmonics, *Nature* 471: 574, 2012.

[8] D. C. Marinica, A. K. Kazansky, P. Nordlander, J. Aizpurua, A. G. Borisov, Quantum Plasmonics: Nonlinear Effects in the Field Enhancement of a Plasmonic Nanoparticle Dimer, *Nano Lett.* 12: 1333, 2012.

[9] S. M. Morton, L. Jensen, A discrete interaction model/quantum mechanical method to describe the interaction of metal nanoparticles and molecular absorption, *J. Chem. Phys.* 135: 134103, 2011.

[10] Y. Gao, D. Neuhauser, Dynamical Quantum-Electrodynamics Embedding: Combining Time-Dependent Density Functional Theory and the Near-Field Method, *J. Chem. Phys.* 137: 074113, 2012.

[11] J. L. Payton, S. M. Morton, J. E. Moore, L. Jensen, A discrete interaction model/quantum mechanical method for simulating surface-enhanced Raman spectroscopy, *J. Chem. Phys.* 136: 214103, 2012.

[12] J. Yan, Z. Yuan, S. Gao, End and Central Plasmon Resonances in Linear Atomic Chains, *Phys. Rev. Lett.* 98: 216602, 2007.

[13] J. Cai, P. Ruffieux, R. Jaafar, M. Bieri, T. Braun, S. Blankenburg, M. Muoth, A. P. Seitsonen, M. Saleh, X.Feng, K. Müllen, R. Fasel, Atomically Precise Buttom-Up Fabrication of Graphene Nanoribbons, *Nature* 466: 470, 2010.

[14] R. M. Martin, *Electronic Structure: Basic Theory and Practical Methods*, Cambridge University Press, 2004.

[15] E. Runge, E. K. U. Gross, Density-functional theory for time-dependent systems, *Phys. Rev. Lett.* 52: 997, 1984.

[16] *Fundamentals of Time-Dependent Density Functional Theory*, Eds. M. A. L. Marques, N. T. Maitra, F. M. S. Nogueira, E. K. U. Gross, A. Rubio, Springer, Heidelberg, 2012.

[17] J. Yan, J. J. Mortensen, K. W. Jacobsen, K. S. Thygesen, Linear density response function in the projector aufgmented wave method: Applications to solids, surfaces, and interfaces, *Phys. Rev. B* 83: 245122, 2011.

[18] M. Walter, H. Häkkinen, L. Lehtovaara, M. Puska, J. Enkovaara, C. Rostcaard, J. J. Mortensen, Time-dependent density-functional theory in the projector augmented-wave method, *J. Chem. Phys.* 128: 244101, 2008.

[19] J. Enkovaara, C. Rostgaard, J. J. Mortensen, *et al.*, Electronic structure calculations with GPAW: a real-space implementation of the projector augmented-wave method, *J. Phys.: Condens. Matter* 22: 253202, 2010.

[20] https://wiki.fysik.dtu.dk/gpaw/

[21] P. E. Blöchl, Projector augmented-wave method, *Phys. Rev. B* 50:17953, 1994.

[22] C. Cocchi, D. Prezzi, A. Ruini, M. J. Caldas, E. Molinari, Optical Properties and Charge-Transfer Excitations in Edge-Functionalized All-Graphene Nanojunctions, *J. Phys. Chem. Lett.* 2: 1315, 2011.

[23] C. Cocchi, D. Prezzi, A. Ruini, E. Benassi, M. J. Caldas, S. Corni, E. Molinari, Optical Excitations and Field Enhancement in Short Graphene Nanoribbons, *J. Phys. Chem. Lett.* 3: 924–929, 2012.

[24] C. Xia, C. Yin, V. V. Kresin, Photoabsorption by Volume Plasmons in Metal Nanoclusters, *Phys. Rev. Lett.* 102: 156802, 2009.

[25] A. Sakko, A. Rubio, M. Hakala, K. Hämäläinen, Time-Dependent Density Functional Approach for the Calculation of Inelastic X-Ray Scattering Spectra of Molecules, *J. Chem. Phys.*, 133: 174111, 2010.

[26] D. E. Chang, A. S. Sorensen, P. R. Hemmer, M. D. Lukin, Strong coupling of single emitters to surface plasmons, *Phys. Rev. B* 76: 035420, 2007.

[27] G. T. Bae, C. M. Aikens, TDDFT and CIS Studies of Optical Properties of Dimers of Silver Tetrahedra, *J. Phys. Chem. A* 116: 8260, 2012.

Optical Forces Induced by Metal Nanoparticle Clusters

Jordi Sancho-Parramon[1,2*], Salvador Bosch[2]

[1]Rudjer Boskovic Institute, Zagreb, Croatia
[2]Applied Physics and Optics Department, University of Barcelona, Barcelona, Spain
*corresponding author, E-mail: jsancho@irb.hr

Abstract

The strong field localization generated between closely placed metal particles excited by electromagnetic radiation induces intense forces on small polarizable objects. In this study we investigate the optical forces that can be generated in the vicinity of metal nanoparticle clusters using fully electrodynamic numerical simulations. The influence of the cluster configuration as well as of the excitation parameters is analyzed.

1. Introduction

Optical trapping appears to be a promising way to control the position of small objects with nanometric precision. In this sense, optical tweezers have been shown to be a useful tool to trap objects in the focal region of tightly focused beams [1]. The key issue is the gradient of electromagnetic field generated at the focus that induces a dipole force on polarizable particles. This force, proportional to the field intensity gradient, drives the particles towards the region where the field is largest. However, due to the diffraction-limited field distribution that can be achieved with conventional optics, nanometric control of the position of small objects requires large laser power beams. Such requirement is not suitable for objects that might be damaged when exposed to strong irradiation, for instance, biological samples.

In order to surpass this restriction, the use of optical near-fields for trapping has been proposed as alternative, since near-field distributions are not diffraction-limited. In this sense nanometric optical tweezers have been suggested for precise trapping of very small objects based on the strong field gradient generated around nanoparticle surfaces [2]. Using this principle, nanoscale control of objects has been experimentally demonstrated at nanostructured substrates containing metal particle pairs [3,4] enabling even stacking and sorting of objects [5]. Such trapping configurations exploit the strongly enhanced and localized near field generated at the gap between particles as result of the coupling of individual particle plasmon resonances [6].

In the present study we analyze the potential of metal clusters for efficient optical trapping of small objects. In particular, we focus on the influence of different configurations of particle pairs and of the characteristics of the radiation exciting the cluster. The evaluation of the potential for trapping for each configuration is performed by calculating the near field distribution in the cluster structure. For this purpose we use fully electrodynamic simulations, i.e., a generalized Mie theory that can take into account different particle clusters and illumination conditions. The numerical simulations evidence how the trapping potential of focused beams can be boosted by the presence of metal nanoparticles in the focal region and aid in choosing the best particle configurations for optimal trapping.

2. Theory

A general sketch of the system investigated is shown in Fig. 1. We assume a plane wave travelling in the $-z$ direction with a wave-vector (0, 0, $-k$) and focused by an aplanatic lens with numerical aperture NA = $n_m \cdot \sin \alpha$ where n_m is the refractive index in the image space and α is the angular semi-aperture of the lens. The presence of a cluster of small particles and an object to be trapped in the focal region may significantly modify the incident electromagnetic field distribution. The focus of the system is located at $x = y = z = 0$. In order to evaluate how an object can be trapped it is necessary to compute: i) the field distribution of the focused plane wave, ii) the electromagnetic response of the cluster of particles and the object to be trapped to this incident field distribution, and iii) the force exerted by the resulting total field distribution on the object to be trapped.

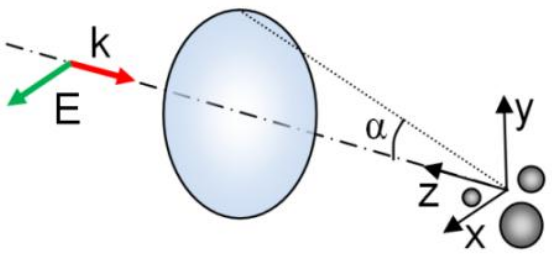


Figure 1: Scheme of the system considered in the numerical simulations. A cluster of particles located in the focal region of a lens is excited by the incident focused beam.

2.1. Focal field distribution

The distribution of light in the focal region of a high numerical aperture lens can be calculated using the Richards-Wolf theory [7]. Imposing the aplanatism condition, the electric field at a point **r** in the focal region, $\mathbf{E_f}$, can be computed with the following diffraction integral:

$$\mathbf{E_f}(\mathbf{r}) = \frac{-i}{\lambda}\int_0^{\alpha} d\theta \sin\theta \int_0^{2\pi} d\phi \mathbf{E}_{ref} \exp(-i\mathbf{k}\cdot\mathbf{r}), \quad (1)$$

where λ is the vacuum wavelength and $\mathbf{E}_{ref}$ is the field refracted by the lens that can be calculated from the incident plane wave by geometrical optics. **k** is a wavector with module *k* and with direction given by (θ, ϕ), that are the polar and azimuthal angles in a spherical coordinate system. Actually, the above diffraction integral is the angular spectrum representation of the focal field, i.e., the field at focus can be interpreted as a sum of plane waves with polarizations and weights determined by the propagation direction [8].

2.2. Electromagnetic response of particles

The interaction of a cluster of arbitrary sized and shaped particles with electromagnetic radiation is a complex problem that usually can be only solved by numerical resolution of Maxwell equations. However, if the particles of the cluster and the object to be trapped are spherical, the solution can be found in a in a semi-analytical way using the generalized Mie theory [9]. Briefly, the incident, scattered and internal fields are expanded in vector spherical harmonics, that are combination of spherical harmonics and Bessel functions. Then, imposing boundary conditions at the surface of every particle, the expansion coefficients of the scattered and internal fields can be calculated from those of the incident field by solving a linear system of equations. In order to solve this system of equations is necessary to use vector addition theorems that connect vector spherical harmonics with different origins, i.e., particle centers. The dimension of the system of equations is determined by the number of terms in the field expansion. Therefore, the higher accuracy is required, the larger the size of the system of equations and thus, the computational load.

The expansion coefficients for an incident plane wave are well known [9]. Generally speaking, for an arbitrary field distribution is always possible to find the expansion coefficients numerically [10]. Nevertheless, for a focused field distribution given by Eq. 1, different authors have proposed multipole expansions of the diffraction integral for linearly polarized plane waves [11] or cylindrical vector beams [12] illuminating the lens. These expansions can be easily related to the vector spherical harmonics expansion used in the generalized Mie theory. We have recently used such expansions to analyze plasmon coupling in tightly focused beams [13-14].

2.3. Calculation of forces and related parameters

Once the electromagnetic field distribution is known, the time-averaged force acting over an object is given by [8]:

$$\langle \mathbf{F} \rangle = \int_S \langle \vec{\vec{\mathbf{T}}} \rangle \cdot d\mathbf{s} \quad (2)$$

where $\langle \vec{\vec{\mathbf{T}}} \rangle$ is the time-averaged Maxwell stress tensor and the integral is performed over a surface enclosing the object. The Maxwell stress tensor can be directly calculated from the electromagnetic field as:

$$\vec{\vec{\mathbf{T}}} = \left[\varepsilon_m \mathbf{E}\otimes\mathbf{E} + \mu_m \mathbf{H}\otimes\mathbf{H} - \frac{1}{2}\left(\varepsilon_m E^2 + \mu_m H^2\right) \vec{\vec{\mathbf{I}}} \right], \quad (3)$$

where **E** and **H** stand for the electric and magnetic fields, *E* and *H* are their magnitudes and ε_m and μ_m the medium permittivity and permeability. Alternatively, a simplified computation framework can be used if the particle to be trapped is much smaller than the wavelength and the field acting over the particle can be locally approximated to a plane wave. If, in addition, the particle is non-absorbing, the average force can be calculated as [15]:

$$\langle \mathbf{F} \rangle = \frac{\alpha n_m}{2c} \nabla I_{exc}, \quad (4)$$

where *c* is the speed of light in vacuum, I_{exc} is the intensity of the electromagnetic field exciting the particle (i.e., without the presence of the particle) and α is the particle polarizability, that can be calculated from the Clausius-Mossotti relation:

$$\alpha = 3V \frac{\varepsilon_p - \varepsilon_m}{\varepsilon_p + 2\varepsilon_m}, \quad (5)$$

with *V* being the particle volume and ε_p the particle permittivity. Equation 4 represents the gradient force and states that small particles are driven to the regions with largest field intensity. Around this equilibrium position, the restoring force exerted on the particle has a linear dependence with small displacements Δx, enabling to define the trap stiffness as:

$$k_{trap} = -\frac{\langle \mathbf{F} \rangle}{\Delta x} \quad (6)$$

In addition, an important parameter to quantify the stability of the optical trap to Brownian motion is the trapping potential, defined as the work that has to be done to bring a particle from a given position $\mathbf{r_0}$ to infinity:

$$U(\mathbf{r_0}) = -\int_{\infty}^{\mathbf{r_0}} \langle \mathbf{F} \rangle \cdot d\mathbf{r} \quad (7)$$

Finally, a convenient way to quantify how effective is a given illumination configuration for work as an optical trap is the trapping efficiency, **Q**, defined as:

$$\mathbf{Q} = \langle \mathbf{F} \rangle \frac{c}{n_m P_{inc}} \quad (8)$$

where P_{inc} is the power of the incident beam.

3. Results and discussion

In the following we shall assume that the radiation illuminating the lens is a plane wave linearly polarized in the *x*-direction and with λ = 1064 nm. The power incising on the lens is set to 100 mW. The object to be trapped is a small sphere with radius 1 nm and refractive index 1.5. The medium in the image space is assumed to be water (n_m = 1.33). For the cluster of particles we consider Au with complex refractive index 0.26+6.97i at the radiation wavelength. We observed that for all the studied cases, there are no significant differences when the force acting on the glass particle is calculated either by Eq. 2 or Eq. 4.

3.1. Focused beam trapping vs. plasmon field trapping

First, we aim to illustrate the enhancement of trapping by a focused beam if the strong near field associated to the plasmon resonance is used. Fig.2 shows the intensity of the incident beam at the focal plane (left) for a lens with NA = 1.2 and the total field when two gold particles with radius *R* = 80 nm and interparticle distance *d* = 20 nm are located over the *x*-axis, i.e., at *x* = ± 90 nm, *y* = *z* = 0. The strong electromagnetic coupling between the particles [13] results in charge accumulation in the zones where the particles are facing each other and the formation of a hot-spot, i.e., region of nanometric dimensions and a large field enhancement (over two orders of magnitude with respect to the incident field intensity for the given configuration).

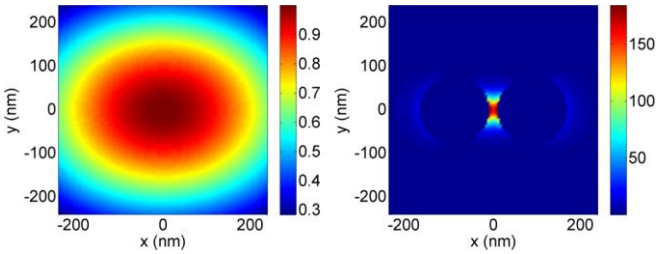


Figure 2: Intensity (a.u.) distribution at the focal plane for the incident focused beam (left) and with the presence of the Au particles (right).

The large intensity gradient that can be achieved by plasmon coupling compared to the one that can be attained by conventional focusing gives place to much stronger forces, as shown in Table 1, where several force-related parameters are compared when the glass 1-nm particle is located over the *y*-axis of the focal plane.

Table 1: Optical trapping parameters for 1 nm glass particle (see text for details on illumination)

	no Au particles	with Au particles
k_{trap} (pN/μm)	2.2x10^{-5}	0.32
Q_y (maximum)	7.2e-9	9.7e-6
U_{min} (in k_BT) (T = 300 K)	-2.87e-5	-0.0373

3.2. Illumination conditions

The influence of the degree of focusing on the trapping efficiency is shown in Fig.3. The configuration is the same as described in the previous section and the only parameter that is changed is the numerical aperture of the system. For a focused beam, weaker focusing leads to lower intensity gradient and, therefore, to smaller optical force. In addition, the position where force is maximal, i.e., where the intensity gradient is largest, varies with the dimension of the focal spot size, that increases as the NA is reduced. This is not the case for the plasmon-based trapping, where the position where the force is maximal is entirely dictated by the spatial extension of the hot-spot. The absolute value of the force also decreases when the NA of the system is lowered. Since the field enhancement is nearly independent of the NA, the force decrease can be basically associated to the lower incident field intensity at the focus when the NA of the system is reduced. Indeed, it appears that tight focusing is not requested to enable trapping of small particles by plasmon coupling, as even under standard illumination conditions, trapping of molecules can take place if the space between metal particles is in the range of few nanometers, leading to a field enhancement of several orders of magnitude [16].

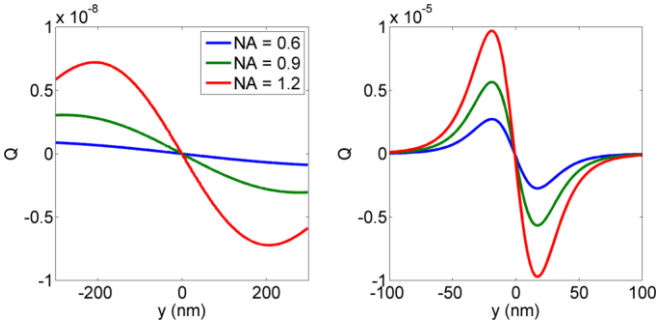


Figure 3: NA dependence of the trapping efficiency for a 1 nm glass particle located on the *y*-axis of the focal plane without (left) and with (right) the presence of Au particles.

We have also investigated other illumination conditions, such as different linearly polarized plane waves or cylindrical vector beams, but it appears that the largest gradient, and therefore, force, is always achieved through the hot-spot generated by a polarization parallel to the particle pair.

3.3 Cluster configuration

Finally, we study the effect or re-scaling the dimensions of the Au pair of particles. Thus, in addition to the above configuration with particle radius *R* = 80 nm and interparticle distance *d* = 20 nm, we consider also the case with *R* = 40 nm and *d* = 10 nm and *R* = 20 nm and *d* = 5 nm, i.e., the whole system is re-scaled a factor 2 and 4. The wavelength dependence of the magnitude of the field enhancement at the focus (between the particles) is shown in Fig. 4. The maximum of field enhancement is associated to the excitation of the coupled plasmon mode, which shifts

to longer wavelength the larger the particle. On the other hand, due to radiative damping, large particles give place to a reduced near-field enhancement in comparison with small particles. In addition, decreasing the interparticle distance amplifies the coupling strength and gives place to larger field enhancements [17]. Overall, the maximum field enhancement at the wavelength considered in the present simulations is obtained with the R = 80 nm, d = 20 nm configuration.

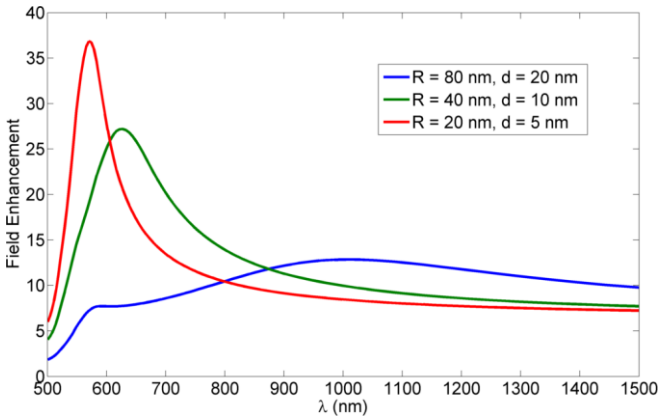


Figure 4: Electric field enhancement at the focus when different Au particle pairs are located over the x axis of the focal plane ($x = \pm(R + d/2)$, $y = z = 0$).

The trapping efficiency and optical trapping potential of these different particle pairs is shown in Fig. 5. Although the field enhancement is lower for smaller particle pairs, the maximum force is larger since the size of the hot spot is reduced and therefore the intensity gradient can be larger than for bigger particles [18]. On the other hand, a smaller spatial extension of the trapping region leads to a narrower, but also smaller in magntiude, optical trapping potential.

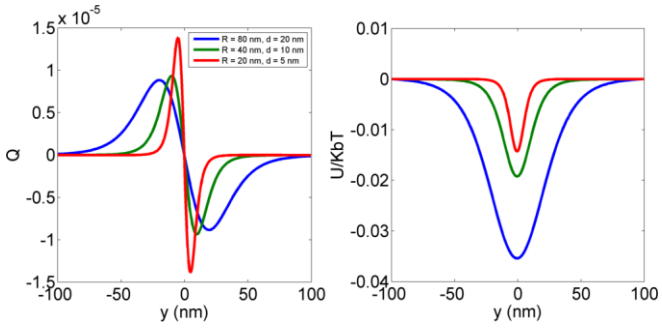


Figure 5: Trapping efficiency (left) and optical trapping potential (right) for different Au particle pairs configurations located over the x axis of the focal plane ($x = \pm(R + d/2)$, $y = z = 0$).

4. Conclusions

The potential of plasmon coupling for trapping of nanometric sized objects has been investigated by numerical simulations. Our approach takes into account with no approximation: i) the description of focused light as field exciting the metal nanoparticles, ii) the modification of this field distribution by the electromagnetic response of the metal nanoparticles and iii) the forces exerted over a small dielectric particle. It is shown that the strong field gradients generated by plasmon coupling and that are confined in nanometric-sized regions lead to optical forces that are several orders of magnitude larger than those that can be obtained in absence of the metal particles. In addition, the influence of the illumination conditions and of the cluster dimensions enables to elucidate what system configurations are more suitable for optimizing the trapping of nano-objects.

Acknowledgements

JSP acknowledges the financial support of the Government of Catalonia through a Beatriu de Pinós post-doctoral grant. The authors also acknowledge the support of the project FIS2012-38244-C02-02 of the Spanish Ministry of Economy and Competitivity.

References

[1] A. Ashkin, Acceleration and trapping of particles by radiation pressure, *Phys. Rev. Lett.* 24: 156–159, 1977.

[2] L. Novotny, R. X. Bian, and X. S. Xie, Theory of nanometric optical tweezers, *Phys. Rev. Lett.* 79: 645–648, 1970.

[3] A. N. Grigorenko, W. Roberts, M. R. Dickinson, and Y. Zhang, Nanometric optical tweezers based on nanostructures substrates, *Nat. Photonics* 2: 365–670, 2008

[4] M. Righini, P. Ghenuche, S. Cherukulappurath, V. Myroshnychenko, F. J. García de Abajo, and R. Quidant, Nano-optical Trapping of Rayleigh particles and Escherichia coli bacteria with resonant optical antennas, *Nano Lett.*, 9: 3387–3391, 2009.

[5] B. J. Roxworthy, K. D. Ko, A. Kumar, K. H. Fung, E. K. C. Chow, G. L. Liu, N. X. Fang, and K. C. Toussaint, Jr, Application of plasmonic bowtie nanoantenna Arrays for optical trapping, stacking, and sorting, *Nano Lett.* 12: 796-801, 2012.

[6] J. R. Krenn, A. Dereux, J. C. Webber, E. Bourillot, Y. Lacroute, J. P. Goudonnet, G. Schider, W. Gotschy, A. Leitner, F. R. Aussenegg, amd C. F. R. Girard, Squeezing the optical near-field zone by plasmon coupling of metallic nanoparticles, *Phys. Rev. Lett.* 82: 2590–2593, 1999.

[7] B. Richards and E. Wolf, Electromagnetic diffraction in optical systems. II. Structure of the image field in an aplanatic system. Proc. Royal Soc. Lond. 253(1274): 358-379, 1959.

[8] L. Novotny and B. Hecht. *Principles of Nano-optics*. Cambridge university press, 2006.

[9] J. M. Gérardy and M. Ausloos, Absorption spectrum of clusters of spheres from the general solution of

Maxwell's equations. II. Optical properties of aggregated metal spheres, *Phys. Rev. B* 25: 4204-4229, 1982.

[10] C. F. Bohren and D. R. Huffman, *Absorption and scattering of light by small particles*. Wiley-Vch, 2008.

[11] C. J. R. Sheppard and P. Török, Efficient calculation of electromagnetic diffraction in optical systems using a multipole expansion, *J. Mod. Optics* 44:803-818, 1997.

[12] R. Borghi, M. Santarsiero, and M. A. Alonso, Highly focused spirally polarized beams, *J. Opt. Soc. Am. A*, 22:1420-1431, 2005.

[13] J. Sancho-Parramon, Near-field coupling of metal nanoparticles under tightly focused illumination, *Opt. Lett*. 36:3527-3529, 2011

[14] J. Sancho-Parramon and S. Bosch., Dark modes and Fano resonances in plasmonic clusters excited by cylindrical vector beams, *ACS nano 6:8415-8423*, 2012.

[15] A. Rohrbach and E. Stelzer, Optical trapping of dielectric particles in arbitrary fields, *J. Opt. Soc. Am. A*, 18:839-853 (2001).

[16] H. Xu and M. Käll, Surface-plasmon-enhanced optical forces in silver nanoaggregates, *Phys. Rev. Lett.* 89:246802, 2002.

[17] U. Kreibig and M. Vollmer, *Optical properties of metal clusters*, Springer Series in Materials Science, 1995.

[18] A. A. E. Saleh and J. A. Dionne, Toward efficient optical trapping of sub-10-nm particles with coaxial plasmonic apertures, *Nano Lett.* 12:5581-558, 2012.

Dielectric Sensing based on Energy Tunneling in Wire-loaded Microstrip Cavities

Abdullah Nauroze[1], Omar Sidiqui [2*], Rashad Ramzan[3], and Omar Ramahi[4]

[1]National University of Computer and Emerging Sciences (FAST-NU), Islamabad-44000, Pakistan
[2]Taibah University, Madinah, Saudi Arabia
[3]United Arab Emirates University, AlAin-15551, UAE
[4] University of Waterloo, Waterloo, Ontario, Canada
*corresponding author, E-mail: omarsiddiqui2@gmail.com

Abstract

The electromagnetic energy tunneling which takes place in narrow channels and bends loaded with epsilon-near-zero materials or resonant wires is accompanied by very intensive electric fields. The resulting transmission response is, therefore, highly frequency selective. Hence such configurations can be employed in highly sensitive dielectric detection. In this paper, the energy tunneling set-up is created in a microstrip environment using resonant wires. The dependence of various wire and microstrip parameters on the sensitivity of the sensor is studied. The microstrip technology, compared to the rectangular waveguides, is low cost, robust, easily manufactured and suitable for planar integration.

1. Introduction

The dispersion regimes supporting energy tunneling are identified by diminishing group velocities along one of the structure's axes of symmetry and the flatness of the dispersion surfaces, leading to permittivities that are close to zero. Hence such materials have also been termed as epsilon-near-zero materials (ENZ) [1-3]. When these materials are interfaced with free space, a strongly directive electromagnetic propagation is observed where energy tunnels or squeezes through sub-wave length apertures [1-3]. The property of high field build-up in these narrow channels can be exploited to obtain highly sensitive dielectric sensors [4]. A rectangular waveguide arrangement that supports energy tunneling is depicted in Fig. 1a. It is a 180^o short-circuited bend where two rectangular waveguides are connected through a narrow aperture 'A' filled with an ENZ material [5]. More recently, analogous energy-tunneling effects have also been observed in waveguide bend loaded with wires. The metallic wires, in such configuration are directed parallel to the electric (E) field [6]. It can be inferred, at least in a qualitative manner, that the tunneling can also take place in other guided media when the wires are placed to match the direction of dominant electric field component. To support this argument, a microstrip structure is studied which is formed by placing two microstrip transmission lines on top of each other with a common ground, as shown in Fig. 1b. The wire is placed in front of the conductor backing inside the aperture that connects the two microstrip lines.

Two simulation studies are performed using Agilent's HFSS, first with the air substrate and second with a Rogers

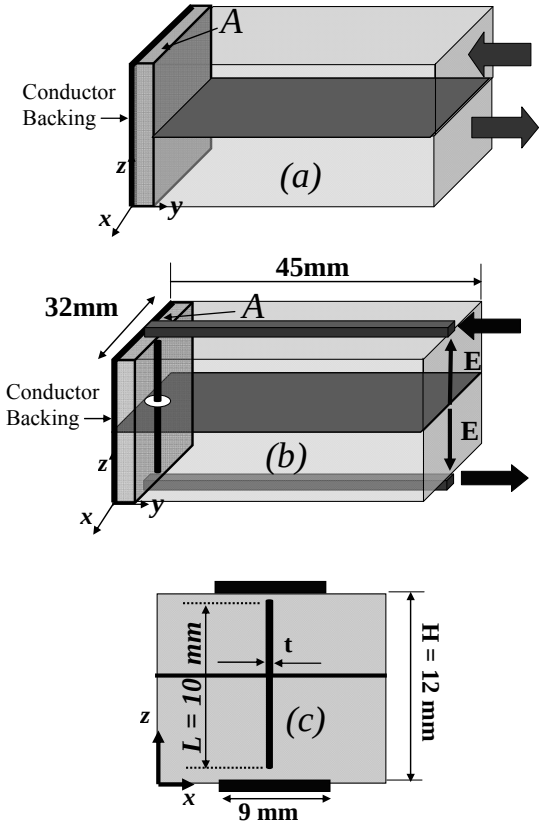


Figure 1: (a) Two short-circuited wave guides connected with ENZ material and (b) Side view of views of the proposed microstrip wire-loaded structure. (c) Back view of the microstrip structure with t=80μm

6002 (ε_r = 2.95) for the dimensions depicted in Fig. 1 (b and c). As depicted in Fig. 2, the proposed cavity indeed supports the tunneling mode that is highly sensitive to the dielectric material that fills the cavity. A resonance frequency shift of −1.335 GHz is noted for the permittivity shift +1.95. This resonance shift is due to the change in the effective length of the same physical metallic wire in the new dielectric environment. Simulation studies are performed to determine and characterize the geometric parameters of the microstrip structure that affect the sensitivity. The knowledge of these parameters will serve as basis to design a practical sensor exploiting the existence of

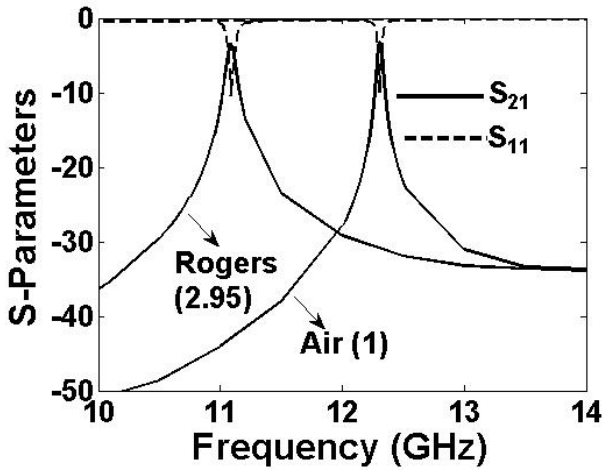


Figure 2: Simulation Results for the microstrip structure (Fig.1) with air and rogers as substrate.

energy tunneling phenomenon in microstrip structures. The microstrip transmission lines are planar, rugged, much easier to fabricate, extremely low cost, and easily excitable compared to the rectangular waveguides.

2. A Practical Sensor Design

Since electric fields are concentrated in the region closed to the wire [5], it is not required to replace the whole cavity with the dielectric sample whose permittivity is to be measured. Instead, a smaller sample can be placed in such a way that it fills some of the aperture 'A' (see Fig. 1b). Consider the RT Duroid cavity simulated in Section 1. With the given dimensions, each of the microstrip line has a standard characteristic impedance of 75Ω. The coaxial cables and SMA connectors are available in both flavors of 50Ω and 75Ω standard impedances. We selected 75Ω as it gives microstrip dimensions which are more manufacturing friendly compared to dimensions dictated by 50Ω standard impedance.

Taking into consideration the practical implementation constraints, two cylindrical sections representing the dielectric samples are introduced on each side of the metallic wire, as depicted in Fig. 3. In practice, these cylinders will serve as cavities to house dielectric samples and can be drilled from the upper to the lower microstrip line in the form of through-hole PCB vias. To demonstrate the sensor operation, the cylinders are considered to be made up of air. Replacing some parts of the Rogers 6002 material with air cylinders corresponds to decreasing the aperture's cumulate effective permittivity. This localized change is in permittivity effects the intense electric field coupled (tunneled) through the wire placed between upper and lower microstrip at the far end thus changing the resonance frequency of the tunneled energy. The transmission coefficients (S_{21}) are simulated for the two cases depicted as shown in Fig. 3. Consider the first case in which two air cylinders placed close to the microstrip edges (Fig. 3a), each having a volume ($\pi w^2 H/4$) of 0.54 mm^3 . A resonance frequency shift from 11.08 GHz to 11.16 GHz is observed in Fig. 4. Note that this 70 MHz frequency shift is obtained by a mere 0.0031% volume perturbation to the overall cavity volume (32x45xH mm^3). When the air cylinders are moved closer to the wire at distance of 1.75mm compared to 3.5mm in last case, the resonant frequency shift increases from 70MHz to 240MHz. The result is expected since the cylinders close to the wire perturb the stronger electric fields compared to the same size cylinders placed further away.

3. Sensitivity Analysis

In this section, a parametric study is presented to show the effect of different parameters on the sensor's performance. Consider the effect of increasing the sample's volumetric perturbation on the sensitivity of detection system. This is done by increasing the numbers of air cylinders around the energy tunneling wire. In comparative study four uniformly spaced air cylinders are placed at 1.75mm and compared with the two air cylinders placed at

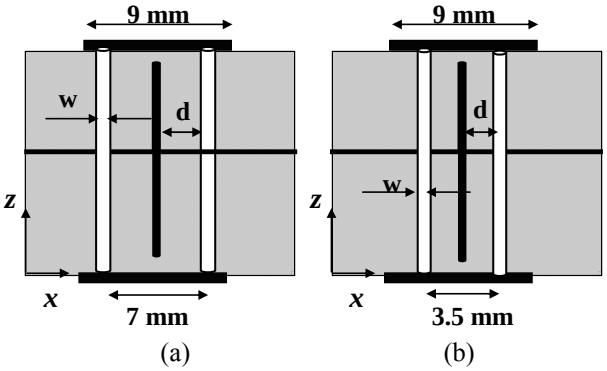


Figure 3: Two air cylinders (w = 240μm) representing the dielectric samples are placed at different distances from the wire (a) d = 3.5mm (b) d = 1.75mm

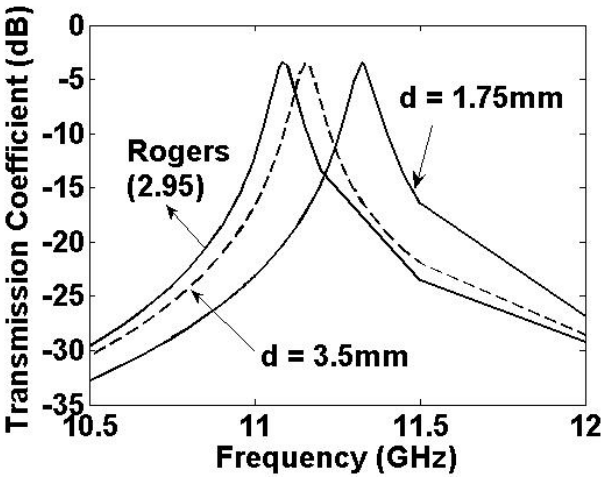


Figure 4: Simulation Results for the Rogers microstrip cavity perturbed by two air cylinders located at a distance of 1.75mm and 3.5mm from the wire

3.5mm distance from the wire as shown in the inset of Fig. 5. It is worth noting that the resonant frequency for four uniformly spaced air cylinders with distance d=1.75mm is almost same as for two cylinders placed at the same distance from the wire. This is due to stronger electric field coupling between the wire and the nearby air cylinders as compared to ones placed further away. However, the operational bandwidth remains constant in both cases.

Now let's consider a case when multiple equally spaced wires of same dimensions are placed in the microstrip structure (see inset of Fig. 6). An increase in operational bandwidth is noticed as the number of wires is increased. This bandwidth increase is the result of the lesser field concentration on individual wires as the power is now tunneled through multiple wires. Moreover, multiple resonances are observed because all the wires do not experience the uniform field due to the nature of quasi-TEM fields that are set up in a microstrip environment compared to pure TEM transmission in parallel-plate waveguides. To further increase the bandwidth, multiple wires of different lengths can be placed in the cavity. Consider the case when a second wire of 7.5mm is placed parallel to the 10mm wire in the microstrip cavity. The s-parameters plotted in Fig. 7 show and an additional resonance at a frequency of approximately 18 GHz. This additional resonance can be arbitrarily placed at a desire frequency location which depends on the samples' permittivities and length of the tunneling wire.

4. Conclusions and Future Work

In this paper, a novel dielectric detection system is presented which is designed by exploiting the wire-based energy tunneling in microstrip transmission line structures. It has been shown that energy tunneling phenomenon is narrow band and highly frequency sensitive due to an intense concentration of electric fields around the metallic wire which is placed in two top and bottom microstrip at far end without physically shorting the microstrips. Full-wave electromagnetic simulations are done to carry out a sensitivity analysis which shows the methods and paremeters to further improve and refine the physical design of the sensor.

We are now in process of manufacturing a physical sensor using conventional low cost PCB technology. The current hurdles are non-standard PCB thickness and design of a convenient mechanism to launch EM test signal in 9mm wide microstrip transmission line using of-the-shelf standard SMA connectors without reflection.

References

[1] A. Alu and N. Engheta, "Light Squeezing through Arbitraily Shaped Plasmonic Channels and Sharp Bends," Physical Review B, vol. 78, pp. 035440-035445, July 2008.

[2] A. Alu, M. Silveirinha, and N. Engheta, "Transmission-Line Analysis of Epsilon-Near-Zero (ENZ)-Filled Narrow Channels" Phsyical Review E, Vol. 78, 016604 (10 pages), 23 July 2008.

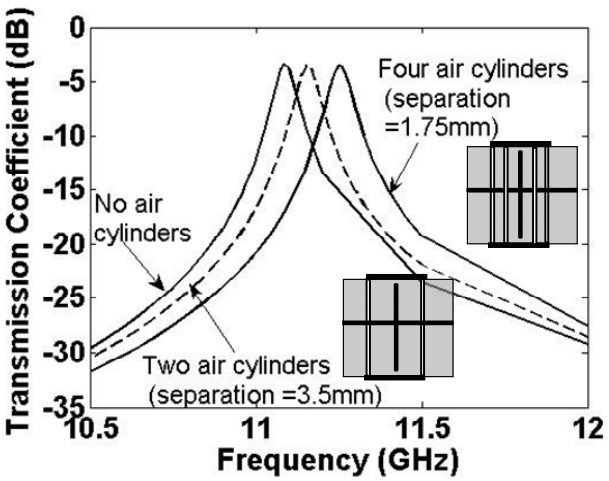


Figure 5: S- parameters for microstrip cavity perturbed by different number of uniformly spaced air cylinders.

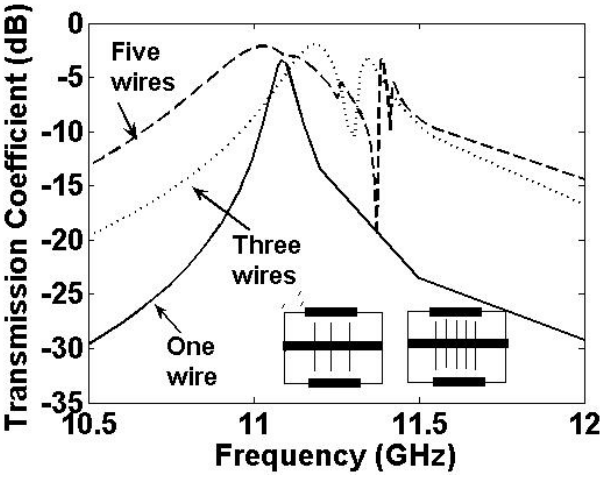


Figure 6: Transmission coefficients (S_{21}) for microstrip cavity with different number of uniformly spaced wires

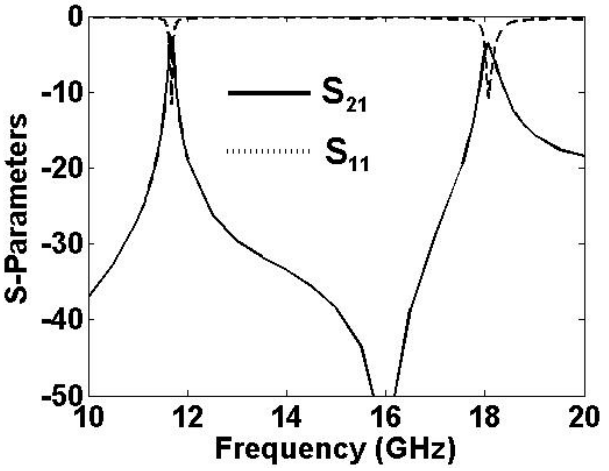


Figure 7: Effect of number of wires of different length on the resonances frequency of microstrip structure

[3] M. G. Silveirinha and N. Engheta, “Theory of supercoupling, squeezing wave energy, and field confinement in narrow channels and tight bends using epsilon near-zero metamaterials” Phys. Rev. B., vol. 76, no. 24, , pp. 245109 (1) -245109(17), Dec. 2007Y. Kawaguchi, T. Tsukahara, M. Motozawa, Experimental and numerical investigations of turbulent drag reduction phenomena by additives, *Proc. ASCHT09*, Jeju, Korea, pp. 23−32, 2009.

[4] A. Alu and N. Engheta, "Dielectric Sensing in Epsilon-Near-Zero Narrow Waveguide Channels," Physical Review B, Vol. 78, 045102 (5 pages), July 3, 2008.

[5] M. G. Silveirinha and N. Engheta, “Tunneling of Electromagnetic Energy through Sub-Wavelength Channels and Bends Using Epsilon-Near-Zero (ENZ) Materials,” Phys. Rev. Lett., vol. 97, no. 15, pp. 157403-157406, October 2006.

[6] O.F. Siddiqui and O. Ramahi,, "A Novel Dielectric Detection System Based on Wire-Loaded Waveguides", IEEE Microwave and Wireless Components Letters, vol. 21, no.2 ,Feb. 2011.

Hybrid and quantum materials

The Influence of Debonding on The Mechanical Properties of Hybrid Nanocomposites

Waleed K. Ahmed[1,*]

[1]Faculty of Engineering, United Arab Emirates University, Al Ain, UAE
*corresponding author, E-mail: w.ahmed@uaeu.ac.ae

Abstract

The present investigation explores the impact of the debonding in a hybrid nanocomposite on the mechanical properties under elastic condition. 3D-axisymmetric finite element model of a representative volume element is adopted in the analysis. Mainly, RVE is consist of carbon nanofiber confined by matrix and subjected to axial tension. Moreover, a longitudinal debonding is proposed along the interfacial nanofiber/matrix, modeled and investigated. As a result, FE results demonstrate a significant influence of the debonding on the mechanical properties..

1. Introduction

Nanocomposites are a novel class of composite materials where one of the constituents has dimensions in the range 1–100 nm [1]. They can be produced by embedding reinforcement in the form of nanofibres or nanotubes in a matrix such as a polymer in a similar manner to conventional composite materials [2]. Nanocomposites is considered as one of the growing areas of nanotechnology, since CNTs have remarkable mechanical properties and is intensively used as reinforcements in polymers and other matrices to form what is nowadays is called "Nanocomposite materials"[3]. Nanofibers in general, and the nanotubes in particular, can be hundred times stronger than steel and even more than six times lighter, become as a candidate for aerospace application [4].Moreover, nanotubes show increasing in composite strength by as much as 25% [5]. Nanocomposites' reinforcement can include nanofibers, nanoplatelets and nanoclay. These reinforcements are functionalized with additives, by this means resulting in a strong interfacial bond with the matrix [1]. Mainly, there are three mechanisms of interfacial load transfer between nanofiber and the matrix, which are the weak van der Waals force and the reinforcement, chemical bonding, and micromechanical interlocking [6]. Mainly, there are two causes behind a mechanically strong or weak nanocomposite material which affects the stiffness, the matrix interface with the nanofibres and the stress transfer. As the nanocomposite subjected to mechanical loading, stress concentrations will take place at the matrix/nanofibre interface which will eventually lead weakness of the nanocomposite and eventually lead to damage nucleation, initiation, growth and final non-tolerated failure [7]. There are two probable sources of damage nucleation in nanocomposites; poor wetting of the nanofibres by the polymer and the aggregation of the nanofibres [8]. Both cases produce polymer rich nanocomposite portions that are likely to experience low stress to failure. Researchers [9] have observed that one of the reasons that nanocomposites may have a low strain to failure is the high interfacial stress that can lead to nanofibre/matrix debonding. In addition, the stress transfer from the matrix to the reinforcement is the main factor that will dictate the final nanocomposite material strength. It is reported that load transfer through a shear stress mechanism was observed at the molecular level [1]. Moreover, local interfacial properties affect the macrolevel material behavior, like reduction in flexural strength in nanotube/epoxy composite beams due to weakly bonded interfaces [10], as well the reduction in composite stiffness which was attributed to local nanofibers/ nanotube waviness [11], whereas the impact of the nanoholes presence [12], nanoinclusion [13] and the interfacial crack [14] on the interfacial stresses in nanocomposite were investigated using finite element method. As a results, deterioration of the nanocomposite's mechanical properties can be attributed to many factors, therefore it has been attracted many researches to investigate the effective Young's modulus as well as the parameters that play big role in the predicted properties. Gawandi et al [15] investigated the influence of the nanofiber elastic properties and toughening effect of the nanofiber by 3D-FE of a penny-shaped cracked matrix as well as the impact of mismatch. Whereas a representative volume element (RVE) of a simplified 3D model for a wavy carbon nanotube (CNT) is considered [16] to study the stress transfer in (SWCNT) composites. The adopted model was capable of predicting axial as well as interfacial shear stresses along a wavy CNT embedded in a matrix. Moreover, the effects of the waviness of the CNTs and the interfacial debonding between them and the matrix on the effective moduli of CNT–reinforced composites are studied by a simple analytical model to investigate the influence of the waviness and debonding on the effective moduli [17]. A computational numerical-analytical model of nano-reinforced polymer composites is developed taking into account the interface and particle clustering effects [18]. The model was employed to analyze the interrelationships between microstructures and mechanical properties of

nanocomposites. An improved effective interface model which is based on Mori–Tanaka approach and includes the nanoparticle geometry and clustering effects was developed. Yijun et al used advanced boundary element method (BEM) to study curved cracks at the interphases between the fiber and matrix in the fiber reinforced composites, where stress intensity factors (SIFs) are evaluated and the interface cracks at the interphases of fiber-reinforced composites are studied and the effects of the thickness and materials on the SIFs are investigated. The effects of spatial distribution and geometry of carbon nanotubes (CNTs) on the macroscopic stiffness and microscopic stresses of CNT reinforced polymer composites are investigated based on the multi-scale homogenization theory [20], besides the influence of the aspect ratio and volume fraction of CNT, the end gap between two coaxial nanotubes and the distance between two parallel nanotubes on the nanocomposites are also investigated. An extensive review of the work done of experiment, theory of micro-nanomechanics, and numerical analysis on characterizing mechanical properties of nanocomposites is presented [21]. Three different approaches are discussed in finite element modeling, i.e. multiscale representative volume element (RVE) modeling, unit cell modeling, and object-oriented modeling. Also, the mechanism of nanocomposite mechanical property enhancement and the ways to improve stiffness and fracture toughness for nanocomposites are discussed. Unnati et al [22] studied the effects of pinhole defects on the mechanical properties are investigated for wavy carbon nanotubes based nanocomposites using 3-D RVE with long carbon nanotubes. The Young's modulus of elasticity are evaluated for various values of waviness index, as well as type and number of pinhole defects under an axial loading condition. The presence of chemical bonding between functionalized carbon nanotubes and matrix in carbon nanotube reinforced composites is modeled by elastic beam elements representing covalent bonding characteristics by neglecting reinforcing mechanisms in the composite such as relatively weak interatomic Van der Waals forces [23]. The effective mechanical properties of CNT-based composites are evaluated using a square RVE based on the continuum mechanics and with FEM [24]. Besides, formulas to extract the effective material constants from solutions for the square RVEs under two load cases are derived based on the elasticity theory. Rafiee et al [25] investigated the impact of CNTs on the fracture behaviour by estimating J-integral of composites using A 3-D FEM consisting of CNT, interphase and surrounding polymer is constructed. CNT is modeled as a lattice structure using beam elements and the interphase region is simulated using non-bonded interactions. The longitudinal behavior of a CNT in a polymeric matrix is studied [26] using a non-linear analysis of a full 3D multi-scale FEM consisting of carbon nanotube, non-bonded interphase region and surrounding polymer. The bonding between carbon nanotube and its surrounding polymer is treated as van der Waals interactions and corresponding longitudinal, transverse and shear moduli are calculated. Based on molecular mechanics, an improved 3D-FEM for armchair, zigzag and chiral single-walled carbon nanotubes (SWNTs) was developed [27] and the bending stiffness of the graphene layer was considered. The elastic stiffness of graphene was studied and the effects of diameters and helicity on Young's modulus and the shear modulus of SWNTs were investigated. Tserpes and Chanteli evaluated the effective elastic properties of carbon nanotube-reinforced polymers as functions of material and geometrical parameters using a homogenized RVE and 3D FE model. The parameters considered are the nanotube aspect ratio, the nanotube volume fraction as well as the interface stiffness and thickness. Both isotropic and orthotropic material properties have been considered for the MWCNT. Atomistic-based FE analysis is combined with mechanics of materials to evaluate the geometrical characteristics and elastic properties of beams by using 3D FE analysis and a linear behavior of the C–C bonds to estimate the tensile, bending and torsional rigidities of CNTs [29]. A developed FEM based on molecular mechanics to predict the ultimate strength and strain of SWCNT, and the interactions between atoms was modeled by combining the use of non-linear elastic and torsional elastic spring. Mechanical properties as Young's modulus, ultimate strength and strain for several CNTs were calculated [30]. Hernández-Pérez and Avilés [31] investigated the influence of the interphase on the effective properties CNT composites using FEA and elasticity solutions for RVEs and the influence of the thickness and gradient in elastic modulus on the elastic properties and stress distribution of the composite is examined. A proposed SWCNT-FEM, based on the use of nonlinear and torsional spring elements is adopted [32] to evaluate the mechanical properties. The influence of tube diameter and chirality on the Young's modulus of SWCNTs was investigated, armchair, zig-zag and chiral nanotubes, with different size, were tested under uniaxial load.

The present paper investigates through using the finite element analysis the significances of the debonding between the nanofiber and the matrix of nanocomposite. Mainly, the proposed debonding is modeled to be exist between the nanofiber and the matrix as a longitudinal defected zone. Therefore, the impact of this debonding will be studied and discussed in term of the stiffness of the representative volume element(RVE), i.e., effective Young's modulus. Linear elastic analysis is chosen as the basis for the present analysis using finite element analysis. Uniaxial load is imposed to study the case, whereas three different values of the reinforcements' stiffness are used to model the nanofibers' properties. Each case are investigated individually through using traditional package ANSYS to predict normal and shear stresses along the interfacial nanofiber/matrix for both debonded and intact RVE. Representative volume element (RVE) was proposed to model the case, and 3D-axisymmetric dimensional analyses are implemented to model the nanocomposite because of the complexity of the problem.

2. Method of Analysis

Finite element analysis (FEA) has been used by researchers as a powerful tool in investigating the interfacial stresses,

the failure strains as well as the effective Young's modulus of the nanocomposites instead of molecular dynamic simulation [6], since the latter can only deal with physical phenomena at the level of a few nanometers at the present stage, whereas the size of a representative volume of a nanocomposite material ranges from 10 nm upward to several hundreds of nanometers.

It was reported that mostly the smallest dimension of the nanofiber under investigation of the researchers lies in the range 20–50 nm, therefore continuum mechanics assumptions, like the one used in the finite element analysis are still valid at such length scales. Analogous finite element analyses have been reported by [16] with a focus on stiffness analysis incorporating micromechanics theory. In fact, these finite element analyses simplified the complex interaction among the nanoscale reinforcement, matrix and the doable interphase [6].

In this paper, the aim of the finite element analysis (FEA) is to investigate the impact of a proposed debonding between the matrix and the reinforcement, i.e., nanofiber, on the effective Young's modulus of the nanocmoposite. Moreover, the analysis explores the interfacial normal and shear stresses along the nanofiber sides. The FEA modeling was carried out using ANSYS software. In order to simplify the modeling of the study, 3D-axisymmetric dimension analyses were conducted by FEA which is mainly based on a cylindrical representative volume element (RVE) of the namocomposite material. Besides, constituents properties of the nanoreinforcement and the matrix have been obtained used similar to the previous investigators [6]. The proposed RVE model as well as the interfacial debonding used in this study is shown in Fig. 1, whereas Fig. 2 illustrates the 3D axisymmetric FE model and the boundary conditions used in the analysis.

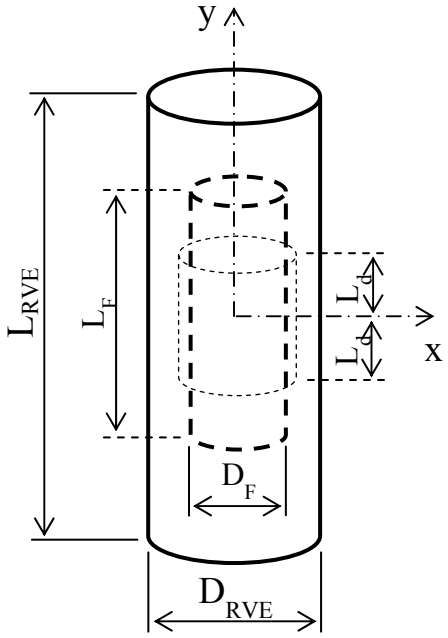


Figure 1: Cylindrical RVE reinforced by nanofiber with circumferential debonding.

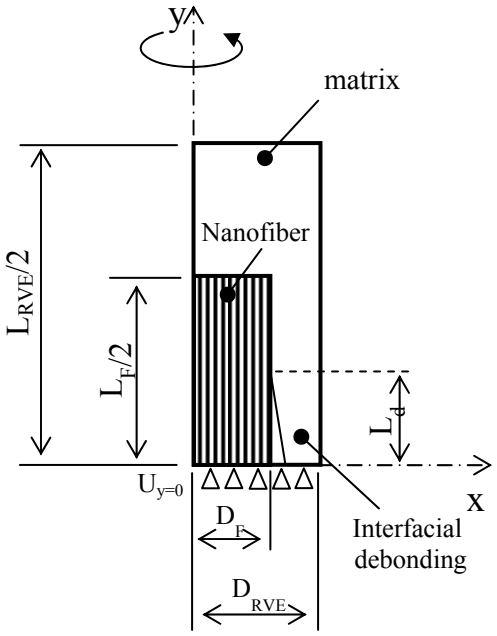


Figure 2: 3D-Axisymmetric FE model with boundary conditions.

Due to complexity of the problem, 3D-axiymmertic finite element analysis is carried out to model the nanofiber composite, i.e., RVE. Four-node quadrilateral element (solid 182) is employed in the investigation through ANSYS software to assess the effective stiffness, i.e., Young's modulus, as well as the interfacial stresses along the nanofiber. The interfacial debonding is modeled as circumferential sharp crack. Tie constraints are applied locally at the interface between the nanofiber and the matrix except for the debonding line L_d in order to represent the interfacial debobding zone. A dense mesh in and around the nanofiber-matrix interface to a relatively coarser mesh utilized for the rest of the RVE.

3. Geometry and Materials Specification

The material properties used in the baseline RVE is epoxy matrix has a Young's modulus of E_m=4 GPa and Poisson's ration of ν_m= 0.4. Analogous to other finite element analyses done previously [6], the nanofiber is considered as transversely isotropic materials [14]. The nanofiber is considered as a carbon fiber of elastic modulus of E_f = 200, 400 and 1000 GPa respectively. A tensile stress of unit nN/nm^2 is applied on the nanocomposite and imposed to be parallel to the longitudinal nanofiber of the nanocomposite, whereas the transvers direction of the nanocompsite is left free of any load.

The adopted cylindrical RVE of the proposed nanocoposite is proposed to have a length of L_{RVE}=120 nm and diameter of D_{RVE}=90 nm. The RVE consist of a matrix of polymer and a nanofiber. The nanofiber has a cylindrical shape of L_f=100nm and D_f=20nm which is equivalent to L_{RVE}/L_f=1.2

and D_{RVE}/D_f=4.5 which can be expressed by a fiber volume fraction of the nanocomposite V_f=4%.

The debonding length along the longitudinal side of the nanofiber L_d of 0, 10, 25, 40 and 50 nm is considered in the analysis for the cases studied, and this value is corresponded to debonding length to the nanofiber's length of L_d/L_f=0, 0.2, 0.5, 0.8 and 1, where intact RVE whenever L_d/L_f=0 which si the standard case, whereas the fully debonding case when L_d/L_f=1. The nanofiber and the matrix in the model are assumed to be bonded perfectly with the exception of the debonding line. Frictionless sliding behavior is assumed between the mismatch's faces.

The level of the local interfacial stresses arises at the debonding line are inspected as well. The defected nanocomposite, i.e., debonded, is investigated under static loading conditions for uniaxial tensile stress. In addition, the debonding length L_d along the longitudinal side of the nanofiber is considered as parameters in the analysis through the analysis. Nanofiber's stiffness is considered as another parameter in the analysis.

The impact of the longitudinal debonding on the longitudinal side of the nanofiber is studied to estimate the effective Young's modulus and for both interfacial normal stresses σ_y along the nanofiber's diameter and the shear stresses τ_{xy} as well as Von Misses stresses along the nanofiber's side. It is important to mention that effective Young's modulus of the nanpocomposite is estimated through longitudinal displacement results by imposing multipoint constraints (MPC) on the cylindrical RVE along RVE's diameter.

4. Results and Discussion

In the FE analysis of the RVE which contains longitudinal debonding, the impact of the debonding to the nanofiber length 2Ld/Lf on the effective Young's as well as the interfacial normal, shear and Von Misses stresses and are investigated in three stages.

In stage I, the effective Young's modulus of the RVE is investigated due to presumed debonding, whereas in stage two the normal and Von Misses stresses along the transverse side of the nanofiber is investigated, whereas in the last stage, the longitudinal shear and Von Mises stresses are estimated. The main parameters in the analysis are the debonding length ratio, i.e., $2L_d/L_f$ which has value of 0, 0.2, 0.5, 0.8 and 1 respectively, whereas the nanofiber's stiffness values are E_f/E_m=50, 100 and 250.
It is observed from Fig. 3 increases in the effective Young's modulus of the intact RVE to be 1.54 times the matrix stiffness for the E_f/E_m=50 case, whereas rises from 1.64 to 1.71 as the E_f/E_m varies from 100 to 250, this attributed to the impact of the reinforcement's stiffness. As the debonding introduces, a significant reduction in the normalized effective Young's modulus of 1.3% when L_d=10 nm, where it is observed to b almost constant between $2L_d/L_f$=0.2 to 0.5. After crossing $2L_d/L_f$=0.6, the second stage reduction in normalized effective Young's modulus occur up to total reduction in stiffness of 6.5% for the E_f=200 GPa whereas this maximum value becomes 7.4% and 9.4% for both E_f=400 and 1000 GPa respectively as the RVE becomes fully debonded in the longitudinal direction. That means, as the debonding increases, the impact of the nanofiber's stiffness becomes negative on the effective Young's modulus.

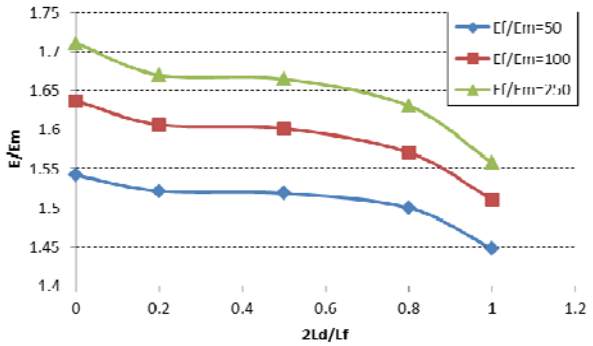


Figure 3: Normalized effective Young's modulus E/E_m versus total debonding length over nanofiber's length.

Normal stress σ_y and Von Misses stresses σ_{von} are estimated along the transverse side of the nanofibers as the debonding progresses through the longitudinal side of the nanofiber. Figure 4 illustrates a drop in normalized σ_y up to 10.7% as debonding approaches 10nm, whereas almost remains constant through the progress of the debonding from L_d=10 to 80nm. Beyond this limit, a significant rise in normalized σ_y observed to be 62.5% as RVE becomes fully debonded, and this attributed to the stresses at the transvers side started to carry the whole applied stresses, and this may cause peeling failure between nanofiber and the matrix. This is for E_f/E_m=50, for the other stiffness ratio, the maximum normalized stress approaches 61.9 and 62.3% for the E_f=400 and 1000 GPa respectively.

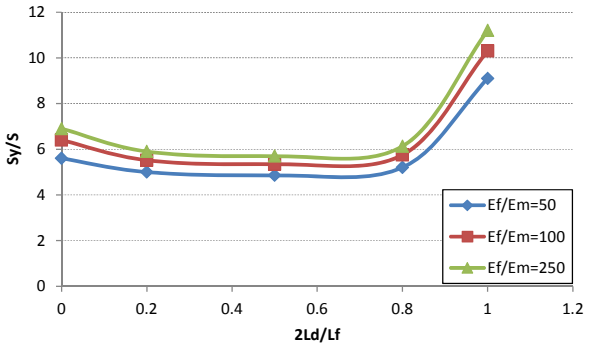


Figure 4: Normalized stress of transverse side σ_y/σ versus total debonding length over nanofiber's length.

In the other hand, the Von Misses stresses along the transverse side shows a quit similar behavior but a little bit higher stresses, as shown in Fig. 5, and this is expected due to combined load effect. As in the normal stresses σ_y, there is a drop in stresses about 15.7% at L_d=10 nm and remains almost steady up to L_d=80 nm. After that an increase in stresses up to 62.6% as RVE becomes fully debonded, and this value exactly the same percentage estimated for normalized σ_y. Again, the impact of the nanofiber's stiffness play opposite role on the escalading Von Misses stresses which have range of 58.4 to 64.3% as E_f=400 to 1000 GPa respectively.

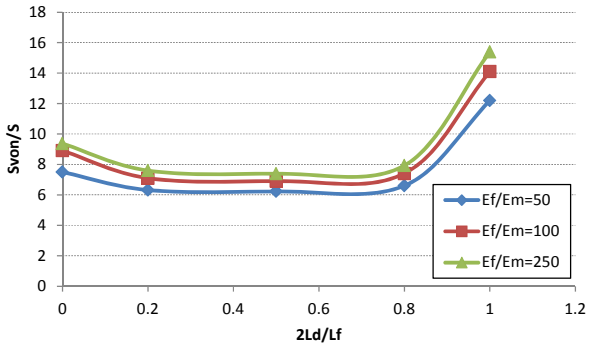


Figure 5: Normalized Von Misses stress of transverse side σ_{Von}/σ versus total debonding length over nanofiber's length.

The third stage of the analysis is to investigate the shear τ_{xy} and the Von Misses stresses on the longitudinal side of the nonofiber. Figure 5 shows that as the debonding increases, a slight increase in normalized shear stresses is observed, which starts from 16.6% at $2L_d/L_f$=0.2, and remains almost stable until the debonding approaches 50% of the nanofiber's length, so it starts to increase to 78.5% at L_d=80 nm and becomes quit steady as RVE being fully debonded. This is for the case where E_f/E_m=50. A similar behavior for the other ration, i.e., E_f/E_m=100 and 250, but with greater level of stresses. The maximum growth in normalized shear stresses can be as 76.4 to 77% for the E_f=400 and 1000 GPa respectively.

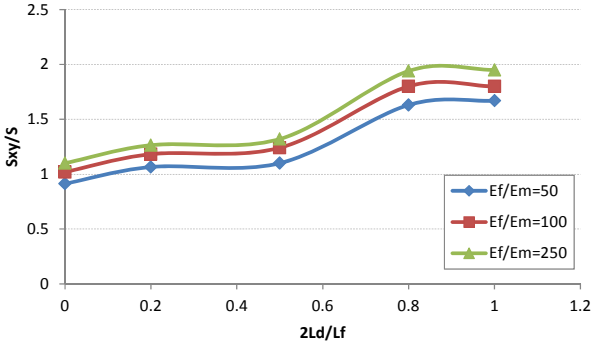


Figure 6: Normalized shear stress of longitudinal τ_{xy}/σ versus total debonding length over nanofiber's length.

On the contrary, Von Misses stresses on the longitudinal side of the nanofiber don't show similar behavior as in the transverse side. The stresses show increase of 25.9% as L_d=10 nm, and remains stable between $2L_d/L_f$=0.2 to 0.8, and then large jump in Von Misses stresses approaches to 181.7% as RVE becomes fully debonded. This analysis for E_f/E_m=50, for the other values, the maximum stresses are 179 and 177.5% whenever E_f=400 and 1000 GPa respectively.

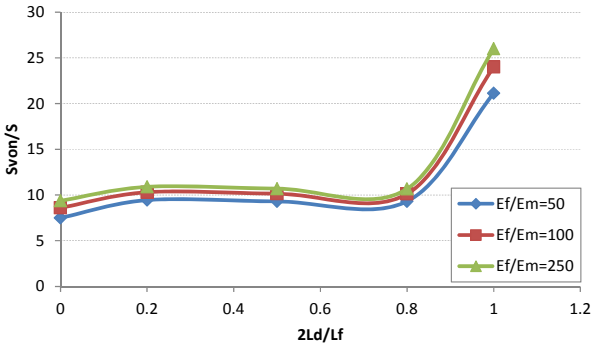


Figure 7: Normalized Von Misses of longitudinal side σ_{Von}/σ versus total debonding length over nanofiber's length.

5. Conclusions

3D-axisymmetric finite element analysis is used to investigate cylindrical RVE with circumferential debonding. Mainly, the debonding has negative impact on the effective stiffness of the nanocomposite, and this is reflected on the increase in the normal stresses on the transverse side as well as the shear stresses along the longitudinal side of the RVE. Whereas Von Misses stresses on the both sides were increased in different levels. The influence of the nanofiber's stiffness on less impact than expected. Eventually, whatever debonding initiation causes, still on of the major factors that lead to the final failure of the nanocomposite due to increasing in the level of the stresses as losing interfacial bonded areas which through stresses pass.

References

[1] L.R. Xu, S. Sengupta, Interfacial stress transfer and property mismatch in discontinuous nanofiber/nanotube composite materials, *J. Nanoscience and Nanotechnology* 10: 1-6, 2005.

[2] P.M. Ajayan, L.S. Schadler, P.V. Braun, *Nanocompsite Science and Technology*, Wiley-VCH Verlag GmbH Co. K GaA, Weinheim, pp.77, 2003.

[3] H.D. Wagner, O. Lourie, Y. Feldman, R. Tenne, Stress-induced fragmentation of multiwall carbon nanotubes in a polymer matrix, *Applied Physics Letter* 72: 188, 1998.

[4] J. Njuguna, K. Pielichowski, Advanced polymer nanocomposites for aerospace applications:

Characterization, *Advanced Eng. Mat.* 6(4): 204-210, 2004.

[5] M.F. Yu, O. Lourie, M. Dyer, Moloni K, T. Kelly, R.S. Ruoff, Strength and breaking mechanism of multi-walled carbon nanotubes under tensile load, *Science* 287(5453): 637-640, 2000.

[6] L.S. Schadler, S.C. Giannaris, P.M. Ajayan, Load transfer in carbon nanotube epoxy composites, *Applied Physics Letter* 73: 3842-3844, 1998.

[7] M. Bourchak, B. Kada, M. Alharbi, K. Aljuhany, Nanocomposites damage characterisation using finite element analysis, *Int. J. of Nanoparticles* 2(1): 467-475, 2009.

[8] L.R. Xu, V. Bhamidipati, W. Zhong, J. Li, C.M. Lukehart, E. Lara-Curzio, K.C. Liu, M.J. Lance, Mechanical property characterization of a polymeric nanocomposite reinforced by graphitic nanofibers with reactive linkers, *J. Comp. Mat.* 38(18): 1563-1582, 2004.

[9] L.R. Xu, S., Interfacial stress transfer and property mismatch in discontinuous nanofiber/nanotube composite materials, *J. Nanoscience Nanotech.* 5(4): 620-626, 2005.

[10] K.T. Lau, S.Q. Shi, L.M. Zhou, H.M. Cheng, Micro-hardness and flexural properties of randomly-oriented carbon nanotube composites, *J. Comp. Mat.* 37(4): 365-376, 2003.

[11] D. Srivastava, C. Wei, K. Cho, Computational nanomechanics of carbon nanotubes and composites, *ASME Appied. Mech. Revision* 56: 215, 2003.

[12] W.K. Ahmed, S.A. Shakir, The influence of nanoholes on the interfacial stresses in discontinuous nanofiber composite, *Proceedings of the International Conference on Bio-Nanotechology: Future Prospects in the Emirates*, Al Ain, UAE, ISBN: 9948-02-135-5, pp. 241-245, 2006.

[13] W.K. Ahmed, F.K. Omar, Y. Haik, The effect of nano-circular inclusion on the interfacial stresses of nano-composite, *First Sharjah International Conference on Nanotecnology. and Its Appl*ications, Sharjah, UAE, (*AIP Conf. Proc.* Vol. 929 Issue 1, pp.38, 8/22/2007), pp.111, 2007.

[14] W.K. Ahmed, Y. Al-Douri, K. Aslantas, Finite element analysis of cracked nano-fiber reinforced composite, *Proc. 6th European Congress on Comp. Methods in Applied Sciences and Engineering (ECCOMAS 2012)*, Vienna University of Technology, Vienna, Austria, ISBN: 978-3-9502481-9-7, pp.383, 2012.

[15] A.A. Gawandi, J.M. Whitney, G.P. Tandon, R.B. Brockman, Three-dimensional analysis of the interaction between a matrix crack and nanofiber, *Composite: Part B* 40: 698-704, 2009.

[16] K. Yazdchi, M. Salehi, The effects of CNT waviness on interfacial stress transfer characteristics of CNT/polymer composites, *Composite: Part A* 42: 1301-1309, 2011.

[17] L.H. Shao, R.Y. Luo, S.L. Bai, J. Wang, Prediction of effective moduli of carbon nanotube–reinforced composites with waviness and debonding, *Composite Structure* 87: 274-281, 2009.

[18] R.D. Peng, H.W. Zhou, H.W. Wang, Leon Mishnaevsky Jr., Modeling of nano-reinforced polymer composites: Microstructure effect on Young's modulus, *Comp. Mat. Science* 60: 19-31, 2012.

[19] Y. J. Liu, N. Xu, Modeling of interface cracks in fiber-reinforced composites with the presence of interphases using the boundary element method, *Mech. Mat.* 32: 769-783, 2000.

[20] D. Luo, W. Wang, Y. Takao, Effects of the distribution and geometry of carbon nanotubes on the macroscopic stiffness and microscopic stresses of nanocomposites, *Comp. Science Tech.* 67: 2947-2958, 2007.

[21] H. Hua, L. Onyebuekea, A. Abatanb, Characterizing and modeling mechanical mroperties of manocomposites-meview and mvaluation, *J. Minerals and Material Characterization and Engineering* 9(4): 275-319, 2010

[22] U. A. Joshi, S. C. Sharma, S.P. Harsha , Analysis of elastic properties of carbon nanotube reinforced nanocomposites with pinhole defects, *Comp. Mat. Science* 50: 3245-3256, 2011.

[23] K.P. Saffar, N.J. Pour, A.R. Najafi, G. Rouhi, A.R. Arshi, and A.Fereidoon, A Finite element model for estimating Young's modulus of carbon nanotube reinforced composites incorporating elastic cross-links, World Academy of Science, *Eng. and Tech.* 23, 2008.

[24] X.L. Chen, Y.J. Liu, Square representative volume elements for evaluating the effective material properties of carbon nanotube-based composites, *Comp. Mat. Scien*ce 29: 1-11, 2004.

[25] R. Rafiee, A. Fereidoon, M. Heidarhaei, Influence of non-bonded interphase on crack driving force in carbon nanotube reinforced polymer, *Comp. Mat. Science* 56: 25-28, 2012.

[26] M.M. Shokrieh, R. Rafiee, On the tensile behavior of an embedded carbon nanotube in polymer matrix with non-bonded interphase region, *Comp. Structure* 92: 647-652, 2010.

[27] X. Lu, Z. Hu, Mechanical property evaluation of single-walled carbon nanotubes by finite element modeling, *Composite: Part B* 43: 1902-1913, 2012.

[28] K.I. Tserpes, A. Chanteli, Parametric numerical evaluation of the effective elastic properties of carbon nanotube-reinforced polymers, *Comp. Structure* (2012), doi: http://dx.doi.org/10.1016/ j.compstruct.2012.12.004.

[29] P. Papanikos, D.D. Nikolopoulos, K.I. Tserpes, Equivalent beams for carbon nanotubes, *Comp. Mat. Scien*ce 43: 345–352, 2008.

[30] M. Meo, M. Rossi, A molecular-mechanics based finite element model for strength prediction of single wall carbon nanotubes, *Mat. Science Eng*. A 454-455: 170-177, 2007.

[31] A. Hernández-Pérez, F. Avilés, Modeling the influence of interphase on the elastic properties of carbon nanotube composites, *Comp. Mat. Science* 47: 926–933, 2010.

[32] M. Meo, M. Rossi, Prediction of Young's modulus of single wall carbon nanotubes by molecular-mechanics based finite element modeling, *Comp. Science Tech.* 66: 1597–1605, 2006.

Exact numeric resolution of the system globally non linear Schrodinger Poisson in order to study the influence of different technological parameters on the performance of AlGaAs/GaAs heterojunction

I. BOUNEB[1], M. MARIR BENABBAS[1]

[1] *Laboratory of MODERNA , Department of ELECTRONIC, University CONSTANTINE, ALGERIA*

bounebilhem@yahoo.fr

abstract : In structures with GaAs, which are the structures most used, because of their physical and electronic nevertheless seems a compromise between the increase of doping and reduced mobility. The use of quantum heterostructures can overcome this limitation by creating a 2D carrier gas. The study of this heterojunction (steep) inevitably involves the resolution of the system of equations Schrödinger-Poisson due to quantum effects that occur at the interface. Our work had as main objectif the numerical resolution of the non linear Schrödinger Poisson system in order to modelised the potential at the interface of a heterojunction AlGaAs/GaAs the system was solved self-consistent Calculations, using projective methods, allowing the integration of Hamiltonian using the Green's functions in the Schrödinger equation for a rigorous self-consistent resolution with the Poisson equation are developed. However, the resolution of this system is made by least square method (fsolve) where the initial vector is very close to the solution (initial vector approximated a square well), which enables the convergence of the overall nonlinear system confirmed for ten basis functions and a clearly defined position of the electric walls. This allowed us to infer the performance of the most influential in the operation of the HEMT as the charge density and the influence of physical parameters such as doping and the rate of Aluminium

This computational physics model that we have made can be applied to all other quantum heterojunction with inversion layer or accumulation.

© 2010 Published by Elsevier Ltd. Selection and/or peer-review under responsibility of [name organizer]

Keywords: nanostructure, quantum well, Poisson - Schrödinger equations, Green function, wave function, surfasic density

INTRODUCTION

A large majority of electronic components is still done based on silicon. Yet a significant number of uses of semiconductors in the areas of civil and military telecommunications naturally leads the actors to innovate, because these applications require the use of power always more important at high frequencies [1].

Thus, an alternative is to use semiconductor materials to delivering superior physical properties of high power and supporting high operating temperatures. Of these, the semiconductor III-V. One of the properties of the family compound semiconductor III-V is indeed the probability of forming heterostructures with a good crystal interface (eg GaAs / AlAsGa)[1]. The gas formed by electrons accumulated at the interface of this heterojunction has two interesting physical properties: a two-dimensional character and a very high mobility, especially at very low temperatures[1].

the two-dimensional quantum structures are generally the easiest systems to achieve technologically. At present, the molecular jet'epitaxie allows the manufacture of semiconductor heterostructures of high quality (eg GaAs / AlAsGa).
The study of this heterojunction (steep) inevitably involves the resolution of the system of equations, Schrödinger-Poisson due to quantum effects that occur at the interface[2].
This work is dedicated to the NUMERIC physical modeling of a quantum well and aim to solve the system of Schrödinger-Poisson equations and the numerical solution of this system was made by the method of least squares.

1. THEORIE

The structure under investigate consists for a N-type AlGaAs layer and a P-type GaAs buffer layer. The nanametric structure has been investigated by using an integral method calculation in the effective mass approximation and the envelope wave function vanishes at the interface [3]. The potential at the interface of heterojunction verify simultaneously the equation of Schrödinger and of Poisson that is why we propose to solve with rigorous way the system of equation Poisson Schrödinger given by the following formula:

$$\begin{cases} Es: \dfrac{-\hbar^2}{2m_e}\Delta\Psi^i(z)+V(z)\Psi^i(z)=E^i\Psi^i(z) \\ Ep: V(z)+\dfrac{\rho(z)}{\varepsilon}=0 \end{cases} \quad (1.1)$$

Δ : The Laplacien operator

$m_{e:}$ effective mass of an electron

$\Psi^i(z)$: Wave function associated with energy level $E^{i.}$

V (z): the potential

$\hbar$: Planck 's constant

$\rho(z)$: Density of free electron it is given by:

$$\rho(z)=\begin{cases} qN_D - q\sum n(E^i)\left|\Psi^i(z)\right|^2 \cdots in\ GaAsAl \\ -qN_A - q\sum n(E^i)\left|\Psi^i(z)\right|^2 \cdots in\ GaAs \end{cases} \quad (1.2)$$

q: electron charge.

qND and -qNA: fixed charge

ND: donors doping rate

NA:acceptors doping rate)

$q\sum n(E^i)\left|\Psi^i(z)\right|^2$: mobile carriers

n (Ei): carrier density (to the energy level of i number) of electrons

obtained by the Dirac Fermi distribution it is given by:

$$n(E^i)=\left(\frac{m_e k_B T}{\pi\hbar^2}\right)\log\left(1+\exp\frac{E_F-E^i}{k_B T}\right) \quad (1.3)$$

E_F: energy level of Fermi.

K_B: Boltzman constant

T: absolute temperature

i: number of state bound possible.

2. different approach of resolution

2.1 approximatifs Méthods –analytic resolution

Content of the difficulty of solving the Poisson-Schrödinger coupled equations ,particular forms of the potential well and the wave function have been proposed.

A) Linear aproximation of a quantum well

The model proposed by Delagebeaudeuf considers a linear potential well [19], the electric field is therefore constant in the well. In the calculation of levels E_n from the Schrodinger equation as a function of field (the only parameter defining the well) is relatively simple and we can write [4]:

$$E_n=\left(\frac{\hbar^2}{2m_e}\right)^{1/3}.\left(\frac{2}{3}\pi qE\right)^{2/3}.\left(n+\frac{3}{4}\right)^{2/3} \quad (2\text{-}1)$$

In reality the assumption of a linear potential well is very simple but can bring with sufficient rigor the behavior of the accumulation layer heterojunction.

B) Approximation d'un puits de potentiel parabolique

- **Assumption of this model**

In this model we consider the potential well of parabolic shape [5]. This choice is a priori arbitrary condition subsequent to the cruel treatment.

Indeed, C. VERSNANYEN have considered that this choice results in some degree the response of space charge in the accumulation area, and if the charge density was uniform this assumption is close to physical reality.

In his calculations he made the following assumptions [5]:

- The well is parabolic, it is characterized by two parameters: its depth V and width Z which determine the field at the interface.
- The position of the Fermi level far from the interface in GaAs is determined by the condition of thermodynamic equilibrium volume .
- The limitation to the first two permits energy levels, sub-bands defined by them contains almost all of the load.

- **Method of resolution**

The calculation of energy levels takes place in from the integration of the Schrödinger equation then leads to the following equation:

$$\sqrt{2m_e}\int_{x1}^{x2}\sqrt{F_n - V(x)}.dx=(n+\frac{1}{2}).\pi\hbar \quad \textbf{(2-2)}$$

This equation (2-2) is coupled to that of the electronic charge density interfacial (NS) in GaAs

$$N_s=D.\frac{kT}{q}\sum_{n=1}^{2}\log(1+\exp(\frac{E_F-E_n}{kT})) \quad \textbf{(2-3)}$$

The calculation proceeds as follows: Starting from a given well depth V, digital convergence and the well width is determined as the interfacial charge calculated from E0 and E1

levels is consistent with that given by the Poisson equation.
The interfacial charge so calculated satisfying the Poisson equation and the particular statistical two-dimensional gas wells across the dish considred.

C) Triangular approximation of the Well

In this approach approximate the potential well is considered infinite and triangular (Figure 1) equal to [6]

$$V(x) = \begin{cases} -Fs.x \\ \\ \infty \end{cases} \quad \textbf{(2-4)}$$

Where F_s is the electric field.

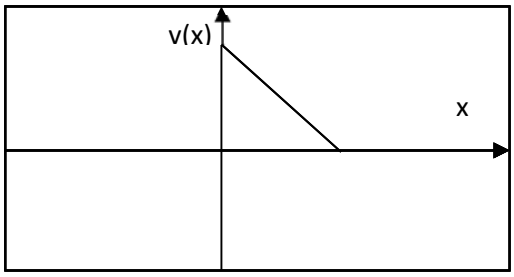


Figure -1 : triangular potential well

Solving the Schrödinger equation can then carry out analytically and gives:

$$E^i = \left(\frac{\hbar^2}{2m_e}\right)^{1/2}\left(\frac{2}{3}.\pi.q.F_S\left(i+\frac{3}{4}\right)\right)^{3/2} \quad \textbf{(2-5)}$$

$$\psi^i(z) = A_i(z)\left[\left(\frac{2.m_e.q.F_s}{\hbar^2}\right).\left(3-\frac{E^i}{q.F_S}\right)\right]$$

(2-6)

Where Ai (z) is the Airy function. To determine the electric field, potential energy must be linéairisée [7] as:

- the potential energy due to the depletion charge varies linearly with z in the vicinity of the interface
  - Reverse potential energy is neglected if the charge depletion is more important than the reversal charge in this case the potential energy of the electrons is written as:

$$V(z) = e.Ez \quad \textbf{(2-7)}$$

Where $E = e.\frac{N_{dep}}{\varepsilon_2}$ is the electric field in the semiconductor 2. This field is constant in the vicinity of the interface to the extent that the potential varies linearly.

- If the reverse charge is not negligible compared with the charge depletion so potential energy is written as approximated forme[6]:

$$V(z) = e.E_{eff}.z \quad \textbf{(2-8)}$$

Avec : $E_{eff} = e.(\frac{N_{dep} + f.n}{\varepsilon_2})$

E_{eff} represents the effective electric field, F is a numerical coefficient the pre-weighting participation reverse charge .

The triangular well approximation is used for its simplicity, the main advantage of this formulation is particularly simple law linking the values of the energy levels with the electric field, allowing the introduction of these expressions in the modeling of component [7].

2.2 Calculation self consistent

Previous methods, which are much simpler to use, have the failure of lack of precision especially when seeking to know the exact shape of the potential and the gas density or even the energy difference between levels. For this there is only one method to solving the system of Schrödinger-Poisson equations is self consistent calculation [7].

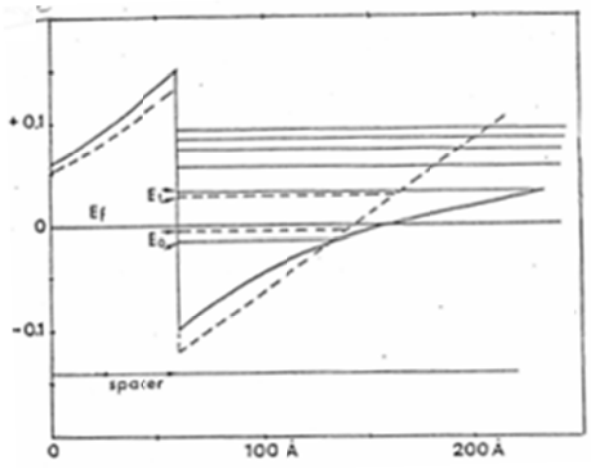


Figure -2 : comparison between the results obtained by the method of

triangular (------) potential and the method of calculating self consistent ( ) [8]

Figure (2) shows a comparison between the results obtained by the triangular method and self-consistent calculation method for heterojunction GaAsAl / GaAs at 300k°.

Note the difference between the energy values of the first two sub-band and that of the bottom of the well, we also see the large gap between potentials for large values of z [8].

The principle of self-consistent method is based on an initial potential well in most cases is triangular for which energy levels and wave functions are solving the Schrödinger equation with this data we solve the equation Poisson to have a new potential for which we solve again the Schrödinger equation and so on. This iterative process is conducted until the difference between the potential from two successive iterations is below a certain value (1mev, 1μev).

A) F.Stern model

The self-consistent numerical solution of F. Stern of the system formed by the Poisson and Schrödinger equation for an inversion layer of the heterojunction Si (p) / SiO2 is based on three major approximation [7].

- the validity of the effective mass approximation .
- the envelope wave function vanishes at the interface.
- the interface states are neglected and their effects and the effects of other charges that may be in SiO2 near the interface are replaced by an equivalent electric field.

The potential image is a function of the difference in dielectric constants of the two materials constituting the heterojunction, it will be neglected in the case of the heterojunction Si (p) / SiO2.

The system to be solved is represented by [7]:

$$\begin{cases} \dfrac{-h^2}{2me}\dfrac{d^2\Psi^i}{dz^2} - qV(z)\Psi^i(z) = E^i\Psi^i(z) \\ \dfrac{d^2V(z)}{dz^2} = \dfrac{-\left[\rho_{dep} - q\sum n_i\left|\Psi\right|^2\right]}{\varepsilon} \end{cases} \quad \textbf{(2-9)}$$

The energy levels of excited states are obtained either from the variational method or from the triangular potential.

B) A.Cappy model

Pour For the numerical solutionself consistent of the system formed by the Poisson and Schrödinger equations for an accumulation layer of the heterojunction GaAsAl / GaAs ,A. Cappy took over the general philosophy of F. Stern for the modeling of inversion layer in the MOS transistor. This approach is based on the following approximations [8] :

- the validity of the effective mass approximation
- the différence of effectives masses in the two semiconductors is neglected.
- limit condition requires that $\psi(-w) = \psi(+w) = 0$
- The wave function is defined as a product of an envelope function and an oscillating term:

$$\psi^i(x, y, z) = \psi^i(z).\exp(i.k_x.x + i.k_y.y)$$

Where k_x, k_y are the wave vectors in the direction parallel to the heterojunction

- The potential energy corresponding to the bottom of the conduction band is written as :

$$V_0(z) = V(z) - \Delta E_C H(z - z_0)$$

where H is the level function.

Two sizes are imposed in this self consistent of A. Cappy [8]:

- The surface density of electrons Ns depends on technological and physical parameters and physical heterojunction (temperature, doping spacer ...).
- The position of the Fermi level: EF=0

From an initial solution V0 (z) given, the energy levels and wave functions are calculated and also the value of the Fermi level.The integration of the Poisson equation gives a new value of potential. as long as the value of the Fermi level is different to zero a new iteration is performed using the new potential as an initial solution..

C) third-order polynomial model

- **Assumption of this model**

La Resolution self consistent of Schrödinger equation - Poisson system based on the following major approximations [9]:

- the validity of the effective mass approximation.
- Ithe wave function vanishes at ∞ .
- the Fermi level is taken as the origin of energies. .

- The initial potential at the interface is approximated by a polynomial of 3rd degree

- **Method of calculation**

For solving the Schrödinger equation of system-Poisson, the method is self consistent with a relaxation parameter to ensure convergence of the iterative process.
This resolution was made by the Galerkin method or the potential is approximated using the basis function which greatly reduces the calculations [9]. Schrödinger equation resolution is divided into two parts which are closely linked:

- determining the wave function.
- determining the energy .

The wave function is expressed using the basis function whose coefficients are determined by the Galerkin method [23] while the energy is calculated from an equation that expresses the condition that the wave function vanishes at the boundary of the heterojunction.

D) integral method

- **Assumption of this model**

Our contribution relationship to the different approaches of the literatures that is we have used integral method where without propose any form either for the potential energy or/and for the wave function, this method is based on Green functions and the moments methods. Green function associated to an equation to the partial derivatives can either be defined calculated, its form depend on the physical function to study in our case the potential, and they also depend on the domain of definition and limits conditions. The mathematical interpretation to the sense of distribution of these conditions is [3]:

$$\Delta G = -\delta(z - z_0) \tag{2.10}$$

The application of the Green function gives to the equation of Poisson the following integral forms:

$$V(z) = \frac{1}{\varepsilon}\int_{\Gamma} G(z/z_0)\rho(z_0)dz_0 \tag{2.11}$$

And therefore the equation of Schrödinger becomes:

$$\frac{-\hbar^2}{2m_e}\Delta\Psi(z) + \frac{1}{\varepsilon}\int_{\Gamma} G(z/z_0)\rho(z_0)dz_0\Psi(z) = E\Psi \tag{2.12}$$

Application of the Galerkin method to the equation (2.10) yields the following equation system:

$$\sum_{n,m}^{N}\left[H_{m,n}(\alpha_1,\alpha_2,\cdots\cdots\alpha_N)\right]\alpha_n = E\sum_{m=n}^{N}\alpha_n.\delta_{mn} \tag{2.13}$$

In which N is the number of basis function used for expanding $\psi_i(z)$; $\alpha_n = \prec \varphi_n \psi \succ$.

The test functions used here are classical solutions obtained for a rectangular well, projected over a Galerkin basis such that

$$\varphi_n = \frac{\sin N\pi(x+w)}{2w}, H_{mn}(\alpha \succ) \tag{2.14}$$

The chosen α_n functions are eigenfunctions of the Hamiltonian of an infinite well with a width 2w, which is much greater than the dimensions of the quantum well under study. In equation (2.13) the unknowns to be determined are α_n and E_m . The resolution of a no linear system (equations 2.13) can be gotten by a choice of an appropriate numeric method. Auto - coherent resolution of the equations Schrödinger - Poisson system where as supposing the existence of only one bound state in the potential well is done appropriately by the numeric methods chosen that have the aim to determine the profile of potential and the wave function associated to one bound state. In this work the numeric resolution is made by least square method[10] , where we approximate the initial vector as a square well what permits the convergence of the system globally no linear confirms for ten basis function and a good determination of electric wall position.
The methods are based on the nonlinear least-squares algorithms witch used in fsolve (FUNCTION IN MATLAB) also used in `lsqnonlin(IN MATLAB)`. The advantage of using a least-squares method is that if the system of equations is never zero due to small inaccuracies, or because it just does not have a zero, the algorithm still returns a point where the residual is small.

4 .Simulation Results

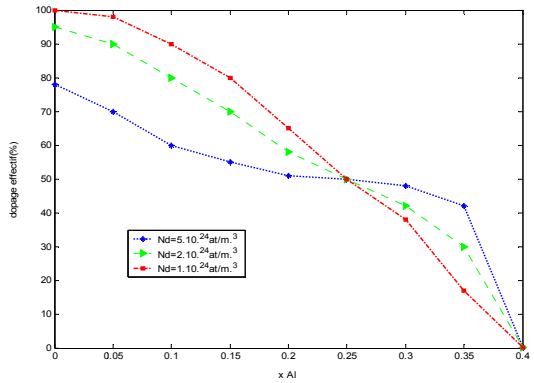


Figure.3 evolution of effective doping with the rate of Aluminum

The values of the donor levels E_{dl} ,E_{dx} OF AlGaAs are equal to the value of the rate of Aluminum of about 0.25, irrespective of doping, it is normal that all curves intersect at the point (x=0.25, $N_{eff}=N_d/2$)(fig).
For values of the rate of Aluminum near to 0.44, the effective doping is near to zero (fig).
For value of the rate of Aluminum near to zero (case of GaAs), doping is about introduced into the initial structure, especially since the doping decreases($N_d=10^{24}at/m^3$) (figure 3).

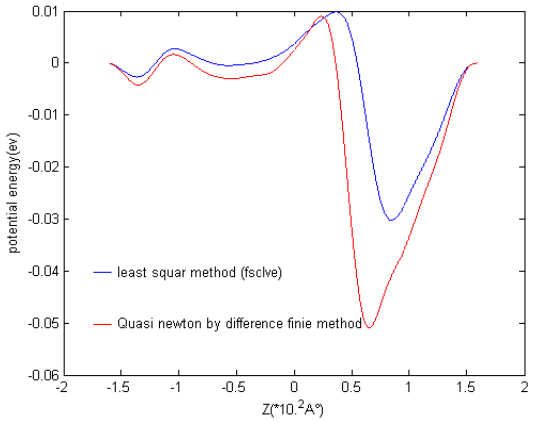


Figure .4: potential energy profile for one bound state

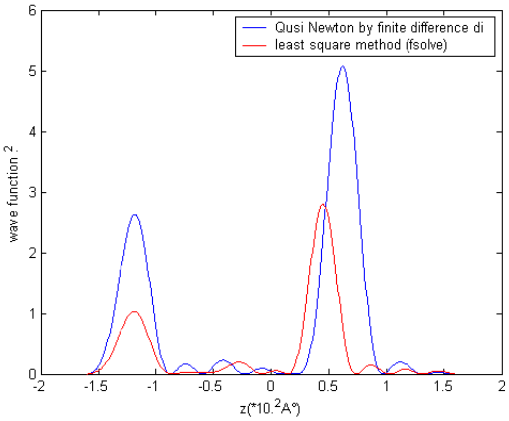


Figure.5. Comparison the result gotten by least squares method (fsolve) with regard to Results reported by the reference [7]

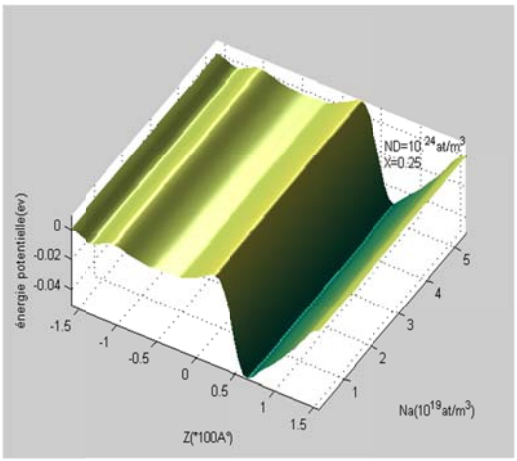


Figure.6. visualisation of the variation of potential energy with N_d

the potential energy is constant when varying the doping atom acceptor (N_a)because we have used inversion layer (figure (6)).

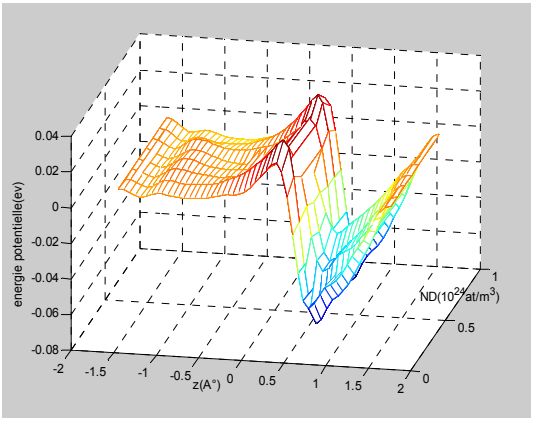


Figure.7. visualisation of the variation of potential energy with ND

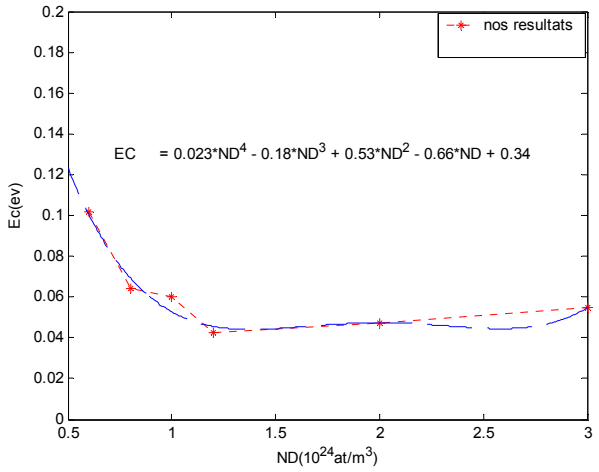


Figure .8 : influence of N_D On ΔE_C

In figure (8) we can see that for a rate of Aluminium about 0.25 ΔE_C decreases as increses ND .and if Nd continues to increase it will tend toward a limit value as oppose to N_S witch increasing when ND increases it will tend toward a limit as if ND continues to incease.

Conclusion

Our work has as main objective the exact numerical solution of Schrödinger-Poisson system witch is globally nonlinear in order to define the potential at the interface of a heterojunction GaAsAl/GaAs

We elaborate a calculus, using projective methods permit the Hamiltonian integration using Green functions in the equation of Schrödinger, for a rigorous resolution auto coherent with the equations of Poisson.

However, the resolution of this system is made by least square method.

This physic –numeric modelisation that we have made can be applied to all other quantum heterojunction with inversion or accumulation layer.

Refference

[1] :R.Castagné, J.P.Duchemin, M.Gloanecet Ch.Rumelhard, « circuits intégrés en Arséniure de galilum », physique, et regles de conception, Masson, **1989**

[2]: « Quantum Well,Wires and Dots», Paul Harrison , **2002**

[3]] Bouneb I., Bennabas Marir M., Modelisation of Accumulation Barrier of Nanostructure AlGaAs/GaAs , in : Advanced research in physics and engineering, Proceedings of the 2nd WSEAS International Conference on NANOTECHNOLOGY (NANOTECHNOLOGY '10), University of Cambridge, UK February 20-22, 2010, pp.131-134

[4] A.Meftah , H.Ajlani, A.Marzouki, R.Chtourou and M.Oueslati, « Electronic Energies in Delta Doped AlGaAs-GaAs Heterostructures », American journal of applied science 5(4):425-439,2008

[5] C .Versnaeyen, « propriétés physiques et expérimentale du transistors à effet de champ à heterojonction AlGaAs /GaAs », these de doctorat , université de LILLEI,**1985**

[6]: B.R. Nag L. R. Carley, G. Declerck, F. M. Klaassen, «Physics of Quantum Well Devices», Kluwer Academic Publishers,**2002**

[7] :F.Stern, « self-consistent results for n-type Si inversion layer », physical rview B, volume 5, Number 12, june **1972**

[8] A.Cappy, « propriétés physiques et performances potentielles des composants submicroniques à effet de champ .structure conventionnel à gaz bidimensionnel », thèse de doctorat en science physique, université des sciences et techniques de LILLE Flandres-Artrois , **1986**

[9] S.E.Benchaiba, B.E.Marir, M.Marir, a new variatianal method for schrodinger's equation ,application to a quantum heterostructure, 5th international conference on advanced semiconductor devices and microsystems (ASOMAM 2004)Slominice Castle, Slavarika, october 17-21,2004

[10] Michel Bierlaire, « Introduction à l'optimisation différentiable », press polytechnique et universitaire romandes, première édition, 2006

Photonic crystals

Soft and Hard regimes of Gap Solitons generation in Planar Bragg Grating

Alexandr Sadovnikov, Andrew Rozhnev, Nikita Ryskin

Saratov State University, Faculty of Nonlinear Processes, Saratov, Russia
*corresponding author, E-mail: SadovnikovAV@gmail.com

Abstract

The 2D model of Bragg grating structure with nonlinear Kerr materials (cubic nonlinearity) was considered. The process of the electromagnetic wave propagation in the nonlinear Bragg grating system has been numerically studied by the straightforward numerical modeling of Maxwell's equation. The possibility of multiple gap soliton generation in these structures was shown. A Finite-Difference-Time-Domain method was used. The transformation of band gap diagram was estimated. The interaction between solitary pulses was studied and discussed. The soft and hard processes of soliton formation were investigated. The efficiency of energy conversion from the energy of continuous wave signal to the energy of pulse signal was computed for different values of the input signal power. The maximum value of energy transmission coefficient was equal to 60-70% of input signal energy.

1. Introduction

The dependence of the refractive index of the materials on the applied electromagnetic field power has lead to an intensive theoretical and practical research of the different devices which can operate on this effect of nonlinear material. The periodical nonlinear structures exhibit attractive properties that make them suitable for novel devices development with wavelength tunable characteristics. The Bragg grating structure represents 1D photonic crystal [1] and is widely used in optical communications systems, as notch filters, in dispersion compensation modules, in pulse compressors, in optical multiplexers and demultiplexers, with an optical circulator, in the all-optical switching devices, all-optical buffers and storing devices, as optical sensor [1].

The waveguiding properties and possibility of soliton propagation in the nonlinear periodic dielectric structures are interesting subjects of intensive exploration during past several decades. The soliton formation is based on the interplay between temporal dispersion and nonlinearity in the system [2]. Typical value of the length at which this balance is achieved varies from a few hundred meters to several kilometers. In the real Bragg grating structures this balance is realized only in a few centimeters [3]. As opposed to the conventional solitons in optical fiber, which can be formed due to the dispersion of the glass material, the solitons in the Bragg grating exist because of the balance between the nonlinearity and the dispersion of the grating. These gap solitons propagate stably through the grating and because of modulation instability in the grating structure the periodic train of pulses can be observed [4].

Is is well known from the general theory of wave propagation in the periodic medium that the dispersion characteristic of these waves consist of the frequency ranges in which the wave can propagate and the forbidden frequency range (band gaps) in which the wave decays and cannot propagate. It is also known [2] that the dispersion characteristics of such waves in the nonlinear media transform so the effect of wave tunneling can be observed. The possibility of nonlinear tunneling was considered in [5] for the first time by the investigation of the propagation of the soliton pulse through a finite potential barrier. The works devoted to the gap soliton formation [6] showed the possibility of full transmission of the signal with the frequency inside the band gap region. The numerical analysis of wave dynamic of nonlinear coupled mode equations [7] was also provided in order to demonstrate the generation of the soliton-like pulses in the finite periodic nonlinear media. The first experimental observation of nonlinear propagation of the signal in fiber Bragg grating demonstrated [8] the soliton propagation at the frequencies near the band gap. The further develop of the nonlinear wave propagation in the structures with the cut-off frequency was presented in the work [9], where the process of soliton generation in such systems is explained by the change of the character of modulation instability in the vicinity of a critical frequency from convective to absolute. This process begins as the wave amplitude increases and the soliton-like pulses start to propagate along the structure.

In this paper the processes of the electromagnetic wave propagation in the nonlinear Bragg grating system was studied. The Finite-Difference-Time-Domain (FDTD) method is applied because it is straightforward solution of the six-coupled field components of the Maxwell's equations.

The paper is organized as follows. In section 2 the model of Bragg grating consisting of periodical layers with Kerr nonlinearity and the numerical simulation method are considered. In section 3 the dispersion of the nonlinear structure is described, the values of nonlinear frequency shift are estimated for the different intensities of input signal. Section 4 includes the results of the simulation of the nonlinear dynamics in Bragg grating – gap solitons generation and propagation. In the Section 5 the

characteristics of gap soliton propagation are analyzed. Finally a summary and conclusions are included in section 6.

2. Model of 2D Bragg grating

2.1. Geometry and material

The model of the two-dimensional nonlinear periodic structure consisting of alternating layers of Kerr nonlinear media is shown in Fig. 1. The waveguide width is $2a = 1$ μm, the period of structure $d = 1$ μm, the linear part of layers' refractive indices $n_1 = 1.45$, $n_2 = 2.0$. The layers consist of the media with positive Kerr-like nonlinearity [2]:

$$n_{I,II} = n_{1,2} + n_{nl}|E|^2, \qquad (1)$$

where $n_{nl} = 3 \cdot 10^{-8}$ μm^2/W – the nonlinear additive to the linear part of refraction index of silica glass. So the nonlinear media with instantaneous third-order nonlinearity responses are analyzed. The wave propagates along the x-direction. The structure is surrounded by vacuum with the refractive index $n = 1$ ($\varepsilon = 1$, $\mu = 1$). The input signal was set in the x_1 plane, which was placed in the lead-in waveguide domain with the refractive index $n_0 = (n_1 + n_2)/2$.

Distance between the x_1 plane and the left boundary of periodical system was sufficient for the excited electromagnetic wave to form the fundamental mode of the planar waveguide with the refractive index n_0. This condition was taken into account in the case of signal excitation with a constant amplitude and frequency. The lead-in section also provided minimization of the reflection of the wave from the structure.

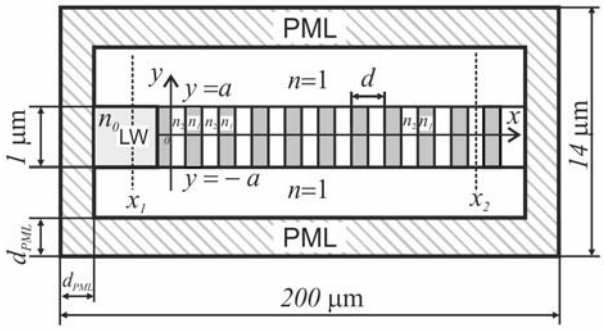


Figure 1: Model of the nonlinear Bragg grating model. PMLs surround the system. LW – the lead-in waveguide.

For the investigation of the nonlinear effect in pure silica glass big values of input signal power are needed because of the small value of the nonlinear additive n_{nl}. At this intensities of total launched power of light the structure of the real Bragg grating can suffer permanent damage. The common method of reduction the threshold intensities for the nonlinear effects near the band gap region is the fabrication of Bragg gratings of increased length and using the chalcogenide glasses.

2.2. Numerical method

For numerical calculations we utilize the FDTD numerical simulation method [10]. The FDTD method has been widely used for solving many problems of the electromagnetic wave propagation in different media. It is a straightforward solution of the six-coupled field components of the Maxwell's equations. This method is based on Yee's algorithm [11] and computes the electric and the magnetic field components by discretizing the Maxwell's equations both in time and space domain and then solving the system of the discretized equations in a time marching sequence by alternatively calculating the electric and magnetic fields in the computational domain. The accuracy of the FDTD method can be significantly improved by using subpixel smoothing of the dielectric function. This smoothing technique requires only preprocessing of the materials geometry and does not change the general FDTD algorithm.

The free electromagnetic code from the MIT MEEP package [12] was used to perform the FDTD computational method. To simulate wave propagation in an open structure the perfectly matched layer (PML) absorbing boundary conditions were applied. The PML has been shown to be one of the most effective boundary condition because it can truncate the simulation space without artificial reflections. Inside the PML domain each field component splits into two subcomponents and the system of the discretized Maxwell's equations slightly modifies. In the MEEP package the modification of PML (Uniaxially Perfectly Matched Layer) is implemented. This reduces the computational time due to the decrease of distance between the boundary of computational space and the electrodynamic structure. In the Fig. 1 the PML regions are depicted with hatching.

The computational domain size was chosen to be 200×14 μm, the size of dielectric periodic structure was 200×1 μm, the number of periods was 190. The thickness of the PML on all boundaries of computational domain was equal to $d_{PML} = 30 \cdot \Delta x = 3$ μm. This value of d_{PML} parameter minimized the wave reflections from the boundary of computational space. The cell size was chosen as $\Delta x = \Delta y = 0.1$ μm, the time step was taken as $\Delta t = 8.13 \cdot 10^{-17}$ s and the value of Courant stability factor [10] was taken to be $S = 0.5$ that satisfies the numerical stability of the method.

3. Band diagram and transmission spectrum

For the FDTD computation of the dispersion diagram the infinite structure in x-direction was considered. This structure represents one-dimensional photonic crystal [1]. The computational domain is shown in Fig. 2. The primitive cell of periodical structure consists of two layers with refractive indices n_I and n_{II} which are dependent on field intensity (1). The upper and lower boundaries of primitive

cell consist of PML, the right and left edges represent periodic boundary conditions for the simulation of infinite structure.

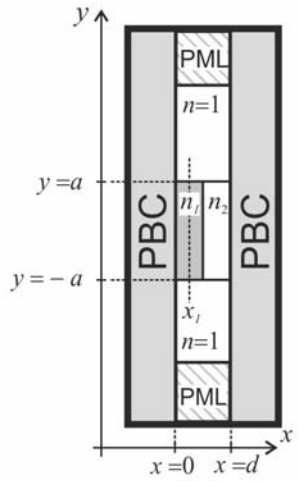


Figure 2: Model of the unit cell of 1D photonic crystal.

We look at the first band gap in the frequency range $0.29 < \Omega < 0.37$, where $\Omega = \frac{\omega a}{2\pi c}$ is the dimensionless frequency, $\omega = 2\pi f$ – the circular frequency of the electromagnetic wave, a – halfwidth of the 2D Bragg grating structure shown in Fig. 1, c – the speed of light in vacuum, $K = \beta a$ is the dimensionless longitudinal wavenumber, β – longitudal wavenumber. The result of the band structure computation is shown in Fig. 3. Different curves correspond to the different value of intensity of input signal. The frequency on the bottom and top of the first photonic band gap named as cut-off frequencies are denoted as Ω_{co1} and Ω_{co2} , respectively. This was done for the dispersion characteristics for the signal with intensity I_1 . For the different intensities of input signal the cut-off frequency was decreased and for the fixed power of the signal the upper branch of dispersion curve changes more than the bottom one.

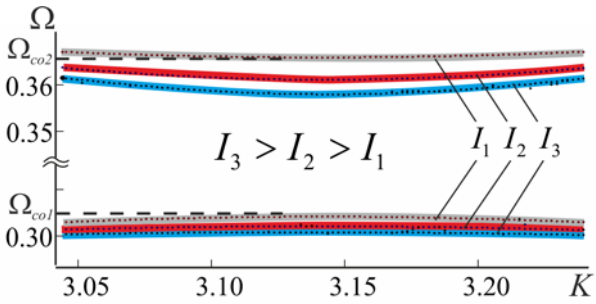


Figure 3: Band diagram for the different values of input signal intensities.

These results of band gap calculation were subsequently compared with the results of the transmission spectrum computation through the non-infinite Bragg grating shown in Fig. 1. The propagation of the Gaussian pulse with center frequency $\Omega = 0.33$ and pulse width $\Delta\Omega = 0.1$ through the grating was considered. The pulse was excited in the plane x_1 . The time-domain response of the transmitted electromagnetic field was monitored inside the Bragg grating in the plane x_2 , which is shown in the Fig. 1. The Fast Fourier Transform of the monitored data in the plane x_2 was performed to obtain the spectra of the time-domain responses. The parameters of the initial Gaussian pulse was chosen to overlay the first photonic band gap of the investigated structure. The amplitude of pulse was chosen to be $A = 1$, so the nonlinear effects was negligibly small.

The result of this simulation is plotted in Fig. 4, where T is the transmission coefficient which defines the amplitude of a transmitted wave relative to an incident wave. In this figure the lower and upper frequency boundary of the firs band gap is denoted by Ω_{co1} and Ω_{co2} , respectively. The good correspondence between the results of the cut-off frequencies computation by estimation of the band gap of 1D photonic crystal (Fig. 3) and transmission spectra analysis (Fig. 4) was achieved.

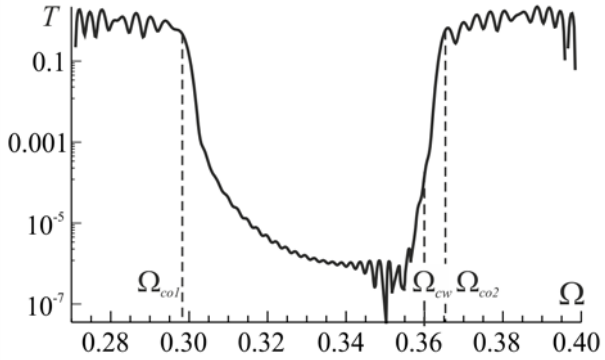


Figure 4: The transmission spectrum through the Bragg grating of the Gaussian pulse with the central frequency $\Omega = 0.33$ and the width $\Delta\Omega = 0.1$.

4. Gap soliton generation

Here we consider the continuous wave (CW) signal propagation through the Bragg grating. The nonlinear dynamics of CW signal propagation in the structure was studied in detail near the upper branch of the photonic band gap, where the dispersion is anomalous and the criterion of modulation instability [2] is satisfied. The modulation instability near the top branch of band gap is similar to that in the nonlinear Schrödinger equation [13].

The form of the CW signal was chosen as

$$E_z(y,t) = A \cdot E_{FM}(y) \sin(2\pi f_{CW} t), \qquad (2)$$

where $f_{cw} = \Omega_{cw} c/a$ is the signal frequency, $E_{FM}(y)$ is the mode profile of the fundamental TE mode of the planar waveguide [14]. The frequency of input signal was chosen to be $\Omega_{cw} = 0.36$. This frequency value is located near the cut-off frequency Ω_{co2} as shown in Fig. 4.

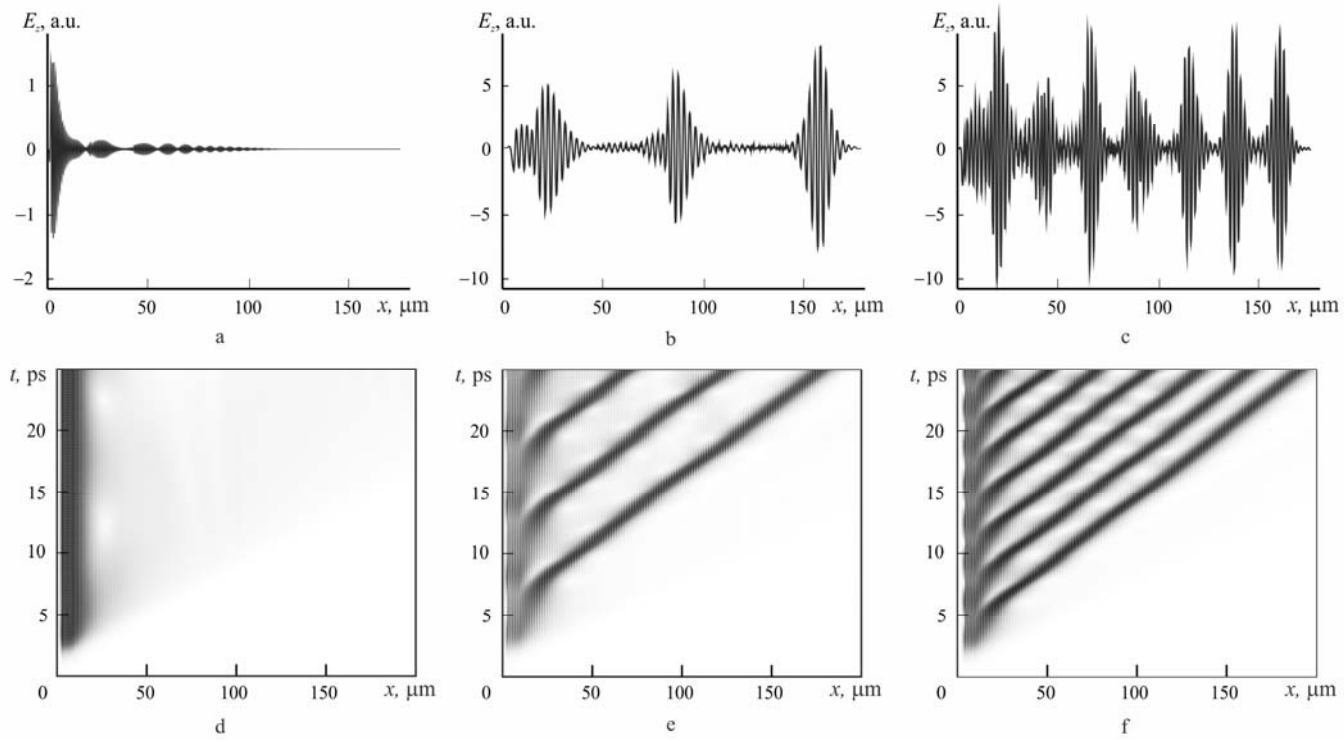


Figure 5: Distribution of the field component $E_z(x)$ and spatio-temporal distribution of $E_z(x)$ along the Bragg grating for the different amplitude values of CW input signal: $A=6$ (a, d), $A=7$ (b, e) and $A=10$ (c, f).

The transmission coefficient at this frequency is approximately equal to the value $T(\Omega_{cw}) \approx 10^{-4}$. A series of simulations was performed with the different value of the amplitude of the input signal denoted by A. When the power of source and therefore amplitude A is small, the electromagnetic wave exponentially decays as it propagates along the structure, as shown in Fig. 5a. Here the distribution of the field component $E_z(x)$ along the system is plotted. The time moment, at which the steady-state regime begins, was shown. The relatively low value of the nonlinear coefficient n_{nl} and small value of signal amplitude correspond to the linear system and the influence of the nonlinear effects is therefore negligibly small.

It was demonstrated that increasing the input signal amplitude one can obtain the signal propagation along the periodical structure. This can be explained as the transformation of the band structures of the periodic nonlinear system and the nonlinear frequency shift, which was depicted in Fig. 3. In the Fig. 5b the propagation of the signal with amplitude $A=7$ is shown. Moreover the signal profile inside the Bragg grating is specifically modulated and the formation of multiple gap-solitons is observed. If the amplitude of initial signal achieved a threshold value the gap-soliton is formed, however as the intensity is increased more gap-solitons are generated. In Fig. 5c the CW signal with amplitude $A=10$ was excited in the x_1 plane in the lead-in waveguide (Fig. 1). The number of the generated gap-solitons per system length (or per time unit) is increased in this case. In the Fig. 5d-f the spatio-temporal dynamics of CW signal propagation are demonstrated. The frequency of CW signal used in this simulation was chosen to be similar to the previous computation of the field distribution along the system. If the amplitude is below the threshold of gap-soliton formation the signal decays along the system, as it is shown in Fig. 5d. When the amplitude of initial signal was chosen to be $A=7$, the train of gap-solitons is formed. This dynamics of solitons generation is demonstrated in Fig. 5e. When the amplitude gets larger ($A=10$ in the Fig. 5f), the period of solitons generation is decreased. If the amplitude reachs the value $A=15$ the distance between solitons is decreased and is so small the the interaction between gap-solitons can be observed at the time $t>15$ ps (Fig. 6). By the solitons interaction their speed is conserved.

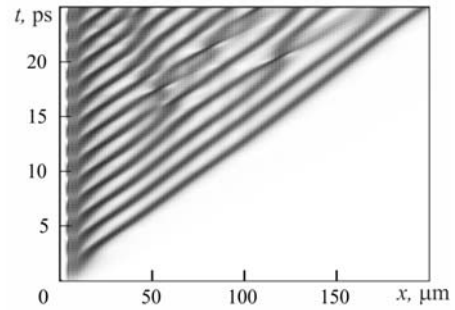


Figure 6: Spatio-temporal distribution of $E_z(x)$ for the amplitude of CW input signal $A = 15$.

5. Characteristics of gap soliton propagation

In this section the different characteristics of gap soliton propagation in nonlinear Bragg grating are studied.

The distances between solitons is decreased as the amplitude gets larger (Fig. 7). This calculation can be done from the spatio-temporal distributions of the field for the different values of the amplitude of input signal A.

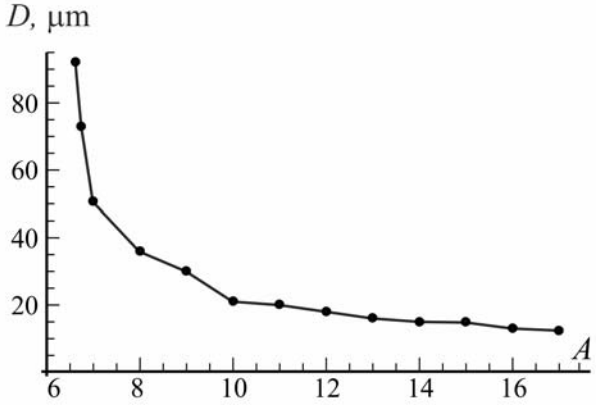


Figure 7: Distance between solitons as a function of input signal amplitude.

The velocity of solitons propagation can be estimated as the trajectory slope in the Fig. 5d-f. The result of this calculation is shown in Fig. 8. The threshold of generation was estimated. It was equal to the value $A_{th} \approx 6.7$. The approximate value is presented because near the threshold of generation the unstable behavior in signal dynamics can be observed – small fluctuation of the field energy at the left side of the grating can lead to the spontaneous gap soliton formation. And the process of solitons generation starts to be nonperiodical. The speed of propagation of solitons is increased as the amplitude A gets larger. There are difficulties in the further calculation of solitons' velocity (at the amplitude values $A > 15$) because the distance between them decreases and regular interactions of solitons occur.

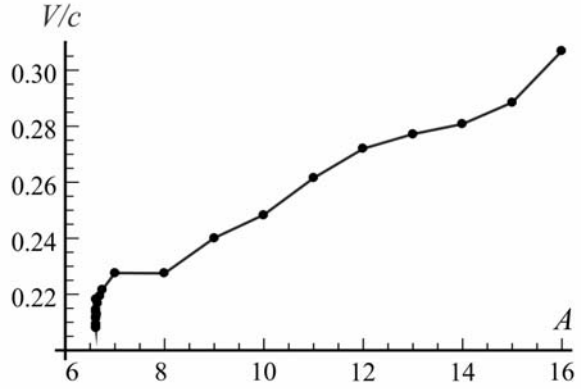


Figure 8: Velocity of solitons propagation at the different values of amplitude of input CW signal.

One of the most important characteristics of the process of generation of solitons is the efficiency of energy transformation from the energy of the input CW signal to the energy of resulting pulse signal:

$$\Sigma = P_r / S_x \qquad (3)$$

where $P_r = E \cdot f_{pulse}$ – time averaged power of output pulse signal, E – energy of electromagnetic field in the pulse, f_{pulse} – pulse repetition rate, S_x – time averaged power of the input signal.

The dependency of Σ vs amplitude A is shown in Fig.9. The efficiency of energy transformation can achieve 60-70 %.

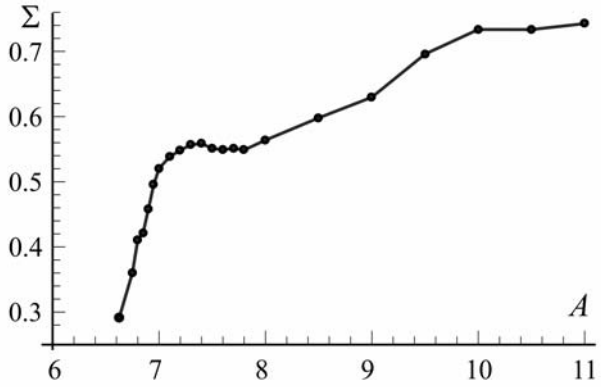


Figure 9:The efficiency of energy transformation for the different amplitudes of input signal.

6. Conclusions

In conclusion, the dynamic of the electromagnetic wave propagation in the 2D nonlinear Bragg grating was numerically studied. The calculation of band gap diagram and estimation of the cut-off frequencies in the periodical structure for the different values of input signal intensities was performed with the FDTD method. The good correspondence between the results of the cut-off frequencies computation and analysis of transmission spectra was shown. It has been shown that the nonlinear frequency shift lead to the possibility of CW signal propagation with the frequency near the upper branch of the photonic band gap. The process of multiple gap soliton formation and propagation in the nonlinear 2D Bragg grating has been observed. As the amplitude of input signal gets larger the distance between soliton-like pulses decreases and interaction between gap solitons can be observed. The quantitative characteristics of soliton propagation were obtained. The maximum value of energy transmission coefficient, which shows the efficiency of energy transformation from the energy of the input CW signal to the energy of soliton-like pulse signal, was equal to 60-70%.

Acknowledgements

This work was supported by the Russian Foundation for Basic Research Grant No 12-07-31009, 11-02-01280-a and by the Grant (project no. 11.G34.31.0030).

References

[1] J.D. Joannopoulos, S.G. Johnson, J.N. Winn, R.D. Meade, *Photonic Crystals: Molding the Flow of Light (Second Edition*), Princeton University Press, Princeton, 2008.

[2] G.P. Agrawal, *Nonlinear Fiber Optics*, 4th ed. Academic Press, San Diego, 2007.

[3] D. Taverner, N.G.R. Broderick, D.J. Richardson, R.I. Laming, M. Ibsen, Nonlinear self-switching and multiple gap-soliton formation in a fiber Bragg grating, *Optics Lett.* 23: 328-330, 1998.

[4] A.B. Aceves, S.Wabnitz, Self-induced transparency solitons in nonlinear refractive periodic media, *Phys. Lett. A* 141: 37-42, 1989.

[5] A.C. Newell, Nonlinear tunneling, *J. Math. Phys.* 19: 1126-1134, 1978.

[6] W. Chen, D.L. Mills, Gap Solitons and the Nonlinear Optical Response of Superlattices, *Phys. Rev. Lett.* 58: 160-163, 1987.

[7] C.M. de Sterke, J.E. Sipe, Switching dynamics of finite periodic nonlinear media: A numerical study, *Phys. Rev. A.* 42: 2858-2871, 1990.

[8] B.J. Eggleton, R.E. Slusher, C.M. de Sterke, P.A. Krug, J.E. Sipe, Bragg grating solitons, *Phys. Rev. Lett.* 76: 1627–1630, 1996.

[9] A.A. Balyakin., N.M. Ryskin, Modulation Instability in a Nonlinear Dispersive Medium Near Cut-Off Frequency, *Nonlinear Phenomena in Complex Systems* 7: 34-42, 2004.

[10] A. Taflove, S.C. Hagness, *Computational Electrodynamics: The Finite-Difference Time-Domain Method*, Artech House, Norwood, 2005.

[11] K.S. Yee, Numerical solution of initial boundary value problems involving Maxwell's equation in isotropic media, *IEEE Transaction on Antennas and propagation* 14: 302-307, 1996.

[12] A.F. Oskooi, D. Roundy, M. Ibanescu, P. Bermel, J.D. Joannopoulos, S.G. Johnson, MEEP: A flexible free-software package for electromagnetic simulations by the FDTD method, *Computer Physics Communications* 181: 687-702, 2010.

[13] C.M. de Sterke, Theory of modulation instability in fiber Bragg gratings, *J. Opt. Soc. Am. B.* 15: 2660-2667, 1998.

[14] H.A. Haus, *Waves and Fields in Optoelectronics*, Prentice-Hall, Englewood Cliffs, N.J., 188-190, 1985.

Photonic Crystal Fiber Propagation Characteristics

Raad Thaher

Department of Electrical Engineering

Al-Mustansiria University-Baghdad-Iraq

E-Mail: raadthaher@yahoo.com

Abstract

Photonic crystal fiber (PCF) is a new class of optical fiber based on the properties of photonic crystals, it have the ability to confine light in hollow cores. in this research paper the propagation characteristics of PCF described using different materials was investigated such as effective area, effective refractive index , numerical aperture and material dispersion for three different materials . It was concluded that zero dispersion occur at less wavelength when there is no silica in the constriction of PCF (i.e. 0.83μm for sapphire (extra ordinary wave).also the three dimension relation between dispersion, bit error rate, and fiber length for the three different materials was presented.

Keywords: BER, Dispersion, Numerical aperture, PCF

1. Introduction

Over the past few years, photonic crystal fiber (PCF) technology has evolved from a strong research – oriented field to a commercial technology providing characteristics such as a wide single-mode wavelength range, a bend-loss edge at a shorter wavelengths, a very large or small effective core area, group velocity, dispersion at visible and near field arrangement of air holes running along the length of the fiber. PCF is now finding applications in fiber-optic communications, fiber lasers, non-linear devices, high-power transmission, highly sensitive gas sensors and other areas.

Research cover the last decades has generated a wide range of rigorous numerical algorithms for modeling PCF ,such as plane wave expansion(PWE),finite difference time domaine, finite element methods.these versatile algorithms have been applied with success to study issues such as dispersion and losses for PC wave-guide.

The common term used in all these numerical methods is to calculate the effective refractive index of PCF because all linear and non-linear propagation properties of PCF can be analysed using effective refractive index.

We consider the type of PCF which consist of pure silica with a cladding and air holes of diameter (d) arranged in a triangular lattice with pitch (Λ).

The effective area is a quantity of great importance. It is originally introduced as a measure of non-linearities, a low effective area gives a high density of power needed for non-linear effect to be significant [1].The effective area can be related to the spot size and it is also important in the context of confinement loss [2],microbending loss[3], macrobending loss splicing loss[4]and numerical aperture[5].

The chromatic dispersion of the PCF s can be determined by:

$$D = -\frac{\lambda}{c}.\frac{d^2 n_{eff}}{d\lambda^2} + D_m \ , n_{eff} = \frac{\beta}{K_o} \ , \ k_o = \frac{2\pi}{\lambda}$$

Where λ, c are wavelength and speed of light respectively in free space

n_{eff} the effective refractive index of the PCF core

D_m the material dispersion

However , the material dispersion can be calculated using sellmeier equation[6].

Their combination leads to signal degradation in optical fibers for telecommunications because the varying delay in arrival time between different components of signal "smearont" the signal in time[7].

2. Theoretical Background [2,5,7]

Maxwell's equations predict the propagation of electromagnetic energy away from time varying source in the form of waves.They can be expressed by:

$$\nabla X\vec{E} = -\frac{dB}{dt} = -jw\mu\vec{H} \qquad (1)$$

$$\nabla X\vec{H} = J + \frac{d\bar{D}}{dt} = (\sigma + jw\epsilon)\vec{E} \qquad (2)$$

$$\nabla . \vec{D} = \rho_v \qquad (3)$$

$$\nabla . \vec{B} = 0 \qquad (4)$$

By taking the curl of equation (1) and substitute in equation (2), we get

$$\nabla^2 E = jw\mu(\sigma + jw\epsilon)\vec{E} = \beta^2 \vec{E} \qquad (5)$$

And by taking the curl of equation (2)and substitute in equation (1)

$$\nabla^2 H = jw\mu(\sigma + jw\epsilon)\vec{H} \qquad (6)$$

Where β: is the propagation constant and can be expressed as

$$\beta = \sqrt{jw\mu(\sigma + jw\epsilon)} = \alpha + j\gamma \qquad (7)$$

Where α is the attenuation constant which defines the rate which the fields of the waves are attenuated as the wave propagates

γ is the phase constant which defines the phase rate at which the phase changes as the wave propagates

From the properties of the medium $(\mu, \epsilon, \sigma)$the attenuation and phase constants can be calculated (i.e. $\beta^2 = jw\mu(\sigma + jw\epsilon) = (\alpha + j\gamma)^2 = \alpha^2 + 2j\alpha\gamma - \gamma^2$)

Therefore

$$\left.\begin{aligned} \alpha &= w\sqrt{\frac{\mu\epsilon}{2}\left(\sqrt{1 + \left(\frac{\sigma}{w\epsilon}\right)^2} - 1\right)} \\ \text{And} \\ \gamma &= w\sqrt{\frac{\mu\epsilon}{2}\left(\sqrt{1 + \left(\frac{\sigma}{w\epsilon}\right)^2} + 1\right)} \end{aligned}\right\} \qquad (8)$$

W is the signal frequency in rad/sec

The propagation constant can express the effective refractive index and the wavelength dispersion as

$$\left.\begin{aligned} D_w(\lambda) &= -\frac{\lambda}{c}.\frac{d^2 n_{eff}}{d\lambda^2} \\ \text{And} \\ n_{eff} &= \frac{\beta(\lambda, n_m)}{K_o} \end{aligned}\right\} \qquad (9)$$

Where n_m is the refractive index of any material, K_o is the wave number

2.1 Dispersion calculation

PCF 's are made of a periodic arrangement of fused silica and air holes running to the parallel axis of the fiber . An essential effect of the transverse periodic structure to alter the effective index for propagation along the direction of the fiber leading to intriguing new dispersive properties

we focus on the dispersion property of PCFs with triangular air silica structure where the central air hole is missing as a high index defect as shown in figure (1)

(d and Λ are air hole diameter and pitch respectively)

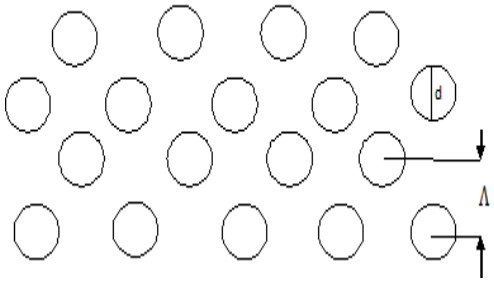


Figure1: All silica photonic crystal fiber

In the PCF design , the air hole diameter to pitch ratio is a key parameter The total dispersion loss of a PCF can be approximated [9] by the sum of waveguide dispersion and material dispersion as

$$D(\lambda) = D_w(\lambda) + \Gamma(\lambda) D_m(\lambda)$$

Where $\Gamma(\lambda)$ is the confinemental factor of silica (≈ 1 for most practical PCF's)

The material dispersion D_m is decided by the material that is used in the PCF. The material dispersion can be directly derived from the Sellmeier formula [10] which can be expressed by

$$n^2(\lambda) = 1 + \frac{\beta_1 \lambda^2}{\lambda^2 - c_1} + \frac{\beta_2 \lambda_2^2}{\lambda^2 - c_2} + \frac{\beta_3 \lambda_2^2}{\lambda^2 - c^2}$$

Where n is the refractive index . β_1 , β_2 , β_3 and c_1 , c_2 , c_3 are experimentally determined sellmeier coefficients .Table (1) shows the coefficients values for the three different materials (borosilicate, silica, sapphire for extra ordinary wave)which will be considered in our research paper.

Table 1 Sellmeier coefficients for three different materials

Material	Coefficient					
	β_1	β_2	β_3	C_1	C_2	C_3
Borosilicate	1.03961212	0.231792344	1.01046945	6.00069867	2.00179144	$1.03560653*10^2$
Fused Silica	0.69616300	0.407942600	0.897479400	$4.67914826*10^{-3}$	$1.35120631*10^{-2}$	97.9340025
Sapphire for extra ordinary wave	1.5039759	0.55069141	6.5927379	$5.48041129*10^{-3}$	$1.47994281*10^{-2}$	$4.0289514*10^2$

Figure (2) shows the relationship between $\eta_{eff}(\lambda)$ with wavelength for the three different materials which shows that the fused silica gives better refractive index for different wavelengths.The waveguide dispersion of PCF is related to the transversal geometrical structure which contributes all the design freedom.

2.2 Effective Area

The effective area is a quality of great importance. it was considered as a measure of non-linearities . A low effective area gives a high density of power needed for non linear effects to be significant [1].However, the effective area can be related to the spot area (w) through

$A_{eff} = \pi w^2$ and thus it is also important in the context of confinement loss , microbending loss , splicing loss ,and numerical aperture .

2.3 Non-linearity Coefficient

The non-linearity coefficient is given by [1]

$$\Psi = \frac{n_2 \omega}{cA_eff} = \frac{2\pi n_2}{\lambda A_{eff}} \qquad (10)$$

Where n_2 is the non-linear index coefficient in the non linear part of the refractive index (that is mean $\delta_n = n_2 |E|^2$). Thus knowledge of A_{eff} is an important starting point in understanding of non-linear phenomena in PCFs.

2.4 Numerical Aperture (NA)

The numerical aperture (NA) relates to the effective area.for a Gaussian field of width z , one has the standard approximate expression

$$\tan\theta = \frac{\lambda}{\pi z} \qquad (11)$$

for half divergence angle θ of light radiated from the end facet of the fiber [8].the corresponding numerical aperture can be expressed as

$$\text{NA}=\sin\theta \cong \left(1 + \pi A_{eff}\right)^{-\frac{1}{2}} \qquad (12)$$

2.4 Macro Bending Loss

For the estimation of the macro-bending loss coefficient the sakai-Kimra formula [11] can be applied to PCFs. This involves the evaluation of the ratio of $\frac{A_e^2}{P}$ where A_e is the amplitude coefficient of the field in the cladding and P is the power carried by the fundamental mode.

The Gassian approximation gives:

$$\frac{A_e^2}{P} = \frac{1}{A_{eff}} \qquad (13)$$

And this was used to calculate the marco bending loss in the PCFs based on fully eigenmodes of maxwell equations.

2.5 Splicing Loss

Splicing loss can be quantified in terms of the concept of effective areas.the splicing of two aligned fibers with effective areas $A_{eff1} and\ A_{eff2}$ will have a power transmission coefficient $T < 1$ is given by

$$T \approx \frac{4A_{eff1}A_{eff2}}{\left(A_{eff1}+A_{eff2}\right)^2} \qquad (14)$$

Due to the mismatch of effective areas.

2.6 The Bit Error Rate (BER)

The bit error rate (BER) can be expressed by[7]

$$BER = \frac{1}{4D(\lambda)*L*\Delta\lambda} \qquad (15)$$

Where L is the fiber length, $\Delta\lambda$ is the spectral width of the light source

3- Results and Conclusions

The results showed the propagation characteristics for different materials (silica, borosilicate, and sapphire) was carried out using MATLAB software program .figure (2) shows the relationship between the refractive index and wavelengths for the silica, borosilicate and sapphire (extraordinary wave). It can be noted that the fused silica and borosilicate graphs are near to each other because the silica enter in the construction in both materials.

Figure (3) shows the effect of (A_{eff} /Pitch) ratio and wavelength for different pitch values. The micro bending loss and diameter was shown in figure (4).However the effective area play an important role in the behavior of PCF because it determines the numerical aperture (NA) and its relation to wavelength as shown in figure (5) which shows the numerical aperture for different effective areas.

The most important factor is the fiber dispersion for the three different materials which is evaluated from Sellimer equation for $\eta_{eff}$and equation (9)which are shown in figures (6),(7),(8) respectively .It can be seen from figure (7) that zero dispersion occur at $1.28\mu m$ for silica ,at $1.19\mu m$ for borosilicate, and $0.83\mu m$ for sapphire (for extraordinary wave).it can be concluded that when there is no silica in the construction of the PCF it will lead low zero dispersion wavelength. Also when the construction contain silica give ,approximately, characteristics near to each other. as a suggestion to modify this work, on can study other materials such as florid or phosphate .in the construction of photonic crystal fibers. Also the bit error rate variation with dispersion for different fiber lengths (for borosilicate , fsed silica,sapphire) are shown in figures (9),(10),(11) respectively. Figure (12)show the three dimension graph between the three variables (fiber length , dispersion and bit error rate)for the different materials as shown in figures(12),(13),(14) respectively .

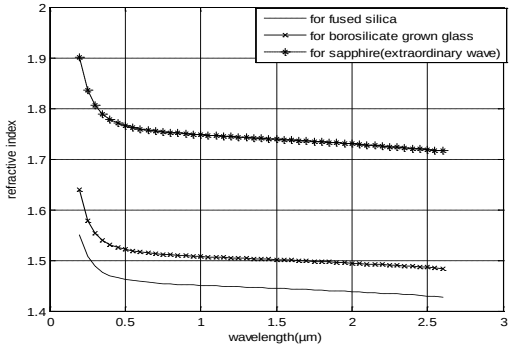


Figure 2: Refractive index & wavelength for different materials

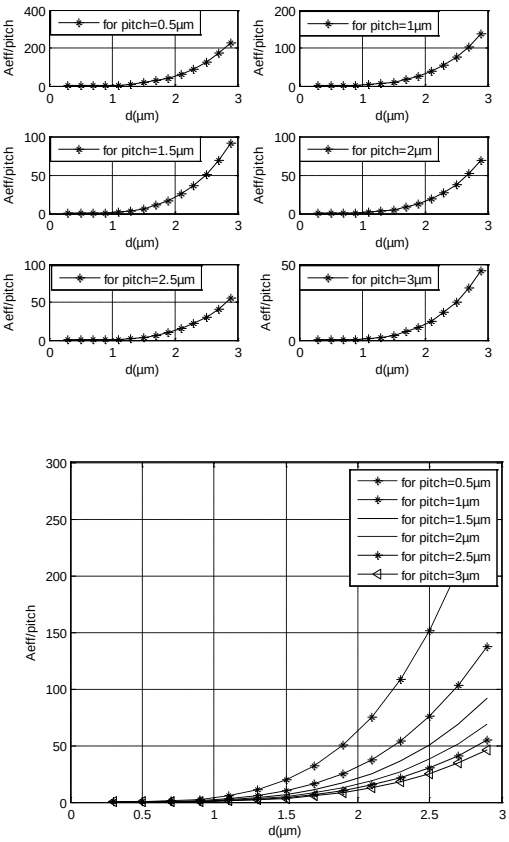


Figure 3: The variation of effective area and diameter for different pitches

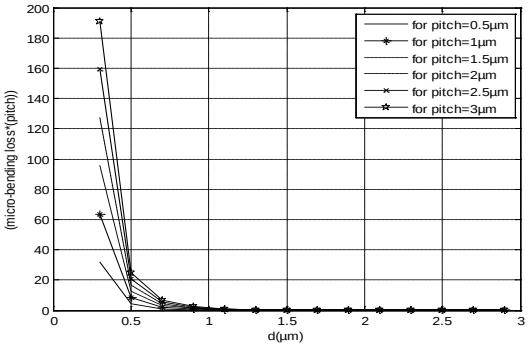


Figure 4: Microbending loss and diameter for different pitches

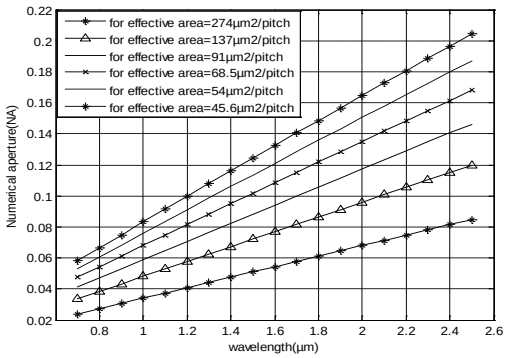


Figure 5: Numerical aperture and wavelength for different effective areas

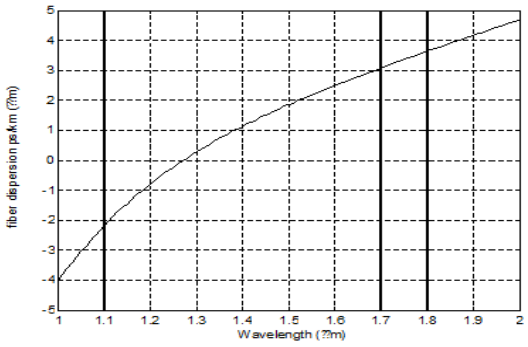


Figure 6: The relation between dispersion &wavelength for fused silica

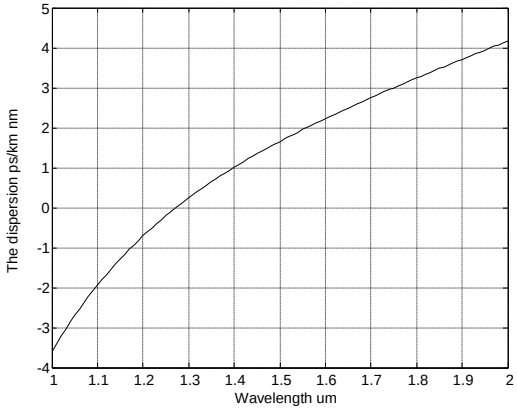


Figure 7: the relation between dispersion and wavelength for borosilicate

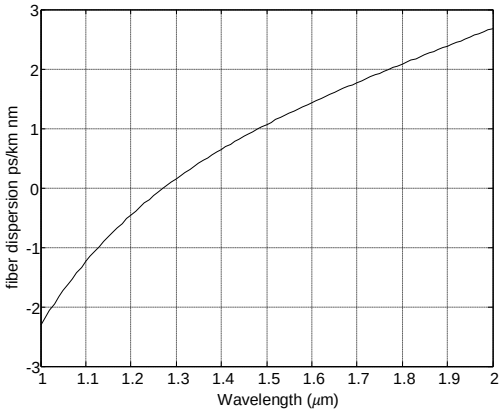


Figure 8: the relation between dispersion and wavelength for sapphire

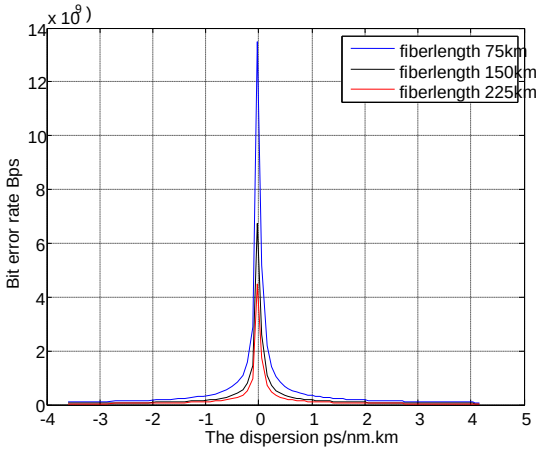


Figure 9: the relation between bit error rate & dispersion for borosilicate

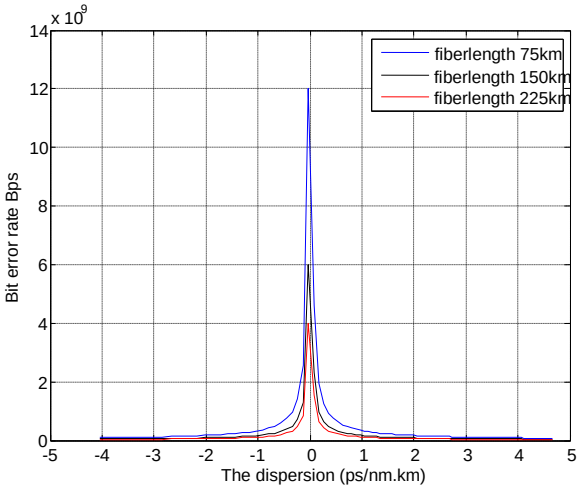


Figure 10: the relation between bit error rate & dispersion for fused silica

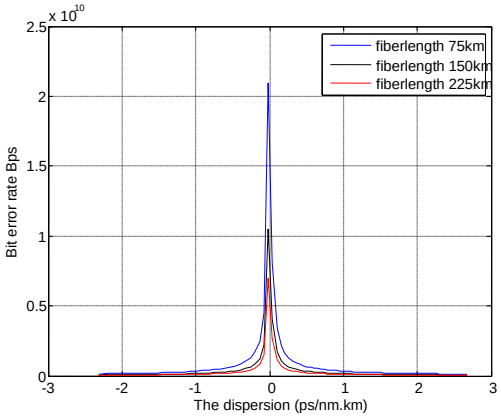


Figure 11: the relation between bit error rate & dispersion for sapphire

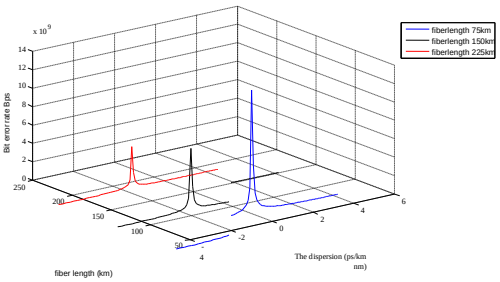


Figure 12: the relation between bit error rate & dispersion for borosilicate in 3-D

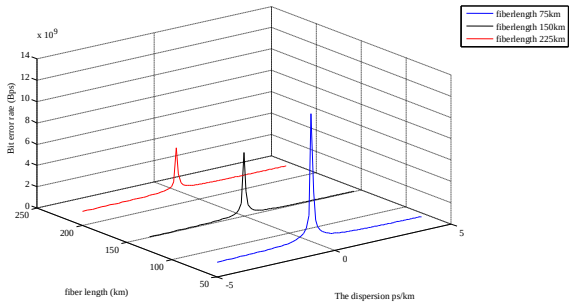


Figure 13: the relation between bit error rate & dispersion for fused silica in 3-D

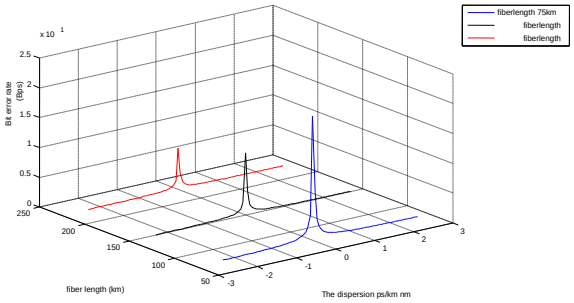


Figure 14: the relation between bit error rate & dispersion for sapphire in 3-D

4. References

G.P.Agrawal , "non-linear fiber optics",Academic press .San Diego,2001.

1. T.P.White,R.C.Mcphedran and M.J.Steel ,"Confinement losses in microstructured optical fibers,"Opt.lett.26,pp1660-1662,2001.

2. K.Peterman,"Fundamental mode microbending loss in graded index and w fibers",Opt.Quantum Electron g,pp 167-175,1977.

3. D.Marcuse,"Loss analysis of single-mode fiber splices" , Bell system.Tech.J.56,pp 703.1977

4. N.A.Mortenson,J.Broeng ,"Numerical aperture of single –mode photonic crystal fibers ",http//arxiv.org/abs/physics/0202073

5. H.Tanzer,"Course materials for EE167",California state university ,Sacramento,2002

6. Fayroz.A.S and Zahraa.H.M,"studying the effect of fiber length on bit error rate and chromatic dispersion for different materials of fiber " Conference of university of technology 2011

7. A.K.Ghatak and K.Thygarajan"Introduction to fiber optics" , Cambridge university pree,Cambridge,1998

8. S.S Mishra et.al ,"Full-Vector finite element method",international jornal of engineering science and technology,vol.2(9),pp4520-4525,2010

9. CHI.Hao and shenLin-fang,"Design of photonic crystal fibers with anomalus dispersion" , optoelectronics letters,Vol.2 , No.1 , Jan 2006

10. J.Sakai and T.Kimura ,"Bending loss of propagation modes in arbitrary-index profile optical fibers",Appl.optics 17,pp 1499-1506,1978

Construction of Dirac Points Using Triangular Supercrystals

Mohammad Hasan Aram, Roya Mohajeri, and Sina Khorasani*

Department of Electrical Engineering,
Sharif University of Technology, Tehran, Iran
*corresponding author, E-mail: khorasani@sina.sharif.edu

Abstract

We show a methodology on how to construct Dirac points that occur at the corners of Brillouin zone as the Photonic counterparts of Graphene. We use a triangular lattice with circular holes on Silicon substrate to create a Coupled Photonic Crystal Resonator Array (CPCRA) which its cavitiy resonators play the role of Carbon atoms in Graphene. At first we draw the band structure of our CPCRA using tight binding method. For this purpose we first designed a cavity which its resonant frequency is approximately at the middle of the first H-polarization band gap of the basis triangular lattice. Then we obtained dipole modes and magnetic field distribution of this cavity using Finite Element Method (FEM). Finally we drew the two bands that construct the Dirac points together with the frequency contour plots for both bands and compared with the Plane Wave Expansion (PWE) and FEM results to prove the existence of Dirac point in the H-polarization band structure of lattices with air holes.

1. Introduction

Since the discovery of graphene in 2004 by K. Novoselov and A. Geim a lot of researchers have found many interesting applications and specifications for this material. The main reason for these specs is its exclusive band structure in which two bands coincide each other at a point in the corners of Brillouin zone called Dirac point. These two bands are linear near this point, thus the electron dispersion can be described by Dirac equation in this region. Graphene is a good material to visualize some relativistic behavior of electrons such as quantum hall effect, Zitterbewegung, and Klein paradox. But because of complex interaction and limited scale, some of these phenomena can not be observed directly[1].

Recently efforts have been made to construct Dirac points in the band structure of optical materials [2]-[8] to examine the existence of mentioned phenomena for photons of electromagnetic fields. Since we have great control on the design of Photonic Crystals (PC), it is simpler to observe these phenomena in them than in graphene. Some of the predicted or examined characteristics of PCs with Dirac point in their band structure are inverse proportionality of photon conductance to the length of crystal [9, 10, 11], Extinction of coherent backscattering [12], Zitterbewegung phenomenon for photons near the Dirac point [1], and one-way light transport [13]. Some novel applications for this kind of crystals have been proposed as well; among them we can mention construction of photonic topological insulators [14] and directional optical waveguide in PCs [15].

In the remaining of this paper we first explain the design of specified supercrystal and then its band structure calculation to show the Dirac point in the H-polarization mode.

2. Crystal design

In order to construct a crystal which is similar to Graphene we should use a triangular lattice as our basis. Also since we want to use tight-binding method to obtain the band structure, we have to create cavities which in addition to form a triangular lattice should have confined electromagnetic field and be separated sufficiently. The triangular basis lattice was supposed to be made of Silicon substrate with circular air holes that their radius is 0.35 of lattice constant, a. The distance between cavities was set to be two times the lattice constant. The cavities were arranged so that every cavity has six cavities in its neighborhood. The designed CPCRA is shown in Fig. 1.

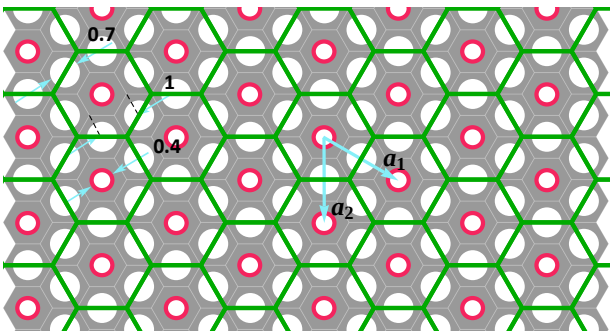


Figure 1: Supercrystal designed in this project. Green hexagons are unit cells of this crystal. $\vec{a}_1$ and $\vec{a}_2$ are primitive vectors

As said above the field of the cavities should be confined to be able to use tight-binding method. To confine the field we have to design the cavity so that its resonance frequency falls inside a band gap of the basis lattice. We know a triangular lattice with circular air holes has a wide gap between its first and second band in H-polarization mode. By changing the cavity radius we brought its resonance frequency near the middle of the band gap. Of course a cavity has different resonance frequencies depending on its field

distribution but since we need two bands to form Dirac cones it seems we should consider a field distribution that is degenerate. So we considered only dipole field. Fig. 2 shows the average amplitude of z component of dipole magnetic field inside cavities with different radii. The magenta band in the figure is the first gap of our basis lattice. The peaks of curves indicate the resonance frequency of each cavity. It can be seen that the resonance frequency of the cavity with radius 0.2a is approximately in the middle of the gap. So we chose this radius for the cavities of our supercrystal.

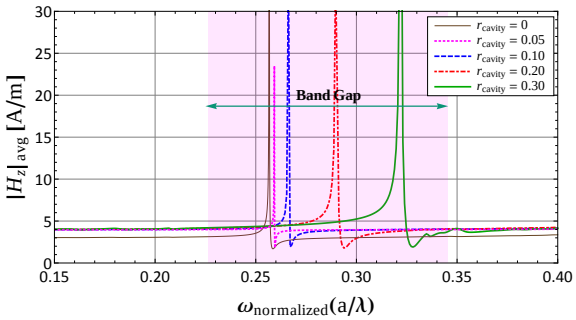


Figure 2: Average amplitude of z component of dipole magnetic field inside cavities with different radii

3. Symmetry analysis

Looking at the structure of the supercrystal in Fig. 1 it is obvious that it has C_{6v} symmetry. The operators of this symmetry group are as follows

$$C_{6v} = \left\{ \begin{array}{c} (\hat{E}), (\hat{C}_6, \hat{C}_6^{-1}), (\hat{C}_3, \hat{C}_3^{-1}), \\ (\hat{C}_2), (\hat{\sigma}_x, \hat{\sigma}'_x, \hat{\sigma}''_x), (\hat{\sigma}_y, \hat{\sigma}'_y, \hat{\sigma}''_y) \end{array} \right\} \quad (1)$$

Three highly symmetric points, the Γ point, $(0,0)$, the K point, $(4\pi/3a, 0)$, and the M point, $(\pi/a, -\pi/\sqrt{3}a)$ in the reciprocal lattice have C_{6v}, C_{3v}, and C_{2v} group symmetry respectively. The T points (between Γ and K), Σ points (between Γ and M), and Λ points (between K and M) have C_{1h} group symmetry. The compatibility relations between adjacent points in the reciprocal lattice is summarized in Table 1.

To find modes of bands in the band structure we have to find irreducible representations of highly symmetric points in reciprocal lattice. The number of a specific mode, A, at a point in the reciprocal lattice can be calculated using the following formula [16].

$$\frac{\sum_{\hat{R}\in\mathscr{G}} N_{\hat{R}}.\mathcal{X}_A(\hat{R})}{number\ of\ elements\ in\ \mathscr{G}} \quad (2)$$

where $\mathscr{G}$ is the group symmetry of the point, $N_{\hat{R}}$ is the number of invariant points of the specified type when the operator $\hat{R}$ is applied to the lattice, and $\mathcal{X}_A(\hat{R})$ is the character of $\hat{R}$ for mode A in that point. To find $N_{\hat{R}}$ we should determine the exact location of each point in the reciprocal lattice. This is done in Fig. 3. Using this figure modes of each point is listed in Table 2.

Table 1: Compatibility relations in the hexagonal lattice

		T	**Λ**	**Σ**
Γ :	A_1	A	–	A
	A_2	B	–	B
	B_1	A	–	B
	B_2	B	–	A
	C_1, C_2	A, B	–	A, B
K :	A_1	A	A	–
	A_2	B	B	–
	C	A, B	A, B	–
M :	A_1	–	A	A
	A_2	–	B	B
	B_1	–	B	A
	B_2	–	A	B

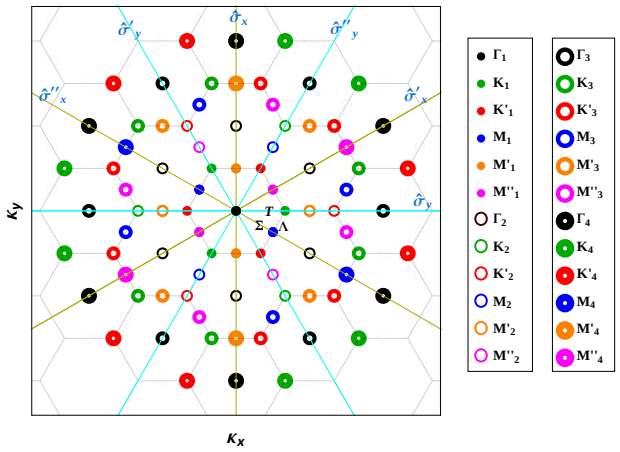


Figure 3: Position of defferent points in the reciprocal lattice

4. Band structure calculation

In this section we calculate the dispersion relation of the two bands which create the Dirac cone in the band structure of the designed supercrystal using tight binding method and then verify these two bands with the band structure obtained by PWE and FE method. The results are in good agreement with each other.

4.1. Tight binding method

It was mentioned that a triangular lattice with air holes has a wide gap between its first and second band in H-polarization mode. So we are interested in the H-polarization bands of the designed CPCRA. In this mode cavities have confined resonant field and tight binding is operative. The cavity field distribution which is studied here is double degenerate hence degenerate tight binding method is applied. If we show each of the electric field distribution of a cavity in its resonant frequency, ν, by $\vec{\mathscr{E}}_{\nu,l}$, $(l = 1, 2)$, then according to the first and the second Maxwell equa-

Table 2: modes of points of reciprocal lattice

Symmetry	*Point*	*Irreducible representations*
$\mathbf{C_{6v}}$	$\mathbf{\Gamma_1}$	A_1
	$\mathbf{\Gamma_2}$	A_1, B_2, C_1, C_2
	$\mathbf{\Gamma_3}$	A_1, B_1, C_1, C_2
	$\mathbf{\Gamma_4}$	A_1, B_2, C_1, C_2
$\mathbf{C_{3v}}$	$\mathbf{K_1}$	A_1, C
	$\mathbf{K_2}$	A_1, C
	$\mathbf{K_3}$	$A_1, A_2, 2C$
	$\mathbf{K_4}$	$A_1, A_2, 2C$
$\mathbf{C_{2v}}$	$\mathbf{M_1}$	A_1, B_1
	$\mathbf{M_2}$	A_1, B_2
	$\mathbf{M_3}$	A_1, A_2, B_1, B_2
	$\mathbf{M_4}$	A_1, B_1

tions we have

$$\nabla \times \nabla \times \vec{\mathscr{E}}_{\nu,l}\left(\vec{r}\right) = \varepsilon_r\left(\vec{r}\right)\frac{\nu^2}{c^2}\vec{\mathscr{E}}_{\nu,l}\left(\vec{r}\right) \tag{3}$$

where $\varepsilon_r\left(\vec{r}\right)$ is the profile of the relative permittivity of a single cavity and c is the speed of light in vacuum. For H-polarization mode, electric field $\vec{\mathscr{E}}_{\nu,l}$, has two components in x and y directions. Because of the orthogonality of eigenmodes of a degenerate field distribution we can write

$$\int \varepsilon_r\left(\vec{r}\right)\vec{\mathscr{E}}^*_{\nu,l}\left(\vec{r}\right)\cdot\vec{\mathscr{E}}_{\nu,k}\left(\vec{r}\right)d^2r = \delta_{lk} \quad , \quad l,k = 1,2 \tag{4}$$

According to Bloch theorem electric field distribution in the entire CPCRA lattice is obtained from the following equation

$$\mathbf{E}_{\vec{\kappa}}\left(\vec{r}\right) = \sum_{n,m=-\infty}^{+\infty}\sum_{l=1}^{2} e^{-i(n\vec{\kappa}\cdot\vec{a}_1+m\vec{\kappa}\cdot\vec{a}_2)}b_l\vec{\mathscr{E}}_{\nu,l}\left(r-n\vec{a}_1-m\vec{a}_2\right) \tag{5}$$

where $\vec{a}_1$ and $\vec{a}_2$ are primitive vectors of the CPCRA that are shown in Fig. 1, $\vec{\kappa}$ is the Bloch wave vector, and b_l is a constant. Similar to Equation (3) we can write

$$\nabla \times \nabla \times \mathbf{E}_{\vec{\kappa}} = \epsilon_r\left(\vec{r}\right)\frac{\omega^2}{c^2}\mathbf{E}_{\vec{\kappa}} \tag{6}$$

for electric field of the entire lattice, where $\epsilon_r\left(\vec{r}\right)$ is the profile of relative permittivity of the whole CPCRA. By replacing $\mathbf{E}_{\vec{\kappa}}$ from equation (5) into equation (6) we have.

$$\begin{aligned}\sum_{n,m=-\infty}^{+\infty}\sum_{l=1}^{2}\Big(e^{-i(n\vec{\kappa}\cdot\vec{a}_1+m\vec{\kappa}\cdot\vec{a}_2)}b_l \\ \nabla\times\nabla\times\vec{\mathscr{E}}_{\nu,l}(\vec{r}-n\vec{a}_1-m\vec{a}_2)\Big) \\ = \epsilon_r\left(\vec{r}\right)\frac{\omega^2}{c^2}\sum_{n,m=-\infty}^{+\infty}\sum_{l=1}^{2}\Big(e^{-i(n\vec{\kappa}\cdot\vec{a}_1+m\vec{\kappa}\cdot\vec{a}_2)} \\ b_l\vec{\mathscr{E}}_{\nu,l}\left(\vec{r}-n\vec{a}_1-m\vec{a}_2\right)\Big)\end{aligned} \tag{7}$$

Now if we put the value of $\nabla \times \nabla \times \vec{\mathscr{E}}_{\nu,l}\left(r-n\vec{a}_1-m\vec{a}_2\right)$ from equation (3) into equation (7) we reach the following equation.

$$\begin{aligned}\nu^2\sum_{n,m=-\infty}^{+\infty}\sum_{l=1}^{2}\Big(e^{-i(n\vec{\kappa}\cdot\vec{a}_1+m\vec{\kappa}\cdot\vec{a}_2)}b_l \\ \varepsilon_r\left(\vec{r}-n\vec{a}_1-m\vec{a}_2\right)\vec{\mathscr{E}}_{\nu,l}\left(\vec{r}-n\vec{a}_1-m\vec{a}_2\right)\Big) \\ = \omega^2\sum_{n,m=-\infty}^{+\infty}\sum_{l=1}^{2}\Big(e^{-i(n\vec{\kappa}\cdot\vec{a}_1+m\vec{\kappa}\cdot\vec{a}_2)}b_l \\ \epsilon_r\left(\vec{r}\right)\vec{\mathscr{E}}_{\nu,l}\left(\vec{r}-n\vec{a}_1-m\vec{a}_2\right)\Big)\end{aligned} \tag{8}$$

Inner product of both sides of equation (8) by $\vec{\mathscr{E}}^*_{\nu,k}\left(r\right)$ and then integration over $x-y$ plane results in

$$\begin{aligned}\nu^2\sum_{n,m=-\infty}^{+\infty}\sum_{l=1}^{2}\Big\{e^{-i(n\vec{\kappa}\cdot\vec{a}_1+m\vec{\kappa}\cdot\vec{a}_2)}b_l \\ \int\Big(\vec{\mathscr{E}}^*_{\nu,k}\left(\vec{r}\right)\cdot\vec{\mathscr{E}}_{\nu,l}\left(\vec{r}-n\vec{a}_1-m\vec{a}_2\right) \\ \varepsilon_r\left(\vec{r}-n\vec{a}_1-m\vec{a}_2\right)\Big)d^2r\Big\} \\ = \omega^2\sum_{n,m=-\infty}^{+\infty}\sum_{l=1}^{2}\Big\{e^{-i(n\vec{\kappa}\cdot\vec{a}_1+m\vec{\kappa}\cdot\vec{a}_2)}b_l \\ \int\vec{\mathscr{E}}^*_{\nu,k}\left(\vec{r}\right)\cdot\vec{\mathscr{E}}_{\nu,l}\left(\vec{r}-n\vec{a}_1-m\vec{a}_2\right)\epsilon_r\left(\vec{r}\right)d^2r\Big\}\end{aligned} \tag{9}$$

If we show the overlap integrals of electric field by

$$\begin{aligned}\alpha^{k,l}_{n,m} = \int\Big(\vec{\mathscr{E}}^*_{\nu,k}\left(\vec{r}\right)\cdot\vec{\mathscr{E}}_{\nu,l}\left(\vec{r}-n\vec{a}_1-m\vec{a}_2\right) \\ \varepsilon_r\left(\vec{r}-n\vec{a}_1-m\vec{a}_2\right)\Big)d^2r\end{aligned} \tag{10}$$

$$\begin{aligned}\beta^{k,l}_{n,m} = \int\Big(\vec{\mathscr{E}}^*_{\nu,k}\left(\vec{r}\right)\cdot\vec{\mathscr{E}}_{\nu,l}\left(\vec{r}-n\vec{a}_1-m\vec{a}_2\right) \\ \epsilon_r\left(\vec{r}\right)\Big)d^2r\end{aligned} \tag{11}$$

we can write equation (9) in an abstract form.

$$\begin{aligned}\nu^2\sum_{n,m=-\infty}^{+\infty}\sum_{l=1}^{2}b_l e^{-i(n\vec{\kappa}\cdot\vec{a}_1+m\vec{\kappa}\cdot\vec{a}_2)}\alpha^{k,l}_{n,m} \\ = \omega^2\sum_{n,m=-\infty}^{+\infty}\sum_{l=1}^{2}b_l e^{-i(n\vec{\kappa}\cdot\vec{a}_1+m\vec{\kappa}\cdot\vec{a}_2)}\beta^{k,l}_{n,m}\end{aligned} \tag{12}$$

It is seen from equations (10) and (11) that $\alpha^{k,l}_{n,m} = \left(\alpha^{k,l}_{-n,-m}\right)^*$ and $\beta^{k,l}_{n,m} = \left(\beta^{k,l}_{-n,-m}\right)^*$. on the other hand for centrosymmetric permittivity profiles, $\alpha^{k,l}_{n,m}$ and $\beta^{k,l}_{n,m}$ are real valued [17]. We can assume

$$\alpha^{k,l}_{n,m} \simeq \beta^{k,l}_{n,m} \simeq 0 \quad , \quad (2 \leq |n|, |m|) \tag{13}$$

for weak coupling conditions. Thus equation (12) can be

written in an approximate form.

$$\nu^2 \sum_{l=1}^{2} b_l \Big(\alpha_{0,0}^{k,l} + 2\mathbf{Re}\Big\{ \alpha_{1,0}^{k,l} e^{-i(\vec{\kappa}\cdot\vec{a}_1)} + \alpha_{-1,1}^{k,l} e^{i(\vec{\kappa}\cdot\vec{a}_1 - \vec{\kappa}\cdot\vec{a}_2)} + \alpha_{0,1}^{k,l} e^{-i(\vec{\kappa}\cdot\vec{a}_2)} \Big\} \Big) \tag{14}$$

$$\simeq \omega^2(\vec{\kappa}) \sum_{l=1}^{2} b_l \Big(\beta_{0,0}^{k,l} + 2\mathbf{Re}\Big\{ \beta_{1,0}^{k,l} e^{-i(\vec{\kappa}\cdot\vec{a}_1)} + \beta_{-1,1}^{k,l} e^{i(\vec{\kappa}\cdot\vec{a}_1 - \vec{\kappa}\cdot\vec{a}_2)} + \beta_{0,1}^{k,l} e^{-i(\vec{\kappa}\cdot\vec{a}_2)} \Big\} \Big)$$

This equation can be simplified as

$$\nu^2 \sum_{l=1}^{2} b_l \Big(\alpha_{0,0}^{k,l} + 2\alpha_{1,0}^{k,l} \cos(\vec{\kappa}\cdot\vec{a}_1) + 2\alpha_{-1,1}^{k,l} \cos(\vec{\kappa}\cdot\vec{a}_1 - \vec{\kappa}\cdot\vec{a}_2) + 2\alpha_{0,1}^{k,l} \cos(\vec{\kappa}\cdot\vec{a}_2) \Big) \tag{15}$$

$$\simeq \omega^2(\vec{\kappa}) \sum_{l=1}^{2} b_l \Big(\beta_{0,0}^{k,l} + 2\beta_{1,0}^{k,l} \cos(\vec{\kappa}\cdot\vec{a}_1) + 2\beta_{-1,1}^{k,l} \cos(\vec{\kappa}\cdot\vec{a}_1 - \vec{\kappa}\cdot\vec{a}_2) + 2\beta_{0,1}^{k,l} \cos(\vec{\kappa}\cdot\vec{a}_2) \Big)$$

We can write equation (15) in a compact matrix form as

$$\nu^2 \big[\mathbb{A}(\vec{\kappa})\big] \begin{bmatrix} b_1 \\ b_2 \end{bmatrix} = \omega^2(\vec{\kappa}) \big[\mathbb{B}(\vec{\kappa})\big] \begin{bmatrix} b_1 \\ b_2 \end{bmatrix} \tag{16}$$

where matrices $\big[\mathbb{A}(\vec{\kappa})\big]$ and $\big[\mathbb{B}(\vec{\kappa})\big]$ are equal to

$$\big[\mathbb{A}(\vec{\kappa})\big] = \begin{bmatrix} \alpha_{0,0}^{1,1} & \alpha_{0,0}^{1,2} \\ \alpha_{0,0}^{2,1} & \alpha_{0,0}^{2,2} \end{bmatrix} + 2\cos(\vec{\kappa}\cdot\vec{a}_1) \begin{bmatrix} \alpha_{1,0}^{1,1} & \alpha_{1,0}^{1,2} \\ \alpha_{1,0}^{2,1} & \alpha_{1,0}^{2,2} \end{bmatrix} + 2\cos(\vec{\kappa}\cdot\vec{a}_2) \begin{bmatrix} \alpha_{0,1}^{1,1} & \alpha_{0,1}^{1,2} \\ \alpha_{0,1}^{2,1} & \alpha_{0,1}^{2,2} \end{bmatrix} + 2\cos\big(\vec{\kappa}\cdot(\vec{a}_1 - \vec{a}_2)\big) \begin{bmatrix} \alpha_{-1,1}^{1,1} & \alpha_{-1,1}^{1,2} \\ \alpha_{-1,1}^{2,1} & \alpha_{-1,1}^{2,2} \end{bmatrix} \tag{17}$$

$$\big[\mathbb{B}(\vec{\kappa})\big] = \begin{bmatrix} \beta_{0,0}^{1,1} & \beta_{0,0}^{1,2} \\ \beta_{0,0}^{2,1} & \beta_{0,0}^{2,2} \end{bmatrix} + 2\cos(\vec{\kappa}\cdot\vec{a}_1) \begin{bmatrix} \beta_{1,0}^{1,1} & \beta_{1,0}^{1,2} \\ \beta_{1,0}^{2,1} & \beta_{1,0}^{2,2} \end{bmatrix} + 2\cos(\vec{\kappa}\cdot\vec{a}_2) \begin{bmatrix} \beta_{0,1}^{1,1} & \beta_{0,1}^{1,2} \\ \beta_{0,1}^{2,1} & \beta_{0,1}^{2,2} \end{bmatrix} + 2\cos\big(\vec{\kappa}\cdot(\vec{a}_1 - \vec{a}_2)\big) \begin{bmatrix} \beta_{-1,1}^{1,1} & \beta_{-1,1}^{1,2} \\ \beta_{-1,1}^{2,1} & \beta_{-1,1}^{2,2} \end{bmatrix} \tag{18}$$

Using equation (16) we can write the dispersion relation as follows

$$\omega(\vec{\kappa}) = \nu \sqrt{\text{Eigen value}\Big\{ \big[\mathbb{B}(\vec{\kappa})\big]^{-1} \big[\mathbb{A}(\vec{\kappa})\big] \Big\}} \tag{19}$$

Since $\big[\mathbb{A}(\vec{\kappa})\big]$ and $\big[\mathbb{B}(\vec{\kappa})\big]$ are 2×2 matrices and have two eigenvalues, equation (19) has two solutions that gives two bands of the band structure. $\omega(\vec{\kappa})$ variations obtained from this equation is plotted in Figs. 4 and 5 as constant frequency contours in reciprocal lattice. Each figure shows one solution of equation (19). Fig. 6 shows the band structure calculated by this method.

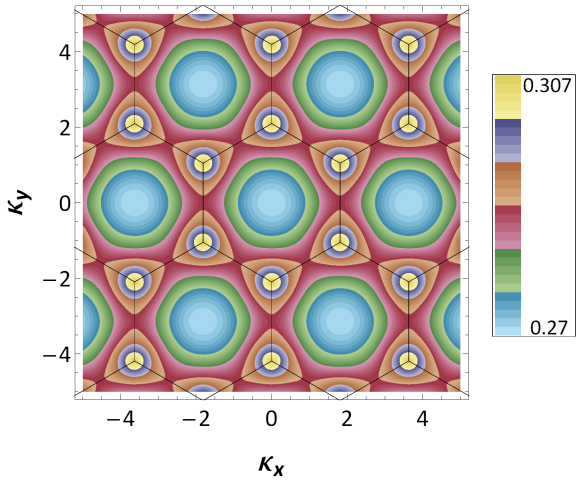


Figure 4: $\omega(\vec{\kappa})$ variations in reciprocal lattice for the first band obtained by tight binding method

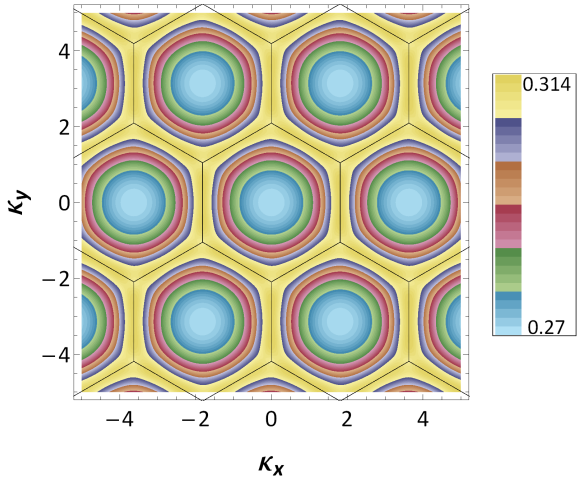


Figure 5: $\omega(\vec{\kappa})$ variations in reciprocal lattice for the second band obtained by tight binding method

4.2. Plane wave expansion method

In this method the dispersion relation is obtained by solving an eigenvalue equation too. But unlike the tight binding in this method nearly all of the bands are obtained. From the first and the second Maxwells equations we have

$$\nabla \times \mathbf{E}(\vec{r},t) = -\mu_0 \frac{\partial}{\partial t} \mathbf{H}(\vec{r},t) \tag{20}$$

$$\nabla \times \mathbf{H}(\vec{r},t) = \epsilon_0 \epsilon(\vec{r}) \frac{\partial}{\partial t} \mathbf{E}(\vec{r},t) \tag{21}$$

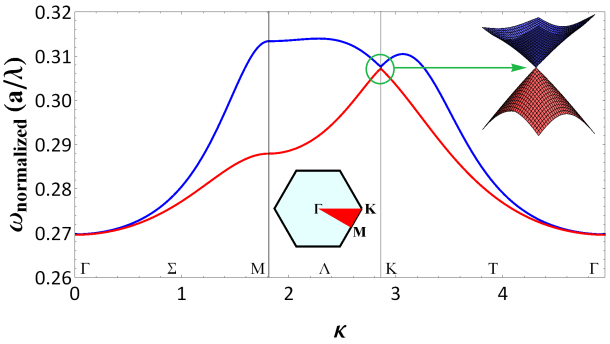


Figure 6: band structure calculated by tight binding method

If we take curl of both sides of equation (21) and then replacing the value of $\nabla \times \mathbf{E}(\vec{r})$ from equation (20) in it we reach

$$\nabla \times \left(\frac{1}{\epsilon(\vec{r})} \nabla \times \mathbf{H}(\vec{r},t) \right) = -\frac{1}{c^2} \frac{\partial^2}{\partial t^2} \mathbf{H}(\vec{r},t) \qquad (22)$$

By considering sinusoidal steady state magnetic field

$$\mathbf{H}(\vec{r},t) = \mathbf{H}(\vec{r})\, e^{-j\omega t} \qquad (23)$$

equation (22) becomes a phasor equation.

$$\nabla \times \left(\frac{1}{\epsilon(\vec{r})} \nabla \times \mathbf{H}(\vec{r}) \right) = \frac{\omega^2}{c^2} \mathbf{H}(\vec{r}) \qquad (24)$$

It is possible to show that in the H-polarization mode equation (24) becomes the following equation for the z component of $\mathbf{H}(\vec{r})$

$$\nabla \cdot \left(\frac{1}{\epsilon(\vec{r})} \nabla \cdot H_z(\vec{r}) \right) = -\frac{\omega^2}{c^2} H_z(\vec{r}) \qquad (25)$$

Now we define $\eta(\vec{r}) \equiv 1/\epsilon(\vec{r})$. Because of the periodicity of permittivity in a photonic crystal lattice we can write the Fourier series expansion for it as follows.

$$\eta(\vec{r}) = \sum_{m,n} \eta_{m,n} e^{-j(m\vec{b}_1 + n\vec{b}_2).\vec{r}} = \sum_{\mathbf{G}} \eta_{\mathbf{G}} e^{-j\mathbf{G}.\vec{r}} \qquad (26)$$

In this equation $\vec{b}_1$ and $\vec{b}_2$ are primitive vectors of reciprocal lattice. Using Bloch theorem we can write $H_z(\vec{r})$ as

$$H_z(\vec{r}) = e^{-j\vec{\kappa}.\vec{r}} \sum_{\mathbf{G}} \varphi_{\mathbf{G}}(\vec{\kappa})\, e^{-j\mathbf{G}.\vec{r}} \qquad (27)$$

By replacing $\eta(\vec{r})$ and $H_z(\vec{r})$ from equations (26) and (27) into equation (25) we obtain the following eigenvalue equation.

$$\sum_{\mathbf{G}'} \sum_{\mathbf{G}} \Big(\eta_{\mathbf{G}'}\, \varphi_{\mathbf{G}}(\vec{\kappa}) (\vec{\kappa} + \mathbf{G}) \cdot (\vec{\kappa} + \mathbf{G} + \mathbf{G}') \qquad (28)$$
$$e^{-j(\mathbf{G}+\mathbf{G}').\vec{r}} \Big) = \frac{\omega^2}{c^2} \sum_{\mathbf{G}} \varphi_{\mathbf{G}}(\vec{\kappa})\, e^{-j\mathbf{G}.\vec{r}}$$

We can simplify this equation by changing variables. The simplified eigenvalue equation to be solved is

$$\sum_{\mathbf{G}'} \eta_{\mathbf{G}'-\mathbf{G}}\, \varphi_{\mathbf{G}'}(\vec{\kappa}) (\vec{\kappa} + \mathbf{G})^2 = \frac{\omega^2}{c^2} \varphi_{\mathbf{G}}(\vec{\kappa}) \qquad (29)$$

In practice it is not possible to consider all of the Fourier series coefficients, thus we take coefficients with indices not greater than a specified number *N*. Then the final eigenvalue equation becomes

$$\sum_{p,q=-N}^{N} \eta_{p-m,q-n}\, \varphi_{p,q}(\vec{\kappa}) \left(\vec{\kappa} + (m\vec{b}_1 + n\vec{b}_2) \right)^2 \qquad (30)$$
$$= \frac{\omega^2}{c^2} \varphi_{m,n}(\vec{\kappa})$$

Dashed curves in Fig. 7 are the band structure obtained by solving equation (30). Modes of each band are also determined in this figure.

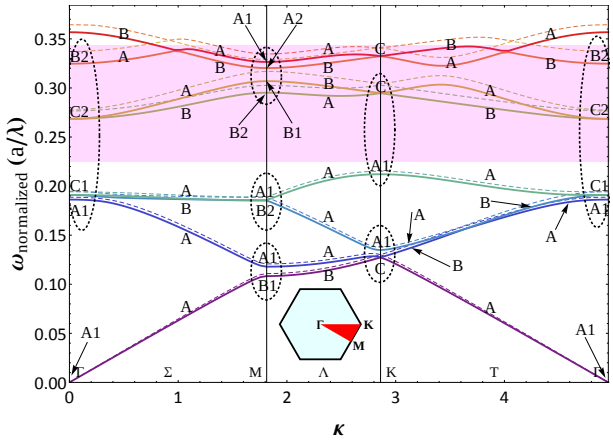


Figure 7: Band structure of designed supercrystal. Dashed and continuous curves are results of PWE and FE methods respectively. The magenta band is the first H-polarization band gap of triangular basis lattice.

4.3. Finite element method

One of the numerical methods to calculate photonic crystal band structure is FEM. In general FEM is a method to solve partial differential equations numerically. In FEM a very complicated problem is divided into small elements that can be solved according to each other [18]. Continuous curves in Fig. 7 are results of FEM for the band structure of our supercrystal.

5. Conclusions

In this project we first designed a triangular CPCRA with air holes in Silicon substrate. Then we calculated its band structure in H-polarization mode using tight binding, plane wave expansion, and finite element methods and proved the existence of Dirac points at the corners of Brillouin zones.

Acknowledgement

We have benefited from discussions with Dr. S. M. Etemadi. This research is supported by National Elite Foundation of Iran.

References

[1] Xiangdong Zhang, Observing Zitterbewegung for Photons near the Dirac Point of a Two-Dimensional Photonic Crystal, *Phys. Rev. Lett.* 100, 113903 (2008)

[2] Li-Gang Wang, et al., Realization of Dirac point with double cones in optics, *Optics Letters*, Vol. 34, Issue 10, pp. 1510-1512 (2009)

[3] Or Peleg, et al., Conical Diffraction and Gap Solitons in Honeycomb Photonic Lattices, *Phys. Rev. Lett.* 98, 103901 (2007)

[4] Kazuaki Sakoda, Dirac cone in two- and three-dimensional metamaterials, *Optics Express* , Vol. 20, Issue 4, pp. 3898-3917 (2012)

[5] C. T. Chan, et al., Dirac Dispersion in Two-Dimensional Photonic Crystals, *Advances in Opto-Electronics* Volume 2012, Article ID 313984

[6] B Wunsch, et al., Dirac-point engineering and topological phase transitions in honeycomb optical lattices, *New Journal of Physics* 10 (2008) 103027

[7] Wei Zhong and Xiangdong Zhang, Dirac-cone photonic surface states in three-dimensional photonic crystal slab, *Optics Express* , Vol. 19, Issue 15, pp. 13738-13749 (2011)

[8] Xueqin Huang, et al., Dirac cones induced by accidental degeneracy in photonic crystals and zero-refractive-index materials, *Nature Materials* 10, 582586 (2011)

[9] Xiangdong Zhang, Demonstration of a new transport regime of photon in two-dimensional photonic crystal, *Physics Letters A* Volume 372, Issue 19, (2008)

[10] R. A. Sepkhanov, et al., Extremal transmission at the Dirac point of a photonic band structure, *Phys. Rev. A* 75, 063813 (2007)

[11] R.A. Sepkhanov, C.W.J. Beenakker, Numerical test of the theory of pseudo-diffusive transmission at the Dirac point of a photonic band structure, *Optics Communications* Volume 281, Issue 20, (2008)

[12] R. A. Sepkhanov, et al., Extinction of coherent backscattering by a disordered photonic crystal with a Dirac spectrum, *Europhysics Letters* 85 14005, (2009)

[13] Tetsuyuki Ochiai and Masaru Onoda, Photonic analog of graphene model and its extension: Dirac cone, symmetry, and edge states, *Phys. Rev. B* 80, 155103 (2009)

[14] Alexander B. Khanikaev, et al, Photonic topological insulators, *Nature Materials* (2012)

[15] F. D. M. Haldane and S. Raghu, Possible Realization of Directional Optical Waveguides in Photonic Crystals with Broken Time-Reversal Symmetry, *Phys. Rev. Lett.* 100, 013904 (2008)

[16] Kazuaki Sakoda, *Optical Properties of Photonic Crystals*, Springer, second edition, 2005.

[17] S. Khorasani, *Applied Quantum Mechanics*, (in persian) Delarang Publishers, Tehran, 2011.

[18] `http://en.wikipedia.org/wiki/Finite_element_method`

Propagation effects in a polymer-based photonic liquid crystal fiber

T. R. Wolinski[1], M.Tefelska[1*], K. Milenko[1], K. Rutkowska[1], A. W. Domanski[1], S. Ertman[1], K. Orzechowski[1], M. Sierakowski[1], E. Nowinowski-Kruszelnicki[2], and R. Dabrowski[2]

[1]Faculty of Physics, Warsaw Univ. of Technology, Koszykowa 75, 00-662 Warszawa, Poland
[2]Military Univ. of Technology, Warszawa, Poland
[*]corresponding author: martef@if.pw.edu.pl

Abstract

In this paper propagation effects induced by thermal tuning of photonic band gaps (PBGs) in a polymer photonic crystal fiber (Pol-PCF) infiltrated with a specially designed liquid crystal (LC) are observed. When temperature increases PBGs in the transmission spectrum are narrowing and moving towards shorter wavelengths. However, when temperature approaches the nematic-isotropic phase transition, PBGs are getting wider and shift back towards longer wavelengths.

1. Introduction

Over the past decade photonic crystal fibers (PCFs) [1] have attracted an increasing scientific interest due to a great number of potential applications. Optical wave guiding in a PCF is governed by one of two principal mechanisms responsible for light trapping within the core: a classical propagation effect based on the modified total internal reflection (mTIR or index guiding) and the photonic band gap effect, which occurs if the refractive index of the core is lower than the mean refractive index of the cladding region. Infiltrating the air-holes with liquid crystals introduces highly-tunable photonic structures, called photonic liquid crystal fibers (PLCFs) [2-7]. Due to high electro-, magneto-, and thermo-optic responses of LCs, their refractive indices may be relatively easily changed by physical fields and highly influence propagation conditions within PLCFs. One of the most spectacular phenomena was the successful realization of temperature-induced switching between two mechanisms of light propagation, which was demonstrated for silica-glass based PLCFs [3]. Recently more attention has been directed towards polymer photonic crystal fibers (Pol-PCFs) [8-12]. Plastic materials like polymethyl methacrylate (PMMA – acrylic glass which has a refractive index of 1.4914 at 588nm) as well as polycarbonate (PC for which the refractive index is 1.5849 at 588nm) are very interesting optical materials with high mechanical strength and white light transmittance of 93% for PMMA (for a thickness of 3mm and within a spectral band of 380nm÷780nm) and 87% for PC (of the same thickness and within spectral band of 480nm÷680nm. Among the key advantages of microstructured polymer optical fibers are their high flexibility and greater resistance to mechanical stress than in the case of silica glass fibers. Thanks to that it is possible to create a variety of microstructured polymer photonic structures and in particular those with a large refractive index contrast between the core and the cladding.

The best-known technique to fabricate Pol-PCFs is adapted from silica-glass PCFs manufacturing technology but in the case of polymer-based fibers the temperature is much lower than for silica glass fibers. A properly prepared polymer structure is then fused and drawn with a fiber drawing tower described in details elsewhere [13,14]. Microstructured polymer optical fibers can be also fabricated by drilling holes in a preform [13,14].

In recent years losses of Pol-PCF fibers (which are relatively high and result mainly from the manufacturing process and the fiber material) have been the most important issue considered and improved. Presently the loss for a single-mode Pol-PCF has been reduced from 32dB/m to 0.7 dB/m [15,16].

2. Materials

Due to the fact that PMMA is dissolved in many organic solvents including liquid crystals, the special 1781A-2' LC mixture which prevents reaction with the PMMA material was synthesized. In our experiment a few-mode (FM-340 KIRIAMA) polymer photonic crystal fibers and the 1781A-2' nematic LC mixture were used.

2.1. Properties of FM-340 Pol-PCF

The FM-340 Pol-PCF (Fig.1) was manufactured at Kiriama company. It has a 15-μm diameter solid core and is composed of 6 concentric rings of air-holes periodically distributed in the PMMA cladding. The outer coating is made of PC. The parameters of the Pol-PCF fiber are presented in Table 1 and its transmission spectrum is shown in Fig. 2 (black line). Fiber losses in the visible are at the level of a few dB/m. In the near infrared, a high-loss peak around 900 nm is observed.

Table 1: Parameters of polymer photonic crystal fiber FM-340.

FM-340	
Fiber diameter	340 μm
Core diameter	15 μm
Loss @ 650nm	1 dBm

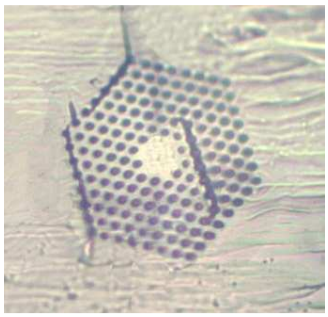


Figure 1: FM-340 polymer photonic crystal fiber.

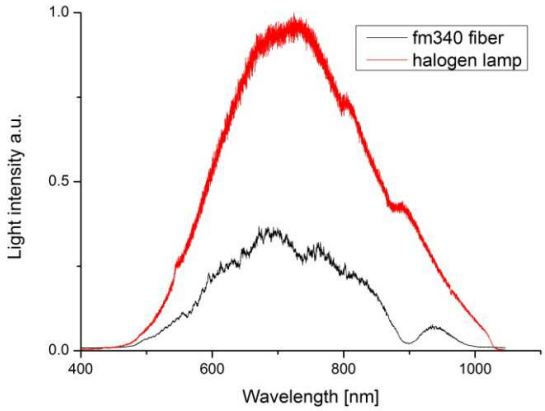
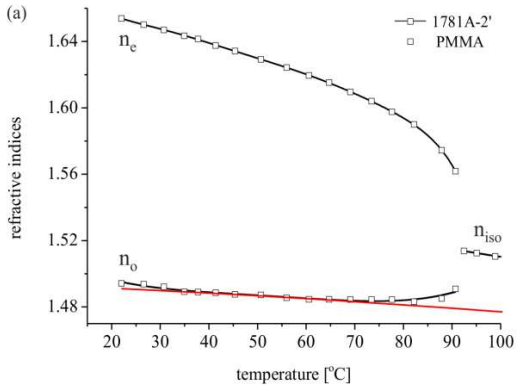


Figure 2: Normalized transmission spectrum of the FM-340 Pol-PCF. Spectrum of the halogen lamp used as a light source is also presented (red line).

2.2. Properties of 1781A-2' LC mixture

A specially designed 1781A-2' nematic mixture was synthesized at the Military University of Technology (Warsaw, Poland). Its chemical composition was modified in order to prevent reaction with the PMMA material. 1781A-2' LC is characterized by the phase transition (N-Iso) at 92.4°C and in a wide range of temperatures (corresponding to the nematic phase) its ordinary refractive index n_o is close to the refractive index of the PMMA. The temperature characteristic of refractive indices for 1781A-2' is presented in Fig. 3a while its chromatic dispersion at 25°C is shown in Fig. 3b.



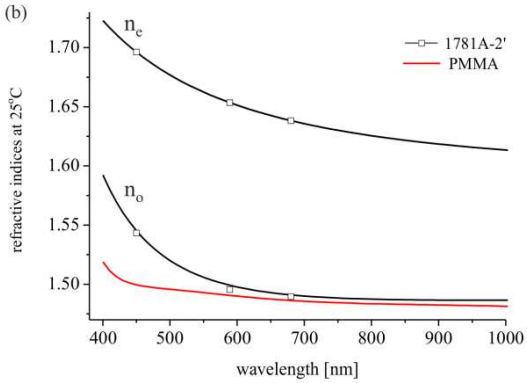


Figure 3: Refractive indices of the 1781A-2' nematic LC (at the wavelength of 589nm) as a function of temperature (a) and at the temperature of 25°C (b), where n_o is an ordinary and n_e is an extraordinary refractive index of the nematic phase, n_{iso} is a refractive index in an isotropic phase. Refractive index of PMMA is also shown for comparison [17, 18].

2.3. Polymer photonic liquid crystal fiber (Pol-PLCF)

The Pol-PCF was infiltrated with the 1781A-2' LC mixture by using capillary forces forming a polymer photonic liquid crystal fiber (Pol-PLCF). This infiltration method applied suggests planar orientation of molecules in the Pol-PLCF fiber [19]. However, the molecules orientation has not been controlled in experimental conditions. Most of the techniques of the LC molecules orientation in micro-capillaries require the use of strong organic solvents and/or high temperature, which may be destructive for polymer microstructured fibers. It is why we have decided not to use any aligning layers and preserve the original microstructure.

3. Numerical Results

In order to identify the temperature-dependence of light guidance in the Pol-PLCF of interest, a custom-written numerical scheme based on the vector-field FDFD mode solver (with Yee-mesh) [20] has been applied. It has been also checked that the results of analogous simulations - performed with commercial software (COMSOL, Multiphysics), based on the finite elements methods - are quantitatively and qualitatively consistent (with the compatibility of effective indices up to at least fifth place after the decimal point for the same mode). Specific values of refractive indices taken for simulations (for particular wavelengths and temperatures) have been approximated and extrapolated with the use of the dispersion equations and material characteristics shown in Fig. 3. Specifically, the diagonal form of the electric permittivity tensor for LC (with values of n_o^2, n_o^2, n_e^2 on its diagonal) has been used, thus following an assumption of the planar orientation of the LC molecules within the Pol-PCF. Figure 5 shows the numerical results for the effective index of the fundamental core-mode of the Pol-PLCF sample as a function of the wavelength and temperature. It is worth mentioning that in

the presented cases PBG-guiding modes dominate due to the refractive indices of LC being higher than those of PMMA (approximated for the same conditions). The insets in the upper right hand corner of Fig. 5 show exemplary intensity profiles for the fundamental (core-guiding) modes (with their patterns dependent on the wavelength). As it is typical for the PBG-guiding mechanism, for some wavelengths there are no core-guiding modes, which corresponds to the gaps in the Pol-PLCF transmission spectrum (e.g. measured in experimental conditions). The results obtained suggest that when temperature increases, the bands in the transmission spectrum are narrowing and moving towards shorter wavelengths. However, when temperature approaches a value characteristic for the nematic-isotropic phase transition, the bands are getting wider and shift back to longer wavelengths. It is worth noting that for all temperatures considered, there are no core-guiding modes for the wavelengths longer than 715nm (whereas numerical simulations have been performed up to 1100nm).

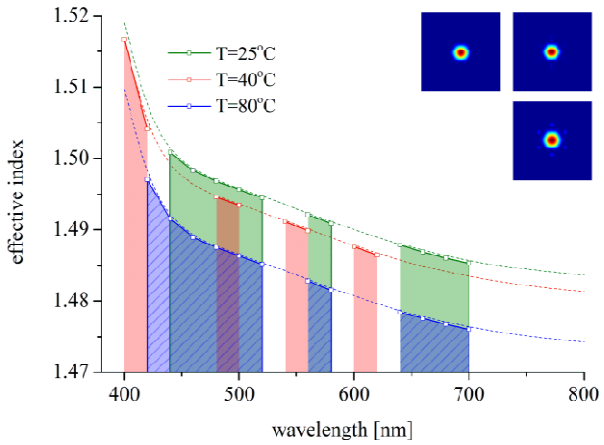


Figure 5: Effective index of the fundamental mode in the Pol-PLCF as a function of the wavelength for three different temperatures of 28°C, 40°C and 80°C. Dispersion curves for the PMMA at the same temperatures are plotted as dashed lines for comparison. The insets in the upper right hand corner show typical intensity profiles obtained for the fundamental (core-guiding) modes in the Pol-PLCF of interest (please note that only the central part of calculation window is presented).

4. Experimental results

The experimental setup is shown in Fig. 4. It consists of a halogen lamp (Ocean Optics Mikropack, with a spectrum shown in Fig. 2) as a light source, Ocean Optics USB4000 spectrometer with an 0.2 nm optical resolution as a detector and Peltier module used to heat a section of the Pol-PLCF in order to thermally tune its photonic band gaps.

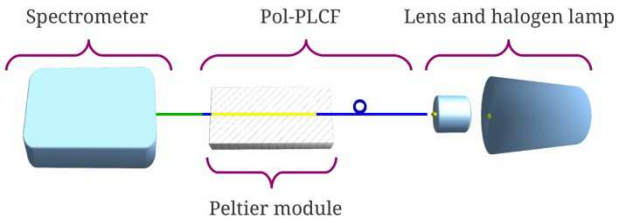


Figure 4: Experimental setup.

The FM-340 fiber was infiltrated with the 1781-A2' liquid crystal. The length of the fiber was 350mm and the length of the infiltrated part was 30mm as obtained for an infiltration time of 10 minutes. After the infiltration of the polymer photonic crystal fiber, the fiber transmission curve shows formation of a single and wide photonic band gap (Fig. 6). The width of the band gap is 106nm. The thermal tuning of the photonic band gap in a polymer photonic liquid crystal fiber obtained for the range of 28.6°C to 91.1°C is shown in Figs. 6 and 7. Similar results of temperature PBGs tuning in PLCF made of silica glass were presented elsewhere [3, 5]. It can be noticed that increasing temperature causes the band gap to shift towards lower wavelengths (Fig. 6). We have also observed a narrowing of the photonic band gap, which can be attributed to limitations of the light source. The maximum shift is obtained for ~62°C and the PBG position changes of about 104nm. For temperatures higher than 62°C the band gap starts to shift towards longer wavelengths (Fig. 7).

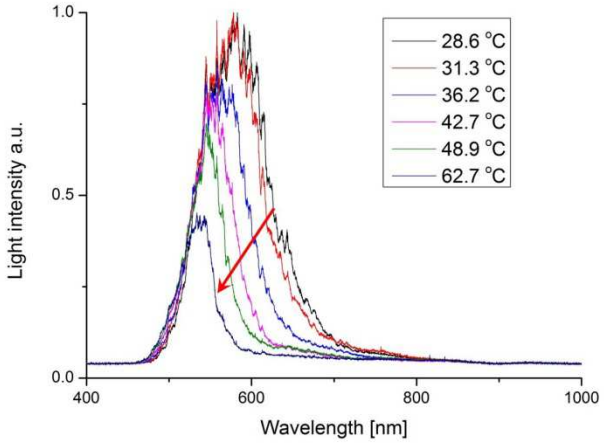


Figure 6: Temperature tuning of photonic band gaps within the temperature range from 28.6°C to 62.7°C. Infiltrated section of FM-340 Pol-PCF is 30mm long.

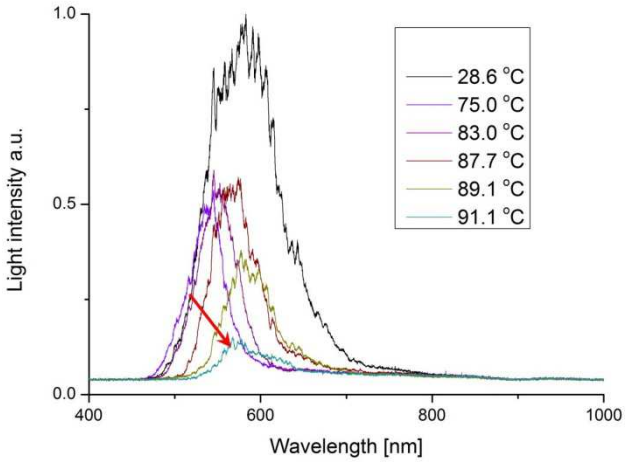


Figure 7: Temperature tuning of photonic band gaps within the temperature range from 75.0°C to 91.1°C. Transmission in 28.6°C (in black) is used as a reference. Infiltrated section of FM-340 Pol-PCF is of the length of 30mm.

When the part of the LC infiltrated fiber length is shorter than 30mm as shown previously, the photonic band gap effect is still observed but wavelengths from outside the band gap are not suppressed. In the case shown in Figs. 8-10, the infiltration length of LC in Pol-PCF was 10mm. The resulting photonic band gap is wider than for an infiltration length of 30mm and it is 133nm-wide. The rising external temperature up to 63°C (Fig. 8) causes the narrowing of the photonic band gap and the reduction of propagating light intensity. In the temperature range from 64°C to 85°C the photonic band gap is widening and its intensity is restored (Fig. 9). For temperatures above 85°C the widening of the photonic band gap and its shift towards higher wavelengths are observed (Fig. 10).

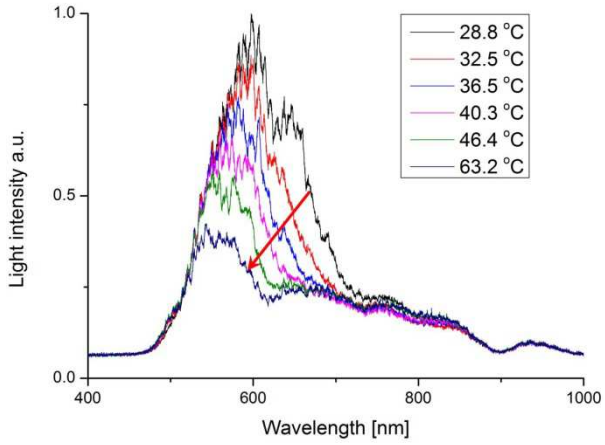


Figure8: Temperature tuning of photonic band gaps, within the temperature range from 28.8°C to 63.2°C. Infiltrated section of FM-340 Pol-PCF is of the length of 10mm

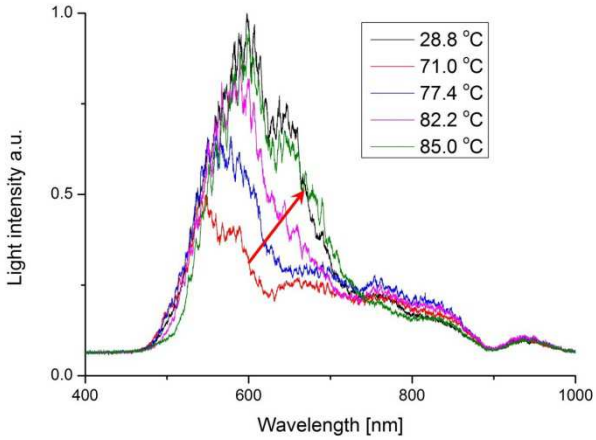


Figure 9: Temperature tuning of photonic band gaps, within the temperature range from 71.0°C to 85.0°C. Transmission spectrum obtained for 28.8°C is used as a reference. Infiltrated section of FM-340 Pol-PCF is of the length of 10mm.

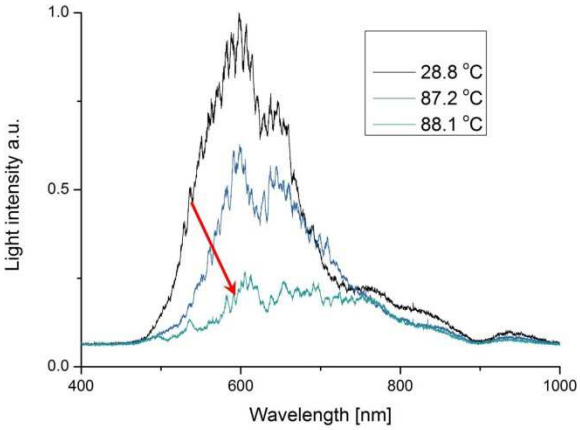


Figure 10: Temperature tuning of photonic band gaps, within the temperature range from 85.0°C to 88.1°C. Transmission spectrum obtained for 28.8°C is used as a reference. Infiltrated section of FM-340 Pol-PCF is of the length of 10mm.

Thermal tuning of the photonic band gaps in the polymer photonic liquid crystal fiber observed at the output facet of the Pol-PLCF fiber, for the range from 24.3°C to 89.1°C is shown in Fig. 11. We observe a variation in the propagated wavelengths as the temperature changes.

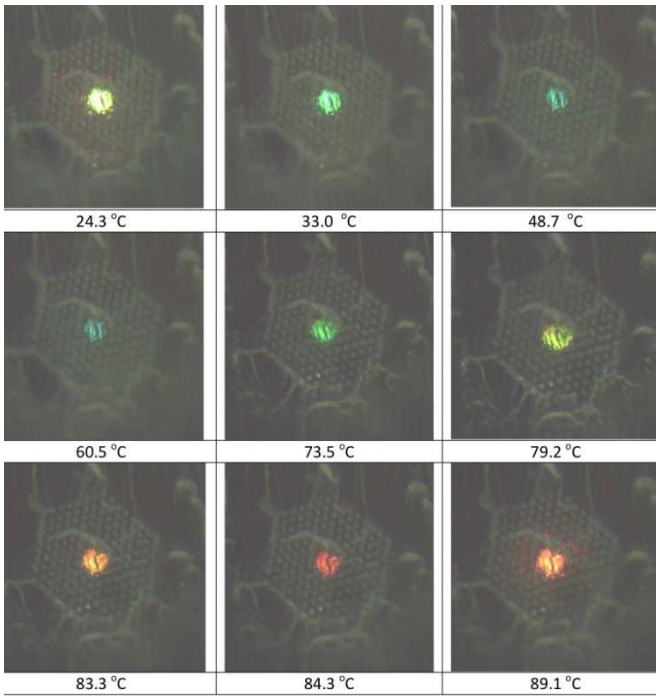


Figure 11: Thermal tuning of the band gaps in FM-340 Pol-PLCF.

5. Conclusions

To conclude, a novel polymer photonic liquid crystal fiber (Pol-PLCF) with PBG temperature-induced tuning effect was demonstrated along with a theoretical analysis of propagation properties of the polymer photonic crystal fiber infiltrated with a liquid crystal. The formation of the photonic band gap and its shift due to a change in temperature were also presented. Preliminary experimental results demonstrated transmission spectra for two different infiltration lengths of the polymer liquid crystal fiber. The observed PBG temperature tuning effect agrees qualitatively with the theoretical predictions.

The polymer photonic crystal fibers (Pol-PCFs) presented here offer possibilities for developing photonic devices with new functionalities. The photonic band gap tuning in Pol-PLCF described in this paper could be used for building tunable filters, which can find practical applications in fiber-optic based spectroscopy.

Acknowledgements

This work was supported by the Polish National Science Centre (NCN) under the grant no. 2011/01/B/ST7/05015. One of the authors (K.R.) would like to acknowledge Homing Plus Programme (2010-2/11) granted by the Foundation for Polish Science and co-financed by the European Regional Development Fund.

References

[1] P.St.J. Russell, Photonic Crystal Fibers, *Science* 299(5605): 358−262, 2003.

[2] T.T.Larsen, A. Bjarklev, D.S. Hermann, and J. Broeng, Optical devices based on liquid crystal photonic bandgap fibers, *Opt. Express* 11(20): 2589−2596, 2003.

[3] T.R. Wolinski, K. Szaniawska, S. Ertman, P. Lesiak, A.W. Domanski, R. Dabrowski, E. Nowinowski-Kruszelnicki, and J. Wojcik, Influence of temperature and electrical fields on propagation properties of photonic liquid crystal fibers, *Meas. Sci. Technol*. 17: 985–991, 2006.

[4] K. Milenko, T.R. Wolinski, P. Shum, and J.J. Hu, Temperature-Sensitive Photonic Liquid Crystal Fiber Modal Interferometer, *IEEE Photonics J.* 4(5): 1855−1860, 2012.

[5] M.M. Tefelska, S. Ertman, T.R. Wolinski, P. Mergo, and R. Dabrowski, Large area multimode photonic band gap propagation in photonic liquid crystal fiber, *IEEE Photon. Technology Lett*. 24: 631−633, 2012.

[6] T.R. Wolinski, Photonics Liquid Crystal Fiber Sensors for Safety and Security Monitoring in Photonics sensing: principle and applications for safety and security monitoring, Eds. G. Xiao and W.J. Bock, John Wiley and Sons, pp 147−182, 2012.

[7] T.R. Woliński, S. Ertman, D. Budaszewski, M. Chychłowski, A. Czapla, R. Dąbrowski, A.W. Domański, P. Mergo, E. Nowinowski-Kruszelnicki, K.A. Rutkowska, M. Sierakowski, M. Tefelska, Emerging photonic devices based on photonic liquid crystal fibers, *Phot. Lett. Poland* 3(1): 20−22, 2011.

[8] J. Wójcik, P. Mergo, J. Klimek, G. Wójcik, K. Skorupski, J. Pędzisz, J. Kopeć, Technology of high birefringent microstructured polymer optical fibers, *Phot. Lett. Poland* 2(1): 4−6, 2010.

[9] J. Witt, M. Steffen, M. Schukar, K. Krebber, Investigation of sensing properties of microstructured polymer optical fibres, *Proc. SPIE* 7714: 77140F−77140F-12, 2010.

[10] W. Yuan, L. Wei, T.T. Alkeskjold, A. Bjarklev, O. Bang, Thermal tunability of photonic bandgaps in liquid crystal infiltrated microstructured polymer optical fibers, *Opt. Express* 17: 19356−19364, 2009.

[11] Y. Zhang, L. He, H. Ji, S. Yang, M. Chen, S. Xie, Tunable attenuator based on polymer microstructured optical fibers, *Optoelectr. Lett.* 3(1): 47−49, 2007.

[12] A. Argyros, M.A. van Eijkelenborg, S. D. Jackson, R.P. Mildren, Microstructured polymer fiber laser, *Opt. Lett.* 29: 1882−1884, 2004.

[13] G. Barton, M.A. van Eijkelenborg, G. Henry, M.C.J. Large, J. Zagari, Fabrication of microstructured polymer optical fibres, *Opt. Fiber Technol.* 10: 325−335, 2004.

[14] Y. Zhang, K. Li, L. Wang, L. Ren, W. Zhao, R. Miao, Casting preforms for microstructured polymer optical fibre fabrication, *Opt. Express* 14: 5541−5547, 2006.

[15] M.C. Large, R. Lwin, A. Argyros, S. G. Leon-Saval, Low loss microstructured Polymer Optical Fibre

(mPOF), Optical Fiber Communication Conference, OSA Technical Digest (CD) paper OWS6, 2011.

[16] J. Zubia, J. Arrue, Plastic Optical Fibers: An Introduction to Their Technological Processes and Applications, *Opt. Fiber Technol.* 7: 101−140, 2001.

[17] S.N. Kasarova *et al.*, Analysis of the dispersion of optical plastic materials, *Opt. Mater.* 29: 1481−1490, 2007.

[18] M. Kovacevic *et al.*, Temperature Dependence Analysis of Mode Dispersion in Step-Index Polymer Optical Fibers, *Acta Phys. Pol. A* 116(4): 649−651, 2009.

[19] T.R. Woliński, P. Lesiak, A.W. Domański, K. Szaniawska, S. Ertman, R. Dąbrowski, J. Wójcik, Polarization optics of microstructured liquid crystal fibers, *Mol. Cryst. Liq. Cryst.* 454:333−350, 2006

[20] K.A. Rutkowska, L.W. Wei, Full-Vectorial Description of the Light Guidance in Anisotropic Photonic Liquid Crystal Fibers, *Acta Phys. Pol. A*, 122(5): 880−890, 2012.

Influence of Ag doping on structural and optical properties of ZnO thin films synthesized by sol-gel technique

A. Chelouche[1], D.djouadi[1], H. Merzouk[1], A .Aksas[1]

[1] Laboratoire du Génie de l'Environnement (LGE), Université de Béjaia, Algérie

E-mail: hamid.merzouk@yahoo.fr

Abstract

Thin films of Ag-ZnO samples deposited on glass substrates with different percentage of Ag content (1, 2 and 3 at %) were synthesized, at room temperature, by a dip-coating sol-gel method. The obtained samples are hexagonal wurtzite structure. The average grain size of deposits is about 5 nm. Up to 3 at %, c-axis lattice parameter shifts towards higher value which indicates that silver atoms replace Zn atoms in the crystal lattice. As shown by the DRX spectra, growth rate in the (101) direction is favored by the presence of silver ions in the ZnO struture. The layers present a homogeneous crystallites distribution, as we can remark it on SEM micrographs and exhibit a very low roughness according to AFM images. The entire samples exhibit a transmission value greater than 80%, in the visible region, while the maximum is obtained for those doped at 2 at %. Energy band varies between 3.15 eV and 3.25 eV. The wider gap obtained is that of the ZnO layer doped with 1at%. It's worth noting a strong UV emission observed on PL spectrum, performed at very low temperature (77K), for silver doped ZnO compared to that of pure ZnO.

1. Introduction

The synthesis and applications of nanoscale structures based on zinc oxide was the subject of intense investigation in recent years. This is mainly due to the special properties of ZnO as a wide gap (3.37 eV) and large exciton binding energy (60meV) at room temperature. These features have made this material an excellent candidate for applications such as semiconductor luminescent emitting in the spectral region Blue-UV [1-3].

A large number of ZnO nanostructures have been synthesized by various methods such as magnetron sputtering [4], laser ablation [5], electron beam evaporation [6], ultrasonic pyrolysis [7], and the sol-gel [8]. Among the different methods of preparation, the sol-gel method is easier to implement and is generally carried out at near room temperature. This technique should also be promising for doping ZnO nanostructures since it consists of mixing, beforehand, dopant sources with zinc atoms precursors. In addition, the preparation of thin films by this method minimizes intrinsic defects and gives good optical quality samples [9].

The silver is one of the most promising dopant. Once introduced into ZnO, it behaves as an acceptor and is actively involved in improving the low temperature photoluminescence UV emission. Ruiqun et al. obtained, the PL spectra of pure and Ag-doped nanowires at 10 K using wet oxidation doping process [10]. Xu, Jin et al. have conducted PL studies, at

130K, on thin films substrates using sol-gel method [11].To our knowledge, there are no photoluminescence studies carried out at the liquid nitrogen temperature (77 K) on Ag-doped ZnO thin films using sol-gel technique. Influence of Ag doping on structural and optical properties of ZnO nano thin films synthesized by sol–gel technique is little studied.

In this work, microstructure and optical properties, in particular the low temperature photoluminescence UV spectra, of Ag-doped ZnO nanostructures are studied. Thin films of Ag doped ZnO were prepared by the sol-gel method and deposited on glass substrates by dip-coating technique. The effects of silver ions concentration on structural, morphological and optical properties of as deposited films were studied. The low temperature (77 K) UV emission is discussed.

1. Experimental procedure

Di-hydrate zinc acetate, ethanol, diethanolamine (DEA) and nitrate are used respectively as silver precursor, solvent, stabilizer and source doping. The doping level Ag / Zn varies from 1 to 3%. The deposition of thin films was performed by dip-coating. The pulling speed was set at 20 mm / min. After each deposition, the sample is dried at 200 ° C for 40 minutes. This process is repeated for each of the three deposited layers. Finally, thin films prepared were annealed in air in a muffle furnace at 500 ° C.

The thin films prepared were characterized by X-ray diffraction (XRD) at grazing incidence using the PanAnalytical diffractometer. X-rays are produced from a CuK radiation source (wavelength 1.54 Å), an acceleration voltage of 40 kV and a current of 30 mA. The SEM images were obtained by Zeiss scanning electron microscope and AFM images were obtained with a VEECO microscope type. The optical transmittance spectra were obtained using a Safas uvmc2 UV-Visible. The photoluminescence spectra were recorded using Jobin-Yvon HR460 spectrophotometer. The samples were excited by a laser of wavelength 244 nm.

2. Results and discussion

Pure ZnO and Ag-doped ZnO thin films X-ray diffraction are shown in Figure 1. Spectra present hexagonal wurtzite structure. The lattice parameter value (c) has increased from 5.177 Å (pure ZnO) to 5.300 Å (Ag 3%-ZnO) while the parameter "a" remains practically constant for all deposits. This shows the substitution of zinc atoms by those of silver in the crystal lattice [11, 12]. The high intensity of the (101) peak indicates that heterogeneous nucleation is easier in the presence of silver ions, which favors the growth rate in this direction. On the other hand, the average crystallite size (~5 nm) calculated by the Scherrer method [13] is not modified by the addition of small amounts of silver atoms.

Scanning electron microscopy (SEM) images (figure 2) show a homogeneous distribution of crystallites for our prepared simples.

Silver doped ZnO thin films (1, 2 and 3%) topographies obtained by atomic force microscopy (AFM) are shown in Figure 3. The best roughness is found for ZnO layers doped with 2% silver atoms.

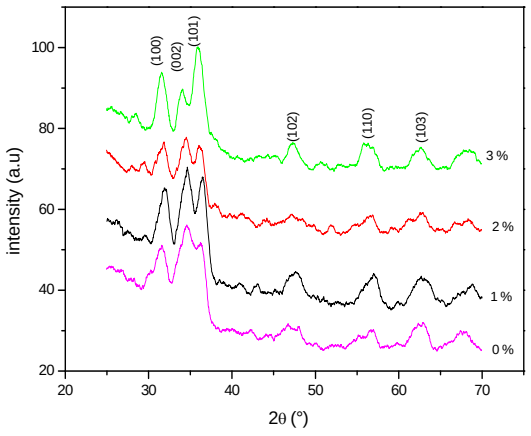


Figure 1: X-ray diffraction spectra of the ZnO and Ag-doped ZnO films

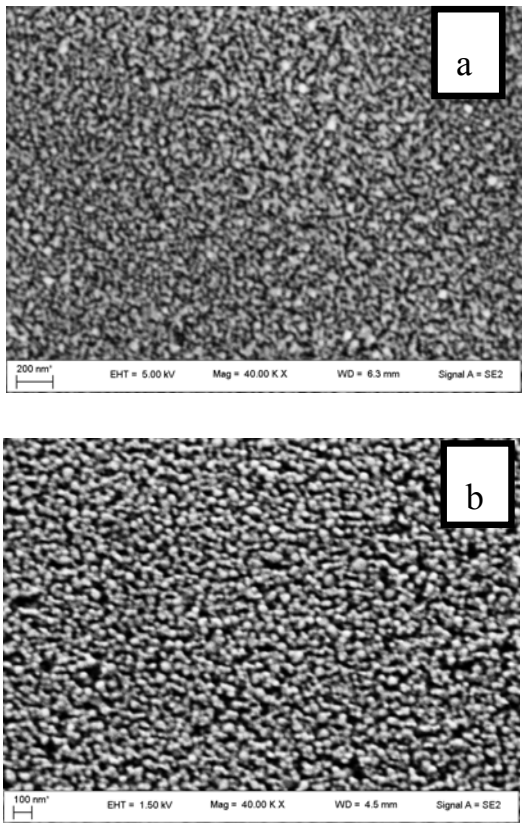


Figure 2: SEM micrograph of ZnO (a) and Ag 3%-doped ZnO (b)

The UV-visible optical transmission spectra are given figure 4a. The average value of the visible transmission is greater than 80%. The 2at% Ag- doped ZnO layer shows the maximum transmission value in the near UV and visible. The transmission threshold of this layer is slightly shifted towards shorter wavelengths. From the UV-visible optical transmission data, curves giving the absorption coefficient α as a function of photon energy hν are plotted (Figure 4b) following the relationship:

$$[\alpha\ (h\nu)]^2 = (h\nu - Eg) \qquad (1)$$

Band gap energy values (Eg) obtained by linear extrapolation (for $\nu \neq 0$,when $\alpha \longrightarrow 0, h\nu \longrightarrow Eg$) vary from $3,15$ eV to $3,25$ eV. The wider energy band gap value is obtained for 2 % Ag-doped ZnO films.

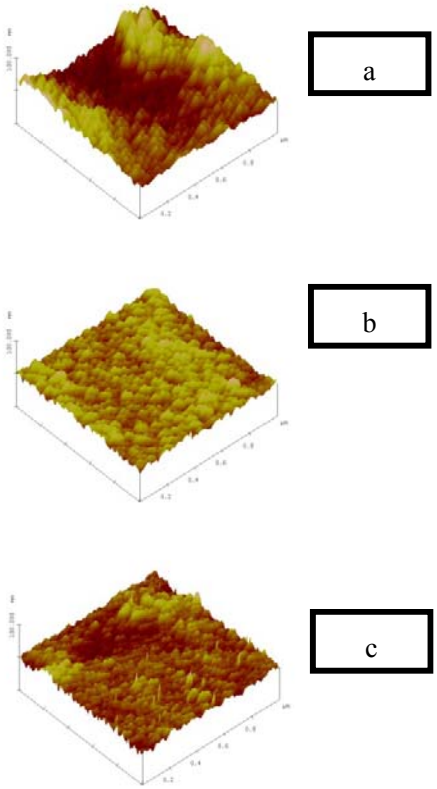


Figure 3: Topography of Ag doped ZnO thin films: 1% (a), 2% (b) and 3% (c).

Figure 6 and Figure 7 show the photoluminescence spectra (PL) at very low temperature (77 K) of, respectively, pure ZnO and Ag doped ZnO films. At liquid nitrogen temperature, it is worth noting a sharp increase of the UV emission for Ag-doped samples compared to undoped ones. Thus, the excitons in the ZnO scatter less when their concentration is increased. And most excitonic recombination leads to stronger UV emission [14].

ZnO thin films present three bands centered on 3.36, 3.32 and 3.26 eV while four bands centered on 3.36, 3.32, 3.24 and 3.16 eV followed by a shoulder at 3.10 eV appear for Ag (3%) doped-ZnO samples. The peak at 3.36 eV is attributed to the radiative recombination of free excitons (FX) and the peak at 3.32 eV is due to the recombination of bound excitons (BX) [15, 16].

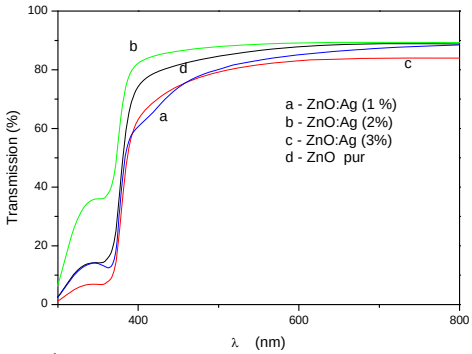


Figure 4: Transmittance spectra of ZnO and Ag - ZnO films

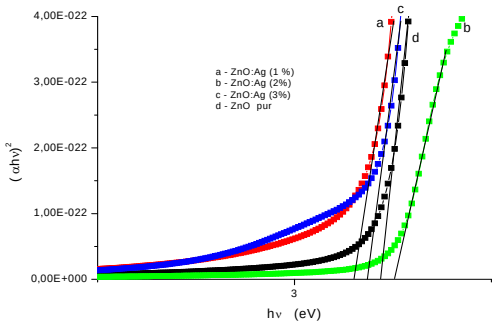


Figure 5: Plot of $(\alpha h\upsilon)^2$ vs. photon energy

Transitions assisted by optical phonon replicas are located at positions 3.24 (1LO), 3.16 eV (2LO) and 3.1 eV (3LO). 1LO and 2LO peaks are absent for the pure ZnO.

For Ag-doped ZnO, the most important emission at 77K is that due to 2LO optical phonon and the DX exciton emission is larger than the FX exciton emission contrary to undoped ZnO. This indicates that doping with silver increases DX and 2LO emissions. It is probable that the peak at 3.16 eV is not only due to 2LO but also to electrons transition from the conduction band to an acceptor level A+. This level is the result of the introduction of the silver as an acceptor in the ZnO.

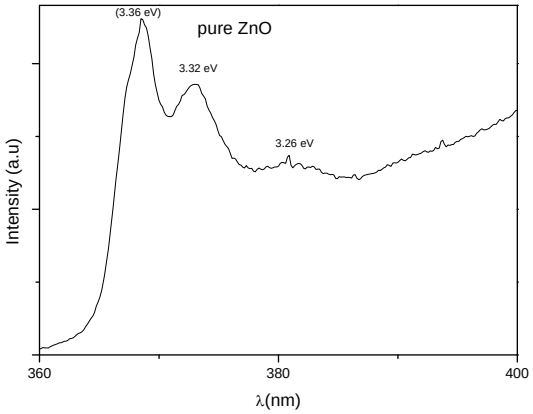


Figure 6: PL spectra at 77K of Ag 3%-doped ZnO

Conclusion

The concentrating effect of Ag doping on structural and optical properties of ZnO films prepared by sol gel method were studied. The films exhibited the monocrystalline structure with hexagonal wurtzite.

The surface morphology of the Ag-doped ZnO films is homogenous.

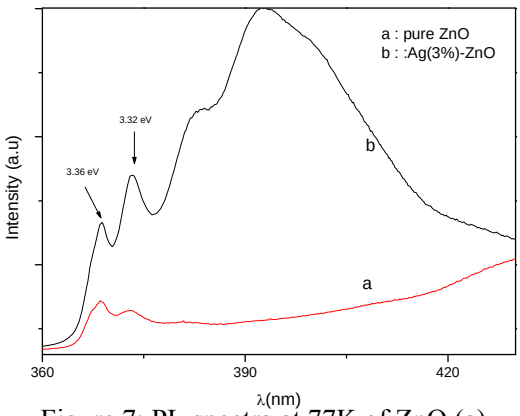


Figure 7: PL spectra at 77K of ZnO (a) and Ag 3%-doped ZnO (b)

The best roughness is found for ZnO layers doped with 2%. We note that doping favors c-axis orientation

which proves the substitution of zinc atoms by those of silver in the crystal lattice. The high intensity of the (101) peak indicates that heterogeneous nucleation is easier in the presence of silver ions, which favors the growth rate in this direction. Entire films exhibit high optical transmission rates (>80%), while the 2at% Ag- doped samples present the maximum values in the near UV and visible. The wider gap is obtained for 1at% Ag-ZnO layer.

The photoluminescence spectra at very low liquid nitrogen temperature (77 K) of pure ZnO and Ag doped ZnO films show a sharp increase of the UV emission for Ag-doped samples compared to undoped ones. ZnO thin films present three bands centered on 3.36, 3.32 and 3.26 eV while four bands, centered on 3.36, 3.32, 3.24 and 3.16 eV followed by a shoulder at 3.10 eV, appear for Ag (3%) doped-ZnO samples. The peak at 3.36 eV is attributed to the radiative recombination of free excitons (FX) while the related peak to 3.32 eV is due to the recombination of bound excitons (BX).

References

[1]M. Krunks, A. Katerski, T. Dedova, I. OjaAcik, A. Mere, Sol. Energ. Mat. Sol. 92, 1016 (2008).

[2] S.C. Ko, Y.C. Kim, S.S. Lee, S.H. Choi, S.R. Kim, Sensor. Actuat. A-Phys. 103, 130 (2003).

[3] M.C. Carotta, A. Cervi, V. di Natale, S. Gherardi, A. Giberti, V. Guidi, D. Puzzovio, B. Vendemiati, G. Martinelli, M. Sacerdoti, D. Calestani, A. Zappettini, M. Zha, L. Zanotti, Sensor. Actuat. B-Chem. 137, 164 (2009).

[4] E. Fortunato, P. Nunes, D. Costa, D. Brida, I. Ferreira, R. Martins, Vacuum. 64, 233 (2002).

[5] Y-W. Song, K. Kim, S.Y. Lee, Thin Solid Films 518, 1318 (2009).

[6] D.R. Sahu , S.Y.Lin, J.L.Huang, Appl. Surf. Sci 253, 4886 (2007).

[7] K. Liu, B. F. Yang , H. Yan, Z. Fu , M. Wen,Y. Chen , J. Zuo , Appl. Surf. Sci. 255, 2052 (2008).

[8] S.W. Xue, X.T. Zu, W.G. Zheng, H.X. Deng, X. Xiang, Physica B, 381 209 (2006).

[9] Y.F. Yang, M.M. Al-Jassim, S.H. Wei, Appl. Phys. Lett. 89, 181912 (2006).

[10] R.Chen, C. Zou1, J. Bian, A. Sandhu, W. Gao, Nanotechnology, **22 105706** (2011).

[11] X. Jin, Z. Zi-Yu, Z. Yang, L. Bi-Xia, F. Zhu-Xi, Chin.Phys.Lett. 22 2031 (2005).

[12] J. Xu, Z-Y. Zhang, Y. Zhang, B-X. Lin, Z-X. Fu, Chin. Phys. Lett. 22, 2031(2005).

[13] X.B. Wang, C. Song, K.W. Geng, F. Zeng, F. Pan, J. Phys. D: Appl. Phys. 39, 4992 (2006).

[14] K. Liu, B.F. Yang, H. Yan, Z. Fu, M. Wen, Y. Chen, J. Zuo, Appl. Surf. Sci. 255, 2052 (2008).

[15] H. Merzouk, A. Chelouche, S. Saoudi, D. Djouadi, A. Aksas**,** Appl. Phys. A 109, 841 (2012).

[164]. R. Chen, C. Zou, J. Bian, A. Sandhu, W. Gao Nanotechnology 22, 105706 (2011).

[17] C. Li, Y. Lv, L. Guo, H. Xu, X. Ai, J. Zhang, J. Lum. 122–123, 415 (2007).

[18] H. Zhang, J. Lu, X. Yang, Z. Ye, J. Huang, B. Lu, L. Hu, Y. Li, Y. Zhang, D. Li, Cryst. Eng. Comm. 14, 4501 (2012).

Inverse design and topology optimization of novel Photonic Crystal broadband passive devices for Photonic Integrated Circuits

Imanol Andonegui[1]*, Isidro Calvo[2], and Angel J. Garcia-Adeva[1]
*Imanol Andonegui, E-mail: imanol_andonegui@ehu.es

[1]Departamento de Fisica Aplicada I, E.T.S. Ingenieria de Bilbao, Universidad del Pais Vasco (UPV/EHU), Alda. Urquijo s/n, 48013 Bilbao, Spain
[2]Departamento de Ingenieria de Sistemas y Automatica, E.U. Ingenieria Tecnica de Vitoria, Universidad del Pais Vasco (UPV/EHU), C/ Nieves Cano 12, 01006 Vitoria, Spain

Abstract

We report on the application of various optimization methods as a very promising simulation approach for the design of true integrated optical devices by means of inverse design. We show that these techniques provide a global optimum towards one or various functional objectives at a reasonable computational cost. The results obtained by these methods are far better than intuitive design procedures and clearly outperform trial-and-error based models. We illustrate their performance by using a series of inverse-designed practical photonic devices.

1. Introduction

Photonic crystals (PC) have generated a surge of interest in the last decades as they offer the possibility to control the propagation of light to an unprecedented level. The prospect of attaining a fully functional photonic device that tackles light propagation in subwavelength scale requires breaking the spatial symmetry of PCs. These topologies enhance additional functionalities and enable a higher level of control in complex light paths. However, creating novel designs based upon aperiodic PC clusters entails dealing with numerous sensitive and correlated parameters. In addition, investigating all feasible combinations of structural parameters for a particular application demands a lot of computational effort, which scales exponentially with the number of parameters. Therefore, the challenging problem of designing such PC structures belongs to the class of the NP-complete optimization problems.

Currently, the process of designing a PC structure that ultimately complies with a certain required objective is still based on intuitive assumptions rather than using a rigorous mathematical technique. However, designing structures founded on intuition, usually yields to non-optimum scenarios. Beyond these assumptions, creating PC structures to fulfill multiple conflicting objectives highly hinders the design procedure.

In contrast with intuition-based approaches, we show in the present manuscript that global optimization heuristic and evolutionary algorithms are specially well suited to deal with the noisy and non-linear nature of disordered PCs. In this work, we report a number of inverse designed novel passive devices using two alternative heuristic methods, namely the fast simulated annealing technique (FSA) [1] and the harmony search (HS) [2] algorithm and an evolutionary algorithm called Non dominated Sort Genetic Algorithm 2 (NSGA2) [3]. The optimized complex systems obtained by means of these techniques clearly outperform intuitive based models. These procedures support a constrained search of the parameter space and hence they can render PC topologies that are fully compatible with CMOS fabrication technology. We found that these methods are easily applicable to most of PC engineering design problems since they do not require any detailed knowledge of the structure of the problem and they can rely on the solver of the problem as a blackbox. Therefore, we exploit the advantages of implementing a stochastically-driven optimization process and the rapidity and accuracy of the finite element method (FEM) in order to design fully functional optical components, such as sharp bend PCWGs, compact power splitters, PCWG crossings and wavelength selective routing mechanisms, and high quality factor and reduced modal area cavities.

2. Optimization and inverse design

Heuristics are typically used when there is no known way to find an optimal solution, or when it is desirable to give up finding the optimal solution for an improvement in run time. They do not attempt to find the best result to a certain problem, albeit they do their best in order to achieve a close to optimal solution, which is normally more than enough in NP-Complete problems. There are two fundamental reasons that favor the use of these methods: on the one hand, they are easily adapted to face new problems and, on the other hand, they provide a proper balance between the degree of complexity involved and the quality of the obtained results. When studying novel PC systems based upon non-periodic scatterer systems, the number of possible configurations becomes extremely large. For the sake of simplicity, let us consider a simple PC model, e.g. an arrangement of holes drilled in a dielectric material, wherein, one must decide whether to plug a hole with bulk material or to leave it at is in order to guide the light through a certain path. Regarding to this case, the amount of possible configurations

grows rapidly with the number of holes that comprise the PC cluster (*N)*; i.e. the number of distinct configurations grows up to 2^N. Nonetheless, even this simple case entails dealing with a large amount of possible configurations, and it is evidently impractical to analytically solve each of them. Thus, we must resort to seek for an approximation that minimizes the computational effort.

Heuristic algorithms comprise two fundamental features: the divide-and-conquer process, in which the problem is divided into a more manageable subsets and the iterative improvement that performs a sequential downhill optimization.

2.1. Inversion by FSA

The Simulated annealing (SA) technique is a well known meta-heuristic ground state search method that has been commonly applied to combinatorial optimization (CO) problems. It aims to find the optimum state of a specific problem with non-zero probability for accepting uphill solutions. However, the classical SA scheme enhances the acceptance of worse solutions in the early stage of the optimization process in a non-local form. Thus, these initial PC arrangements are most likely to be disregarded later on and, the throughput of the optimization method decreases. Consequently, several alternative SA schemes have been proposed so far [4, 5]. In this work, we employ the fast simulated annealing (FSA) algorithm [1]. The FSA algorithm reduces significantly the required running time of the standard SA algorithm by performing a semi-local search and enhances the efficiency of the optimization process by further controlling the number of uphill moves. Besides, we have included a re-annealing scheme that aids to bound the search space of less sensitive parameters relative to the ranges of more sensitive parameters.

2.2. Inversion by IHS

The HS algorithm is a meta-heuristic optimization algorithm inspired by musical improvisation processes, which aims to achieve a perfectly melodic harmony. This harmony, in music, is analogous to finding the optimality in an optimization process. HS was proposed by Geem in 2001 [2] and thenceforth it has been widely applied to a variety of combinatorial optimization problems [6, 7, 8]. Trying to characterize the process of musical improvisation, Geem pointed that any musician in the process of composition has three options for suggesting a new note: play a tune exactly in the way he has memorized, play something similar to a stored melody (eg. slightly adjusting the pitch), or compose new notes randomly. Based on these three options, Geem et al., made a new quantitative optimization process. These three corresponding components became: memory usage of harmonies, pitch adjustment and randomization. However, the local search procedure of HS does not ensure a high performance [9]. In this context, Mahadavi et al. [9] proposed a new method for enhancing the local search and convergence of HS through dynamic adaptation of both pitch adjusting rate (*PAR*) and bandwidth. In addition, we have included a further randomization operator proposed in [10].

2.3. Inversion by NSGA-II: multiobjective formulation

Former heuristic methods, namely the FSA and IHS optimization methods, in its native meta-heuristic formulation, have proven to be a very valuable computational tools for inverse designing. Nevertheless, there are many situations wherein multiple simultaneous objectives must be fulfilled. Moreover, usually there is no way to elucidate a PC structure that produces an optimum for each of the competing objectives. This is due to the existence of conflicts between both objectives. In these cases, multi-objective evolutionary algorithms (MOEAs) allows one to find multiple Pareto-optimal solutions in a single run; i.e., they provide a sparse number of alternative solutions that simultaneously optimize all objectives. This is a fact of a great practical value for designing novel PC devices such as e.g. photonic crystal resonant cavities that possess a high Q factor and a low modal volume or PC wavelength division multiplexers, just to cite some. In this paper, we use a computationally fast elitist multi-objective evolutionary algorithm, NSGA-II, which uses a spread non-dominating sorting approach.

2.4. Solving harmonic TM propagation using FEM

FEM is a general purpose numerical method for solving partial differential equations that it is especially well suited for dealing with electromagnetic problems in geometries of arbitrary complexity. Recently, we pointed out that FEM is a reliable and fast computational method for calculating important electromagnetic quantities in the stationary regime [11], such as the transmittance spectra in PC clusters. Furthermore, it combines very good with iterative processes such as the optimization methods described in sections 2.1 and 2.2. On the other hand, the finite-difference time-domain (FDTD) method is the most widespread method for the PC topology analysis, but as mentioned in [11], its variable convergence time makes it less suitable for an iterative hard search problem. For simplicity, in this paper, we have used an approach consisting of optimizing a two-dimensional PC and, later, calculating the corresponding merit function (the transmittance mainly) for the corresponding 3D slab extruded from the 2D template. In a later work, we will report calculations performed directly on the PC slabs [12]. All the PC designs sketched in the present work share a triangular lattice made of $0.35a$ radii holes drilled into a Si material. This bulk material was set to an index of refraction of 3.46, which is appropriated at optical wavelengths. We restricted our analysis to TM modes.

3. Inverse designed PCWG sharp bends

PCs can modify and even inhibit the density of photonic states inside the crystal. In addition, if the symmetry of the crystal lattice along one of its main crystalline directions is broken, evanescent, standing waves and/or traveling single

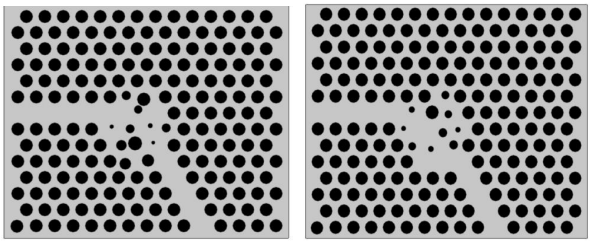


Figure 1: Left: Inverse designed model of a 60° waveguide using the IHS algorithm. Right: Inverse designed waveguide of a 60° model using the FSA algorithm.

or multiple modes may break through the band gap leading to novel nanoscale optical waveguides (PCWGs). In this situation, the light is guided at subwalength scale with minimal propagation losses. Furthermore, the band gap guiding mechanism allows to create unprecedented waveguide curvatures while it preserves an efficient guiding along extremely sharp corners. PCWG bends, unless conventional curved dielectric waveguides, are not limited to a critical curvature angle of the order of millimeters, instead, they can offer a much more compact way to guide light along curved light paths. This fact opens the possibility of building essential stages for novel integrated optoelectronics, small-scale all-optical circuits and overall for semiconductor device miniaturization. Reducing the reflection from the bend region in a large bandwidth has been widely investigated in the literature [13, 14, 15, 16]. The first results on PC waveguide bends were reported by Mekis et al. [13], where the transmission through a 90° bend in a 2D photonic crystal with a square lattice structure was investigated. Several techniques have been used so far in order to improve the transmission of the PC bends [14, 17, 18]. A simple 60° PC bend can be introduced in a triangular structure as shown in Fig .1. Due to the existance of a PBG, light is confined to the bend region and no power will be radiated out of the waveguide. In this simple bend structure the discontinuity along the guidance path causes large reflection and hence it provides low transmission. The main reason for the low transmission is that the mismatch at the bend region stimulates higher order modes that are evanescent in the PC waveguide. The PC bend consists of two parts: a waveguide in the Γ–K direction and another one in the Γ–M direction. In a simple bend structure, the coupling of energy between these parts is not efficient and, therefore, the transmission of the bend is low (see Fig .2).

The situation radically changes, however, when we apply our optimization algorithms to this waveguide. The resulting topologies obtained by using the HS and FSA algorithms, respectively, are depicted in Fig .1. It can be seen that the optimized topologies present a significant improvement in the transmittance on the selected dimensionless frequency range from 0.26 to 0.28, as shown in in Fig .2. The structural modifications carried out by our heuristic algorithms resulted in a shift of the waveguide modes and hence brings about a better coupling of the energy from the Γ–M to the Γ–K direction waveguides. As a consequence, the bandwidth increases and the spectrum is flatter.

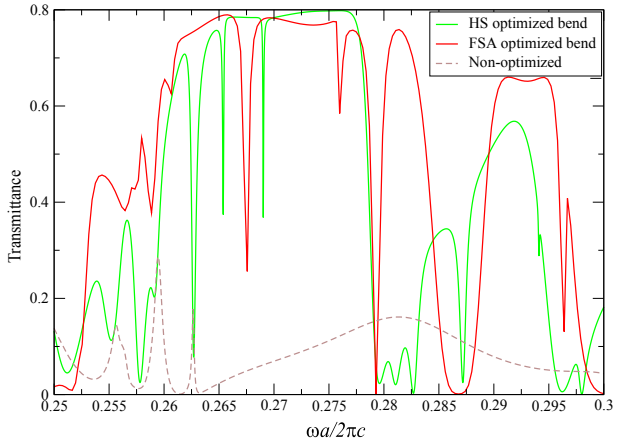


Figure 2: Transmittance calculation comparison for PCWG curved geommetries obtained from the IHS, and FSA algorithms, together with the transmittance of a straight W1 PCWG and the transmittance of a non-optimized structure.

4. Inverse design of ultracompact Y-junction power splitters

A power-splitter device is one of the most essential and functional devices required in future PICs, i.e., optical power splitters are key building blocks in any photonic system. In addition, the optical waveguide splitter is an important device in integrated optical interconnect systems. Equal amount of power distribution in each branch is a fundamental function in electronics. Standard splitters follow the X and Y shape, but these systems usually present high transmission losses.

Here we pose some novel power-splitting schemes in two-dimensional PC using the standard approach of an Y-junction (or branch) structure, which has been widely criticized for having a poor transmittance [19, 20]. Some of the drawbacks that have been attributed to such configurations are mainly due to the existence of sharp 120° bends. However, in [12], we demonstrate that by means of heuristic, one can minimize the reflectance of curved waveguides even for systems requiring high bandwidth. Even though some reasonably good configurations are known for the microwave region power splitting [21], none of them seems to be easily made using PC technology on optical wavelength scale. Focusing on a practical design, we performed an heuristic optimization in order to overcome these problems. In this context, new half power splitting schemes are proposed (see Fig .3) using a symmetric structure. Besides, these splitter configurations divide the input power equally at the output ports without significant reflection or radiation losses. Moreover, since they are built following the PC standards, they comply with the size compactness requirements of future PICs.

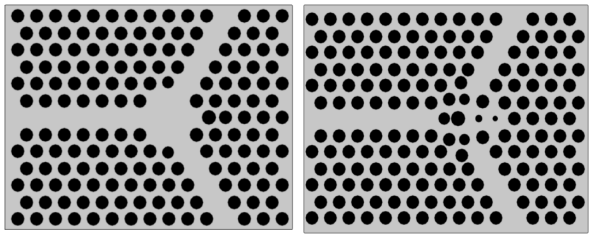


Figure 3: Left: Inverse designed model of a Y-junction splitter using the IHS algorithm. Right: Inverse designed of a Y-junction splitter model using the FSA algorithm.

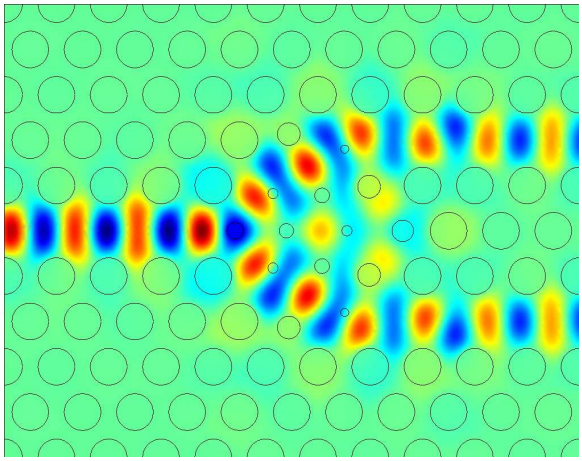


Figure 4: Geometry and mode profile calculated within the harmonic regime using FEM and a monochromatic plane wave source excited in the westernmost W1 boundary for $f = 0.275$.

5. A Photonic Crystal Line Defect Waveguide Integrated with a Multimode Interference Block (MMI) based Power Splitter

The Y-junction configurations presented in previous section operate within a broad bandwidth, they present negligible losses, and they possess a very compact size. However, they require an additional sharp bend stage that further complicates the whole splitter design yielding to a very challenging structure. Alternatively, we have applied inverse design technique to a different geommetry that does not contain these inconveniences. This structure consists of three disjointed elements, namely an input waveguide, a short interference section (MMI block) and two symmetric output waveguides. Therefore, the incoming field interacts with the interference stage in such a way that the field is split and redirected equally into both output waveguides. This structure allows to couple the split light power directly into the output ports and therefore, the overall design is simplified. Fig . 4 depicts the power splitting of an incoming monochromatic field and the shape of the inverse designed structure.

Fig. 5 shows that both algorithms succeed in the task

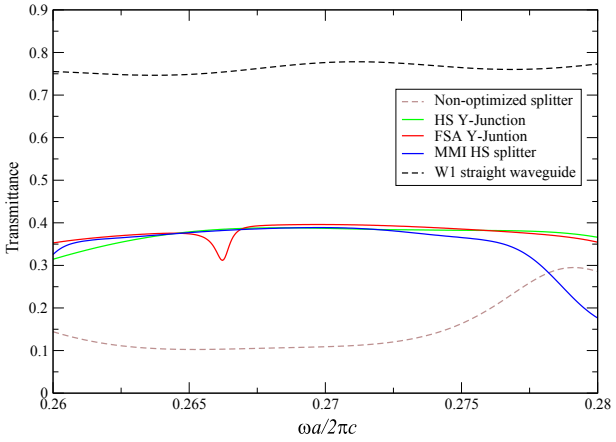


Figure 5: Transmittance spectra comparison for both FSA and IHS Y-junction splitter models, a splitter model comprised witha MMI and a non-optimized Y-junction splitting geommetry. The dashed black line indicates the transmittance spectra of a reference straight PCWG of the same length as the Y-junction model.

of maximizing the half-splitting for both, the Y-junction and the MMI like splitting structures along the 0.26–0.28 frequency range, up to an extremely wide operating bandwidth that almost covers the entire passband of the selected guided mode. Yet, the maximization of the transmittance over frequency range 0.26–0.28 ensures that the transmittance losses due to the splitter mechanism are almost inhibited. Regarding the transmittance of the W1 PCWG it should be pointed out that the amplitude of the transmittance of the isolated W1 PCWG lies below the theoretical value of 1. This fact is due to the presence of absorption boundaries surrounding the simulation domain.

5.1. Inverse design of an optical cross-connect and wavelength multiplexing structure

Optical cross-connect interconnects (OXC) are the key fundamental element for a high-speed all-optical signal switching system. In contrast with the present digital OXC systems, this PC based optical OXC deals with multiple high speed optical signals that are switched in the optical domain in their entirety and do not require any prior multiplexing stage or optical-to-electrical conversion. In this context, we present a fully bidirectional WDM and OXC compatible with chip-scale silicon photonics. This device is comprised by two parallel PCWG sections joined by an inverse designed interference stage that produces a mode matching between opposite waveguides through a reasonable bandwidth. In addition, the most widespread configuration of add/drop multiplexing devices that, in general, are constructed including an array waveguide diffraction grating or fiber gratings, demand a significantly large bend radius, and so the overall device dimensions scale accordingly. Our simulations reveal that this component outperforms previous approaches, as it permits to couple waveguide modes using a short and compact PC geometry comprised by only

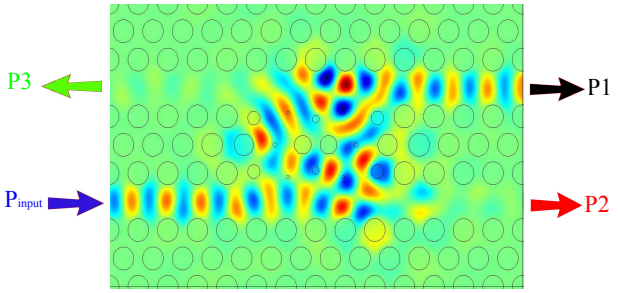


Figure 6: Convergence of the HS algorithm across an optimized tapering structure. The final structure is shown in the inset.

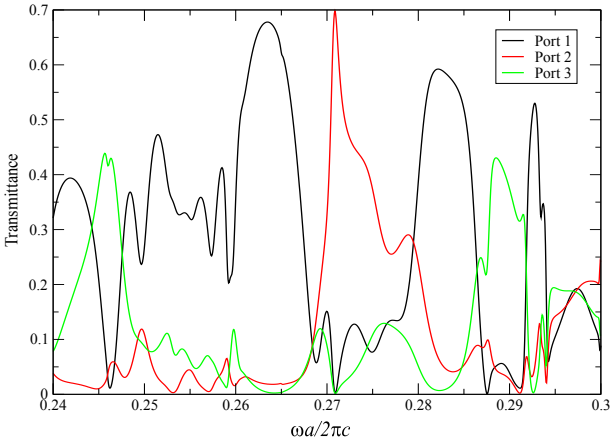


Figure 7: Transmittance spectra for the cross connect system depicted in Fig. 6. The incoming light is thenceforth routed to one of the output ports according to the wavelength. Noticeably, reflection and cross-talk losses are almost negligible.

a few holes and allows miniaturizing the crossing and multiplexing functionalities, as shown in Fig. 6.

Fig. 7 depicts the transmittance flux calculated at the boundary of each output port. Therein, it is shown that almost the entire input power is redirected through a unique port and moreover, this structure changes this procedure according to the input signal wavelength. We believe that this system could serve as an optical signal encoding source for a OCDMA system, as long as it allows for an efficient, low loss and fast routing of WDM signals through an optical networks architecture.

6. Inverse designed PC resonant cavities with high quality factor and reduced modal area

When the periodic lattice of a PC is intentionally broken, there is the possibility to trap light within this imperfection. Following this principle, a wide variety of novel functional devices can be designed. On the one hand, PC point defect cavities rely on the Bragg reflection confinement strength, which allows to confine light and yielding extremely high quality factors (Q). On the other hand the spatial localization of trapped modes within these cavities present extremely low mode volumes. These facts make PC cavities an attractive field for developing novel potential applications in quantum information technology. Nevertheless, implementing both optimal criteria simultaneously is a challenging task, since both objectives are somehow competing ones. Therefore, in this section, we resort to the NSGA-II MOEA in order to find topologies that optimize both objectives in a balanced way. In this case, we focused our research on structures presenting good criteria within donor state cavities. The optimization process of the NSGA-II run is schematically shown in Fig.8. There, the Pareto-optimal front it shifted to higher values of quality factors and to minimum values of modal area (A), during the process of optimization. Two of the proposed resonant cavities are depicted in the inset of Fig. 8, corresponding to a resonant cavity with a dipole aspect and a high Q value and a resonant cavity that is reminiscent of the whispering gallery mode observed in microdisk resonant cavities.

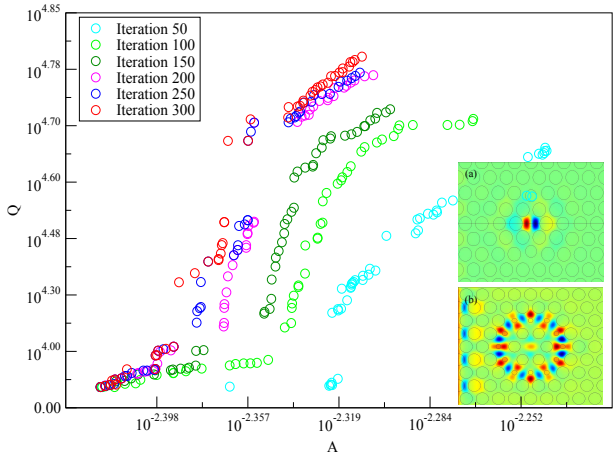


Figure 8: Convergence of the optimal Pareto-fronts through the MOEA optimization run. Both objectives scale as the iterative process evolves. The modal area was calculated as in [22], where $A = \frac{\int \epsilon(r)H^2(r)d^2r}{(\epsilon(r)H^2(r))_{max}}$. The insets show (a) a dipole PC resonator provided by a high Q of 62.168 ,and a dodecapole resonant mode with a Q factor of 37.000

7. Conclusions

In this paper, novel PC passive devices are proposed using single objective heuristic algorithms, namely the FSA and IHS algorithms together with a MOEA algorithm called NSGA-II, for more challenging designs. We report on sharp bends structures providing a near 100% intrinsic bending efficiency for a broad bandwidth, two alternative power splitter structures that equally divide the incoming power supply without significant reflection losses. In addition, we report on a cross-connect structure formed by two parallel PCWGs that simultaneously acts as a broadband WDM. Last but not least, we report on a fast elitist multi-objective Genetic Algorithm approach as a design tool for designing PC cavities that exhibit simultaneously high quality factors

and reduced modal areas.

Acknowledgement

We would like to thank the Basque Government for financial support under the SAIOTEK 2012 (ref. S-PE12UN043) programme. One of us, I.A., wants to thank the Vicerrectorado de Euskara y Plurilinguismo de la UPV/EHU for financial support under the PhD Fellowships 2011 programme.

References

[1] H. Szu and R. Hartley, Fast simulated annealing, *Phys. Lett. A*, 122: 157–162, 1987.

[2] Z. W. Geem, J. H. Kim, G. V. Loganathan, A New Heuristic Optimization Algorithm: Harmony Search, *Simulation*, 76: 60–68, 2009.

[3] K. Deb, A. Pratap, S. Agarwal, T. Meyarivan, A Fast and Elitist Multiobjective Genetic Algorithm: NSGA-II, *IEEE Trans. on Evolut. Comput.*, 6: 182–68, 2002.

[4] B. Apolloni, C. Caravalho, D. De Falco, Quantum stochastic optimization, *Stoch. Proc. Appl.* 33: 233-244, 1989.

[5] L. Ingber, Adaptative simulated annealing (ASA): lessons learned, *J. Control Cybern.*, 25: 33–54, 1996.

[6] R. Forsati, A.T. Haghighat, M. Mahdavi, Harmony search based algorithms for bandwidth-delay-constrained least-cost multicast routing, *Comp. Communications*, 31: 2505–2519, 2008.

[7] Z.W. Geem, Harmony Search in Water Pump Switching Problem, *Adv. Nat. Comp*, 3612: 751-760, 2005.

[8] R. Zhang and L. Hanzo, Iterative Multiuser Detection and Channel Decoding for DS–CDMA Using Harmony Search, *IEEE Sig. Proc. Let.*, 16: 917 - 920, 2009.

[9] M. Mahdavi, M. Fesanghary,E. Damangir, An improved harmony search algorithm for solving optimization problems, *Appl. Math. Comput.*, 188: 15671579,2007.

[10] I. Landa-Torres, S. Gil-Lopez, S. Salcedo-Sanz, J. Del Ser, J.A. Portilla-Figueras, A novel grouping harmony search algorithm for the multiple-type access node location problem, *Expert Sys. Appl*, 39: 52625270, 2012.

[11] I. Andonegui and A. J. Gacia-Adeva, The finite element method applied to the study of two-dimensional photonic crystals and resonant cavities, *Opt. Express* (to be published).

[12] I. Andonegui and A. J. Gacia-Adeva (unpublished).

[13] A. Mekis, J.C. Chen, I. Kurland, S. Fan, P. R. Villeneuve, J. D. Joannopoulos, High Transmission through Sharp Bends in Photonic Crystal Waveguides, *Phys. Rev. Lett.*, 77:3787–3790, 1996.

[14] A. Chutinan and S. Noda Waveguides and waveguide bends in two-dimensional photonic crystal slabs, *Phys. Rev. B*, 62:4488–4492, 2000.

[15] A. Mekis, S. Fan, J. D. Joannopoulos Bound states in photonic crystal waveguides and waveguide bends, *Phys. Rev. B*, 58:4809–4817, 1998.

[16] A. Chutinan, M. Okano, S. Noda Wider bandwidth with high transmission through waveguide bends in two-dimensional photonic crystal slabs, *Applied Physics Letters*, 80:1698–1700, 2002.

[17] J. Smajic, C. Hafner, D. Erni, Design and optimization of an achromatic photonic crystal bend, *Opt. Express*, 11:1378–1384, 2003.

[18] P. Borel, A. Harpth, L. Frandsen, M. Kristensen, P. Shi, J. Jensen, O. Sigmund, Topology optimization and fabrication of photonic crystal structures, *Opt. Express*, 12:1996–2001, 2004.

[19] S. Boscolo, M. Midrio, T. F. Krauss, Y-junction in photonic crystal channel waveguides: high transmission and impedance matching, *Opt. Lett.*, 27:1001–1003, 2002.

[20] S. Fan, S. G. Johnson, J.D. Joannopoulos, C. Manolatou, H. A. Haus, Waveguide branches in photonic crystals *J. Opt. Soc. Am. B*, 18:162–165, 2001.

[21] M. Bayindir, B. Temelkuran, E. Ozbay, Photonic-crystal-based beam splitters *Appl. Phys. Lett.*, 77:3902–3904, 2000.

[22] R. Coccioli, M. Boroditsky, K. W. Kim, Y. Rahmat-Samii, E. Yablonovitch, Smallest possible electromagnetic mode volume in a dielectric cavity *IEEE Proc. Optoelectronics*, 145:391–397, 1998.

Eigenmodes Analysis in 2-D Lorentz-Type Frequency-Dependent Photonic Crystals

Amin Gul HANIF[1*], Toru UNO[2], and Takuji ARIMA[3]

Tokyo University of Agriculture and Technology
2-24-16 Naka-cho, Koganei-shi, Tokyo, Japan 184-0012
[*]50009834203@st.tuat.ac.jp

Abstract

Electromagnetic wave propagation in metamaterials including photonic crystals has been widely investigated due to their inherent capabilities for developing novel devices in optics, microwave and antenna engineering. In reality, most of the materials are frequency-dependent; on the other hand, it is necessary to investigate how the performance of photonic crystals depends on frequency. In this paper, it is shown that the eigenmodes can be accurately calculated in two-dimensional Lorentz-type frequency-dependent photonic crystals using a new finite-difference frequency-domain (FDFD) algorithm.

1. Introduction

Recently, remarkable progress has been made in the field of photonic crystals (PCs) due to their various applications in optics, microwave, and antenna engineering [1-4]. The band diagram of PCs has been analyzed for frequency-independent materials. Recently, interest has been grown in the analysis of frequency-dependent or dispersive PCs for novel applications. Therefore, accurate modeling of the band diagram of PCs composed of frequency-dependent materials is highly desirable to efficiently analyze the wave propagation phenomena over a wide range of frequencies in microwave and optical disciplines.

Several numerical methods have been used to compute the band diagram of two-dimensional (2-D) PCs. The most commonly applicable methods are the plane-wave expansion (PWE) method [4], the finite-difference time-domain (FDTD) method [5, 6], and the finite-difference frequency-domain (FDFD) method [3, 7]. The PWE method is very simple and easy to apply. However, the resultant matrix of the PWE method is dense and large, thus making its computation heavy for large problems. Moreover, it suffers from slow convergence of the Fourier transform of the dielectric function [3, 8].

The FDTD method is a well-known electromagnetic computational method, which is also applicable for frequency-dependent materials [9]. However, in some cases, the FDTD method does not have enough accuracy for band diagram calculation of PCs. To improve the accuracy of the conventional FDTD method, several FDTD algorithms have been developed. Although the accuracy of the FDTD has been improved, it is still not adequate. There is possibility of losing the resonant frequencies if the excitation and monitor points are not properly positioned in the calculation domain [5, 7]. In addition, spurious modes may occur in the band diagram calculation because of low spatial resolution [10]. Moreover, the FDTD has difficulties in resolving of the degenerating eigenmodes [5]. For further accuracy of the band diagram calculation, Johnson et al. applied the filter-diagonalization method (FDM) [11] for band diagram calculation of PCs [12, 13]. FDM gives better accuracy than the straight forward calculating of the spectral peaks. The FDM can calculate the nearly degenerating eigenfrequencies, but it is difficult to distinguish those eigenfrequencies when they are very close or overlap to each other because they appear in the same or very closed frequency.

Conversely, the FDFD method is highly accurate in band diagram computation of 2-D PCs [14-20]. Because the FDFD method does not utilize spectral analysis to be in trouble for detecting spectral peaks. The FDFD method simply uses the eigenvalue equation to compute the eigenvalues of the characteristic matrix composed of field coefficients. Therefore, the FDFD is capable to compute the eigenfrequencies accurately even if they are very close to each other or degenerate. Yang [14] proposed a FDFD method based on discretizing the Helmholtz equation in the homogeneous sub-regions and field matching at the central grid point. After that, various 2-D FDFD algorithms were developed for band diagram calculations of PCs. Nevertheless, it has not been possible to compute the band diagram for lossy or any other type of frequency-dependent materials with the FDFD method. Lately, we developed an improved 2-D FDFD algorithm that contains electrical conductivity in its formulation and that allows the calculation of the band diagram of 2-D lossy PCs [18]. In addition, we have proposed new 2-D FDFD algorithms for band diagram calculations of Debye-type and Drude-type frequency-dependent PCs [19, 20].

In this paper, we propose a new FDFD algorithm for band diagram analysis of 2-D PCs composed of Lorentz-type frequency-dependent materials. As this FDFD algorithm uses only the eigenvalue equation, therefore, there is no chance to miss the eigenfrequency for any of the band points. This algorithm allows accurate computation of propagation modes in Lorentz-type frequency-dependent PCs. To confirm the accuracy of this FDFD algorithm, the results are compared with the FDTD method. The comparison verifies high accuracy and stability of this FDFD algorithm.

2. Formulation

formulation has been developed for TM_z mode, single-pole Lorentz-type frequency-dependent materials. In the Maxwell's equations in frequency domain

$$\nabla \times \mathbf{E} = -j\omega\mu_0\mu_r \mathbf{H} \tag{1}$$

$$\nabla \times \mathbf{H} = j\omega\varepsilon_0\varepsilon_r \mathbf{E} \tag{2}$$

ε_r and μ_r are the relative permeability and permittivity, respectively. Here, the relative permittivity ε_r is replaced with the single-pole Lorentz type frequency-dependent relative permittivity $\varepsilon_r^{'}$

$$\varepsilon_r^{'} = \varepsilon_\infty + (\varepsilon_s - \varepsilon_\infty)\frac{\omega_p^2}{\omega_p^2 + 2j\omega\delta_p - \omega^2} \tag{3}$$

where ε_∞ is relative permittivity at infinite frequency, ε_s is the relative frequency at static or zero frequency, ω_p is the frequency of the pole pair (the undamped resonant frequency of the medium), ω is the angular frequency, and δ_p is the damping coefficient. Discretizing equations (1) and (2), using Yee's mesh as shown in Fig. 1(a), and further arrangement of the equations yields the following matrix equation.

$$j\omega\begin{bmatrix} \varepsilon_0\boldsymbol{\varepsilon}_{rz}^{'} & 0 & 0 \\ 0 & -\mu_0\boldsymbol{\mu}_x & 0 \\ 0 & 0 & -\mu_0\boldsymbol{\mu}_y \end{bmatrix}\begin{bmatrix} \mathbf{E}_z \\ \mathbf{H}_x \\ \mathbf{H}_y \end{bmatrix} = \begin{bmatrix} 0 & -\mathbf{V}_y & \mathbf{V}_x \\ \mathbf{U}_y & 0 & 0 \\ -\mathbf{U}_x & 0 & 0 \end{bmatrix}\begin{bmatrix} \mathbf{E}_z \\ \mathbf{H}_x \\ \mathbf{H}_y \end{bmatrix} \tag{4}$$

where $\boldsymbol{\varepsilon}_{rz}^{'}$ is a diagonal matrix composed of Lorentz relative permittivity at the grid points; $\mathbf{V}_x, \mathbf{V}_y, \mathbf{U}_x$, and $\mathbf{U}_y$ are square matrices containing space-differential operators along x and y directions; $\boldsymbol{\mu}_x$ and $\boldsymbol{\mu}_y$ are diagonal matrices of relative permeability at the grid points; $\mathbf{H}_x$, $\mathbf{H}_y$, and $\mathbf{E}_z$ are column matrices containing the field values. Periodic boundary conditions, on the square unit cell as shown in Fig. 1(b), are applied in the space-differential operators [3]. For simplicity, equation (4) is reduced to

$$-\omega^2\varepsilon_0\,\boldsymbol{\varepsilon}_{rz}^{'}\mathbf{E}_z - \mathbf{A}\mathbf{E}_z = 0 \tag{5}$$

Where $\mathbf{A}$ is a sparse matrix composed of space differential operators and the inverse of relative permeability matrices

$$\mathbf{A} = \frac{1}{\mu_0}(\mathbf{V}_y * \boldsymbol{\mu}_x^{-1} * \mathbf{U}_y + \mathbf{V}_x * \boldsymbol{\mu}_y^{-1} * \mathbf{U}_x) \tag{6}$$

we place the value of $\boldsymbol{\varepsilon}_{rz}^{'}$ into equation (5) that yields

$$-\omega^2\varepsilon_0(\boldsymbol{\varepsilon}_\infty + \frac{\boldsymbol{\Delta\varepsilon}\boldsymbol{\omega}_p^2}{\boldsymbol{\omega}_p^2 + 2j\omega\,\boldsymbol{\delta}_p - \omega^2\mathbf{I}})\mathbf{E}_z = \mathbf{A}\mathbf{E}_z \tag{7}$$

where $\boldsymbol{\Delta\varepsilon} = \boldsymbol{\varepsilon}_s - \boldsymbol{\varepsilon}_\infty$ and $\mathbf{I}$ is the identity matrix.

Let $\mathbf{B} = \boldsymbol{\Delta\varepsilon}\boldsymbol{\omega}_p^2$ then we can write

$$-\omega^2\varepsilon_0\mathbf{B}^{-1}\boldsymbol{\varepsilon}_\infty\mathbf{E}_z - \frac{\omega^2\varepsilon_0\mathbf{I}}{\boldsymbol{\omega}_p^2 + 2j\omega\boldsymbol{\delta}_p - \omega^2\mathbf{I}}\mathbf{E}_z = \mathbf{B}^{-1}\mathbf{A}\mathbf{E}_z \tag{8}$$

$$-\omega^2\varepsilon_0\boldsymbol{\omega}_p^2\mathbf{B}^{-1}\boldsymbol{\varepsilon}_\infty\mathbf{E}_z - 2j\omega^3\varepsilon_0\boldsymbol{\delta}_p\mathbf{B}^{-1}\boldsymbol{\varepsilon}_\infty\mathbf{E}_z + \omega^4\varepsilon_0\mathbf{B}^{-1}\boldsymbol{\varepsilon}_\infty\mathbf{E}_z - \omega^2\varepsilon_0\mathbf{E}_z = \boldsymbol{\omega}_p^2\mathbf{B}^{-1}\mathbf{A}\mathbf{E}_z + 2j\omega\boldsymbol{\delta}_p\mathbf{B}^{-1}\mathbf{A}\mathbf{E}_z - \omega^2\mathbf{B}^{-1}\mathbf{A}\mathbf{E}_z \tag{9}$$

$$-\omega^2\varepsilon_0\mathbf{B}\boldsymbol{\omega}_p^2\mathbf{B}^{-1}\boldsymbol{\varepsilon}_\infty\mathbf{E}_z - 2j\omega^3\varepsilon_0\mathbf{B}\boldsymbol{\delta}_p\mathbf{B}^{-1}\boldsymbol{\varepsilon}_\infty\mathbf{E}_z - \omega^2\varepsilon_0\mathbf{B}\mathbf{E}_z - \mathbf{B}\boldsymbol{\omega}_p^2\mathbf{B}^{-1}\mathbf{A}\mathbf{E}_z - 2j\omega\mathbf{B}\boldsymbol{\delta}_p\mathbf{B}^{-1}\mathbf{A}\mathbf{E}_z + \omega^2\mathbf{A}\mathbf{E}_z = -\omega^4\varepsilon_0\boldsymbol{\varepsilon}_\infty\mathbf{E}_z \tag{10}$$

Multiplying both sides of equation (10) by $-\frac{1}{\varepsilon_0}\boldsymbol{\varepsilon}_\infty^{-1}$ yields

$$\omega^2\,\boldsymbol{\varepsilon}_\infty^{-1}\mathbf{B}\boldsymbol{\omega}_p^2\mathbf{B}^{-1}\boldsymbol{\varepsilon}_\infty\mathbf{E}_z + 2j\omega^3\,\boldsymbol{\varepsilon}_\infty^{-1}\mathbf{B}\boldsymbol{\delta}_p\mathbf{B}^{-1}\boldsymbol{\varepsilon}_\infty\mathbf{E}_z + \omega^2\,\boldsymbol{\varepsilon}_\infty^{-1}\mathbf{B}\mathbf{E}_z + \boldsymbol{\varepsilon}_\infty^{-1}\mathbf{B}\boldsymbol{\omega}_p^2\mathbf{B}^{-1}\frac{\mathbf{A}}{\varepsilon_0}\mathbf{E}_z + 2j\omega\boldsymbol{\varepsilon}_\infty^{-1}\mathbf{B}\boldsymbol{\delta}_p\mathbf{B}^{-1}\frac{\mathbf{A}}{\varepsilon_0}\mathbf{E}_z - \omega^2\boldsymbol{\varepsilon}_\infty^{-1}\frac{\mathbf{A}}{\varepsilon_0}\mathbf{E}_z = \omega^4\mathbf{E}_z \tag{11}$$

Substituting the coefficients

$$\mathbf{C} = 2j\,\boldsymbol{\varepsilon}_\infty^{-1}\mathbf{B}\boldsymbol{\delta}_p\mathbf{B}^{-1}\boldsymbol{\varepsilon}_\infty \quad ; \quad \mathbf{D} = \boldsymbol{\varepsilon}_\infty^{-1}\mathbf{B}\boldsymbol{\omega}_p^2\,\mathbf{B}^{-1}\boldsymbol{\varepsilon}_\infty \quad ; \quad \mathbf{E} = \boldsymbol{\varepsilon}_\infty^{-1}\mathbf{B}$$

$$\mathbf{F} = -\boldsymbol{\varepsilon}_\infty^{-1}\frac{\mathbf{A}}{\varepsilon_0} \quad ; \quad \mathbf{G} = 2j\boldsymbol{\varepsilon}_\infty^{-1}\mathbf{B}\,\boldsymbol{\delta}_p\mathbf{B}^{-1}\frac{\mathbf{A}}{\varepsilon_0} \quad ;$$

$$\mathbf{H} = \boldsymbol{\varepsilon}_\infty^{-1}\,\mathbf{B}\boldsymbol{\omega}_p^2\,\mathbf{B}^{-1}\frac{\mathbf{A}}{\varepsilon_0} \tag{12}$$

into equation (11) yields

$$\omega^3\mathbf{C}\mathbf{E}_z + \omega^2(\mathbf{D}+\mathbf{E}+\mathbf{F})\mathbf{E}_z + \omega\mathbf{G}\mathbf{E}_z + \mathbf{H}\mathbf{E}_z = \omega^4\mathbf{E}_z \tag{13}$$

Equation (13) can be summarized in the following eigenvalue equation.

$$\mathbf{H}\mathbf{Z} = \omega\mathbf{Z} \tag{14}$$

where

$$\mathbf{H} = \begin{bmatrix} \mathbf{C} & \mathbf{D}+\mathbf{E}+\mathbf{F} & \mathbf{G} & \mathbf{H} \\ \mathbf{I} & \mathbf{0} & \mathbf{0} & \mathbf{0} \\ \mathbf{0} & \mathbf{I} & \mathbf{0} & \mathbf{0} \\ \mathbf{0} & \mathbf{0} & \mathbf{I} & \mathbf{0} \end{bmatrix} \quad \text{and} \quad \mathbf{Z} = \begin{bmatrix} \omega^3\mathbf{E}_z \\ \omega^2\mathbf{E}_z \\ \omega\mathbf{E}_z \\ \mathbf{E}_z \end{bmatrix} \tag{15}$$

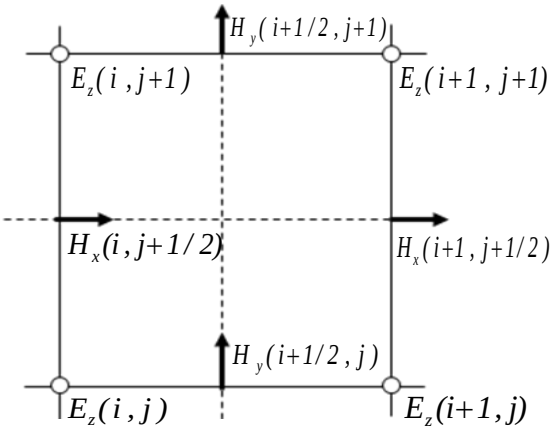
The quantity ω is the eigenvalue of matrix **H,** from which one finds the normalized eigenfrequency $\omega\, a/2\pi c$, where a is periodic length and c is the speed of light in vacuum.

3. Numerical Results

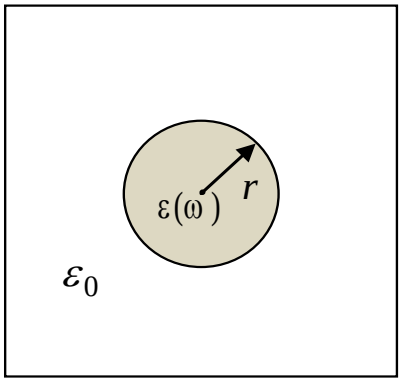
For numerical analysis, a 2-D PCs composed of Lorentz-type frequency-dependent periodic cylinders with square lattice is considered. As shown in Fig. 1(b), the unit cell contains only one cylinder with radius r and has periodic length a. The ratio r/a = 0.2, a =1 mm, and $\Delta x = \Delta y = 0.025\,\text{mm}$. Arnoldi Algorithm [21] is used to compute the eigenvalues of the characteristic matrix in the FDFD algorithm. In the FDTD calculation, the recursive-convolution (RC) approach [5] is used to model the Lorentz-type frequency-dependent PCs. In order to confirm the validity of the new FDFD algorithm and analyze the frequency effect on the Lorentz-type PCs, different values of the frequency-dependent permittivity are used.

First the validity of this FDFD algorithm is confirmed by setting the relative permittivity at infinite frequency (ε_∞) equal to the relative permittivity at zero or static frequency (ε_s) and then the computed eigenfrequencies are compared to the eigenfrequencies of the conventional dielectric PCs case. The eigenfrequencies must agree well because by setting ε_∞ equal to ε_s the imaginary part of the relative permittivity of Lorentz-type frequency-dependent PCs approaches to zero and its real part equals to the relative permittivity of the conventional dielectric PCs. Figure 2 shows the comparison of normalized frequency of the first six (1st to 6th) eigenmodes of the Lorentz-type PCs, $\omega_p = 1.256*10^{10}$, $\delta_p = 1.256*10^9$, $\varepsilon_s = 8.9$, and $\varepsilon_\infty = 8.9$, and pure dielectric PCs, $\varepsilon_r = 8.9$. The normalized frequency computed by this FDFD algorithm for Lorentz-type PCs and conventional FDFD method for pure dielectric PCs agree well, because the relative permittivity of Lorentz-type PCs equals to the relative permittivity of pure dielectric PCs, that confirms the validity of this new FDFD algorithm.

Figure 3 shows the normalized frequency of the first six(1st to 6th) eigenmodes of the band diagram computed by the new FDFD algorithm and FDTD methods. The parameters of the frequency-dependent relative permittivity are set $\omega_p = 1.256*10^{10}$, $\delta_p = 1.256*10^9$, $\varepsilon_s = 8.9$, and $\varepsilon_\infty = 4.0$. Both methods agree well in this calculation, except that, the FDTD method calculates some unexpected values for Γ and M points in the irreducible Brillouin zone because at these points some of the modes degenerate and the FDTD method has difficulties in the calculation of the degenerating eigenmodes because they appear very close or at the same frequency. In addition, FDTD has low accuracy in the calculation of the higher eigenmodes because some of the higher eigenmodes arise closer to each other, acquire closer frequencies, and cause to create abnormality in the FDTD calculation. However, the new FDFD algorithm simply uses the eigenvalue equation and is capable to calculate all of the eigenmodes accurately even if they are degenerated.



(a)



(b)

Figure 1: (a) Yee's mesh for TM mode analysis (b) The square unit cell

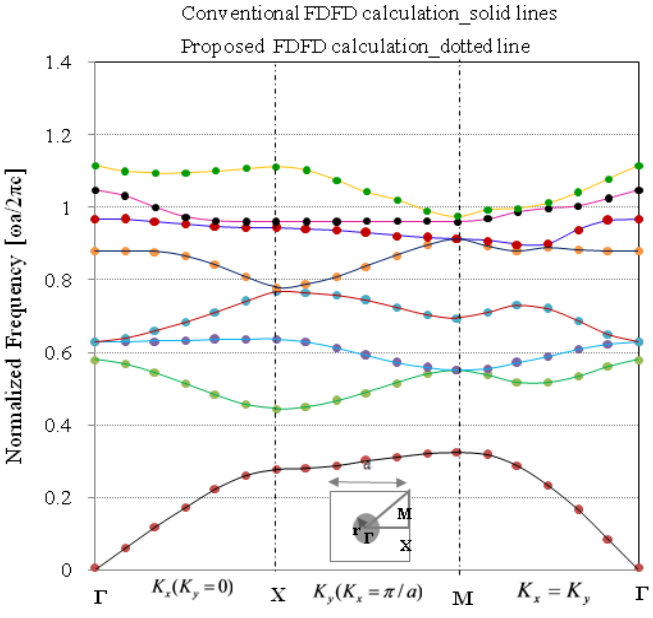


Figure 2: Comparison of the new FDFD algorithm and the conventional FDFD method

Figure 4 shows the normalized frequency of the first six(1st to 6th) eigenmodes computed by the new FDFD algorithm and FDTD method considering the following values $\omega_p = 1.256*10^{10}$, $\delta_p = 1.256*10^{9}$, $\varepsilon_s = 8.9$, and $\varepsilon_\infty = 2.0$. Similarly, as shown in figure 3, both methods agree well in this calculation, except for Γ and M points of the irreducible Brillouin zone. In these points, the eigenmodes degenerate and the FDTD method has difficulties to clearly calculate them. Because the eigenfrequencies of the degenerated modes appear very close to each other that the FDTD detects one frequency for both eigenmodes and misses the other frequency. Also, FDTD issued some irregular value for higher eigenmodes as seen at the top of the figure.

Figure 5 shows the comparison of the FDFD algorithm and FDTD method using the values $\omega_p = 1.256*10^{11}$, $\delta_p = 1.256*10^{10}$, $\varepsilon_s = 8.9$, and $\varepsilon_\infty = 6.0$. In this case, the FDFD and FDTD results are more compatible comparing to the results of figure 3 and figure 4. Because using these values of ω_p and δ_p in the Lorentz-type relative permittivity, the imaginary part of the relative permittivity is decreased for the eigenfrequencies of figure 3 and figure 4. FDTD uses spectral analysis for detecting eigenfrequencies of the eigenmodes. In the spectral analysis, if the imaginary part of the relative permittivity increases then it causes to increase the width of each spectral peak. When the width of each spectral peak increases then the closer modes are appearing under a single peak and FDTD detect only a single frequency for these eigenmodes instead of separate frequencies for each eigenmode. This causes to create abnormality in the FDTD calculation for those relative permittivities that have higher imaginary part. However, the FDFD algorithm is capable to accurately calculate the band diagram for all values of the relative permittivity because it only uses the eigenvalue equation and does not need spectral analysis to calculate eigenfrequencies.

Figure 6 shows the effect of variation of the relative permittivity on normalized frequency using the new FDFD algorithm. In this calculation, the values of ω_p and δ_p are set $1.256*10^{10}$ and $1.256*10^{9}$ respectively. First, the values of ε_∞ or $\varepsilon(\text{Inf.})$ and ε_s are set 8.9 and 8.9 respectively. Secondly, the values of ε_∞ and ε_s are set 4.0 and 8.9 respectively. The normalized frequencies are computed for both cases and then compared as shown in figure 6. The result confirms that as the net relative permittivity decreases then the normalized frequency increases and if the net relative permittivity increases then the normalized frequency decreases.

Similarly, figure 7 confirms the effect of variation of the relative permittivity on normalized frequency using the new FDFD algorithm. In this calculation, the values of ω_p and δ_p are set the same as in the calculation of figure 6. In first case, the values of ε_∞ and ε_s are set 8.9 and 8.9 respectively. In second case, the values of ε_∞ and ε_s are set 2.0 and 8.9 respectively. The normalized frequencies are computed for both cases and then compared as shown in figure 7. The result further confirms that as the net relative permittivity decreases then the normalized frequency increases and if the net relative permittivity increases then the normalized frequency decreases.

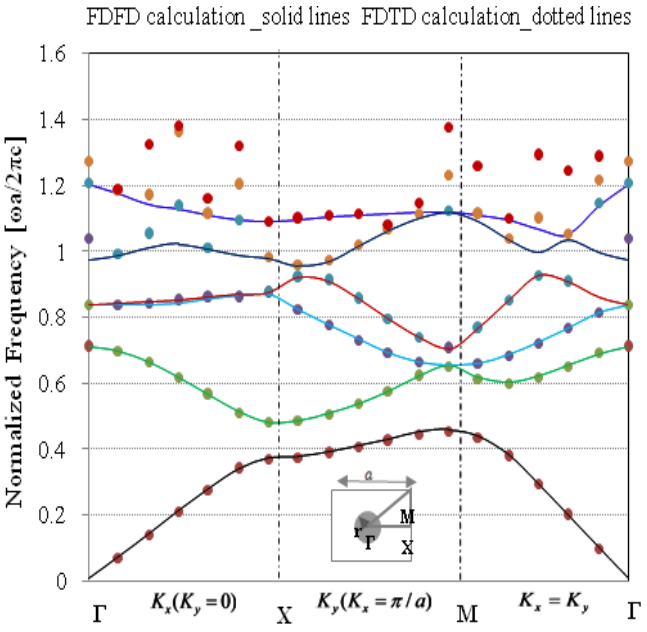


Figure 3: Comparison of new FDFD algorithm and FDTD method for $\varepsilon_\infty = 4$.

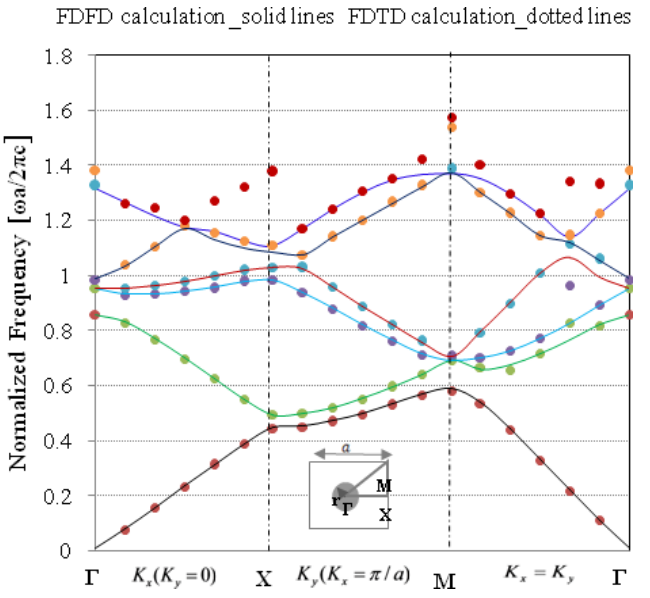


Figure 4: Comparison of new FDFD algorithm and FDTD method for $\varepsilon_\infty = 2$.

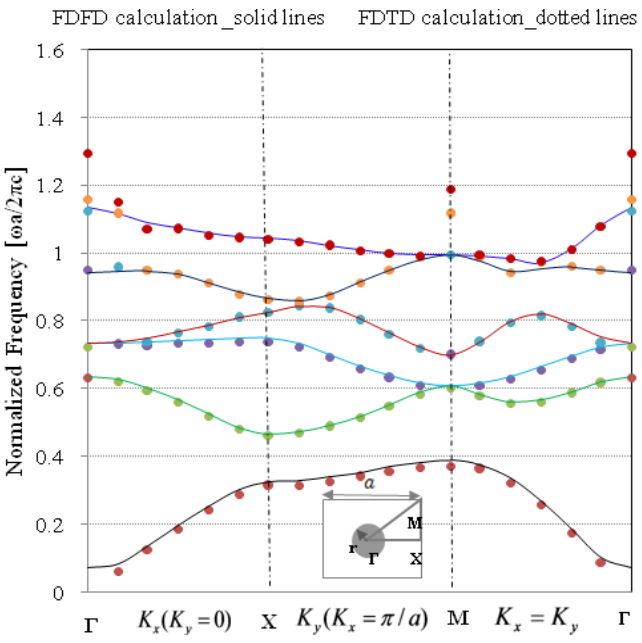


Figure 5: Comparison of new FDFD algorithm and FDTD method for $\varepsilon_\infty = 6$.

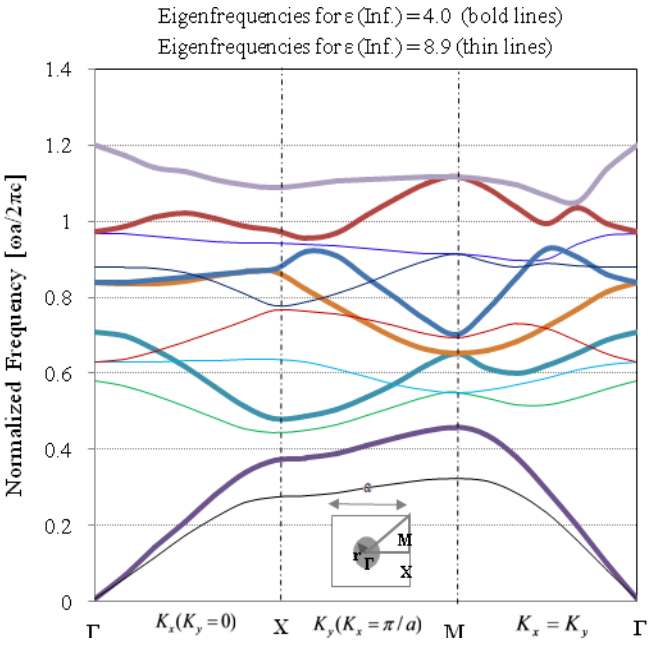


Figure 6: Comparison of the band structures calculations for $\varepsilon_\infty = 8.9$ and $\varepsilon_\infty = 4.0$ using the new FDFD algorithm.

4. Discussion

As mentioned earlier, most of the materials are frequency-dependent and it is necessary to investigate how the performance of photonic crystals depends on frequency. Several numerical methods have been used to compute the band diagram of 2-D PCs. However, these methods have some limitations in the band diagram computation of frequency-dependent PCs as discussed in the introduction section. In this paper, a new 2-D FDFD algorithm is proposed to compute the band diagram of Lorentz-type frequency-dependent PCs. The validity, accuracy, and stability of this FDFD algorithm is confirmed in section 3, numerical results, for Lorentz-type frequency-dependent PCs.

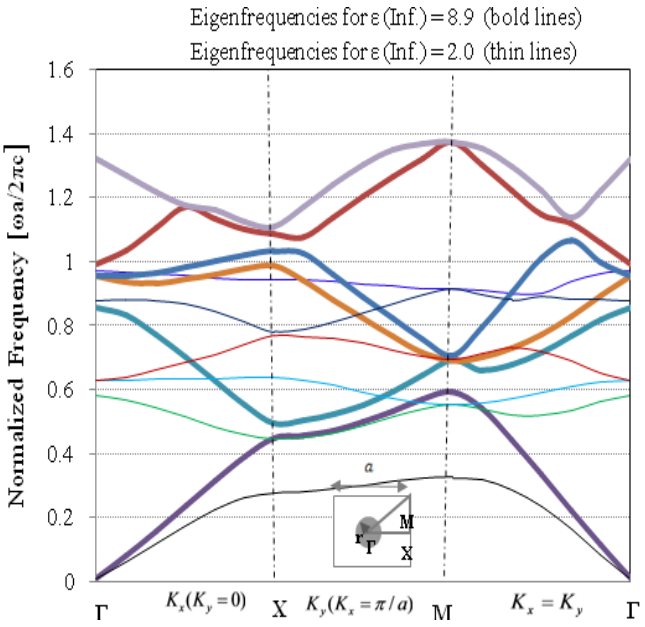


Figure 7: Comparison of the band structures calculations for $\varepsilon_\infty = 8.9$ and $\varepsilon_\infty = 2.0$ using the new FDFD algorithm.

5. Conclusions

In this paper, eigenmodes of 2-D Lorentz-type frequency-dependent PCs are analyzed using a new FDFD algorithm. The validation of this FDFD algorithm is confirmed by its comparison to the traditional FDFD method for dielectric PCs and the FDTD method. The simulation results of this FDFD algorithm for band diagram analysis of Lorentz-type frequency-dependent PCs are compared with the FDTD method that confirm high accuracy and stability of the FDFD algorithm. The FDFD algorithm successfully computes eigenfrequencies of the degenerate modes appearing in band points of the irreducible Brillouin zone. This algorithm relies only on linear algebra and directly uses the eigenvalue equation; thus it can accurately analyze the band diagram of different types of Lorentz frequency-dependent PCs.

References

[1] J. D. Joannopoulos, R. D. Meade and J. N. Winn, *Photonic Crystals: Modeling the flow of light*, princeton University press, 2008.

[2] F. Yang and Y. Rahmat-Samii, *Electromagnetic Band Gap Structures in Antenna Engineering*, Cambridge

University Press, New York, 2009.

[3] K. Yasumoto, *Electromagnetic Theory and Application for Photonic Crystal*s, CRC press, Boca Raton, FL, 2006.

[4] K. Sakoda, *Optical Properties of Photonic Crystals*, 2nd Ed., Springer-Verlag, Berlin Heidelberg, 2005.

[5] A. Taflove and S. C. Hagness, *Computational Electrodynamic : The Finite-Difference Time-Domain Method*, 3rd Ed., Artech House, Norwood, MA, 2005.

[6] T. Uno, *Finite - Difference Time – Domain Method for Electromagnetic Field and Antenna Analysis*, Corona Publishing Co. LTD. 1998 (in Japanese).

[7] Y. C. Chiang, Y. P. Chiou, and H. C. Chang, Finite - Difference Frequency - Domain Analysis of 2-D Photonic Crystals With Curved Dielectric interfaces , *Lightwave Tech*., vol. 26, no. 8, Apr. 2008.

[8] H. S. Sozuer, J. W. Haus, and R. Inguva, Photonic bands: convergence problems with the plane - wave method, *Phys. Rev. B*, 45, 13, 962-13, 972, 1992.

[9] D. F. Kelley and R. J. Luebbers, Piecewise Linear Recursive Convolution for Dispersive Media Using FDTD, *IEEE Trans. on Antenna and Propagat.*, vol. 44, no. 6, June 1996.

[10] Y. Hao and R. Mittra, *FDTD Modeling of Metamaterials: Theory and applications*, Artech House , Norwood, MA, Chap. 4, 2009.

[11] Mandelshtam, V. A., and H. S. Taylor, Harmonic inversion of time signals and its applications, *J. Chem Phys*., vol. 107, 1997, pp. 6756-6769.

[12] Johnson, S. G., S. Fan, A. Mekis, and J. D. Joannopoulos, Multiple - cancellation mechanism for high - Q cavities in the absence of a complete photonic band gap, *Applied Phys. Lett*., vol. 78, 2001. pp. 3388 -3390.

[13] [online]: http://ab-initio.mit.edu/harminv/

[14] H. Y. D. Yang, Finite difference analysis of 2 - D photonic crystals, *IEEE Trans. Microwave Theory Tech*., vol. 44, no. 12, pp. 2688–2695, 1996.

[15] S. Guo, F. Wu. S. Albin, and R. S. Rogowski, photonic band gap analysis using finite-difference frequency-domain method, *Optics Express* 1741, vol. 12, no. 8, Apr. 2004.

[16] C. P. Yu and H. C. Chang, Compact finite-difference frequency - domain method for the analysis of two-dimensional photonic crystals, *Opt. Exp*., vol. 12, no. 7, pp. 1397–1408, 2004.

[17] Y. L. Li, Q. Z. Xue, and C. H. Du, Two-Dimensional Metallic Photonic Crystal with Point Defect Analysis Using Modified Finite-Difference Frequency-Domain Method, *Lightwave Tech*., vol. 28, no. 2, Jan. 2010.

[18] A. G. Hanif, T. Uno, and T. Arima, FDFD and FDTD analysis of 2 - Dimensional lossy photonic crystals, *IEICE Elect. Express*, vol. 8, no. 9, pp. 695-698,2011.

[19] A. G. Hanif, T. Uno, and T. Arima, Finite-Difference Frequency - Domain Algorithm for Band Diagram Calculation of 2 - D Photonic Crystals Composed of Debye Type Dispersive Materials, *IEEE Antenna and Wireless Propagat. Lett.*, Vol. 11, 41-44, 2012.

[20] A. G. Hanif, T. Arima, and T. Uno, New Derived Finite - Difference Frequency - Domain Method Used for Band Structure Analysis of 2 - D EBG Structure Composed of Drude -Type Dispersive Media, *IEICE Elect. Express*, vol. 9, no. 11, pp. 951-957, 2012.

[21] http://www.caam.rice.edu/software/ARPACK/

Plasmon-enhanced photovoltaics, photocatalysis, and solar fuels

Enhanced Light Absorption in Thin-Film Tandem Solar Cells using a Bottom Metallic Nanograting

Xuanru Zhang[1], Wei Wang[2], Zhiang Li[2], Honglei Cai[2], Jijun He[2], Randy J. Knize[3], Bin Xiang[2,*] and Yalin Lu[1,2,3]*

[1] Advanced Applied Research Center, Hefei National Laboratory for Physical Science at the Microscale, University of Science and Technology of China, Hefei, Anhui, 230026, P. R. China
[2] CAS Key Laboratory of Materials for Energy Conversion, Department of Material Science and Engineering, University of Science and Technology of China, Hefei, Anhui, 230026, P. R. China
[3] Laser Optics Research Center, Physics Department, United States Air Force Academy, Colorado Springs, CO 80840, USA
*corresponding author, E-mail: binxiang@ustc.edu.cn, yalin.lu@usafa.edu

Abstract

We introduced a metallic nanograting structure at the bottom of thin-film tandem solar cells, and carried out an investigation into the light absorption in the top and bottom cells via electromagnetic simulation. It indicated that broadband and polarization-insensitive light absorption enhancement was obtained in the bottom cell while the light absorption in the top cell remained unchanged by the influence of this metallic nanograting. It caused that overall carrier generation enhancement can be achieved as much as 60% for both polarization. This light absorption enhancement effect can survive in a wide range of cell thickness and nanograting geometries, which enables us to reduce the thickness of the bottom cell with minimal impact on light absorption. Thereby, it reduces the solar cell production cost in the meanwhile it enhances the solar cell efficiency by the decrease of light-generated carrier recombination rate.

1. Introduction

Plasmonic solar cell is a type of thin-film solar cells which has the capability of trapping light in the thin absorbing layer by the plasmonic (metallic) nanostructures, resulting in the increase of the total light absorption [1-7]. Plasmons are thought to be useful because the absorbed energy is proportional to the electric field squared, and the near-field enhancement of the plasmons causes a larger absorption in a smaller volume. Both localized surface plasmons (LSPs) excited in metallic nanoparticles and surface plasmon polaritons (SPPs) propagating at the metal/semiconductor interface are of great interest. The plasmonic nanostructures can be on top of, within, or at the bottom of the absorbing layer in a solar cell.

The rectangular grating structure is widely chosen for its simple geometry, and easy fabrication [1, 4, 5]. The grating structure applied in a solar cell was firstly reported by Atwater in 2007[4-6]. By placing the grating on top of the cell, large light absorption enhancement was achieved in a narrow spectral range for transverse magnetic (TM) waves, where the SPPs were resonantly excited. However, the absorption for transverse electric (TE) waves were suppressed, since the top metallic gratings acted as a reflect mirror for TE waves [5]. It suggested that the technique of top metallic grating was narrow-band, polarization sensitive, and blocked a fairly amount of incident photons. Our group proposed a structure in 2010 that placed the metallic nanograting at the bottom of the active layer[7]. This design not only free up those photons blocked by surface nanostructures, but also achieved broadband and polarization in-sensitive enhancement; as kinds of resonant effects collaborated. 30% integrated light absorption enhancement integrated over the solar spectrum was achieved in amorphous silicon thin-film solar cells.

In this paper, we place a metallic nanograting at the bottom of the absorbing layer in a tandem solar cells, which is composed of multi-junctions of absorbing materials with different band gaps [8].

The tandem solar cells were introduced to avoid the trade-off between the maximum absorption spectrum band and the maximum voltage. We took the amorphous silicon (a-Si, band gap 1.7 ev)/microcrystalline silicon (μc-Si, band gap 1.1 ev) tandem solar cells as an example [9]. Up to now, most researches are devoted to reducing the thickness of the top cell, considering the unstability of a-Si caused by light induced degradation [10]. Intermediate reflector layers with lower refractive index are introduced, such as transparent conducting oxide indium tin oxide (ITO) or zinc oxide (ZnO), to trap short wavelength light in the thin top layer [10-13]. However, little attention is paid on the naturally poor light absorption of silicon in infrared. To achieve enough absorption of infrared light, the bottom cell is usually of several micrometers, which raises the production cost and declines the light generated carrier collection efficiency due to the increase of the recombination rate.

With the structure of a metallic (silver) nanograting at the bottom of the a-Si/μc-Si tandem solar cell, we investigated the light absorption of the top and bottom cell via numerical calculation. Different from the effect of the top metallic grating, our technique gives rise to broadband and polarization-insensitive absorption enhancement in the bottom cell, on the other hand the high absorption of the top

cell remains unchanged. Over 40% integrated light absorption enhancement and 60% integrated carrier generation enhancement factor is achieved in the bottom cell. By varying the configuration parameters, it indicates that the light absorption enhancement can survive in a wide range of cell thickness and grating geometries. In addition, our study demonstrates that an Ag/Al bimetallic nanograting structure with less Ag cost provides us with the same light absorption enhancement as that of Ag nanograting structure. Our bottom nanograting technique opens up a pathway to cut down the solar cell manufacture cost by reducing the solar cell thin film thickness.

2. Computational methods

The 3-dimensional (3-D) and 2-dimensional (2-D) schematics of the solar cell with the metallic nanograting were shown in Fig. 1. Indium tin oxide (ITO) has been widely used a transparent conductor because of its high conductivity and high transparency. On top of the cell, a thin layer of ITO with a thickness of T_1 acted as the top transparent electrode. An interlayer electrode was a layer of ITO with T_2 thickness. The cell bottom electrode was a silver nanograting, on top of planar silver film as back-reflector as shown in Fig 1. The grating slits were filled with suitable dielectric materials, here chosen as ITO. Different dielectrics used here can tune the dielectric environment of the nanograting, thus the optical properties. To determine the thickness of the silver back-reflector, our numerical investigation indicated that a thickness of 100 nm was enough to reflect all light back into the cell. Two active layers of amorphous silicon (a-Si) and microcrystalline silicon (μc-Si) were sandwiched by the three electrodes, with thicknesses of T_2 and T_4 respectively. The structural parameters used were marked in Fig. 1 (b). In the following discussions, we compared this tandem cell structure with the planar structure, which consisted of Top ITO (T_1)/a-Si (T_2)/interlayer ITO (T_3)/μc-Si (T_4)/back ITO (T_5)/silver. In order to maximize the absorption, it is important to investigate the absorption's dependence on all the structural parameters. However, to simplify our discussion and focus on the effects of the grating, we fixed T_1 and T_3 to be 80 nm and 20 nm, and a-Si thickness T_2= 100 nm.

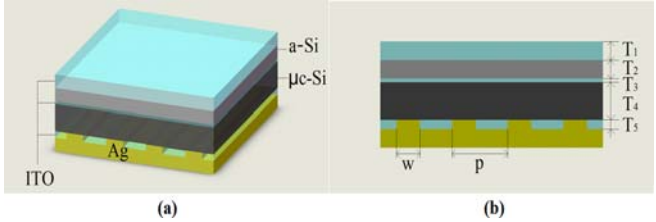


Fig. 1 Schematic (a) and cross section view (b) of the proposed tandem solar cell structure, with the structural parameters to be used in the simulation.

In order to match the solar spectrum with the absorption band of the two silicon materials, a wavelength range of 270 nm to 1200 nm was selected. The frequency-dependent dielectric constants of the four materials used in our study were interpolated from experimental data reported by ref [14, 15]. The modeling software we used is commercially available 2D finite element method (FEM) software Comsol 3.5a. The computational domain was considered as a single unit cell surrounded by bilateral periodic boundaries including top and bottom perfect matching layers (PMLs)[16]. The steady-state electromagnetic field distributions across the structure and the light absorption in the two silicon layers were investigated in this paper. The light absorption was calculated as the integral of the Poynting vectors over the surface of the active layer.

3. Results and Discussion

We compared the absorption spectrums of the structures with and without the metallic gratings (blue line versus red line) in Fig. 2. The geometry parameters were: T_4=200 nm, p=350 nm, w=100 nm, T_5=50 nm. As shown in Fig. 2(a, c), light absorption of the top cell changed little in the presence of the nanograting while the absorption of the bottom cell was greatly enhanced (Fig 2 b, d) in a wide spectrum. According to the effect of the gratings, the absorption spectrum can be roughly divided into three regions: 400-800 nm, 800-1000 nm, and > 1000 nm. For 400- 800 nm region, the absorptions changed little for both polarizations, as the silicon material absorbed radiation in this spectrum very well[14]. The radiation at this region came from the residue of the top cell. For 800- 1000 nm (which is beyond the band gap of a-Si), the absorption was enhanced by the grating structure, with different shapes for TM and TE polarizations. For > 1000nm region where silicon's absorption was small, the absorption of TM waves was enhanced to a considerable level; while the absorption of TE was still near to zero.

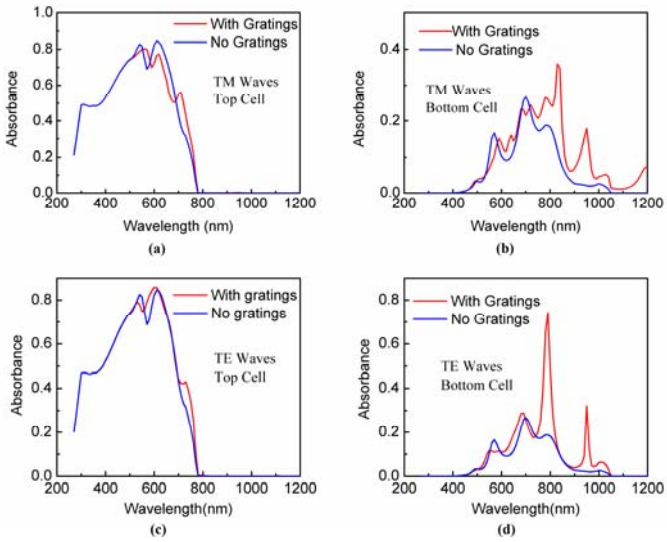


Fig. 2 Absorbance of the top (a and c) and bottom (b and d) cells for both polarization, for the structure with and without the gratings. The geometric parameters are: T_4=200 nm, p=350 nm, w=100 nm, T_5=50 nm.

To investigate the enhancement effect mechanism, 2D map of the absorption enhancement spectrum by varying the configuration parameters and incident wavelengths for both polarizations was simulated as shown in Fig. 3. The peak shift in 400-800 nm was linearly dependent on μc-Si thickness, but exhibited independence on the grating period, for both polarizations. In the cell structure without adding

nanograting, these peaks in 400-800nm were also observed as shown in Fig. 2 and the shift trends for both polarizations are similar. We attributed it to the Fabry-Perot (FP) resonances, which existed with cavity length > λ/2 (λ is the effective wavelength, standing for the product of the free space wavelength and the refractive index)[17]. For the 800-1000 nm region, several bright peaks exhibited dependences on both the μc-Si thickness and the grating period. These may be ascribed to the planar waveguide resonances. The wave vector mismatch between the free propagating light and the guide mode can be achieved by the diffraction of the grating. The peaks for TM and TE waves were slightly different, as the grating was 1-dimensional and produced polarization dispersion. For the region > 1000 nm, the peaks exist for TM waves only. It could be due to the surface plasmon resonances, which also need wave vector compensation from the grating, and can be excited by the TM waves only [18].

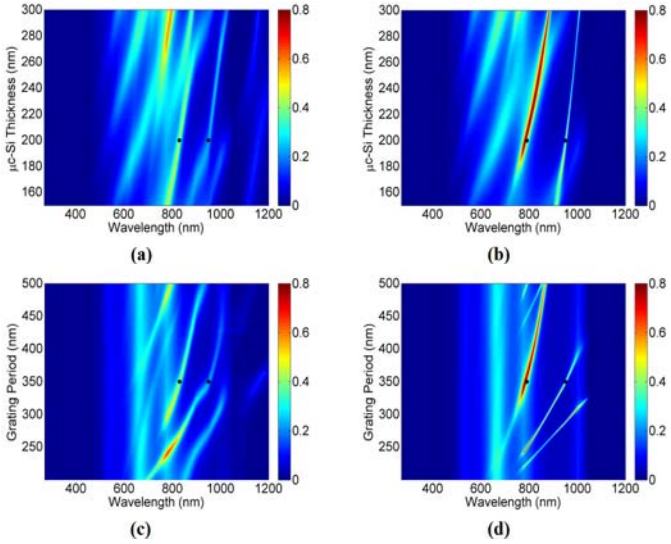


Fig. 3 Mapping the absorbance of the bottom cell with μc-Si thickness T_4 (a and b) and the grating period p (c and d), under TM (a and c) and TE (b and d) polarizations. The black dots correspond to the absorption peaks with structural parameters the same as those in Fig.2.

To further confirm the mechanisms, we plotted the normalized and time-averaged electromagnetic field distributions in Fig. 4. The wavelengths were at the absorption peaks in Fig. 2. The waveguide modes are clearly demonstrated in (a), (b), (c) and (d). For TM waves, the scattering from the silver grating caused a near-field enhancement at the silver-silicon interface, though it didn't perfectly match surface plasmon. The scattering enhancement collaborated with the waveguide modes, so the field enhancement factors of TM waves were larger than TE waves' (as shown in the color bars), and the absorption peaks were broader (as shown in Fig. 2). Fig. 4 (c) and (f) are at 1130 nm, where enhancement only occurs for TM waves. The FP and waveguide resonances participate little in this spectrum region, as the wavelength is quite large relative to the cavity thickness. For TM waves, a clear surface plasmon pattern is shown in Fig. 4(c).

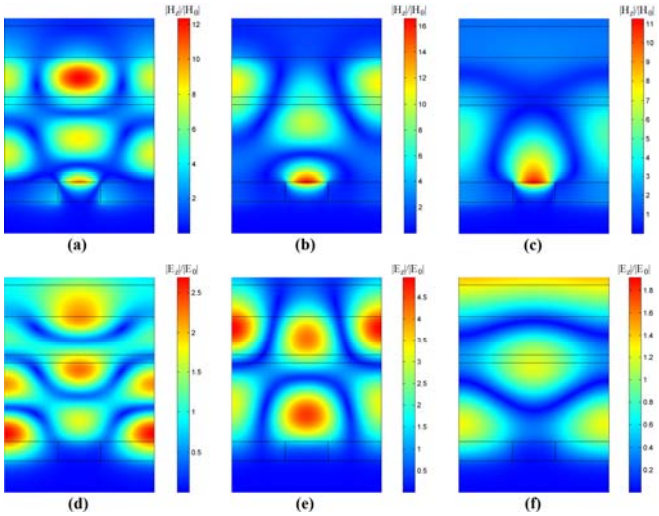


Fig. 4 Normalized and time-averaged electromagnetic field distributions for TM (a, b and c) and TE (d, e and f) waves, at 830 nm (a), 950 nm (b), 1130 nm (c), 790 nm (d), 950 nm (e) and 1130 nm (f).

To further confirm the mechanisms, we plotted the normalized and time-averaged electromagnetic field distributions in Fig. 4. The wavelengths were at the absorption peaks in Fig. 2. The waveguide modes are clearly demonstrated in (a), (b), (c) and (d). For TM waves, the scattering from the silver grating caused a near-field enhancement at the silver-silicon interface, though it didn't perfectly match surface plasmon. The scattering enhancement collaborated with the waveguide modes, so the field enhancement factors of TM waves were larger than TE waves' (as shown in the color bars), and the absorption peaks were broader (as shown in Fig. 2). Fig. 4 (c) and (f) are at 1130 nm, where enhancement only occurs for TM waves. The FP and waveguide resonances participate little in this spectrum region, as the wavelength is quite large relative to the cavity thickness. For TM waves, a clear surface plasmon pattern is shown in Fig. 4(c).

To evaluate the overall absorption enhancement effect over the whole solar spectrum, we define two functions $A_{enhance}$ and $N_{enhance}$. $A_{enhance}$ is defined as the total energy absorption enhancement, calculated using

$$A_{enhance} = \frac{\int I(\lambda) A_{grating}(\lambda) d\lambda}{\int I(\lambda) A_{planar}(\lambda) d\lambda}, \qquad (1)$$

where $I(\lambda)$ is the normalized AM 1.5 solar spectrum, $A_{grating}$ is the absorption spectrum of the investigated structure with gratings, and A_{planar} is the absorption spectrum of the comparison planar structure with only planar back reflector. $N_{enhance}$ is defined as the total carrier generation enhancement, calculated via

$$N_{enhance} = \frac{\int I(\lambda) A_{grating}(\lambda) \cdot (hc/\lambda)^{-1} d\lambda}{\int I(\lambda) A_{planar}(\lambda) \cdot (hc/\lambda)^{-1} d\lambda}, \qquad (2)$$

which includes the different quantum energy of photons of different wavelengths. (We assume uniform internal quantum efficiency (IQE) over the solar spectrum)

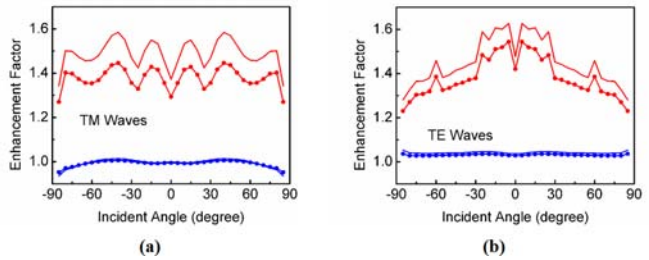


Fig. 5 Energy absorption (dotted line) and carrier generation (solid line) enhancement integrated over the solar spectrum for TM (a) and TE (b) polarizations, as a function of the incident angle. The geometric parameters are: T_4=200 nm, p=350 nm, w=100 nm, T_5=50 nm.

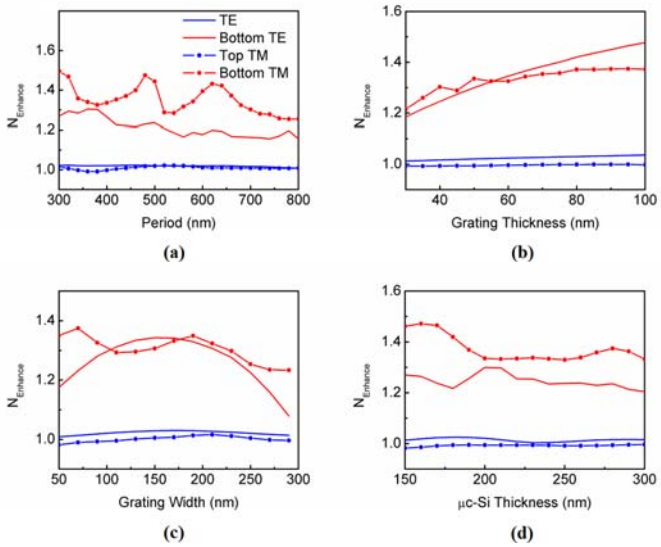


Fig. 6 Carrier generation enhancement factors evolving with the grating period p (a), grating thickness T_5 (b), grating width w (c), and μc-Si thickness T_4 (d), for both the top (blue) and bottom (red) cells, for TM (dotted line) and TE (solid line) polarizations.

In Fig. 5, we investigated the effect of the incident angle on the overall enhancement. As shown in the absorption spectrum (Fig. 2), the grating made less impact on the light absorption of the top cell (blue lines). For the bottom cell, the enhancement effect oscillated with the incident angle in tiny amplitude. An overall carrier generation enhancement of 60% was achieved for both polarizations. Although the absolute absorption decreased at large incident angles due to the large reflection at the air/ITO interface, the absorption enhancement exhibited little dependence on the incident angle, and was even larger than normal incident case. It was ascribed to multiple effects participating in the enhancement mechanism.

The structural parameter dependence of the light absorption enhancement was discussed in Fig. 6. The other structural parameters were fixed when varying one of them. It suggests that the enhancement effect can survive in a wide range of grating parameters, which is of importance for applications in solar cells, as well as it allows relaxing tolerance for nanofabrication, and may reduce the production cost. By the study of the cell-thickness dependence of the enhancement effect as shown in Fig 6(c), it enables us to achieve the enhanced light absorption for large range of μc-Si thicknesses.

4. Further discussion

Considering that the electromagnetic field concentrated at the top surface of the grating and penetrated little into the grooves (Fig. 4), we proposed an Ag/Al bimetallic structure (in the inset in Fig. 7 (a)). Compared to Ag metallic nanograting, modeling results presented that this bimetallic structure was able to provide the same performance of light absorption enhancement as shown in Fig 7.

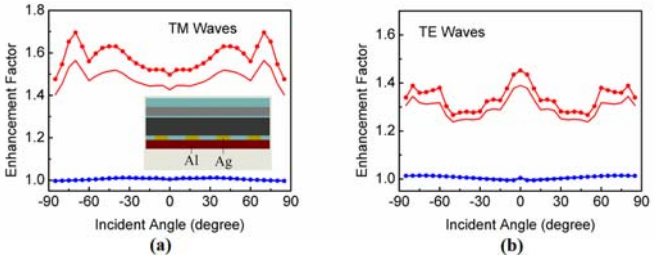


Fig. 7 Enhancement factors as functions of incident angle for both TM (a) and TE (b) polarizations, for the Ag/Al bimetallic structure; with dotted line for carrier generation enhancement and solid line for absorption enhancement, red line for the bottom cell and blue line for the top cell. The geometric parameters are the same as that in Fig. 5 with T_4=200 nm, p=350 nm, w=100 nm, T_5=50 nm. The inset is a schematic of the Ag/Al bimetallic structure.

5. Conclusions

In conclusion, we introduced a metallic nanograting to the bottom of the a-Si/μc-Si thin-film tandem solar cell. While maintaining a similar absorption in the top cell, the light absorption in the bottom cell was greatly enhanced in a wide spectrum. Three mechanisms, the Fabry-Perot resonance, planar waveguide mode and surface plasmon resonance, are involved in different wavelength regions. Overall carrier generation enhancement of 60% is achieved. Due to the multiple effect included in, the enhancement exhibits little dependence on the incident angle and structural parameters. The Ag/Al bimetallic structure shows similar enhancing effect with much lower production cost. Since the design has no demand for the materials of the solar cell, extending the similar design into other active materials such as organic tandem cells can be expected.

Acknowledgements

This work was supported by the National Basic Research Program of China (2012CB922001).

References

[1] H. A. Atwater and A. Polman, Plasmonics for improved photovoltaic devices, *Nature Materials* **9**, pp. 205-213, 2010

[2] D. Derkacs, S. H. Lim, P. Matheu, W. Mar, and E. T. Yu, Improved performance of amorphous silicon solar cells via scattering from surface plasmon polaritons in nearby metallic nanoparticles, *Appl. Phys. Lett.* **89**, 093103, 2006.

[3] P. Matheu, S. H. Lim, D. Derkacs, C. McPheeters, and E. T. Yu, Metal and dielectric nanoparticle scattering for improved optical absorption in photovoltaic devices, *Appl. Phys. Lett.* **93**, 113108, 2008.
[4] R. A. Pala, J. White, E. Barnard, J. Liu, and M. L. Brongersma, Design of Plasmonic Thin-Film Solar Cells with Broadband Absorption Enhancements, *Advanced Materials* **21**, pp. 3504-3509, 2009.
[5] C. Min, J. Li, G. Veronis, J.-Y. Lee, S. Fan, and P. Peumans, Enhancement of optical absorption in thin-film organic solar cells through the excitation of plasmonic modes in metallic gratings, *Appl. Phys. Lett.* **96**, 133302, 2010.
[6] V. E. Ferry, L. A. Sweatlock, D. Pacifici, and H. A. Atwater, Plasmonic Nanostructure Design for Efficient Light Coupling into Solar Cells, *Nano Letters* **8**, pp. 4391-4397, 2008.
[7] W. Wang, S. Wu, K. Reinhardt, Y. Lu, and S. Chen, Broadband Light Absorption Enhancement in Thin-Film Silicon Solar Cells, *Nano Letters* **10**, pp.2012-2018, 2010.
[8] W. Shockley and H. J. Queisser, Detailed balance limit of efficiency of p-n junction solar cells, *Journal of Applied Physics* **32**, pp. 510-519, 1961.
[9] A. Shah, J. Meier, E. Vallat-Sauvain, C. Droz, U. Kroll, N. Wyrsch, J. Guillet, and U. Graf, Microcrystalline silicon and 'micromorph' tandem solar cells, *Thin Solid Films* **403**, pp. 179-187, 2002.
[10] J. Krc, K. Brecl, F. Smole, and M. Topic, The effects of enhanced light trapping in tandem micromorph silicon solar cells, *Solar Energy Materials and Solar Cells* **90**, pp. 3339-3344, 2006.
[11] T. Soederstroem, F. J. Haug, X. Niquille, V. Terrazzoni, and C. Ballif, Asymmetric intermediate reflector for tandem micromorph thin film silicon solar cells, *Appl. Phys. Lett.* **94**, 063501, 2009.
[12] J. Uepping, A. Bielawny, R. B. Wehrspohn, T. Beckers, R. Carius, U. Rau, S. Fahr, C. Rockstuhl, F. Lederer, M. Kroll, T. Pertsch, L. Steidl, and R. Zentel, Three-Dimensional Photonic Crystal Intermediate Reflectors for Enhanced Light-Trapping in Tandem Solar Cells, *Advanced Materials* **23**, pp. 3896-3900, 2011.
[13] K. Ding, T. Kirchartz, B. E. Pieters, C. Ulbrich, A. M. Ermes, S. Schicho, A. Lambertz, R. Carius, and U. Rau, Characterization and simulation of a-Si:H/mu c-Si:H tandem solar cells, *Solar Energy Materials and Solar Cells* **95**, pp. 3318-3327, 2011.
[14] E. D. Palik, *Handbook of Optical Constants of Solid* (Acdemic, 1985).
[15] D. Mergel and Z. Qiao, Dielectric modelling of optical spectra of thin In_2O_3 : Sn films, *Journal of Physics D-Applied Physics* **35**, pp.794-801, 2002.
[16] J. M. Jin, *The Finite Element Method in Electromagnetics* (Wiley, 2002).
[17] M. Born and E. Wolf, *Principles of Optics* (Cambridge University Press, 1999).
[18] S. A. Maier, *Plasmonics: Fundamentals and Applications* (Springer, 2007).

VO_2-based multilayers with enhanced luminous transmittance and switching properties

Yuan Zhao[1], Xuanru Zhang[2], Randy J. Knize[3], and Yalin Lu[1,2,3]*

[1] CAS Key Laboratory of Materials for Energy Conversion, Department of Material Science and Engineering, University of Science and Technology of China, Hefei, Anhui, 230026, P. R. China
[2] Advanced Applied Research Center, Hefei National Laboratory for Physical Science at the Microscale, University of Science and Technology of China, Hefei, Anhui, 230026, P. R. China
[3] Laser Optics Research Center, Physics Department, United States Air Force Academy, Colorado Springs, CO 80840, USA
*corresponding author, E-mail: yllu@ustc.edu.cn, yalin.lu@usafa.edu

Abstract

We studied optical properties of VO_2/Al:ZnO(AZO)/glass multilayer films near the semiconductor-metallic (S-M) transition of VO_2, when changing the temperature across the S-M transition. It was found that both VO_2/AZO/glass films with a periodic VO_2 stripe grating and ZnO/VO_2/AZO/glass multilayer structures showed much enhanced luminous transmittance and the solar modulation ability. The optical transmission properties of the films could be tuned by changing either VO_2 or AZO layer thicknesses. The obtained results may lead to a potential application in thermochromic smart building windows for energy saving.

1. Introduction

Energy-saving windows can significantly reduce the energy consumption of buildings and vehicles. To achieve the optimized energy-saving performance, it is critical to modulate the solar irradiation of such windows via common routes of material selection and/or structural design [1, 2]. In the solar spectrum, ultraviolet (UV), visible and near-infrared (NIR) light account for 8%, 43% and 48%, respectively, in terms of the energy distribution [3]. Among them, UV irradiation is harmful to both human skin and in-house furniture, and thus should be blocked entirely by the windows; while visible light is essential for having a clear vision inside; and NIR carries solar heat and should be treated according to different seasons and out-door weather conditionss [4]. Simply to say, windows with high NIR transmittance are needed in cold days; however, windows should be highly reflective to NIR for maintaining a comfortable indoor temperature in hot days. Automatic switching between the two statuses requires a new window smart enough and responsive fast enough to the out-door temperature changing, without using any external forces such as the electrical voltage in common electrochromatic windows.

As an important component for making energy-saving smart windows, chromogenic materials sensing and responding to external stimuli have attracted intensive research interest in recent years [2, 5-8]. Among the materials studied, thermochromic vanadium dioxide (VO_2) undergoes a reversible first-order semiconductor-to-metallic (S-M) phase transition at a critical temperature (T_c) under a few types of external excitations, such as thermal excitation [9], electrical excitation [10], and optical excitation [11]. In the temperature range below T_c, VO_2 is in the semiconducting state with a monoclinic structure. As temperature increases to above T_c, it is in metallic state with a rutile lattice. With this structural transition, a dramatic change in the optical properties occurs when the transmission for NIR switches between a transparent state and an opaque state [12, 13]. Besides, during the phase transition the UV light is always almost fully absorbed; the transmission of visible light remains almost unaffected [14]. Bulk-like VO_2 has a transition temperature of Tc ≈ 68°C [9, 15], which is too high for building-related applications, even for the summer time around majority areas of the world. Fortunately, it has been reported that Tc can be adjusted to near room temperature by doping [16-18], or by reducing its dimension to thin films or nanoparticles [19]. For example, it was stated that the tungsten doping in VO_2 could lower the T_c to ~40°C [20]. Compared to other types of energy-saving windows, such as electrochromic [5, 8, 21], photochromic [22] or gasochromic [23] energy-saving windows, VO_2 based thermochromic energy-saving smart windows are more attractive due to the relatively simple structure, cost-effective materials to be used, fast response to environmental temperature changes [24], and 'true smartness' to the environment.

A few research groups have reported the use of noble metals [25] or oxides [4, 13, 26, 27] combined with VO_2 in order to improve the optical performance that is otherwise insufficient if using VO_2 films only. For example, when combining VO_2 with transparent conducting oxides (TCO) as multilayers, both visible transmission and low-emissivity were improved due to TCO's high reflectivity for both middle and far infrared radiation. Pt/VO_2 structure, combining VO_2 with continuous Platinum film on the top, was also proposed, and high reflectivity in infrared and low-emissivity were achieved. However, all such improvements come along with a decrease in luminous transmission and

NIR modulation ability. A room to maximize the performance via optimizing both structural design and material selection will definitely exist. Unfortunately, not much work, especially a thorough investigation via modeling and simulation, has been done in the past.

In this research, we attempted to optimize the structure for achieving a much improved luminous transmission and a much enhanced NIR modulation via modeling and simulation. Preliminarily, we have focused on the VO_2 and ZnO materials systems, due to that one of the doped ZnO, aluminum doped zinc oxide (Al:ZnO or AZO), is a widely used electrode material in solar cell industries. Fabrication of large area Al:ZnO thin films is relatively easy and cost-effective. We have systematically explored the optical properties of multilayer structures composing of VO_2 and AZO on glass substrates, over a wide temperature range across the VO_2 phase transition temperature and over a range of structural parameters. We further introduced a stripe grating of VO_2 and an antireflection layer ZnO in order to further improve the luminous transmittance and NIR modulation ability. Our simulations suggested that VO_2-based multilayer films combining with specific structural design could provide a promising route to the enhanced properties of VO_2 as next generation energy-saving smart windows.

2. Computational methods

2.1 Structure

Figure 1 shows the schematic of the structures studied in this work. Basically the structure composes of VO_2, AZO, ZnO and glass. Two forms of VO_2 were used: continuous film and periodic gratings (slit width 50 nm and period 200 nm). For VO_2/AZO/glass films, we mapped the VO_2 thickness from 0.02μm to 0.2μm continuously, and changed the AZO thickness from 0 (no AZO layer) to 200nm at an interval of 50 nm. A wavelength range from 0.35 to 2μm, covering the major solar spectrum from UV to NIR, was swept through in the investigation. Dielectric constants (complex refractive indices *n* and *k*) of VO_2 used in our simulations were taken from the interpolation of the experimental spectroscopic data reported by others [28, 29]. Dielectric constants of ZnO and AZO were taken from the data in the Reference [30]. In the wavelength range studied here, the K9 glass's dispersion is small compared to those of AZO and VO_2, and was thus neglected. A constant refractive index of 1.51 was used for K9 glass. The simulations were carried out using a commercially available 2-dimensional (2D) finite element method (FEM) software (Comsol 3.4a) [31]. For modeling the multilayer structures with two infinite horizontal dimensions, the computational domain was considered as a single unit cell surrounded by either periodic boundary conditions or by perfectly matching layer (PML)[32]. The light was incident to the film surface and the transmittance was calculated from the electromagnetic field distributions obtained.

2.2. Luminous, solar and NIR solar transmittances

Performance of the thermochromic energy-saving smart windows can be indicated by luminous (T_{lum}, 380~780 nm), solar (T_{sol}, 350~2000 nm), NIR solar ($T_{NIR,sol}$, 780~2000 nm) transmittance, solar modulation ΔT_{sol}, NIR solar modulation $\Delta T_{NIR,sol}$, as defined in the following,

$$T_{lum} = \int \phi_{lum}(\lambda) T(\lambda) d\lambda / \int \phi_{lum}(\lambda)\, d\lambda \quad (1)$$

$$T_{sol} = \int \phi_{sol}(\lambda) T(\lambda) d\lambda / \int \phi_{sol}(\lambda)\, d\lambda \quad (2)$$

$$T_{NIR,sol} = \int \phi_{NIR,sol}(\lambda) T(\lambda) d\lambda / \int \phi_{NIR,sol}(\lambda)\, d\lambda \quad (3)$$

$$\Delta T_{sol} = T_{sol,s} - T_{sol,m} \quad (4)$$

$$\Delta T_{NIR,sol} = T_{NIR,sol,s} - T_{NIR,sol,m} \quad (5)$$

Here $T(\lambda)$ denotes the spectral transmittance at the wavelength λ; ϕ_{lum} is the standard luminous efficiency function for the photonic vision; ϕ_{sol} and $\phi_{NIR,sol}$ are spectral solar irradiance and NIR solar irradiance for an air mass of 1.5 [33], where *s* and *m* stand for semiconducting and metallic phase of VO_2, respectively.

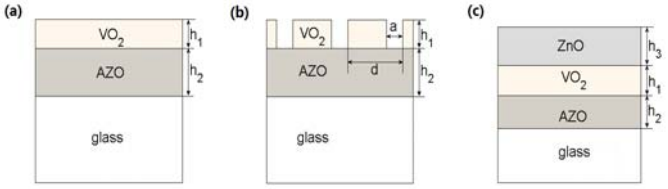


Figure 1 Schematic view of the structures: (a) VO_2/AZO/glass films with VO_2 layer thickness 'h_1' and AZO layer thickness 'h_2'; (b) VO_2/AZO/glass films with stripe gratings in VO_2 having VO_2 layer thickness 'h_1', AZO layer thickness 'h_2', slit width 'a', period 'd'; (c) ZnO/VO_2/AZO/glass films with VO_2 layer thickness 'h_1', AZO layer thickness 'h_2' and ZnO layer thickness 'h_3'.

3. Results and Discussion

3.1 Effect of adding AZO layer

We first investigated the structure of VO_2/AZO/glass films [Fig. 1(a)]. Figure 2 shows the normal incident transmittance and absorbance spectra of the structures with different AZO thicknesses and 40 nm continuous VO_2 film in the semiconducting or metallic phase. We can see from Figure 2(a) that the optical transmittance in NIR region for the metallic VO_2 reduces as the AZO thickness increases. This can be attributed to the stronger absorption of thick AZO and enhanced multiple interface reflections in longer wavelengths. However, the visible transmittance remains about the same independent on the AZO thickness due to weaker absorption in the visible light. On the contrast, for the structure with VO_2 in the semiconducting state, the transmittance was first enhanced with introducing a thin AZO layer and then reduced when the AZO thickness is bigger than 100 nm. This may be explained by the possibility that the planar cavity resonance response plays a leading role in the thin AZO films, while gradually stronger absorption (Figure 2(b)) and multiple interface reflections play an increasingly important role for thick AZO films. This cavity effect can be seen much clearly in the s AZO 200 nm spectrum. On the other hand, owing to the huge photoionization absorption in VO_2 for high energy UV photons, the transmission in UV is always weak for both

semiconducting and metallic phases of VO_2. The integral luminous, solar and NIR solar transmittance and their modulation during SMT are summarized in Table 1.

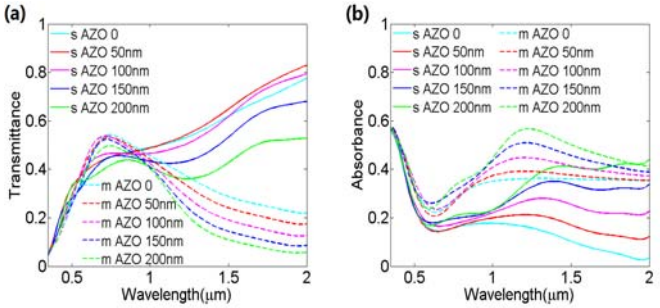


Fig. 2 Transmittance (a) and absorbance (b) spectra for VO_2/AZO/glass films having different AZO layer thicknesses, with 's' standing for semiconducting VO_2 (25°C) and 'm' for metallic VO_2 (90°C). The VO_2 layer thickness 'h_1' is fixed at 40 nm.

Table 1 Optical and SMT Properties for VO_2/AZO/glass Films with Different AZO Layer Thicknesses.

Structure	d_{AZO} (nm)	T_{lum} (%) S	T_{lum} (%) M	T_{sol} (%) S	T_{sol} (%) M	ΔT_{sol} (%)	$T_{NIR,sol}$ (%) S	$T_{NIR,sol}$ (%) M	$\Delta T_{NIR,sol}$ (%)
VO_2/AZO	0	33.24	35.98	40.69	37.86	2.83	52.66	41.96	10.70
	50	37.25	38.77	42.75	37.92	4.83	53.50	39.40	14.10
	100	37.23	38.99	41.73	36.59	5.14	51.57	36.70	14.87
	150	33.39	35.88	38.62	34.49	4.13	47.05	34.20	12.85
	200	34.52	36.50	36.31	33.44	2.87	41.70	32.09	9.61

As shown in Figure 2 and Table 1, the VO_2/AZO double-layered films maintained VO_2's thermochromic property across the phase transition, with improved luminous transmittance and NIR solar modulation ability as the AZO thickness was increased. From the results shown in Figure 2(a) we can see that the 75 nm thickness is not too thin but still maintains acceptable bi-status transmittance contrasts over a fairly large NIR wavelength range. Thus, the AZO thickness of 75 nm was selected in our subsequent simulations for studying the influence of other parameters. The AZO thin film with such a thickness can also be fabricated with high quality relatively conveniently [4, 30].

3.2 Structure-tunable properties

With a fixed thickness of 75 nm for AZO, the transmittance of VO_2/AZO/K9 multilayer structure was mapped over a wavelength range of from 0.35 to 2μm and over a VO_2 thickness range of from 0.02μm to 0.2μm in both the semiconducting [Fig. 3(a)] and metallic phases [Fig. 3(b)]. Obviously, the transmittance is high when the VO_2 layer is thin, but it reduces monotonously as the VO_2 layer thickness, because of the gradually enhanced absorption and multiple interface reflections of VO_2. Figure 4 shows integrated data on luminous, solar and NIR solar transmittance derived from the spectra in Figure 3. It can be seen that the variations of T_{lum}, T_{sol} and $T_{NIR,sol}$ are consistent with the spectral variations in Figure 3, on condition that requiring a noticeable luminous transmittance T_{lum} to 40%, the modulation of $T_{NIR,sol}$ doesn't exceed 15%. Figure 3 and Figure 4 give the necessary instructions to further windows design for selecting proper VO_2 thickness.

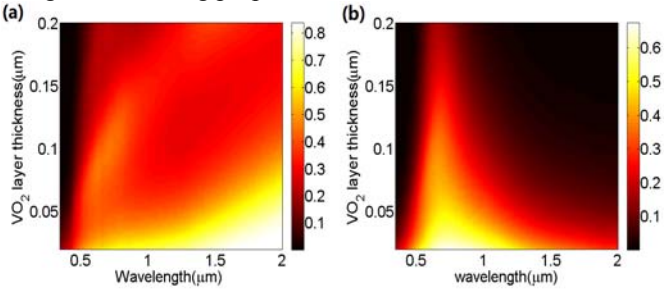


Fig. 3 Mapping transmittance for VO_2/AZO/glass films with varying VO_2 layer thickness in semiconducting (a) and metallic phase (b). The AZO layer thickness 'h_2' is fixed at 75 nm.

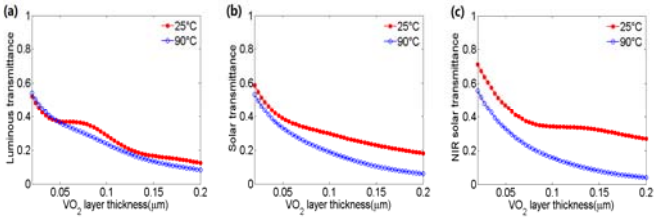


Fig. 4 Integral luminous (a), solar (b) and NIR solar (c) transmittance for VO_2/AZO/glass films with various VO_2 layer thickness in semiconducting and metallic phase. The AZO layer thickness 'h_2' is fixed at 75 nm. Lines with solid red and open blue symbols are computed at 25°C and 90°C, respectively.

3.3 Temperature-agile tunable Properties

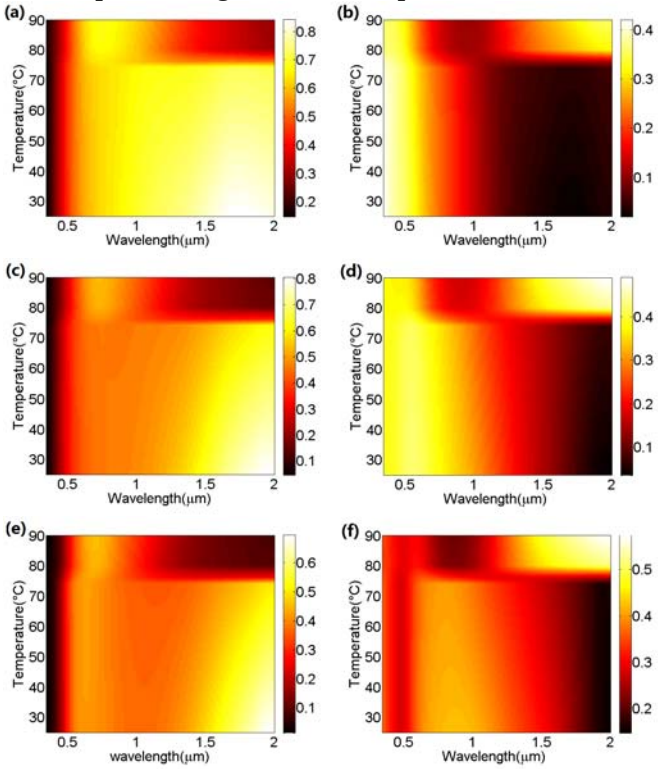


Fig. 5 Mapping transmittance (a, c, e) and reflectance (b, d, f) spectra for VO_2/AZO/glass films with varying temperature and VO_2 layer thicknesses ((a, b) for 20 nm,

(c, d) for 40 nm, (e, f) for 60 nm). The AZO layer thickness 'h_2' is fixed at 75 nm.

Figure 5 shows the optical transmittance and reflectance spectra with varying temperature and VO_2 layer thickness, when the AZO layer was fixed at 75nm. Here we neglected a possible reduction of the VO_2's S-M phase transition temperature caused by overlapping the VO_2 with AZO [4] [14] [25], and fixed the phase transition temperature at ~68°C in all the following simulations. A noticeable phenomenon is the abrupt change (from high to low) in optical transmittance when the VO_2 layer changes its state from semiconductor to metal. This change occurs mainly in the visible to NIR wavelength range, which shifts to longer wavelengths when the VO_2 thickness increases from 20 to 60 nm. This change can be explained by overlapping the intense absorption and multiple interface reflections. As VO_2 layer thickness increases, the shut off effect for NIR incidence becomes better, which makes us to tune the windows property by changing the VO_2 film thickness.

4. Structural optimation

To improve the luminous transmittance and to strengthen NIR solar modulation, two special designs, either a VO_2 gratings instead of continuous VO_2 film or an antireflection layer ZnO on the top, were introduced. The VO_2/AZO/glass films with one-dimensional stripe VO_2 grating and ZnO/VO_2/AZO/glass multilayer films structure has been displayed in Fig. 1(b) and Fig. 1(c), respectively.

Figure 6 shows the normal incident transmittance spectra for VO_2/AZO/glass films with a stripe grating in VO_2 and ZnO/VO_2/AZO/glass films in its semiconducting and metallic phases. Clearly, the transmission of both structures were enhanced for both phases of VO_2 over the spectrum of from visible to NIR region, when compared to VO_2/AZO/glass films with continuous VO_2 films as discussed above. The reason of why the transmission are enhanced after adding stripe gratings in VO_2 can be explained by the Effective Medium Theory (EMT) [12, 34-36]. When un-polarized electromagnetic waves are incident on the sub-wavelength grating, the VO_2 gratings act as a mean medium and the waves transmit through the gratings, owing to the grating size is far less than the incident wavelength. While for multilayer structure, it complies with the interference principle. The integral luminous, solar and NIR solar transmittance and their modulation during S-M phase transition are summarized in Table 2.

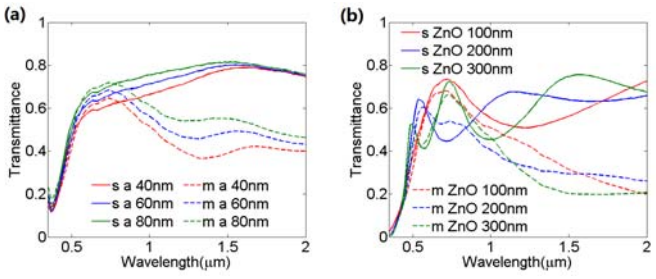


Fig. 6 (a). Transmittance spectra for VO_2/AZO/glass films with stripe gratings in VO_2 having different slit width 'a' with period of 0.2 μm. (b) Transmittance spectra for ZnO/VO_2/AZO/glass films having different ZnO layer thicknesses. In both structures, VO_2 layer is fixed at 40 nm, AZO layer is fixed at 75 nm, 's' in the legend stands for semiconducting VO_2 and 'm' for metallic phase.

Table 2 Optical and SMT properties for VO_2/AZO/glass Films with Stripe Gratings in VO_2 for Different Slit Width and ZnO/VO_2/AZO/glass Films for Different ZnO Layer Thicknesses

Structure	a/d_{ZnO} (nm)		T_{lum} (%)		T_{sol} (%)		ΔT_{sol}	$T_{NIR,sol}$ (%)		$\Delta T_{NIR,sol}$
			S	M	S	M	(%)	S	M	(%)
VO_2(G) /AZO	a	40	52.97	52.72	56.99	48.82	8.17	68.87	49.18	19.69
		60	56.79	56.37	60.68	53.22	7.46	72.77	54.81	17.96
		80	60.44	60.04	64.15	57.58	6.57	76.09	60.11	15.98
ZnO/VO_2 /AZO	d_{ZnO}	100	53.24	50.22	53.28	46.30	6.98	58.67	47.19	11.48
		200	58.13	55.28	51.61	41.58	10.03	59.84	38.84	21.00
		300	45.56	45.10	50.30	41.93	8.37	57.62	40.76	16.86

As shown in Figure 6 and Table 2, the grating design in VO_2 layer and ZnO/VO_2/AZO multilayer structure maintain the thermochromic property of VO_2, with improved luminous transmittance (>50%) and NIR solar modulation ability. Especially, in ZnO/VO_2/AZO multilayer structure, when the thickness of ZnO layer is 200 nm, the integrated values of T_{lum} are 58.13% and 55.28% at 25°C and 90°C, respectively. The corresponding changes across the phase transition, ΔT_{sol} and $\Delta T_{NIR,sol}$, are 10.03% and 21.00%, respectively. These values are comparable to those of five-layered TiO_2/VO_2/TiO_2/VO_2/TiO_2 films, where T_{lum} are 45.00% and 42.00% at 20°C and 90°C, respectively, and the corresponding modulation data of ΔT_{sol} 12.00%. The above structure design may give some instructions to further windows design for achieving better optical properties.

5. Conclusions

In summary, VO_2/AZO/glass multilayer films near the semiconductor-metal (S-M) transition of VO_2 was proposed and fully investigated by simulations. VO_2/AZO/glass films with stripe VO_2 gratings design and ZnO/VO_2/AZO/glass multilayer structure showed a much enhanced luminous transmittance and NIR solar modulation ability. In addition, the transmission properties of the films could be tuned by changing VO_2 and AZO layer thicknesses. Such properties can be explained by photoionization of UV photons, EMT, multiple interface reflections, absorption and planar cavity effect. The results may lead to the possible application of VO_2 in VO_2-based thermochromic windows.

Acknowledgements

This work was supported by the National Basic Research Program of China (2012CB922001) and the US Air Force Office of Scientific Research (AFOSR).

References

[1] C.G. Granqvist, *Applied Physics A Solids and Surfaces* 52, pp. 83, 1991

[2] S.S. Kanu ,R. Binions, *Proceedings of the Royal Society a Mathematical Physical and Engineering Sciences* 466, pp. 19, 2010

[3] C.G. Granqvist, *Solar Energy Materials and Solar Cells* 91, pp. 1529, 2007
[4] L. Kang, Y. Gao, H. Luo, J. Wang, B. Zhu, Z. Zhang, J. Du, M. Kanehira ,Y. Zhang, *Solar Energy Materials and Solar Cells* 95, pp. 3189, 2011
[5] A. Pawlicka, *Recent Patents on Nanotechnology* 3, pp. 177, 2009
[6] X. Gong, J. Li, S. Chen ,W. Wen, *Applied Physics Letters* 95, 251907, 2009
[7] D. Cupelli, F.P. Nicoletta, S. Manfredi, G. De Filpo ,G. Chidichimo, *Solar Energy Materials and Solar Cells* 93, pp. 329, 2009
[8] A. Anders, J.L. Slack ,T.J. Richardson, *Thin Solid Films* 517, pp. 1021, 2008
[9] F. Morin, *Physical Review Letters* 3, pp. 34, 1959
[10] G. Stefanovich, A. Pergament ,D. Stefanovich, *Journal of Physics-Condensed Matter* 12, pp. 8837, 2000
[11] A. Cavalleri, C. Toth, C.W. Siders, J.A. Squier, F. Raksi, P. Forget ,J.C. Kieffer, *Physical Review Letters* 87, 018149, 2001
[12] S.Y. Li, G.A. Niklasson ,C.G. Granqvist, *Journal of Applied Physics* 108, 063525, 2010
[13] N.R. Mlyuka, G.A. Niklasson ,C.G. Granqvist, *Solar Energy Materials and Solar Cells* 93, pp. 1685, 2009
[14] Z. Zhang, Y. Gao, H. Luo, L. Kang, Z. Chen, J. Du, M. Kanehira, Y. Zhang ,Z.L. Wang, *Energy & Environmental Science* 4, pp. 4290, 2011
[15] E.E. Chain, *Applied Optics* 30, pp. 2782, 1991
[16] N.R. Mlyuka, G.A. Niklasson ,C.G. Granqvist, *Applied Physics Letters* 95, 171909, 2009
[17] C. Sihai, M. Hong, D. Jun ,Y. Xinjian, *Applied Physics Letters* 90, 101117, 2007
[18] M. Tazawa, P. Jin ,S. Tanemura, *Applied Optics* 37, pp. 1858, 1998
[19] L. Dai, C. Cao, Y. Gao ,H. Luo, *Solar Energy Materials and Solar Cells* 95, pp. 712, 2011
[20] J.M. Wu ,L.B. Liou, *Journal of Materials Chemistry* 21, pp. 5499, 2011
[21] B.P. Jelle ,G. Hagen, *Journal of the Electrochemical Society* 140, pp. 3560, 1993
[22] C.O. Avellaneda, L.O.S. Bulhoes, *Solid State Ionics* 165, pp. 117, 2003
[23] V. Wittwer, M. Datz, I. Ell, A. Georg, W. Graf ,G. Walze, *Solar Energy Materials and Solar Cells* 84, pp. 305 2004
[24] P. Jin, G. Xu, M. Tazawa ,K. Yoshimura, *Applied Physics a-Materials Science & Processing* 77, pp. 455, 2003
[25] L. Kang, Y. Gao, Z. Chen, J. Du, Z. Zhang ,H. Luo, *Solar Energy Materials and Solar Cells* 94, pp. 2078, 2010
[26] Z. Chen, Y. Gao, L. Kang, J. Du, Z. Zhang, H. Luo, H. Miao ,G. Tan, *Solar Energy Materials and Solar Cells* 95, pp. 2677, 2011
[27] N.R. Mlyuka, G.A. Niklasson ,C.G. Granqvist, *Physica Status Solidi a-Applications and Materials Science* 206, pp. 2155, 2009
[28] J.B.K. Kana, J.M. Ndjaka, G. Vignaud, A. Gibaud ,M. Maaza, *Optics Communications* 284, pp. 807, 2011
[29] A. Gavini, C. Kwan, *Physical Review* B 5, pp. 3138, 1972
[30] Y. Okuhara, T. Kato, H. Matsubara, N. Isu ,M. Takata, *Thin Solid Films* 519, pp. 2280, 2011
[31] COMSOL 3.4a Reference Manual 3.4, 2006
[32] A. Lavrinenko, P.I. Borel, L.H. Frandsen, M. Thorhauge, A. Harpoth, M. Kristensen, T. Niemi ,H.M.H. Chong, *Optics Express* 12, pp. 234, 2004
[33] Annual Book of ASTM Standards, *American Society for Testing and Materials* 12, pp. 176, 1987
[34] G.-G. Kang, Q.-F. Tan, W.-L. Chen, Q.-Q. Li, W.-Q. Jin ,G.-F. Jin, *Acta Physica Sinica* 60, 014218, 2011
[35] I. Yamada, J. Nishii ,M. Saito, *Applied Optics* 47, pp. 4735, 2008
[36] I. Richter, P.C. Sun, F. Xu ,Y. Fainman, *Applied Optics* 34, pp. 2421, 1995

Broadband Spectroscopy of Nanoporous-Gold Promoter

S. Kuwano-Nakatani[1], Y. H. Han[1] , T. Takahashi[2] and T. Awano[1*]

[1] Tohoku Gakuin University, Japan
[2]Research Reactor Institute, Kyoto University, Japan
[*]corresponding author: awano@tjcc.tohoku-gakuin.ac.jp

Abstract

The efficiency of UV photocatalysis on TiO_2 particles was increased by mixing TiO_2 particles with nanoporous gold (NPG) with pore diameters of 10–40 nm. This means that NPG acts as a promoter in the photocatalytic reaction of TiO_2. Broadband spectroscopic results from millimeter wave to ultra violet of NPG membrane are discussed to estimate plasmonic effect on the catalysis.

1. Introduction

It is well known that bulk Au is inert. However, Au nanoparticles with several-nanometer-scale sizes are catalytically active for several chemical reactions such as the decomposition of formaldehyde and oxidation of CO[1,2]. The catalytic activity depends on the size of nanoparticles. The nanoparticles with diameters in the range of 2 to 5 nm show the highest activity for oxidation[3]. Nanoporous Au (NPG) with 10–50 nm pore size also shows catalytic activity for oxidation[2].

Recently, TiO_2 is being widely used for photocatalysis of various materials. TiO_2 has a different activity with crystal structure for different wavelengths. It has been reported that composite materials of TiO_2 with Au or Pt nanoparticles enhance TiO_2 catalytic activity[4]. TiO_2 plays an active role in the decomposition of water to generate OH radicals. It is supposed that the plasmonic electromagnetic effect of Au or Pt enhances the catalytic activity of TiO_2. In addition, since pores of NPG are able to trap the TiO_2 particles on its surface, NPG seems to be a photocatalytic nanocomposite because of enhancement of the catalytic activity by the electromagnetic effect. We have found that NPG acts as a promoter to produce OH radicals using TiO_2 [5]. We report optical properties of NPG in this paper to investigate electromagnetic and plasmonic origin of the promotor effect.

2. Experimental

NPG films were obtained by nitric acid etching of Ag from $Au_{35}Ag_{65}$ alloy films with about 100 nm thickness. The average pore diameter was 10–40 nm, according to the dealloying temperature and time. Figure 1 shows SEM images of NPG films with average pore diameters of 20 nm (a) and 42 nm (b). The other samples were confirmed to have average pore diameters of 11 and 33 nm.

Reflectivity spectra of the NPG films on quartz plate were measured over four regions: (1) millimeter wave region was measured using a coherent transition radiation induced by the LINAC facility of Research Reactor Institute, Kyoto University; (2) far-infrared region was measured using synchrotron radiation by UVSOR facility of Institute for Molecular Science. This region was also measured using a Martin-Puplett interferometer JASCO FARIS-1 with a

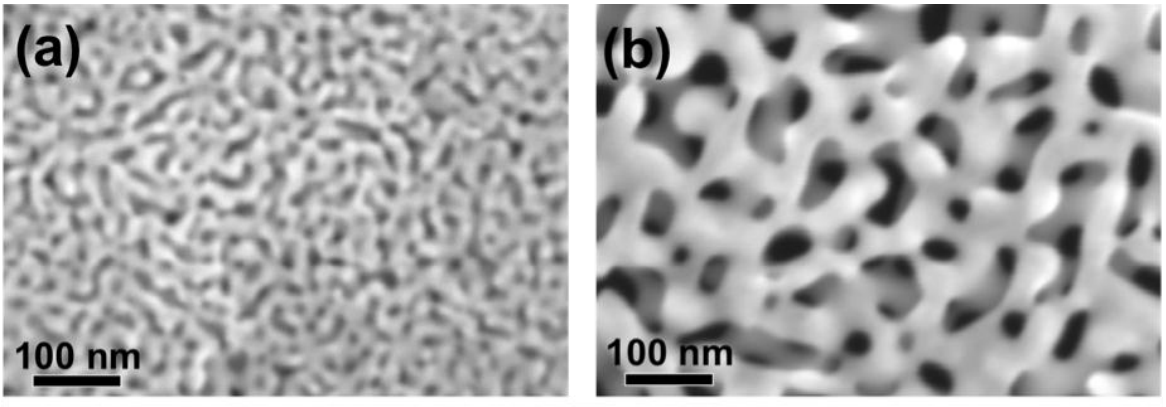


Figure 1: SEM images of NPG films. Pore diameter is (a) 20 nm and (b) 42 nm.

conventional mercury light source; (3) infrared region was measured using JASCO FT-4100 spectrometer; (4) near infrared, visible and ultraviolet region.

3. Results and discussion

3.1. Promoter effect

Anatase (25 nm average diameter) and rutile (85 nm average diameter) TiO_2 particles were in the ratio 4:1. The mixture of NPG, TiO_2, and spin trapping agent was irradiated by Black-light with wave length 365 nm. The spectra for the estimation of the amount of induced OH radicals were measured by X-band ESR. No OH radical was formed by the $Au_{35}Ag_{65}$ alloy film or NPG film alone during the Black-light irradiation. Besides, the coexistence of TiO_2 particles and NPG films enhanced the production of the OH radical. ESR signals of the OH-radical spin adduct were observed, and it was confirmed that NPG is a promoter for photocatalysis on TiO_2. Fig. 2 shows the efficiency of OH radical productivity vs. average pore sizes. The maximum efficiencies normalized by that of an $Au_{35}Ag_{65}$ alloy film was 1.5 at average pore diameter of 20 nm. No enhancement was observed at pore diameters over 40 nm. This peak seems to be due to that the average particle diameter of the anatase TiO_2 particles, which are sensitive to the irradiated Black-light, was 25 nm. Therefore, the active anatase TiO_2 particles appear to dispersively infiltrate into the pores of Au and tightly stick to the pore surface. This seems to enhance the promoter effect of Au on TiO_2.

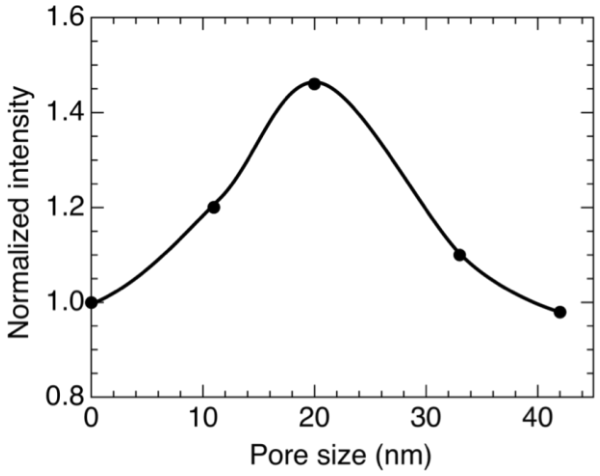


Figure 2: OH-radical production efficiency as a function of average pore diameter.

3.2. Spectroscopic results

3.2.1. Reflectivity spectra

Fig. 3 shows broadband reflectivity spectra of NPG with various average pore sizes. The horizontal axis is in a logarithm to show the wide spectral range. Fine structures in IR spectra are due to CO_2 and H_2O in atmosphere. Measurement of the lack region at terahertz wave is under way at the UVSOR facility. Peaks at 0.06eV are due to reflection of the substrate quartz. It is especially strong at

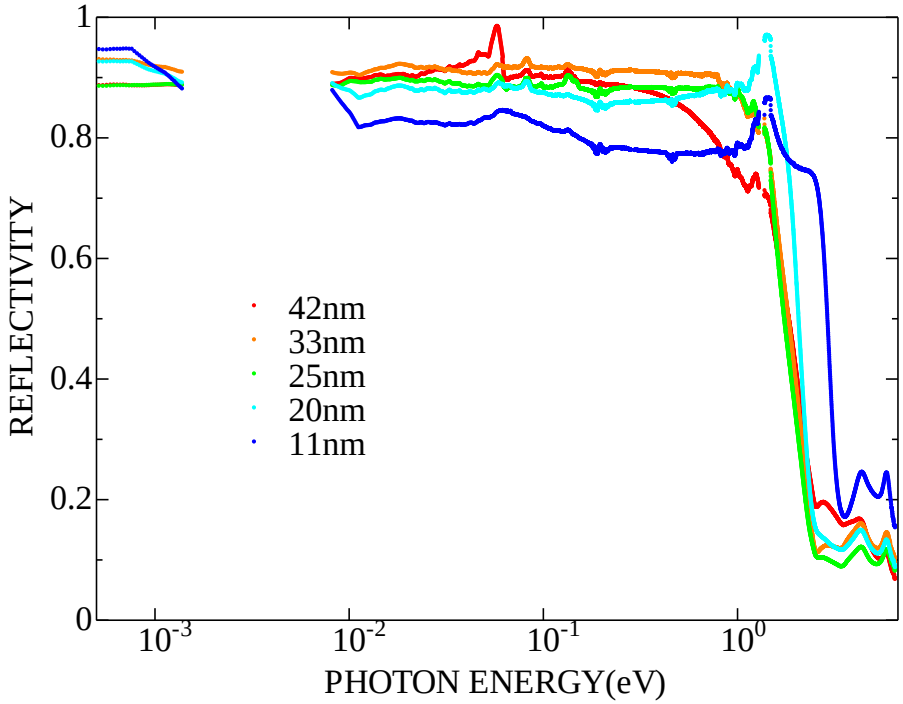


Figure 3: Reflectivity spectra of NPG membranes on quartz substrates. Average pore diameters of the five samples with diameter on the order of 42 nm to 11 nm are shown in the NIR-UV figure.

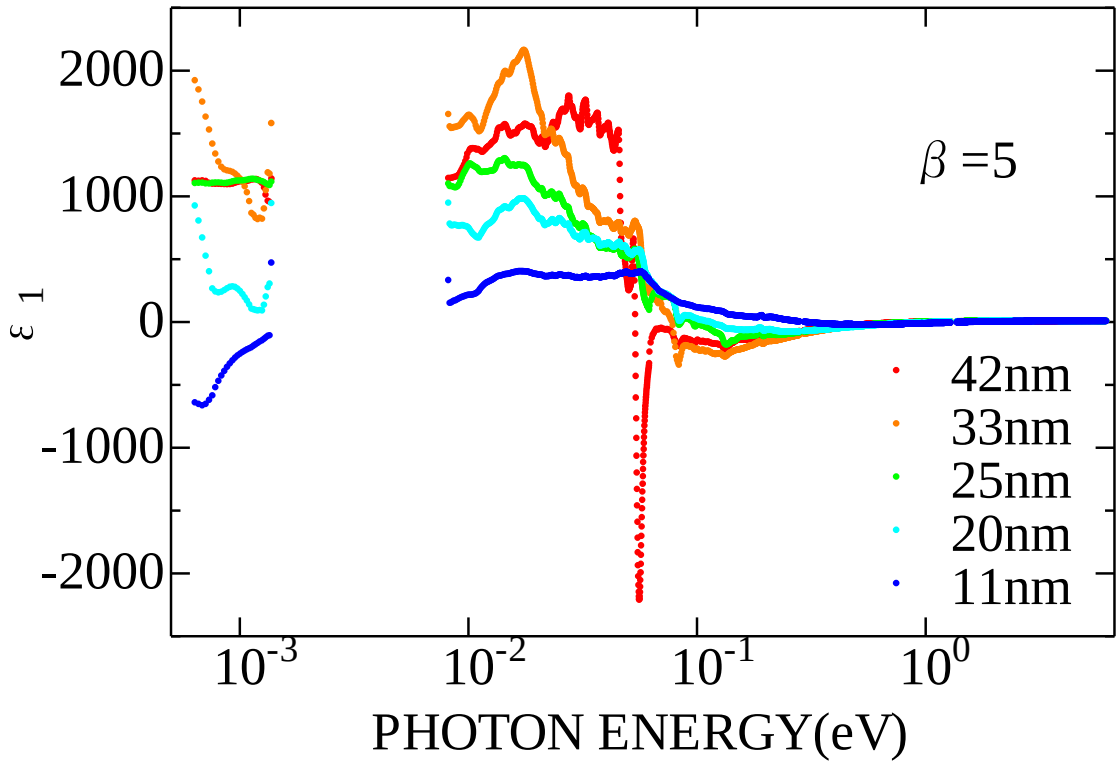


Figure 4: Dielectric constant spectra (real part) of NPG membranes on quartz substrates. The extrapolation exponent index of the reflectivity at high energy $\beta = 5$.

42nm pore sample because of void content (low average density) of the large porous thin film. Small structures at infrared region are due to absorption by CO_2 and H_2O in atmosphere. Peaks at 1.45eV are due to reflectivity dip of the reference Al mirror. Plasmonic characteristic spectral changes were observed from IR to UV region. They depend on the pore size.

3.2.2. Dielectric constants

Dielectric constants are obtained by Kramer-Kronig analysis. The measured reflectivity spectra were wide enough to obtain dielectric constants by calculation from it. The reflectivity spectra were extrapolated as constant to connect smoothly at low energy side and terahertz region. They were extrapolated as exponential decrease function to connect smoothly. The optimum exponent coefficients were scattered largely. Fig. 4 and 5 show dielectric constants at the exponent $\beta = 5$ to see the pore size dependence of optical properties. Fig. 4 shows real parts of the dielectric constant. The large structures at 0.06eV are due to the reflection of the substrate quartz. Spectra at low energy region change as sequent by pore sizes except the case of 42nm. This seems to be due to low average density of gold by pore volume.

Fig. 5 shows imaginary parts of the dielectric constant. Lower figure shows a log-log plot to show the region from infrared to UV. The large structures at 0.06eV are due to the reflection of the substrate quartz. Spectra at low energy region change as sequent by pore sizes except the case of 42nm as in the ε_1 spectra. It is clearly observed in the lower figure that the spectra of large and intermediate pore sizes show linear decrease which means these spectra decrease as power function in the region from 0.1 to 1eV. The ε_2 spectra shows absorption intensity for transverse wave. To investigate plasmonic absorption for longitudinal wave, energy loss function spectra obtained from these dielectric constants spectra are discussed in the next section.

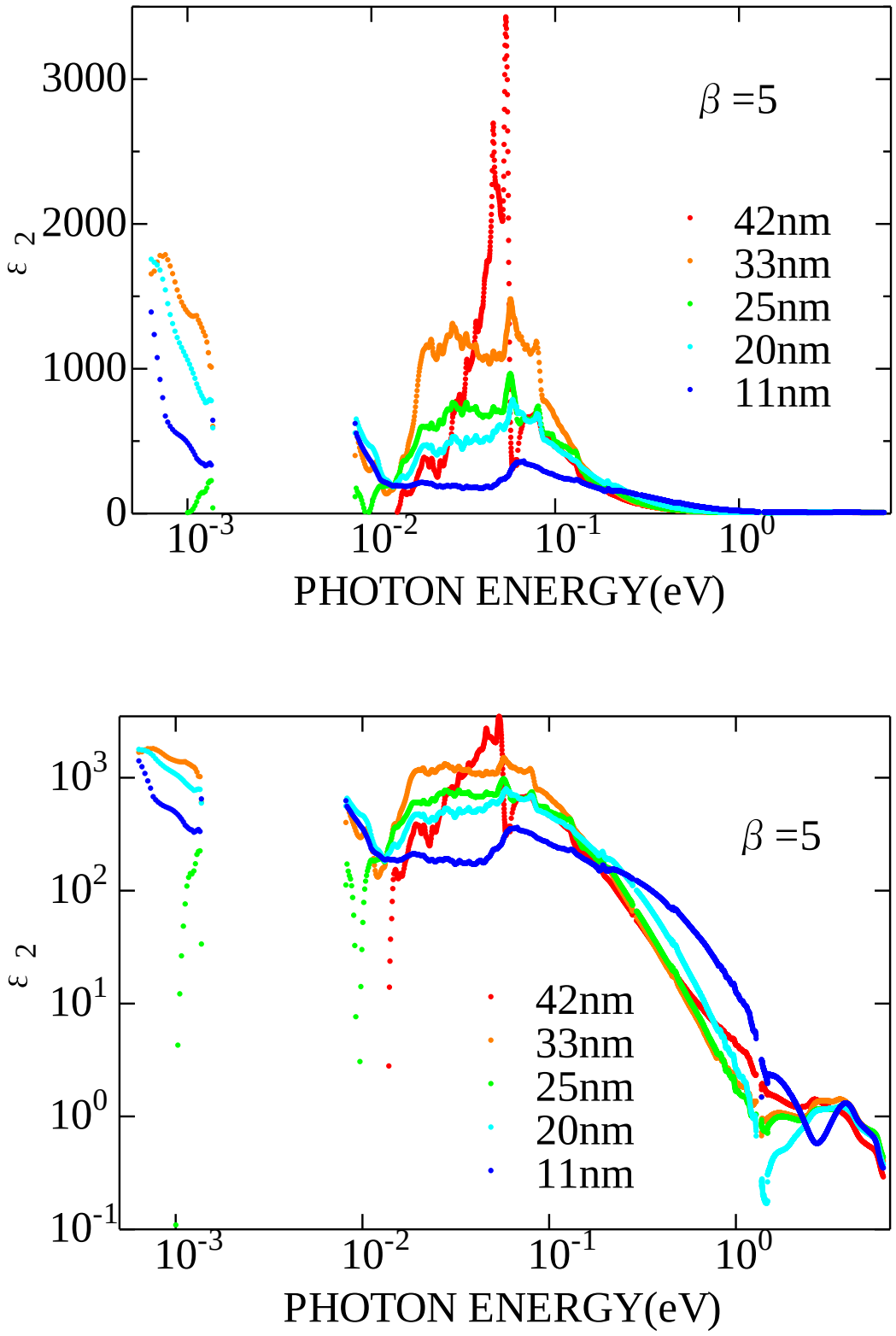


Figure 5: Dielectric constant spectra (imaginary part) of NPG membranes on quartz substrates. The above figure is semi-log plot and the below one is log-log plot. The extrapolation exponent index of the reflectivity at high energy $\beta = 5$.

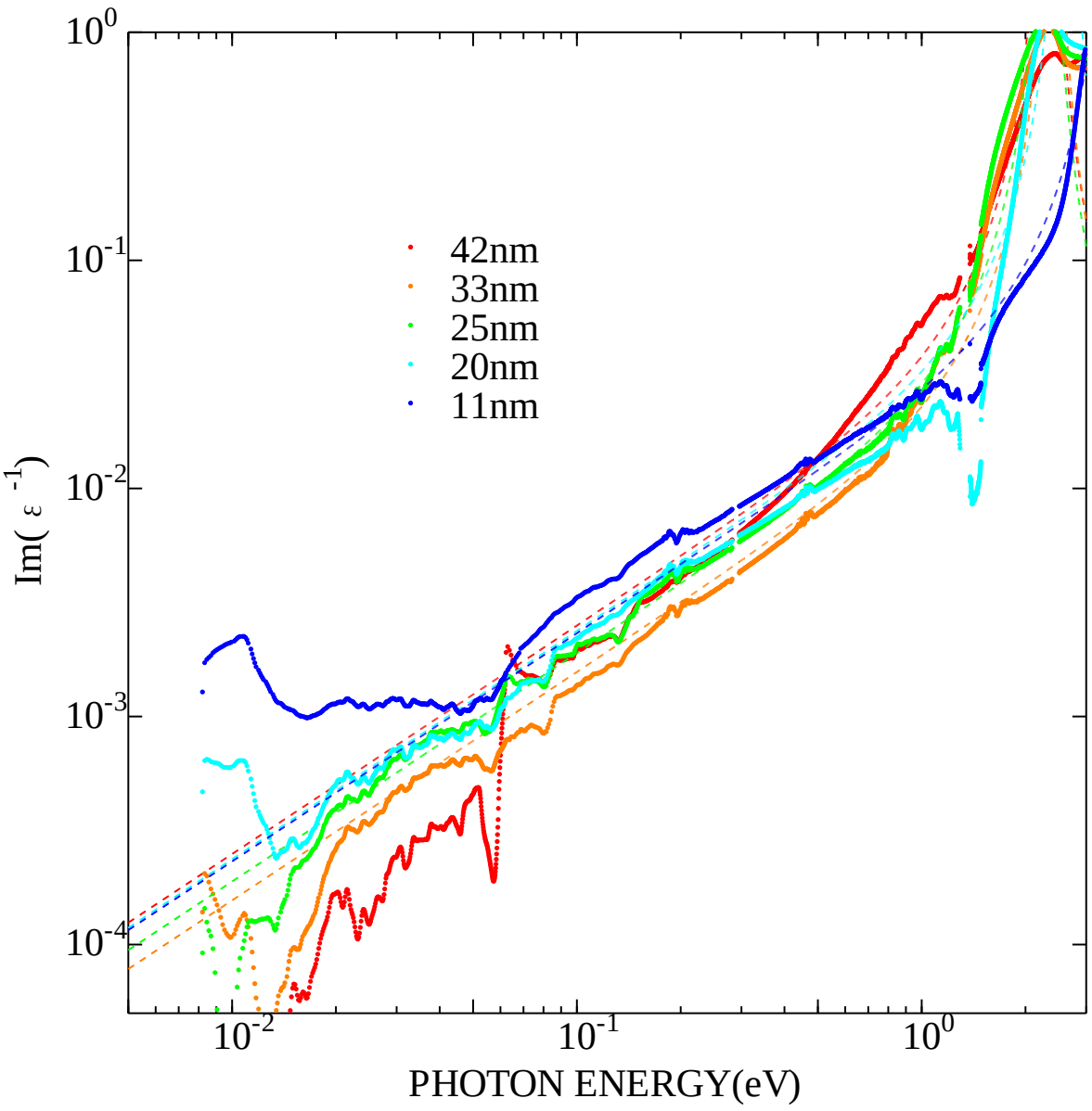


Figure 6: Drude curve fitting of the energy loss function spectra of NPG membranes on quartz substrates. Dashed lines show fitting curves for each pore size sample.

3.2.3. Plasmon fitting

Plasmon fitting by classical Drude model in energy loss function spectra is shown in fig. 6. In Drude model, dielectric constant is

$$\varepsilon = \varepsilon_\infty (1 - \frac{\omega_p^{\ 2}}{\omega^2 + \gamma^2} + i \frac{\gamma \omega_p^{\ 2}}{\omega(\omega^2 + \gamma^2)}),$$

where $\omega_p = \sqrt{\frac{4\pi N e^2}{m^* \varepsilon_\infty}}$ is the plasma frequency, γ is dumping factor and ε_∞ is dielectric constant at high frequency. Energy loss function, Im(1/ ε), is proportional to absorption intensity by transverse wave. The plasmon fitting parameters are summarized in Table 1. Systematic decrease of the plasma frequency with pore size increment was observed. Plasma frequency of bulk gold is 8.6eV, therefore, these ω_p for pore samples are much small. The promoter effect seems to be related with small values of these parameters. The origin of pore size dependence of the promoter effect is still not clear.

Table 1: Plasmon parameters.

pore size(nm)	ω_p(eV)	γ (eV)	ε_∞
42	2.3	0.06	2.2
33	2.4	0.01	9
25	2.3	0.025	4
20	2.6	0.02	8
11	3.6	0.03	10

4. Conclusions

Promoter effect was discovered on NPG/TiO_2 system. The detail enhance mechanism of the promoter effect is not clear yet. However, we could observe that smaller plasmon parameters on NPG than those on bulk gold.

Acknowledgements

Part of this work was done under the visiting researcher program of Research Reactor Institute, Kyoto University and UVSOR facility of Institute for Molecular Science.

References

[1] Bierner, J. et al., Surface-chemistry-driven actuation in nanoporous gold, *Nature Materials* 8: 47–51, 2009.

[2] Wittstock, A., V. Zielasek, J. Biener, C. M. Friend, M. Bäumer, Nanoporous Gold Catalysis for Selective Gas-Phase Oxidative Coupling of Methanol at Low Temperature, *Science* 327: 319-322, 2003.

[3] Haruta, M., When Gold Is Not Noble: Catalysis by Nanoparticles, *Chem. Rec*..3: 75-87, 2003.

[4] Haruta, M., Nanoparticulate Gold Catalysis for Low-Temperature CO Oxidation, *J. New Mat. Electrochem. Sys.* 7: 163-172, 2004.

[5] Kuwano-Nakatani S., T. Ando, K. Oba and Y.H. Han, to be published.

Design Consideration for Plasmonic Solar Cells Based on Ag Nanoparticles

Razan R. Nejm[1], Mousa Hussein[1], Ahmed Ayesh[2]

[1] Department of Electrical Engineering, United Arab Emirates University, Al Ain, , United Arab Emirates
[2] Department of Physics, United Arab Emirates University, Al Ain, , United Arab Emirates
*corresponding author, E-mail: r.radwan@uaeu.ac.ae

Abstract

A plasmonic solar cell based on silver (Ag) nanoparticles is modeled and studied theoretically in this paper as a preliminary study for future experimental work. Ag nanoparticles were deposited on a silicon (Si) substrate surface and are excited by normally incident light source propagating from air into silicon surface. Two main parameters were the interest of study, nanoparticles (NPs) size, period and number and dielectric environment. NPs parameters show enhancement in the forward scattering power, whereas dielectric environment can be controlled to enhance and tune the resonance region.

1. Introduction

Most renewable energy investments are spent on materials and researches, especially solar energy market which attracted researchers and manufacturers from different sectors. 40% of a solar module cost made from crystalline silicon is the cost of the silicon wafers. This fact draws the attention of the researchers over the past ten years toward thin-film solar cells which have thicknesses usually in the range 1-2 μm, and are deposited on cheap substrates such as glass, plastic or stainless steel. Although many researches are carried to find alternative type of solar cell materials, silicon solar cells are still the dominant type in the market and have the best share in the research. [1]

According to Solar Market Research and Analysis (Solarbuzz) report in 2010, the total global cell production increased 108%, with crystalline silicon up 117% and thin film up 62% [2]. Decreasing the cell thickness raised light absorption problem. This creates new challenge and active research area for thin film solar cells people by looking for solutions to enhance its absorption for light especially the near band-gap light.

Light trapping showed great results after depositing metallic nanoparticles on the surface of the solar cells. [1, 3-5] Silver (Ag) and Gold (Au) nanoparticles respectively, showed the best results although other metallic nanoparticles were used. S. Pillai et. al. [6] deposited Ag nanoparticles on semiconductor surface using thermal evaporation of thin layers of silver. They observed a significant enhancement of the absorption for both thin-film and wafer-based structures at wavelengths close to the band gap of Si. They reported a sevenfold enhancement for wafer-based cells at $\lambda = 1200$ nm and up to sixteen fold enhancement at $\lambda = 1050$ nm for 1.25 μm thin silicon-on-insulator (SOI) cells. D. M. Schaadt et. al. [7] deposited spherical Au nanoparticles on a silicon (Si) pn semiconductor junction surface. Their work showed enhancement in absorption within the semiconductor, which increased the photocurrent response in pn junction diodes over wavelength ranges that correspond closely to the nanoparticle plasmon resonance wavelengths. They found that at or near the plasmon resonance wavelengths, photocurrent response increased between 50%–80% relative to that of the Si pn junction diode itself.

This paper investigates light scattering from Ag nanoparticles numerically by varying the adjustable parameters experimentally (the next step) in order to determine some fundamental design principles. Nanoparticles size, period, density and adding insulator layer effect were studied using FDTD method.

2. Numerical Simulation

Numerical simulations using FDTD from optiwave company was used. Ag NPs on a c-Si substrate was modeled using Drude-Lorentz model. Using more than one NP in the study is due to the importance of interparticle coupling effect which is neglected in the most theoretical works. Two observation points were used to observe the backward and forward scattering power in the solar cell placed behind the source by 0.02um and inside the C-Si substrate respectively. All the results are depending on the calculated back/forward scattered fields are as a function of wavelength.

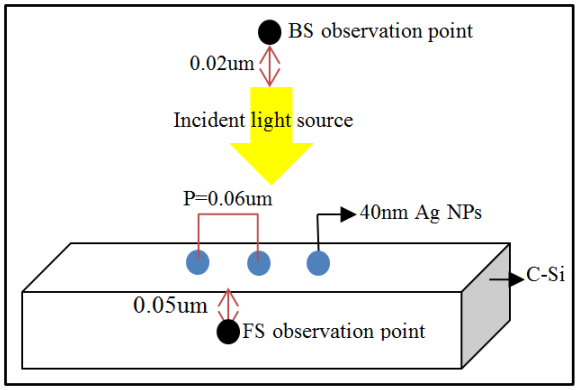


Figure 1: Reference device structure

A normally incident source is used to illuminate a finite c-Si substrate. Three silver spherical NPs with diameter of 40nm on the c-Si substrate was our reference as shown schematically in Fig.1.

NPs number, size (D) and spacing between them (p) were studied first. NPs number was changed with saving the distance from boundaries and other parameters to study the nanoparticles density effect only. The size effect was studied by changing the sphere diameter only without changing the spacing between the spheres. Then the period between the NPs was changed too.
Next, insulating layer between the NPs and the Si substrate was added to increase the distance between the nanoparticles and the substrate. Different types were used SiO2, TiO2, Si3N4, Mica, GaAs and ITO with constant thickness equal to 20nm to study the type effect only, were 20 nm is the typical thickness of SiO2 used for coating Si solar cells [8].

3. Results and Discussion

When the number of NPs is increased, an improvement in forward scattering is expected. Fig.2 shows the opposite, as the number decrease the performance enhanced.

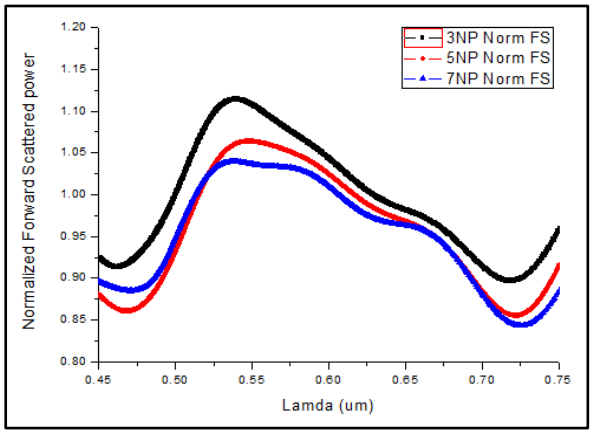


Figure 2: Normalized forward scattered power as NPs number change.

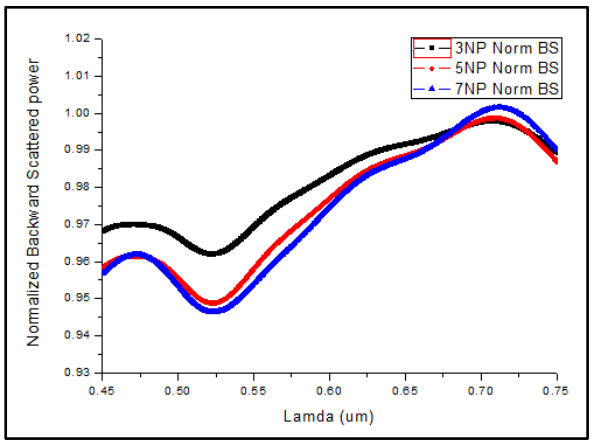


Figure 3: Normalized backward scattered power as NPs number change.

Three Ag NPs show the best enhancement around λ=507nm than others. Increasing NPs number showed reduction in power scattered into the Si. 7Nps showed less scattered power to thus obtain from 3Nps but with widening resonance range. This improve that the forward scattering is not subjected to increasing the nanoparticles number on the surface. This can be related to the loss of the power as the metal NPs increased on the Si surface due to increasing of signal absorption by the NPs [9]. However 7NP showed the highest backward scattered power around λ=705nm compared to the 3NPs which scatter comparable power for the entire region (Fig.3).

The period between the nanoparticles doesn't show recognizable enhancement. Period between the NPs changed from 0.05 um to 0.08 um as shown in Fig.4. Although it is not clear to the reader, less distance between the NPs enhanced the scattered power in Si with very small fraction.

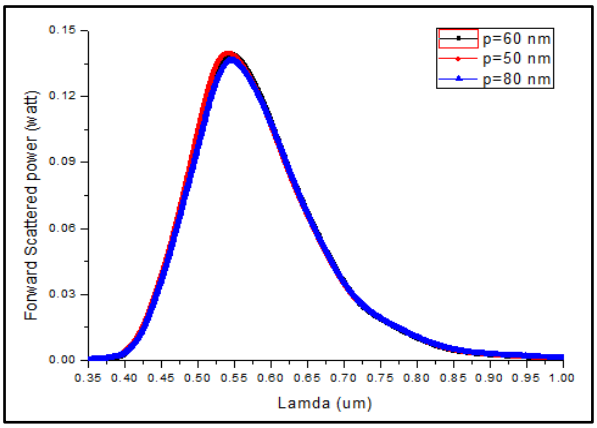


Figure 4: Forward scattering power as NPs period change.

The last parameter to change in the NPs is their diameter. As the diameter size of the NPs increased from 20 nm to 50 nm (Fig.5), the distance between the substrate and the NP increased too whereas the distance between the NPs itself decrease. This showed the forward scattering increases as the sphere diameter is increase where the distance between the NPs was saved.

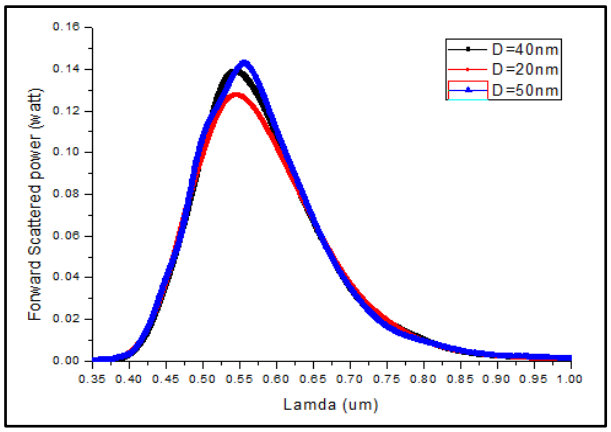


Figure 5: Forward scattering power as NPs size change

Repeating the same experiment with saving the distance between the NPs edges showed different results. Decreasing the NPs size and decreasing the distance between them as well shows enhancement in the forward scattering power. This is due the fact that decreasing the NP diameter decreases the average spacing to the substrate. Less spacing increases the probability of losing the scattered light in the air and allows efficient coupling and more scattering light to propagate in silicon. [10-11].

After that, insulating layer between the NPs and the substrate was added. Different types were studied (figures not show). SiO_2 and Mica layers showed almost similar improvement as their refractive indexes are closed. Si_3N_4 showed higher enhancement than the latter two dielectrics with wider and red shifted resonance region. On the other hand TiO_2 layer showed the best improvement in the scattered power value, red shifted and wider resonance range compared to the reference output. From the obtained results it was clear that increasing the dielectric refractive index improves the forward scattering efficiency and widening the resonance region [12].

4. Conclusions

Different parameters can be controlled to tune the solar cell efficiency. This paper studied the most important and applicable parameters nanoparticles dimensions and dielectric environment.

It was found that increasing the nanoparticles number is not efficient as decreasing the particles diameter and the spacing between them. Also coating the substrate with high refractive index insulator layer increases its absorbance.

Acknowledgements

The authors wish to acknowledge the support provided by the United Arab Emirates University.

References

[1] K. R. Catchpole and A. Polman, *Plasmonic solar cells*, Opt. Express 16, 21793-21800 (2008)

[2] Solarbuzz. Global PV Market. 2010; Available from: http://www.solarbuzz.com/facts-and- figures/market-facts/global-pv-market.

[3] Spinelli, P., et al., *Optical Impedance Matching Using Coupled Plasmonic Nanoparticle Arrays*, Nano Letters. 11(4): p. 1760-1765.

[4] Ferry, V.E., J.N. Munday, and H.A. Atwater, *Design Considerations for Plasmonic Photovoltaics*, Advanced Materials. 22(43): p. 4794-4808.

[5] Pillai, S. and M.A. Green, Plasmonics for photovoltaic applications, Solar Energy Materials and Solar Cells. 94(9): p. 1481-1486.

[6] [6] Pillai, S., et al., *Surface plasmon enhanced silicon solar cells*. Journal of Applied Physics, 2007. 101(9): p. 093105-093105-8.

[7] [7] Schaadt, D.M., B. Feng, and E.T. Yu, *Enhanced semiconductor optical absorption via surface plasmon excitation in metal nanoparticles*, Applied Physics Letters, 2005. 86(6): p. 063106.

[8] [8] Mokkapati, S., et al., *Designing periodic arrays of metal nanoparticles for light-trapping applications in solar cells*, Applied Physics Letters, 2009. 95(5): p. 053115-3.

[9] Marrocco, V., et al., *Efficient plasmonic nanostructures for thin film solar cells*. p. 77250L-77250L.

[10] Catchpole, K.R. and A. Polman, *Design principles for particle plasmon enhanced solar cells*, Applied Physics Letters, 2008. 93(19): p. 191113-3.

[11] Akimov, Y., K. Ostrikov, and E. Li, *Surface Plasmon Enhancement of Optical*, Absorption in Thin-Film Silicon Solar Cells. Plasmonics, 2009. 4(2): p. 107-113.

[12] Beck, F.J., A. Polman, and K.R. Catchpole, *Tunable light trapping for solar cells using localized surface plasmons*, Journal of Applied Physics, 2009. 105(11): p. 114310-7.

Transformational electromagnetics

Fundamentals of designing Cylindrical High Order Transformation Optics Invisibility Cloaks using Silver-Silica Metamaterials

K. S. Elassy*
*Arab Academy for Science, Technology, and Maritime Transport, Egypt
kareemsalah@live.com

Abstract

Metamaterials are known to have effective properties that are distinctive from their composites; they have engineered designed properties that are not found in nature. In order to be able to design a metamaterial, we should establish well understanding of the properties of the constituents to eventually be capable of engineering new effective parameters of the metamaterial, just like a recipe that we should be familiar with its ingredients to deliver a good cook. We perform a detailed analytical study for the effective parameters and the constituents' parameters of Silver-Silica metamaterial that describe the optical response of the mixture at different sizes of the inclusions' particles and different volume fractions of the silver and silica components. We also propose the optimum value of the volume fraction to achieve a broadened resonance optical response for the metamaterial. Finally, a design of a non-magnetic optical cloaking device using high order transformation optics is also proposed with the proper volume fractions of Silver and Silica.

1. Introduction

Metamaterials applications are arising exponentially every day; they are used in negative index materials [1] super lens [2] , hyper lens [3], black holes [4], chiral Metamaterials [5] and even a variety of invisibility cloaks as carpet cloaks[6], non-magnetic cloaks[7], magnetic cloaks [8], and other transformation optics cloaks [9]. The special aspect about metamaterials is the flexibility of having tailored desired properties according to the unit structural that is called meta-atoms. The effective parameters of the metamaterials which are the macroscopic parameters are dominant over the parameters of the constituents. The key feature of manipulating the optical response of the metamaterials is the presence of metals in the structural unit, and what is vital about the metals especially at the nano scale is the existence of surface plasmons that act as the gate for the propagation of the electromagnetic wave inside the metamaterials. Therefore, a composite structure of metal-dielectric mixture is vital for controlling the optical response of the metamaterials, and the effective parameters are according to the meta-atoms shape and volume fraction of the components [10].

Controlling the structure and the size of the constituent particles gives out different values for the permittivities, consequently different values for the refractive index, resulting in a variety of optical response of absorption and reflection according to the real and imaginary parts of the parameters. In this work we show a simplified explanation for the parametric analysis of Silver-Silica composite metamaterial assuming spherical particles of the inclusions by Bruggeman effective medium theory (EMT) [11]. We start with analysis for the Silica dielectric parameters followed by the optical response of the metals, and finally the composite structure response. [12]

2. Theory

2.1. The Optical Response of a Typical Dielectric (Silica)

Although the permittivity of a typical dielectric is usually approximated to a real positive number, this is not the case for all the optical range. Figure 1 shows the frequency-dependent permittivity of a typical transparent dielectric such as Silica.

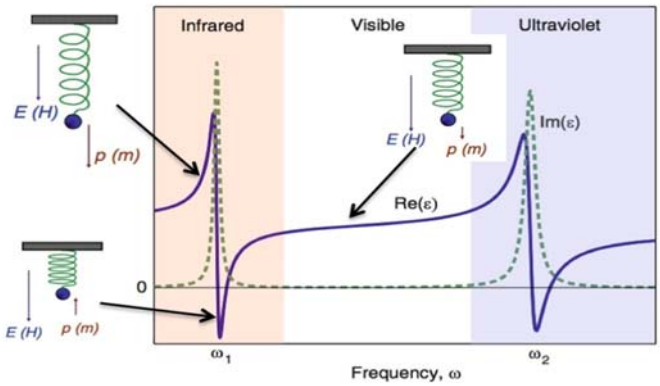


Figure 1 ε(ω) of a typical dielectric with ω_1 and ω_2 corresponding to the lattice resonance and electron transition resonance [13]

Two resonant frequencies, ω_1 and ω_2, can be noticed. In the mid-infrared range, and due to photon absorption of the core electrons, the former resonance, ω_1, is occurred. The latter one, ω_2, on the other hand, occurs in the ultraviolet range due to the bandgap of the crystal. [13] At each resonance, the dielectric function shows a Lorentz line shape associated with a peak in the imaginary part of the permittivity. These peaks indicate material losses, and in-between the two resonances, the approximation of a constant positive

real value to the permittivity becomes valid. This flat response in the visible range is the reason why Silica is observed as a transparent material.

Only slightly after each resonance, where the real part of $\varepsilon(\omega)$ for dielectrics can take negative values, thus the response of the material in this range is opposite to the driving force of the applied field. In contradiction, in general cases where the frequency is below the resonance or far beyond it, the function is usually positive. Consequently, the response of the material is able to follow the driving force with no delay. However, the optical response of Fused Silica at the nano scale is different from the bulk response [14].

$$\varepsilon(\omega) = 1 + \sum_j \frac{S_j \omega_j^2}{\omega_j^2 - \omega^2 - i\omega\gamma_j} \qquad (1)$$

- where ω_j is the resonance frequency of the jth mode, and S_j and γ_j are the strength and damping constant of the jth mode, respectively.

2.2. The Optical Response of a Metal (Silver)

As opposed to dielectric materials, which are characterized by a positive permittivity at optical frequencies, the real part of the dielectric function for noble metals is distinctively negative. In a negative permittivity material, the oscillation of free electrons is out of phase with respect to the driving field. Therefore, at the interface between a metal and a dielectric, most of the incident photons are reflected back [13]. The real part of permittivity is almost constant at different ε_∞ which indicates the interband transitions [15]. At optical frequencies, the effect of the modified damping constant Γ_1 will be dominant only for the imaginary part of the permittivity in (2), a proportional relation is observed between $\varepsilon''(\omega)$ and Γ_1. Therefore the imaginary part of the dielectric constant will depend on the size of the metal structure R in (3).

$$\varepsilon(\omega) = \varepsilon'(\omega) + i\varepsilon''(\omega) = \varepsilon_\infty - \frac{\omega_p^2}{\omega^2} + i\frac{\omega_p^2 \Gamma_1}{\omega^3} \qquad (2)$$

$$\Gamma_1 = \Gamma + \frac{v_F}{R} \qquad (3)$$

$$n'^2 = [\varepsilon' + \sqrt{\varepsilon'^2 + \varepsilon''^2}]/2 \quad ; \quad n''^2 = [-\varepsilon' + \sqrt{\varepsilon'^2 + \varepsilon''^2}]/2 \qquad (4)$$

2.3. where ε_∞ is a valid replacement of the frequency-dependent permittivity at longer wavelengths away from the interband resonance, and v_F is the material's Fermi velocity [13].

The width of the surface plasmon resonance of metallic particles increases as the particle size decreases due to confinement effects that modify the metal dielectric function. This effect is developed from the change in the mean free path of the electrons as the physical boundary of the metal particles is lessen, and since Γ_1 depends on the mean free path, therefore $\varepsilon''(\omega)$ will be affected. In the limit of very low particle concentration, particle size can be directly related to the plasmon width [16-17]. More details about the optical properties of silver at nano scale in [18] Figure 1 shows $\varepsilon'(\omega)$ and $\varepsilon''(\omega)$ versus the wavelength for bulk silver, while Figure 2 show at different sizes of silver particles. It is obvious that when the dimension of the metal is tens of nanometers or smaller, the magnitude of $\varepsilon''(\omega)$ is substantially larger than its bulk value. This feature should be taken into account in the design and simulation of most optical metamaterials with metal-dielectric meta- atoms [19].

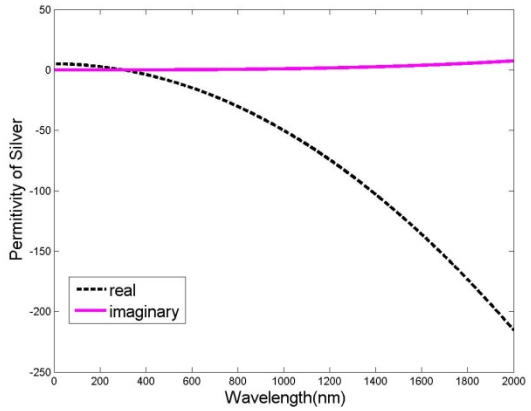


Figure 1 $\varepsilon'(\omega)$ and $\varepsilon''(\omega)$ of bulk silver

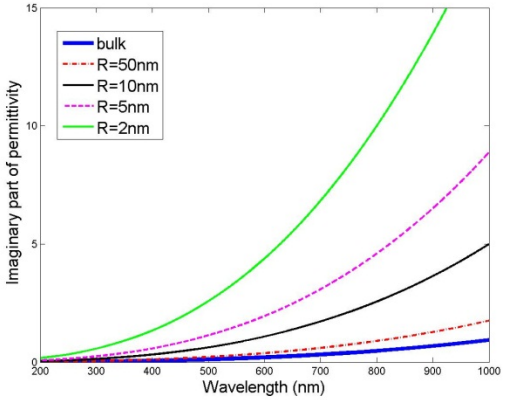


Figure 2 The imaginary part of the dielectric constant of silver at different sizes of the silver spherical particles.

A better way to illustrate this point is to study the refractive index of metal. From (4) along with (2), we can obtain the complex refractive index of metals, as plotted in **Erreur ! Source du renvoi introuvable.** for silver. At optical frequencies, $\varepsilon'' \ll |\varepsilon'|$ holds for the permittivity function of metals, therefore the refractive index has a pronounced imaginary part while the real part of the index is only slightly larger than zero. From the Fresnel equations, we know that the reflection coefficient expressed by $(n_1 - n_2)/(n_1 + n_2)$ must have an absolute value of unity [20] when n_1 is real and n_2 is purely imaginary. As a result, at the boundary between a dielectric and a noble metal, almost all light is reflected as long as the wavelength is

substantially longer than that of the interband transitions. Another phenomenon resulting from the large value of n'' is that light can only penetrate through a very thin layer of the noble metals. This travelling distance, called the skin depth, is the inverse of the absorption. [15]

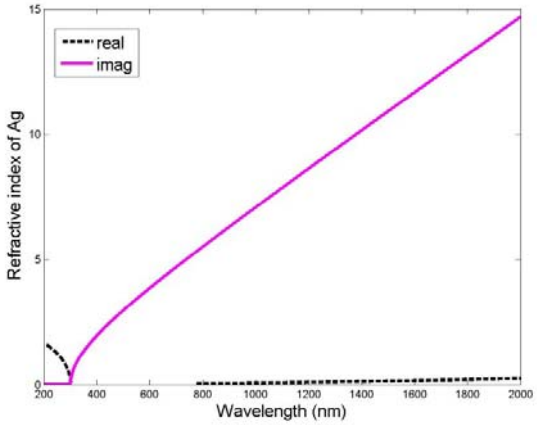


Figure 3 The real and imaginary parts of the refractive index of silver versus wavelength

2.4. The Optical Response of a Silver-Silica Composite

In order to estimate the effective parameters of a composite medium without being restricted by the low-frequency cases for the Maxwell–Garnett theory (MGT), Bruggeman made a great improvement to the MGT by finding a way to treat the two constituent materials on equal footing. The technique is assuming 2 complementary inclusions in a host, where $f_1 + f_2 = 1$ [21], and the host is the effective parameter.

$$\varepsilon_{eff} = \frac{1}{4}[(3f_1 - 1)\varepsilon_1 + (3f_2 - 1)\varepsilon_2 \pm \sqrt{[(3f_1 - 1)\varepsilon_1 + (3f_2 - 1)\varepsilon_2]^2 + 8\varepsilon_1}} \quad (5)$$

where ε_{eff} is the effective permittivity, ε_1 is the permittivity of the metal inclusions, ε_2 is the permittivity of the dielectric which is equal 3.8 for the silica at the visible range, f_1 and f_2 are the filling fraction of the metal and the dielectric in the composite respectively.

Metal-dielectric composites with effective dielectric function that obey the previous expressions can show a negative real part of the effective permittivity function $(Re\{\varepsilon_{eff}\} < 0)$ which absolute value can be adjusted by controlling the filling fraction [21] as shown in **Erreur ! Source du renvoi introuvable.**. As concentration increases, the interaction among particles induces additional broadening. It is shown that for noble metals the contribution of interparticle interaction to plasmon resonance width cannot be neglected even at volume concentrations of a few percent.

a)

b)

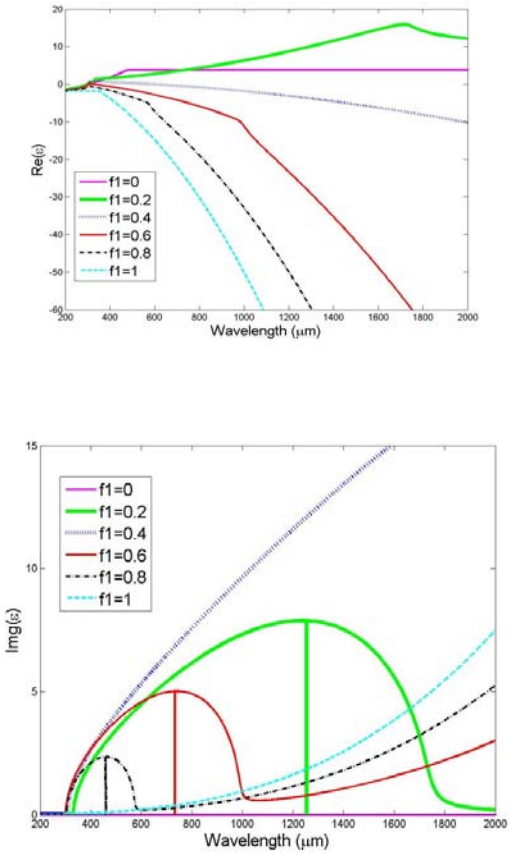


Figure 5 a) The real and b) imaginary parts of the effective permittivity of silver-silica composites for a series of metal volume fractions.

Bruggeman's Effective Medium Theory (EMT) predicts a critical filling fraction for metal, which is known as the percolation threshold. It represents the minimum volume fraction of conducting particles needed for the formation of a continuous conducting pathway [11]. In **Erreur ! Source du renvoi introuvable.**-b, we see that the resonance band in ε_{eff} is very broad in the curve where f=0.4. In fact, this peak can extend to an infinite bandwidth if the filling fraction approaches 1/3, which is the percolation threshold for a three-dimensional metal-dielectric composite. The percolation in a mixture indicates that the magnitude of the metal permittivity $|\varepsilon_1|$ is much larger than the permittivity of the dielectric component ε_2. The real part of ε_{eff} approaches the silver permittivity with increasing metal filling fraction f, which is a rather intuitive result. Interestingly, the imaginary part of ε_{eff} shows a broadened resonance peak due to the electromagnetic interactions between the metal and dielectric grains. If the constitutes of this mixtures is arranged to form a planar arrays of nearly-touching metallic nanoparticles, thus yielding well confined guided mode [22].

Figure 4 The real and imaginary part of the effective permittivity of silver-silica composites at volume fraction (f=0).

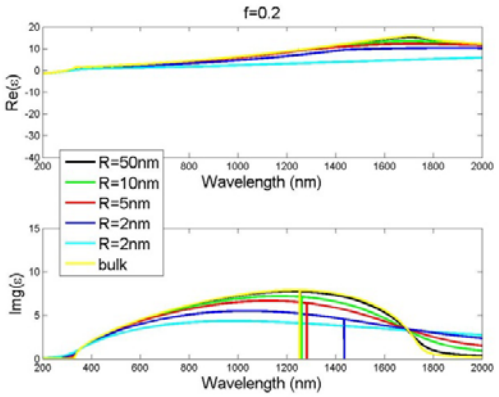


Figure 5 a) The real and b) the imaginary part of the effective permittivity of silver-silica composites for a different sizes of silver inclusion at volume fraction (f=0.2).

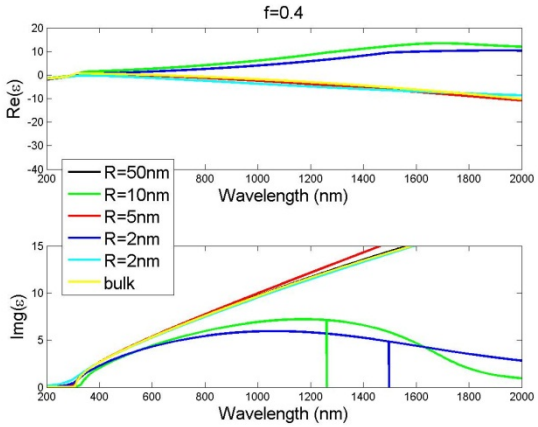


Figure 6 a) The real and b) the imaginary part of the effective permittivity of silver-silica composites for a different sizes of silver inclusion at volume fraction (f=0.4).

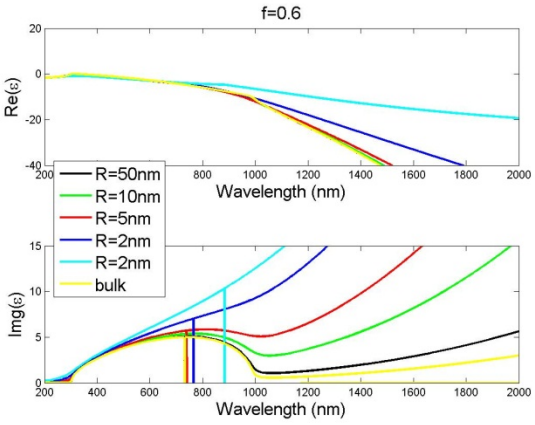


Figure 7 a) The real and b) the imaginary part of the effective permittivity of silver-silica composites for a different sizes of silver inclusion at volume fraction (f=0.6).

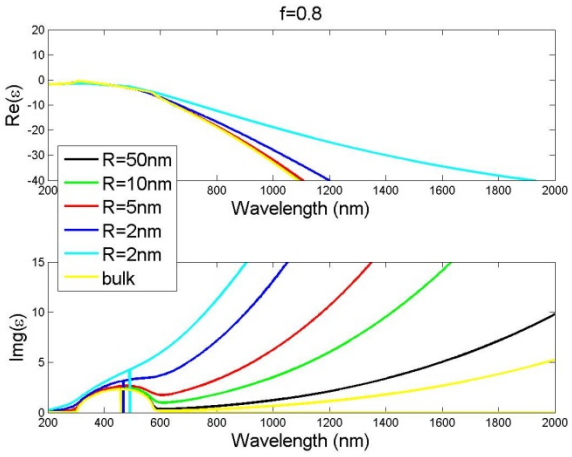


Figure 8 a) The real and b) the imaginary part of the effective permittivity of silver-silica composites for a different sizes of silver inclusion at volume fraction (f=0.8).

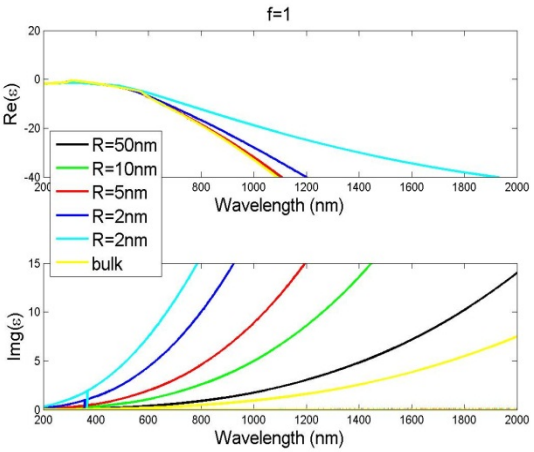


Figure 11 a) The real and b) the imaginary part of the effective permittivity of silver-silica composites for a different sizes of silver inclusion at volume fraction (f=1).

Figures 6-11 show the real and the imaginary part of the effective permittivity of silver-silica composites for different sizes of silver inclusion at different volume fractions. . The volume fraction represent the concentration of the metal (silver) in the composite (silver-silica), so when f=0 as shown in Figure 6 this means that the composite consists of dielectric only so we observe that the real part of the effective permittivity equals 3.8 which is positive value ,and the imaginary one equals zero .By increasing the value of the volume fraction the composite approaches a pure metal , this explains the decrement of the value of the real part of the effective permittivity from 3.8 at f=0 till reaches a negative value at volume fraction equal one.

The imaginary part of the effective permittivity shows a broadened resonance peak due to the electromagnetic interaction between the metals and the dielectric substrate, the metal-dielectric composite acts as dielectric medium for small metal concentrations of less than one third of the volume fraction, beyond the percolation threshold which occurs at f=0.4 as shown in fig.5b. The percolation threshold

is the minimum volume fraction that satisfies the mixture will conduct (surface plasmons allow propagation of wave). The composite acts as a dilute metal with an effective permittivity proportional to $f - 1/3$.

$$\frac{\varepsilon}{\varepsilon_1} = \begin{cases} \frac{1}{2}(3f_1 - 1), & if\ \frac{1}{3} < f_1 \leq 1 \\ 0, & if\ 0 < f_1 \leq \frac{1}{3} \end{cases} \quad (6)$$

It is observed in Figure 6 that the broadened resonance (peeks) increasing from f=0 (pure dielectric) tell reaches maximum at f=0.4 then decreases from f=0.6 tell reaches zero at f=1 (pure metal). It is noted that at f=0.4 is the optimum value that provide the most sufficient coupling between the electromagnetic wave and the metamaterials.

3. Design

In this section, a design of a non-magnetic optical cloaking device is proposed; however, we must first analyze a periodically layered composite with two isotropic constituent materials aligned in a parallel manner as shown in **Erreur ! Source du renvoi introuvable.**. The bulk permittivities of the two constituents are ε_1 and ε_2, respectively. The volume filling fraction of material 1 is noted as f_1, so the second constituent has a filling factor of $f_2 = 1 - f_1$.

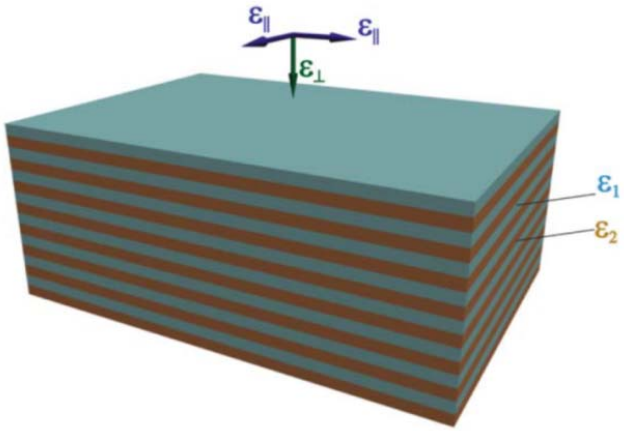


Figure 9 Schematic of a layered metal-dielectric structure, with the permittivities of the two constituents given as ε_1 and ε_2, respectively. Two principal effective permittivities, $\varepsilon_\parallel$ and $\varepsilon_\perp$.[13]

In such a system, there are two principle situations to be studied: when the external electric field is either parallel or perpendicular to the planar interfaces.

$$\varepsilon_\parallel = f_1\varepsilon_1 + f_2\varepsilon_2 \quad (7)$$

$$\varepsilon_\perp = \frac{\varepsilon_1\varepsilon_2}{f_2\varepsilon_1 + f_1\varepsilon_2} \quad (8)$$

The two extremes in equations (7) and (8) are called the Wiener bounds to permittivity, which indicate the absolute values of the effective permittivity of the whole composite in two extreme situations. [23-24] The Wiener bounds of a Silver-Silica layered composite is plotted in Figure 13.

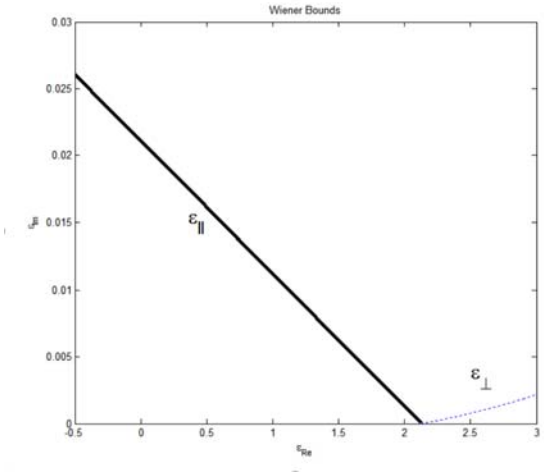


Figure 10 The Wiener bounds, $\varepsilon_\parallel$ and $\varepsilon_\perp$, of a Silver-Silica layered composite

To achieve optical cloaking, we use the design proposed in [25]. The device has a cylindrical geometry, as shown in Figure 11, and using high order transformation optics. Transformation optics is a field of a study which enables a precise control over electromagnetic fields by distorting the Cartesian coordinate system according to our design. The mathematical fundamentals and equations of the transformation technique are presented in [26].

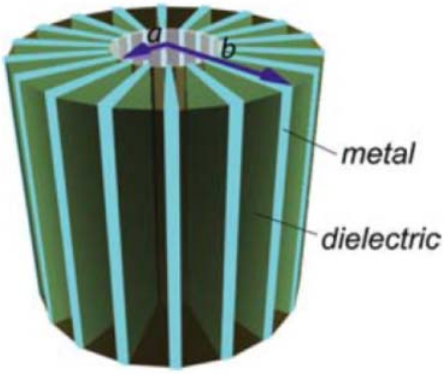


Figure 11 Schematic of a cylindrical non-magnetic cloak with high-order transformations for TM polarization. [25]

The dielectric material that is used here is silica (silicon dioxide), and the metal is silver. We will subject the device to an electromagnetic wave of a wavelength of 532 nm. The electric permittivities of the two constituent materials at this wavelength are as follow: $\varepsilon_{SiO_2} = 2.13$ and $\varepsilon_{Ag} = -10.6 + 0.14i$.

3.1 Constraints

Three main constraints must be put in consideration when designing the device. **First**, the main and most important constraint in the design is the thickness of the metal slabs, which shouldn't exceed the skin depth. As a result, the first step in designing the device is calculating the skin depth of silver.

From (9) and (4), we can calculate the skin depth of the silver at wavelength of $\lambda = 532\ nm$; we find it about 13 nm. So we take the thickness of the silver slap to be 10 nm.

$$\delta = \frac{\lambda_0}{4\pi n''} \qquad (9)$$

where δ is the skin depth, λ_0 is the wavelength of the wave and n'' is the imaginary part of the refractive index of silver.

Second, the device must satisfy a graded-index manner as the electromagnetic wave moves from the outer radius to the inner one. The cylindrical geometry of the device forces us to perform a coordinate transformation function $r = g(r')$ from (r', θ', z') to (r, θ, z). This transformation compresses the region $r' < b$ to a concentric shell $a < r < b$. For a purely non-magnetic TM mode, equation (10) shows that ε_r varies from 0 at the inner boundary of the cloak $(r = a)$ to 1 at the outer surface $(r = b)$. [27]

$$\varepsilon_r = \left(\frac{r'}{r}\right)^2 \qquad (10)$$

The **third** and final constraint is the proper volume fractions, f_1 and f_2, of Silver and Silica, respectively, at both boundaries of the cloak. At the inner boundary $(r = a)$, we derive the Silver volume fraction f_1 which satisfies the effective permittivity $\varepsilon_\parallel = 0$ from the Wiener bounds plotted in Figure 10 and expressed in equation (7). We note that $\varepsilon_\parallel$ in equation (7) corresponds to ε_r in equation (10). The same steps are done for the outer boundary of the cloak $(r - b)$.

By performing the previous step, we find that f_1 at the outer radius is approximately equal to 0.0887666, and at the inner radius equal to 0.167321.

Since the thickness of the silver slap is 10 nm for all the region, therefore we can calculate the lengths of the arcs at the outer and inner radii. At the outer radius, and in order to satisfy the metal filling fraction, we must take the thickness of the silica to be 102.65 nm and 49.765 nm at the inner radius.

Now we assume that the angle between the metal slaps is 3^0; therefore, we can calculate the lengths of the outer and inner radii. By calculations, we find that the outer radius is equal to 2.15 um, and the inner radius is equal to 1.14 um.

4. Conclusions

From our study for the optical response of silver-silica composite metamaterial we have concluded that the parameters of the mixture responses in an independent manner from constituents of the metamaterial as it depend mainly on the structure of the meta-atom. We studied the parameters of the typical Silica, then the parameters of the silver particles at different sizes, then the effective parameters of silver-silica composite at different volume fractions and different sizes of the metal particles. We have shown that the optical response changes correspondingly according to the volume fraction of the component, and the critical volume fraction for the silver in which the metamaterials exhibits broadened resonance response due to the propagation of the surface plasmons oscillation.

Acknowledgements

Acknowledgements belong here.

References

[1] Park N, Min B (2011) A terahertz metamaterial with unnaturally high effective refractive index. Nature 470, 369-373.

[2] Fang N, Zhang X (2003) Imaging properties of a metamaterial superlens. Appl. Phys. Lett. 82, 161.

[3] Hakkarainen, Setälä T, Friberg AT (2012) Near-field imaging of interacting nano objects with metal and metamaterial superlenses. New J. Phys. 14 043019.

[4] Climente, Alfonso (2012) Omnidirectional broadband acoustic absorber based on metamaterials. Appl. Phys. Lett. 100, Issue: 14.

[5] Li Z, Alici KB, Caglayan H, Kafesaki M, Soukoulis CM, Ozbay E (2012) Composite chiral metamaterials with negative refractive index and high values of the figure of merit. Optics Express, Vol. 20, Issue 6, 6146-6156.

[6] Fischer J, Ergin T, Wegener M (2011) Three-dimensional polarization-independent visible-frequency carpet invisibility cloak. Opt. Lett. 36, 2059-2061.

[7] Huang L, Zhou D, Wang J, Li Z, Chen X, Lu W (2011) Generalized transformation for nonmagnetic invisibility cloak with minimized scattering. JOSA B, Vol. 28, Issue 4, 922-928.

[8] Gömöry F, Solovyov M, Šoucl J, Navau C, Prat-Camps J, Sanchez A (2012) Experimental realization of a magnetic cloak. Science, Vol. 335, No. 6075, 1466-1468.

[9] Chen H, Chan CT, Sheng P (2010) Transformation optics and metamaterials. Nature Materials 9, 387-396.

[10] "Metamaterials and Plasmonics: Fundamentals, Modelling, Applications," Proceedings of the NATO Advanced Research Workshop on Metamaterials for Secure Information and Communication Technologies Marrakech, Morocco 7-10 May 2008.

[11] Sancho-Parramon J, Janicki V, Zorc H (2010) On the dielectric function tuning of random metal-dielectric nanocomposites for metamaterial applications. Optics Express, Vol. 18, Issue 26, 26915-26928.

[12] Smith DR. Electromagnetic Metamaterials. http://people.ee.duke.edu/~drsmith/metamaterials.htm. (Feb. 2013)

[13] Shalaev VM, Cai W. Optical metamaterials: fundamentals and applications. DOI 10.1007/978-1-4419-1151-3 1. Springer Science+Business Media, LLC, 233 Spring Street, New York,NY 10013, USA. 2010

[14] Miloslavsky VK, Makovetsky ED, Ageev LA, Beloshenko KS (2009) Fused silica as a composite nanostructured material. Optika Spektroskopiya, 2009, Vol. 107, No. 5, 854–859.

[15] Pinchuk A, von Plessen G, Kreibig U (2004) Influence of interband electronic transitions on the optical absorption in metallic nanoparticles. J. Phys. D: Appl. Phys. 37 3133

[16] Sancho-Parramon J (2009) Surface plasmon resonance broadening of metallic particles in the quasi-static

approximation: a numerical study of size confinement and interparticle interaction effects. Nanotechnology, 20(23), 23576.
[17] Sancho-Parramon J, Janicki V, Loncari M, Zorc H, Dubcek P, Bernstroff S (2011) Optical and structural properties of Au-Ag islands films for plasmonic applications.
[18] Kelly KL Coronado E, Zhao LL, Schatz GC (2003) J. Phys. Chem. B, 107 (3), 668-677.
[19] Sonnichsen C (2001) Plasmons in metal nanostructures.
[20] Skaar J (2006) Fresnel equations and the refractive index of active media. Physics Optics 41.20.Jb, 42.25.Bs
[21] Shalaev VM (2000) Nonlinear optics of random media: fractal composites and metal-dielectric film. (Springer Verlag, STMP-158, Berlin, Heidelberg,).
[22] Sainidou R, de Abajo G (2008) Plasmon guided modes in nanoparticle metamaterials. Opt. Express Vol. 16, Issue 7, pp. 4499-4506.
[23] Shalaev VM, W. Cai W, Chettiar UK, Kildishev AV (2008) Designs for Optical Cloaking with High-Order Transformations. *Birck and NCN Publications,* Paper 174, 2008.

Frequency selective structures and high impedance surfaces

Analytical Model of a Self-complementary Connected Antenna Array on High Impedance Surface

Xavier Begaud[1], Fabrice Linot[1,2], Michel Soiron[3], Christian Renard[2]

[1]Institut Mines-Télécom, Télécom ParisTech, France
[2] THALES Systèmes Aéroportés, Elancourt, France
[3] SART, France
*corresponding author, E-mail: Xavier.Begaud@telecom-paristech.fr

Abstract

This paper presents an analytical model to design a self-complementary connected antenna array above artificial materials like High Impedance Surfaces (HIS). Objective of this model is to perform parametric studies to facilitate deeper understanding of a complex antenna array with a significantly shorter computation time than with electromagnetic simulators. The model of the complete structure has been designed in receiving mode when structure is illuminated with a plane wave and by using transmission line model and ABCD matrix. Applying an interesting property which gives equivalence between the input impedance in transmit mode and the surface impedance in receiving mode, the impedance match of the self-complementary connected antenna array can be quickly calculated. It is also simple to evaluate the influence of the incidence angle on the reflection coefficient of a self-complementary connected antenna array above Perfect Electric Conductor (PEC) or HIS. PEC or artificial materials can modify the antenna array behavior by either increasing the bandwidth or by adding additional bandwidths. All these results have been verified to be accurate by numerical simulations done with Ansys HFSS.

1. Introduction

This work has been carried out in the framework of research on wideband and low-profile antenna arrays for airborne applications. Among wideband antennas, self-complementary antennas have a theoretically infinite bandwidth and are good candidates to fix the input impedance of such antennas [1]. In this work, the antenna consists of checkerboard array of square conducting patches on an electrically thin dielectric substrate. Without dielectric, an infinite array of this form is self-complementary and therefore well matched to half free space impedance according to the Babinet's principle. The patches are fed with balanced excitation at their corners [2] generating a dual linear polarized field (Fig. 1).

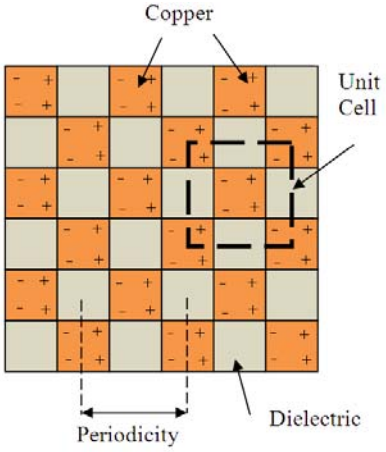


Figure 1: Finite Self-complementary connected phased antenna array composed of 18 patches.

Designing unidirectional antennas is required on many platforms in order to obtain outward radiation and to preserve the interior against any electromagnetic pollution. In wideband applications the most common solution is to place the antenna above an absorbing cavity, but this solution is bulky for low frequency applications. Another efficient technique is to use a reflector made of a very good electrical conductor to retrieve the backward radiation lost in the previous solution. This technique is optimal at the middle of the bandwidth where a constructive interference phenomenon is obtained by placing the reflector at a quarter wavelength (at central frequency) from the antenna radiating face. But this solution is inherently limited in bandwidth and can rarely exceed an octave. Among artificial materials, High impedance Surfaces (HIS) have remarkable characteristics. While a good electrical conductor imposes a reflection phase of π between incident and reflected electric fields, HIS do not introduce any phase shift. Hence it becomes possible to position the antenna closer to the new reflector. As a consequence, the antenna is unidirectional and thin.

In this work, an analytical model will be proposed to calculate an infinite self-complementary connected antenna array located above a HIS or PEC and will be detailed in the following paragraphs.

2. Analytical model of a checkerboard antenna above HIS

The antenna, with or without HIS, can be considered like a stack of dielectric and metallic layers. We assume that the antenna is illuminated by a plane wave. Each layer, metallic or dielectric, can then be represented by an ABCD matrix [3]. Consequently, the surface impedance of this structure can be determined by the product of the ABCD matrices of each layer of the stack.

2.1. Analytical model of a self-complementary connected antenna array

The radiating part of the antenna is composed of a checkerboard array of square metallic patches located above an electrically thin dielectric substrate. Antenna is assumed illuminated by a plane wave under a particular incidence. So, the antenna can be modeled by two-port network, with the parameters of defined hereafter. The ABCD matrix linking the input and output tensions and currents is given by the following equation:

$$\begin{bmatrix} V_e \\ I_e \end{bmatrix} = \begin{bmatrix} A & B \\ C & D \end{bmatrix} \begin{bmatrix} V_s \\ I_s \end{bmatrix} \quad (1)$$

The ABCD matrix of cascade connection of N two-ports networks can be determined by the product of the ABCD matrices representing each network.

For a dielectric layer with thickness *d*, the terms of the ABCD matrix are given by the relation [3]:

$$\begin{bmatrix} \cos(k_i d) & jZ_{diel}^{TE/TM} \sin(k_i d) \\ jY_{diel}^{TE/TM} \sin(k_i d) & \cos(k_i d) \end{bmatrix} \quad (2)$$

Where Z_{diel} and Y_{diel} are respectively the impedance and admittance of the plane wave for both TE and TM polarization in the dielectric. Their expressions are given by the equations (3) and (4):

$$Z_{diel}^{TE} = \frac{\eta_0 k_0}{k_i} \quad (3)$$

$$Z_{diel}^{TM} = \frac{\eta_0 k_i}{\varepsilon_{ri} k_0} \quad (4)$$

where $\eta_0 = 120\pi$ is the free space impedance, k_0 is the free space wave number, k_i is the wave number in the dielectric host defined by:

$$k_i = k_0 \left(\varepsilon_{ri} - \sin^2 \theta_{diel}\right)^{-1/2} \quad (5)$$

θ_{diel} represents the incident angle of the wave in the dielectric medium with a relative permittivity ε_{ri}.

The metallic layer is described by the simple following ABCD matrix:

$$\begin{bmatrix} 1 & Z \\ 0 & 1 \end{bmatrix} \quad (6)$$

Where Z is the surface impedance of the self-complementary grid (only the metallic patches).
This surface impedance of an infinite antenna array is calculated with a 3D electromagnetic simulator prior to build the model. In this simulation the antenna array is considered in a receiving mode where all generators are replaced by their internal equivalent impedance. Then this result will be used for the rest of the optimization and no other 3D electromagnetic simulations are required.

2.2. Analytical model of artificial materials

Artificial surfaces may be modeled with a transmission line model when illuminated by a plane wave. Luukkonen [4] proposed an analytical model to design artificial surfaces facilitating their use for different applications. HIS are modelled as a parallel connection of grid impedance and surface impedance of the grounded dielectric slab. Here the HIS is composed of a planar array of metallic square patches with no via printed on a grounded dielectric slab with thickness h and relative permittivity ε_r. The width of each square patch is w, the gap between neighbouring patches is g and the lattice period P=w+g (Fig. 2).

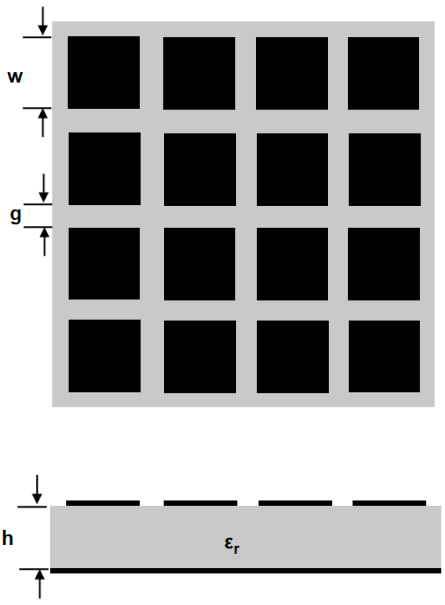


Figure 2: High Impedance Surface consisting of metallic square patches printed on a grounded dielectric slab

The surface impedance of HIS can be represented by the parallel connection of grid impedance Z_g, modeling the

metallic shape array, with grounded dielectric impedance Z_d [4].

$$Z_s^{-1} = Z_g^{-1} + Z_d^{-1} \quad (7)$$

The surface impedance Z_s can be calculated by the following equations when the structure is excited respectively by a plane wave polarized in TM or TE mode [4]:

$$Z_s^{TM} = \frac{j\omega\mu \frac{\tan(\beta h)}{\beta} \cos^2\theta_2}{1 - 2k_{eff}\alpha \frac{\tan(\beta h)}{\beta} \cos^2\theta_2} \quad (8)$$

$$Z_s^{TE} = \frac{j\omega\mu \frac{\tan(\beta h)}{\beta} \cos^2\theta_2}{1 - 2k_{eff}\alpha \frac{\tan(\beta h)}{\beta} \left(1 - \frac{2}{\varepsilon_r + 1}\sin^2\theta\right)} \quad (9)$$

where $\mu=\mu_0$ is the absolute permeability of the substrate, β is the propagation constant defined by:

$$\beta = \sqrt{k^2 - k_t^2} \quad (10)$$

$$k = k_0\sqrt{\varepsilon_r} \quad (11)$$

k is the wave number in the substrate and k_t is the tangential wave number component imposed by the incident plane wave:

$$k_t = k_0\left[1 - \cos^2\theta\right]^{1/2} \quad (12)$$

The refracted angle θ_2 is calculated from the refraction law:

$$\theta_2 = \arcsin\left(\frac{\sin\theta}{\sqrt{\varepsilon_r}}\right) \quad (13)$$

The α term in expressions (9) and (10) represents the grid factor and is equal to:

$$\alpha = \frac{k_{eff}P}{\pi} \log\left(\frac{1}{\sin\frac{\pi g}{2P}}\right) \quad (14)$$

Furthermore k_{eff} is the wave number in the effective host medium:

$$k_{eff} = k_0\sqrt{\varepsilon_{eff}} \quad (15)$$

The effective permittivity of an equivalent uniform medium can be approximated in this case by [3]:

$$\varepsilon_{eff} = (\varepsilon_r + 1)/2 \quad (16)$$

The grid parameters are g the gap between two adjacent patches and P the periodicity of the metallic square patches (Fig. 2).

2.3. Analytical model of the antenna array above artificial materials

Finally, the complete model of the antenna above a HIS is built with the antenna model loaded by the HIS model (Fig. 3). The surface impedance Z_e of the complete antenna can be determined from expression (17):

$$Z_e^{TE/TM} = \frac{AZ_s^{TE/TM} + B}{CZ_s^{TE/TM} + D} \quad (17)$$

The global structure is illuminated by a plane wave in free space. The impedance Z_s represents the surface impedance of the artificial material used.

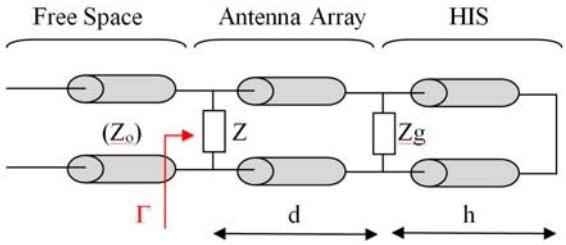


Figure 3: Equivalent model of a self-complementary connected antenna array loaded with HIS.

The reflection coefficient Γ of the multilayer structure modeled by its ABCD matrix is then calculated with relation (18):

$$\Gamma = \frac{Z_s^{TE/TM} - Z_0^{TE/TM}}{Z_s^{TE/TM} + Z_0^{TE/TM}} \quad (18)$$

With Z_0 the free space impedance polarized in TE or TM mode respectively defined by:

$$Z_0^{TM} = \eta_0 \cos\theta \quad (19)$$

$$Z_0^{TE} = \eta_0 / \cos\theta \quad (20)$$

Finally, we used an interesting property given by Cavalo et al. [5]. The authors have shown that the reflection coefficient of an infinite phased array antenna can be

calculated either in transmit or in receive mode. So, finding the surface impedance of the antenna array is equivalent to calculate the input impedance. This is the reason why the infinite complete structure is characterized in receiving mode.

3. Self-complementary connected antenna array over PEC and artificial surfaces

In this part, the analysis using the analytical model is performed and results are compared to numerical results obtained with HFSS. In order to highlight the influence of the artificial reflector on the reflection coefficient of the antenna array, we consider here a single layer antenna (Fig. 4).

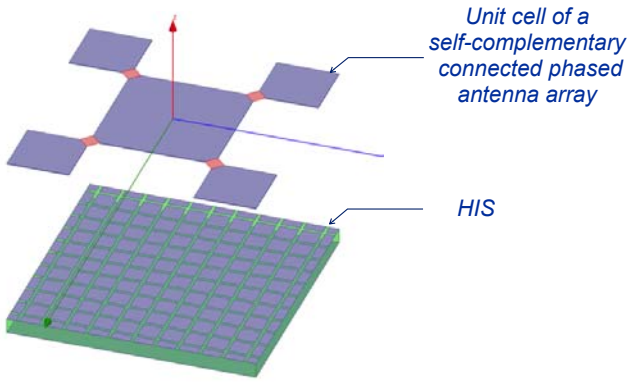


Figure 4: Unit cell of a self-complementary connected antenna array above HIS (dielectric layers are hidden).

Nevertheless, the results presented here are valid for a multilayer stacking [6]. For the numerical simulations, only one cell is considered where periodical boundaries are applied.

3.1. Antenna array above a PEC reflector

First, we consider a Perfect Electric Conductor (PEC) as reflector. This case represents a conventional case and will be considered as a reference. This reference case will be used to verify the validity of the analytical model and also the property enounced by Cavalo et al. [5]. The ground plane is located at a quarter wavelength *(at 8.5 GHz)* distance from the infinite antenna array printed on dielectric. To simplify the analysis, the substrate is considered as free space. The metallic reflector is considered as a PEC, i.e. has a reflection coefficient equal to -1. Hence, the back radiation generated by the radiating elements is reflected by the metallic reflector with a π reflection phase for electric field. As the metallic reflector is placed at a quarter wavelength distance at f_0 away from the radiating elements, the PEC reflector provides at this frequency a constructive interference phenomenon for the forward radiation. At f=17GHz, a destructive interference phenomenon is observed resulting from short-circuit of the antenna array. The reflection coefficient of the antenna calculated with analytical and numerical methods is plotted on Fig. 5.

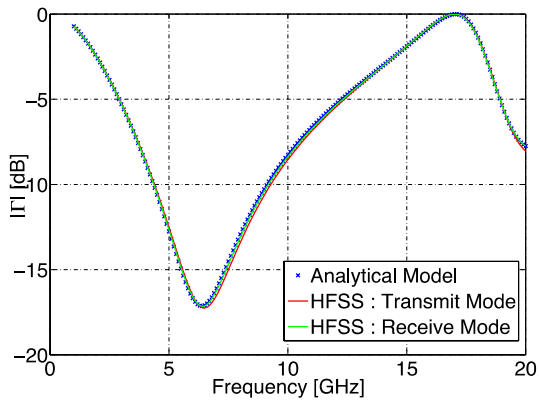
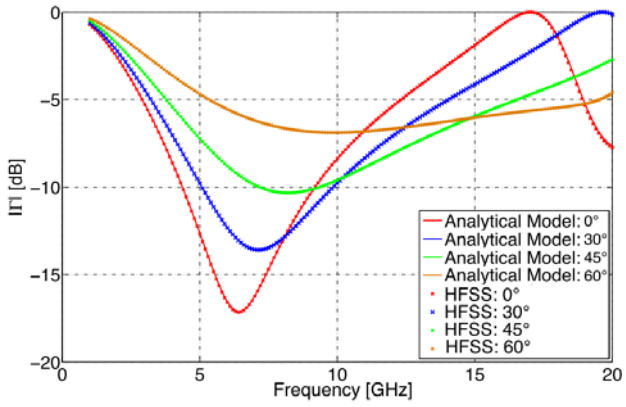
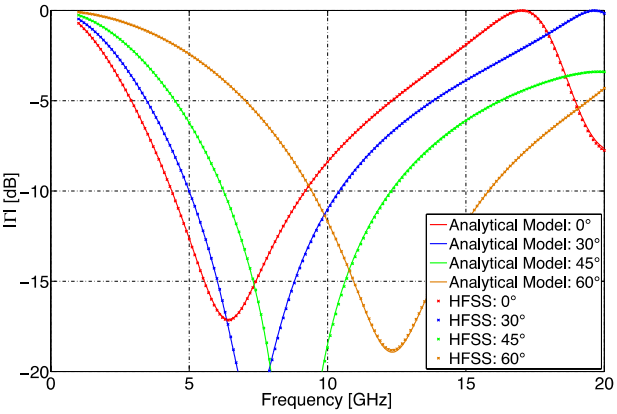


Figure 5: Reflection coefficient of an infinite antenna array above a PEC reflector in receive and transmit modes

The comparison is done when the infinite antenna array is considered in a receiving mode, i.e. illuminated by a plane wave (analytical model and HFSS) and in transmitting mode (all antenna ports are excited simultaneously and with the same amplitude and phase with HFSS) (Fig. 5).
A very good agreement between the analytical and numerical results is observed when the antenna array is calculated in a receiving and transmitting mode (Fig. 5).



a)



b)

Figure 6: Reflection coefficient versus frequency of a self-complementary connected antenna array above a PEC reflector for TM (a) and TE polarizations (b).

The antenna array is now only considered in a receiving mode. On Fig. 6 is plotted the reflection coefficient of a self-complementary connected antenna array for several incident angles for both TE and TM polarization.
The effect of the increase of the incident angle is less sensitive in TM than in TE polarization. In TM mode, when increasing the incident angle, the reflection coefficient of the antenna array increases without large variations of the resonant frequency. The -10dB bandwidth is slightly reduced when the antenna is illuminated by an incident plane wave with angle up to 30°. However, the antenna is mismatched as the incident angle increases showing that good results can be obtained from 0° to 45° with this simple multilayer structure. In TE mode, the reflection coefficient of the antenna array is quite stable when the incident angle increases despite the shift of the resonance frequency toward high frequencies. The numerical results are very close to the ones obtained analytically. Hence, it is possible to quickly evaluate an infinite antenna array in receiving mode with this analytical model.

3.2. Antenna array above a HIS

The self-complementary connected antenna array is now placed above a HIS. This reflector is composed of a periodic array of metallic square patches (P=1.7mm, g=0.1mm, Fig. 2) printed on a grounded dielectric (h=0.762mm, ε_r=10.35). The HIS behaves like a Perfect Magnetic Conductor (PMC) at f=13GHz. The reflection coefficient versus frequency of the infinite antenna array on a high impedance reflector is plotted on Fig. 7.

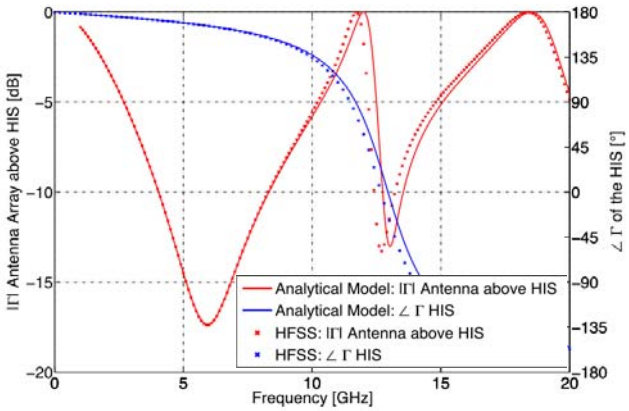


Figure 7: Comparison between analytical and numerical results: reflection coefficient of the infinite antenna array above HIS reflector and reflection phase diagram.

By fixing the height of the antenna to $\lambda_0/4$ at the frequency f_0, the HIS will impose a π reflection phase between incident and reflected electric fields in antenna plane and a 0° reflection phase at $2f_0$. The classical solution of a PEC ground plane only allows having a single operation bandwidth around frequency f_0 (Fig.6). The use of a high impedance reflector gives a second bandwidth around frequency $2f_0$ (Fig. 7).
The radiation pattern of the antenna array can be estimated by the product of the array factor with the radiation pattern of the unit cell. With this formulation one can easily obtain

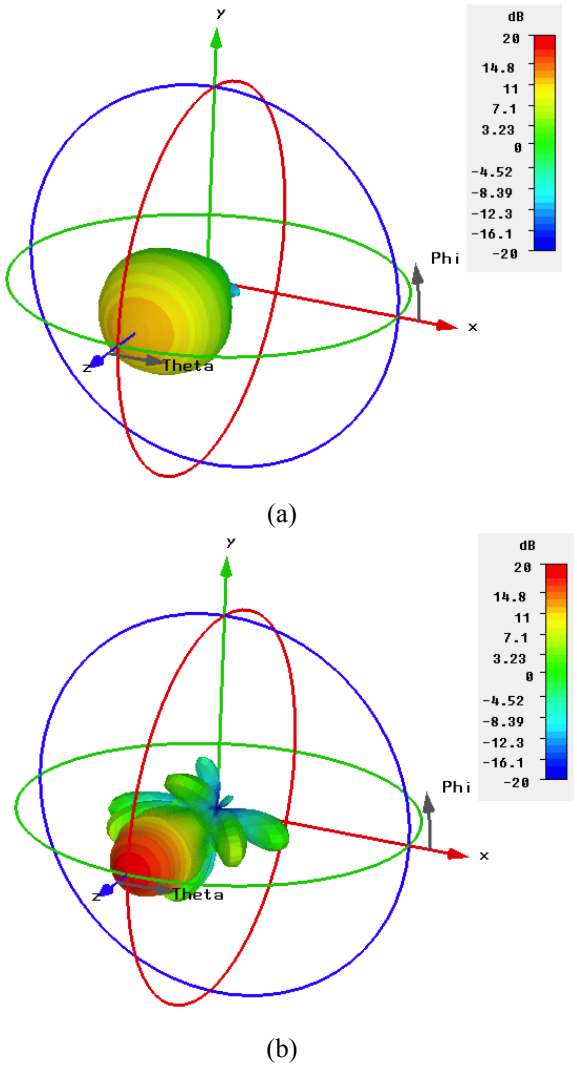


Figure 8: Radiation pattern of a self-complementary connected antenna array. Realized Gain at: (a) f=6.5GHz, (b) f=13GHz.

approximate radiation patterns of the whole structure. The realized gain of a self-complementary connected antenna array made of 5x5 elements located above HIS is plotted on Fig. 8 (a single polarization is activated). These preliminary results show that the antenna array exhibits a directive radiation pattern at the center of the two selected bandwidths defined in Fig. 7.
Moreover by the modification of the HIS parameters it is possible to shift the antenna resonant frequency or to add other bandwidths. A solution for increasing the antenna bandwidth is to use HIS designed with several resonances spread over the total bandwidth [6] or to use an active HIS able to modify the resonant frequency of the reflector [6]. This analytical model is also accurate to design an ultra thin absorber [7] and a self-complementary connected antenna array positioned above an absorbing HIS [6].

4. Conclusions

An analytical model allowing evaluation of the reflection coefficient of a self-complementary connected antenna array above several specific reflectors has been presented. Comparisons between results obtained with this method and computations HFSS show a very good agreement. Hence, the analytical method allows performing parametric studies of the antenna with shorter computer time compared to the time required by an electromagnetic 3D computer code. In this way, such 3D electromagnetic tool should only be used in the final steps of the antenna design.

Acknowledgment

The present work has been led in the framework of the ITP SIMCLAIRS competed program. France, United Kingdom and Sweden have mandated the European Defence Agency (EDA) to contract the Project with a Consortium composed of THALES SYSTEMES AEROPORTES France, acting as the Consortium Leader, SELEX Galileo Ltd, THALES UK Ltd and SAAB AB.

References

[1] Y. Mushiake, Self-complementary antennas, *IEEE Antennas Propagation Magazine*, Vol.34, No.6, pp.23-29, 1992.

[2] M. Gustafsson, Use of dielectric sheets to increase the bandwidth of a planar self-complementary antenna array, *IEEE Antennas and Propagation Society International Symposium 2006*, pp. 2413-2416, 2006.

[3] D.M. Pozar, Microwave Engineering, *2nd Edition, Wiley*, pp.206-213, 1998.

[4] O. Luukkonen, C. Simovski, G. Granet, G. Goussetis, D. Lioubtchenko, A.V. Räisänen and S.A. Tretyakov, Simple and Accurate Analytical Model of Planar Grids and High-Impedance Surfaces Comprising Metal Strips or Patches, *IEEE Transactions on Antennas and Propagation*, Vol.56, No.6, pp.1624-1632, 2008

[5] D. Cavallo, A. Neto and G. Gerini, Green's Function Based Equivalent Circuits for Connected Arrays in Transmission and in Reception, *IEEE Transactions on Antennas and Propagation*, Vol.59, No.5, pp.1535-1545, 2011.

[6] F. Linot, Apport des Surfaces à Haute Impédance à la conception d'antennes réseaux compactes et d'antennes réseaux à très large bande passante, *PhD Thesis Telecom ParisTech*, April 7th 2011.

[7] F. Linot, X. Begaud, M. Soiron, C. Renard, M. Labeyrie, Characterization of a loaded high impedance surface, *International Journal of Microwave and Wireless Technologies*, Vol.1, Special Issue 06, pp. 483-487, 2009.

Design and measurement of a thin and light absorbing material for space applications

Yenny Pinto[1], Julien Sarrazin[2], Anne Claire Lepage[1], Xavier Begaud[1], Nicolas Capet[3]

[1]Institut Mines-Télécom, Télécom ParisTech, France
[2]UMPC Univ. Paris 06, UR2, L2E, Paris, France
[3]Centre National d'Etudes Spatiales, France

*corresponding author, E-mail: pintobal@telecom-paristech.fr

Abstract

This paper presents the design, realization and measurement of a thin lightweight absorbing material for space applications. Absorber design is based on High Impedance Surfaces (HIS) loaded with resistors and known as a Resistive High Impedance Surface (RHIS). The behaviour of RHIS is analysed at normal and oblique incidences for TE and TM polarizations. Prototypes have been realised and measured. Final design has a reflection coefficient less than -15dB in S-Band [2-2.3GHz] at normal incidence and till an angular dispersion of 40° for waves in TE polarization, and 35° for waves in TM polarization. Simulation results are validated by measurement.

1. Introduction

Absorbing material can be used to reduce the reflection of electromagnetic waves on a surface. For space applications, these materials may for example be placed on the satellite in order to reduce interference between antennas. Conventional design methods consist in the insertion of losses on the surface of the material. The Salisbury screen [1] is an example of this approach in which a resistive layer is placed on top of a metal surface at a distance equal to a quarter wavelength. The major drawback of this resonant structure is to operate on a narrow band of frequencies. The Jaumann absorber [2], consisting of several resistive layers spaced approximately by a quarter wavelength, operates over a wide band. However, this technique greatly increases the thickness of the structure.

In 2002, Engheta proposed to introduce metamaterials in the design of absorbers [3]. This approach has represented a technological breakthrough as it allows reducing drastically the thickness. Thus, in [4] the use of a High Impedance Surface (HIS) associated with a resistive material as absorber is presented. This type of structure, called Resistive High Impedance Surface (RHIS), consists in a FSS (Frequency Selective Surface) over a grounded dielectric slab. The FSS is usually a periodic array of printed patterns loaded with resistors or resistive sheets in order to achieve absorption. Such a material has the advantage of being lightweight and thin.

In this article, RHIS is optimized for good absorption performance ($|\Gamma| < -15$dB) in the band ([2 - 2.3GHz] 14%) at normal incidence, while fulfilling specific constraints for space applications as a low mass density (<2.5 kg/m²) and a thickness less than 50 mm. This structure is also analyzed at oblique incidence for TE and TM polarizations.

The paper is organized as follows: in the next Section, the design of the RHIS structure is described, in Section 3 the experimental validation and results are presented, and finally in Section 4 conclusions are given.

2. RHIS Design

The RHIS structure is composed of square patches interconnected by resistors on top of a grounded dielectric slab. Figure 1 shows the unit cell of the RHIS structure. It is composed of square copper patches over Rogers RO4003 substrate (ε_r = 3.38 + / -0.05). Below, are a honeycomb layer (ε_r = 1.08+ / -0.05) and the ground plane, consisting of a copper film. Interconnecting patches, resistors are formed with TICER resistive film with width W_{res} = 0.53mm, resistivity 100Ω/square and thickness t = 0.1µm which provides a resistance of 377 Ω.

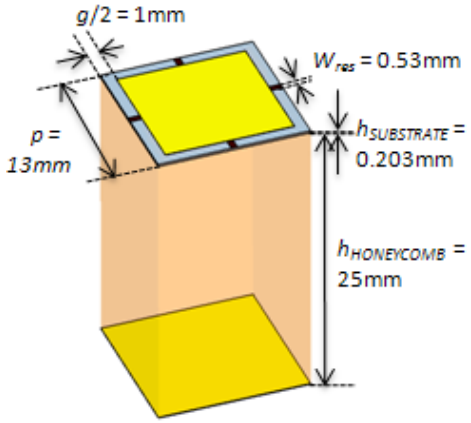


Figure 1: Unit Cell of RHIS.

The structure is simulated and optimized using the CST Microwave Studio (frequency solver) [5]. For simulations, only one cell is considered and periodical boundaries are applied.

2.1. Simulation results

The structure is optimized to obtain a reflection coefficient lower than -15dB (|Γ| < -15dB) in a wider band ([1.6 - 2.3GHz] 36%) than required ([2 - 2.3GHz] 14%) for normal incidence, in order to compensate, to some extent, the expected performance degradation when the incidence angle increases. This structure is also analyzed at oblique incidence for TE and TM polarizations. The simulations results are given in figures 2 and 3. A good absorption performance (|Γ| < -15dB) in the targeted band [2 - 2.3GHz] is observed at normal incidence for both polarizations. When the angular dispersion increases, the absorption level decreases and the frequency band shifts. Consequently, a reflection coefficient lower than -15dB in the 2-2.3 GHz band is limited to an angular dispersion of 40° for waves in TE polarization, and 35° for waves in TM polarization.

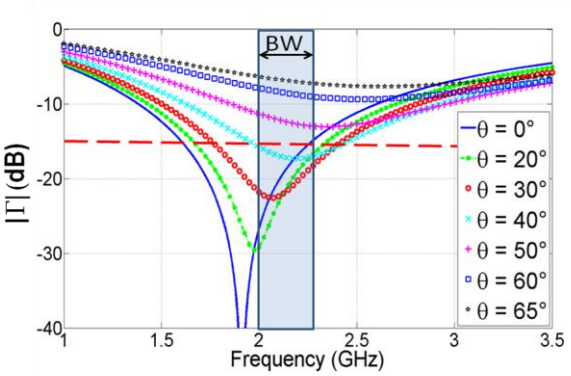


Figure 2: Simulated reflection coefficient at normal and oblique incidence. TE polarization (BW: required bandwidth).

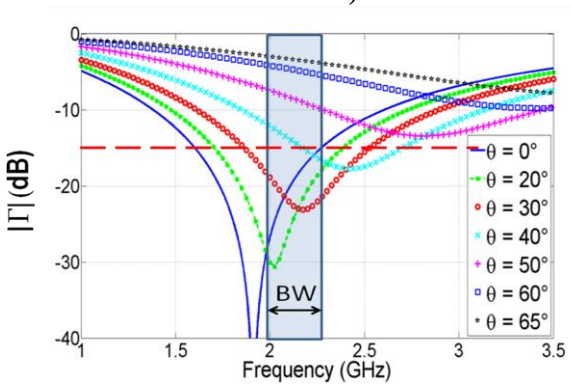


Figure 3: Simulated reflection coefficient at normal and oblique incidence. TM polarization (BW: required bandwidth).

3. Experimental validation

3.1. Prototype

Figure 4 shows the prototype. It is composed of three layers. The first one is a Rogers RO4003 substrate with the patches and the resistive sheet (TICER 100 Ω/square) above it. This layer has a thickness of 0.203 mm. The second layer consists in a honeycomb with a 25 mm thickness, and the third one is the ground plane (a copper sheet of 35 µm). All the layers are added together using double-sided adhesive film. The total thickness of the structure is about 25.3 mm (~0.17λ at 2.1GHz), thereby meeting the specifications.

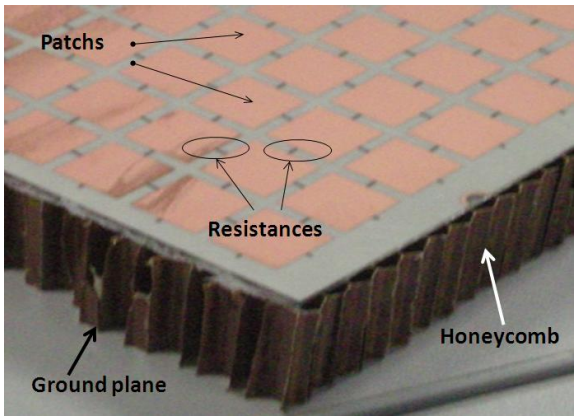


Figure 4: Prototype.

The total size of the prototype is 578x428 mm and the mass density is about 2.4 kg/m^2. Two prototypes are realized in order to validate the fabrication process and to compare the measurement.

3.2. Measurement setup

The measurement of the reflection coefficient of the absorbing material is carried out in three stages:

- Measurement with a reference metallic plane ($\Gamma_{_PEC}$)
- Measurement with the RHIS structure ($\Gamma_{_RHIS}$)
- Calculation of the reflection coefficient of material under test by using (1).

$$|\Gamma| = \frac{|\Gamma_{_RHIS}|}{|\Gamma_{_PEC}|} \qquad (1)$$

The reflection coefficient is measured using two horn antennas. These are positioned in front of the Material Under Test (MUT). The two horn antennas are connected to a network analyzer E5071C Agilent. The measurement setup at normal incidence is shown in Figure 5.

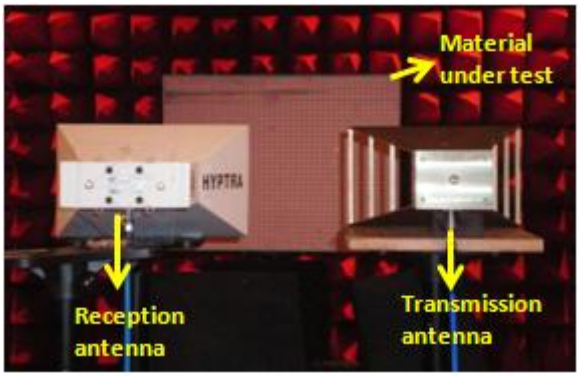


Figure 5: Measurement setup at normal incidence.

The antennas are positioned (Fig. 6) at a distance (d_{am}) of MUT and are separated by a distance (d_a). The material is positioned at a height of 1.15 m above the ground. Two different scenarios are investigated: a measurement in the laboratory and in an anechoic chamber. The objective is then to estimate if the RHIS structure is efficient in a perturbed environment like a laboratory.
The Figure 6 illustrates the measurement setup at oblique incidence. The distance between the antenna and MUT is d_{am} =107 cm. MUT is fixed and the antennas are displaced according to incidence angle (θ_i=θ_r).

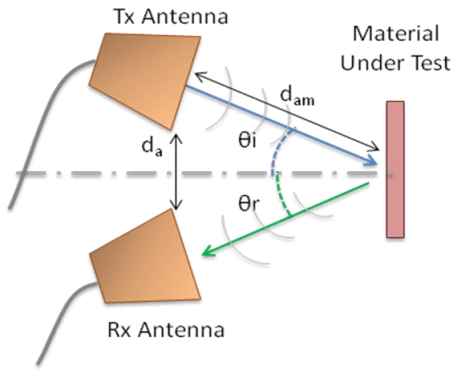


Figure 6: Measurement setup at oblique incidence.

3.3. Measurement results

Measurements were realized in two different environments. The first environment is an anechoic chamber where the conditions are suitable to eliminate external interferences and absorb reflections of electromagnetic waves. Second measurements are realized in a laboratory without ideal conditions. The figure 7 shows results at normal incidence comparing the measurements from two different environments and simulation. A good agreement between results is obtained however a shift in frequency band is observed. The influence of the environment is noticeable. Indeed, measurement in laboratory presents more oscillations than measurements in anechoic chamber. In order to explain the oscillations presence, different measurements, where the distance between antennas and material is changed are performed.
First, the distance (d_{am}) is changed from near field (d_{am}=35cm) to far field (d_{am} =130cm).

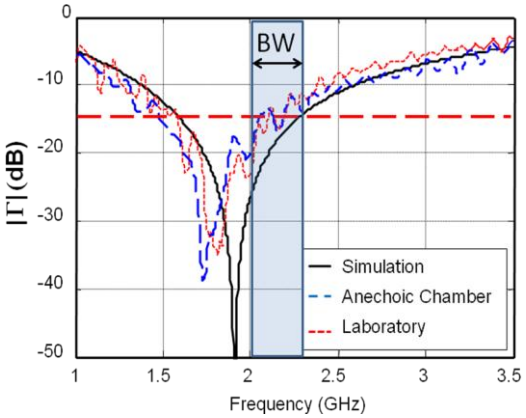


Figure 7: Comparison between simulation and measurements results at normal incidence (d_a= 8 cm, d_{am} =107cm).

The results are displayed in Figure 8. Differences in absorption levels are observed when measurements are realized in the near field. For all cases, the percentage of the frequency shift (according to simulation result) is about 10%. The oscillations are present in all cases.

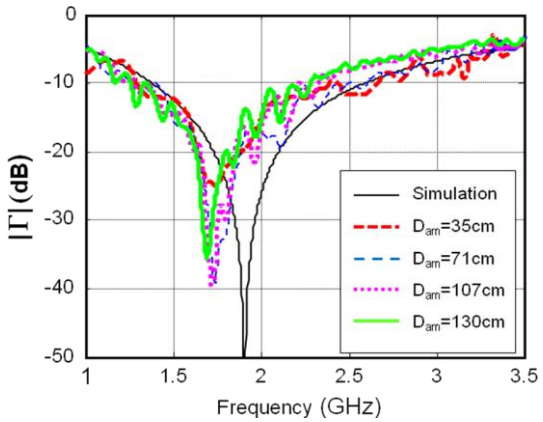


Figure 8: Inluence of the measurement distance (d_{am}) on the reflection coefficient (normal incidence, d_a= 8 cm).

Then, the influence of the separating distance between the antennas (d_a) is shown in figure 9.

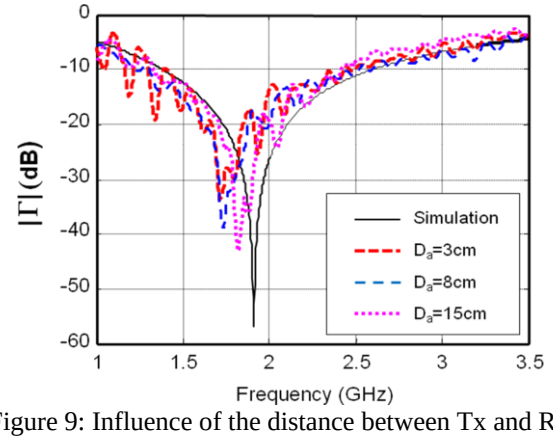


Figure 9: Influence of the distance between Tx and Rx Antennas (d_a) on the reflection coefficient (at normal incidence and with d_{am}= 107 cm).

The oscillations amplitude increases when the value of d_a decreases. Thus the coupling between the antennas is probably the cause of the oscillations. Moreover, this coupling may have an impact on measurements performances at oblique incidence.

For oblique incidence, the measurements are performed for angles 45 ° and 60 °. The results are plotted in figures 10 and 11 for TE polarization. All the following measurement have been realized in the laboratory (Fig. 10, 11, 12 and 13) with d_{am}= 107 cm. There is an agreement, but differences in frequency and level are observed. At oblique incidence for 45° and 60° requirements are not reached. In fact, after 35° bandwidth shifts to low frequencies and level increases.

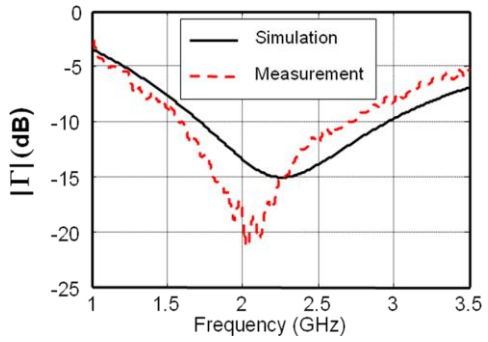


Figure 10: Comparison between simulation and measurements results at oblique incidence (45°). TE polarization.

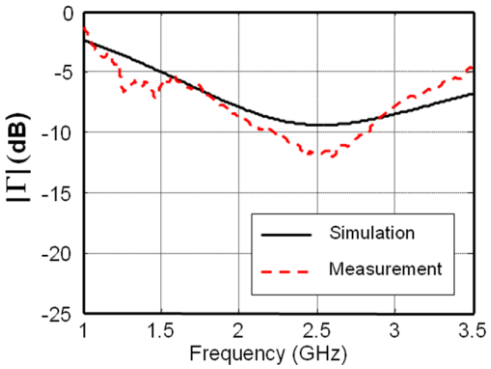


Figure 11: Comparison between simulation and measurements results at oblique incidence (60°). TE polarization.

Measurements for TM polarization are presented in figure 12 and 13.

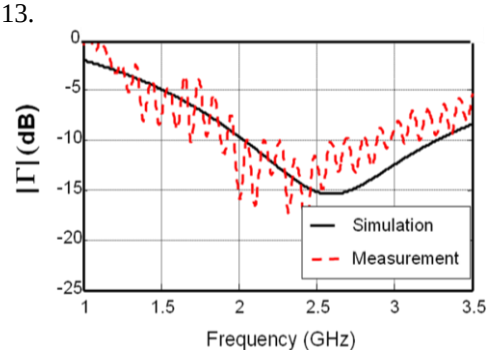


Figure 12: Comparison between simulation and measurements results at oblique incidence (45°). TM polarization.

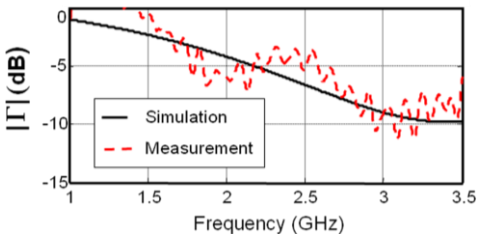


Figure 13: Comparison between simulation and measurements results at oblique incidence (60°). TM polarization.

Shifts in frequency and level can be explained by different ways:

- The imperfections of realisation.
- The simulation does not take into account the presence of the glue.
- The resistance value is not accurate and has a tolerance of + / - 10%.
- The permittivity value of honeycomb is not accurate.

In order to find explanations, further investigation will be driven to highlight and reduce all these uncertainties.

4. Conclusion

The design, realization and measurement of a thin lightweight absorbing material for space applications has been presented. Absorber design was based on High Impedance Surfaces (HIS) loaded with resistors and known as a Resistive High Impedance Surface (RHIS). The behaviour of RHIS has been analysed at normal and oblique incidences for TE and TM polarizations. Simulation results have been compared to measurement. Measurements were realized in two different environments: anechoic chamber and laboratory. There was a good agreement, despite some differences in frequency and level. Shifts in frequency and level can be explained by the imperfections of realisation, tolerances of materials and the glue not taken into account in the simulation.

Final design has a reflection coefficient less than -15dB in S-Band [2-2.3GHz] at normal incidence and till an angular dispersion of 40° for waves in TE polarization, and 35° for waves in TM polarization.

References

[1] W. W. Salisbury, *«Absorbent body for electromagnetic waves»*, U.S. Patent 2599944, June 1952.

[2] L. J. Du Toit, *«The Design of Jaumann Absorbers»*, IEEE Antennas and Propagation Magazine, vol. 36, no. 6, pp. 17-25, Dec. 1994.

[3] N. Engheta, *«Thin absorbing screens using metamaterial surfaces»*, IEEE Antennas and Propagation Symposium, vol. 2, pp. 392-395, 2002

[4] F. Costa, A. Monorchio, and G. Manara, *«Analysis and Design of Ultra Thin Electromagnetic Absorbers Comprising Resistively Loaded High Impedance*

Surfaces», IEEE Transactions on Antennas and Propagation, vol. 58, no.5, pp.1551-1558, May 2010.

[5] F. Linot, X. Begaud, M. Soiron, C. Renard and M. Labeyrie, *«Characterization of a loaded high impedance surface»*, International Journal of Microwave and Wireless Technologies, 1, pp 483-487, 2009.

Conception of Compact Patch Antenna Loaded With CRLH Metamaterial

Oussama Tabbabi[1], Mondher Labidi[1], Fethi Choubani[1], and Jacques David[2]

[1]Innov'com Research Laboratory, Higher School of Communications of Tunis,
Sup'Com University of Carthage, Tunisia
[2]ENSEEIHT (INPT) Laboratory France

Abstract

In This paper, a novel rectangular patch antenna is proposed and studied based on the Metamaterial Composite Right Left Handed (CRLH) transmission line (TL) model. It is a miniaturized Zeroth Order Resonance (ZOR) antenna designed on Reactive Impedance Surface (RIS). The miniaturization is provided by the use of vias that increase the Left Handed (LH) inductor and then push down the (LH) region. Simulated result at zeroth order resonance show improvement in the antenna gain by increasing a number of vias.

1. Introduction

Several Metamaterial realizations were presented using Transmission Line theory. They were done by [1-4], where a mushroom structure [2] is used for the realization of the High Impedance Surface (HIS) [5]. Microstrip antenna loaded with this CRLH metamaterial is able to excite the negative order resonance and provide decreased resonance frequencies [6]. It is shown that they have a good radiation and small size.

The basic structure of the CRLH metamaterial antenna as shown in Fig 1 is consist of (n) CRLH structures, ground plane, substrate and patch on the top of the substrate, a via connects the patch and the ground plane, and there is a gap between the adjacent patches. The Left Handed (LH) capacitance is provided by coupling of adjacent top patches while the LH inductance is provided by a via connected to the ground plane.

2. Antenna configuration and performance

Introducing the proposed antenna geometry, it consists of CRLH structure with two unit cells. Each unit cell consists of a ground plane, substrate, and patch on the top of the substrate. Three configurations are presented; the first one without mushrooms, the second one with one mushroom mushrooms inserted into each unit cell and the third has three vias per cell.

The antenna is printed on a thin substrate with dielectric constant $\varepsilon_r \approx 2.2$ and dimensions of $40 \times 40 \times 1.58 mm^3$. Two patches are printed on the substrate and each patch has dimensions of $15 \times 7.3 mm^2$ with a gap between the two patches of 0.2mm. A microstrip line, of $15 \times 1.54 mm^2$, is used to feed the first patch through a gap of 0.2mm. A vias with radius 0.12mm are used in each unit cell to introduce the shunt inductance. The gap between the patches is used to introduce the series capacitance.

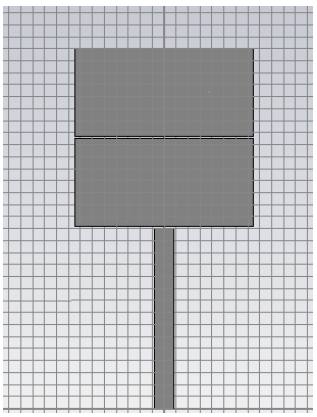


Figure 1: Microstrip antenna based on CRLH metamaterial

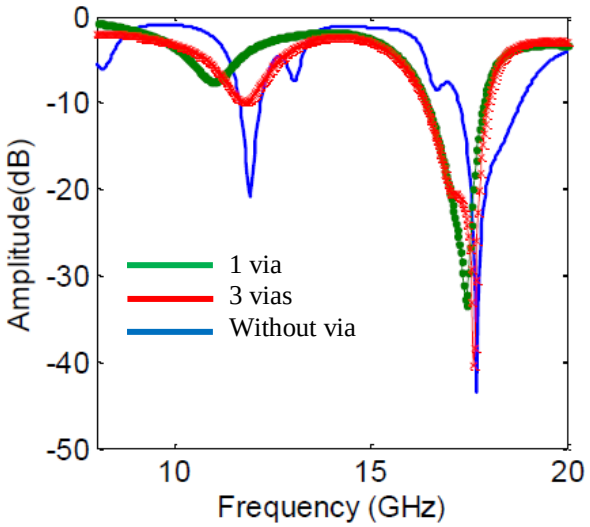


Figure 2: Effect of the mushroom on the return loss of the CRLH antenna.

The return loss properties of the usual patch antenna and the proposed CRLH antenna are plotted on figure 2. Also the electric filed distribution is visualized to convince the design of the true ZOR phenomenon.

The results of simulation show that the antenna has two resonances at the frequency 11.9GHz, and 17.3GHz. The return loss at the first resonance for one vias is -8dB, whereas it is -9.8dB for three vias. At the second resonance for one vias is -34dB, whereas it is -41dB for three vias.

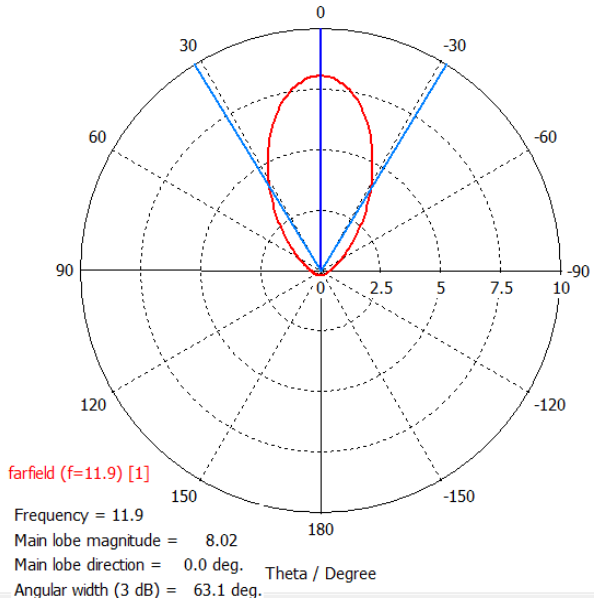


Figure 3: Simulated far-field pattern at first order resonant frequency of a patch antenna without via

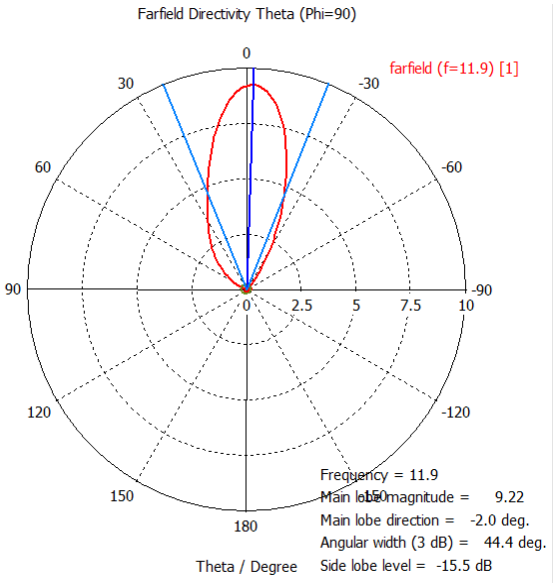


Figure 4: Simulated far-field pattern at first order resonant frequency of a patch antenna with 1 via per patch

Fig 3, 4 and 5 show the far-field radiation pattern results at 11.9GHz. The maximum gain is 8.02dB for without-via configuration, 9.22dB for one via configuration and 11.22dB for three vias configuration.

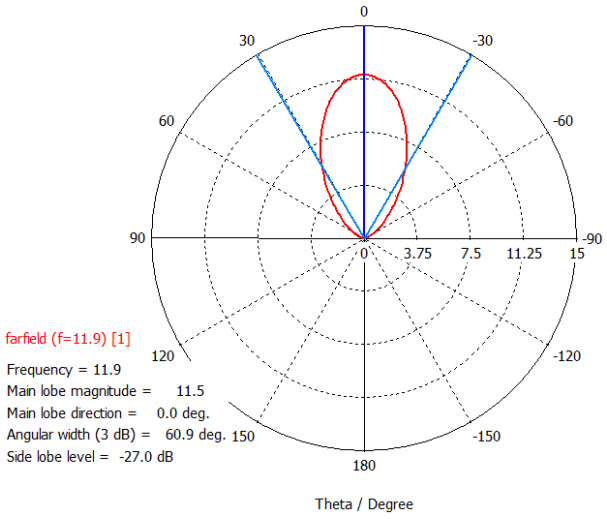


Figure 5: Simulated far-field pattern at first order resonant frequency of a patch antenna with 3 vias per patch

It is shown, that by increasing the number of mushrooms structure, the first operating frequency has been pushed up from 10.9GHz to 11.8GHz. It should be pointed out that the number of mushroom structure can be further increased to reduce the antenna dimension.

3. Conclusions

A novel planar antenna using CRLH structures and loaded with vias has been presented and studied. The designed antennas use the theory of the CRLH-TL to realize negative permeability and permittivity in the LH region. It is shown improving of gain can be obtained by increasing a vias number.

References

[1] A. Sanada, C. Caloz, and T. Itoh, Planar distributed structures with negative refractive index, IEEE Trans Microwave Theory Tech 52 (2004).

[2] C. Caloz and T. Itoh, *Electromagnetic Metamaterials: Transmission Line Theory and Microwave Applications*, Wiley, Hoboken, NJ, 2006.

[3] A. Lai, C. Caloz, and T. Itoh, Composite right/left-handed transmission line metamaterials. *IEEE Microwave Mag* (2004), 33–50.

[4] F. Qureshi, M.A. Antoniades, and G.V. Eleftheriades, A compact and low-profile metamaterial ring antenna with vertical polarization, *IEEE Antennas Propag* Lett 4 (2005), 333–336.

[5] D. Sievenpiper, L. Zhang, R. F. J. Broas, N. G. Alexopolus, and E. Yablonovitch, High-impedance lectromagnetic surfaces with a forbidden frequency band, *IEEE Trans. Microwave Theory Tech*., vol. 47, pp. 2059–2074, 1999.

[6] H. R. Stuart and A. Pidwerbetsky, Electrically small antenna elements using negative permittivity resonators, *IEEE Trans. Antennas Propag*., vol. 54, no. 6, pp. 1644–1653, Jun. 2006.

Analytical and numerical modelling of complex materials and structure

Microwave scattering diagrams of three-layered SiC-metamaterial/ gyrotropic ferrite-SiC cylinders

Juozas Bucinskas[1], Liudmila Nickelson[2,3], Romanas Martavicius[2]

[1]Physics Department, Vilnius University, Vilnius, Lithuania
[2]Vilnius Gediminas Technical University, Vilnius, Lithuania
[3]The State Research Institute Center for Physical Sciences and Technology, Vilnius, Lithuania
*corresponding author, E-mail: lucynickelson@gmail.com

Abstract

We present here for the first time the rigorous solution of boundary diffraction problem about the microwave scattering by a multilayered 2D cylinder. The cylinder layers may be made of isotropic or uniaxial anisotropic or electrically and (or) magnetically gyrotropic materials. The number and thickness of layers may have arbitrary values in our solution. We calculated scattering diagrams (a radial component of real part of the Poynting vector) inside and outside of cylinder using the solution. Here we present scattering diagrams from three - layered cylinder made of SiC and metamaterial UCSD30815 or saturate magnetized ferrite ISCh4. Diagrams were computed for wave incidence angles $\theta=\pi/2$, $\pi/3$, $\pi/6$ inside of metamaterial/ferrite layer at the distance 1 mm and outside of cylinder at the distance 2.5 mm from the cylinder axis.

Keywords: scattering problem, novel rigorous solution, partial domain method, multilayer cylinder, isotropic, uniaxial anisotropic, electrically and magnetically gyrotropic materials.

1. Introduction

Boundary problems of microwave scattering by cylinder obstacles made of conductor, dielectric, metamaterial, semiconductor and ferrite materials have been studied for a long period of time because the problems are very important in radar, satellite, optical imaging system, signal processing, security system, atmospheric science, invisible cloak realization technologies [1-6]. The different microwave elements like a conductor cylindrical plate or other material scattering bodies located close to an antenna can improve the total antenna characteristics, e.g. enhance an antenna bandwidth and reduce antenna sizes [7].

For this reason very important to develop new electrodynamical methods and algorithms for solving of listed problems. A new iterative technique based on the *T*-matrix approach is proposed for the electromagnetic (EM) scattering by dielectric cylinders with finite length. The incident, scattered, and internal fields are expressed in terms of the spherical harmonics [2]. An algorithm for the investigation of scattering properties of multilayered metamaterial and some other materials is given in [3]. Here the incident EM field source is an infinite line with an electric current. The algorithm is based on the eigenfunction expansion and has wide possibilities for numerical investigations [3]. In the article [4] is given the EM analysis of uniaxial multilayer cylinders and is described the developed algorithm of spectral-domain Green's functions of uniaxial multilayer structures with arbitrary number of layers. The full-wave scattering theory was used in [5] to solve a diffraction problem about a magneto-dielectric anisotropic coated cylinder of infinite length when the one is normally illuminated by a transverse magnetic (TM) polarized plane wave. A fast solution for rigorously deriving spatial-domain dyadic Green's functions for the planar multilayer uniaxial media is presented in [6]. The validation of the proposed algorithm and the accuracy of the dyadic Green's function are proved in the mentioned article.

The solution of scattering problem for a multilayered infinite length cylinder with isotropic magneto-dielectric layers is presented in our articles [8, 9] and with uniaxial anisotropic layers, when the anisotropy axis was parallel to a cylinder axis, is given in [10]. In both cases, the solutions of tasks were presented as a superposition of transversal electric (TE) and transversal magnetic (TM) waves.

Here we are going to describe more general solution of diffraction problem about the microwave scattering by a multilayered cylinder of infinite length containing also ε- and (or) μ- gyrotropic layers. This general solution cannot be taken as a superposition of TE and TM waves.

2. Problem formulation and theoretical consideration

The main task for solving of the scattering problem for a multilayer cylinder is to find a solution of Maxwell's equations for an every layer of the cylinder.

We used the partial domain method for solution of the scattering problem and the standard boundary condition, i.e. the equalization of tangential components of electrical and magnetical field components on the surface between layers with different mediums.

When a cylinder layer substance possesses the gyrotropy (magnetize ferrite or/and semiconductor) then the substance properties are described by tensors of the permeability $\hat{\mu}$ or/and the permittivity $\hat{\varepsilon}$ in the Cartesian coordinates in the form:

$$\hat{\mu}=\begin{vmatrix}1+\chi_\mu & i\nu_\mu & 0\\ -i\nu_\mu & 1+\chi_\mu & 0\\ 0 & 0 & \mu_p\end{vmatrix},\quad \hat{\varepsilon}=\begin{vmatrix}1+\chi_\varepsilon & i\nu_\varepsilon & 0\\ -i\nu_\varepsilon & 1+\chi_\varepsilon & 0\\ 0 & 0 & \varepsilon_p\end{vmatrix}. \qquad (1)$$

The solution of the Maxwell's equations is not possible to express through the superposition of TE and TM waves in general case, i.e. when the material of cylinder layer is described by one of tensors (1) or both ones (1), as well as the incident EM wave propagation is not perpendicular to the cylindrical axis, i.e. the incidence angle $\theta \neq 90°$. Below we are going to present in detail the new method of the Maxwell's equations' solution for the general case of scattering problem which is more complicated than partial ones.

Our solution let us to summarize the geometry of cylinder cladding, where the concentric layers can be made of isotropic, uniaxial anisotropic materials as well as the gyrotropic materials that are described by tensors (1) when the layers can be placed in any order, and the core of cylinder could be made of a perfectly conducting material.

The relations of the cyclic coordinates with the basic unit vectors $\vec{e}_{+1}$, $\vec{e}_{-1}$, $\vec{e}_0$ and the Cartesian system orts $\vec{n}_x$, $\vec{n}_y$, $\vec{n}_z$ .are

$$\vec{e}_{+1}=-\frac{1}{\sqrt{2}}(\vec{n}_x+i\vec{n}_y),\quad \vec{e}_{-1}=\frac{1}{\sqrt{2}}(\vec{n}_x-i\vec{n}_y),$$
$$\vec{e}_0=\vec{n}_z \qquad (2)$$

and the corresponding relations for the covariant coordinates are:

$$x_{+1}=-\frac{1}{\sqrt{2}}(x+iy),\quad x_{-1}=\frac{1}{\sqrt{2}}(x-iy),\quad x_0=z\ . \qquad (3)$$

The permeability and permittivity tensors in the cyclic coordinates have the forms:

$$\hat{\mu}=\begin{vmatrix}\mu_{+1} & 0 & 0\\ 0 & \mu_{-1} & 0\\ 0 & 0 & \mu_p\end{vmatrix},\quad \hat{\varepsilon}=\begin{vmatrix}\varepsilon_{+1} & 0 & 0\\ 0 & \varepsilon_{-1} & 0\\ 0 & 0 & \varepsilon_p\end{vmatrix}\ , \qquad (4)$$

where
$\varepsilon_{+1}=1+\chi_\varepsilon+\nu_\varepsilon$, $\varepsilon_{-1}=1+\chi_\varepsilon-\nu_\varepsilon$, $\mu_{+1}=1+\chi_\mu+\nu_\mu$, $\mu_{-1}=1+\chi_\mu-\nu_\mu$. It should be noted that the both tensors (1) in the cyclic coordinates became diagonal ones (4). It is known that in the Cartesian system coordinate if the tensors have the form (4) then there are non-diagonal terms of these tensors in the cyclic coordinates.

The cylindrical symmetry of the cylinder suggests using the cylindrical coordinate system. It can be written the relations on the basis of formula (3):

$$x_{+1}=-\frac{1}{\sqrt{2}}\rho e^{i\varphi},\quad x_{-1}=\frac{1}{\sqrt{2}}\rho e^{-i\varphi},\quad x_0=z\,. \qquad (5)$$

Covariant coordinates can be introduced by the common rules and be written in the form:

$$x^{+1}=\frac{1}{\sqrt{2}}\rho e^{-i\varphi},\quad x^{-1}=-\frac{1}{\sqrt{2}}\rho e^{i\varphi},\quad x^0=z \qquad (6)$$

The Maxwell's equations for harmonic EM fields (when the time dependency is determined as $\exp(i\omega t)$) are written on the projections:

$$ihH_{+1}-\nabla_{+1}H_0=\gamma_{+1}E_{+1}, \qquad (7.1)$$

$$\nabla_{-1}H_0-ihH_{-1}=\gamma_{-1}E_{-1}, \qquad (7.2)$$

$$\nabla_{-1}H_{+1}-\nabla_{+1}H_{-1}=\gamma_pE_0, \qquad (7.3)$$

$$ihE_{+1}-\nabla_{+1}E_0=-\beta_{+1}H_{+1}, \qquad (7.4)$$

$$\nabla_{-1}E_0-ihE_{-1}=-\beta_{-1}H_{-1}, \qquad (7.5)$$

$$\nabla_{-1}E_{+1}-\nabla_{+1}E_{-1}=-\beta_pH_0. \qquad (7.6)$$

Here $\nabla_j=\frac{\partial}{\partial x^j}$, $\gamma_j=\omega\varepsilon_0\varepsilon_j$, $\beta_j=\omega\mu_0\mu_j$, $j=\{+1,-1,p\}$, $\omega=2\pi f$ is an angular frequency of incident microwave, f is the operating frequency, ε_0 is the free space permittivity, μ_0 is the free space permeability.

$$\nabla_{+1}=-\frac{1}{\sqrt{2}}\left(e^{i\varphi}\frac{\partial}{\partial\rho}+\frac{i}{\rho}e^{i\varphi}\frac{\partial}{\partial\varphi}\right),$$

$$\nabla_{-1}=\frac{1}{\sqrt{2}}\left(e^{-i\varphi}\frac{\partial}{\partial\rho}-\frac{i}{\rho}e^{-i\varphi}\frac{\partial}{\partial\varphi}\right),\quad \nabla_0=\frac{\partial}{\partial z}\,. \qquad (8)$$

A further reorganization in the system (7) is more convenient to perform after the integral Fourier transformation with respect to the coordinate x^0.

We have deduced expressions (9.1-9.3) when equations (7.1) and (7.4) with respect to unknown functions E_{+1} and H_{+1} and system equations (7.2) and (7.5) with respect to unknown functions E_{-1} and H_{-1} has been resolved:

$$E_{+1}=\frac{1}{\beta_{+1}\gamma_{+1}-h^2}\left\{ih\nabla_{+1}E_0-\beta_{+1}\nabla_{+1}H_0\right\}, \qquad (9.1)$$

$$H_{+1}=\frac{1}{\beta_{+1}\gamma_{+1}-h^2}\left\{\gamma_{+1}\nabla_{+1}E_0+ih\nabla_{+1}H_0\right\}, \qquad (9.2)$$

$$E_{-1}=\frac{1}{\beta_{-1}\gamma_{-1}-h^2}\left\{ih\nabla_{-1}E_0+\beta_{-1}\nabla_{-1}H_0\right\}, \qquad (9.3)$$

$$H_{-1}=\frac{1}{\beta_{-1}\gamma_{-1}-h^2}\left\{-\gamma_{-1}\nabla_{-1}E_0+ih\nabla_{-1}H_0\right\}. \qquad (9.4)$$

Here h is the Fourier parameter. We have received the coupled differential equation system (10) with respect to unknown functions E_0 and H_0 from (7.3) and (7.6).

$$\left\{-\nabla_{-1}\frac{\gamma_{+1}}{\beta_{+1}\gamma_{+1}-h^2}\nabla_{+1}-\nabla_{+1}\frac{\gamma_{-1}}{\beta_{-1}\gamma_{-1}-h^2}\nabla_{-1}+\gamma_p\right\}E_0$$
$$-ih\left\{\nabla_{-1}\frac{1}{\beta_{+1}\gamma_{+1}-h^2}\nabla_{+1}-\nabla_{+1}\frac{1}{\beta_{-1}\gamma_{-1}-h^2}\nabla_{-1}\right\}H_0=0, \qquad (10.1)$$

$$ih\left\{\nabla_{-1}\frac{1}{\beta_{+1}\gamma_{+1}-h^2}\nabla_{+1}-\nabla_{+1}\frac{1}{\beta_{-1}\gamma_{-1}-h^2}\nabla_{-1}\right\}E_0$$
$$+\left\{-\nabla_{-1}\frac{\beta_{+1}}{\beta_{+1}\gamma_{+1}-h^2}\nabla_{+1}-\nabla_{+1}\frac{\beta_{-1}}{\beta_{-1}\gamma_{-1}-h^2}\nabla_{-1}+\beta_p\right\}H_0=0. \quad (10.2)$$

It is possible to find the analytical solution of system (10) when the permeability and permittivity tensors (4) are independent on the coordinates. In this case the system (10) can be written:

$$\begin{aligned}&\{\Delta_\perp+q_1\}\ E_0-iq_2\Delta_\perp H_0=0,\\ &ip_2\Delta_\perp E_0+\{\Delta_\perp+p_1\}\ H_0=0,\end{aligned} \quad (11)$$

where
$$q_1=\frac{2\varepsilon_p k^2 S_{+1}S_{-1}}{\varepsilon_{+1}S_{-1}+\varepsilon_{-1}S_{+1}}, \quad (12.1)$$
$$q_2=\frac{\xi Z_0\left(S_{+1}-S_{-1}\right)}{\varepsilon_{+1}S_{-1}+\varepsilon_{-1}S_{+1}}, \quad (12.2)$$
$$p_1=\frac{2\mu_p k^2 S_{+1}S_{-1}}{\mu_{+1}S_{-1}+\mu_{-1}S_{+1}}, \quad (12.3)$$
$$p_2=\frac{\xi}{Z_0}\frac{S_{+1}-S_{-1}}{\mu_{+1}S_{-1}+\mu_{-1}S_{+1}}, \quad (12.4)$$
$$\Delta_\perp=\frac{1}{\rho}\frac{\partial}{\partial\rho}\rho\frac{\partial}{\partial\rho}+\frac{1}{\rho^2}\frac{\partial}{\partial\varphi^2}, \quad (12.5)$$
$$S_{\pm1}=\varepsilon_{\pm1}\mu_{\pm1}-\xi^2, \quad (12.6)$$
$$k=\frac{\omega}{c}=\omega\sqrt{\varepsilon_0\mu_0}, \quad (12.7)$$
$$\xi=\frac{h}{k},\quad Z_0=\sqrt{\frac{\mu_0}{\varepsilon_0}}=120\pi. \quad (12.8)$$

We can see from formulae (11) and (12) that both equations of system (11) uncoupled when $\varepsilon_{+1}\mu_{+1}=\varepsilon_{-1}\mu_{-1}$ or when the incident EM wave propagates normally to the axis of the cylinder ($\xi=0$). In the last two cases the solution is simpler and can be expressed through the superposition of TE and TM modes. The solution of the system (11) is sought in the form of infinite series:

$$E_0=\sum_{m=-\infty}^{\infty}E_{0m}(\rho)\exp(im\varphi), \quad (13.1)$$
$$H_0=\sum_{m=-\infty}^{\infty}H_{0m}(\rho)\exp(im\varphi). \quad (13.2)$$

The substitution of functions (13) into the system of equations (11) and using the orthogonality of functions $\exp(im\varphi)$ let us to obtain the ordinary differential equation system with respect to unknown functions E_{0m} and H_{0m}.

$$\left\{\frac{1}{\rho}\frac{\partial}{\partial\rho}\rho\frac{\partial}{\partial\rho}-\frac{m^2}{\rho^2}+q_1\right\}E_{0m}$$
$$-iq_2\left\{\frac{1}{\rho}\frac{\partial}{\partial\rho}\rho\frac{\partial}{\partial\rho}-\frac{m^2}{\rho^2}\right\}H_{0m}=0, \quad (14.1)$$

$$ip_2\left\{\frac{1}{\rho}\frac{\partial}{\partial\rho}\rho\frac{\partial}{\partial\rho}-\frac{m^2}{\rho^2}\right\}E_{0m}$$
$$+\left\{\frac{1}{\rho}\frac{\partial}{\partial\rho}\rho\frac{\partial}{\partial\rho}-\frac{m^2}{\rho^2}+p_1\right\}H_{0m}=0. \quad (14.2)$$

We have sought the solution of the differential equations' system (14) in the form:

$$E_{0m}=C_m^{(e)}Q_m(\lambda\rho), \quad (15.1)$$
$$H_{0m}=C_m^{(h)}Q_m(\lambda\rho), \quad (15.2)$$

where $C_m^{(e)}$, $C_m^{(h)}$ are constants, $Q_m(\lambda\rho)$ is a cylindrical function of any kind with integer index m. When we substitute expressions (15) into equations (14) we get:

$$\left\{-\lambda^2+q_1\right\}C_m^{(e)}+iq_2\lambda^2C_m^{(h)}=0, \quad (16.1)$$
$$-ip_2\lambda^2C_m^{(e)}+\left\{-\lambda^2+p_1\right\}C_m^{(h)}=0. \quad (16.2)$$

We find the parameter λ values from the coupled system of equations (16) based on the requirements of the existence of nontrivial solution. The system (16) has nontrivial solution when the condition (17) is satisfied.

$$\begin{vmatrix}q_1-\lambda^2 & iq_2\lambda^2\\ -ip_2\lambda^2 & p_1-\lambda^2\end{vmatrix}=0. \quad (17)$$

The equation (17) is the biquadratic equation with respect to the parameter λ:

$$\lambda^4(1-q_2p_2)-\lambda^2(q_1+p_1)+q_1p_1=0. \quad (18)$$

The solution of the biquadratic equation (18) is:

$$\lambda^2_{1,2}=\frac{1}{(1-q_2p_2)}\times\left\{\frac{p_1+q_1}{2}\pm\sqrt{\left(\frac{p_1-q_1}{2}\right)^2+q_1p_1q_2p_2}\right\}. \quad (19)$$

The denominator of expression (19) can be represented as $1-q_2p_2=$

$$\frac{\left(\mu_{+1}+\mu_{-1}\right)\left(\varepsilon_{+1}+\varepsilon_{-1}\right)}{\left(\varepsilon_{+1}S_{-1}+\varepsilon_{-1}S_{+1}\right)\left(\mu_{+1}S_{-1}+\mu_{-1}S_{+1}\right)}. \quad (20)$$

Expression (20) for substrata that are described by the permeability and (or) permeability tensors (4) cannot be equal zero, for this reason the solutions (19) everywhere are finite. We introduce a notation for convenience:

$$\omega_1=+\sqrt{\lambda_1^2}, \quad (21.1)$$
$$\omega_2=+\sqrt{\lambda_2^2}. \quad (21.2)$$

The solution of the ordinary differential equation system (14) are:

$$E_{0m} = C_{1m} Q_m(\omega_1\rho) + C_{2m} Q_m(\omega_2\rho), \quad (22.1)$$

$$H_{0m} = P_1 C_{1m} Q_m(\omega_1\rho) + P_2 C_{2m} Q_m(\omega_2\rho). \quad (22.2)$$

Here the coefficients are:

$$P_1 = \frac{i(q_1 - \lambda_1^2)}{q_2\lambda_1^2}, \quad P_2 = \frac{i(q_1 - \lambda_2^2)}{q_2\lambda_2^2}. \quad (23)$$

In this way, we get just a single pair system (14) solutions, because for the cylindrical functions with the integer indexes is valid the ratio $Q_m(-z) = (-1)^m Q_m(z)$, z is an argument of a certain function. If we take instead of $Q_m(\lambda\rho)$ other independent solution of the Bessel equation then we get another couple of independent solutions of system (14).

The general solution of the radial function for a cylindrical gyrotropic layer can be written:

$$E_{0m} = A_m^{(1)} Q_m^{(1)}(\omega_1\rho) + A_m^{(2)} Q_m^{(2)}(\omega_1\rho) + A_m^{(3)} Q_m^{(1)}(\omega_2\rho) + A_m^{(4)} Q_m^{(2)}(\omega_2\rho), \quad (24.1)$$

$$H_{0m} = A_m^{(1)} P_1 Q_m^{(1)}(\omega_1\rho) + A_m^{(2)} P_1 Q_m^{(2)}(\omega_1\rho) + A_m^{(3)} P_2 Q_m^{(1)}(\omega_2\rho) + A_m^{(4)} P_2 Q_m^{(2)}(\omega_2\rho). \quad (24.2)$$

Here $Q_m^{(1)}$ is the first kind and $Q_m^{(2)}$ is the second kind of Bessel equation' solutions.

A selection of function kind depends on a layer's place in the multilayer cylinder. The approach to the implementation of this procedure is the same as in our articles [8-10].

It is worth to mention that if $\xi \neq 0$ and at least one of the coefficients of expression (24.1) is not equal to zero, then the components of the electrical E_0 and magnetical H_0 fields are not equal to zero at the same time, i.e. the waves are hybrid ones and a solution in form of superposition TE and TM modes is not exist.

The system equations (14.1) and (14.2) uncoupled when

$$q_2 = 0 \ \cup \ p_2 = 0. \quad (25)$$

We can see from formulae (12.2) and (12.4) that both equality satisfy when 1) $\xi = 0$ or (and) 2) $\mu_{+1}\varepsilon_{+1} = \mu_{-1}\varepsilon_{-1}$. We can write the problem solution as a superposition of TE and TM waves at these two cases.

The condition $\xi = 0$ means that the incident EM wave propagates in the perpendicular direction to the cylinder axis. In this case the argument of radial function for the TE wave is $\sqrt{p_1}\rho$ and, accordingly, of the TM wave is $\sqrt{q_1}\rho$. Because in the general case the arguments of radial functions are different for this reason a degeneration of solutions vanish and we can separate the TE and TM modes with the same index m .We can distinguish these modes by the space distribution of electrical and magnetical fields.

Please pay attention that cases 1) $\xi = 0$ and 2) $\mu_{+1}\varepsilon_{+1} = \mu_{-1}\varepsilon_{-1}$ differ significantly. In the first case q_1 and p_1 are equal:

$$q_1 = 2k^2 \frac{\varepsilon_p \mu_{+1}\mu_{-1}}{\mu_{+1} + \mu_{-1}}, \quad p_1 = 2k^2 \frac{\mu_p \varepsilon_{+1}\varepsilon_{-1}}{\varepsilon_{+1} + \varepsilon_{-1}}, \ P_1 = P_2 = 1.$$

The expression for second case is valid for a uniaxial medium:

$\mu_{+1} = \mu_{-1} = \mu_t$ $\varepsilon_{+1} = \varepsilon_{-1} = \varepsilon_t$, $S_{+1} = S_{-1} = \varepsilon_t\mu_t - \xi^2$ and we have:

$$q_1 = k^2 \frac{\varepsilon_p}{\varepsilon_t}\left(\varepsilon_t\mu_t - \xi^2\right), \ p_1 = k^2 \frac{\mu_p}{\mu_t}\left(\varepsilon_t\mu_t - \xi^2\right), \quad P_1 = P_2 = 1.$$

Such expressions were early presented in our work [10].

Condition 2) can be satisfied do not only for uniaxial medium but also when $S_{+1} = S_{-1} = S$. Then the value of parameter λ again can be described by relations (16) and expression can be written:

$$q_1 = 2k^2 \frac{\varepsilon_p S}{\mu_{+1} + \mu_{-1}}, \quad p_1 = 2k^2 \frac{\mu_p S}{\varepsilon_{+1} + \varepsilon_{-1}}, \quad P_1 = P_2 = 1.$$

These expressions dependent also on the angle ϑ, which is between the wave vector of the incident wave and the cylinder axis, because $\xi = \cos\vartheta$.

Amplitudes $A_m^{(l)}$, $l = 1,...,4$ of different layers are matched by standard boundary conditions on an interface of the cylindrical layers filled with different materials. The boundary conditions require the equality of the tangential component of EM field on the interface between two different materials. Matching procedure is the same as in [8], [10]. We can express the transverse EM field components after substituting the relations (24) into expressions (9) and at the same time we have the solution of the Maxwell's equations.

The analysis of microwave scattering distribution is usually accompanied by defining the radial components of the Poynting vector at fixed distances on the cylinder axis, i.e. microwave scattering diagram (pattern). Scattering and absorption characteristics depend on the material properties of the scattering body, its geometry, frequency, propagating direction and polarization of the incident wave. The scattered energy per oscillation period per unit length is pretty convenient for the investigation of scattering phenomena here. This quantity is proportional to the scattering (absorption) cross section per unit length. The Poynting vector radial component is equal to

$$P_\rho = \frac{i}{\sqrt{2}}\left(E_{+1}H_0^* + E_0 H_{-1}^*\right)\exp(-i\varphi) + \frac{i}{\sqrt{2}}\left(E_0 H_{+1}^* + E_{-1}H_0^*\right)\exp(i\varphi). \quad (26)$$

In the formula (26) is presented the ρ component of energy flux density at the point $\vec{r} = \rho\vec{n}_\rho$. The average scattered (absorbed) energy over the oscillation period for the unit length of cylinder on a cylinder area of radius ρ is:

$$W = \frac{1}{2}\int_0^{2\pi} \rho P_\rho(\rho,\varphi)d\varphi. \quad (27)$$

There are sets of coefficients $A_m^{(l)}$, $l = 1,...,4$ in the case of multilayered cylinder. These coefficients define the EM fields inside the layer that contains the points $\vec{r} = \rho\vec{n}_\rho$.

If the points are on the external surface of the cylinder, then we use the amplitude of scattered (reflected) waves only.
We can find the scattered power values per oscillation period for the unit cylinder length according to the same formula (27). It is easy to obtain analytical expressions (28) and (29) for integral (27).

$$W=\frac{\rho}{4k}\sum_{m=-\infty}^{\infty}\left\{-\frac{\xi}{S_{+1}}E_m^{+1}H_m^{0*}-\frac{\xi}{S_{-1}}E_m^{-1}H_m^{0*}\right.$$
$$-\frac{iZ_0\mu_{+1}}{S_{+1}}H_m^{+1}H_m^{0*}+\frac{iZ_0\mu_{-1}}{S_{-1}}H_m^{-1}H_m^{0*}+\frac{i\varepsilon_{+1}^*}{Z_0S_{+1}^*}E_m^0E_m^{+1*}$$
$$\left.-\frac{i\varepsilon_{-1}^*}{Z_0S_{-1}^*}E_m^0E_m^{-1*}+\frac{\xi^*}{S_{+1}^*}E_m^0H_m^{+1*}+\frac{\xi^*}{S_{-1}^*}E_m^0H_m^{-1*}\right\} \quad (28)$$

where

$$E_m^0=A_m^{(1)}Q_m^{(1)}(\omega_1\rho)+A_m^{(2)}Q_m^{(2)}(\omega_1\rho)$$
$$+A_m^{(3)}Q_m^{(1)}(\omega_2\rho)+A_m^{(4)}Q_m^{(2)}(\omega_2\rho) \quad (29.1)$$

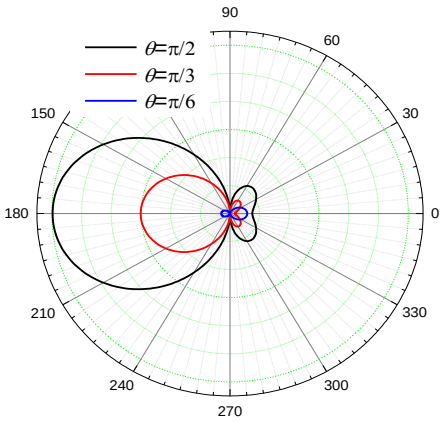
$$H_m^0=A_m^{(1)}P_1Q_m^{(1)}(\omega_1\rho)+A_m^{(2)}P_1Q_m^{(2)}(\omega_1\rho)$$
$$+A_m^{(3)}P_2Q_m^{(1)}(\omega_2\rho)+A_m^{(4)}P_2Q_m^{(2)}(\omega_2\rho) \quad (29.2)$$

$$E_m^n=A_m^{(1)}\omega_1Q_{m+n}^{(1)}(\omega_1\rho)+A_m^{(2)}\omega_1Q_{m+n}^{(2)}(\omega_1\rho)$$
$$+A_m^{(3)}\omega_2Q_{m+n}^{(1)}(\omega_2\rho)+A_m^{(4)}\omega_2Q_{m+n}^{(2)}(\omega_2\rho), \quad (29.3)$$
$$n=+1,-1$$

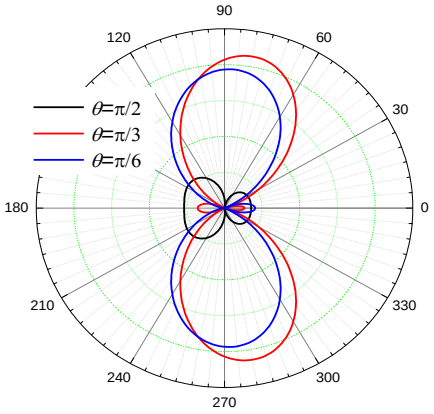
$$H_m^n=A_m^{(1)}\omega_1P_1Q_{m+n}^{(1)}(\omega_1\rho)+A_m^{(2)}\omega_1P_1Q_{m+n}^{(2)}(\omega_1\rho)$$
$$+A_m^{(3)}\omega_2P_2Q_{m+n}^{(1)}(\omega_2\rho)+A_m^{(4)}\omega_2P_2Q_{m+n}^{(2)}(\omega_2\rho), \quad (29.4)$$
$$n=+1,-1.$$

Parameters and numerical calculations

Here we present the scattering microwave power diagrams of three-layered cylinder (Figs 1-3). The core of cylinder has radius 0.5 mm, the middle layer radius is 1.5 mm and the external cylinder radius is 2.0 mm. Numerical calculations were made for the incident plane harmonic monochromatic microwave with the operating frequency f =12 GHz. Our computer program is written in Fortran.
The core of cylinder and it external layer are made of SiC material. This material is useful because it can operate at high-temperature, high-power, high-radiation conditions. The SiC permittivity ε_1=6.5-i0.0005 and the permeability μ_1=1 were taken from [11]. The middle layer can be made from a metamaterial or a gyrotropic ferrite. The metamaterial UCSD30815 complex permittivity ε_2= -4.95-i0.2 and the permeability μ_2= -2.5+ i0.25 were taken from [12]. In this work the permeability tensor components of gyrotropic ferrite ISCh4 are defined taking into account ferrite losses by using a dissipative term in T. Hilbert form as in [13]. The permittivity tensor elements (4) of ferrite are: μ_{+1} =6.757-i0.00301 and μ_{-1} =3.814-i0.00072, μ_p =1 and ε_{fer}=13.5-i0.0005. The variation of the scattering power of microwave at different points on cylindrical surfaces of radius r is shown in Figs 1-3. Here are given the scattering power distributions at wave incidence angles: θ=π/2 (denoted by the black line), θ=π/3 (red), θ=π/6 (blue). The wave incidence angle θ is the angle between a cylinder axis and a direction of incident wave propagation.



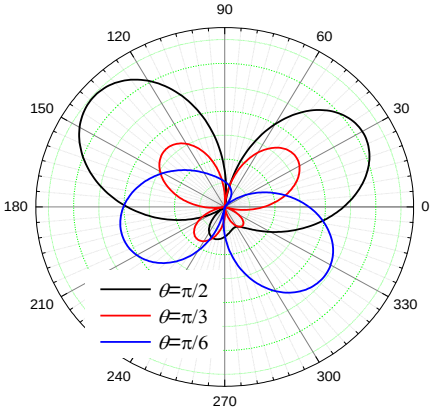
(a)



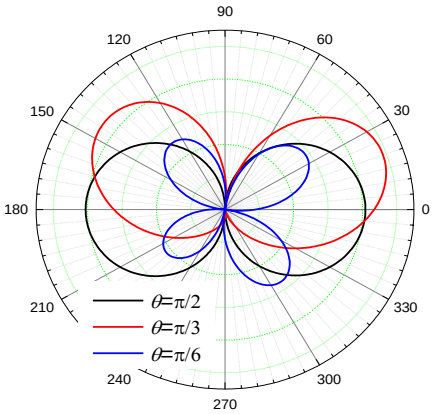
(b)

Figure 1: Scattering diagrams of SiC-metamaterial-SiC layered cylinder at the distance from the axis of cylinder equal to 1mm for parallel (a) and perpendicular (b) polarizations.

The comparison of scattering diagrams of cylinders with the different middle layers (metamaterial or gyrotropic ferrite) shows that exist strong dependencies of the scattering characteristics on the middle layer constitutive parameters and the polarization of incident microwave.

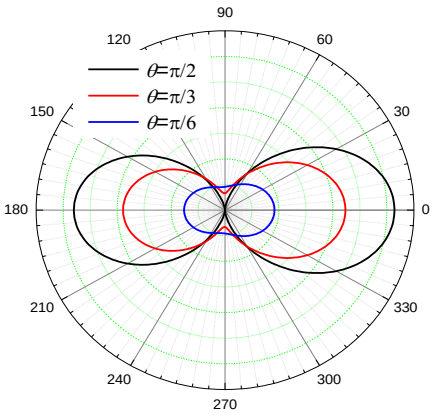


(a)

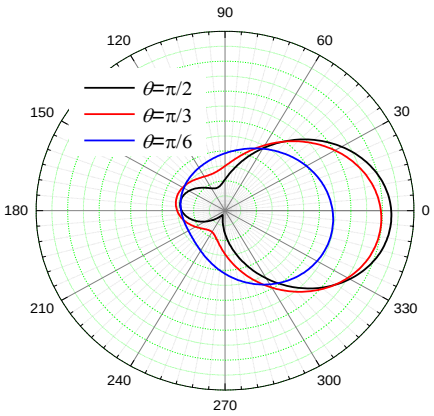


(b)

Figure 2: Scattering diagram of SiC- gyrotropic ferrite -SiC layered cylinder at the distance from the cylinder axis equal to 1mm for parallel (a) and perpendicular (b) polarizations.



(a)



(b)

Figure 3: Scattering diagrams of layered cylinder at the distance from the cylinder axis equal to 2.5 mm for parallel polarizations when cylinder made of SiC- metamaterial -SiC (a) and SiC- gyrotropic ferrite –SiC (b).

On the base structures like the considered cylinders can be created controllable by magnetic field antenna reflectors that can re-direct a radiation.

3. Conclusions

The rigorous solution of boundary diffraction problem about the microwave scattering by a multilayered cylinder with electrically and (or) magnetically gyrotropic substrata is presented here. The harmonic EM wave may incident on the layered cylinder at arbitrary incidence angles. Scattering diagrams of the SiC- metamaterial-SiC cylinder and the SiC- gyrotropic ferrite –SiC cylinder are analyzed. We discovered the special distribution of the radial component of the Poynting vector for gyrotropic cylinders (Fig. 3.1).

References

[1] R.W.P. King, T.T. Wu, *The Scattering and Diffraction of Waves*, Massachusetts: Harvard University Press, Cambridge, 1959.

[2] W.Z. Yan, Y. Du, H. Wu, D.W. Liu, B.I. Wu, EM Scattering From a Long Dielectric Circular Cylinder, *PIER* 85: 39–67, 2008.

[3] C.W. Qiu, H.-Y. Yao, S.-N. Burokur, S. Zouhdi, L.-W. Li, Electromagnetic Scattering Properties in a Multilayered Metamaterial Cylinder, *IEICE Trans. Commun*. E90-B: 2423–2429, 2007.

[4] B. Ivsic, Z. Sipus, S. Hrabar, Analysis of Uniaxial Multilayer Cylinders Used for Invisible Cloak Realization, *IEEE Trans. Antennas Propag.* 5(57): 1521–1527, 2009.

[5] Y. Ni; L. Gao, C.-W. Qiu, Achieving Invisibility of Homogeneous Cylindrically Anisotropic Cylinders, *Plasmonics*. 3(5): 251-258, 2010.

[6] P.-P. Ding, C.-W. Qiu, S. Zouhdi, S.P. Yeo, Rigorous Derivation and Fast Solution of Spatial-Domain Green's Functions for Uniaxial Anisotropic Multilayers Using Modified Fast Hankel Transform Method, *IEEE Trans. MTT*, 2(60): 205-217, 2012.

[7] S.M. Mazinani, H.R. Hassani, A Novel Omnidirectional Broadband Planar Monopole Antenna with Various Loading Plate Shapes, *PIER* 97: 241–257, 2009.

[8] J. Bucinskas, L. Nickelson, V. Sugurovas, Microwave Scattering and Absorption by a Multilayered Lossy Metamaterial–Glass Cylinder, *PIER* 105: 103–118, 2010.

[9] L. Nickelson, J. Bucinskas, Microwave Diffraction Dependencies of a Conductor Cylinder Coated with Twelve Glass and Semiconductor Layers on the *n*-Si Specific Resistivity, Electronics and Electrical Engineering 9(115): 47-50, 2011.

[10] J. Bucinskas, L. Nickelson, V. Sugurovas, Microwave Diffraction Characteristic Analysis of 2D Multilayered Uniaxial Anisotropic Cylinder, *PIER* 109: 175–190, 2010.

[11] T.A. Baeraky, Microwave Measurements of the Dielectric Properties of Silicon Carbide at High Temperature, *Egypt. J. Sol.* 2(25): 263–273, 2002.

[12] D.R Smith, P. Rye, D.C. Vier, A.F. Starr, J.J. Mock, Design and Measurement of Anisotropic Metamaterials that Exhibit Negative Refraction, *IEICE Trans. Electron.*, 3(E87-C): 359–370, 2004.

[13] L. Nickelson and V. Shugurov. *Singular Integral Equation Methods for the Analysis of Microwave Structures*. Leiden – Boston, 2005.

The wave functions of the crystal lattice energy bands

Iskakova Kulpash[1], Akhmaltdinov Rif[2], Amanova Aysara[3],

[1]chair ISE, associate professor, KazNPU after by Abai, Kazakhstan
[2]chair A&CE, KasOU Almaty, Kazakhstan
[3]Department Chemical and Technology student, KazNU after by Al-Farabi, Almaty Kazakhstan
*corresponding author, E-mail: ahmanovakulpash@yahoo.com

Abstract

Properties of crystalline solid-state structures are determined by the energy state of the electron-nuclear systems and the behavior of the electronic assemblies in crystalline magnetic fields.

1. Introduction

Properties of crystalline solid-state structures are determined by the energy state of the electron-nuclear systems and the behavior of the electronic assemblies in crystalline magnetic fields. They have the lattice periodicity (an electron in a periodic potential). Therefore, the tasks quantify and predict the properties of materials is often limited opportunity quite correctly describe and experimentally determine the distribution of energy levels in different structures.

2. The wave functions of the crystal lattice energy bands

In the opinion of Wigner and Seitz "If one had a great calculating machine, one might apply it to the problem of solving the Schrödinger equation for each metal and obtain thereby the interesting physical quantities, such as the cohesive energy, the lattice constant, and similar parameters. It is not clear, however, that a great deal would be gained by this. Presumably the results would agree with the experimentally determined quantities and nothing vastly new would be learned from the calculation. It would be preferable instead to have a vivid picture of the behavior of the wave functions, a simple description of the essence of the factors which determine the cohesion and an understanding of the origin of variation in properties" [1].

The problem of calculating the energy band structure is one of the main problems of solid state physics. Namely band theory is the theoretical basis for the other physical models to understand and explain many physical and technical properties of solids. This primarily refers to the crystals, which are widely used in modern computing, microelectronics, and in the manufacture of construction materials, etc.

However, the calculation of the energy bands of solids is a very complex mathematical problem. This is due to the need to consider the interaction of an infinite number of particles (the many-body problem) in determining the potential. As a result, to determine the levels of energy in the classical version of the theory is required to solve differential and integral equations for the potential to be submitted in the form of a series with an infinite number of members [2], [3].

The main source of problems in all existing methods for calculating the band structure of solids is that originally entered the assumptions that are made in the form of a formal mathematical description, realized in the form of programs and the result is the same assumptions that were made originally. Any new information beyond what is assumed a priori is not generated. The apparent futility of this approach lies behind the enormous confusion and complexity of each cycle of such works.

We consider the crystal as a system of all its constituent elements, the properties of which are determined by the crystal system and there are no outside the crystal in a free state, used a nonlinear superposition of the interactions of these elements are not made outside the assumption of a crystal structure and its size. The known properties of the crystal experiments, for example, the frequency of the elements in the arrangement should be obtained as a consequence of the approach, not postulated in advance.

In the case of the successful development of this theoretical approach will be made a contribution to the solution of the fundamental problem of determining the energy spectrum of electrons in a periodic potential methods of computing. This determines the relevance and practical importance of the work.

The purpose of this work is to develop accurate methods of crystal potentials and wave functions, which would allow to calculate the energy spectra of the electron states in various solids without fitting and use of corrective factors. Assumed that the results of the calculations will be tested on the crystals of copper, which will act in this case as a model system.

The central object, with whom we were dealing with is a wave function. There are construction of the wave function only on the basis theoretical studies that focus on numerical methods. But the quantity of these constructions is clearly smaller. One advantage of this method is to obtain a one-dimensional periodic wave function without translational

periodicity in the space of complex numbers. Interestingly, the imaginary and real parts of the calculated wave function without the use of assumptions about its frequency are obtained periodic with a period equal to the lattice constant. The amplitudes of the wave functions with increasing values of energy in energy bands increase in the nodes of crystal lattice. Consequently the probability densities increase at these points. This means that the higher the energy of the test electron, the closer it can be in the field of the atomic core. Figure 1 shows all the components of the calculation scheme of the core-intercore method for the second state. It is clearly seen near the center of origin because of the large number of cores and intercores as in the total real part and in the total imaginary part of the wave vector there are strong oscillations. This behavior of the wave vector due to the fact that the crystal is modeled with finite small size in the 7th core of the axis Ox. The central (4th) core lies in the depths of the crystal model. Therefore, the oscillations in it take the form of a delta function with a very narrow splash. Oscillations on the side (boundary) of the cores are blurred and are therefore available to them to portray. With an increase in size of the crystal such delta functions repeate periodically in the points that are on the same level of the envelope. However, this period does not correspond to the period of the envelope — the largest number of delta functions are at the center of a finite crystal, the number of the delta-function is reduced away from the center of the crystal.

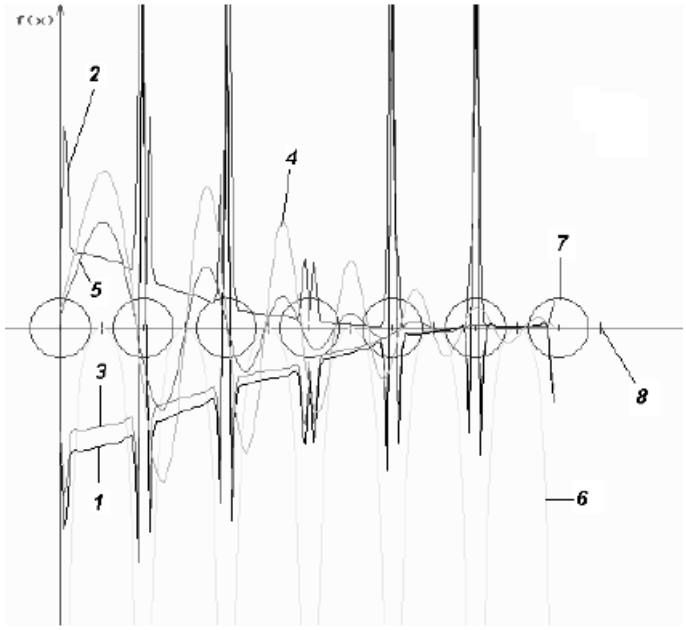


Figure 1 — Functions of the 2nd state. 1 — the total real part of the wave function of all cores and intercores; 2 — the probable of the test electron position; 3 — the imaginary part of the wave functions of all cores and intercores; 4 — the real part of a wave function of some one core and the surrounding six intercores; 5 — the imaginary part of the wave function of some one core and surrounding six intercores, 6 — crystal potential, 7 — core; 8 — intercore center.

These results are consistent with the assumptions set out on the basis of works of Fermi, Pasta and Ulam. In the formation of the monovalent cuprous crystal is socialized one electron from each atom, while on the upper shell of the atom appears defect. We assume that an overlapping of wave functions at the defect level occurs in this process, and the other electronic levels of the ion are the same as in the isolated atom. The direct determination of the potential on the configuration space shows how the potential of the core ion changes depending on the level of the electron filling. In the transition of an electron from shell to shell of the various states of the electrons, each electron shell shields the external space of the charges, which are inside the shell. On the inner surface of the shell due to the screening induced charge of opposite sign [4, 5]. When an electron moves in the intercore space, the crystal potential is equal to the sum of the potentials of all cores and the sum of the potentials of all the parts of the intercores. Then to determine the band structure the obtained relatively on these potentials wave function can be used. We know the wave functions $\psi_j(\vec{x},\vec{k}_x)$ relatively to the zero of the atomic core, fixed at the origin. The are 321 such cores in total including 0th. In the traditional methods functions of the isolated atoms is regarded. And in our case we obtain the functions of not isolated atoms but the functions of the crystal atoms. Generally in a crystal does not exist isolated atom, and the wave functions of the core ions overlap by the defective shells and defective shells, in turn, overlap intercore spaces, or, in other words, the elements of the lattice for the socialization of the electrons. The geometry itself of the construction of the wave functions shows that the isolated atom does not exist, and the coordinates of each core ion can be associated with an arbitrary origin. In the methodology of constructing of the wave function we are not using the unit cell broadcast to the entire crystal, but we consider the crystal as a single system.The interactions of the structural elements of the crystal are compensated, i.e. the object of study is in equilibrium and there is no need to define the energies of the interaction between all the elements. Instead, we define the potential of the interaction of the elements of the entire system with nonlinearity or disturbing factor. Consequently, the fundamental question of the model is to describe the interactions in the crystal by the pair approximation considering many partial interactions.

Functions $\psi_j(\vec{x},\vec{k}_x)$ satisfy the conditions of the Bloch functions. Let's find the eigenvalues of the energy levels of the crystal depending on the states of the wave function. The functional dependence of the energy states from the wave vector is given by:

$$E_j(\vec{k}_x) = \frac{\Delta_x \psi_j(\vec{x},\vec{k}_x)}{\psi_j(\vec{x},\vec{k}_x)} + V(\vec{r}). \qquad (1)$$

Here the wave function is defined in the complex plane, and the energy is the real value. Separating the real and imaginary parts of (1), we obtain the following expression for determining the values of the energy levels

$$\mathrm{E_j}(\vec{\mathrm{k}}_\mathrm{x}) = \frac{\mathrm{ad+bf}}{\mathrm{d^2+f^2}}, \qquad (2)$$

where j — number of the energy level, $a = Re\Delta_x\psi_j(\vec{x},\vec{k}_x)$, $b = I_m\Delta_x\psi_j(\vec{x},\vec{k}_x)$, $d = Re\psi_j(\vec{x},\vec{k}_x)$, $f = I_m\psi_j(\vec{x},\vec{k}_x)$.

The energy levels obtained from the equation (2) are periodic functions in the wave vector space:

$$E_j(\vec{k}_x + \vec{g}) = E_j(\vec{k}_x),$$

where g - reciprocal lattice vector.

Without taking the condition of the periodicity it is obtained periodic dependence of the energy $E_j(\vec{x}, \vec{k}_x)$ from one-dimensional wave vector $\vec{k}_x$ with period $2\,\vec{k}_x/a_0$ (where a_0 — lattice constant) over the entire crystal. In Figures 2 it is shown plots of the energy $E_j(\vec{x}, \vec{k}_x)$, of the coordinates of $\vec{x}$ and wave vector $\vec{k}_x$ for the first five states of copper.

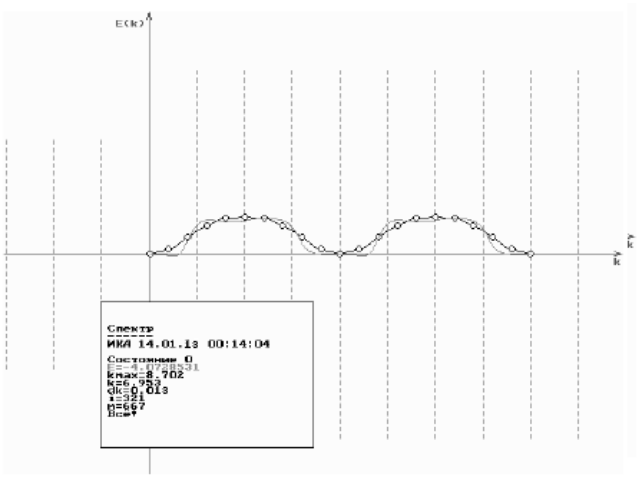


Figure 2 — The energy $E_j(\vec{x}, \vec{k}_x)$ for the state of copper n = 0.

In copper the upper electron layer is composed of eleven electrons: $3d^{10}4s^1$. For these eleven electrons it is necessary six zones. The calculated data of the energy bands of copper obtained Burdick show that for all wave vectors k the structure of the six zones passes in fiveband structure. The energy of the five zones is in the range of 2 eV to 5 eV below the Fermi energy. The energy of the sixth zone ranges from 7 eV to 9 eV. Lower threshold energy is below the Fermi energy, the top one is above the Fermi energy. The threshold of excitation of electrons from the conduction band in the upper zone is reached at the point where the neck of the Fermi surface intersects the hexagonal face of the Brillouin zone.

3. Conclusions

Inside the metal effect of the positive ions on the free electron offset is average. Turned out on the outer layer of positive ions electron electric force acts on the part of the attraction of these ions. The potential energy of an electron in the metal is less than outside it. Valence electrons determine one of the most fundamental differences — the division of solid metals and dielectrics. The difference between the dielectric and the metal is determined by the presence or absence of solid partially filled energy band. The basis of allocation of the two mentioned types of solid-state is the electron distribution not in the real space, but in the wave vector space. You may notice that the electrons in metals are generally not as concentrated near the ions, as in dielectrics.

References

Wigner E.P. and Seitz F., Solid State Physics 1, 97 (1955)

Iskakova K.A., Ahmaltdinov R.Ph., Possibilities of the modifications of the method of calculation of wave function and zonal spectrum of crystal structure, PCI-2010 «12th International Conference on the Physics and Chemistry of Ice». Sapporo, Japan.

Iskakova K.A., Ahmaltdinov R.Ph., Modelling and calculation of FCC structures and principles of the algorithm structure Si, 88th annual meeting of the German Mineralogical Society, 19–22. September 2010 Munster, Germany.

Ashcroft N.W., Mermin N. Solid State Physics, Nauka, Moscow, 1979, Vol 2.

Matveev A.N., Electricity and Magnetism, Moscow: High School, 1983.463 p.

Theory and Simulation of Cavity Quantum Electro-Dynamics in Multi-partite Quantum Complex Systems

Moslem Alidoosty Shahraki[1], Sina Khorasani[1*], and Mohammad Hasan Aram[1]

[1]School of Electrical Engineering, Sharif University of Technology, P. O. Box 11365-9363, Tehran, Iran

*corresponding author, E-mail: *khorasani@sina.sharif.edu*

Abstract

The cavity quantum electrodynamics of various complex systems is here analyzed using a general versatile code developed in this research. Such quantum multi-partite systems normally consist of an arbitrary number of quantum dots in interaction with an arbitrary number of cavity modes. Initially, the coefficients matrix of the system is computed and numerically measured. For this purpose, the general time-dependent state of the most complex system has been rigorously specified and solved. As an example, a nine-partition system is simulated under different coupling regimes, consisting of eight emitters interacting with one cavity mode. Two-level emitters (e.g. quantum dots) are assumed to have an arrangement in the form of a linear chain, defining the mutual dipole-dipole interactions. It was observed that plotting the system trajectory in the phase space reveals a chaotic behavior in the so-called ultrastrong coupling regime. The behavior again confirms the results in our previous works, with stronger disorder particularly for atomic operator and phase plot. In order to study the computational complexity of our code, various multipartite systems consisting of one to eight quantum dots in interaction with one cavity mode were solved individually. Computation run times and the allocated memory for each system were measured.

1. Introduction

Cavity quantum electrodynamics is a branch of quantum optics, which studies the interaction of quantum optical systems and confined radiation in a cavity [1]. For the first time, Jaynes and Cummings and independently Paul presented a model to describe the interaction of a two level quantum emitting system with one cavity mode [2,3]. Quantum entangled states have turned into a frontier topic of interest due to their various potential applications in quantum telecommunication, information and computing.

Programmable multimode quantum networks [4] are generated from various multimode entangled states, enabling the capability of switching between different linear optical networks. Simulation of multipartite many body systems has recently become feasible for the case of electronic wavefunctions in solids where nearly accurate analytical methods have been found [5]. However, precise numerical simulation of multi-partite quantum systems is known to be an intractable problem, in particular when entanglement information is to be kept. For this purpose, simulation of quantum systems composed of few partitions can be hardly done on a personal computer, while existing supercomputers hardly can simulate as many as only 50 partitions [6]. The only known solution so far has been to perform the simulation using physical real simulators [6]. But usefulness of such physical systems is obviously limited to the class of problems they can deal with.

It is the purpose of the present research to demonstrate the feasibility of full-scale simulation of multi-partite quantum systems on personal computers. We have developed an extensive code which is capable of solving arbitrarily complex quantum systems. We demonstrate the usefulness of this code by solving an example encompassing eight quantum dots interacting with one radiation mode. While the code is generally capable of solving for larger number of partitions, memory restrictions on the laptop PC (intel Core i3 2.4GHz, 4GB RAM) used for this purpose has prevented us to explore more complex systems. We have simulated the weak, strong, and ultrastrong coupling regimes and confirm the onset of quantum chaos as a result of ultrastrong coupling, in agreement with our previously published simulations.

The theory has been based on an extension of the JCPM model [2-3], and specification of all possible ket states. The appropriate generalized JCPM must describe the interaction between emitters as dipole-dipole terms, as well as the interaction of emitters with multi-mode fields as field-dipole terms. For this purpose, a special notation and formulation has been invented [7], in conjunction with a major correction to the JCM model [8-10].

In [7], the model Hamiltonian is transformed to the Heisenberg's interaction picture, and the subsequent Rabi equations were numerically solved in which RWA (Rotating Wave Approximation) was vital. This transformation is normally used in the context of quantum optics [1]. However, subsequent studies [8-10] revealed that application of Heisenberg's transformation to the interaction picture will produce mathematically incorrect solutions, markedly under the ultrastrong coupling. It is because the free-running solutions for field and atomic operators in ultrastrongly coupled systems oscillate largely non-sinusoidal. Due to this fact, error could be avoided by solving the system directly in the Schrödinger space without

any approximation, rather than the Heisenberg's interaction picture [10,11]. In our most recent preprint [11] we analyzed a real quantum system modeled as a three-level system [12,13], and another seven partition quantum system consisting of six quantum dots in interaction with one cavity mode [14].

In this present paper we are going to report our study on the behavior of a complex nine partition quantum system analyzed again under various coupling strengths. Here, emitters are assumed to have a linear chain arrangement, so that the dipole-dipole terms for non-neighboring dots vanish. Under a similar two-dimensional configuration [6], many exciting applications are expected where a quantum dot transition is put in resonance with a photonic Dirac point's frequency [15]. We also study the computational complexity of multi-partite systems versus the number of partitions for two algorithms based on full and sparse matrices. Counter-intuitively, usage of sparse matrices results in longer computational times compared to full matrices, while allocating the same order of memory.

2. Theory and Algorithm

Required theory and algorithm are explained completely in [11], however the basic definitions are explained here in brief. The initial point of our methodology is to specify the most general time-dependent system ket state to represent all possible entangled states, and the related generalized operating Hamiltonian. Then the time-dependent state of the most general possible system will be given by

$$|\varphi(t)\rangle = \sum_{A,F} \phi(A,F)|A\rangle|F\rangle$$

$$|A\rangle = \bigotimes_{n=1}^{k} \left|{}^{n}_{r_n}\right\rangle = \left|{}^{1}_{r_1}\right\rangle \left|{}^{2}_{r_2}\right\rangle \ldots \left|{}^{n}_{r_n}\right\rangle \qquad 1<r_n<B_n \qquad (1)$$

$$|F\rangle = \bigotimes_{\nu=1}^{\omega} |f_\nu\rangle = |f_1\rangle|f_2\rangle\ldots|f_\omega\rangle \qquad 0<f_\upsilon<N$$

Here, $|A\rangle$ is supposed to be the ket state of the different energy levels of emitters, k is the total number of emitters, $|F\rangle$ is the ket state of the cavity modes, f_ν is the number of photons in ν-th cavity mode number, and ω is the total number of cavity modes. $\left|{}^{n}_{r_n}\right\rangle$ expresses the eigenstate of the n-th quantum dot residing at its r_n-th energy level. Also, the subscript A refers to the different energy level states of light emitters and B_n is the number of energy levels. F refers to the different cavity modes occupied with photons and N is the maximum number of photons which possibly occupies a cavity mode. $|\varphi(t)\rangle$ is a superposition of all possible states of the system, including atom and field states, and each state has a time dependent coefficient equal to $\phi(A,F)$ [11].

The generalized Hamiltonian $\hat{\mathbb{H}} = \hat{\mathbb{H}}_0 + \hat{\mathbb{H}}_{\mathbf{r\cdot E}} + \hat{\mathbb{H}}_{\mathbf{r\cdot r}}$ is [11]

$$\hat{\mathbb{H}}_0 = \sum_{n,i} E_i^n \hat{\sigma}_i^n + \sum_\nu \hbar\Omega_\nu \hat{a}_\nu^\dagger \hat{a}_\nu$$

$$\hat{\mathbb{H}}_{\mathbf{r\cdot E}} = \sum_{n,i<j} \left(\gamma_{nij}\hat{\sigma}_{i,j}^n + \gamma^*_{nij}\hat{\sigma}_{j,i}^n\right)\sum_\nu \left(g_{nij\nu}\hat{a}_\nu + g^*_{nij\nu}\hat{a}_\nu^\dagger\right) \qquad (2)$$

$$\hat{\mathbb{H}}_{\mathbf{r\cdot r}} = \sum_{n<m,i<j} \left(\eta_{nij}\hat{\sigma}_{i,j}^n + \eta^*_{nij}\hat{\sigma}_{j,i}^n\right)\left(\eta_{mij}\hat{\sigma}_{i,j}^m + \eta^*_{mij}\hat{\sigma}_{j,i}^m\right)$$

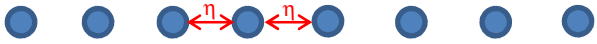


Figure 1: Assumed Light Emitting Systems Arrangement

with $\hat{\mathbb{H}}_0$ describing the system energy without interaction, $\hat{\mathbb{H}}_{\mathbf{r\cdot E}}$ describing the light-emitter interactions, and $\hat{\mathbb{H}}_{\mathbf{r\cdot r}}$ representing interactions between any possible pair of emitters such as dipole-dipole terms. Coefficients γ_{nij} are matrix elements of dipole operator of n-th emitter. The strength of the dipole interaction between n-th emitter and ν-th mode of cavity is given by $g_{nij\nu}$ with the transition i-th and j-th energy levels. Coefficients η_{nij} are proportional to the strength of the dipole generated while another emitter undergoes a transition between i-th and j-th levels. E_i^n indicates the i-th energy of the n-th emitter $\hat{a}_\nu^\dagger$ and $\hat{a}_\nu$ are the field creation and annihilation operators, which respectively increase and decrease the number of photons in the ν-th cavity mode by one, $\hat{\sigma}_{s,k}^l$ is ladder operator which makes the l-th emitter to switch from k-th to s-th level.

Now, the governing Schrödinger equation is

$$\frac{\partial}{\partial t}|\varphi(t)\rangle = -\frac{i}{\hbar}\mathbb{H}|\varphi(t)\rangle \qquad (3)$$

which can be recast into the form with the closed-form solution

$$\frac{d}{dt}\{\Phi(t)\}_{N\times1} = [M]_{N\times N}\{\Phi(t)\}_{N\times1} \qquad (4)$$

$$\{\Phi(t)\} = e^{[M]t}\{\Phi(0)\} \qquad (5)$$

In our code both sides of (3) are compared and coefficients will be arranged as elements of an N×N square matrix $[M]_{N\times N}$, where N is the total number of possible states. Then (3) is rewritten as (4), which admits an analytical solution (5) subject to the initial conditions $\{\Phi(0)\}$. We have also developed an efficient, stable, and accurate method to evaluate (5) [8,11,14]. Then, it would be possible to evaluate the probabilities and expectation values accurately under different coupling regimes.

3. Numerical Analysis Results

Here we study a nine-partition quantum optical system. First the system is characterized, then the state coefficients and subsequent required values to study the system behavior are evaluated precisely. The values are probabilities and expectation values of atomic and ladder operators.

3.1. Characterization

It is supposed that this nine partition system consists of eight identical light emitters (such as quantum dots) which are limited to two different energy level states. We take on a transition energy of 1eV between the ground and excited state. Light emitters are assumed to have a linear chain arrangement as Fig. 1, where dipole-dipole interactions between each dot and only the two neighbors is non-zero. This interaction has the typical magnitude of 5meV. It is furthermore supposed that transition dipole moment in these quantum dots is 96 Debye, in accordance with the typical values calculated elsewhere [12,13]. We let one resonant cavity mode with frequency ω_λ and the Rabi frequency $G_{e,g}$ to exist given by

Table 1. Rabi frequencies.

$E_0(\frac{kV}{cm})$	$G_{e,g}(\frac{Rad}{s})$	$\frac{G_{e,g}}{\omega_\lambda}$
20	6.0676×10^{12}	0.004
200	6.0676×10^{13}	0.04
2000	6.0676×10^{14}	0.4

$$\omega_\lambda = \frac{E_i - E_g}{\hbar} = \frac{1}{\hbar} = 1.5177\times10^{15} \qquad (6)$$

$$G_{e.g} = \frac{1}{\hbar}\left(E_0\hat{E}\right)\cdot\left\langle\psi_e\left|e\mathcal{R}\right|\varphi_g\right\rangle \qquad (7)$$

Here, $\langle\psi_e|e\mathcal{R}|\varphi_g\rangle$ is the transition dipole moment, $E_0\hat{E}$ is the applied electrical field vector, and $\hbar$ is reduced Plank constant. Now electrical fields due to the propagating field and by comparing the Rabi frequencies with the optical frequency ω_λ, different coupling regimes are simulated. According to (7), Rabi frequencies are given in Table 1, for weakly, strongly, and ultrastrongly coupled systems.

Based on the data in Table 1, for the weakest applied electric field with $G_{e,g} = 0.004\omega_\lambda$, the system is in the weak coupling regime. In a stronger electric field with $G_{e,g} = 0.04\omega_\lambda$ the coupling regime is strong. The strongest electric field provides $G_{e,g} = 0.4\omega_\lambda$, that takes the coupling regime into the ultrastrong domain.

In this system, we assume the maximum possible number of occupying photons in the cavity mode to be eight. Therefore the general time dependent state of the system according to the (1) is

$$\begin{aligned}
&|\varphi(t)\rangle = \sum_{r_{1\ldots7},r_8=e,g}\sum_{f=1}^{8}\phi(A,f)|A\rangle|f\rangle \\
&|A\rangle = \bigotimes_{n=1}^{8}\left|\begin{matrix}n\\ r_n\end{matrix}\right\rangle = \left|\begin{matrix}1\\ r_1\end{matrix}\right\rangle\left|\begin{matrix}2\\ r_2\end{matrix}\right\rangle\ldots\left|\begin{matrix}8\\ r_8\end{matrix}\right\rangle \qquad 1<r_\eta<2 \\
&|f\rangle = |f_1\rangle \qquad 0<f_1<8
\end{aligned} \qquad (8)$$

in which $r_1, \ldots, r_8$ are the quantum dots. The related Hamiltonian of this system according to (2) will be

$$\begin{aligned}
&\hat{\mathbb{H}}_0 = \sum_{n=0,i=e,g}^{8} E_i^{\,n}\hat{\sigma}_i^n + \hbar\Omega\hat{a}^\dagger\hat{a} \\
&\hat{\mathbb{H}}_{\mathbf{r}\cdot\mathbf{r}} = \sum_{n<m,i<j}(\eta_{nij}\hat{\sigma}_{i,j}^n + \eta^*_{nij}\hat{\sigma}_{j,i}^n)\left(\eta_{mij}\hat{\sigma}_{i,j}^m + \eta^*_{mij}\hat{\sigma}_{j,i}^m\right) = \\
&\sum_{n=1<m=2,i=g<j=e}^{n=7m=8}(\eta_{nij}\hat{\sigma}_{i,j}^n + \eta^*_{nij}\hat{\sigma}_{j,i}^n)(\eta_{mij}\hat{\sigma}_{i,j}^m + \eta^*_{mij}\hat{\sigma}_{j,i}^m) \\
&\hat{\mathbb{H}}_{\mathbf{r}\cdot\mathbf{E}} = \sum_{n=0,i=g<j=e}^{8}(\gamma_{nij}\hat{\sigma}_{i,j}^n + \gamma^*_{nij}\hat{\sigma}_{j,i}^n)(g_{nij}\hat{a} + g^*_{nij}\hat{a}^\dagger)
\end{aligned} \qquad (9)$$

A coherent field has been considered as initial state. The extended initial condition, based on the existing relations for an arbitrary quantum optic system [11] the initial coherent field for this system is:

$$\begin{aligned}
&\left|\phi(t_0)\right\rangle = \frac{1}{\sqrt{2^8 R}}\sum_{n=0}^{8}\sqrt{\frac{\lambda^n}{n!}e^{-\lambda}}\,|n\rangle\sum_{r_1\ldots r_8=g,e}\left|r_1,r_2,r_3,r_4,r_5,r_6,r_7,r_8\right\rangle \\
&R = \sum_{n=0}^{8}\left|\sqrt{\frac{\lambda^n}{n!}e^{-\lambda}}\right|^2
\end{aligned} \qquad (10)$$

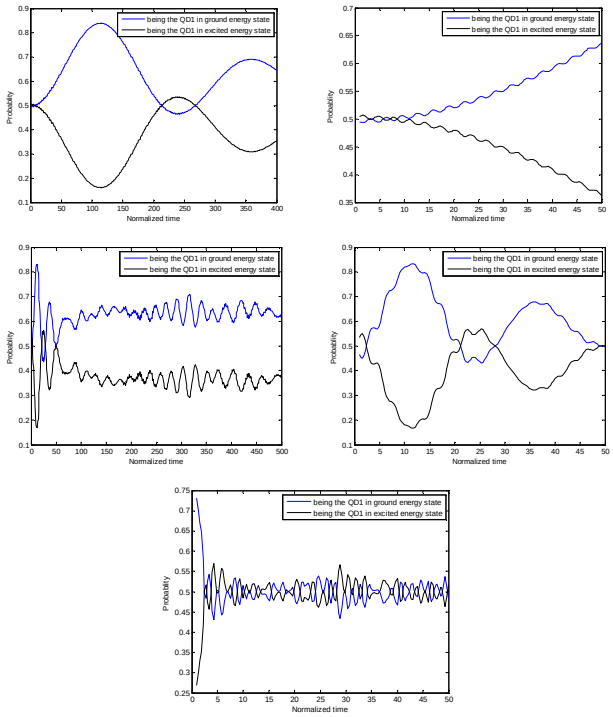


Figure 2: Presence probability of the first quantum dot plotted for both ground and excited states. First, second and third rows are in weak coupling regime, strong coupling regime and ultrastrong coupling regime respectively.

3.2. Presence probability with coherent initial state

According to (1), the presence probability of an arbitrary light emitting system such as l, being at a typical energy level such as k, is simply [9]

$$P = \sum_{A-\{\eta\}=1f_1,f_{2,\ldots},f_V=0}^{B_n}\sum^{N}\left|\phi(r_1,r_2,\ldots,r_{l\to k},r_n,f_1,\ldots f_v)\right|^2 \qquad (11)$$

Subsequently, the presence probability of a quantum dot being at its ground and excited energy level was measured according to

$$\begin{aligned}
&P = \sum_{A-\{\eta\}=g}\sum_{f_1=0}^{8}\left|\phi\left(r_{1\to g},r_2,\ldots,r_8,f_1\right)\right|^2 \\
&P = \sum_{A-\{\eta\}=e}\sum_{f_1=0}^{8}\left|\phi\left(r_{1\to e},r_2,\ldots,r_8,f_1\right)\right|^2
\end{aligned} \qquad (12)$$

These probabilities for all eight quantum dots were plotted. Fig. 2 presents the presence probability of first quantum dot for weak, strong, and ultrastrong coupling. As the coupling constant increases, anonymous oscillations increases and the chaotic behavior of ultrastrong coupling can be seen again in this system as in previous works [11].

3.3. Field operators in different coupling regimes

The behavior of field annihilation and creation operators is calculated in this work, too. The expectation value of the annihilation operator is obtained as [11]

$$\left\langle \varphi(t)|\hat{a}_{\nu}|\varphi(t)\right\rangle = \sum_{A,F}\sqrt{f_{\nu}}\phi^{*}\left(A,f_{\nu}-1\right)\ \phi\left(A,f_{\nu}\right) =$$
$$\sum_{r_{1,2\cdots n-1},r_{n}=1}^{B_{n}}\ \sum_{f_{1},f_{2\cdots\nu},f_{m}=0}^{N}\sqrt{f_{\nu}}\phi^{*}\left(r_{1},r_{2},\ldots,r_{n},f_{1},f_{2},\ldots,f_{\nu}-1\ldots,f_{m}\right) \quad (13)$$
$$\times\phi\left(r_{1},r_{2},\ldots,r_{n},f_{1},f_{2},\ldots,f_{\nu},\ldots,f_{m}\right)$$

So, the expectation value of annihilation operator is found as

$$\left\langle \varphi(t)|\hat{a}_{\nu}|\varphi(t)\right\rangle =$$
$$\sum_{r_{1\ldots5},r_{6}=g,e}\ \sum_{f_{1}=0}^{8}\sqrt{f_{1}}\phi^{*}\left(r_{1},r_{2},r_{3},r_{4},r_{5},r_{6},f_{1}\right)\ \phi\left(r_{1},f_{1}\right) \quad (14)$$

Phase space plots and flat phase plots of the real and imaginary values of the expectation value as functions of normalized time are shown in Fig. 3, respectively for weakly, strongly, and ultrastrongly coupled systems.

As it is observed, by increasing the coupling constant and entering into ultrastrong regime the system behaves very chaotic, marking a disordered behavior. Also, the corresponding phase changes nonlinearly. This behavior was also seen in complex ultrastrongly coupled multipartite systems analyzed before [8-11,14], with the difference that in the previous works, the corresponding phase would undergo abrupt random-like step changes. But as it is seen that not only by increasing the partitions the behavior is not the same as before, but also it is very disordered in shorter time durations and seems to be constant in long durations.

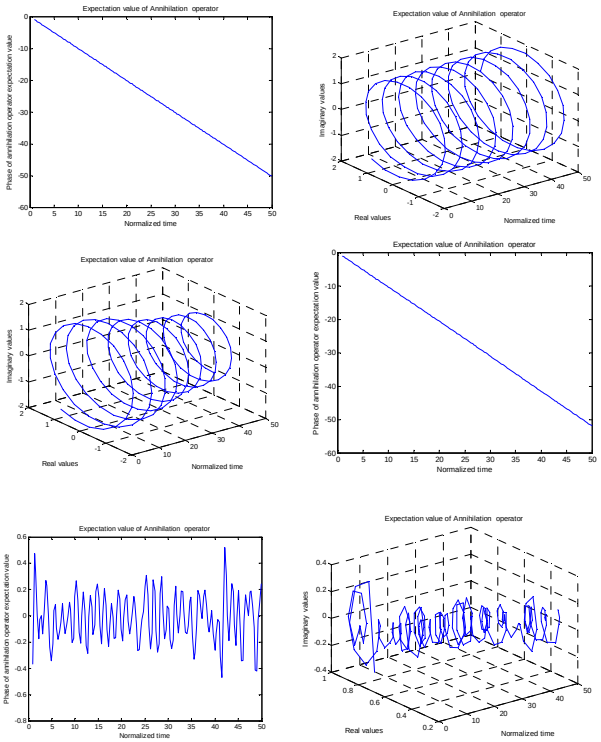


Figure 3: Phase space and phase plots of expectation value of annihilation operator. First, second and third rows are in weak coupling regime, strong coupling regime and ultrastrong coupling regime, respectively.

3.4. Expectation value of the atomic ladder operator

The behavior of ladder operator has been also computed, with the expectation value of annihilation operator in an arbitrary quantum optic system being [11]

$$\left\langle \varphi(t)|\hat{\sigma}_{s,k}^{l}|\varphi(t)\right\rangle =$$
$$\sum_{A-\{\eta\},F}\phi^{*}\left(A_{\eta\to s},F\right)\left\langle F\left|\left\langle A_{\eta\to s}\right|\phi\left(A_{\eta\to k},F\right)\right|A_{\eta\to s}\right\rangle|F\rangle$$
$$=\sum_{A-\{\eta\},F}\phi^{*}\left(A_{\eta\to s},F\right)\times\ \phi\left(A_{\eta\to k},F\right) \quad (15)$$
$$=\sum_{A-\{\eta\}=1f_{1},f_{2},\ldots,f_{m}=0}^{B_{n}}\ \sum^{N}\phi^{*}\left(r_{1},r_{2},r_{l}\to s,\ldots,r_{n},f_{1},f_{2},\ldots,f_{m}\right)$$
$$\times\ \phi\left(r_{1},r_{2},\ldots,r_{n}\to k,f_{1},f_{2},\ldots,f_{m}\right)$$

Here, only the second dot as an example is presented here (all other dots have the same typical behavior). So by using (15) the expectation value of ladder operator for transition of every quantum dot from excited energy level to ground energy level will be

$$\left\langle \varphi(t)|\hat{\sigma}_{g,e}^{2}|\varphi(t)\right\rangle =\sum_{r_{1,3,4,5},r_{6}=g,e}\ \sum_{f_{1}=0}^{8}\phi^{*}\left(r_{1},r_{2\to g},r_{3},r_{4},r_{5},r_{6},r_{7},r_{8},f_{1}\right) \quad (16)$$
$$\times\phi\left(r_{1},r_{2\to g},r_{3},r_{4},r_{5},r_{6},r_{7},r_{8},f_{1}\right)$$

Three-dimensional and phase plots of the real and imaginary values of the measured expectation value as functions of normalized time duration in Figs. 4, show chaotic behavior and nonlinearity in ultrastrong coupling regime is observed.

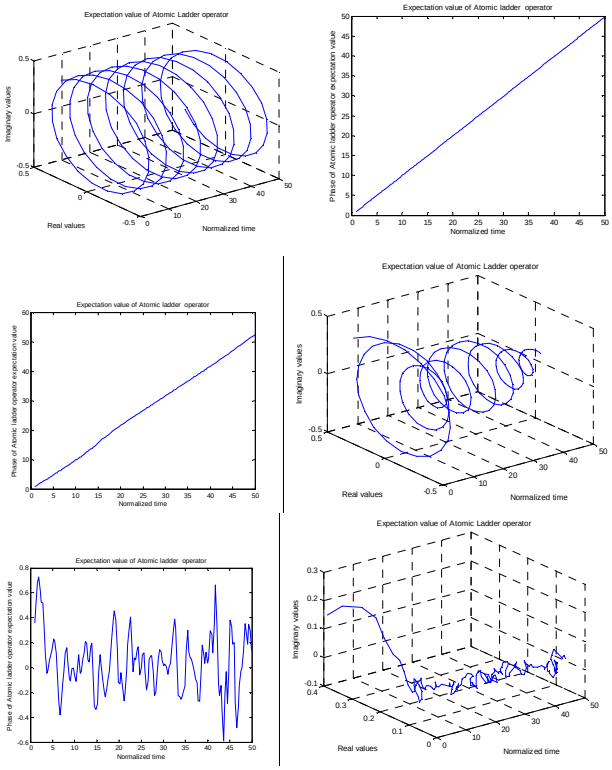


Figure 4: Phase space and phase plots of expectation value of atomic ladder operator, first, second and third rows are in weak coupling regime, strong coupling regime and ultrastrong coupling regime, respectively.

Table 2: Run time and Memory allocation

Partition Num.	Sparse Matrix		Full Matrix	
	Run Time(s)	Memory	Run Time(s)	Memory
2	0.42	343MB	0.53	338 MB
3	0.70	343MB	0.468	341 MB
4	1.94	344MB	0.69	343 MB
5	11.74	347MB	2.60	347 MB
6	90.52	353MB	18.84	353 MB
7	1.31×10^{3}	382MB	1.66×10^{2}	376 MB
8	2.35×10^{4}	510MB	1.58×10^{3}	467 MB
9	5.65×10^{5}	1030MB	1.72×10^{4}	930 MB

In this system, disordered behavior increases significantly and the same anonymous behavior in phase space and phase plots even seems to begin from strong coupling regime. Moreover the amplitude of the real and imaginary parts decreases so much.

4. Computation of Complexity

According to (1), the number of possible states of a quantum optic system equals to

$$M = (N+1)^{Cavitym} \times (enrgylev)^{QDno} \qquad (17)$$

where N is the maximum number of occupying photons in cavity modes, with the number of *Cavitym*. *QDno* is number of light emitting systems that each one has *energylev* number of energy levels.

So it is obvious that the computational complexity will be a strong function of the number of system partitions according to (17). Since the number of possible states in an analyzing system would be so large, it was inevitable to provide an extensive computer code to tackle such systems with an arbitrary number of states. Therefore, a very comprehensive MATLAB software has been developed to achieve this goal.

In the software we firstly utilized full matrixes to provide the initial desired matrix and compute the state coefficient matrix, however due to the limited full matrix dimensions the selection of a system complexity was limited. For example, consideration of a system larger than ten partitions (9 QDs in interaction with 1 *Cavitym* with 7 photons) was not possible on the PC we were using. Hence we revised the codes with sparse matrixes. Sparse matrix squeezes out any zero element of a full matrix, so that it made possibility to consider a system as large as 2^{28} possible states for example a 26 partition system (25 QDs in interaction with 1 *Cavitym* with 7 photons). However, the necessity of eigenvalue computation in the process of state measurement, the sparse matrices allocate more amount of RAM, resulting in increased run time process. So, as long as the eigenvalue extraction is not satisfactorily efficient, use of sparse matrices counter-intuitively would increase the computational complexity.

In order to study the trend of complexity and its relation to the number of system partitions, various having two to nine partitions were solved, through the measurement of their state coefficient matrix. Meanwhile the run time process and allocated memory in those systems are presented in Table 2.

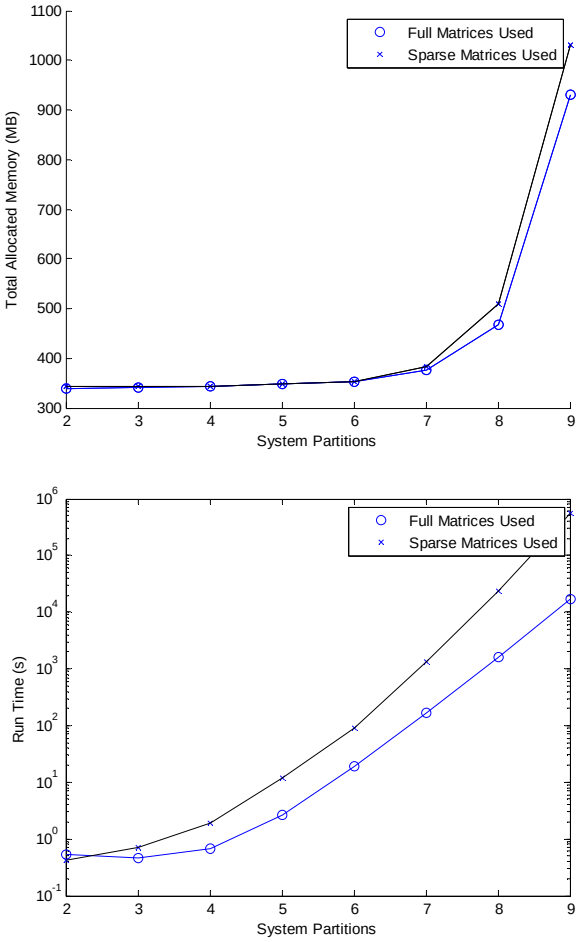


Figure 5: Allocated memory and run time of software processing. First plot is allocated memory in both full and sparse matrix utilization. Second plot is the run time for full matrix application and sparse matrix, respectively.

Run time and memory allocation for analyzed selected systems are plotted in Fig. 5 to illustrate the computational complexity of our algorithms and code. According to the obtained results, by increasing the number of partitions both the required RAM and computational burden surge exponentially. We estimate that the overall efficiency of the algorithm based on full matrices is proportional of 9.6^{M} with M defined in (17), whereas for sparse matrices one would expect a computational burden proportional to 17.8^{M}.

5. Conclusions

In this paper, the cavity quantum electrodynamics of a complex system with nine partitions has been analyzed. The fundamental methodology to tackle such systems theoretically was mentioned. In the ultrastrong coupling regimes, similar to our previous works, a remarkable chaotic behavior has been again observed. However, it appears that the chaotic behavior is pronounced at larger number of partitions. Also, phase plots illustrate strong disorder along with a different behavior not seen earlier, which showed abrupt stepwise phase changes. Then, we

repeated our simulation for various complex systems, while monitoring the overall run time and allocated memory. Since the coefficients matrix is largely sparse, we would normally anticipate that sparse algorithms would cause less computational burden. Strikingly, it was observed that it was not the case, and we would relate this counter-intuitive conclusion to the inefficiency of existing eigenvalue extraction methods for sparse matrices.

Acknowledgements

This work was supported in part by Iranian National Science Foundation (INSF) under Grant 89001329.

References

[1] W. P. Schleich, *Quantum Optics in Phase Space*, 1st ed. Berlin: Wiley-VCH, 2001.

[2] E. T. Jaynes, F. W. Cummings, Comparison of quantum and semiclassical radiation theories with application to the beam maser, *Proc. IEEE*, vol. 51, no. 1, pp. 89-109, Jan. 1963.

[3] H. Paul, Induzierte Emission bei starker Einstrahlung, *Ann. Phys*., vol. 466, pp. 411-412, 1963.

[4] S. Armstrong et al., Programmable multimode quantum network, *Nature Commun.*, vol. 3, 1026, 2012.

[5] G. H. Booth et al., Towards an exact description of electronic wavefunctions in real solids, *Nature*, vol. 493, pp. 365-370, 2013.

[6] J. Cai et al., A large-scale quantum simulator on a diamond surface at room temperature, *Nature Phys.*, vol. 9, 2013; doi:10.1038/nphys2519.

[7] A. H. Sadeghi, A. Naqavi, and S. Khorasani, Interaction of Quantum Dot Molecules with Multi-mode Radiation Fields, *Scientia Iranica*, vol. 17, pp. 59-70, 2010.

[8] E. Ahmadi, H. R. Chalabi, A. Arab, S. Khorasani, Cavity Quantum Electrodynamics in the Ultrastrong Coupling Regime, *Scientia Iranica*, vol. 18F(3), pp. 820-826, 2011.

[9] E. Ahmadi, H. R. Chalabi, A. Arab, S. Khorasani, Revisiting the Jaynes-Cummings-Paul model in the limit of ultrastrong coupling, *Proc. SPIE*, vol. 7946, 79461W, 2011.

[10] A. Arab and S. Khorasani, Fully automated code for exact and efficient analysis of quantum optical systems in the regime of ultrastrong coupling, *Proc. SPIE*, vol. 8268, 82681M, 2012.

[11] M. Alidoosty Shahraki and S. Khorasani, Cavity quantum electrodynamics of multipartite systems, arXiv: 1211.1584, 2012.

[12] F. Karimi and S. Khorasani, Optical Modulation by Conducting Interfaces, arXiv:1211.1413, 2012.

[13] F. Karimi and S. Khorasani, Ultrastrong optical modulation in waveguides with conducting interfaces, *Proc. SPIE*, vol. 8631, 863123 (2013).

[14] M. Alidoosty Shahraki, F. Karimi, and S. Khorasani, Detailed Simulation of Cavity Quantum Electro-dynamics in III/V Heterostructure Well/Waveguide Structures, *Technical Digest of 4th International Topical Meeting on Nanophotonics and Metamaterials*, 3-6 Jan. 2013, Seefeld, Austria.

[15] M. H. Aram, R. Mohajeri, S. Khorasani, Construction of Dirac points using Triangular supercrystals, *4th International Conference on Metamaterials, Photonic Crystals, and Plasmonics*, Dubai, 2013.

The investigation of the photonic waveguide structure made of silicon carbide by means of the method of the Singular Integral Equations

Tatjana Gric[1,2], Liudmila Nickelson[1,2], Romanas Martavicius[1]

[1]Vilnius Gediminas Technical University, Vilnius, Lithuania
[2]Center for Physical Sciences and Technology, Semiconductor Physics Institute, Vilnius, Lithuania
*corresponding author, E-mail: tatjana.gric@gmail.com

Abstract

Here we present the analyses of the open (without a metal screen) ridged and photonic waveguide structures by means of the electrodynamical rigorous method of the Singular Integral Equations (SIE). The waveguides are made of a lossy silicon carbide (SiC) material. We have discovered peculiarities of the dispersion characteristics.

We have found out the numerical solutions to the complex wave equations. The dispersion characteristics of both waveguide structures are numerically analyzed and compared with each other. It was found out that the losses of modes propagating in the waveguide structure with air openings (channels) are smaller than the losses in the waveguide structure without air openings. We came to the conclusion that it is possible to optimize the dispersion characteristics by adding the openings of different shapes and sizes into waveguide structures.

Keywords. Eigenvalue problems, complicated boundary conditions, the Singular Integral Equations' method, ridged waveguide structure, photonic waveguide structure, dispersion characteristics, phase constant, attenuation constant, silicon carbide, losses, microwave range.

1. Introduction

A large number of publications on the development of production technology of the advanced SiC electronic devices in the microwave and terahertz range points to the relevance of this topic [1–3]. The reason of importance of this topic is excellent properties of SiC material to solve the technical problems of our days. SiC has become an increasingly important material in numerous applications including, development of high power, high voltages, high temperature, high critical breakdown field, high frequency, high-radiation condition devices. In additional SiC possess other superb behavior, i.e. high hardness and strength, chemical and thermal stability, high melting point, oxidation resistance, high erosion resistance. The use of modern materials in waveguide technology is progressive approach today.

The second direction of development of novel waveguide technology is the topology complication of waveguide systems. In the last decade a lot of engineering effort was given into developing the photonic waveguides with complex configurations.

The semiconductor photonic waveguide devices have been constructed in [4]. The article [5] reports on the numerical analysis of the reflectivity of electromagnetic waves for several one-dimensional photonic crystal structures. A waveguide consisting of one-dimensional photonic crystal is shown to be promising for optical interconnection on a semiconductor wafer. The fabrication of optical directional couplers with the waveguides and their fundamental characteristics are demonstrated in [6]. The modulation efficiency, response time, and pump power of a terahertz-beam intensity modulator by using an organic photonic crystal slab structure with high quality factor "defect cavity" are theoretically investigated in [7]. The photonic waveguide structures have the wide area of applications. The structures that can find applications in mid- and long-wave infrared regions are analyzed in [8]. The lithographically patterned VO2 thin films grown by pulsed laser deposition have been integrated with silicon-on-insulator photonic waveguides to demonstrate a compact in-line absorption modulator for use in photonic circuits [9]. The physical principles behind the phenomenon of slow light in photonic crystal waveguides, as well as their practical limitations, are discussed and put into context in [10]. This includes the nature of slow light propagation, its bandwidth limitation, the scaling of linear and nonlinear interactions with the slowdown factor as well as issues such as losses, coupling into and the tuning of slow modes. Applications in all-optical signal processing appear to be the most promising outcome of the phenomena discussed.

Our contribution in these topics is the numerical investigation of the ridged and photonic waveguide structures made of silicon carbide (SiC) with taking into account losses in the material.

2. The integral representation of solution to Maxwell's equations

The Maxwell's equations for this boundary problem have been solved by means of the electrodynamically rigorous SIE method. This method attracts much attention due to its positive features. The shape of the cross-section of the investigated waveguide structure may be very complicated

(Fig. 1). In Fig. 1 the contour L separates materials with different permittivities and permeabilities. We assume that the area S^- is the waveguide surrounding waveguide media. All the boundary conditions are satisfied in the electrodynamical problem. We present here our researches of the ridged waveguide which boundary surfaces are parallel to the *x*- and *y*- axes. At the boundary which is parallel to the *x*-axis we assume that $E_x^+|_{Lx} = E_x^-|_{Lx}$. At the boundary which is parallel to the y-axis we assume that $E_y^+|_{Ly} = E_y^-|_{Ly}$, where contour L is composed from segments *Lx* and *Ly*. At all the boundaries we assume that $E_z^+|_L = E_z^-|_L$. The analogical boundary conditions are satisfied for the magnetic field. The longitudinal components of the electric $E_z(\vec{r})$ and magnetic $H_z(\vec{r})$ fields at the contour L have the integral representation:

$$E_z(\vec{r}) = \int_L \mu_e(\vec{r}_s) H_0^{(2)}(k_\perp r')ds,$$
$$H_z(\vec{r}) = \int_L \mu_h(\vec{r}_s) H_0^{(2)}(k_\perp r')ds, \qquad (1)$$

where $H_0^{(2)}$ is the Hankel function of the zeroth order and the second kind.

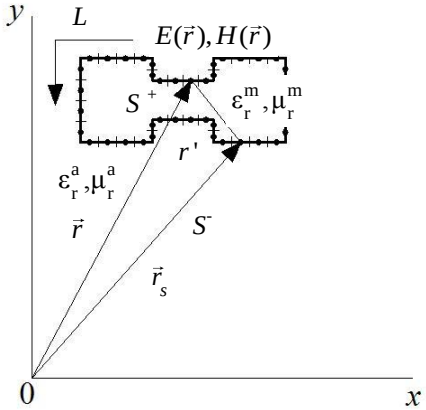


Figure 1: Geometry of an complicated cross-section rod waveguide and the SIE method notations

Here the magnitude *s* is the *arc* abscissa and *ds* is an element of contour L. The magnitudes $\mu_h(\vec{r}_s)$ and $\mu_e(\vec{r}_s)$ are the unknown functions satisfying the Hölder condition. We apply the Krylov–Bogoliubov method whereby the contour is divided into *n* segments and the integration along a contour L is replaced by a sum of integrals over the segments. The expressions of all the electric field components are presented below.

The longitudinal components of the electric field for the area S^+ and S^- are:

$$E_z^+ = \sum_{j=1}^{n} \mu_e^+(s_j) \int_{\Delta L} H_0^{(2)}(k_\perp^+ r')ds\,,$$
$$E_z^- = \sum_{j=1}^{n} \mu_e^-(s_j) \int_{\Delta L} H_0^{(2)}(k_\perp^- r')ds\,. \qquad (2)$$

After substitution of the longitudinal field components (2) in the transverse component formulae we obtain the expressions at the contour points:

$$\left(E_x\right)^+ = -\frac{2\mu_0\mu_r^m\omega\cos\theta}{\left(k_\perp^+\right)^2}\mu_h^+(s_j) - \qquad (3)$$
$$-V_+\left[k_\perp^+\sum_{j=1}^{n}\left(\mu_h^+\left(s_j\right)\right)\int_{\Delta L} H_1^{(2)}(k_\perp^+ r')\frac{y_S - y_0}{r'}ds\right] +$$
$$+Q_+\left[k_\perp^+\sum_{j=1}^{n}\left(\mu_e^+(s_j)\right)\int_{\Delta L} H_1^{(2)}(k_\perp^+ r')\frac{x_S - x_0}{r'}ds\right],$$

$$\left(E_x\right)^- = \frac{2\mu_0\mu_r^a\omega\cos\theta}{\left(k_\perp^-\right)^2}\mu_h^-(s_j) - \qquad (4)$$
$$-V_-\left[k_\perp^-\sum_{j=1}^{n}\left(\mu_h^-\left(s_j\right)\right)\int_{\Delta L} H_1^{(2)}(k_\perp^- r')\frac{y_S - y_0}{r'}ds\right] +$$
$$+Q_-\left[k_\perp^-\sum_{j=1}^{n}\left(\mu_e^-(s_j)\right)\int_{\Delta L} H_1^{(2)}(k_\perp^- r')\frac{x_S - x_0}{r'}ds\right],$$

$$\left(E_y\right)^+ = -\frac{2\mu_0\mu_r^m\omega\cos\theta}{\left(k_\perp^+\right)^2}\mu_h^+(s_j) - \qquad (5)$$
$$-Q_+\left[k_\perp^+\sum_{j=1}^{n}\left(\mu_e^+\left(s_j\right)\right)\int_{\Delta L} H_1^{(2)}(k_\perp^+ r')\frac{y_s - y_0}{r'}ds\right]$$
$$-V_+\left[k_\perp^+\sum_{j=1}^{n}\left(\mu_h^+\left(s_j\right)\right)\int_{\Delta L} H_1^{(2)}(k_\perp^+ r')\frac{x_s - x_0}{r'}ds\right],$$

$$\left(E_y\right)^- = \frac{2\mu_0\mu_r^a\omega\cos\theta}{\left(k_\perp^-\right)^2}\mu_h^-(s_j) - \qquad (6)$$
$$-Q_-\left[k_\perp^-\sum_{j=1}^{n}\left(\mu_e^-\left(s_j\right)\right)\int_{\Delta L} H_1^{(2)}(k_\perp^- r')\frac{y_s - y_0}{r'}ds\right]$$
$$-V_-\left[k_\perp^-\sum_{j=1}^{n}\left(\mu_h\left(s_j\right)\right)^-\int_{\Delta L} H_1^{(2)}(k_\perp^- r')\frac{x_s - x_0}{r'}ds\right],$$

where $\chi_+ = i\varepsilon_0\varepsilon_r^m\omega\Big/\left(k_\perp^+\right)^2$, $\chi_- = i\varepsilon_0\varepsilon_r^a\omega\Big/\left(k_\perp^-\right)^2$, $V_+ = i\mu_0\mu_r^m\omega\Big/\left(k_\perp^+\right)^2$, $V_- = i\mu_0\mu_r^a\omega\Big/\left(k_\perp^-\right)^2$, $Q_+ = ih\Big/\left(k_\perp^+\right)^2$, $Q_- = ih\Big/\left(k_\perp^-\right)^2$, $h = h' - ih''$ is the complex propagation constant where h' is the real part (phase constant) and h'' is the imaginary part (attenuation constant, losses) of the value h. The field components and the values of the unknowns functions $\mu_h(s_j)$ and $\mu_e(s_j)$ are noted in the upper–right corner with the sign

corresponding to different area S^+ or S^-, i.e., the unknowns functions inside of waveguide are $\mu_e^+(s_j)$, $\mu_h^+(s_j)$ and outside of waveguide are $\mu_e^-(s_j)$, $\mu_h^-(s_j)$. These functions at the same contour point are different for the field components in the regions S^+ and S^-, i.e. $\mu_{e,h}^+(s_j) \neq \mu_{e,h}^-(s_j)$. The magnitude $k_\perp^+ = \sqrt{k^2\varepsilon_r^m\mu_r^m - h^2}$ is the transversal propagation constant for the SiC medium in the area S^+ and $k_\perp^- = \sqrt{h^2 - k^2\varepsilon_r^a\mu_r^a}$ is the transverse wave numbers in the area S^- (Fig. 1). Magnitudes $\varepsilon_r^m = \mathrm{Re}(\varepsilon_r^m) - i\mathrm{Im}(\varepsilon_r^m)$ and $\mu_r^m = \mathrm{Re}(\mu_r^m) - i\mathrm{Im}(\mu_r^m)$ are the complex permittivity and the complex permeability of the SiC media. Magnitudes ε_r^a and μ_r^a are the permittivity and the permeability of air around the waveguide. The value $k = \omega/c$ is the wavenumber in air, $\omega = 2\pi f$, where f is an operating frequency. The contour L is divided into n segments and the length of a segment is $\Delta L = L/n$ where the limits of integration in the formulas (2–6) are the ends of each segment ΔL. $H_1^{(2)}$ is the Hankel function of the first order and the second kind. The angle θ is equal to $g \cdot 90°$ with g from 1 till 4 for rectangular contours in the formulae (3–6). The expressions for the magnetic field components are similar. The system of the algebraic equations obtained from the boundary conditions is homogeneous. The condition of solvability is obtained equalizing the determinant of the system to zero. The determinant is our dispersion equation. We have used the Müller's method to find the complex roots. The roots of the dispersion equation give the propagation constants of waveguide modes. After obtaining the propagation constants of desired modes we can determinate the EM field of these modes (see, formulae 2–6). For the correct formulated problem the solution is one–valued and stable with respect to small changes of the coefficients and the contour form [11].

3. The numerical results

The EM wave propagation properties of open SiC ridged waveguide and photonic waveguide can be analyzed in terms of their dispersion curves, i. e. the normalized complex propagation constant versus the frequency. Our developed algorithm let us investigate the dispersion characteristics of the main mode as well as the all spectrum of the waveguide higher eigenmodes. Because the operation mode of many microwave devices is the main one of waveguide structures wherefore the main mode is the subject of our special interest. Here we present dispersion characteristics of the main mode only.

We have investigated the ridged (Fig. 2) and photonic (Fig. 3) waveguide structures by the SIE method that let us to satisfy the exact boundary conditions, i.e. take into account the real topology of the waveguide cross section. Our computer code is written in MATLAB.

The external shape and dimensions of both waveguides Figs 1&2 are the same: $a = b = 7$ mm, s = $d = 1$ mm, l = 3mm. The photonic waveguide additionally has rectangular openings inside of waveguide body determined by sizes $x = 0.2$ mm, $y = 0.5$ mm, $z = 1$ mm.

Both waveguides have in the middle of cross-section a narrow part with the width s and the height d where the EM field energy is focusing. These structures can be used as concentrates of EM energy in this narrow part. Furthermore in order to increase of the waveguide functionality it is rationally to make channels in the waveguide body for a laser radiation, or for controlling of EM properties by filling openings (channels) with gases or liquids or for placing electronic elements inside of channels. The air openings inside of photonic waveguide may lead to a reduction in main mode losses.

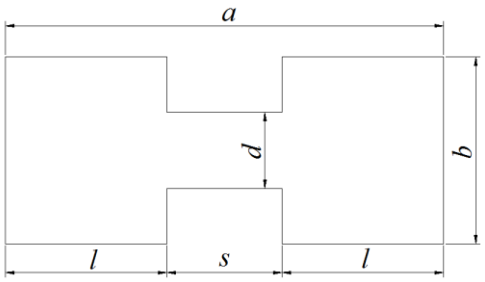


Figure 2: The ridged waveguide structure.

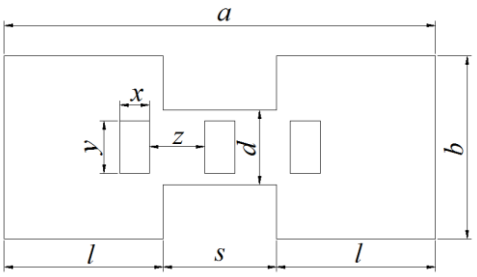
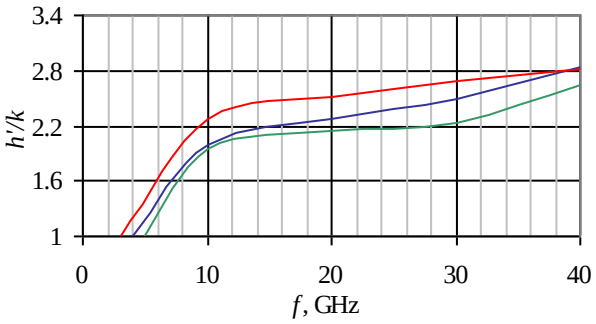


Figure 3: The photonic waveguide structure .

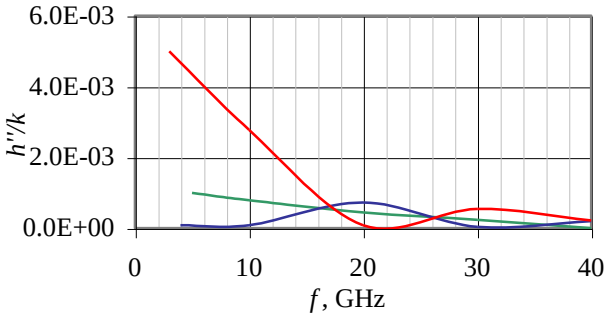
We analysed dispersion characteristics of both waveguides at different temperatures therefore the general SiC material advantage is ability to operate at high temperatures. This ability of SiC can be use to control EM properties of waveguides by temperature too.

We have calculated the dispersion characteristics for both waveguides (Figs 1&2) at three different temperatures T. The dispersion curves of the main mode at T=1500ºC are denoted by the red colour. The permittivity of the SiC is 8-2j in this case [12] at the cutoff frequency of the main mode. The dispersion curves at T=1000ºC and 20ºC are denoted by the blue and green lines correspondingly. The permittivity of the SiC is 7-j and is 6-0.5j in the last two cases. The permeability of the surrounding air and waveguide SiC material were accepted in our calculations equal to 1.

In the Figs 3(a) & 4(a) are presented the real part of the complex propagation constant of main mode, i.e. the phase constant $h' = 2\pi/\lambda$, λ is a main mode wavelength, correspondingly, for waveguides Figs 1 & 2.



(a)

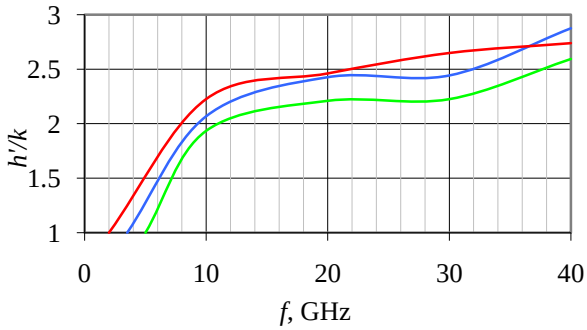


(b)

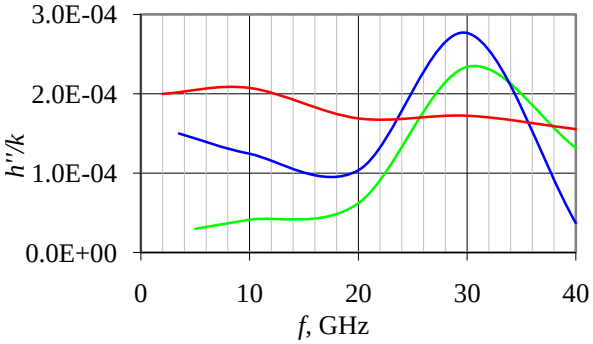
Figure 4: The complex dispersion characteristics of the ridged waveguide structure (Fig. 2): (a) – the dependence of the phase constant upon the frequency, (b) - the dependence of the attenuation constant (losses) upon the frequency.

We see, analyzing the phase constants of both waveguides, the temperature is higher the value *h'* is usually larger, i.e. with an increasing of temperature *T* the mode wavelength λ decreases. This can be explained by the fact that with an increasing of temperature increase also the values of the real and imaginary parts of SiC permittivity.

The cutoff frequency f_{cut} of mode is shifted to the left on the dispersion curve graphs (Figs 4(a), 5(a), i.e. f_{cut} is moved in the low frequency range when *T* increases from 20 till 1500° C. The ridged waveguide values of f_{cut} are a little bet larger in comparison with the f_{cut} values of photonic waveguide.



(a)



(b)

Figure 5: The complex dispersion characteristics of the photonic waveguide (Fig. 3): (a) – the dependence of the phase constant upon the frequency, (b) - the dependence of the attenuation constant (losses) upon the frequency.

We can see this especially for temperatures 1000ºC and 1500 ºC. That means that air openings are shifted the value f_{cut} in the low frequency region.

We can see that the mode wavelength of the ridged waveguide (λ~1/ *h'*) is shorter in comparison with the wavelength of the photonic waveguide which has openings inside of it. This result was predictable by common electrodynamical considerations, because the effective permittivity of composite material (SiC and air openings inside if it) of the photonic waveguide is less than the one of ridged waveguide. The phase constant of both waveguides increases rapidly from the cutoff frequency to approximately to 12 GHz and then the dispersion curves' growth slows down and curves become slightly sloping at the higher frequencies (see Figs 4(a), 5(a)). It is possible to explain the rapid growth of values *h'* in such way. The mode wavelength λ commensurate with the waveguide elements' sizes *d*, *s*, *a*, *b* (Figs 1&2) at the frequency range between the cutoff frequency and ~12 GHz. For this reason EM wave strongly "feel" the shape of waveguide, i.e. the boundary conditions. In this case the largest part of an electric field is distributed in the air space around the waveguide near the interface of SiC at the mentioned frequencies. Moreover the imaginary part of the SiC permittivity dependent inversely proportional to the frequency, i.e. the losses of SiC decrease with increasing of frequencies. This fact also promotes the involvement of the EM wave inside of waveguide material. In other words with increasing frequency also increases the part of the EM wave energy which is distributed into SiC material. We can observe a kind of saturation of EM wave drawing at waveguide body at higher frequencies. The saturation happened because almost the all EM field energy already is inside of the waveguide SiC material. For this reason any increase of the frequency does not influent appreciably on the EM field distribution when *f* is large ~ 12 GHz and we see that at higher frequencies dispersion characteristic curves vary slightly.

The common character of the phase constant dependency on frequencies is a traditional one, for example, like for usual open dielectric waveguides [13].

We can achieve the optimal electrodynamical characteristics of waveguide by identifying of cross-section and dimensions of specific waveguide elements like such as *x, y, z, d, s*.

It is interesting to compare the loss of EM wave energy of both waveguides (Fig, 1&2). We see do not traditional dependences of attenuation constants of the ridged (Fig. 4(b)) and the photonic (Fig. 5(b)) waveguides. As you would expect the second waveguide losses lower than in the first one. We see that the losses of both waveguides are differing on the one order. The difference in losses can be easily explained by the fact that there are openings in the photonic waveguide (Fig. 2) and when the mode propagates through the air undergoes less attenuation. The attenuation constant both waveguides dependent on the temperature, we know that the higher temperature is the larger the real and imaginary part of permittivity of SiC are. In spite of this, we can see (Figs 4(b), 5(b)) that the attenuation constant of main mode at the temperature 1500°C may be smaller than at temperatures 1000 or 20°C. We can watch the special dependence of losses for the photonic waveguide. The attenuation constant throughout the entire range f at T=1500°C is almost unchangeable. Hence the signal modulation by the mode losses may be weak at high temperatures.

We see the curve extremes of attenuation constants (Fig. 5(b) at f = 30 GHz when T=1000°C and 20 °C and the wavenumber k at 30 GHz is equal to 2π. It could be a dimensional resonance of EM wave, which has the wavelength $\lambda_{T=1000}$~0.42 mm or $\lambda_{T=20}$~0.45 mm (see Fig. 5(a)) with the photonic waveguide elements: s = d = 1 mm, x = 0.2 mm, y = 0.5 mm, z = 1 mm.

Conclusions

We created a new computer algorithm for investigation of open dielectric type waveguides with a complicated shape of cross-section and made of materials that may have very high losses. We have made the electrodynamical analysis of the two novel waveguide structures by means of the Singular Integral Equations' method. The dispersion characteristics of two different waveguide structures were analyzed. It was found out that the attenuation constant of main mode propagating in the photonic waveguide structure with air openings are smaller than the losses in the ridged waveguide structure without air channels. As a result, the developed algorithm which let us investigates a very complicated 2D waveguide structures that can be performed of present-day materials with large losses.

References

[1] M. Mukherjee, *Silicon Carbide Based Transit Time Devices: The New Frontier in High-power THz Electronics, Properties and Applications of Silicon Carbide*, Edited by: Rosario Gerhardt, ISBN 978-953-307-201-2, InTech, pp. 143-169, 2011

[2] D. Alfano, *Spectroscopic properties of carbon fibre reinforced silicon carbide composites for aerospace applications. Properties and Applications of Silicon Carbide*, Edited by: Rosario Gerhardt, ISBN 978-953-307-201-2, InTech, pp. 231-250, 2011.

[3] G. Pandraud, P.J. French, P.M. Sarro, PECVD Silicon Carbide Waveguides for Multichannel Sensors, *Proc. IEEE SENSORS*, Atlanta, Georgia, USA, pp. 395-398, 2007.

[4] S. Oku, Y. Shibata, Semiconductor photonic waveguide structures made by a reactive beam etching technique, *Proc. Indium Phosphide and Related Materials International Conference*, Nara, Japan, pp. 75–78, 2001.

[5] H. Taniyama, Waveguide structures using one-dimensional photonic crystal, *J. Appl. Phys.* 91(6): 3511–3515, 2002.

[6] H. Yamada, T. Chu, S. Ishida and Y. Arakawa, Optical directional coupler based on Si-wire waveguides, *IEEE J. Sel. Top. Quant.* 12(6): 1371–1379, 2006.

[7] J. S. Li, S. Zouhdi, Ultrafast and low-power terahertz modulator based on organic photonic crystal, *Opt. Commun.* 285: 953−956, 2012.

[8] S. Stankovic, M. Milosevic, B. Timotijevic, P.Y. Yang, E.J. Teo, J. Crnjanski, P. Matavulj and G.Z. Mashanovich, Silicon photonic waveguides for near- and mid-infrared regions, *Acta Phys. Pol. A* 112(5), 1019−1024, 2007.

[9] R. M. Briggs, I. M. Pryce, and H. A. Atwater, Compact silicon photonic waveguide modulator based on the vanadium dioxide metal-insulator phase transition, *Opt. Express* 18(11), 11192–11201, 2010.

[10] T. F. Krauss, Slow light in photonic crystal waveguides, *J. Phys. D: Appl. Phys.* 40, 2666–2670, 2007.

[11] T. Gric, L. Nickelson and S. Asmontas, Electrodynamical characteristic particularity of open metamaterial square and circular waveguides, *Prog. Electromagn. Res.* 109, 361–379, 2010.

[12] T. A. Baeraky, Microwave measurements of the dielectric properties of silicon carbide at high temperature, *Egypt. J. Sol.* 25(2), 263–273, 2002.

[13] S. Asmontas, L. Nickelson, A. Bubnelis, Martavicius, J. Skudutis, Hybrid Mode Dispersion Characteristic Dependences of Cylindrical Dipolar Glass Waveguides on Temperatures, *Electronics and Electrical Engineering* 10(106), 83-86, 2010.

Electrodynamical analysis of metamaterial waveguides coated with silicon carbides

L. Nickelson[1,2], A. Bubnelis[1,2], S. Asmontas[1]

[1]State Research Institute Center for Physical Sciences and Technology, Lithuania
[2]Vilnius Gediminas Technical University, Lithuania
*corresponding author, E-mail: lucynickelson@gmail.com

Abstract

Here we present our calculation results of electromagnetic (EM) field intensity and vector distributions as well as the dispersion characteristic (phase and attenuation constants) of open two-layered cylindrical waveguides. Waveguides are consisted a metamaterial core which coated by a silicon carbide (SiC) layer. The electrodynamical analysis was performed for three waveguides with the metamaterial core radii r are equal to 1.0, 2.0, 3.0 mm when the external waveguide radius $R = 5$ mm. We discovered a narrow frequency range when the waveguides have the very large attenuations. We find also the very important feature of the waveguides that the ones may have a one – mode regime with a very low attenuation of the hybrid propagating mode in the frequency range from 12.5 to 16 GHz. The electric and magnetic field intensity (strength) and their vector distributions in the waveguide transversal cross-section were calculated in about 26000 points and 1680 points on the radius 2R.

Keywords: eigenvalue problem, partial area method, SiC-metamaterial cylindrical waveguide, numerical analysis, electric field, magnetic field, dispersion characteristics, phase constant, attenuation constant, silicon carbide, double-negative metamaterial, losses, microwave range.

1. Introduction

The technological potential of metamaterials for developing novel devices offers a very promising alternative that could potentially overcome the limitations of current technology. Artificial materials with unusual electrodynamical properties are increasingly being used to develop high-frequency devices with special features. The use of the metamaterials can be seen more often in devices such as antennas, radars, scattering structures, waveguides, cloaking devices [1–4].

In order to create a new microwave device it is necessary to know the main electrodynamical characteristics of metamaterial structures on the basis of which the device is supposed to be created. There are insufficient of articles about the distributions of the EM field in the waveguide and structures [5, 6].

We present here electric and magnetic fields distributions in the transversal and the longitudinal cross-sections as well as the phase and attenuation constants of open two-layered cylindrical waveguides. The waveguides have the core of UCSD30815 metamaterial and the coated layer of silicon carbide (SiC). The parameters of materials were taken from [7, 8].

2. Electrodynamical waveguide model

The model of our investigated waveguide contains three isotropic areas for electrodynamical solution of the problem. Metamaterial core, SiC coating layer and the air outside the waveguide. The solution of this boundary problem was fulfilled by the partial area method in the rigorous electrodynamical formulation. The electrodynamical problem can be solved by using the Maxwell's equations in differential form [9].

In accordance with the boundary conditions is formed the system of linear equations. The dispersion equation is written in the form of determinant D of the eighth order (1). Determinant order depends on quantity of boundaries of layers in the waveguide. The solutions of this dispersion equation is complex propagation constant $h = h' - \mathrm{i}h''$. The real part h' is a wave propagation constant (or phase constant) and the imaginary part h'' is an attenuation constant (losses). The phase constant is inversely proportional to the wavelength λ in the waveguide $h' = 2\pi/\lambda$.

$$D = \begin{vmatrix} d_{11} & 0 & d_{13} & 0 & 0 & 0 & d_{17} & 0 \\ d_{21} & d_{22} & d_{23} & d_{24} & 0 & 0 & d_{27} & d_{28} \\ 0 & d_{32} & 0 & d_{34} & 0 & 0 & 0 & d_{38} \\ d_{41} & d_{42} & d_{43} & d_{44} & 0 & 0 & d_{47} & d_{48} \\ 0 & 0 & d_{53} & 0 & d_{55} & 0 & d_{57} & 0 \\ 0 & 0 & d_{63} & d_{64} & d_{65} & d_{66} & d_{67} & d_{68} \\ 0 & 0 & 0 & d_{74} & 0 & d_{76} & 0 & d_{78} \\ 0 & 0 & d_{83} & d_{84} & d_{85} & d_{86} & d_{87} & d_{88} \end{vmatrix} \quad (1)$$

When searching the complex roots of the dispersion equation, we are calculating values of the determinant D for value h in a specific range. The resulting function $D(h, f = const.)$ has the shape of complex surface. The complex roots of the dispersion equation are clearly visible on the surface and have a form of sharp cones at minima points of the surface. At this points function $D(h, f) \to 0$.

This methodology of searching complex roots allows calculating the dispersion characteristics with high losses in the waveguides. This approach is versatile, but it requires more computational resources. For some tasks, can be used the special mathematical methods to find complex roots, such as the Muller's method. It requires much less resources but have some limitations.

The components of determinant *D* are expressed by formulas (2)–(25):

$$d_{11} = d_{32} = J_m(k_\perp^{(1)} r), \tag{2}$$

$$d_{13} = d_{34} = -J_m(k_\perp^{(2)} r), \tag{3}$$

$$d_{17} = d_{38} = -N_m(k_\perp^{(2)} r), \tag{4}$$

$$d_{21} = d_{42} = \frac{h}{\left(k_\perp^{(1)}\right)^2} \cdot \frac{m}{r} \cdot J_m(k_\perp^{(1)} r), \tag{5}$$

$$d_{22} = \frac{\mathrm{i}\omega\mu_0\mu_r^{(1)}}{k_\perp^{(1)}} \cdot J'_m(k_\perp^{(1)} r), \tag{6}$$

$$d_{23} = d_{44} = -\frac{h}{\left(k_\perp^{(2)}\right)^2} \cdot \frac{m}{r} \cdot J_m(k_\perp^{(2)} r), \tag{7}$$

$$d_{24} = -\frac{\mathrm{i}\omega\mu_0\mu_r^{(2)}}{k_\perp^{(2)}} \cdot J'_m(k_\perp^{(2)} r), \tag{8}$$

$$d_{27} = d_{48} = -\frac{h}{\left(k_\perp^{(2)}\right)^2} \cdot \frac{m}{r} \cdot N_m(k_\perp^{(2)} r), \tag{9}$$

$$d_{28} = -\frac{\mathrm{i}\omega\mu_0\mu_r^{(2)}}{k_\perp^{(2)}} \cdot N'_m(k_\perp^{(2)} r), \tag{10}$$

$$d_{41} = -\frac{\mathrm{i}\omega\varepsilon_0\varepsilon_r^{(1)}}{k_\perp^{(1)}} \cdot J'_m(k_\perp^{(1)} r), \tag{11}$$

$$d_{43} = \frac{\mathrm{i}\omega\varepsilon_0\varepsilon_r^{(2)}}{k_\perp^{(2)}} \cdot J'_m(k_\perp^{(2)} r), \tag{12}$$

$$d_{47} = \frac{\mathrm{i}\omega\varepsilon_0\varepsilon_r^{(2)}}{k_\perp^{(2)}} \cdot N'_m(k_\perp^{(2)} r), \tag{13}$$

$$d_{53} = d_{74} = J_m(k_\perp^{(2)} r), \tag{14}$$

$$d_{55} = d_{76} = -H_m^{(2)}(k_\perp^{(3)} r), \tag{15}$$

$$d_{57} = d_{78} = N_m(k_\perp^{(2)} r), \tag{16}$$

$$d_{63} = d_{84} = \frac{h}{\left(k_\perp^{(2)}\right)^2} \cdot \frac{m}{r} \cdot J_m(k_\perp^{(2)} r), \tag{17}$$

$$d_{64} = \frac{\mathrm{i}\omega\mu_0\mu_r^{(2)}}{k_\perp^{(2)}} \cdot J'_m(k_\perp^{(2)} r), \tag{18}$$

$$d_{65} = d_{86} = -\frac{h}{\left(k_\perp^{(3)}\right)^2} \cdot \frac{m}{r} \cdot H_m^{(2)}(k_\perp^{(3)} r), \tag{19}$$

$$d_{66} = -\frac{\mathrm{i}\omega\mu_0\mu_r^{(3)}}{k_\perp^{(3)}} \cdot H'^{(2)}_m(k_\perp^{(3)} r), \tag{20}$$

$$d_{67} = d_{88} = \frac{h}{\left(k_\perp^{(2)}\right)^2} \cdot \frac{m}{r} \cdot N_m(k_\perp^{(2)} r), \tag{21}$$

$$d_{68} = \frac{\mathrm{i}\omega\mu_0\mu_r^{(2)}}{k_\perp^{(2)}} \cdot N'_m(k_\perp^{(2)} r), \tag{22}$$

$$d_{83} = -\frac{\mathrm{i}\omega\varepsilon_0\varepsilon_r^{(2)}}{k_\perp^{(2)}} \cdot J'_m(k_\perp^{(2)} r), \tag{23}$$

$$d_{85} = \frac{\mathrm{i}\omega\varepsilon_0\varepsilon_r^{(3)}}{k_\perp^{(3)}} \cdot H'^{(2)}_m(k_\perp^{(3)} r), \tag{24}$$

$$d_{87} = -\frac{\mathrm{i}\omega\varepsilon_0\varepsilon_r^{(2)}}{k_\perp^{(2)}} \cdot N'_m(k_\perp^{(2)} r), \tag{25}$$

where $J_m(k_\perp^{(1,2)} r)$ is the Bessel function of the m-th order, $N_m(k_\perp^{(2)} r)$ is the *m*-th order Neumann function, $H_m^{(2)}(k_\perp^{(3)} r)$ is the Hankel function of the second kind. $J'_m(k_\perp^{(1,2)} r)$, $N'_m(k_\perp^{(2)} r)$, $H'^{(2)}_m(k_\perp^{(3)} r)$ are the derivatives of cylindrical functions. $k_\perp^{(1)} = \sqrt{k^2 \varepsilon_r^{(1)} \mu_r^{(1)} - h^2}$ is the transversal propagation constant for the waveguide core medium, $k_\perp^{(2)}$ and $k_\perp^{(3)}$ accordingly are transversal propagation constants for the coating layer and the air layer outside the waveguide. The value $k = c/\omega$ is the wave number in a vacuum. $\varepsilon_r^{(1,2,3)}$ and $\mu_r^{(1,2,3)}$ are the relative permittivity and the relative permeability of corresponding layer of the waveguide. Variable *r* is here a radial coordinate.

3. Analysis of the dispersion characteristics and distribution of the EM fields

We present here our calculation results on investigations of the open two-layer cylindrical metamaterial-SiC waveguides in frequency range 11–16 GHz. We analyzed only modes with the azimuthal index $m = 1$ because the main mode of cylinder waveguides has this EM field symmetry.

As it known SiC has privileges because it can operate at high-temperature, high-power, high-radiation conditions, high melting point. SiC have excellent mechanical properties, as the high hardness and strength, and etc.

The external radius of waveguides are constant and equal to $R = 5$ mm in our calculations. The radius of metamaterial core is changing. The waveguide materials depict by the complex permittivity and permeability, which were taken of articles [7, 8]. Our computer code is written in MATLAB language. The code let us take into account high losses in materials.

The real and imaginary parts of complex propagation constant dependencies on the frequency at three metamaterial core radii are shown in Figs. 1, 2. We have calculated normalized phase constant (Fig. 1) and attenuation constant (Fig. 2) when the waveguide metamaterial core radius is 1.0 mm, 2.0 mm and 3.0 mm. Dispersion characteristics of the waveguide have an unusual form, which is highly dependent on the metamaterial core radius as well as on the magnitudes and signs of permittivity and permeability of UCSD30815 metamaterial at certain frequencies.

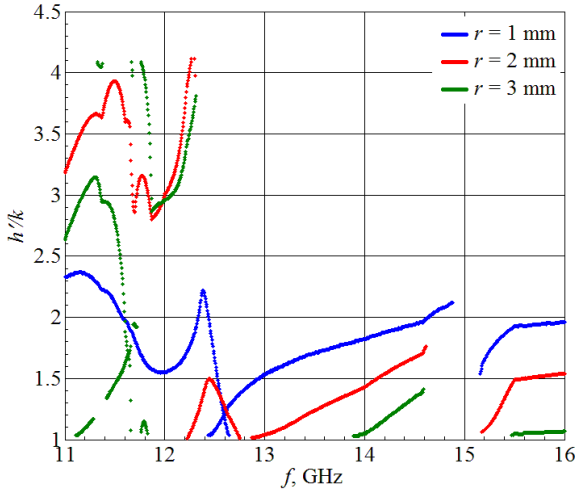


Figure 1: Normalized phase constant dependences of layered metamaterial-SiC waveguide on frequency f at different metamaterial core radii r.

We can observe the resonance behavior of phase and attenuation constants at the frequency range 11–12.75 GHz. The metamaterial is double-negative one with the sharp resonance pikes of the permittivity and the permeability at this frequencies. It is special large the metamaterial magnetic losses here [7]. All propagating modes are the hybrid ones with all 6 components of EM field.

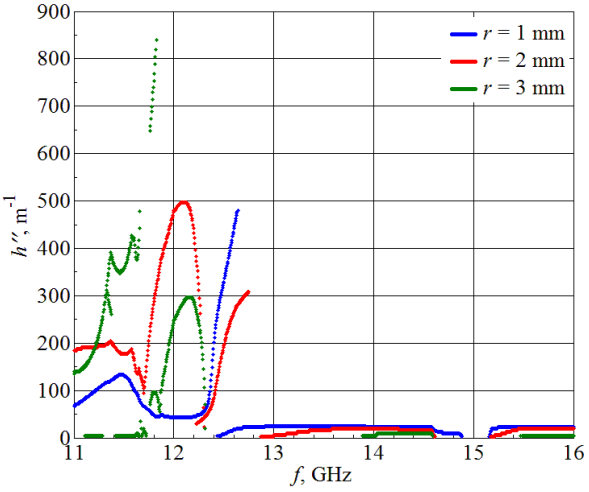


Figure 2: Attenuation constant dependences of metamaterial-SiC waveguide on frequency f at different metamaterial core radii r.

The frequency range 11–16 GHz may be subdivided into three areas on the behavior of dispersion curves. The first area is $\Delta f_1 \sim 11$–12.75 GHz; the second area is $\Delta f_2 \sim 12.75$–15 GHz and the third area is $\Delta f_3 \sim 15$–16 GHz.

The dispersion characteristics have very intricate shapes along the first area Δf_1 for all three investigated waveguides when radii of metamaterial core are equal to 1.0–3.0 mm. For this reason we describe these dependencies in details.

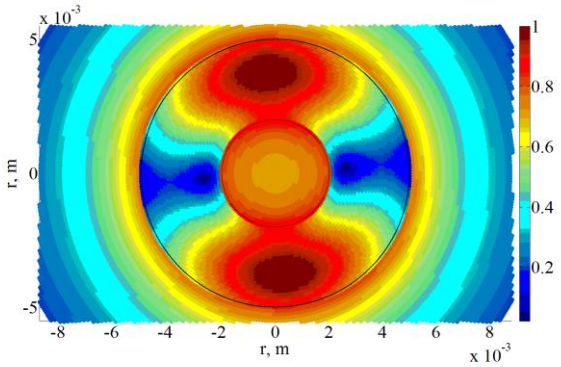


Figure 3: Electric field intensity in the transversal cross-section of metamaterial-SiC waveguide at frequency $f = 13.5$ GHz.

There is only one propagating mode when the core metamaterial radius r is 1.0 mm (blue colour) until $f \sim 12.4$ GHz. The value of phase constant is changing wavy and the magnitude gradually varies from maximum to minimum and then again growing till maxima at $f \sim 12.3$ GHz. The attenuation constant of this single mode has a very large value in area Δf_1 and increases dramatically between $f \sim 12.3$–12.6 GHz. There are two propagating modes at $f \sim 12.4$–12.7 GHz when r is 1.0 mm. The cutoff frequency of the higher mode is 12.4 GHz. The attenuation constant of the first mode is very large and the second one is small enough.

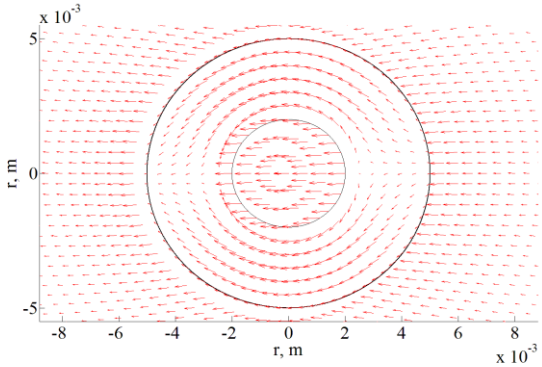


Figure 4: Electric field vector distribution in transversal cross-section of metamaterial-SiC waveguide at frequency $f = 13.5$ GHz.

We see that the curve of phase constant has sharp resonant crests which have various sizes when the metamaterial core radius $r = 2$ mm (red colour). And the branch of h' curve finished at $f \sim 12.3$ GHz and then a new peak appears at higher frequencies $f \sim 12.2$–12.4 GHz. It can be assumed that the first wave vanished it existence at certain f and a new mode with a different structure of EM field started to propagate at $f \sim 12.2$ GHz. The last mode

can propagate only in a narrow frequency range. This wave can be used in the designing of microwave switches.

Values of attenuation constant h'' of waveguide with r = 2 mm at most frequencies are large in comparison with waveguide of radius r = 1 mm. The central maximum of $h''_{r=2\text{mm}}$ (red color) reaches 500 m^{-1} (4.34 dB/mm).

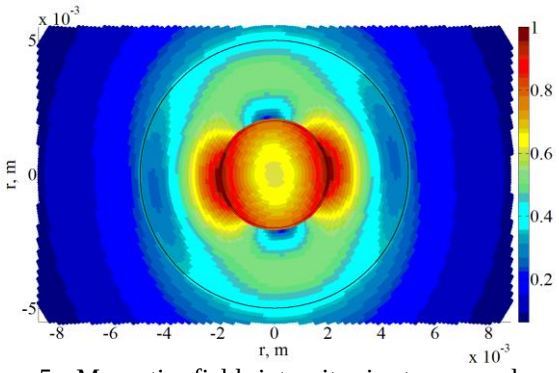


Figure 5: Magnetic field intensity in transversal cross-section of metamaterial-SiC waveguide at frequency f = 13.5 GHz.

Especially complicated dispersion characteristics for waveguide with the largest metamaterial core, when r = 3.0 mm (green colour). As we can see in Figs. 1 and 2 that there are four or more independent dispersion characteristic branches which have the form of the parabola part, two small and large letters V and the inverted letters V in the area Δf_1. The attenuation constants these propagating modes differ from each other and for one of modes can reach 850 m^{-1}. This bunch of modes exists only till f ~ 12.3 GHz. It should be noted that there is not a one mode-regime of the waveguide with r = 3.0 mm at f ~ 12.3–13.8 GHz.

The EM wave attenuation (h'') of modes is very high in the first area Δf_1 and the waveguides could be used in absorbing devices.

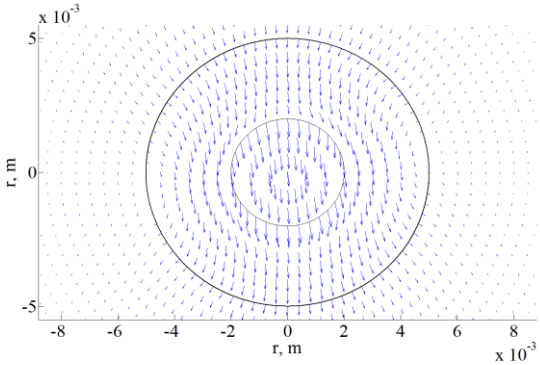


Figure 6: Magnetic field vector distribution in the transversal cross-section of metamaterial-SiC waveguide at frequency f = 13.5 GHz.

The shape of dispersion characteristics of all three waveguides (r = 1.0–3.0 mm) in the second area Δf_2 are traditional as for usual open dielectric cylindrical waveguides [9]. The cutoff frequencies of the propagating modes in area Δf_2 are 12.45 GHz, 12.87 GHz, 13.9 GHz, when the metamaterial core radii are 1 mm, 2 mm and 3 mm, respectively. We see that the value of cutoff frequency is noticeably larger when the core radius r is bigger in spite that the external radius R of waveguide is constant. When the core radius is equal or more than 2 mm than on the waveguide can propagate only one wave with a low attenuation in Δf_2.

In the third area Δf_3 also waveguides operate in one-mode regime. It is important for transmission of EM energy by last waveguides. A frequency gap exists between the dispersion characteristics of eigenmodes that can propagate at Δf_2 and Δf_3 frequencies. Therefore not be interference of modes.

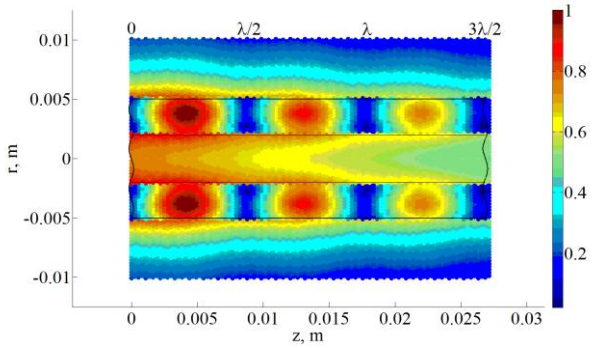


Figure 7: Electric field intensity distribution on the longitudinal cross section of the metamaterial-SiC waveguide at frequency f = 13.5 GHz.

Transverse electric and magnetic field distribution of intensities (strengths) of the propagating mode when the metamaterial core radius is 2 mm and the thickness of SiC layer is 3 mm are presented in Figs. 3, 5 at frequency f = 13.5 GHz. We would like to draw your attention that the metamaterial permittivity is real and approximately equal to -2.5 and the complex permeability equal to zero.

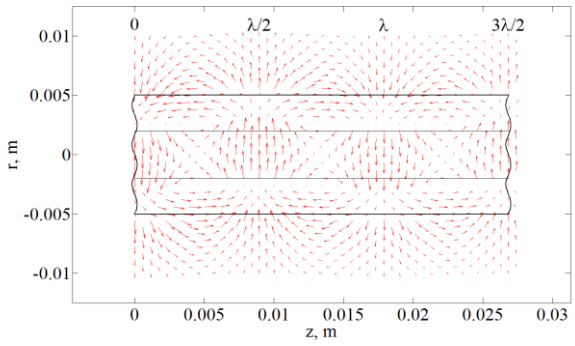


Figure 8: Longitudinal electric field vectors of the metamaterial-SiC waveguide at frequency f = 13.5 GHz.

We calculated components of EM field in the transversal cross-section with the radius equal to 2R, i.e. inside and outside of waveguide. Field intensity is calculated for each point of transverse or longitudinal cross-section by geometrically summing three components of electric ($\vec{E}_r$; $\vec{E}_\varphi$; $\vec{E}_z$) or magnetic ($\vec{H}_r$; $\vec{H}_\varphi$; $\vec{H}_z$) field vectors. We can see that the electric and magnetic fields are localized in the SiC layer, outside of metamaterial core. The color of EM distribution in figures is proportional to the value of the electrical and magnetical fields.

The visualizations of electric and magnetic field intensity in the longitudinal cross-section of the waveguide are presented in Figs. 7, 9. Since the metamaterial and SiC are the lossy substrata, it can be seen that the EM wave attenuates with propagating along waveguide, i.e. the intensity of the EM field become less. At frequency of 13.5 GHz the EM wave is attenuated by approximately 1.5 times after about 3 cm of propagation.

Electric and magnetic field vectors in the transverse and longitudinal sections of the waveguide are presented in Figs. 4, 6, 8, 10. The arrows indicate the direction of the field, and their length is proportional to the field intensity at fixed points. The transverse components of electric and magnetic fields are $\vec{E}_r$, $\vec{E}_\varphi$, $\vec{H}_r$ $\vec{H}_\varphi$ and the longitudinal components are $\vec{E}_z$, and $\vec{H}_z$.

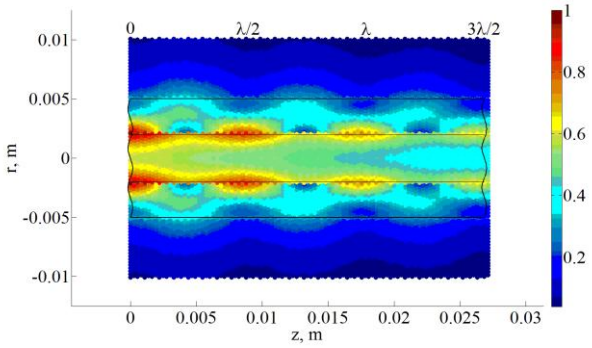


Figure 9: Magnetic field intensity (longitudinal cross section) of metamaterial-SiC waveguide at frequency f = 13.5 GHz.

We can see that the transverse cross-sections (Figs. 4, 6) electric and magnetic field vectors are normal to each other. In addition we can observe a shift between the vectors E and H (Figs. 8, 10) in the longitudinal section because the media are lossy [10].

During the simulation, we observed that the electric and magnetic fields are more concentrated in the coating SiC layer near the interface of waveguide metamaterial core with increasing frequency. It can be seen that the electric field extends into the air outside the waveguide more than magnetic field (Figs. 3, 5, 7, 9).

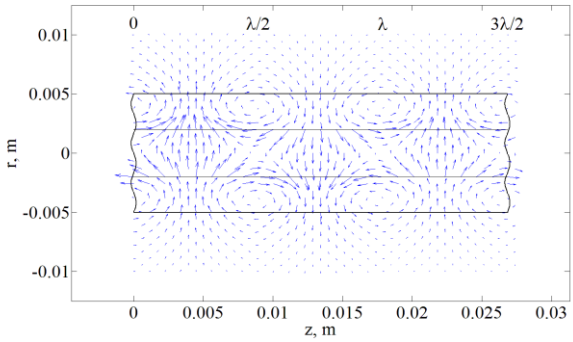


Figure 10: Longitudinal magnetic field vectors of metamaterial-SiC waveguide at frequency f = 13.5 GHz.

The EM field intensity distributions show that the wave energy almost entirely fades in the free space outside of waveguide in the distance less than the one mode wavelength.

4. Conclusions

We have developed the algorithm for visualization of electric and magnetic field in the two-layered isotropic lossy waveguide. The dispersion characteristics of open metamaterial-SiC layered waveguide at different metamaterial core radii are given.

In the frequency range 12.8–16 GHz can propagate only one mode. The attenuation of this hybrid propagating mode is small and slightly dependent on the frequency.

EM field distributions are analyzed for the waveguide with metamaterial core radius r = 2 mm in the space with radius 10 mm. Presented visualization of transverse and longitudinal electric and magnetic fields in the waveguide at frequency f = 13.5 GHz.

The strongest concentration of the electric and magnetic fields are inside of SiC layer in the area of metamaterial core interface. The electric and magnetic field maximal localizations are in different places of the waveguide perimeter.

References

[1] E. O. Liznev, A. V. Dorofeenko, H. Liu, A.P. Vinogradov, S. Zouhdi, Epsilon-near-zero material as a unique solution to three different approaches to cloaking, *Appl. Phys. A* 2(10): 321–325, 2010.

[2] C.-W. Qiu, S. Zouhdi, and Y. L. Geng, Shifted Resonances in Coated Metamaterial Cylinders: Enhanced Backscattering and Near-Field Effects, *Physical Review E* 77: 046604, 2008.

[3] K. Vafi, A. R. M. Javan, M. S. Abrishamian, N. Granpayeh, dispersive behavior of plasmonic and metamaterial coating on achieving transparency, *J. of Electromagn. Waves and Appl*. 22, 941–952, 2008.

[4] Q.-Y. Wen, H.-W. Zhang, Q.-H. Yang, Z. Chen, B.-H. Zhao, Y. Long, Y.-L. Jing, *Perfect Metamaterial Absorbers in Microwave and Terahertz Bands*, Metamaterial, Edited by Xun-Ya Jiang, InTech, pp. 501–512, 2012.

[5] Z. J. Wang and J. F. Dong, Analysis of guided modes in asymmetric left-handed slab waveguides, *PIER* 62: 203–215, 2006.

[6] L. Nickelson, T. Gric, S. Asmontas, R. Martavicius, Electric field distributions of the fast and slow modes propagated in the open rod SiC waveguide, *Electronics and Electrical Engineering* 5(93): 87–90, 2009.

[7] D. R. Smith and et al., Design and measurement of anisotropic metamaterials that exhibit negative refraction, *IEICE Trans. Electron*. 3 (E87-C): 359–370, 2004.

[8] T. A. Baeraky, Microwave measurements of the dielectric properties of silicon carbide at high temperature, *Egypt. J. Sol*. 2(25): 263–273, 2002.

[9] S. Asmontas, L. Nickelson, A. Bubnelis, R. Martavicius, J. Skudutis, Hybrid mode dispersion characteristic dependencies of cylindrical dipolar glass waveguides on temperatures, *Electronics and Electrical Engineering* 10(106): 83–86, 2010.

[10] D.J. Griffiths, *Introduction to Electrodynamics*, Prentice Hall, Upper Saddle River, New Jersey, 1999.

Technologies and applications

Simulation and Design of a Bandpass Filter on Metasubstrates

V. P. Silva Neto*, C. F. L. Vasconcelos, M. R. M. L. Albuquerque, and A. G. D'Assunção

Universidade Federal do Rio Grande do Norte, 59072-970, Natal, RN, Brazil
* corresponding author, E-mail: valdemir.neto@yahoo.com.br

Abstract

This work presents an analysis of the microstrip bandpass filter on metamaterial substrates. The filter is composed of two ring resonators with quarter-wavelength side-coupled sections. The filter input is provided, as well as the output port, using a quarter-wavelength side-coupled microstrip line section. Simulations by finite element method have been carried out to verify the effect of the metamaterial substrate properties on the filter performance, and to compare these results to those obtained considering isotropic substrate.

1. Introduction

Metamaterials have received a great deal of attention due to their unusual electromagnetic properties unavailable in conventional materials. By tuning the geometrical structure of the metamaterial element, we can control the material electromagnetic responses [1–4]. Then, these engineered materials can be used in a variety of printed circuit applications such as filters, impedance transformers, couplers, and antennas [5–7].

Dielectric resonators have many attractive features such as low cost fabrication, compact size, and integration capacity with active devices. These structures found potential applications as basic construction elements in the development of several microwave circuits. Over the years, several works have been devoted to studying the behavior of resonator, such an elementary element of planar filters on isotropic substrates [8–10]. Therefore, it is interesting to study bandpass filters supported by metamaterial substrates, and taking into account the advantages of the dielectric and magnetic anisotropies on the transmission properties of these structures.

The purpose of this work is to investigate the performance of a bandpass filter on a complex material with both electric and magnetic anisotropies. The filter is realized by two single dielectric resonators in cascade. Some characteristics such as central frequency, bandwidth, input adaptation, insertion loss, and rejection of the transmission zeros of bandpass filters supported by metamaterials are presented and discussed. Numerical results are obtained by simulations using the finite element method.

2. Theory

2.1. Synthesis of a single microstrip resonator

The microstrip resonator under consideration is based on the concept of wavelength ring resonator, shown in Fig. 1(a). The simplified diagram of the quarter-wavelength resonator [9] with identical coupled lines is depicted in Fig. 1(b).

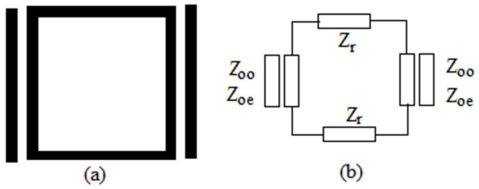


Figure 1: (a) Ring resonator. (b) Simplified diagram of the resonator.

The total perimeter of the ring is equal to one wavelength at the central frequency f_0 in the bandwidth of the filter, which is the same resonant frequency of the resonator. The resonator frequency response is controlled by the even- and odd-mode characteristic impedances, Z_{0e} and Z_{0o}, of the coupled lines, and also by the characteristic impedance of the ring Z_r. The bandpass filter is composed of two resonators in cascade and two access lines of 50 Ω, as depicted in Fig. 2.

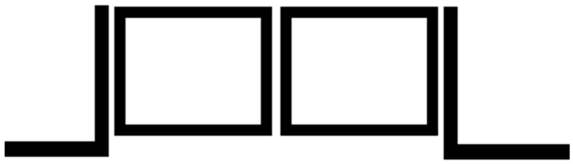


Figure 2: Bandpass microstrip filter geometry.

The even- and odd-mode coupled line characteristic impedances, Z_{0e} and Z_{0o} are, respectively, defined as:

$$Z_{0e} = \frac{1}{Y_{0e}}, \qquad Z_{0o} = \frac{1}{Y_{0o}}. \tag{1}$$

where Y_{0e} and Y_{0o} are the corresponding characteristic admittances.

To synthesize the resonator, firstly we choose an arbitrary and suitable value for Z_{0e}, in order to obtain the frequency response with the poles being too close to each other. These poles allow to control the position of the transmission zeros frequencies. The even- and odd-mode admittances are, respectively, given by [9]:

$$Y_{0e} = \frac{1}{Z_{0e}} \tag{2}$$

$$Y_{0o} = \frac{1}{Z_{0o}} = \frac{T_Z Y_{0e}}{Z_r\left(2Y_{0e} - \frac{T_z}{Z_r}\right)} \tag{3}$$

with

$$Z_r = \frac{2T_Z x + T_Z^2 Y_{0e} Z_0 + Y_{0e}\left(-Z_0 + S_Q - x\sqrt{\frac{P+Q+R}{Y_{0e}x^2}}\right)}{2xY_{0e}} \tag{4}$$

$$T_z = \frac{\sin\left(\frac{\pi f_{tz}}{2f_0}\right)^2}{1+\cos\left(\frac{\pi f_{tz}}{2f_0}\right)^2} \tag{5}$$

where T_z is a parameter that allows to control the first transmission zero frequency (f_{tz}), x takes into account the ripple on the bandwidth, and f_0 is the central frequency of the bandwidth. The other parameters P, Q, R, and S_Q can be determined by using the following equations [9]:

$$P = 4xZ_0T_z^3 - Y_{oe}Z_0^2T_z^4\left(x^4-2\right) + 4T_z x\left(S_Q - Z_0\right) \tag{6}$$

$$Q = 2Z_0T_z^2Y_{oe}\left(Z_0\left(x^2-2\right)+S_Q\right) \tag{7}$$

$$R = -2Z_0Y_{oe}\left(Z_0\left(x^2-2\right)+2S_Q\right) \tag{8}$$

$$S_Q = \sqrt{\left(1-x^2\right)\left(T_z^2-1\right)^2 Z_0^2} \tag{9}$$

It is important to highlight that the bandwidth of the response increases as the ratio between f_{tz} and f_0 decreases. This will lead to an increase of the difference between Z_{0e} and Z_{0o}, as the coupling level becomes greater. Thus, if Z_{0e} and the ripple are fixed, decreasing the ratio f_{tz}/f_0 will decrease Z_{oo}.

2.2. Metamaterial modeling

In this work, we consider that homogeneous anisotropic metamaterials used as substrates in planar filter design are modeled according to the analytical formulation presented in [3], with enhanced positive values of electric permittivity and magnetic permeability for microwave applications.

The anisotropic characteristics of the electric permittivity and magnetic permeability are obtained with a periodic array of split ring resonators (SRR), as shown in Fig. 3.

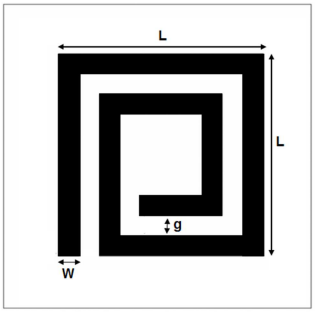


Figure 3: Spiral loop geometry used in modeling the planar filter metamaterial substrate.

The spiral SRR is embedded in a dielectric medium with $\varepsilon_r = 10.7$, and thickness h = 1.57 mm. The physical dimensions of the structure are L = 16 mm, W = g = 1.3 mm. The parameter extractions are accomplished using metamaterial unit cell containing spiral loop to characterize the metamaterial by effective magnetic permeability and effective electric permittivity as defined by [3].

The filter metasubstrate is characterized by uniaxial permittivity and permeability tensors which are given as follows:

$$\vec{\varepsilon} = \varepsilon_0\begin{bmatrix} \varepsilon_{xx} & 0 & 0 \\ 0 & \varepsilon_{yy} & 0 \\ 0 & 0 & \varepsilon_{zz} \end{bmatrix} \tag{10}$$

$$\vec{\mu} = \mu_0\begin{bmatrix} \mu_{xx} & 0 & 0 \\ 0 & \mu_{yy} & 0 \\ 0 & 0 & \mu_{zz} \end{bmatrix} \tag{11}$$

We also assume that variations of the effective permittivity and effective permeability enable four possible configurations of the metamaterial tensors, named as [6, 7]:

- Case 1

$$\vec{\varepsilon} = \varepsilon_0\begin{bmatrix} 1 & 0 & 0 \\ 0 & 1 & 0 \\ 0 & 0 & \varepsilon_{eff} \end{bmatrix}; \quad \vec{\mu} = \mu_0\begin{bmatrix} \mu_{eff} & 0 & 0 \\ 0 & \mu_{eff} & 0 \\ 0 & 0 & 1 \end{bmatrix}. \tag{12}$$

In Case 1, the components of the permittivity tensor assume values $\varepsilon_{xx} = \varepsilon_{yy} = 1,\ \varepsilon_{zz} = \varepsilon_{eff}$. The permeability elements are $\mu_{xx} = \mu_{yy} = \mu_{eff},\ \mu_{zz} = 1.$

- Case 2

$$\vec{\varepsilon} = \varepsilon_0\begin{bmatrix} \varepsilon_r & 0 & 0 \\ 0 & \varepsilon_r & 0 \\ 0 & 0 & \varepsilon_{eff} \end{bmatrix}; \quad \vec{\mu} = \mu_0\begin{bmatrix} 1 & 0 & 0 \\ 0 & 1 & 0 \\ 0 & 0 & \mu_{eff} \end{bmatrix}. \tag{13}$$

In Case 2, both effective permittivity and effective

permeability components are along the z-axis. The dielectric host medium has relative permittivity ε_r and relative permeability $\mu_r = 1$. Hence, $\varepsilon_{xx} = \varepsilon_{yy} = \varepsilon_r$, $\varepsilon_{zz} = \varepsilon_{eff}$, and $\mu_{xx} = \mu_{yy} = 1$, $\mu_{zz} = \mu_{eff}$.

- Case 3

$$\ddot{\varepsilon} = \varepsilon_0 \begin{bmatrix} \varepsilon_{eff} & 0 & 0 \\ 0 & \varepsilon_{eff} & 0 \\ 0 & 0 & \varepsilon_r \end{bmatrix}; \quad \ddot{\mu} = \mu_0 \begin{bmatrix} 1 & 0 & 0 \\ 0 & 1 & 0 \\ 0 & 0 & \mu_{eff} \end{bmatrix}. \qquad (14)$$

In Case 3, we consider that $\varepsilon_{xx} = \varepsilon_{yy} = \varepsilon_{eff}$, $\varepsilon_{zz} = \varepsilon_r$, and $\mu_{xx} = \mu_{yy} = 1$, $\mu_{zz} = \mu_{eff}$.

- Case 4

$$\ddot{\varepsilon} = \varepsilon_0 \begin{bmatrix} 1 & 0 & 0 \\ 0 & 1 & 0 \\ 0 & 0 & \varepsilon_{eff} \end{bmatrix}; \quad \ddot{\mu} = \mu_0 \begin{bmatrix} 1 & 0 & 0 \\ 0 & 1 & 0 \\ 0 & 0 & \mu_{eff} \end{bmatrix}. \qquad (15)$$

In Case 4, we consider that $\varepsilon_{xx} = \varepsilon_{yy} = 1$, $\varepsilon_{zz} = \varepsilon_{eff}$, and $\mu_{xx} = \mu_{yy} = 1$, $\mu_{zz} = \mu_{eff}$.

3. Results and Discussions

Figure 4 shows the effective permeability response to frequency variation of a periodic array of SRRs, as depicted in Fig. 3 (L= 16 mm, g = w = 1.3 mm), which displays the resonant behavior as predicted in [3]. The effective permeability results are used to calculate the frequency response of the bandpass filter printed on metasubstrate.

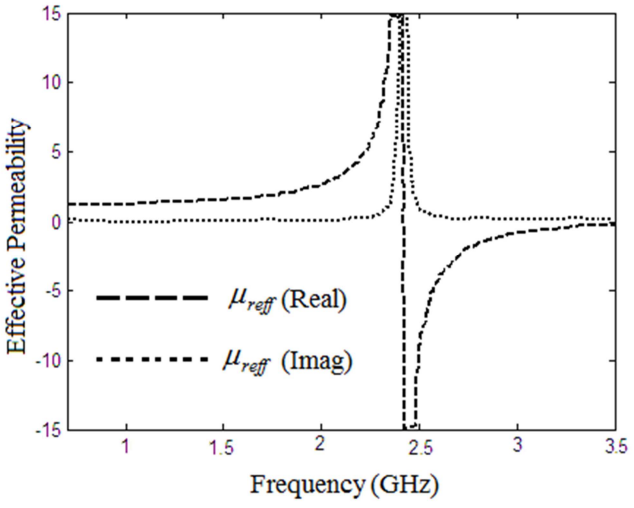


Figure 4: Effective permeability as a function of frequency for SRR medium.

Here, the effective magnetic permeability value is chosen μ_{eff} = 3.1, such as selected in [3], but at 2.2 GHz because the proposed filter is centered around this frequency.

Following, we present numerical results for bandpass filters as a function of the frequency. The filter parameters are obtained by simulations using the Ansoft HFSS. The substrate has thickness h = 1.7mm.

Figure 5 depicts curves for the filter on isotropic substrate ($\varepsilon_r = 10.7$). In the first band, centered at 1.7 GHz, the filter has return loss of –18 dB, while the insertion loss is –2 dB. In the second band, centered at 2.04 GHz, the filter has no good response, because it is not properly adapted to the input port (S_{11} = –8 dB).

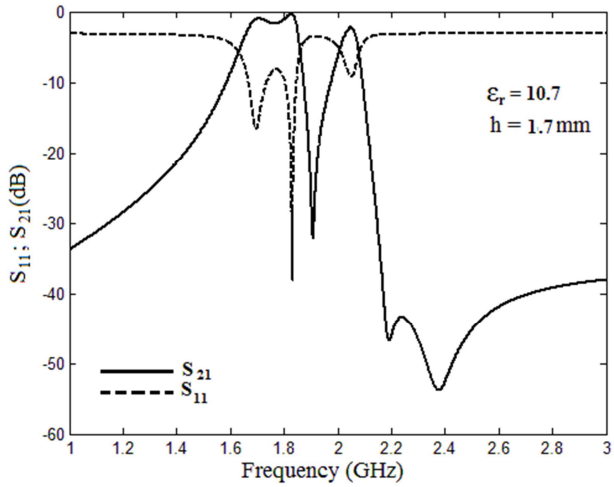


Figure 5: Frequency response of the filter on isotropic substrate.

Figure 6 presents the results for the insertion loss and return loss of the filter printed on metamaterial, labeled Case 1. The filter has frequency response in two frequency bands. In the first band, the insertion loss is –5 dB and the return loss is –14 dB. In the second band, the filter has S_{11} = –18.5 dB and the transmission loss is –2 dB. The first relative bandwidth is very close (2%), while in the second transmission the bandwidth is 10% approximately.

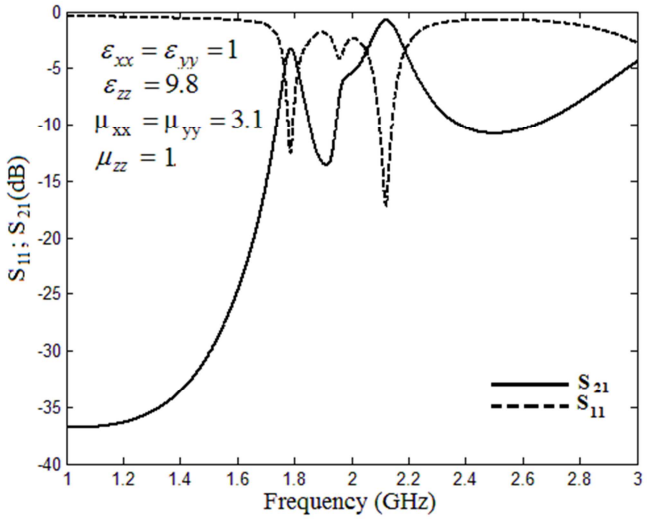


Figure 6: Frequency response of the filter on metasubstrate labeled Case 1.

Figure 7 depicts the filter behavior on metamaterial labeled Case 2. In the first band, the filter has fractional bandwidth of 15.20 % at 1.87 GHz, insertion loss of –3 dB, and maximum return loss of –22 dB. The second band has relative bandwidth of 5.4 % at 2.2 GHz, with insertion loss of –2.4 dB and return loss of –28 dB. The filter exhibits a good performance in both frequency bands.

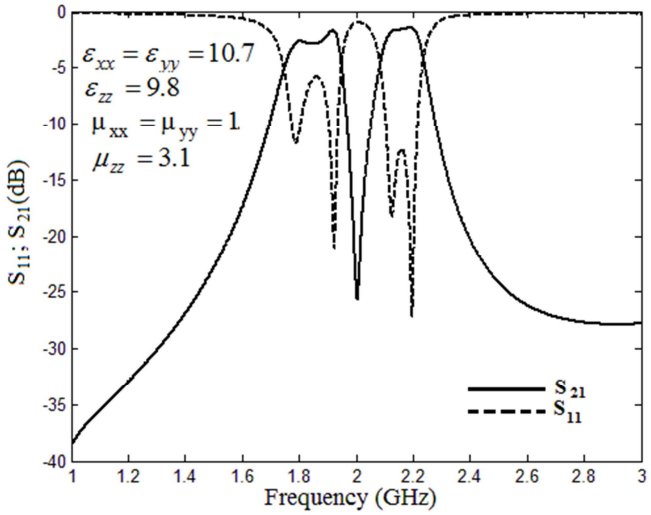


Figure 7: Frequency response of the filter on metasubstrate labeled Case 2.

Figure 8 shows the frequency responses of the filter supported by metasubstrate, as illustrated in Case 3. In the first and second bands, respectively, the levels of insertion loss are –3.50 dB and –1.58 dB, and return losses of –17.80 dB and –29.42 dB are obtained, with fractional bandwidth of 17.7 % at 1.89 GHz and 11.3 % at 2.18 GHz.

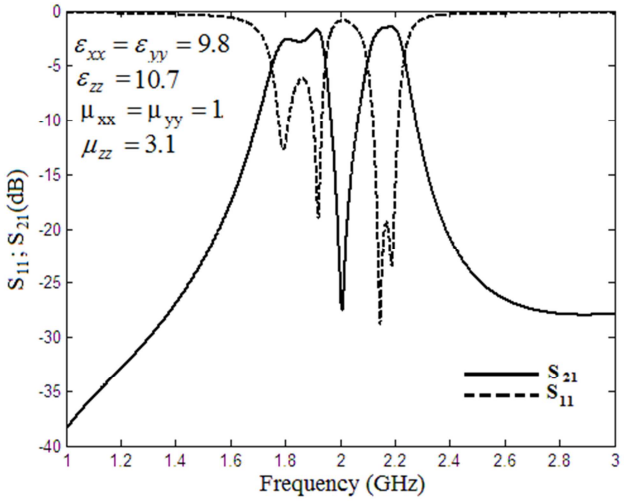


Figure 8: Frequency response of the filter on metasubstrate labeled Case 3.

In Fig. 9, designed curves show that the bandpass filter on metamaterial substrate (Case 4) has very good responses, due to the input adaptation in the two frequency bands. In the first band, the filter is centered at 1.63 GHz with relative bandwidth of 14.4 %, insertion loss of –4.0 dB, and return loss of –23.5 dB. In the second band, the filter is centered at 1.9 GHz with relative bandwidth of 13.15 %, insertion loss of –1.80 dB, and return loss of –30 dB, approximately. This bandpass filter can be used in microwave system applications, such as a duplex component.

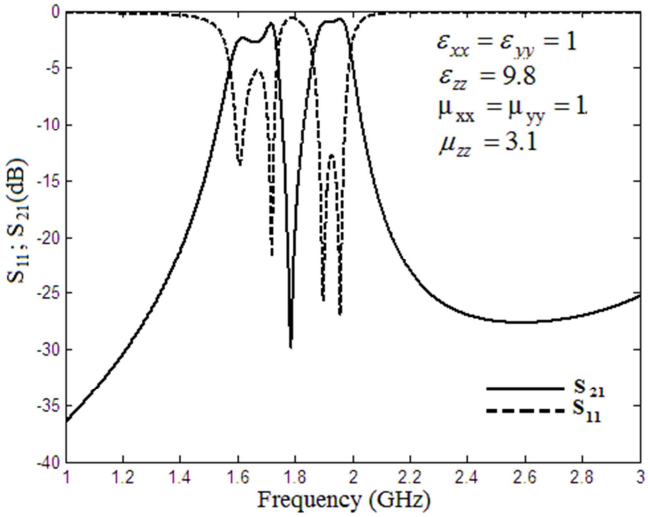


Figure 9: Frequency response of the filter on metasubstrate labeled Case 4.

Tables I and II, respectively, summarize the values for the main parameters of the filters, in order to make a comparison among their performances.

Table 1: Performances of bandpass filter in the first band.

Material	f_0 (GHz)	S_{21} (f_0) (dB)	S_{11} (f_0) (dB)	BW (%)
Isotropic $\varepsilon_r = 10.7$	1.70	–2.0	–18.0	16.5
Metamaterial Case 1	1.80	–5.0	–14.0	2.0
Metamaterial Case 2	1.87	–3.0	–22.0	15.2
Metamaterial Case 3	1.89	–3.5	–17.8	17.7
Metamaterial Case 4	1.63	–4.0	–23.5	14.4

Table 2: Performances of bandpass filter in the second band.

Material	f_0 (GHz)	$S_{21}(f_0)$ (dB)	$S_{11}(f_0)$ (dB)	BW (%)
Isotropic $\varepsilon_r = 10.7$	2.04	–3.00	–8.00	5.00
Metamaterial Case 1	2.18	–2.00	–18.50	10.00
Metamaterial Case 2	2.20	–2.40	–28.00	5.40
Metamaterial Case 3	2.18	–1.58	–29.42	11.30
Metamaterial Case 4	1.90	–1.80	–30.00	13.15

From the tables, it can be seen the influence of the magnetic permeability in the filter response, mainly in the return loss S_{11} and relative bandwidth BW. The filter printed on metamaterial, named Case 1, has no good performance, hence the permeability tensor has significant influence in the frequency responses of the filter.

4. Conclusions

It is pointed out that the anisotropy of the substrate material has a great influence on the filter performance and cannot be neglected in the design of bandpass filters. The proposed bandpass filters have two passbands in the frequency response. The first band is due to the length of the two rings which is approximately equal to one wavelength at the central frequency of the band. The second one is due to the coupling of the two ring resonators. From the curves, we can conclude that metasubstrate enables the use of the filter as a duplex component, because it has a good frequency response in two bands with the frequencies being too close to each other. We achieved the necessary flexibility to obtain frequency responses, controllable bandwidths, and compact dimensions. These structures can be of interest in those applications where miniaturization and compatibility with planar circuit technology are key issues.

Acknowledgements

We thank the Brazilian Research Agencies CNPq, CAPES and FAPERN for partial financial support.

References

[1] N. Engheta, R.W. Ziolkowski, A positive future for double-negative metamaterials, *IEEE Trans. Microwave Theory Tech.* 53: 1535-1556, 2005.

[2] J. R. Smith, D.C. Vier, N.Kroll, S. Schultz, Direct calculation of permeability and permittivity for a left-handed metamaterial, *Appl. Phys. Letters* 77(14): 2246-2248, 2000.

[3] K. Buell, H. Mosallaei, K. Sarabandi, A substrate for small patch antennas providing tunable miniaturization factors, *IEEE Trans. Microwave Theory Tech.* 54: 135-146, 2006.

[4] Z. Li, K. Aydin, E. Ozbay, Determination of the effective constitutive parameters of bianisotropic metamaterials from the reflection and transmission coefficients, *Phys. Review E*: 79, 026610-1–026610-7, 2009.

[5] T. Itoh, C. Caloz, *Electromagnetic Metamaterials: Transmission Line Theory and Microwave Applications*, Wiley, New Jersey, pp. 4-9, 2006.

[6] C.F.L. Vasconcelos, S.G. Silva, M.R.M.L. Albuquerque, J.R.S. Oliveira, A.G. d'Assunção, Full wave analysis of annular ring microstrip antenna on metamaterial, *IEEE Trans. Magn.* 47: 1110-1113, 2011.

[7] C.F.L. Vasconcelos, M.R.M.L. Albuquerque, G.M.F. Freitas, and A.G. d'Assunção, Study of a microstrip antenna on anisotropic metamaterials, *Applied Physics A*, 10.1007/s00339-013-7554-1, 2013.

[8] I.C. Hunter, *Theory and Design of Microwave Filters*, IEE Press, London, U.K., 2000.

[9] M.K.M. Salleh, G. Prigent, O. Pigaglio, R. Crampagne, Quarter-wavelength side-coupled ring resonator for bandpass filters, *IEEE Trans. Microw. Theory Tech.* 56: 156-162, 2008.

[10] K.K.M. Cheng, Design of dual-mode ring resonators with transmission zeros, *Electron. Letters* 33: 1392-1393, 1997.

Metamaterial-Inspired Displacement Sensor with High Dynamic Range

Zahra Shaterian, Ali K. Horestani, and Christophe Fumeaux

School of Electrical & Electronic Engineering,
The University of Adelaide, Adelaide, Australia
*corresponding author, E-mail: zshaterian@eleceng.adelaide.edu.au

Abstract

This article presents a displacement sensor based on broadside coupled Split Ring Resonators (SRRs) coupled to a microstrip line. In contrast to previous SRR-based displacement sensors, the proposed sensor benefits from a high dynamic range limit and since the displacement sensing is based on a precisely measurable shift in the resonance frequency, rather than change in the depth of resonance, the proposed sensor benefits from a higher immunity to noise. Also, it is shown that the sensitivity of the sensor in terms of the frequency shift is improved by introducing tapered tips in the SRR design.

1. Introduction

Metamaterials were originally proposed as artificially engineered bulk materials composed of electrically small particles that are able to create a specified material's effective permittivity and/or permeability [1]. The metamaterial basic elements, such as split ring resonators (SRRs), have also found applications for high-quality resonators [2], compact filters [3] and planar directive antennas [4]. Because of their high quality factor resonance, subwavelength dimensions, and the sensitivity of the resonance to the constituent materials and physical dimensions, SRRs are also appropriate to be used in the design of high sensitivity and high resolution sensors [5, 6, 7]. Recently, displacement sensors based on SRR-loaded coplanar waveguide (CPW) have been proposed [8, 9]. This paper proposes a displacement sensor based on a microstrip line loaded with broadside coupled SRRs (BC-SRRs). This sensor can be seen as compact transmission line based realization of the free-space pressure sensor array of [10]. In contrast to other displacement sensors [11, 12], in which a fundamental dynamic range limit was dictated by the CPW's lateral dimension, the proposed sensor has virtually no dynamic range limit. It is also shown that the sensitivity of the sensor can be increased by using tipped SRRs.

2. Displacement sensor based on broadside coupled split ring resonators

Figures 1(a) and (b) illustrate the side and top view of the proposed displacement sensor, which is composed of a microstrip line loaded with a pair of BC-SRRs. Each BC-SRR is composed of two U-shaped split-rings printed on different layers, on top of each other and open in opposite directions. Note that in the proposed structure one of the rings is printed on the same layer as the microstrip line, so it is fixed, and the second one is on the top layer of a second substrate, which can be displaced along the direction of the microstrip line, as shown by the red arrows in the figure. The aim of the proposed sensor is to measure this displacement. The BC-SRR can be modeled as a parallel LC resonator [13], in which the equivalent capacitance corresponds to the capacitance of the overlapping metallic area of the two U-shaped rings and the equivalent inductance corresponds to the rectangular loop formed by the two U-shaped rings. In the configuration shown in the figure, an increase in the displacement d of the upper ring results in a decrease in the equivalent capacitance and an increase in the equivalent inductance of the BC-SRR. However, as will be shown in the simulation results, the change in the equivalent capacitance is dominant, which results in shifting the resonance frequency to higher frequencies. The shift in the resonance frequency can therefore be used to sense the amount of displacement along the direction of the microstrip line.

Based on this sensor concept, a specific geometry is designed by electromagnetic simulations using Rogers RO4003 substrates with relative permittivity of 3.38 and copper metallization with thickness of $35\,\mu\mathrm{m}$. The thickness of the bottom and top substrates are 1.524 mm and 0.203 mm, respectively. The width of the microstrip line is $w = 3.3\,\mathrm{mm}$ which corresponds to a $50\,\Omega$ characteristic impedance. The dimensions of the BC-SRRs are mentioned in the caption of Fig. 1.

Fig. 1(c) depicts the simulated transmission coefficients of the sensor for the displacement d varying from 0 mm to 9 mm in steps of 1 mm. The figure demonstrates the increase in resonance frequency for increasing displacement d. The resonance frequency can thus be used as measure for the amount of displacement. The dynamic range of the proposed sensor is not limited and can be increased by using longer BC-SRRs.

Fig. 1(d) and (e) illustrate the side and top view of an improved version of the sensor with tipped BC-SRRs in which, compared to the uniform BC-SRR, a higher rate of change of capacitance versus displacement is achieved. Fig. 1(f) depicts the simulated transmission coefficients of the sensor for the displacement d varying between 0 mm and 9 mm in steps of 1 mm. Comparing the total frequency

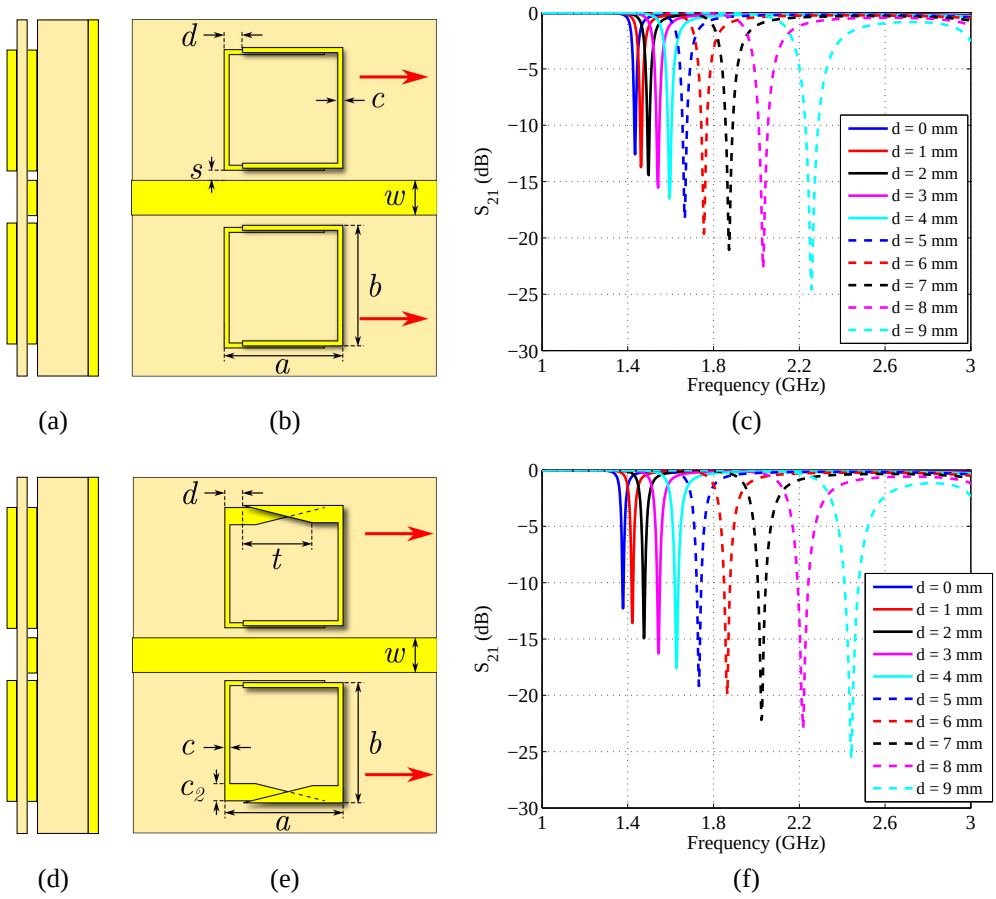


Figure 1: (a) Side view and (b) top view of the displacement sensor based on uniform BC-SRRs. Dimensions of the structure are $a = 10.2$ mm, $b = 12.4$ mm, $c = 0.4$ mm and $s = 0.2$ mm. (c) Simulated transmission coefficients of the structure for different displacements $d = 0$ mm to $d = 9$ mm in steps of 1 mm. (d) Side view and (e) top view of the displacement sensor based on tipped BC-SRRs. All dimensions are the same as in (b) except the tipped part of the resonator for which $c_2 = 3$ mm and $t = 7.7$ mm. (f) Simulated transmission coefficients of the structure for different displacements $d = 0$ mm to $d = 9$ mm in steps of 1 mm.

shift for 9 mm displacement in Fig. 1(c) and (f), the sensor with tipped BC-SRRs achieves a 29% improvement in the displacement sensitivity in terms of frequency, i.e. 1060 MHz shift vs. 820 MHz shift for the sensor with uniform resonators.

3. Conclusion

This work has presented a high dynamic range displacement sensor based on U-shaped BC-SRR. The proposed transmission line based sensor benefits from a dynamic range that can be tailored to suit applications, without the limitations of previously published SRR-based displacement sensors. Furthermore, it has been shown that the sensitivity of the sensor can be significantly improved by using tipped BC-SRRs. Also, since the proposed sensor is based on shifting in the resonance frequency rather than the resonance depth, the sensor benefits from a higher immunity to the environmental noise.

References

[1] J. J. Yang, M. Huang, and J. Sun, "Double negative metamaterial sensor based on microring resonator," *IEEE Sensors Journal*, vol. 11, no. 10, pp. 2254–2259, 2011.

[2] A. Horestani, Z. Shaterian, S. Al-Sarawi, and D. Abbott, "High quality factor mm-wave coplanar strip resonator based on split ring resonators," in *36th International Conference on Infrared, Millimeter and Terahertz Waves (IRMMW-THz)*. IEEE, 2011, pp. 1–2.

[3] A. Horestani, Z. Shaterian, W. Withayachumnankul, C. Fumeaux, S. Al-Sarawi, and D. Abbott, "Compact wideband filter element based on complementary split-ring resonators," in *Smart Nano-Micro Materials and Devices*, vol. 8204. International Society for Optics and Photonics, 2011, p. 55.

[4] S. Enoch, G. Tayeb, P. Sabouroux, N. Guérin, and P. Vincent, "A metamaterial for directive emission,"

Physical Review Letters, vol. 89, no. 21, 2002, art. no. 213902.

[5] M. Huang and J. Yang, "Microwave sensor using metamaterials," *Wave Propagation*, pp. 13–36, 2011.

[6] W. Withayachumnankul, K. Jaruwongrungsee, C. Fumeaux, and D. Abbott, "Metamaterial-inspired multichannel thin-film sensor," *IEEE Sensors Journal*, no. 5, pp. 1455–1458, 2012.

[7] S. A. Taya and M. M. Shabat, "Sensitivity enhancement in optical waveguide sensors using metamaterials," *Applied Physics A: Materials Science and Processing*, vol. 103, no. 3, pp. 611–614, 2011.

[8] J. Naqui, M. Durán-Sindreu, and F. Martín, "Novel sensors based on the symmetry properties of split ring resonators (SRRs)," *Sensors*, vol. 11, no. 8, pp. 7545–7553, 2011.

[9] A. K. Horestani, C. Fumeaux, S. F. Al-Sarawi, and D. Abbott, "Displacement sensor based on diamond-shaped tapered split ring resonator," *Sensors Journal, IEEE*, vol. 13, no. 4, pp. 1153 –1160, 2013.

[10] E. Ekmekci and G. Turhan-Sayan, "Metamaterial sensor applications based on broadside-coupled SRR and V-shaped resonator structures," in *IEEE International Symposium on Antennas and Propagation (APSURSI)*. IEEE, 2011, pp. 1170–1172.

[11] J. Naqui, M. Durán-Sindreu, and F. Martín, "Alignment and position sensors based on split ring resonators," *Sensors*, vol. 12, no. 9, pp. 11 790–11 797, 2012.

[12] J. Naqui, M. Duran-Sindreu, and F. Martin, "On the symmetry properties of coplanar waveguides loaded with symmetric resonators: Analysis and potential applications," in *IEEE MTT-S International Microwave Symposium Digest (MTT)*, 2012, pp. 1 –3.

[13] R. Marqués, F. Mesa, J. Martel, and F. Medina, "Comparative analysis of edge- and broadside-coupled split ring resonators for metamaterial design-theory and experiments," *IEEE Transactions on Antennas and Propagation*, vol. 51, no. 10, pp. 2572–2581, 2003.

Planar metamaterial-based MIMO Antennas

D. A. Ketzaki[1], D. K. Ntaikos[1], I. T. Rekanos[2] and T. V. Yioultsis[1*]

[1] Dept. of Electrical and Computer Engineering, Aristotle University of Thessaloniki, Greece
[2] Physics Div., Dept. of Mathematics, Physics, and Computational Sciences, Aristotle Univ.Thessaloniki, Greece
[*]corresponding author: traianos@auth.gr

Abstract

A systematic design of planar MIMO antennas with significantly reduced mutual coupling is presented, based on the concept of metamaterials. Split ring resonators are placed in the space between antenna elements, providing high levels of isolation without essentially affecting the simplicity and planarity of the antennas. The designs are further explained and justified by a rigorous parameter retrieval, based on a proper inverse problem methodology, thus addressing the problem of material characterization for 1D rows of resonators or single resonators.

1. Introduction

The concept and application of metamaterials, i.e. periodic formations with synthetic material properties has drawn significant attention over the last years [1]. This basic concept has matured, encompassing a broad range of synthetic materials with artificial electric and magnetic properties of many kinds. A particularly exciting fact about metamaterials is that their properties can be exploited to control and enhance propagation or radiation characteristics of electronic and photonic circuits, including antennas.

Among many applications, metamaterials have been utilized to enhance antenna characteristics, including metamaterial-based small antennas [2]-[5]. The fundamental idea is that the coupling of the radiator to the metamaterial cell is exploited to alter the antenna radiation properties, including its matching to the feeding transmission line. In a sense, the resonator effectively acts as a "metamaterial shell" that surrounds the antenna. Although this canonical structure has provided a clear route toward the design of compact antennas, individual small resonators are employed in practice, with their geometric features and dimensions being carefully chosen to obtain operation at the desired resonance frequency. An interesting fact about this category of antennas is that the metamaterial effects and properties seem to manifest themselves at a single-cell level as well, even though the original metamaterial concept refers to bulky three-dimensional periodic formations.

In addition, metamaterial properties and particularly their ability to control electromagnetic wave propagation have been used to reduce mutual coupling in multiple-input multiple output (MIMO) antennas [6]. However, the resulting structures can be bulky and hard to fabricate.

In this paper, we provide a systematic process and a series of new designs for entirely planar metamaterial-enhanced MIMO monopole antennas, by properly placing split ring resonators (SRRs) between individual monopoles. A critical feature of this approach is that the metamaterial concept is utilized at a single-cell level, since it can be confirmed that the synthesized material properties (in this case a negative magnetic permeability) can be present even at such a scale. The overall synthesis process relies firstly on tracing and localizing the primary paths and routes of electromagnetic wave propagation. Subsequently, metamaterial samples, in the form of individual resonators, can be placed at the exact locations of interest to suppress unwanted flows of electromagnetic energy that contribute to mutual coupling. More importantly, the metamaterial properties can be approximately synthesized in an independent manner, by means of a supplementary computational analysis that involves only a unit cell of the metamaterial structure, i.e. a single resonator. Hence, the design of the radiating elements and metamaterials are performed separately, with only minimal modifications and fine tuning of the composite antenna.

2. Antenna Design

The antenna design is based on the property of negative permeability, by first tracing the primary paths of wave propagation. The next step involves the design of the resonator elements to be placed between the antennas. The geometric parameters of the ring resonator are carefully selected by a finite-element based computational analysis to achieve resonance close to the frequency of 2.45 GHz. This will provide the basic mechanism to suppress the substrate modes that induce coupling. Finally, individual ring resonators are placed between the antennas, acting in a sense as a metamaterial "shell" or "screen" that can either enhance the individual antenna radiation properties or regulate coupling between them. We note that the applied parameter retrieval procedure addresses the problem of 1D rows of metamaterial unit cells or single SRRs, by a properly designed computational inverse problem formulation, as it is it is impossible to employ any simple slab EM analysis formulas in such a case. Thus, we attempt to address the fundamental question whether it is the periodic metamaterial aggregate that provides the meta-behavior or an indication of its properties can be traced at the level of rows of unit

cells or single resonators.

The antenna designs are based on planar printed microstrip-fed monopole antennas (Fig. 1). The comparison between coupling before and after the insertion of the metamaterial structure is shown in Fig. 1 and 2. Obviously, coupling is considerably reduced, while matching is also achieved in a wide frequency band.

A further interesting point to investigate is whether regulating, instead of minimizing mutual coupling may beneficially affect channel capacity, since this is considered a highly important feature in the design and operation of MIMO antennas. In particular, coupling may be beneficial for element distances between 0.1λ and 0.2λ. This characteristic, thereby, should be taken into account when miniaturization becomes a critical issue.

Considering that mutual coupling could lead to increased channel capacity, under certain circumstances, and that the ring resonator structures are expected to regulate propagation between the MIMO antenna elements, a prospective use of such metamaterial-based structures would be challenging. Towards this direction, an investigation of the channel capacity when both the receiver and the transmit antennas are metamaterial enhanced MIMO monopole arrays has been accomplished.

For this purpose, the proposed structure has been chosen both as a transmit and as a receive antenna. Since it is expected that the change of the SRRs reentrant faces' lengths, s_1 and s_2 for the two resonators, could mostly affect mutual coupling between elements, we considered these as design parameters. The channel environment is assumed to include several randomly distributed point scatterers, and the capacity is computed both for the case when mutual coupling between the two antenna elements is taken into account and the case when the antenna elements are assumed to be uncoupled.

The overall MIMO channel structure has been simulated and the first results, in terms of the channel capacity, are shown in Fig. 3. For comparison purposes, the capacity levels for the reference antenna (without SRR structures), both for the case when mutual coupling is included in the analysis (red grid) and the case when the array elements are considered uncoupled (blue grid), have been added. As it can be seen, the MIMO system comprising the reference two-monopole antennas seems to exhibit higher capacity values when the mutual coupling effect is taken into account for the channel capacity computation. This feature has been expected, since the monopole interelement distance has been chosen to be slightly larger than 0.1λ. On the other hand, the change of the SRR geometric parameters s_1 and s_2 clearly affects the values of the channel capacity through the impact on the S-parameters of the monopole elements. Obviously, there are combinations of s_1 and s_2, for which the MIMO system exhibits capacity comparable to that of the no- SRR case, while the reflection coefficient is successfully kept below -10 dB (Fig. 4).

This investigation is considered indicative, showing a marginal but noticeable gain in system capacity. However, it could provide a perspective of a more general use of the metamaterial based inclusions for the controlling of propagation between the MIMO array elements, reenforcing the capability for further investigation towards this direction.

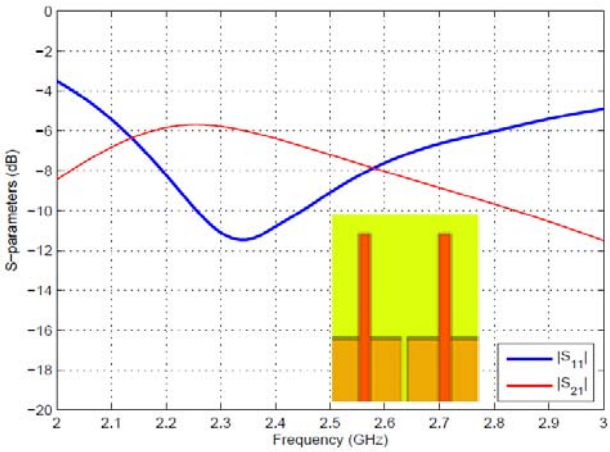


Figure 1: Reflection and transmission (coupling) of the two element MIMO monopole antenna, before the insertion of the metamaterial structure.

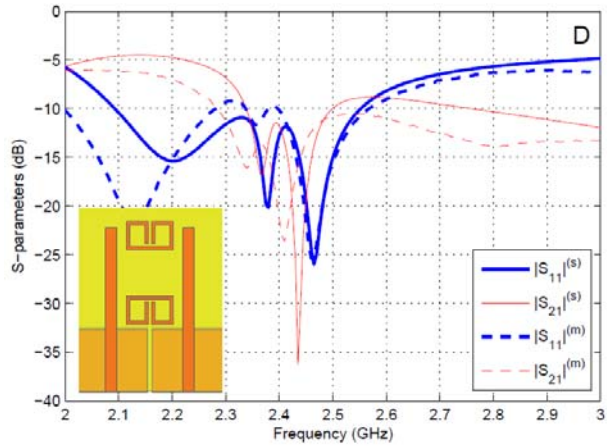


Figure 2: Reflection and transmission (coupling) of the two element MIMO monopole antenna after the insertion of the metamaterial structure.

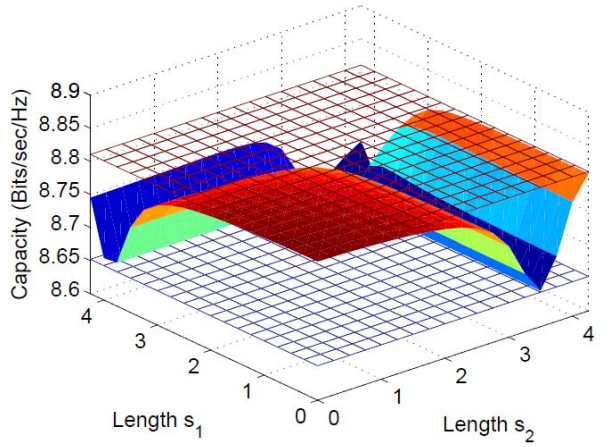


Figure 3: Computed channel capacity for combinations of the SRR reentrant faces' lengths.

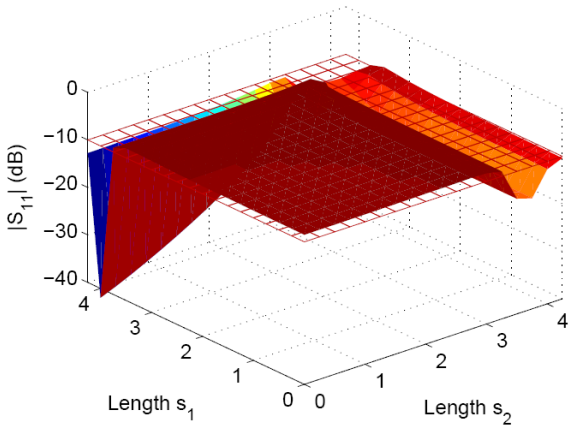


Figure 4: Reflection oefficient of a MIMO array element for different combinations of lengths s_1 and s_2.

Other, more complex variations have been also fabricated, like the four-element ultra compact MIMO antenna (Fig. 4), where metamaterial samples are used to make individual elements compact, while other ones are invoked to result in particularly low values of correlation coefficients (Fig.5).

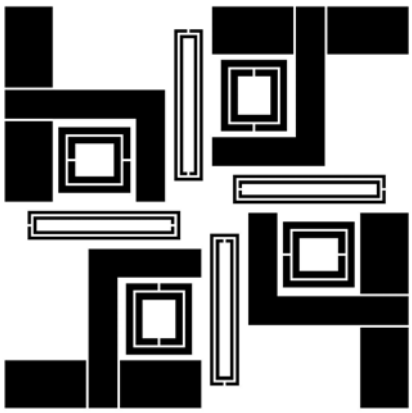


Figure 5: A four element compact MIMO Antenna.

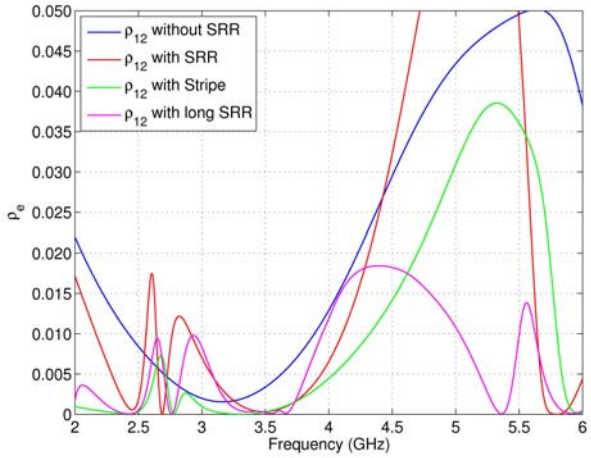


Figure 6: obtained values of correlation coefficients.

Acknowledgements

This research has been co-financed by the European Union (European Social Fund - ESF) and Greek national funds through the Operational Program "Education and Lifelong Learning" of the National Strategic Reference Framework (NSRF) - Research Funding Program: THALES: Reinforcement of the interdisciplinary and/or inter-institutional research and innovation (Project ANEMOS).

References

[1] D. R. Smith, W. J. Padilla, D. Vier, S. C. Nemat-Nasser and S. Schultz S., Composite medium with simultaneously negative permeability and permittivity, *Phys. Rev. Lett.*, 84: 4184–4187, 2000.

[2] A. Erentok and R. W. Ziolkowski, Metamaterial-inspired efficient electrically small antennas, *IEEE Trans. Antennas Propag.*, 56: 691–707, 2008.

[3] M. A. Antoniades and G. V. Eleftheriades, A broadband dual-mode monopole antenna using NRI-TL metamaterial loading, *IEEE Antennas Wirel. Propagat. Lett.*, 8: 258–261, 2009.

[4] T. Kokkinos and A. P. Feresidis, Low-profile folded monopoles with embedded planar metamaterial phase-shifting lines, *IEEE Trans. Antennas Propag.*, 57: 2997–3008, 2009.

[5] J. Zhu, M. A. Antoniades, and G. V. Eleftheriades, A compact tri-band monopole antenna with single-cell metamaterial loading, *IEEE Trans. Antennas Propag.*, 58: 1031-1038, 2010.

[6] M. M. Bait-Suwailam, M. S Boybay and O. M. Ramahi, Electromagnetic coupling reduction in high–profile monopole antennas using single–negative magnetic metamaterials for MIMO applications, *IEEE Trans. Antennas Propag.*, 58: 2894–2902, 2010.

Nano-aperture design to enhance optical transmission using the shape optimization procedure

H. Lim[1], N. Heo[1], J. Choi[2] and J. Yoo[3*]

[1]Graduate School of Mechanical Engineering, Yonsei University, Seoul, Korea
[2]Samsung Electronics, Co. Ltd., Suwon, Korea
[3]School of Mechanical Engineering, Yonsei University, Seoul, Korea
*corresponding author, E-mail: yoojh@yonsei.ac.kr

Abstract

In the optics field, many researchers have proposed various shape of nano-aperture whose transmission efficiency is over 1 challenging the prediction of the diffraction limit. This study suggests a systematic design approach of a nano-aperture for the purpose of enhancing optical transmission .

For nano-aperture design, we adapted phase field shape optimization method using the reaction diffusion equation with double well potential. It is adapted for obtaining simplified structure by controlling the diffusion coefficient. Through the design process, we have designed an unprecedented form of the aperture and compared its performance was with traditional shapes.

1. Introduction

As the technology related with the nano-sized metallic aperture has been improved, various shapes of the aperture such as making a slit in the vicinity of the aperture [1] and changing the shape of the apertures [2-4] have been widely applied to several fields such as the optical data storage and antenna systems [5, 6]. Those shapes were invented using the principle of the surface plasmon resonance (SPR) to improve the transmission rate extraordinary. A recent study based on the numerical method using the finite difference time domain method (FDTD) has proven the high transmission efficiency of the nano-aperture numerically [7].

Since the earliest concept proposed by Bendsøe and Kikuchi [8], topology optimization has been regarded as one of the most promising methods for concept design of continuum structures and it can be applied various physical field, such as elastic, thermal, acoustic, and electromagnetic field [9-11] and it can be applied dynamic problem [12] or time varying field problem[13]. This research aims to obtain the optimal cross sectional shape of the metal layer in a nano-aperture system to enhance the wave transmission through a nano-aperture. It is noteworthy that the structure scale is too small to admit complex shapes if the real application would be taken into account. Therefore, this study adopts the double well potential (DWP) combined optimization method as well as the topology optimization method based on the reaction diffusion (RD) equation not only for avoiding gray scale representation but also for obtaining simplified structure by controlling the diffusion coefficient.

The proposed optimization method is applied to the nano-scale aperture design of a vertical-cavity surface-emitting laser (VCSEL) system and we use the finite element method (FEM) to analyze the electromagnetic field wave propagation and the design objective is defined as maximizing the energy flux at the measuring area under the aperture structure.

2. Analysis Model

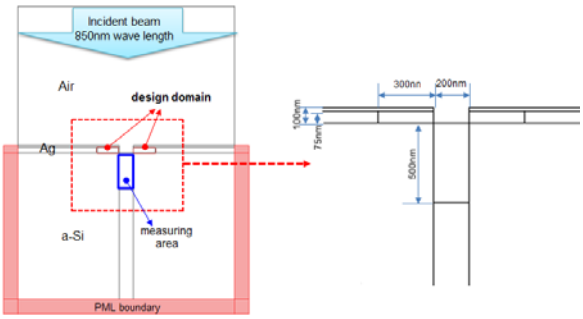
2.1. Finite element modeling

The initial model of nano-aperture is represented in Figure 1(a). In this study, the nano-aperture model is composed of three parts. At first, the 850nm wavelength incident light which is fixed in near infrared wavelength range, goes from the upper air portion. Subsequently, it passes through the nano-aperture and propagates amorphous silicon (a-Si) layer in Fig. 1(a). Perfectly matched layers (PML) are set around silver (Ag) and a-Si layer. The design domain has 75nm depth and 300nm width Ag layer designated in the red box as shown in Fig. 1(a). The part becomes a new structure by topology optimization process.

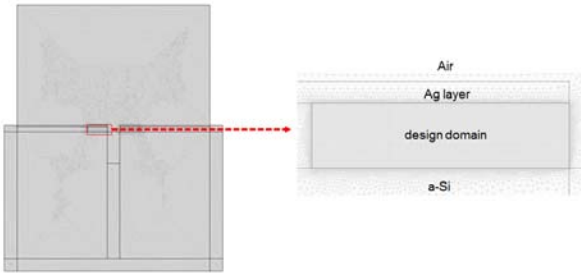
Table 1 shows the relative permittivity of each material in this system. The design objective is to maximize the field strength intensity in the measuring domain in Fig. 1(a) and we evaluated it by calculating the Poyinting vector value of the area. The prototype model is set as the whole design domain is filled with Ag material. Fig. 1(b) displays the finite element model of prototype design and an Ag layer part is enlarged to show the very fine element size. It is discretized for all element sizes not to exceed 20nm. The numerical analysis results from the two-dimensional FEA using 45000 quadrilateral elements in the design domain and 153844 triangular elements in other domains. The FEA is implemented by commercial FE analysis package COMSOL^{TM} and the optimization process is carried out by Matlab programs.

Table 1: Material properties used for the analysis

Material	Air	Ag	a-Si
relative permittivity	1	$-32.22+1.73i$	$14.62+0.50i$



(a)



(b)

Figure 1: Initial model of the nano-aperture: (a) schematic of the analysis model and (b) element description for FEM.

2.2. Wave analysis

Regardless of the exciting frequency, the electromagnetic wave propagation can be analyzed by solving Maxwell's equations representing the electric and magnetic field strength profile. Maxwell's equations for time-varying fields are as follows:

$$\nabla \times \nabla \times \mathbf{E} = -\mu\varepsilon \frac{\partial^2}{\partial t^2}\mathbf{E} \tag{1}$$

$$\nabla \times \nabla \times \mathbf{H} = -\mu\varepsilon \frac{\partial^2}{\partial t^2}\mathbf{H} \tag{2}$$

where **H** is the magnetic field strength and **E** is electric field strength. ε and μ represent the electric permittivity and the magnetic permeability, respectively.

This study is targeting two-dimensional (2D) design of the nano-aperture cross-sectional shape, the transverse magnetic (TM) mode analysis governed by Eq. (2) is required. In case of fixed excitation frequency of ω, the wave propagation in 2D by the SP phenomenon can be analyzed by the following governing equation [14]:

$$\nabla \cdot \left(\frac{1}{\varepsilon_r} \nabla \mathbf{H}_z \right) = -\frac{\omega^2}{c_0^{\,2}} \mathbf{H}_z \tag{3}$$

where c_0 is the light speed in the air and ε_r is the relative permittivity. The magnetic field strength **H** has only the *z*-directional magnetic field strength component H_z in 2D TM model analysis. The subscript 0 of the electric permittivity and the magnetic permeability means the property in the air. This study employed the PML boundary condition in order to avoid the wave reflection from the boundaries.

$$\frac{1}{S_x^{\,2}}\frac{\partial}{\partial x}\left(\frac{1}{\varepsilon_r}\frac{\partial}{\partial x}H_z\right)+\frac{1}{S_y^{\,2}}\frac{\partial}{\partial y}\left(\frac{1}{\varepsilon_r}\frac{\partial}{\partial y}H_z\right)=\frac{1}{c_0^{\,2}}\frac{\partial}{\partial t^2}H_z \tag{4}$$

where $S_x = 1 - j(x - x_{PML})^2 D$ and $S_y = 1 - j(x - y_{PML})^2 D$. x_{PML} and y_{PML} represents the basis locations of the PML boundary, respectively and D is the numerical damping coefficient [15].

3. Topology Optimization

The RD equation used for topology optimization in this study is formulated as

$$\frac{\partial \phi(\mathbf{x},t)}{\partial t} = \alpha \nabla^2 \phi(\mathbf{x},t) - \frac{\partial W(\phi, H_z)}{\partial \phi} \tag{5}$$

$$\frac{\partial \phi}{\partial \mathbf{n}} = 0 \quad on \ \partial\Omega \tag{6}$$

where ϕ is the design variable which represents a phase field parameter and **n** is the unit vector normal to $\partial\Omega$. Because this study deals with wave propagation in transverse magnetic (TM) mode, the *z*-directional magnetic field strength H_z is considered as a state varible. α is the diffusion coefficient and its change is closely related to the interfacial energy; therefore, it influences complexity of the optimized configuration.

When the structural optimization problem is to minimize objective function considering the equality volume constraint, the optimization problem is determined as follows:

$$\begin{aligned} &\textbf{minimize} \quad \Psi\left(\phi,\ H_z(\phi)\right) \\ &\textbf{subject to} \quad h(\phi) = \textstyle\int_\Omega \phi\, dx - V_{req} \int_\Omega dx \le 0,\ \ 0 \le \phi \le 1 \end{aligned} \tag{7}$$

where Ψ is the objective function, $h(\phi)$ means the volume fraction constraint and V_{req} is the required volume fraction. To deal with the objective function and design constraints simultaneously, the augmented Lagrangian is defined as

$$\bar{\Psi}(\phi, H_z, \lambda) = \eta\Psi(\phi, H_z) + \lambda\hat{h}(\phi) + \frac{\gamma}{2}\hat{h}(\phi)^2 \tag{8}$$

Here, λ and γ represent the Lagrange multiplier and the penalty parameter, respectively. Note that the modified constraint function $\hat{h}(\phi)$ is

$$\hat{h}(\phi) = \max\left[h(\phi), -\frac{\lambda}{r}\right]. \tag{9}$$

The parameter η to normalize the design sensitivity is defined as [16]

$$\eta = \frac{\int_\Omega dx}{\left\| \partial \Psi / \partial \phi \right\|_{L^2(\Omega)}}. \quad (10)$$

The gradient of the augmented Lagrangin with respect to the phase field ϕ becomes

$$\frac{\partial \bar{\Psi}(\phi, H_z, \lambda)}{\partial \phi} = \eta \frac{\partial \Psi(\phi, H_z)}{\partial \phi} + \frac{\partial \hat{h}(\phi)}{\partial \phi}\left[\lambda + \gamma \hat{h}(\phi)\right]. \quad (11)$$

If the phase field parameter follows the evolution scheme expressed in (5) and (6), only the diffuse interface of the domain represented parameter is moving. The velocity to the moving direction can be determined by the sensitivity analysis using the artificial DWP. The DWP W is set as follows:

$$W(\phi, H_z) = aw(\phi) + \eta \frac{\partial \Psi(\phi, H_z)}{\partial \phi} g(\phi) + \lambda \hat{h}(\phi) + \frac{\gamma}{2} \hat{h}(\phi)^2$$
$$where\ w(\phi) = \phi^2 (1-\phi)^2,\ \ g(\phi) = \phi^3 (6\phi^2 - 15\phi + 10). \quad (12)$$

$aw(\phi)$ is a smooth Dirac delta function with constant a that influences the diffuse interfacial layer thickness and $g(\phi)$ is a smooth Heaviside function. $\partial \Psi / \partial \phi$ is the sensitivity value of the design objective Ψ. The range of Dirac delta function and Heaviside function is $0 \le \phi \le 1$.

Combining the Eq. (5) and Eq. (12), we get a modified reaction diffusion equation:

$$\frac{\partial \phi}{\partial t} = \alpha \nabla^2 \phi - aw'(\phi) - \eta \frac{\partial \Psi(\phi, H_z)}{\partial \phi} g'(\phi) + \frac{\partial \hat{h}}{\partial \phi}\left[\lambda + \gamma \hat{h}(\phi)\right] \quad (13)$$

Because $g'(\phi)$ is zero when ϕ is 0 and 1, the sensitivity outside diffusion layer becomes zero.

During the design process, refractive index values in the design domain are changed according to the variation of the design variable, i.e., the phase field parameter ϕ based on the following formulation [14, 15]:

$$n = n(\phi) = n'_{Ag} + \phi^p (n'_{a-Si} - n'_{Ag}) + i(n''_{Ag} + \phi^p (n''_{a-Si} - n''_{Ag})) \quad (14)$$

where n'_{Ag} and n'_{a-Si} are real parts of the refractive index of the Ag layer and the a-Si part, respectively, and n''_{Ag} and n''_{a-Si} are their imaginary part values. The relative permittivity is the square of the refractive index as $\varepsilon_r = n^2$.

4. Numerical Result

In this section, the result variation according to several design parameter variation is evaluates. The objective is maximizing the energy flux represented by the Poynting vector. The objective value of the prototype model which has no grating is measured as 1.76e-38 W/m^2 and it is set to the normalized value of 1.

For the optimization result by the ordinary phase field method using DWP, the initial distribution of material has a decisive effect on the result of final shape [17]. Therefore, we have investigated results for five different initial configuration definitions as can be seen in Table 2. First three cases have different number of Ag nano-particles to check the SP effect around the nano-particles and its related shape changes. The influence of grating structure, which is widely used in SP wave propagation, is also evaluated in last two cases. The volume fraction constraint is fixed to 0.6 in this verification process. If nano-particles are taken into account in the initial configuration, optimization results are almost identical to each other as can be confirmed in the table. In case of initial shape with grating structure, both the resultant shapes and objective values are a little bit different.

In previous investigations, the diffusion coefficient α is fixed to 1.0e-3. However, it is necessary to confirm the influence of the variation of α and it is essential in nano-structure design to compromise between the performance and the manufacturing feasibility. Fig. 2(a) represents initial phase parameter distribution of the aperture. To confirm the coefficient effect, relatively complex initial shape is chosen. Figs. 2(b)-(d) show the optimal material distribution for diffusion coefficient of 1.0e-3, 1.0e-4 and 1.0e-5, respectively, with 0.6 volume fraction. As the coefficient value is getting smaller, optimized configurations become more complicated and it is natural in results by the phase field method [18]. Normalized objective values for the three cases are evaluated as 1.51, 2.21 and 2.04 at each of cases.

5. Conclusions

In this study, we designed the cross sectional shape of a nano-aperture of a VCSEL system and obtained remarkably improved performance. The suggested design method has been successfully applied to metallic structure design considering the SP effect. It is also confirmed that the material distribution near the aperture hole is crucial to maximize the intended performance. Although this study is limited only for 2D cross-sectional design, this approach will be expanded in three-dimensional structural design for electromagnetic field devices.

Acknowledgements

This work was supported by the National Research Foundation of Korea (NRF) grant funded by the Korea government (MEST) (No. 2012-0005701).

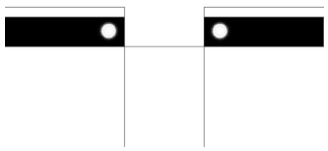
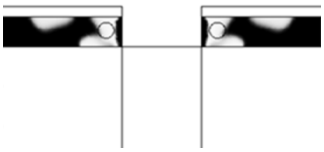
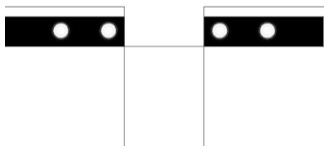
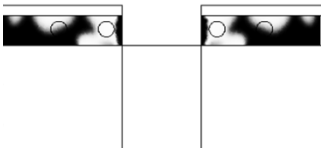
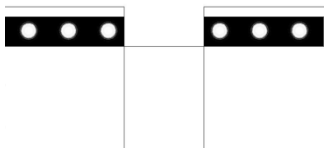
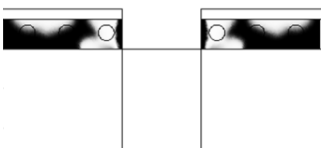
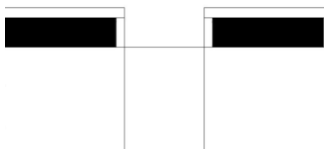
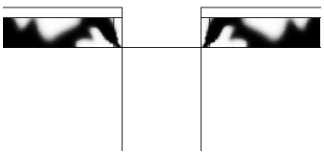
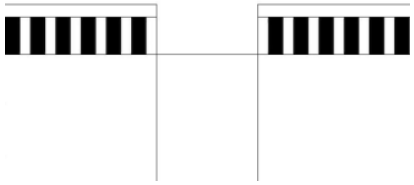
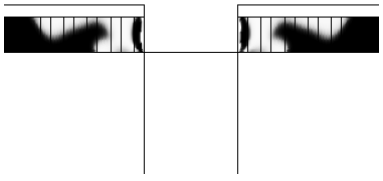
References

[1] F. J. Garcia-Vidal, H. J. Lezec, T. W. Ebbesen, L. Martin-Moreno, Multiple paths to enhance optical transmission through a single subwavelength slit, *Physical Review Letters* 90: 213901, 2003.

[2] F. J. Garcia-Vidal, H. J. Lezec, T. W. Ebbesen, L. Martin-Moreno, Multiple paths to enhance optical

transmission through a single subwavelength slit, *Physical Review Letters* 90: 213901, 2003.

Table 2: Optimization result dependency according to the initial configuration.

Volume fraction = 0.6 (fixed)			
Initial configuration	Optimal topology	Normalized objective value of initial distribution	Normalized objective value of optimal result
		0.84	1.75
		0.87	1.74
		0.93	1.73
		0.94	1.49
		1.06	1.51

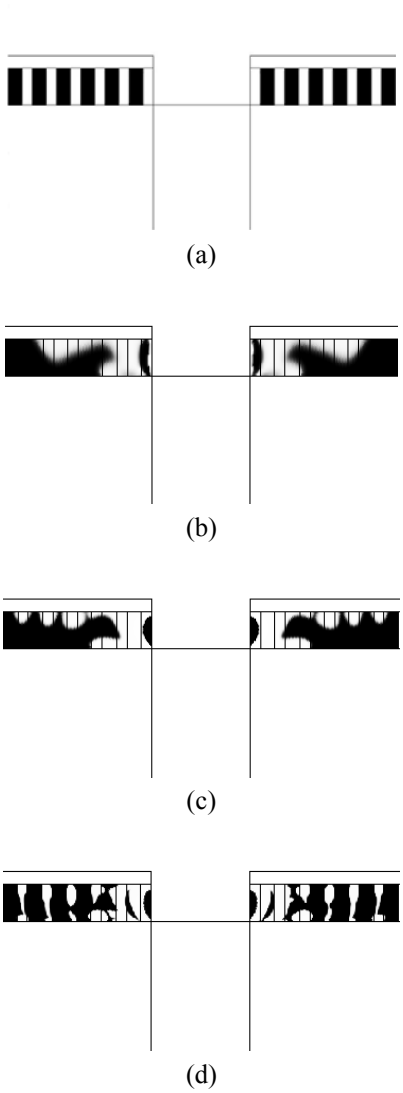


Figure 2: Variation of diffusion coefficient; (a) initial configuration, (b) $\alpha = 1\times10^{-3}$, (c) $\alpha = 1\times10^{-4}$ and (d) $\alpha = 1\times10^{-5}$.

[3] F. J. Garcia-Vidal, H. J. Lezec, T. W. Ebbesen, L. Martin-Moreno, Multiple paths to enhance optical transmission through a single subwavelength slit, *Physical Review Letters* 90: 213901, 2003.

[4] J. A. Matteo, D. P. Fromm, Y. Yuen, P. J. Schuck, W. E. Moemer, L. Hesselink, Spectral analysis of strongly enhanced visible right transmission through single C-shaped nanoapertures, *Applied Physics Letters* 85: 640-648, 2004.

[5] X. L. Shi, R. L. Thornton, L. Hesselink, Ultrhigh light transmission through a C-shaped nanoaperture, *Opt. Lett* 28: 1320-1322, 2003.

[6] L. Wang, S. M. Uppuluri, E. X. Jin, X. Xu, Nanolithography using high transmission nanoscle bowtie apertures, *Nano Lett* 6: 361-364, 2006.

[7] R. D. Grober, R. J. Schoelkopf, D. E. Prober, Optical antenna: towards a unity efficiency near-field optical probe, *Appl. Phys. Lett* 70: 1354-1356, 1997.

[8] X. Shi, L. Hesselink, Mechanism for Enhancing Power Throughput from Planar Nano-Apertures for Near-Field Optical Data Storage, *The Japan Society of Applied Physics* 41: 1632-1635, 2002.

[9] L. Wang, X. Xu,, Numerical study of optical nanolithography using nanoscale bow-tie-shaped nano-apertures, *Journal of microscopy* 229: 483-489, 2008.

[10] M. P. Bendsøe, N. Kikuchi, Generating optimal topologies in structural design using a homogenization method, *Comput. Methods Appl. Mech. Engrg* 71: 197-224, 1988.

[11] C. B. W. Pedersen, T. Buhl, O. Sigmund, Topology synthesis of large-displacement compliant mechanisms, *Int. J. Numer. Methods Engrg* 50: 2683-2705, 2001.

[12] D. N. Dick, D. A. Lowther, Composite microstructure of permeable material for the optimized material distribution method of automated design, *IEEE Trans. Magn* 33: 1828-1831, 1997.

[13] Y. Tsuji, K. Hirayama, T. Nomura, K. Sato, S. Nishiwaki, Design of optical circuit devices using topology optimization method with function-expansion-based refractive index distribution, *IEEE Photonics Technology letters* 20: 982-984, 2008.

[14] A. R. Diaz, N. Kikuchi, Solutions to shape and topological eigenvalue optimization problems using a homogenization method, *Int. J. Numer. Methods Engrg* 35 : 1487-1502, 1992.

[15] J. Dahl, J. S. Jensen, O. Sigmund, Topology optimization for transient wave propagation problems in one dimension, *Struct. Multidisc. Optim* 36: 585–595, 2008.

[16] H. Soh, J. Yoo, Improved surface plasmonic wave propagation of a prism coupler through optimal grating structure design, *J. Electromagn. Waves and Appl* 25: 629-640, 2011.

[17] J. Andkjær, S. Nishiwaki, T. Nomura, O. Sigmund, Topology optimization of grating couplers for the efficient excitation of surface plasmons, *J. Opt. Soc. Am. B* 27: 1828-1832, 2010.

[18] J. S. Choi, K. Izui, S. Nishiwaki, A. Kawamoto, T. Nomura, Rotor pole design of IPM motors for a sinusoidal air-gap flux density distribution, *Struct. Multidiscip. Optimiz* 46: 445-455, 2012.

[19] A. Takezawa, S. Nishiwaki, M. Kitamura, Shape and topology optimization based on the phase field method and sensitivity analysis, *J. Comput. Phys* 229: 2697–2718, 2010.

[20] J. S. Choi, T. Yamada, K. Izui , S. Nishiwaki , J. Yoo, Topology optimization using a reaction-diffusion equation, *Comput. Methods Appl. Mech. Engrg* 200: 2407–2420, 2011.

Recent progress on numerical methods for metamaterial analysis

On the use of a Hierarchical Multi-level Building Block Basis Function Scheme in Periodic Plasmonic Structures

X. Zheng[1], V. K. Valev[2], V. Volskiy[1], Guy A. E. Vandenbosch[1*], and V. V. Moshchalkov[3]

[1] Department of Electrical Engineering (ESAT – TELEMIC), KU Leuven, Leuven, Belgium
[2] Cavendish Laboratory, Department of Physics, University of Cambridge, Cambridge, United Kingdom
[3] Nanoscale Superconductivity and Magnetism, Pulsed Fields Group, Department of Physics, KU Leuven, Leuven, Belgium
*corresponding author: guy.vandenbosch@esat.kuleuven.be

Abstract

A Volumetric Method of Moments (V-MoM) algorithm is applied to predict the plasmonic responses of chiral metamaterials. This algorithm is based on the use of a multi-level building block basis function scheme, in combination with a dedicated Kummer transformation in the calculation of periodic Green's functions. The validity of the algorithm is demonstrated by analyzing a Ninja Star periodic structure. Circular Dichroism (CD) is observed in both simulations and experiments.

1. Introduction

In the last decade, plasmonic metamaterials have been constantly drawing attention from physicists, chemists, and electrical engineers, due to their predesigned exotic electromagnetic properties at nanoscale, e.g., plasmon induced transparency [1], optical rotation [2], circular dichroism [3] and asymmetric transmission [4] in chiral metamaterials, etc.. In general, the interaction of light with nano-plasmonic structures can be modeled in the framework of classical electrodynamics. Thus, the classic Method of Moments (MoM) algorithm can be adapted and applied in the field of nano-plasmonic applications [5].

In the implementation of the Method of Moments algorithm for plasmonic metamaterials, two key aspects must be respected. On the one hand, because the thickness of nanostructures is comparable with the skin depth of metals at optical frequencies, the electromagnetic wave penetrates the structures. The dispersive material properties of metals start to play a role and the currents flowing in the structures must be considered as **three-dimensional (3D) ones**. Therefore, the original Method of Moments algorithm must be extended to a volumetric one with 3D current basis functions (rooftops) introduced. For 3D rooftops, half rooftops can exist individually on the ground that the boundary charge now is a surface charge rather than a line charge, which doesn't result in any singularities of the electric field. Based on this observation, pairing half rooftops on smaller and smaller hexahedral or tetrahedral building blocks can be used to describe the boundary of the plasmonic structures in more detail.

On the other hand, due to the periodicity of metamaterials, periodic Green's functions must be calculated for the coupling matrix which describes the interactions amongst the 3D current basis functions. However, the evaluation of the periodic Green's function is always hampered by a poor convergence when the source point z' and the observation point z are collocated at the same z value. This numerical difficulty can be circumvented by applying the Kummer transformation and sensibly adding and subtracting so-called asymptotes. Details on the Kummer transformation and the choice of the asymptotic series will be elaborated in the following sections.

In this work, firstly, the relation between the dimensionality of a charge density and the (possible) electric field singularity is briefly reviewed. Then, a multi-level meshing scheme for periodic structures based on these observations is illustrated. Secondly, the Kummer transformation is introduced and a recently proposed choice of asymptotic series [6] is illustrated. Last but not least, as a validation, the surface plasmons induced by left and right circularly polarized light in a Ninja Star [3] nanostructure are calculated with our in-house developed Volumetric Method of Moments (V-MoM) based software, MAGMAS [7-9] and compared with SHG microscopy images.

2. Hierarchical Multi-level Building Block Basis Function Scheme

In this section, we shall first briefly investigate the relation between the dimensionality of a charge density and the (possible) electric field singularity. Then, by complementing a larger rooftop with smaller rooftops, we illustrate a multi-level meshing scheme for the periodic structures under consideration.

2.1. Charge Density and Electric Field

Take the electric field in free space generated by a stand-alone half rooftop **J(r')** (current basis function) as an illustrative example

$$\mathbf{E}(\mathbf{r}) = -j\omega\mu_0 \int_{s'} g(r,r')\mathbf{J}(\mathbf{r}')ds' - \frac{1}{\varepsilon_0}\nabla \int_{s'} g(r,r')\left(\frac{\nabla\cdot\mathbf{J}(\mathbf{r}')}{-j\omega}\right)ds' - \frac{1}{\varepsilon_0}\nabla \int_{b'} g(r,r)\left(\frac{\mathbf{n}\cdot\mathbf{J}(\mathbf{r}')}{-j\omega}\right)db'. \tag{2.1}$$

$g(r,r') = e^{-jk|r-r'|} \Big/ 4\pi|r-r'|$ is the free space scalar Green's function. The first two terms and the last term in Eq. (2.1) are integrated with respect to the source region s' and the boundary b' surrounding the source region, which is one dimension lower than the integral domain of the first two terms. $\mathbf{n}$ is the unit vector normal to the boundary b'. $\left(\mathbf{n}\cdot\mathbf{J}(\mathbf{r}')/-j\omega\right)$ represents the charge accumulated on the boundary due to the normal current arriving there. The general expression for the contribution of a charge density to the electric field can thus be written as

$$\nabla \int_{source} \frac{e^{-jk|r-r'|}}{4\pi|r-r'|}\rho d(source). \qquad (2.2)$$

The source domain can be 3D, 2D, 1D, or 0D (a point), depending on the situation. An overview of the types of source current and the types of boundary charge can be found in Table 1.

TABLE 1: Overview of S' and B' for different cases

Type of Source Current	Type S'	Type B'	Dimension Charge on B'
Volume Current	Volume	Surface	2D
Surface Current	Surface	Line	1D
Line Current	Line	End points of line	0D

When an observation point approaches a source point, the electric field in (2.2) becomes proportional to,

$$\frac{1}{|r-r'|}\int_{source}\frac{1}{|r-r'|}\rho d(source). \qquad (2.3)$$

For different charge densities, the (possibly) resultant singularities in the electric field, the electric energy density and the energy are tabulated in Table 2.

TABLE 2: Types of singularity for different charge dimensionalities: r is the distance to the charge on B which has to be considered in the limit to zero.

Boundary B	Electric Field	Electric Field Energy Density	Energy in dV around B
Surface (2D)	No Singularity	No Singularity	No Singularity
Line (1D)	$\sim\frac{1}{r}$	$\sim\frac{1}{r^2}$	$\sim\log(r)$
Point (0D)	$\sim\frac{1}{r^2}$	$\sim\frac{1}{r^4}$	$\sim\frac{1}{r}$

2.2. Hierarchical Multi-level Building Block Basis Function Scheme

At optical frequencies, because the skin depth is comparable with the thickness of the nanostructures, the current flowing in the nanostructures has to be considered as a volumetric one. According to Table 2, this 3rd dimension uplifts the physical limits, i.e. the surface charge does not induce any singularities, and renders us the possibility of using a hierarchical scheme as depicted in Fig. 1. At the edges of a structure, the actual boundary is reconstructed with an increased resolution by adding blocks where necessary of half the size of the blocks of the previous level. In Fig. 1, for example, there are three levels. The blocks of level 1 are used throughout the interior of the structure. At the boundary, they are supplemented by blocks of level 2, with half the size of the blocks of level 1.

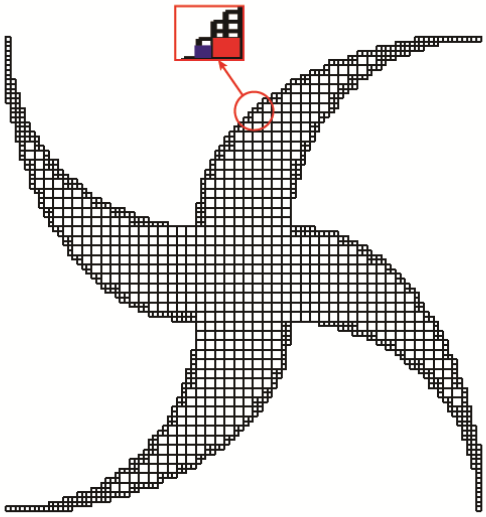


Fig.1. Illustration of hierarchical use of 3D half rooftops in a binary scheme, red: level 1; blue: level 2.

3. Evaluation of the Periodic Green's Function

For infinitely large periodic arrays, the spatial domain periodic Green's function can be derived from the spectral Green's function [10-13],

$$G(x,y;z,z') = \sum_m\sum_n \tilde{G}(k_{mn};z,z')e^{-j(k_{mx}x+k_{ny}y)} \qquad (2.4)$$

$\tilde{G}(k_{mn}, z, z')$ is the Green's function in spectral domain. k_{mn} is the wave number in xy plane, $\sqrt{k_{mx}^2 + k_{ny}^2}$. $k_{mx} = k_x^{inc} + 2\pi m / d_x$ and $k_{ny} = k_y^{inc} + 2\pi n / d_y$ are the wave numbers in x and y directions with d_x and d_y the periods in these directions. $k_{inc}^x = k_0 \sin\theta\cos\varphi$ and $k_{inc}^y = k_0 \sin\theta\sin\varphi$ are the x and y projections of the total incident wave number k_0.

The series in Eq. (2.4) has a poor convergence when the source point z' approaches the observation point z, which can be circumvented by applying a Kummer transformation [14],

$$G(x,y) = G^{spectral}(x,y) + G^{spatial}(x,y), \tag{2.5}$$

$$G^{spectral}(x,y) = \sum_m \sum_n \left[\tilde{G}(k_{mn}) - \tilde{G}^{as}(k_{mn}) \right] e^{-j(k_{mx}x + k_{ny}y)}, \tag{2.6}$$

$$G^{spatial}(x,y) = \sum_m \sum_n \tilde{G}^{as}(k_{mn}) e^{-j(k_{mx}x + k_{ny}y)}. \tag{2.7}$$

By adding and subtracting the asymptote terms, the Kummer transformation separates the original series into two parts: 1) (2.6) is a function of small wave numbers; 2) the asymptotes (2.7) are functions of large wave numbers, so that the numerical evaluation of (2.6) and (2.7) can be conducted easily in spectral domain and in spatial domain, respectively. In the spatial domain, Eq. (2.7) can be expanded as,

$$G^{spatial}(x,y) = \sum_m \sum_n g^{as}(\rho_{mn}) e^{-j(mk_x^{inc}d_x + nk_y^{inc}d_y)}. \tag{2.8}$$

ρ_{mn} is $\sqrt{(x + md_x)^2 + (y + nd_y)^2}$. And $g^{as}(\rho_{mn})$ and $\tilde{G}^{as}(k_{mn})$ form a Fourier transform pair. The series in Eq. (2.8) is easily convergent except at the point where $x, y \to 0$ and $z \to z'$. Thus, Eq. (2.8) can be further split as,

$$G^{spatial}(x,y) = -g^{as}(\rho_{00}) + \sum_{exc.\ m=0} \sum_{exc.\ n=0} g^{as}(\rho_{mn}) e^{-j(mk_x^{inc}d_x + nk_y^{inc}d_y)}. \tag{2.9}$$

It is clearly shown that the first term in Eq. (2.9) is the main reason for the poor convergence in Eq. (2.4). Since we successfully extract the singularity from (2.4), we can sensibly construct the asymptotic series [6] to annihilate the problematic terms, both in spectral domain,

$$\tilde{G}^{as}(k_\rho) = \frac{\left(1 - e^{-k_\rho t}\right)^m e^{-k_\rho \Delta}}{k_\rho^m}. \tag{2.10}$$

and in spatial domain, for $m = 1$,

$$g^{as}(\rho) = \frac{1}{\sqrt{\rho + \Delta^2}} - \frac{1}{\sqrt{\rho + (\Delta + t)^2}}. \tag{2.11}$$

More details on the selection of (2.10) and (2.11) and the associated acceleration techniques can be found in [6].

4. Results

In this section, a Ninja Star periodic nano-plasmonic structure is analyzed by our in-house developed Volumetric Method of Moments (V-MoM) based software and compared with the experimental Second Harmonic Generation microscopy images.

The Ninja Star structure is made of Au (35 nm)/Cr (5 nm) and deposited on SiO_2 (100 nm)/Si layers. The dimensions of the structure and the periods in x and y directions can be directly measured from the SEM image as shown in Fig. 2. In the MAGMAS simulation set up, a two-level hierarchical mesh as shown in Fig. 1 is employed to model the structure in xy plane with two segments in z direction for the Au [15] layer and one segment for the Cr [16] layer. The SiO_2 layer is modeled as an infinitely large layer in xy plane of thickness 100 nm. The subsequent Si layer is taken as a half space.

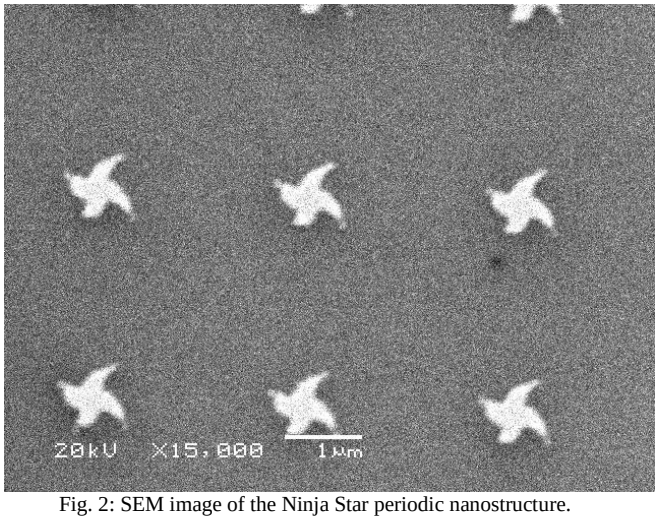


Fig. 2: SEM image of the Ninja Star periodic nanostructure.

In the experiment, the left and right circularly polarized laser pulses centered around 800 nm are shone on the structures and the reflected light is collected by the SHG microscope. More details about the experimental setup can be found in [3]. A pronounced Second Harmonic Generation – Circular Dichroism (SHG-CD) effect can be read from Fig. 3 (c) and (d). In the simulations (shown in Fig. 3 (a) and (b)), the Ninja stars whose arms screw in the clockwise direction are more sensitive to the left circularly polarized light than

the right circularly polarized light. It is clearly seen that our simulations are in very good agreement with the experiments.

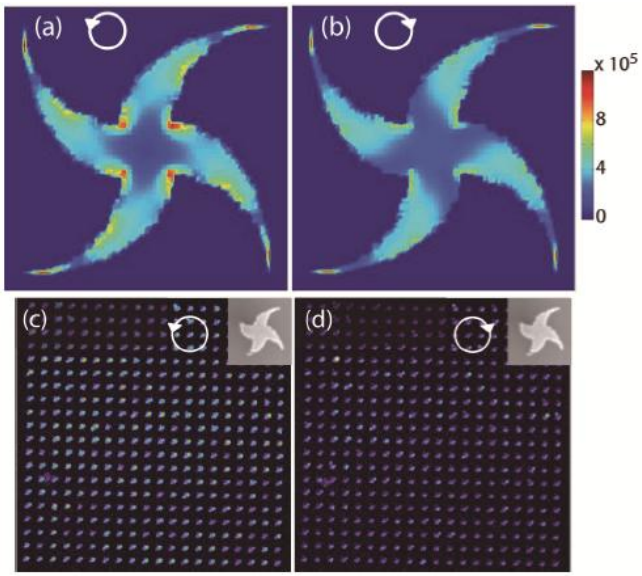


Fig. 3: (a) and (b) Numerical simulation of the polarization currents induced in the top mesh layer of the nanostructures in response to left-hand, in (a), and right-hand, in (b), circularly polarized light. The direction of rotation for circularly polarized light is indicated with the oriented white circles. The Second Harmonic Generation (SHG) is sensitive to chirality and is homogenous throughout the arrays. The SHG response was recorded for left-hand, in (c), and right-hand, in (d), circularly polarized light. SEM micrographs are shown in the insets.

5. Conclusions

In summary, within the framework of the Volumetric Method of Moment (V-MoM) algorithm, a meshing scheme using a binary hierarchical mesh with multiple levels, together with a dedicated Kummer transformation in the calculation of the periodic Green's function, is introduced and investigated. The implemented algorithm successfully predicts the circular dichroism in the nano-plasmonic Ninja Star metamaterial, also experimentally observed with SHG microscopy.

Acknowledgements

The research described in this paper has received funding from the Fund for Scientific Research Flanders (FWO-V) of the Flemish government, through the FWO project G.0897.10N, and from the Katholieke Universiteit Leuven and the Flemish Government through Methusalem Funding. The work of V. K. Valev is supported by the FWO – V, Consorcios Regionales de Experimentación Agricola, and the Engineering and Physical Sciences Research Council under Grant EP/G060649/1.

References

[1] Shuang Zhang, Dentcho A. Genov, Yuan Wang, Ming Liu, and Xiang Zhang, "Plasmon-Induced Transparency in Metamaterials", *Phys. Rev. Lett.*, 101, 047401 (2008)

[2] E. Plum, X.-X. Liu, V. A. Fedotov, Y. Chen, D. P. Tsai, and N. I. Zheludev, *"*Metamaterials: Optical Activity without Chirality*"*, Phys. Rev. Lett. **102**, 113902.

[3] V. K. Valev, B. D. Clercq, X. Zheng, D. Denkova, E. J. Osley, S. Vandendriessche, A. V. Silhanek, V. Volskiy, P. A. Warburton, G. A. E. Vandenbosch, M. Ameloot, V. V. Moshchalkov and T. Verbiest, "The role of chiral local enhancements below the resolution limit of Second Harmonic Generation microscopy," *Opt. Exp.*, Vol. 20, No. 1, 256 -264, 2012.

[4] V. A. Fedotov, P. L. Mladyonov, S. L. Prosvirnin, A. V. Rogacheva, Y. Chen, and N. I. Zheludev, "Asymmetric Propagation of Electromagnetic Waves through a Planar Chiral Structure," Phys. Rev. Lett. **97**, 167401.

[5] G. A. E. Vandenbosch, V. Volski, N. Verellen, V. V. Moshchalkov, "On the use of the method of moments in plasmonic applications," Radio Science, vol. 46, May 2011, rS0E02.

[6] V. Volskiy, and G. A. E. Vandenbosch, "Quasi 3D Mixed Potential Integral Equation Formulation for Periodic Structures," IEEE Trans. Antennas Propag., Accepted.

[7] G. A. E. Vandenbosch and A. R. de Capelle, "Mixed-potential integral expression formulation of the electric field in a stratified dielectric medium," IEEE Trans. Antennas Propag., vol. 40, pp. 806–817, 1992.

[8] M. Vranken and G. A. E. Vandenbosch, "Hybrid dyadic-mixed-potential and combined spectral-space domain integral equation analysis of quasi-3-d structures in stratified media," IEEE Trans. Microw. Theory Tech., vol. 51, no. 1, p. 216225, Jan. 2003.

[9] Y. Schols and G. A. E. Vandenbosch, "Separation of horizontal and vertical dependencies in a surface/volume integral equation approach to model quasi 3-d structures in multilayered media," IEEE Trans. Antennas Propag., VOL. 55,NO. 4, pp. 1086–1094, 2007.

[10] A. F. Peterson, S. L. Ray and R. Mittra, *Computational Methods for Electromagnetics*, *IEEE Press*, 1998.

[11] G. Valerio, P Baccarelli, P. Burghignoli and A. Galli, "Comparative analysis of acceleration techniques for 2D and 3D Green's functions in periodic structures along one and two directions", *IEEE Trans AntennasPropagation*, Vol. 55, No. 6, 1630-1643, 2007.

[12] N. Guerin, S. Enoch and G. Tayeb, "Combined method for the computation of the doubly periodic Green's function," *Journal Electromagn. Waves and Appl.*, Vol. 15, No. 2, 205-221, 2001.

[13] G. Valerio, P. Baccarelli, S. Paulotto, F. Frezza, A. Galli, "Regularization of mixed- potential layerd media Green's function for efficient interpolation procedures in planar periodic structures, *IEEE Trans Antennas Propagation*, Vol. 57, No. 1, 122-134, 2009.

[14] N. Guerin, Dardenne X, and C. Craye, Accelerated computation of the Free Space Green's function gradient of infinite phased arrays of dipoles, *IEEE*

Trans Antennas Propagation, Vol.57, No.10, 3430-3434, 2009

[15] P. B. Johnson and R. W. Christy, "Optical Constants of the Noble Metals", *Phys. Rev. B*, 6, 4370-4379 (1972)

[16] *SOPRA N&K Database*

Selective mode suppression in microstrip differential lines by means of electric-LC (ELC) and magnetic-LC (MLC) resonators

J. Naqui, M. Durán-Sindreu, and F. Martín

GEMMA/CIMITEC, Departament d'Enginyeria Electrònica,
Universitat Autònoma de Barcelona, 08193-BELLATERRA (Barcelona), Spain
*corresponding author: Ferran.Martin@uab.cat

Abstract

In this paper, it is demonstrated that the so-called electric-LC (ELC) resonators, and their dual counterparts, the magnetic-LC (MLC) resonators, are useful for the selective suppression of either the differential or the common mode in microstrip differential lines. The key point to mode suppression is the alignment of the electric (differential mode) or magnetic (common mode) walls of the line with the resonator. It is shown that by simply rotating the resonators 90^o we can selectively choose the suppressed mode at the resonator's fundamental resonance frequency. The theory is validated through full-wave electromagnetic simulation and supported by the lumped element equivalent circuit models of the proposed structures.

1. Introduction

Split-ring resonators (SRRs) [1] and their complementary counterparts (CSRRs) [2] (Fig. 1) have been extensively used for the implementation of metamaterials and many devices based on them [3]. One of the applications of these metamaterial resonators is the selective mode suppression in 3-wire transmission lines where two fundamental modes can propagate along them. Specifically, SRRs etched in the back substrate side of a CPW with their symmetry plane (*x*-*z* plane) aligned with the symmetry plane of the line, are useful to suppress the parasitic slot mode of the line at their fundamental resonance, while they are transparent for the CPW (common) mode [4] [Fig. 2(a)]. CSRRs, on the other hand, have been applied to suppress the common mode in microstrip differential lines and balanced circuits [5]. In these applications, the CSRRs must be etched in the ground plane with their symmetry plane aligned with the symmetry plane of the differential line [Fig. 2(b)].

The key aspect to suppress either the differential or the common mode, keeping the other mode unaltered, is the perfect alignment of electric or magnetic walls between the line and the resonator. Thus, for the CPW loaded with symmetrically etched SRRs, the electric wall of the SRR at their symmetry plane is responsible for the slot mode suppression, since the CPW exhibits an electric wall at the symmetry plane for this mode. For a microstrip differential line, the symmetry plane is a magnetic wall for the common mode. Therefore, by symmetrically etching a CSRR in the ground plane, where the symmetry plane is also a magnetic wall, the common mode is suppressed at the fundamental CSRR resonance, whereas the differential mode is kept unaltered.

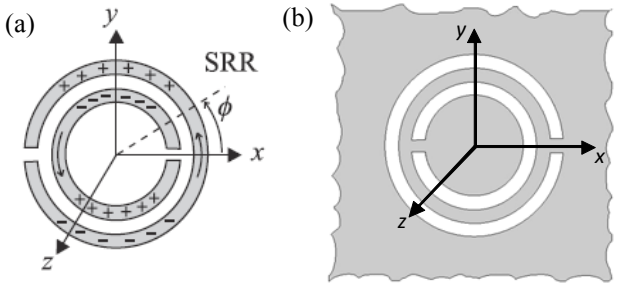


Figure 1: Typical topology of an SRR (a) and a CSRR (b). The distribution of charges for the SRR at the fundamental resonance is also indicated (notice that the symmetry plane is an electric wall). From the Babinet principle, it follows that the CSRR exhibits a magnetic wall at the symmetry plane.

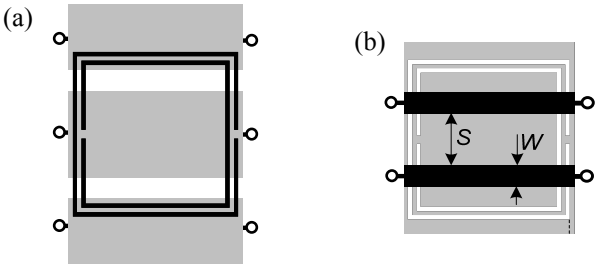


Figure 2: CPW loaded with a symmetrically etched SRR (a) and microstrip differential line loaded with a symmetrically etched CSRR (b).

SRRs/CSRRs exhibit bianisotropy [3,6,7], which means that they can be excited by means of a uniform axial time-varying magnetic/electric field, or by means of an electric/magnetic field orthogonally applied to the symmetry plane of the particle. When these particles (SRRs or CSRRs) are loading elements of a transmission line, it is clear that the driving fields generated by the line are not uniform. Nevertheless, it has been demonstrated that both CPW and

microstrip lines loaded with symmetrically etched SRRs and CSRRs, respectively, exhibit mixed coupling between the line and the resonators for those line modes that are suppressed [8]. These modes are the slot mode for the CPWs, and the common mode for the differential microstrip lines (single microstrip lines with symmetrically etched CSRRs do also exhibit mixed coupling).

In this paper, alternative resonators are considered, namely, the so-called electric-LC resonator, ELC [Fig. 3(a)] [9], or its complementary particle, the magnetic-LC resonator, MLC [Fig. 3(b)]. Such resonators do not exhibit bianisotropy and they are bisymmetric, one of the symmetry planes being a magnetic wall and the other one being an electric wall at the fundamental resonance (see Fig. 3). The selective mode suppression with ELC and MLC resonators in microstrip differential lines is discussed on the basis of symmetry properties. The theory is validated through electromagnetic simulation and supported by means of lumped element equivalent circuit models.

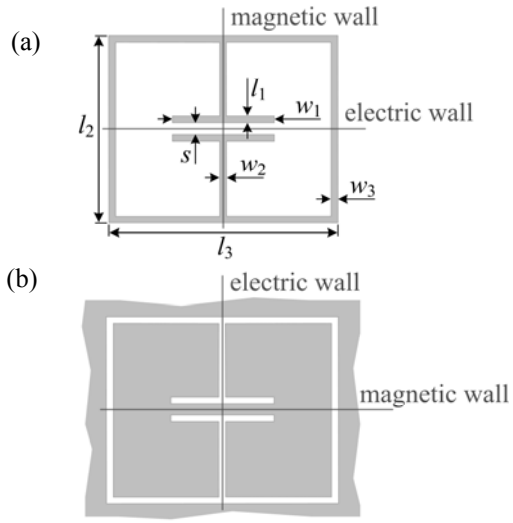


Figure 3: Typical topology of an ELC (a) and a MLC (b) resonator. The nature of the symmetry planes is indicated.

2. ELC and MLC resonators

The ELC resonator [Fig. 3(a)] was proposed by Schurig *et al*. for the implementation of resonant-type negative permittivity metamaterials, as an alternative to the well known wire media, described by the Drude model [9]. The ELC resonator consists of two closed inductive loops connected to a common capacitor. At the fundamental resonance, the instantaneous current is clockwise in one loop and counterclockwise in the other loop, thus giving rise to a net displacement current in the central capacitor. Therefore, at the fundamental resonance, the magnetic moment associated with currents in both loops cancels and the particle cannot be excited by a uniform time-varying magnetic field applied in the axial direction. However, there is still an electric dipole moment associated with the capacitor. Thus, the ELC resonator can be electrically driven (or coupled) by means of an electric field applied in the particle plane in the direction orthogonal to the electric wall. Notice that due to current symmetry, the vertical symmetry plane in Fig. 3(a) is a magnetic wall for the fundamental resonance.

For the MLC, we can invoke the Babinet principle and conclude that this particle exhibits magnetic and electric walls, rotated 90^o as compared to those of the ELC. In other words, the particle cannot be excited by means of a uniform axial time-varying electric field, but it can be driven by means of a magnetic field applied in the particle plane, in the direction orthogonal to the magnetic wall.

3. Microstrip differential lines loaded with ELCs and MLCs

As it was discussed before [5], if a transmission line is loaded with a symmetric resonator with aligned symmetry planes, and the symmetry plane of the line and resonator are of the same nature (electric or magnetic walls), signal propagation at the fundamental resonance is inhibited (i.e., a transmission zero appears). However, the line is transparent if such symmetry planes are distinct. In particular, if we consider a microstrip differential line, there are 4 cases of interest for selective mode suppression, depicted in Figs. 4 and 5. In Figs. 4(a) and (b), the differential line is loaded with an ELC etched on the upper side of the substrate, with a relative orientation of 90^o between the loading elements. According to these orientations, it is expected that the structure of Fig. 4(b) is transparent for the common mode and produces a notch for the differential mode, contrarily to Fig. 4(a).

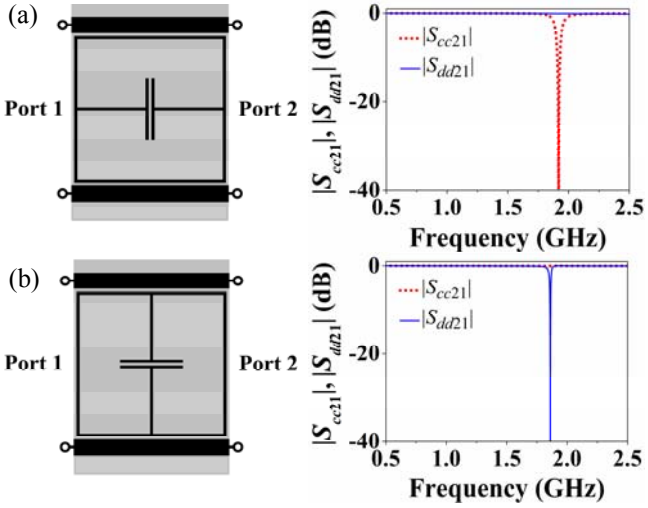


Figure 4: Microstrip differential line loaded with an ELC with the electric (a) and magnetic (b) wall aligned with the symmetry plane of the line. The substrate is *Rogers RO3010* with thickness h = 1.27 mm and dielectric constant ε_r = 11.2. Line dimensions are: W = 1.1 mm and S = 10.4 mm. ELC dimensions are: w_1 = 4 mm, $w_2 = w_3 = l_1 = s$ = 0.2 mm, $l_2 = l_3$ = 10 mm.

In Figs. 5(a) and 5(b), the differential line is loaded with a MLC resonator etched in the ground plane. In this case the situation is reversed since the electric and magnetic walls of ELCs and MLCs are interchanged. The transmission coefficients for the differential (S_{dd21}) and common (S_{cc21}) modes of the structures of Figs. 4 and 5 have been inferred by means of the *Agilent Momentum* commercial software. These results (also depicted in Figs. 4 and 5) validate the selective mode suppression achievable in these differential lines by merely rotating the resonators 90º.

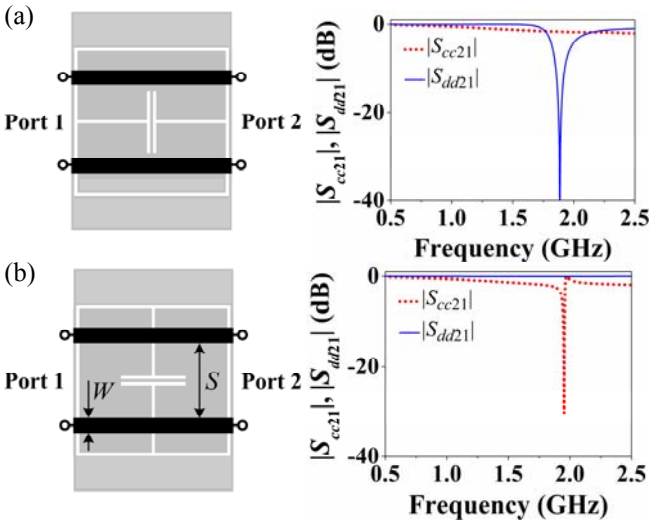


Figure 5: Microstrip differential line loaded with a MLC with the magnetic (a) and electric (b) wall aligned with the line. The substrate is *Rogers RO3010* with thickness h = 1.27 mm and dielectric constant ε_r = 11.2. Line dimensions are: W = 1 mm and S = 5 mm. MLC dimensions are: w_1 = 4 mm, $w_2 = w_3 = l_1 = s$ = 0.2 mm, and $l_2 = l_3$ = 10 mm.

It is important to emphasize that the driving fields of the particles are not uniform. Indeed, in the configuration of Fig. 4(a), the ELC cannot be excited by the electric field generated by the differential line in the common mode. However, for this mode, the magnetic fields generated by both lines have contra-directional axial components on the upper and lower part of the ELC, sufficient to excite the particle. Therefore, the ELC resonator is excited by means of the magnetic field generated by the line under common mode operation. Similarly, in the configuration of Fig. 5(a), the MLC is excited under differential mode operation thanks to the electric field generated by the pair of lines, which is able to induce an electric dipole moment and a net current flow in the ground plane, across the symmetry plane of the lines (or across the electric wall of the MLC). Thus, the terminology of these particles does not obey to the nature of the driving fields in the considered configurations (the reason is that the fields are not uniform). However, the original nomenclature, given by Schurig *et al.* [9] to the resonator of Fig. 3(a), i.e. ELC, is preserved. For coherence, the resonator of Fig. 3(b) is called MLC particle by the authors.

4. Lumped element equivalent circuit models

Let us now consider the lumped element equivalent circuit models of the structures of Figs 4 and 5. In Fig. 4(a), the ELC can only by excited by the magnetic field generated by the line (common mode), but not by the electric field, due to the particle orientation. Similarly, for the MLC of Fig. 5(a), excitation under differential mode operation is only possible through the electric field generated by the line. For Figs. 4(a) and 5(a), particle excitation under differential and common mode, respectively, is more complex, since both electric and magnetic coupling between the line and the resonator must be considered. Let us thus start with the lumped element equivalent circuit models of the structures of Figs. 4(b) and 5(b), where mixed coupling is not present.

The model of the ELC-loaded differential line of Fig. 4(a) is depicted in Fig. 6(a). The electric and magnetic coupling between the pair of lines has been neglected due to the significant separation between both lines (necessary to accommodate the ELC). Thus, the even mode (common mode related) and the odd mode (differential mode related) characteristic impedances are, respectively, $Z_e \approx Z_o \approx 50\ \Omega$. L and C are the per-section inductance and capacitance, respectively, of the individual lines, the ELC resonator is modeled by the inductances L_e and by the capacitance C_e, and the magnetic coupling between the lines and the resonator is accounted for through the mutual inductance M. The equivalent circuit models for common (or even) and differential (or odd) mode excitation are depicted in Figs. 6(b) and (c). For the common mode, the symmetry plane is an open circuit, and the model is identical to that of an SRR-loaded line, giving a notch in the transmission coefficient at resonance [10,11]. For the differential mode, the symmetry plane is a short circuit and the ELC no longer plays an active role. Therefore, the line is transparent for this mode. We have considered the structure of Fig. 7 (inset), and we have extracted the circuit parameters for the common mode from the electromagnetic simulation of the frequency response for this mode. The agreement between the circuit and electromagnetic simulation is remarkable. Notice that the topology of the ELC of Fig. 7 has been modified (as compared to Fig. 4) in order to reduce the electrical size of the particle (under these conditions the lumped element circuit model is valid in a wider range of frequencies).

The model of the MLC loaded differential line of Fig. 5(a) is depicted in Fig. 8(a). L and C model the per-section line inductance and capacitance, respectively. However, notice that C acts as the coupling capacitance between the lines and the MLC. The resonator is modeled by the inductance L_m and the capacitances C_m. Finally, the particle is capacitively connected through the ground plane through the slot capacitances modeled by C_g. The common and differential mode models are depicted in Figs. 8(b) and 8(c), respectively. For the common mode, the resonator is opened, and the resulting model is that of a transmission line, i.e. the structure is transparent. For the differential mode, there is a short in the symmetry plane, and the circuit model is identical to that of a CSRR loaded microstrip line,

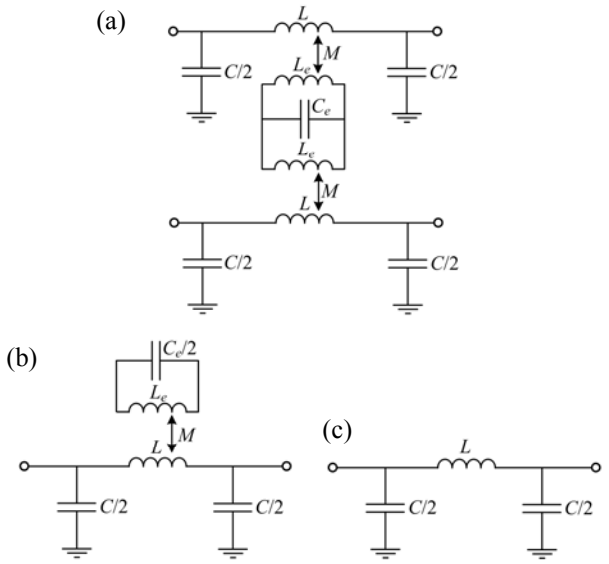


Figure 6: (a) Lumped element equivalent circuit model of the ELC loaded differential line of Fig. 4(a); (b) circuit model for the even mode; (c) circuit model for the odd mode.

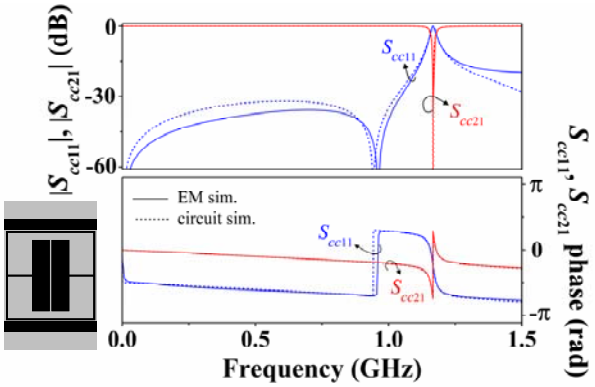


Figure 7: Frequency response (common mode) for the structure in Fig. 4(a) with $l_1 = 2$ mm and $w_1 = 8$ mm and for its circuit model in Fig. 6(b). Circuit parameters are: L = 4.57 nH, C = 2.20 pF, L_e = 4.57 nH, C_e = 8.14 pF, and M = 1 nH.

providing a notch in the transmission frequency for such mode at resonance. We have considered the structure of Fig. 9 (inset), and we have extracted the circuit parameters for the differential mode from the electromagnetic simulation of the frequency response for this mode. The agreement between the circuit and electromagnetic simulation is also good.

Let us now focus on the lumped element equivalent circuit models that result by rotating the MLC and the ELC 90º, that is, the models describing the structures of Figs. 4(a) and 5(a), where both magnetic and electric coupling must be considered. For the structure of Fig. 4(b), the circuit model is that depicted in Fig. 10(a). The resonator has been rotated, and the coupling capacitances, C_a, have been added to account for electric coupling. Indeed, since the symmetry plane in the configuration of the structure of Fig. 4(b) is an electric wall for the differential mode, electric coupling is the main driving mechanism of the particle for this mode. The circuit models for the common and differential modes are depicted in Figs. 10(b) and 10(c), respectively, where it is clear that the common mode is not able to excite the particle and the structure is transparent for this mode. Conversely, the differential mode produces a notch in the transmission coefficient, as the equivalent circuit model of such mode confirms. We have considered the structure of Fig. 11 (inset) and we have tuned the coupling capacitance, optimizing slightly the rest of parameters corresponding to Fig. 7 (the geometry of the differential line and ELC are identical) in order to match the frequency response for the circuit model (differential mode) to that inferred from the electromagnetic simulation. The agreement is reasonable taking into account that those element parameters corresponding to Fig. 7 have been considered.

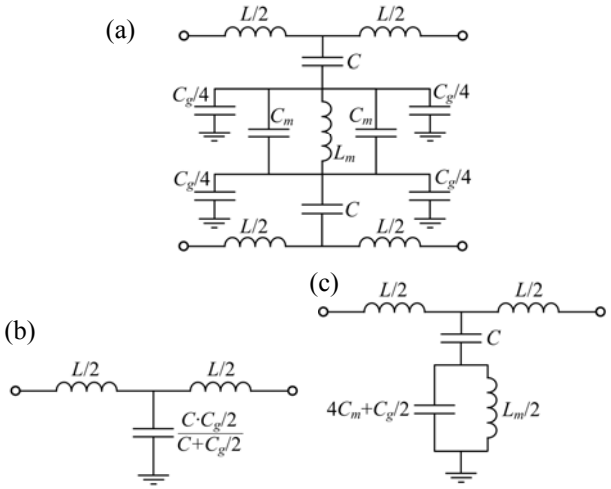


Figure 8: (a) Lumped element equivalent circuit model of the MLC loaded differential line of Fig. 5(a); (b) circuit model for the even mode; (c) circuit model for the odd mode.

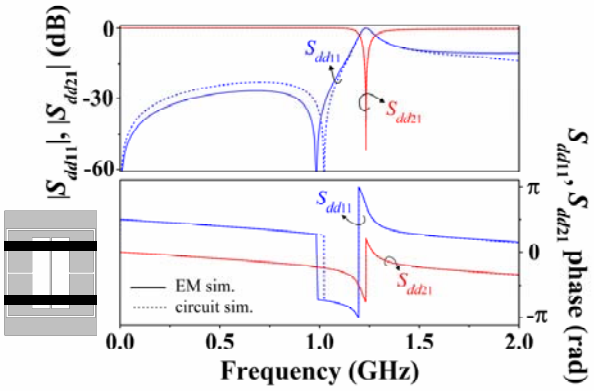


Figure 9: Frequency response (differential mode) for the structure in Fig. 5(a) with $l_1 = 2$ mm and $w_1 = 8$ mm and for its circuit model in Fig. 8(c). Circuit parameters are: L = 6.07 nH, C = 1.53 pF, $4C_m + C_g/2$= 7.47 pF, and L_m = 3.71 nH.

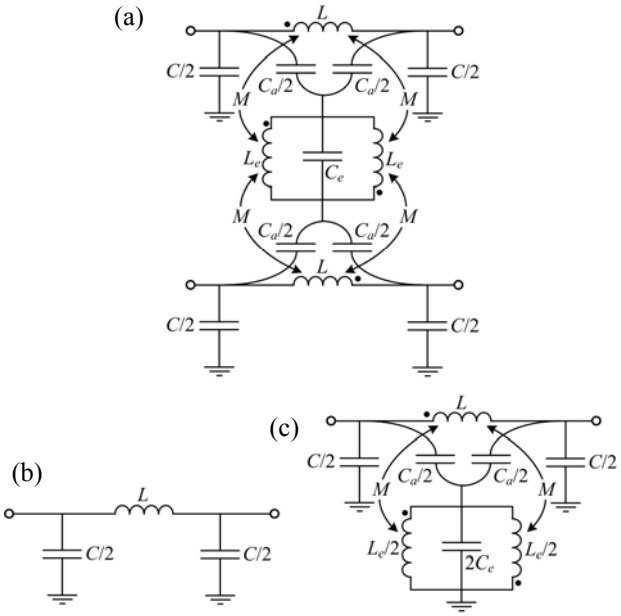


Figure 10: (a) Lumped element equivalent circuit model of the ELC loaded differential line of Fig. 4(b); (b) circuit model for the even mode; (c) circuit model for the odd mode.

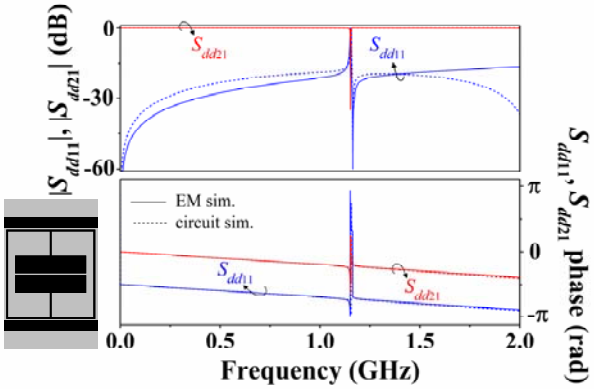


Figure 11: Frequency response (differential mode) for the structure shown in Fig. 4(b) with $l_1 = 2$ mm and $w_1 = 8$ mm and for its circuit model in Fig. 10(c). Circuit parameters are: L = 4.62 nH, $C = 2.02$ pF, $L_e = 4.6$ nH, $C_e = 8.14$ pF, $M = 1$ nH, and $C_a = 0.4$ pF.

The MLC-loaded differential line of Fig. 5(b) is modeled by the circuit of Fig. 12(a). This is obtained by rotating the particle and splitting the coupling capacitance. Moreover, magnetic coupling has been introduced and is accounted for by the mutual inductances M. The equivalent circuit models for the common and differential modes [Figs. 12(b) and 12(c), respectively], indicate that in this case, the structure is transparent for the differential mode, whereas a notch appears for the common mode. Again, the electromagnetic simulation for the common mode is compared to the circuit simulation for such mode (Fig. 13), and the agreement is also good, thus confirming the validity of the proposed model.

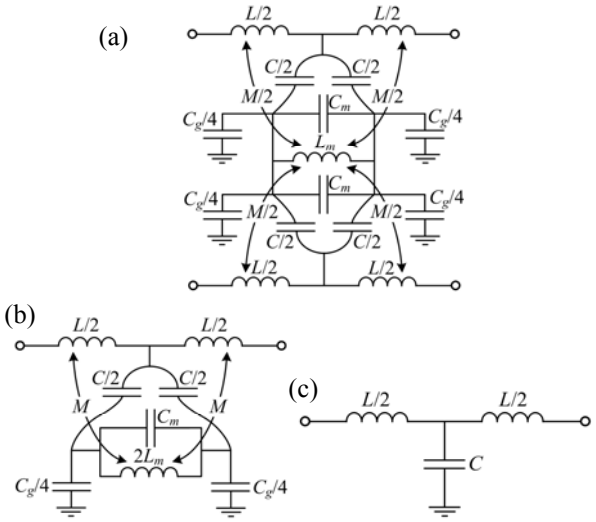


Figure 12: (a) Lumped element equivalent circuit model of the MLC loaded differential line of Fig. 5(b); (b) circuit model for the even mode; (c) circuit model for the odd mode.

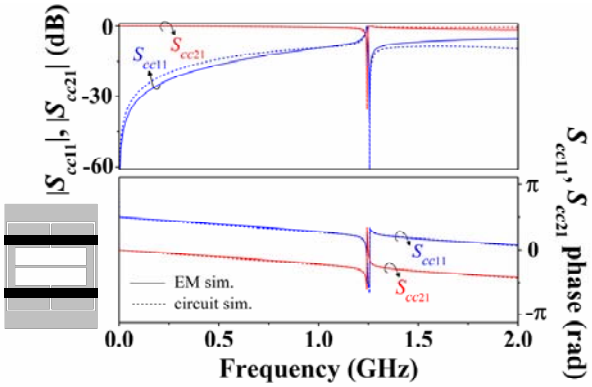


Figure 13: Frequency response (common mode) for the structure shown in Fig. 5(b) with $l_1 = 2$ mm and $w_1 = 8$ mm and for its circuit model in Fig. 12(b). Circuit parameters are: L = 9.3 nH, $C = 1.53$ pF, $L_m = 3.64$ nH, and C_m = 0.93 pF, C_g = 7.5 pF, and $M = 0.5$ nH.

5. Conclusions and future work

In conclusion, it has been demonstrated that the differential and common modes in microstrip differential lines can be selectively suppressed by loading the lines with either ELC or MLC bisymmetric resonators. Key to this selective mode suppression at the fundamental resonance frequency of the particles is the presence of a magnetic and an electric wall, orthogonally oriented, in these resonators. Hence, it is possible to either suppress the common or the differential mode by simply rotating the considered particle (ELC or MLC) 90°. We have proposed lumped element circuit models for microstrip differential lines loaded with both resonators for the two considered orientations, and the agreement between the frequency responses inferred from circuit and electromagnetic simulations is good. These structures can be useful for common mode suppression in differential lines and balanced circuits [5], or for the

implementation of sensors based on symmetry properties, such as rotation sensors [14]. As compared to the structures used in [5], based on CSRRs, the structure of Fig. 4(b) is able to suppress the common mode, keeping the ground plane unaltered. On the other hand, implementing a circular structure based on the configuration of Fig. 4, it is possible to implement a rotation sensor (similar to that based on the CPW structure reported in [14]) in microstrip technology. Work is in progress in these directions.

Acknowledgements

This work has been supported by MICIIN-Spain (projects TEC2010-17512 and CSD2008-00066) and by AGAUR-*Generalitat de Catalunya*, through project 2009SGR-421. Jordi Naqui is also in debt to MINECO (Spain) for supporting his work through the FPU grant AP2010-0431.

References

[1] J.B. Pendry, "Magnetism from conductors and enhanced nonlinear phenomena", *IEEE Trans. Microw. Theory Tech*., vol. 47, pp. 2075-2084, Nov.1999.

[2] F. Falcone, T. Lopetegi, J. D. Baena, R. Marqués, F. Martín, and M. Sorolla, "Effective negative-ε stop-band microstrip lines based on complementary split ring resonators," *IEEE Microwave and Wireless Components Letters*, vol. 14, pp. 280-282, June 2004.

[3] R. Marqués, F. Martín, M. Sorolla, *Metamaterials with negative parameters: theory, design and microwave applications*, John Wiley & Sons Inc., USA, 2008.

[4] J. Naqui, M. Durán-Sindreu, F. Martín, "Selective mode suppression in coplanar waveguides using metamaterial resonators", *Appl. Phys. A - Materials Science and Processing*, vol. 109, pp. 1053-1058, Dec. 2012.

[5] J. Naqui, A. Fernández-Prieto, M. Durán-Sindreu, F. Mesa, J. Martel, F. Medina, and F. Martín, "Common mode suppression in microstrip differential lines by means of complementary split ring resonators: theory and applications", *IEEE Transactions on Microwave Theory and Techniques*, vol. 60, pp. 3023-3034, Oct. 2012.

[6] R. Marques, F. Medina and R. Rafii-El-Idrissi, "Role of bi-anisotropy in negative permeability and left handed metamaterials", *Phys. Rev. B*, vol. 65, paper 144441, 2002.

[7] R. Marqués, F. Mesa, J. Martel and F. Medina, "Comparative analysis of edge and broadside couple split ring resonators for metamaterial design. Theory and Experiment", *IEEE Trans. Ant. Propag*., vol. 51, pp.2572-2582, Oct. 2003.

[8] J. Naqui, M. Durán-Sindreu, and F. Martín, "Modeling Split Ring Resonator (SRR) and Complementary Split Ring Resonator (CSRR) Loaded Transmission Lines Exhibiting Cross Polarization Effects", *IEEE Antennas and Wireless Propagation Letters*, to be published.

[9] D. Schurig, J. J. Mock, and D. R. Smith, "Electric-field-coupled resonators for negative permittivity metamaterials", *Appl. Phys. Lett*., vol. 88, paper 041109, 2006.

[10] F. Martín, F. Falcone, J. Bonache, R. Marqués and M. Sorolla, "Split ring resonator based left handed coplanar waveguide", *Appl. Phys. Lett*., vol. 83, pp. 4652-4654, December 2003.

[11] F. Aznar, J. Bonache and F. Martín, "Improved circuit model for left handed lines loaded with split ring resonators", *Appl. Phys. Lett*., vol. 92, paper 043512, February 2008.

[12] J.D. Baena, J. Bonache, F. Martín, R. Marqués, F. Falcone, T. Lopetegi, M.A.G. Laso, J. García, I Gil, M. Flores-Portillo and M. Sorolla, "Equivalent circuit models for split ring resonators and complementary split rings resonators coupled to planar transmission lines", *IEEE Transactions on Microwave Theory and Techniques*, vol. 53, pp. 1451-1461, April 2005.

[13] J. Bonache, M. Gil, O. García-Abad and F. Martín, "Parametric analysis of microstrip lines loaded with complementary split ring resonators", *Microwave and Optical Technology Lett.*, vol. 50, pp. 2093-2096, August 2008.

[14] J. Naqui, M. Durán-Sindreu, F. Martín, "Transmission Lines Loaded with Bisymmetric Resonators and Applications", *IEEE MTT-S Int. Microwave Symp*., June 2013, Seatle (USA).

Multifrequency and Low Profile Metamaterial-Inspired Antennas

S. DAKHLI[1, 2]. H. RMILI[3*], J. M. FLOC'H[4], F. CHOUBANI[1] and K. MAHDJOUBI[2]

[1]Innov'Com Laboratory, SUPCOM,University of Carthage, Tunis, Tunisia.

[2]IETR, University of Rennes 1, #263, Av. Général Leclerc, CS 74205, 35042 Rennes Cedex, France.

[3]King Abdulaziz University, Electrical and Computer Engineering Department, Jeddah, Saudi Arabia.

[4]IETR, INSA, #20 avenue buttes des coësmes, 35043 Rennes Cedex, France.

[*]Hatem RMILI: hmrmili@kau.edu.sa

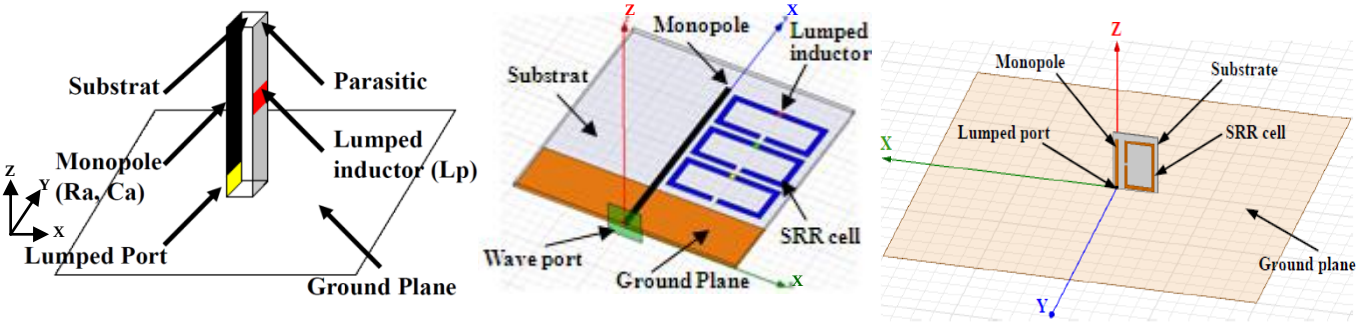
Abstract-In this paper several low profile and multifrquency metamaterial inspired antennas are designed. All these antennas are based on the electric coupling between the parasitic element and the driven monopole element. The simulated and measured results of the return loss, efficiency and radiation patterns are reported.

1. Introduction

The rapid progress of wireless devices for communication has increased the requirement of efficient, low profile, light weight and low cost electrically small antennas (ESAs). A variety of antennas has been engineered with metamaterials and metamaterial-inspired constructs in order to improve their performances in terms of bandwidth [1] and efficiency [2] as well as to achieve novel functions [3-4]. In this work, we use new type of parasitic elements with different shapes in order to obtain a multifrequency behavior. This technique leads to new resonance frequencies lower than that of the exciting monopole. Three families of antennas are studied: each one is composed of a monopole antenna and some parasitic elements.

2. Antennas Design and Fabrication

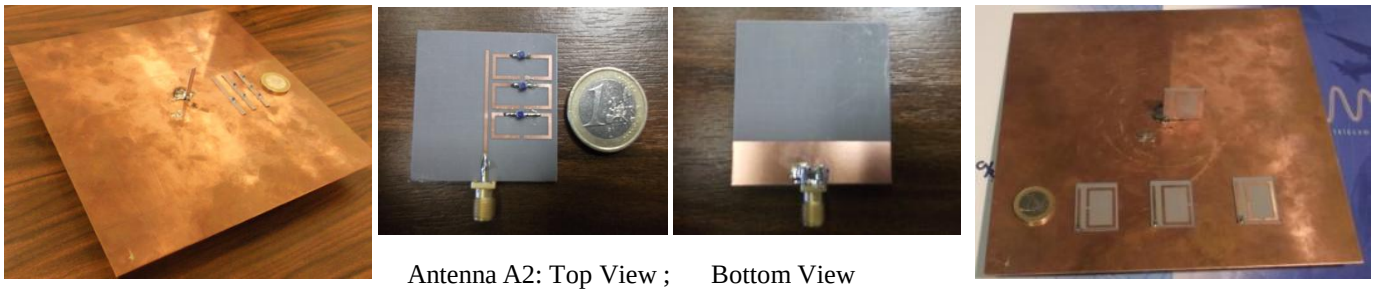
Figure.1 presents the structures of the proposed antennas A1, A2 and A3. For the three structures, we have used a Rogers Duroid TM 5880 substrate of thickness 0.8mm and relative permittivity ε_r = 2.2, and a monopole antenna of 25mm long 1.5mm wide, having a resonance frequency of 2.45GHz and a bandwidth of 400MHz. In simulation, the A1 and A3 antennas are excited by a lumped port of 50Ω input impedance while the A2 antenna is excited by a wave port of 50Ω input impedance. The antennas are simulated by ANSYS-HFSS software.



Antenna A1 [4] Antenna A2 [5] Antenna A3 [6]

Figure 1. The structures of the three proposed antennas.

The prototypes are simulated, optimized, realized and finally characterized. Fig. 2 presents photos of the realized prototypes.



Antenna A1 Antenna A2: Top View ; Bottom View Antenna A3

Figure 2. Photos of the realized prototypes.

3. Equivalent Circuit Model

An equivalent circuit model (Fig.3) is proposed in order to describe the operation of the antenna system.

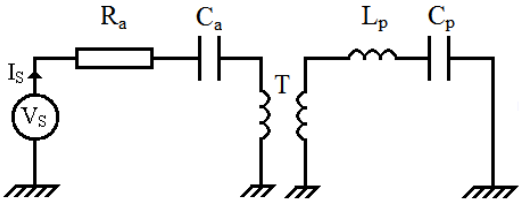


Figure.3. Equivalent circuit model of the antenna system.

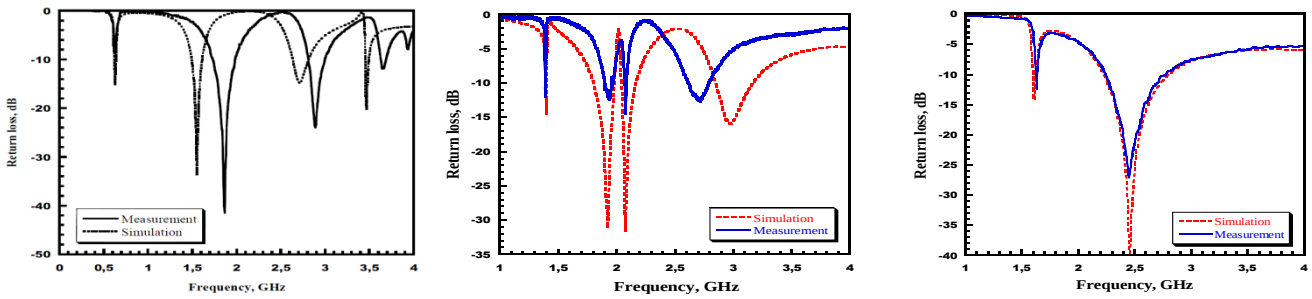
To a lower frequency, the monopole and the coupling elements are electrically small. The monopole acts as a RC circuit (R_a,C_a). Whereas the parasitic element acts like a LC circuit (L_p,C_p).The coupling between the two elements is ensured by a transformer T. The resonant frequency of the circuit model is approximately [3]:

$$f_{res} = \frac{1}{2\pi}\sqrt{\frac{C_a+C_p}{L_p.(C_a.C_p)}} \quad (1)$$

4. Results

a. Return Loss

Figure.4 illustrates the measured and simulated return loss for the different antennas.



Antenna A1 Antenna A2 Antenna A3

Figure 4. Measured and Simulated Return loss for the three prototypes.

According Fig.4, the addition of the parasitic elements generates a new resonance frequencies lower than that of the exciting monopole. We can notice a good agreement between numerical and experimental results.

Table I summarizes simulated and measured resonant frequencies for the proposed antennas, deduced from Fig. 4.

TABLE I:

SIMULATED AND MEASURED RESONANCE FREQUENCIES FOR THE FOUR PROPOSED ANTENNAS

	Simulated resonant frequencies (GHz)				**Measured resonant frequencies (GHz)**			
Antenna	F_0	F_1	F_2	F_3	F_0	F_1	F_2	F_3
A1	0.63	1.56	2.7	3.48	0.63	1.86	2.89	3.64
A2	1.438	1.858	1.991	2.881	1.397	1.931	2.082	2.692
A3	1.606	2.455	-	-	1.635	2.445	-	-

b. Efficiency and Radiation Pattern

Table I collects the simulated and measured overall efficiency (OE) of the four proposed antennas at the lower and the higher frequencies. OE is the ratio of the radiated power P_{rad} to the input power P_{in}, as given by the following expression [3]:

$$OE = \frac{P_{rad}}{P_{in}} \tag{2}$$

TABLE I:

SIMULATED AND MEASURED OVERALL EFFICENCY (OE) FOR THE FOUR PROPOSED ANTENNAS

	Simulated Overall Efficiency (OE %)	**Measured Overall Efficiency (OE %)**
Antenna	F_0	F_0
A1	82.4	71.5
A2	42.5	35.6
A3	96.2	82.3

According to the table II, a high overall efficiency (OE) is obtained for A1 and A3 antennas at the lower frequencies. For the A1 antenna the OE = 96% at F_0 = 631MHz. For the A3 antenna OE = 82% at F_0 =1.606GHz. For The A2 antenna, we obtain a lower efficiency than that of the A1 and A3 antennas at the lower frequencies due to its reduced ground plane.

Fig.5 presents the simulated results of 3D radiation patterns of the proposed antennas at the resonance frequencies.

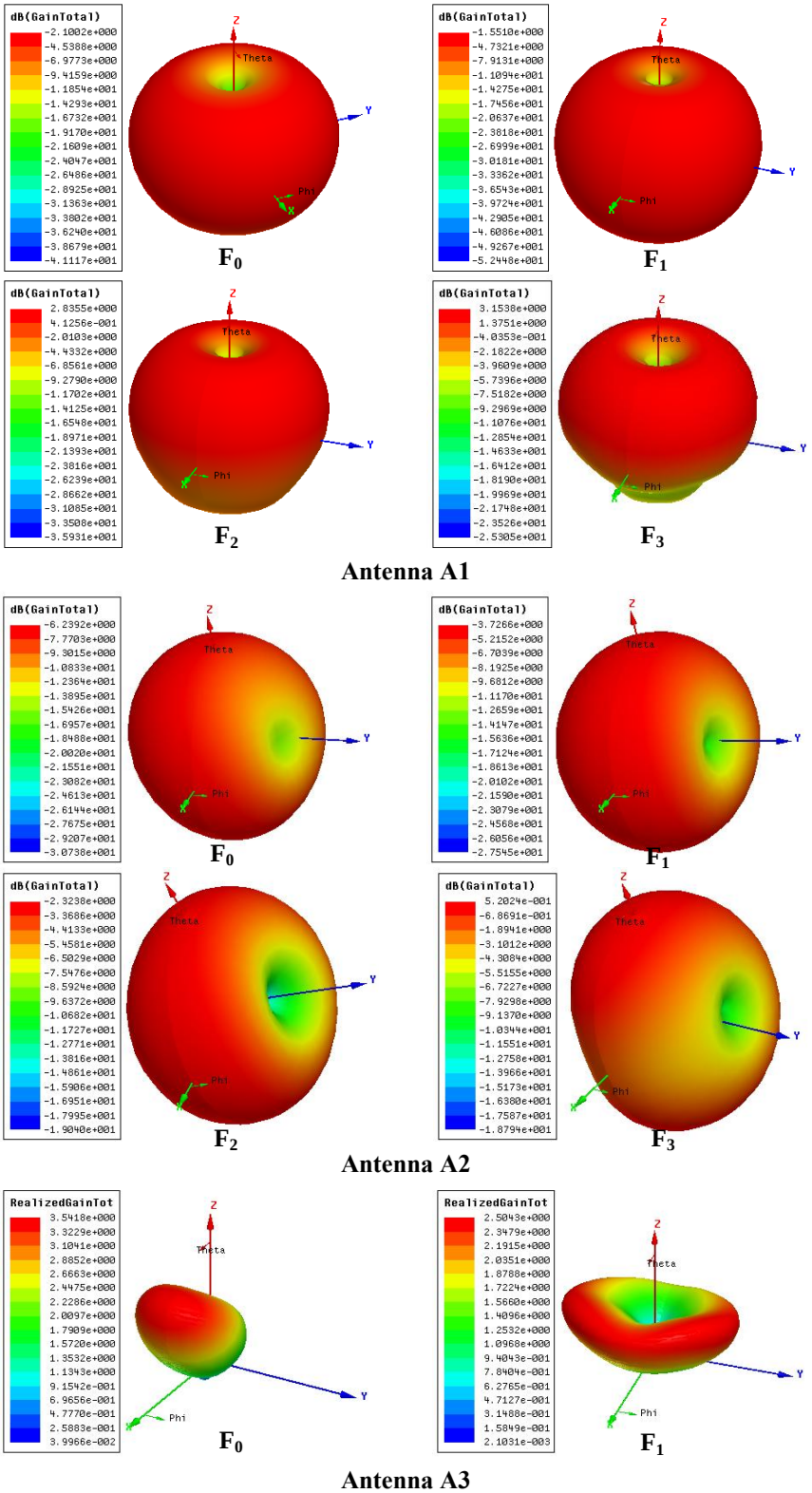


Figure 5. Simulated 3D Radiation Patterns for the studied antennas.

All these structures behave like a single monopole antenna at the different resonance frequencies from both S_{11} (Fig. 4) and radiation point of view (Fig.5), except of the case of the A3 Antenna when we can notice an unusually directive beam at the lower frequency F_0.

5. Conclusion

A family of low profile and multifrequency metamaterial inspired antennas is reported. We have used different shape of parasitic elements to reduce the profile of the monopole antenna and/or to create multifrequency behavior. The simulated and measured results of the return loss, efficiency and radiation patterns are presented and discussed.

REFERENCES

1. P. Jin and R.W. Ziolkowski, «Broadband, Efficient, Electrically Small Metamaterial-Inspired Antennas Faciltated by Active Near Field Resonant Parasitic Elements, » *IEEE Trans. Antennas Propag.*, vol. 58, pp 318-327, Feb. 2010.
2. A. Erentok and R.W. Ziolkowski, "Metamaterial-Inspired Efficient Electrically Small Antennas," IEEE Trans. Antennas Propag, vol. 56, pp. 691-707, Mar. 2008.
3. R.W.Ziolkowski, Efficient Electrically Small Antenna Facilitated by a Near-Field Resonant Parasitic," Antenna and Wireless Propagation Letters IEEE, vol. 7, pp. 581 – 584, Sep. 2008.
4. S. Dakhli, K. Mahdjoubi, H. Rmili, J.M Floc'h and H. Zangar, «Compact, Mulifunctional Metamaterial-Inspired Monopole Antenna, » *European Conference on Antennas and Propagation, EUCAP*, Prague, Czech Republic, proceeding, pp 1967-1970, Mar.2012.
5. S. Dakhli, J.M Floc'h, H. Rmili, K. Mahdjoubi, and H. Zangar, «A Novel Multifrequency and Low Profile Metamaterial-Inspired Monopole Antennas, » *Meditteranean Microwave Symposium, MMS*, Istanbul, Turkey, Sep.2012.
6. S. Dakhli, K. Mahdjoubi, J.M Floc'h, H. Rmili, and H. Zangar, «Efficient,Metamaterial-Inspired Loop-Monopole Antenna with Shaped Radiation Pattern,» *Loughborough Antenna and Propagation Confrerence, LAPC*, Loughborough, England, proceeding, pp 1-4, Nov 2012.

A Robustness Analysis of the Numerical Computation of Green's Dyadics in Bianisotropic Media

Ignace Bogaert

Department of Information Technology (INTEC),
Ghent University, Ghent, Belgium
E-mail: Ignace.Bogaert@intec.UGent.be

Abstract

The robustness of a previously developed numerical algorithm for the computation of the four Green's dyadics in homogeneous bianisotropic materials is theoretically analyzed. The lossy bianisotropic materials are identified as a class of materials for which the numerical computation is provably robust. This is of great importance for applications in boundary integral equations because the vast majority of bianisotropic materials are lossy at nonzero frequencies.

1. Introduction

In the past, boundary integral equations (BIEs) for scatterers consisting of isotropic materials have received considerable research attention. For example, fast methods were invented to multiply the associated method of moment (MoM) matrix with an arbitrary vector, enabling iterative solvers with an $\mathcal{O}(N)$ or $\mathcal{O}(N \log N)$ complexity per iteration [1–3]. In addition, efficient physics-based preconditioners were constructed to lower the number of iterations in such solvers [4]. This has resulted in BIEs becoming a mature technology that allows the solution of extremely large scattering problems [5].

Given the success of BIEs for isotropic materials, it is of both theoretical and practical importance to look for ways to extend BIEs to more general materials. In this contribution, the focus will be on the extension to bianisotropic materials. Some work has already been done in this area, for example for a uniaxial material [6]. The constitutive equations of a generic bianisotropic material classical frequency-domain electromagnetics are:

$$\boldsymbol{d}(\boldsymbol{r}) = \bar{\bar{\varepsilon}} \cdot \boldsymbol{e}(\boldsymbol{r}) + \bar{\bar{\xi}} \cdot \boldsymbol{h}(\boldsymbol{r}), \tag{1a}$$

$$\boldsymbol{b}(\boldsymbol{r}) = \bar{\bar{\zeta}} \cdot \boldsymbol{e}(\boldsymbol{r}) + \bar{\bar{\mu}} \cdot \boldsymbol{h}(\boldsymbol{r}). \tag{1b}$$

Here, $\bar{\bar{\varepsilon}}$ is the permittivity tensor and $\bar{\bar{\mu}}$ is the permeability tensor. The tensors $\bar{\bar{\zeta}}$ and $\bar{\bar{\xi}}$ are the magnetoelectric coupling tensors. For isotropic materials, all the material tensors become scalars times the unit tensor $\mathbb{1}$.

To apply BIEs to bianisotropic materials, four Green dyadics are needed. These four Green dyadics correspond to the electric and magnetic fields generated by elementary electric and magnetic currents:

$$\boldsymbol{e}(\boldsymbol{r}) = \bar{\bar{G}}_{ee}(\boldsymbol{r}) \cdot \boldsymbol{j} + \bar{\bar{G}}_{em}(\boldsymbol{r}) \cdot \boldsymbol{m}, \tag{2a}$$

$$\boldsymbol{h}(\boldsymbol{r}) = \bar{\bar{G}}_{me}(\boldsymbol{r}) \cdot \boldsymbol{j} + \bar{\bar{G}}_{mm}(\boldsymbol{r}) \cdot \boldsymbol{m}, \tag{2b}$$

where the vectors $\boldsymbol{j}$ and $\boldsymbol{m}$ are the directions of the elementary dipoles, i.e. the electric and magnetic currents are given by

$$\boldsymbol{j}(\boldsymbol{r}) = \boldsymbol{j}\delta(\boldsymbol{r}), \tag{3a}$$

$$\boldsymbol{m}(\boldsymbol{r}) = \boldsymbol{m}\delta(\boldsymbol{r}). \tag{3b}$$

The availability of the Green dyadics is indispensable for applying BIEs to bianisotropic materials. Indeed, the Green dyadics are required to compute the MoM matrix elements, without which no BIE can be discretized nor solved. Unfortunately, despite fantastic progress over the past decades [7–9], no analytical formulas exist for the Green dyadics of a general bianisotropic material. The absence of such analytical expressions for the Green dyadics poses a serious practical problem and has, in the past, severely hindered the development of boundary integral equations for bianisotropic materials.

To get around this problem, a method was proposed for the all-numerical computation of the bianisotropic scalar Green function (BSGF) and its derivatives [10, 11]. This capability is sufficient for the computation of the Green dyadics because these only depend on the fourth- and lower-order derivatives of the BSGF. The computation method presented in [10, 11] relies on an expansion of the BSGF into Gegenbauer polynomials such as the Legendre or Chebyshev polynomials. These expansions can be made arbitrarily accurate in a finite cubical region and a covering of $\mathbb{R}^3$ with such cubical regions can provide the BSGF everywhere. Such a scheme has the additional advantage that the Gegenbauer expansion serves as a very accurate tabulation of the BSGF, meaning that the BSGF can be precomputed and stored in the form of these Gegenbauer expansions.

In this contribution, it will be rigorously shown that the computation approach proposed in [10, 11] does not fail in a 'hard' way when it is applied to lossy bianisotropic materials. More specifically, no divisions by zero nor infinities are encountered when executing the program. Also, the integrands of numerically evaluated integrals are always exponentially decaying. Of course, this does not exclude the

occurrence of subtle numerical cancelations that can lead to inaccurate results. Neither does it rule out that the method can become slow for certain limiting cases. However, it is still a very strong statement about the robustness of the method, especially when keeping in mind that the class of lossy bianisotropic materials has 72 real free parameters. The paper is laid out as follows: first, a brief overview of the BSGF evaluation method proposed in [10, 11] is given. Then, a number of surprising and general properties of lossy bianisotropic materials are proved. These properties are subsequently used to show that the possible problems the proposed method may suffer from never occur if the bianisotropic material is lossy.

2. Computation of the BSGF

For a detailed derivation of the BSGF, we refer to [10, 11]. However, the definition of the BSGF and its relation to the Green dyadics will be repeated here to fix the notation and make the paper more self-contained. The BSGF is defined as

$$G(\boldsymbol{r}) = \frac{1}{8\pi^3} \int_{\mathbb{R}^3} \frac{e^{j\boldsymbol{s}\cdot\boldsymbol{r}}}{D(\boldsymbol{s})} \mathrm{d}\boldsymbol{s}, \tag{4}$$

with $D(\boldsymbol{s})$ the so-called Helmholtz determinant [12]

$$D(\boldsymbol{s}) = \mathrm{Det}\left[\mathsf{P}(\boldsymbol{s})\right], \tag{5}$$

which is defined by means of the 6×6 matrix

$$\mathsf{P}(\boldsymbol{s}) = \begin{bmatrix} \bar{\bar{\varepsilon}} & \bar{\bar{\xi}} - \boldsymbol{s} \times \mathbb{1} \\ \bar{\bar{\zeta}} + \boldsymbol{s} \times \mathbb{1} & \bar{\bar{\mu}} \end{bmatrix}. \tag{6}$$

The symbol $\mathbb{1}$ denotes the 3×3 unit matrix, such that

$$\boldsymbol{s} \times \mathbb{1} = \begin{bmatrix} 0 & -s_z & s_y \\ s_z & 0 & -s_x \\ -s_y & s_x & 0 \end{bmatrix}. \tag{7}$$

It can be shown that the four Green dyadics, which relate electric and magnetic currents with the electric and magnetic fields they generate, are given by

$$\begin{bmatrix} \bar{\bar{G}}_{ee}(\boldsymbol{r}) & \bar{\bar{G}}_{em}(\boldsymbol{r}) \\ \bar{\bar{G}}_{me}(\boldsymbol{r}) & \bar{\bar{G}}_{mm}(\boldsymbol{r}) \end{bmatrix} = \frac{j\omega^2}{8\pi^3} \int_{\mathbb{R}^3} e^{j\omega\boldsymbol{s}\cdot\boldsymbol{r}} \mathsf{P}^{-1}(\boldsymbol{s}) \, \mathrm{d}\boldsymbol{s}. \tag{8}$$

This can be rewritten as

$$\begin{aligned} \begin{bmatrix} \bar{\bar{G}}_{ee}(\boldsymbol{r}) & \bar{\bar{G}}_{em}(\boldsymbol{r}) \\ \bar{\bar{G}}_{me}(\boldsymbol{r}) & \bar{\bar{G}}_{mm}(\boldsymbol{r}) \end{bmatrix} &= \frac{j\omega^2}{8\pi^3} \mathsf{A}\left(-j/\omega\boldsymbol{\nabla}\right) \int_{\mathbb{R}^3} \frac{e^{j\omega\boldsymbol{s}\cdot\boldsymbol{r}}}{D(\boldsymbol{s})} \mathrm{d}\boldsymbol{s}, \\ &= j\omega^2 \mathsf{A}\left(-j/\omega\boldsymbol{\nabla}\right) G(\omega\boldsymbol{r}). \end{aligned} \tag{9}$$

Here, $\mathsf{A}(\boldsymbol{s})$ is adjugate matrix of $\mathsf{P}(\boldsymbol{s})$:

$$\mathsf{A}(\boldsymbol{s}) = D(\boldsymbol{s})\mathsf{P}^{-1}(\boldsymbol{s}). \tag{10}$$

After some calculations, it can be shown that the 36 components of $\mathsf{A}(\boldsymbol{s})$ are polynomials of degree four in the components of $\boldsymbol{s}$. Therefore, the representation (9) is well-defined and shows that only fourth- and lower-order derivatives of the BSGF are required.

The BSGF can now be expanded in Gegenbauer polynomials [13]:

$$G(\boldsymbol{r} + \boldsymbol{c}) = \sum_{p_x, p_y, p_z = 0}^{\infty} Q_{\boldsymbol{p}} \, C_{p_x}^{\nu}\!\left(\frac{x}{a_x}\right) C_{p_y}^{\nu}\!\left(\frac{y}{a_y}\right) C_{p_z}^{\nu}\!\left(\frac{z}{a_z}\right), \tag{11}$$

for all $\boldsymbol{r}$ in the range $\square_{\boldsymbol{c},\boldsymbol{a}}$. The range $\square_{\boldsymbol{c},\boldsymbol{a}}$ is a cuboidal region centered around $\boldsymbol{c}$ and with sides $2a_x$, $2a_y$ and $2a_z$. The expansion coefficients $Q_{\boldsymbol{p}}$ are computed from definition (4) by using the polynomial's orthogonality with respect to the associated weight function. This allows the usage of some analytical results [11] to obtain

$$Q_{\boldsymbol{p}} = \int_{\mathbb{R}^3} \frac{\mathcal{F}_{\boldsymbol{p}}(\boldsymbol{s})}{D(\boldsymbol{s})} \mathrm{d}\boldsymbol{s}. \tag{12}$$

with only minor restrictions on ν and with the function $\mathcal{F}_{\boldsymbol{p}}(\boldsymbol{s})$ given by

$$\mathcal{F}_{\boldsymbol{p}}(\boldsymbol{s}) = e^{j\boldsymbol{s}\cdot\boldsymbol{c}} F_{p_x}^{\nu}(s_x a_x) F_{p_y}^{\nu}(s_y a_y) F_{p_z}^{\nu}(s_z a_z), \tag{13}$$

$$F_n^{\nu}(u) = i^n (\nu + n) \frac{J_{\nu+n}(u)}{u^{\nu}}. \tag{14}$$

Finally, complex contour integration is used to compute the integrals (12). Indeed, the function $F_n^{\nu}(u)$ is entire, which means that the only complex poles in the integrand are due to zeros in the Helmholtz determinant. Let us write the reciprocal of the Helmholtz determinant as a partial fraction expansion

$$\frac{1}{D(\boldsymbol{s})} = \frac{1}{D_z} \sum_{m=1}^{4} \frac{\alpha_m(s_x, s_y)}{s_z - \eta_m(s_x, s_y)}, \tag{15}$$

where $\eta_m(s_x, s_y)$ is the mth root of the Helmholtz determinant on a line parallel to the z-axis:

$$D([s_x, s_y, \eta_m(s_x, s_y)]) = 0, \tag{16}$$

and

$$D_z = \lim_{s_z \to \infty} \frac{D([0, 0, s_z])}{s_z^4}. \tag{17}$$

Assuming that the range $\square_{\boldsymbol{c},\boldsymbol{a}}$ lies entirely above the xy-plane, this leads to the following result

$$Q_{\boldsymbol{p}} = \frac{2\pi j}{D_z} \int_{\mathbb{R}^2} \sum_{\substack{m=1 \\ \Im\eta_m > 0}}^{4} \alpha_m \mathcal{F}_{\boldsymbol{p}}([s_x, s_y, \eta_m]) \mathrm{d}s_x \mathrm{d}s_y. \tag{18}$$

Here, the dependence of α_m and η_m on s_x and s_y was dropped for brevity. The case in which $\Im\eta_m$ is exactly zero was neglected for reasons that will become apparent in Section 3.

Finally, the integrals (18) are numerically computed using an adaptive numerical integration algorithm. It will be assumed that the adaptive integration routine can robustly integrate functions that do not contain singularities and that

converge to zero in an exponential fashion when moving away from the origin in the s_x, s_y-plane. Therefore, to prove the robustness of the BSGF computation for lossy bianisotropic materials, it needs to be proven that the integrand in (18) satisfies these requirements. This will be done in the next Section.

3. Robustness for Lossy Materials

Lossy bianisotropic materials are defined as satisfying the inequality [14]

$$\Im\left\{\boldsymbol{V}^H \cdot \begin{bmatrix} \bar{\bar{\varepsilon}} & \bar{\bar{\xi}} \\ \bar{\bar{\zeta}} & \bar{\bar{\mu}} \end{bmatrix} \cdot \boldsymbol{V}\right\} < 0, \forall \boldsymbol{V} \in \mathbb{C}^6 \setminus \{\boldsymbol{0}\}. \quad (19)$$

As will be shown, lossy materials exhibit a number of properties that are very useful for the numerical evaluation of (18). First, it will be proved that the Helmholtz determinant cannot have purely real zeros. Secondly, it will be proved that the Helmholtz determinant always has four complex zeros on an arbitrary line in $\boldsymbol{s}$ space, exactly two of which have positive imaginary part. Lastly, the repercussions of these results on the computation of (18) are discussed.

3.1. No Real Zeros

One of the most basic properties of the Helmholtz determinant of a lossy bianisotropic material is the fact that it does not allow real zeros $\boldsymbol{s} \in \mathbb{R}^3$. Indeed, if such a root $\boldsymbol{s}_0$ would exist, then this would mean that there exist a nonzero complex vector $\boldsymbol{V}_0$ such that

$$\mathsf{P}(\boldsymbol{s}_0) \cdot \boldsymbol{V}_0 = 0. \quad (20)$$

This in turn implies that

$$\boldsymbol{V}_0^H \cdot \mathsf{P}(\boldsymbol{s}_0) \cdot \boldsymbol{V}_0 = \boldsymbol{V}_0^H \cdot \begin{bmatrix} \bar{\bar{\varepsilon}} & \bar{\bar{\xi}} \\ \bar{\bar{\zeta}} & \bar{\bar{\mu}} \end{bmatrix} \cdot \boldsymbol{V}_0 = 0, \quad (21)$$

which contradicts criterium (19).

3.2. Always Four Roots

In a similar way, it can be proved that the Helmholtz determinant of a lossy material, restricted to a line in $\boldsymbol{s}$-space, always admits four complex zeros. Mathematically, this means that the equation

$$D(\boldsymbol{s}_1 + \eta \boldsymbol{s}_2) = 0, \boldsymbol{s}_1 \in \mathbb{R}^3, \boldsymbol{s}_2 \in \mathbb{R}^3, \quad (22)$$

always has four solutions for η. To prove this, a necessary and sufficient condition is that the coefficient of η^4 in this polynomial is nonzero. This coefficient can be shown to be

$$\begin{aligned} \lim_{\eta\to\infty} \frac{D(\boldsymbol{s}_1 + \eta \boldsymbol{s}_2)}{\eta^4} &= D_4(\boldsymbol{s}_2), \\ &= (\boldsymbol{s}_2 \cdot \bar{\bar{\varepsilon}} \cdot \boldsymbol{s}_2)\,(\boldsymbol{s}_2 \cdot \bar{\bar{\mu}} \cdot \boldsymbol{s}_2) \\ &\quad - \left(\boldsymbol{s}_2 \cdot \bar{\bar{\zeta}} \cdot \boldsymbol{s}_2\right)\left(\boldsymbol{s}_2 \cdot \bar{\bar{\xi}} \cdot \boldsymbol{s}_2\right), \end{aligned} \quad (23)$$

where $D_4(\boldsymbol{s})$ is the fourth-degree part of the Helmholtz determinant. Now, if this polynomial coefficient could become zero, this would imply the existence of a complex vector $\boldsymbol{V}_1$ of the form

$$\boldsymbol{V}_1 = \begin{bmatrix} a\boldsymbol{s}_2 \\ b\boldsymbol{s}_2 \end{bmatrix}, \quad (24)$$

such that

$$\boldsymbol{V}_1^H \cdot \begin{bmatrix} \bar{\bar{\varepsilon}} & \bar{\bar{\xi}} \\ \bar{\bar{\zeta}} & \bar{\bar{\mu}} \end{bmatrix} \cdot \boldsymbol{V}_1 = 0. \quad (25)$$

Again, this contradicts criterium (19).

Surprisingly, this result can be used to prove that there are exactly two zeros with positive imaginary part and two zeros with negative imaginary part. To start, it is easily verified that this property holds for any lossy *isotropic* material. Furthermore, it is always possible to continuously perturb the isotropic material into an arbitrary lossy bianisotropic material, whilst keeping the perturbed material lossy. Now invoke the fact that the zeros of a polynomial vary continuously as a function of the polynomial coefficients as long as the highest-degree coefficient remains bounded away from zero, and the fact that the imaginary part of the zeros cannot become zero (otherwise there would exist a real zero). It can then be concluded that the two zeros of the isotropic material's Helmholtz determinant with positive imaginary part are continuously perturbed into two zeros, also with positive imaginary part, for any lossy bianisotropic material. A similar reasoning can be made for the two zeros with negative imaginary part.

3.3. Consequences for the BSGF Computation

The results from Subsections 3.1 and 3.2 can be used to address concerns about the evaluation of the integrals (18). For example, the test whether $\Im\eta_m > 0$ becomes numerically very robust due to the knowledge that there will never be a purely real η_m. Also, the division by D_z is never a problem because the right hand side of (23) never becomes zero.

Other possible sources of problems are the partial fraction coefficients α_m, which can become infinite when the two zeros with positive imaginary part coincide. However, through careful implementation of the summation, and because the two zeros with negative imaginary part cannot coincide with the other zeros, this singularity can be removed. Therefore, it can be concluded that the integrand of (18) does not contain singularities.

Finally, it remains to be shown that the integrand converges to zero exponentially fast. To this end, the behavior of η_m for large s_x and s_y must be investigated. Therefore, consider equation (16) with $s_x = q\cos\phi$ and $s_y = q\sin\phi$ and q a large real number:

$$D([q\cos\phi, q\sin\phi, \eta_m(q\cos\phi, q\sin\phi)]) = 0. \quad (26)$$

After dividing by q^4 and taking the limit, the following is

obtained

$$D_4([\cos\phi, \sin\phi, \lim_{q\to\infty} \frac{1}{q}\eta_m(q\cos\phi, q\sin\phi)]) = 0. \quad (27)$$

This means that

$$\eta_m(q\cos\phi, q\sin\phi) \to q\psi_m(\phi), \quad (28)$$

for large q, where $\psi_m(\phi)$ is the solution to

$$D_4([\cos\phi, \sin\phi, \psi_m(\phi)]) = 0. \quad (29)$$

Again, two of the four $\psi_m(\phi)$ have a positive imaginary part. Due to the factor $e^{j\boldsymbol{s}\cdot\boldsymbol{c}}$ in the integrand of (18), this implies an exponential convergence to zero as $s_x^2 + s_y^2 \to \infty$.

4. Conclusion

The numerical computation of the BSGF and its derivatives by means of the method proposed in [10, 11] has been proved to be robust against 'hard' breakdowns for all lossy bianisotropic materials. Since all passive bianisotropic materials exhibit at least some loss at nonzero frequencies, this shows that this numerical computation strategy has wide applicability, e.g. for modeling circulators or other microwave components.

Acknowledgement

The work of Ignace Bogaert is supported by a postdoctoral grant from the Fund for Scientific Research Flanders (FWO-Vlaanderen).

References

[1] L. Greengard and V. Rokhlin, "A fast algorithm for particle simulations," *Journal of Computational Physics*, vol. 73, no. 2, pp. 325–348, Dec. 1987.

[2] W.C. Chew, J. Jin, E. Michielssen, and J. Song, *Fast and Efficient Algorithms in Computational Electromagnetics*. Artech House, 2001.

[3] I. Bogaert, J. Peeters, and F. Olyslager, "A nondirective plane wave MLFMA stable at low frequencies," *IEEE Transactions on Antennas and Propagation*, vol. 56, no. 12, pp. 3752–3767, December 2008.

[4] F. Andriulli, K. Cools, H. Bagci, F. Olyslager, A. Buffa, S. Christiansen, and E. Michielssen, "A multiplicative calderon preconditioner for the electric field integral equation," *IEEE Transactions on Antennas and Propagation*, vol. 56, no. 8, pp. 2398–2412, 2008.

[5] J. Song, C.C. Lu, and W.C. Chew, "Multilevel fast multipole algorithm for electromagnetic scattering by large complex objects," *IEEE Transactions on Antennas and Propagation*, vol. 45, no. 10, pp. 1488–1493, Oct. 1997.

[6] G. Mumcu, K. Sertel, and J. Volakis, "Surface integral equation solutions for modeling 3-d uniaxial media using closed-form dyadic green's functions," *Antennas and Propagation, IEEE Transactions on*, vol. 56, no. 8, pp. 2381 –2388, aug. 2008.

[7] F. Olyslager and I. V. Lindell, "A pedigree of bianisotropic media." in *Proceedings of the 8th International Conference on Electromagnetics of Complex Media (Bianisotropics 2000), 27-29 September 2000, Lisbon, Portugal*, 2000, pp. 153–158.

[8] F. Olyslager and I. Lindell, "Electromagnetics and exotic media: a quest for the holy grail," *Antennas and Propagation Magazine, IEEE*, vol. 44, no. 2, pp. 48 –58, apr 2002.

[9] I. Lindell and F. Olyslager, "Generalized decomposition of electromagnetic fields in bi-anisotropic media," *Antennas and Propagation, IEEE Transactions on*, vol. 46, no. 10, pp. 1584 –1585, oct 1998.

[10] I. Bogaert, "Accurate Computation and Tabulation of the Scalar Green Function for'Bi-anisotropic Media and its Derivatives," in *Proceedings of the conference of the Applied Computational Electromagnetics Society*, Columbus, Ohio, USA, 10-14 April 2012.

[11] ——, "Computing Green's Functions for Bianisotropic Materials," in *Proceedings of the International Conference on Electromagnetics in Advanced Applications*, Cape Town, South Africa, 2–7 September 2012.

[12] B. Jakoby and F. Olyslager, "Asymptotic expansions for greens dyadics in bianisotropic media," *Progress on Electromagnetics Research*, vol. 12, pp. 277–302, 1996.

[13] F. W. J. Olver, D. W. Lozier, R. F. Boisvert, and C. C. W., *NIST Handbook of Mathematical Functions*. Cambridge University Press, 2010.

[14] I. V. Lindell and F. M. Dahl, "Conditions for the parameter dyadics of lossy bianisotropic media," *Microwave and Optical Technology Letters*, vol. 29, no. 3, pp. 175–178, May 2001.

Multifrequency and Low Profile Metamaterial-Inspired Antennas

S. DAKHLI[1, 2], J. M. FLOC'H[3], F. CHOUBANI[1] and K. MAHDJOUBI[2] and H. RMILI[4*],

[1]Innov'Com Laboratory, SUPCOM,University of Carthage, Tunis, Tunisia.

[2]IETR, University of Rennes 1, #263, Av. Général Leclerc, CS 74205, 35042 Rennes Cedex, France.

[3]IETR, INSA, #20 avenue buttes des coësmes, 35043 Rennes Cedex, France.

[4]King Abdulaziz University, Electrical and Computer Engineering Department, Jeddah, Saudi Arabia.

[*]Hatem RMILI: hmrmili@kau.edu.sa

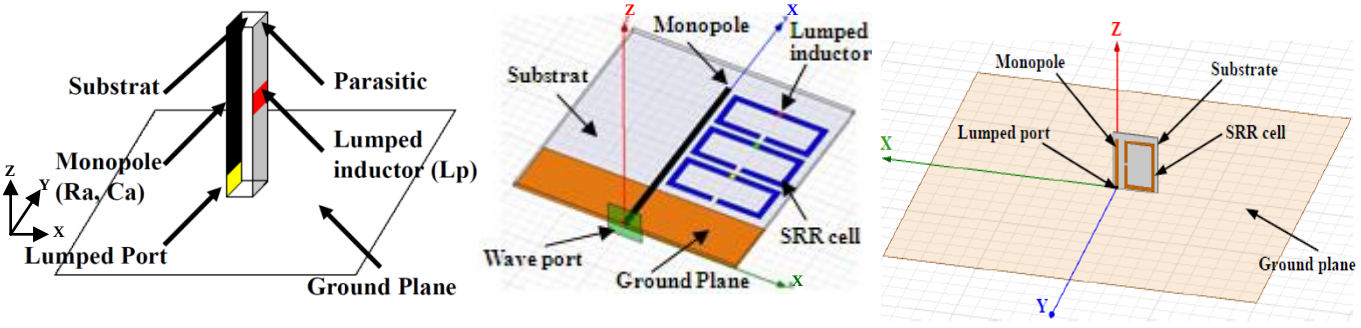
Abstract-In this paper several low profile and multifrquency metamaterial inspired antennas are designed. All these antennas are based on the electric coupling between the parasitic element and the driven monopole element. The simulated and measured results of the return loss, efficiency and radiation patterns are reported.

1. Introduction

The rapid progress of wireless devices for communication has increased the requirement of efficient, low profile, light weight and low cost electrically small antennas (ESAs). A variety of antennas has been engineered with metamaterials and metamaterial-inspired constructs in order to improve their performances in terms of bandwidth [1] and efficiency [2] as well as to achieve novel functions [3-4]. In this work, we use new type of parasitic elements with different shapes in order to obtain a multifrequency behavior. This technique leads to new resonance frequencies lower than that of the exciting monopole. Three families of antennas are studied: each one is composed of a monopole antenna and some parasitic elements.

2. Antennas Design and Fabrication

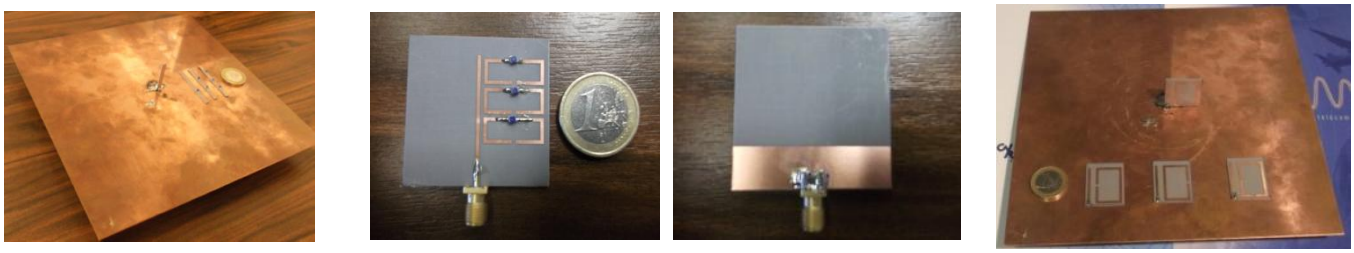
Figure.1 presents the structures of the proposed antennas A1, A2 and A3. For the three structures, we have used a Rogers Duroid TM 5880 substrate of thickness 0.8mm and relative permittivity ε_r = 2.2, and a monopole antenna of 25mm long 1.5mm wide, having a resonance frequency of 2.45GHz and a bandwidth of 400MHz. In simulation, the A1 and A3 antennas are excited by a lumped port of 50Ω input impedance while the A2 antenna is excited by a wave port of 50Ω input impedance. The antennas are simulated by ANSYS-HFSS software.



Antenna A1 [4] Antenna A2 [5] Antenna A3 [6]

Figure 1. The structures of the three proposed antennas.

The prototypes are simulated, optimized, realized and finally characterized. Fig. 2 presents photos of the realized prototypes.



Antenna A1 Antenna A2: Top View ; Bottom View Antenna A3

Figure 2. Photos of the realized prototypes.

3. Equivalent Circuit Model

An equivalent circuit model (Fig.3) is proposed in order to describe the operation of the antenna system.

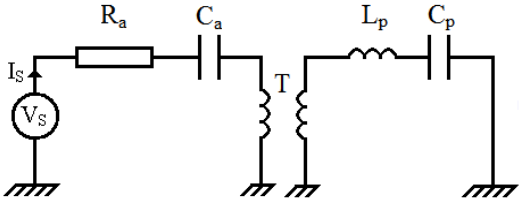


Figure.3. Equivalent circuit model of the antenna system.

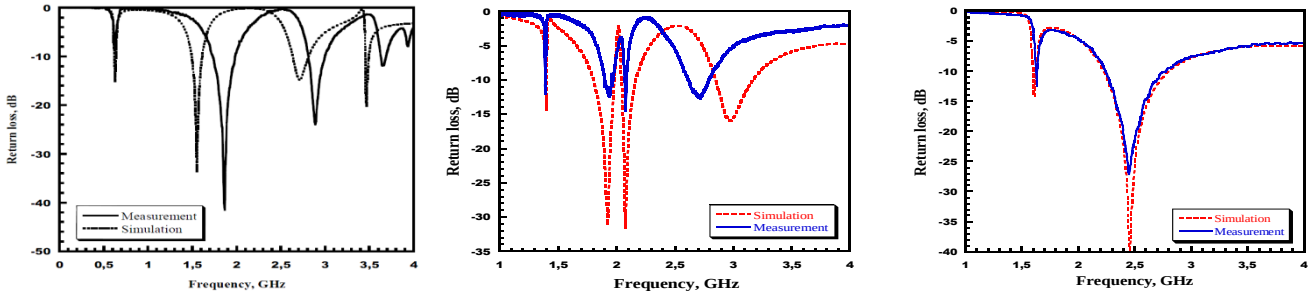
To a lower frequency, the monopole and the coupling elements are electrically small. The monopole acts as a RC circuit (R_a,C_a). Whereas the parasitic element acts like a LC circuit (L_p,C_p).The coupling between the two elements is ensured by a transformer T. The resonant frequency of the circuit model is approximately [3]:

$$f_{res} = \frac{1}{2\pi}\sqrt{\frac{C_a+C_p}{L_p.(C_a.C_p)}} \quad (1)$$

4. Results

a. Return Loss

Figure.4 illustrates the measured and simulated return loss for the different antennas.



Antenna A1 Antenna A2 Antenna A3

Figure 4. Measured and Simulated Return loss for the three prototypes.

According to Fig.4, the addition of the parasitic elements generates a new resonance frequency lower than that of the exciting monopole. We can notice a good agreement between numerical and experimental results.

Table I summarizes simulated and measured resonant frequencies for the proposed antennas, deduced from Fig. 4.

TABLE I: SIMULATED AND MEASURED RESONANCE FREQUENCIES FOR THE FOUR PROPOSED ANTENNAS

	Simulated resonant frequencies (GHz)				**Measured resonant frequencies (GHz)**			
Antenna	F_0	F_1	F_2	F_3	F_0	F_1	F_2	F_3
A1	0.63	1.56	2.7	3.48	0.63	1.86	2.89	3.64
A2	1.438	1.858	1.991	2.881	1.397	1.931	2.082	2.692
A3	1.606	2.455	-	-	1.635	2.445	-	-

b. Efficiency and Radiation Pattern

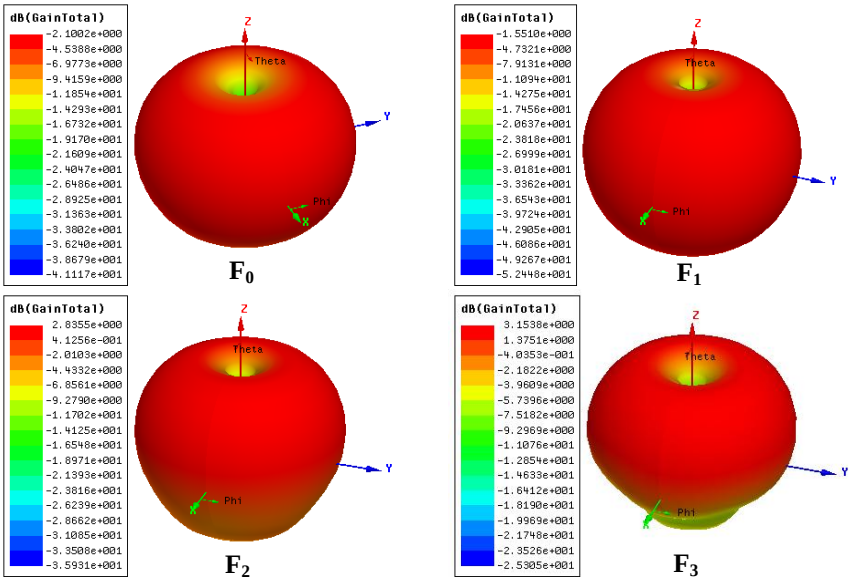
Table I collects the simulated and measured overall efficiency (OE) of the four proposed antennas at the lower and the higher resonant frequencies. OE is the ratio of the radiated power P_{rad} to the input power P_{in}, as given by the following expression [3]:

$$OE = \frac{P_{rad}}{P_{in}} \tag{2}$$

TABLE II: SIMULATED AND MEASURED OVERALL EFFICENCY (OE) FOR THE FOUR PROPOSED ANTENNAS

	Simulated Overall Efficiency (OE %)	**Measured Overall Efficiency (OE %)**
Antenna	F_0	F_0
A1	82.4	71.5
A2	42.5	35.6
A3	96.2	82.3

According to Table II, a high overall efficiency (OE) is obtained for A1 and A3 antennas at the lower frequencies. The overall efficiency is 96% at F_0 = 631MHz, and 82% at F_0 =1.606GHz For antennas A1 and A3, respectively, whereas A2 antenna presents, at the lower frequencies, a lower efficiency than those of antennas A1 and A3 due to its reduced ground plane. Fig.5 presents simulated 3D radiation patterns of the proposed antennas at their resonance frequencies.



Antenna A1

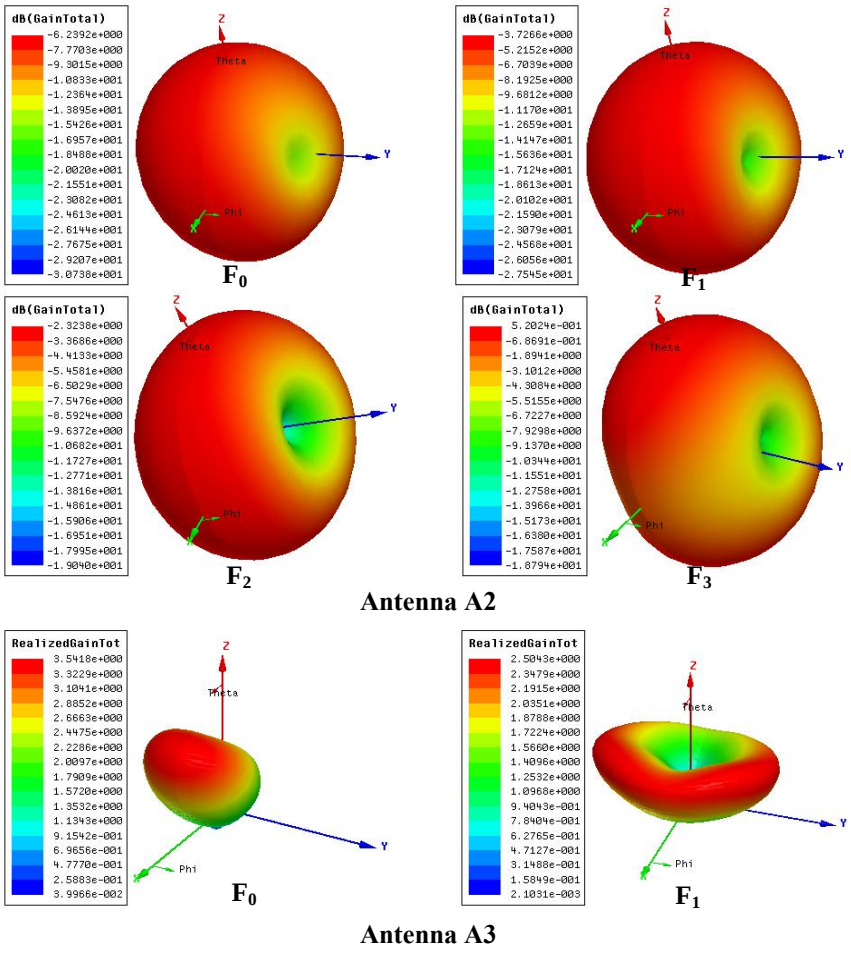


Figure 5. Simulated 3D Radiation Patterns for the studied antennas.

We can deduce from Fig. 5 that all the studied structures are characterized by a monopole-like radiation pattern behave except the case of Antenna A3when we can notice an unusually directive beam at the lower frequency F_0.

5. Conclusion

A family of low profile and multifrequency metamaterial inspired antennas is reported. We have used different shapes of parasitic elements to reduce the size of the monopole antenna and/or to create multiband behavior. Both simulated and measured results of the impedance matching, overall efficiency and radiation patterns are satisfying, and the obtained structure are suitable for wireless communication systems.

REFERENCES

1. P. Jin and R.W. Ziolkowski, «Broadband, Efficient, Electrically Small Metamaterial-Inspired Antennas Faciltated by Active Near Field Resonant Parasitic Elements, » *IEEE Trans. Antennas Propag.*, vol. 58, pp 318-327, Feb. 2010.
2. A. Erentok and R.W. Ziolkowski, "Metamaterial-Inspired Efficient Electrically Small Antennas," IEEE Trans. Antennas Propag, vol. 56, pp. 691-707, Mar. 2008.
3. R.W.Ziolkowski, Efficient Electrically Small Antenna Facilitated by a Near-Field Resonant Parasitic," Antenna and Wireless Propagation Letters IEEE, vol. 7, pp. 581 – 584, Sep. 2008.

4. S. Dakhli, K. Mahdjoubi, H. Rmili, J.M Floc'h and H. Zangar, «Compact, Mulifunctional Metamaterial-Inspired Monopole Antenna, » *European Conference on Antennas and Propagation, EUCAP*, Prague, Czech Republic, proceeding, pp 1967-1970, Mar.2012.
5. S. Dakhli, J.M Floc'h, H. Rmili, K. Mahdjoubi, and H. Zangar, «A Novel Multifrequency and Low Profile Metamaterial-Inspired Monopole Antennas, » *Meditteranean Microwave Symposium, MMS*, Istanbul, Turkey, Sep.2012.
6. S. Dakhli, K. Mahdjoubi, J.M Floc'h, H. Rmili, and H. Zangar, «Efficient,Metamaterial-Inspired Loop-Monopole Antenna with Shaped Radiation Pattern,» *Loughborough Antenna and Propagation Confrerence, LAPC*, Loughborough, England, proceeding, pp 1-4, Nov 2012.

Antennas on Quasi Synthetic Media

Chinwe C. Njoku[1], William G. Whittow[1], (J) Yiannis C. Vardaxoglou[1*]

[1]School of Electronic, Electrical & Systems Engineering, Loughborough University, Loughborough, LE11 3TU, UK
* E-mail: J.C.Vardaxoglou@lboro.ac.uk

Abstract

This paper examines the differences and/or similarities between some of the commonly used canonical equations describing the effective permittivity and permeability of heterogeneous substrates with dielectric or metallic inclusions, at microwave frequencies. Graphical results are presented for the different structures considered. Simulated results from heterogeneous mixtures with both dielectric and metallic inclusions are presented, and compared with results from the canonical equation representation. Simulated results of a patch antenna on a heterogeneous medium and on its homogenous equivalent have also been presented.

1. Introduction

The overall goal of this research is to one day, be able to apply nanomaterial fabrication techniques to the production of microwave antenna systems, such that these systems are made in one process. As such, an important aspect is to understand the electromagnetic (EM) properties of heterogeneous structures which are structures consisting of small-scale inclusions in a homogenous host. Heterogeneous structures have been of interest to engineers and physicists alike as they provide additional degrees of freedom when designing various electromagnetic structures. These heterogeneous structures can be applied to the design of microwave antennas to control the dielectric and possibly the magnetic properties, thus allowing the creation of novel substrates with pre-determined characteristics. EM advantages related to bandwidth, efficiency and size may be achieved as a by-product of being able to control the material's EM properties. In previous work, it has been shown that a larger bandwidth can be achieved with an as yet unrealizable substrate with equal permittivity and permeability [1]. In addition, using textured dielectrics in which the permittivity of the substrate is mapped to the electric field intensity, such as with a patch antenna, has been shown to improve antenna performance [2–5]. Fig. 1 shows an example of how these inclusions can be smoothly varied in a substrate to dictate the local effective permittivity.

Lord Rayleigh in [6] was the first reported person to examine these structures in the mid-19th century but more commonly used is the paper by Lewin in [7]. Since his analysis in 1946, extensions, modifications and alternatives to his equations for the effective permittivity, ε_{eff} and effective permeability, μ_{eff} of a semi-infinite heterogeneous structure with spherical inclusions have been published [8–13]. An initial analysis carried out by the authors in [14] in which these different canonical equations for the ε_{eff} and μ_{eff} are listed and briefly explained, is being extended in this paper. These equations are compared and analysed in further detail here.

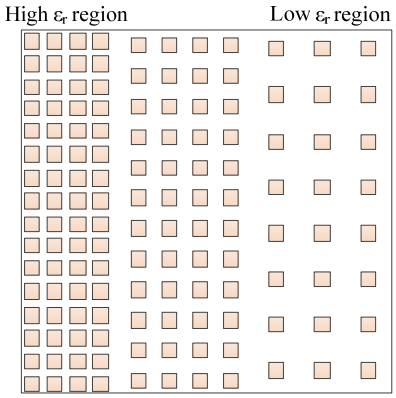


Figure 1: A sketch showing how the permittivity can be varied within the substrate by changing the spacing of the inclusions (not to scale)

Section 2 highlights the differences and similarities between the different effective medium theories in order to determine which of these theories are robust enough to cover the structures investigated in this research, and which ones were not suitable. Mathematical manipulations and application of assumptions/conditions such as using metallic inclusions and using uniform inclusion spacing in all three axes, were carried out on some of the equations to show their similarities. Section 3 presents some graphical results using these equations while Section 4 investigates a heterogeneous structure with both dielectric and metallic inclusions and presents simulated results of different configurations. The complete simulation and inversion process of the scattering (S-) parameters has been described in detail and used in [15], [16]. A patch antenna on a heterogeneous substrate with dielectric cubic inclusions and on the homogenous equivalent substrate, have been simulated and the return loss values presented in Section 5. Finally, conclusions are given in Section 6. The values of ε and μ given here are absolute values (except otherwise stated) and relative to those of free space, ε_o and μ_o.

2. Comparative Analysis

2.1. Mathematical Comparisons

By assuming conducting spheres in a cubic array and using algebraic manipulations, it is shown below that the equations from [7] and [10] for the ε_{eff} and μ_{eff} of these heterogeneous structures are similar to each other. These equations are given respectively in equations (1) and (2).

$$\varepsilon_{eff} = \varepsilon_1\left(1 + 3p/\left(\frac{\varepsilon_p+2\varepsilon_1}{\varepsilon_p-\varepsilon_1} - p\right)\right);$$
$$\mu_{eff} = \mu_1\left(1 + 3p/\left(\frac{\mu_p+2\mu_1}{\mu_p-\mu_1} - p\right)\right) \quad (1)$$

where (ε_1, μ_1) are the ε and μ of the host medium; $p = \frac{4}{3}\pi a^3/s^3$ is the inclusions' volume ratio; (a, s) are the radius and centre-to-centre spacing of the inclusions; (ε_p, μ_p) are the effective ε and μ of the inclusions, given by:

$$\frac{\varepsilon_p}{\varepsilon_2} = \frac{\mu_p}{\mu_2} = \frac{2(sin\theta - \theta cos\theta)}{(\theta^2-1)sin\theta + \theta cos\theta} = F(\theta) \quad (1b)$$

where the constant, $\theta = ka\sqrt{\mu_2\varepsilon_2}$; $k = 2\pi/\lambda$ and $\lambda =$ operating wavelength; (ε_2, μ_2) are the bulk ε and μ of the inclusion material.

$$\varepsilon_{eff} = 1 + \frac{N\alpha_1}{1-\alpha_1 C} \qquad \mu_{eff} = 1 + \frac{N\beta_1}{1-\beta_1 C} \quad (2)$$

where α_1, β_1 are the inclusion's electric and magnetic polarisabilities, N is the density of the inclusions and C is the interaction constant.

The electric and magnetic polarisabilities for spherical inclusions are given by: $\alpha_1 = 4\pi a^3$ and $\beta_1 = -2\pi a^3$ [10] respectively. Assuming uniform spacing, s in the x, y, and z directions,

$$C = \frac{1}{\pi s^3}[1.202 - 16\pi^2 K_0(2\pi)] \quad (2a)$$

where $K_0(\cdot)$ is the modified Bessel function of the second kind and reduces to $C = 1.06/\pi s^3$ using the approximation for the Bessel function for large variables. Substituting this into equation (2) gives,

$$\varepsilon_{eff} = \frac{1+8.33a^3/s^3}{1-4.24a^3/s^3} \qquad \mu_{eff} = \frac{1-4.16a^3/s^3}{1+2.12a^3/s^3} \quad (3)$$

As discussed in [7], for metal particles, ε_p is much greater than ε_1. Thus the expression for permittivity in equation (1) reduces to

$$\varepsilon_{eff} = \varepsilon_1[1 + 3p/(1-p)] \quad (4a)$$

Substituting the expression for $p = 4\pi a^3/s^3$ reduces the expression in the square brackets above to $\frac{1+8.38a^3/s^3}{1-4.19a^3/s^3}$, which is very similar (± 0.05 difference in the multipliers of a^3/s^3) to the expression for ε_{eff} in equation (3). Since a "lightweight binder" like Polyfoam which has a dielectric constant of 1.05 [17] is used in the analysis in [10], ε_1 can be approximated to ε_0.

Also, using the approximation for μ_{eff}, if the particles are non-magnetic such that $\mu_p \to 0$, the expression for permeability in equation (2) is reduced to

$$\mu_{eff} = \mu_1(1 - 3p/2 + p) \quad (4b)$$

Substituting for p, reduces the expression in the bracket above to $\frac{1-4.19a^3/s^3}{1+2.09a^3/s^3}$, which is again similar to (3). Since the binder material is non-magnetic, $\mu_1 \approx \mu_0$.

From the foregoing calculations, the expressions for the ε_{eff} and μ_{eff} of a dielectric host containing spherical particles, obtained in [7] and [10] are almost the same assuming: uniform simple cubic spacing, non-magnetic spherical conducting inclusions and a host permittivity close to that of air, $\varepsilon_0 = 1$.

Furthermore, the expressions for the effective parameters by Collin [10] as shown in equation (2) are similar to those of Cai et al [8] as shown in equation (5).

$$\varepsilon_{eff} = 1 + \frac{N\alpha_1}{1-N\alpha_1/3} \qquad \mu_{eff} = 1 + \frac{N\beta_1}{1-N\beta_1/3} \quad (5)$$

In [10], the interaction constant for equally-spaced spheres was obtained as $C = 1.06/\pi s^3$. In this case, $N = s^{-3}$, and therefore $C = N \times 1.06/\pi$. Since $\frac{1.06}{\pi} \cong 1/3$, substituting in equation (2) yields $\varepsilon_{eff} = 1 + \frac{N\alpha_1}{1-N\alpha_1/3}$, which is the same as Cai's equation in [8]. The equations in [10] also suggest that they can be applied to mixtures with non-uniform spacings along the x, y and z axes.

Although [8–10], [12] have used polarisabilities in their determination of effective constitutive parameters, they have represented these expressions differently. As an example, the expression for polarisability in equation (4) [8] and that in [12] yield very similar graphs as shown in Fig. 2 when used to plot the ε_{eff} against frequency, even though they are mathematically not exactly equal. In addition, although there is a '4π' product difference in their equations for the effective properties appearing in the numerator and denominator as in [12], the 4π's cancel each other out. Another disparity is in the expressions for polarisability in [8] and [12] which is due to the presence of the host medium's refractive index value in the expression in [12].

2.2. General Comparisons

The limit of the validity of formulas is that the spherical particles should not be densely packed. This is similar to that in [10] whose validity is based on the relationship between the obstacles' dimension and their spacing. Notable is the difference in the representation of the *Clausius-Mossotti* equation by Sihvola [9] from that used in equation (5) by Cai et al [8], by the presence of the 'ε_1' term in the denominator. This is because equation (5) by Cai et al from [8] takes into account the EM properties of the inclusions but not that of the host or assumes the host has EM properties close to that of free space.

The difference between the *Maxwell-Garnett* equation and Lewin's formula from [7] is that while Lewin makes the particles exhibit an effective ε and μ due to their small size, *Maxwell-Garnett* assumes that the smaller size particles have the same EM properties as when in their bulk forms. As the value of θ (see equation (1b)) changes from being very small to being large and complex as the size-to-wavelength ratio increases, this variation in permittivity

decreases. The value of the expression for θ in [7], [13], [18] differs with the size parameter, x $(= ka\sqrt{\varepsilon_1\mu_1})$ in [8], [12], in that the effect of ε_2 and μ_2 are not accounted for. $\sqrt{\varepsilon_2\mu_2}$ in the expression for θ is equal to the refractive index of the material of the particle, say n_2, while x uses the refractive index of the host medium, n_0.

Kolmakov et al in [13] adopts the formula by Sihvola in [9] for mixtures with more than one size of spherical inclusions to write an expression for ε_{eff} and μ_{eff} of a heterogeneous medium with a single-size sphere but having two different frequency-dependent polarisabilities. It takes into account the fact that the radii, the polarisabilities, the volume fractions and volume densities of the spheres will vary in magnetic and electric resonance modes. This is the primary difference from Lewin's study in [7] where these variations are not taken into account. The spheres have different radii and were arranged accordingly. In their study the particle spacing was also taken to be much smaller than the wavelength – in line with the conditions for formulae validity in [7]. Numerical simulations were carried out on dielectric spherical and cylindrical particle arrays and it was found out that when the inclusions' spacing was close to a wavelength, or even approximately half of the wavelength, the effective medium approach is not best suited for such mixtures [13]. This is because "the particle interferes with the normal behaviour" of the host in [7].

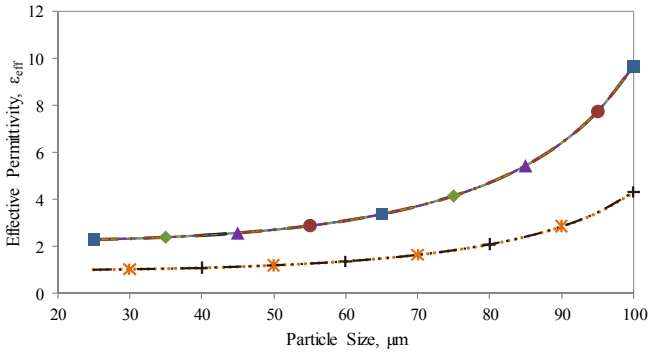
Other minor differences are that: the difference in the formulas for effective constitutive parameters in [7], [10] and [11] can be attributed to the product term difference of ε_o in their expressions for dipole moment, $\overline{\boldsymbol{p}}$.

3. Graphical Results

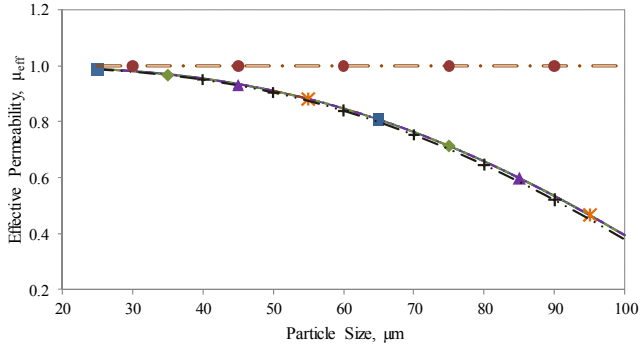
In order to further highlight the similarities and differences between these equations, a variation of the ε_{eff} and μ_{eff} with particle size are given in Fig. 2. Data used: frequency, $f =$ 3 GHz, spacing, $s =$ 200 µm, inclusion radius, $a =$ 1-100 µm, the dielectric host medium, $\varepsilon_1 =$ 2.25 (tan $\delta =$ 0.001). The inclusions are made of Copper ($\sigma = 5.8 \times 10^7$S/m); the relative permittivity of Copper was obtained as $\varepsilon_2 = (1.2 - j103.5) \times 10^6$, from first principles using the Drude model [19], $\mu_1 = \mu_2 = 1$.

The results from [8] and [10] agree with each other but do not agree with those from [7], [9], [12], [13] as [8] and [10] do not include the value of the host permittivity, ε_1 in their equations and so will only agree with the others when the host permittivity, $\varepsilon_1 \cong 1$. Even though $\mu_1 = \mu_2 = 1$, μ_{eff} reduces with increase in the inclusions' volume fraction because the inclusions are metallic and may create diamagnetism with the medium when illuminated by an external magnetic field. This diamagnetic effect has been reported in previous work [20]. But due to the denominator term, $\mu_2 - \mu_1$ being equal to 0 in [9], this results in its $\mu_{eff} = 1$.

Formulations from [9], [10] do not have frequency terms, therefore only equations from [7], [8], [12], [13] are used to understand the effect of variation of the operating frequency with the EM properties of the heterogeneous mixture as shown in Fig. 3. Here, it is assumed that the permittivities of the host and the inclusions are constant with frequency. Data used: 1-30 GHz; $a =$ 100 µm, $s =$ 220 µm, $\mu_1 = \mu_2 = 1$, $\varepsilon_1 =$ 2.25 (tan $\delta =$ 0.001) and $\varepsilon_2 = (1.2 - j103.5) \times 10^6$.



(a)



(b)

Figure 2: Variation of (a) ε_{eff} and (b) μ_{eff} with spherical inclusion size, a, from [7] (—■—), [8] (—•ж•—), [9] (═•═•●•═•═), [10] (—••+••—), [12] (— —◆— —) and [13] (▪▪▲▪▪).

As shown in Fig. 3, ε_{eff} from [8] differs significantly from the others because $\varepsilon_1 > 1$ which is not included in its equation for ε_{eff}. The other results agree over the frequency range considered. For the case of μ_{eff}, all the results from the equations agree with each other. As the frequency increases an initial reduction in the μ_{eff} from 1 is seen, and then μ_{eff} remains nearly constant at approximately 0.5. This may be due to the rather high value of ε_2 for metallic inclusions.

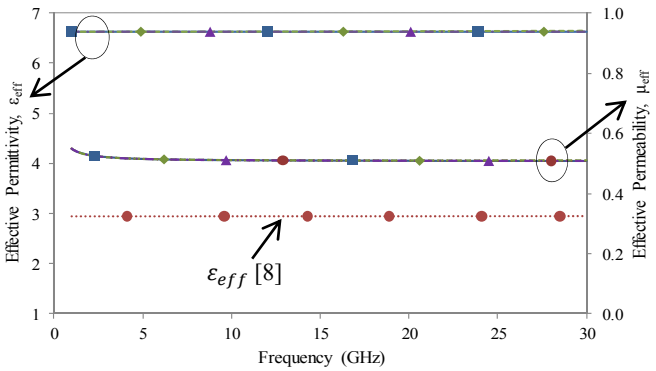
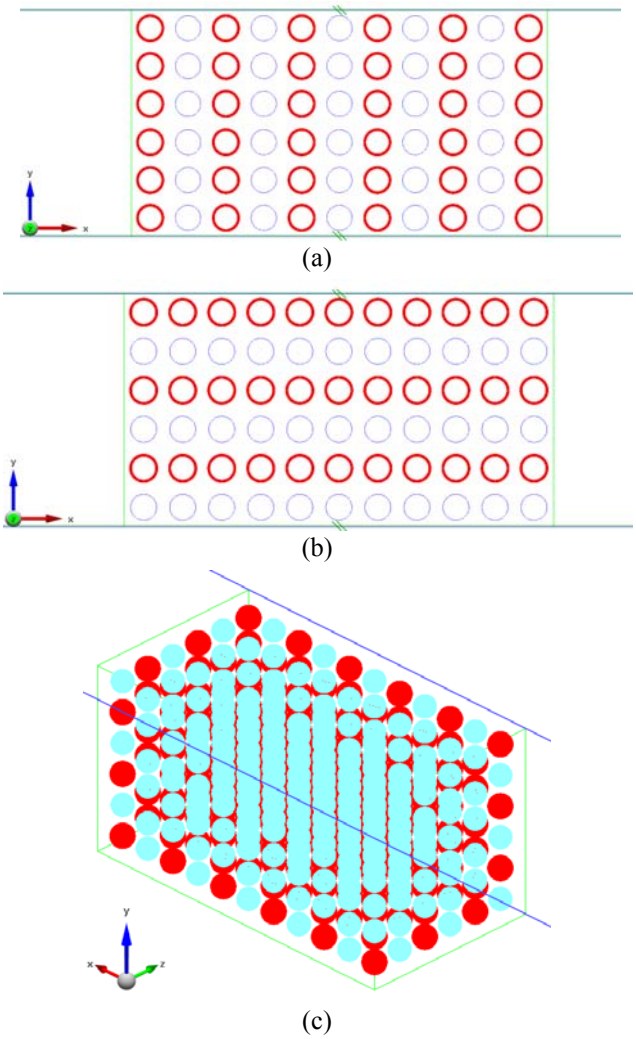


Figure 3: Variation of ε_{eff} and μ_{eff} with frequency from [7] (—■—), [8] (▪▪●▪▪), [12] (--◆--) and [13] (—•▲•—).

4. Mixed Inclusions

More advanced studies are carried out in [9], [21] for mixtures that include two or more homogenous material particles of equal or different sizes. This can also allow the creation of anisotropic materials. Here, the effective permittivity is a function of summation terms where the volume fractions of each included material and their respective permittivities are examined separately. The different arrangements of these structures examined in this section are shown in Fig. 4. In this section, analytical results are compared with FDTD simulations in conjunction with a retrieval algorithm for the ε_{eff} and μ_{eff}.



(a)

(b)

(c)

Figure 4: (a) *y*-oriented, (b) *x*-oriented and (c) alternating arrays of metallic (red, thick circles) and dielectric (blue, thin circles) inclusions in a homogenous host. The orientations refer to the orientations of the columns/rows of the metallic inclusions shown in bold red lines in (a) and (b).

Using the inversion process as described in [15] for extracting the ε_{eff} and μ_{eff} of heterogeneous structures, the results shown in Fig. 5 were obtained. Data used: f = 1-20 GHz, a = 100 µm, s = 300 µm, ε_1 = 2.25 (tan δ = 0.001), ε_{2a} = 4.40 (tan δ = 0.02), $\varepsilon_{2b} = (1.2 - j103.5) \times 10^6$ (Copper), $\mu_1 = \mu_{2a} = \mu_{2b} = 1$; where $(\varepsilon, \mu)_{2a,2b}$ represents the ε and μ of the different inclusions. A 6-by-6 array was used in the plane of the infinite/symmetry boundaries, that is, the yz-plane, and the structure had 11 layers, implying a thickness of 3.3 mm in the direction of propagation of the plane wave – the *x*-axis. Perfect Electric and Perfect Magnetic Conductor (PEC and PMC) boundary conditions are used along the *z*- and *y*-axes respectively. They act as symmetry planes to create an infinite structure along those boundaries. Absorbing boundary conditions are used in the *x*-axis to minimize reflections as the wave travels. An in-depth description of these boundaries is given in [15]. Fig. 5 shows the ε_{eff} and μ_{eff} of the structures in Fig. 4 and includes the cases when the spheres are either all dielectric or all metallic.

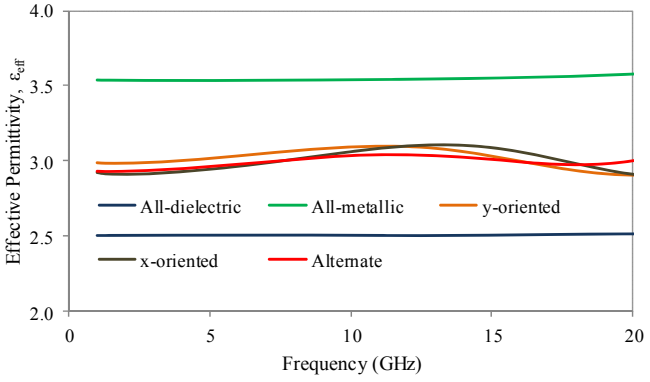
As shown in Fig. 5, as the volume fraction of the metallic inclusions increases, the ε_{eff} increases while the μ_{eff} decreases, as expected. Table 1 gives a summary of the important properties of these heterogeneous media, where p_d and p_m are the volume fractions of the dielectric and metallic inclusions respectively. Even though spherical inclusions are used, the orientation of the rows of metallic/dielectric spheres has been shown to have an effect on the ε_{eff}. As shown, the extracted values of ε_{eff} from the simulation-inversion process agrees well with the analytical results from [9] as shown in equation (6):

$$\varepsilon_{eff} = \varepsilon_1 + 3\varepsilon_1 \frac{\sum_{k=2}^{K} p_k \frac{\varepsilon_k - \varepsilon_1}{\varepsilon_k + 2\varepsilon_1}}{1 - \sum_{k=2}^{K} p_k \frac{\varepsilon_k - \varepsilon_1}{\varepsilon_k + 2\varepsilon_1}} \qquad (6)$$

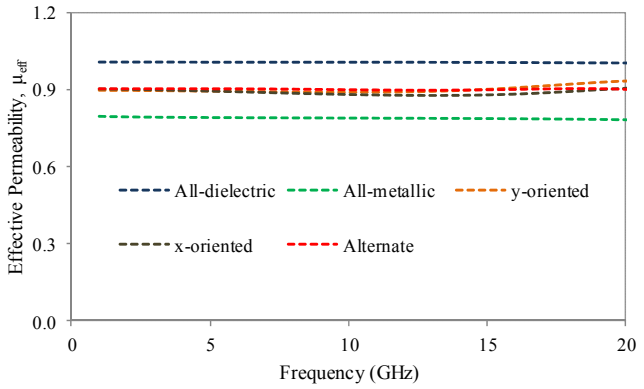
where k represents the different inclusions. The extracted values are the average values over the frequency range examined. There are no results for the μ_{eff} from [9] as μ_{eff} = 1, in all cases as explained in Section 3. With increased volume fractions of the metallic inclusions, the ε_{eff} will further increase while the μ_{eff} will decrease.

Table 1: Summary of simulated results

	p_d	p_m	ε_{eff}	ε_{eff} [9]	μ_{eff}
y-oriented	0.071	0.085	3.04	3.01	0.89
x-oriented	0.078	0.078	2.97	2.97	0.89
Alternate	0.078	0.078	2.98	2.97	0.90
All-dielectric	0.155	-	2.51	2.51	1.00
All-metallic	-	0.155	3.54	3.49	0.79



(a)



(b)

Figure 5: Variation of (a) ε_{eff} (continuous) and (b) μ_{eff} (dashed) with frequency for different heterogeneous mixtures

5. Patch Antenna

As mentioned earlier, heterogeneous mixtures can be used as antenna substrates. In this section, the geometry and simulated results of simple example are given. Fig. 6 shows the geometry of a simple inset-fed patch antenna on a heterogeneous medium with dielectric cubic inclusions. Data used: patch dimensions: 24 mm by 27.76 mm, transmission line width = 3.12 mm, inset feed depth = 8 mm, cube length, $l = 0.5$ mm, spacing, $s = 0.75$ mm, thickness of the substrate, $d_s = 1.5$ mm, $\varepsilon_1 = 2.08$ (tan $\delta = 0.0004$), $\varepsilon_2 = 12.94$ (tan $\delta = 0.006$), $\mu_1 = \mu_2 = 1$. The ε_{eff} for the heterogeneous medium is 3.55 (tan $\delta = 0.0016$) obtained from equation (1), and is used as the permittivity for the homogeneous equivalent. The return loss, S_{11}, for these two structures are shown in Fig. 7. The results show good agreement with the resonant frequency of the heterogeneous substrate (3.21 GHz) being slightly lower than that of the homogenous equivalent (3.25 GHz). Previous work by the authors in [22], [23] have shown this to be the case for spherical and metallic inclusions. The radiation efficiencies are 93.52% and 92.82% for the homogenous and heterogeneous respectively which again show good agreement. These good agreements provide further confidence that the canonical equations accurately predict the effective EM properties of these heterogeneous media. This shows that the match is maintained and reasonable efficiencies are possible.

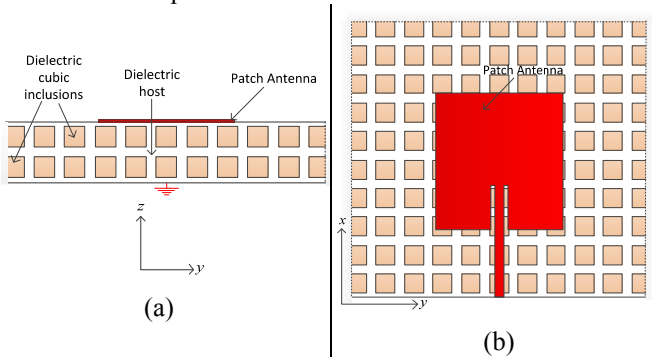


Figure 6: (a) Side view and (b) top view of inset-fed patch antenna on a heterogeneous substrate (not drawn to scale)

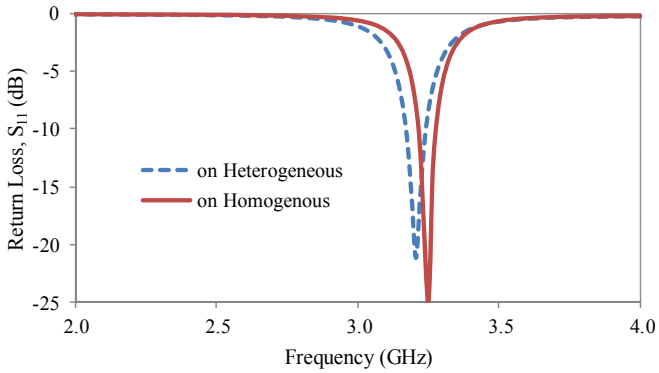


Figure 7: Simulated S_{11} of same sized patch on a homogenous (continuous) and heterogeneous (dashed) substrates with dielectric cubic inclusions

6. Conclusions

Canonical equations from different authors have been compared with each other and with simulated results. Even though the equations appear to be different, on closer inspection and under certain assumptions, they can be shown to be quite similar to each other. Heterogeneous mixtures with more than one type of inclusion have been simulated with the results showing good agreement with the equivalent canonical equation. An example patch antenna on a heterogeneous substrate with dielectric cubic inclusions have been simulated and shown to have good agreement with when the patch antenna is on its homogenous equivalent substrate.

Acknowledgements

This work was supported by EPSRC under Grant No. EP/I01490X/1.

References

[1] M. I. Kitra, C. J. Panagamuwa, P. McEvoy, J. (Yiannis) C. Vardaxoglou, and J. R. James, "Low SAR ferrite handset antenna design," *IEEE Transactions on Antennas and Propagation*, vol. 55, no. 4, pp. 1155–1164, Apr. 2007.

[2] G. Kiziltas, D. Psychoudakis, J. L. Volakis, and N. Kikuchi, "Topology design optimization of dielectric substrates for bandwidth improvement of a patch antenna," *IEEE Transactions on Antennas and Propagation*, vol. 51, no. 10, pp. 2732–2743, Oct. 2003.

[3] C.-C. Chen and J. L. Volakis, "Bandwidth broadening of patch antennas using nonuniform substrates," *Microwave and Optical Technology Letters*, vol. 47, no. 5, pp. 421–423, Dec. 2005.

[4] D. Psychoudakis, Y.-H. Koh, J. L. Volakis, and J. H. Halloran, "Design method for aperture-coupled microstrip patch antennas on textured dielectric substrates," *IEEE Transactions on Antennas and Propagation*, vol. 52, no. 10, pp. 2763–2765, Oct. 2004.

[5] D. Psychoudakis, J. L. Volakis, Z. N. Wing, S. K. Pillai, and J. W. Halloran, "Enhancing UHF antenna

functionality through dielectric inclusions and texturization," *IEEE Transactions on Antennas and Propagation*, vol. 54, no. 2, pp. 317–329, Feb. 2006.

[6] Lord Rayleigh, "On the influence of obstacles arranged in rectangular order upon the properties of a medium," *Philosophical Magazine*, vol. 34, pp. 481–502, 1892.

[7] L. Lewin, "The electrical constants of a material loaded with spherical particles," *IEE-Part III: Radio Comm. Eng.*, vol. 94, no. 27, pp. 65–68, 1947.

[8] X. Cai, R. Zhu, and G. Hu, "Experimental study for metamaterials based on dielectric resonators and wire frame," *Metamaterials*, vol. 2, no. 4, pp. 220–226, 2008.

[9] A. Sihvola, *Electromagnetic Mixing Formulas and Applications*. London: IET, 1999.

[10] R. E. Collin, *Field Theory of Guided Waves*. New York: IEEE Press, 1991.

[11] W. T. Doyle, "The Clausius-Mossotti problem for cubic arrays of spheres," *Journal of Applied Physics*, vol. 49, no. 2, pp. 795–797, 1978.

[12] W. T. Doyle, "Optical properties of a suspension of metal spheres," *Physical Review B*, vol. 39, no. 14, pp. 9852–9858, 1989.

[13] I. A. Kolmakov, L. Jylha, S. A. Tretyakov, and S. Maslovki, "Lattice of dielectric particles with double negative response," in *28th Gen. Ass. Int. Union Radio Sci. (URSI)*, 2005.

[14] C. C. Njoku, W. G. Whittow, and J. C. Vardaxoglou, "Comparative study of nanomaterials' effective properties using canonical formations," in *Loughborough Antennas & Propagation Conference (LAPC)*, 2010, pp. 413–416.

[15] C. C. Njoku, W. G. Whittow, and Y. C. Vardaxoglou, "Simulation methodology for synthesis of antenna substrates with micro-scale inclusions," *IEEE Transactions on Antennas and Propagation*, vol. 60, no. 5, pp. 2194–2202, 2012.

[16] C. C. Njoku, W. G. Whittow, and Y. C. Vardaxoglou, "Effective permittivity of heterogeneous substrates with cubes in a 3-D Lattice," *IEEE Antennas and Wireless Propagation Letters (Special Issue on Metamaterials)*, vol. 10, pp. 1480–1483, 2011.

[17] R. Asmatulu, B. Geist, W. B. Spillman, and R. O. Claus, "Dielectric constant and breakdown field studies of electrostatic self-assembled materials," *Smart Materials and Structures*, vol. 14, no. 6, pp. 1493–1500, Dec. 2005.

[18] C. L. Holloway, E. F. Kuester, J. Baker-Jarvis, and P. Kabos, "A double negative (DNG) composite medium composed of magnetodielectric spherical particles embedded in a matrix," *Antennas and Propagation, IEEE Transactions on*, vol. 51, no. 10, pp. 2596–2603, 2003.

[19] J. C. Vardaxoglou, "Optical switching of frequency selective surface bandpass response," *Electronics Letters*, vol. 32, no. 25, pp. 2345–2346, 1996.

[20] I. Awai, O. Mizue, and A. K. Saha, "Artificial dielectric resonator made of spherical metal particles," *IEICE Transactions on Electronics*, vol. E92–C, no. 1, pp. 72–76, 2009.

[21] W. M. Merrill, R. E. Diaz, M. M. LoRe, M. C. Squires, and N. G. Alexopoulos, "Effective medium theories for artificial materials composed of multiple sizes of spherical inclusions in a host continuum," *IEEE Transactions on Antennas and Propagation*, vol. 47, no. 1, pp. 142–148, 1999.

[22] C. C. Njoku, W. G. Whittow, and Y. C. Vardaxoglou, "Designing microwave patch antennas using heterogeneous substrates," in *European Conference on Antennas and Propagation (EuCAP)*, 2012, pp. 886–888.

[23] W. G. Whittow, C. C. Njoku, and J. C. Vardaxoglou, "Designing multi-band and high bandwidth antennas with heterogeneous substrates," in *IEEE Tropical Conference on Antennas and Propagation in Wireless Communications (APWC)*, 2012, pp. 748–751.

Plasmonic antennas, lenses and metasurfaces

Long-range interaction of localized surface plasmons in periodic and random patterns of Au nano-narticles

Yoshiaki Nishijima[1], Lorenzo Rosa[2], Saulius Juodkazis[2,3],

[1]Department of Electrical and Computer Engineering, Graduate School of Engineering, Yokohama National University, Japan
[2]Faculty of Engineering and Industrial Sciences, Swinburne University of Technology, Australia
[3]Melbourne Centre for Nanofabrication, Australia
*corresponding author, E-mail: nishijima@ynu.ac.jp

Abstract

The plasmon resonance of periodic and random arrays of Au-nanodiscs and nano-squares was investigated experimentally and numerically. By randomization, plasmon resonance spectra become broadened, however, the electromagnetic field enhancement is augmented by a factor of 10-10^2 times at some specific wavelength as shown by the finite elements time domain (FDTD) calculations. The spatial localization takes place at a fewer hot-spots. The randomized structures are promising for the applications in opto-electronics, sensing, and light harvesting.

1. Introduction

The localized surface plasmon resonances (LSPRs) are generated by nanostructures of noble metals such as gold, silver and copper, which are attractive and promising materials in the field of opto-electronics, photochemistry, and solar energy applications. Also it is important tool for the detection of small number of molecules with high sensitivity, high selectivity using surface enhanced Raman scattering (SERS) and surface enhanced infrared absorption spectroscopic measurements (SEIRA) [1–7]. Recently configuration of a nano-pattern has been paid much of attention for controlling the wide-angle light-plasmon coupling [8–12] [13]. In the case of plasmon resonance, one nanostructure itself play as a resonator to the light and is coupled to other resonators in close vicinity. Configuration of the pattern of nano-particles becomes important for propagation scattering and active emission (spaser) similarly to the photonic crystals and is currently actively researched. Apparently, random patterns of nano-particles are increasing efficiency of organic solar cells [14].

Periodic arrays of nanostructures which are widely produced by top-down nanotechnology techniques, have the Bragg diffraction dominant effects and scatters light into diffracting modes, they appear as resonant scattering bands in extinction. The diffracted light departs from surface and is lost for light harvesting. However, when periodicity of pattern is broken by randomization, spectroscopic properties and electromagnetic(EM) field enhancement are modified favorably for light harvesting. The benefit of studying the (quasi)-random structure is promising for cost reduction of fabrication. The quality of tools used in nanofabrication is developing rapidly with advances in the accuracy down to the nanometer sized gaps, high through-put, high reproductivity at lower electron beam acceleration voltages and less danage to the substrate [15]. The (quasi-)random patterns of nanoparticles can be created not only by top-down methods but also by bottom-up approach including the chemical synthesis. Therefore for the large large area applications (such as white light applications like LEDs, solar cells, photo catalysis and so on) better understanding of the plasmon resonances and EM-field enhancement is required.

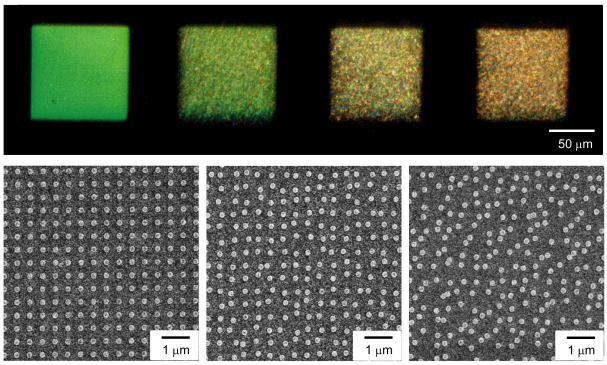


Figure 1: Optical dark-field image of the randomization effect of nanoparticles on a 100 × 100 μm^2 area; from left to the right the randomness is increasing. (b) SEM images of a gradually randomized periodic gold nano-disc array structures.

In this study, we demonstrate how randomization affects the optical extinction spectra of well-defined arrays of gold nano-disks and squares as disorder is gradually increased. The experimental results are analyzed numerically and shows significant EM-field enhancement favorable for the spectrally broad light enhancement.

2. Experiments

Arrays of nano-disks were fabricated by top-down approach using electron beam (EB) lithography and lift-off technique as reported earlier [8, 16]. EB resist (ZEP-520A

ZEON Co.) was coated on the glass substrate by spin coating (3000 rpm for 2 minutes). Top of resist was covered with charge dissipating agent (ESPACER, Showa Denko Co.). Patterns of gold nano-disks are CAD generated by the random-walk method starting from a perfectly periodic pattern, with increasing the mean free length of random walking. After EB drawing process and development, 2 nm of Cr (as the adhesion layer) and 25 nm of Au has been coated with thermal evaporation. Then, EB resist with residual metal over-coating was removed by organic solvent; the obtained gold nano-disc structures were used for experiments. Transmission spectra were measured with a confocal microscope system, composed of a microscope ($10^{\times}$ objective lens with numerical aperture $NA = 0.5$, pinhole of 100 μm diameter from Optiphoto2, Nikon Co.) and an optical spectrum analyzer (Q8381A, Advantest Co.).

3. Results and Discussions

3.1. Experimental analysis of periodic and random patterns

Figure 1 shows the optical dark field images and scanning microscopy images of 500 nm periodic/random arrays of nano-disks. By randomization, a green color (which is caused by the first-order diffraction of the $\Lambda = 500$ nm period pattern) has disappeared and a red color (scattering light by the tail of plasmon resonance) has gradually appeared in the images.

Quantitatively, the analysis of randomness can be achieved by Fourier transform of the CAD pattern or 2D correlation of the SEM images. The appearance of the FFT images is informative and qualitatively conveys perception of the effect of randomness, as shown in Figure 2. The 2D correlation was calculated using the SEM images shown in Figure 1. The 2D correlation method is used to detect similarities between two 2D patterns, which have previously been prepared for analysis in a matrix format. The following equation defines the 2D correlation between two matrices (images) a and b:

$$g(i,j) = \Sigma_m \Sigma_n a(m,n) b(m-i, n-j) \qquad (1)$$

where i, j and m, n are the pixel indices the x- and y-planes. The 2D correlation region is limited to the central 8.6×8.6 μm^2 area due to desktop computer memory constraints. The $a(m,n)$ and $b(m,n)$ matrices are normalized by $\Sigma_{m,n} a(m,n)^2$ and $\Sigma_{m,n} b(m,n)^2$, respectively, which measure the autocorrelations of each of the matrices. Peaks that appear in the correlation factor are defined by the discrete function $g(i,j)$, calculated by shifting one of the two images with respect to the other by a number of pixels i in the x-direction and j in the y-direction (see Equation 1). When the all nano-discs overlap for a specific shift, as in the case of perfect superposition, the correlation function $g(i,j)$ peaks over several pixels (x,y) (Figure 2(a)). When the pattern has less defined periodicity, just a few pixels will overlap outside of the perfect superposition, making the correlation peak narrower as in Figure 2(b). In the fully randomized case, only the single peak at (0,0) appears, as outside perfect superposition the overlap of the images is immediately lost.

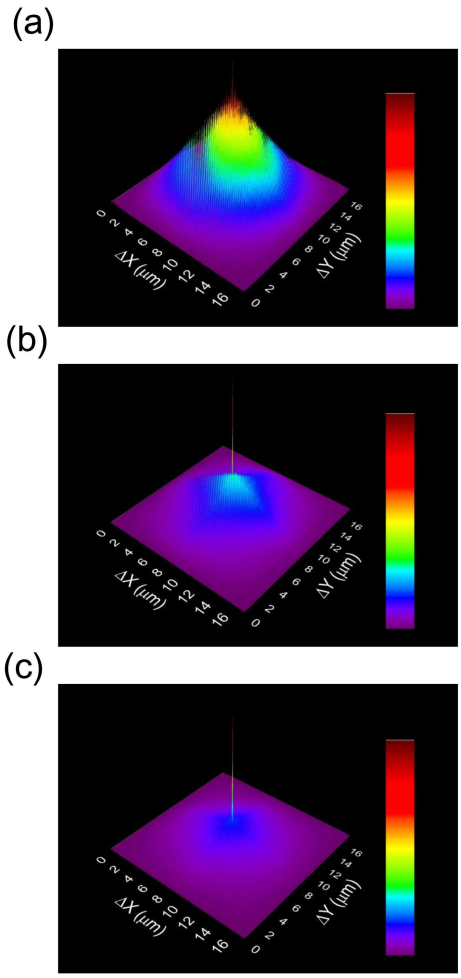


Figure 2: 2D correlation plots of the $g(i,j)$ correlation function obtained from the SEM images shown in Figure 1 for (a) periodic structure, (b) partially random, and (c) fully random; the color scale bar goes from 0 to 10^{-4} in linear scale. The SEM image used here is same as Figure 1.

These numerical 2D correlation results are in good agreement with the FFT of the SEM images. Interestingly, even though the scattering by the periodic pattern gradually disappeared (see Figure 1), periodic features in the 2D correlation function were still recognizable. The main tendency of the narrowing the 2D correlation peak as randomness increases is the same whether one analyzes the CAD or the SEM patterns.

Typical extinction spectra for periodic and randomized arrays of nano-discs are shown in Figure 3. While the diameter of discs was kept constant, increasing the period Λ from 450 to 750 nm caused the extinction peak to shift, at first to the red and then to the blue spectral side, with decreasing extinction values due to the reduced surface coverage (particle density). When the extinction is normalized to

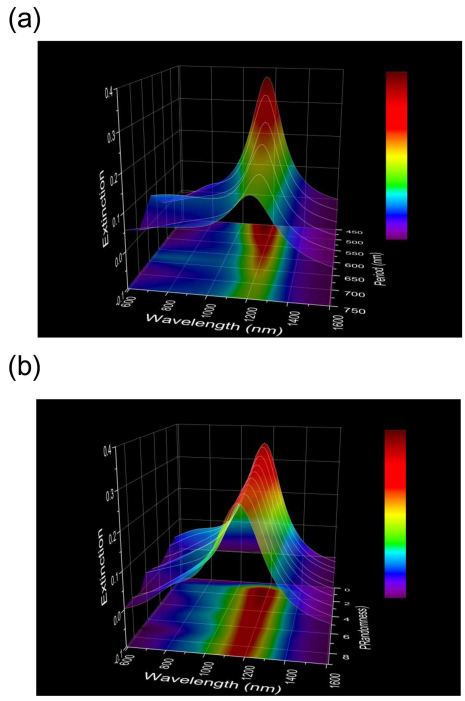


Figure 3: (a) Experimental extinction spectra of periodic arrays with periods between $\Lambda = 450$ nm and 700 nm, at 50 nm regular intervals of period Λ. (b) Extinction spectra for $\Lambda = 550$ nm for gradually increasing randomization.

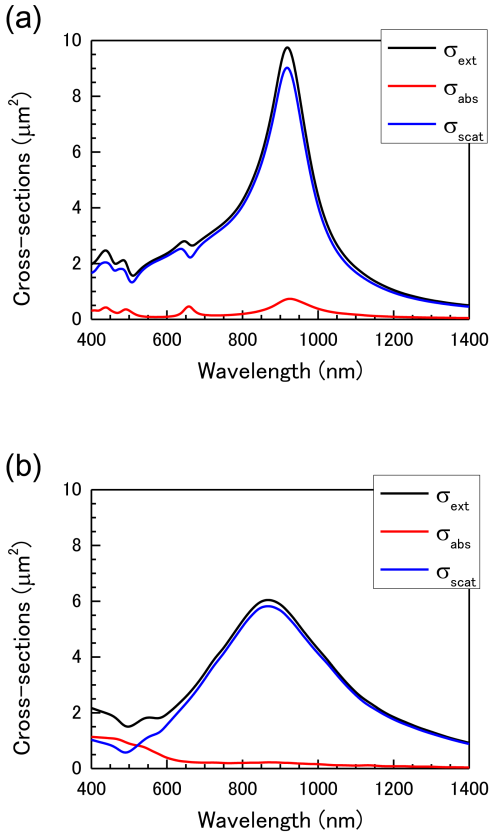


Figure 4: Optical cross-sections for extinction σ_{ext}, absorption σ_{abs}, and scattering σ_{scat}, of (a) periodic and (b) random array patterns obtained from FDTD calculations.

the density, the pattern with period $\Lambda = 550$ nm is close to the maximum extinction value and has the narrowest spectral peak. This is caused by the coupling of plasmon resonance and first-order diffraction [8,12]. When the matching occurs between the diffraction conditions and plasmon resonance, a 10 times stronger EM-field enhancement is obtained, as compared with the pattern where the diffraction wavelength does not overlap with the plasmon resonance. However, the strongest enhancement and the surface density have a trade-off relationship, and sometimes increasing the number of field enhancement hot-spots by increasing the density of nano-particles can be advantageous, even if the resonant diffraction and particle extinction conditions are not matched.

As randomization is increased, the plasmon resonance slightly blue shifts, decreasing the extinction value, and broadens the spectral width (see Figure 3(b)). As shown in the optical microscopy image, the internal diffraction condition is removed by the randomization process. This tendency becomes stronger when using thicker nano-discs of 65 nm thickness. Part of the scattered light leaves the surface, and part experiences total internal reflection at large angles and is bound to the surface. The surface-bound wave is scattered by the nano-particles and its effects on extinction and enhancement are analysed in the next Section 3.2.

3.2. FDTD analysis of periodic and random pattern

In order to study the response of the ordered and disordered patterns, we designed and simulated a layout based of the $\Lambda = 600$ nm period case, as it has better response to the short-wavelength range, as visible in Figure 3. To better exploit the calculation resources available, we first did a preliminary study on smaller-size square particles better suited for the structured mesh of the FDTD method. This was acceptable for the study, as the long-wavelength resonance will mostly experience a shift, while short-wavelength response is dominated by the material characteristics. The comparison stands as the size of the particles is unchanged while the layout is randomized.

For the 3D-FDTD simulation, the structure was enclosed in a domain with a size of $6.6 \times 6.6 \times 0.5$ μm^3, so as to contain exactly 11 periods of the periodic structure. The layout consists of a glass layer on which the gold nano-blocks are placed; the size of the blocks is $200 \times 200 \times 65$ nm^3, and they are automatically positioned according to the layout description used for the e-beam lithography. Perfectly matched layers (PMLs) are used on the domain boundaries to avoid edge reflection. The central 5×5 periods are excited by a total-field scattered-field (TFSF) source, dividing space into two distinct regions: in-

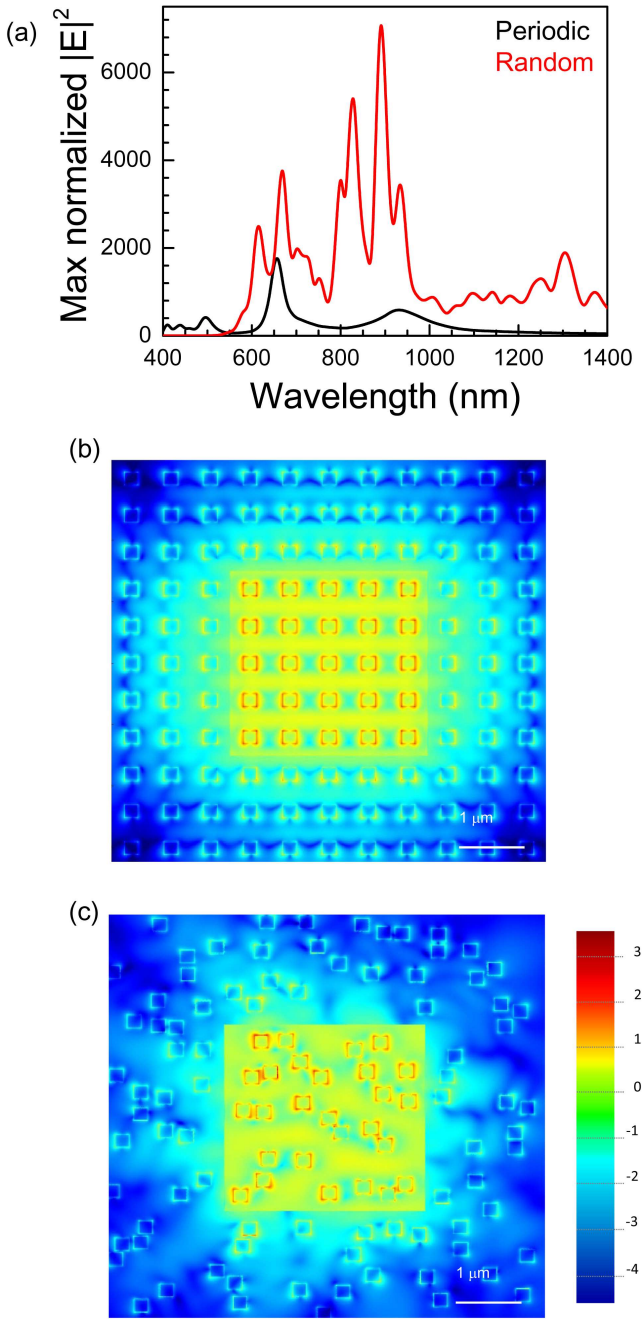


Figure 5: (a) Maximum normalized E-field intensity enhancement on the top surface of the 200 × 200 nm nano-blocks for the periodic and random layouts. Below, the intensity enhancement distribution at 900 nm wavelength in logarithmic scale on the top block surface for (b) periodic and (c) random layouts. The central box-like region corresponds to the total-field region of the TFSF source, and the outer region to the scattered-field one.

side the TFSF volume the total field is calculated, while outside the volume the scattered field is, permitting to evaluate separately extinction, absorption, and scattering cross-section of the region enclosed. [5] The space left between the TFSF boundary and the domain boundary is needed to avoid spurious coupling and resonances between the discontinuities introduced by these two boundaries. In the case of the random layouts, the layout is slightly adjusted to avoid the blocks crossing the non-physical boundary of the TFSF source, though this does not influence the response significantly because of the averaging effect of having a large number of blocks in the domain.

The central part is illuminated with a bandwidth between 400 and 1400 nm wavelength, measuring absorption, scattering, and extinction cross-sections and the E-field intensity enhancement normalized to source intensity. The material models for silica glass and gold are taken from the Lumerical built-in library. The reflected and transmitted power is collected by two monitors at opposite ends of the domain in the z-direction and projected to the far-field at 1 m distance in the positive and negative half-space by the Fraunhöfer integral formulation implemented in Lumerical. The effect of staircase approximation is addressed by reducing the square mesh size in the z-direction to 0.2 nm (or about $\lambda/5000$), forcing the use of a supercomputer on a 3D mesh totaling around 2 million mesh points. The simulation times ranged from 1 to 2 hours and total memory occupancy ranged from 60 to 80 GB, with increasing times and memory according to greater mesh complexity for the random layouts. The simulations have been performed on the Green II machine at Swinburne University, with 86 nodes available, each of them having 16 calculation cores and carrying 64 GB memory. Workload has been subdivided by employing one 8-node cluster per simulation, for a total of 256 cores.

Figure 4 shows the optical cross-sections for extinction σ_{ext}, absorption σ_{abs}, and scattering σ_{scat}, of the periodic and random patterns obtained from FDTD simulations.

With increasing randomization, the cross-section spectra broaden and the peaks blue-shift. This feature reprodices well the experimental results of transmission measurements shown in Figure 2. Additionally, in the case of random patterns, absorption cross-section σ_{abs} (which gives account of the loss in the metal), was reduced in the random pattern when in the maximum extinction condition. This increases the scattering efficiency compared to the periodic pattern, albeit with lower extinction. In the case of the random structure, each nano-disk has a slightly different resonance wavelength because of different long-range interaction, thus the randomly-scattered light is spread over a wider range of wavelengths. Spectrally broader plasmon resonances like this are favorable in practical light harvesting applications.

As in our previous report, the electro-magnetic field enhancement is up to 10-10^2 times larger in the partly disordered patterns, suggesting "hot-spot-like" strong localized enhancement as was observed in the previous case [8] (see Figures 5(b) and (c)). The periodic pattern has strong hot-spots on the corners and edges perpendicular to the irradiation light polarization, reaching values as high as 500. In the random pattern, enhancement hot-spots also appear on the corners and edges, also depending on the polarization of

the irradiation light but with much less regularity. The top enhancement spots also move from block to block depending on wavelength, but are frequently located where corners face each other, creating a nano-gap.

We analyzed the maximum field enhancement value over all the calculation area that is flush with the top of the nano-blocks, plotted against the irradiation light wavelength. The results are shown in Figure 5.

In the case of the periodic array (Figure 5(a)), the maximum intensity spectra have a profile similar to the cross-sections. Therefore, the profile broadens around 1000 nm wavelength to a maximum intensity of 500 times the source. Interestingly, around 660 nm we observe a narrow and strong peak (where normalized intensity reaches 1700). The same feature can be seen in the absorption cross-section and we can see a small distortion in the scattering and extinction cross-sections in Figure 4(a). This narrow and strong enhancement of the EM field is due to a Fano-like resonance coupling between plasmon resonance and diffraction [16–20]. As we previously reported, EM field enhancement strongly depends on the plasmon resonance wavelength and its periodicity [8]. It is important to control the coupling of plasmon resonance and diffraction for efficient EM field enhancement. However, in the random pattern, EM enhancement features become quite different from the periodic pattern. Maximum enhancement reaches 7000, which is 14 times as large as the periodic pattern at the plasmon peak wavelength. Its profile is also related to the plasmon resonance, however it is not smooth and has many peaks. Even around 1300 nm wavelength, which has weaker extinction than peak wavelength, still it shows 1000 times enhancement (two times higher than the periodic pattern). This strong enhancement would appear as long as the plasmon resonance exists. The features of random array structures (broadband resonance and low extinction loss with strong enhancement) can be especially promising as materials for white-light applications such as organic/inorganic LEDs, photo-voltaic devices and solar cells, photo-detectors, and photochemical processes like photo catalysts. Also, the broadband resonance and narrow, strong enhancement features appearing in Figure 5 are significant in that they will contribute to sensitivity in SERS and SEIRA applications. As already discussed widely discussed in literature, the SERS intensity is dependent on the EM field enhancement both at excitation and scattering wavelengths. In case of the plasmon resonance of a periodic structure, it is difficult to tune both excitation and Raman scattering to the maximum EM-enhancement wavelength. However, in the random substrate, we have a strong wideband enhancement which can cover a wide range of SERS signals. We also have the possibility to enhance a specific signal, which can increase specific molecular selectivity in SERS measurements [21].

4. Conclusions

In this study, we have demonstrated the effect of periodic and random particle patterns on the plasmonic resonance. An increase of extinction and a broader plasmon resonance occurs with increasing the randomness in the case of nano-disks as can be visualized by dark-field. FDTD calculations show an augmentation of the enhancement by more than two orders of magnitude for the random configuration of nano-squares with spectral broadening and field enhancement effects. Broad band and narrow peak appearance in the enhancement profile is shown by FDTD calculations. This unique features have potential to be applied to both the white light harvesting and for SERS/SEIRA sensing. Recently, the enhancement of SERS intensity by an order of magnitude as compared to that on periodic patterns [22] is demonstrated on laser-ablated ripples [23]. The randomness of the hot-spots on scale of tens-of-nanometers is attributable for this effect and SERS sensitivity can be increased to detect gaseous precursors of explosives [24]. This is achieved without compromise of spatial uniformity over sensing surface since SERS intensity is integrated over hot-spots occurring within 2-5 μm diameter laser focus of the SERS readout.

Acknowledgement

Authors thank Prof. T. Baba (Yokohama National University) for discussions and facility supports. We are also grateful to Prof. Jacob Khurign (Johns Hopkins University) and Prof. H. Fujiwara (Hokkaido University) for the fruitful discussions. This work was financially supported by the Amada Foundation, the Research Foundation for Opt-Science and Technology, and The Ministry of Education, Culture, Sports, Science and Technology(MEXT), Japan. SJ ts thankful for support by ARC Discovery DP130101205 grant.

References

[1] Link, S. and El-Sayed, M. A., "Size and temperature dependence of the plasmon absorption of colloidal gold nanoparticles," *The Journal of Physical Chemistry B* **103**(21), 4212–4217 (1999).

[2] Shekhah, O., Liu, J., Fischer, R. A., and Woll, C., "Mof thin films: existing and future applications," *Chem. Soc. Rev.* **40**, 1081–1106 (2011).

[3] Valev, V. K., Smisdom, N., Silhanek, A. V., De Clercq, B., Gillijns, W., Ameloot, M., Moshchalkov, V. V., and Verbiest, T., "Plasmonic ratchet wheels: Switching circular dichroism by arranging chiral nanostructures," *Nano Letters* **9**(11), 3945–3948 (2009). PMID: 19863052.

[4] Michaels, A. M., Nirmal, M., and Brus, L. E., "Surface enhanced raman spectroscopy of individual rhodamine 6g molecules on large ag nanocrystals," *Journal of the American Chemical Society* **121**(43), 9932–9939 (1999).

[5] Sawai, Y., Takimoto, B., Nabika, H., Ajito, K., and Murakoshi, K., "Observation of a small number of molecules at a metal nanogap arrayed on a solid surface using surface-enhanced raman scattering," *Journal of the American Chemical Society* **129**(6), 1658–1662 (2007).

[6] Tsuboi, Y., Shoji, T., Kitamura, N., Takase, M., Murakoshi, K., Mizumoto, Y., and Ishihara, H., "Optical trapping of

quantum dots based on gap-mode-excitation of localized surface plasmon," *The Journal of Physical Chemistry Letters* **1**(15), 2327–2333 (2010).

[7] Nishijima, Y., Nigorinuma, H., Rosa, L., and Juodkazis, S., "Selective enhancement of infrared absorption with metal hole arrays," *Opt. Mater. Express* **2**, 1367–1377 (Oct 2012).

[8] Nishijima, Y., Rosa, L., and Juodkazis, S., "Surface plasmon resonances in periodic and random patterns of gold nano-disks for broadband light harvesting," *Opt. Express* **20**, 11466–11477 (May 2012).

[9] Khurgin, J. B. and Sun, G., "Impact of disorder on surface plasmons in two-dimensional arrays of metal nanoparticles," *Applied Physics Letters* **94**(22), 221111 (2009).

[10] Albooyeh, M., Morits, D., and Tretyakov, S. A., "Effective electric and magnetic properties of metasurfaces in transition from crystalline to amorphous state," *Phys. Rev. B* **85**, 205110 (May 2012).

[11] Khunsin, W., Brian, B., Dorfmuller, J., Esslinger, M., Vogelgesang, R., Etrich, C., Rockstuhl, C., Dmitriev, A., and Kern, K., "Long-distance indirect excitation of nanoplasmonic resonances," *Nano Letters* **11**(7), 2765–2769 (2011).

[12] Lamprecht, B., Schider, G., Lechner, R. T., Ditlbacher, H., Krenn, J. R., Leitner, A., and Aussenegg, F. R., "Metal nanoparticle gratings: Influence of dipolar particle interaction on the plasmon resonance," *Phys. Rev. Lett.* **84**, 4721–4724 (May 2000).

[13] Rosa, L., Sun, K., Mizeikis, V., Bauerdick, S., Peto, L., and Juodkazis, S., "3d-tailored gold nanoparticles for light field enhancement and harvesting over visible-ir spectral range," *J. Chem. Phys. C* **115**, 5251–5256 (2011).

[14] Poh, C.-H., Rosa, L., Juodkazis, S., and Dastoor, P., "FDTD modeling to enhance the performance of an organic solar cell embedded with gold nanoparticles," *Opt. Mater. Express* **1**, 1326–1331 (2011).

[15] Juodkazis, S. and Rosa, L., "Surface defect mediated electron hopping between nanoparticles separated by a nanogap," *physica status solidi - rapid research letters* **4**(10), 244–246 (2010).

[16] Nishijima, Y. and Akiyama, S., "Unusual optical properties of the au/ag alloy at the matching mole fraction," *Opt. Mater. Express* **2**, 1226–1235 (Sep 2012).

[17] Wu, D., Jiang, S., Cheng, Y., and Liu, X., "Fano-like resonance in symmetry-broken gold nanotube dimer," *Opt. Express* **20**, 26559–26567 (Nov 2012).

[18] Rodriguez, S. R. K., Abass, A., Maes, B., Janssen, O. T. A., Vecchi, G., and Gómez Rivas, J., "Coupling bright and dark plasmonic lattice resonances," *Phys. Rev. X* **1**, 021019 (Dec 2011).

[19] Gopinath, A., Boriskina, S. V., Feng, N.-N., Reinhard, B. M., and Negro, L. D., "Photonic-plasmonic scattering resonances in deterministic aperiodic structures," *Nano Letters* **8**(8), 2423–2431 (2008). PMID: 18646833.

[20] Auguié, B. and Barnes, W. L., "Collective resonances in gold nanoparticle arrays," *Phys. Rev. Lett.* **101**, 143902 (Sep 2008).

[21] Marimuthu, A., Christopher, P., and Linic, S., "Design of plasmonic platforms for selective molecular sensing based on surface-enhanced raman spectroscopy," *The Journal of Physical Chemistry C* **116**(17), 9824–9829 (2012).

[22] Buividas, R., Stoddart, P. R., and Juodkazis, S., "Laser fabricated ripple substrates for surface-enahnced Raman scattering," *Annalen der Physik* **524**(11), L5 – L10 (2012).

[23] R.Buividas, Rosa, L., Šliupas, R., Kudrius, T., Šlekys, G., Datsyuk, V., and Juodkazis, S., "Mechanism of fine ripple formation on surfaces of (semi)transparent materials via a half-wavelength cavity feedback," *Nanotechnology* **22**, 055304 (2011).

[24] Chou, A., Jaatinen, E., Buividas, R., Seniutinas, G., Juodkazis, S., Izake, E. L., and Fredericks, P. M., "SERS substrate for detection of explosives," *Nanoscale* **4**(23), 7419 – 7424 (2012).

Metamaterial Patch Antenna Radiation Pattern Agility

S. M. CHAKER, M. BOUZOUAD.

Telecommunication Signal and Systems Laboratory,
BP 37G, Route de Ghardaïa, 03000, Laghouat, Algérie.
*corresponding author, E-mail: m.bouzouad@mail.lagh-univ.dz

Abstract

In this paper we address the introduction of antenna radiation pattern agility using an agile metamaterial. We design an agile metamaterial having two different behaviors which can be controlled by an external command. This agile metamaterial is used to design an agile lens which comprises two grids each composed of two regions: the first one constitutes a focusing zone (FZ) and the second one the lens body. The focusing zone parameters—refraction index, size, shape and position in the grid— can be modified using an external switching system (OFF or ON stat) by modifying the FZ parameters one can control the patch antenna radiation pattern main lobe beamwidth and direction (pointing angle) in E- and H- planes.

1. Introduction

Among the most important metamaterial applications in the antenna field we can mention the antenna performances enhancement and size reduction [1], [2], [3]. However, antenna characteristics control remains a major challenge of metamaterial use in the antenna domain. The goal is to design agile antennas [4], [5], of which it is possible to change the antenna characteristics using an external control system. This makes telecommunications systems more flexible. Generally, in this kind of structures Ferooelectrique films [6] or switching elements (diodes, MEMs, etc…) are used to ensure the agility [7], [8]. Agile antennas can be classified in two categories: i) Frequency agile antennas for which we can vary their operating frequency, ii) Radiation pattern agile antennas for which we can change their radiation pattern characteristics (pointing direction, main lobe beamwidth, etc…). These antennas can be used for telecommunication applications, metrology (detection angles of arrival) and also for RADAR applications [9].

We are interested in this study, with the patch antenna radiation pattern agility. The aim is to steer the radiation pattern using a lens based on an agile metamaterial (programmable). Note that the use of a metamaterial based lens above a patch antenna improves also the antenna directivity considerably (16 dB instead of 7 dB for the antenna alone) [9].

2. Antenna radiation pattern Agility

Figure 1 shows our studied agile radiation pattern antenna. The structure is formed by a patch antenna atop which is disposed an agile metamaterial lens. The elementary cell of the agile metamaterial is made of a disconnected cross like conducting strips, printed on a dielectric substrate. The disconnected branches of the cross can be joined with a switching devices (Diodes, MEMs, etc…). This modifiable unit cell (Figure 1-a and -b) allows us introducing the metamaterial agility. According to the switches state (ON or OFF), we design the unit cell to have two different commutable behaviors. The first one corresponding to the disconnected cross type (switch ON) behaving like an effective medium with a refraction index n_1 higher than unity and the second one corresponding to the connected cross type (switch OFF) having a positive and close to zero refraction index n_2.

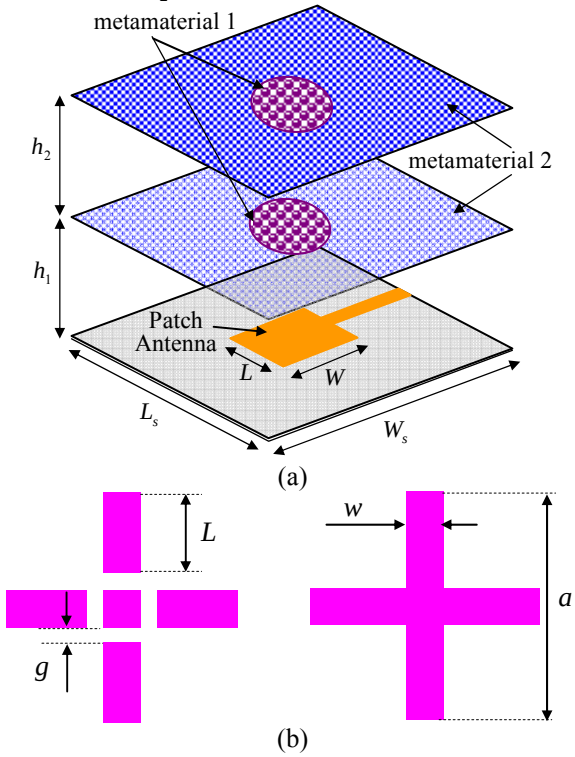


Figure 1: a) Agile radiation pattern radiating structure, b) agile metamaterial elementary cell (disconnected and connected cross).

The obtained programmable metamaterial is used to realize the grids of the agile lens. These grids are made up of two regions (Figure 2- a), the first one forming a focusing zone (FZ) and the second one, the lens body (host medium). The refraction index (n_1 or n_2), the size, shape and position of the FZ can be programmed by acting on the switching devices (state ON or OFF). Modifying the FZ parameters (size, shape, position, and refraction index), allows us to control the antenna radiation pattern properties (main lobe direction (pointing angle) and beamwidth in both E- and H-plane.

3. Agile metamaterial characterization

The metamaterial elementary motifs (Figure 1- b) are printed on a dielectric substrate of permittivity $\varepsilon_r = 2.2$ and a thickness $h = 0.8$ mm [9].

3.1. The metamaterial unit cell size determination

The patch antenna operating frequency is 40 GHz, hence the corresponding wavelength in free space is 8 mm. Accordingly, the greatest dimension of the metamaterial unit cell must be much lower than the operating wavelength, to respect the homogenization conditions [11]. So, we fixed it to 2 mm (lower than $\lambda/3 \approx 2.66$ mm).

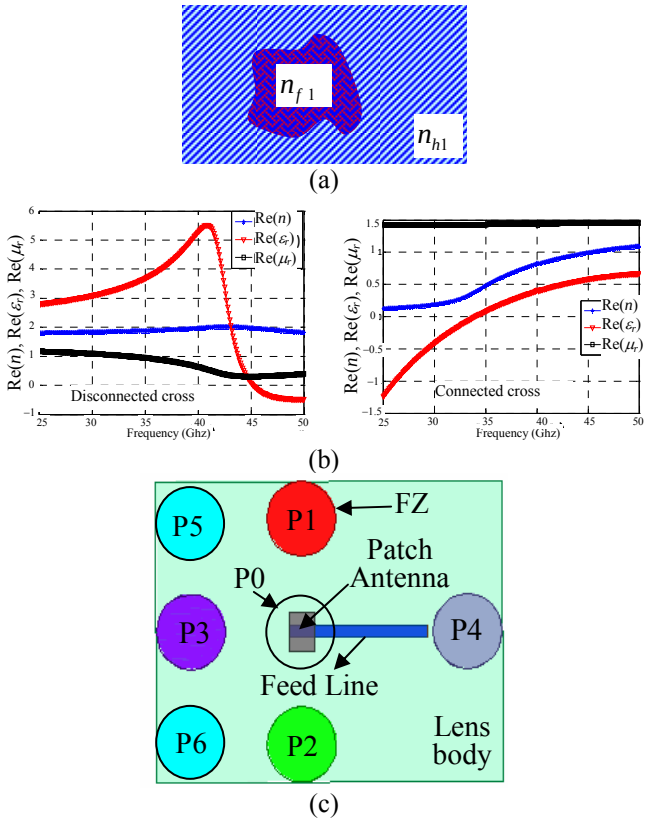


Figure 2: a) Agile lens grid: host medium with refraction index n_{f1} and FZ with index n_{h1}, b) Used metamaterial refraction indices profiles, c) different positions of the FZ.

We used a parametric study to obtain the unit cell optimum sizes, of the two metamaterials types, to attain the desired refraction indexes profiles (Figure 2-b). The refraction index contrast of both the metamaterial types used is about $\Delta n = 0.95$. The cross branch conducting strips are separated by a gap $g = 0.25$ mm and have a length L =0.675 mm, a width $w = 0.15$ mm, and a metallization thickness $t = 0.035$ mm.

The study shows also that the agile radiating structure directivity is maximum when the host mediums of the first grid and the focusing zone of the second grid of the agile lens are based on a connected cross type metamaterial and the host mediums of the second grid and the focusing zone of the first grid are based on a disconnected cross type metamaterial.

The constitutive parameters (ε_{reff} and μ_{reff}) and the refraction index of the agile metamaterials are obtained using the Fresnel inversion method starting from the *S* parameters, obtained by the HFSS simulation software (commercial code).

4. Results and discussion

Table 1 and Figure 3 show the agile radiating antenna radiation pattern steering, obtained by the positioning of the FZ. When placed between positions P1 and P2 (Figure 2-c), the FZ acts only on E-plane of the radiation pattern. The main lobe is rotated on both sides of the $\theta = 0°$direction.

Table 1. Agile antenna radiation pattern main angle direction θ_{max} versus FZ positions.

FZ positions	E-Plan	H-Plan
	θ_{max} (deg)	θ_{max} (deg)
P0	0	5.0
P1	-8,7	6,1
P2	8,7	6,1
P3	0,5	11,8
P4	0,4	36.0

The amplitude of the rotation angle is about 8.7° (Table 1). Whereas, the focusing zone acts only on the H-plane of the radiation pattern when it's placed between positions P3 and P4 (Figure 2-c). The FZ positioned in P3 rotates the main beam pattern by 11.8° and by 36° if it is positioned in P4. Normally the main lobe rotation angle corresponding to position P4 should be negative, but due to the undesirable radiation from the antenna feed line perturbs drastically the radiation pattern and makes difficult to determine the radiation pattern main lobe pointing angle. However, in Figure 3 it's clearly shown that the radiation pattern corresponding to position P3 can be obtained by a rotation clockwise of that corresponding of position P4. We note that the amplitude of main lobe pointing rotation angle is a bout 8° in the plan E. This is not sufficient for the radiation pattern steering. This can be explained by the weak contrast Δn between the refraction index of the two metamaterials used to design the agile lens (the host medium and the focusing zone).

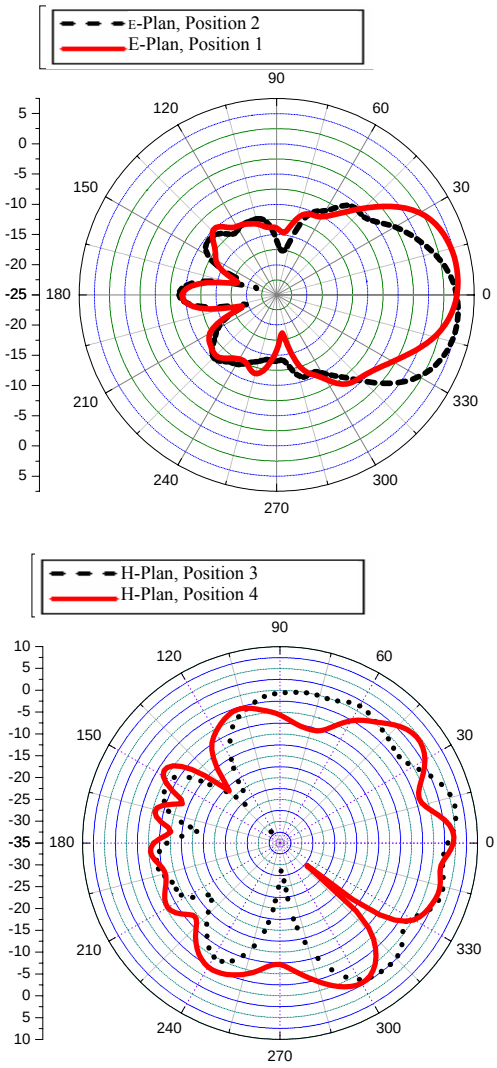


Figure 3: Radiation pattern steering of the agile radiating structure by positioning the FZ.

4.1. Effect of the material refraction index contrast

To improve the agile metamaterial lens steering performances, we increase the refraction index contrast between the two metamaterials used to realize the host medium and the FZ. We choose for the connected cross type metamaterial a low refraction index ($n = 0.5$) and for the disconnected cross type metamaterial a higher refraction index ($n = 2$). Hence, the refraction index contrast is $\Delta n = 1.5$ instead of $\Delta n = 0.95$ for the previous lens described in section 3.1.

Table 2 and Figure 5 show that the radiation pattern main lobe rotation angle amplitude is 15° in the E-plane. We observe an improvement of about 6.8° compared to that obtained by the low contrast refraction index lens. In the H-plane, for the same reasons mentioned above, the rotation angle amplitude is difficult to determine. It can be estimated to (2.0°-4.3° = -2.3°) clockwise and (13.0°-4.3° = 8.7°) counterclockwise.

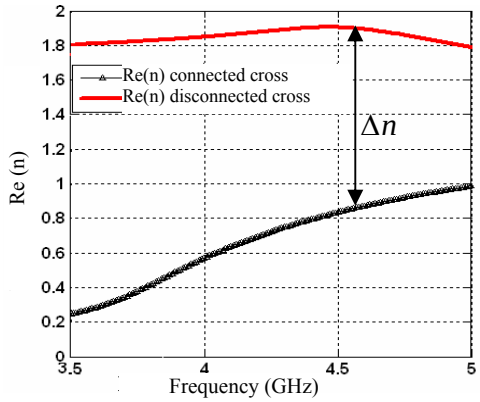


Figure 4: Used metamaterial refraction indices profiles.

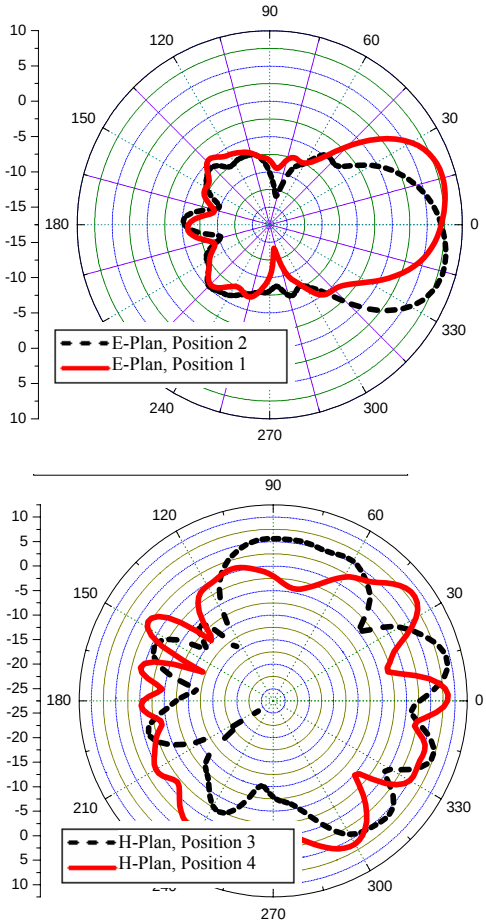


Figure 5: Radiation pattern steering of the agile radiating structure by positioning the FZ, with a high contrast agile metamaterial lens ($\Delta n = 1.5$).

Table 2. Agile antenna radiation pattern main angle direction θ_{max} versus FZ positions, with a high contrast agile lens ($\Delta n = 1.5$).

FZ positions	E-Plan	H-Plan
	θ_{max} (deg)	θ_{max} (deg)
P0	0.0	4.3
P1	-15.5	7.2
P2	15.4	7.2
P3	0,5	13
P4	0,6	2

4.2. Effect of the focusing zones and patch antenna alignment

In addition to the refraction index contrast, the alignment of the focusing zones with the patch antenna is another parameter witch can be used to improve the agile metamaterial lens radiation pattern steering capability. Indeed, the previous results are obtained with the two focusing zones disposed one on the other and were not aligned with the patch antenna as is depicted in Figure 6-a. Now, we will position the two focusing zones so they will be on the same alignment with the patch antenna (Figure 6-b).

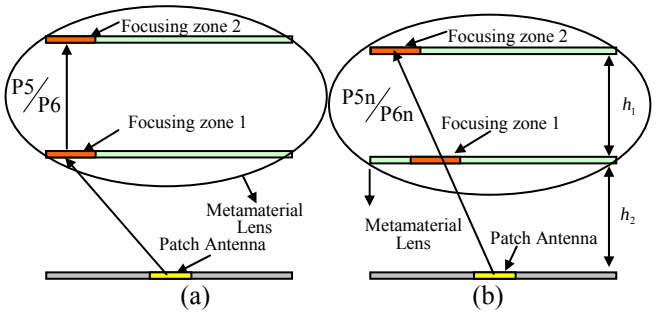


Figure 6: Patch antenna with the agile metamarerial lens: a) with not aligned FZs, b) with aligned FZs,.

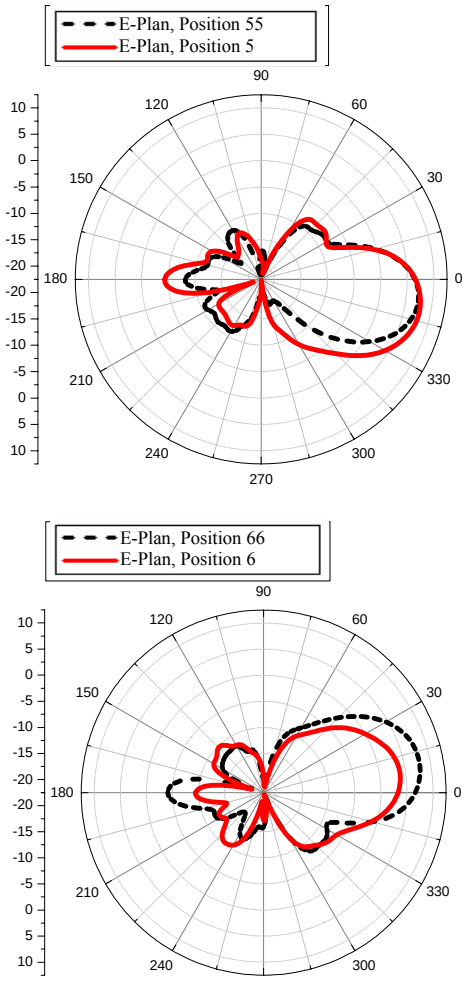


Figure 7: Radiation pattern steering of the agile radiating structure by positioning the aligned and not aligned FZ.

As is shown in Figure 2-c and Figure 6, to the positions 5 and 6 with not aligned focusing zones, we correspond the new positions 5n and 6n with the two focusing zones aligned with the patch antenna. Figure 7 shows a comparison of the antenna radiation patterns in E-plane corresponding to the aligned and not aligned positions 5n and 5, respectively 6n and 6 of the focusing zones. We observe clearly that the alignment of the focusing zones reduces the radiation main lobe beamwidth and improves the antenna gain.

5. Conclusion

In this study, we highlight the possibility of introducing patch antenna radiation pattern agility by using an agile metamaterial lens. In the E-plane, the different results obtained show clearly the main lobe radiation pattern steering, due to the FZ positioning. Whereas, in the H-plane, the presence of secondary side lobes degrades strongly the radiation pattern and the steering effect becomes less visible. The antenna gain and the amplitude of main lobe pointing angle depend uppon the alignement of the FZs and the refraction index contrast of the two materials used to realize the agile metamaterial lens (host medium and FZ).

We have introduced the metamaterial agility by designing a modifiable elementary unit cell based on a disconnected cross shape equipped with MEMs switches. According to the state of the MEM switches (ON or OFF), the metamaterial refraction index flips between two values n_1 close to zero and n_2 greater than the unity.

References

[1] J. Dalin, “Gain improvement of a microstrip patch antenna using metamaterial superstrate with the zero refractive index”, International Conference on Microwave and Millimeter Wave Technology (ICMMT), May 2012; China.

[2] M. Bouzouad. « Analyse et conception d’antennes microruban sur des substrats bandes interdites électromagnétique ». Thèse de Doctorat d’État. École nationale polytechnique d’Alger, décembre 2007.

[3] J. Cha and Y. Kuga. “A steerable array antenna using controllable 4-bit dielectric slab phase shifters on a coplanar waveguide at 24 Ghz”, Microwave and optical technology letters, Vol.49, n°12, 2007.

[4] L. Mercier, « Synthèse de propriété d’agilité électromagnétique par des matériau artificiel périodique intégrant des micocomposants : Application à la conception d’antenne à résonateur BIE configurable », Doctorat d’université de Limoges, 2005.

[5] H. Boutayeb, « Etude des structures périodiques planaires et conformées associées aux antennes. Applications aux communications mobiles », Thèse de doctorat, Université de Rennes, Décembre 2003.

[6] S. ABADEI, S. Gevorgian, C. R. Cho, A Grishin, J. Anderasson et T. Lindback, ‘DC field dependent properties of NaKNbO3/SiO2/Si structures at millimeter-wave frequencies” Applied Physics letters, Vol. 78, p.1900-1902, 2001.

[7] P. Blondy, C. Champeaux, P. Tristant, D. Mercier, D. Cros, A. Catherinot, P.Guillon « Application of RF MEMS to tunable filters and matching networks » IEEE MTT, 2001.

[8] A. Pothier « Conception, réalisation et test de micro-commutateurs micro-électromécaniques et application aux circuits hyperfréquences reconfigurables »; Thèse de doctorat, Université de Limoges, décembre 2003.
[9] L. Leger, T. Monédière, B. Jecko, 'Enhancement of gain and radiation bandwidth for a planar 1-D EBG antenna', IEEE Antennas and Wireless Propagation Letters, Vol. 15, N° 9, September 2005.
[10] F. Bendelala, M. Bouzouad, A. Benabdelkrim, I. Huynen, « Optimisation des dimensions du motif élémentaire d'une grille métamatériau utilisée pour améliorer la directivité d'une antenne imprimée travaillant à 43 GHz », 17èmes Journées Nationales Microondes, Brest, France, 18-19-20 Mai 2011.
[11] C.R. Simovski et al., "Homogenization of Planar Bianisotropic Arrays on the dielectric interface", Electromagnetics, 22 : p. 177-189, 2002.

Active Terahertz Metamaterials

Terahertz band gaps based on TEM mode by photonic crystals inside parallel-plate waveguide

Eui Su Lee and Tae-In Jeon*

Division of Electrical and Electronics Engineering, Korea Maritime University, Busan 606-791, South Korea
*corresponding author, E-mail: jeon@hhu.ac.kr

Abstract

We report an experimental and simulation study of terahertz (THz) band gap properties by using slits and grooves inside tapered parallel-plate waveguide (PPWG) with TEM mode. The Bragg and non-Bragg stop bands obtained from the slits (groove) embedded between the two surfaces of the PPWG plates can be used as notch filters and low-pass filters. When the air gap between the metal plates of the PPWG is controlled using a motor controlled translation stage or piezo-actuator, a tunable THz notch filter can be obtained.

1. Introduction

We use experimental measurements and FDTD simulations to investigate the THz band gaps properties by positioning metal slits at the center of the air gap or metal grooves on the surface of PPWG [1-3]. Recently, THz notch filter properties have been studied using single groove inside a PPWG [4,5]. The frequency of notch filter was very sensitive according to the air gap variation in the PPWG, leading to a feasibly tunable THz notch filter. We experimentally demonstrates tunable THz notch filter by adjusting the air gap using a piezo-actuator. The frequency of the tunable notch filter can be controlled by adjusting the DC voltage to the piezo-actuator.

2. Non-Bragg stop band : Tunable Notch filter

2.1. Experimental setup

Figure 1 schematically shows the tunable THz notch filter setup, which is composed of a tapered aluminum block and a flat stainless plate with a single groove on the surface [4]. The tapered aluminum block consists of a tapered area with a 3° angle and a flat area. A flat stainless plate, which is the lower part of the PPWG, has dimensions of 50 mm (length), 24 mm (width), and 100 μm (thickness). The single groove, fabricated by a micro-photochemical etching method, is embedded in the flat plate. The single groove is located 6.5 mm from the right edge, which is in the middle of the 13 mm flat surface of the upper plate. Because a vertically polarized (y-direction) THz field propagates to the PPWG, only TM modes exist. We prepared two types of single grooves. Sample A has a 70 μm wide and a 28 μm deep groove, and sample B has a 105 μm wide and a 40 μm deep groove, as shown in the image in Fig. 1(a,b). Figure 1(c) shows the definition of the depth and width of the groove. A motor-controlled translation stage is connected to a flat stainless plate to adjust the air gap of the PPWG, and the tapered aluminum plate is fixed. After measuring the notch filter properties, we replaced the motor-controlled translation stage with a piezo-actuator in order to adjust the air gap using a DC voltage source, as shown in Fig. 1.

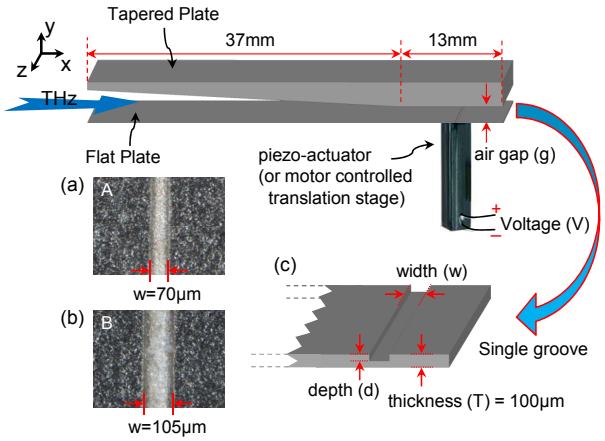


Figure 1 : Schematic diagram of the PPWG [4]. A single groove is embedded into the lower flat plate, which is attached to a piezo-actuator (or a motor-controlled translation stage). (a, b) Optical micrograph of the single groove. Samples A and B show 70 and 105-μm groove widths and 28 and 40-μm groove depths, respectively. (c) Expanded view of the groove.

2.2. Data analysis

Figure 2(a) and (b) show the amplitude spectra of the measured THz pulses with the 100- and 140-μm air gaps, respectively, for samples A (red) and B (black) where sample A has a 70 μm wide and a 28 μm deep groove, and sample B has a 105 μm wide and a 40 μm deep groove [4]. When the air gaps are increased, the resonance frequencies shift to lower frequency region and also the resonance width gradually becomes narrower. Like the property of the notch filter resonance in the TE_1 mode, that in the TEM mode is also excellent [5]. Unlike the TE_1 mode, which has a cutoff frequency, the notch filter resonances of the TEM mode can

be obtained for the entire frequency region by adjusting the air gap. Figure 2(c) shows the absorbance of the notch filter resonance with different air gaps ranging from 60 to 240 μm. The resonant frequency shifts to a low frequency range and the absorbance becomes small with an increase in the air gap. The resonant frequencies of the notch filter of sample A are 0.62 and 1.75 THz when the air gaps are 240 and 60 μm, respectively. The frequency tuning sensitivity (FTS) is given as Δf/Δg, where Δf is the resonance frequency shift and Δg is the air gap variation. Therefore, the FTS of the THz notch filter is 6.28 GHz/μm, which is compared to 1.36 GHz/μm obtained from the band gap [3].

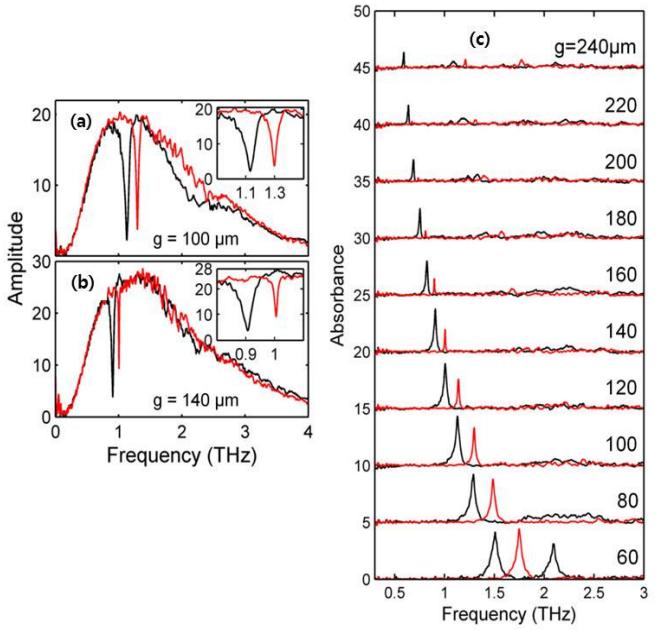


Figure 2 : THz notch filter properties by single groove inside PPWG [4]. (a) 100 μm air gap (sample A: upper red, sample B: lower black). (b) 140 μm air gap. (c) Absorbance spectra in samples A and B when varying the air gaps from 60 to 240-μm. Because the weight of the flat stainless plate is only 0.95 g, the piezo-actuator can support the plate. Instead of mechanical movement by the motor-controlled translation stage, the piezo-actuator makes its length longer and shorter by controlling the DC (or AC) voltage supplied to the piezo-actuator. Therefore, the motor-controlled translation stage is replaced by the piezo-actuator, which is 30-mm long (Piezomechanik, model No. PSt-HD 200/7x7/40), as shown in Fig. 1.

2.3. FDTD Simulation

Figure 3 shows the resonant frequency shift according to the difference in the air gap when it ranges from 60 to 240 μm for sample A and from 60 to 320 μm for sample B [4]. The solid lines indicate the numerical fitting lines, which are defined as

$$f_r(g) = \frac{c}{2\times\left[d_{eff}(g)+g\right]}, \qquad (1)$$

where c is the speed of light in a vacuum; g is the air gap; and d_{eff} is the effective groove depth, which is defined as (d – Δd(g)). Also, Δd(g) is the height from the groove bottom, which has a very weakly distributed THz field compared to the space above of the groove. Therefore, the height is not considered to determine the effective groove depth.

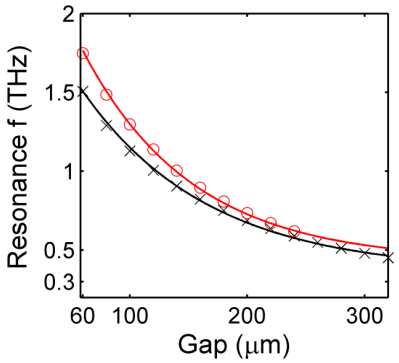


Figure 3 : The resonant frequency shift of the notch filters according to the air gaps [4]. The solid lines are numerical fitting lines. Red circles and black squares indicate sample A and B, respectively.

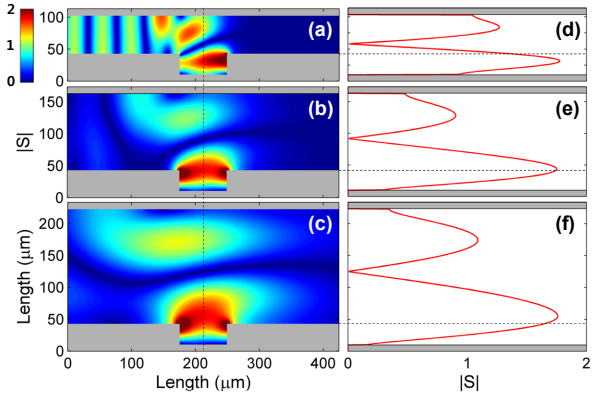


Figure 4 : Poynting vectors around the groove (w = 75, d = 32 μm). The air gap and resonant frequency are (a) 60 μm and 1.69 THz, (b) 120 μm and 1.1 THz, and (c) 180 μm and 0.8 THz, respectively. (d)-(f) Each figure indicates the amplitude of Poynting vectors along the vertical line which shows middle of the groove.

Figure 4 shows the distribution of Poynting vectors around the groove with the different air gap and resonance frequency. In this case, the THz field is not fully distributed on the groove bottom. Therefore the effective groove depth (d_{eff}) is introduced as indicated in the Eq. (1). The energy flux density is confined in the effective groove depth (space) and the air gap. The energy density of the other frequencies moves to the output of the PPWG; however, only the energy density of the notch filter frequency is tied-up at groove. This situation makes the notch filter resonate at the measured THz bandwidth. The process of building up the notch filter resonance by the single groove is identical to that of the single slit measurement, non-Bragg stop band [2]; the only difference is the THz field reflection by the groove bottom and the THz field passing through the slit. When the THz fields are reflected from the metal waveguide surface or the groove bottom, which are considered as perfect conductors in the THz frequency region, the images of the

THz fields exist inside the metal. According to image theory, the THz field pattern in the groove waveguide is identical to that in the folded THz field halfway along the horizontal center of the slit [1,3]. Therefore, the formation of notch filter resonance by the single groove can be explained in terms of the resonance of the single slit [2].

3. Bragg stop band : Low-pass filter

3.1. Experimental setup and FDTD simulation

The experimental setup is illustrated schematically in Fig. 5(a) [2]. The angle of the tapered part is 3°; it has twice the coupling coefficient of the cylindrical silicon lens used in PPWG. Moreover with no silicon lenses in the waveguide, multiple reflections are eliminated from the measurement. The total length of the flat surface of the TPPWG is k=6 mm. The protruded length of the stainless steel sheet in the tapered part is ℓ=7 mm, and this can separate the incoming THz beam into two parts. A THz beam propagating along slits with a period P inside the TPPWG has a Bragg stop band with strong resonance at a Bragg frequency

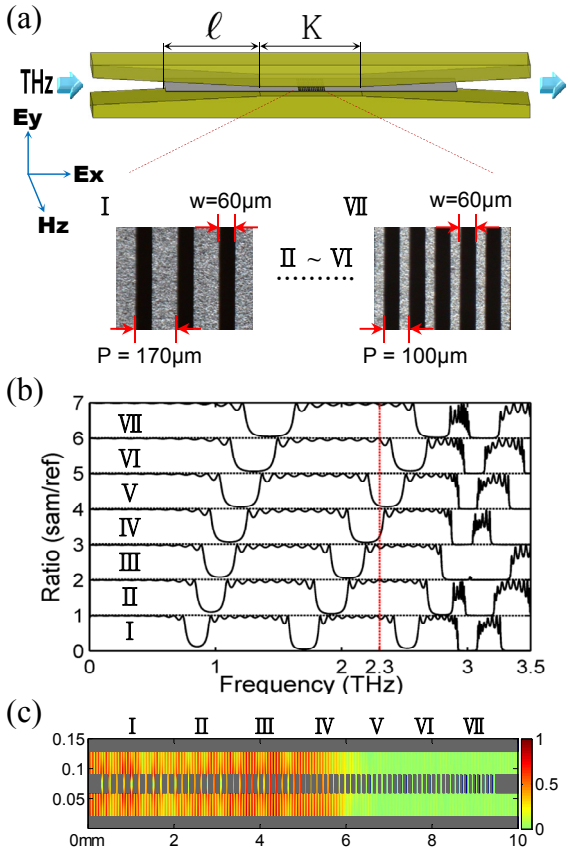


Figure 5 : (a) Diagram of TPPWG and slit images in region I and region VII. Areas from region II to region VI are not shown in the figure but these areas are continuously connected. (b) Bragg stop band positions in each region. The red vertical dashed line indicates 2.3 THz. (c) FDTD simulation of E field intensity distribution for 2.3 THz continuous wave source. [2]

Table 1. Dimensions of each region of the slit used in LPF [2]. Each region has 10 slits (N) and 60-μm width (w).

Region	I	II	III	IV	V	VI	VII
Period P [μm]	170	150	140	130	120	110	100
Width w [μm]	60						
Number of Slits N [ea]	10						

f_{Bragg} = mc/(2P), where m is an integer and c is the speed of light. The bandwidth of the Bragg stop band broadens as the period gets narrower at the Bragg stop band positions in the high frequency range. Using such characteristics, if slits with different periods are arrayed in a line on a metal sheet, an LPF can be implemented to completely eliminate the high frequency component after cutoff frequency. To design such an LPF, slits with equal width of 60 μm and 7 different periods of slit pattern were designed as shown in Table 1. Since each region has 10 identical slits, the total number of the slits is 70. Figure 5(a) shows images of some of the slits in region I and region VII; slits were made of stainless steel with a thickness of 30 μm. Figure 5(b) shows the FDTD simulation results for Bragg stop bands when the air gap is 38 μm. As shown in the Fig. 5(b), the first and second Bragg resonance frequencies corresponding to the slits of region I are located at 0.85 and 1.7 THz, respectively. The bandwidths of each Bragg stop band are 0.19 THz and 0.24 THz, where the bandwidths are measured at a width at 3 dB. The first and second Bragg stop bands of each of the 7 slit patterns are overlapped. Moreover, the first Bragg stop band of region VII (from 1.23 THz to 1.62 THz) and the second Bragg stop band of region I (from 1.58 THz to 1.82 THz) overlap. Only a THz field whose frequency range is below the first Bragg stop band of the slits of region I can propagate to the exit of the waveguide. Therefore, the characteristics of LPF depend on the first Bragg stop band of region I. The LPF can be predicted to have a 0.76 THz cutoff frequency, 55 dB power transmission in the cutoff region, and 84 GHz transition width (a drop from 90% to 10%) at the cutoff region. In order to confirm that the slits block the propagation of this particular THz component, FDTD simulation was performed using a THz continuous wave (CW) source. As shown in the red vertical dashed line in Fig. 5(b), a 2.3 THz CW source propagates through regions I, II, and III. However, the Bragg stop band of the slits of region IV includes 2.3 THz, which prevents the THz beam propagation along the air gap. Figure 5(c) displays a simulation with a 38-μm air gap and a 2.3 THz CW source. Region IV prevents the THz beam propagation to the higher regions.

3.2. Measurement : Low-pass filter

A THz beam propagating along slits with a period P inside a PPWG has a Bragg stop band with strong resonance at a Bragg frequency. The bandwidth of the Bragg stop band broadens as the period gets narrower at the Bragg stop band positions in the high frequency range. Using such characteristics, if slits with different periods are arrayed in a line on a metal sheet, an LPF can be implemented to completely eliminate the high frequency component after cutoff frequency. Figure 6(a) shows the amplitude of the output spectrum with cutoff frequency at 0.78 THz [2]. As

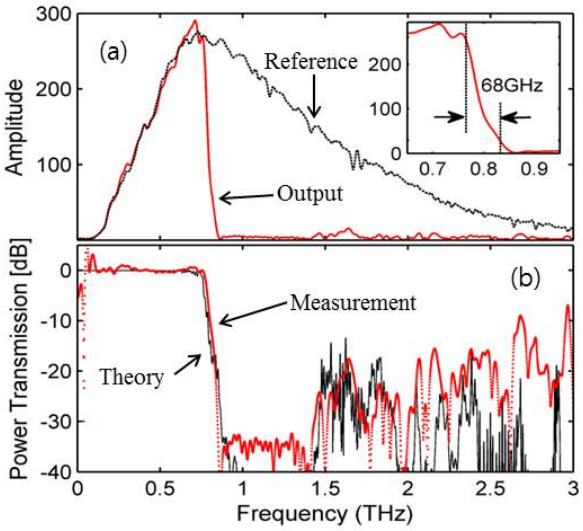


Figure 6 : (a) The spectra of the reference and output. The inset shows expended figure near the cutoff frequency. (b) Comparison of power Transmission in the measurement and FDTD simulation. [2]

shown in the inserted figure, the magnitude response changes from pass band to stop band. The transition width is about 68 GHz. The power transmission in the cutoff region of the LPF is measured at about 35 dB. The experimental result is in good agreement with the FDTD simulation, which is represented with a measurement as shown in Fig. 6(b).

4. Conclusions

We demonstrate a tunable THz notch filter and low-pass filter using groove and slit inside a PPWG with the TEM mode. When the air gap was controlled within the range of 60 to 240 μm for sample A, the resonant frequency of sample A changes from 1.75 to 0.62 THz. Therefore, the tunable sensitivity of the single notch filter is approached to 6.28 GHz/μm. The measured resonant frequencies of the notch filters were found to agree well with the calculations used to determine the effective groove depth. Moreover, we performed the LPF based on multiple Bragg stop bands using different slit period. The transition width of the cutoff is only 68 GHz and the cutoff region of power transmission is 35 dB.

Acknowledgements

This work was supported by the National Research Foundation of Korea (NRF) grant funded by the Korea government (MEST) (No. 2008-0062257 and No. 2010-0009070), and was supported by the Grant of the Korean Health Technology R&D Project; Ministry for Health, Welfare & Family Affairs of Korea (A101954).

References

[1] E. S. Lee, Y. B. Ji, and T.-I. Jeon, "Terahertz band gap properties by using metal slits in tapered parallel-plate waveguides," *Appl. Phys. Lett. Vol. 97(18)*, 181112, 2010.

[2] E. S. Lee, S. G. Lee, C. S. Kee, and T.-I. Jeon, Terahertz notch and low-pass filters based on band gaps properties by using metal slits in tapered parallel-plate waveguides, *Opt. Express,* Vol. 19, pp. 14852-14859, 2011.

[3] E. S. Lee, J. K. So, G. S. Park, D. S. Kim, and T.-I. Jeon, Terahertz band gaps induced by metal grooves inside parallel-plate waveguides, *Opt. Express,* Vol. 20, pp. 6116-6123, 2012.

[4] E. S. Lee and T.-I. Jeon, Tunable THz notch filter with a single groove inside parallel-plate waveguides, *Opt. Express,* Vol. 20, pp. 29605-29612, 2012.

[5] R. Mendis and D. M. Mittleman, Comparison of the lowest-order transverse-electric (TE_1) and transverse-magnetic (TEM) modes of the parallel-plate waveguide for terahertz pulse applications, *Opt. Express*, Vol. 17(17), pp. 14839-14850, 2009.

A bottom-up approach towards metamaterials and plasmonics

Plasmonic collective coherent radiance and collective resonance state at the loss compensation condition near metal nanoparticle

Vitaliy Pustovit1[1], Arkadiy Chipouline[2] and Augustine Urbas[1],

[1]Materials and Manufacturing Directorate, Air Force Research Laboratory,
Wright Patterson Air Force Base, Ohio 45433, United States
[2]Institute of Applied Physics, Friedrich Schiller University Jena, Max-Wien-Platz 1, D-07743 Jena, Germany
*corresponding author, E-mail: pustovit.vitaliy.ctr@wpafb.af.mil

Abstract

We present for the first time (to the best of our knowledge) a unified microscopic theory of the response of plasmonic nanoparticles assisted by optical gain media. Our approach combines the rigorous Mie scattering equations for the plasmonic structure and well known in laser physics density matrix formalism, allowing correct description of different relaxation and energy exchange channels in the system. We identify mechanism of plasmonic collective coherent radiance of the aggregate similar to conventional laser taking into account as well specific for the plasmonic resonator effects, i.e. energy relaxation into the dark modes. We demonstrate that the total loss compensation leads to the laser resonator type collective resonance states that could cause a stimulated emission.

1. Introduction

Radiation of an active molecule near a metal nanostructure supporting a surface or localized plasmon is attracting renewed interest due to possible biosensing and metamaterials applications [1]. While early studies mainly focused on fluorescence properties of the molecules (decay time, luminescent enhancement/inhibition) near rough metal films, recent advances in near-field optics and in chemical control of molecule- nanostructure complexes spurred a number of experiments on single metallic nanoparticles (NPs) optically coupled through the near fields with dye molecules or semiconductor quantum dots [2]. Emission of a photon by a molecule-NP aggregate involves several processes which have to be taken into account: Forster resonance energy transfer (FRET) from an excited molecule to the NP and back, irreversible energy relaxation of the electron oscillations in NP (ohmic losses), radiative and nonradiative molecule decay into environment (thermo bath), and FRET between the molecules surrounding NP. The two mentioned FRET mechanisms determine the scenario of the dynamics for the aggregate "molecules+NP". The first scenario assumes that the interaction between the molecules dominates over the influence of the NP, but NP enhances the coherence between the molecules. In this case the emission is dominated by three superradiant states with the same quantum yield as a single emitter, leading to a drastic reduction of ensemble radiated energy down to just thrice of that by a single emitter, the remaining energy being dissipated in the metal through subradiant states [3, 4]. This scenario can be called "Dicke Scenario" that underlines an importance of the interaction between the molecules for the collective state formation. We call the second scenario a "Laser Scenario", where the primary mechanism of the resulted cooperative emission is caused by the FRET between the molecules and plasmons rather than Dicke radiative coupling between the molecules. In this case the influence of the plasmon on the internal quantum dynamics of the molecules overcomes the interaction between the molecules, and NP plays a role of a resonator (in full analogy with a laser) which sets coherence on the quantum dynamics of the molecules. We establish a complete description of the optical response of the system "molecules+NP" based on Greens functions, which allows us to investigate high molecular coverage of metal nanoparticle with either regular or random distribution of dye molecules, and which is applicable for the both "Dicke" and "Laser" scenarios. Moreover, we included in the description an external resonance field, which can change the compound system dynamics qualitatively giving rise to a multistable operation [5]. The latter is important for applications, where the resonant field is used to read the system response. Based on the established description we focus our attention here on the "Laser scenario" for the cases of presence and absence of the external field.

2. The model

We study the optical response of an aggregate made of a single spherical nanoshell with silver core of radius ($R_c = 30\,\text{nm}$) covered with a silica layer ($\epsilon_r = 2.2$, and thickness h) and surrounded by N fluorescent dyes located on the silica surface at positions $\mathbf{r}_j$, with $j = 1, 2, ..N$ (we set origin $\mathbf{r} = \mathbf{0}$ at center), all at the same radial distance $R = R_c + h$ from the center [see Fig. 1]. The aggregate is illuminated by an incident plane wave with electric field E_{ext}. We assume that the aggregate has a spherical symmetry, with a uniform (regular or statistical) distribution of active molecules around the NP. In order to find a field generated/scattered by the aggregate, we have to describe coupled dynamics of NP and the molecules, which we denote as p_j. We assume that the molecules can be to

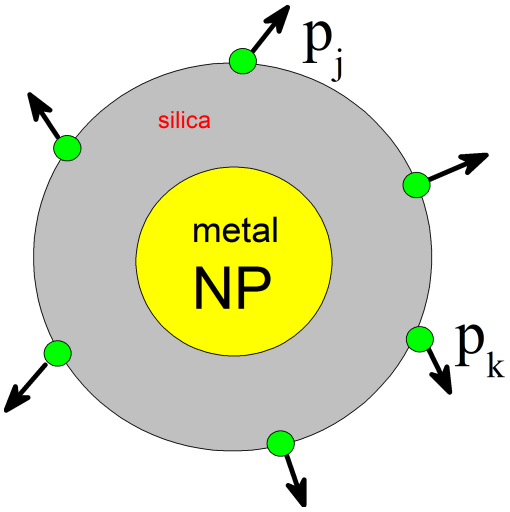


Figure 1: (color online) The aggregate made by one nanoparticle NP (nanoplasmonic sphere) and a layer of N dyes. Whole set of radiative and nonradiative coupling mechanisms between dyes and the nanoparticle is taken into account.

a first approximation described by a pumped two level system in the frame of the standard density matrix approach [6]. For the steady state operation mode and in the frame of the resonance approximation (which is sometimes called a rotating wave approximation, see [6]), the internal molecule dynamics is given by:

$$\tilde{\rho}_{12}\left[\frac{1}{\tau_2}+i(\omega-\omega_{21})\right]=\frac{i\mu_m A^* N}{\hbar},$$
$$\frac{(N-N_0)}{\tau_1}=\frac{i\mu_m\left[A\tilde{\rho}_{12}-A^*\tilde{\rho}^*_{12}\right]}{2\hbar},$$
$$N_0=\frac{W\tilde{\tau}_1-1}{W\tilde{\tau}_1+1},\quad \tau_1=\frac{\tilde{\tau}_1}{W\tilde{\tau}_1+1} \qquad (1)$$

Here ρ_{22}, ρ_{11} and ρ_{12}, ρ^*_{12} are the diagonal and non-diagonal elements, respectively; τ_2 and τ_1 are the constants describing phase and energy relaxation processes due to the interaction with a thermostat; $\omega_{21}=(E_2-E_1)/\hbar$ is the transition frequency between levels 2 and 1; W is the phenomenological pump rate, μ_m is the dipole moment of the molecule, A - is the amplitude of the local field at the point of the molecule $E=\frac{1}{2}(A(t)exp(-i\omega t)+A(t)^*exp(i\omega t))$. The field A is a sum of all fields acting on the molecule, namely the external field E_{ext}, the field from the NP E_{NP}, and the field from the other molecules $\mathbf{E}_{mol,i}=\sum_{i\neq j}^{N}\mathbf{E}_{mol,j}(\mathbf{r}_i)$. In order to find a total field we use standard Mie theory approach, namely we start from the Helmholz equation in microscopic form:

$$\nabla\times\nabla\times\mathbf{E}-\epsilon\frac{\omega^2}{c^2}\mathbf{E}=\frac{4\pi\omega^2}{c^2}\sum_{i=1}^{N}\mathbf{p}_j(\omega,|\mathbf{E}_j|^2)\delta(\mathbf{r}-\mathbf{r}_j) \qquad (2)$$

Here $\mathbf{p}_j(\omega,\mathbf{r}_j,|\mathbf{E}_j|^2)$ are the dipole moments of the molecules, is the dielectric constant of the metal for inside the NP and the dielectric constant of the dielectric layer and air outside respectively. Solution of this equation is the field at each point, including the points where the molecules are situated, and it is actually the field which affects the molecule internal quantum dynamics and which has to be substituted into 1. The expression for the solution of 2 has been found in [3]:

$$\mathbf{E}(\mathbf{r}_i,\omega)=\mathbf{E}_h(\mathbf{r}_i,\omega)$$
$$+\frac{4\pi\omega^2}{c^2}\sum_{j=1}\mathbf{G}(\omega,\mathbf{r}_i,\mathbf{r}_j,|\mathbf{E}_j|^2)\mathbf{p}_j(\omega,\mathbf{r}_j,|\mathbf{E}_j|^2) \qquad (3)$$

Here $\mathbf{E}_h(\mathbf{r}_i,\omega)$ is the solution of (2) without right side (homogeneous Helmholz equation) and is not zero in case of the presence of the external field E_{ext}. From 1 polarization of the molecule can be found straightforwardly:

$$\mathbf{p}_j(\omega,\mathbf{r}_j,|\mathbf{E}_j|^2)=\alpha_j(\omega,\mathbf{r}_j,|\mathbf{E}_j|^2)\mathbf{E}(\mathbf{r}_j,\omega),$$
$$\alpha_j(\omega,\mathbf{r}_j,|\mathbf{E}_j|^2)=\left(\frac{\mu_m}{\hbar}\right)^2\left[\tau_2^2(\omega_{12}-\omega)-i\hbar\tau_2\right]$$
$$\times\left[\frac{W\tau_1-1}{(1+\tau_2^2(\omega_{21}-\omega)^2(1+W\tau_1))+|\mathbf{E}_j|^2/|\mathbf{E}_s|^2}\right] \qquad (4)$$

Solution (4) accounts for all molecule-nanoparticle interactions (multipolar) as well as molecule-molecule interactions. The dyadic Green's function $\mathbf{G}(\omega,\mathbf{r}_i,\mathbf{r}_j,|\mathbf{E}_j|^2)=(1-\delta_{ij})\mathbf{G}_0(\omega,\mathbf{r}_i,\mathbf{r}_j,|\mathbf{E}_j|^2)+\mathbf{G}_{sc}(\omega,\mathbf{r}_i,\mathbf{r}_j,|\mathbf{E}_j|^2)$ (see Ref.[3]), where represents the electric field at r_i due to an electric dipole at r_j. The symbol δ_{ij} is the Kronecker delta and, accordingly, the term G_0 accounts for the free space (direct) when $j\neq k$, and the term G_{sc} represents the NP scattered contribution. Substituting 4 into 3 we get:

$$\mathbf{E}(\mathbf{r}_i,\omega)=\mathbf{E}_h(\mathbf{r}_i,\omega)+\sum_j\mathbf{T}(\omega,\mathbf{r}_i,\mathbf{r}_j,|\mathbf{E}_j|^2)\mathbf{E}(\mathbf{r}_j,\omega),$$
$$\mathbf{T}(\omega,\mathbf{r}_i,\mathbf{r}_j,|\mathbf{E}_j|^2)=\frac{4\pi\omega^2}{c^2}\mathbf{G}(\omega,\mathbf{r}_i,\mathbf{r}_j)\alpha_j(\omega,\mathbf{r}_j,|\mathbf{E}_j|^2), \qquad (5)$$

System (5) is the master system of equations, which is suggested to describe the field distribution produced by the considered aggregate.

3. "Laser scenario" without external field

First, consider the situation without any external field, which means $\mathbf{E}_h(\mathbf{r}_i,\omega)=0$:

$$\mathbf{E}(\mathbf{r}_i,\omega)=\sum_j^N\mathbf{T}(\omega,\mathbf{r}_i,\mathbf{r}_j,|\mathbf{E}_j|^2)\mathbf{E}(\mathbf{r}_j,\omega),$$
$$\mathbf{T}(\omega,\mathbf{r}_i,\mathbf{r}_j,|\mathbf{E}_j|^2)=\frac{4\pi\omega^2}{c^2}\mathbf{G}(\mathbf{r}_i,\mathbf{r}_j,\omega)\alpha_j(\omega,\mathbf{r}_j,|\mathbf{E}_j|^2), \qquad (6)$$

Physically, this corresponds to the nanolaser, and the solution depends critically on the level of pump W. In case of $W\tau_1<1$ the imaginary part of the polarizability of the molecule corresponds to losses, and system (6) has only one trivial solution $\mathbf{E}(\mathbf{r}_i,\omega)=0$. The case $W\tau_1>1$ nevertheless does not guarantee the nontrivial solution, because

of the nontrivial solution (stable nanolaser generation) assumes compensation of all losses in the system: relaxation losses (which is taken into account by τ_1), losses in the metal of the NP (which are taken into account by the imaginary part of the dielectric constant of the NP), and radiative losses, which are taken into account by the Mie scattering formalism. It is important to note, that the developed here approach takes into account one more mechanism of losses, namely energy transfer between to the modes. The NP has set of eigen modes, which could be radiative (with the nonzero dipole moment) and nonradiative (with zero dipole moment). The energy transfer from the radiative to the nonradiative modes evidently increases the total losses to be overcome and hence increases a pump threshold for the nanolasers. Investigation of this problem in details requires more comprehensive analysis and is left for future publications.

The first equation in (6) can be rewritten as:

$$\left[\hat{\mathbf{I}} - \sum_j^N \mathbf{T}(\omega, \mathbf{r}_i, \mathbf{r}_j, |\mathbf{E}_j|^2)\right] \mathbf{E}(\mathbf{r}_i, \omega) = 0 \qquad (7)$$

and has a nontrivial solution only in case of zero determinant:

$$det\left[\hat{\mathbf{I}} - \sum_j^N \mathbf{T}(\omega, \mathbf{r}_i, \mathbf{r}_j, |\mathbf{E}_j|^2)\right] = 0 \qquad (8)$$

which is basically equivalent to two equations:

$$Re\left(det\left[\hat{\mathbf{I}} - \sum_j^N \mathbf{T}(\omega, \mathbf{r}_i, \mathbf{r}_j, |\mathbf{E}_j|^2)\right]\right) = 0,$$
$$Im\left(det\left[\hat{\mathbf{I}} - \sum_j^N \mathbf{T}(\omega, \mathbf{r}_i, \mathbf{r}_j, |\mathbf{E}_j|^2)\right]\right) = 0, \qquad (9)$$

for unknowns ω and $|\mathbf{E}_j|^2$. Two equations (9) evidently cannot determine the all $|\mathbf{E}_j|^2$; the number of unknowns is equal to the number of the molecules. Physically it would correspond to the conclusion, that there are many solutions for $|\mathbf{E}_j|^2$ which could satisfy (9), which means that the steady state of the system "moleculs+NP" corresponds to the permanent jumps between the possible redistribution of the various combinations of the $|\mathbf{E}_j|^2$, which satisfy (9). We assume here for simplicity, that all molecules experience the same field, e.g. $|\mathbf{E}_j|^2 \equiv |\mathbf{E}_0|^2$; in this case the intensity in equations (9) can be taken as a parameter. It is worth noticing that the algorithm of consideration is the same as for the problem of laser generation, or more recently appeared the problem of spaser steady state operation [7]. In the following we will restrict our analysis to the case of dyes with identical radial polarizability. For that particular case the operator elements $\mathbf{G}(\omega, \mathbf{r}_i, \mathbf{r}_j, |\mathbf{E}_0|^2)$ are taken in the near-field approximation and can be represented analytically (all molecules are oriented perpendicular to the surface of the NP, as in Ref.[3]):

$$G(\omega, r_i, r_j, |\mathbf{E}_0|^2) = -\frac{(1-\delta_{ij})\eta_{ij}}{r_{ij}^3} + \sum_l \frac{\alpha_l(\omega)(l+1)^2 P_l(\cos\gamma_{ij})}{r_j^{l+2} r_i^{l+2}}$$
$$+i\frac{2}{3}k^3 \cos\gamma_{ij}\left[1 + 2\alpha_1(\omega)(\frac{1}{r_j^3} + \frac{1}{r_i^3}) + \frac{4|\alpha_1|^2}{r_i^3 r_j^3}\right]. \qquad (10)$$

Here α_l represents the lth multipolar polarizability of the nanoshell with metal core and dielectric shell and α_1 is a polarizability of nanoshell in the dipolar approximation $l = 1$; $P_l(\cos\gamma_{ij})$ denotes the Legendre polynomial of order l, where γ_{ij} is the angle between dye locations $\mathbf{r}_j$ and $\mathbf{r}_i$, whereas $\eta_{ij} = 1 + \sin^2(\gamma_{ij}/2)$.

4. "Laser scenario" with external field

For the case of an external field under the same approximations which have been assumed for the elaboration of (10):

$$\mathbf{E}(\mathbf{r}_i, \omega) = \mathbf{E}_h(\mathbf{r}_i, \omega) + \frac{4\pi\omega^2}{c^2}\alpha(\omega, \mathbf{r}_j, |\mathbf{E}_0|^2) \times \sum_j^N \mathbf{G}(\omega, \mathbf{r}_i, \mathbf{r}_j, |\mathbf{E}_0|^2)\mathbf{E}(\mathbf{r}_j, \omega), \qquad (11)$$

Solution of (11) can be written in terms of eigen vectors/eigen functions:

$$\mathbf{E}(\mathbf{r}_i, \omega) \sim \sum_{n=1}^N \frac{|q_n\rangle \ \langle q_n|\mathbf{E}_h(\mathbf{r}_i, \omega)\rangle}{(\omega - \omega_{12} - \Delta\omega_n) + i(1/\tau_2 - \Delta\gamma_n)} \qquad (12)$$

where $|q_n\rangle$ are eigenvectors of the matrix $\hat{G}$. The mostly pronounced modes are selected by the conditions of zeroing of the real and imaginary parts of the denominator of (12):

$$\omega = \omega_{12} + \Delta\omega_n(\omega, |\mathbf{E}_0|^2),$$
$$\Delta\gamma_n(\omega, |\mathbf{E}_0|^2) = 1/\tau_2 \qquad (13)$$

Solution of (13) as like as in previous case of absence of the external field gives the resonant frequencies and intensity at the points of molecules (remember that the intensity is assumed to be the same for all molecules). In contrast with the solution of (9), system (13) is expected to have one or several possible solutions.

Acknowledgement

This work was supported in part by the European Science Foundation short visit grant "New Approaches to Biochemical Sensing with Plasmonic Nanobiophotonics" and AFRL Materials and Manufacturing Directorate Applied Metamaterials Program.

References

[1] N. I. Zheludev, The road ahead for metamaterials, *Science* 328: 582–583, 2010.

[2] M. A. Noginov, G. Zhu, A. M. Belgrave, R. Bakker, V. M. Shalaev, E. E. Narimanov, S. Stout, E. Herz, T. Suteewong and U. Wiesner, Demonstration of a spaser-based nanolaser, *Nature* 460: 1110–1113, 2009.

[3] V.N. Pustovit and T. V. Shahbazyan, Plasmon-mediated superradiance near metal nanostructures, *Phys. Rev. B* 82: 075429, 2010.

[4] V.N. Pustovit and T. V. Shahbazyan, Cooperative emission of light by an ensemble of dipoles near a metal nanoparticle: The plasmonic Dicke effect, *Phys. Rev. Lett.* 102: 077401, 2009.

[5] E. S. Andrianov, A. A. Pukhov, A. V. Dorofeenko, A. P. Vinogradov, and A. A. Lisyansky, Forced synchronization of spaser by an external optical wave, *Optics Express* 19: 24849–24857, 2011.

[6] A. Chipouline, S. Sugavanam, V. A. Fedotov, A. E. Nikolaenko, Analytical model for active metamaterials with quantum ingredients, *J. Opt.* 14: 114005–114013, 2012.

[7] M. Stockman, Spaser action, loss-compensation, and stability in plasmonic systems with gain,*Phys. Rev. Lett.* 106: 156802, 2011.

Plasmonic nanocomposites

Enhancement of GaAs/InGaAs Quantum Well Emission by disordered Gold Nanoparticle Arrays

Hongwei Gao[1], Jinghua Teng[2], SooJin Chua[1,2], Ning Xiang[1*]

[1] Department of Electrical and Computer Engineering, National University of Singapore, Singapore, Singapore 117576, Singapore
[2] Institute of Materials Research and Engineering, Singapore, Singapore 117602, Singapore
*corresponding author, E-mail: elexn@nus.edu.sg

Abstract

Coupling effect of locallized surface Plasmon (LSP) with InGaAs/GaAs QW emission is demonstrated experimentally. The LSP resonance is generated by disordered Au nanodisk arrays on the InGaAs/GaAs QW surface. More than 2-fold QW PL enhancement is observed. Theoretical simulations also indicated that the disorder of Au structure enlarged the angle for which light can be radiated out. The bigger angle is of benefit to enhance PL intensity.

1. Introduction

Recently large amount of attention has been attracted to the effects of field enhancement in the vicinity of metallic nanostructures. It is well understood that this field enhancement is caused by the collective oscillations of electrons in metals structured in the subwavelength scale, which is called localized surface plasmon (LSP). LSP can induce local optical fields which may exceed the average optical fields of the incident light by orders of magnitude. It has been demonstrated that various optical effects can be enhanced near the resonantly excited metal nanoparticles. Single metallic nanoparticle was reported to be able to enhance the nearby electrical field and the photoluminescence intensity of single active molecule [1]. However, the effect caused by single metallic nanoparticle is relatively weak. Subsequently, ordered arrays of metallic nanoparticles with a separation comparable to the free space wavelength of radiation has been predicted [2] and observed [3,4] with the spectrally narrow directional extinction resonances, which would be useful for high sensitivity applications [5, 6]. Recently, the ordered arrays of metallic nanoparticles were also applied to enhance photoluminescence from optoelectronic devices, especially in the visible range, and obtained great progress [7]. However, for the near infrared range, for example, 980 nm LEDs, there still lacks the results. Here, investigation of LSP effects generated by ordered and disordered Au nanodisk arrays on InGaAs/GaAs QW structures is reported. More that 2-fold enhancement of PL has been observed on the sample with the disordered Au nanodisks.

For fluorescence enhancement applications, closely spaced ordered arrays is a significant disadvantage since the energy from the excited active layer is coupled into "dark modes" and gets dissipated there. For the case of a periodic structure with a square lattice, Khurgin and Sun [8] has indicated theoretically that the modes with $q<2\pi/\lambda$ (less than the free space wavevector) are radiative (bright) and can be coupled out at the angle of θ (q) $=\sin^{-1}(q\lambda/2\pi)$, where q is wavevector and λ is wavelength in free space. Besides the bright modes, other modes are the nonradiative or dark modes which cannot be coupled outside. When some degree of disorder is introduced to the lattice, LSP modes mixing will occur, which makes partial dark modes to become bright modes. We have observed this effect experimentally, and in this paper we report the direct evidence for this disorder effect.

2. Experiment

In our experiments, three samples were studied. Sample A was $InGa_{0.18}As_{0.82}$/GaAs quantum well (QW) grown by molecular beam epitaxy technique, which consisted of 12 nm $In_{0.18}Ga_{0.82}As$ (herein after referred as InGaAs) well and 20 nm GaAs cap layer. Sample B was constructed by disordered Au structure fabricated on the surface of the as grown InGaAs/GaAs QW, and Sample C was ordered Au nanodisk arrays on the top of as grown InGaAs/GaAs QW. Laser interference lithography (LIL) was employed to pattern the Sample B and the Sample C. Two times exposure process was used to generate square lattice of photoresist. The lattice constant can be controlled by laser wavelength

and the angle between incident beam and reflected beam. Near circular openings of photoresist were formed due to the surface tension after development. Au was deposited on the patterns and Au disks were formed after lift-off process. In our process, there exists a great opportunity to fabricate disordered Au nanostructures because the residual photoresist after development can affect the disk formation. Therefore, the disordered Au nanodisks (Sample B) were formed by directly depositing 10 nm Au to the patterns generated by the LIL. The nearly ordered Au disks (Sample C) were formed on the photoresist patterns of which O_2 RIE treatment was performed before Au deposition. Fig.1a and Fig.1b show SEM images of Sample B and Sample C, respectively. It is observed that disordered Au nanodisk arrays both in shape and position were formed on top of the InGaAs/GaAs QW surface for sample B, while the nearly ordered Au nanodisk arrays were formed for Sample C. The coverage of the Au nanodisks (area ratio to the underneath GaAs surface) for sample B and Sample C are 14% and 44% respectively.

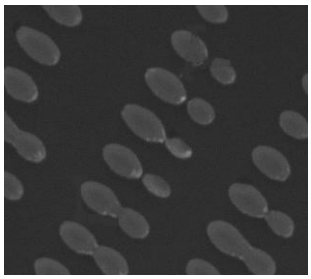


Figure 1a The SEM image of random Au nanodisk arrays for Sample B

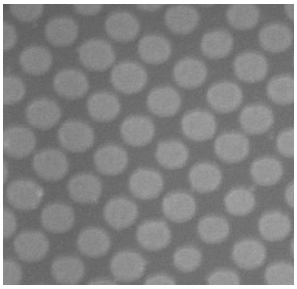


Figure 1b. The SEM image of ordered Au nanodisk arrays for Sample C

The reflectance spectrum was measured by a UV-IR microspectrophotometer from normal incidence. A commercial RPM2000 rapid photoluminescence mapper was employed to collect the PL signal.

3. Results and Discussion

Fig. 2 shows the PL spectra from Sample A (blue curve), Sample B (black curve), and Sample C (red curve) measured at room temperature. For Sample A, the QW emission peak was observed at 993 nm. Strong enhancement of the QW PL was observed for Sample B. The peak intensity increased to 2.02-fold compared to that of Sample A, with QW emission peak wavelength blue-shifted to 982 nm. However, for the Sample C, the QW emission peak intensity decreased to almost 10% of that of Sample A, and its peak wavelength blue-shifted to 986 nm.

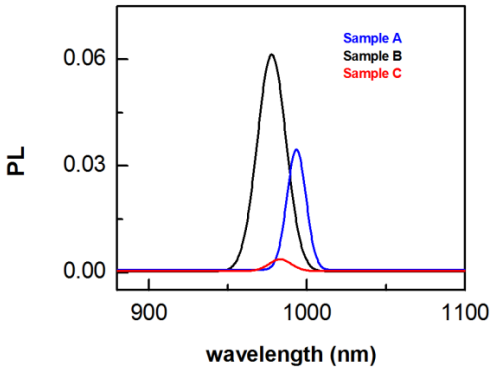


Figure 2 PL spectra of Sample A (blue curve), Sample B (black curve), and Sample C (red curve)

If we consider the surface emission area, for sample B, whose area ratio of Au nanodisk to the underneath GaAs surface was ~14%, both of the excitation and emitting light would be reduced to 14% of that of Sample A. Therefore, the real enhancement of PL for the sample B should be more than 2.02 fold. For Sample C, of which area ratio was 44%, would reduce to 44% of that of Sample A. However, the peak intensity of the InGaAs QWs emission from Sample C decreases nearly 90%, and is about 10% of that of Sample A. The PL intensity difference may be attributed to the coupling effect between QW emission and LSP. The exciting energy in the QW is transferred into the LSPs mode in the Au nanostructure if the energy of LSPs is close to the band gap energy of InGaAs QW. It leads to a hybridized excitation. First, the excited electron-hole pairs generated in the QW relaxes by emitting energy into LSP modes. This LSP resonance energy coupling mode subsequently offers a large density of states with a fast coupling rate. It provides a fast path for electron-hole recombination. The energy can be coupled to both LSP bright modes and LSP dark modes. However, only those coupled to the LSP bright modes can be radiated out in the form of light. Those coupled to LSP dark modes would be thermally dissipated. Therefore, during this process, not only the degree of localization of an average SP mode for a given wavelength plays an important role, but also the degree to which the light can be extracted out by bright mode [8] is of importance.

To verify the enhancement mechanism, measurement of reflectance spectrum for Sample B and Sample C were conducted. Fig.3 shows the experimental results. A broad dip is observed from 800 nm to 1200 nm for Sample B (black curve), while a relatively narrow and deep dip is clearly seen from 900 nm to 1100 nm for Sample C (red curve). The reflectance spectra reveal that around the InGaAs QW emission peak wavelength (993 nm), the higher field intensity was confined by Sample C. This would obtain an efficient coupling between LSP and QW emission to enhance the QW PL intensity. However, our experiment shows the QW PL intensity from Sample C decreased

dramatically, the opposite to our expectation. This may be attributed to the greater interparticle coupling between more closely spaced Au nanoparticles which drew the enhanced field into the lateral gaps between Au nanoparticles, and thus less light was extracted from the sample surface. If only consider the density of state, there would be lower PL intensity can be collected for Sample B. However, the random Au structure induces the larger angle of bright mode LSP which allowed more light to be radiated out. In the case of Sample B, due to the disorder, the dispersion relation became $\omega_q=\omega_0+\Delta\omega[\cos(q_x a)+\cos(q_y a)]/4$, where ω_0 is the isolated LSP resonance frequency, and $\Delta\omega=4\omega_0 r^3/a^3$ is a LSP bandwidth, *a* is the lattice constant, *r* is the size of Au particle. In our experiment, the disorders of both particle size and shape of Sample B can cause the mixing of LSP modes with different wavevectors, which broaden the resonance dip. With the spreading out of LSP modes, the angular spread of the light emitted by the array can be estimated roughly as $\Delta\theta\sim\lambda\Delta q/2\pi$. More PL light can be emitted out with the increased angle for bright mode.

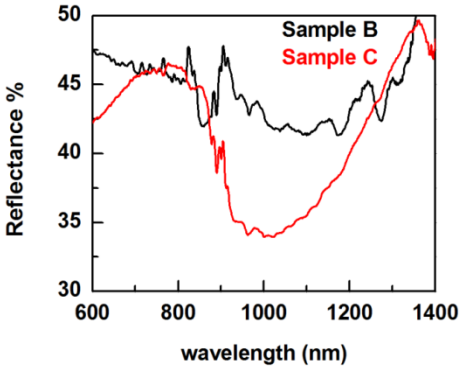


Fig. 3. Reflectance spectrum of Sample B (black curve) and of Sample C (red curve)

In order to obtain further support on our speculation, numerical simulation was performed using finite-difference time-domain (FDTD) software, Lumerical. The geometry used for this three-dimensional simulation was based on SEM images for Sample B and Sample C. Electrical dipole (centre at 993 nm, span of 60 nm), representing the QW emission, was placed to 20 nm below the surface of GaAs, and was acted as light source in this system. Light intensity in the center plane of Au structures and in the plane of 100 nm above the Au structures for both samples were monitored to observe how much light that can be emitted out. The far field projections for both samples were also collected to see the angular distribution of the collected signal. Fig.4 shows the simulated spectra of electrical field's intensity varies with wavelength in different planes for both samples. Comparing the electrical field's intensity in the plane of Au structure for Sample B and Sample C (black curve in Fig. 4a and Fig. 4b), we can see that more light are confined in the plane of Au structure for Sample C, which agrees well with our speculation. It is observed from Fig 4a that around half of the energy in the plane of Au structure was radiated out to free space for Sample B. From Fig 4b, less than 5% of energy got radiated out for Sample C. Although high electrical field was confined by the Au structure for Sample C, the majority of light were consumed in lateral direction due to the interparticle coupling between the closely spaced Au particles, which is the disadvantage for coupling of LSP with QW emission [9]. Insets of Fig. 4a and Fig.4b show the far field projections for Sample B and Sample C respectively. It is observed that the angle of the bright mode for Sample B is 10 degree bigger than that for Sample C, and it would allow more energy to be radiated out for Sample B. Thus, we believe that the enhancement of the PL intensity for Sample B is indeed caused by the randomness of Au structure. Further investigation on the carrier decay dynamics by time resolved PL peak intensity decay measurement will be carried out and reported elsewhere.

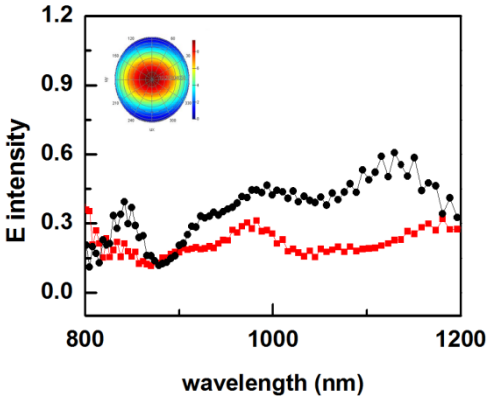


Figure 4a Spectra of electric field intensity varies with wavelength in the plane of Au structure (black curve) and 100 nm above the Au structure (red curve) for Sample B, inset is the far field projection for Sample B

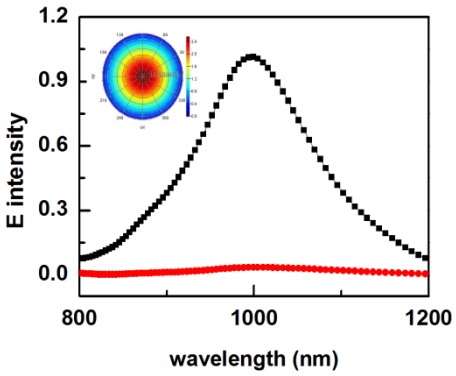


Figure 4b Spectra of electric field intensity varies with wavelength in the plane of Au structure (black curve) and 100 nm above the Au structure (red curve) for Sample C, inset is the far field projection for Sample C

4. Conclusions

In conclusion, we have demonstrated the impact of disorder of Au nanoparticle arrays on the LSP enhancement in InGaAs/GaAs QW emission. LSP bright mode is enlarged

and the degree of LSP coupling to be extracted to the outside of the sample is significantly enhanced by the disorder. With the disordered Au nanoparticle arrays, more than 2 fold of PL enhancement has been achieved. To our best knowledge, this is the first report on the PL enhancement from InGaAs/GaAs QWs by LSP generated by a disorderly distributed metallic structure.

Acknowledgements

This work is supported by Singapore Ministry of Education (grant number MOE2009-T2-1-086).

References

[1] G.Sun, J.B.Khurgin, R.A.Soref, Applied Physics Letter, 94,101103, (2009)

[2] S. Zou, N. Jarel, and G. C. Schatz, J. Chem. Phys. 120, 10871 (2004).

[3] Y. Chu, E. Schonbrun, T. Yang, and K. B. Crozier, Appl. Phys. Lett. 93,181108 (2008).

[4] B. Augui é and W. L. Barnes, Phys. Rev. Lett. 101, 143902 (2008).

[5] S. A. Maier, M. L. Brongersma, P. G. Kik, and H. A. Atwater, Phys. Rev.B 65, 193408 (2002).

[6] G. A. Wurtz, J. S. Im, S. K. Gray, and G. P. Widerrecht, J. Phys. Chem. B107, 14191 (2003).

[7] Cheng Hsueh Lu, Chia Chun Lan, Yen Lin Lai, Advanced material, 21,4719-4723, (2011)

[8] J.B.Khurgin, G.Sun, Applied Physics Letter 94,221111, (2009)

[9] Julie S.Biteen, Luke A. Sweatlock, J. Phys. Chem. C, 111, 13372-13377, (2007)

Tunable metamaterials and plasmonics devices

Plasmonic Waveplate: Incident Polarization Modulation

Shan Huang [1], Jie Li[1], Feng Lin[1], Zheyu Fang[1,*], and Xing Zhu[1, 2,*]

[1]School of Physics, State Key Laboratory for Mesoscopic Physics, Peking University, Beijing 100871, China

[2]National Center for Nanoscience and Technology, Beijing 100190, China

[*]zhyfang@pku.edu.cn; zhuxing@pku.edu.cn

Abstract- We demonstrate that the rectangular nanohole arrays perforated in a 100 nm gold film can perform to tune polarization direction of the transmitted light with maximum rotation angle of about 30 degrees. Theoretical analysis with the three-dimensional finite-difference time-domain simulations indicate this phenomenon is attributed to the excitation of the surface plasmon wave on the gold film surface and the resonance of localized surface plasmon in the hole. With multiple plasmon resonances, the plasmonic waveplate can realize a multi-wavelength polarization modulation. Our results may be useful to understanding the physical mechanism of enhanced plasmon mediated transmission and potential applications in plasmonic optical components.These instructions provide you with the basic guidelines for preparing the 2-page summary for META. An abstract (limited to 80 words max) should appear on the top of the page, after the title of the paper in chapter titled "Abstract" (without chapter number), after the names of the authors and the contact information of the corresponding author.

1. Introduction

Surface plasmon polaritons (SPPs) are electromagnetic surface waves exist at the interface of dielectric and metal layers with high field confinement and enhancement [1]. SPPs are sensitive to the localized environment, which have many applications for nanophotonics device by realizing optical manipulations with metal nanostrcutures, such as field enhanced nanoscale focusing[2-4], plasmonic waveguide [5-7], optical nano-antenna [9-11], and plasmonic photodetector and transistor [11-14].

Extra-ordinary optical transmission (EOT), a phenomenon that the optical transmission efficiency can be enhanced by periodic nanostrcutures, is a typical phenomenon of the SPPs induced optical manipulation [15, 16]. EOT in periodic nanohole arrays exhibits strong wavelength dependence, which has been used as plasmonic color filter [17, 18]. Since SPPs can be only excited by the incident light with the TM polarization, the polarization of the incident light is an important factor to influence the EOT properties, especially in the anisotropic nanostructures, such as elliptical hole arrays [19-21], rectangular hole arrays [22,23], and circular hole arrays with quadrate periodicity [24]. For elliptical hole arrays, the transmission spectrum shows different peaks for two orthogonal linear polarization of the incident white light [21]. For the quadrate hole arrays, the transmission efficiency of the light and the ratio between transmission efficiencies of horizontal and vertical polarized light can be continuously tuned [24]. Besides the transmission intensity, the transmission polarization was also reported can be modulated in the process of EOT by using bull's eye and nanoslit structure, which can be explained as the phase change of the excited SPP waves. [25, 26]. However, the rotation angle is limited by the nanostructure geometry and incident polarization, and the principle of this kind transmission polarization tuning is still unclear, which hampers its application for the future optical waveplate and polarizer device.

In this work, we experimentally demonstrate and theoretically calculate a plasmonic waveplate based on different Au nanohole arrays. We find the transmission polarization can be effectively rotated relative to the incident light and can be tuned with various nanostructure geometries. A theoretical analysis proves that this kind polarization rotation is caused by the different transmission efficiencies of longitudinal and transverse SPP modes. Further with the finite-difference time-domain (FDTD) simulations, this plasmonic nanohole configuration is found can have a potential application for the optical wavelength selection.

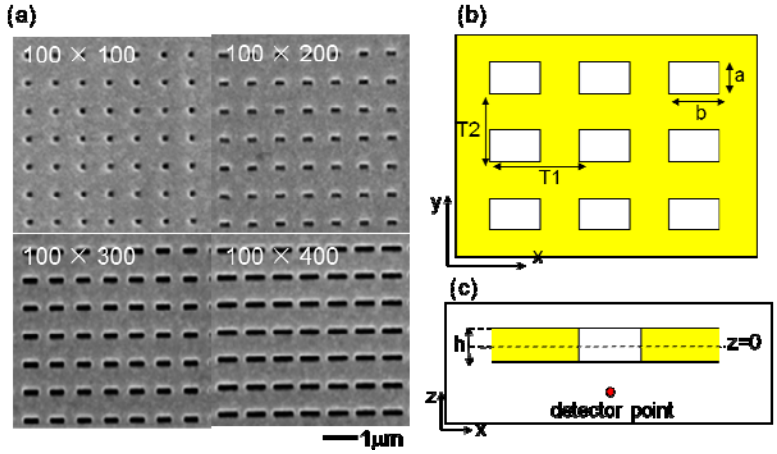


Fig. 1. (a) Scanning electron microscopy images of nanohole arrays with different aspect ratio (100 nm × 100 nm, 100 nm × 200 nm, 100 nm × 300 nm, and 100 nm × 400 nm); (b) Schematic drawing of a free-standing gold film perforated with rectangular holes. The thickness of the gold film is *h*. The hole has a cross section of *a* × *b*. The periods of the hole array are T1 and T2 in *x* and *y* axis, respectively; (c) A cross section of the a single unit cell of the hole array. The electric field is detected at the point 100 nm below the gold film.

2. Sample preparation and FDTD simulation

A gold film with 100 nm thickness was deposited by thermal evaporation on a quartz substrate. The 20 × 20 quadrate nanohole arrays were fabricated with focused ion beam (FIB) milling method (NOVA 200, FEI). Figure 1(a) shows the scanning electron microscopy (SEM) images of the hole arrays with different aspect ratio. The period of the array was fixed at 600 nm in the transverse and longitudinal directions (corresponding to x and y axis in the Fig. 1(a)). The incident light polarization was controlled by a polarizer combined with a half waveplate as a polarization controller. A linear polarized semiconductor laser beam with a wavelength of 671 nm passed through the polarization controller and then focused onto the sample by using a 10 × microscope objective. The output light pass through a polarizer and then collected by an optical fiber. The intensity of the transmission was recorded by an avalanche photo detector (APD).

The finite-difference time-domain (FDTD) simulations were also applied to analyze the experimental results. The model of the simulation is shown in Fig. 1(b). A free-standing perforated gold film is placed in the middle of the space. The relative dielectric function of the gold is given by the modified Debye model [27]. The incident polarization angle is defined as the angle between the polarization orientation and the *x* axis. The x and y component of the transmission electric field are detected at a point 100 nm below the gold film, as illustrated in Fig. 1(c). Therefore, the transmission polarization angle is determined by $\theta'=arctan(E_x/E_y)$.

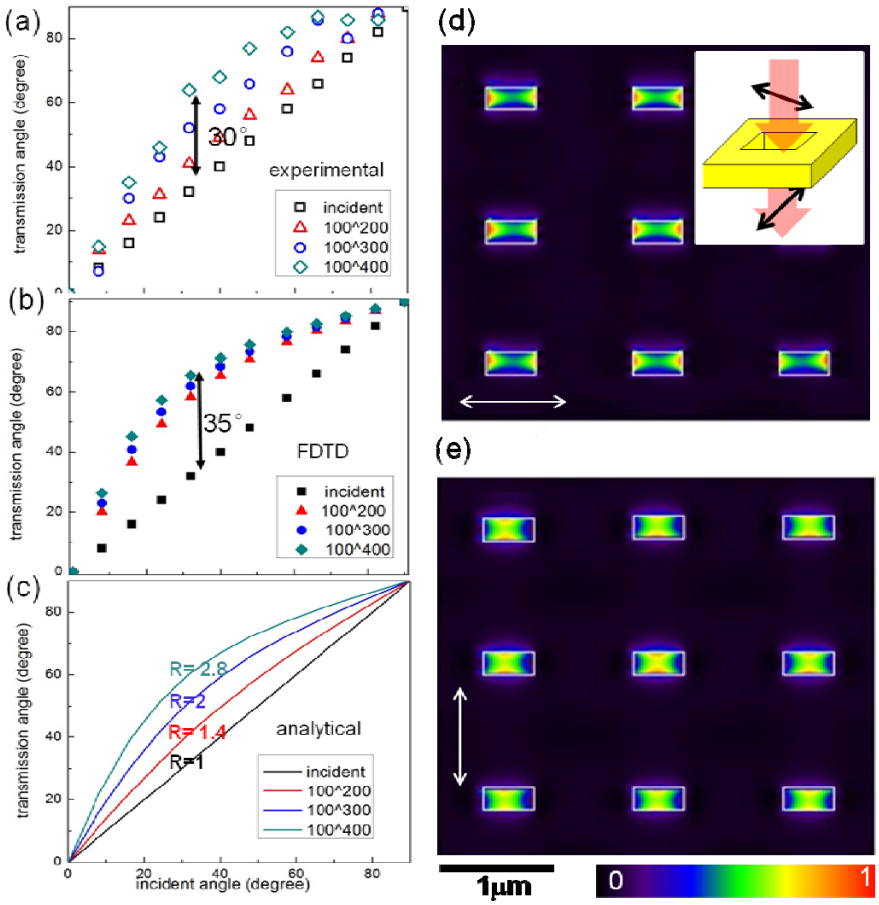


Fig. 2. (a) The experimental measured transmission polarization angle θ as a function of the incident light polarization angle θ for hole arrays with different aspect ratio. The maximum rotation angle is about 30° occurring on 100 nm × 400 nm hole arrays; (b) The FDTD simulation results for the corresponding hole arrays, which agree well with the experimental results. (c) The analytically calculated results. (d-e) FDTD simulated electric field distributions of LSP modes resonance in transverse (d) and longitudinal (e) directions.

3. RESULTS AND DISCUSSION

The nanohole arrays act as a plasmonic waveplate for the transmitted light shows an obvious polarization rotation relative to the incident light, as shown in Fig. 2(a). The rotation angle defined as the polarization direction difference between the incident and transmitted light ($\Delta\theta=\theta-\theta'$). For the rectangular nanohole array, we find when increasing θ from 0° to 90°, the $\Delta\theta$ first increases and then decrease with a maximum value obtained around $\theta=45°$. Moreover, under the same incident polarization direction, the rotation angle $\Delta\theta$ can achieve a maximum value about 30° when increases of the nanohole's aspect ratio from 100 × 200 nm to 100 × 400 nm holes. Figure 2(b) is the FDTD simulations by using the same experimental parameters, which shows a good agreement with the experiment observations, where the simulation maximum value of the rotation angle 35° is recorded for the 100 × 400 nm holes. Noted that the rotation angle $\Delta\theta$ for the square hole array (100 × 100 nm) is always 0°.

To further understand this polarization rotation, we develop an analytical method to actually calculate the rotation angle. There are three steps for the SPPs and light interaction, 1) the incident light excited SPP wave, 2) SPP wave transmitted through the holes, and 3) the SPP wave coupled with the transmitted light. For the exciting process, two kind of SPP modes are excited, including the SPP wave excited by the periodic configurations and the localized

surface plasmons (LSPs) resonant in the holes which are related with the array's periodicity and the individual hole structure [28-31]. For the period induced SPP waves, its wave vector can be written as[28, 29]:

$$\vec{K}_{sp} = p\frac{2\pi}{L}\vec{u}_x + q\frac{2\pi}{L}\vec{u}_y \quad (1)$$

where $\vec{u}_x$ and $\vec{u}_y$ are the unit reciprocal lattice vectors of the periodic hole array in the x and y directions, p and q are the integers determining the propagation modes of the SP wave. The LSPs is related to geometry of the hole structure. For the rectangular hole, the resonance of LSP can also be separated into two independent components, perpendicular to the short edge (along x axis) and the long edge (along y axis) of the hole. In other words, the two kind of SPPs both have independent components in the directions of x and y axis for the rectangular hole arrays, and the components in this two directions denoted as|1,0□ and |1,0□.

Fig. 2(d-e) shows the electric field distribution of the two components with FDTD simulation. Obviously, for the incident polarization angle θ=0°, only the |1,0□ can be excited, and for 90°, the |0,1□ is excited. For the incident light with polarization angle θ, the excited SPPs can be described as $cos\theta$|1,0□+$sin\theta$|1,0□.

In the transmission process, the energy loss include the coupling loss, the Ohm loss and the scattering loss caused by the defects. For rectangular holes, the loss in the two directions is unequal, and the corresponding transmission efficiencies denote as T_{01}, T_{10}, respectively. We can get the relationship between the polarization angles of incident light and transmitted light:

$$\tan\theta' = \sqrt{\frac{T_{10}}{T_{01}}}\tan\theta = R\tan\theta \quad (2)$$

where, we defined $R = \sqrt{T_{10}/T_{01}}$, which is independent on the polarization angle of the incident light. The calculated results are shown in Fig. 2(c), which fits the experimental results very well, with R =1.4, 2, 2.8 for 100 nm × 200nm, 100 nm × 300 nm, 100 nm × 400 nm hole arrays. For 100 nm × 100 nm hole arrays, T_{01}=T_{10} and R=1, the polarization angle of transmitted light showed no rotation.

According to Eq. (2), we can also calculate the polarization dependence of the transmitted intensity for light with polarization angle θ as

$$T_\theta \propto R^2 \sin^2\theta \quad (3)$$

Fig. 3(a) shows the polarization dependence of the transmitted intensity, which is proportional to $sin^2\theta$. The maximum transmission occurs when the light was polarized parallel to the short side of the rectangle holes. The experimental and calculated results fit very well, which is consistent with the previous work in Ref. 21.

Obviously, the parameter R can represents the degree of the polarization rotation. It can be used as an important parameter to characterize the optical properties the plasmonic waveplate, which is only related with the configuration of the nanohole array.

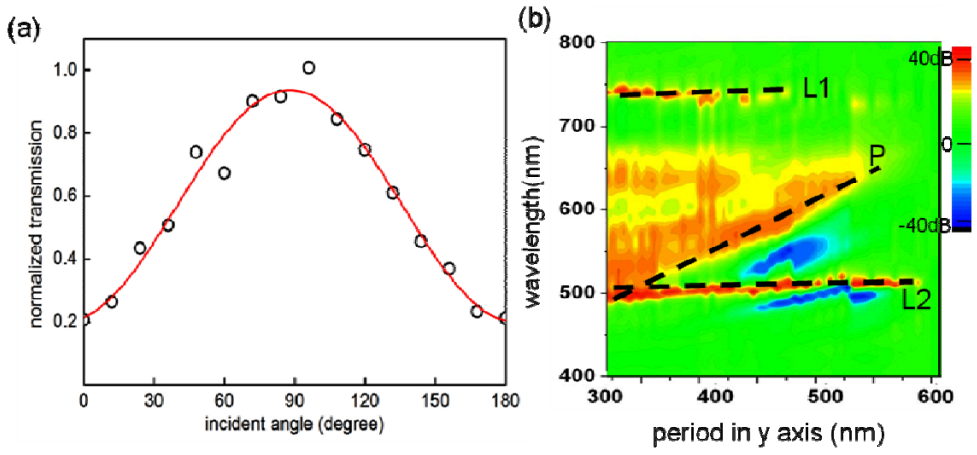


Fig. 3. (a) The polarization dependence of transmission intensity of hole arrays 100 nm × 400 nm, normalized to the maximum value. (b) The mapping of simulated value of R, by scanning of the incident wavelength and the period of hole arrays in y axis.

At last, we investigated the resonant wavelength dependent on the period with FDTD simulated. The FDTD are proposed with the period of the hole arrays in y axis change from 300 nm to 700 nm with an increment of 10 nm and the period in x axis fixed at 600 nm. The incident wavelength changes from 400 nm to 800 nm with increment of 10nm. The size of the nanoholes are set as 120 nm × 120 nm. The simulation results exhibit three obvious bands, as shown in Fig. 3(b), which corresponding with three SPPs resonance modes, because R is associated with the SPPs transmission efficiency, only at the resonant wavelength, the value of R is much larger than 1. Line *P* with the resonant wavelength increases linearly with the period, arises from the resonance of the SP waves, because the resonance of the SP wave is totally determined by the period of the hole array as described in Eq. (1). And line *L1* and *L2*, with the resonant wavelength at about 500nm and 740nm mainly invariant with increase of the period, is related to two LSP resonance bands, because the LSP resonance is determined by the hole structure and independence on the period of the nanohole arrays. For a metallic hole with a diameter much smaller than the wavelength λ of the LSP mode, the resonant LSP modes can be easily obtained using the electrostatic approximation[32]:

$$\frac{\varepsilon(\omega)}{\varepsilon} = -\frac{l+1}{l} \tag{4}$$

Where $\varepsilon(\omega)$ is a frequency-dependent dielectric function of metal and ε is the dielectric constant of the surrounding medium, and l is an integer, $l = 1,2,3\ldots$. The observed LSP resonant bands can be designed as the dipole mode ($l = 1$), and the quadrupole mode ($l = 2$).

From Fig. (3), we can find that the plasmonic wave plate can realize multi-wavelength polarization modulation. For example, for the period of 400 nm hole arrays, the value of R is non-one and polarization rotated for the incident wavelength of about 500nm, 550nm and 740nm.

3. Conclusions

We have realized a plasmonic waveplate with a polarization rotation angle of 30°. The ratio (R) of the transmission efficiency of SPP modes in x and y directions, which is only related with the configuration of the nanohole arrays, is found as a critical parameter to characterize the wave plate properties,. We further observed multiple polarization rotation effect bands, resulted from the SP wave propagation on the Au film and SP localized resonance in the

nanoholes, which can be used for a multi-wavelength polarization modulation. Confirmed by both theory and FDTD simulations, our wave plate configuration can be used for the future controllable optoelectronic device applications, such as the plasmonic mediated transmission and selection.

Acknowledgments

The work is supported by the National Basic Research Program of China (973 Program) Grant No. 2012CB933004, and the National Science Foundation of China (Grant No. 61176120 and No. 60977015).

For **equations**,

$$\nabla \times \overline{E}\left(\overline{r},t\right) = -\frac{\partial \overline{B}\left(\overline{r},t\right)}{\partial t} \tag{1}$$

Figures and Tables: Give each figure and table a separate concise caption. It begins with Figure or Table, followed by the appropriate Arabic numeral and period. The maximum width of figure or table may not exceed 17 cm. Make symbols, line thickness, and lettering in proper scale in relation to the overall figure size.

Acknowledgements, if any, including all funding information, should be gathered into a brief statement at the end.

REFERENCES

1. W. L. Barnes, A. Dereux, and T. W. Ebbesen, "Surface plasmon subwavelength optics," Nature 424, 824-830 (2003).
2. Z. Y. Fang, Q. A. Peng, W. T. Song, F. H. Hao, J. Wang, P. Nordlander, and X. Zhu, "Plasmonic Focusing in Symmetry Broken Nanocorrals," Nano Lett 11, 893-897 (2011).
3. S. Thongrattanasiri, A. Manjavacas, and F.J. Garcia de Abajo, "Complete optical absorption in periodically patterned grahphene." Phys. Rev. Lett. 108, 047401 (2012)
4. W. B. Chen, D. C. Abeysinghe, R. L. Nelson, and Q. W. Zhan, "Plasmonic Lens Made of Multiple Concentric Metallic Rings under Radially Polarized Illumination," Nano Lett 9, 4320-4325 (2009).
5. N. Large, L. Saviot, J. Margueritat, J. Gonzalo, C. N. Afonso, A. Arbouet, P. Langot, A. Mlayah, and J. Aizpurua, "Acousto-plasmonic hot spots in metallic nano-objects".Nano. Lett. 9 3732–3738 (2009),
6. Z. Y. Fang, C. F. Lin, R. M. Ma, S. Huang, and X. Zhu, "Planar Plasmonic Focusing and Optical Transport Using CdS Nanoribbon," Acs Nano 4, 75-82 (2010).
7. B. Wild, L. N. Cao, Y. G. Sun, B. P. Khanal, E. R. Zubarev, S. K. Gray, N. F. Scherer, and M. Pelton, "Propagation Lengths and Group Velocities of Plasmons in Chemically Synthesized Gold and Silver Nanowires," Acs Nano 6, 472-482 (2012).
8. A. A. Yanik, R. Adato, S. Erramilli, and H. Altug, "Hybridized nanocavities as single-polarized plasmonic antennas," Opt Express 17, 20900-20910 (2009).
9. Z. Y. Fang, L. R. Fan, C. F. Lin, D. Zhang, A. J. Meixner, and X. Zhu, "Plasmonic Coupling of Bow Tie Antennas with Ag Nanowire," Nano Lett 11, 1676-1680 (2011).
10. V. Giannini, Y. Francescato, H. Amrania, C. C. Phillips, and S. A. Maier, "Fano Resonances in Nanoscale Plasmonic Systems: A Parameter-Free Modeling Approach," Nano Lett 11, 2835-2840 (2011).
11. Z. Y. Fang, Z. Liu, Y. M. Wang, P. M. Ajayan, P. Nordlander, and N. J. Halas, "Graphene-Antenna Sandwich Photodetector," Nano Lett 12, 3808-3813 (2012).
12. Z. Fang, Y. Wang, Z. Liu, Pulickel M. Ajayan, Frank H.L. Koppens, Peter Nordlander, and N. J. Halas., "Plasmon-Induced Doping of Graphene," ACS Nano, 6, 10222-10228, (2012).

13. M. W. Knight, H. Sobhani, P. Nordlander, and N. J. Halas, "Photodetection with Active Optical Antennas," Science 332, 702-704 (2011).
14. Z. Y. Fang, J. Y. Cai, Z. B. Yan, P. Nordlander, N. J. Halas, and X. Zhu, "Removing a Wedge from a Metallic Nanodisk Reveals a Fano Resonance," Nano Lett 11, 4475-4479 (2011).
15. T. W. Ebbesen, H. J. Lezec, H. F. Ghaemi, T. Thio, and P. A. Wolff, "Extraordinary optical transmission through sub-wavelength hole arrays," Nature 391, 667-669 (1998).
16. R. Gordon, A. G. Brolo, D. Sinton, and K. L. Kavanagh, "Resonant optical transmission through hole-arrays in metal films: physics and applications," Laser Photonics Rev 4, 311-335 (2010).
17. H. S. Lee, Y. T. Yoon, S. S. Lee, S. H. Kim, and K. D. Lee, "Color filter based on a subwavelength patterned metal grating," Opt Express 15, 15457-15463 (2007).
18. C. Genet, and T. W. Ebbesen, "Light in tiny holes," Nature 445, 39-46 (2007).
19. R. Gordon, M. Hughes, B. Leathem, K. L. Kavanagh, and A. G. Brolo, "Basis and lattice polarization mechanisms for light transmission through nanohole arrays in a metal film," Nano Lett 5, 1243-1246 (2005).
20. Y. M. Strelniker, "Theory of optical transmission through elliptical nanohole arrays," Phys Rev B 76, 085409 (2007).
21. R. Gordon, A. G. Brolo, A. McKinnon, A. Rajora, B. Leathem, and K. L. Kavanagh, "Strong polarization in the optical transmission through elliptical nanohole arrays," Phys Rev Lett 92, 037401 (2004).
22. K. L. van der Molen, K. J. Klein Koerkamp, S. Enoch, F. B. Segerink, N. F. van Hulst, and L. Kuipers, "Role of shape and localized resonances in extraordinary transmission through periodic arrays of subwavelength holes: Experiment and theory," Phys Rev B 72, 045421 (2005).
23. Q. A. Zhao, C. Li, Y. S. Zhou, and H. Y. Wang, "The mechanism of the polarization dependence of the optical transmission in subwavelength metal hole arrays," J Phys-Condens Mat 23, 015005 (2011).
24. X. F. Ren, G. P. Guo, Y. F. Huang, Z. W. Wang, and G. C. Guo, "Influence of unsymmetrical periodicity on extraordinary transmission through periodic arrays of subwavelength holes," Appl Phys Lett 90, 161112 (2007).
25. A. Drezet, C. Genet, and T. W. Ebbesen, "Miniature Plasmonic Wave Plates," Phys Rev Lett 101, 043902 (2008).
26. E. H. Khoo, E. P. Li, and K. B. Crozier, "Plasmonic wave plate based on subwavelength nanoslits," Opt Lett 36, 2498-2500 (2011).
27. H. F. Gai, J. Wang, and Q. Tian, "Modified Debye model parameters of metals applicable for broadband calculations," Appl Optics 46, 2229-2233 (2007).
28. Y. Zeng, Y. Fu, X. S. Chen, W. Lu, and H. Agren, "Selective excitation of surface-polariton Bloch waves for efficient transmission of light through a subwavelength hole array in a thin metal film," Phys Rev B 76, 35427 (2007).
29. Y. Zeng, Y. Fu, X. S. Chen, W. Lu, and H. Agren, "Dynamics of the damping oscillator formed by the collective generation of surface polaritons for extraordinary light transmission through subwavelength hole arrays in thin metal films," Phys Rev B 76, 125409 (2007).
30. A. Mary, S. G. Rodrigo, L. Martin-Moreno, and F. J. Garcia-Vidal, "Theory of light transmission through an array of rectangular holes," Phys Rev B 76, 195414 (2007).
31. Z. Y. Fang, Y. R. Zhen, L. R. Fan, X. Zhu, and Peter Nordlander, "Tunable wide-angle plasmonic perfect absorber at visible frequencies", Phys. Rev. B, 2012, 85: 245401
32. M. Yang, Z. P. Fu, F. Lin, and X. Zhu, "Incident angle dependence of absorption enhancement in plasmonic solar cells," Opt Express 19, A763-A771 (2011).

New advances in optically magnetic materials for nanophotonics

Scattering forces on magneto-dielectric particles and the electromagnetic momentum density

Manuel I. Marqués[1,2*], and Juan Jose Sánez[2,3]

[1]Departamento de Física de Materiales, Universidad Autónoma de Madrid, 28049, Madrid, Spain
[2]Instituto de Ciencia de Materiales Nicolás Cabrera, 28049, Madrid, Spain
[3]Departamento de Fśica de la Materia Condensada, 28049, Madrid, Spain
*corresponding author, E-mail: manuel.marques@uam.es

Abstract

In this paper we analyze the non-conservative forces on magneto-dielectric particles in special configurations where the scattering force is not proportional to the average value of the Poynting vector. Based on these results, we revisit the concept of electromagnetic momentum density.

1. Introduction

After the pioneering experimental work by Ashkin and coworkers [1] , the mechanical action of light on small particles have been extensively used to trap and manipulate small particles [2, 3, 4] or to induce significant optical forces between particles [5, 6, 7]. Some recent proposals like the optical tractor beams [8, 9, 10, 11, 12], have renewed the interest in this field.

Small dielectric particles compared with the radiation wavelength develop an electric dipole moment that is drawn by intensity gradients and that competes with the radiation pressure due to the momentum transferred from the photons to the particle. Actually, light forces on small dielectric particles are described as the sum of the dipole or gradient force and the radiation pressure or scattering force [13, 14].

Radiation pressure is usually considered proportional to the Poynting vector. However this is not the case for inhomogeneous waves. For non-homogeneous waves there is also an additional contribution to the scattering force [15], which has been shown to be a non-conservative force proportional to the curl of the spin angular momentum of the light field [16]

This second contribution to the scattering force may be essential to understand the behaviour of nano particles under non-homogeneous waves. For example both, forces coming from the Poynting vector and spin forces, must be considered in order to understand the scattering forces in the focal volume of microscope objectives [17, 18, 19, 20].

These non-homogeneous light fields may be also produced by an appropriate manipulation of interfering laser beams. For example, it is possible to generate local vortices and complex Poynting vector patterns [21] leading to a complex dynamics of nanoparticles [22, 23, 24]. These interesting field configurations are usually based on the interference between linearly polarized fields. Recently, the forces on a small dipolar particle and the electromagnetic momentum density in a configuration consisting in two perpendicular circularly polarized stationary waves have been analysed [25]. The fields distribution for this particular configuration shows regions in which the electric and magnetic fields are parallel corresponding to a null Poynting vector. Although the average value of the momentum density, proportional to the Poynting vector, is zero in these regions, a non-negligible scattering forces due to light's spin force was found.

In this paper we will review this result and we will extend it to the case of magneto dielectric particles. We will also discuss about a proposal for a new definition of the average value of the momentum density for free propagating electromagnetic fields based on the total scattering forces.

2. Scattering forces with null Poynting vector in dielectric nanoparticles

Let us consider a small dielectric particle and let us treat it as a point dipole proportional to the external field, $\mathbf{p} = \epsilon_0 \alpha \mathbf{E}$ where $\alpha(\omega) = \alpha'(\omega) + i\alpha''(\omega)$ is the complex polarizability and ω the frequency of the electromagnetic field. The total time averaged scattering force may be written as the sum of two terms; a scattering force proportional to the Poynting vector and a scattering force proportional to the curl of the spin angular momentum of light [16]:

$$\langle \boldsymbol{F} \rangle = \sigma \left\{ \frac{1}{c} \langle \boldsymbol{S} \rangle \right\} + \sigma \Big\{ c \boldsymbol{\nabla} \times \langle \boldsymbol{L}_S \rangle \Big\} \tag{1}$$

where $\sigma = k\alpha''$ is the particle's extinction cross section. The time averaged Poynting vector is,

$$\langle \boldsymbol{S} \rangle = \mathrm{Re}\{\mathbf{E} \times \mathbf{H}^*\}/2 \tag{2}$$

and the curl of the spin density of the light field is given by,

$$\langle \boldsymbol{L}_S \rangle = \epsilon_0 \left\{ \mathbf{E} \times \mathbf{E}^* \right\} / (4\omega i) \tag{3}$$

Let us analyse the average value of the scattering force when the small dielectric particle is placed in a electromagnetic field consisting in two perpendicular circularly polarized stationary waves with wavelength λ and wave vector

of modulus $k = 2\pi/\lambda$, propagating in the X-Y plane and with a different of phase of $\pi/2$.

$$\boldsymbol{E_1} = (e^{ikx} - e^{-ikx})\frac{1}{\sqrt{2}}(0,1,i) \quad (4)$$

$$\boldsymbol{E_2} = (e^{iky} - e^{-iky})\frac{i}{\sqrt{2}}(1,0,i) \quad (5)$$

The value of the total scattering force is given by [25]

$$\langle F_x\rangle = -\alpha'' k\epsilon_0[\cos(kx)\sin(ky)] \quad (6)$$
$$\langle F_y\rangle = \alpha'' k\epsilon_0[\cos(ky)\sin(kx)] \quad (7)$$
$$\langle F_z\rangle = 0 \quad (8)$$

while the Poynting vector is given by [25]

$$\langle S_x\rangle = -\epsilon_0 c[\cos(kx)\sin(ky) + \sin(kx)\cos(ky)] \quad (9)$$

$$\langle S_y\rangle = -\langle S_x\rangle \quad (10)$$
$$(11)$$
$$\langle S_z\rangle = 0 \quad (12)$$

In points given by

$$y = -x \pm \frac{m\lambda}{2} \quad (13)$$

being m an integer number, the electric and magnetic fields are parallel, implying an average value of the Poynting vector equal lo zero. However, the total scattering force on this points is non zero.

If the scattering force is considered to be a momentum exchange with the light field then, in this points, we have an anomalous situation where the scattering force is non zero but the electromagnetic linear momentum density, proportional to Ponting vector, is zero. Let us analyze if this anomalous situation also holds in the case of small magnetic particles.

3. Scattering forces with null Poynting vector in magneto-dielectric nanoparticles

The optical scattering force on magnetic particles have been analysed in Ref. [26, 27]. If the magnetic moment induced by the electromagnetic field is given by $\mathbf{m} = (\alpha_m/\mu_0)\mathbf{B}$ then the total scattering optical force is given by

$$\langle \boldsymbol{F}\rangle = \sigma_m\left\{\frac{1}{c}\langle \boldsymbol{S}\rangle\right\} + \sigma_m\Big\{c\boldsymbol{\nabla}\times\langle \boldsymbol{L}_{SM}\rangle\Big\} \quad (14)$$

where $\sigma_m = k\alpha_m''$ is the particle's magnetic extinction cross section and the curl of the magnetic spin density of the light field is given by,

$$\langle \boldsymbol{L}_{SM}\rangle = (1/\mu_0)\left\{\mathbf{B}\times\mathbf{B}^*\right\}/(4\omega i) \quad (15)$$

The Poynting vector has not changed with respect to the previous case but, in order to calculate the total scattering force on the magnetic particle, we must calculate the new force due to the curl of the magnetic spin density of the light field. This curl of the spin density is given by

$$\boldsymbol{\nabla}\times\langle \boldsymbol{L}_{SM}\rangle|_x = (\epsilon_0/c)[\cos(kx)\sin(ky)] \quad (16)$$
$$\boldsymbol{\nabla}\times\langle \boldsymbol{L}_{SM}\rangle|_y = -(\epsilon_0/c)[\cos(ky)\sin(kx)] \quad (17)$$
$$\boldsymbol{\nabla}\times\langle \boldsymbol{L}_{SM}\rangle|_z = 0 \quad (18)$$

Once we know the spin density we may calculate the total scattering force:

$$\langle F_x\rangle = -\alpha_m'' k\epsilon_0[\cos(ky)\sin(kx)] \quad (19)$$
$$\langle F_y\rangle = \alpha_m'' k\epsilon_0[\cos(kx)\sin(ky)] \quad (20)$$
$$\langle F_z\rangle = 0 \quad (21)$$

Again it is possible to find regions where the Poynting vector is zero but the average value of the scattering forces, due to the existence of a magnetic spin density with a value of the curl different from zero, is not null (see Figure 1).

The scattering forces for magnetic and dielectric particles are different but, in this particular case, the dynamical trend of both kind of particles, dielectric and magnetic, are going to be the same. We should say that this is not always the case. For example, in the case of linearly polarized beams, a s-polarization implies a null value of the spin force for the dielectric particle and a value different from zero for the magnetic particle. And, for p-polarization, the situation is just the opposite [16].

For small particles with a non- negligible electric and magnetic induced dipole there is also an extra contribution to the force given by the interaction between both dipoles, magnetic and electric [26, 27]. But, for pure scattering forces (coming solely from the imaginary parts of the polarizability) the contribution from this mixing term is proportional to the average value of the Poynting vector [28].

4. A electromagnetic linear momentum density proposal

By summarizing the results presented in this paper, we may say that even with a null average value of the Poynting vector, a magneto dielectric particle experiences a pure scattering force given by

$$\langle \boldsymbol{F}\rangle = \sigma\Big\{c\boldsymbol{\nabla}\times\langle \boldsymbol{L}_S\rangle\Big\} + \sigma_m\Big\{c\boldsymbol{\nabla}\times\langle \boldsymbol{L}_{SM}\rangle\Big\} \quad (22)$$

Then, it seems natural to redefine the electromagnetic linear momentum density as the sum of the forming contribution coming from the Poynting vector ($\boldsymbol{S}/c^2$) and the curls of the electric and magnetic spin densities, such that the electromagnetic momenta flow lines correspond directly with the scattering light forces [25]. The term added is

solenoidal so it has no influence on the conservation laws obtained from Maxwell equations.

$$\langle \boldsymbol{p_{new}} \rangle = \frac{\langle \boldsymbol{S} \rangle}{c^2} + (\boldsymbol{\nabla} \times \langle \boldsymbol{L}_S \rangle) + (\boldsymbol{\nabla} \times \langle \boldsymbol{L}_{SM} \rangle) \quad (23)$$

Where first and second terms are exchanged by the electromagnetic field with a dielectric particle while first and third therms are exchanged when the particle is magnetic.

The average value of the electromagnetic momentum interacting with a dielectric particle may be also written as

$$\langle \boldsymbol{p_e} \rangle = \frac{i\epsilon_0}{4\omega} \sum_{i=x,y,z} (E_i \boldsymbol{\nabla} E_i^* - E_i^* \boldsymbol{\nabla} E_i) \quad (24)$$

while for the magnetic particle it may be written as

$$\langle \boldsymbol{p_m} \rangle = \frac{i}{4\omega\mu_0} \sum_{i=x,y,z} (B_i \boldsymbol{\nabla} B_i^* - B_i^* \boldsymbol{\nabla} B_i) \quad (25)$$

Note how both expression are the natural vectorial extension of the density of linear momentum for a scalar field Ψ in quantum mechanics [25],

$$\frac{i\hbar}{2}(\Psi \boldsymbol{\nabla} \Psi^* - \Psi^* \boldsymbol{\nabla} \Psi) \quad (26)$$

A possible vale for a instantaneous electromagnetic linear momentum density for monochromatic harmonic fields in vacuum, with average value like the one obtained in 24, is given by

$$\boldsymbol{p_e} = \epsilon_0 \sum_{i=x,y,z} E_i \boldsymbol{\nabla} A_i \quad (27)$$

being $\boldsymbol{A}$ the gauge invariant transverse vector potential [29], while and average value like 25 is obtained with

$$\boldsymbol{p_m} - \frac{1}{\mu_0 c} \sum_{i=x,y,z} B_i \boldsymbol{\nabla} C_i \quad (28)$$

being $\boldsymbol{C}$ the dual transformation of the vector potential $\boldsymbol{A}$ [30, 31]. These terms are usually named as the orbital parts of the electromagnetic linear momentum density.

Interestingly, by considering the transverse gauge [29] for the free electromagnetic fields, the following linear momentum density $\hat{\boldsymbol{p}}$ is obtained directly from the canonical stress energy tensor [32]

$$\hat{p}_i = \frac{S_i}{c^2} + \epsilon_0 \boldsymbol{\nabla}(\boldsymbol{E} A_i) \quad (29)$$

and it is easy to show that in vacuum

$$\hat{\boldsymbol{p}} = \boldsymbol{p_e} \quad (30)$$

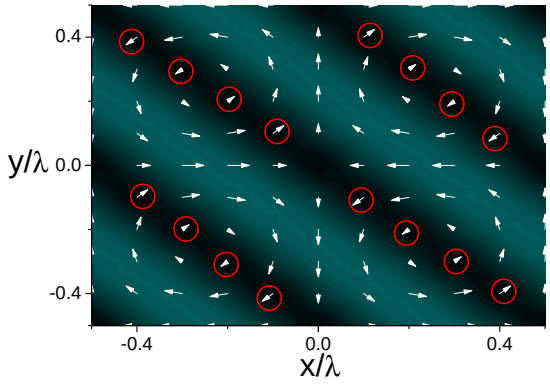


Figure 1: Scattering force on a magnetic particle for the configuration consisting in two perpendicular, circularly polarized, stationary waves with wavelength λ propagating in the X-Y plane and with a difference on the phase $\phi = \pi/2$. The colour map represents the magnitude of the Poynting vector (darker for lower values). Red circles highlight the scattering forces which are different from zero in a region with null value of the Poynting vector.

So we are tempted to say that, if instead of considering the usual symmetric stress energy tensor, we consider the canonical stress energy tensor [32], a value of the electromagnetic linear momentum density, proportional to the scattering forces on dielectric particles, is directly obtained.

However, we must be very careful because the canonical stress energy tensor has a major drawback, it is not symmetric. This asymmetry has two main consequences: First, the instantaneous time variation of the electromagnetic energy density ($\nabla \boldsymbol{S}$) is not longer proportional to the instantaneous divergence of linear momentum density ($c^2 \nabla \hat{\boldsymbol{p}}$). Second, for a non symmetric stress energy tensor the electromagnetic angular momentum is, in general, not conserved [32]. Although we should point out that the total angular momentum derived from the calculation of $\boldsymbol{r} \times \hat{\boldsymbol{p}}$, usually known as the orbital angular momentum of light, is conserved [33].

There is finally a major drawback to the linear momentum density obtained directly from the canonical stress energy tensor; it only applies when light is interacting with dielectric particles. What about magnetic particles? We could say that the linear momentum exchanged by light interacting with magnetic particles $\boldsymbol{p_m}$ is obtained also from the canonical stress energy tensor, but in this case the dual electromagnetic fields must be considered [30, 31].

5. Conclusions

We have analysed the scattering force for crossed circularly polarized standing waves where the field distribution shows regions in which the electric and magnetic fields are parallel corresponding to a null Poynting vector. We have shown that, although the average value of the momentum density, proportional to the Poynting vector, is zero in these regions,

there are scattering forces acting on small dielectric particles due to lights spin force We have extended these results to small particles presenting both, electric and magnetic responses We have discussed the intriguing interplay between the momentum and spin densities and the actual force on magneto-dielectric particles. The total scattering force reported suggests a new definition of the average value of the momentum density, for free propagating electromagnetic fields, proportional to the full scattering forces. We hope this discussion will open intriguing basic new possibilities about the concept of the electromagnetic momentum flow.

Acknowledgement

This work was supported by the Spanish MEC through grants No. FIS2009-13430-C02 and No. CSD2007-00046 (Consolider NanoLight) and by the Comunidad de Madrid Microseres Project No. S2009/TIC-1476.

References

[1] A. Ashkin, Acceleration and Trapping of Particles by Radiation Pressure, Phys. Rev. Lett. **24** (1970) 156-159.

[2] A. Ashkin, J.M. Dziedzic, J. E. Bjorkholm, and S. Chu, Observation of a single-beam gradient force optical trap for dielectric particles, Opt. Lett. **11** (1986) 288-290.

[3] D.G. Grier, A revolution in optical manipulation, Nature **424** (2003) 810-816.

[4] K.C. Neuman and S.M. Block, Optical trapping, Rev. Sci. Instrum. **75** (2004) 2787-2895.

[5] M.M. Burns, J.-M. Fournier and J.A. Golovchenko, Optical Binding, Phys. Rev. Lett. **63** (1989) 1233-1236.

[6] R. Gómez-Medina, and J.J. Sáenz, Unusually Strong Optical Interactions between Particles in Quasi-One-Dimensional Geometries, Phys. Rev. Lett. **93** (2004) 243602-243605.

[7] K. Dholakia and P. Zemánek, Gripped by light: optical binding, Rev. Mod. Phys. **82** (2010) 1767-1791.

[8] J. Chen, J. Ng, Z. Lin, and C. T. Chan, Optical pulling force, Nature Photonics **5** (2011) 531-534.

[9] J.J. Sáenz, Optical forces: Laser tractor beams, Nature Photon. **5** (2011) 514-515.

[10] A. Novitsky, C.-W Qiu and H. Wang, Single Gradientless Light Beam Drags Particles as Tractor Beams, Phys. Rev. Lett. **107** (2011) 203601-1-203601-4.

[11] S. Sukhov and A. Dogariu, Negative Nonconservative Forces: Opti cal Tractor Beams for Arbitrary Objects, Phys. Rev. Lett. **107** (2011) 203602-1-203602-4.

[12] A. Salandrino and D. N. Christodoulides, Reverse optical forces in negative index dielectric waveguide arrays, Opt. Lett. bf36 (2011) 3103-3105.

[13] L. Novotny and B. Hecht, *Principles of Nano-Optics*, Cambridge University Press, Cambridge 2006.

[14] M. Nieto-Vesperinas, P.C. Chaumet and A. Rahmani, Near-field photonic forces, Phil. Trans. R. Soc. Lond. A **362** (2004) 719-737.

[15] V. Wong and M. Ratner, Gradient and nongradient contributions to plasmon-enhanced optical forces on silver nanoparticles, Physical Review B **73**, (2006) 075416-1-075416-6 .

[16] S. Albaladejo, M. I. Marqués, M. Laroche and J. J. Sáenz, Scattering Forces from the Curl of the Spin Angular Momentum of a Light Field, Phys. Rev. Lett. **102** (2009) 113602-1-113602-4.

[17] I. Iglesias and J. J. Sáenz, Scattering forces in the focal volume of high numerical aperture microscope objectives, Opt. Commun. **284** (2011) 2430-2436.

[18] I. Iglesias and J. J. Sáenz, Light spin forces in optical traps: comment on "Trapping metallic Rayleigh particles with radial polarization", Opt. Express **20** (2012) 2832-2834.

[19] Q. Zhan, Trapping metallic Rayleigh particles with radial polarization: reply to comment, Opt. Express **20**, (2010) 6058-6059.

[20] A. Bekshaev, K. Y. Bliokh, M. Soskin, Internal flows and energy circulation in light beams. Journal of Optics **13** (2011) 053001-1-053001-32.

[21] A. Hemmerich and T. W. Hänsch , Radiation pressure vortices in two crossed standing waves, Phys. Rev. Lett. **68**, (1992) 1492-1495 .

[22] S. Albaladejo, M. I. Marqués, F. Scheffold, and J. J. Sáenz, Giant enhanced diffusion of gold nanoparticles in optical vortex fields, Nano Lett. **9** (2009) 3527-3531.

[23] I. Zapata, S. Albaladejo, J.M.R. Parrondo, J.J. Sáenz and F. Sols,. Deterministic Ratchet from Stationary Light Fields. Phys. Rev. Lett., **103** (2009) 130601-1-130601-4.

[24] S. Albaladejo, M. I. Marqués, and J. J. Sáenz, Light control of silver nanoparticle's diffusion, Opt. Express **19** (2011) 11471-11478.

[25] M. I. Marqués, and J. J. Sáenz, Scattering forces and electromagnetic momentum density in crossed circularly polarized standing waves, Opt. Lett **37** (2012) 2787-2789; Opt. Lett **37** (2012) 4470.

[26] P. C. Chaumet and A. Rahmani, Electromagnetic force and torque on magnetic and negative-index scatterers Opt. Express **17** (209) 2224-2234.

[27] M. Nieto-Vesperinas, J.J. Sáenz, R. Gómez-Medina and L. Chantada, Optical forces on small magnetodielectric particles, Opt. Express **18** (2010) 11428-11443.

[28] R. Gómez-Medina, M. Nieto-Vesperinas and J. J. Sáenz, Nonconservative electric and magnetic optical forces on submicron dielectric particles, Phys. Rev. A **83** (2011) 033825-033832.

[29] See f.i. J. D. Jackson, Classical Electrodynamics, 3er ed., page 241.

[30] K.Y. Bliokh, A. Y. Bekshaev and F. Nori, Dual electromagnetism: Helicity, spin, momentum and angular momentum, arXiv:1208.4523

[31] R.P. Cameron and S. M. Barnett, Electric-Magnetic symmetry and Noether's theorem New Journal of Physics **14** (2012) 123019-123046.

[32] See f.i. J. D. Jackson, Classical Electrodynamics, 3er ed., page 605.

[33] See f.i. L. Mandel and E. Wolf, Optical coherence and quantum optics, page 488.

Emerging technology in plasmonics

Optimizing Silicon-Plasmonic Waveguides for $\chi^{(3)}$ Nonlinear Applications

Alexandros Pitilakis, Odysseas Tsilipakos and Emmanouil E. Kriezis

Department of Electrical and Computer Engineering,
Aristotle University of Thessaloniki, Thessalniki, Greece
*corresponding author, E-mail: alexpiti@auth.gr

Abstract

Hybrid silicon-plasmonic waveguides constitute an appealing platform for integrated photonic circuitry. They merge the technical maturity and prevalence of the SOI platform with the subwavelength confinement of plasmonic waveguides, essential for accessing enhanced nonlinear response at micron length-scales. Employing full-wave numerical simulations complemented with Schrödinger equation techniques, we propose nonlinear waveguide designs for Kerr-effect applications exhibiting minimized impairments due to free-carrier effects, thus raising the power-ceiling imposed on standard silicon waveguides.

1. Introduction

Nonlinear phenomena emanating from the third order susceptibility $\chi^{(3)}$ hold the key to efficient all-optical signal processing in integrated photonics. Circuitry based on standard silicon-on-insulator (SOI) waveguides [1] presents limited potential for micron-length-scale Kerr-type nonlinear applications due to the large interaction length-scales required: typically longer than 1 mm [2, 3]. Furthermore, silicon exhibits two-photon absorption (TPA) in the telecom band, which in turn, apart from introducing additional losses, gives rise to free-carrier effects (FCEs), namely dispersion (FCD) and, more importantly, absorption (FCA). The magnitude of FCEs increases quadratically with the optical power. Thus, FCA limits the maximum on-chip average power to a few tens of milliwatts; above this threshold, it drastically quenches the optical power. On the other hand, purely plasmonic waveguides [4] can allow for subwavelength confinement significantly boosting the nonlinear response and thus reducing the required interaction length. However, they suffer from substantial Ohmic losses, a fundamental barrier for any nonlinear application .

Hybrid silicon-plasmonic (HSP) waveguides [5] present a fair compromise between silicon and plasmonic traits, with respect to the potential for Kerr-type nonlinear applications [6]. Fusing index-contrast and plasmonic guiding mechanisms, they confine the optical field in a nanosized low-index dielectric gap, formed between a metal and a high-index silicon area. If the dielectric additionally possesses a high nonlinear index n_2, then the nonlinear parameter γ quantifying the Kerr-effect strength acquires orders-of-magnitude larger values than those typical of SOI waveguides ($\gamma \approx 100\ \mathrm{m}^{-1}\mathrm{W}^{-1}$). More importantly, HSP waveguides offer a two-fold advantage over SOI ones with respect to FCE impairments. Specifically, as the optical field is confined primarily inside the dielectric gap, not only is the relative TPA magnitude (r_{TPA}) decreased, but, in addition, TPA-generated free-carriers (residing only inside the silicon area) do not significantly overlap with the optical field. These two aspects mean that the overall FCE perturbation is considerably decreased, even further than nonlinear-slot waveguides [3]. In view of these attributes, HSP waveguides offer increased potential for Kerr-related nonlinear applications in compact integrated photonic components at length scales in the order of tens of microns, while also allowing for higher on-chip powers, if that is necessary.

2. Nonlinear Figure-of-Merit

In order to establish a common ground for the comparison of nonlinear waveguides, we define a figure-of-merit (FoM) that provides a qualitative measure of the impact of all discussed nonlinear phenomena, namely, the Kerr effect, TPA and FCEs. We start off with a basic FoM for TPA-free waveguides defined as

$$\mathcal{F} = \gamma \times L_{\mathrm{prop}} = \gamma/\alpha \tag{1}$$

and measured in W^{-1}. In this equation, $L_{\mathrm{prop}} = 1/\alpha$ is the propagation length, i.e., the e-folding distance of the optical power, due to linear propagation losses (α). The nonlinear parameter (γ) is the real-part of its complex-valued counterpart

$$\gamma_c = \frac{3\omega\varepsilon_0}{4\mathcal{N}^2} \sum_{\mu,\alpha,\beta,\gamma}^{x,y,z} \iint_{\infty} \chi^{(3)}_{\mu\alpha\beta\gamma} e^*_\mu e_\alpha e^*_\beta e_\gamma \, dxdy, \tag{2}$$

that is rigorously extracted [2] from the electric-field distribution ($\mathbf{e}$) and the cross-sectional profile of the $\chi^{(3)}$-tensor. The latter has a real and an imaginary part, associated with the Kerr-index (n_2) and the TPA-coefficient (β_{TPA}), respectively [1]. Finally, $\mathcal{N}$ is a normalization-integral quantifying the axial power-flow $\mathcal{N} = \mathrm{Re}\{\iint (\mathbf{e} \times \mathbf{h}^*) \cdot \hat{\mathbf{z}}\, dxdy\}$.

It can be shown that the input-power (P_{in}) required for a particular Kerr-type nonlinear application is proportional to $1/\mathcal{F}$. For instance, when the waveguide length is fixed at $L = L_{\mathrm{prop}}$, then spectral FWHM-doubling of

a guassian pulse requires $P_{\text{in}} \approx 4/\mathcal{F}$, nonlinear switching (due to desynchronization) of a directional coupler occurs at $P_{\text{in}} \approx 9/\mathcal{F}$, and a given degenerate four-wave-mixing (FWM) efficiency η requires a CW pump power of $P_{\text{in}} \approx 3\eta^{0.5}/\mathcal{F}$ [3].

Subsequently, in order to evaluate the influence of TPA and FCEs, a power-dependent FoM can be derived according to $\mathcal{F}' = \gamma' \times L'_{\text{prop}}$. For this purpose, the effective quantities γ' and L'_{prop} are introduced by applying correction terms to the nonlinear parameter and propagation length, respectively. These correction terms scale with the input-power and are derived from a nonlinear Schrödinger equation (NLSE) formulation [2] and, more specifically, from the phase and amplitude of the complex-envelope of a signal propagating along a nonlinear waveguide. Both primed quantities are smaller than the respective non-primed ones; FCD counteracts the self-focusing Kerr-effect leading to a reduced effective nonlinear parameter ($\gamma' < \gamma$), while both TPA and FCA are responsible for additional losses that lower the effective propagation length ($L'_{\text{prop}} < L_{\text{prop}}$). The defined $\mathcal{F}'$ is useful when studying how the Kerr-performance of a particular waveguide deteriorates under the effect of TPA and FCE as the power level increases. However, when optimizing or comparing different waveguides it is useful to quantify the relative importance of FCEs; it can be shown that the latter increases with the dimensionless FCE scaling factor

$$f_{\text{fc}} = r_{\text{TPA}} \times \Pi_{\text{Si}} \tag{3}$$

where r_{TPA} is the tangent of the complex-valued nonlinear parameter of Eq. (2), i.e., $r_{\text{TPA}} = \text{Im}\{\gamma_c\}/\text{Re}\{\gamma_c\}$, and Π_{Si} is the fraction of the optical-intensity residing inside silicon-areas of the cross-section

$$\Pi_{\text{Si}} = \frac{\iint_{\text{Si}} |\mathbf{e}|^2 \, dxdy}{\iint_{\infty} |\mathbf{e}|^2 \, dxdy} \leq 1. \tag{4}$$

For typical SOI-waveguides, where the light is guided mostly inside the Si-core, $r_{\text{TPA}} \approx 0.25$ and $\Pi_{\text{Si}} > 0.5$ [2] leading to $f_{\text{fc}} > 0.1$. On the contrary, HSP waveguides are expected to have considerably smaller values of f_{fc} since light is guided almost exclusively inside the dielectric gap, i.e., mostly outside the Si-area.

3. Waveguide Optimization

We base our hybrid silicon-plasmonic waveguide design on the generic planar conductor-gap-silicon (CGS) waveguide [7] and extend the dielectric and metal regions laterally. For the dielectric gap material, we select the DDMEBT nonlinear polymer [3] possessing linear and nonlinear indices of $n = 1.8$ and $n_2 = 1.7 \times 10^{-17}$ m^2/W, respectively, while the metal is silver for minimal Ohmic losses at $\lambda = 1550$ nm ($n_{\text{Ag}} = 0.14 - j11.4$). In order to boost the plasmonic confinement even further, we introduce an inverted metal rib [6] or wedge [8], laterally aligned with the underlying silicon waveguide [Fig. 1(a),(b)]. The corresponding intensity distributions (TM_{00} mode) are plotted

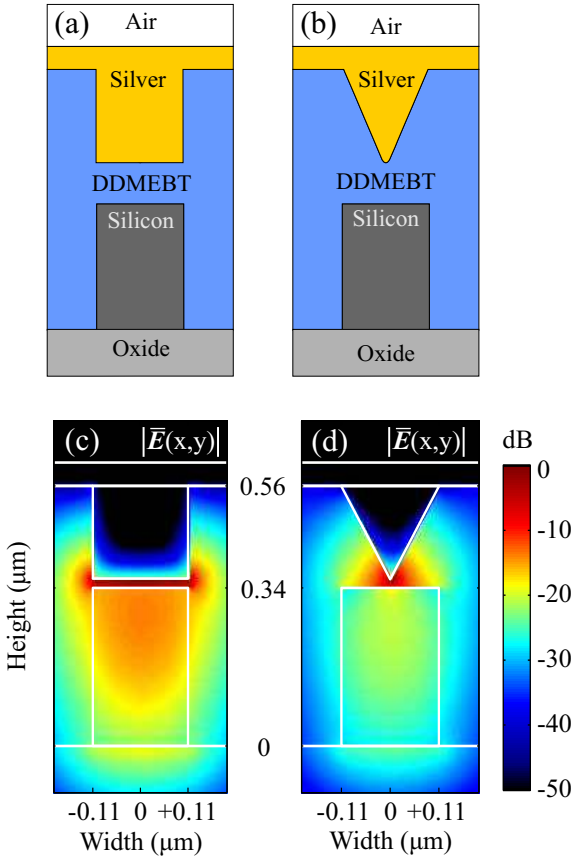


Figure 1: Cross-sections of (a) the inverted metal-rib and (b) the wedge hybrid silicon-plasmonic waveguide designs. (c) and (d): Typical intensity distributions at 1550 nm for the fundamental TM_{00} mode supported for a 20 nm gap. The nonlinear polymer is DDMEBT and the metal is silver.

in Fig. 1(c),(d). Other approaches are also possible for enhancing the mode confinement and improving the nonlinear response, for instance patterning the metal film into a stripe having a width comparable to the silicon wire or less.

The most crucial parameter of these hybrid silicon-plasmonic waveguide designs is the gap size (g). In Fig. 2 we plot both the nonlinear FoM ($\mathcal{F}$) and the FCE-scaling factor (f_{fc}) for a broad range of gap sizes (5–300 nm). One can readily confirm that the metal-wedge design offers considerable improvement in the FoM compared to the metal-rib designs as the gap decreases below 50 nm. The metal-rib designs exhibit an $\mathcal{F}$-peak at about 20 nm, and then the performance starts to drop as the losses become overwhelming. On the contrary, the $\mathcal{F}$ of the metal-wedge design continues to increase even below 5 nm gaps, owing to the enhanced field-confinement at the wedge-tip. As an example, for a gap of 20 nm the wedge design exhibits $\gamma \approx 6.7 \times 10^3$ m^{-1}W^{-1} (thus significantly outperforming standard SOI waveguides) and $L_{\text{prop}} \approx 43$ μm, amounting to $\mathcal{F} = 0.3$ W^{-1}. The factor f_{fc} is approximately 5×10^{-4}, which is orders of magnitude smaller than the f_{fc} exhibited by Si-wires, indicating that the relative importance of FCEs is rather limited. These figures can be further improved by

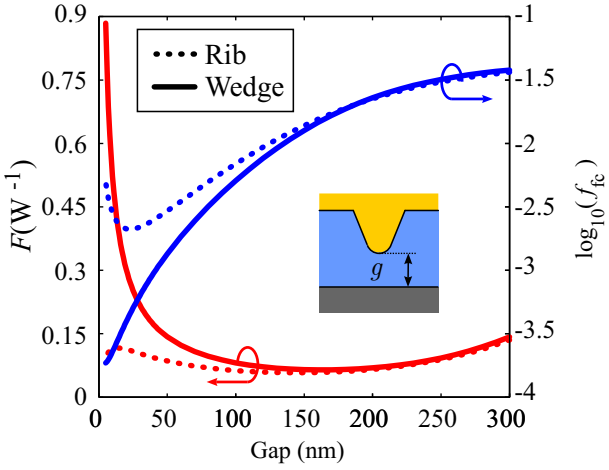


Figure 2: Nonlinear figure-of-merit $\mathcal{F}$ and FCE-scaling factor f_{fc} as a function of gap, for the two waveguide designs. The silicon ridge is in all cases $W \times H = 220$ nm $\times$ 340 nm, the silver film is 50 nm thick and the inverted metal-rib/wedge is $W \times H = 220$ nm $\times$ 200 nm. The wedge-angle is approximately 57° and its tip curvature is 1 nm.

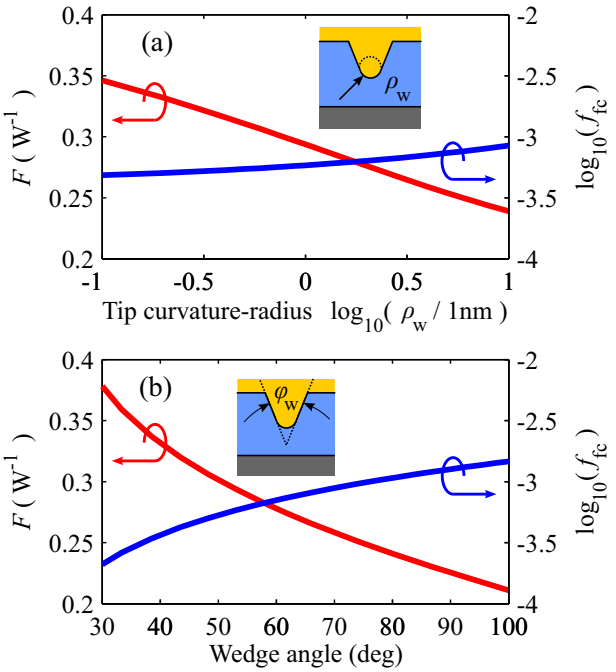


Figure 3: Nonlinear figure-of-merit $\mathcal{F}$ and FCE-scaling factor f_{fc} as a function of (a) wedge-tip radius for $\varphi_w = 53.2^\circ$ and (b) wedge-angle for $\rho_w = 1$ nm. The nonlinear gap is set at 20 nm, the silicon ridge is $W \times H = 220 \times 340$ nm^2, the silver film is 50 nm thick and the inverted metal-wedge height is 100 nm.

optimizing all waveguide parameters which can even lead to $\gamma > 10^4$ m^{-1}W^{-1}.

Focusing on the inverted metal-wedge design, it can be intuitively inferred that acute wedges will lead to improved performance, mostly thanks to the extreme field-confinement at the wedge-tip, which boosts the nonlinear-parameter since $\gamma \propto A_{\text{eff}}^{-1}$, where A_{eff} is the effective mode-area. To this end, we investigate the effect of the wedge-angle (φ_w) and its tip's curvature radius (ρ_w) on the resulting FoM. In our design, the nonlinear gap-size is set to 20 nm (being a reasonable compromise between mode confinement and fabrication challenge), the silicon ridge is set to $W \times H = 220 \times 340$ nm^2, the silver film is 50 nm thick and the inverted metal-wedge height (measured from the tip of the wedge to the bottom of the silver-film) is set to 100 nm. Varying φ_w is done by changing the wedge's lateral width, while varying ρ_w also amounts to a small change of the wedge-width in order to maintain the same wedge-height, wedge-angle and nonlinear-gap. The results are depicted in Fig. 3, where $\varphi_w = 53.2^\circ$ in Fig. 3(a) and $\rho_w = 1$ nm in Fig. 3(b). It is evident that the nonlinear figures-of-merit for HSP waveguides based on this design improve as the wedge becomes more acute, even though the increase is not as pronounced as with respect to the nonlinear gap. Additionally, it was found that obtuse wedges do no significantly restrict the performance; for instance, an acute wedge of $(\varphi_w, \rho_w) = (30^\circ, 0.1\text{ nm})$ leads to $\mathcal{F} > 0.6$ W^{-1} while an obtuse wedge of $(\varphi_w, \rho_w) = (100^\circ, 10\text{ nm})$ leads to $\mathcal{F} < 0.2$ W^{-1}. This means that the fabrication error-tolerance of this design is quite high and the penalty factor between the above two extreme combinations barely exceeds 3.

Finally, addressing some fabrication considerations, we note that the Si-rib width as well as possible lateral offsets between the wedge and the Si-rib do not have a major impact on the aforementioned figures-of-merit.

4. Validation

In order to validate the findings of the previous Section, we adopt the vectorial nonlinear Schrödinger equation (NLSE) framework of Daniel and Agrawal [2] that monitors the evolution of the field's complex-envelope along the waveguide. We calculate all parameters affecting the nonlinear response (losses, Kerr-effect, TPA and FCE) in terms of this NLSE formulation using our custom vector finite-element based mode-solver. Focusing on the CW or quasi-CW regimes, we drop all time-derivatives from the NLSE and record the nonlinear phase-shift ($\Delta\Phi_{\text{NL}}$) and the insertion-losses (IL) as a function of the input-power and the waveguide-length. The $\Delta\Phi_{\text{NL}}$ is extracted from the phase of the output-envelope and has positive contribution from the Kerr-effect ($\propto \gamma L_{\text{eff}} P_{\text{in}}$) and negative contribution from the FCD ($\propto f_{\text{fc}} L_{\text{eff}} P_{\text{in}}^2$); the latter tends to reduce the refractive-index inside silicon, proportionally to the TPA-generated free-carrier density, thus opposing the Kerr-effect which increases the refractive-index. The overall-IL are extracted from the amplitude of the output-envelope and depend on linear (ohmic, Rayleigh-scattering, surface-roughness) as well nonlinear loss-mechanisms, i.e. TPA and FCA.

Subsequently, we compare these CW-metrics for three nonlinear waveguides, namely our HSP-wedge design, a

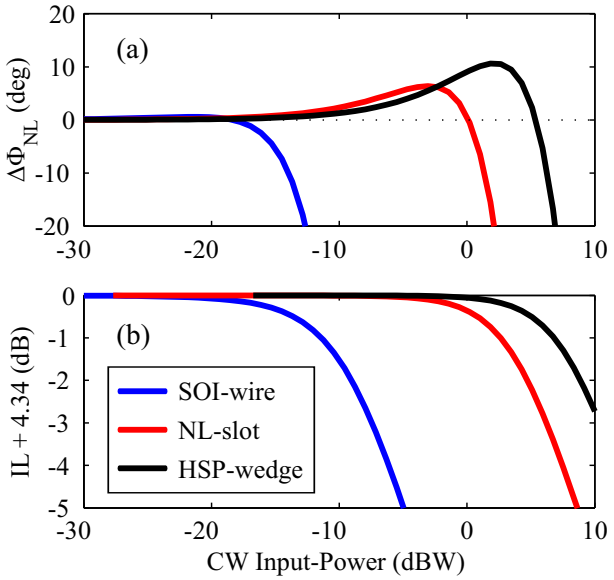


Figure 4: NLSE-calculated nonlinear (a) phase-shift and (b) insertion losses, as a function of the CW input-power along three waveguide designs of L_{prop} length. The SOI-wire is 400×340 nm^2 and operates in the fundamental TE-mode with nominal 1 dB/cm losses. The NL-slot is 140 nm-wide and formed between two 200×220 nm^2 Si-wires and operates in a TE-mode with nominal 1.6 dB/mm losses [3]. The HSP is made of a 20 nm gap separating a 200×220 nm^2 Si-wire from an Ag-wedge of 100 nm height with a tip-radius of 1 nm and operates in a TM-mode. The free-carrier effective lifetime was conservatively considered equal to 1 nsec in all three cases.

typical SOI-wire [2] and a nonlinear-slot [3]. For the purpose of comparison, the SOI-wire cladding and the nonlinear-slot are also filled with the same nonlinear polymer (DDMEBT) and the waveguide-length is equal to the L_{prop} of each design. In Fig. 4(a) we observe that the HSP has a higher FCD power-threshold than the SOI and slot design. This threshold can be defined as the power above which the negative-contribution of FCD overwhelms the positive one from the Kerr-effect, amounting to a negative slope in the $\Delta\Phi_{\text{NL}}$-vs.-P_{in} curve. For the HSP design this threshold-power is well above 0 dBW. The same holds true for the power-threshold associated with the nonlinear-IL, i.e., the overall-IL minus the linear-losses over $L = L_{\text{prop}}$, which amount to 4.34 dB. This power-threshold can be defined as the power where the nonlinear losses impose an additional 1 dB, i.e. $(\text{IL}+4.34) \approx -1$ dB, and is also well above 0 dBW for the HSP design. From Fig. 4 we can deduce that, in the CW-case, the power-threshold associated with FCD is generally lower, i.e. more strict, than the threshold associated with FCA. Let us finally note that the TPA-losses become important in much higher powers meaning that FCA is usually the dominant nonlinear loss mechanism. For the extrapolation of these remarks to the pulsed-regime, please refer to Section 5.

Finally, we note that these results for CW-radiation were corroborated by means of full-wave beam-propagation method simulations [9], and an excellent agreement between the full-wave method and the NLSE-approach was observed.

5. Discussion

The important attributes of the HSP nonlinear waveguide design, apart from being SOI/CMOS-compatible, are the very compact size, the high nonlinearity and the increased FCE power-threshold. The latter is crucial for Kerr-effect applications at interaction-lengths well below 1 mm. Assuming an effective free-carrier lifetime of 1 nsec [2], typical SOI waveguides have an FCE-ceiling in the order of 10 mW (CW), while the respective for HSP waveguides is above 1 W; this is reflected on the orders-of-magnitude smaller FCE-scaling factor f_{fc}. Moreover, SOI waveguides provide a higher FoM ($\mathcal{F} \approx 5$ W^{-1}), albeit on substantially longer length scales ($L_{\text{prop}} \approx 1$ cm). The interaction lengths can be reduced with nonlinear-slot designs [3] at the cost of a ten-fold decrease in $\mathcal{F}$. However, even though (or, exactly because) they avoid the metal-presence, these designs are still approximately two orders-of-magnitude longer than the respective HSP ones, and they achieve approximately equivalent figures-of-merit ($\mathcal{F}$ and f_{fc}).

Evidently, the pulsed-regime performance will be considerably improved with respect to the FCE power-thresholds observed for the CW-regime. This is true for pulses with duration shorter than the carrier-lifetime ($\tau_{\text{fc}} \approx 1$ ns) and for low repetition-rates [10]. The reason behind this improvement is that even though the FCE are triggered instantaneously due to TPA, they are not given the time to considerably affect short-pulses due to their delayed response. In this manner, both FCD and FCA power-thresholds are at least 10–20 dB higher than the CW-ones, e.g. for guassian pulses shorter than τ_{fc}. This allows for higher powers and, consequently, much more pronounced Kerr-effect than the $\Delta\Phi_{\text{NL}} \ll \pi$ anticipated in the CW-regime [11]. Even for NRZ systems and/or high repetition-rates, the FCE power-thresholds are still higher than those calculated for CW-radiation. In overall, the estimates of Fig. 4, in and of themselves, are very pessimistic for most practical applications and mainly provide relative figures for the power levels at which FCE become important in different waveguide designs. Nevertheless, in the present work they can be employed as measures for comparative waveguide assessment and optimization, since it is well understood that the FCE-penalization always scales with the factor f_{fc}, in the pulsed as well as the CW-regime.

6. Conclusion

We have investigated the potential of hybrid silicon-plasmonic waveguides for Kerr-effect applications in integrated photonic components. A set of figures-of-merit for the overall characterization of silicon-comprising nonlinear waveguides has been established, taking into account the two-photon absorption and free-carrier effects.

Using these FoM, we have optimized an HSP waveguide design employing an inverted metal wedge and have acquired record-high nonlinear-parameter values approaching 10^4 $m^{-1}W^{-1}$. Furthermore, we have shown that the power-ceiling above which the FCE and TPA overwhelm the Kerr-effect is approximately two orders-of-magnitude higher compared to standard SOI waveguides. Finally, our findings have been corroborated with vectorial nonlinear Schrödinger equation techniques and full-wave beam-propagation numerical simulations, validating the proposed optimization approach.

Acknowledgement

This research has been co-financed by the European Union (European Social Fund – ESF) and Greek national funds through the Operational Program "Education and Lifelong Learning" of the National Strategic Reference Framework (NSRF) – Research Funding Program: Heracleitus II. Investing in knowledge society through the European Social Fund.

References

[1] Q. Lin, O.J. Painter, G.P. Agrawal, Nonlinear optical phenomena in silicon waveguides: Modeling and applications, *Opt. Express*, Vol. 15, No. 25, 16604–16644, 2007.

[2] B.A. Daniel, G.P. Agrawal, Vectorial Nonlinear Propagation in Silicon Nanowire Waveguides: Polarization Effects, *J. Opt. Soc. Am. B*, Vol. 27, No. 5, 956–965, 2010.

[3] C. Koos, P. Vorreau, T. Vallaitis, P. Dumon, W. Bogaerts, R. Baets, B. Esembeson, I. Biaggio, T. Michinobu, F. Diederich, W. Freude, J. Leuthold, All-Optical High-Speed Signal Processing with Silicon-Organic Hybrid Slot Waveguides, *Nat. Photonics*, Vol. 3, 216–219, 2009.

[4] M.L. Brongersma, R. Zia, J.A. Schuller, Plasmonics - The missing link between nanoelectronics and microphotonics, *Appl. Phys. A*, Vol. 89, No. 2, 221–223, 2007.

[5] R.F. Outlon, V.J. Sorger, D.A. Genov, D.F.P. Pile,X. Zhang, A hybrid plasmonic waveguide for subwavelength confinement and long-range propagation, *Nat. Photonics*, Vol. 2, No. 8. 496–500, 2008.

[6] A. Pitilakis, O. Tsilipakos, E.E. Kriezis, Nonlinear Effects in Hybrid Plasmonic Waveguides, in *Proceedings of 14th International Conference on Transparent Optical Networks*, Coventry, United Kingdom, July 2012, Art. No. 6254436.

[7] M. Wu, Z. Han, V. Vien, Conductor-Gap-Silicon Plasmonic Waveguides and Passive Components at Subwavelength Scale, *Opt. Express*, Vol. 18, 11728–11736, 2010.

[8] A. Boltasseva, V.S. Volkov, R.B. Nielsen, E. Moreno, S.G. Rodrigo, S.I. Bozhevolnyi, Triangular metal wedges for subwavelength plasmon-polariton guiding at telecom wavelengths, *Opt. Express*, Vol. 16, No. 8, 5252–5260, 2008.

[9] O. Tsilipakos, A. Pitilakis, A.C. Tasolamprou, T.V. Yioultsis, E.E. Kriezis, Computational Techniques for the Analysis and Design of Dielectric-Loaded Plasmonic Circuitry, *Opt. Quant. Electron.*, Vol. 42, 541–555, 2011.

[10] L. Yin, G.P. Agrawal, Impact of two-photon absorption on self-phase modulation in silicon waveguides, *Opt. Lett.*, Vol. 32,No.14,2031–2033, 2007.

[11] E. Dulkeith, Y.A. Vlasov, X. Chen, N.C. Panoiu, R.M. Osgood, Jr., Self-phase-modulation in submicron silicon-on-insulator photonic wires, *Opt. Express*, Vol. 14, No. 12, 5524–5534, 2006.

Rigorous characterization of surface plasmonic waveguides and guided-wave devices for THz system.

B.M.A. Rahman, C. Themistos, H. Tanvir, A. Quadir, and C. Markides
City University London Northampton Square, London EC1V 0HB, UK

ABSTRACT

A rigorous full-vectorial modal solution approach based on the finite element method is used to find the propagation properties of THz waveguides supporting plasmonic modes. As plamonic modes are very lossy, design approaches are presented here to reduce their modal losses. Design of several THz devices, including quantum cascade lasers, power splitters and narrow-band filters are also presented.

Keywords- Surface Plasmon modes, THz waveguides; THz devices, finite element method**.**

1. INTRODUCTION

The terahertz (THz) region occupies a large portion of the electromagnetic spectrum, located between the microwave and optical frequencies and normally is defined as the band ranging from 0.1 to 10 THz. In recent years, this intermediate THz radiation band has attracted considerable interest, because it offers significant scientific and technological potential for applications in many fields, such as sensing [1], imaging [2] and spectroscopy [3]. However, waveguiding in this intermediate spectral region is a major challenge and strong dielectric and conductive losses in the terahertz frequency range have been a major problem for waveguiding. The conventional guiding structures exemplified by microstrips, coplanar striplines and coplanar waveguides [4] are highly lossy and dispersive. However, so far the most promising dielectric waveguides have been the use of photonic crystal fibers at terahertz frequencies [5, 6] and metal coated guides [7] at terahertz frequencies. In this paper, various types of practical metal coated plasmonic waveguides are evaluated and design optimization of Quantum Cascade Lasers, MMI-based power splitters and narrow-band filters are presented, by using full-vectorial finite element method [8].

2. THZ WAVEGUIDES

Dielectric waveguides in silica, silicon, polymer, and other semiconductors materials have been widely used at optical frequencies: however most of these materials are very lossy at the lower terahertz frequency range. Since air has lower loss than all the known dielectric materials, sub-wavelength air-clad dielectric waveguides [9] have been considered for THz guidance. Photonic crystal fibres (PCF), which have many air-holes running along the waveguide, has also been considered for THz guidance. So far most of the PCFs that have been considered have been fabricated from silica or non-silica glasses, due to their low loss in the optical frequency range, but the material loss of silica is prohibitively high at THz frequencies. Only recently, Han *et al*. [5] have fabricated a PCF for THz using high-density polyethylene (HDPE) with modal loss values of 0.2 cm^{-1} and Goto *et al*. [6] have reported a PCF-like waveguide using Teflon tubes and filaments with loss values of 0.5 cm^{-1}, showing their potential. More recently, a porous core sub-wavelength guide has also been reported [10] to increase the power in the air claddings or air-holes. Recently, we have also reported the design of PCF with porous core [11], where maximum 60% power confinement in the air-holes has been achieved.

Amongst the various THz waveguides that have also been suggested, the metal-clad waveguides supporting surface plasmon modes are showing the greatest promise as low-loss waveguides for use both in active components and as passive waveguides. Several waveguide structures incorporating metallic layers have been reported, such as low-loss and flexible hollow polycarbonate waveguide with copper and dielectric inner coatings, deposited by using a liquid chemistry approach [12]. A metal-coated hollow glass waveguide (HGW) [13] with an inner silver/polystyrene-coating is considered for the better understanding of the various loss mechanisms and subsequently design optimization of a low-loss THz waveguide. For this waveguide the thickness of the silica tube (*s*) is taken as 0.5 mm and the bore radius (*a*) of the HGW as 2 mm. The thickness of the silver cladding (*t*) and polystyrene layer (*p*) are taken as t μm and p μm, respectively. The complex refractive index of the polystyrene, the silver metal cladding layers and the silica ring are taken as n_p=1.58 –j0.0036, n_m=308-j532 and n_s=1.96 –j0.0061, respectively at an operating frequency of 2.5 THz. At this

frequency, as the air is also not absolutely loss-free, to represent this loss factor its complex refractive index is taken as $1.0 - j\ 1.1x10^{-6}$.

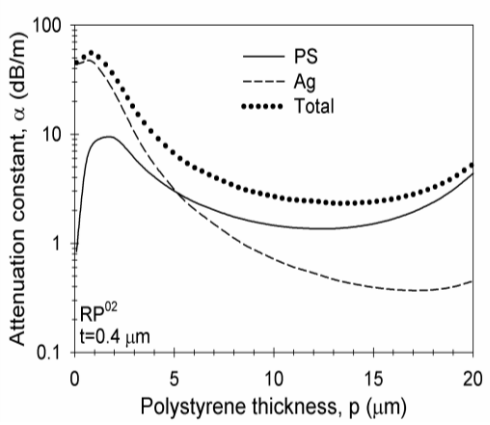


Figure 1. Attenuation constant with the polystyrene thickness, *p*, for *t*=0.4μm for a 2 mm bore waveguide.

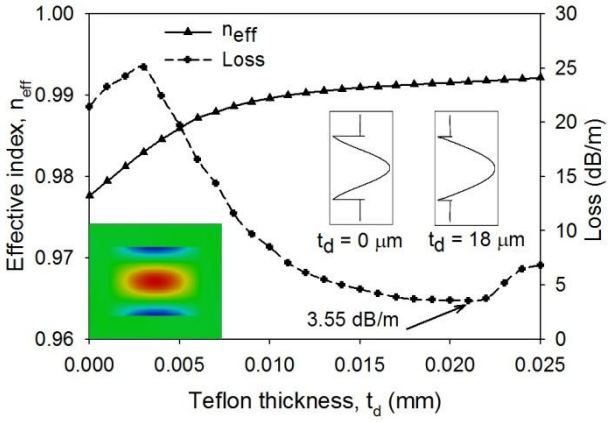


Figure 2. Effective index and loss with Teflon thickness for the H^x_{10} mode in a rectangular waveguide.

There are two metal/dielectric interfaces, which can support surface plasmon modes (SPM), one the outer silver/silica boundary and the other at the inner silver/polystyrene (or air, when p = 0 μm) boundary. This waveguide supports two SPMs along these two metal/dielectric interfaces. The refractive indices of the inner and outer cladding materials being very different, the two SPMs have widely different propagation constants and they do not interact with each other. However, at the right and left hand sides of the metal/dielectric interfaces, when the same electric-wall boundary condition is imposed, the H_x field is forced to be zero at the metal boundary and no SPM exists. Another mode with the dominant H_y field, would form a similar SPM; however, at the left and the right interfaces. The H_y field profile of this mode is similar to the H_x field profile, but rotated by 90 degrees. These two modes have identical propagation constants and being degenerate, they can be superimposed to form radially polarized RP-like modes. The superposition of their field profiles indicates a rotationally symmetric profile similar to those reported for dielectric clad metal waveguides supporting surface plasmon modes at optical frequencies [14].

The loss values of the fundamental plasmonic mode increases with the PS thickness and not shown here. The attenuation characteristics of the RP^{02} mode, with the variation of the polystyrene thickness, for a silver thickness t = 0.4 μm, is shown in Fig. 1, where the loss contribution of the polystyrene and silver layers has also been examined. As can be seen from the above characteristics, the total attenuation shows a maximum and a minimum loss at a polystyrene thickness of about 1 μm and 13 μm, respectively. The attenuation curves due to the polystyrene and the silver layer exhibit similar trend with the total attenuation. Throughout the range of polystyrene thicknesses examined, the optical power confinement in the inner air-core is of the order of 99.9%, thus contributing a constant attenuation of about 0.25 dB/m. For a polystyrene thickness lower than 5 μm, the total attenuation is affected mainly due to the metal attenuation but as the polystyrene thickness increases above 5 μm the total attenuation is mainly governed by the loss in the polystyrene layer. This mode shows a greater promise to achieve low-loss guidance through a metal clad dielectric waveguides. It would also be easier to couple this mode since the field profile is also very close to a Gaussian shape [13]. The modal loss of this waveguide, when design is optimized, is significantly lower than most of the THz waveguides reported so far, as most of the power is being guided in the central air-hole region.

Next this novel approach is considered to design and optimize a low-loss rectangular core metal waveguide. If we consider its height and widths are different then the polarized modes will not be degenerate. In our more recent work [15], we have shown that similarly a polarization maintaining rectangular core air-core dielectric-clad metal-coated waveguide can also be less lossy. A thin metal coating would support plasmonic modes, but these are relatively lossy. However, a Teflon coating on the gold layer can draws field away from the lossy conducting layer and loss may reduce considerably. Figure 2 shows the variation of the loss value with the Teflon thickness for the H^x_{12} mode in an air-core 1mm x 0.6 mm rectangular waveguide with 0.7 μm gold coating at 2.5 THz. It can be seen that at the optimum 21 μm Teflon thickness, the loss value can be 3.5 dB/m, one of the lowest reported so far [15]. The evolution of third order mode for no Teflon coating to a near Gaussian profile for 18 μm Teflon coating are shown as insets.

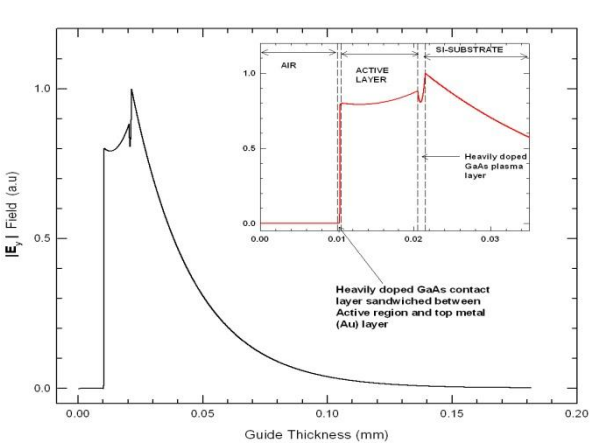


Figure 3. Field profile of $\mathbf{E_y}$ mode in a THz Quantum Cascade Laser. The field inside the confinement layers is shown on the inset.

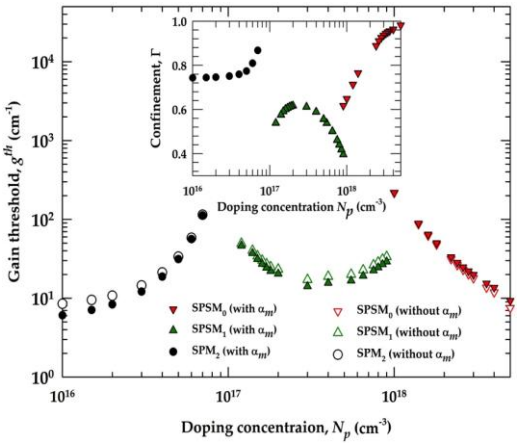


Figure 4. Gain threshold of several plasmonic modes.

Quantum cascading lasers [16] are emerging as efficient high power THz source for many important applications, such as imaging and sensing. However, for the THz frequency, the wavelength is large and it is not possible to grow the semiconductor materials comparable to the operating wavelength. For this reason, for THz QCL often smaller height needs to be considered and plasmonic confinement is used in that direction. The plasmonic confinement in the vertical direction is shown in Fig.3, which clearly shows the mode formation at the metal-dielectric interfaces. However, it is easily possible to have a wider guide, so mostly dielectric confinement is used in horizontal direction. The gain threshold for such QCL is shown in Fig.4. Because of the wider guides, the gain threshold difference between the fundamental and higher order (lateral) modes are very small. This allows possibility of mode hopping for any external changes. A novel design approach is considered [17] using slotted upper metal clad, to enhance the gain threshold of the higher order modes. Fig. 5 clearly shows that gain threshold of the higher order modes are increased for slotted-electrode designs. For the future THz system, it is essential to design various integrated guided-wave components. In that spirit, it is shown here that a compact power splitter can b designed by using the MMI principle. In Fig. 6, it is shown here that an efficient power splitter can be designed by using a 35 μm long multimoded section [18].

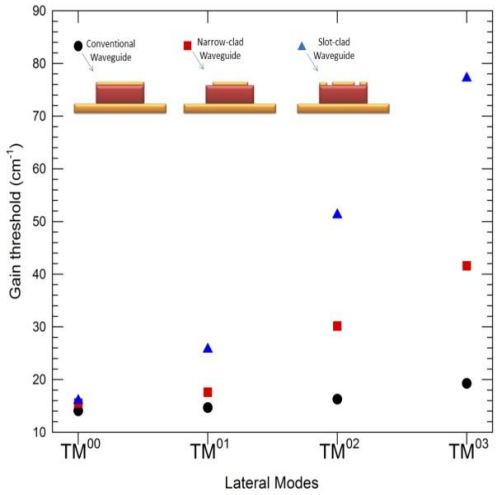


Figure 5. Gain Threshold of the lower order modes for different waveguides

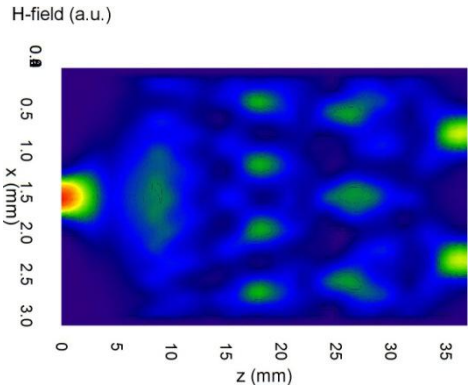


Figure 6 FDTD Simulation of the MMI 3dB coupler

Finally, a Terahertz frequency range band-stop filter for molecular sensing [19], where two 5 μm wide band-stop filter stubs with a length of 192 μm and 83 μm are placed at a 400 μm apart along the direction of propagation, as shown in the right inset of Fig.7, has been considered. Initially the above device has been simulated without a polysterene film on top of the metal layer, using the FDTD approach and the variation of the insertion loss with the frequency is presented in Fig.10. As can be seen from the above frequency response, the device exhibits two resonant frequencies due to the stubs at about 600 and 800 GHz, with a minimum insertion loss of about -55 and -30 dB.

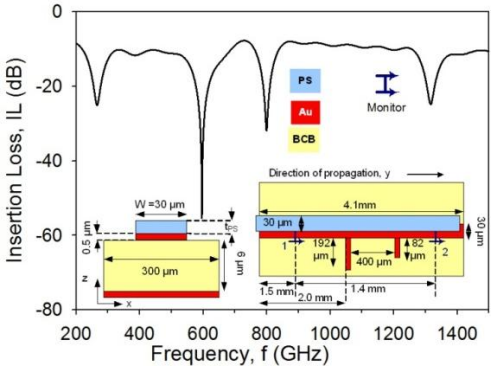


Figure 7 Insertion Loss with frequency for the microstrip filter

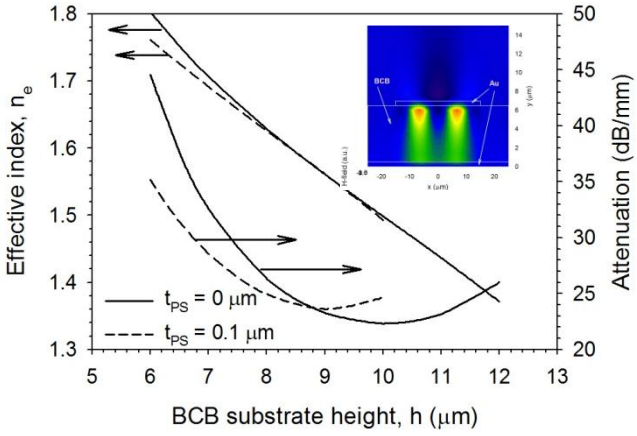


Figure 8 Variation of the effective index and attenuation with BCB substrate height of the microstrip line. (mode shown as inset)

Initially, the fundamental Quasi-TEM mode of the microstrip line, has been obtained using the FEM and the magnetic H_x field profile of the above mode is presented as inset in Fig.8 The effective index and attenuation of the above mode were found to be 1.803 and 44.59 (dB/mm), respectively. The effect on the propagation characteristics of the device of a polysterene layer along the top of the metal layer has then been examined, using the FEM. For a polysterene thickness of 0.1 μm the effective index and attenuation constant of the device were found be 1.76 and 35.21 (dB/mm), respectively, thus slightly lower compared with the corresponding values obtained for the plain metallic structure. However, as the polysterene thickness increases, both the effective index and the attenuation increase and for a thickness of 0.5 μm of the above material the loss level reaches the value obtained for the structure without the polysterene film. As the polysterene thickness further the attenuation increase much above the corresponding value obtained for the structure without the above film deposition (not shown here), and therefore, it can be concluded that attenuation reduction of the above device can only be achieved for a very thin polysterene film deposition.

The BCB substrate height, *h*, has then been varied and the effective index and attenuation of the microstrip structure with no polysterene layer on top of the metal and that with a 0.1 μm film thickness of the above material have been examined and presented in Fig.8. As can be seen from the above characteristics, as the substrate height increases both the effective index and the attenuation decrease, with the corresponding values of the structure with the polysterene film being lower than those obtained for the device without it. At a substrate height of about 9 μm, the above corresponding values are about the same for both the structures examined. However, the device with the polysterene film exhibits minimum attenuation at the above substrate height and as the substrate height increases further the attenuation of the structure with the polysterene layer becomes higher than that obtained for the structure without the above material.

3. CONCLUSION

A finite-element approach, based on a full-vectorial **H**-field formulation, has been used to study the detailed modal properties of metal clad waveguides supporting plasmonic modes operating in the THz frequency range. It is shown here that by using a thin but optimized dielectric over-layer plasmonic loss in a hollow-core waveguide can also be reduced. It is also shown here that by using a novel slot-type electrode, the differential loss of the higher order modes can be significantly increased to reduce mode hopping. Finally, simple guided-wave devices such as power splitters and band-pass filters are also presented here. The design approach used here can be extended to optimize not only THz waveguides but also more advanced guided-wave devices for future THz integrated circuits (TIC).

REFERENCES

[1] R. H. Jacobsen, D. M. Mittleman, and M. C. Nuss, "Chemical recognition of gases and gas mixtures with terahertz waves," *Optics Lett*., **21**, no.24, pp. 2011-2013, 1996.

[2] Q. Chen, Z. Jiang, G. X. Xu, and X. C. Zhang, "Near-field terahertz imaging with a dynamic aperture," *Optics Lett*., **25**, no.15, pp.1122-1124, 2000.

[3] J. Q. Zhang and D. Grischkowsky, "Waveguide terahertz time-domain spectroscopy of nanometer water layers," *Optics Lett*., **29**, no.14, pp.1617-1619, 2004.

[4] M. Y. Frankel, S. Gupta, J. A. Valdmanis and G. A. Mourou, "Terahertz attenuation and dispersion characteristics of coplanar transmission-lines," *IEEE Trans. Microwave Theory Tech*., **MTT-39**, no.6, pp.910-916, 1991.

[5] H. Han, H. Park, M. Cho, and J. Kim, "Terahertz pulse propagation in plastic photonic crystal fiber," *Appl. Phys. Lett*, **80**, no.15, pp.2634-2636, 2002.

[6] M. Goto, A. Quema, H. Takahahi, S. Ono, and N. Sarukura, "Teflon photonic crystal fiber as terahertz waveguide," *Jpn. J. Appl. Phys*, Part 2 **43**, L317-L319, 2004.

[7] R. W. McGowan, G. Gallot, and D. Grischkowsky, "Propagation of ultrawideband short pulses of Terahertz radiation through submillimeter diameter circular waveguides," *Opt. Lett*, vol. **24**, no. 20, pp. 1431-1435, Oct 1999.

[8] B. M. A. Rahman and J. B. Davies, "Finite-element analysis of optical and microwave waveguide problems," *Trans. Microwave Theory Tech*, **MTT-32**, no.1, pp.20-28, 1984.

[9] L. J. Chen, H. W. Chen, T. F. Kao, J. Y. Lu and C. K. Sun, "Low-loss subwavelength plastic fiber for terahertz waveguiding", Opt. Lett., vol. 31, no. 3, pp. 308-310, 2006.

[10] A. Hassani, A. Dupuis, and M. Skorobogatiy, "Porous polymer fibers for low-loss terahertz guiding" Opt. Express, vol. 16, no. 9, pp. 6340–6351, 2008.

[11] M Uthman, B. M. A. Rahman,, Design and characterization of low-loss porous-core photonic crystal fiber, IEEE Photonics J, vol. 4, no. 6, pp.2314-2325, Dec 2012.

[12] J. A. Harrington, R. George, P. Pederson, and E. Mueller, "Hollow polycarbonate waveguides with inner Cu coatings for delivery of terahertz radiation," *Opt Express*, vol. **12**, no.21, pp. 5263-5268, Oct. 2004.

[13] C. Themistos, B. M. A. Rahman, M. Rajarajan, K. T. V. Grattan, B. Bowden, and J. A. Harrington, "Characterization of Silver/Polystyrene (PS)-coated hollow glass waveguides at terahertz frequency," *J. Lightwave. Technol.*, vol. **25**, no. 9, September 2007.

[14] C. Themistos, B. M. A. Rahman, and K. T. V. Grattan, "TM/TE modal solution for sub-micron lossy metal-clad optical fibers," *Proc. Inst. Electr. Eng. – Optoelecton.*, vol. **145**, no. 3, pp. 171-177, June 1998.

[15] B.M.A. Rahman, A. Quadir, H. Tanvir and K.T.V. Grattan, "Characterization of Plasmonic Modes in a Low-Loss Dielectric-Coated Hollow Core Rectangular Waveguide at Terahertz Frequency," *IEEE Photonics Journal*, vol.3, pp.1054-1066, 2011.

[16] J. Faist, F.Capasso, D. L. Sivco, C. Sirtori, A. L. Hutchison, A. Y. Cho, "Quantum cascade laser," *Science*, vol.**264**, pp. 553-556, 1994.

[17] H. Tanvir, B.M.A. Rahman and K.T.V. Grattan, "Impact of "Ghost" Mode Interaction in Terahertz Quantum Cascade Lasers," IEEE Photonics Journal, vol.3, pp.926-935, 2011

[18] C. Markides, C. Themistos, H. Tanvir, B.M.A. Rahman, and K.T.V. Grattan, "Multimode Interference 3dB splitters in hollow core metallic waveguides for low loss THz wave transmission", IEEE *J. Selected Topics in Quantum Electron*. Vol. 19, pp.8500606-8500704, Feb. 2013.

[19] J. Cunningham, C. Wood, A. G. Davies, I. Hunter, E. H. Linfield, and H. E. Beere, "Terahertz frequency range band-stop filters," *Applied Physics Letters*, vol.86,p.213503, 2005.

Singularities & broken symmetries of systems with gain and loss structu

Soliton scattering in the chain of optical waveguides including $\mathcal{PT}$- symmetric defect

Sergey V. Suchkov[1*], Sergey V. Dmitriev[1], Andrey A. Sukhorukov [2], Igor V. Barashenkov[3], Elina R. Andriyanova[4], Karina M. Badgetdinova[4], Yuri S. Kivshar[2]

[1]Institute for Metals Superplasticity Problems, RAS, Ufa 450001, Russia
[2]Nonlinear Physics Centre, Research School of Physics and Engineering, Australian National University, Canberra ACT 0200, Australia
[3]Department of Mathematics, University of Cape Town, Rondebosch 7701, South Africa
[4]Department of General Science, Ufa State Aviation Technical University, Ufa, Russia
*corresponding author, E-mail: sergey.v.suchkov@gmail.com

Abstract

We study the sensitivity of light dynamics to the internal phase of propagating pulses in the two types of $\mathcal{PT}$-symmetric models. The first is a waveguide array with an embedded pair of waveguides with gain and loss, called $\mathcal{PT}$-coupler, and the second is a planar coupler which models a chain of $\mathcal{PT}$-symmetric couplers. For the first model we investigate the soliton scattering on the mode localized on the coupler, while for second model we study the collision of two breathers. For both models we find that the light dynamics is sensitive to the internal phases of the interacting pulses. Particularly, the $\mathcal{PT}$-symmetry breaking can take place or not, depending on the internal phases of two signals having identical other parameters.

1. Introduction

Under the parity-time ($\mathcal{PT}$) symmetry constraint non-Hermitian Hamiltonians can have an entirely real eigenvalue spectrum [1]. For optical structures the necessary condition for the $\mathcal{PT}$-symmetry of a Hamiltonian with a complex potential, $V(x)$, can be reduced to the condition $V(x) = V^*(-x)$ [2] which can be realized by combining a spatially symmetric profile of the refractive index with symmetrically positioned gain and loss regions. Photonic structures composed of coupled waveguides with loss and gain offer new possibilities for shaping optical beams and pulses compared to conservative structures. Such structures can be designed as optical analogues of complex $\mathcal{PT}$- symmetric potentials, which can have a real spectrum corresponding to the conservation of power for optical eigenmodes, however the beam dynamics can demonstrate unique features distinct from conservative systems due to nontrivial wave interference and phase transition effects [2]. Recently the possibility of creation of $\mathcal{PT}$ -symmetric optical coupler, a pair of waveguides with gain in one of them and loss in another, was demonstrated experimentally [3, 4, 5].

In the present study we consider two models, one is the waveguide array with an embedded $\mathcal{PT}$ -coupler and another one is the chain of such couplers. For the first model the problem of interaction of the soliton with the coupler is analysed and for the second model we investigate the outcome of breather-breather collisions. In both cases we focus on the effect of the internal phases of the solitary waves on the collision outcome and particularly on the $\mathcal{PT}$ -symmetry breaking. Note that the non-trivial effects of the solitary wave phases on their collision outcomes have been reported for the conservative nonlinear Shrödinger equation [6, 7, 8].

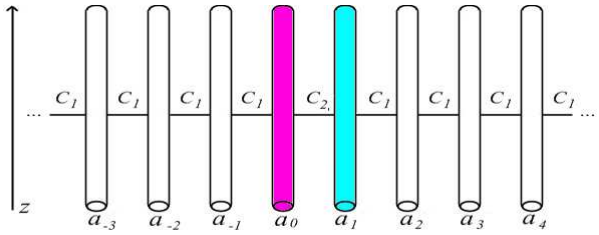


Figure 1: A scheme of optical waveguide array composed of conservative waveguides with embedded $\mathcal{PT}$-symmetric pair of waveguides with gain and loss at $j = 0, 1$, correspondingly, where j is the waveguide number.

2. Array of optical waveguides with embedded $\mathcal{PT}$-symmetric element

Firstly, we consider a chain of coupled optical waveguides with an embedded pair of $\mathcal{PT}$-symmetric waveguides schematically shown in Fig. 1. Light propagating through the waveguide array can be described by the following set of discrete nonlinear Shrödinger equations,

$$i\frac{da_j}{dz} + C_1 a_{j-1} + C_1 a_{j+1} + |a_j|^2 a_j = 0,\ j \neq 0, 1, \quad (1)$$

$$i\frac{da_0}{dz} + i\rho a_0 + C_1 a_{-1} + C_2 a_1 + |a_0|^2 a_0 = 0, \quad (2)$$

$$i\frac{da_1}{dz} - i\rho a_1 + C_2 a_0 + C_1 a_2 + |a_1|^2 a_1 = 0, \quad (3)$$

where z is the propagation coordinate along the waveguides, C_1 and C_2 are the coupling constants describing the interaction between waveguides, ρ is the gain-loss coef-

ficient, a_j are the optical mode amplitudes, and j is the waveguide number. This model was studied in our recent works [9, 10, 11]. In the present study we focus on the effect of phase sensitivity of light dynamics in this model.

Since the array is composed of conservative waveguides on either sides of the $\mathcal{PT}$-coupler, far from the defect Eqs. (1) admit conventional approximate solutions for self-localized beams (solitons) that can propagate through the waveguide array [12, 13] for $j < 0$ and $j > 1$,

$$a_j = A\mathrm{sech}[\delta(j - j_0 - 2C_1 vz)]e^{i[v(j-j_0)+\beta_s z+\alpha]}, \quad (4)$$

where A defines the soliton amplitude, $\delta = A\sqrt{\gamma/2C_1}$ is the inverse width, v is the normalized velocity, $\beta_s = (\delta^2 - v^2 + 2)C_1$ is the propagation constant, j_0 is the initial position, and α is the initial phase of the soliton. For conservative systems, it is known that it is possible to flexibly control the soliton scattering by exciting a localized mode at a defect [14, 15]. The study of interaction between a soliton and a localized mode in the model with gain and loss may lead to new effects.

Properties of the mode localized on the $\mathcal{PT}$-coupler can be determined analytically in the linear regime [9]. The modes exist for $C_1 < C_2$, and their profiles are found from the linearized system (1) as

$$\begin{aligned} a_j(z) &= Bq^{-j}\exp(-i\beta_l z), j \le 0, \\ a_j(z) &= Bq^{j-1}\exp(-i\beta_l z + i\varphi), j \ge 1, \end{aligned} \quad (5)$$

where

$$\begin{aligned} \beta_{l_{1,2}} &= \pm\left(\overline{\rho}^2 - \overline{C_1}^2 - 1\right)\left(1 - \overline{\rho}^2\right)^{-1/2} C_2, \\ q_2 &= \frac{1}{q_1} = -\frac{\beta_{l_{1,2}}}{2C_1} + \left(\frac{\beta_{l_{1,2}}^2}{4C_1^2} - 1\right)^{1/2} \\ \varphi_1 &= -\arcsin\overline{\rho}, \;\; \varphi_2 = \pi + \arcsin\overline{\rho}. \end{aligned} \quad (6)$$

Here B is the mode amplitude and β_l is the propagation constant. For $C_2 < C_1$ the localized mode is not supported because its propagation constant lies within the spectrum of extended plane waves of the waveguide array surrounding the $\mathcal{PT}$-coupler.

In order to obtain high-amplitude localized modes, we use a special numerical procedure. We start from the initial conditions defined by Eq. (5) to excite a low-amplitude mode, and then pump it up by setting in Eq. (1) the gain coefficient equal to $-(\rho + \epsilon)$ and the loss coefficient equal to $(\rho - \epsilon)$, where $\epsilon > 0$ is a small quantity. Thus, the gain will exceed the loss, and the energy of the localized mode will grow. This way we have got modes with amplitudes $B = \{1.2, 1.4, 1.6, 1.89\}$, for the model parameters $C_1 = 2$, $C_2 = 4$, $\rho = 1.5$, which were obtained by setting $\epsilon = 0.0025$ and the initial conditions defined by Eq. (5) with $\beta_l = -4.787$, $q = 0.54$, $\varphi = -0.38$, and $B = 1$. We find that the modes with $B > 1.89$ are unstable due to the nonlinear $\mathcal{PT}$-symmetry breaking, similar to an instability in an isolated nonlinear $\mathcal{PT}$-coupler [16]. The parameters of the incident soliton are chosen as follows: $A = 0.5$, $j_0 = -50v$, and $\beta_s = 3.65$.

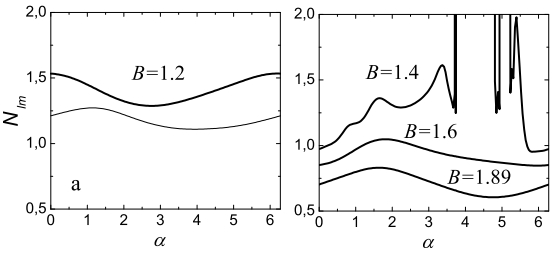


Figure 2: Change of the localized mode energy due to the interaction with the soliton, N_{lm}, as the function of the initial phase of the incident soliton, α. The model parameters are $C_1 = 2$, $C_2 = 4$, and $\rho = 1.5$; soliton amplitude is $A = 0.5$. Thick and thin lines correspond to the soliton incident from the left ($v = 0.5$) and from the right ($v = -0.5$), respectively. The initial amplitude of the localized mode, B, is indicated by labels.

We revealed that the interaction of the soliton with the localized mode can result in $\mathcal{PT}$-symmetry breaking or in a stable dynamics depending only on the internal phases of the two considered modes. To study this effect in more detail we define the parameter N_{lm} as a ratio of the localized mode energy after the passing of the soliton to its initial value. We find that N_{lm} depends on the initial soliton phase, α. Figure 2(a) shows the dependence of N_{lm} on α for the localized mode with the amplitude $B = 1.2$. Thick and thin lines show the results for the soliton incident from the left ($v = 0.5$) and from the right ($v = -0.5$), respectively. In Fig. 2(b) N_{lm} is shown as a function of α for the localized modes with the amplitudes $B = 1.4$, $B = 1.6$, and $B = 1.89$ for the soliton moving from the left ($v = 0.5$). For the soliton moving from the right, the interaction with the high-amplitude localized mode leads to $\mathcal{PT}$-symmetry breaking (the fact that the $\mathcal{PT}$-symmetry breaking occurs for smaller values of the localized mode amplitudes in the case when the incident soliton firstly hits the element with gain does not seem surprising).

As follows from Fig. 2, the interaction of the soliton with the localized mode depends on the parameters of the mode and the soliton in a nontrivial way. In particular, for the localized mode amplitude $B = 1.4$, there exists a range of the soliton initial phase, α, where the $\mathcal{PT}$-symmetry breaking occurs and the mode energy diverges.

In practice it is difficult to control the phases of the soliton and the localized mode at the time of interaction. In such circumstances, for the known signal amplitudes and soliton velocity one can only estimate the probability of $\mathcal{PT}$-symmetry breaking considering the phases are homogeneously distributed random variables. Let us discuss the probabilistic approach to the investigation of interaction between two breathers propagating in the model of planar $\mathcal{PT}$-coupler.

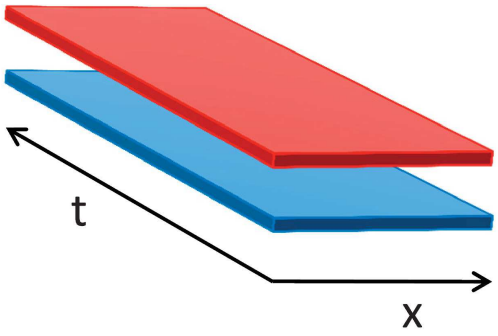


Figure 3: A scheme of the planar $\mathcal{PT}$-coupler. The red waveguide undergoes gain and the blue one loss.

2.1. Interaction of breathers in the model of planar $\mathcal{PT}$-coupler

Similar effect of phase sensitivity is observed in the model of planar $\mathcal{PT}$-symmetric coupler schematically shown in Fig. 3.

We notice that this model can be treated as a continuum limit of the chain of $\mathcal{PT}$-symmetric couplers which was studied in several works [17, 18, 19, 20, 21].

Light dynamics governed by the following pair of nonlinear Shrödinger equations

$$\begin{aligned} iu_t + u_{xx} + 2|u|^2u = -v + i\rho u, \\ iv_t + v_{xx} + 2|v|^2v = -u - i\rho v. \end{aligned} \tag{7}$$

Here t stands for the spatial coordinate, while x for the transverse one, $\rho > 0$ is a gain/loss coefficient, $|u|^2$ and $|v|^2$ define light intensity. In the work [21] it was demonstrated that this model supports the breather solutions propagating without noticeable changes in their profiles along the t coordinate. It was found that the initial conditions for a static breather can be taken in the form

$$\begin{aligned} u(t) = a + b, \;\; v(t) = e^{i\theta}b - e^{-i\theta}a, \\ a = \sqrt{\epsilon}[A_0 + \epsilon A_1 + O(\epsilon^2)], \\ b = \sqrt{\epsilon}[B_0 + \epsilon B_1 + O(\epsilon^2)], \end{aligned} \tag{8}$$

where

$$\begin{aligned} A_0 = \frac{e^{-i(\omega_0-\epsilon)t}}{\sqrt{3}}\mathrm{sech}\left(\sqrt{\epsilon}(x-x_0)\right)\times \\ \left[1 - \frac{\epsilon}{102\omega_0}\left(6 + \mathrm{sech}(x-x_0)^2\right)\right], \\ B_0 = \frac{e^{i(\omega_0+\epsilon)t}}{\sqrt{3}}\mathrm{sech}\left(\sqrt{\epsilon}(x-x_0)\right)\times \\ \left[1 + \frac{\epsilon}{102\omega_0}\left(6 + \mathrm{sech}(x-x_0)^2\right)\right], \\ A_1 = \frac{e^{i\epsilon t}}{6\sqrt{3}\omega_0}\mathrm{sech}^3\left(\sqrt{\epsilon}(x-x_0)\right)\times \\ \left[e^{i(3\omega_0 t+2\theta)} - 4i\rho e^{-i(3\omega_0 t+\theta)}\right], \\ B_1 = -\frac{e^{i\epsilon t}}{6\sqrt{3}\omega_0}\mathrm{sech}^3\left(\sqrt{\epsilon}(x-x_0)\right)\times \\ \left[4i\rho e^{i(3\omega_0 t+2\theta)} + e^{-i(3\omega_0 t+\theta)}\right], \\ \theta = \arcsin\rho, \quad \omega_0 = \cos\theta. \end{aligned} \tag{9}$$

Here ϵ defines the breather amplitude, x_0 is the initial breather position. Using the Galilean transformation it is possible to obtain from (9) a moving breather solution.

If the $\mathcal{PT}$-symmetry breaking transition happens, one can say that all the information in the system is lost. It is thus important to study the conditions when such transition takes place.

The breather solution is more general then the soliton one and we will study the interaction between two breathers. We consider a simple case when the two breathers have equal amplitudes and opposite velocities. For our simulations we fix $x_0 = \pm 22.136$ and take the absolute value for breather velocities $V = 2$. The period of amplitude oscillation of breather, $T = \pi/\omega_0$, is divided into 24 equal parts and we do simulations for each value of t from this set. Thus we carry out 576 simulations to cover all possible phases of breather collisions. In Fig. 4 one can see the result of breather collisions for the amplitudes $A = \sqrt{\epsilon} = 0.3, 0.4, 0.5$ and for $\rho = 0.5, 0.7, 0.9$. The abscissa and the ordinate indicate the numbers i and j, respectively, defining the initial value of the left and right breathers as follows $t_{\text{left}} = i\frac{T}{24}$ and $t_{\text{right}} = j\frac{T}{24}$. Black points show the parameters for which the $\mathcal{PT}$-symmetry braking does not take place, while the white ones stand for the $\mathcal{PT}$-symmetry breaking. We have also considered the cases when the gain/loss coefficient is $\rho = 0.1,\ 0.3$ and for all three considered values of the breather amplitude, we found that the $\mathcal{PT}$- symmetry breaking does not take place.

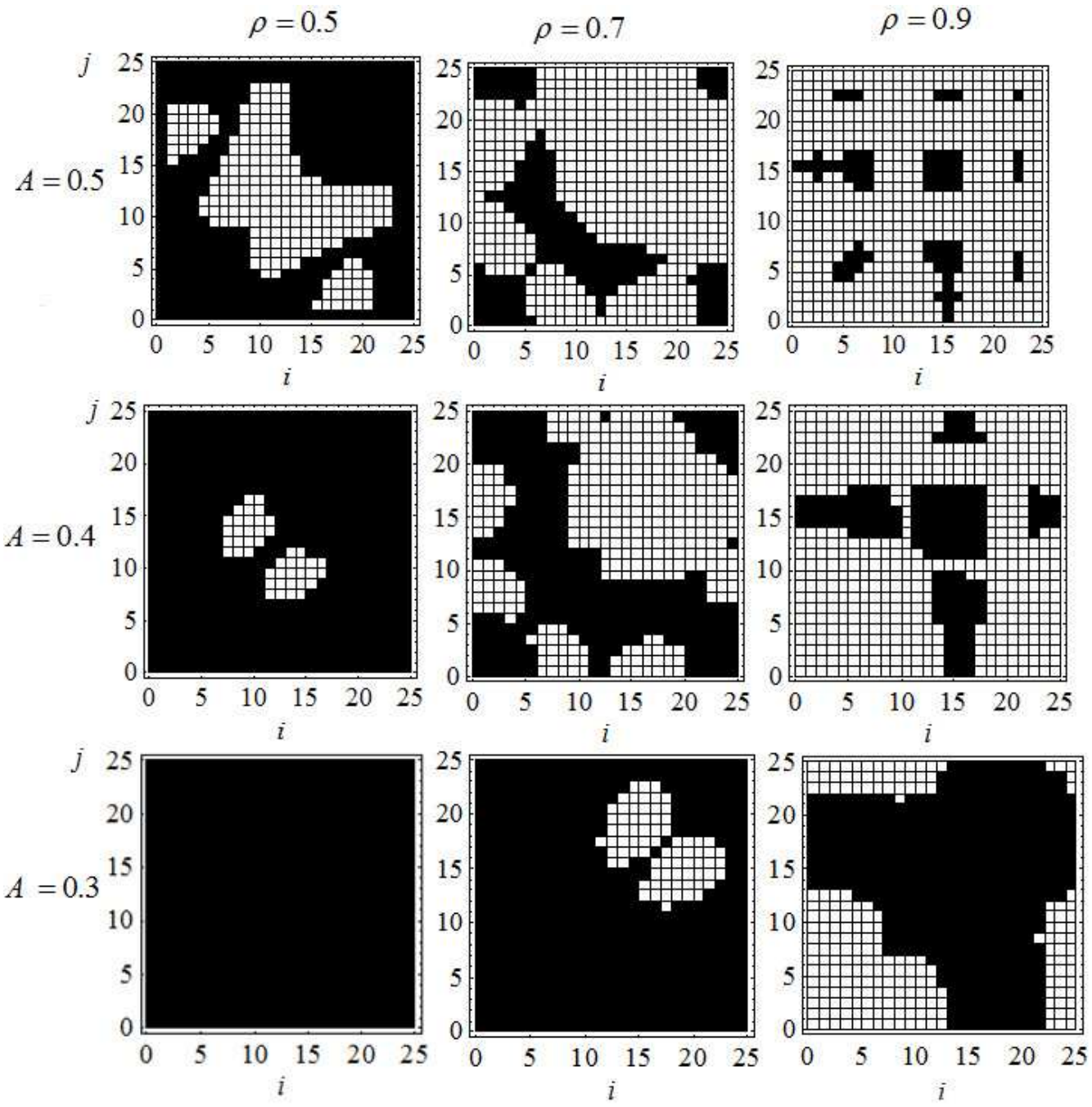


Figure 4: White areas of the initial breather phases where $\mathcal{PT}$-symmetry breaking takes place for different breather amplitudes and different values of the gain/loss parameter. The numbers i and j define the initial value of the left and right breathers as follows $t_{\text{left}} = i\frac{T}{24}$ and $t_{\text{right}} = j\frac{T}{24}$.

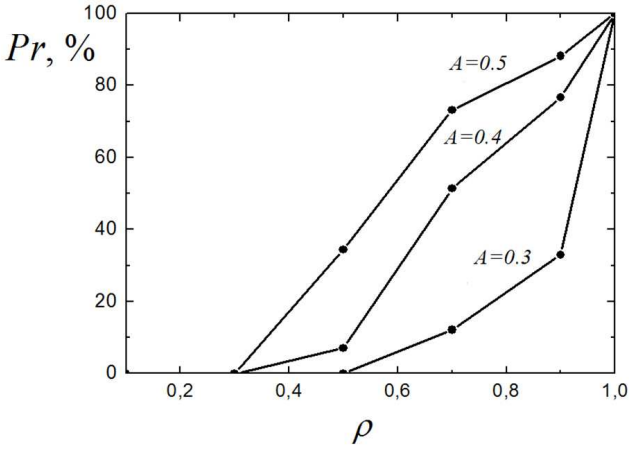


Figure 5: Probability of $\mathcal{PT}$-symmetry breaking as the function of ρ for the three studied values of the breather amplitude.

Using the obtained results we estimate the probability of $\mathcal{PT}$-symmetry breaking for the collision of two breathers as the function of gain/loss coefficient ρ for the three studied breather amplitudes (see Fig. 5). Here we assume that phases of breathers are homogeneously distributed random variables. Thus the probability of the $\mathcal{PT}$-symmetry breaking, Pr, is equal to the ratio of the white area in Fig. 2 to the whole area.

3. Conclusions

In this paper we investigate the effect of phase sensitivity of light dynamics propagating in the $\mathcal{PT}$-symmetric lattices. In contrast to the conservative structures, in the studied systems the interaction of signals can lead not only to some energy exchange between them but also to the $\mathcal{PT}$-symmetry breaking, which is undesirable for information transmission systems. Using two model systems as examples we demonstrated that the interaction between signals has probabilistic nature. The probability of the $\mathcal{PT}$-symmetry breaking was estimated numerically.

Acknowledgement

The work was supported by the Russian Foundation for Basic Research, grants 12-02-315-06 mol_a and 11-08-97057-p_povoljie_a, by the Australian Research Council (including Future Fellowship FT100100160).

References

[1] C. M. Bender, C. Boettcher, *Phys. Rev. Lett* 80, 5243–5246, 1998.

[2] R. El-Ganainy, K. G Makris, D. N. Chistodoulides, and Z. H. Musslimani, *Opt. Lett.* 32, p.2632, 2007.

[3] C. E. Ruter, K. G. Makris, R. El-Ganainy, D. N. Christodoulides, M. Segev, D. Kip, *Nature Physics* 6, pp. 192–195, 2010.

[4] A. Guo, G. J. Salamo, D. Duchesne, R. Morandotti, M. Volatier-Ravat, V. Aimez, G. A. Siviloglou D. N. Cristodoulides, *Phys. Rev. Lett.* 103, p.093902, 2011.

[5] A. Regensburger, C. Bersch, M.-A. Miri, G. Onishchukov, D. N. Christodoulides, and U. Peschel, *Nature* 488, p. 167, 2012.

[6] I. E. Papacharalampous, D. J. Frantzeskakis, P. G. Kevrekidis, B. A. Malomed. *Phys. Rev. E* 68, p. 466041, 2003.

[7] S. V. Dmitriev, T. Shigenari, *Chaos* 12, pp. 324-331, 2002.

[8] S. V. Dmitriev, D. A. Semagin, T. Shigenari, A. A. Sukhorukov, *Phys. Rev. E* 66, p. 046609, 2002.

[9] S. V. Dmitriev, S. V. Suchkov, A. A. Sukhorukov, and Yu. S. Kivshar, Scattering of solitons in nonlinear waveguide arrays on a pair of $\mathcal{PT}$-symmetric waveguides with balanced gain and loss, *Phys. Rev. A* 84, p. 013833, 2011.

[10] A. A. Sukhorukov, S. V. Dmitriev, S. V. Suchkov, and Yu.S. Kivshar, Nonlocality in $\mathcal{PT}$-symmetric waveguide arrays with gain and loss, *Opt. Lett.* 37, pp. 2148–2150, 2012.

[11] S. V. Suchkov, A. A. Sukhorukov, S. V. Dmitriev, Yu. S. Kivshar, Scattering of the discrete solitons on the $\mathcal{PT}$-symmetric defects, *EPL* 100, p. 54003, 2012.

[12] Yu. S. Kivshar, G. P. Agrawal, *Optical solitons. From fiber to photonic crystals*, Academic Press, 2003.

[13] A. V. Yulin, D. V. Skryabin, and P. S. J. Russel, Transition radiation by matter-wave solitons in optical lattices, *Phys. Rev. Lett.* 91, p. 260402, 2003.

[14] Yu. S. Kivshar, Z. Fei, and L. Vazquez, Resonant soliton-impurity interactions, *Phys. Rev. Lett.* 67, p. 1177, 1991.

[15] K. Forinash, M. Peyrard, and B. Malomed, Interaction of discrete breathers with impurity modes, *Phys. Rev. E* 49, p.3400, 1994.

[16] A .A. Sukhorukov, Z. Y. Xu, and Yu. S. Kivshar, Nonlinear suppression of time reversals in $\mathcal{PT}$-symmetric optical couplers, *Phys. Rev. A* 82, p. 043818, 2010.

[17] S. V. Suchkov, B. A. Malomed, S. V. Dmitriev, and Yu. S. Kivshar, Solitons in a chain of parity-time-invariant dimers, *Phys. Rev.* **E** 84, p 046609, 2011.

[18] S. V. Suchkov, S. V. Dmitriev, B. A. Malomed, and Yu. S. Kivshar, Wave scattering on a domain wall in a chain of $\mathcal{PT}$-symmetric couplers, *Phys. Rev. A* 85, p. 033825, 2012.

[19] R. Driben and B. A. Malomed, Stability of solitons in parity-time-symmetric couplers, *Opt. Lett.* 36, pp. 4323–4325, 2011.

[20] N. V. Alexeeva, I. V. Barashenkov, A. A. Sukhorukov, and Yu. S. Kivshar, Optical solitons in $\mathcal{PT}$-symmetric nonlinear couplers with gain and loss, *Phys. Rev. A* 85, p. 063837, 2012.

[21] I. V. Barashenkov, S. V. Suchkov, A. A. Sukhorukov, S. V. Dmitriev, and Yu. S. Kivshar, Breathers in $\mathcal{PT}$-symmetric optical couplers, *Phys. Rev. A* 86, p. 053809, 2012.

$\mathcal{PT}-$Symmetric Nonlinear Metamaterials and Zero-Dimensional Systems

G. P. Tsironis and N. Lazarides

Department of Physics, University of Crete, P. O. Box 2208, 71003 Heraklion, Greece;
&
Institute of Electronic Structure and Laser, Foundation for Research and Technology-Hellas,
P.O. Box 1527, 71110 Heraklion, Greece
*corresponding author, E-mail: nl@physics.uoc.gr

Abstract

A one dimensional, parity-time ($\mathcal{PT}$)-symmetric magnetic metamaterial comprising split-ring resonators having both gain and loss is investigated. In the linear regime, the transition from the exact to the broken $\mathcal{PT}$-phase is determined through the calculation of the eigenfrequency spectrum for two different configurations; the one with equidistant split-rings and the other with the split-rings forming a binary patterns ($\mathcal{PT}$ dimer chain). The latter system features a two-band, gapped spectrum with its shape determined by the gain and loss coefficients as well as the inter-element coupling. In the presense of nonlinearity, the $\mathcal{PT}$ dimer chain configuration with balanced gain and loss supports nonlinear localized modes in the form of a novel type of discrete breathers below the lower branch of the linear spectrum. These breathers, that can be excited from a weak applied magnetic field by frequency chirping, can be subsequently driven solely by the gain for very long times. The effect of a small imbalance between gain and loss is also considered. Fundamendal gain-driven breathers occupy both sites of a dimer, while their energy is almost equally partitioned between the two split-rings, the one with gain and the other with loss. We also introduce a model equation for the investigation of classical $\mathcal{PT}$ symmetry in zero dimensions, realized by a simple harmonic oscillator with matched time-dependent gain and loss that exhibits a transition from oscillatory to diverging motion. This behavior is similar to a transition from the exact to the broken $\mathcal{PT}$ phase in higher-dimensional $\mathcal{PT}-$ symmetric systems. A stability condition relating the parameters of the problem is obtained in the case of piecewise constant gain/loss function that allows the construction of a phase diagram with alternating stable and unstable regions.

1. Introduction

The investigation of artificial materials whose properties can be tailored has recently attracted a lot of attention. Considerable research effort has been invested in the developement of artificial structures that exhibit properties not found in nature. Two recent and well known paradigms are the metamaterials, that provide full access to all four quadrants of the real permittivity - permeability plane [1], and the parity - time ($\mathcal{PT}$) symmetric systems, whose properties rely on a delicate balance between gain and loss. The latter belong to a class of 'synthetic' materials that do not obey separately the parity ($\mathcal{P}$) and time ($\mathcal{T}$) symmetries but instead they do exhibit a combined $\mathcal{PT}$ symmetry. The ideas and notions of $\mathcal{PT}-$symmetric systems have their roots in quantum mechanics where $\mathcal{PT}-$symmetric Hamiltonians have been studied for many years [2]. The notion of $\mathcal{PT}$ symmetry has been recently extended to dynamical lattices, particularly in optics, where photonic lattices combining gain and loss elements offer new possibilities for shaping optical beams and pulses. Soon after the developement of the theory of $\mathcal{PT}-$symmetric optical lattices [3, 4], the $\mathcal{PT}-$symmetry breaking was experimentally observed [5, 6, 7]. Naturally, such considerations have also been extended to nonlinear lattices [8, 9] and oligomers [10], and $\mathcal{PT}-$related phenomena like unidirectional optical transport [11], unidirectional invisibility [12], and Talbot effects [13] were theoretically demonstrated. Moreover, it has been shown that optical solitons [8, 14, 15, 16], nonlinear modes [17], and breathers [18, 19] may also be supported by $\mathcal{PT}-$symmetric systems. Moreover, the application of these ideas in electronic circuits [20], not only provides a platform for testing $\mathcal{PT}-$related ideas within the framework of easily accessible experimental configurations, but also provides a direct link to metamaterials whose elements can be modeled with equivalent electrical circuits.

Conventional metamaterials comprising resonant metallic elements operate close to their resonance frequency where unfortunately the losses are untolerably high anid hamper any possibility for their use in device applications. The pathways to overcome losses are either to replace the metallic parts with superconducting ones [21] or to construct active metamaterials by incorporating active constituents that provide gain through external energy sourses. The latter has been recently recognized as a very promising technique for compensating losses [22, 23]. A particular electronic component that may provide both gain and nonlinearity in a metamaterial is the tunnel (Esaki) diode which features a current-voltage characteristic with a negative resistance part [24]. Left-handed transmission lines with successful implementation of Esaki diodes have been recently realized [25], although other electronic components may be employed as well for loss compensation [26]. Thus, the fabrication of $\mathcal{PT}-$symmetric metamaterials with balanced gain and loss

is feasible with the present technology in the microwaves, combining highly conducting split-ring resonators (SRRs) and negative resistance devices in a way similar to that in electrical circuits [20]. In this prospect, the SRR equivalent circuit parameters and the bias of the negative resistance device sould be properly adjusted to provide gain and equal amount of loss as well as real eigenfrequencies in a finite frequency range of the gain/loss parameter.

In the following we present a one-dimensional, discrete, equivalent circuit model for an array of SRRs with alternatingly gain and loss in the two different configurations (Section 2). In Section 3 we present linear eigenfrequency spectra for systems with small number of SRRs and we obtained the relation that provides the eigefrequencies for large systems. It is shown that $\mathcal{PT}-$symmetric metamaterials undergo spontaneous symmetry breaking from the exact $\mathcal{PT}$ phase (real eigenfrequencies) to the broken $\mathcal{PT}$ phase (at least a pair of complex eigenfrequencies), with variation of the gain/loss coefficient. In Section 4, where nonlinearity becomes important, the generation of long-lived nonlinear excitations in the form of discrete breathers (DBs) [27] is demonstrated numerically. These novel gain-driven DBs result by a purely dynamical proccess, through the matching of the input power through the gain mechanism and internal loss. In Section 5 we introduce a model $\mathcal{PT}-$symmetric system in zero dimensions, realized by a harmonic oscillator with balanced time-periodic gain and loss, that exhibits extraordinary properties and multiple critical (phase transition) points. Section 6 contains the conclusions.

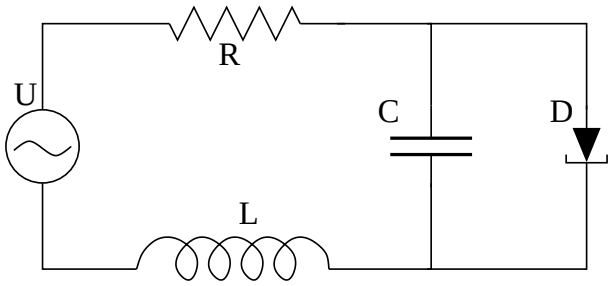


Figure 1: Electrical equivalent circuit for a split-ring resonator loaded with a tunnel (Esaki) diode.

2. Equivalent circuit modelling and Dynamic Equations

Consider a metalic split-ring resonator (SRR) that can be regarded as an RLC electrical circuit featuring Ohmic resistance R, inductance L, and capacitance C. A tunnel (Esaki) diode [24] is connected in parallel with the capacitance C of the SRR (Fig. 1) forming thus a nonlinear metamaterial element with gain. Esaki diodes exhibit a well defined negative resistance region in their current-voltage characteristics that has a characteristic $'N'$ shape. A bias voltage applied to the diode can move its operation point in the negative resistance region and then the SRR-diode system

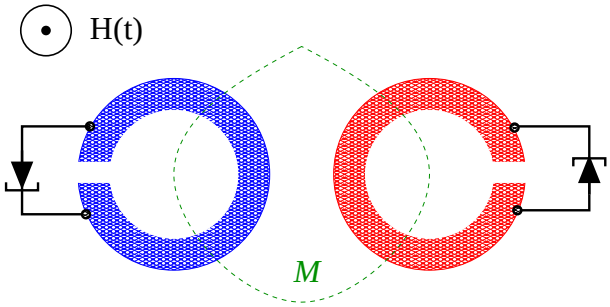


Figure 2: (Color online) Schematic of a $\mathcal{PT}-$symmetric metadimer comprising two tunnel diode-loaded SRRs in an alternating magnetic field $H(t)$. The SRRs are coupled magnetically through their mutual inductance M. Different bias in the diodes may create a balanced gain/loss structure.

gains energy from the source.

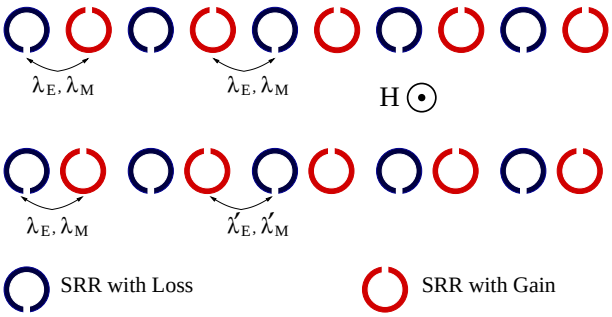


Figure 3: (Color online) Schematic of a one-dimensional $\mathcal{PT}-$symmetric metamaterial. Upper panel: all the SRRs are equidistant. Lower panel: the separation between SRRs is modulated according to a binary pattern ($\mathcal{PT}$ dimer chain). The applied field is such that the magnetic component is perpendicular to the plane of the split-ring resonators.

A metadimer comprising two SRRs loaded with tunnel diodes in an external alternating magnetic field is shown in Fig. 2. The equivalent circuit parameters R, C, and L of the SRRs and the bias in the diodes have been adjusted so that: (i) the two elements have the same eigenfrequencies; (ii) one of the SRRs has gain while the other has equal amount of loss. Then, the pair of SRRs is a $\mathcal{PT}-$symmetric metadimer, that may be employed for the construction of one-dimensional $\mathcal{PT}-$symmetric metamaterials, which moreover are nonlinear due to the tunnel diodes. The alternating magnetic field induces an electromotive force in each SRR due to Faraday's law which in turn produce currents that couple the SRRs magnetically through their mutual inductance M (Fig. 2). The coupling strength between SRRs is rather weak due to the nature of their interaction (magnetoinductive), and has been calculated accurately by several authors [28, 29]. The SRRs may also be coupled electrically, through the electric dipoles that develop in their slits. Thus, in the general case one has to consider both magnetic and electric coupling between

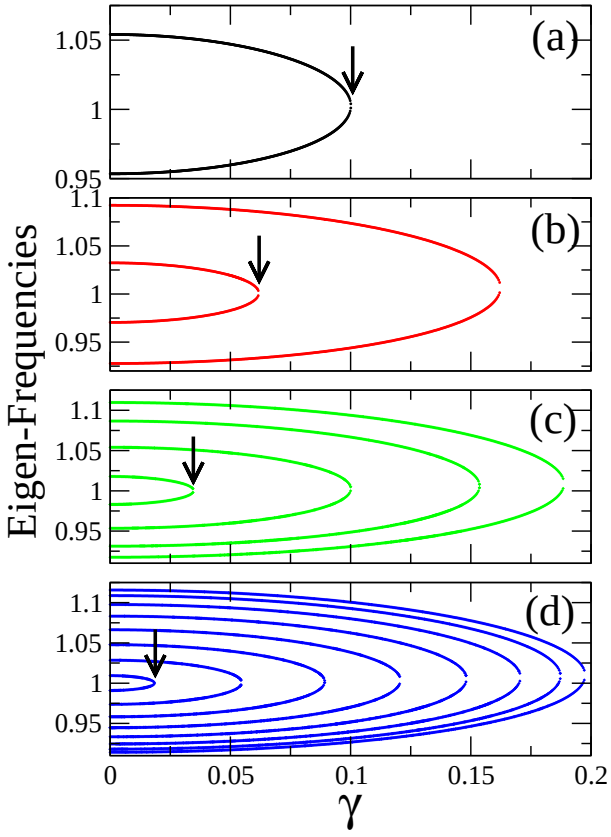


Figure 4: (Color online) Frequency eigenvalues of the free $\mathcal{PT}-$symmetric SRR array as a function of the gain/loss parameter γ for $\lambda_E = 0$, $\lambda_M = -0.1$, and (a) $N = 2$; (b) $N = 4$; (c) $N = 8$; (d) $N = 16$. The arrows indicate the critical point γ_c for the exact-to-broken $\mathcal{PT}$ phase transition. Only the real eigenfrequencies is shown for clarity.

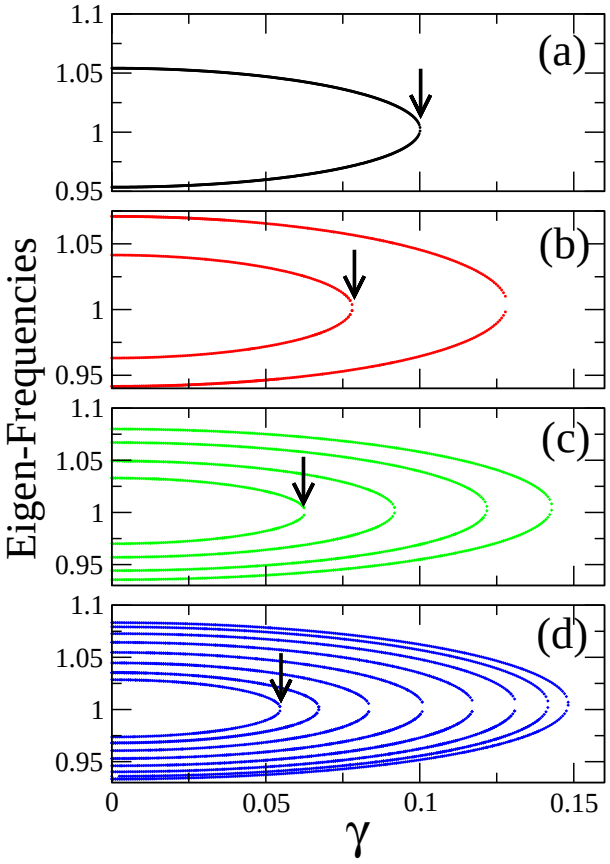


Figure 5: (Color online) Frequency eigenvalues of the free $\mathcal{PT}-$symmetric dimer chain as a function of the gain/loss parameter γ for $\lambda_E = \lambda'_E = 0$, $\lambda_M = -0.1$, $\lambda_M = -0.05$, and (a) $N = 2$; (b) $N = 4$; (c) $N = 8$; (d) $N = 16$. The arrows indicate the critical point γ_c for the exact-to-broken $\mathcal{PT}$ phase transition. Only the real eigenfrequencies is shown for clarity.

SRRs. However, for particular relative orientations of the SRR slits the magnetic interaction is dominant, while the electric interaction can be neglected in a first approximation [30, 31, 32]. As can be seen in Fig. 3, the $\mathcal{PT}-$symmetric metadimers can be arranged in a one-dimensional lattice in two distinct configurations; one with all the SRRs equidistant and the other with the SRRs forming a $\mathcal{PT}$ dimer chain.

Within the framework of the equivalent circuit model, a set of discrete differential equations have been used to describe the dynamics in nonlinear magnetic metamaterials [33, 34, 35, 29]. Takining into account the binary structure of the $\mathcal{PT}$ dimer chain, the dynamics of the $\mathcal{PT}-$symmetric metamaterial with balanced gain and loss is governed by the equations [19] (in normalized form)

$$\begin{aligned} &\lambda'_M \ddot{q}_{2n} + \ddot{q}_{2n+1} + \lambda_M \ddot{q}_{2n+2} \\ &+\lambda'_E q_{2n} + q_{2n+1} + \lambda_E q_{2n+2} \\ &+\alpha q_{2n+1}^2 + \beta q_{2n+1}^3 + \gamma \dot{q}_{2n+1} = \varepsilon_0 \sin(\Omega\tau) \end{aligned} \quad (1)$$

$$\begin{aligned} &\lambda_M \ddot{q}_{2n-1} + \ddot{q}_{2n} + \lambda'_M \ddot{q}_{2n+1} \\ &+\lambda_E q_{2n-1} + q_{2n} + \lambda'_E q_{2n+1} \\ &+\alpha q_{2n}^2 + \beta q_{2n}^3 - \gamma \dot{q}_{2n} = \varepsilon_0 \sin(\Omega\tau) \end{aligned} \quad (2)$$

where λ_M, λ'_M and λ_E, λ'_E are the magnetic and electric coupling coefficients, respectively, with $\lambda_{E,M} > \lambda'_{E,M}$ and $\lambda_{E,M}\lambda'_{E,M} > 0$, α and β are dimensionless nonlinear coefficients, γ is the gain/loss coefficient ($\gamma > 0$), ε_0 is the amplitude of the external driving voltage, while Ω and τ are the driving frequency and temporal variable, respectively, normalized to the inductive-capacitive (LC) resonance frequency ω_0 and inverse LC resonance frequency ω_0^{-1}, respectively, $\omega_0 = 1/\sqrt{LC_0}$ with C_0 being the linear capacitance. The values selected for the nonlinear coefficients $\alpha = -0.4$, $\beta = 0.08$ are typical for a diode and they provide a soft on-site nonlinear potential. They can be obtained from a Taylor expansion of the capacitance to voltage relation of an equivalent circuit diode model, that gives a very good approximation for weakly driven systems [36, 35].

3. Linear Eigenfrequency Spectra and Critical Point

In order to obtain the critical value of $\gamma = \gamma_c$ that separates the exact $\mathcal{PT}-$phase, where all the eigenvalues are real, from the broken $\mathcal{PT}-$phase, where at least a pair of eigen-

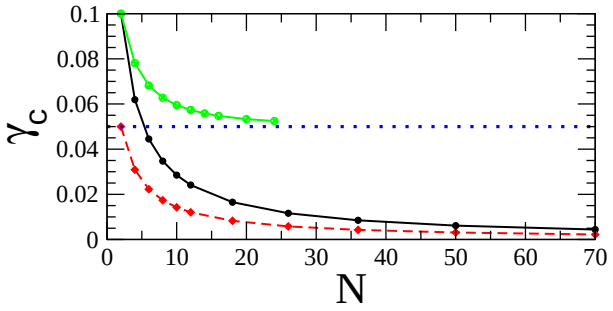


Figure 6: (Color online) Dependence of the critical gain/loss parameter value γ_c on the number of SRRs, N, for magnetically coupled SRRs in both the equidistant and dimer chain configuration. The black squares and the red diamonds have been calculated for the former configuration with $\lambda_M = -0.1$ and $\lambda_M = -0.05$, respectively. The green circles have been calculated for the latter configuration with $\lambda_M = -0.1$, $\lambda'_M = -0.05$. The lines serve as a guide to the eye.

values is complex, we calculate the frequency spectrum. This is a straightforward procedure for systems with relatively small number of SRRs; the roots of the determinant of the linearized Eqs. (1) and (2) for $\varepsilon_0 = 0$ are obtained with a root-finding algorithm and then plotted against the gain/loss parameter γ. In Figs. 4 and 5, the real eigenfrequencies of $\mathcal{PT}-$symmetric metamaterials in both configurations are shown as a function of γ, while the arrows indicate the critical point γ_c in each case. Thus, for $\gamma < \gamma_c$ all eigenvalues are real, while in the opposite case at least a pair of eigenvalues has become complex. As we can see from the figures, for $\gamma > \gamma_c$ more and more eigenfrequency pairs become complex with increasing γ, until they all become complex for a particular value of γ. Moreover, as we can see from an inspection of Figs. 4 and 5, obtained for the equidistant SRR configuration and the $\mathcal{PT}$ dimer chain, respectively, the value of γ_c decreases rapidly with increasing number of SRRs N for the former configuration, while it tends to a constant value for the latter configuration. This can be seen more clearly in Fig. 6, where the critical point γ_c is plotted as a function of N for both configurations. For the curves corresponding to equidistant SRRs (corresponding to two different values of the magnetic coupling coefficient λ_M) we see that γ_c is smaller as the magnetic coupling coefficient λ_M lowers. However, in both curves corresponding to equidistant SRRs the value of the critical point γ_c tends to zero with increasing N. In contrast, for the $\mathcal{PT}$ dimer chain configuration, the value of γ_c tends to a constant finite value which approximatelly equals the absolute difference of the magnetic coupling coefficients λ_M and λ'_M (see below).

For large systems, we can obtain a condition that determines the critical point γ_c as a function of the magnetic coupling constant(s). In the standard way, we substitute into the linearized Eqs. (1) and (2) for $\varepsilon_0 = 0$ the trial solutions

$$q_{2n} = A\exp[i(2n\kappa - \Omega\tau)], \quad (3)$$
$$q_{2n+1} = B\exp\{i[(2n+1)\kappa - \Omega\tau]\}, \quad (4)$$

where κ is the normalized wavevector. Then, by requesting nontrivial solutions for the resulting stationary problem, we obtain

$$\Omega^2_\kappa = \left(-b \pm \sqrt{b^2 - 4ac}\right)/(2a), \quad (5)$$

where

$$a = 1 - (\lambda_M - \lambda'_M)^2 - \mu_\kappa\mu'_\kappa, \quad (6)$$
$$b = \gamma^2 - 2\left[1 - (\lambda_E - \lambda'_E)(\lambda_M - \lambda'_M)\right] + \varepsilon_\kappa\mu'_\kappa + \varepsilon'_\kappa\mu_\kappa, \quad (7)$$
$$c = 1 - (\lambda_E - \lambda'_E)^2 - \varepsilon_\kappa\varepsilon'_\kappa, \quad (8)$$

and $\varepsilon_\kappa = 2\lambda_E\cos(\kappa)$, $\varepsilon'_\kappa = 2\lambda'_E\cos(\kappa)$, $\mu_\kappa = 2\lambda_M\cos(\kappa)$, $\mu'_\kappa = 2\lambda'_M\cos(\kappa)$. In the following, we neglect the electric coupling between SRRs, i.e., $\lambda_E = \lambda'_E = 0$, for simplicity. Then, Eq. (5) reduces to

$$\Omega^2_\kappa = \frac{2 - \gamma^2 \pm \sqrt{\gamma^4 - 2\gamma^2 + (\lambda_M - \lambda'_M)^2 + \mu_\kappa\mu'_\kappa}}{2(1 - (\lambda_M - \lambda'_M)^2 - \mu_\kappa\mu'_\kappa)}. \quad (9)$$

The condition for having real Ω_κ for any κ then reads

$$\cos^2(\kappa) \geq \frac{\gamma^2(2 - \gamma^2) - (\lambda_M - \lambda'_M)^2}{4\lambda_M\lambda'_M}. \quad (10)$$

It is easy to see that for $\lambda_M = \lambda'_M$ corresponding to the equidistant SRR configuration, the earlier condition cannot be satisfied for all κ's for any positive value of the gain/loss coefficient γ, implying that a large $\mathcal{PT}-$symmetric SRR array (Fig. 3, upper panel) will be in the broken phase. To the contrary, for $\lambda_M \neq \lambda'_M$, i.e., for a $\mathcal{PT}$ dimer chain (Fig. 3, lower panel), the above condition is satisfied for all κ's for $\gamma \leq \gamma_c \simeq |\lambda_M - \lambda'_M|$, ($\gamma^4 \simeq 0$). In the exact phase ($\gamma < \gamma_c$), the $\mathcal{PT}-$symmetric dimer array has a gapped spectrum with two frequency bands, as shown in Fig. 7. The width of the gap separating the bands decreases with decreasing $|\lambda_M - \lambda'_M|$ for fixed γ. For $\gamma \simeq \gamma_c$ the gap closes, some frequencies in the spectrum acquire an imaginary part and the $\mathcal{PT}$ metamaterial enters into the broken phase. Note that the gain/loss coefficient γ has little effect on the dispersion curves of the $\mathcal{PT}$ dimer chain (compare with the dotted curves where γ is set to zero), as long as the sign in front of γ alternates from one SRR to another.

4. Gain-Driven Breather Excitations

For a gapped linear spectrum, large amplitude linear modes become unstable in the presence of driving and nonlinearity. If the curvature of the dispersion curve in the region of such a mode is positive and the lattice potential is soft, large amplitude modes become unstable with respect to formation of DBs in the gap below the linear spectrum [37]. For the parameters used in Fig. 7, the bottom of the lower

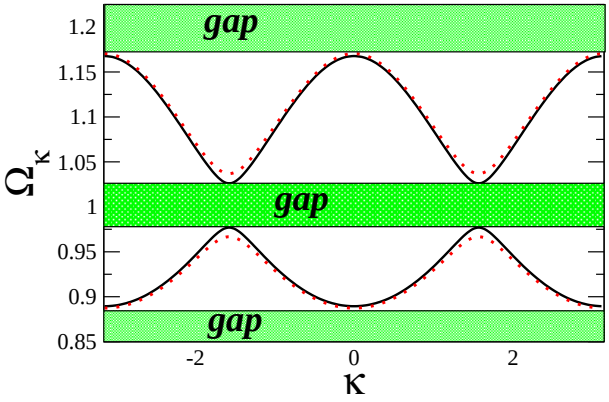


Figure 7: (Color online) Frequency bands for a $\mathcal{PT}-$symmetric dimer chain with balanced gain and loss for $\lambda_M = -0.17$, $\lambda'_M = -0.10$, and $\gamma = 0.05$ (black solid curves); $\gamma = 0$ (red dotted curves). The gaps are indicated in green (dark) color.

band is located at $\Omega_0 \simeq 0.887$, where the curvature is positive. The corresponding period at the bottom of the lower band is $T_0 = 2\pi/\Omega_0$. Moreover, the SRRs are subjected to soft on-site potentials for the selected values of the nonlinear coefficients α and β. Then, DBs can be generated spontaneously by a frequency chirped alternating driver; after turning off the driver, the breathers are driven solely by gain. A similar procedure has been applied succesfuly to lossy nonlinear metamaterials with a binary structure [34, 38, 39] The results are illustrated in Figs. 8 and 9, where the case of a slight imbalance between gain and loss and its effect on breather generation has been also considered. In these figures, a density plot of the local energy E_n of a $\mathcal{PT}-$symmetric metamaterial is shown on the $n-\tau$ plane for two different values of the driving amplitude ε_0.

In the following, the integration of Eqs. (1) and (2) implemented with the boundary condition

$$q_0(\tau) = q_{N+1}(\tau) = 0, \tag{11}$$

that accounts for the termination of the structure in finite systems, is performed with a 4th order Runge-Kutta algorithm with fixed time-step. In order to prevent instabilities that will result in divergence of the energy at particular sites in finite time, we consider a longer dimer chain with total number of SRRs $N + 2N_\ell$; then we replace the gain with equivalent amount of loss at exactly N_ℓ SRRs at each end of the extended chain. In other words, we embed the $\mathcal{PT}-$symmetric dimer chain into a geometrically identical lossy chain, in order to help the excess energy to go smothly away during evolution living behind stable (or at least very long-lived) breather structures.

We use the following procedure described in detail in Ref. [19]:

• At time $\tau = 0$, we start integrating Eqs. (1) and (2) from zero initial state without external driving for $500\,T_0 \simeq 3500$ time units (t.u.) to allow for significant developement of large amplitude modes.

• At time $\tau \simeq 3500$ t.u. the driver is switched-on with low-amplitude ε_0 and frequency slightly above Ω_0 ($1.01\,\Omega_0 \simeq 0.894$). The frequency is then chirped downwards with time to induce instability for the next 10600 t.u. ($\sim 1500\,T_0$), until it is well below Ω_0 ($0.997\,\Omega_0 \simeq 0.882$). During that phase, a large number of excitations are generated that move and strongly interact to each other, eventually merging into a small number of high amplitude breathers and multi-breathers.

• At time $\tau \simeq 14100$ t.u. (point A on Figs. 8 and 9), the driver is switched off and the DBs that have formed are solely driven by the gain. They continue to interact for some time until they reach an apparently stationary state and get trapped at particular sites. The high density segments between the points A and C in Figs. 8 and 9 precisely depict those gain-driven DB structures.

• At time $\tau \sim 440000$ t.u. (point C on Figs. 8 and 9), the gain is replaced everywhere by equal amount of loss, and the breathers die out rapidly. Note that the above procedure of breather generation is very sensitive to parameter variations of the external fields. Even though the values of the driving amplitudes in Figs. 8 and 9 are rather close (i.e., $\varepsilon_0 = 0.085$ and 0.095, respectively), the breather structures as well as their numbers are different. In Fig. 8(b), in the balanced gain/loss case, we observe two distinct structures that have been formed that correspond to a relatively high amplitude multi-breather and a low amplitude breather. These structures remain stationary during the long time interval they have been followed ($> 56000\,T_0$). In Figs. 8(a) and 8(c), gain and loss are not perfectly matched; in Fig. 8(a) loss exceeds gain by a small amount while in in Fig. 8(c) gain exceeds loss by the same small amount. Notably, breather excitations may still be formed through the frequency chirping procedure in the presence of a small amount of either net gain or net loss. Indeed, as we may observe comparing Figs. 8(a) and 8(c) with Fig. 8(b), the same structures are formed [except the low amplitude breather that is not visible in Fig. 8(c)]. However, both in Figs. 8(a) and 8(c) we can see a slow gradual widening of the high amplitude multibreather: when loss exceeds gain the multibreather losses its energy at a low rate, with its excited sites that are closer to its end-points gradually falling down to a low amplitude state. Similarly, when gain exceeds loss, the high amplitude multibreather slowly gains energy and becomes wider. In both cases, breather destruction will take place in a time-scale that depends exponentially on the gain/loss imbalance. Thus, in an experimental situation, where gain/loss balance is only approximate, it will be still possible to observe breathers at relatively short time-scales. Similar observations hold for Fig. 9 as well. In this figure, we observe three relatively high amplitude multibreather structures that are formed both in the balanced and the imbalanced case. Here we also observe that instabilities may appear after long time intervals of apparently stationary breather evolution as well. Whenever this happens, they start moving through the lattice until they get once more trapped at different lattice sites. In Fig. 9(b)

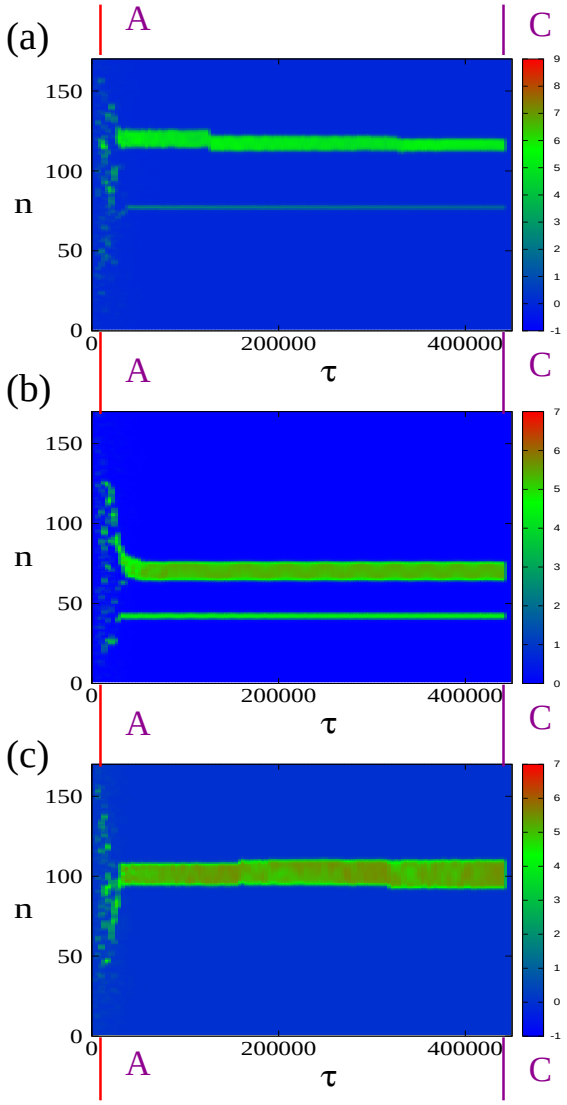


Figure 8: (Color online) Spatiotemporal evolution of the energy density E_n for a $\mathcal{PT}-$symmetric dimer chain with $N = 70$, $N_\ell = 10$, $\Omega_0 = 0.887$, $\gamma = 0.002$, $\lambda_M = -0.17$, $\lambda'_M = -0.10$ ($\lambda_E = \lambda'_E = 0$), $\varepsilon_0 = 0.085$, $\gamma = 0.002$ and (a) excess loss 0.2%; (b) balanced case; (c) excess gain 0.2%.

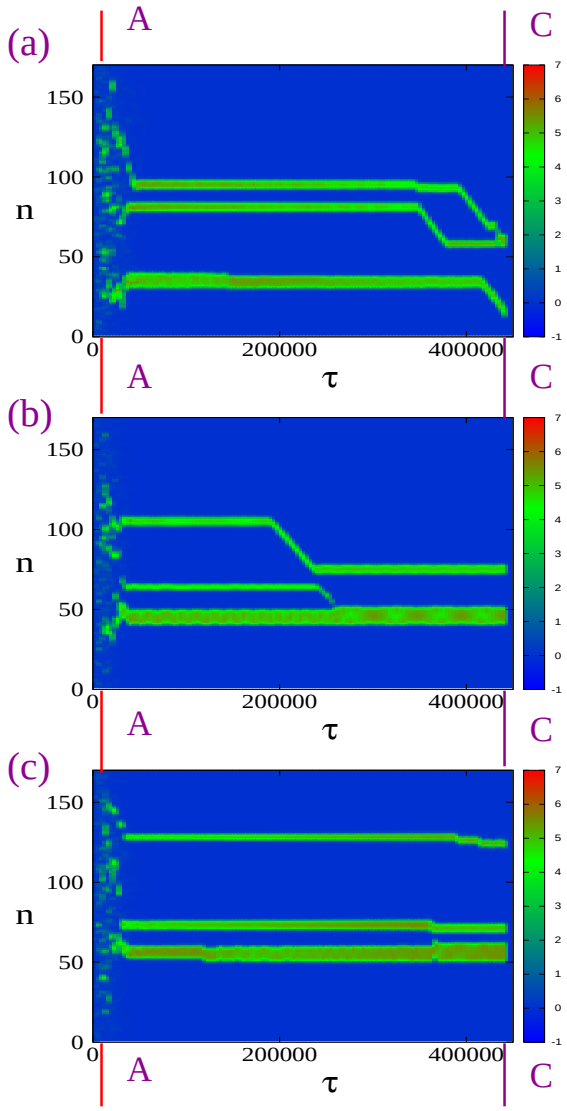


Figure 9: (Color online) Spatiotemporal evolution of the energy density E_n for a $\mathcal{PT}-$symmetric dimer chain with $N = 70$, $N_\ell = 10$, $\Omega_0 = 0.887$, $\gamma = 0.002$, $\lambda_M = -0.17$, $\lambda'_M = -0.10$ ($\lambda_E = \lambda'_E = 0$), $\varepsilon_0 = 0.095$, $\gamma = 0.002$ and (a) excess loss 0.2%; (b) balanced case; (c) excess gain 0.2%.

such an instability appears between $200000 - 250000$ t.u. for the two narrower multibreather structures. The one of them gets trapped a few tenths lattice sites away from its previous position, while the other (the narrowest) collides and it is absorbed by the wide multibreather located at n 50.

5. Classical $\mathcal{PT}-$Symmetry in Zero Dimensions

In the classical domain, in all cases of $\mathcal{PT}-$symmetric systems investigated so far, the combination of time-reversal and parity symmetries is utilized: In a given time-evolution if we reverse time while "reflecting" position and momentum, we must retrace the original path. The parity operation requires that the system is extended either in continuous or discrete space in order to be able to perform this operation. We show here that this is not necessary and that the features of the $\mathcal{PT}$ -symmetric systems can be preserved in "zero" dimensions where the parity symmetry is trivial.

We consider the following simple harmonic oscillator:

$$\ddot{x} + 2\theta(t)\dot{x} + \omega_0^2 x = 0, \tag{12}$$

where $x \equiv x(t)$ is the equilibrium dislacement of a mass (the charge in an RLC cirquit), ω_0 the resonant oscillator frequency while $\theta(t)$ is a time-dependent "damping" term; both ω_0 and $\theta(t)$ are scaled to the mass (impedance of the circuit). We take $\theta(t)$ to be periodic with period T, viz.

$\theta(t+T) = \theta(t)$ while its values may be both positive and negative, i.e., for some part of the period the oscillator experiences damping while in the rest of the period time amplification, or anti-damping. We investigate the osillator evolution after long time and the stability of the motion. Instead of adressing a general periodic function $\theta(t)$ we focus on a simple form that makes the problem readily solvable, viz. we take

$$\theta(t) = \begin{cases} +\gamma & \text{if } 0 \le t < \tau_1; \\ -\gamma & \text{if } \tau_1 \le t < \tau_2. \end{cases} \tag{13}$$

where $T = \tau_1 + \tau_2$ and taking the plus (minus) sign in front of the coefficient γ (γ is defined as a positive constant, $\gamma > 0$, that may assume any value between zero and unity) we have in the first (second) part of the cycle loss (gain). With this form of piecewise constant function $\theta(t)$ we can easily solve Eq. (12) for the loss (L) segment of time duration τ_1 and gain (G) segment of duration τ_2. The form of Eq. (13) permits to view the problem as mapping of the position-velocity vector at a given time to the position-velocity vector at a later time; if in the begining of the gain (loss) period (assuming $t = 0$) we have position and velocity equal to $(x_0,\ \dot{x}_0)$. Then after the evolution during time τ (τ_1 or τ_2, respectively) we obtain:

$$\begin{pmatrix} x \\ \dot{x} \end{pmatrix} = M_{G/L}(\tau) \begin{pmatrix} x_0 \\ \dot{x_0} \end{pmatrix} \tag{14}$$

where for gain we have

$$M_G(\tau_1) = \frac{e^{\gamma\tau_1}}{\delta} \times \begin{pmatrix} \delta\cos\delta\tau_1 - \gamma\sin\delta\tau_1 & \sin\delta\tau_1 \\ -\omega_0^2\sin\delta\tau_1 & \delta\cos\delta\tau_1 + \gamma\sin\delta\tau_1 \end{pmatrix} \tag{15}$$

and for the loss respectively

$$M_L(\tau_1) = \frac{e^{-\gamma\tau_2}}{\delta} \times \begin{pmatrix} \delta\cos\delta\tau_2 + \gamma\sin\delta\tau_2 & \sin\delta\tau_2 \\ -\omega_0^2\sin\delta\tau_2 & \delta\cos\delta\tau_1 - \gamma\sin\delta\tau_2 \end{pmatrix} \tag{16}$$

where $\delta = \sqrt{\omega_0^2 - \gamma^2}$. Using the mapping, we may obtain long time evolution after N periods T as a repetitive application of the matrices $M_G(\tau_1)$ and $M_L(\tau_2)$ to an arbitraty initial state $(x_0,\ \dot{x}_0)$. Since the matrices $M_{L/G}(\tau)e^{\pm\gamma\tau}$ are unimodular, the long time evolution with be dominated by the exponetial term $\exp[N\gamma(\tau_1 - \tau_2)]$; this leads trivially to exponential growth ($\tau_1 > \tau_2$) or exponential decay ($\tau_1 < \tau_2$). As a result we consider the more interesting case with $\tau_1 = \tau_2 = \tau \equiv T/2$; in this case the gain and loss power is perfectly matched during the period T. The combined propagation matrix after one period (assuming first gain) is simply $M(T) = M_L(\tau)M_G(\tau)$, i.e.,‘

$$M(T) = \frac{1}{\delta^2} \begin{pmatrix} M_{11} & M_{12} \\ M_{21} & M_{22} \end{pmatrix} \tag{17}$$

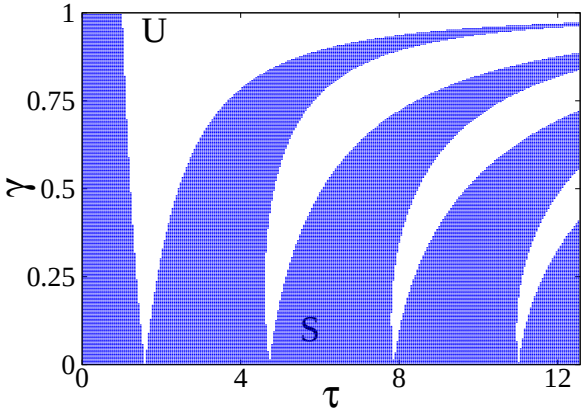


Figure 10: (Color online) Phase diagram on the $\gamma - \tau$ plane for the harmonic oscillator with time-dependent "damping" term, obtained from Eq. (27). The stability region is indicated in blue (dark) color.

where M_{ij} are given by

$$M_{11} = -\gamma^2 + \omega_0^2\cos(2\phi), \tag{18}$$
$$M_{12} = +2\sin\phi(\delta\cos\phi + \gamma\sin\phi) \tag{19}$$
$$M_{21} = -2\omega_0^2\sin\phi(\delta\cos\phi - \gamma\sin\phi) \tag{20}$$
$$M_{22} = -\gamma^2 + \omega_0^2\cos(2\phi) \tag{21}$$

and $\phi = \delta\tau \equiv \delta T/2$. The matrix M is clearly also unimodular with eigenvalues $e^{i\mu}$ and $e^{-i\mu}$; since the trace of a matrix is invariant we find

$$\cos\mu = \frac{-\gamma^2 + \omega_0^2\cos 2\phi}{\delta^2}. \tag{22}$$

Stability Equation.- Eq. (22) can be re written as

$$\cos\mu = \frac{1 - B^2\cos 2\phi}{1 - B^2} = 1 + \frac{2B^2\sin^2\phi}{1 - B^2} \tag{23}$$

with $B = \frac{\omega_0}{\gamma}$. In order to have stable motion it is necessary that $|\cos\mu| \le 1$, or $-1 \le 1 + \frac{2B^2\sin^2\phi}{1-B^2} \ge 1$, leading to

$$-2 \le \frac{2B^2\sin^2\phi}{1 - B^2} \le 1 \tag{24}$$

Eq. (24) has solutions only for $|B| > 1$ or $|\gamma| < \omega_0$, for $\omega_0 > 0$; in the latter case we find

$$|\cos\phi| \ge \left|\frac{\gamma}{\omega_0}\right| \tag{25}$$

The range thus of allowed values for the angle ϕ ($\gamma > 0$) is

$$\frac{\gamma}{\omega_0} \le \cos\phi \le 1$$
$$-1 \le \cos\phi \le -\frac{\gamma}{\omega_0} \tag{26}$$

We note that there are multiple allowed solutions marked by the the lines $\cos\phi = \pm\gamma/\omega_0$, i.e., for the three parameters of the problem γ, $T = 2\tau$ and ω_0 the transcedental equation

$$\cos(\delta\tau) = \begin{cases} +\frac{\gamma}{\omega_0} & \text{for } 2n\pi - \pi/2 < \delta\tau < 2n\pi + \pi/2; \\ -\frac{\gamma}{\omega_0} & \text{for } 2\pi n + \pi/2 < \delta\tau < 2\pi n + 3\pi/2, \end{cases}$$

where $n = 0, \pm 1, \pm 2, ..$, marks the onset of the transition from stable to unstable evolution. This is the equivalent to the $\mathcal{PT}$ transition from the exact (stable) to the broken (unstable) phace in this zero-dimensional problem. Using Eq. (25) we construct a $\mathcal{PT}$ phase diagram on the $\tau - \gamma$ plane (Fig. 10), where the blue (dark) color indicates regions of stability. If we fix one of the parameters, variation of the other drives the oscillator through alternatingly stable and unstable regions, as can be readily observed from Fig. 10.

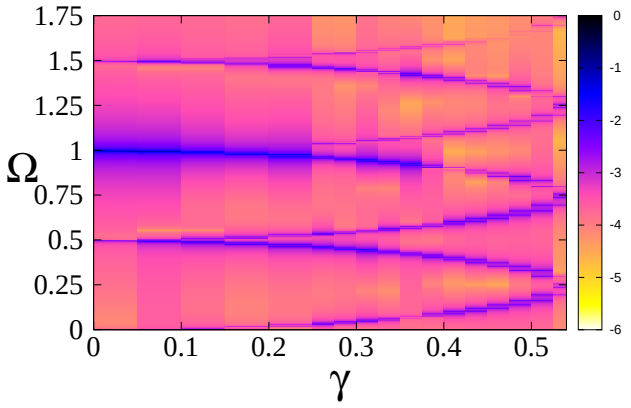


Figure 11: (Color online) Density plot of the logarithm of the frequency spectra of $x(t)$, $y = \log_{10}\{PS[x(t)]\}$, as a function of γ. The discrete frequency components of the spectra for each value of γ are indicated with blue (darker) color.

Introducing the frequency $\omega = 2\pi/T \equiv \pi/\tau$ we define the reduced parameters $\Omega = \omega/\omega_0$ and $\tilde{\gamma} = \gamma/\omega_0$. Then, the equation that controls the stability regions becomes

$$\left| \cos\left[\frac{\pi\sqrt{1-\gamma^2}}{\Omega} \right] \right| = \gamma, \tag{27}$$

where the tilde has been dropped. Eq. (27) has solutions for $|\gamma| < 1$; for different reduced frequencies Ω we obtain different number of solutions of the earlier equation, the number of the latter icreases with decreasing frequency ω. Once we have the solutions of Eq. (27) we can find the regimes of stability and instability. Consider the resonant case $\Omega = 1$ where the external frequency of gain/loss alternation matches the self-frequency of the oscillator. Besides the trivial solution at $\gamma = 0$, numerical solution of Eq. (27) gives $\gamma_1 \approx 0.676$ so that the stable region is in the range $0 \leq \gamma \leq \gamma_1$. For $\Omega = 0.5$ the corresponding solutions are $\gamma_1 \approx 0.54$, $\gamma_2 \approx 0.80$, and $\gamma_3 \approx 0.90$ with two stability regions, i.e., $0 \leq \gamma \leq \gamma_1$ and $\gamma_2 \leq \gamma \leq \gamma_3$.

The stable solutions of Eq. (12) as a function of time t are in general quasi-periodic oscillations whose spectral content varies both with τ and γ. For an illustration, we consider a particular value of τ, i.e., $\tau = 2\pi$ ($\Omega = 0.5$) for which the boundaries of the stability regions have been calculated. For the interval with relatively low values of γ, $0 \leq \gamma \leq \gamma_1 \simeq 0.54$, that is more physically relevant, we present a density plot of the logarithm of the frequency spectra of $x(t)$, $y = \log_{10}\{PS[x(t)]\}$, as a function of γ (Fig. 11). In this figure, the discrete frequency components of the spectra for each value of γ are indicated in dark (blue) color. For $\gamma = 0$ and very close to zero, the only frequency appearing in the spectrum is the eigenfrequency of the oscillator $\Omega \simeq 1$. With increasing γ, the frequency components at $\Omega \simeq 1 \pm 0.5$ become more and more important. At about $\gamma = 0.15$ these half-integer frequency components start spliting into pairs of frequencies that are symmetric around the half-integer values. The separation between these pairs increases with further increasing γ, and the frequency components from neighboring pairs come closer and closer together until they eventually merge for γ approaching its critical value 0.54.

6. Conclusions

We have investigated theoretically a $\mathcal{PT}-$symmetric nonlinear metamaterial relying on gain and loss. Eigenfrequency spectra for linearized systems of either small and large N and two different configurations were calculated and the critical points γ_c were determined. Large $\mathcal{PT}-$symmetric metamaterials with the dimer chain configuration exhibit phase transitions for the exact to the broken $\mathcal{PT}-$symmetry phase, while large $\mathcal{PT}-$symmetric metamaterials with the equidistant SRR configuration are always in the broken $\mathcal{PT}$ phase.

In the presence of nonlinearity, we have demonstrated numerically the a $\mathcal{PT}-$symmetric dimer chain supports localized excitations in the form of discrete breathers. Breathers are excited by a purely dynamical process, with a frequency chirped external magnetic field that induces instability in a zero initial state. Subsequently, the nonlinearity focuses energy around points that have acquired high amplitude leading to the formation of localized structures. The external field is then switched off and those localized structures are then solely driven by the gain, the excess energy lives the system through its lossy parts at the ends, leading eventually to breather generation.

Remarkably, slight imbalance between gain and loss does not destroy the breathers instantly; they can stiil be generated through the frequency chirping procedure and they can be regarded as stationary for relatively short time intervals. In the long term, the imbalanced breathers either gain constantly energy and diverge or lose constantly energy and vanish. The time-scale for the latter events depends exponentially from the amount of imbalance.

We have introduced a "zero-dimensional" $\mathcal{PT}$ system that can be realized by a harmonic oscillator with a "damping" term that provides balanced gain and loss, through alternation of the sign of the damping coefficient. We consider a piecewise linear gain/loss function and obtain a stability condition, i.e., a relation between the parameters of the problem. We thus obtain a "phase diagram" with parameter regions where oscillatory (stable) motion and diverging (unstable) motion occur. BY crossing the stability

boundary marks the onset of the transition from stable to unstable evolution that is equivalent to the $\mathcal{PT}$ transition from the exact to the broken phase in this zero-dimensional problem.

Acknowledgement

This research was partially supported by the THALES

Project ANEMOS, co-financed by the European Union (European Social Fund - ESF) and Greek National Funds through the Operational Program Education and Lifelong Learning of the National Strategic Reference Framework (NSRF) Investing in knowledge society through the European Social Fund.

References

[1] N. I. Zheludev, "The road ahead for metamaterials," *Science*, vol. 328, pp. 582–583, 2010.

[2] D. W. Hook, "Non-hermittian potentials and real eigenvalues," *Ann. Phys. (Berlin)*, vol. 524 (6-7), p. A106, 2012.

[3] R. El-Ganainy, K. G. Makris, D. N. Christodoulides, and Z. H. Musslimani, "Theory of coupled optical pt-symmetric structures," *Opt. Lett.*, vol. 32, pp. 2632–2634, 2007.

[4] K. G. Makris, R. El-Ganainy, D. N. Christodoulides, and Z. H. Musslimani, "Beam dynamics in pt-symmetric optical lattices," *Phys. Rev. Lett.*, vol. 100, p. 103904, 2008.

[5] A. Guo, "Observation of pt-symmetry breaking in complex optical potentials," *Phys. Rev. Lett.*, vol. 103, p. 093902, 2009.

[6] C. E. Rüter, K. G. Makris, R. El-Ganainy, D. N. Christodoulides, M. Segev, and D. Kip, "Observation of paritytime symmetry in optics," *Nature Physics*, vol. 6, pp. 192–, 2010.

[7] A. Szameit, M. C. Rechtsman, O. Bahat-Treidel, and M. Segev, "Pt-symmetry in honeycomb photonic lattices," *Phys. Rev. A*, vol. 84, p. 021806(R), 2011.

[8] S. V. Dmitriev, A. A. Sukhorukov, and Y. S. Kivshar, "Binary parity-time-symmetric nonlinear lattices with balanced gain and loss," *Opt. Lett.*, vol. 35, pp. 2976–2978, 2010.

[9] A. E. Miroshnichenko, B. A. Malomed, and Y. S. Kivshar, "Nonlinearly pt-symmetric systems: Spontaneous symmetry breaking and transmission resonances," *Phys. Rev. A*, vol. 84, p. 012123 (4pp), 2011.

[10] K. Li and P. G. Kevrekidis, "Pt-symmetric oligomers: Analytical solutions, linear stability, and nonlinear dynamics," *Phys. Rev. E*, vol. 83, p. 066608 (7pp), 2011.

[11] H. Ramezani, T. Kottos, R. El-Ganainy, and D. N. Christodoulides, "Unidirectional nonlinear pt-symmetric optical structures," *Phys. Rev. A*, vol. 82, p. 043803 (6pp), 2010.

[12] Z. Lin, H. Ramezani, T. Eichekraut, T. Kottos, H. Cao, and D. N. Christodoulides, "Unidirectional invisibility induced by pt-symmetric periodic structures," *Phys. Rev. Lett.*, vol. 106, p. 213901 (4pp), 2011.

[13] H. Ramezani, D. N. Christodoulides, V. Kovanis, I. Vitebskiy, and T. Kottos, "Pt-symmetric talbot effects," *Phys. Rev. Lett.*, vol. 109, p. 033902, 2012.

[14] S. V. Suchkov, B. A. Malomed, S. V. Dmitriev, and Y. S. Kivshar, "Solitons in a chain of parity-time invariant dimers," *Phys. Rev. A*, vol. 84, p. 046609, 2011.

[15] V. Achilleos, P. G. Kevrekidis, D. J. Frantzeskakis, and R. Carretero-González, "Dark solitons and vortices in pt-symmetric nonlinear media: From spontaneous symmetry breaking to nonlinear pt phase transitions," *Phys. Rev. A*, vol. 86, p. 013808 (7pp), 2012.

[16] N. V. Alexeeva, I. V. Barashenkov, A. A. Sukhorukov, and Y. S. Kivshar, "Optical solitons in pt-symmetric nonlinear couplers with gain and loss," *Phys. Rev. A*, vol. 85, p. 063837 (13pp), 2012.

[17] D. A. Zezyulin and V. V. Konotop, "Nonlinear modes in finite-dimensional pt-symmetric systems," *Phys. Rev. Lett.*, vol. 108, p. 213906 (5pp), 2012.

[18] I. V. Barashenkov, S. V. Suchkov, A. A. Sukhorukov, S. V. Dmitriev, and Y. S. Kivshar, "Breathers in pt-symmetric optical couplers," *Phys. Rev. A*, vol. 86, p. 053809 (12pp), 2012.

[19] N. Lazarides and G. P. Tsironis, "Gain-driven discrete breathers in pt-symmetric nonlinear metamaterials," *Phys. Rev. Lett.*, vol. 110, p. 053901 (5pp), 2013.

[20] J. Schindler, A. Li, M. C. Zheng, F. M. Ellis, and T. Kottos, "Experimental study of active lrc circuits with pt symmetries," *Phys. Rev. A*, vol. 84, p. 040101(R), 2011.

[21] S. M. Anlage, "The physics and applications of superconducting metamaterials," *J. Opt.*, vol. 13, pp. 024 001–10, 2011.

[22] A. D. Boardman, "Active and tunable metamaterials," *Laser Photonics Rev.*, vol. 5, p. 287, 2010.

[23] L.-M. Si, T. Jiang, K. Chang, T.-C.Chen, X. Lv, L. Ran, and H. Xin, "Active microwave metamaterials incorporating ideal gain devices," *Materials*, vol. 4, pp. 73–83, 2011.

[24] L. Esaki, "New phenomenon in narrow germanium $p - n$ junctions," *Phys. Rep.*, vol. 109, pp. 603–605, 1958.

[25] T. Jiang, K. Chang, L.-M. Si, L. Ran, and H. Xin, "Active microwave negative-index metamaterial transmission line with gain," *Phys. Rev. Lett.*, vol. 107, p. 205503, 2011.

[26] W. Xu, W. J. Padilla, and S. Sonkusale, "Loss compensation in metamaterials through embedding of active transistor based negative differential resistance circuits," *Opt. Express*, vol. 20, p. 22406, 2012.

[27] S. Flach and A. V. Gorbach, "Discrete breathers - advances in theory and applications," *Phys. Rep.*, vol. 467, pp. 1–116, 2008.

[28] O. Sydoruk, A. Radkovskaya, O. Zhuromskyy, E. Shamonina, M. Shamonin, C. stevens, G. Faulkner, D. Edwards, and L. Solymar, "Tailoring the near-field guiding properties of magnetic metamaterials with two resonant elements per unit cell," *Phys. Rev. B*, vol. 73, p. 224406, 2006.

[29] N. N. Rosanov, N. V. Vysotina, A. N. Shatsev, I. V. Shadrivov, D. A. Powell, and Y. S. Kivshar, "Discrete dissipative localized modes in nonlinear magnetic metamaterials," *Opt. Express*, vol. 19, p. 26500, 2011.

[30] F. Hesmer, E. Tatartschuk, O. Zhuromskyy, A. A. Radkovskaya, M. Shamonin, T. Hao, C. J. Stevens, G. Faulkner, D. J. Edwardds, and E. Shamonina, "Coupling mechanisms for split-ring resonators:theory and experiment," *Phys. Stat. Sol. (b)*, vol. 244, pp. 1170–1175, 2007.

[31] I. Sersić, M. Frimmer, E. Verhagen, and A. F. Koenderink, "Electric and magnetic dipole coupling in near-infrared split-ring metamaterial arrays," *Phys. Rev. Lett.*, vol. 103, p. 213902, 2009.

[32] N. Feth, M. König, M. Husnik, K. Stannigel, J. Niegemann, K. Busch, M. Wegener, and S. Linden, "Electromagnetic interaction of spit-ring resonators: The role of separation and relative orientation," *Opt. Express*, vol. 18, pp. 6545–6554, 2010.

[33] N. Lazarides, M. Eleftheriou, and G. P. Tsironis, "Discrete breathers in nonlinear magnetic metamaterials," *Phys. Rev. Lett.*, vol. 97, pp. 157 406–4, 2006.

[34] M. I. Molina, N. Lazarides, and G. P. Tsironis, "Bulk and surface magnetoinductive breathers in binary metamaterials," *Phys. Rev. E*, vol. 80, p. 046605, 2009.

[35] N. Lazarides, V. Paltoglou, and G. P. Tsironis, "Nonlinear magnetoinductive transmission lines," *Int. J. Bifurcation Chaos*, vol. 21, pp. 2147–2156, 2011.

[36] B. Wang, J. Zhou, T. Koschny, and C. M. Soukoulis, "Nonlinear properties of split-ring resonators," *Opt. Express*, vol. 16, p. 16058, 2008.

[37] M. Sato, B. E. Hubbard, A. J. Sievers, B. Ilic, D. A. Czaplewski, and H. G. Graighead, "Observation of locked intrinsic localized vibrational modes in a micromechanical oscillator array," *Phys. Rev. Lett.*, vol. 90, p. 044102 (4pp), 2003.

[38] N. Lazarides, M. I. Molina, and G. P. Tsironis, "Breather induction by modulational instability in binary metamaterials," *Acta Physica Polonica A*, vol. 116 (4), pp. 635–637, 2009.

[39] ——, "Breathers in one-dimensional binary metamaterial models," *Physica B*, vol. 405, pp. 3007–3011, 2010.

Plasmonic Biosensors

Metal island film based structures for sensing using spectrophotometry and ellipsometry

V. Janicki[1,2*], J. Sancho-Parramon[1,2], S. Bosch[2] and H. Zorc[1]

[1]Ruđer Bošković Institute, Croatia
[2]University of Barcelona, Spain
*corresponding author, E-mail: janicki@irb.hr

Abstract

Metal island films (MIF) are good candidates for sensors due to environment refractive index sensitive localized surface plasmon resonance (SPR). The strong near field enhancement in the vicinity of the island surface can be even higher if metal layer (ML) is placed close to MIF. Structures containing MIF with and without ML are prepared and sensitivities of spectrophotometric and ellipsometric features of the measurements compared. It is shown that simple MIF is preferable for ellipsometric and the one including ML for spectrophotometric sensing.

1. Introduction

Metal island films, consisting of two-dimensional ensembles of metal particles deposited on a substrate, have strong potential for plasmonic biosensing. SPR of isolated particles is highly sensitive to refractive index changes of the environment, enabling to detect presence of different analytes [1]. MIFs are attractive candidates for the production of performance- and cost-efficient sensors. For this reason, sensing using MIF is typically based on shift of the maximum of the SPR band upon changes of dielectric environment. In addition, the strong near field enhancement taking place close to the island surface, allows amplification of Raman signal [2] or infrared absorption [3] of closely located molecules. The near field enhancement is largest for very small particles and inter-particle distances, which are typically few nanometers in the case of MIF. Strong coupling between SPR of metal nanoparticles and propagating surface plasmon of a nearby metal film (polariton), enhances this electric near field largely [4-6]. This work compares sensitivity of MIF-based plasmonic structures, consisting of a single MIF layer or including a compact ML nearby MIF, to the quantity of dielectric material surrounding the metal nanoparticles.

2. Experimental

The samples were prepared by electron beam evaporation in a modified Varian 3117 chamber. The quartz substrates were positioned onto a rotating calotte to ensure a uniform thickness of the layers over the sample surface. Base pressure was $6 \cdot 10^{-6}$ Torr. Prior to the deposition of Au island film the samples were preheated to 250°C to enhance metal island growth [7, 8]. Mass thickness of the layers was controlled by a quartz crystal monitor. Deposition rates were 10Å/s for SiO_2 and 1Å/s for Au.

The first type of sample structure is quartz/MIF/SiO_2 (MIF* serial) and the second quartz/Au/SiO_2/MIF/SiO_2 (AuMIF* serial). These samples are designed to test the sensing potential of MIF, as they would simulate the effect of adsorbed analyte layers at MIF. The samples within one serial differ in the mass thickness of capping SiO_2 layer (d_{capp}), that was 3, 6, 9 and 12 nm. Additional samples having structure quartz/MIF, quartz/Au, quartz/Au/SiO_2 and quartz/Au/SiO_2/MIF were deposited as well. The mass thickness of compact Au ML is 70 nm and of the spacer SiO_2 layer between ML and MIF is 12 nm. All the corresponding layers are prepared in the same electron beam deposition process. Therefore, their thicknesses and optical parameters in the both structures are assumed to be the same.

Spectroscopic (reflectance *R* and transmittance *T*) and ellipsometric measurements of the two series of samples are analysed. *R* and *T* are measured in the range 300-1100 nm at Prkin Elmer Lambda 25 Spectrometer, and ellipsometric functions Ψ and Δ in the range 4.35-0.57 eV (that corresponds to 285-2175 nm), at incidence angles 25°, 45°, 55°, 65° and 80° at Woollam VASE Ellipsometer. Additionally, *T* is measured at ellipsometer in the same range as Ψ and Δ, at normal incidence.

3. Modeling and characterization

It has been shown in a previous study that Au metal island films deposited in the same conditions as here have dimensions that are much smaller than the wavelength of the performed measurements [7]. For this reason it is not expected significant scattering. Therefore, in the analysis of the spectral characteristics, absorptance *A* defined as *A=1-T-R* was included as well.

MIF layers of the studied samples contain not only Au metal islands, but also SiO_2 from the capping layer that fills the space between the islands. The samples having structure quartz/Au, and quartz/Au/SiO_2 were analyzed as first. The obtained optical constants and thicknesses of Au layer and SiO_2 under layer were used as known parameters in modelling of the rest of the samples.

In order to obtain thicknesses and optical parameters of the layers, the measurements were analyzed by WVASE32 software. Since the optical parameters of

MIF are influenced by the parameters of the dielectric environment, it was expected that they would change with d_{capp}. For this reason the MIF and the capping layer were modelled as one effective layer (see Fig.1.). The optical parameters of dielectric constants (real and imaginary ε_1 and ε_2) of this layer were modelled with a sum of Gauss oscillators [8]. Variation of the constants with d_{capp} of each model was monitored.

The maxima or minima in the spectra having significant central wavelength (λ_o) shift or change of the intensity (I_o) with d_{capp} were analysed. Sensitivity was calculated as $S_x = dx/dd$, where x denotes λ_o or I_o of the spectral features and d is mass thickness of SiO_2 deposited above Au islands.

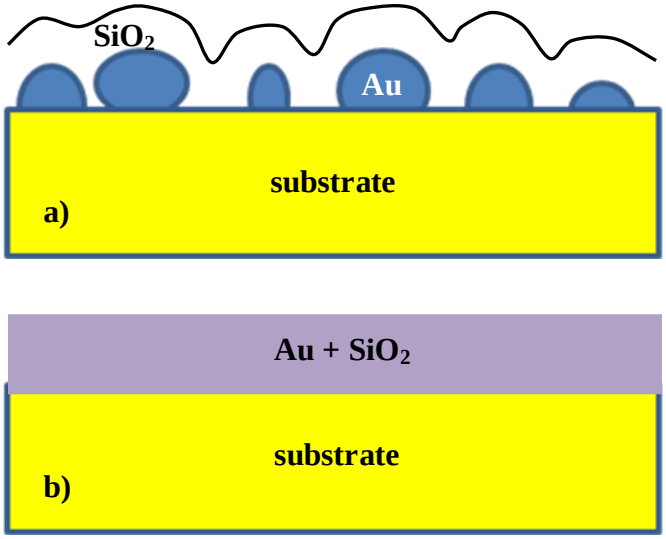
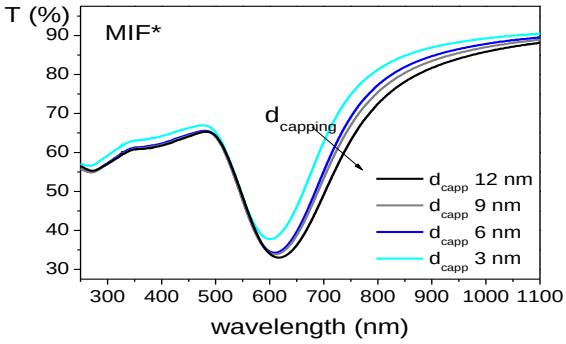
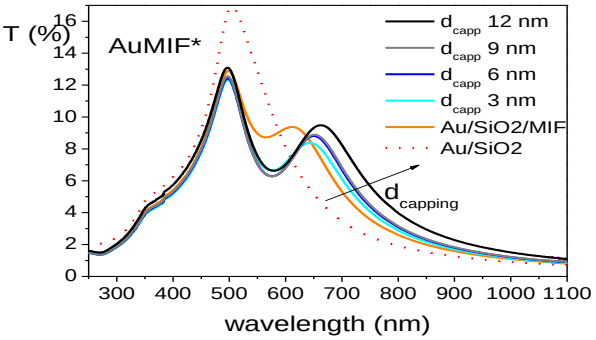


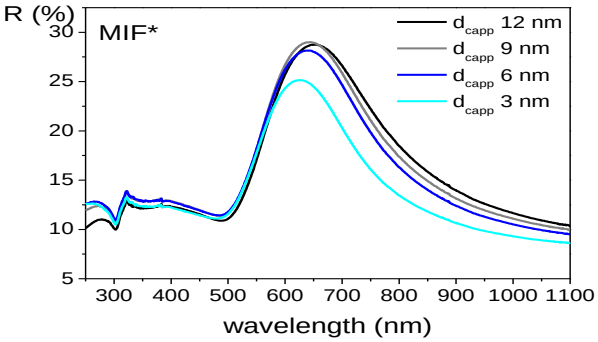
Figure 1. Schematic presentation of a MIF* sample consisting of Au island film covered with capping SiO_2 layer (a) and the corresponding model used in optical characterization (b).

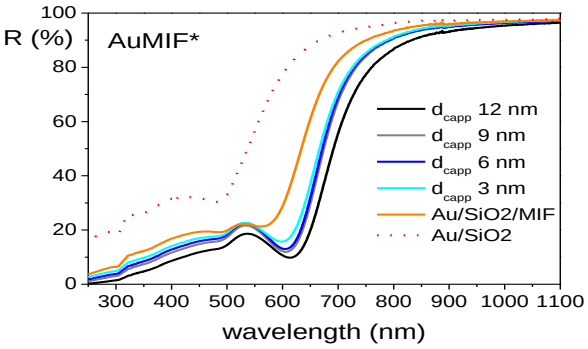
4. Results and discussion

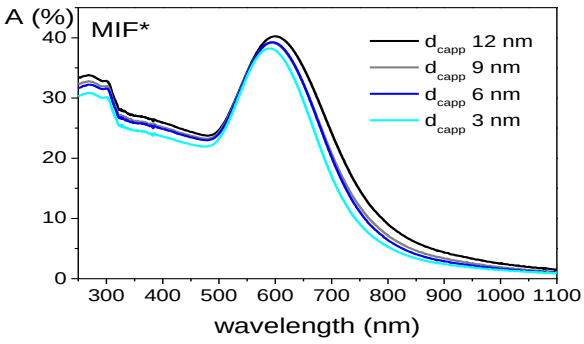
The spectra originating from spectrophotometric and ellipsometric measurements are presented in Fig.2 and Fig.3. These spectra show that I_o and λ_o of the peaks are significantly changing with d_{capp}. Dielectric constants of MIF layers obtained as the result of optical characterization based on ellipsometric measurements are presented in Fig.4.











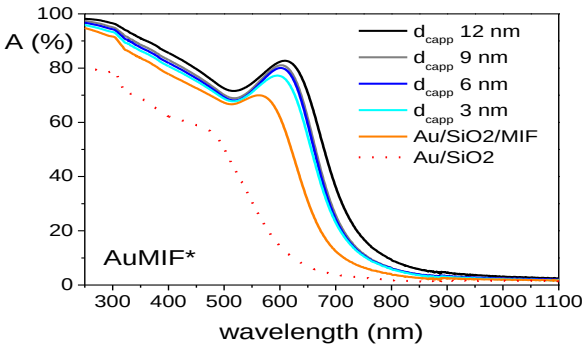


Figure 2. Spectrometric measurements showing characteristic change of spectra due to increase of d_{capp}. Measurements of Au/SiO_2 and Au/SiO_2/MIF are presented for comparison.

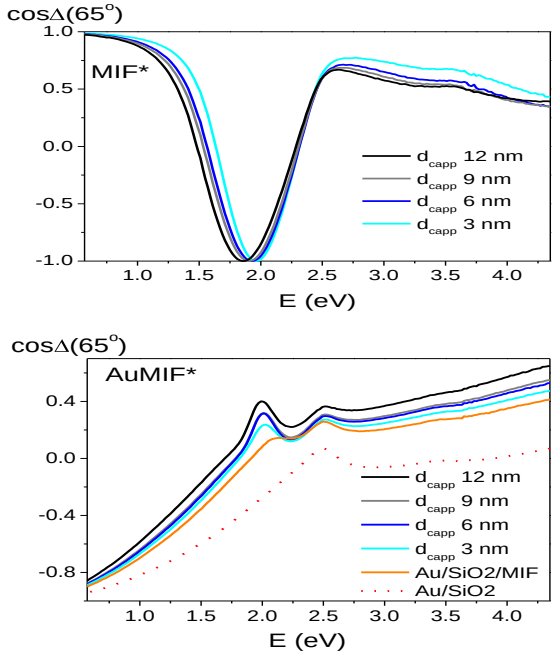


Figure 3. The changes of cosΔ(65°) with d_{capp}.

The calculated sensitivities are presented in Tab.1. and Tab.2. In order to compare intensity sensitivities S_I of different measurements, they were all normalized to 0-100% scale. Quantity I_c is defined as $I_c = \sin 2\Psi \cos\Delta$, that is really measured by ellipsometer. The changes of cosΔ(65°) with d_{capp} are presented in Fig. 4.

It is found that AuMIF* serial transmittance peak shift sensitivity $S_{\lambda 0}(T_{AuMIF*})$ is higher than the one of MIF*. Since T measurements are simple and widely available, this makes AuMIF* structure more practical for sensing purposes. $S_{\lambda 0}(A_{AuMIF*})$ also shows higher value than the one of MIF*. However, $S_{\lambda 0}$ (R_{MIF*}) has the highest sensitivity of all the spectrometric measurements. Generally, S_I shows lower values for this kind of measurements than $S_{\lambda 0}$. S_I(AuMIF*) is higher than S_I(MIF*). Regarding ellipsometric measurements, shift sensitivities of MIF* are significantly higher than for AuMIF*. In the case of S_I the situation is opposite. However, comparing shift and intensity sensitivities obtained from ellipsometry, S_I values are lower. Dielectric functions ε_1 and ε_2 obtained from optical characterization based on ellipsometric measurements show high values of $S_{\lambda 0}$(MIF*), having S_I higher than those resulting from AuMIF*.

Quantities the most sensitive to spectral shift are shown to be cosΔ(65°) and I_c(65°), both obtained for ellipsometric measurements of MIF*. High sensitivity of Δ function in this case originates from the fact that generally it is sensitive to properties of surfaces [9]. It means that it carries the information about the very surface of the sample, which corresponds to MIF covered with capping SiO_2. Contrary to this, R or Ψ, for example, are dominated with intrinsic properties of the sample [10, 11]. Corresponding measurements performed at other angles do not show so high change of Δ as for 65°. This shows the importance of choosing the angle having the highest sensitivity for the measurements.

High spectral shift sensitivities originate from the expected sensitivity of SPR to the change of the environment. This is confirmed by high values of $S_{\lambda 0}$ $(\varepsilon_1, \varepsilon_2)$ of MIF*. On the contrary, spectral shifts of AuMIF* dielectric permittivity are poor. One possible explanation might be that the coupling of localized surface plasmon in MIF and surface polariton in ML is screening the influence of change of environment to SPR by its strength. In this case increasing the distance between MIF and ML, by thicker spacer, the coupling should become weaker [4]. Modelling of the studied structures of samples could check for the optimal design of the proposed sensors.

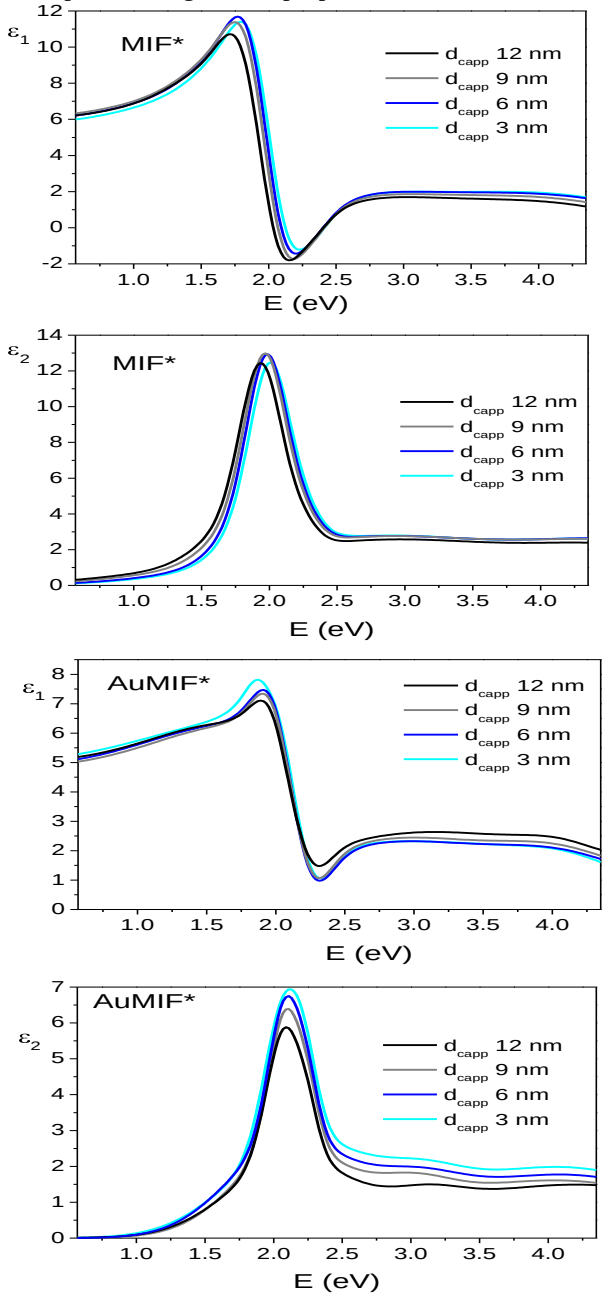


Figure 4. Dielectric functions of MIF layers obtained as the result of optical characterization based on ellipsometric measurements.

Table 1: Sensitivities of the measurements

	$S_{\lambda o}$		S_{Io} (nm^{-1})	
	MIF*	AuMIF*	MIF*	AuMIF*
T	1.67	**1.93**	**-0.49**	0.11
R	**2.93**	1.53	0.39	**-0.63**
A	1.07	**1.47**	0.2	**0.58**
$\psi(45^o)$	1.28	1.11	< 0.1	< 0.1
$\psi(80^o)$	**2.83**	< 0.1	< 0.1	< 0.1
$\cos\Delta(45^o)$	0.58	**1.25**	0.16	**0.65**
$\cos\Delta(65^o)$	**4.31**	1.23	< 0.1	**0.82**
$I_c(65^o)$	**3.68**	0.47	-0.34	**0.47**

Table 2: Sensitivities of dielectric permittivities obtained from optical characterization

	$S_{\lambda o}$		S_{Io} (nm^{-1})	
	MIF*	AuMIF*	MIF*	AuMIF*
ε_1	**2.77**	0.56	0.2	-0.12
ε_2	**2.24**	< 0.1	< 0.1	-0.10

5. Conclusions

Overall, AuMIF* structure is preferable for sensing in the case of spectrometric measurements, while ellipsometric measurements give advantage to MIF* structure having high values of spectral shift sensitivity. These results offer a guideline for design of MIF based sensing structures depending on the availability of optical measurements.

Acknowledgements

Vesna Janicki would like to thank European Science Foundation (ESF) for the activity entitled 'New Approaches to Biochemical Sensing with Plasmonic Nanobiophotonics (PLASMON-BIONANOSENSE) Exchange Grant 3853.

References

[1] A. Vaskevic, I. Rubinstein, Localized Surface Plasmon Resonance Sensing (LSPR) Spectroscopy in Biosensing, *Handbok of Biosensors and Biochips*, Wiley, 2007.

[2] M. Moskovits, Surface-enhanced Raman spectroscopy: a brief retrospective, *J. Raman Spectrosc.*, Vol. 36, No. 36, pp. 485-496, 2005.

[3] M. Osawa, Surface Enhanced Infrared Absorption, *Topics Appl. Phys.*, Vol. 81, pp. 163-187, 2001.

[4] H. R. Stuart, D. G. Hall, Enhanced dipole-dipole interaction betwen elementary radiators near surface, *Phys. Rew. Lett.*, Vol. 80, pp. 5663-5666, 1998.

[5] Y. Chu, K. B. Crozier, Experimental study of the interaction between localized and propagating surface plasmons, *Opt.Lett*., Vol. 34, No. 3, pp. 244-246, 2009.

[6] L. C. T. Shoute, Multilayer substrate-mediated tuning resonance of plasmon and SERS EF of nanostructured silver, *ChemPhysChem.*, Vol 11, pp.2539-2545, 2010.

[7] M. Lončarić, J. Sancho-Parramon, M. Pavlović, H. Zorc, P. Dubček, A. Turković, S. Bernstorff, G. Jakopic, A. Haase, Optical and structural characterization of silver island films on glass substrates, *Vacuum*, Vol. 24, pp. 188-192, 2010.

[8] M. Lončarić, J. Sancho-Parramon, H. Zorc, Optical properties of gold island films - a spectroscopic ellipsometry study, *Thin Solid Films*, Vol. 519, pp. 2946-2950, 2011.

[9] A. V. Tikhonravov, M. K. Trubetskov, A. V. Krasilnikova, E. Masetti, A. Duparre, E. Quesnel, D. Ristau, Investigation of the surface micro-roughness of fluoride films by spectroscopic ellipsometry,*Thin Solid Films*, Vol. 397, pp. 229-237, 2001.

[10] A. V. Tikhonravov, M. K. Trubetskov, A. V. Krasilnikova, Spectroscopic ellipsometry of slightly inhomogeneous nonabsorbing thin films with arbitrary refractive-index profiles: theoretical study, *Appl. Opt.* Vol. 37, pp. 5902-5911, 1998.

[11] K. Lodewijks, W. Van Roy, G. Borghs, L. Lagae, P. Van Dorpe, Boosting the figure-of-merit of LSPR-based refractive index sensing by phase-sensitive measurements, *Nano Lett.*, Vol. 12, pp. 1655-1659, 2012.

Nanoparticles and nanosystems

Assemblies from Metallic and Semiconducting Nanocrystals

*Ingolf Kahle,[†] Stefan Krause,[§] Cornelius Krasselt,[§] Alexander Jakob,[‡] Alexander Oehlke,[†] Colin Georgi,[‡] Steffen Schulze,[II] Heinrich Lang,[‡] Michael Hietschold,[II] Stefan Spange,[†] and Christian von Borczyskowski,[§] **

[†],Department of Polymer Chemistry, Chemnitz University of Technology, 09111 Chemnitz, Germany.

[§] Department of Optical Spectroscopy and Molecular Physics, Chemnitz University of Technology,

09126 Chemnitz, Germany.

[‡] Department of Inorganic Chemistry, Chemnitz University of Technology, 09111 Chemnitz, Germany.

[II] Department of Solid Surfaces Analysis, Chemnitz University of Technology, 09126 Chemnitz, Germany.

*Corresponding Author: Christian von Borczyskowski, Chemnitz University of Technology, Institute of Physics, Reichenhainerstr. 70, D-09107 Chemnitz, Germany. E-mail: borczyskowski@physik.tu-chemnitz.de; Fax: +49 (0) 371 531 833035; Tel: +49 (0) 371 531 33035.

Abstract Optical properties of nanomaterials such as semiconductor and metal quantum dots are important for sensor and photovoltaic applications. They often show quantum size effects. We report on optical, microscopic and AFM investigations on bulk and single quantum objects. Of special interest is the investigation of Ag metal nanoaggregates formed in zeolites or self-aggregated assemblies from organic dyes and semiconductor quantum dots. The synthesis of fluorescent silver nanoparticles with a size diameter of about 1 nm using a silver (I) carboxylate and zeolite Y is presented. Here, the defined structure of the zeolite serves both as size directing and stabilizing. The Ag aggregates in the zeolite cages exhibit fluorescence even after storage under ambient conditions for almost one year. In addition, single Ag particles could be investigated outside the cages by fluorescence microscopy. This introduces highly sensitive tool with respect to sensor applications. With respect to photovoltaic applications energy transfer among the constituents of heterogeneous nanomaterials is of great importance. Extension into the UV regime is established via the chemical surface functionalization of ZnSe quantum dots (QDs) with fluorescent styrylpyridine dyes, the formation of which has a strong effect on the optical properties of both, the QDs and the dye.

KEYWORDS

Silver, ZnSe semiconductor quantum dots, nanoparticles, luminescence, zeolites, photoblinking, styrylpyridine, single particle spectroscopy, nanoassemblies

1. Introduction

In many areas of science, such as biomedical technology, industrial and food processing, healthcare and environmental monitoring, a demand exists for optical sensors with high sensitivity and ease of handling [1-4]. Among these are fluorescent probes which can be investigated easily by different optical techniques with high sensitivity and which have been already applied in the fields of chemical sensing and biosensing [5-7]. Therefore, the development of new effective (e.g. photostable, high quantum yield, large Stokes shift) fluorescent probes is still an attractive topic. Organic dyes and recently developed semiconductor quantum dots (QDs) are very promising as fluorescence probes but are limited by several characteristics. Fluorescent dyes exist in a variety of organic chemical structures and optical properties but suffer from low absorption cross section and tend to photobleach especially in presence of oxygen [8-9]. QDs show high quantum yields and absorption cross sections, size-tunable narrow emissions and minimal photobleach. However, they are limited by their harsh and toxic conditions in the synthesis and their large physical size which may hinder their use for *in-vivo* applications and as fluorescent reporters of binding events [10-12]. It is a challenge to develop new fluorophores without these problems. Because of their non-toxicity, photostability, high emission rates and large Stokes shifts, few-atom silver nanoparticles offer a new class of promising fluorescenct probes. We report on a precise size control via zeolite template assisted synthesis and the optical and microscopic identification of single Ag nanoparticles.

While Ag particles might serve as efficient non-toxic fluorescent probes, colloidal semiconductor nanocrystals offer due to their structural or chemical composition and surface functionalization a large manifold of modifications with respect to their (tunable) optical properties. Semiconductor nanocrystals, also known as quantum dots (QDs), have been extensively investigated over the past several decades due to their unique and excellent optical properties, such as size-dependent photoluminescence (PL) with high PL quantum yield, narrow emission profiles, and good resistance to photo degradation [13-18]. These properties have made QDs interesting candidates for applications in various fields, including optoelectronics and sensors such as bio-imaging, LEDs, and displays [19-25]. Avoiding toxic Cd as component is essential in sensors for biological application. Therefore, the development of non-toxic and water soluble quantum dots is a challenge. ZnSe would be an interesting candidate for those applications. To amplify the optical properties of ZnSe QDs, the surface of them can be functionalised with suitable fluorescent dyes. For this purpose, pyridine ring containing dyes are especially usefull because the electron density of the lone electron pair at the nitrogen of the pyridine ring is sufficient to bind at the ZnSe surface, as has been shown previously for CdSe or CdSe/ZnS [26, 27]. We report for the first time on ZnSe based QD-dye nanoassemblies and demonstrate the modification of the optical properties of such systems.

2. Experimental

2.1 Synthesis of Ag particles

Zeolite Y (H.C. Starck; H-form; SiO_2/Al_2O_3 ratio ~ 90), $AgNO_3$ (Acros; 99+ %), $HO_2C(CH_2OCH_2)_3H$ (Sigma-Aldrich 90+ %) and triethylamine (Sigma-Aldrich 99+ %) were used without further purification. All used solvents were redistilled over appropriate drying agents prior to use. The silver(I) precursor *$[AgO_2C(CH_2OCH_2)_3H]$* was synthesized according to literature by the reaction of silver nitrate with 2-[2-(2-methoxyethoxy)-ethoxy]acetic acid in presence of NEt_3 in a mixture of ethanol/acetonitrile (20:1 (v/v)) at ambient temperature [26]. An amount of 1 g zeolite Y (H form) was heated at 180 °C for 2 h under vacuum to remove water adsorbed in the pores of the material. Subsequently, the zeolite was loaded with $[AgO_2C(CH_2OCH_2)_3H]$ by incipient wetness impregnation. Therefore, 100 mg of the silver complex was dissolved in a small amount of dichloromethane (2 ml) and

added drop-wise via syringe to the zeolite which was placed in an evacuated Schlenk vessel. After shaking for 12 h, the zeolite was dried under vacuum at ambient temperature before it was heated to about 280 °C for 2 h. The obtained powder was dispersed in water and treated with ultrasonic (55 W, 15 min) to remove silver particles grown at the external surface. A formation of silver oxide can be excluded since it decomposes at temperatures higher than 230 °C.

2.2 Formation of QD-dye nanoassemblies

All used solvents were redistilled over appropriate drying agents prior to use. All commercial organic compounds were used without further purification. For synthesis of styrylpyridines or styrylquinolines benzoylchloride (1 mmol) was added to a solution of pyridine or lepidine (1 mmol) in 3 ml toluene. After stirring for 20 min benzaldehyde (1 mmol) was added and the mixture was stirred under reflux for 5 h. After cooling to room temperature, 10% NaOH solution in water (2 ml) was added drop-wise. The resulting precipitate was filtered off and recrystallised from ethanol to afford the product.

QD-dye aggregates have been obtained by titration experiments. To a solution of ZnSe QDs in toluene ($2.5 \cdot 10^{-5}$ mol/l) a defined amount of the respective dye solution (in toluene) was added (with concentrations ranging from $1 \cdot 10^{-5}$ mol/l to $1.2 \cdot 10^{-4}$ mol/l). Each mixture was investigated by fluorescence experiments.

2.3 Characterization

UV/Vis spectra were recorded for Ag particles in reflection on a Zeiss multi-channel spectrometer system MCS 601/CLD using a deuterium lamp (210-620 nm) and a CLX 75W/Sch xenon lamp (290 - 900 nm) as light sources. Fluorescence spectroscopy was performed at a FluoroMax®-4 spectrometer from HORIBA Jobin Yvon (cuvette d=10 mm). ^{1}H and ^{13}H spectra of dye molecules in solution were measured at room temperature with a Bruker Avance 250 spectrometer at 250 and 69.9 MHz respectively. Elemental analyses were performed with a Vario-EL-analyser. Diffuse reflectance IR Fourier transform (DRIFT) spectra were recorded using a BIORAD FTS 165 spectrometer with a praying mantis device. The samples were mixed with dry KBr. Pure potassium bromide was used as reference. Differential Scanning Calorimetry analyses were performed with a DSC 30 from Mettler Toledo under nitrogen flow (50 ml/min) with a heating rate of 10 K/min.

Thermogravimetry (TG) and mass spectrometry were carried out with a Mettler Toledo TGA/DSC 1 HT simultaneous thermal analyzer. Measurements were carried out in the temperature range from 40 to 600 °C with a heating rate of 10 K min^{-1} in an atmosphere of argon (20 ml/min). Atomic Force Microscope (AFM) investigations revealed a diameter of 1nm for the isolated Ag clusters.

Transmission electron microscopy (TEM) images were obtained with a 200 kV Philips CM20 FEG transmission electron microscope. For sample preparation, a copper grid (Ø = 3.0 mm) was dipped into a water suspension of the zeolite powder with embedded silver particles and kept under atmospheric conditions for drying before usage. Scanning electron microscopy (SEM) was performed on a NanoNovaSEM (Philips) with a Schottky Field Emission Gun.

For investigations of individual Ag particles a home-built wide field microscope was used [27]. The sample was excited with the 514 nm line of an argon/krypton-ion laser (Coherent, Innova 70C). For this, the laser beam was focused on the backfocal plane of a 100x objective with a numerical aperture of NA = 0.9 (Zeiss, Epiplan Neofluar). The emitted light of the tracers was collected by the same objective and focused via a lens (focal length 250 mm) onto a back-illuminated electron multiplying charge-coupled device (EMCCD) camera (Princeton instruments, PentaMax, cooled down to -30 °C) in the frame-transfer mode, which was used as a photon detector. The fluorescence signal of the particles is separated from backscattered excitation light using a dichroic beamsplitter and a long pass filter.

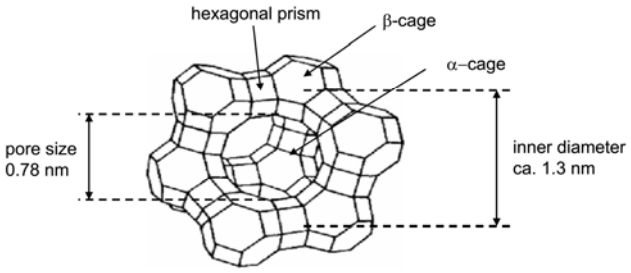
Laser scanning measurements were performed with a Zeiss LSM 510 (excitation at 488 nm). For this the powder was depositet on silicon wafer with 100 nm thermally grown SiO_2 from water solution by evaporation.

3. Results and discussion

3.1 Formation of silver aggregates in zeolite cages

Different routes for synthesizing silver nanoparticles are described in literature. In most cases these particles are prepared in solution by the addition of reducing- and stabilizing agents which prevent the formation of aggregates [28-32]. Lin *et al* also described the synthesis of silver nanoparticles without further reducing agents by electrochemical means [33]. But this method requires a fairly elaborate setup and the obtained nanoparticles were stable for only 7 days. The formation of silver nanoparticles on and within silica and their anti-bacterial and catalytic effect is also reported [34, 35]. However, in most cases an additional reducing agent is indispensable and the control of size is still a challenge.

Fluorescent nanoparticles with a diameter between 1 and 2 nm could be simply synthesized without additional reducing agents by using the silver(I) carboxylate [$AgO_2C(CH_2OCH_2)_3H$] as precursor and zeolite Y. The defined structure of the zeolite serves both as size director and a stabilizer for the silver nanoparticles (Scheme 1) [36, 37].



Scheme 1 Structure of faujasite (zeolite Y) consisting of $[SiO_4]^{4-}$ and $[AlO_4]^{3-}$ tetrahedra, linked by oxygen atoms [36]

The thermal conversion process of the silver (I) complex inside the zeolite Y was investigated by thermogravimetric analysis (TG) (Fig. 1).

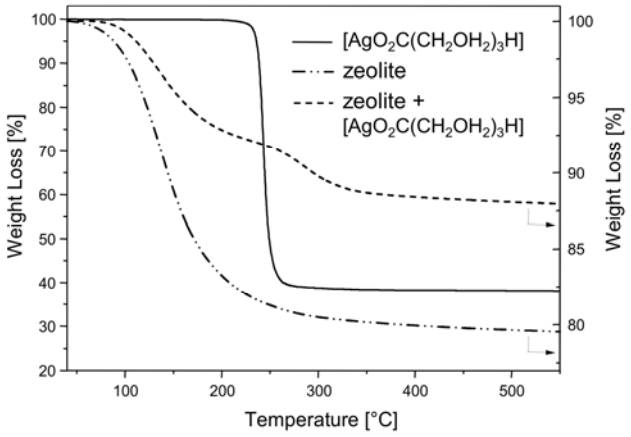


Fig. 1 TG traces for the thermal heating of the silver (I) complex, zeolite Y, and zeolite Y containing about 10 wt% of the silver precursor ([$AgO_2C(CH_2OCH_2)_3H$])

A first weight loss appears at about 100 °C for the pure zeolite Y (weight loss of about 20 %) and zeolite loaded with the precursor (weight loss of about 6 %). Zeolites are hygroscopic materials often used as drying agents. Therefore, this first weight loss is assigned to adsorbed water due to a short storage under ambient conditions prior to the TG measurements. The thermal degradation of the precursor inside the zeolite occurs between 200 and 300 °C (second weight loss of about 6 %) and is in the same region of the pure silver (I) complex. Additional mass spectrometry analyses for the zeolite Y

loaded with silver (I) carboxylate confirmed previous findings of a thermal decomposition of pure [$AgO_2C(CH_2OCH_2)_3H$] where the main fragments were CH_3^+ (m/z = 15), CH_4^+ (m/z = 16), CO^+ (m/z = 28), CHO^+ (m/z = 29) and CO_2^+ (m/z = 44) [26]. Note that a m/z of 44 could also be assigned to fragments from the glycol units of the complex ($C_2H_4O^+$). Comparable to the pure silver (I) complex, the mass loss of the precursor inside the zeolite was also about 60 %, which is in accordance with the theoretical percentage calculated for the formation of elemental silver (37.8 %). With respect to these findings, we conclude that the zeolite matrix does not affect the thermal behavior of the silver (I) carboxylate.

The formation of metallic silver was confirmed by electron diffraction (see supporting information). As the SEM image shows, the size distribution of the zeolite is in the range of several µm, while the encapsulated silver particles are mostly between 1 and 2 nm diameter as shown by TEM investigations. This agrees with the inner pore diameter of the zeolite Y (Fig. 2). Even after treatment with ultrasonic in order to remove larger aggregated silver particles, a few particles in the range of 5-15 nm are still present at the surface. Further studies to investigate the stability of the hybrid material were performed *via* dialysis for 1 week in ultrapure water. We observed that a small percentage of silver nanoparticles could be washed out while the main part remains in the zeolite. However, these silver nanoparticles could be deposited onto a silicon wafer from solution and were investigated *via* atomic force microscopy (AFM). By this, a particle size of about 1 nm was confirmed (see supporting information).

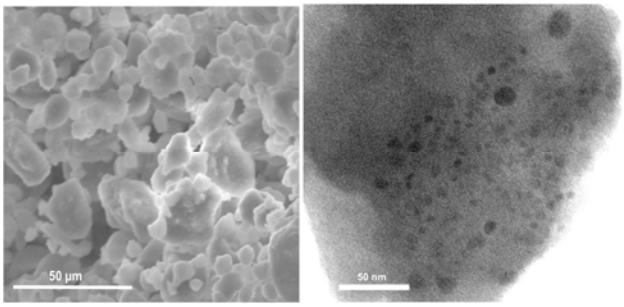


Fig. 2 SEM (left) and TEM (right) images of zeolite powder with encapsulated silver particles

The obtained powders are yellow to brownish and show a strong fluorescence under the UV excitation (UV lamp with 8 W; λ = 254 nm). Although the size-dependent behavior of silver nanoparticles is not fully understood it is clear that the emission originates from particles consisting of only a few Agatoms [38]. In silver nanoparticles the motion of electrons is restricted and interactions are expected to be influenced by the surface. The resulting optical properties are determined by collective oscillations of conduction electrons by interaction with light which is called “surface plasmon resonance”. A further reduction in size to few-atom nanoparticles results in discrete energy levels. This allows the interaction with light by electronic transitions between these energy levels.

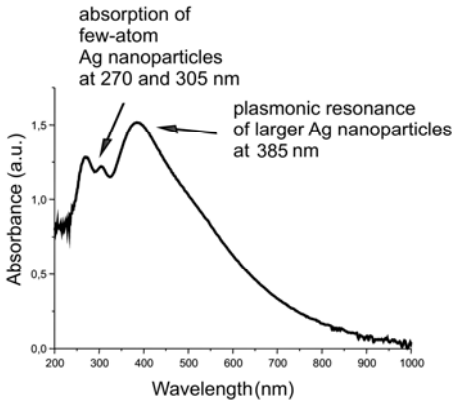


Fig. 3 UV/Vis absorption spectrum of silver nanoparticles encapsulated in zeolite Y

The UV/Vis absorption spectrum shows two bands at 270 and 305 nm and a broad plasmon resonance band at 385 nm, which is typical for spherical silver nanoparticles (Fig. 3) [39]. The two bands at 270 and 305 nm can be assigned to small silver nanoparticles consisting of only several atoms with respect to the atomic radius of silver (Ø = 0.288 nm) and previously reported absorption spectra of such silver clusters (Ag_n cluster with $n \leq 9$) which were investigated in cryogenic inert gas matrices [40]. Similar UV/Vis absorption bands of Ag_8 and Ag_9 were found in the same region. However, different matrices will lead to shifts of the absorption bands as there is a strong influence on the cluster stabilization energy, geometrical structure of the embedded clusters and oscillator strength of different transitions. Nevertheless, strong UV/Vis absorption bands should still be in a similar range while much weaker bands are also found in the visible range. Analog observations are reported for silver clusters embedded in mordenite or erionite channels which were formed by reduction of silver ions in a H_2 flow [41]. Referring to Harbich *et al.*, those optical transitions are associated to the *s*-electrons which is in contrast to other metals (Au and Cu) which show a strong coupling of *d*-electrons [40].

It is known that plasmonic metal nanoparticles strongly absorb light but generally they do not fluoresce or only very weakly. In the present case we observe a strong emission in the range between 400 and 600 nm. The recorded excitation spectrum, which belongs to the emission at 465 nm, clearly shows that this emission originates from the few-atom silver particles (Fig. 4). The excitation spectrum does not correspond directly to the absorption spectrum (Fig. 3). Neither the UV nor the plasmon absorption is pronounced in excitation. Additionally, there is a strong Stokes-shift between excitation and emission. This can be understood by taken recent investigations on Ag-clusters into account which show absorption over a broad range changing with size and structure. The fluorescence is extremely red shifted, since absorbed photons cascade down to the lowest energy level [40, 42].

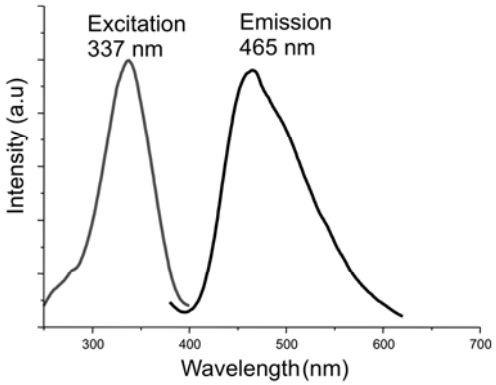


Fig. 4 Excitation and emission spectra of silver nanoparticles encapsulated in zeolite Y (suspension in water)

Investigation with laser scanning microscopy showed a non-regular spatial distribution of the silver nanoparticles within the zeolite matrix (see Fig. 5). In addition, individual silver nanoparticles could be further investigated by fluorescence microscopy. Therefore, the powder was suspended in ultrapure water (1 mg/4 ml) and spin-coated onto a silicon wafer with 100 nm thermally grown SiO_2 at 3000 rpm. These particles were excited with a 514 nm laser beam (500 mW). The fluorescence was imaged onto a CCD camera. Using a 530 nm long pass filter the fluorescence was separated from the excitation light. As a result, only emission above 530 nm according to size and structure of a sub-ensemble of Ag clusters could be observed.

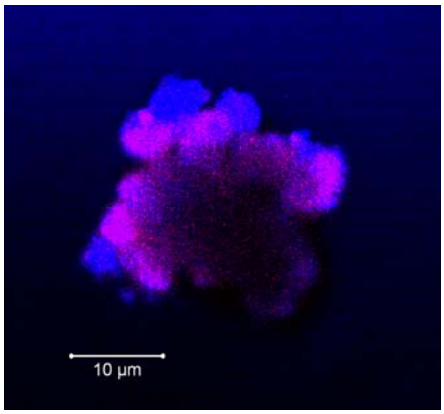


Fig. 5 Representative image of a large zeolite particle from laser scanning microscope (blue area: reflection; red area: fluorescence)

Fig. 6 shows a typical image taken with the wide field fluorescence microscope, where photoblinking behavior of the individual particles was observed. Most of the diffraction limited spots displayed blinking that persisted over a long period (several seconds to minutes) of observation. Similarly, Lakowicz *et al.* reported about silver nanostructures deposited on glass that showed luminescence blinking when excited at high irradiance [43]. They found small silver fractal surfaces photoactivated at much lower irradiances (<30 W/cm^2), as compared to both colloids and silver island films coated on glass (>100 W/cm^2).

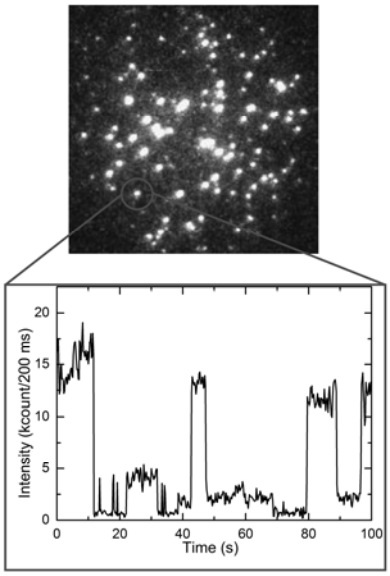


Fig. 6 Representative image taken with a wide field fluorescence microscope. The marked area shows a single particle blinking in intensity and the related time-trace

This aspect further supports our findings about the small few-atom nanoparticles within the zeolite matrix. In dependence of the excitation power we found that fluorescence could already be observed at relatively low irradiance of about 10 W/cm^2 (see supporting information).

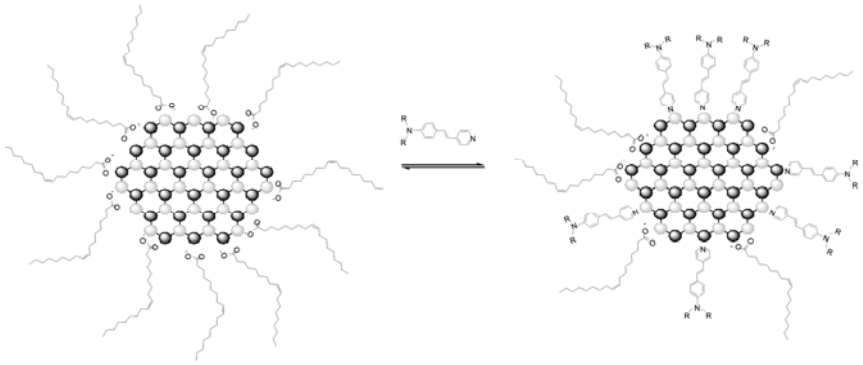
By illumination of the sample with high excitation power (P_{ex} = 1mW) we further observed a photobleaching of the particle luminescence (see supporting information). This bleaching might be caused by laser-generated defects at the particle surfaces and was monitored as a function of time following a bi-exponential time dependence (see supporting information).

Due to the sensitivity of silver against sulfur containing compounds, we further investigated the material by treatment with H_2S for several hours. In expectation of obtaining silver sulfide nanoparticles with completely different optical characteristics, we observed that only the larger particles on the zeolite surface were affected. The plasmon resonance band at 385 nm was not present in the UV/Vis spectrum after H_2S treatment, while the absorption bands at 270 and 305 nm were still observed. In addition, the powder still shows fluorescence with a maximum at 450 nm which is slightly shifted hypsochromically with respect to the emission spectrum before H_2S treatment (see supporting information). This behavior might be caused by adsorbed silver sulfide or H_2S. Silver nanoparticles show strong response to the polarity of the surrounding medium which is reflected in solvato-fluorochromic properties [44]. Therefore, we conclude that the as-synthesized silver nanoparticles consisting of only a few atoms are stabilized through the zeolite matrix which is supported by their optical properties after storage under ambient conditions as well as after treatment with H_2S.

3.2 Surface functionalization of ZnSe QDs with fluorescent styrylpyridine dyes

QDs are usually stabilized with an organic layer of ligands to prevent aggregation. These ligands (often trioctylphosphine oxide (TOPO) or long chain amines and organic acids) play a key role during nanocrystal synthesis, as they form a monolayer (capping) that slows down crystal growth and stabilizes the nanocrystals in suspension [10, 11]. The improvement of photoluminescence efficiency [45], chemical reactivity [38], the formation of two-dimensional and three-dimensional aggregates [46, 47], and the attachment of quantum dots to surfaces is accessible by tuning the nature of the ligand [48]. Further studies were concerned with surface modifications to render QDs water soluble [49, 50]. Moreover, coating the surface of nanocrystals with organic dye molecules provides a new class of materials which will be important for photovoltaic, fluorescence markers in biological or medical applications or as LEDs [51, 52].

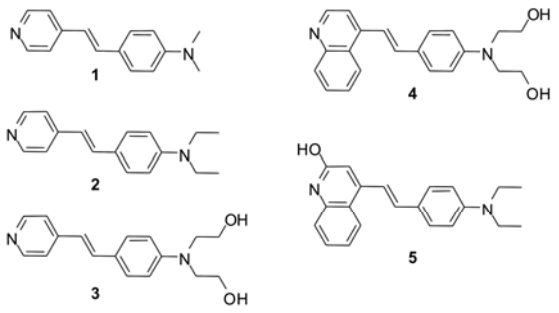
The intrinsic optical properties of ZnSe, used in the present experiment, are determined by the band gap energy (BGE) which is 2.7 eV as compared to CdS (2.42 eV), CdSe (1.73 eV), and CdTe (1.49 eV) [24, 25]. The larger BGE energy of ZnSe is of disadvantage for several optical applications as compared to analogous Cd compounds, because the UV/Vis absorption and emission of ZnSe occurs at higher energy in the visible spectrum (UV, blue to green). The empty Zn^{2+} sites on the surface of ZnSe are electron deficient which are able to interact with electron rich parts of a molecule. This concept is used to stabilize the quantum dots by such ligands which contain lone electron pairs suitable to enter the electron deficient sites on the surface of QDs. Accordingly, the choice of dyes for surface functionalisation of QDs is determined by their electronic properties of the active sites which should overcome the binding strength of the original ligands (oleic acid, TOPO) (see Scheme 2). Furthermore, it is desired that the interaction of the dye with the quantum dot surface is detectable by UV/Vis spectroscopy. A further rrequirement is that the UV/Vis emission of the linked dye is clearly separated from that of the ZnSe QDs. For this purpose, pyridine ring containing dyes are especially useful because the electron density of the lone electron pair at the nitrogen of the pyridine ring is sufficient to bind at the ZnSe surface, as has been shown previously for CdSe or CdSe/ZnS [27].



Scheme 2 Schematic presentation of ligand exchange on a ZnSe QD surface using styrylpyridine molecules

Therefore, several pyridyl substituted fluorescent dyes (4-(4-*N*,*N*-dimethylaminostyryl) pyridine (**1**), 4-(4-*N*,*N*diethylaminostyryl) pyridine (**2**), 4 (4Bis(2hydroxyethyl)aminostyryl)pyridine (**3**), 4-(4-Bis(2-hydroxyethyl)styryl)quinoline (**4**), and 4-(4-N,Ndiethylaminostyryl)-2-hydroxyquinoline (**5**)) were used to functionalize the surface of ZnSe nanoparticles (see Scheme 3). The base strengths of styrylpyridines are slightly higher compared to that of pyridine itself which is known to be able to displace ligands such as TOPO or oleic acid from semiconductor nanocrystal surfaces [43].

The formation of QD-dye assemblies via spontaneous adsorption of functional dye molecules on the surface of ZnSe nanocrystals is assumed to be a dynamic process during which the dye molecules and the originally ligands (oleic acid) are in rapid equilibrium. Advantageously, the pyridine moiety of those dyes is conjugated with the chromophoric system by which a surface functionalization of the QDs is directly and readily measurable by means of fluorescence spectroscopy. The pyridine ring is electron withdrawing. Its electron withdrawing strength is similar to that of nitrobenzene. Therefore, electron



Scheme 3 Molecular structures of pyridyl functionalized dye molecules for ligand exchange reaction on ZnSe QD surfaces.

donating substituents in the 4-position of the pyridine ring enhance the push-pull character. The Lewis acid attack of Zn^{2+} ions upon the lone electron pair of the nitrogen improves the electron withdrawing character of those dyes which is measurable by a bathochromic shift in the UV/Vis absorption and emission bands as seen by the model reaction of **1** with a Zn-salt (see Fig. 7).

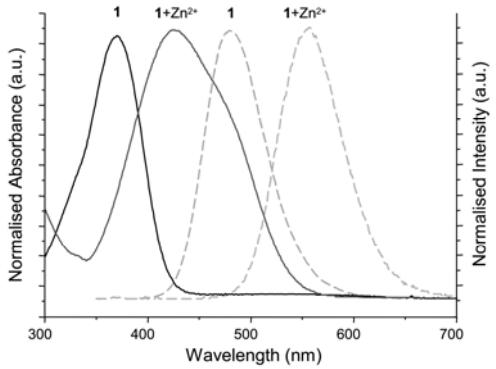


Fig. 7 Influence on UV/Vis absorption- and emission band of **1** by complexation of Zn^{2+} ions in methanol (solid lines: UV/Vis absorption bands; broken lines: emission bands)

Related to these features, a bond between the dye and the electron-poor metal atoms at the surface of ZnSe nanocrystals through the pyridyl ring reduces the electron density at the nitrogen heteroatom in a similar way, although not to the same extent, which leads to a slight increase of the push-pull character of the chromophor. As a consequence a bathochromic shift of the emission band is the result and could be simply observed by optical measurements (see Fig. 8). The emission maximum of dye **1** in toluene is observed at 430 nm and shifted bathochromically by 16 nm upon titration to a ZnSe solution indicating the formation of dye-ZnSe nanoassembly. All used pyridyl substituted dyes except the quinoline derivative **4** show similar effects upon titration to a ZnSe solution, a bathochromic shift of 10 nm to 17 nm of the dye emission band (see Table 1 and supporting information). Simultaneously, a quenching of the nanocrystal photoluminescence which is assigned to an energy transfer from the Qd to the dye is observed.

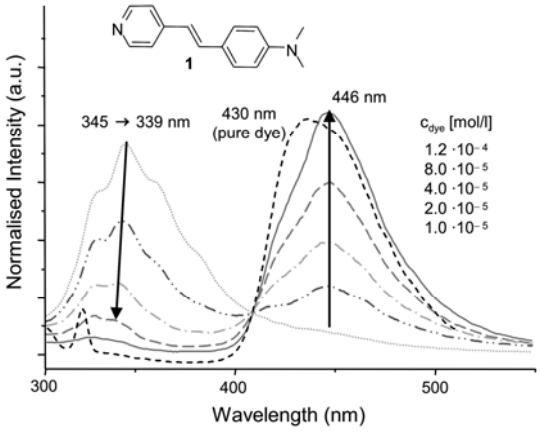


Fig. 8 Increase of Luminescence spectra of pure **1** (at 430 nm) and **1**-ZnSe nanoassembly (at 446 nm) with increasing dye concentration (dotted to solid line) after titration to a ZnSe solution (2.5·10-5 mol/l)

Table 1 Observed emission maxima of pure dye solution and dye/ZnSe nanoassemblies after excitation at 295 nm.

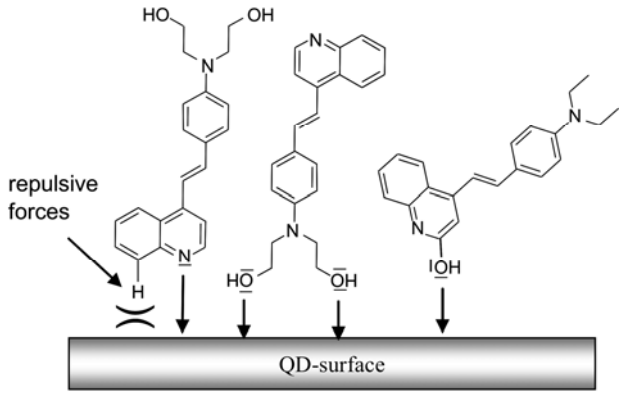
Dye	λ_{ZnSe}(nm)[a]	λ_{dye} (nm)[b]	$\lambda_{dye/ZnSe}$(nm)[c]	L(nm)

1	345	430	446	16
2	345	433	450	17
3	345	430	446	16
4	345	465	465	-
5	345	475	485	10

[a] emission maxima of ZnSe in toluene; [b] emission maxima of the dye in toluene; [c] emission maxima of the dye in dye/ZnSe assemblies in toluene

We note that the PL emission band of the ZnSe is not typical for QDs with respect to the structured band shape. This is attributed to several trap states due to non-uniformity of the particles (discussed in more detail in the supporting information). The two bands at longer wavelengths (345 and 360 nm) are much more affected by due to quenching upon titration with dye solution as compared to the band at 330 nm which is well explained by the spectral overlap of ZnSe emission- and dye absorption bands (supporting information). This supports the hypothesis of excitation energy transfer from ZnSe particles to the surface-bonded dyes.

The strongest shifts of the dye emission bands upon titration to ZnSe solution were observed for styrylpyridines **1** to **3** accompanied by a slight blue shift of the ZnSe emission band by about 6 nm which is still not fully understood. Dye **4** is not able to coordinate to the QD surface via the nitrogen hetero-atom due to steric hindrance (see Scheme 4). The annelated ring in quinoline derivatives plays a similar role as ortho-nitrogen in pyridine rings for which it is known that an adsorption onto QD surfaces des not take place due toi steric hindrance [27]. According to geometric reasons in the case of the styrylquinoline derivative **4**, an anchoring of the nitrogen lone pair orbital can occur only for an orientation of the dye nearly parallel to the QD surface. From the absence of a bathochromic UV/Vis shift of the emission band in the latter case, we conclude that a parallel orientation of the dye with respect to the QD surface is not favored. Therefore, the observed quenching of the nanoparticles emission can only come through an interaction of the particle surface with the OH groups of the dye. While the assemblies of ZnSe nanoparticles and dye **3** were soluble in ethanol, we assume that the bonding proceeds via the nitrogen hetero atom and/or the free OH groups. This is not observed for dye **4** which supports our suggestion of a preferred interaction between free OH groups of **4** and the QD surface. The introduction of an OH group in 2-position of the quinoline ring leads to a new type of styrylquinolines which seems to be able to form nanoassemblies with ZnSe QDs affecting the chromophoric system. The partially negative charged oxygen atom of **5** is able to interact with the ZnSe surface with less steric hindrance. However, this interaction between the oxygen and nanocrystal surface is only of weak nature compared to that of the stronger basic pyridyl nitrogen with ZnSe resulting in a weaker bathochromic shift of the emission band.



Scheme 4 Different binding behavior of dyes **4** and **5** at the QD surface

4. Conclusions

In summary, we presented a synthesis route for fluorescent silver nanoparticles via zeolite templates consisting of only a few atoms. Beside these, some larger silver particles in the range of 5 to about 15 nm in diameter are present on the surface of the zeolite Y. For this reason, a significant plasmon resonance band is observed at 385 nm in the UV/Vis spectrum of the zeolite/Ag powder. Importantly, the silver particles were prepared without any additional reducing agents in the zeolite Y matrix by using a silver(I) carboxylate. Thereby, the structure of the inorganic matrix serves both as size director and as stabilizer. The obtained powders exhibit a detectable fluorescence even after storage under ambient conditions for several months (see supplement).

The investigation of individual Ag clusters with sizes of about 1 nm *via* wide field microscopy showed a photoblinking in time domains of up to a few seconds, a time scale which is in most cases irrelevant with respect to biological applications [44]. Thus, both the synthetic route and the material itself show great potential for application in many research fields, such as biological imaging, optical sensing, and single-molecule studies. Especially the investigation of Ag nanoparticles with respect to excitation energy transfer is a promising perspective because the silica substrate might be further modified, for example with fluorescent dyes.

With respect to excitation energy transfer in the UV range, we have presented a concept for the functionalisation of ZnSe QD surfaces with fluorescent pyridyl substituted dyes which affects both, the chemical and optical properties and therefore leads to new class of nanoassembled material. Advantageously, this process is readily detectable by means of fluorescence spectroscopy. In this regard, a variety of ZnSe–dye assemblies with high potential for application as LEDs or bioimaging sensors might be available via a very simple preparation route. The creation of white light emitting diodes by surface modification of QDs with fluorescent styrylpyridine dyes is, for example, an interesting field which will be further investigated.

Concluding, we demonstrated that both metal and semiconductor nanoparticles are subject to modifications via the environment which results both in size selection and tuning of optical properties of (self-aggregated) nanoassemblies.

Acknowledgements

We thank Martin Neumann for AFM measurements and Dr. Frank Rauscher, Bayer Technology Services for providing the ZnSe quantum dots. Financial support from the Fonds der Chemischen Industrie and BAYER Technology Services is gratefully acknowledged.

References

1. J. Shi, Y. Zhu, X. Zhang, W. R. G. Baeyens, A.M. Garcia-Compana, Trends Anal. Chem. 23, 351 (2004)
2. P. C. A. Jeronimo, A.N. Araujo, M. Conceicao, B. S. M. Montenegro, Talanta 72, 13 (2007)
3. J. R. Lakowicz, Probe design and chemical sensing in: Topics in Fluorescence Spectroscopy, ed. J. R. Lakowicz, Plenum Press, New York , vol. 4 (1994)
4. L. Prodi, New J. Chem. 29, 20 (2005)
5. L. Shang, S. Dong, Biosen. Bioel. 24, 1569 (2009)
6. S. Bonacchi, D. Genovese, R. Juris, M. Montalti, L. Prodi, E. Rampazzo, N. Zaccheroni, Angew. Chem. 123, 2 (2011)
7. A. Tanimura, A. Nezu, T. Morita, R. J. Turner, Y. Tojyo, J. Biol. Chem. 279, 38095 (2004)
8. Y. Zhou, J. Zhou, Anal. Chem. 76, 5302 (2004)
9. P. Demechenko, Anal. Biochem. 343, 122 (2005)
10. P. J. Alivisatos, Phys. Chem. 100, 13226 (1996)
11. H. Weller, Angew. Chem. 105, 43 (1993)
12. M. Niemeyer, Angew. Chem. Int. Ed. 40, 4128 (2001)
13. B. Dong, L. Cao, G. Su, W. Liu, Chem. Commun., 46, 7331 (2010)
14. W. C. W. Chan and S. Nie, Science, 281, 2016 (1998)
15. A. P. Alivisatos, J. Phys. Chem., 100, 13226 (1996)
16. H. Weller, Angew. Chem., 105, 43, (1993)
17. C. M. Niemeyer, Angew. Chem., Int. Ed., 40, 4128 (2001)
18. A. P. Alivisatos, Nature, 437, 664 (2005)
19. D. E. Gómez, I. Pastoriza-Santos and P. Mulvaney, Small, 1, 238 (2005)
20. M. Y. Han, X. H. Gao, J. Z. Su and S. Nie, Nat. Biotechnol., 19, 631 (2001)
21. A. L. Rogach, D. Nagesha, J. W. Ostrander, M. Giersig and N. A. Kotov, Chem. Mater., 12, 2676 (2000)
22. Y. Chan, J. P. Zimmer, M. Stroh, J. S. Steckel, R. K. Jain and M. G. Bawendi, Adv. Mater., 16, 2092 (2004); N. Insin, J. B. Tracy, H. Lee, J. P. Zimmer, R. M. Westervelt and M. G. Bawendi, ACS Nano, 2, 197 (2008)
23. S. Ravindran, S. Chaudhary, B. Colburn, C. S. Ozkan, Nano Lett., 3, 447 (2003)
24. B. G. Streetman, S. Banerjee, in Solid state electronic Devices, Prentice Hall, New Jersey, 5, 524 (2000)

25. O. Madelung, in Semiconductors-basic data, Springer, Berlin, 2 (1996)

26. S. F. Jahn, A. Jakob, T. Blaudeck, P. Schmidt, H. Lang, R. R. Baumann, Thin Solid Films 518, 3218 (2010)

27. E. I. Zenkevich, T. Blaudeck, A. M. Shulga, F. Cichos, C. von Borczyskowski, J. Lumin., 122, 784 (2007); D. Kowerko, S. Krause, N. Amecke, M. Abdel-Mottaleb, J. Schuster, C. von Borczyskowski, Int. J. Mol. Sci., 10, 5239 (2009); D. Kowerko, J. Schuster, N. Amecke, M. Abdel-Mottaleb, R. Dobrawa, F. Würthner, C. von Borczyskowski, Phys. Chem. Chem. Phys., 12, 4112 (2010)

28. I. R. Díez, H. A. Ras, in Advanced Fluorescence Reporters in Chemistry and Biology II: Moleculear Construction, Polymers and Nanoparticles, Springer Ser. Fluoresc. 9, 307 (2010)

29. Z. Jiang, W. Yuan, H. Pan, Spectrochim. Acta Part A 61, 2488 (2005)

30. H. Xu, K. S. Suslick, Adv. Mater. 22, 1078 (2010)

31. B. Adhikari, A. Banerjee, Chem. Mater. 22, 4364(2010)

32. L. Maretti, P. S. Billone, Y. Liu, J. C. Scaiano, J. Am. Chem. Soc. 131, 13972 (2009)

33. Y. C. Lin, L. H. Lin, Electrochem. Commun. 6, 1163 (2004)

34. M. Steffan, A. Jakob, P. Claus, H. Lang, Catal. Commun. 10, 437 (2009)

35. L. Jiang, W. Wang, D. Wu, J. Zhan, Q. Wang, Z. Wu, R. Jin, Mater. Chem. Phys. 104, 230 (2007)

36. D. Wöhrle, G. Schulz-Ekloff, Adv. Mater. 6, 875 (1994)

37. M. Warnken, K. Lázá, M. Wark, Phys. Chem. Chem. Phys. 3, 1870 (2001)

38. Z. Hens, D. V. Tallapin, H. Weller, D. Vanmaekelbergh, Nano Lett., 81,4245 (2002)

39. J. J. Mock, M. Barbic, D.R. Smith, D. A. Schultz, S. Schultz, J. Chem. Phys. 116, 6755 (2002)

40. S. Lecoultre, A. Rydlo, J. Buttet, C. Félix, S. Gilb, W. Harbich, J. Chem. Phys. 134, 184504 (2011)

41. J. S. Ogden, N. E. Bogdanchikova, J. M. Corker, V. P. Petranovskii, Eur. Phys. J. D 9, 605 (1999)

42. S. A. Mitchell, J. Farell, G. A. Kenny-Wallace, G. A. Ozin, J. Am. Chem. Soc. 102, 7702 (1980)

43. D. Geddes, A. Parfenov, I. Gryczynski, J. R. Lakowicz, J. Phys. Chem. B 107, 9989 (2003)

44. I. Díez, M. Pusa, S. Kulmala, H. Jiang, A. Walther, A. S. Goldmann, A. H. E. Müller, O. Ikkala, R. H. A. Ras, Angew. Chem. Int. Ed. 48, 2122 (2009)

45. C. M. Donega, S. G. Hickey, S. F. Wuister, D. Vanmaekelbergh, A. Meijerink, J. Phys. Chem. B., 107, 489 (2003)

46. U. Banin, Y. W. Cao, C. B. Murray, S. O´Brian, Nature, 423, 968 (2003)

47. E. P. A. M. Bakkers, Z. Hens, A. Zunger, A. Franceschetti, L. P. Kouwenhoven, L. Gurevich, D. Vanmaekelbergh, Nano Lett., 1, 551 (2001)

48. M. Cho, K. Lim, K. Woo, Chem. Commun., 46, 5584 (2010)

49. M.-Q. Zhu, E. Chang, J. Sun, R. A. Drezek, J. Mater. Chem., 17, 800 (2007)

50. A. Sukhanova, J. Devy, L. Venteo, H. Kaplan, M. Artemyev, V. Oleinkov, D. Klimov, M. Pluot, J. H. M. Cohen, I. Nabier, Anal. Biochem., 324, 60 (2004)

51. A. Hagfeldt, M. Graetzel, Acc. Chem. Res., 33, 269 (2000)

52. E. Jang, S. Jun, H. Jang, J. Lim, B. Kim, Y. Kim, Adv. Mater., 22, 3076 (2010)

The study of magnetic properties of Ge nanoparticles

Yung Liou
Institute of Physics, Academia Sinica, Taipei, Taiwan, ROC

*corresponding author, E-mail: yung@phys.sinica.edu.tw

Abstract

Room-temperature ferromagnetism was observed in Ge nanoparticles fabricated by different methods. The magnitudes of the saturation magnetization in these samples were different from the other methods, but the largest saturation magnetizations were always measured in samples with smaller sizes and higher densities of Ge nanoparticles. The saturation magnetization was determined by both the size and inter-particle distance of Ge nanoparticles.

1. Introduction

Nanoparticles due to size effect may exhibit properties different from their bulk counterpart. By reducing the size of a material, degenerate energy bands split into discrete levels at the band edge which make nanoparticles possess different stable structures unlike their bulk materials. The surface effect is also significant in nanoparticles due to their large surface to volume ratio. Dangling bonds or unsaturated spins appeared inside the nanostructure or on the surface of nanoparticles may induce the un-expected magnetism. Ferromagnetism observed in many non-magnetic materials, such metallic (Au and Pd) nanoparticles [1, 2], semiconductor (CdSe and GaN) nanoparticles [3, 4], and carbon nanostructures (nanofoam, graphene etc.) [5, 6], has been related to the structural defects, surface effect, charge transfer or quantum size effect. However, magnetism in most nanoparticles is weak and below room temperature. Semiconductors possessing large room temperature magnetism have long been pursued for their potential applications in spintronics. Room-temperature ferromagnetism in p-type Si single crystal wafers has been observed during ion implantation (50 KeV, Si and Ar) or neutron irradiation [7](Dubroca 2006). Paramagnetic defects were believed to be one of the factors responsible for the observed magnetism. Room-temperature ferromagnetism in Ge nanostructures and nanoparticles were reported recently [8]. The observed magnetism was attributed to the quantum size effect and the magnetic coupling among Ge nanoparticles.

2. Experiments

Ge nanoparticles with various sizes were fabricated by different methods, such as thermal evaporation, inert gas condensation and co-sputtering. Densely packed two-dimensional layer of polystyrene nanospheres with sizes from 20 to 500 nm were used. High purity intrinsic Ge (6N) were used to fabricate nanoparticles with different sizes. A low deposition rate of about 1 Å/min was operated in the thermal evaporation process at base pressures of about $1x10^{-7}$ Torr. Different helium pressures were used in inert gas condensation. The argon gas pressure was kept at $5x10^{-3}$ Torr in co-sputtering. Different analytical tools, such as transmission electron microscopy (TEM), scanning electron microscopy (SEM) and atomic force microscope (AFM) were used to characterize the surface morphology and particle sizes. Vibrating sample magnetometer (VSM) and super conducting quantum interference device (SQUID) were used to measure the magnetization of the nanoparticles at room temperature and low temperatures, respectively.

3. Results and Discussion

The rough surfaces covered with nanospheres provided unconventional templates for the island-like film growth. The size of the islands (nanoparticles) was determined by the curvature of the nanosphere and the thickness of the film. Ge nanoparticles were generated either on tops of or at the concaved spaces among nanospheres. Fig. 1 shows the SEM images of 5 nm thick Ge films on different polystyrene nanospheres. Most evaporated Ge films were covered the tops of nanospheres. Parts of Ge vapor may pass through spaces among large nanospheres and directly deposited on the substrate. Ge films may also accumulate on the concaved spaces among small nanospheres. Continuous films were formed when the film was thick enough to cover both tops and concaved spaces.

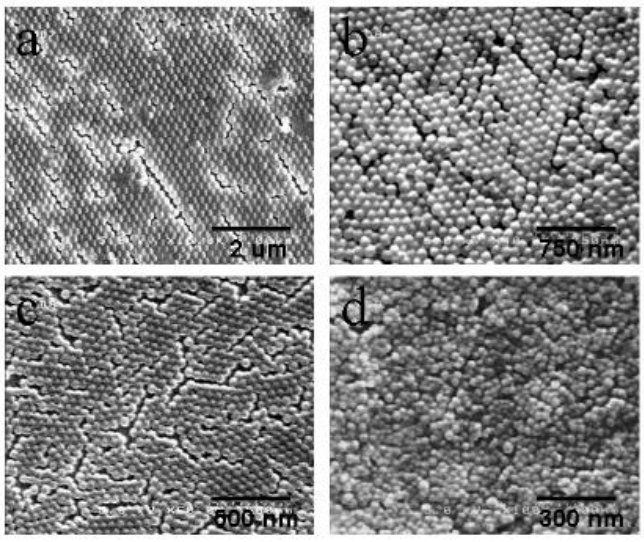


Fig. 1. SEM images of 5 nm Ge films on (a) 200 nm, (b) 100 nm, (c) 50 nm and (d) 30 nm polystyrene nanospheres.

The magnetic properties of the Ge nanosparticles were measured mainly with VSM at room-temperature since the transition temperatures of the Ge nanoparticles were over 300 ^{o}C. SQUID was only used to measure the temperature dependence of the magnetization at low temperatures. The diamagnetic contribution in the magnetic measurements was mainly come from the Si substrates. Si substrates with nanospheres were also diamagnetic.

Ge layers directly deposited on Si substrates without nanospheres were also diamagnetic. The diamagnetic contribution from the Si substrates and the nanospheres has been subtracted away from the magnetization loops for easy comparison. Room temperature magnetization loops plotted versus the external magnetic field for samples with 5 nm thick Ge layers deposited on different polystyrene nanospheres were shown in fig. 2. Hysteresis loops with small remanence and coercivity were clearly seen. In the sample with 5 nm thick Ge layer on the nanospheres with a 20 nm in diameter, the remanent magnetization was only about 50 emu/cm^3 and the coercive field was only about 35 Oe. The paramagnetic behavior may be attributed to the softness and the disorder of the magnetic moments in Ge nanoparticles.

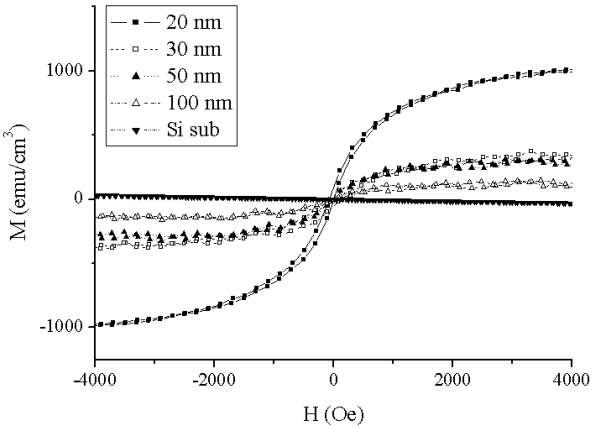


Fig. 2. M-H loops of Ge nanoparticles on different sizes of nanospheres and Si substrate.

A plot of the summary of all samples with saturation magnetizations (room-temperature) versus the thickness of Ge layers deposited on different nanospheres (polystyrene) was shown in fig. 3. It is clearly shown the majority of the Ge layers were non-magnetic. Magnetism was only observed on few samples with thin Ge layers (< 10 nm) on small polystyrene nanospheres (< 100 nm). Thick Ge films always showed the diamagnetic property which may support us to rule out the inclusion of magnetic impurities. It was also noticeable that the decline of the magnetism in Ge nanoparticles with layer thickness less than 5 nm on different polystyrene nanospheres with sizes less than 100 nm.

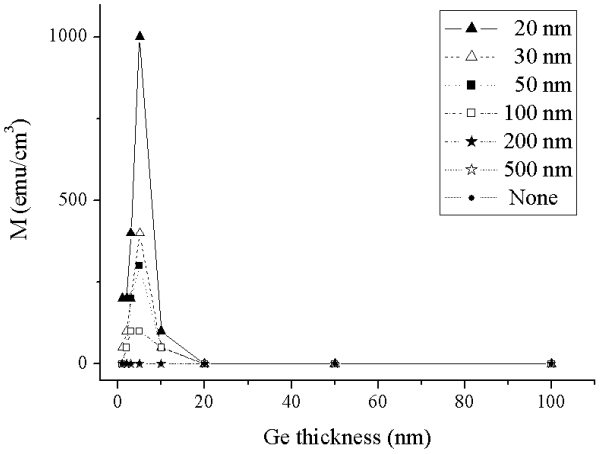


Fig.3. Summary of saturation magnetizations of different thick Ge films on different sizes of nanospheres.

Different Ge nanoparticles have also been collected in inert gas condensation method by adjusting the helium pressures. In Fig. 4, the TEM plane view images show different sizes of Ge particles fabricated at different He pressures. The Ge particles collected at high pressures (1 Torr) and at the center area of the copper plate were agglomerated into large particles with an average size over 20 nm, as shown in Fig. 4(a). Most of Ge particles were amorphous but parts of them were crystalline. Ge particles were uniformly distributed when collected at locations away from the center region. As the helium pressures were decreased from 0.1 to 0.01 Torr, the average sizes of Ge particles were decreased (11.5 nm, 4.5 nm and 1.5 nm), as shown in Fig. 4(b), 4(c) and 4(d), respectively.

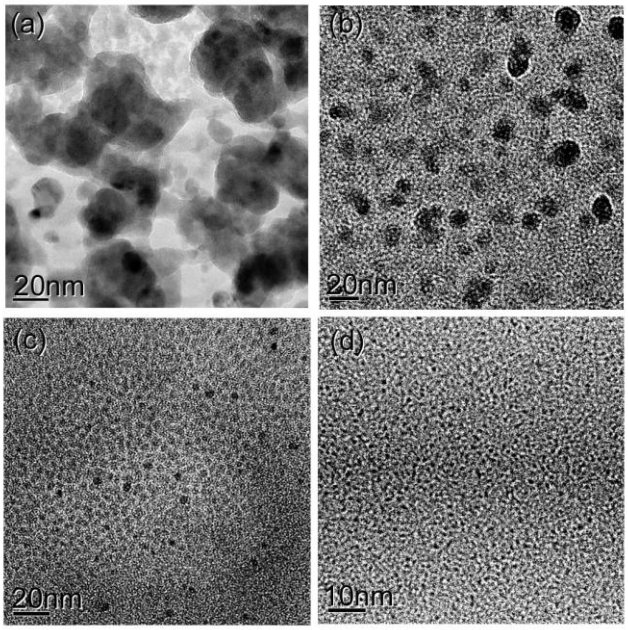


Fig. 4. TEM images of Ge particles collected in He pressure of (a) 1 Torr, (b) 0.1 Torr, (c) 0.05 Torr and (d) 0.01 Torr.

In Fig. 5, different magnetizations were shown in the M-H loops of above four samples (a - d, corresponding to the four samples in Fig.4, from Fig. 4(b) to Fig. 4(d)). The magnetization of these

samples was affected by both the size and the density of Ge nanoparticles.

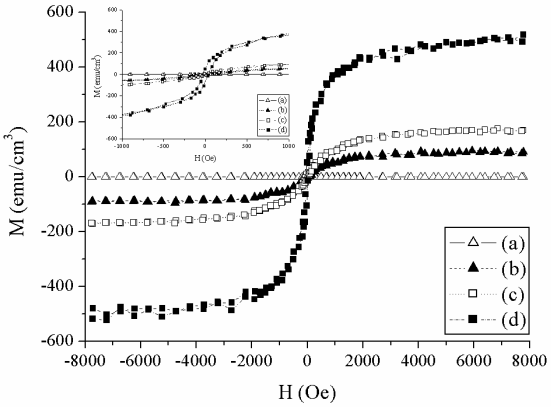


Fig. 5. M-H loops of different magnetizations of Ge particles (inlet is the enlarged loops at small fields).

By co-sputtering, Ge nanoparticles have been mixed into other different matrix materials, such as Al, Cu, Sb, Bi and SiO_2, and the magnetic properties have been investigated. The magnitudes of the saturation magnetization in these samples were much smaller than other methods, but the largest saturation magnetizations were always measured in samples with smaller sizes and higher densities of Ge nanoparticles. The ferromagnetism always disappeared if large Ge particles or Ge continuous films were formed. The detail will be discussed elsewhere. The room-temperature ferromagnetism was attributed to the magnetic coupling among Ge nanoparticles, in which magnetic moments in Ge nanoparticles might arise from the size effect however both the defect and surface effects might also be included.

4. Conclusions

Magnetic properties in Ge nanoparticles fabricated with different methods have been discussed. The magnetic moments in the Ge particles were determined by the size and the nanostructure. The measured room-temperature ferromagnetism was determined by the magnetic coupling among Ge nanoparticles which was affected by the inter-particle distance or the density of the nanoparticles.

Acknowledgements

This work has been done by my graduate students and research assistants in the past several years. Their contributions are acknowledged. The continuous support of the National Science Council of Taiwan, Republic of China is also acknowledged.

References

[1] Y. Yamamoto, T. Miura, M. Suzuki, N. Kawamura, H. Miyagawa,T. Nakamura, K. Kobayashi, T. Teranishi, and H. Hor, Direct observation of ferromagnetic spin polarization in gold nanoparticles, *Phys. Rev. Lett.*, 93, 116801, 2004.

[2] T. Shinohara, T. Sato, and T. Taniyama, Surface ferromagnetism of Pd fine particles, *Phys. Rev. Lett.*, 91, 197201, 2003.

[3] S. Neeleshwar, C. L. Chen, C. B. Tsai, Y. Y. Chen, C. C. Chen, S. G. Shyu, and M. S. Seehra, Size-dependent properties of CdSe quantum dots, *Phys. Rev. B*, 71, 201307 (R), 2005.

[4] A. J. Zaleski, M. Nyk, and W. Strek, Magnetic studies of GaN nanoceramics, *Appl. Phys.Lett.*, 90, 042511, 2007.

[5] D. Arcon, Z. Jaglicic, A. Zorko, A. V. Rode, A. G. Christy, N. R. Madsen, E. G. Gamaly, and B. Luther-Davies, Origin of magnetic moments in carbon nanofoam, *Phys. Rev. B*, 74, 014438, 2006.

[6] O. V. Yazyev, and L. Helm, Defect-induced magnetism in grapheme, *Phys. Rev. B*, 75, 125408, 2007.

[7] T. Dubroca, J. Hack, R. E. Hummel, and A. Angerhofer, Quasiferromagnetism in semiconductors, *Appl. Phys. Lett.*, 88, 182504, 2006.

[8] Y. Liou, and Y. L. Shen, Y. Magnetic properties of germanium quantum dots, *Adv. Mater.*, 20, 779, 2008